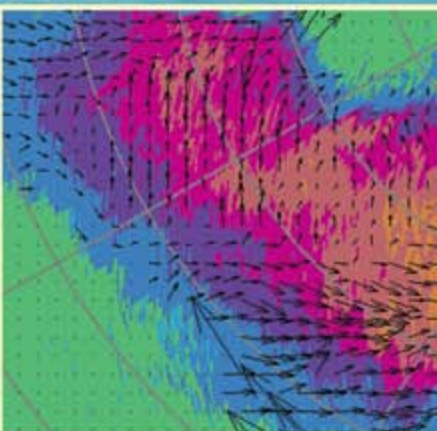
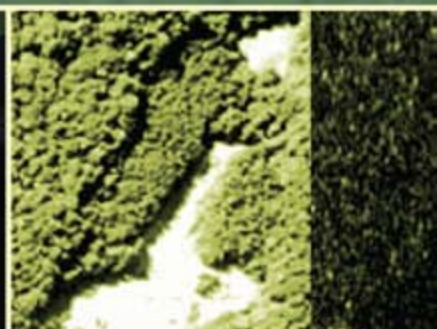


PRINCIPLES OF MODERN RADAR

RADAR APPLICATIONS



William L. Melvin, James A. Scheer (Editors)

Principles of Modern Radar

Principles of Modern Radar

Vol. III: Radar Applications

William L. Melvin

Georgia Institute of Technology

James A. Scheer

Georgia Institute of Technology



Edison, NJ
scitechpub.com



Published by SciTech Publishing, an imprint of the IET.
www.scitechpub.com
www.theiet.org

Copyright © 2014 by SciTech Publishing, Edison, NJ. All rights reserved.

No part of this publication may be reproduced, stored in a retrieval system or transmitted in any form or by any means, electronic, mechanical, photocopying, recording, scanning or otherwise, except as permitted under Sections 107 or 108 of the 1976 United States Copyright Act, without either the prior written permission of the Publisher, or authorization through payment of the appropriate per-copy fee to the Copyright Clearance Center, 222 Rosewood Drive, Danvers, MA 01923, (978) 750-8400, fax (978) 646-8600, or on the web at copyright.com. Requests to the Publisher for permission should be addressed to The Institution of Engineering and Technology, Michael Faraday House, Six Hills Way, Stevenage, Herts, SG1 2AY, United Kingdom.

While the author and publisher believe that the information and guidance given in this work are correct, all parties must rely upon their own skill and judgement when making use of them. Neither the author nor publisher assumes any liability to anyone for any loss or damage caused by any error or omission in the work, whether such an error or omission is the result of negligence or any other cause. Any and all such liability is disclaimed.

Editor: Dudley R. Kay
Cover Design: Brent Beckley

10 9 8 7 6 5 4 3 2 1

ISBN 978-1-89112-154-8 (hardback)
ISBN 978-1-61353-032-0 (PDF)

Typeset in India by MPS Limited
Printed in the USA by Sheridan Ltd
Printed in the UK by CPI Group (UK) Ltd, Croydon

Contents

Preface xi

Reviewer Acknowledgements xv

Editors and Contributors xvii

1 Radar Applications 1

- 1.1 Introduction 1
- 1.2 Historical Perspective 2
- 1.3 Radar Measurements 5
- 1.4 Radar Frequencies 6
- 1.5 Radar Functions 8
- 1.6 U.S. Military Radar Nomenclature 9
- 1.7 Topics in Radar Applications 10
- 1.8 Comments 14
- 1.9 References 15

2 Continuous Wave Radar 17

- 2.1 Introduction 17
- 2.2 Continuous Wave Radar 21
- 2.3 Frequency Modulated CW Radar 26
- 2.4 Other CW Radar Waveform Designs 63
- 2.5 FMCW Radar Applications 67
- 2.6 References 82

3 MMW Radar Characteristics and Applications 87

- 3.1 Introduction 87
- 3.2 The MMW Spectrum 88
- 3.3 Propagation at Higher Frequency 89
- 3.4 Antenna Beamwidth Considerations 93
- 3.5 MMW Performance Limitations 94
- 3.6 Typical Seeker or Smart Munition Configuration 98
- 3.7 MMW Radar Applications 108

- 3.8 MMW Future Trends 112
- 3.9 Further Reading 113
- 3.10 References 114

4 Fire-Control Radar 117

- 4.1 Introduction 117
- 4.2 Airborne Fire-Control Radar 123
- 4.3 Surface-Based Fire-Control Radar 160
- 4.4 Electronic Counter Countermeasures 170
- 4.5 The “AN” Equipment-Designation System 172
- 4.6 References 173
- 4.7 Further Reading 173

5 Airborne Pulse-Doppler Radar 175

- 5.1 Introduction 175
- 5.2 Geometry 177
- 5.3 The Doppler Shift and Motivation for Doppler Processing 181
- 5.4 Range and Doppler Distribution of Clutter 185
- 5.5 Contours of Constant Doppler and Range 196
- 5.6 Example Scenario 199
- 5.7 Pulse-Doppler Conceptual Approach 203
- 5.8 Ambiguities, Folded Clutter, and Blind Zones 216
- 5.9 Overview of PRF Regimes 226
- 5.10 High PRF Mode 228
- 5.11 Medium PRF Mode 235
- 5.12 Low PRF Mode 246
- 5.13 Summary 248
- 5.14 References 249

6 Multifunction Phased Array Radar Systems 251

- 6.1 Introduction 251
- 6.2 Operational Concepts and Military Utilities 254
- 6.3 MPARS Sizing and Performance Evaluation 257
- 6.4 ESA Overview 262
- 6.5 Radar Control and Resource Management 268
- 6.6 MPARS Technologies 276
- 6.7 MPARS Testing and Evaluation 280

- 6.8 Netcentric MPARS Applications 281
- 6.9 References 283
- 6.10 Further Reading 283

7 Ballistic Missile Defense Radar 285

- 7.1 Introduction 285
- 7.2 BMD Radar System Requirements 292
- 7.3 Radar Development for Ballistic Missile Defense 298
- 7.4 BMD Radar Design 307
- 7.5 BMD Radar Performance Estimation 312
- 7.6 References 321
- 7.7 Further Reading 322

8 Ground-Based Early Warning Radar (GBEWR): Technology and Signal Processing Algorithms 323

- 8.1 Introduction 323
- 8.2 Phased Array Antenna 335
- 8.3 Transceiver 342
- 8.4 Waveforms and Signal Processing 348
- 8.5 Tracking 352
- 8.6 Electronic Counter-Countermeasures (ECCM) Capabilities 357
- 8.7 Special Functions 359
- 8.8 Conclusions and Further Reading 376
- 8.9 References 377

9 Surface Moving Target Indication 383

- 9.1 Introduction 383
- 9.2 SMTI Radar Operation 390
- 9.3 Signal Models 393
- 9.4 SMTI Metrics 400
- 9.5 Antenna and Waveform Considerations 405
- 9.6 Clutter-Mitigation Approaches 410
- 9.7 Detection Processing 418
- 9.8 Angle and Doppler Estimation 421
- 9.9 Other Considerations 424
- 9.10 Summary 426
- 9.11 Further Reading 427
- 9.12 References 427

10	Space-Based SAR for Remote Sensing	431
10.1	Introduction	431
10.2	Historical Perspective	438
10.3	Orbits	451
10.4	Design Considerations for the Spaceborne SAR	457
10.5	Special Modes and Capabilities	473
10.6	Design Example: Germany's TerraSAR-X	482
10.7	Summary	493
10.8	References	494
10.9	Further Reading	498

11	Passive Bistatic Radar	499
11.1	Introduction	499
11.2	Bistatic Radar	505
11.3	Passive Bistatic Radar Waveforms	509
11.4	The Signal Environment	519
11.5	Passive Bistatic Radar Techniques	524
11.6	Examples of Systems	527
11.7	Conclusions	536
11.8	References	537
11.9	Further Reading	540

12	Air Traffic Control Radar	543
12.1	Introduction – The Task of Air Traffic Control (ATC)	543
12.2	System Requirements/Mission	552
12.3	Design Issues	558
12.4	The Future of ATC Radar	582
12.5	Summary	585
12.6	Further Reading	585
12.7	Acknowledgments	585
12.8	References	585

13	Weather Radar	591
13.1	Introduction	591
13.2	Typical Weather-Radar Hardware	595
13.3	The Radar-Range Equation for Weather Radar	598
13.4	Doppler Processing	603

- 13.5 Hydrological Measurements 609
- 13.6 Characteristics of Some Meteorological Phenomena 615
- 13.7 Sun Echoes and Roost Rings 623
- 13.8 Advanced Processing and Systems 623
- 13.9 References 632
- 13.10 Further Reading 634

14 Foliage-Penetrating Radar 635

- 14.1 Introduction 635
- 14.2 History of Battlefield Surveillance 637
- 14.3 Foliage-Penetrating SAR Collection Systems 642
- 14.4 FOPEN Clutter Characteristics 645
- 14.5 Image Formation 654
- 14.6 Radio Frequency Interference 665
- 14.7 Target Detection and Characterization 676
- 14.8 Summary 684
- 14.9 References 685
- 14.10 Further Reading 688

15 Ground-Penetrating Radar 691

- 15.1 Overview 691
- 15.2 Pulsed Ground-Penetrating Radar System Design 697
- 15.3 GPR System Implementation and Test Results 731
- 15.4 Conclusions 746
- 15.5 References 746

16 Police Radar 749

- 16.1 Introduction 749
- 16.2 The History of Technologies that Enabled Police Radar 750
- 16.3 Review of Homodyne Radar Principles 751
- 16.4 The First Police Radar 753
- 16.5 The Cosine Error Caused by Improper Operation 754
- 16.6 The Next-Generation S-band Radar 755
- 16.7 The Move to X-band – 10 GHz 758
- 16.8 A Second Method Used to Achieve the Ferro-Magnetic Circulator Function 763
- 16.9 Moving Radar with Improved Detection Range Capability 764

16.10	Moving-Mode Police Radar Operation	766
16.11	Alternative Phase-Locked Loop Signal-Processing Approach	770
16.12	The Move to K-band Frequencies	771
16.13	Police Radar Moves to the Ka-band and Utilizes Digital Signal Processing	772
16.14	Other Police Operating Modes Made Possible by DSP	774
16.15	Summary	777
16.16	References	777
16.17	Further Reading	778
Index		779

Preface

Principles of Modern Radar: Radar Applications is the third of the three-volume series of what was originally designed to be accomplished in one volume. As the final volume of the set, it finishes the original vision of a complete yet bounded reference for radar technology. This volume describes fifteen different system applications or class of applications in more detail than can be found in Volumes I or II.

As different as the applications described, there is a difference in how these topics are treated by the authors. Whereas in Volumes I and II there is strict adherence to chapter format and level of detail, this volume has a wider dynamic range of technical depth. Some system applications lend themselves to a deeper level of technical description than others.

What This Book Addresses

Certainly, there are many applications for which radar technology can be applied. Each chapter in *Principles of Modern Radar: Radar Applications* discusses a particular (selected) application or class of applications for the use of radar as a sensor. Not all applications for radar as a sensor are addressed in this volume, nor could they be. However, a varied selection of applications are included, providing a fairly broad cross section of surface-based and aerospace systems, defense-oriented as well as commercial technologies, and European as well as American systems.

It was difficult to determine which system applications should be selected for this volume. Some areas of technology are so new that intellectual property rights restricted us from developing a complete picture of those applications. In other cases, classification issues were at play. Even considering these issues, there are many other radar applications that might have been covered, and a selection had to be made. We hope you are pleased with our choices.

Why This Book Was Written

The original vision for PoMR was to provide the radar community with a single resource that described the latest radar technology, as driven largely by advancements in digital signal-processing (DSP) capability. Since DSP technology is maturing at such a fast pace, the ability to employ advanced techniques grows with it. The growth of these new techniques influences the development of advanced antenna techniques as well as subsystem radio-frequency and intermediate frequency hardware. The first two volumes in this series describe basic principles, some of which are true for legacy systems and some of which have experienced relatively recent use, as well as specific advanced techniques in the use of this technology. So, the first two volumes provide a complete picture of radar technology from the first principles to the advanced techniques in use today. With the publication of the first two volumes, it was natural to complete the original vision by preparing this volume describing selected modern radar applications.

Who Should Read This Book

Different from Volumes I and II, this volume is not intended as a textbook for the university environment. Rather, it was originally developed to be largely readable by the layperson, who might not necessarily have all the mathematical and scientific background to fully appreciate the material in the first two volumes. That stated, this volume is also intended to fill in some detail, reinforce or expand on fundamental technological issues described in the first two volumes, and round out understanding of system issues, at least for a selection of applications.

How the Chapters Are Structured

The framework for each chapter was written roughly to answer the following questions: What are the system requirements? What are the particular radar issues associated with these requirements? How specifically are these features incorporated in the system?

Examples of specific systems representing the class of applications discussed herein support the answers to these questions. Since different radar technology communities sometimes use different, or unique, symbols and abbreviations, many chapters have a separate table of abbreviations and symbols. It would be more difficult to read if all of the abbreviations and symbols were consolidated at the end of the book. Since this volume is not expected to be used as a university text, no student questions are included.

The History of the PoMR Series

As discussed in the prefaces of Volumes I and II, the PoMR series was originally planned as one volume, entitled *Principles of Modern Radar: Basic Principles, Advanced Techniques, and Radar Applications*. The resulting number of chapters and sheer amount of the material suggested two volumes: the *Basic Principles* volume and the *Advanced Techniques and Radar Applications* volume. True to form, as Volume II emerged, it was separated into two volumes, resulting in the current set of three volumes.

Volume I was written to provide a modern look at the fundamental technology and design issues related to radar technology in general. It provides an in-depth look at the modern signal-processing techniques available today, many that were not supported by the computing resources (signal- and data-processing technology) available even ten years ago. Volume II was prepared to demonstrate specific signal-processing techniques that are not required in every system in development but are relatively new to the field of radar. The current volume, *Radar Applications*, cites specific examples of the use of basic principles and advanced techniques.

It is interesting to note that many of the signal-processing techniques in use today were first discussed in the early (World War II era) series prepared at the MIT Radiation Laboratory.¹ The techniques were known, but available signal-processing technology

¹This refers to a twenty-one-book series of topics related to radar technology titled *MIT Radiation Laboratory Series*, McGraw Hill Book Company, New York, NY, 1948.

did not support implementation until modern digital signal-processing equipment became available.

Acknowledgements

As editors for this volume, we are very grateful to the publisher, Dudley Kay, for his enduring support and encouragement. Special thanks also go to Brent Beckley for all of his efforts on the sales and marketing front. We are also grateful to Dudley and Brent for gathering and managing the unusually numerous volunteer reviewers whose participation as a “community effort” over the course of the three-volume series has been remarkable and inspiring.

Most important, though, we remain thankful to our families for their patience, love, and support as we prepared materials, revised, reviewed, coordinated, and repeated. This book, like the others, represents time away from the ones we love. We thank them for their understanding, kindness, and support.

To Our Readers

We hope the reader will enjoy this book! Radar is and will continue to be an immensely exciting and diverse field of engineering.

Please report errors and refinements. We know from the publication of the first two volumes that even the most diligently reviewed and edited book is bound to contain errors in the first printing. It can be frustrating to see such errors persist, even in many subsequent printings. We continue to appreciate SciTech Publishing’s commitment to correct errors and enhance the book with each printing. So, it remains a “community effort” to catch and correct errors and improve the book. You may send your suspected errors and suggestions to:

pomr3@scitechpub.com

This email will reach us and SciTech concurrently so we can confer and confirm the modifications gathered for scheduled reprints. You are always welcome to contact us individually as well.

Bill Melvin
Atlanta, GA

Jim Scheer
New Bern, NC

Reviewer Acknowledgements

SciTech Publishing – IET gratefully acknowledges the manuscript reviewing efforts from the following members of the international radar and electronic warfare community. Refinements to the book’s content and expression for the benefit of all readers represent the blessing of ‘a community effort’.

Ron Aloysius, Northrop Grumman Corporation, USA
Edward R. Beadle, Harris Corporation, USA
Lee Blanton, General Atomics Corporation, USA
Neal Brune, Esterline Defense Technologies, USA
Kernan Chaisson, Captain, USAF (retired)
I-Ting Chiang, Qualcomm, USA
Jean Yves Chouinard, Universite Laval, Canada
Patrick Dever, Northrop Grumman Corporation, USA
John Erickson, Wright-Patterson Air Force Base, USA
Phillip Fitch, University of South Australia, Australia
Riccardo Fulcoli, Selex ES, Italy
Gaspere Galati, Università di Roma Tor Vergata, Italy
Frank Gekat, Selex Systems Integration, Germany
Martie Goulding, MDA Corporation, Canada
Hugh Griffiths, University College London, UK
Stephen Harman, QinetiQ, UK
Stephen Hogue, Harris GCSD, USA
Michael Inggs, University of Cape Town, South Africa
Stephane Kemkemian, Thales Airborne Systems, France
Peter Knott, Fraunhofer Institute for High Frequency Physics and Radar Techniques, Germany
Thodoris G. “Ted” Kostis, University of the Aegean, Greece
Anthony Leotta, ADL Associates, USA
David Long, Brigham Young University, USA
John Milan, Consultant, USA
Lee Moyer, Technology Service Corporation, USA
Karl-Erik Olsen, Norwegian Defence Research Establishment, Norway
A. M. (Tony) Ponsford, Raytheon Canada Ltd., Canada
Pinaki S. Ray, University of Adelaide, Australia
Earl Sager, Consultant, USA
John SantaPietro, The MITRE Corporation, USA
Margaret M. “Peggy” Swassing, 412th Test Engineering Group (Edwards AFB), USA
Firooz Sadjadi, Lockheed Martin Corporation, USA
John Sahr, University of Washington, USA
Alexander Singer, Thales Group, Canada
Koen van Caekenberghe, HiSilicon, Belgium

Editors and Contributors

Volume Editors



Dr. William Melvin

Volume Editor-in-Chief and Multiple Chapter Author

William Melvin is Director of the Sensors and Electromagnetic Applications Laboratory at the Georgia Tech Research Institute and an Adjunct Professor in Georgia Tech's Electrical and Computer Engineering Department. His research interests include systems engineering, advanced signal processing and exploitation, and high-fidelity modeling and simulation. He has authored more than 180 publications in his areas of expertise and holds three patents on adaptive radar technology. Among his distinctions, Dr. Melvin is a Fellow of the IEEE, with the follow citation: "For contributions to adaptive signal processing methods in radar systems." He received the PhD, MS, and BS (with High Honors) degrees in Electrical Engineering from Lehigh University.



Mr. James A. Scheer

Associate Volume Editor and Chapter 1 Author

Jim Scheer has forty years of hands-on experience in the design, development, testing, evaluation, and analysis of radar systems. He currently consults and works part-time for GTRI and teaches radar-related short courses. He began his career with the General Electric Company (now Lockheed Martin Corporation), working on the F-111 attack radar system. In 1975, he moved to GTRI, where he worked on radar system applied research until his retirement in 2004. Mr. Scheer is an IEEE Life Fellow and holds a BSEE degree from Clarkson University and the MSEE degree from Syracuse University. His primary interests are in the area of coherent radar performance prediction and evaluation.

Chapter Contributors



Mr. Chris Baker

Chris Baker is the Ohio State Research Scholar in Integrated Sensor Systems at The Ohio State University. Until June 2011, he was the Dean and Director of the College of Engineering and Computer Science at the Australian National University (ANU). Prior to this, he held the Thales-Royal Academy of Engineering Chair of intelligent radar systems based at University College London. He has been actively engaged in radar

systems research since 1984 and is the author of more than 200 publications. His research interests include coherent radar techniques, radar signal processing, radar signal interpretation, electronically scanned radar systems, radar imaging, and natural and cognitive echo-locating systems. He is the recipient of the IEE Mountbatten premium (twice) and the IEE Institute premium, and he is a Fellow of the IET. He is a Visiting Professor at the University of Cape Town, Cranfield University, University College London, Adelaide University, Wright State University, and Nanyang Technical University.



Mr. Bill Ballard

William Ballard is a Senior Research Associate at the Georgia Tech Research Institute Sensors and Electromagnetic Applications Laboratory. He is also the course director of the popular Georgia Tech Professional Education Airborne Fire Control Systems short course. He is a retired U.S. Navy Commander with more than 3,500 hours and 912 traps in the A-6 Intruder. He has served on the faculty at the NATO School (SHAPE) in Oberammergau, Germany where he taught NATO Maritime Operations, Conventional Weapons Employment, and Naval NBC Defense. Both his bachelor's and master's degrees in Mechanical Engineering and Management Science are from Georgia Tech.



Mr. Melvin L. Belcher

Mel Belcher is a Principal Research Engineer at Georgia Tech Research Institute (GTRI). He has worked in the development and analysis of phased array radars systems for more than three decades. He has focused on air- and missile-defense applications and has also contributed to airborne radar and space surveillance radar efforts. His professional interests include systems engineering, active electronically scanned arrays, and signal and data processing. He currently serves as the Technical Director of the Sensors Knowledge Center within the Missile Defense Agency. He founded and led the Air and Missile Defense Division at GTRI. He served as Chief Engineer for Radar Futures at Northrop Grumman Mission Systems from 2005 through 2010. He received the MSEE from Georgia Institute of Technology and the BEE from Auburn University.



Mr. Lee Blanton

Lee Blanton is a radar engineer with General Atomics Aeronautical Systems, Inc., where he supports development of radars for unmanned aerial vehicles (UAVs). His thirty-five-year career in industry has focused primarily on radars for airborne, missile-borne, and spaceborne applications with additional work in the areas of satellite communication and electronic warfare systems. His spaceborne radar experience includes design studies for the proposed Venus Orbiting Imaging Radar and its successor, the Magellan Venus Radar Mapper, as well as concept studies for spaceborne radars for the Air Defense Initiative (ADI), the Strategic Defense Initiative (SDI), and imaging radar applications.



Dr. Mark E Davis

Mark Davis has forty-five years of experience in government and industry in developing technology and systems for radar and electronic systems. After retirement in 2008, he established *MEDavis Consulting* as a sole proprietorship to serve the radar science and technology community. He served at DARPA as Deputy Director Information Exploitation Office from 2006 to 2008. Prior to this assignment, he was the Technical Director for Air Force Research Laboratory Space Based Radar Technology (1998–2006) and Program Manager in DARPA Information Systems Office for Counter CC&D technologies (1995–1998). His interests are in radar and microwave system design, phased array antennas, and adaptive signal processing.

Dr. Davis is a Life Fellow of the IEEE and Military Sensing Symposia and is Chair of the IEEE Radar Systems Panel. He has a PhD in Physics from The Ohio State University and bachelor's and master's degrees in Electrical Engineering from Syracuse University.



Dr. Antonio De Maio

Dr. Antonio De Maio was born in Sorrento, Italy, on June 20, 1974. He received the DrEng degree (with honors) and the PhD degree in information engineering, both from the University of Naples Federico II, Naples, Italy, in 1998 and 2002, respectively. From October to December 2004, he was a Visiting Researcher with the U.S. Air Force Research Laboratory, Rome, New York. From November to December 2007, he was a Visiting Researcher with the Chinese University of Hong Kong. Currently, he is an Associate Professor with the University of Naples Federico II. His research interest lies in the field of statistical signal processing, with emphasis on radar detection, optimization theory applied to radar signal processing, and multiple-access communications.

Dr. De Maio is an IEEE Fellow and the recipient of the 2010 IEEE Fred Nathanson Memorial Award as the young (less than forty years of age) AESS Radar Engineer 2010 whose performance is particularly noteworthy as evidenced by contributions to the radar art over a period of several years, with the following citation for “robust CFAR detection, knowledge-based radar signal processing, and waveform design and diversity.”



Dr. Alfonso Farina

Alfonso Farina received the doctorate degree in electronic engineering from the University of Rome (I), Italy, in 1973. In 1974, he joined Selenia, now SELEX Electronic Systems, where he has been a Manager since May 1988. He was Scientific Director in the Chief Technical Office. He was the Director of the Analysis of Integrated Systems Unit, Director of Engineering in the Large Business Systems Division, and Chief Technology Officer of the Company (SELEX Sistemi Integrati). Today he is Senior Advisor to CTO of SELEX ES. From 1979 to 1985, he has also been a Professor of radar techniques with the University of Naples. He is the author of more than 500 peer-reviewed technical publications as well

as the author of books and monographs. He has been nominated Fellow of IEEE, international fellow of the Royal Academy of Engineering, United Kingdom, and Fellow of EURASIP. He has been appointed member in the Editorial Boards of *IET Radar, Sonar and Navigation (RSN)* and of *Signal, Image, and Video Processing Journal (SIVP)*. He has been the General Chairman of the IEEE Radar Conference, 2008. He is a Fellow of the Institution of Engineering and Technology (IET), United Kingdom. He is also the recipient of the 2010 IEEE Dennis J. Picard Gold Medal for Radar Technologies and Applications with the following citation: “For continuous, innovative, theoretical and practical contributions to radar systems and adaptive signal processing techniques.”



Mr. E. F. Greneker

Mr. E. F. Greneker was employed by Georgia Tech Research Institute (GTRI) for thirty-three years before his retirement as a Principal Research Scientist. He was responsible for the establishment of the GTRI Severe Storms Research Center (SSRC) and served as the founding Director of the SSRC. During his career with GTRI he directed more than sixty major sponsored research projects for many U.S. government agencies and the military services. Many of these sponsored projects related to the use of radar for national security purposes. Other projects included using radar to track insects, and police radar. He has authored more than 85 papers, journal articles, and the chapter on police radar in this book. He is a Senior member of the IEEE. He holds five U.S. patents, with others and two as sole inventor. While employed by GTRI, he consulted to government agencies through his consulting firm, Greneker and Associates, Inc.

After retiring from GTRI, he started his own business, RADAR Flashlight, LLC (RFLLC). RFLLC performed research for the Defense Advanced Research Projects Agency and the U.S. Army on topics relating to detecting humans through a wall using radar. RFLLC also performed research for the U.S. Air Force on radar detection of moving targets from an unmanned aerial vehicle. Mr. Greneker's current interests include remote sensing, both optical and radar, passive radar, radar applications for highway safety, and radar used for security purposes.



Mr. Hugh Griffiths

Hugh Griffiths was educated at Hardye's School, Dorchester, and Keble College, Oxford University, where he received the MA degree in Physics in 1978. He also received the PhD (1986) and DSc (Eng) (2000) degrees from the University of London. He holds the THALES/Royal Academy of Engineering Chair of RF Sensors at University College London. From 2006 to 2008, he served as Principal of the Defence College of Management and Technology, at the Defence Academy, Shrivenham. From 1982 to 2006, he was with University College London as Head of the Department of Electronic and Electrical Engineering from 2001 to 2006. His research interests include radar sensor systems and signal processing (particularly synthetic aperture radar and bistatic

and multistatic radar and sonar) as well as antennas and antenna measurement techniques. He has published more than 400 papers and technical articles on these subjects.

Professor Griffiths was awarded the IET A F Harvey Prize in 2012 for his work on bistatic radar. He has also received the IERE Lord Brabazon Premium Award in 1984, the IEE Mountbatten and Maxwell Premium Awards in 1996, and the IEEE Nathanson Award in 1996. He served as President of the IEEE AES Society for 2012–13. He has been a member of the IEEE AESS Radar Systems Panel, which he chaired from 2006 to 2009, and is Editor-in-Chief of the journal *IET Radar, Sonar, and Navigation*. He was Chairman of the IEE International Radar Conference RADAR 2002 in Edinburgh, United Kingdom. He also serves on the Defence Scientific Advisory Council for the U.K. Ministry of Defence. He is a Fellow of the IET, Fellow of the IEEE, and in 1997 was elected to Fellowship of the Royal Academy of Engineering.



Mr. Stephane Kemkemian

Stephane Kemkemian graduated in Aerospace Engineering from ISAE, Toulouse, France. He began his career at Thales working on RDY and RBE2 radar prototypes (radars for the Mirage-2000 and Rafale fighters, respectively). He is now senior expert with the Technical Directorate of Thales Airborne Systems. He holds around thirty patents and is the author of about twenty papers. He is senior member of the French SEE and founding member of the IEEE AESS French chapter.



Dr. Richard C. Liu

Richard C. Liu received his BS, MS, and PhD degrees in radio engineering from Xi'an Jiaotong University, Xi'an, China, in 1982, 1984, and 1988, respectively. Since 1988, he has been with the Department of Electrical and Computer Engineering, University of Houston, Houston, TX, where he is currently a Professor and the Director of the Well Logging Laboratory and the Subsurface Sensing Laboratory. His research areas include resistivity well logging, tool simulation, tool hardware design, electromagnetic telemetry systems, ground-penetrating radar, sensor technology, wireless telecommunication systems, short-range radio, and RF and microwave circuit design. Dr. Liu has published more than 160 technical papers in these areas.

Dr. Liu is a senior member of IEEE, member of the Society of Professional Well Logging Analysts, the Environmental and Engineering Geophysics Society, and the Society of Core Analysts.



Mr. Aram Partizian

Aram Partizian is a Senior Research Scientist at GTRI, where he contributes to the design, development, and field-testing of advanced radar electronic warfare technologies. He has more than thirty years of experience in radar and the electronic warfare field, including software and system engineering roles at Raytheon Company prior to joining Georgia Tech. He earned a BA in Physics from Oberlin College in 1977.



Mr. Samuel Piper

Samuel O. Piper is a GTRI Fellow and Principal Research Engineer, and since 2002 has served as Chief of the Radar Systems Division in the Sensors and Electromagnetic Applications Laboratory in GTRI. He has more than forty years of experience in radar systems engineering and analysis. He serves as coordinator for the Georgia Tech Principles of Continuous Wave (CW) Radar short course. He earned a master's degree in EE from Georgia Tech.



Mr. John Porcello

John Porcello is a Senior Research Engineer for the Georgia Tech Research Institute (GTRI). John designs, develops, and implements digital signal processing (DSP) algorithms in FPGAs for a wide range of applications, including radar and communications. John has more than twenty years of experience as an engineer and is a Senior Member of the IEEE and a private pilot.



Mr. Jay Saffold

Jay Saffold is the Chief Scientist for RNI and has more than twenty years of engineering experience in both military and industry research in RF tags, virtual reality, digital databases, soldier-tracking systems, millimeter wavelength (MMW) radar, multimode (MMW and optical) sensor fusion, fire-control radar, electronic warfare, survivability, signal processing, and strategic defense architecture. He lectures annually for GTRI on remote sensing and signal processing. He has authored or coauthored more than 104 technical papers and reports. He holds a BSEE degree from Auburn University.



Dr. Luca Timmoneri

Luca Timmoneri is a Vice President of SELEX ES, where he is currently Chief Technical Officer of the Land and Naval Division. His working interests span from the area of synthetic aperture radar, to radar STAP, to detection and estimation with application to tridimensional phased array radar, to parallel-processing architectures.

Dr. Timmoneri is the author of several peer-reviewed papers (also invited). He is the coauthor of three tutorials presented at International IEEE radar conferences. He received the 2002, 2004, and 2006 AMS (now SELEX ES) CEO Award for Innovation Technology; the 2003 AMS (now SELEX Sistemi Integrati) MD Award for Innovation Technology; the 2004 Finmeccanica Innovation Award; and the 2013 Oscar Masi Award for industrial innovation of the Italian Association for Industrial Research.



Mr. John Trostel

John Trostel is a senior research scientist and Director of the Severe Storms Research Center at the Georgia Tech Research Institute (GTRI). His fields of specialization include the meteorology of severe storms, development of data-acquisition and analysis systems, effects of meteorological phenomena on MMW propagation and backscatter, and

general physics and meteorological expertise. He was part of a GTRI team tasked to support the FAA in the development of a Multifunction Phased Array Radar (MPAR) system and was involved in investigations of MMW backscatter characteristics of snow-covered ground, atmospheric acoustics, and underwater sonar development. He is an active member of the American Meteorological Society, National Weather Association, American Geophysical Union, and American Physical Society.

Radar Applications

*William L. Melvin, Ph.D., and James A. Scheer,
Georgia Institute of Technology, Atlanta, GA*

Chapter Outline

1.1	Introduction	1
1.2	Historical Perspective	2
1.3	Radar Measurements	5
1.4	Radar Frequencies	6
1.5	Radar Functions	8
1.6	U.S. Military Radar Nomenclature	9
1.7	Topics in Radar Applications	10
1.8	Comments	14
1.9	References	15

1.1 | INTRODUCTION

Radio detection and ranging (radar) involves the transmission of an electromagnetic wave to a potential object of interest, scattering of the wave by the object, receipt of the scattered energy at the receive site, and signal processing applied to the received signal to generate the desired information product. Originally developed to detect enemy aircraft during World War II, radar has through the years shown diverse application, not just for military consumers, but also for commercial customers. Radar systems are still used to detect enemy aircraft, but they also keep commercial air routes safe, detect speeding vehicles on highways, image polar ice caps, assess deforestation in rain forests from satellite platforms, and image objects under foliage or behind walls. A number of other radar applications abound.

This book is the third in a series. *Principles of Modern Radar: Basic Principles*, appearing in 2010, discusses the fundamentals of radar operation, key radar subsystems, and basic radar signal processing [1]. *Principles of Modern Radar: Advanced Techniques*, released in 2012, primarily focuses on advanced signal processing, waveform design and analysis, and antenna techniques driving tremendous performance gains in radar system capability [2]. This third text, *Principles of Modern Radar: Radar Applications*, combines the developments of *Basic Principles* and *Advanced Techniques* to illustrate a myriad of radar applications.

Principles of Modern Radar: Radar Applications is comprised of three sections:

- *Tactical Radar*, covering continuous wave radar, with application to missile seekers and other low-cost radar needs; millimeter wave radar, used in areas such as battle-field fire-control systems and automotive radar; fire-control radar principles; airborne pulse Doppler radar, the heart of airborne interceptor radar; multifunction radar used to search, track, and engage airborne targets and employing sophisticated and costly phased array antennas, processing software, and resource management; and ballistic missile defense radar.
- *Intelligence, Surveillance, and Reconnaissance*, including early warning detection of aircraft and missiles preceding handoff to a tracking radar; surface moving target indication, used to detect and monitor targets on Earth's surface; and spaceborne surveillance used to remotely monitor Earth resources, cultural sites, and military facilities.
- *Specialized Applications*, including passive radar, which uses noncooperative sources of illumination and receivers displaced a considerable distance from the various transmit sites; air traffic control radar; weather radar; foliage-penetrating radar; ground- and materials-penetrating radar; and police radar.

Individual chapters discuss the aforementioned topics within these three sections in further detail, identifying key considerations and the practical application of radar technology, principles, and techniques to accomplish the specific radar objective: detecting, locating, and tracking targets moving on Earth's surface; imaging a stationary target under foliage; detecting approaching or receding targets from an airborne pulse Doppler radar; detecting and tracking ballistic missiles from large, ground-based phased array radar; protecting ground troops from mortar attack using mobile, counterbattery surface radar; and so on.

1.2 | HISTORICAL PERSPECTIVE

The earliest radar developments appear to have taken place independently in a number of countries. World War II accelerated the development of radar to address the direst of situations. That military application has served as a primary motivation for radar technology development complicates an exposition on its history due to sundry requirements for secrecy. Consequently, spirited debate amongst radar developers over who deserves acclaim for certain innovations is not uncommon.

Reference [3] provides a remarkable overview of the earliest beginnings of radar. The possibility of a system to detect objects based on reflected electromagnetic waves dates to the 19th century and the work of Heinrich Hertz, with James Clerk Maxwell's work on electromagnetism suggesting this possibility. Other great minds invariably associated with the earliest beginnings of radar include Christian Hulsmeyer, Nikola Tesla, Guglielmo Marconi, Sir Robert Wattson-Watt, and Hoyt Taylor. As [3] discusses, highly protected programs to develop radar took place leading up to and during World War II in a number of countries, including England, France, Germany, Japan, Canada, and the United States. Robust radar programs were further known to exist in the Soviet Union, Italy, and the Netherlands.

The detection of air raids was of paramount importance during World War II. Generally, surface-based radars, such as the British Chain Home radar system [4], were developed for this purpose. These original surveillance radars provided an early warning function so citizens could take shelter and service personnel could launch interceptor aircraft. The interceptors similarly required radar to acquire and engage enemy bombers and provide self-protection from enemy escort aircraft. Early warning and fire-control radar were also necessary for naval shipboard protection. World War II applications solidified the need for microwave transmitters and receivers and pulsed waveforms. As pointed out in [4], this period of extensive innovation involved the efforts of multiple researchers and engineers, resulting in radar having no single lineage, but a collection of forefathers.

The earliest radar experiments involved continuous waveforms and bistatic configurations to achieve sufficient isolation between transmitter and receiver [4, 5]. The technology available at the time could only support detection; range information was not available to the operator. Moreover, many of these initial investigations involved longer wavelengths – in the vicinity of 60 cm or greater. A requirement for range information and improved spatial accuracy led to microwave developments and pulsed radar modes. For years beyond World War II, noncoherent pulsed radar systems were used for a number of important applications.

A coherent radar employs a stable, coherent oscillator to transmit and receive signals. In this manner, the radar keeps track of the phase of the receive signal over time. A time-varying phase leads to a frequency shift in the receive signal. If the range between the radar and the object of interest is changing, the time it takes the signal to propagate to the object and return to the radar is $\tau(t) = 2r(t)/c$, where $r(t)$ is the time-varying range and c is the velocity of propagation (nominally, the speed of light). The corresponding phase is $\phi(t) = \omega\tau(t)$, where ω is frequency in radians. Frequency is the time-derivative of phase, $\dot{\phi}(t) = \omega\partial\tau(t)/\partial t$. Suppose $r(t|t = nT) = r_0 + n\Delta r$, with T the sample time, n the sample index, r_0 the initial range, and Δr the constant change in range between sample times resulting from a constant velocity target. The corresponding derivative of the phase function is $\dot{\phi}(t|t = nT) = (4\pi/\lambda)(\Delta r/\Delta t)$, with Δt the change in time; we recognize $\Delta r/\Delta t$ as the radial velocity (or range-rate), v_r , and $\dot{\phi}(t|t = nT) = \omega_d = (4 * \pi/\lambda) * v_r$ (or, $f_d = 2v_r/\lambda$ in Hz) as the well-known Doppler shift [4, 6].

The ability to take advantage of the target Doppler shift was revolutionary, providing the radar with additional information on target motion and enabling a mechanism to better separate target returns from those of background clutter due to reflections from Earth's surface or even from weather phenomenon. Thus, the extensive development of coherent radar systems followed the major accomplishments of the World War II era and occupied the minds of radiofrequency scientists and engineers for subsequent decades. The pulsed Doppler mode is the cornerstone of modern radar technology, integral to surface and aerospace military radar systems. Pulsed Doppler radar has important civilian and commercial applications, permeating everyday life in the form of television weather newscasts with detailed radar weather maps and air traffic control radar making the skies safe for travelers of all types. Coherent continuous wave radars are also important, providing target Doppler information for applications ranging from missile engagement to police traffic surveillance.

Coherency also makes all-weather terrain and stationary target mapping possible via a technology known as *synthetic aperture radar* (SAR) [2, 6–8]. SAR was invented

in the 1950s, with Carl Wiley of Goodyear Aircraft Company viewed as its originator, and multiple parties greatly contributing to its development. The primary objective of SAR is to create a high-resolution map of the scene reflectivity; the resulting product has image-like quality and is generally interpreted by a trained analyst. In its most basic form, SAR uses knowledge of the collection geometry, generating a matched filter tailored to the phase history of a particular, resolvable, stationary scatterer of interest. As previously discussed, the phase history is $\phi(t) = \omega\tau(t)$, where in this case the change in range over time typically leads to a nonlinear characteristic for $\tau(t)$, and consequently a response comprised of time-varying frequency. The SAR is built and deployed in such a way that ideally the various scatterers possess unique phase histories, though practically there are basic limitations affecting the quality of the reflectivity estimate. Image-formation processing is the series of steps applied to the phase history data to generate the SAR map.

SAR has played important military roles in areas such as nuclear arms treaty monitoring and battlefield surveillance, preparation, and damage assessment. Meeting these stringent and critical applications required extraordinary effort to achieve pristine coherency over relatively long periods of time – data are collected over periods of hundreds of milliseconds to tens of minutes or more, a duration required to traverse sufficient viewing angle to achieve a desired cross-range resolution – and conceive computationally feasible approaches to approximate the matched filter condition. Indeed, system coherency and signal-processing algorithm development have served as hallmarks of SAR technology development. Early SAR image formation used optical signal-processing methods, with digital signal-processing techniques replacing the former after a relatively extended period of time needed for available technology to sufficiently advance. With some delay, civil applications of SAR emerged, including Earth resources monitoring, polar ice cap monitoring, and extraterrestrial planetary exploration.

Over the past twenty years or so, the radar community has significantly focused on radar subsystem hardware improvement, signal-processing algorithm development and implementation, and diverse applications. The development of phased array radar has been a major undertaking and a critical step in radar deployment for air and missile defense and multimode airborne radar systems [9]. Advances in computing technology have made digital beamforming (DBF) and space-time adaptive processing (STAP) possible [2, 9–11]. DBF and STAP are key elements in radar electronic protection, superior clutter mitigation techniques, and advanced concepts such as passive radar where DBF makes “pulse chasing” feasible [5]. Radar’s diverse applications made possible through technology maturation include through-the-wall radar for law enforcement support; the detection, location, and characterization of dismount targets (persons of interest traversing Earth’s surface) from airborne radar [12]; remote sensing of ocean currents; border surveillance; gait analysis for threat monitoring (e.g., detection of a perimeter breach by unauthorized personnel) and medical diagnosis (e.g., assessment of indicators of traumatic brain injury); automotive radar for intelligent highways; and the development of low-cost passive surveillance radar hosting off of commercial communications broadcasts [13].

Radar has proven its importance to society. As such, radar development and implementation has generally received favorable treatment under situations of competing interest. An emerging conflict over spectrum allocation among users of the electromagnetic spectrum will intensify, leading radar developers to innovate and conceive new technology and capabilities [14]. In addition to spectrum, energy is

placing pressure on radar: The proliferation of wind farms as an alternative energy source creates a whole new class of interference requiring mitigation to ensure effective radar performance. Radar will also be asked to solve new and challenging problems, such as identification of humans in emergency management situations resulting from such natural phenomena as earthquakes; the detection of small vessels traversing the littoral zone expanse; and the beneficial exploitation of multipath in urban settings to enable non-line-of-sight radar detection and tracking of objects [15].

This book summarizes and puts into perspective a select number of important and modern radar applications, as well as the requisite constituent technology. As such, it builds on the exposition set forth in the first two volumes of the *Principles of Modern Radar* series [1, 2].

1.3 | RADAR MEASUREMENTS

Radar operation requires an active source of illumination. Monostatic and cooperative bistatic radar use a coordinated transmitter. Noncooperative bistatic radar exploits the transmissions from other electronic systems, including radio towers, communication transmit antennas, and other radars. Cooperative systems attempt to tailor the transmit waveform to the extent possible to maximize important radar quality measures, such as signal-to-noise ratio (SNR), signal-to-interference-plus-noise ratio (SINR), range resolution, target class separation, and resilience to radiofrequency interference (RFI).

The radar generates its product based on target-induced modulation of the reflected waveform. Radar design allows access to the following primary measurements:

- Fast-time – collected at the analog-to-digital converter rate, these voltages correspond to sampling in the range dimension.
- Slow-time – collected at the pulse repetition interval (PRI), the corresponding voltages are the pulse-to-pulse measurements for a given range cell. The Fourier transform of slow-time is Doppler.
- Spatial – samples generated at the output of a multichannel or multibeam receive antenna, where each channel or beam has its own receive chain. Angle information follows from the Fourier transform of the spatial channel measurements; the inverse transform of the multibeam output restores spatial sample information. The measured angle corresponds with azimuth, elevation, or cone, where cone is an ambiguous measurement related to a specific direction cosine in the antenna coordinate system.
- Polarimetric – consists of two basic forms, dual-polarization and quad-polarization. In dual-polarization, the transmit polarization is fixed and the receive antenna collects orthogonal polarizations (e.g., the transmitter sends out a vertically polarized wave, and the receiver collects both vertical and horizontal polarizations). Quad-polarized operation requires the transmitter to interleave transmissions of orthogonal polarizations, and the receiver simultaneously collects two orthogonal polarizations as in the dual-polarized case.
- Multipass – the radar can collect data at a common operating frequency, polarization, and bandwidth over distinct orbits and then process the data to look for scene changes. When the processing is coherent from pass to pass, the mode is called

coherent change detection (CCD); naturally, noncoherent change detection operates on magnitude-only data from pass to pass. Change detection makes it possible to detect subtle changes in the scene, such as the presence of tire tracks on a dirt road or areas of trampled grass.

It is the purpose of the radar signal processor to operate on the radar measurements and generate the radar data product. A data signal processor, such as a tracker, operates on this output to assist the operator or analyst in interpreting events.

Regarding radar measurements, it is worth pointing out the difference between monostatic, bistatic, and multistatic systems [2]. The radar transmitter and receiver are collocated in monostatic radar. The bistatic configuration employs transmit and receive sites separated by an appreciable distance [5]; the distance is not precisely defined, but it is instructive to consider the bistatic configuration one in which target and clutter-scattering phenomenology are distinct from the monostatic case, and hence include different information content. A cooperative bistatic system controls its illumination source, whereas a noncooperative bistatic system employs illuminators of opportunity. Multistatic radar merges data from multiple bistatic nodes and can yield substantially enhanced geolocation performance resulting from the combination of the diverse target measurements [19].

Invariably, radar applications involve collecting and exploiting distinct measurements to achieve a given mission objective. Different measurement domains enable the radar to better differentiate a desired target from interference and other potential targets. At times, practical considerations – cost, deployment issues, etc. – affect the measurement domains collected by the radar.

1.4 | RADAR FREQUENCIES

Radar operating frequency is chosen based on a number of considerations. Important trade factors include but are not limited to the following.

- **Spatial resolution:** For a fixed aperture size, beamwidth is proportional to $\lambda/L_{a,m}$, where λ is wavelength and $L_{a,m}$ is the aperture length in the m th dimension.
- **Propagation:** Lower frequencies propagate farther and are used in very long range surveillance systems. As frequency increases, so does atmospheric attenuation due to water vapor, rainfall, and other weather effects as well as from dust and suspended particulates [16].
- **Materials penetration:** Radar systems that must find targets under foliage, behind walls, under canopies, or below soil favor lower frequency operation. Foliage-penetrating (FOPEN) radar systems typically operate at frequencies from several tens of megahertz up to 1 GHz; ultrahigh frequency (300 MHz to 1 GHz) is a popular choice, trading off attenuation for resolution. Through-the-wall radar favors L-band (1–2 GHz) as a good trade between attenuation through the wall, resolution, and aperture size.
- **Electromagnetic interference/electromagnetic compatibility (EMI/EMC):** The characteristics of spectrum use in the vicinity of the radar siting or operating environment influence frequency selection. For example, placing a radar in the vicinity of a

high-power communications transmitter influences frequency selection and the general system design.

- Electronics: The availability and cost of electronic components at a given frequency influence the design. There are many radar systems built at X-band, for instance, leading to lower-cost electronics than at Ku-band, making it more challenging to justify Ku-band designs without other compelling factors.
- Target properties: Target phenomenology varies with frequency selection [16, 17].
- Fractional bandwidth limitations: High resolution requires wider waveform bandwidth and design consideration to accommodate dispersion and hardware mismatch effects. Generally, instantaneous bandwidths drive the system design up to higher operational frequency as a means of simplification.
- Radiofrequency interference: Radar frequency may be selected to avoid operating in a band covered by jamming systems [2, 18].

Table 1-1 summarizes the radar frequency operating bands. Specific frequency allocations for radar are designated by governing bodies: the International Telecommunications Union (ITU) in particular, with coordination among other national agencies.

Example applications for the various frequencies are given in Table 1-1. The nomenclature relates to the function. For example:

- the “L” in “L-band” refers to long range application;
- Ku is “K under” and Ka is “K above,” respectively, due to their frequency ranges relative to K-band;

TABLE 1-1 ■ Radar Frequency Bands

Frequency	Range	Example Application(s)
High frequency (HF)	3–30 MHz	Ground-penetrating radar, over-the-horizon radar (OTHR), very long range surveillance radar
Very high frequency (VHF)	30–300 MHz	Foliage-penetrating radar, very long range surveillance radar
Ultrahigh frequency (UHF)	300–1,000 MHz	Foliage-penetrating radar, airborne surveillance radar, long range ballistic missile defense radar
L-band	1,000–2,000 MHz	Weapons location radar, air traffic control radar, long range surveillance radar
S-band	2,000–4,000 MHz	Naval surface radar, weapons location radar, weather radar
C-band	4,000–8,000 MHz	Weather radar
X-band	8,000–12,000 MHz	Fire-control radar, air interceptor radar, ground-mapping radar, ballistic missile-tracking radar
Ku-band	12,000–18,000 MHz	Air-to-ground SAR and surface-moving target indication
K-band	18,000–27,000 MHz	Limited due to absorption
Ka-band	27,000–40,000 MHz	Missile seekers, close-range fire-control radar
Millimeter wave (mmw)	40,000–300,000 MHz	Fire-control radar, automotive radar, law enforcement imaging systems, airport scanners, instrumentation radar

- the “X” in X-band stands for “X marks the spot,” due to the common use of this frequency for fire-control systems (some suggest that the X is the roman numeral representing 10, the approximate center frequency in GHz for the X-band); and
- “C-band” is a “compromise” between a selection of X-band and S-band.

The radar center wavelength is given as $\lambda_o = c/f_o$, where f_o is the center frequency. Wavelengths on the order of a millimeter technically start just slightly above 30 GHz.

1.5 | RADAR FUNCTIONS

All radar systems operate on the same physical principle: an active source illuminates a target, a receiver then collects scattered target energy, and a processor generates the radar product (e.g., dots on a screen representing target detections or a synthetic aperture radar image). From this basic concept of radar operation arise different radar functions. Radar mode design implements variants of these core functions: search, track, and recognition. In general, the purpose of the core radar functions falls into one of two primary categories, as given in [2]:

- *moving target indication* (MTI), with subsequent steps to estimate target motion and type, perhaps followed by a tracker to refine target position and velocity estimates and predict where the target will next appear; or
- *radar imaging*, the process of collecting data, estimating radiofrequency reflectivity over the local coordinates of interest, and then mapping the estimates to a georeferenced framework.

In *search*, the radar system attempts to acquire targets of interest. Examples include an airborne early warning (AEW) radar scanning the sky for incoming aircraft and an air interceptor (AI) radar scanning for enemy fighter aircraft. In a similar vein, imaging radar typically “lay down” a certain number of beams per specified time interval to collect spotlight SAR data, or scan a certain area on Earth’s surface in stripmap mode with the objective of searching for certain target types; in the former case, the target of interest might be a missile launcher, whilst in the latter scenario the analyst may be trying to identify deforestation or degradation of polar ice caps.

Oftentimes, radar systems that implement the search function are called *surveillance radar*. The surveillance radar may detect the same target multiple times, thereafter tracking the target through the skill of the radar analyst via something tantamount to “grease pencil markings on a radar display” or by feeding radar measurements into an automated tracker; however, the radar continues to search for new targets with a very similar scan pattern and waveform previously employed to generate existing target indications; and, as already suggested, the nuances of correlating these target detections from scan to scan are left to either the analyst or an automated tracker. Radar resources are not diverted upon detecting a given target; rather, if engagement is to occur, the surveillance radar “hands off” the target to a tracking radar.

The *tracking* function involves focusing radar resources more acutely on a particular target or set of targets. The radar dedicates resources to ensure adequate measurements

are collected to maintain track quality. Information from the tracker is used to direct the transmit beam to anticipated target locations. For example, an L-band search radar persistently detects an incoming target, thereafter handing off the acquired target to an X-band tracking radar that refines estimates of target state (position, velocity, and possibly acceleration) by frequently collecting target measurements. The product from the tracking radar function is subsequently provided external to the radar system to a command-and-control function.

It is possible that a single radar performs both search and track. Moreover, a single radar can, under the appropriate set of constraints, simultaneously implement both functions in what is known as *track-while-scan*. In track-while-scan, sufficient radar timeline is available so that, between required tracker updates, the radar can allocate its resources to search for new targets or reacquire targets dropped by the tracker.

In addition to searching for targets and placing them in track, *recognition* is another important function. Recognition involves coarsely or finely determining the target type through the following steps: discrimination, classification, and identification. Discrimination bins the target according to level of interest – for example, a potential military target versus generic ground traffic. Classification determines the threat category, such as ground transport, tank, or missile launcher. Identification then narrows the assessment to a particular target class, such as the tank, missile launcher, helicopter, or aircraft model. Different levels of recognition place varying demands on radar resources: discrimination only requires relatively coarse resolution, whereas identification requires greater information and hence higher resolution. These demands force the radar system to modify its operation in a manner distinct from search and track functions.

Recognition may take place at the hands of a trained analyst. An overview of automatic target recognition is given in [2].

1.6 | U.S. MILITARY RADAR NOMENCLATURE

Radar nomenclature acknowledges many different radar applications. Table 1-2 shows the nomenclature system used to catalog radar systems in the U.S. military. The first letter designates the platform, the second the equipment type, and the third the

TABLE 1-2 ■ Some Elements of the Joint Electronics Type Designation System (JETDS)^a

Platform	Equipment Type	Application
A – Airborne	L – Countermeasures	G – Fire control or searchlight directing
F – Ground fixed	P – Radar	N – Navigation
M – Ground mobile	Y – Processing	Q – Special or multipurpose
S – Surface ship	B – Communications security	Y – Surveillance
T – Ground transportable	Q – Sonar	R – Receive (passive) only
U – Ground utility	W – Armament	S – Detecting, range and bearing, search
B – Underwater		
G – Ground		
K – Amphibious		
P – Man portable		

^aThe Joint Army–Navy Nomenclature System was previously used to catalog electronic equipment.

application; typically, these letters are preceded by the designation “AN/” (for joint service Army–Navy equipment) and followed by the model number. For example:

- The AN/APY-1 is the radar on the E-3A and E-3B Sentry Airborne Warning and Control System (AWACS). AN/APY-1 reads as “Army–Navy equipment,” airborne platform, radar, surveillance, model number 1. The AN/APY-2 is the radar on the E-3C AWACS and includes a maritime capability.
- The AN/APG-63 is the radar used on the F-15E fighter aircraft. APG-63 stands for airborne platform, radar, fire-control, model number 63.
- The AN/TPQ-53 is the Quick Reaction Capability Radar, sometimes called the Enhanced Firefinder radar. TPQ-53 stands for ground transportable, radar, multi-purpose, model number 53. The TPQ-53 is a counterbattery radar used to defend ground troops from rocket, artillery, and mortar attack. The TPQ-53 is replacing the TPQ-36 Firefinder radar.
- The AN/SPY-1 is part of the U.S. Navy’s Aegis Combat System. It is a passive, phased array surveillance radar used to protect the ship from air and missile attack. SPY-1 stands for shipborne platform, radar, surveillance, model number 1.

A vast array of radar systems comprise the U.S. military inventory, covering a tremendously wide range of applications. Moreover, military radar innovation has led to civil and commercial opportunities. This book considers a number of different radar applications, discussing key issues, constraints, and technology resulting in a particular radar capability.

1.7 | TOPICS IN RADAR APPLICATIONS

This book is organized into three sections: tactical radar; intelligence, surveillance, and reconnaissance (ISR) radar; and specialized radar applications. Topics assigned to a particular section are done so based on predominant use but may hold broader applicability.

1.7.1 Tactical Radar

Tactical radar systems are used to execute an action within a limited timeframe, as opposed to information gathering that indirectly supports future activities. As a military example, tactical radar is used to track and engage an incoming missile. Police radar is used to evaluate speeds of individual vehicles relative to allowable limits and is a civilian safety example. Determination of liquid levels in industrial storage tanks, known as *level gauge measurement*, is a commercial example.

Continuous wave (CW) radar systems imply low-cost, low-complexity radar. These radar systems typically operate at short range, and their applications include missile seekers, altimeters, active protection systems used to direct a kinetic kill response at incoming rockets, police radar, and automotive safety. Chapter 2 discusses CW radar in detail, covering the basic configuration types; CW radar performance issues and analysis; modulated CW waveforms, including the commonly used linear frequency modulated CW (FMCW) waveform; and applications leveraging the benefits of CW radar.

Chapter 3 discusses millimeter wave (mmw) radar. As mentioned earlier, the millimeter wave regime technically ranges from 30 GHz to 300 GHz. The shorter

wavelength is appealing for compact radar applications, as would be the case on a missile, in an unmanned aerial vehicle (UAV), or in a personal conveyance. A key benefit of the higher frequency is narrower beamwidth for a fixed aperture size, an important consideration for target engagement and operation in clutter-limited environments. A mmw radar can operate using both CW and pulsed waveforms; current applications tend to favor CW, consistent with the discussion in Chapter 2. Other mmw radar applications include concealed weapon imaging, automotive radar, and autonomous landing systems. In each of these applications, the short wavelength benefits the system application: higher resolution for concealed weapon imaging and autonomous landing; and compact system design with appropriately narrow beamwidth yielding finer angular resolution, as well as improved electromagnetic compatibility, in support of effective automotive radar. As discussed in Chapter 3, interest in mmw radar continues to grow; this interest will lead to improvements in the cost and performance of mmw electronic components.

Fire-control systems seek to detect, track, and recognize targets as part of the engagement process. While a number of sensor modalities can be used for fire control, radar proves very appealing, as Chapter 4 discusses, due to its improved range performance and all-weather capability relative to infrared and optical sensors. There is a broad range of fire-control radar systems supporting a number of missions, including air-to-air combat, air-to-ground fixed-site targeting, shipboard protection, and ballistic missile defense. Chapter 4 broadly considers fire-control radar objectives, implementation considerations, and example systems. This information is a good segue into subsequent chapters.

Pulse Doppler waveforms are a critical element of current and future radar systems. This waveform is the mainstay of most radar modes; the pulse Doppler waveform is particularly useful since it provides superior transmit-to-receive isolation. While SAR, AEW, and surface moving target indication (SMTI) all use pulse Doppler variants, air-to-air pulse Doppler radar is the focus of Chapter 5. Chapter 5 discusses basic airborne pulse Doppler radar principles and concepts, characterizes target and clutter Doppler properties as seen from an airborne platform, and examines the various pulse repetition frequency (PRF) selections.

The design of the antenna subsystem plays a critical role in modern radar capability and sophistication. Multifunction phased arrays offer superlative performance, since a single radar can carry out multiple tasks. As Chapter 6 describes, multifunction phased arrays provide beam agility through fine control of the elements comprising the antenna. Surface air and missile defense radars, such as the AN/TPY-2 Terminal High Altitude Area Defense (THAAD) radar, and airborne radars, such as the AN/APG-81 radar on the F-35 Lightning, provide multifunction capabilities to search, provide track-while-scan on many targets, and support weapons engagement. The multifunction phased array radar rapidly focuses a beam in space, transmits and receives an appropriate waveform for that specific objective, and then rapidly moves the beam electronically to the next dwell position. In addition to leveraging advanced antenna technology, multifunction phased array radar systems require detailed software architectures to manage system resources. Chapter 6 discusses resource management, as well as multifunction phased array design and performance assessment.

Ballistic missile defense (BMD) is an important application for multifunction phased array radar. BMD is an extraordinarily challenging problem, dealing with vast detection ranges and targets of lower RCS and higher velocity than typically seen in other applications. The BMD problem is sometimes stated as “hitting a bullet with a

bullet” due to its complexity. Chapter 7 describes in detail BMD radar and its corresponding reliance on large, costly, and highly capable phased array radar systems. These phased array radar systems provide exquisite sensitivity and agility to detect, track, and engage ballistic missile targets. Moreover, as Chapter 7 describes, the radar systems comprising the BMD system usually accomplish other important missions as well, including shipboard defense for Aegis BMD, space situational awareness at some of the large ground-based radar sites, and measurement and signature intelligence (MASINT).

1.7.2 ISR Radar

ISR radar systems gather information in support of other actions. Examples include the collection of spotlight SAR imagery to determine if activity is taking place in the vicinity of a missile site and detection of troop movement using ground moving target indication (GMTI) radar [20].

Radar systems dedicated to early warning are also considered ISR assets. Early warning served as the original motivation for radar development. The British Chain Home radar is among the earliest early warning radar systems, and it played a pivotal role in the Battle of Britain during World War II. Since these early days, early warning radar systems continue to flourish, and many experts recognize their capabilities as critical to national defense. These early warning radar systems feed into command-and-control networks and provide handoff to tracking and engagement radar. Ground-based, shipborne, and airborne variants exist. Chapter 8 focuses on ground-based early warning radar, complementing some of the discussion in Chapter 7 on ballistic missile warning. Discussion in Chapter 8 covers the objectives of early warning radar; antenna, transceiver and electronics, signal processing, tracking, and electronic protection design considerations; and characteristics of fielded early warning radar systems. This chapter provides international exposure to the topic.

Chapter 9 covers SMTI radar design and implementation. (GMTI is the most prominent instantiation of SMTI.) SMTI is a radar mode whose fielded history started in the early 1990s with Joint STARS [20]. This chapter discusses the fundamentals of SMTI, including clutter and target modeling, performance measures, system design considerations, and signal-processing requirements. Clutter mitigation is a critical topic in SMTI, and substantial effort is devoted in Chapter 9 to this topic. As described in the chapter, at its very essence, SMTI radar attempts to discriminate the angle-Doppler response of a potential target from the background clutter. The chapter describes an end-to-end detection processing chain and a standard approach to bearing and Doppler estimation. An overview of several critical topics affecting SMTI implementation, such as the impact of heterogeneous clutter on detection performance and requirements for dismount detection, conclude the chapter.

Deploying radar on Earth-orbiting satellites is appealing due to the access such platforms provide. In recent years, international interest in developing and deploying satellite-based synthetic aperture radar has exploded. Spaceborne SAR has numerous applications, including remote sensing of natural resources, monitoring of oceans and gulfs, emergency management, and treaty monitoring. Chapter 10 discusses spaceborne SAR. The chapter presents an array of internationally developed SAR systems, exhaustively covers a number of critical design issues and considerations, and describes SAR implementation and performance assessment applied to spaceborne

assets. The chapter summarizes the characteristics of a number of operational spaceborne SAR systems.

1.7.3 Specialized Applications

Innovation in radar technology continues. Advances in RF electronics and antenna technology, as well as remarkable improvements in high-performance computing, enable the conception and deployment of numerous new radar capabilities. This section of the book examines the emerging or specialized applications of radar technology.

Passive bistatic radar systems exploit ambient signals, such as those from broadcast stations and communications towers, to detect and localize moving targets. Original observations on radar potential were a result of target-induced modulation on noncooperative signals viewed at a receive site; early radar systems were bistatic owing to a requirement to isolate the transmit and receive function, and the history of radar in general and that of the bistatic topology are inseparable. The availability of lower-cost electronic components and computing devices is a key enabler in the design and deployment of passive bistatic radar, and it is a primary reason for an international surge of interest in this area. Chapter 11 discusses passive bistatic radar in detail, providing a historical perspective; details of bistatic radar geometry and fundamental operation; characteristics of plausible, passive bistatic radar waveforms, such as FM and DTV broadcast, cell-tower emissions, and wireless computer network signals, via the complex ambiguity function; processing requirements; and a survey of some practical systems. Digital modulation has been a boon to passive bistatic radar interest, owing to the potential for reasonably good range resolution. As Chapter 11 details, digital signal processing (DSP) is critical to passive bistatic radar utility, allowing the receive site to broadly capture scattered transmit energy through the formation of multiple surveillance receive beams; enabling direct path receipt and creation of the replica signal needed for pulse compression; allowing pulse compression implementation with different Doppler hypotheses to filter scaled, time-delayed versions of the replica signal; and providing a mechanism to mitigate the impact of the strong, direct path signal interfering with the surveillance channels.

Chapter 12 discusses radar application to air traffic control. Air traffic control radar systems are used throughout the world to maintain safe and efficient aviation. These radar systems have a long and proud heritage. While the role of air traffic control radar is evolving due to direct broadcast navigation systems, radar will continue to be pivotal in commercial aviation safety. Chapter 12 looks at the objectives of air traffic control, discusses the purpose of primary and secondary surveillance radar capabilities, and describes design issues for both surveillance modes; this chapter considers requirements for detection of weather effects as well.

From its earliest days, it was known that radar detects weather phenomenon. Most people are familiar with radar due to its extensive use on weather newscasts, and the term *Doppler radar* is widely recognized for this reason. Chapter 13 discusses weather radar in detail, surveying available weather-surveillance radar systems, describing the radar range equation and Doppler processing for weather surveillance, characterizing weather volume reflectivity, and discussing the manifestation of distinct effects (e.g., rainstorm versus tornado) in the weather-surveillance radar product. In addition to weather radar outputs showing up on the evening news, terminal Doppler weather radar detect downbursts and wind shear in support of aviation safety, and aircraft use radar to

avoid localized weather. The incorporation of polarization to characterize raindrop size is a current endeavor. Advanced concepts for weather surveillance include the Multifunction Phased Array Radar (MPAR), the newest design from the Federal Aviation Administration (FAA) whose purpose includes replacing aging air traffic control radar and providing a simultaneous capability to monitor weather.

During the Vietnam War, insurgents realized they were safely hidden under foliage from the X-band fire-control radars of the time. Shorter wavelengths associated with higher-frequency radar are known to poorly penetrate foliage. The need to detect and engage troops under foliage drove the development of foliage-penetrating radar. Of all the technologies available for surveillance of concealed targets, radar is the most appealing. Chapter 14 discusses the history of FOPEN radar and then focuses on key issues around forming SAR images using lower-frequency, ultrawideband airborne radar. The chapter characterizes propagation through foliage as a function of frequency, examines clutter and target properties, and details SAR image-formation processing. Due to the overlap of FOPEN radar waveforms with a preponderance of other signal sources, radiofrequency interference mitigation techniques are critical in FOPEN; in this regard, Chapter 14 discusses waveform design approaches and both transmit and receive-side waveform notching. FOPEN radar systems leverage polarization to assist in separating manmade and natural objects and in enhancing target characterization, important issues included in this chapter's exposition.

Ground-penetrating radar (GPR) is used to detect buried mines in military applications. GPR is also widely used by commercial industry to detect buried utilities. Moreover, GPR is used in archaeology and has been deployed in emergency management situations to detect life signs under rubble. An extensive discussion on GPR application, principles, and system design is given in Chapter 15. GPRs typically operate at lower frequencies of several MHz, but they can be deployed at operating frequencies in the microwave regime; frequency selection is a function of the properties of the material to penetrate, as well as target features. The system typically couples to the surface via direct contact of the transmit and receive antenna system. Chapter 15 discusses hardware implementation issues and provides sample product outputs. The chapter also more broadly discusses materials-penetrating applications, such as the characterization of objects within concrete building material.

The final application considered in this book is police radar. Police radar is used to calculate the speed of roadway traffic. As in the case of weather radar, police radar is well known to the general public. Chapter 16 discusses police radar in significant detail. Current police radar systems are CW (see Chapter 2), operate at X-band, and apply Doppler processing to generate range-rate estimates. These radar systems were initial by-products of radar development during World War II, thereafter leveraging technology readily available at the time to implement product improvement. This chapter also discusses sources of error in police radar application and steps taken to improve deployment.

1.8 | COMMENTS

While titled *Radar Applications*, this book is only able to cover select applications due to the vastness of the radar discipline; in this sense, *Select Radar Applications* is a more precise title. Important topics are excluded from the text for practicality's sake, something we certainly regret.

The reader may also notice that some topics are not basic principles, nor are they techniques; they appear closer in alignment to applications. The chapters on CW radar and mmw radar fall into this category. So, an argument can be made that *Select Radar Technology and Applications* is even more accurate titling.

This consternation aside, we hope the reader benefits from the detailed descriptions provided in this book, *Radar Applications*. The chapters herein build on the legacy of the first two books in the *Principles of Modern Radar* series; taken as a whole, many important aspects of modern radar principles, techniques, and applications have been covered.

1.9 | REFERENCES

- [1] M.A. Richards, J.A. Scheer, and W.A. Holm, Editors, *Principles of Modern Radar: Basic Principles*, SciTech Publishing, Raleigh, NC, 2010.
- [2] W.L. Melvin and J.A. Scheer, Editors, *Principles of Modern Radar: Advanced Techniques*, IET/SciTech Publishing, Raleigh, NC, 2012.
- [3] J.B. McKinney, "Radar: a case history of an invention," *IEEE AES Systems Magazine*, Vol. 21, No. 8, Part II, August 2006.
- [4] M.I. Skolnik, *Introduction to Radar Systems, 2nd Ed.*, McGraw Hill, New York, NY, 1980.
- [5] N.J. Willis, *Bistatic Radar*, Technology Service Corporation, Silver Spring, MD, 1995.
- [6] G.W. Stimson, *Introduction to Airborne Radar, 2nd Ed.*, IET/SciTech Publishing, Edison, NJ, 1998.
- [7] W.G. Carara, R.S. Goodman, and R.M. Majewski, *Spotlight Synthetic Aperture Radar: Signal Processing Algorithms*, Artech House, Inc., Norwood, MA, 1995.
- [8] C.V. Jakowatz, D.E. Wahl, P.H. Eichel, D.C. Ghiglia, and P.A. Thompson, *Spotlight-Mode Synthetic Aperture Radar: A Signal Processing Approach*, Kluwer Academic Publishers, Boston, 1996.
- [9] R.J. Mailloux, *Phased Array Antenna Handbook*, Artech House, Boston, MA, 1994.
- [10] W.L. Melvin, "A STAP overview," *IEEE AES Systems Magazine – Special Tutorials Issue* (Ed. Prof. Peter Willett), Vol. 19, No. 1, January 2004, pp. 19–35.
- [11] W.L. Melvin, "Space-time adaptive processing for radar," *Elsevier Electronic Reference in Signal, Image and Video Processing*, Academic Press, 2013.
- [12] R.K. Hersey, W.L. Melvin, and E. Culpepper, "Dismount modeling and detection from small aperture moving radar platforms," in *Proceedings 2008 IEEE Radar Conference*, May 2008, Rome, Italy.
- [13] K. Olsen and K. Woodbridge, "Performance of a multiband passive bistatic radar processing scheme – Part II," *IEEE AES Systems Magazine*, Vol. 27, No. 11, November 2012, pp. 4–14.
- [14] M. Cotton *et al.*, "Developing forward thinking rules and processes to fully exploit spectrum resources: an evaluation of radar spectrum use and management," in *Proceedings of ISART 2011*, NTIA Special Publication SP-12-485, July 27–30, 2011, Boulder, Colorado. See <http://www.its.bldrdoc.gov/publications/2669.aspx>.
- [15] L.B. Fertig, M.J. Baden, J.C. Kerce, and D. Sobota, "Localization and tracking with multipath exploitation radar," in *Proceedings 2012 IEEE Radar Conference*, Atlanta, GA, May 7–11, 2012.
- [16] F.E. Nathanson, *Radar Design Principles, 2nd Ed.*, SciTech Publishing, Inc., New Jersey, 1999.

- [17] E.F. Knott, J.F. Schaeffer, and M.T. Tuley, *Radar Cross Section, 2nd Ed.*, SciTech Publishing, Raleigh, NC, 2004.
- [18] D.C. Schleher, *Electronic Warfare in the Information Age*, Artech House, Boston, Massachusetts, 1999.
- [19] W.L. Melvin, R. Hancock, M. Rangaswamy, and J. Parker, “Adaptive distributed radar,” in *Proceedings 2009 International Radar Conference*, Bordeaux, France, October 2009.
- [20] J.N. Entzminger, C.A. Fowler, and W.J. Kenneally, “JointSTARS and GMTI: past, present and future,” *IEEE Transactions on Aerospace and Electronic Systems*, Vol. 35, No. 2, April 1999, pp. 748–761.

Continuous Wave Radar

*Christopher J. Baker, Ohio State University, Electro Science lab,
Department of Electrical and Computer Engineering, and
Samuel O. Piper, Georgia Tech Research Institute, Sensors and
Electromagnetic Laboratory*

Chapter Outline

2.1 Introduction	17
2.2 Continuous Wave Radar.	21
2.3 Frequency Modulated CW Radar	26
2.4 Other CW Radar Waveform Designs	63
2.5 FMCW Radar Applications	67
2.6 References.	82

2.1 | INTRODUCTION

Continuous wave (CW) radar systems continuously transmit an illumination signal and simultaneously continuously receive echo reflections scattered from objects. If an illuminated object is stationary, the frequency of the echo signal is unchanged from that transmitted. However, if an object is moving, then the frequency of the echo signal is altered due to the Doppler effect. By detecting this *Doppler frequency*, the object’s motion can be determined. The faster the object moves in a given direction, the larger the Doppler frequency. The operation of a CW radar system is shown schematically in Figure 2.1-1.

CW radar systems are generally used in compact, short-range, low-cost applications and are often manufactured using solid-state technology. CW radar systems have

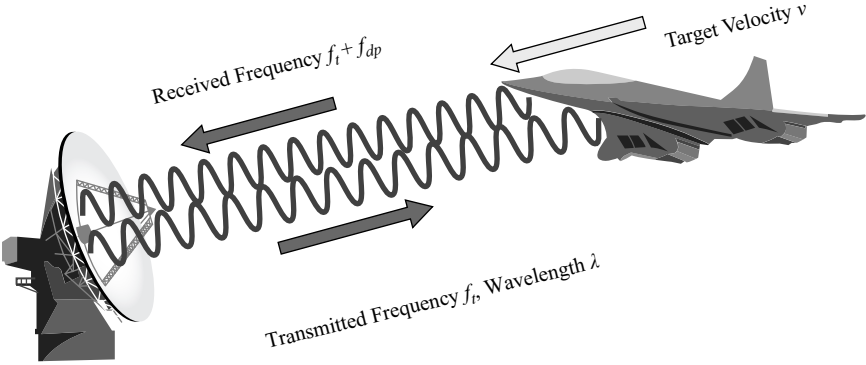


FIGURE 2.1-1 ■ A CW Radar Using the Doppler Shift to Detect a Moving Object.

been used in a wide variety of applications such as the measurement of liquid levels in industrial storage tanks, vehicular speed determination for police speed guns, short-range navigation, missile seekers, fusing, battlefield surveillance, aircraft detection, and automobile cruise control. Indeed, as automobile radar systems are set to become standard for every new car manufactured, CW radar systems may shortly become the most commonplace of any radar variant.

The Doppler effect, on which simple CW radar relies, is caused by relative motion. If we consider the signal in Figure 2.1-1, the echoes that return to the radar are effectively compressed by the action of the moving object (or expanded if the object were moving away from the radar). This compression acts to reduce the wavelength of the reflected signals at the receiver, so the observed frequency is increased. The higher the speed of the object, the greater the wavelength compression and therefore an increase in the Doppler frequency shift is observed.

The velocity of an object in the radial direction with respect to the radar is related to the Doppler frequency shift, f_{Dop} by

$$V = \frac{\lambda f_{Dop}}{2} \quad (2.1-1)$$

where

- V = radial velocity of the object (m s^{-1}),
- λ = wavelength of the CW signal (m), and
- f_{Dop} = Doppler frequency (Hz).

In other words, the Doppler frequency is scaled by the wavelength of the illuminating signal to convert it to a measurement of velocity, and the factor 2 represents the two-way path traveled in transmission and reception.

The simple concept just outlined is known as an *unmodulated* CW radar system in that a pure tone is used to measure the Doppler shift from a moving object. A drawback of such a CW radar system is that it is unable to detect stationary objects or measure the range to an object (because range is ambiguous to a wavelength). These limitations can be overcome by modulation of the transmitted signal. The modulation imparts a code on the CW signal as a function of time and therefore radial range. For example, the frequency of the transmission can be linearly changed as a function of time. In this way a particular value of frequency represents a particular time delay and hence can be associated with a particular range. In fact, linear FM modulation is probably the most common form used and will be examined in detail in the next section. This type of system is known as *frequency modulated continuous wave (FMCW) radar*. Figure 2.1-2 illustrates the relationship between frequency and time for this form of modulation.

The time delay, Δt , between the transmitting frequency and the frequency of the echo signal, at any instant in time, is proportional to the distance to an object. The time taken for an echo to be received is given by

$$\Delta t = \frac{2R}{c} \quad (2.1-2)$$

where

- R = range from the radar to the object (m) and
- c = velocity of light (m s^{-1}).

From Figure 2.1-2 we can see that knowledge of the linear rate of change of the transmitted signal and the difference frequency, f_d , between the transmitted and received

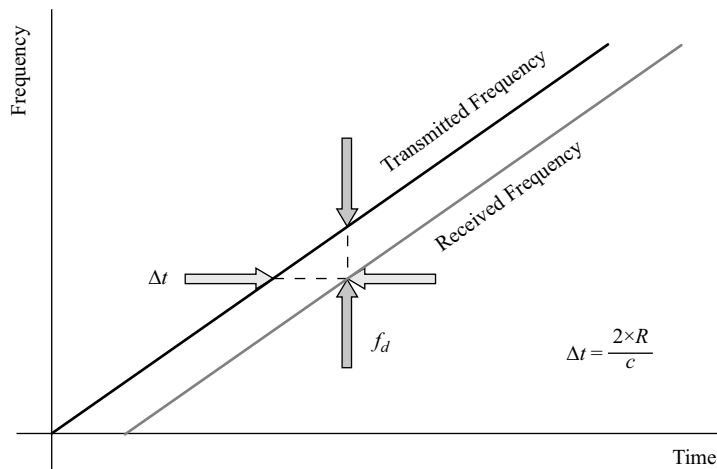


FIGURE 2.1-2 ■ The Relationship between Frequency and Time for a Linear FMCW Radar System.

signals allows computation of the time, Δt , for an echo to be received and hence for the range, R , to a detected object to be determined.

Figure 2.1-3 shows a schematic illustration of a CW signal composed of a single frequency tone. The amplitude is plotted as a function of the distance traveled by the wave. Thus, the distance between successive peaks is the wavelength, λ . If a similar plot were produced but with time on the horizontal scale, then the peak-to-peak length would be the period of the signal and its inverse the signal frequency.

The relationship between frequency, f (Hz), and wavelength, λ (m), is given by

$$f = \frac{c}{\lambda} \tag{2.1-3}$$

where

c = velocity of light (m s^{-1}).

Critical to the understanding of the operation of CW radar is the notion of phase. *Phase* represents the precise location within a cycle of a signal. It is common to refer phase to the points in time at which the amplitude of the signal becomes zero; it is measured in degrees or radians. A single cycle of a tone maps out 360 degrees or 2π radians of phase. This is equivalent to a vector equal in length to the amplitude of the signal rotating through 360 degrees, that is, making one complete revolution of a circle. By comparing the phase of the outgoing transmit signal with the incoming received signal, fine motion estimation is possible. Figure 2.1-4 illustrates the concept of phase and relative phase.

This chapter on CW radar systems focuses on the essential techniques and technologies widely used in today’s systems. The foundations and application of modulated

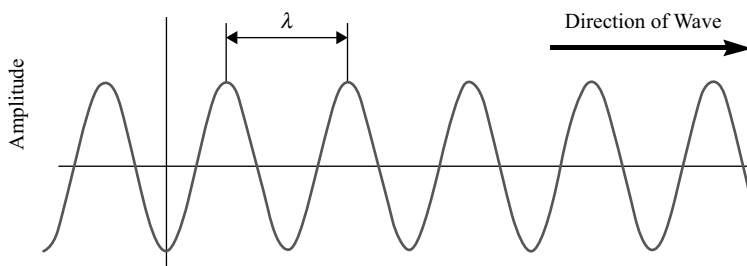
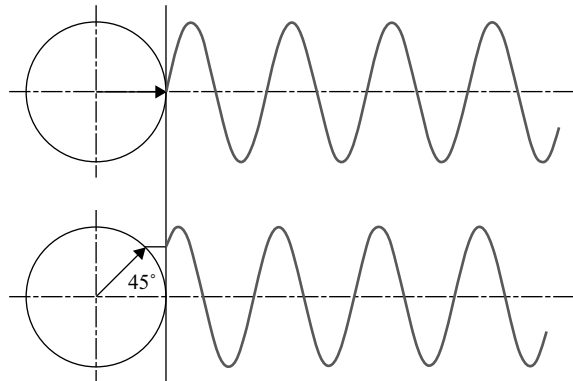


FIGURE 2.1-3 ■ A Portion of a CW Signal.

FIGURE 2.1-4 ■ The Top Signal Is Said to Exhibit a Phase of Zero Degrees and the Bottom a Phase of 45 Degrees (with regard to the Top Signal).



and especially FMCW radar are laid out in the next section. This is followed by a brief discussion of more advanced CW concepts that employ phase and other forms of frequency modulation. Section 2.5 examines the range of applications that exploit the CW technique and summarize a number of the systems used to address these applications.

The following is a list of symbols and abbreviations used in this chapter.

SYMBOLS AND ABBREVIATIONS ASSOCIATED WITH CW RADAR

ACC	adaptive cruise control
ADC	analog-to-digital converter
AGC	automatic gain control
B	Bandwidth
B_b	beat frequency bandwidth for point target
c	propagation velocity = $3.0 \times 10^8 \text{ ms}^{-1}$
CPI	coherent processing interval
CW	continuous wave
DAC	digital to analog converter
dB	decibels
dBc	decibels relative to the carrier
dBHz	decibels relative to one Hz bandwidth
dBK	decibels relative to standard temperature
dBm	decibels relative to a milliWatt
ES	electronic support
f	radar frequency
F	noise figure
f_b	beat frequency
f_d	difference frequency
f_{Dop}	Doppler frequency shift
FFT	fast Fourier transform
f_m	modulation frequency
FM	frequency modulation
FMCW	frequency modulated continuous wave
FOV	field of view

GHz	GigaHertz
G_p	Processing gain
GSPS	Gigasample per second
k	Boltzmann's constant
K	Kelvin
kHz	kiloHertz
km	kilometer
LO	local oscillator
L_r	receiver losses
m	meter
MHz	MegaHertz
ms	millisecond
m/s, ms^{-1}	meter/second
mW	milliWatt
ns	nanosecond
P_i	incident power
P_r	reflected power
R	range
RCS	radar cross section
RF	radio frequency
RPC	reflected power canceller
SNR	signal-to-noise ratio
STC	sensitivity time control
T	reference temperature
t_d	round-trip propagation time
T_m	modulation period
t_r	delay between RF and LO paths for internal reflections
V	target velocity relative to the radar
VCO	voltage-controlled oscillator
VSWR	voltage standing wave ratio
wrt	with respect to
Δf_b	beat frequency resolution
ΔF	frequency deviation, bandwidth of the transmit waveform
$\Delta F'$	effective bandwidth of the transmit waveform
ΔR	range resolution
ΔR_0	ideal range resolution
ΔT	time resolution
μs	microsecond

2.2 | CONTINUOUS WAVE RADAR

CW radars can utilize any part of the RF electromagnetic spectrum just like their pulsed counterparts, and examples exist all the way through from HF to W band. The principal

advantages of CW radars include simplicity, low cost, and small volume – but how do these come about? As CW radars transmit continuously, their peak power and average power are the same. Consider a pulsed radar with a typical pulse length of 1 micro-second and a pulse repetition frequency of 1,000 Hz. A peak power of 1 kW is required to transmit an average power of just 1 W. A transmitter with a peak power of 1 kW makes for a complex and potentially costly system. A CW radar with a peak or average output power of 1 W is straightforward using compact, relatively simple solid-state technology that sometimes costs just a few dollars.

A disadvantage of CW radars, though, is reduced dynamic range because of simultaneous transmission and reception. Transmission is continuous and therefore competes with the weak reflected echo signal, which it can easily swamp, thus preventing detection of objects. Of course, the Doppler imparted by a moving target helps mitigate this as the transmission is, in effect, at zero Doppler. This improves the isolation between the transmit and receive signals. To further improve matters, it is usual to use separate antennas for transmission and reception arranged to keep the transmit signal from “leaking” across into the receive antenna. Close-in objects can also cause reflections into the receive antenna, and these again compete with objects detected at longer ranges and also limit sensitivity to slow-moving objects. This usually imparts a limit on the maximum transmit power whereby further increases simply increase the leakage and do not result in an increased detection range. It is largely for this reason that CW radar systems tend to be used in shorter-range applications and consequently tend to be lower in transmission power and smaller in size. There have been one or two exceptions to this and Figure 2.2-1 shows a military 5N62 Square Pair “Guidance and Illumination Radar” capable of a 140–160 NMI range. The larger parabolic antenna is for the transmit signal, and the smaller parabolic section antenna is for reception. Note the dividing blade

FIGURE 2.2-1 ■
Semimobile
Configuration of the
Improved K-1M
Cabin with 5N62
Square Pair FMCW
Radar on Display at
Kecel in Hungary.



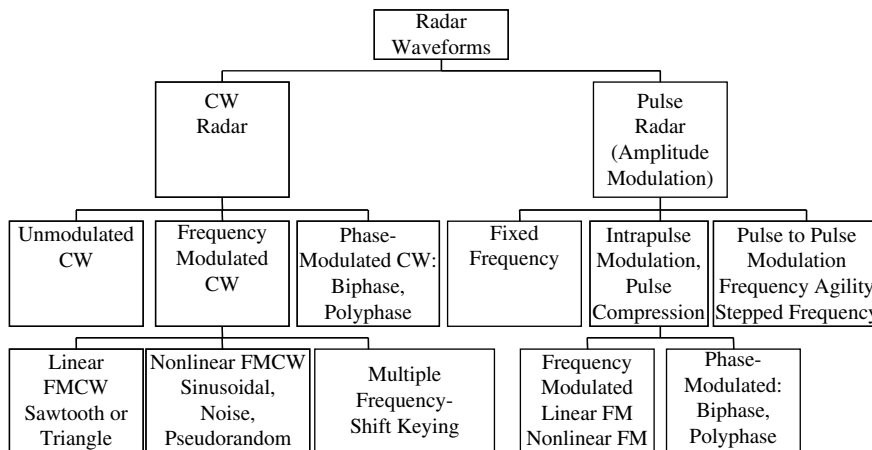


FIGURE 2.2-2 ■ Radar Waveform Hierarchy Showing CW Radar Waveforms.

(termed a *knife*); it is employed to avoid spillover of the transmit signal into the receive antenna, which would otherwise degrade isolation between transmission and reception and hence reduce detection range. The transmit power is 100 kW CW, and this physical method for improving isolation between the transmission and reception paths is necessary to cope with such high powers. This form of CW radar is much more the exception than the rule, with most being of modest power (usually 1 W or less) and of small physical size.

Another feature of some CW radars is that they can operate with a single radio frequency source without the requirement for a separate local oscillator (LO). The relatively low peak transmit power is attractive for solid-state transmit sources and amplifiers that are inherently peak power limited. CW radars also inherently have a lower probability of intercept (LPI) as Electronic Surveillance Measures (ESM) receivers are triggered by the peak power intercepted [1–3].

Figure 2.2-2 shows a segmentation of radar waveforms that are separated into CW and pulsed types. CW and pulsed waveforms are both able to host a wide variety of differing forms of modulation. This wide variety of waveform types, in turn, provides the radar designer with a range of options that allow the performance for a given application to be optimized.

CW radar has been in use since World War II and has found widespread application. Perhaps, not unsurprisingly, the applications where CW has found significant and sustained traction are those where low cost, small size, and short range drive system design. Table 2.2-1 lists the most common applications of CW radar system; many have maximum ranges of less than 1 km. As is usually the case with radar, there are notable exceptions such as over-the-horizon (OTH) radars. OTH radars achieve good transmit-to-receive isolation by separating the transmitter and receiver by approximately one hundred kilometers and are thus able to see out to ranges well beyond the horizon.

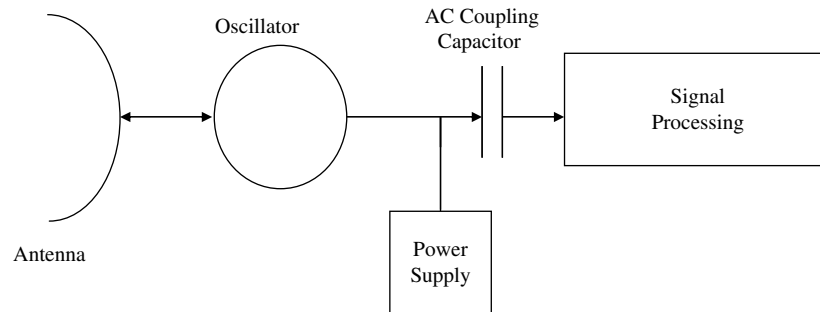
2.2.1 CW Radar: Configuration Types

We briefly introduce the principal CW radar front-end configuration types and discuss their relative merits. Three main forms are examined: (1) autodyne, (2) homodyne, and (3) heterodyne.

The simplest of all the configurations is the autodyne. Its configuration uses a free-running oscillator as the transmission source. Figure 2.2-3 shows the block diagram for

TABLE 2.2-1 ■ CW Radar Applications

Radar altimeters
Police radars
Missile seekers
Active protection systems
Artillery and missile fuses
Doppler navigators
Buried object detection
Short-range navigation
Ship docking
Automobile automatic cruise control, collision avoidance
Meteorology, weather sensing
Tank-level measurement
Radar cross section (RCS) measurement range
Over-the-horizon radar – long range

FIGURE 2.2-3 ■ Autodyne CW Radar Block Diagram.

the autodyne configuration (sometimes referred to as a *self-mixing oscillator* or *self-oscillating mixer*). While stationary targets are not detectable with this CW radar configuration, the return signal from moving targets experiences a Doppler frequency shift. The different transmit and receive frequencies are mixed via the oscillator nonlinearities, yielding a difference frequency equal to the Doppler shift.

This difference or beat frequency passes via capacitive coupling to the radar for signal processing. Police speed radar systems generally use the autodyne configuration in the form of a Gunn oscillator source. It is also suitable for intrusion alarms and automatic door opener sensors. However, the simple autodyne CW radar configuration has relatively poor sensitivity, as the noise floor is broadband and the received signal competes with that being transmitted [4] and this limits detection range and velocity estimation.

Relative to the autodyne configuration, the homodyne CW radar configuration offers improved sensitivity because of better performance when using a separate mixer and because of the greater transmit-to-receive isolation with separate antennas for transmit and receive. Figure 2.2-4 shows a block diagram of a homodyne CW radar with the transmit signal coupled to the mixer. While a transmit–receive switch cannot be used with CW waveforms, a single-antenna CW radar configuration is feasible (see Figure 2.2-5). This requires a transmit–receive diplexer, such as a circulator, to separate the transmit and receive signals. Different polarizations on transmit and receive have also been used in some CW radars to enhance isolation, although this can add expense.

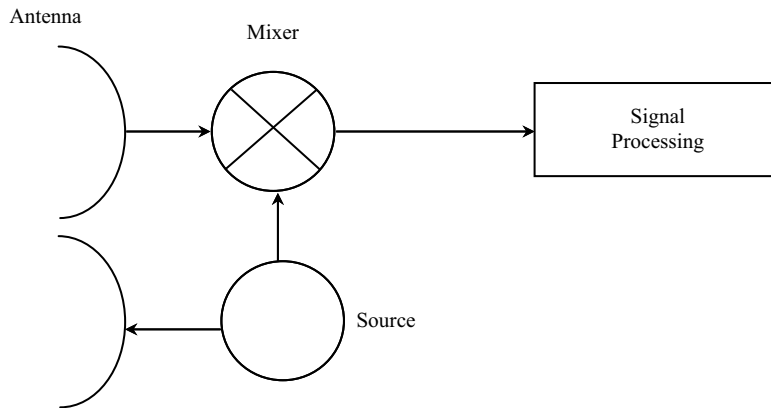


FIGURE 2.2-4 ■ Homodyne CW Radar Block Diagram with Separate Antennas for Transmit and Receive.

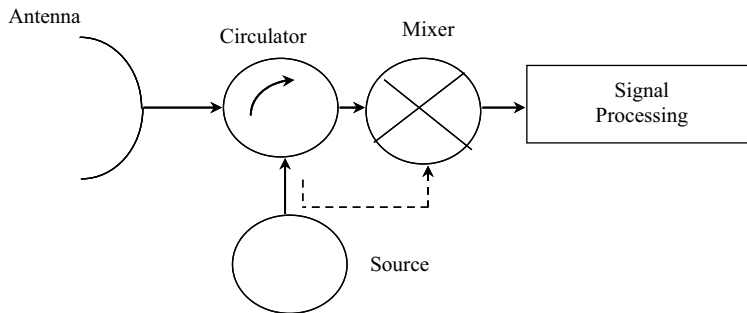


FIGURE 2.2-5 ■ Single Antenna Homodyne CW Radar Block Diagram.

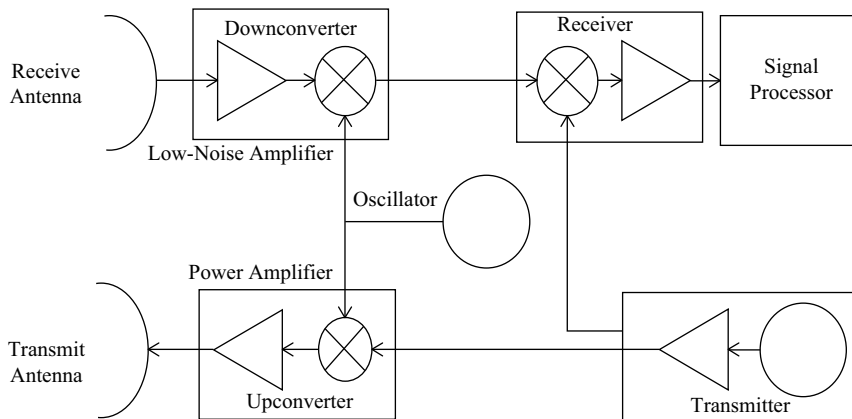


FIGURE 2.2-6 ■ Heterodyne CW Radar Block Diagram.

All approaches have a degree of coupling or leakage that ultimately limits the isolation and hence maximum detection range.

Finally, the heterodyne CW radar configuration offers another improvement in performance but at the cost of further complexity [5]. As shown in Figure 2.2-6, the transmit modulation is imparted at a convenient *intermediate frequency* (IF) and then mixed with the local oscillator to the desired carrier frequency. The receive signal is mixed with the local oscillator, and the signal processing is done at IF. An important advantage of the heterodyne configuration is moving the received signal frequency farther from the transmit frequency because both amplitude modulation and phase modulation noise

power of the transmit signal decreases with separation from the carrier. Filtering improves performance still further by reducing the effects of otherwise broadband noise. The design approach depicted in Figure 2.2-6 offers the potential for good performance with separate transmit and receive antennas enabling good isolation, an RF power amplifier (PA) for higher transmit power, a low noise amplifier (LNA) before the mixer for lower noise figure, and heterodyne mixing for lower amplitude and phase noise.

The technology underpinning the design and implementation of CW radar systems is relatively simple and lends itself well to large-volume production in solid-state form. Indeed, the development of FMCW radar technology is resulting in short-range, low-cost systems that have high performance and are able to resolve objects separated by as little as 20 cm in radial range. The main limitation is the ease with which long detection ranges can be achieved. However, there are very many applications in which long range is not a design driver and thus CW systems can be a natural solution. In the next section, linear FMCW modulation is examined in detail, as this is the workhorse of most modern CW systems. FMCW offers a combination of performance and cost that make it highly attractive for many applications, especially for the rapidly emerging area of automotive radar systems, which has enormous commercial potential.

2.3 | FREQUENCY MODULATED CW RADAR

In this section, we introduce the linear frequency modulated waveform for CW radar systems. We have already discussed how unmodulated CW radar systems can measure target velocity via the Doppler frequency shift and target direction with a directional antenna; they cannot measure range, however. Measuring range requires a timing reference encoded onto the transmit waveform. In CW systems, this is applied by modulating the frequency or phase of the signal to be transmitted. Although there are other forms of frequency modulation, such as sinusoidal and nonlinear FM, we concentrate on the linear case as it enables the key principles to be introduced and is the most widespread form of modulation in use in CW radar systems today. We also describe the process by which the signal-to-noise ratio and range resolution may be estimated in a linear FMCW radar system together with limits on system performance.

2.3.1 The Linear FMCW Waveform

Figure 2.3-1 shows the transmit and receive frequency of an FMCW radar waveform as a function of time. The waveform illustrated is a sawtooth linear FMCW waveform. The receive signal comes from the echo of a target located a distance R from the transmitter. The resulting beat frequency, f_b , is the instantaneous difference in frequency between the transmit and receive waveforms. Measurement of the beat frequency allows us to determine the range to a target because it is directly related to target delay. The duration of the linear modulation is set so that it lasts longer than the round-trip transit time for the most distant target to be observed, thus avoiding ambiguities.

In Figure 2.3-1 the total peak-to-peak frequency deviation is ΔF and is termed the *modulation bandwidth*. The modulation period, T_m , is the time between repetitions of the sawtooth waveform. Together these two quantities (along with their repetition) form a triangle similar but offset to that formed by the beat frequency, f_b , and the transit time delay, t_d (the time difference between the transmit and receive waveforms, that is, the

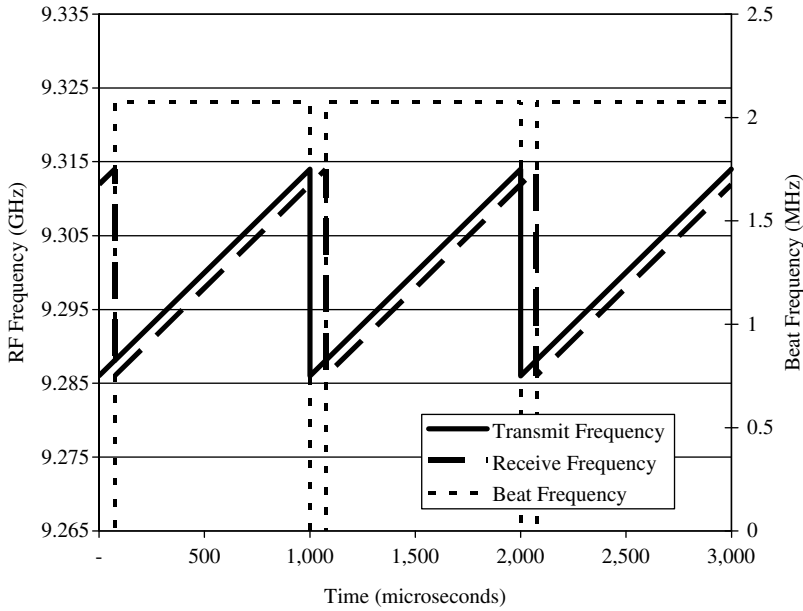


FIGURE 2.3-1 ■ Transmit-and-Receive Frequency as a Function of Time with Beat Frequency Shown.

range to a target). A relation can thus be formed between the modulation bandwidth, the modulation period, the beat frequency, and the transit time that leads to the determination of range to a target:

$$\frac{f_b}{t_d} = \frac{\Delta F}{T_m} \quad (2.3-1)$$

where

- f_b = beat frequency,
- t_d = round-trip propagation time delay,
- ΔF = modulation bandwidth, and
- T_m = modulation period.

The round-trip propagation time, t_d , is proportional to range and is given by

$$t_d = \frac{2R}{c} \quad (2.3-2)$$

where

- R = range to target and
- c = propagation velocity = 3.0×10^8 m/s.

Substituting for t_d in equation 2.3-1 and rearranging terms leads to the following expression, known as the *FMCW equation*, which relates beat frequency and range:

$$f_b = \frac{\Delta F 2R}{T_m c} \quad (2.3-3)$$

The beat frequency is the product of the frequency sweep slope (i.e., the total frequency deviation divided by the modulation period) and the transit time. Thus, for the

parameters shown in Figure 2.3-1, assuming a 28-MHz modulation bandwidth and a 1-ms modulation period, the resulting beat frequency is 2.1 MHz, which equates to a target located at a range of 11.1 km.

Other formulations of the FMCW radar equation may be constructed. For example, a sawtooth waveform modulation period, T_m , is the inverse of the modulation frequency, f_m and thus the FMCW equation can be written as

$$f_b(\text{sawtooth}) = \Delta F f_m \frac{2R}{c} \quad (2.3-4)$$

If the modulation type is a triangular waveform, then there is an additional factor of 2 in the numerator because the period of the triangle wave, including both upswEEP and downswEEP, is twice that of the sawtooth wave for the same frequency slew rate:

$$f_b(\text{triangle}) = \frac{\Delta F 4R}{T_m c} \quad (2.3-5)$$

The Doppler effect will shift the frequency of the received signals for moving targets, and the beat frequency for an FMCW sawtooth waveform that swEeps up in frequency is given by

$$f_b = \frac{-\Delta F 2R}{T_m c} + \frac{2Vf_0}{c} \quad (2.3-6)$$

Equation 2.3-6 shows the measured beat frequency to be dependent on both Doppler velocity and target range. In other words, moving targets will appear at an incorrect range. The ambiguity resulting from this “range-Doppler” coupling can be resolved if the waveform employs two frequency slew rates or slopes. The triangle waveform with alternate up and down frequency swEeps is a common choice. For the triangle waveform, range is linearly proportional to the difference in the upswEEP and downswEEP beat frequencies, and velocity is proportional to the sum of the beat frequencies. For the triangle waveform, the upswEEP and downswEEP beat frequencies are given by

$$f_b(\text{triangle, upswEEP}) = \frac{-\Delta F 4R}{T_m c} + \frac{2Vf_0}{c} \quad (2.3-7)$$

and

$$f_b(\text{triangle, downswEEP}) = \frac{\Delta F 4R}{T_m c} + \frac{2Vf_0}{c} \quad (2.3-8)$$

so that range, R , is given by

$$R = \frac{T_m c}{8\Delta F} (f_{b(\text{downswEEP})} - f_{b(\text{upswEEP})}) \quad (2.3-9)$$

and velocity, V , by

$$V = \frac{-c}{4f_0} (f_{b(\text{downswEEP})} + f_{b(\text{upswEEP})}) \quad (2.3-10)$$

Thus, for a single target there are two equations and two unknowns – range and velocity – and hence we can solve for these two quantities. Figure 2.3-2 shows this graphically where separate target range and velocity measurements are made using a triangular modulation waveform. The intersection of the two lines provides the solution to equations 2.3-7 and 2.3-8. The two lines on the graph represent the two different beat frequencies derived from the two different slopes of the triangular modulation and hence

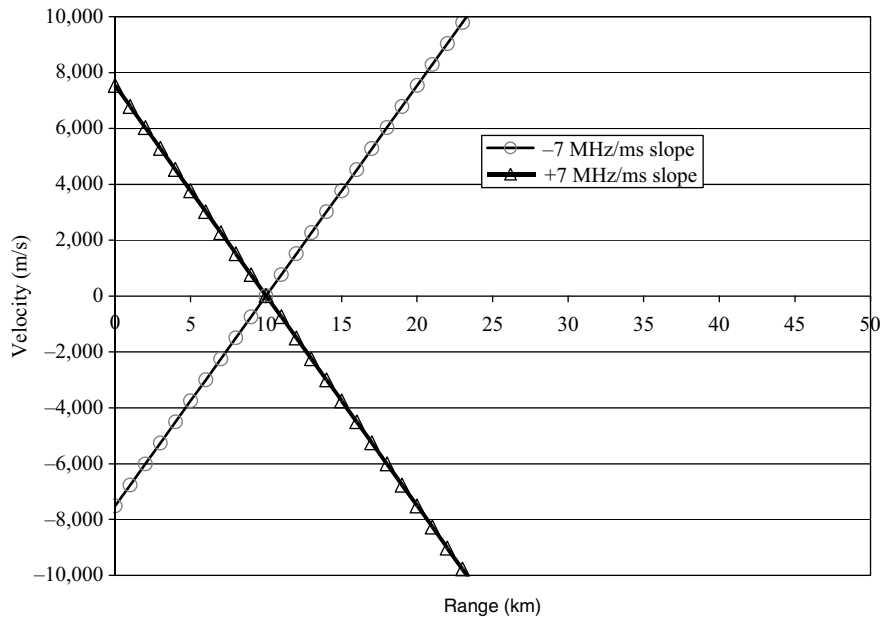


FIGURE 2.3-2 ■ Target Range and Velocity Estimation Using Two Different Beat Frequencies Generated by the Two Different Slopes of a Triangular Waveform.

the actual target range and velocity. In this example, the target range is 10 km and the target was stationary.

For multiple targets, an FMCW waveform with multiple pairs of slopes can resolve the range-Doppler ambiguities. The number of FMCW slope pairs that can be supported ultimately determines the number of targets that are resolvable.

2.3.2 Linear FMCW Waveform Trades

In practice, choosing FMCW waveform parameters for a given application requires careful consideration of numerous trade-offs. These trade-offs are necessary to ensure that measurements can be made with sufficient accuracy and precision and hence enable determination of target range and velocity within desired limits. The key trade-offs are summarized in Table 2.3-1; they broadly consist of decreasing and increasing the modulation bandwidth, the modulation period, and the beat frequency. We next consider how these parameters influence measurement accuracy.

Decreasing the modulation bandwidth reduces the RF bandwidth over which the antenna and other front-end components must operate; generally, this requires simpler components, so costs can be reduced. Decreasing the modulation bandwidth also favors higher output powers and lower amplitude and phase noise. Increasing the modulation bandwidth offers improved range resolution and lower radiated power spectral density. Improved range resolution allows spatial information about targets to be determined, and this can be exploited for modes of operation such as target recognition. Lower radiated power spectral density can reduce the likelihood of the emissions being intercepted because they are spread over a wider frequency range so that the power transmitted per unit frequency is reduced.

Decreasing the modulation period will increase both the slope of the modulation and the magnitude of the beat frequency. This helps avoid interference with other forms of modulation that could be applied such as conical scanning demodulation for improved angular location of targets, automatic gain control (AGC), or other internal processing

TABLE 2.3-1 ■ FMCW Waveform Trade-offs

Waveform Parameter	Reasons to Decrease	Reasons to Increase
Modulation bandwidth	<ul style="list-style-type: none"> • Narrower bandwidth RF components • Higher power sources available • Lower amplitude and phase noise 	<ul style="list-style-type: none"> • Finer ideal range resolution • Lower radiated power spectral density • Increased slope • Increased beat frequency
Modulation period	<ul style="list-style-type: none"> • Increased slope • Increased beat frequency • Avoids interference with conical scan and other modulations • Reduced beat frequency chirp or smear due to target motion • Increased unambiguous velocity 	<ul style="list-style-type: none"> • Increased transmit and receive overlap • Increased coherent processing interval • Increased effective processed transmit bandwidth and power • Better range and Doppler resolution • Narrower bandwidth linearizer
Beat frequency	<ul style="list-style-type: none"> • Lowered ADC sample frequency • Narrower bandwidth range bin filters • Less beat frequency bandwidth required to cover given range swath • Greater source phase noise correlation 	<ul style="list-style-type: none"> • Lower amplitude and phase noise at greater separation from carrier

control loops. Increasing the modulation period increases the interval over which processing can be carried out coherently (the coherent-processing interval or CPI). A longer CPI offers the potential for finer receiver frequency resolution and consequently finer range and Doppler resolution. Increasing the modulation period also decreases the modulation frequency and decreases the required bandwidth for the frequency sweep linearity compensation circuitry [6] but at the loss of finer range and Doppler resolution.

The FMCW beat frequency signal is estimated via a bank of narrowband filters that form range resolution bins. The beat frequency is usually digitized and the filter bank generated via a fast fourier transform (FFT). This permits convenient application of weighting functions to reduce range side-lobes. The analog-to-digital converter (ADC) and digital processing must have wide dynamic range because radar returns from near and far ranges are present simultaneously. For a 1-ms modulation period, with 500-MHz frequency deviation and 1-km range, the beat frequency is 3.3 MHz, requiring an ADC sampling rate of at least twice that frequency to avoid aliasing. For lower beat frequencies, the receiver filter bandwidth required for each range bin is less for a given range resolution. It also follows that the total receiver bandwidth required to cover a given range swath is less. For higher beat frequencies, a given Doppler shift corresponds to a smaller apparent shift in range.

If the linear FMCW radar operates with a constant beat frequency (as might be the case when a limited bandwidth analog frequency filter bank forms the range bins), then the frequency sweep slope must be changed to keep the beat frequencies of interest within the bandwidth of the filters as the range of interest changes. As the transit time decreases for shorter ranges, the slope must increase to keep the beat frequency constant. For constant frequency deviation, this requires shorter modulation periods at shorter

range. Since range resolution is proportional to the product of the range and the ratio of the filter bandwidth to the filter center frequency, the linear FMCW waveform approach has the coarsest range resolution at the longest range.

2.3.3 FMCW Signal-to-Noise Ratio (SNR) Estimation

In this section, a methodology is presented for estimating the signal power to noise ratio for both point targets and from area clutter. Example calculations use the PILOT radar as an exemplar. The PILOT radar was originally developed by the Philips Corporation of the Netherlands (now part of the Saab group) as a surveillance sensor for both civil and military applications. The low peak powers of PILOT make it much less likely to be intercepted by an enemy electronic support (ES) system and therefore particularly attractive for short- to medium-range military surveillance.

In CW radar, both system noise power and AM and FM noise are important in determining the overall performance, including the computation of SNR. Amplitude and phase noise will be examined in the next section. As with any radar system, the received signal power, P_r , is given by the radar equation:

$$P_r = \frac{P_t G_t G_r \lambda^2 \sigma}{(4\pi)^3 (R)^4 L} \quad (2.3-11)$$

where

P_t = transmit power,

G_t = transmit antenna gain,

G_r = receive antenna gain,

λ = wavelength,

σ = target radar cross section,

R = slant range, and

L = loss.

The noise power is given by the following equation,

$$N = kT_0BF \quad (2.3-12)$$

where

k = Boltzmann's constant = 1.38×10^{-23} W/(Hz K),

T_0 = reference temperature = 290 K,

B = bandwidth, and

F = noise figure.

This expression assumes that the receiver components have a physical temperature of 290 K and that the antenna is pointed at an absorbing surface such as the earth.

The noise floor of the radar determines the fundamental limit on detection range and is dominated by the performance of the low-noise amplifier if used, or the mixer otherwise. Table 2.3-2 shows a calculation of the noise floor using the PILOT radar parameters. The noise floor allows us to assess the detection performance of the radar by designing the system such that the echo signal is sufficiently larger than the noise so that acceptable values for the probability of detection and false alarm occur. As a rule of thumb, this implies a minimum SNR of 10 dB or greater for reliable detection performance.

TABLE 2.3-2 ■ PILOT FMCW Radar Noise Power Calculation

Symbol	Description	Value	Units	Value (dB)
k	= Boltzmann's constant	= 1.38E-20	mW/(Hz K)	= -198.6 dBm/(Hz K)
T_0	= Reference temperature	= 290	K	= 24.6 dBK
B	= Bandwidth	= 1,000	Hz	= 30.0 dBHz
F	= Noise figure	= 3.2		= 5.0 dB
N	= Receiver noise power	=		= -139.0 dB

TABLE 2.3-3 ■ PILOT FMCW Radar Signal Power Calculation

Symbol	Description	Value	Units	Value (dB)
P_t	= Average transmit power	= 1	W	= 30.0 dBm
G_t	= Transmit antenna gain	= 1,000		= 30.0 dBi
G_r	= Receive antenna gain	= 1,000		= 30.0 dBi
λ^2	= Wavelength ²	= (0.032) ²	m ²	= -29.8 dBsm
σ	= RCS	= (100) ²	m ²	= 20.0 dBsm
$(4\pi)^3$	= 1984	= 1984		= -33.0 dB
R^4	= (Slant range) ⁴	= (44.4) ²	km ⁴	= -185.9 dBsm
P_r	Target signal power			= -138.7 dBm

Table 2.3-3 illustrates an example radar range equation computation for the PILOT radar parameters. The table shows that the signal power for a 20-dBsm target RCS at a range of 44 km is -139 dBm. Note that the output power is only 1 W, typical of this class of FMCW surveillance radar systems. An output power of 1 W is less than most mobile phones; we can see how a signal of this strength might be hidden among many other existing emissions in the complex and congested electromagnetic spectrum. Most mobile phones, for example, have an output of between 2 W and 3 W. The antenna gain of 30 dBi and a wavelength of 3.2 cm (corresponding to the 9.3-GHz nominal RF center frequency) are also consistent with radars of this class. In this tabular calculation, the parameter values are converted to decibels, terms in the numerator of equation 2.3-11 are added, and terms in the denominator are subtracted.

The maximum transmit power for the PILOT radar is 1 W, but lower power levels are selectable in 10-dB increments down to 1 mW for shorter ranges.

The four lower curves in Figure 2.3-3 show the echo signal power for the PILOT radars as a function of range for different selections of output power levels. The noise floor of the radar is also shown sitting at the calculated value of -139 dBm. In addition, the four upper curves show the power levels received by an intercept system as a function of range and PILOT transmitter power. The figures in the box at the top right-hand corner show the maximum radar-detection range and the equivalent intercept range as a function of transmitter power. The intercept ESM is assumed to have a high sensitivity of -80 dBmi. For this example, the detection range of the PILOT radar always exceeds the range at which it can be detected by an ESM system. For this reason, the PILOT radar was often referred to as being “undetectable.” In reality, the probability of detection is much lower than would be the case with an equivalent conventional pulsed radar, but it may still be detected by equipment with sufficient sensitivity. Further, the preceding is a free space computation and does not account for clutter, multipath, and so on. For example, the

addition of a forward scatter multipath signal component from a smooth or a rough surface will cause a variation in the range at which an ESM is able to detect the radar.

To further illustrate use of the radar range equation across the spectrum of CW radar types, we now examine its application to a level gauge measurement FMCW system. Many materials are kept in tanks used on industrial sites. They might contain noxious substances or for other reasons are not easily accessed. The level-measurement radar provides a means of determining the fill height of the tank without human intervention. Radar makes an ideal measurement tool, and the FMCW technique is used routinely. Figure 2.3-4 shows such a radar system mounted on a tank containing a liquid with a level to be measured.

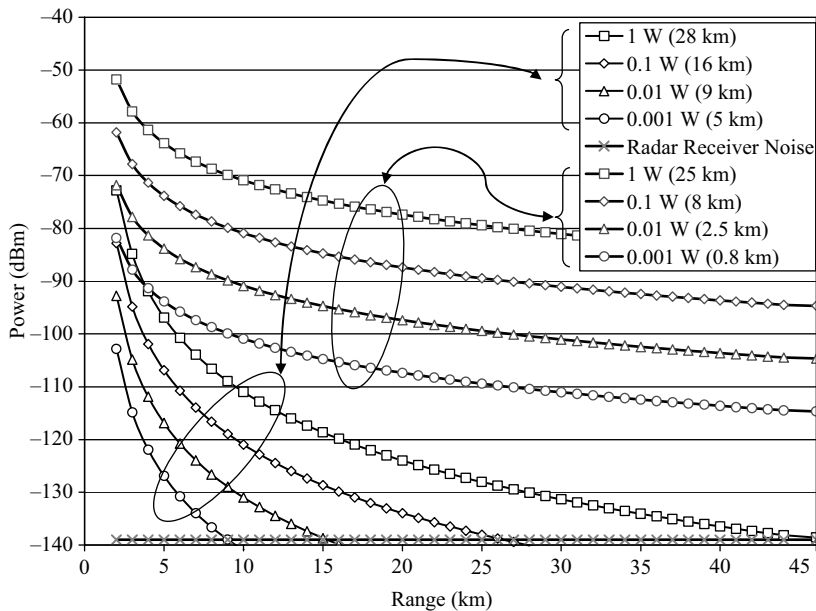


FIGURE 2.3-3 ■ PILOT FMCW Radar Signal Power as a Function of Range along with the Radar Power at an Intercept Receiver.

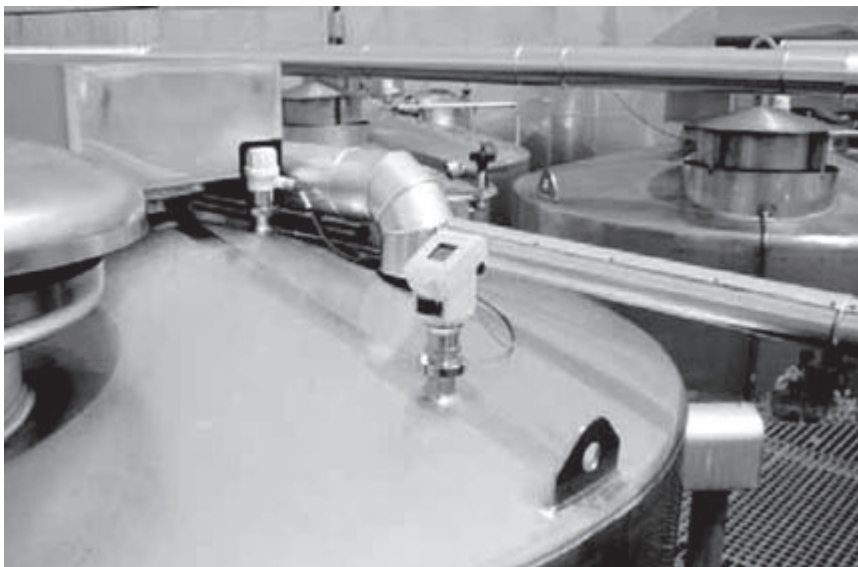
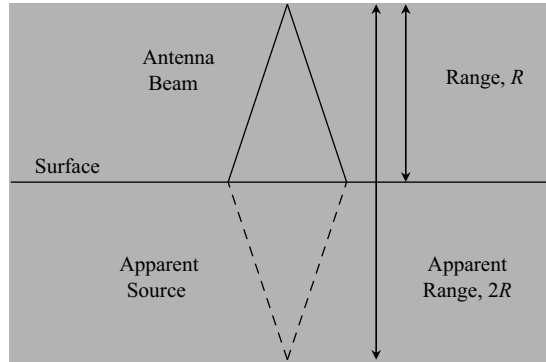


FIGURE 2.3-4 ■ Liquid Level Measurement Radar Mounted on an Industrial Tank.

FIGURE 2.3-5 ■
Modified Bistatic
Radar Equation for
Vertical Incidence.



The detection range may be as little as 1 m; in this case, the time to receive an echo is approximately 6.27 nanoseconds, a demanding measurement task for any radar system. We begin by modifying the radar equation into the bistatic form. This is done so the transmitter can be thought of as being located at its image position due to the reflection from the surface of the liquid as shown in Figure 2.3-5. In effect, this modifies the radar equation into a form closely resembling that of a communications link budget equation. The range measured by the system is therefore twice the actual liquid level height ($2R$) and the reflectivity coefficient of the liquid (or substance), ρ , is used rather than area-normalized RCS, σ^0 , to account for the reflectivity from the surface. The radar equation may be written as

$$\text{SNR} = \frac{P_t G_t G_r \lambda^2}{(4\pi)^2 (2R)^2 L k T_0 B_n F_n} (\rho) \quad (2.3-13)$$

where

P_t = transmit power,

G_t = transmit antenna gain,

G_r = receive antenna gain,

λ = wavelength,

ρ = reflectivity coefficient,

R = slant range,

L = loss,

k = Boltzmann's constant = 1.38×10^{-23} W/(Hz K),

T_0 = reference temperature = 290 K,

B_n = noise bandwidth, and

F_n = noise figure.

For CW radars used in level gauge applications, the surface of metals and conductive liquids such as acids and concentrated saline will reflect almost all of the incident power. FMCW radars generally work well for dielectric constants, or relative permittivity, greater than 2. The relative permittivity of water is 80. The relative permittivity of oils is approximately 3.5, and they reflect approximately 10 percent or -10 dB of the incident power. The relative permittivity of hydrocarbons is approximately 1.5, so they reflect 1 percent or -20 dB. The relative permittivity of a vacuum is 1, and the relative permittivity of most gases is approximately 1.

TABLE 2.3-4 ■ SNR Calculation for Level Gauge CW Radar

Symbol	Description	Value	Units	Value (dB)
P_t	= Average transmit power	= 1	mW	= 0.0 dBm
G_t	= Transmit antenna gain	= 100		= 20.0 dBi
G_r	= Receive antenna gain	= 100		= 20.0 dBi
λ^2	= Wavelength ²	= (0.012) ²	m ²	= -38.3 dBsm
ρ	= Reflectivity coefficient	= 0.01		= -20.0 dB
$(4\pi)^2$	= $(4\pi)^2$	= 158		= 22.0 dB
$(2R)^2$	= $(2 * \text{Range})^2$	= (200) ²	m ²	= 46.0 dBsm
L	= Loss	= 10		= 10.0 dB
k	= Boltzmann's constant	= 1.38E-20	mW/(Hz K)	= -198.6 dBm/(Hz K)
T_0	= Reference temperature	= 290	K	= 24.6 dBK
B_n	= Noise bandwidth	= 100	Hz	= 20.0 dBHz
F_n	= System noise figure	= 1,000		= 30.0 dB
SNR	= Signal-to-noise ratio	= 588		= 27.7 dB

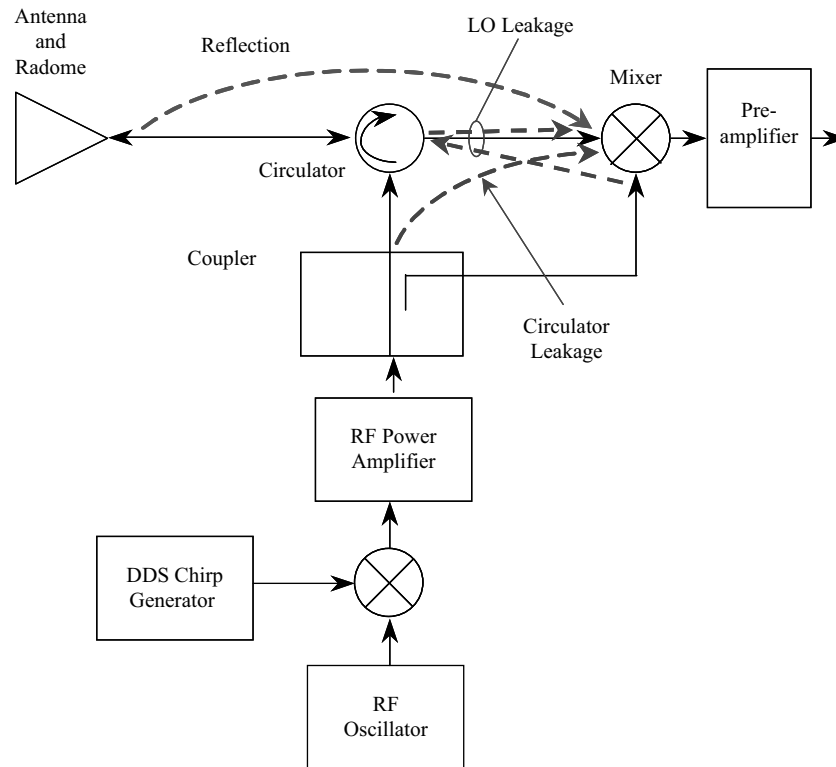
Table 2.3-4 illustrates the SNR calculation for a level gauge at 100-m range with 1-mW transmit power, 20-dBi antenna gain, 0.12-m wavelength, 10-dB loss, -20-dB reflectivity coefficient, 100-Hz bandwidth, and 30-dB noise figure. The parameters are typical of level gauge FMCW measurement radar systems. An increase in power will result in higher levels of signal to noise. However, this does not necessarily translate into improved measurement accuracy as this is usually limited by reverberation caused by reflections from the sides of the tank competing with the reflection from the surface of the liquid. Note also the high value of the system noise figure. This is not atypical of the more simple forms of FMCW radar and is a reflection of performance and cost trade-offs.

Sensitivity time control (STC) is a mechanism used to keep the dynamic range of the received echo power matched to the receiver. STC is the programmed variation of the gain or sensitivity of a radar receiver as a function of time within each pulse repetition interval or observation time so that the receiver is not overloaded by strong echoes or by clutter at close ranges. For FMCW, range is proportional to frequency, and the STC function can be realized by high-pass filtering of the beat frequency signal. Since the radar equation tells us that target return power is proportional to range to the fourth power, a 12-dB/octave, or 40-dB/decade high-pass filter, will provide the STC function and hence reduce the receiver dynamic range requirement. Since ADC technology forces a trade-off between faster sample rates and wider dynamic range, this STC filtering enhances the utilization of limited dynamic range ADCs.

2.3.4 Amplitude and Phase Noise

For CW radars the amplitude and phase noise sidebands of the transmitter can couple into the receiver and degrade the system noise figure if they exceed the thermal noise level. While AM noise levels are generally much lower than phase modulated noise levels, they may dominate the system noise figure because as described below phase noise correlation effects reduce the effective phase noise level. Stove provides an example in which the AM noise degrades the system noise figure by 3 dB and while the FM noise is 60 dB greater than the AM noise there is a 70 dB phase noise correlation effect which results in negligible phase noise degradation of system noise figure [7]. Phase noise in FMCW radar systems can be significantly higher than thermal noise. This

FIGURE 2.3-6 ■
Antenna Reflection
and Circulator
Leakage Paths in
FMCW Homodyne
Radar Front End.



is due to transmitter to receiver leakage; reflections from close in clutter and noise inherent in components such as voltage-controlled oscillators (VCOs). Phase noise subsequently results in errors in the phase-measuring capability of the radar system. Phase noise is a function of frequency and is usually presented as the ratio of signal power to noise power in a given frequency band that is offset from the transmitter carrier frequency. This section introduces transmitter phase noise effects, including those due to front-end reflections and leakage. Figure 2.3-6 highlights potential antenna reflection and circulator leakage paths in an FMCW radar front end along with the role of the mixer, which also introduces phase noise into the system.

The phase noise may be calculated by summing (in logs) all the relevant contributions from the power source through to insertion losses associated with individual components and the appropriate value of phase noise power density at the frequency of operation. Table 2.3-5 shows an example calculation to estimate the phase noise power for the PILOT radar exemplar. This calculation yields a phase noise estimate of -112 dBm due to antenna reflection in a 1-kHz bandwidth at a beat frequency of 1.4 MHz. Significantly, this is more than 27 dB greater than the thermal noise for a 5-dB noise figure. The performance can be improved by providing more isolation between the transmitter and the receiver paths. This is achieved using separate antennas to transmit and receive or by introducing a reflected power canceller. For example, with 30-dB additional isolation provided by a reflected power canceller, the phase noise power is reduced to -142 dBm, which is 3 dB less than the thermal noise for a 5-dB noise figure. This assumes a 1-W or 30-dBm source power that is attenuated 0.5 dB by the isolator

TABLE 2.3-5 ■ Antenna Reflection Phase Noise Power Calculation

Parameter	Value	Units
Source power (1 W)	30.0	dBm
Isolator insertion loss	-0.5	dB
Total loss for 20-dB LO coupler	-0.5	dB
Circulator insertion loss	-0.5	dB
Antenna power reflection coefficient – for 2:1 VSWR	-9.5	dB
Circulator insertion loss	-0.5	dB
Phase noise power density at 1.4 MHz	-130.0	dBc/Hz
Phase noise correlation factor at 1.4 MHz – for 3.3-ns time difference	-30.7	dB
Range bin bandwidth (1 kHz)	30.0	dBHz
Antenna reflection phase noise power at 1.4 MHz in 1-kHz bandwidth	-112.2	dBm
Reflected power canceller	-30.0	dB
Antenna reflection phase noise power at 1.4 MHz in 1-kHz bandwidth after reflected power canceller	-142.2	dBm

and another 0.5 dB by the coupler that provides the LO drive signal. The circulator insertion loss is 0.5 dB, so a power of 28.5 dBm is presented to the antenna port.

Using the same source to transmit and receive a signal reduces the effect of the source phase noise because the noise of the received signal is correlated to that of the transmitted signal [6]. The phase noise correlation factor is termed K^2 , and it depends on the offset frequency from the carrier and the delay between the transmitted and received signals. For FMCW homodyne radar systems, the carrier offset is the beat frequency, f_b . The delay t_r is the difference between the source to mixer LO port path and the source to antenna reflection to mixer RF port path. We can write:

$$K^2 = 2 \bullet [1 - \cos(2\pi f_b t_r)] \quad (2.3-14)$$

Since

$$\sin^2 \alpha = \frac{1}{2}(1 - \cos 2\alpha) \quad (2.3-15)$$

then

$$K^2 = 4\sin^2(\pi f_b t_r) \quad (2.3-16)$$

or

$$K^2 \cong 4(\pi f_b t_r)^2, \quad \text{for small products of } f_b \text{ and } t_r \quad (2.3-17)$$

This example assumes that the delay is 3.3 ns, corresponding to a 1-m free space path length difference between the path from the source to the mixer LO port and from the source to the antenna reflection to mixer RF port. This yields a correlation factor of $K^2 = -30.7$ dB. Adjusting the LO path length to cancel the strongest reflected signal path will improve the phase noise correlation and reduce the reflected noise component. This technique will be less effective for applications where antenna scanning results in a changing distance to the reflection point (such as for radome reflections). This static cancellation will also increase the path and decrease the phase noise correlation for other reflected signals and internal leakage signals. Static cancellation will have limited bandwidth.

Lower beat frequencies result in greater phase noise power density and correlation. The phase noise correlation factor is approximately proportional to the square of the beat frequency when the product of f_b and t_r is small. Over regions where the source phase noise follows a 20-dB/decade slope, these effects will approximately cancel one another, resulting in approximately constant noise power as a function of beat frequency. The phase noise closer to the carrier may typically follow a 30-dB/decade slope, resulting in greater noise for lower beat frequencies.

A number of methods have been used to improve phase noise performance, and they generally rely on cancellation techniques that attempt to minimize losses. Figure 2.3-7 shows an example schematic of part of the ELVA FMCW radar system (this is a 200-mW FMCW radar developed for traffic-control applications) in which a phase shifter is inserted between the circulator and antenna to help cancel the antenna reflected power and circulator leakage that otherwise increases the system noise figure and degrades the sensitivity of the radar [8]. Figure 2.3-8 shows the measured power reflected from the antenna along with the power after phase shifter tuning. As an example consider frequencies from 93.8 GHz to 93.9 GHz where the antenna reflection decreases from 26 dB to 29 dB below the transmit level. After phase-shifter cancellation, the power is at least 35 dB below the transmit level. This also highlights that phase-shift cancellation is only effective over a limited bandwidth. For wide bandwidth cancellation, a time-delay method is necessary.

Johnson and Brooker [9] describe a reflected-power canceller (RPC) used in a 94-GHz FMCW radar. This manually adjustable vector RPC permits adjustment of the amplitude and the time delay of a signal used to cancel front-end reflections in order to minimize the performance degradation that would otherwise result. The PILOT radar

FIGURE 2.3-7 ■
Block Diagram of
ELVA-1 Front End.

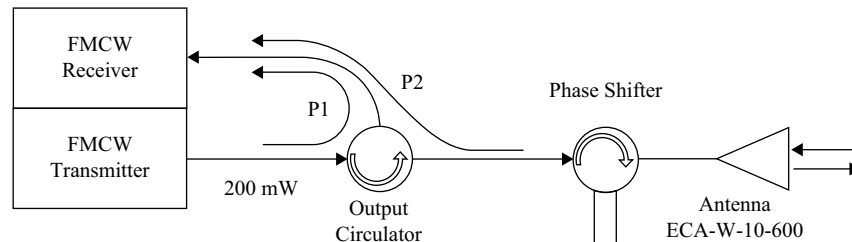
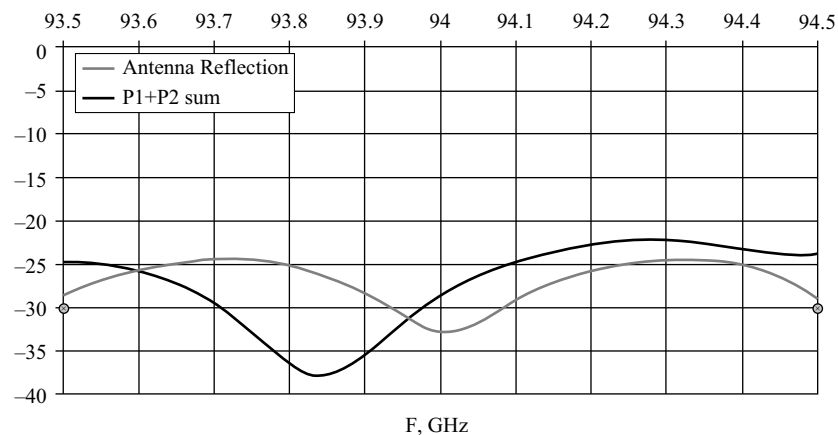


FIGURE 2.3-8 ■
ELVA-1 MMW
FMCW Radar
System Antenna
Reflection Power as
a Function of
Frequency.



system exploits a dynamic version of RPC as shown in Figure 2.3-9. The RPC uses an X-band vector modulator to adaptively inject a signal with the appropriate amplitude and phase before the mixer to cancel reflected power and thus enhance sensitivity. The RPC offers a 30-dB transmit-to-receive isolation improvement for PILOT, from 20 dB without the RPC to 50 dB with. This compares favorably with the less elegant but pragmatic solution of using separate transmit and receive antennas to achieve sufficient isolation. Table 2.3-6 lists the isolation improvements achieved with four different antennas and signal bandwidths [10].

Mathematically, if a phasor of amplitude A is cancelled using a separate phasor of amplitude, a , and phase error, θ , the resulting normalized residual power can be obtained from the law of cosines:

$$\left(\frac{\rho}{A}\right)^2 = 1 + \left(\frac{a}{A}\right)^2 - 2\frac{a}{A}\cos(\theta) \quad (2.3-18)$$

It is possible to parameterize the problem using the phase of the residual, allowing the complete set of possible canceling phase and amplitudes to be plotted for any given residual power. In terms of the phase, φ , of the residual phasor, the relative amplitude of the canceling phasor is given by

$$\left(\frac{a}{A}\right)^2 = 1 - 2\frac{\rho}{A}\cos(\varphi) + \left(\frac{\rho}{A}\right)^2 \quad (2.3-19)$$

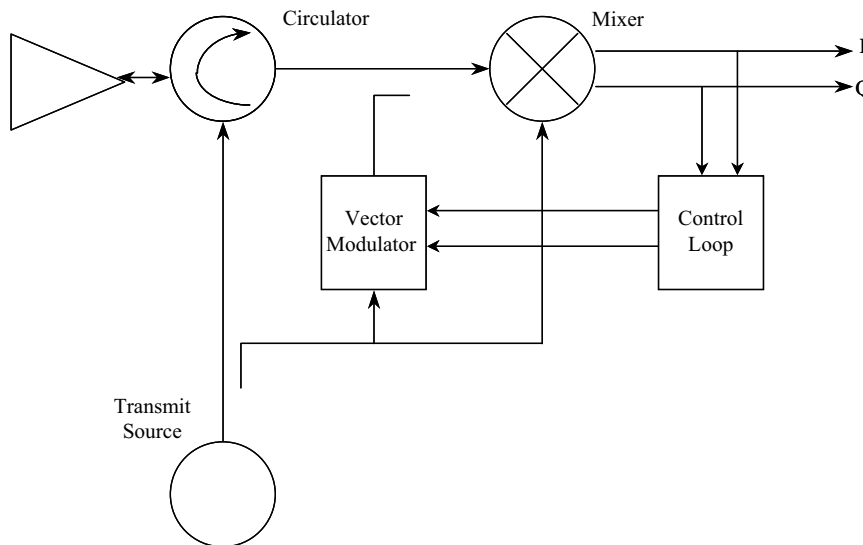


FIGURE 2.3-9 ■ Reflected Power Canceller Block Diagram.

TABLE 2.3-6 ■ Reflected Power Canceller Isolation Improvement Performance

Improvement	Bandwidth	Antenna
40 dB	1,200 MHz	“Perfect antenna”
33 dB	400 MHz	2.1-m (7-ft) navigation
40 dB	650 MHz	Small navigation
35 dB	1,000 MHz	1.5-m (5-ft) navigation

The corresponding phase error of the canceling phasor can be obtained from the law of sines:

$$\sin(\theta) = \frac{\rho}{a} \sin(\varphi) \quad (2.3-20)$$

Figure 2.3-10 shows contours of amplitude and phase errors for cancellation ratio values of -40 dB, -35 dB, and -30 dB. With perfect cancellation amplitude ($a = A$), a residual power of -30 dB is obtained with $\theta = 1.8^\circ$. With perfect phase cancellation, -30 dB is obtained with a relative amplitude of -0.279 dB or $+0.270$ dB.

The cancellation phase is constant for a static target or for static clutter and a fixed frequency. However, for linear FM (i.e., a quadratic phase modulation) and a static target, the cancellation phase changes as a function of frequency. If the reflection point is moving, dynamic adaptivity is required. Any lag in the cancellation control loop will lead to a cancellation phase error. An important system characteristic is the loop response time (loop delay), which essentially determines the depth of the cancellation for the FMCW radar. As the frequency sweeps, the delay difference between the feed-through path and the leakage path causes a time-varying phase difference. For the linear FM case, this will form a frequency difference that is proportional to frequency sweeping rate and the delay difference. This is captured as follows

$$\Delta f = \frac{\Delta f_{\text{sweep}}}{T_p} t_D \quad (2.3-21)$$

where

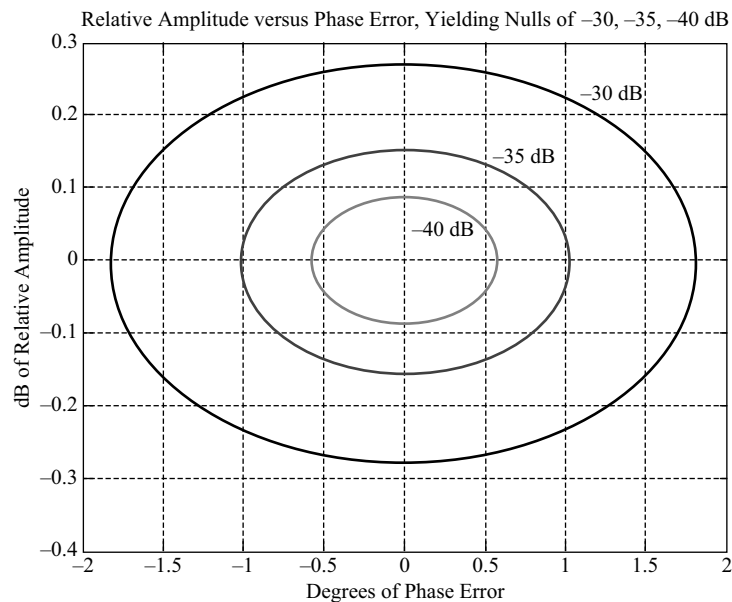
Δf = frequency difference between leakage signal and reference signal,

Δf_{sweep} = frequency sweep bandwidth,

T_p = pulse repetition time, and

t_D = maximum RF delay mismatch.

FIGURE 2.3-10 ■
Contours of
Amplitude and
Phase Errors for -40
dB, -35 dB, and
 -30 dB Cancellation
Ratios.



To compensate this frequency difference, a time-varying error vector has to be generated through the detection of the frequency difference and the extraction of phase information. Because of the finite response time of the loop, the controlling error vector variation always lags behind the phase difference variation, limiting the cancellation performance:

$$\Delta\phi = 360^\circ \cdot \Delta f \cdot t_s \quad (2.3-22)$$

where

$\Delta\phi$ = phase error in degree between leakage signal and feed through signal and

t_s = maximum loop response time.

Substituting equation 2.3-21 into equation 2.3-22,

$$\Delta\phi = 360^\circ \cdot \frac{\Delta f_{\text{sweep}}}{T_p} \cdot t_D \cdot t_s \quad (2.3-23)$$

Lin *et al.* [11, 12] determined that for a 2-GHz total frequency deviation and a 10-ms modulation period, with a 200-MHz/ms sweeping rate and a 1-ns RF delay mismatch, a 35-dB cancellation requires a phase error of less than 1° . The cancellation loop response time should be less than 13.8 μs , which corresponds to at least 73.5-kHz bandwidth and requires a real-time cancellation control loop. Thus, from equation 2.3-23, we have

$$\Delta\phi = 360^\circ \cdot \frac{2 \text{ GHz}}{10 \text{ ms}} \cdot 1 \text{ ns} \cdot 13.6 \mu\text{s} = 360^\circ \cdot 0.00272 = 0.98^\circ$$

For the PILOT FMCW radar parameters in the short-range mode with a 70-MHz frequency deviation and a 1-ms modulation period (and assuming a 1-ns delay mismatch), the cancellation control loop response time must be 40 μs , corresponding to a 25-kHz loop bandwidth. From 2.3-22, we have

$$\Delta\phi = 360^\circ \cdot \frac{70 \text{ MHz}}{1 \text{ ms}} \cdot 1 \text{ ns} \cdot 40 \mu\text{s} = 360^\circ \cdot 0.0028 = 1^\circ$$

and in the long-range mode the PILOT frequency deviation is reduced to 7 MHz; with a ten times lower frequency sweep slope, the response time can increase correspondingly by ten times to 400 μs . This equates to a 2.5-kHz loop bandwidth such that the phase error is maintained at 1° ; for example,

$$\Delta\phi = 360^\circ \cdot \frac{7 \text{ MHz}}{1 \text{ ms}} \cdot 1 \text{ ns} \cdot 400 \mu\text{s} = 360^\circ \cdot 0.0028 = 1^\circ$$

The phase noise for FMCW radar is a function of frequency. Figure 2.3-11 shows examples of both a simulated and a measured transmitter phase-modulated (PM) noise spectrum for the MMIC-based 77-GHz radar front-end block diagram shown in Figure 2.3-12. Note that the PM noise is approximately -100 dBc/Hz at a 1-MHz offset from the carrier and that the slope is approximately 30 dB/decade. Laloue *et al.* [13] used a commercially available nonlinear simulator to compute the amplitude-modulated (AM) and PM signal distortion introduced by the nonlinearities of the transmitter on an FMCW signal. They characterized this radar transmitter driven by a sawtooth FMCW

FIGURE 2.3-11 ■
 Simulated and
 Measured
 Transmitter PM
 Noise Spectrum.

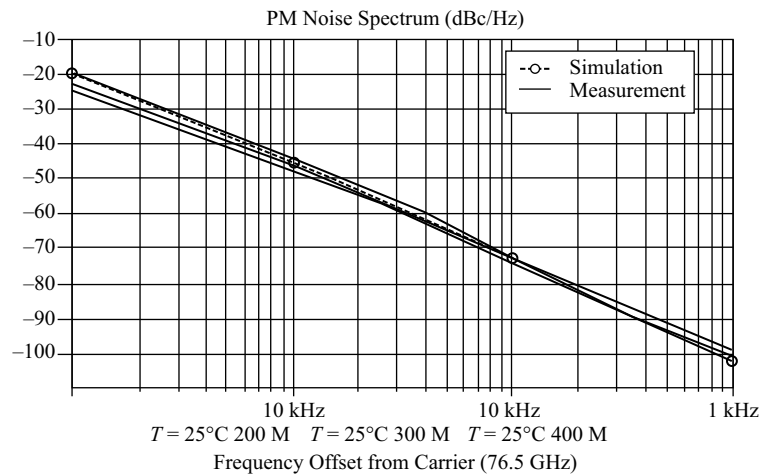
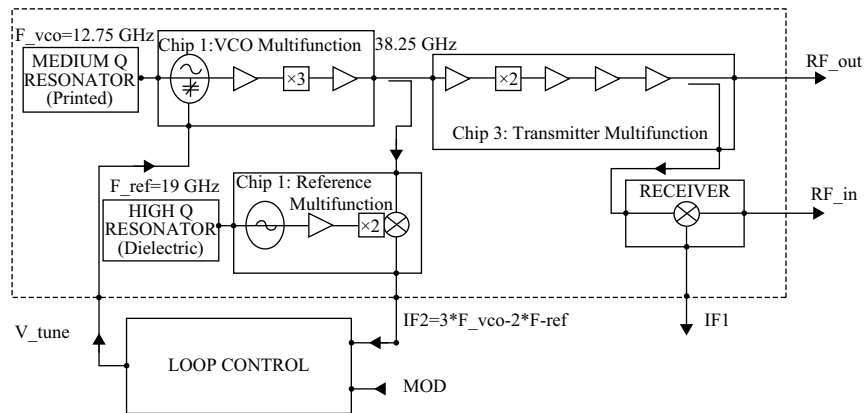


FIGURE 2.3-12 ■
 Block Diagram of an
 MMIC-based 77-
 GHz Radar Front
 End.



signal issuing from a VCO and successfully compared measured and simulated PM-to-AM conversion coefficients.

Figure 2.3-13 shows an example of the phase noise spectrum for *dielectric resonant oscillators* (DROs) that are both *free-running* (FRDRO) and *phase-locked* (PLDRO) while operating at 14 GHz. Both have approximately -140 dBc/Hz phase noise at 1 MHz. The FRDRO phase noise increases approximately 20 dB/decade below 1 MHz, while the PLDRO increases approximately 10 dB/decade, with a plateau around 100 kHz [14].

Interruption of the FMCW waveform avoids simultaneous transmit and receive, thus improving sensitivity and allowing longer-range operation. This variation of FMCW – interrupted (IFMCW) – involves turning the transmitter on and off such that the transmission time is matched to the round-trip propagation time and the reception time. This, of course, reduces the transmit duty cycle by a factor of 2, which reduces the average transmit power by at least 3 dB. This waveform approach also offers the benefit of reducing the transmit phase noise effects by more than the loss in average transmit power so that overall the SNR is enhanced (G Brooker [15] page 329).

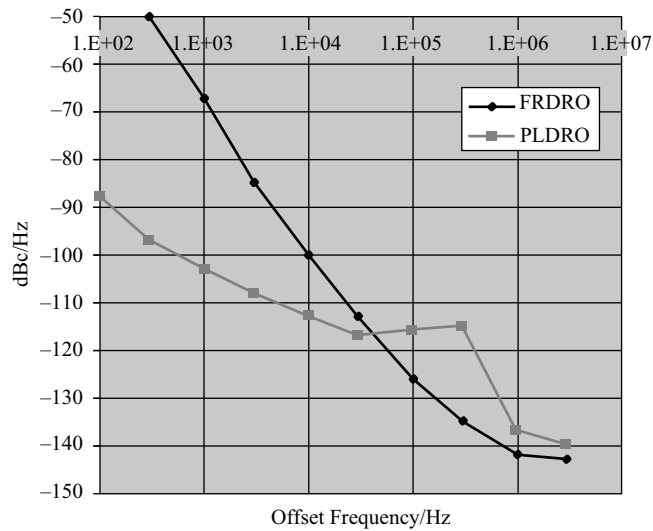


FIGURE 2.3-13 ■ Phase Noise for an FRDRO and a PLDRO Operating at 14 GHz.

Brooker *et al.* [15, 16] reported on an airborne IFMCW imaging radar that employed a 120-MHz frequency deviation triangle waveform with two fixed 20- μ s transmit intervals and 20- μ s receive intervals on the up-sweep and two on the down-sweep. The 20- μ s transmit interval results in no eclipsing for targets at the 3-km maximum range. For targets at shorter ranges down to the 1.5-km minimum, the increase in eclipsing loss is more than compensated by the increase in SNR due to the effect of the inverse of range to the fourth power. Almorox-Gonzalez *et al.* [17, 18] reported an IFMCW radar that staggered the modulation period to help reduce spurious harmonics.

2.3.5 Area Clutter RCS

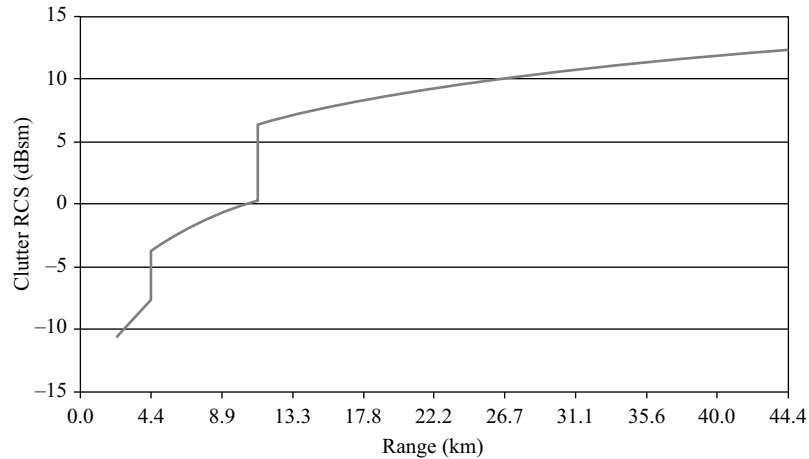
Unwanted reflections from the scattering environment in the form of clutter will dominate radar performance if the echo power of the clutter is significantly above that of system noise. Volumetric clutter, such as that caused by weather, is usually small, and its contribution at short range is rarely significant. However, surface clutter as caused by reflections from the surface of the land or sea and reverberations in a level-measurement radar system can result in echoes significantly above the noise floor.

Consider the following example. The RCS of area clutter, σ_c , is the product of the area-normalized backscatter, σ^0 , and the radar resolution cell area, A_c . If we assume an area-normalized backscatter coefficient, $\sigma^0 = -30$ dB; a range, $R = 44$ km; an azimuth beamwidth, $\theta_{az} = 1.3^\circ$; and range resolution, $\Delta CR = 24$ m, then the clutter RCS, σ_c , is approximately 17 m² or 12 dBsm as given by

$$\begin{aligned}
 \sigma_c &= \sigma^0 A_c = \sigma^0 R \frac{\theta_{az}}{\sqrt{2}} \delta_R \\
 &= (0.01) \left[(44,448 \text{ m}) \left(\frac{0.023 \text{ radian}}{1.4} \right) \right] (24 \text{ m}) \\
 &= (0.01)(713 \text{ m})(24 \text{ m}) \\
 &= 17.1 \text{ m}^2 = 12.3 \text{ dBsm}
 \end{aligned}$$

Figure 2.3-14 shows the predicted RCS of sea clutter as a function of range for the PILOT system. The calculations assume a -30 -dB sigma zero for the return from the

FIGURE 2.3-14 ■
Sea Clutter RCS as
a Function of Range.



sea at shallow grazing angles and a one-way half-power azimuth beamwidth of 1.3° , which corresponds to uniform illumination of a 1.25-m azimuth aperture. At the 44-km maximum range, the RCS of the sea clutter is 12 dBsm, which is just 8 dB less than the 20-dBsm target RCS assumed in Table 2.3-4. In other words, the signal-to-clutter ratio is 8 dB, and targets have to be detected against this background, which is higher than system-induced noise. The clutter may also have non-noiselike statistical properties such as a longer-tailed distribution than is the case for noise, resulting in a further performance degradation.

2.3.6 Range Resolution

FMCW radar systems are capable of very-high-range resolution that enables not just high-range measurement accuracy but allows production of high-range resolution profiles (HRRP). This also permits the FMCW technique to be used in a synthetic aperture radar (SAR) mode to generate high-resolution two-dimensional imagery. The range resolution of a linear FMCW homodyne radar is fundamentally limited by the transmit bandwidth. In addition, it will also have limits imposed by transmit-and-receive waveform overlap, receiver frequency resolution, and frequency sweep nonlinearities. For any radar waveform, the range resolution is linearly proportional to the time resolution (i.e., the pulse length for an unmodulated pulsed radar) or inversely proportional to the transmit waveform bandwidth (or the modulation bandwidth for a pulsed radar or an FMCW radar):

$$\Delta R_0 = \frac{c\Delta T}{2} = \frac{c}{2\Delta F} \quad (2.3-24)$$

where

ΔR_0 = ideal range resolution,

ΔT = time resolution, and

ΔF = bandwidth of the transmit waveform.

For PILOT, the bandwidths of the transmitted FMCW waveforms are 70 MHz, 28 MHz, and 7 MHz with corresponding ideal range resolution of 2.1 m, 5.4 m, and 21.4 m, respectively.

As seen earlier range measurement is also a function of the beat frequency which must therefore be estimated as accurately as possible. The PILOT radar system uses a sawtooth linear FMCW waveform with 1-kHz modulation frequency and a corresponding 1-ms modulation period. The three range settings of PILOT (4.4 km, 11 km, and 44 km) have corresponding total frequency deviations of 70 MHz, 28 MHz, and 7 MHz, respectively. For ranges out to 4.4 km, with corresponding transit times up to 30 μ s, the frequency slew rate slope is 70 MHz/ms that yields a maximum beat frequency of 2.07 MHz. For the 11-km and 44-km maximum range modes, the slope is decreased proportionally so that the maximum beat frequency remains 2.07 MHz. The parameters for PILOT are shown in Table 2.3-7.

Figure 2.3-15 shows the beat frequency, f_b , spectrum from 0 MHz to 2.048 MHz for the 70-MHz bandwidth and a modulation period of 1 ms. A single stationary point target echo results in a beat frequency at 1.4 MHz, corresponding to its range of 3 km. For example,

$$f_b = \frac{\Delta F}{T_m} \frac{2R}{c} = \frac{70 \text{ MHz}}{1 \text{ ms}} \frac{2(3 \text{ km})}{3 \times 10^8 \text{ m/s}} = (70 \text{ MHz/ms})(20 \mu\text{s}) = 1.4 \text{ MHz} \quad (2.3-25)$$

TABLE 2.3-7 ■ PILOT Waveform and Receiver Parameter Summary

Range Setting	4.4	11	44	km	Given
FMCW waveform	Sawtooth	Sawtooth	Sawtooth		Given
Frequency deviation, peak to peak	70	28	7	MHz	Given
Ideal time resolution	14	36	143	ns	Calculated
Ideal range resolution	2.1	5.4	21.4	m	Calculated
Range resolution claimed	2.4	6.0	24.0	m	Given
Modulation frequency	1	1	1	kHz	Given
Modulation index	70,000	28,000	7,000		Calculated
Modulation period	1	1	1	ms	Calculated
Frequency slew rate	70	28	7	MHz/ms	Calculated
Beat frequency/range ratio	467	187	47	Hz/m	Calculated
Range/beat frequency ratio	0.002	0.005	0.021	m/Hz	Calculated
Maximum transit time	30	74	296	μ s	Calculated
Overlap	97.0%	92.6%	70.4%		Calculated
Maximum beat frequency	2.07	2.07	2.07	MHz	Calculated
Minimum beat frequency interval	970	926	704	μ s	Calculated
Minimum beat frequency spectral width	1,031	1,080	1,421	Hz	Calculated
Range resolution limit	2.2	5.8	30.5	m	Calculated
Analog-to-digital converter sample rate	4,096	4,096	4,096	MHz	Assumed
FFT length	4,096	4,096	4,096	Points	Given
FFT length	1,000	1,000	1,000	μ s	Calculated
FFT frequency sample spacing	1,000	1,000	1,000	Hz	Calculated
FFT range sample spacing	2.1	5.4	21.4	M	Calculated
Window	Hamming	Hamming	Hamming		Assumed
Window frequency resolution (6 dB)	1.81	1.81	1.81	Sample	Calculated
Window frequency resolution (6 dB)	1,810	1,810	1,810	Hz	Calculated
Window range resolution (6 dB)	3.9	9.7	38.8	M	Calculated
Doppler frequency shift	62.0	62.0	62.0	Hz/(m/s)	Calculated
Range error due to Doppler	0.13	0.33	1.33	m/(m/s)	Calculated

Figure 2.3-16 is a zoom of the 1.4-MHz single target return showing the beat frequency spectrum from 1.38 MHz to 1.42 MHz (i.e., corresponding to ranges from 2,957 m to 3,043 m). The plot shows sidelobes at approximately -13 dB that are consistent with a $\sin x/x$ or sinc function response for a single-point target.

Figure 2.3-17 shows transmit-and-receive frequency as a function of time for two targets. The plot shows the beat frequency as a function of time. For the far-range target,

FIGURE 2.3-15 ■
Beat Frequency Spectrum for Single Stationary Point Target at 3-km Range.

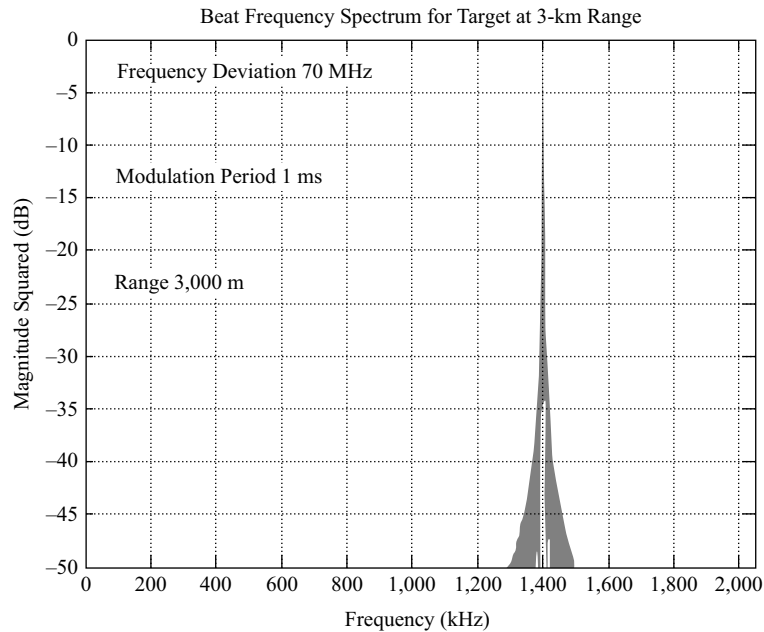
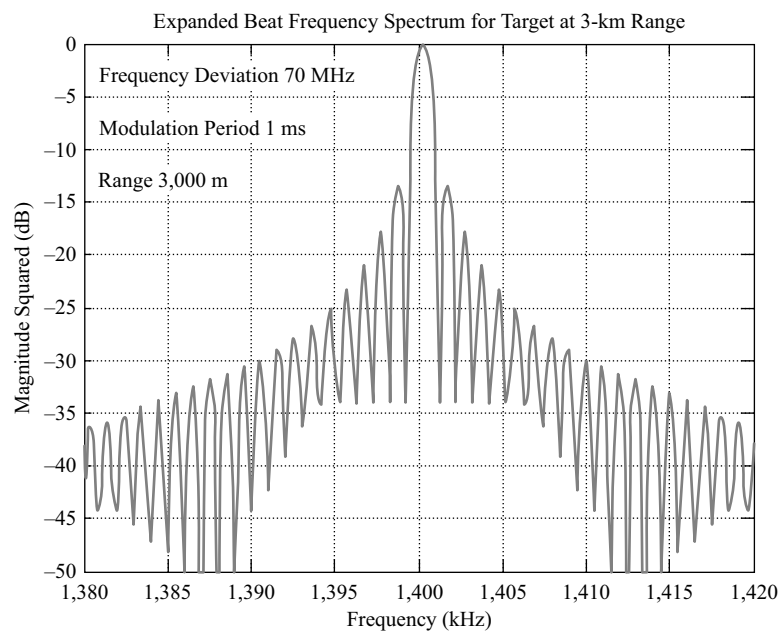


FIGURE 2.3-16 ■
Expanded Beat Frequency Spectrum for Single Stationary Point Target at 3-km Range.



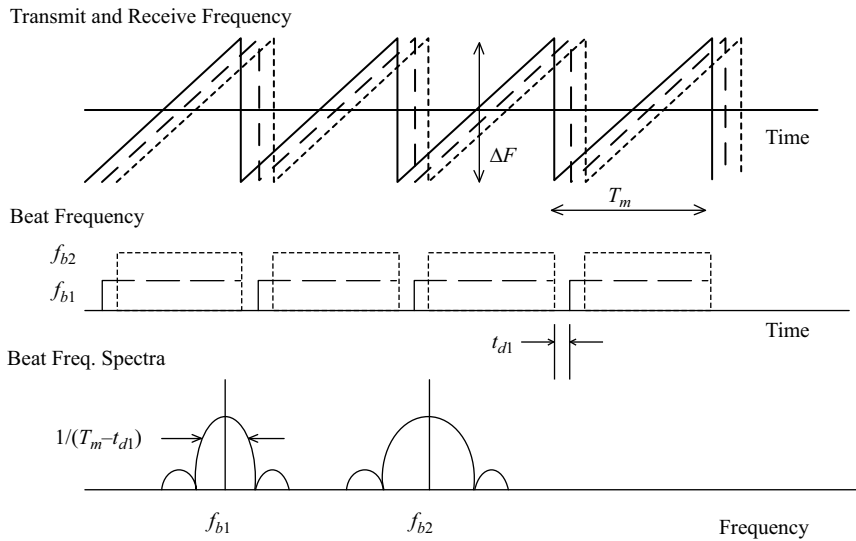


FIGURE 2.3-17 ■ Homodyne Linear FMCW Overlap.

the beat frequency is larger, as is the transit-time gap after the beginning of the frequency sweep. In the beat frequency spectrum, the nearer-range target has a lower frequency than the far-range target. The spectral width is greater for the longer-range target because the overlap in time is less.

The beat frequency bandwidth, B_b , of a single-point target is given by

$$B_b = \frac{1}{T_m - t_d - t_{\text{sweep recovery}}} \quad (2.3-26)$$

where

B_b = beat frequency bandwidth of target,

T_m = modulation period,

t_d = round-trip propagation time delay, and

t_s = sweep recovery time.

Thus, again, for the PILOT radar with 1-ms modulation period, for a target at a range of 44-km with a 296- μs transit time, and assuming negligible sweep-recovery time, the spectral width of difference frequency is 1,421 kHz, or 42 percent wider than a short-range target, as shown here:

$$B_b = \frac{1}{T_m - t_d} = \frac{1}{1,000 \mu\text{s} - 296 \mu\text{s}} = \frac{1}{704 \mu\text{s}} = 1,421 \text{ kHz} \quad (2.3-27)$$

Partial overlap between the transmit and receive waveforms causes this broadening of the spectral width of the beat frequency. Figure 2.3-18 shows the beat frequency spectrum for a single point at 30-km range with 7-MHz frequency deviation. The beat frequency is the same as in Figure 2.3-15 because of the ten-time increase in range and transit time is offset by the ten time reduction in reduction in frequency deviation and sweep slope. However, the target return broadens by over 20 percent due to the change in overlap from 98 percent to 80 percent.

A further source of broadening of the beat frequency is due to target motion causing ambiguity between range and Doppler known as *range-Doppler coupling*. Figure 2.3-19 shows the beat frequency spectrum for a single-point target at 3-km range with 32-m/s relative radial velocity. The target velocity is sufficient to shift the target return beat frequency by 2 kHz to 1.402 MHz as shown here:

$$f_b = \frac{\Delta F}{T_m} \frac{2R}{c} + \frac{2v}{\lambda} = \frac{7 \text{ MHz}}{1 \text{ ms}} \frac{2(30 \text{ km})}{3 \times 10^8 \text{ m/s}} + \frac{2(32 \text{ m/s})}{0.032 \text{ m}} = 1,400 \text{ kHz} + 2 \text{ kHz}$$

$$= 1.402 \text{ MHz} \quad (2.3-28)$$

FIGURE 2.3-18 ■
Beat Frequency Spectrum for Single Stationary Point Target at 30-km Range with 80 Percent Overlap.

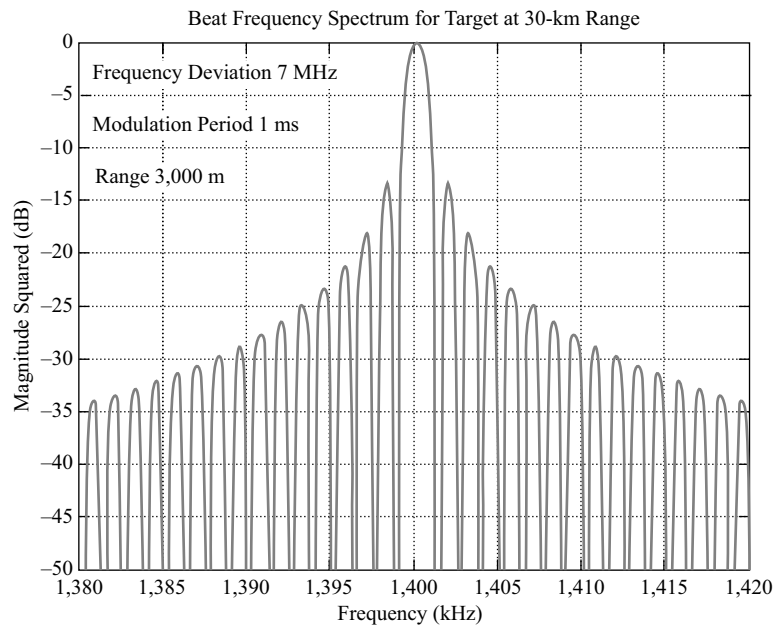
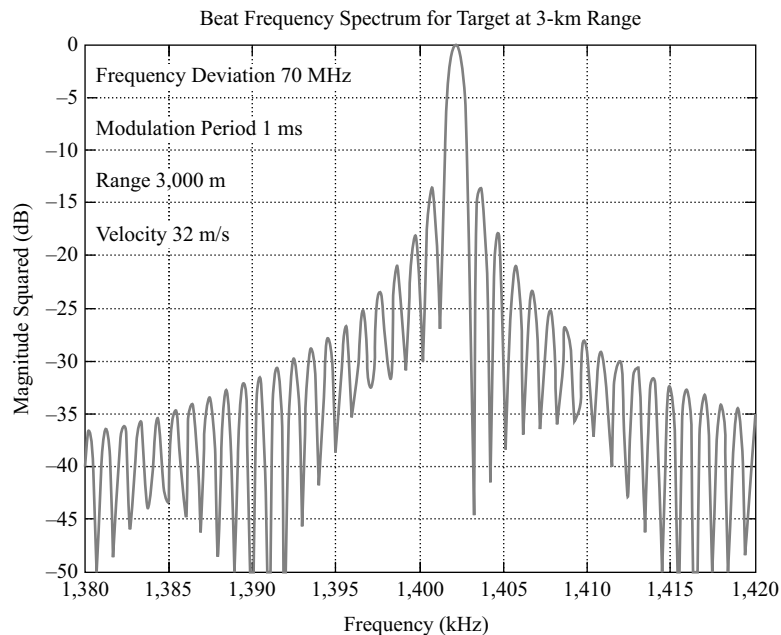


FIGURE 2.3-19 ■
Beat Frequency Spectrum for Single-Point Target at 3-km Range with 32-m/s Velocity.



This is also equivalent to shifting the return by two 2-m range bins. This 1.402-MHz beat frequency thus ambiguously also corresponds to a stationary target at 3,004-m range.

When the target is moving, there is also a beat frequency chirp during the modulation period due to the relative velocity between the radar and target in addition to the beat frequency components due to range and velocity. If the relative velocity is less than the range resolution divided by the modulation period, then the error will be less than a frequency or range bin. For the preceding moving target example, the beat frequency chirp is only 34 Hz as shown by the following computation:

$$f_{b\text{-chirp}}(t) = \frac{4\Delta F}{T_m c} \left(1 - \frac{V}{c}\right) Vt \cong 2 \frac{\Delta F}{T_m} \frac{2Vt}{c} = \frac{70 \text{ MHz}}{1 \text{ ms}} \frac{4Vt}{3 \times 10^8 \text{ m/s}}$$

$$f_{b\text{-chirp}}(t = T_m) = \frac{70 \text{ MHz}}{1 \text{ ms}} \frac{4V(1 \text{ ms})}{3 \times 10^8 \text{ m/s}} = \frac{4(70 \text{ MHz})}{(3 \times 10^8 \text{ m/s})} V = (0.933 \text{ m}^{-1})V$$

$$f_{b\text{-chirp}}(t = T_m, V = 32 \text{ m/s}) = (0.933 \text{ m}^{-1})V = (0.933 \text{ m}^{-1})32 \text{ m/s} = 34 \text{ Hz}$$

For the 7-MHz frequency deviation used by the PILOT in the far-range mode, the FM modulation would decrease by 3 Hz. Figure 2.3-20 shows how this results in an increase in the beat frequency sidelobe levels for a case in which the velocity is very high, taking a value of 1.6 km/s. A velocity of this magnitude is so high that the beat frequency is approximately 1.493 kHz higher at the end of the modulation period than at the beginning. Even with a velocity this high, the error only corresponds to approximately 1.5 range bins (note also that sidelobes are only marginally higher).

Having examined the spectrum of the beat frequency under various different target conditions, we now consider how well the different beat frequencies can be resolved. This enables the limits on range resolution to be evaluated. The FMCW radar receiver will include frequency filters to form the range bins. The spectral output of the range bin filter will be the convolution of the mixer output beat frequency spectrum and the filter

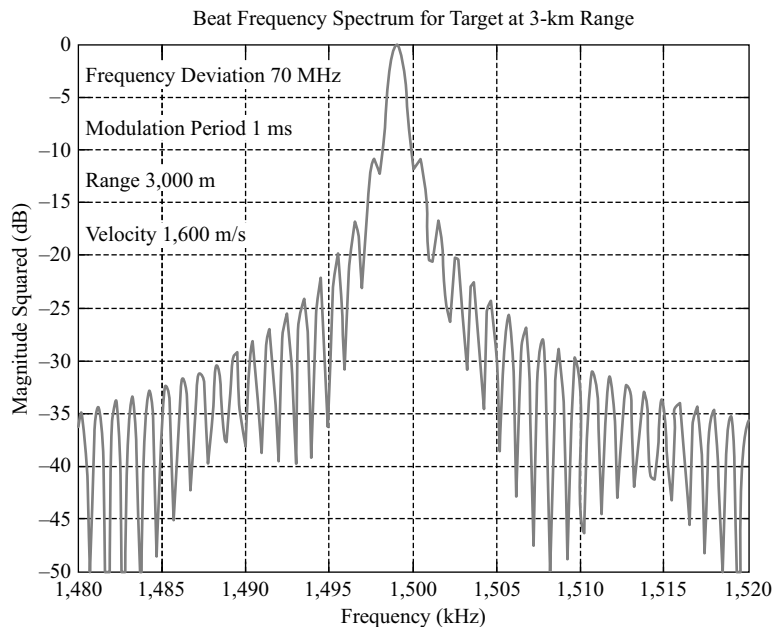


FIGURE 2.3-20 ■
Beat Frequency Spectrum for Single-Point Target at 2-km Range with 1,600-m/s Velocity.

spectral characteristic. The bandwidth of the matched filter will be approximately equal to the inverse of the modulation period less the transit time and any sweep recovery time. Wider bandwidth filters may be used when the frequency sweep nonlinearities broaden the mixer output spectrum beyond the inverse of the modulation period. While analog range bin filters can be used to form the range bins, digital signal processing is attractive for many modern FMCW radar applications. Coarser beat frequency resolution and consequently degraded range resolution will result from using sequences shorter than modulation period. Weighting to reduce frequency and range sidelobes will also broaden the filter bandwidth. The zero-padding technique can be used for narrower bandwidth filters, thus improving both frequency and range resolution.

For the ADC at the mixer output to comply with the sampling theorem, the sampling rate f_s must be at least two times the maximum beat frequency, or

$$2f_{bmax} \leq f_s \quad (2.3-29)$$

where

f_{bmax} = maximum beat frequency and

f_s = sampling frequency.

Substituting for f_{bmax}

$$2 \left(\frac{\Delta F}{T_m} \frac{2R_{max}}{c} + \frac{2V_{max}}{\lambda} \right) \leq f_s \quad (2.3-30)$$

Thus, for a modulation bandwidth of 500-MHz frequency and a modulation period of 1 ms, a stationary target at a range of 1 km results in a beat frequency, f_{bmax} , of 3.3 MHz. Thus, f_s must be sampled at a rate at least greater than twice this value.

$$2 \frac{\Delta F}{T_m} \frac{2R_{max}}{c} = 2(500 \text{ MHz/ms})(6.7 \mu\text{s}) = 2(3.3 \text{ MHz}) = 6.7 \text{ MHz} \leq f_s \quad (2.3-31)$$

Matching the samples processed in the FFT to the modulation period, and requiring that the number of samples be a power of 2, yields

$$T_m = \frac{N}{f_s} = \frac{2^n}{f_s} \quad (2.3-32)$$

where $N = 2^n$ is the number of samples, so that

$$f_s = \frac{2^n}{T_m} \quad (2.3-33)$$

Substituting,

$$2 \frac{\Delta F}{T_m} \frac{2R_{max}}{c} \leq \frac{2^n}{T_m} \quad (2.3-34)$$

so that

$$\frac{4\Delta F R_{max}}{c} \leq 2^n \quad (2.3-35)$$

So a 2^{13} or 8,192-point FFT is needed for the 500-MHz frequency deviation and 1-km range as shown here:

$$\frac{4\Delta FR_{max}}{c} = \frac{4(500 \text{ MHz})(1 \text{ km})}{3 \times 10^8 \text{ m/s}} = 6,667 \leq 2^n = 2^{13} = 8,192 \quad (2.3-36)$$

This can be accomplished by sampling the 1-ms modulation period at 6.7 MHz and appending 1,525 zeroes to pad the sequence length to 8,192, or increasing the ADC sample rate to 8.192 MHz to get 8,192 samples in 1 ms.

Some linear FMCW homodyne FMCW radar systems use coherent-processing intervals that are shorter than the modulation period. This reduces the signal-processing burden since FFTs with fewer points require less processing. Examples include Lear Astronics and TSC [19, 20]. It may also be desirable to only process the interval from the maximum transit time to the end of the modulation period to ensure that any window function applied to the data includes returns from all ranges, avoiding degradation of filter sidelobe response due to misalignment.

Figure 2.3-21 shows the beat frequency spectrum for two stationary-point targets with equal RCS located at a nominal range of 3 km with a separation of 4 m. To be able to resolve these as two targets, they have to be resolvable in beat frequency. The null depth between the two target peaks is very sensitive to changes in the range separation that are comparable to fractions of a wavelength because of interference between the range sidelobes of the returns from the two targets. The range sidelobes are approximately 15 dB below the peaks in this figure. Weighting can be used to reduce the sidelobes at the expense of mainlobe broadening; Figure 2.3-22 shows the reduction in range sidelobes to approximately 40 dB below the peak with a Hamming weighting for

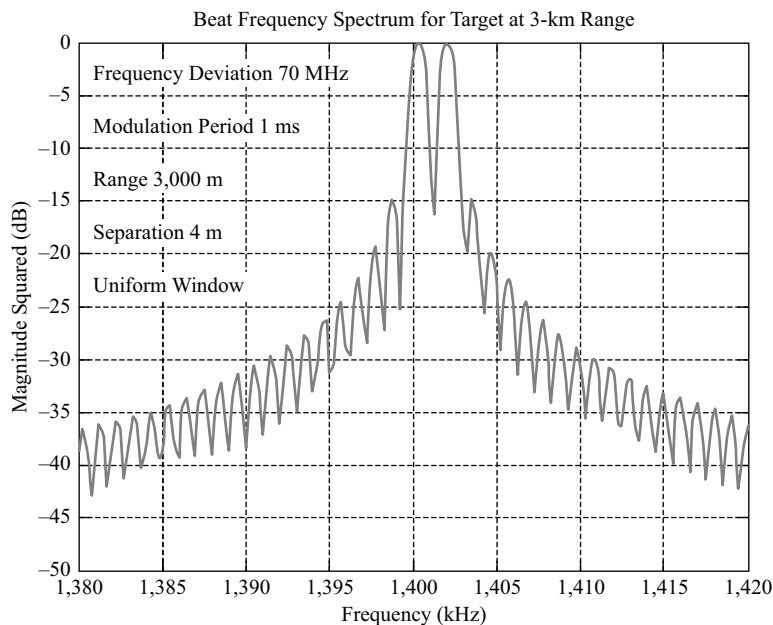
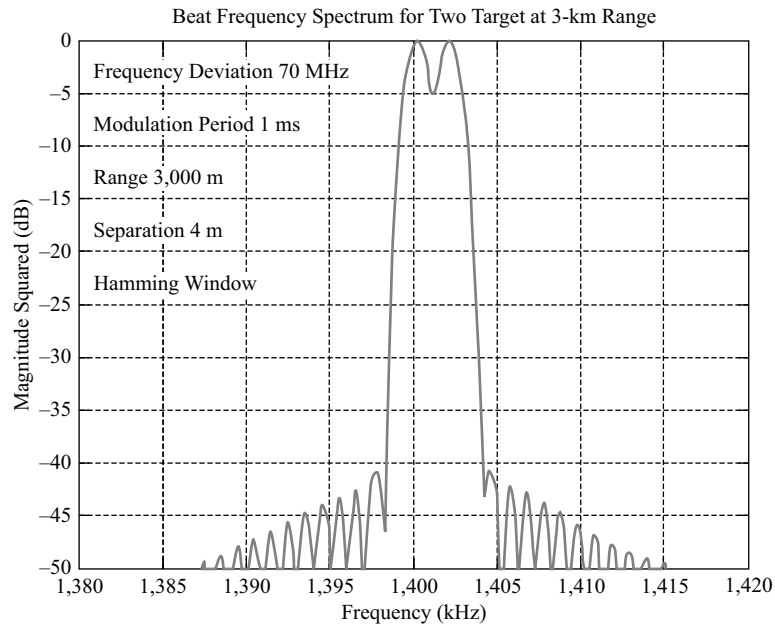


FIGURE 2.3-21 ■ Beat Frequency Spectrum for Two Point Targets at 3-km Range with 4-m Separation and Uniform Window.

FIGURE 2.3-22 ■
Beat Frequency
Spectrum for Two
Point Targets at
3-km Range with
4-m Separation and
Hamming Window.



the same two targets. Note that the depth of the null between the two targets is now much less, and any further reduction could render them unresolved.

The achieved range resolution may be estimated as the square root of the sum of the squares of the beat frequency spectral width and the receiver frequency resolution; it is given by

$$\Delta R = \frac{T_m c}{2\Delta F} \sqrt{\left(\frac{1}{T_m - (2R/c) - t_{sr}}\right)^2 + \Delta f_{receiver}^2} \quad (2.3-37)$$

where

T_m = modulation period,

c = propagation velocity,

ΔF = total frequency deviation,

R = range,

t_{sr} = sweep recovery (or other unprocessed) time, and

$\Delta f_{receiver}$ = receiver frequency resolution.

2.3.7 Frequency Sweep Nonlinearity

Nonlinearities in the frequency sweep result in broadening of the beat frequency spectrum and consequent degradation of the range resolution. Nonlinearities in the frequency sweep can also cause the apparent presence of false targets and the misplacement of real targets, both stationary and moving.

For a VCO, the definition of nonlinearity is the ratio of the deviation from an ideal linear-tuning characteristic relative to the total tuning bandwidth:

$$\text{Nonlinearity}(VCO) = \frac{\text{Nonlinearity Bandwidth}}{\text{Frequency Deviation}} \quad (2.3-38)$$

The design aim for linear FMCW radar is for the deviation to be less than the inverse of the modulation period (the modulation frequency) so that the beat frequency spectrum width will be approximately equal to the frequency and range bin bandwidth to avoid degradation of the range resolution. Thus, the nonlinearity criterion may be expressed as

$$\begin{aligned} \text{Nonlinearity}(VCO - \text{desired}) &= \frac{\text{Nonlinearity Bandwidth}}{\text{Frequency Deviation}} \approx \frac{\text{Modulation Frequency}}{\text{Frequency Deviation}} \\ &= \frac{f_m}{\Delta F} \end{aligned} \quad (2.3-39)$$

Linear FMCW radar engineers often also use the following alternative definition for nonlinearity

$$\text{Nonlinearity}(FMCW) = \frac{\text{Nonlinearity Bandwidth}}{\text{Nominal Beat Frequency}} \quad (2.3-40)$$

So the FMCW nonlinearity criterion is

$$\begin{aligned} \text{Nonlinearity}(FMCW - \text{desired}) &= \frac{\text{Nonlinearity Bandwidth}}{\text{Nominal Beat Frequency}} \\ &\approx \frac{\text{Modulation Frequency}}{\text{Nominal Beat Frequency}} = \frac{f_m}{f_b} \end{aligned} \quad (2.3-41)$$

The alternative definition is useful because it gives the range resolution relative to range. For example, with a 500-MHz total frequency modulation (i.e., a 0.3-m ideal range resolution) and a 1-ms modulation period (a 1-kHz modulation frequency), it is desirable for the variation from an ideal linear FMCW sweep to be less than 1 kHz so that the mixer output spectrum for a point target will be no more than approximately 1-kHz wide. This corresponds to a nonlinearity of 1 kHz relative to the 500-MHz total frequency modulation or 0.0002 percent. For a target at a range of 1 km, the beat frequency is 3.3 MHz. The alternative nonlinearity definition corresponds to a nonlinearity of 1 kHz relative to the 3.3-MHz beat frequency or 0.03 percent. Note that 0.3-m range resolution is 0.03 percent of the 1-km range. Since the frequency deviation is much greater than the beat frequency, the first and more stringent nonlinearity criterion must be used to specify the frequency sweep linearity for the FMCW radar transmitter. The second alternative is useful as an FMCW radar performance metric to represent range resolution relative to the nominal range.

Figure 2.3-23 shows the frequency as a function of tuning voltage for a 35-GHz varactor-tuned Gunn diode oscillator. The difference between the actual tuning characteristic and the best linear fit to the characteristic is approximately 40 MHz. This

corresponds to approximately 8 percent nonlinearity and will result in a severely degraded range resolution.

Some systems compensate for nonlinearities with piecewise linear fits to segments of the tuning characteristic. Figure 2.3-24 shows the residual errors as a function of tuning voltage for ten segments. This reduces the peak error from approximately 40 MHz to ± 0.5 MHz near the center of the bandwidth.

Compensating for frequency sweep nonlinearities is challenging. Often the output frequency as a function of tuning voltage characteristic is sensitive to temperature so that compensation with an open-loop lookup table or polynomial approach has limited

FIGURE 2.3-23 ■ Frequency as a Function of Tuning Voltage for 35-GHz Varactor-Tuned Gunn Diode Oscillator Showing Tuning Nonlinearity.

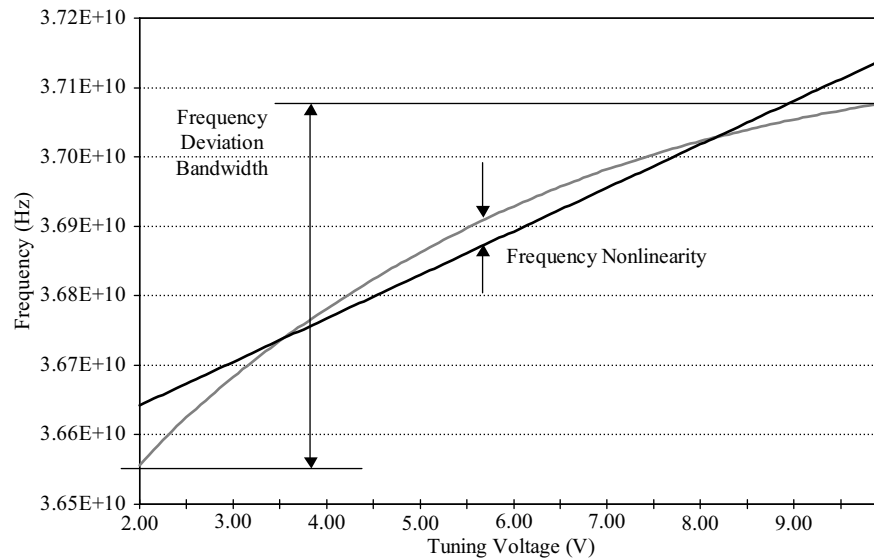
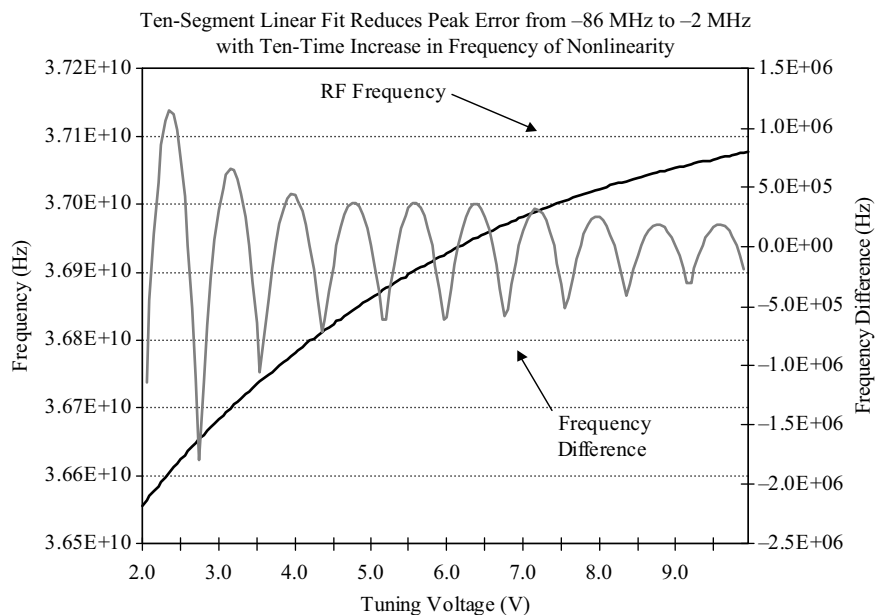


FIGURE 2.3-24 ■ Ten-Segment Linear Fit Reduces Peak Error from -86 MHz to -2 MHz with a Ten-Time Increase in Frequency of Nonlinearity.



performance. For example, Brooker reported significant performance enhancement with closed-loop linearization relative to open-loop analog compensation [16]. Delay-line discriminators are used to measure the slope in a closed-loop linearizer.

The ELVA-1 millimeter wave (MMW) FMCW radar front end uses an active IMPATT frequency multiplier driven by a microwave voltage-controlled master oscillator. The sensitivity and accuracy requirements are met with a triangle waveform generated with an open-loop linearizer to achieve relatively high output power with low noise and good linearity. Table 2.3-8 lists the parameters for the ELVA-1 FMCW radar front end with a 94-GHz RF center frequency. The 100-MHz total frequency deviation corresponds to a 1.5-m ideal range resolution. Figure 2.3-25 shows the beat frequency spectrum for a target at approximately 380-m range. For the triangular linear FMCW waveform with a 100-MHz total frequency deviation, a 5-ms modulation period with 2.5-ms upsweep and a 2.5-ms down sweep, the frequency sweep slope is 40 MHz/ms and the calculated

TABLE 2.3-8 ■ ELVA-1 FMCW Radar Front-End Characteristics

Parameter	Value	Units
RF center frequency	94	GHz
Total frequency deviation	100	MHz
Ideal range resolution, calculated	1.5	m
Modulation period, triangle waveform	5	ms
Sweep time, triangle waveform	2.5	ms
Frequency sweep slope, calculated	40	MHz/ms
Range to target	380	m
Transit time, calculated	2.53	μ s
Calculated beat frequency	101,333	Hz
Measured beat frequency	102,900	Hz
Measured half-power spectral width	700	Hz
Measured half-power spectral width	± 350	Hz
Measured half-power spectral width	± 0.34	Percent of beat frequency
Measured half-power spectral width	± 0.00035	Percent of frequency deviation
Measured range resolution	2.6	m
Ratio of measured to ideal range resolution	1.7	

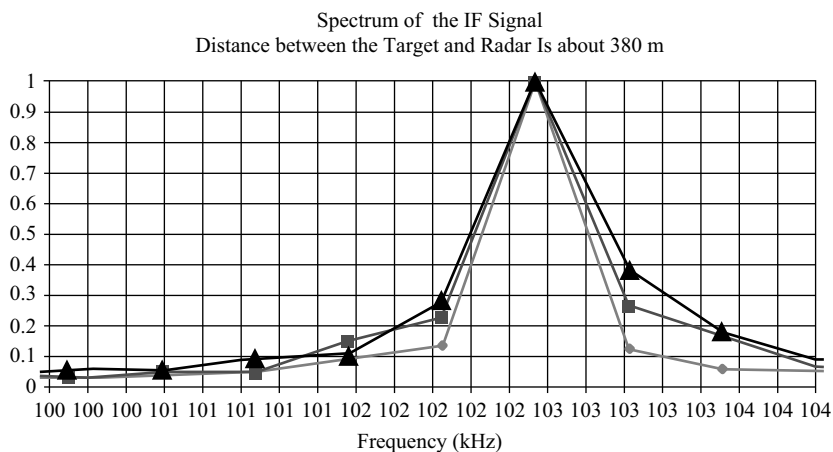


FIGURE 2.3-25 ■ ELVA-1 94 GHz FMCW Radar Beat Frequency Spectrum.

beat frequency is approximately 101 kHz for a range of 380 m. In Figure 2.3-25, the peak target return is centered at approximately 103 kHz with approximately ± 350 -Hz half-power width, which is ± 0.34 percent of the nominal beat frequency and ± 0.00035 percent of the frequency deviation. The corresponding range resolution is approximately 2.6 m, which is 1.7 times greater than the 1.5-m ideal range resolution limit.

Now we consider a second example based on Alliant Techsystems FMCW radar. Figure 2.3-26 shows the beat frequency spectrum for a single 70-m^2 RCS target at 1 km. The half-power spectral width of the target return is approximately 0.3 m. In Figure 2.3-27, the two targets, separated by 0.3 m in range, are resolvable with an approximate 3-dB null between them. The third target is separated by 0.6 m and is even more clearly resolvable. These figures demonstrate a range resolution of approximately 0.3 m, which corresponds to the theoretical limit for 500-MHz total frequency deviation and is indicative of a well-designed linear FM waveform.

FIGURE 2.3-26 ■ Alliant Techsystems FMCW Radar Beat Frequency Spectrum for Single Target.

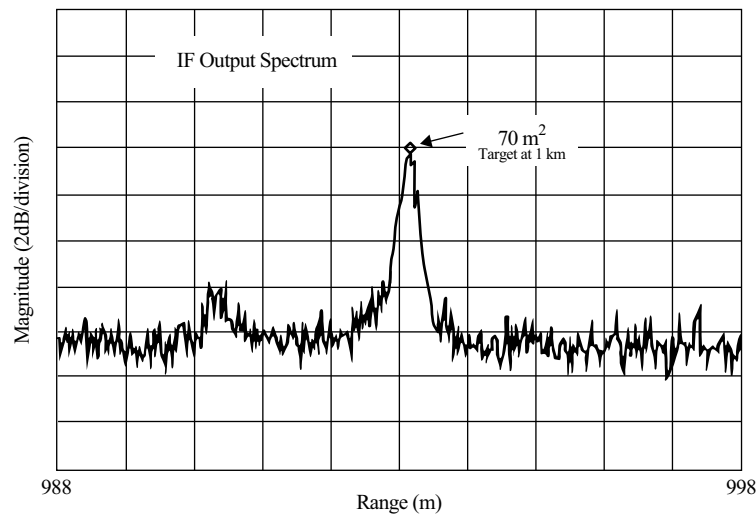
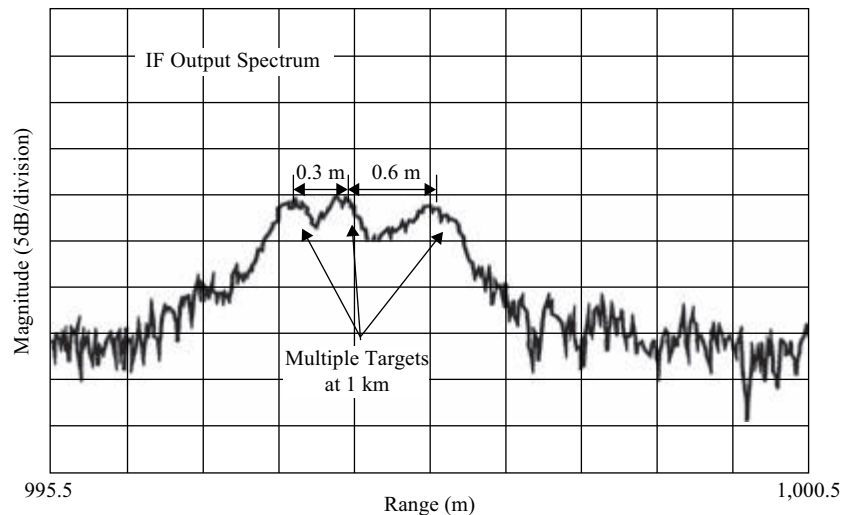


FIGURE 2.3-27 ■ Alliant Techsystems FMCW Radar Beat Frequency Spectrum for Three Targets.



Consideration of sinusoidal nonlinearities is mathematically tractable. The assumption of a sinusoidal nonlinearity is reasonable for describing the variation from an ideal linear frequency sweep due to inherent VCO tuning nonlinearities. These are the result of residual errors after linearizer compensation or quantization in frequency steps. A simple analysis is presented here on the impact of a sinusoidal nonlinearity on the beat frequency. By assuming that the frequency sweep nonlinearity has a sinusoidal characteristic, the standard deviation of the slope of the frequency sweep can be related to the maximum frequency variation from an ideal linear sweep. The frequency during the down sweep is given by

$$F(t) = f_0 + \frac{\Delta F}{2} - \frac{\Delta F}{T}t + A \sin(2\pi ft), \quad 0 < t < T \quad (2.3-42)$$

where

- f_0 = RF center frequency,
- ΔF = total frequency deviation,
- T = modulation period,
- t = time,
- A = nonlinearity amplitude, and
- f = nonlinearity frequency.

Differentiating $F(t)$,

$$\frac{dF(t)}{dt} = -\frac{\Delta F}{T} + (A2\pi f) \cos(2\pi ft) \quad (2.3-43)$$

The ratio of the standard deviation of the slope to the average slope is

$$\frac{\text{Standard Deviation} \left[\frac{dF(t)}{dt} \right]}{\text{Average} \left[\frac{dF(t)}{dt} \right]} = \frac{(A2\pi f)\sqrt{0.5}}{\frac{\Delta F}{T}} = \frac{4.44Af}{\frac{\Delta F}{T}} = \frac{4.44AfT}{\Delta F} \quad (2.3-44)$$

The beat frequency spectral width for a point target and consequently the range resolution will be proportional to the ratio described by equation 2.3-44. For this simple analysis of a sinusoidal nonlinearity, it is evident that target spectral width and range resolution are proportional to both the amplitude and the frequency of the sinusoidal nonlinearity and will deteriorate accordingly.

A more detailed analytical model is now derived for the beat frequency, including a sinusoidal nonlinearity. For a linear FMCW sawtooth waveform, sweeping up in frequency with sinusoidal nonlinearity, the transmit frequency is given by

$$f_t'(t) = f_0 - \frac{\Delta F}{2} + \frac{\Delta F}{T_m}t + A \sin 2\pi ft, \quad 0 < t < T_m \quad (2.3-45)$$

where

- f_0 = RF center frequency,
- ΔF = total frequency deviation,

T_m = modulation period,
 A = sinusoidal nonlinearity amplitude, and
 f = sinusoidal nonlinearity frequency.

The transmit RF phase is given by

$$\phi_t'(t) = 2\pi \int_0^t f_t'(x) dx \quad (2.3-46)$$

and assuming that $f_0 = 0$ for $t = 0$,

$$\phi_t'(t) = 2\pi \left[\left(f_0 - \frac{\Delta F}{2} \right) t + \frac{\Delta F}{2T_m} t^2 + \frac{A}{2\pi f} (1 - \cos 2\pi f t) \right], \quad 0 < t < T_m \quad (2.3-47)$$

So the transmit signal with amplitude a_0 is given by

$$s_t(t) = a_0 \sin 2\pi \left[\left(f_0 - \frac{\Delta F}{2} \right) t + \frac{\Delta F}{2T_m} t^2 + \frac{A}{2\pi f} (1 - \cos 2\pi f t) \right], \quad 0 < t < T_m \quad (2.3-48)$$

The receive signal is the transmit signal delayed in time by the round-trip propagation time to the target and back, t_d , with reduced amplitude, b_0 :

$$s_r(t) = \frac{b_0}{a_0} s_t(t - t_d), \quad t_d < t < T_m \quad (2.3-49)$$

where t_d = transit time, or

$$s_r(t) = b_0 \sin 2\pi \left\{ \left(f_0 - \frac{\Delta F}{2} \right) (t - t_d) + \frac{\Delta F}{2T_m} (t - t_d)^2 + \frac{A}{2\pi f} [1 - \cos 2\pi f (t - t_d)] \right\} \quad (2.3-50)$$

For a homodyne FMCW radar, the receive signal is mixed with the transmit signal so that the mixer output beat frequency signal $s_b(t)$ is

$$s_b(t) = c_0 \cos \left\{ \begin{array}{l} 2\pi \left[\left(f_0 - \frac{\Delta F}{2} \right) t + \frac{\Delta F}{2T_m} t^2 + \frac{A}{2\pi f} [1 - \cos 2\pi f t] \right] - \\ 2\pi \left[\left(f_0 - \frac{\Delta F}{2} \right) (t - t_d) + \frac{\Delta F}{2T_m} (t - t_d)^2 + \frac{A}{2\pi f} [1 - \cos 2\pi f (t - t_d)] \right] \end{array} \right\} \quad (2.3-51)$$

Simplifying,

$$s_b(t) = c_0 \cos 2\pi \left[\left(f_0 + \frac{\Delta F}{2} \right) t_d - \frac{\Delta F}{2T_m} (2t_d t - t_d^2) + \frac{A}{2\pi f} [\cos 2\pi f (t - t_d) - \cos 2\pi f t] \right] \quad (2.3-52)$$

Regrouping,

$$s_b(t) = c_0 \cos 2\pi \left[\left(f_0 - \frac{\Delta F}{2} \right) t_d - \frac{\Delta F}{2T_m} t_d^2 + \frac{\Delta F}{T_m} t_d t + \left(\frac{A}{2\pi f} \right) [\cos 2\pi f (t - t_d) - \cos 2\pi f t] \right] \quad (2.3-53)$$

Since $t_d = 2R/c$,

$$s_b(t) = c_0 \cos 2\pi \left[\left(f_0 - \frac{\Delta F}{2} \right) \left(\frac{2R}{c} \right) - \frac{\Delta F}{2T_m} \left(\frac{2R}{c} \right)^2 + \frac{\Delta F}{T_m} \left(\frac{2R}{c} \right) t + \left(\frac{A}{2\pi f} \right) \left[\cos 2\pi f \left(t - \left(\frac{2R}{c} \right) \right) - \cos 2\pi f t \right] \right] \quad (2.3-54)$$

The beat frequency signal can be written as

$$\begin{aligned} s_b(t) &= c_0 \cos 2\pi(\phi + ft + \varepsilon(t)) \\ \text{where} \\ \phi &= \left(f_0 - \frac{\Delta F}{2} \right) \left(\frac{2R}{c} \right) - \frac{\Delta F}{2T_m} \left(\frac{2R}{c} \right)^2 \\ f &= \frac{2\Delta FR}{T_m c} \\ \varepsilon(t) &= \left(\frac{A}{2\pi f} \right) \left[\cos 2\pi f \left(t - \left(\frac{2R}{c} \right) \right) - \cos 2\pi f t \right] \end{aligned} \quad (2.3-55)$$

For stationary radar and target, the beat frequency signal includes a constant phase term, a constant frequency term, and the nonlinearity term. For constant relative velocity between the radar and the target $R = R_0 + Vt$, substitute that into the beat frequency signal expression:

$$s_b(t) = c_0 \cos 2\pi \left[\left(f_0 + \frac{\Delta F}{2} \right) \frac{2R_0}{c} + \left(f_0 + \frac{\Delta F}{2} \right) \left(\frac{2V}{c} \right) t + \frac{\Delta F}{2T_m} \left(\frac{4R_0^2 + 8R_0 Vt + 4V^2 t^2}{c^2} \right) - \frac{\Delta F}{T_m} \frac{2R_0}{c} t - \frac{\Delta F}{T_m} \frac{2V}{c} t^2 + \left(\frac{A}{2\pi f} \right) \left[\cos 2\pi f \left(t - \frac{2R_0}{c} - \frac{2V}{c} t \right) - \cos 2\pi f t \right] \right] \quad (2.3-56)$$

Combining like terms,

$$s_b(t) = c_0 \cos 2\pi \left[\left[\left(f_0 - \frac{\Delta F}{2} \right) \frac{2R_0}{c} - \frac{2\Delta FR_0^2}{T_m c^2} \right] + \left[\left(f_0 - \frac{\Delta F}{2} \right) \left(\frac{2V}{c} \right) + \frac{2\Delta FR_0}{T_m c} \left(1 - \frac{2V}{c} \right) \right] t + \left[\frac{2\Delta FV}{T_m c} \left(1 - \frac{V}{c} \right) \right] t^2 + \left[\frac{A}{2\pi f} \left[\cos 2\pi f \left(t \left(1 - \frac{2V}{c} \right) - \frac{2R_0}{c} \right) - \cos 2\pi f t \right] \right] \right] \quad (2.3-57)$$

Equation 2.3-57 shows that there is a constant phase term that is dependent on target range and a Doppler frequency shift term that is linearly proportional to velocity. The constant phase term is approximately equal to the number of wavelengths to the target

and back. For $f_0 = 35$ GHz, $\Delta F = 500$ MHz, $c = 3.0 \times 10^8$ m/s, $T_m = 1$ ms, and $R_0 = 1$ km then

$$\phi_b = \left(f_0 + \frac{\Delta F}{2}\right) \frac{2R_0}{c} + \frac{2\Delta FR_0^2}{T_m c^2} = 235,000.0 + 11.1 = 235,011.1 \quad (2.3-58)$$

The beat frequency for moving target and sinusoidal nonlinearity is given by

$$f_b(t) = \left\{ \begin{array}{l} \left[\left(f_0 - \frac{\Delta F}{2}\right) \left(\frac{2V}{c}\right) + \frac{2\Delta FR_0}{T_m c} \left(1 - \frac{2V}{c}\right) \right] + \\ 2 \left[\frac{2\Delta FV}{T_m c} \left(1 - \frac{V}{c}\right) \right] t + \\ A \left[\sin 2\pi f t - \left(1 - \frac{2V}{c}\right) \sin 2\pi f \left(t \left(1 - \frac{2V}{c}\right) - \frac{2R_0}{c}\right) \right] \end{array} \right\} \quad (2.3-59)$$

which can be written as

$$f_b(t) = f_d + f_r + f_c(t) + \varepsilon(t)$$

where

$$f_d = \left(f_0 + \frac{\Delta F}{2}\right) \left(\frac{2V}{c}\right) = 231.7 \text{ Hz}/(\text{m/s})V$$

$$f_r = \frac{-2\Delta FR_0}{T_m c} \left(1 - \frac{V}{c}\right) \cong (-3.3 \text{ kHz}/\text{m})R_0 \quad (2.3-60)$$

$$f_c(t) = 2 \left[\frac{-2\Delta FV}{T_m c} \left(1 - \frac{V}{c}\right) \right] t \cong (-6.7 \text{ kHz}/\text{m})Vt$$

$$\varepsilon(t) = A \left[\sin 2\pi f t - \left(1 - \frac{2V}{c}\right) \sin 2\pi f \left(t \left(1 - \frac{2V}{c}\right) - \frac{2R_0}{c}\right) \right]$$

The effect on the beat frequency chirp can be illustrated with the example shown in Table 2.3-9. For $f_0 = 35$ GHz, $\Delta F = 500$ MHz, $c = 3.0 \times 10^8$ m/s, $T_m = 1$ ms, and

TABLE 2.3-9 ■ Comparison of Constant Range and Constant Velocity Examples

	Constant Range	Constant Velocity	Units
Initial range	1,000.0	1,000.0	m
Range at end of modulation period	1,000.0	999.7	m
Change in range	0.0	0.3	m
Velocity	0	-300	m/s
Initial Doppler frequency shift	0	69,500	Hz
Doppler frequency shift at end of modulation period	0	70,500	Hz
Change in Doppler frequency shift	0	1,000	Hz
Beat frequency	-3,333,333	-3,263,833	Hz
Beat frequency at end of modulation period	-3,333,333	-3,261,833	Hz
Change in beat frequency during modulation period	0	-2,000	Hz

$R_0 = 1$ km, the beat frequency is -3.333 MHz from the start of the target return until the end of the modulation period. For a target approaching with -300 -m/s relative velocity, there will be a 0.3 -m change in range during the modulation period and a 1 -kHz change in Doppler frequency shift due to the change in transmit frequency during the modulation period. Consequently, the beat frequency will decrease from -3.264 MHz initially to -3.262 MHz at the end of the modulation period, which is a beat frequency chirp of approximately 2 kHz. The beat frequency chirp during the frequency sweep induced by the target velocity is approximately twice the modulation frequency in this example.

The beat frequency spectrum is very sensitive to frequency sweep nonlinearities [21, 22] and is illustrated in Figure 2.3-28, which shows the beat frequency spectrum for the two targets at 3 -km range with 4 -m separation. In this case, there is one-half cycle of nonlinearity over the 1 -ms modulation period so the nonlinearity frequency is 500 Hz. The peak deviation from an ideal linear sweep is 50 times the 1 -kHz frequency resolution, so the nonlinearity amplitude is 50 kHz. This 50 -kHz peak nonlinearity is only 0.07 percent of the 70 -MHz total frequency deviation. In this example, the two frequencies are resolvable but only just.

Figure 2.3-29 shows a different example with ten cycles of nonlinearity over the 1 -ms modulation period corresponding to 10 -kHz nonlinearity frequency. The peak deviation from an ideal linear sweep is five times the 1 -kHz frequency resolution, so the nonlinearity amplitude is 5 kHz. Note that the nonlinearity results in spurious range sidelobes that repeat every 10 kHz in beat frequency, or every 21 m in range. The first sidelobes at $1,400 \pm 10$ kHz are only 10 dB below the main target return peaks. This 5 -kHz peak nonlinearity is only 0.007 percent of the 70 -MHz total frequency deviation. This example illustrates the greater sensitivity of the beat frequency spectrum to deviations from ideal linearity when the correlation time of the nonlinearities is shorter.

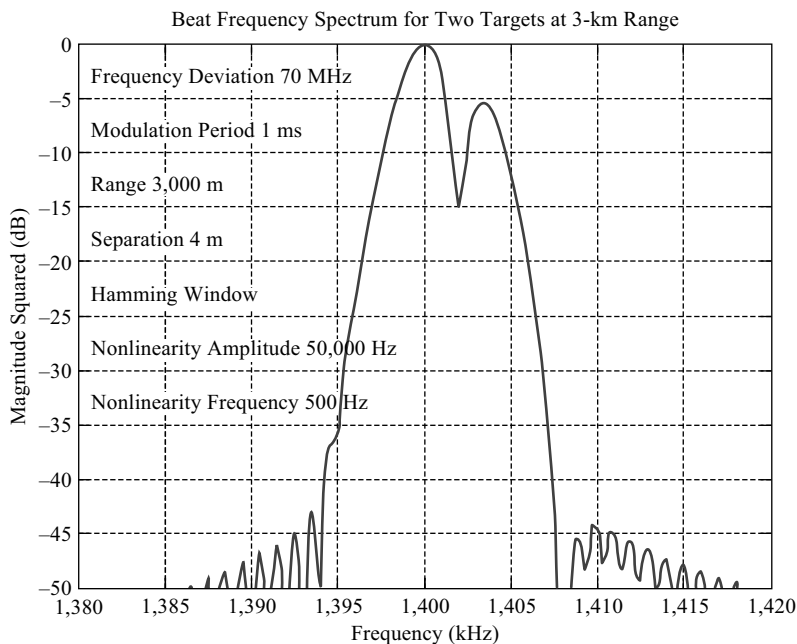
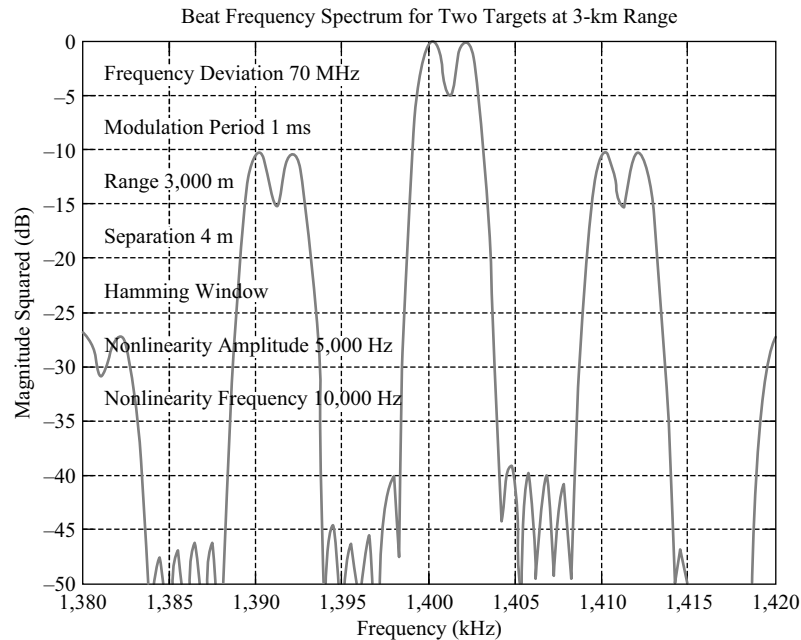


FIGURE 2.3-28 ■ Beat Frequency Spectrum for Two-Point Targets at 3 -km Range with 4 -m Separation, Hamming Window, 50 -kHz Peak Nonlinearity, and 2 -ms Nonlinearity Period.

FIGURE 2.3-29 ■ Beat Frequency Spectrum for Two-Point Targets at 3-km Range with 4-m Separation, Hamming Window, 5-kHz Peak Nonlinearity, and 0.1-ms Nonlinearity Period.



2.3.8 Direct Digital Chirp Synthesizers

An alternative to analog devices is to use direct digital synthesis of the FMCW waveform (although this is not without its own challenges and is the subject of continuing research). One method is to generate the frequency sweep at a lower frequency and then multiply it up to the desired operating frequency. This requires very careful attention to phase noise at the originating frequency because the phase noise increases with the frequency multiplication. For example, Griffiths reported on digitally generating a 40-MHz sweep at 200 MHz, then using two frequency quadrupler stages to yield a 640-MHz sweep at 3.2 GHz [23]. Johnson and Brooker reported on a real-beam FMCW radar that generates a 6-MHz sweep at 7.23 GHz and multiplies up by a factor of 13 to achieve 78-MHz sweep bandwidth at the 94-GHz operating frequency [9]. This approach may be necessary when, for example, the desired frequency deviation is greater than that available from direct digital synthesizer (DDS) technology. Meta *et al.* present a careful analysis of the impact of nonlinearity on FMCW radar performance along with compensation approaches [24]. Brennan *et al.* discuss FMCW sweep linearity requirement.

Direct frequency synthesizer technology can offer highly linear frequency sweeps. For example, the Analog Devices AD9858 is a DDS that features a 10-bit DAC operating up to 1 GSPS. The AD9858 is capable of generating a frequency-agile analog output sine wave up to 400+ MHz. The AD9858 residual phase noise is -140 dBc/Hz at 100-kHz offset for 403-MHz output. Liu *et al.* reported on using an Analog Devices AD9858 DDS in an FMCW radar with 800-MHz frequency deviation and 671-Hz modulation frequency. For the corresponding 1.49-ms modulation period, the desired slope is 537 MHz/ms. The AD 9858 frequency update rate is 125 MHz, so there are 8 ns between frequency changes, corresponding to 4.3-kHz frequency steps as shown in Figure 2.3-30. This quantization of the frequency sweep results in frequency errors that

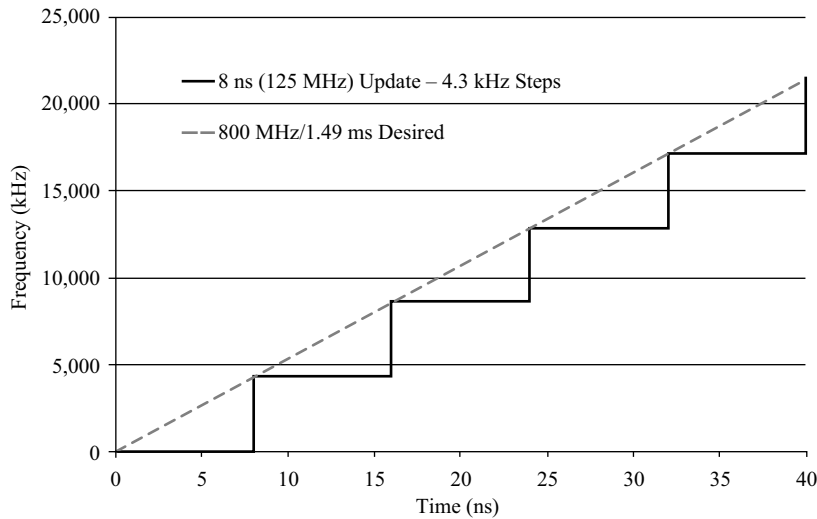


FIGURE 2.3-30 ■
DDS Frequency as a
Function of Time.

are uniformly distributed over 0 to 4,295-Hz, with corresponding 1,240-Hz ($4,295\text{ Hz}/\sqrt{12}$) standard deviation, which is 185 percent of the 671-Hz modulation frequency [25]. This is a rapidly advancing area in which commercial devices are likely to quickly improve their capability.

The Analog Devices AD9912 offers 1 GSPS internal clock speed, up to 400-MHz output directly, integrated 14-bit DAC, and 48-bit frequency tuning word (FTW) so that it can synthesize frequencies in step sizes $<4\ \mu\text{Hz}$. In fact, modern digital lab equipment offers a simple but quite costly approach to direct digital synthesis and has the flexibility that comes with digital waveform generation.

2.4 | OTHER CW RADAR WAVEFORM DESIGNS

In section 2.3, we only considered the linear frequency modulated waveform because this is the workhorse of the vast majority of current CW radar systems. However, it is not the only design of waveform that could be employed. Indeed, the design freedom represented by choice of modulation is one that is being exercised more and more as current technology now allows almost any form of modulation to be superimposed on the carrier frequency of pulsed or CW radar transmissions. Here we consider one example that exploits phase modulation because this form of signal has appeared more regularly in the research literature and has also begun to find its way into real systems. We also consider an alternative type of design that uses multiple frequencies. In general, the carrier frequency can be modulated in frequency, phase, and amplitude or in combinations of these. Indeed, even noise modulations may be used and have potentially attractive properties for CW applications. The coding can be linear or nonlinear.

Phase modulation has found widespread use in pulsed radar and can offer advantages in terms of control of sidelobes and avoidance of interference. Phase-only modulation [26] is similar to phase-modulated pulse compression. The rate at which the phase is varied (the chip rate) determines the bandwidth and hence range resolution of the waveform. Phase coding potentially has the attractive property that full bandwidth

resolution can be realized without loss induced by a weighting function. In other words, weighting can be done with phase without reducing amplitude across the signal and therefore avoiding the resulting loss in power. However, phase modulation can also result in ambiguous Doppler sensitivity, and care has to be exercised in the design of the coding scheme. Honeywell and NASA Ames developed a phase-modulated CW radar for helicopters for low-level flight to help avoid collisions with obstacles and terrain. Figure 2.4-1 shows a developmental phase-modulated CW radar. The radar system has an operating frequency of 35 GHz [27]. It was designed to detect objects such as trees, high-tension cables, fences, wood telephone poles, metal high-tension towers, and ground returns at less than 4° grazing angle to help enable safe low-level flying [28]. Table 2.4-1 lists the main operating parameters of this system.

Table 2.4-1 shows this system using a 32-ns bi-phase chip length. The chip length is the inverse of the chip rate, which determines the bandwidth and hence the range resolution. A chip length of 32 ns corresponds to 4.8-m range resolution. To achieve

FIGURE 2.4-1 ■ Phase-Modulated CW Obstacle Avoidance Radar System: NASA Ames and Honeywell, 20° Vertical by 50° Horizontal Field of View (FOV). Photo: Dominic Hart.



TABLE 2.4-1 ■ Honeywell Phase-Modulated CW Radar Parameters

35-GHz RF center frequency
35-mW transmit power
6-dB receiver noise figure
34-dBi antenna gain
3° beamwidth
25-dB antenna sidelobes
$\pm 45^\circ$ azimuth
$\pm 10^\circ$ elevation
32-ns or 4.8-m (16-ft) bi-phase code chip
1-, 5-, 7-, 11-, and 13-bit codes transmitted
25-kHz receiver bandwidth

chip lengths of this value requires a phase modulator with at least 31.3-MHz bandwidth and thus at least a 62.5-MHz ADC sample rate. The 0.9-km maximum unambiguous range requires a code length of at least 190 chips. This will produce range sidelobe levels of approximately 23 dB. This code is match filtered in a correlator to produce the range-compressed output. A brute-force 190-element correlator will require 190 multiplications every 16 ns or 11.9×10^9 multiplies per second.

Achieving finer range resolution requires a shorter chip length, which itself requires a wider bandwidth phase modulator, faster ADC sample rate, and faster memory. In other words, it requires a more complex and hence more expensive radar system. There is a trade-off in ADC technology between sample rate and dynamic range. For example, increasing the ADC sample rate may limit the available ADC dynamic range. Increasing the maximum unambiguous range or reducing the range sidelobe levels will require a longer code length that will require a longer correlator and thus more multiplications per second. The requirement for processing the fully transmitted bandwidth in the receiver generally limits phase-modulated CW radar to a coarser resolution than is readily achievable in FMCW radar. Table 2.4-2 summarizes the performance of the radar system as a function of chip and code length.

Another approach to waveform design that has found its way from the research literature to use in commercial radar systems is the frequency-shift keying (FSK) or multiple frequency (MF) technique. This technique has been of interest primarily because it is simple to implement and thus consistent with a low-cost design approach. Perhaps as a result, it has found application in the automotive radar, an extremely cost-sensitive industry.

FSK is a variant of FMCW radar. The radar transmits a CW signal with a frequency that is typically changed by two values to equate to the bandwidth of FMCW radar on a microsecond timescale. Processing proceeds in a similar manner to the FMCW radar. The phase difference between the received signals at the different frequency points contains the range data, while the Doppler information is contained in the IF frequency. FSK requires good phase stability but is otherwise simple from a hardware standpoint. The radar, however, requires extensive post-processing to ensure accurate range information. FSK has also been combined in a hybrid form with more conventional FMCW modulations.

TABLE 2.4-2 ■ Phase-Modulated CW Radar

Bi-phase Modulation Parameter	Performance	Requirements
32-ns chip length (1,120 35 GHz cycles per chip)	4.8-m (16-ft) range resolution	31.3-MHz bandwidth phase modulator 62.5-MHz ADC sample rate – 8- to 10-bit (48- to 60-dB) dynamic range (ADC technology limitation) 62.5-MHz memory
190 code length (190 code length \times 32-ns chip length \sim 6- μ s code repetition interval)	0.9-km (3-kft) unambiguous range 23-dB range sidelobe levels	190-element correlator 190 multiplies every 16 ns 11.9×10^9 multiplies per second

In basic form, the frequency FSK CW radar waveform alternates between two discrete frequencies, f_A and f_B , in the transmit signal. The maximum unambiguous range is given by

$$R_{max} = \frac{c}{2(f_A - f_B)} = \frac{c}{2\Delta f} \quad (2.4-1)$$

The coherent-processing interval is the duration of each frequency step. Figure 2.4-2 shows an example of an FSK CW radar waveform for 24-GHz operating frequency with a 500-kHz frequency step and a 5.12-ms CPI. The 500-kHz frequency step corresponds to 300-m maximum unambiguous range.

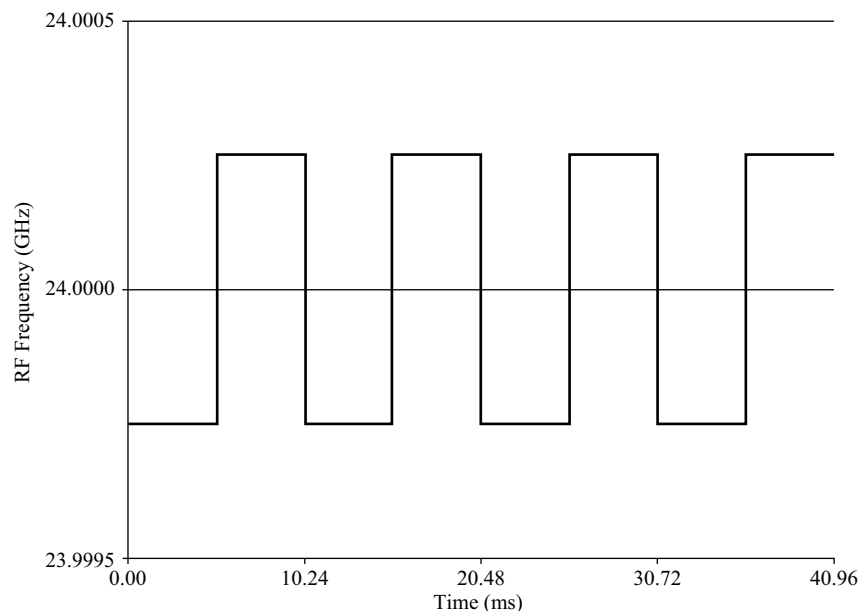
Using a homodyne receiver, the beat frequency signal is sampled N times, and an N -point FFT is performed on that sequence. Targets are detected in the FFT output, that is, in the Doppler-frequency-shift bins corresponding to relative-velocity bins. Due to the relatively small frequency step, a single target will be detected in the same Doppler frequency bin for both frequency-step FFTs but with different phase. The resulting phase difference, $\Delta\phi = \phi_A - \phi_B$ for the two transmit frequencies is proportional to the target range as given by the following equation:

$$R = \frac{c\Delta\phi}{4\Delta f} \quad (2.4-2)$$

The Doppler-frequency-shift resolution is approximately equal to the inverse of the CPI. Thus, a 5.12-ms CPI implies 195-Hz frequency resolution and corresponds to 1.2-m/s velocity resolution at 24 GHz. The system can make a relative phase measurement and hence a range measurement for objects separated by 195 Hz in Doppler frequency shift or 1.2 m/s in velocity.

Figure 2.4-3 shows the block diagram for an FSK CW radar design. For an 800-kHz ADC sample rate, there will be 4,096 samples for each 5.12-ms duration frequency step.

FIGURE 2.4-2 ■
Example of an FSK
CW Radar
Waveform.



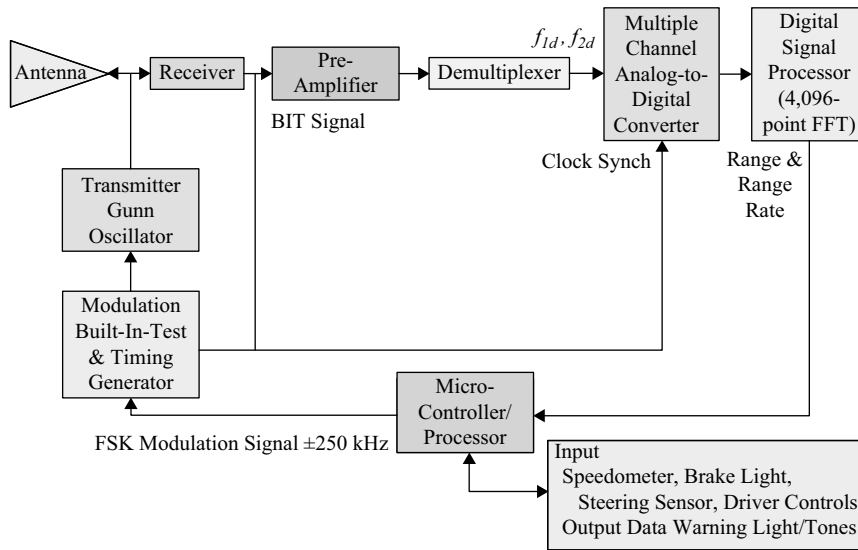


FIGURE 2.4-3 ■
FSK CW Radar
Block Diagram.

Performing a 4,096-point FFT on those samples yields 4,096 frequency bins from 0 to 800 kHz with 195-Hz Doppler-frequency separation, which corresponds to 1.2-m/s relative velocity separation for 24-GHz frequency. For 500-kHz frequency separation, the phase-difference-to-range ratio is 1.2°/m as shown here:

$$\Delta\phi = \frac{4\pi\Delta f R}{c} = \frac{4\pi 500 \text{ kHz}}{3 \times 10^8 \text{ m/s}} R = (0.021 \text{ rad/m})R = (1.2^\circ/\text{m})R \quad (2.4-3)$$

The FSK CW modulation is simple to generate and resolves targets with different velocities, but it is unable to measure the range to stationary targets because they all have the same relative velocity. Meinecke and Rohling propose a composite LFM CW and FSK waveform to overcome this challenge [29]. Will described automotive radar that uses the FSK CW waveform [30].

Overall waveform design for CW radars is still at an early stage. However, high-volume applications such as automotive radar are emerging that will place more emphasis on the design of the waveform. The security of sensed information is one aspect that will drive this. For example, if all vehicles are to have radar systems, then it becomes vital they do not interfere with one another, which will be challenging in a band-limited spectral environment. One approach to this problem may be to use codes that have high isolation from one another. In other words, they exhibit orthogonality such that they cross correlate with a resulting low signal level. Equally, to make the sensors affordable, the methods employed must be simple to implement and fabricate.

2.5 | FMCW RADAR APPLICATIONS

This section describes a number of CW radar applications along with some of the better-known systems, most of which have been developed into commercial products. Just like pulsed radar, CW systems have found their way into almost all types of radar

application. Here we examine surveillance systems, altimeters, aircraft landing aids, missile seekers, automotive radar, level measurement, ranging, weather radar, imaging radar, and space-based radar. Although this list is extensive, it is by no means exhaustive. In this section we hope to show the broad extent of CW radar systems by describing applications that have developed or taken up this attractive sensing technology.

2.5.1 Surveillance

CW radar systems have long been developed for surveillance applications going all the way back to the British Chain Home system developed for early warning of German air raids in World War II. However, the invention of the T/R switch meant that a single antenna could be used to both transmit and receive. This simultaneously both simplified the technology and avoided the greater complexity that comes with bistatic operation. As a result, most radar systems were subsequently of the pulsed type (which, of course, overcomes the transmitter leakage problem). However, from time to time the attractive properties of CW radar (low peak power, excellent Doppler sensitivity, low probability of intercept, etc.) meant that this alternative was subject to periodic research, some of which has subsequently given rise to the development of commercial products. Here we select just a few of the more noteworthy modern surveillance systems.

The PILOT radar from the Saab group was first developed in the 1980s. It performs navigation and detection and was developed for use on ships and submarines. PILOT exploits the FMCW waveform to achieve low probability of intercept (LPI) performance. Table 2.5-1 lists the main parameters of PILOT, and Figures 2.5-1 and 2.5-2 depict the radar equipment. Note that PILOT Mk3 includes frequency agility over a 400-MHz bandwidth from 9.1 GHz to 9.5 GHz. Spreading transmit power over this wide bandwidth enhances its LPI performance and its RPC to permit the system to operate with a single standard-navigation radar antenna. The PILOT maximum transmit power of 1 W gives it the same average power and detection range as pulsed navigation radars (of comparable size), but it enjoys an advantage over simple intercept receivers and antiradiation missile (ARM) receivers that are not matched to the FMCW waveform. In addition, the operator can reduce the transmit power to 1 mW for operation at shorter ranges and against larger targets [31].

A.G. Stove collaborated with M. Jankiraman to describe the development of the FMCW radar that was the precursor to the PILOT and SCOUT radars [32]. Jankiraman describes a very-high-resolution X-band radar with 4-GHz bandwidth and 34-mm range resolution achieved by exploiting parallel operation of eight 500-MHz bandwidth FMCW radar channels [33]. The PILOT radar system aroused much interest when it was first announced, as it was the first to demonstrate that active radar could have a truly low probability of intercept. This meant that a shorter-range active radar-surveillance system could legitimately be considered alongside passive techniques. The PILOT radar has gone on to be a successful commercial product capable of a number of surveillance roles.

A number of other similar systems have been developed. For example, there is the SCOUT radar family manufactured by MSSC (a joint venture of DRS Communications Company, LLC, and THALES Naval Nederland). The basic SCOUT radar shares some of the parameters of the PILOT system. It operates at I-band with transmit power varying from 10 mW to 1,000 mW and instrumented ranges of 4.4, 11.1, and 44 km. The SCOUT antenna beamwidths are 1.2° in azimuth and 11° in elevation. The SCOUT can

TABLE 2.5-1 ■ PILOT, SCOUT, and SQUIRE Radar Parameter Summary

	PILOT	SCOUT Mk2	MSSC SCOUT	SQUIRE
RF center frequency	9.3 GHz, X(I)-band	I-band	I-band (two channels)	J-band
Frequency agility bandwidth	400 MHz	–	–	–
Features	Reflected rower canceller	–	Dual slotted waveguide antenna	–
Output power	1, 10, 100, and 1,000 mW	10 to 1,000 mW	1, 10, 100, and 1,000 mW	10 to 1,000 mW
Receiver noise figure	5 dB	–	3.5 dB	–
Instrumented range	2.4, 6, 24 nm	6, 12, 24 nm	0.75, 1.5, 3, 6, 12, 24 nm	3, 6, 12, 24 nm or 6, 12, 24, 48 nm
Range cell size	2.4, 6, 24 m	3 m at 6 nm scale	6 to 96 m at 0.75 to 24 nm	–
Antenna gain	–	29.5 dBi	30 dBi	–
Number of range cells	–	3,641	512	512
Antenna rotation speed	–	144°/s 24 rpm	144°/s 24 rpm	0, 7, 14°/s
Antenna beamwidth	–	1.2° Azimuth 11° Elevation	1.4° Azimuth 20° Elevation	2.7° Azimuth 7.8° Elevation
Sweep repetition frequency	–	–	1 kHz	–
Frequency sweep	–	–	Up to 54 MHz	–

**FIGURE 2.5-1** ■ PILOT FMCW Radar Transceiver, Signal Processor, and Remote Control Panel.

FIGURE 2.5-2 ■
PILOT FMCW Radar
Transceiver Interior.



also be used for coastal surveillance. The SCOUT Mk2 includes a dual-array antenna for good isolation between the transmitter and receiver. This antenna has 29.5-dBi gain and rotates at 144°/s. Thales Naval Nederland's VARIANT is a lightweight short- to medium-range two-dimensional surveillance radar that includes both a dual-band pulse Doppler radar and an LPI FMCW radar. Table 2.5-1 includes a separate column for the MSSC SCOUT because some of the parameters are slightly different. The Coastal Border Surveillance System (CBSS) combines SCOUT with an electro-optical (EO) system for rapid target detection and identification and classification. As shown in Figure 2.5-3, the system is packaged in a mobile shelter on a high mobility multipurpose wheeled vehicle (HMMWV) or other vehicles and includes a trailer-mounted generator.

Another broadly similar but more modern system is the SQUIRE radar. This is a human-portable, ground surveillance FMCW radar from Thales operating between 10 GHz and 20 GHz that can detect moving targets on or close to the ground, up to a distance of 48 km. The system supplies information to classify detected targets manually or automatically. In addition, it can assist friendly artillery by giving feedback on shell impacts. As shown in Figure 2.5-4, SQUIRE can be carried in two backpacks of approximately 24 kg each.

In 2001, MSSC was awarded a contract to provide a mobile ground surveillance radar system (MGSRS) for an international army border defense guard force. The MGSRS includes the SQUIRE along with electro-optical sensors and controls integrated into an HMMWV. MGSRS can support battlefield surveillance, border control, oil-field and power-station security, and drug-interdiction operations.

Perhaps the most notable recent addition to CW surveillance radars is the Blighter family developed by Plextek in the United Kingdom (U.K.). This is also a lightweight portable system but one that also combines electronic scanning with the FMCW technique. The output power is 1 W with a high-power 4 W option. This has a maximum



FIGURE 2.5-3 ■
Coastal Border
Surveillance System
(CBSS), Including
SCOUT FMCW
Radar.



FIGURE 2.5-4 ■
SQUIRE Ground
Surveillance FMCW
Radar.

detection range of 32 km and can be combined to readily form a network. The Blighter radar is integrated with a lightweight camera system to provide flexible high-performance surveillance; Figure 2.5-5 shows a fielded system.

Also from Thales Naval Nederland, PAGE is an air-surveillance FMCW. It also operates between 10 GHz and 20 GHz and provides early warning and cueing for air targets at ranges up to 20 km. It is intended to work with human-portable air-defense systems such as STINGER, MISTRAL, STARSTREAK, RBS70, and medium-caliber anti-aircraft (AA) guns. PAGE is suitable for integration with a vehicle as well as for mounting on a tripod. Figure 2.5-6 shows the PAGE system.

FIGURE 2.5-5 ■
The Blighter Radar
System.



FIGURE 2.5-6 ■
PAGE Air
Surveillance FMCW
Radar.



Warsaw-based Prezemyslowy Instytut Telekomunikacji (Telecommunications Research Institute) developed an LPI radar for naval and coastal surveillance applications. Designated the CRM-100, the sensor is described as being an FMCW emitter that operates on ten switched frequencies within the 9.3- to 9.5-GHz frequency range. Designed to detect surface targets and provide automatic target tracking and data hand-off to a command post, the CRM-100 is quoted as having an output power of between

1 mW and 1 W and being able to track as many as 40 targets at ranges of between 1.4 km and 44.5 km. In its ground-based application, the CRM-100 appears to comprise a truck-mounted equipment and operator shelter and a deployable mast that is carried on a two-wheel trailer. The radar is described as having an angular resolution of 0.1° and a bearing accuracy of 1° as well as being able to establish target numbers, ranges, bearings, courses, and speeds.

2.5.2 CW Radar Altimeters

FMCW is an attractive mode of operation for measuring height because systems can be made compact and hence flown on small aircraft or on satellites. High-accuracy range finding coupled with the large reflectivity of the ground at vertical incidence make this a commonly used approach for altimetry. Figure 2.5-7 shows the AN/APN-232 Combined Altitude Radar Altimeter (CARA) from NavCom Defense Electronics, Inc., which uses the FMCW waveform in combination with adaptive power control to achieve LPI. As listed in Table 2.5-2 the CARA operates between 4.2 GHz and 4.36 GHz with 100-MHz modulation bandwidth. At the maximum specified range of 15.2 km (50 kft), the maximum radiated power is 1 W for worst-case surface reflectivity; with adaptive power management, typical radiated power is in the low milliwatt range at 152-m (500-ft) altitude. The CARA accuracy is summarized in Table 2.5-2. For an ESM receiver optimized for the CARA waveform, the detection range at 152-m (500-ft) altitude is from 91 m to 213 m (300 ft to 700 ft) for typical ground reflectivity of -13 dB to 0 dB. More than 10,000 CARA systems have been delivered. It is the standard U.S. Air Force (USAF) radar altimeter on the F-4, F15E, F-16, F-111, C-5, C-17, C-130, H-53, and other aircraft platforms [34].

Honeywell has been a consistent manufacturer of a range of radar altimeters. The HG-9550 radar altimeter from Honeywell Defense and Space Electronics Systems has the same range, accuracy, and transmit power as the CARA. The HG-9550 operates at 4.3 GHz. LPI features include power management, frequency agility, and jittered code and pulse repetition frequency (PRF). It is currently in production for the USAF C-120J, the U.K. C-130J, Argentine A-4 upgrade, Korean T-50, and F-16 block 60 [36]. The HG7808 radar altimeter module from Honeywell also operates at C-band, 4.3 GHz, and has a transmit power of up to 1 W or 30 dBm. The maximum altitude is 2.4 km with ± 0.6 m (or ± 2 percent). LPI features include both power management and pseudo random noise (PRN) coding [35].

Thales is another company well known for radar altimetry. Figure 2.5-8 shows the company's AHV-2100 radar altimeter. Designed for helicopters, trainers, and transport aircraft requirements, it has been installed on the NH90 helicopter, CASA 295 transport aircraft, and NIMROD MPA. This FMCW radar altimeter operates in the 4.2- to 4.4-GHz frequency band with power management for good LPI performance. Its accuracy is $1\text{ m} \pm 2$ percent for ranges up to 1,524 m.

TABLE 2.5-2 ■ CARA Accuracy Summary

Accuracy	Altitude
± 0.6 m (± 2 ft)	Up to 30 m (100 ft)
± 2 percent	From 30 m to 1,524 m (100 ft to 5,000 ft)
± 30 m (100 ft)	From 1,524 m to 3,048 m (5,000 ft to 10,000 ft)
± 1 percent	Above 3,048 m (10,000 ft)

FIGURE 2.5-7 ■
AN/APN-232 CARA.



FIGURE 2.5-8 ■
Thales AHV-2100
Radar Rltimeter.



The Thales AHV-2900 radar altimeter operates over the same frequency band as the AHV-2100. However, this system is designed for missiles and unmanned aerial vehicles (UAVs) and is installed on APACHE, RBS15, and STORM SHADOW missiles. Like the AHV-2100, it has power management, offering a maximum range of 9.144 km and $1 \text{ m} \pm 1$ percent accuracy. Figure 2.5-9 shows an example.

The Thales AHV-2500 radar altimeter shown in Figure 2.5-10 is also designed for missiles and UAVs. It operates over the same frequency band as the AHV-2100. However, it offers a shorter maximum range of 1.524 km and $1 \text{ m} \pm 3$ percent accuracy.

2.5.3 Aircraft Landing and Obstacle Avoidance

The avoidance of obstacles and the ability to land in foul weather can be improved using radar sensors. Narrow antenna beamwidths are desirable for radars installed in the nose



FIGURE 2.5-9 ■
Thales AHV-2900
Radar Altimeter.



FIGURE 2.5-10 ■
Thales AHV-2500
Radar Altimeter.

of aircraft, implying MMW operating frequencies. The CW waveform may be employed for high average transmit power and long coherent-processing intervals. Lear Astronics and Technology Service Corporation prototype radars were developed for this application. Table 2.5-3 lists the parameters for the Lear Astronics prototype 94 GHz FMCW radar. The Lear Astronics FMCW radar receiver processing computes four 400- μ s FFTs within each 1,800- μ s modulation period. Thomson CSF's Romeo system was also developed for helicopter obstacle avoidance [19].

Rangwala *et al.* described a W-band sawtooth FMCW prototype radar for helicopter landing with 150-m maximum range, $<1^\circ$ antenna beamwidth, and <0.3 -m

TABLE 2.5-3 ■ Lear Astronics 94 GHz FMCW Radar Parameter Summary

Radar Parameter	Value	Value	Value	Units
RF center frequency	94.3	94.3	94.3	GHz
RF wavelength	3	3	3	mm
FMCW waveform	Sawtooth	Sawtooth	Sawtooth	
Frequency deviation, peak to peak	200.0	100.0	50.0	MHz
Ideal time resolution	5.0	10.0	20.0	ns
Ideal range Resolution	0.75	1.5	3.0	m
Modulation frequency	555.56	555.6	555.6	Hz
Modulation index	360,000	180,000	90,000	
Modulation period	1.8	1.8	1.8	ms
Frequency slew rate	111.11	55.56	27.78	MHz/ms
Beat frequency/range ratio	740.74	370.37	185.19	Hz/m
Maximum range	1.50	3.00	6.00	km
Maximum transit time	10	20	40	μs
Maximum beat frequency	1.11	1.11	1.11	MHz
Analog-to-digital convertor sample rate	2.5	2.5	2.5	MHz
FFT length	1,024	1,024	1,024	Points
FFT length (4 FFTs per sweep)	400	400	400	μs
FFT frequency sample spacing	2,441.41	2,441.41	2,441.41	Hz
FFT range sample spacing	3.30	6.59	13.18	m

range resolution design goals [36]. The prototype had +16-dBm transmit power, ~150-mm diameter horn lens antenna, 500-MHz frequency deviation, and 50-kHz modulation frequency. Honeywell, in Torrance, California has a prototype W-band FMCW radar with up to 800-MHz sweep bandwidth and ~20 mm range resolution. This system has 0.5-W transmit power, 0.65° azimuth beamwidth, and 4.0° elevation beamwidth [37].

2.5.4 Seekers and Active Protection System Sensors

The CW waveform is also used in missile seekers and fuzes for missiles and artillery because those applications require low-cost, compact, lightweight sensors. Missile-seeker design is challenging because it requires fully autonomous operation over the full range of operational conditions. The Brimstone anti-armor missile seeker uses a 94-GHz FMCW radar [37]. The Saab Bofors Dynamics RBS-15 air-to-surface missile has an LPI FMCW radar seeker that employs transmit power management [38].

Active protection systems (APSS) are used on military vehicles to detect and track inbound projectiles such as rocket-propelled grenades and antitank guided missiles. The CW waveform is attractive for this application, which requires rapid response and autonomous operation. APSS using CW radar sensors include the Russian Drozd and Italian Scudo [39]. Scudo uses an X-band dual-frequency CW radar for surveillance, detection, and target tracking out to 500-m range [40].

2.5.5 Automotive CW Radars

Recent years have brought huge interest in automotive radar as technology has matured, and the application offers real potential for improving road safety. Systems are being developed that allow not only adaptive cruise control (ACC) but also collision sensing and avoidance with other cars, road debris, and pedestrians especially. Figure 2.5-11 shows a schematic of an automotive radar system in operation on the highway.

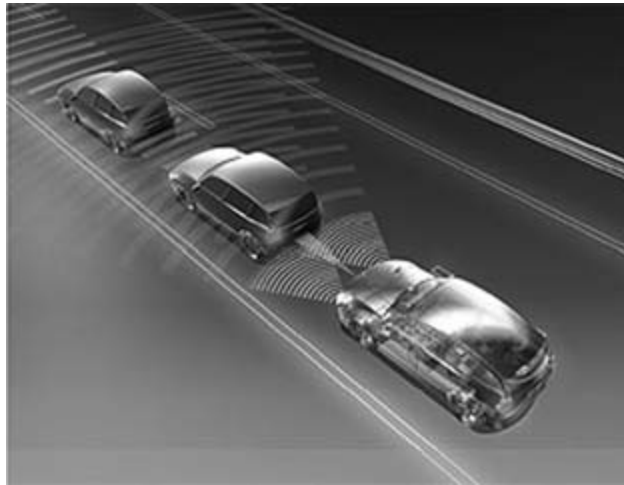


FIGURE 2.5-11 ■ Schematic Illustration of Automotive Radar.

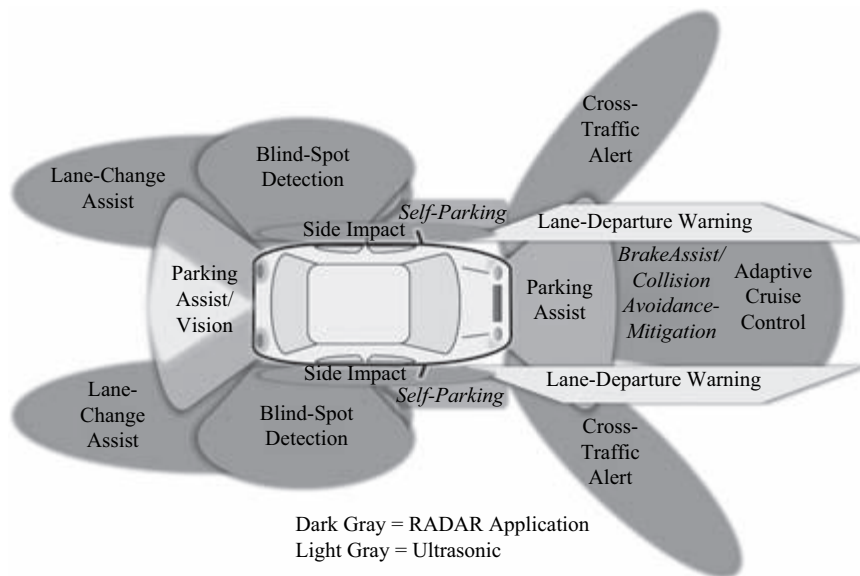


FIGURE 2.5-12 ■ Possible Vehicular Applications for Automotive Radar.

Systems are being developed in two main frequency bands: 24 and 77 GHz. The 77-GHz operating frequency band has been allocated for automotive radar sensors in the United States, Europe, and Japan. FMCW radars have been developed in that band for ACC and collision avoidance. For example, radar-based ACC and collision warning with brake support is currently available on Ford's Edge, Explorer, and Taurus and Lincoln's MKS, MKT, and MKX. The radar detects the vehicle up to 180 m ahead and adjusts the speed of the host vehicle to maintain a safe separation. Steinhauer *et al.* reported on a 76.5-GHz FMCW automotive radar with 200-MHz frequency deviation and 1.3-ms modulation period [41]. Goppelt *et al.* have investigated mutual interference between automotive FMCW radars [42]. Rohling *et al.* describe advanced CW waveforms for automotive radars [43, 44]. Figure 2.5-12 shows the range of vehicular applications that automotive radar could potentially support.

2.5.6 Level-Measurement FMCW Radars

Level measurement is a requirement of many industrial organizations and is a well-established application area for FMCW radar systems. Indeed, many tens of thousands of FMCW radar-level gauges have been sold by Saab, Siemens, Krohne, and others. For example, the Saab TankRadar operates at X-band using the FMCW waveform with 1-GHz frequency deviation and 0.1-s modulation period to achieve 1- to 3-mm accuracy for ranges up to 60 m as long as 1 percent to 4 percent of the power is reflected. The 10-GHz Rosemount 5600 series FMCW radar gauges offer ± 5 -mm accuracy at ranges of up to 50 m. Table 2.5-4 summarizes the parameters for a number of FMCW level gauges.

Figure 2.5-13 shows a radar system that includes a horn antenna for a level-measurement radar system operating at a carrier frequency of 26 GHz from Vega Controls Ltd. The higher frequency of 26 GHz results in a narrower beam, thus reducing the potentially deleterious effects of reverberation that exist in tank environments. There are variations in the internal design of horn antennas. Microwaves are transmitted down a high-frequency cable and coupled into a waveguide. The metal waveguide then directs the microwaves toward the horn of the antenna. A low dielectric material such as polytetrafluoroethylene (PTFE), ceramic, or glass is often used within the waveguide. At the transition from the waveguide to the flared part of the horn antenna, a low dielectric material is machined to a pointed cone. The angle of this cone depends on the dielectric constant of the material. Microwaves emitted from this pointed cone are focused toward the target by the metal horn.

2.5.7 Weather Sensing

Radar has become an indispensable tool for monitoring weather and providing advance warning of extreme events. Meteorologists use S-band zenith-pointing radars for measuring the atmospheric boundary layer. These radars use separate antennas to enhance transmit-to-receive isolation as shown in Figure 2.5-14. The FMCW waveform is employed for high average power and long coherent-processing intervals to achieve the sensitivity needed to detect the small RCS returns from variations in atmospheric density [45, 46]. Williams describes a system operating at C-band for observing precipitation [47]. ProSensing Inc. manufactures solid-state FMCW cloud radars, with up to 400-mW output power, 4.5-dB noise figure, and range resolution down to 1 m. These systems operate at MMW for enhanced cloud reflectivity.

2.5.8 Imaging

Radar imaging offers high resolution in two dimensions, thus providing detailed maps such as representations of Earth's surface. It has been developed primarily using pulsed radar concepts, but the drive for compact low-cost systems is creating interest in the FMCW technique. For example, the increase in the use of unmanned aircraft systems as platforms for surveillance sensors makes the low cost, compact size, and low-power requirements of FMCW radar systems attractive for short-range SAR. The International Research Centre for Telecommunications – Transmission and Radar (IRCTR) has flight-tested an X-band FMCW SAR operating at 9.65 GHz with 520-MHz bandwidth capable of 1- or 2-kHz modulation frequency and sawtooth or triangle modulation [48]. Nouvel *et al.* described an FMCW SAR operating at 35 GHz with 400-MHz bandwidth

TABLE 2.5-4 ■ FMCW Radar Level Gauges

Manufacturer	Saab	Rosemount	L&J Engineering	Krohne	PSM Instrumentation Ltd.	Nivelco Process Control	Solid Applied Technologies Ltd.
Model	TankRadar Rex	5600	evo 2600	BM702A	VG7	PilotTREK	SoltaScan
Frequency band	10 GHz	10 GHz	26 GHz	8.5–9.9 GHz	29 GHz	8–9 GHz	9.1–10.1 GHz
Range		50 m		20 m	40 m	40 m	50 m
Accuracy	±3 mm	±5 mm	±3 mm	±10 mm	±3 mm	±1 mm	<1 mm

FIGURE 2.5-13 ■ A Level-Measurement Radar.
Source: <http://www2.emersonprocess.com/SiteCollection/Images/News%20Images/Rosemount5300.jpg>



FIGURE 2.5-14 ■ S-Band FMCW Atmospheric Boundary Layer Radar.



and 400- μ s upsweep and downsweep for 1.25-kHz modulation frequency [49]. Weiss and Ender also describe an FMCW SAR operating at Ka-band [50].

2.5.9 Over-the-Horizon Radar

Over-the-horizon radar (OTHR) is highly suited to surveillance of extremely large areas. It operates by bouncing transmission off the ionosphere. Figure 2.5-15 shows an

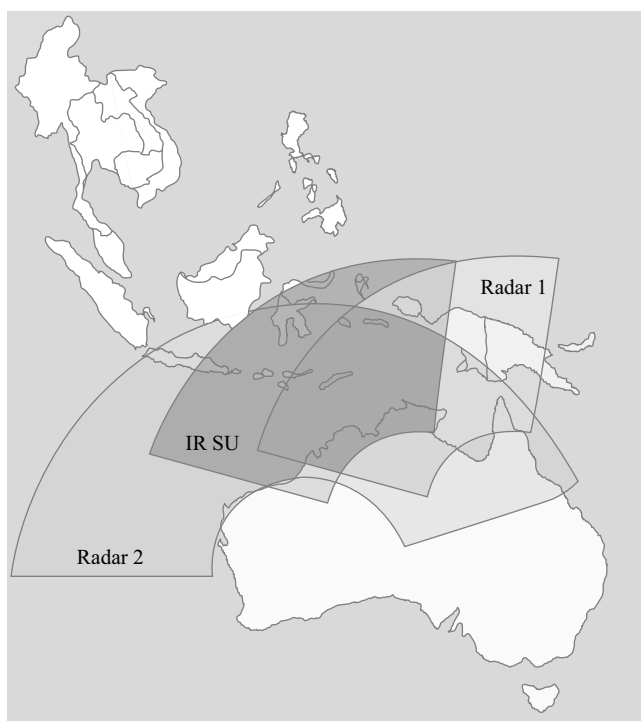


FIGURE 2.5-15 ■
Jindalee OTHR
Radar Coverage.

example of coverage for the Australian Jindalee system, which is capable of providing surveillance across the entire northern coast of Australia.

The linear FMCW waveform is used for OTHR, including the AN/FPS-118 East Coast Radar System (E CRS), West Coast Radar System (W CRS), AN/TPS-71 Relocatable OTHR (ROTHR), and the SRI International Wide Aperture Research Facility (WARF), along with the Australian Jindalee Stage B and Jindalee Operational Radar Network (JORN) Laverton. The mission for these systems is aircraft and ship detection at ranges beyond the radar horizon. The transmit-to-receive site separation is from 80 km to 180 km. These systems operate within the 5- to 32-MHz band in which signals are reflected by the ionosphere. Transmit effective radiated power (ERP) is 75 dBW to 80 dBW. Modulation frequencies are from 4 Hz to 80 Hz with 4- to 100-kHz bandwidth [51, 52, 53].

2.5.10 Space

Placing a radar sensor at high altitude offers the best geometry for global surveillance. Indeed, many pulsed imaging radar systems are currently in orbit and more are planned. A somewhat different concept is the Air Force Space Surveillance System, colloquially known as the Space Fence, a multistatic CW radar system that can detect orbital objects at ranges up to 30,000 km. This unique CW radar system includes six receiving stations and three transmitter sites that operate at different frequencies in the VHF band near 217 MHz. The master transmitter at Lake Kickapoo, Texas, has 99-dBW ERP. The Space Fence radar systems determine target position from Doppler frequency shifts and from interferometry between receive antennas because unmodulated CW radar waveform cannot measure range.

2.6 | REFERENCES

- [1] W. K. Saunders, “CW and FM Radar,” Chapter 14 in *Radar Handbook*, Second Edition, Merrill I. Skolnik, editor, McGraw-Hill, 1990.
- [2] W. K. Saunders, “CW and FM Radar,” Chapter 16 in *Radar Handbook*, M. I. Skolnik, editor, McGraw-Hill, 1970, pp. 16–17.
- [3] I. V. Komarov and Sergey M. Smolskiy, *Fundamentals of Short-Range FM Radar*, Artech House, 2003.
- [4] S. Kaplan, *Wiley Electrical and Electronics Engineering Dictionary*, Wiley-IEEE Press, 2004, ISBN: 9780470547151.
- [5] A. G. Stove, “Linear FMCW Radar Techniques,” *IEE Proceedings*, Part F, Vol. 139, No. 5, October 1992, pp. 343–350.
- [6] B.-O. As, CelsiusTech Electronics, Sweden, “Implementation of FMCW Techniques into Practical Radar Systems,” 1993.
- [7] A. G. Stove, “Measurement of Oscillator Phase and Amplitude Noise at W-band,” Automated RF & Microwave Measurement Society (ARMMS), RF and Microwave Society, 2008 Conference, 7 to 8 April 2008. Retrieved from http://www.armms.org/images/conference/ARMMS_Stove.pdf. Accessed on 14 October 2011.
- [8] James A. Scheer, “The Radar Range Equation,” Chapter 2 in *Principles of Modern Radar, Volume I: Basic Principles*, Mark A. Richards, James A. Scheer, and William A. Holm, editors, SciTech Publishing, Inc., 2010, p. 65.
- [9] D. Johnson and G. Brooker, “Research Radar for Unmanned Navigation,” *2008 International Conference on Radar*, pp. 165–170 [Digital object identifier 10.1109/RADAR.2008.4653911].
- [10] P. D. L. Beasley, A. G. Stove, B. J. Reits, and B.-O. As, “Solving the Problems of a Single Antenna Frequency Modulated CW Radar,” *IEEE Radar Conference*, 1990, pp. 391–395.
- [11] K. Lin, R. H. Messerian, and Y. Wang, “A Digital Leakage Cancellation Scheme for Monostatic FMCW Radar,” *2004 IEEE MTT-S International Microwave Symposium Digest* (IEEE Cat. No. 04CH37535), June 6–11, 2004, Fort Worth, TX, USA, pp. 747–750, Vol. 2, ISBN: 0 7803 8331 1.
- [12] K. Lin and Y. Wang, “Real-Time DSP for Reflected Power Cancellation in FMCW Radars,” *2004 Vehicular Technology Conference, VTC2004-Fall*, 2004 IEEE 60th, September 26–29, 2004, Vol. 6, pp. 3905–3907, ISSN: 1090-3038.
- [13] A. Laloue, J.-C. Nallatamby, M. Prigent, M. Camiade, and J. Obregon, “An Efficient Method for Nonlinear Distortion Calculation of the AM and PM Noise Spectra of FMCW Radar Transmitters,” *IEEE Transactions on Microwave Theory and Techniques*, Vol. 51, No. 8, August 2003, pp. 1966–1976.
- [14] P. D. L. Beasley, “Advances in Millimetre Wave FMCW Radar,” *MRRS-2008 Symposium Proceedings*, Kiev, Ukraine, September 22–24, 2008.
- [15] G. M. Brooker, D. Birch, and J. Solms, “W-Band Airborne Interrupted Frequency Modulated CW Imaging Radar,” *IEEE Transactions on Aerospace and Electronic Systems*, Vol. 41, No. 3, July 2005, pp. 955–972.
- [16] G. Brooker, *Introduction to Sensors for Ranging and Imaging*, SciTech Publishing, 2009, pp. 456–459.

- [17] P. Almorox-Gonzalez, J.-T. Gonzalez-Partida, M. Burgos-Garcia, B. P. Dorta-Naranjo, and J. Gismero, "Millimeter-Wave Sensor with FMICW Capabilities for Medium-Range High-Resolution Radars," *IEEE Transactions on Microwave Theory and Techniques*, Vol. 57, Issue 6, June 2009, pp. 1479–1486 [Digital object identifier 10.1109/TMTT.2009.2019991].
- [18] J. T. Gonzalez-Partida, M. Burgos-Garcia, B. P. Dorta-Naranjo, and F. Perez-Martinez, "Stagger Procedure to Extend the Frequency Modulated Interrupted Continuous Wave Technique to High Resolution Radars," *IET Radar, Sonar & Navigation*, 2007, Vol. 1, Issue 4, pp. 281–288 [Digital object identifier 10.1049/iet-rsn:20060033].
- [19] L. Q. Bui, Y. Alon, and T. Morton, "94 GHz FMCW Radar for Low Visibility Aircraft Landing System," *IEEE MTT-S International MW Symposium Digest*, June 1991.
- [20] R. J. Lefevre, J. C. Kirk, Jr., and R. L. Durand, "Obstacle Avoidance Sensors for Automatic Nap-of-the-Earth Flight," *Proceedings of the 1994 IEEE/AIAA 13th Digital Avionics Systems Conference (DASC)*, November 1994.
- [21] S. O. Piper, "FMCW Range Resolution for MMW Seeker Applications," *IEEE Southeastcon '90*, April 1990.
- [22] S. O. Piper, "Receiver Frequency Resolution for Range Resolution in Homodyne FMCW Radar," National Telesystems Conference, Atlanta, GA, June 1993.
- [23] H. D. Griffiths and W. J. Bradford, "Digital Generation of Wideband FM Waveforms for Radar Altimeters," *Proceedings Radar 87 Conference*, London, October 1987.
- [24] A. Meta, P. Hooeboom, and L. P. Ligthart, "Signal Processing for FMCW SAR," *IEEE Transactions on Geoscience and Remote Sensing*, Vol. 45, No. 11, November 2007, pp. 3519–3532.
- [25] Y. Liu, D. Goshi, K. Mai, L. Bui, and Y. Shih, "Linearity Study of DDS-Based W-Band FMCW Sensor," *Microwave Symposium Digest*, 2009, MTT '09, IEEE MTT-S International, Boston, MA, June 7–12, 2009, pp. 1697–1700, ISSN 0149-645X, Print ISBN 978-1-4244-2803-8, INSPEC Accession Number 10788742 [Digital object identifier 10.1109/MWSYM.2009.5166042].
- [26] M. Jankiraman, "Phase-Coded Waveform," Chapter 5 in *Design of Multi-Frequency CW Radars*, SciTech Publishing, 2007.
- [27] P. Proctor, "Low-Level Collision Avoidance Tested," *Aviation Week and Space Technology*, February 3, 1997.
- [28] K. Raymer and T. Weingartner, "Advanced Terrain Data Processor," *Proceedings of the IEEE/AIAA 13th Digital Avionics Systems Conference (DASC)*, 31 October to November 3, 1994, pp. 636–639.
- [29] M.-M. Meinecke and H. Rohling, "Combination of LFMCW and FSK Modulation Principles for Automotive Radar Systems," *German Radar Symposium GRS2000*, Berlin, October 22–12, 2000.
- [30] J. D. Will, "Monopulse Doppler Radar for Vehicle Applications," *Proceedings of the Intelligent Vehicles '95 Symposium*, September 25–26, 1995, IEEE Catalog 95TH8132, p. 42, ISBN 0-7803-2983-X.
- [31] S. O. Piper and J. Wiltse, "Continuous Wave Radar," in "RF and Microwave Applications and Systems," Chapter 14 in *The RF and Microwave Handbook*, Second Edition, Mike Golio and Janet Golio, editors, CRC Press, 2008.
- [32] M. Jankiraman, Chapter 7 in *Design of Multi-Frequency CW Radars*, SciTech Publishing, 2007.

- [33] M. Jankiraman, Chapter 8 in *Design of Multi-Frequency CW Radars*, SciTech Publishing, 2007.
- [34] P. E. Pace, *Detecting and Classifying Low Probability of Intercept Radar*, Second Edition, Artech House, 2009, pp. 42–45.
- [35] P. E. Pace, *Detecting and Classifying Low Probability of Intercept Radar*, Second Edition, Artech House, 2009, p. 43.
- [36] M. Rangwala, L. Juseop, and K. Sarabandi, “Design of FMCW Millimeter-Wave Radar for Helicopter Assisted Landing,” *2007 IEEE International Geoscience and Remote Sensing Symposium*, IGARSS 2007, pp. 4183–4186 [Digital object identifier 10.1109/IGARSS.2007.4423772].
- [37] D. S. Goshi, Y. Liu, K. Mai, L. Bui, and Y. Shih, “Cable Imaging with an Active W-Band Millimeter-Wave Sensor,” *2010 IEEE MTT-S International Microwave Symposium Digest (MTT)*, May 23–28, 2010, Anaheim, CA, pp. 1620–1623 [Digital object identifier 10.1109/MWSYM.2010.5515781].
- [38] P. E. Pace, *Detecting and Classifying Low Probability of Intercept Radar*, Second Edition, Artech House, 2009, p. 466.
- [39] P. E. Pace, *Detecting and Classifying Low Probability of Intercept Radar*, Second Edition, Artech House, 2009, pp. 58–59.
- [40] Defense Update International. “Active Protection Systems for AFVs,” *Defense Update International Online Defense Magazine*, Issue 1, 2004.
- [41] *Anti-Missile System for Main Battle Tanks*, Lt. Col. Carlo Aimini, Italian Army, International Armaments Technology Symposium and Exhibition, Picatinny Arsenal, NJ, June 14–16, 2004.
- [42] M. Steinhauer, H.-O. Ruoss, H. Irion, and W. Menzel, “Millimeter-Wave-Radar Sensor Based on a Transceiver Array for Automotive Applications,” *IEEE Transactions on Microwave Theory and Techniques*, Vol. 56, No. 2, February 2008, p. 261.
- [43] M. Goppelt, H.-L. Blocher, and W. Menzel, “Analytical Investigation of Mutual Interference Between Automotive FMCW Radar Sensors,” *2011 German Microwave Conference (GeMIC)*, pp. 1–4.
- [44] H. Rohling and M.-M. Meinecke, “Waveform Design Principles for Automotive Radar Systems,” *Proceedings 2001 CIE International Conference on Radar*, pp. 1–4 [Digital object identifier 10.1109/ICR.2001.984612].
- [45] H. Rohling and C. Moller, “Radar Waveform for Automotive Radar Systems and Applications,” *IEEE Radar Conference, 2008, RADAR '08*, pp. 1–4 [Digital object identifier 10.1109/RADAR.2008.4721121].
- [46] S. J. Frasier, “High-Resolution S-Band Profiling of the Atmospheric Boundary Layer,” ARO Grant DAAG-55-98-1-0513, November 4, 2002.
- [47] S. J. Frasier, A. Muschinski, P.-S. Tsai, and M. Behn, “Vertical Velocity Turbulence observed with FMCW Radar,” in the digest of *IEEE International Geoscience and Remote Sensing Symposium*, pp. III 911–III 914, July 2008.
- [48] C. R. Williams, “Inexpensive FM-CW Radar for Boundary-Layer Precipitation Studies,” *IEEE Geoscience and Remote Sensing Letters*, 2011.
- [49] A. Meta and P. Hoogeboom, “Time Analysis and Processing of FM-CW SAR Signals,” available at http://irctr.et.tudelft.nl/sector/rs/articles/2003/irs_meta.pdf.
- [50] J. Nouvel *et al.*, “A Ka Band Imaging Radar: DRIVE on board ONERA Motorglider,” *Proceedings of the IEEE International Geoscience Remote Sensing Symposium*, Denver, CO, August 2006, pp. 134–136.

- [51] M. Weiss and J. H. G. Ender, “A 3D Imaging Radar for Small Unmanned Airplanes – ARTINO,” *Proceedings of EURAD*, Paris, France, October 2005, pp. 209–212.
- [52] J. M. Headrick and S. J. Anderson, “HF Over-the-Horizon Radar,” Chapter 20 in *Radar Handbook*, Third Edition, Merrill I. Skolnik, editor in chief, McGraw Hill, 2008.
- [53] T. H. Pearce, “The Application of Digital Receiver Technology to HF Radar,” *Fifth International Conference on HF Radio Systems and Techniques*, London, England, July 22–25, 1991.

MMW Radar Characteristics and Applications

J. A. Saffold, Research Network Incorporated, Kennesaw, GA

Chapter Outline

3.1 Introduction	87
3.2 The MMW Spectrum	88
3.3 Propagation at Higher Frequency	89
3.4 Antenna Beamwidth Considerations	93
3.5 MMW Performance Limitations	94
3.6 Typical Seeker or Smart Munition Configuration	98
3.7 MMW Radar Applications	108
3.8 MMW Future Trends	112
3.9 Further Reading	113
3.10 References	114

3.1 | INTRODUCTION

Millimeter wave (MMW) radar does not represent a specific radar *application* but a class of radars that operates over the range of frequencies from 30 GHz to 300 GHz. This corresponds to wavelengths measured in millimeters, hence the name. While the first MMW systems were large and bulky, today's systems have higher effective output powers and greater efficiencies in extremely small packages. This chapter will present the unique capabilities and challenges presented by the use of MMW for target detection, tracking, and identification in the current environment for both the defense and commercial market sectors. Implementations and examples are provided along with key operating considerations.

The primary advantage of MMW radar is its short wavelength. As discussed in [1, 2], the antenna beamwidth (in radians) is approximately $1.2\lambda/D$, where λ is the wavelength, and D is the antenna dimension. If space for an antenna is limited, then the shorter the λ , the narrower the antenna beam and similarly the better the tracking precision. Also, the amount of interference from clutter is reduced for a narrow beamwidth compared to a wide beamwidth. Many applications for radar have limited space, such as in missiles, automobiles, and personnel devices. The ability to propagate in small bounded regions allows for circuit miniaturization and higher aperture resolution. While MMW components are still not as efficient as many lower-frequency radio frequency (RF) components, the availability is getting better. For example, a 10-Watt X-band amplifier might be 100 times more efficient (and less costly) than a similar one at W-band.

The primary disadvantage of MMW radar is also related to its short wavelength. At MMW frequencies, the atmospheric effects are increased compared to lower frequencies in the transmission bands. Precipitants and other lofted particulates also have greater impact on the range performance of MMW radar. While poor compared to other radar systems at lower frequencies, MMW radar does penetrate many obscuring phenomena better than IR or optical wavelengths. Specific advantages of MMW over other spectral regions are discussed later in this chapter.

There are many applications for which MMW wavelengths are appropriate for radar sensors. In some cases, current requirements are met using electro-optical (EO) or infrared (IR) systems, however, relatively high absorption of these signals as they propagate through the atmosphere sometimes severely limits their usefulness. In these cases, the use of an MMW replacement or companion sensor is appropriate. In other cases, more conventional microwave frequency sensors are in use, although the narrow beamwidths produced by shorter MMW systems make them a better choice. Given that there are so many specific applications for MMW radars, this chapter will not attempt to describe them all. Indeed, an entire volume would be required to adequately describe these applications. Instead, the specific features of MMW systems will be provided, followed by a summary of classes of applications.

3.2 | THE MMW SPECTRUM

The MMW spectrum is defined by the frequency range from 30 GHz to 300 GHz. Table 3-1 lists the frequency band designations used by the Institute of Electrical and Electronics Engineers (IEEE).

The band designations for frequencies above 110 GHz are generally “millimeter.” As applications and components start to provide performance at these frequencies, appropriate band letters will follow. While initially the MMW region was dominated by military applications such as seekers and missiles, there are many additional applications now in use from the K-band to the W-band (MMW). Cell phones, wireless Internet, digital radio, satellite communications (SATCOM), collision avoidance, automated aircraft landing, and many others are evolving. As illustrated in Figure 3-1, combat identification systems, police radars, and concealed-weapon detection systems are also used in this range, and many others continue to emerge in the commercial market.

For the most part, although the band designations encompass a wide range of frequencies, the actual frequency used for radar would be at a specific one that is at or near the relative null in the absorption characteristics. For example, a Ka-band radar often operates in the range of 34 GHz to 35 GHz, and a W-band system operates in the vicinity of 94–95 GHz. The 140-GHz systems are not prevalent today but will become more

TABLE 3-1 ■ MMW Spectrum Band Designations (IEEE)

Band Designation	Frequency Range
Ka	27–40 GHz
Q / V	40–75 GHz
W	75–110 GHz
Millimeter	110–300 GHz

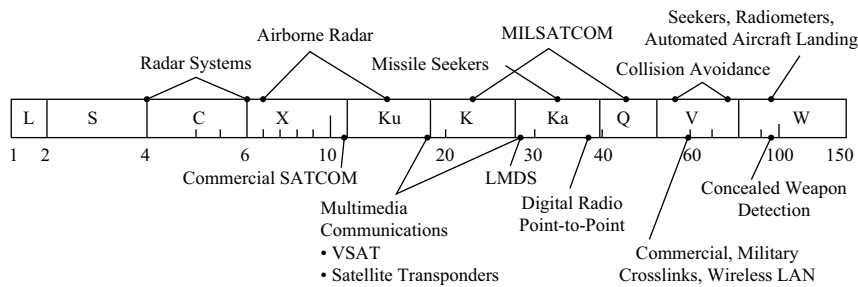


FIGURE 3-1 ■
MMW Spectrum and
Military and
Commercial Use.

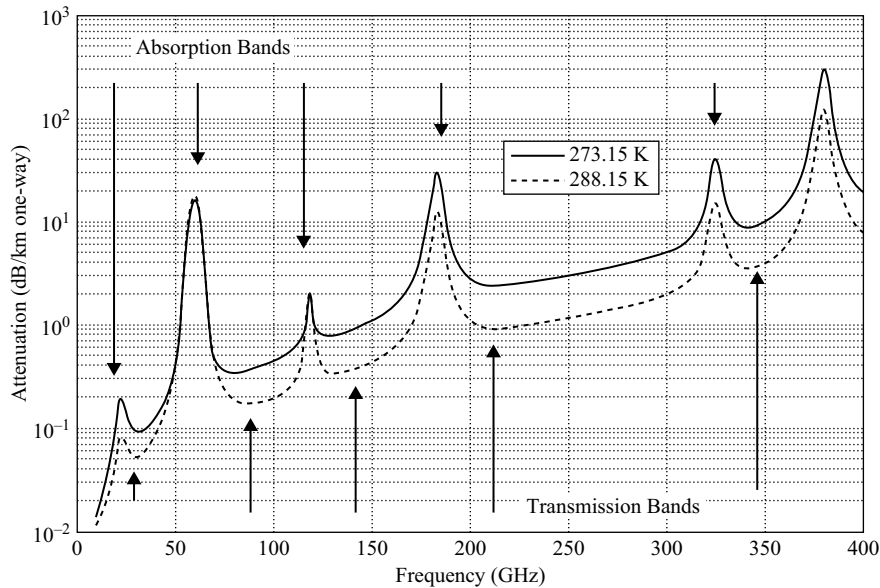


FIGURE 3-2 ■
Radar Transmission
and Absorption
Bands.

popular as component efficiencies and performance increase. The transmission bands are indicated in the classic radar-absorption curves presented in Figure 3-2 [3].

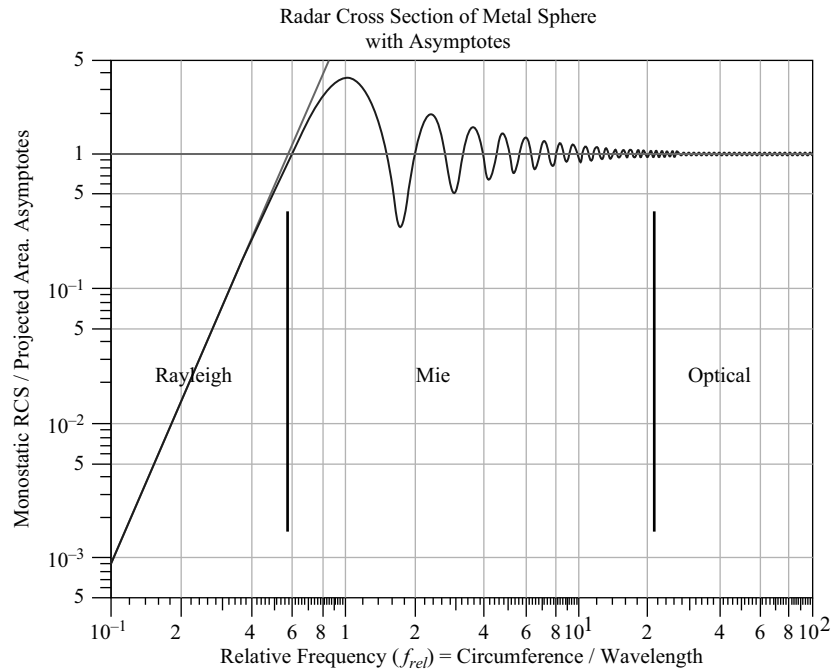
In the figure, note the relative nulls (dips) in attenuation at key frequency locations. Of course, the absorption bands – peaks in attenuation – can be used for covert communications when one only wants a signal to be seen over a certain distance. The absorption bands provide higher signal attenuation at these frequencies.

3.3 | PROPAGATION AT HIGHER FREQUENCY

As previously discussed, the short wavelength afforded by operation in the MMW region can be an advantage and a disadvantage. The short wavelength generally leads to the use of small components, and typical targets tend to have higher reflectivity. On the downside, clutter returns are also higher, and there is increased atmospheric attenuation over the engagement paths. The short wavelength also means that complex scatterers can be further resolved as a contributor to the total reflection data.

The primary reason for this increased contribution of smaller scatterers is the scattering region for an object. According to Rayleigh scattering principles – after Lord

FIGURE 3-3 ■
Scattering from a
Sphere as a
Function of
Wavelength.



Rayleigh [4, 5] – the reflected return from an object (a sphere in this case) varies according to the incident wave’s frequency. Figure 3-3 depicts the monostatic radar cross section (RCS) of a perfectly conducting metal sphere as a function of frequency (computed by Mie theory). In the low-frequency Rayleigh scattering limit where the circumference is less than the wavelength, the normalized RCS is $\sigma/(\pi R^2) \sim 9(kR)^4$. In the high-frequency optical limit, $\sigma/(\pi R^2) \sim 1$.

The x -axis is the relative frequency, defined as the number of wavelengths in the circumference; it is equal to the wave number k times the radius – i.e., $f_{rel} = 2\pi R/\lambda = kR$. The y -axis is the RCS relative to the projected area of the sphere – i.e., $\sigma/(\pi R^2)$. The asymptotes are $\sigma/(\pi R^2) = 9(f_{rel})^4$ in the low-frequency (Rayleigh) region ($\lambda > 2\pi R$), and $\sigma/(\pi R^2) = 1$ in the high-frequency (optical) limit ($\lambda \ll R$).

In the figure, the sphere is fixed and the normalized size is used to quantify changes in the wavelength for the objects return. As a result, smaller physical objects on targets (and clutter) can contribute greater amounts to the total return as the wavelength becomes proportionately small compared to the size of the scatterer. For example, at 95 GHz, the nuts, bolts, rivets, and cracks in a tank shell can provide more than 50 percent of the total target return at some incident angles, whereas at longer wavelengths, the flat and curved surfaces contribute to most of the radar signature.

3.3.1 Atmosphere

Adverse weather conditions have an increased effect on the higher-frequency region. While low cost and small size are a real boon for miniaturized systems, the increased impacts of external factors will tend to limit the maximum range performance of MMW systems. A summary of atmospheric attenuations for two key transmission band frequencies – 35 GHz and 94 GHz – is illustrated in Table 3-2 [6].

TABLE 3-2 ■ Atmospheric Attenuation for Two MMW Bands

Parameter	One-Way Loss (dB/km)	
	35 GHz	94 GHz
Clear air attenuation	0.12	0.4
Rain attenuation (mm/hr)		
0.25	0.07	0.17
1	0.24	0.95
4	1.0	3.0
16	4.0	7.4
Cloud attenuation		
Rain	5.14	35.04
Dry	0.5	3.78
Fog attenuation (g/m ³)		
0.01 (light)	0.006	0.035
0.1 (thick)	0.06	0.35
1.0 (dense)	0.6	3.5
Snow (0 °C)	0.007	0.0028

Adapted from *Infrared and Millimeter Waves, Vol. 4, Millimeter Systems*, Edited by K. J. Button and J. C. Wiltse, Academic Press, 1981.

Measured Tank RCS versus Radar Depression Angle and Target Aspect Angle at 35 Ghz

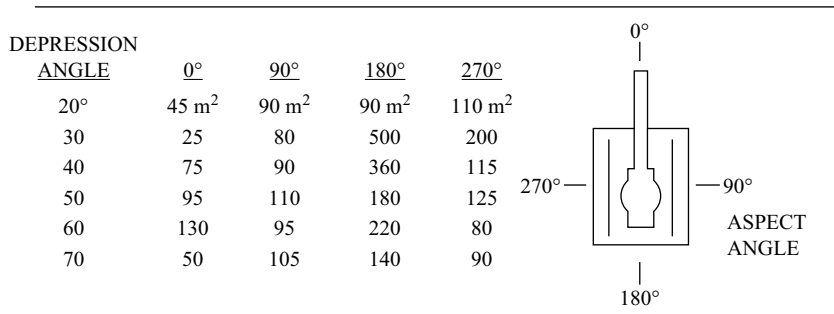


FIGURE 3-4 ■ Measured Tank RCS versus Radar Depression Angle and Aspect at 35 GHz.

While these losses are low compared to optical systems (IR, laser), they are somewhat higher than for microwave or lower-frequency propagation. As indicated, the wave penetration through high-density water volumes is very limited.

At the shorter wavelengths, an ability to “image” targets becomes feasible. This also applies to illuminated terrain or clutter patches by the radar. At the higher carrier frequency, the percent bandwidth needed for resolution on the order of inches is still a small fraction of the center frequency.

3.3.2 Target RCS Characteristics

At MMW, target scatterers of small scale (mm in size) can become significant in the reflected returns. Due to this effect, there are usually more significant scattering centers than for a conventional microwave system, making human-made targets (tanks, cars, tractors, etc.) highly complex and not only giving the return a higher overall RCS but

FIGURE 3-5 ■
Microwave (10-GHz)
Image of Tank
(Simulated).
Courtesy of MRSIM
Software by RNI

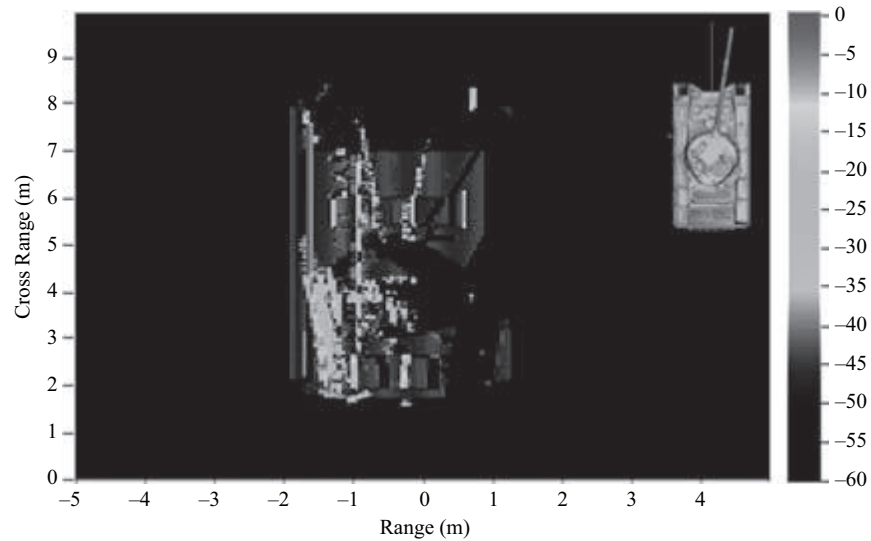
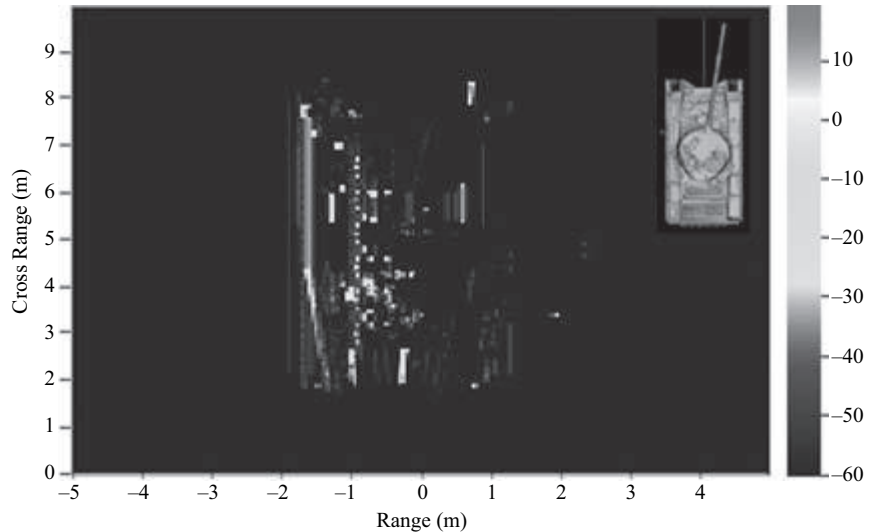


FIGURE 3-6 ■
Millimeter Wave
(95-GHz) Image of
Tank (Simulated).
Courtesy of MRSIM
Software by RNI



also resolving more discrete scattering centers. Figure 3-4 illustrates the average RCS return of resolved scattering centers on a tank target at different engagement angles (depression, azimuth) at 35 GHz.

As discussed, the scatterer contribution (and discrete distribution) is more pronounced at MMW frequencies than at lower frequencies for a human-made target. Figures 3-5 and 3-6 illustrate the computed synthetic aperture radar (SAR) image for a T72 tank at 95 GHz (MMW) and at 10 GHz (microwave) using the Multi Spectral Response Simulation (MRSIM) available from Research Network, Inc. (RNI) [7]. In both cases, the target was at an azimuth angle of 90° and an elevation angle of -30° relative to the MMW sensor. An image of the high-resolution 3-D tank model is also provided in the figures. Also note the overall increase in peak scatterer RCS for the MMW image.

In the MMW image, the numbers of resolved scatterers with higher RCS values are visibly increased over the microwave version and the peak values of the resolved scattering centers are similarly increased.

3.3.3 Terrain

At millimeter wavelengths, clutter scatterers of small scale (mm in size) can have significant RCS values, so clutter reflectivity generally increases over that at lower frequencies. The very makeup of the terrain patch illuminated by the radar can have pronounced effects. Surface roughness affects backscatter. The rougher a given surface is in comparison to a wavelength, the higher the backscatter. So, a given surface such as smooth sand will have a higher backscatter at a millimeter wave frequency than the same surface would have at a lower microwave frequency. Human-made objects such as soda cans, automobiles, and many others made of metallic substances can dominate a terrain's reflectivity. In virtually all cases, when a radar image (2-D or 3-D) is formed over a rural scene, the human-made objects (barns, tractors, etc.) stand out from surrounding natural clutter.

In general, measurements to determine the clutter reflectivity are made over controlled fields for various clutter types of interest. In air-to-ground measurement systems, the data tend to reflect more of the true composite sets embedded in radar terrain patches [8].

For airborne systems attempting to reject clutter, low grazing angles are often chosen to maximize the contrast between distributed clutter and targets. This places the clutter (terrain reflectivity) lower in the target-to-clutter contrast domain. For terrain-sensing systems (such as terrain avoidance or automated landing applications), higher depression (or grazing) angles are chosen to maximize the clutter returns, making terrain the target. As discussed earlier, the target reflectivity is less sensitive to very low angle variations. Figure 3-7 shows the range of clutter-reflectivity values seen as a function of depression angle [9].

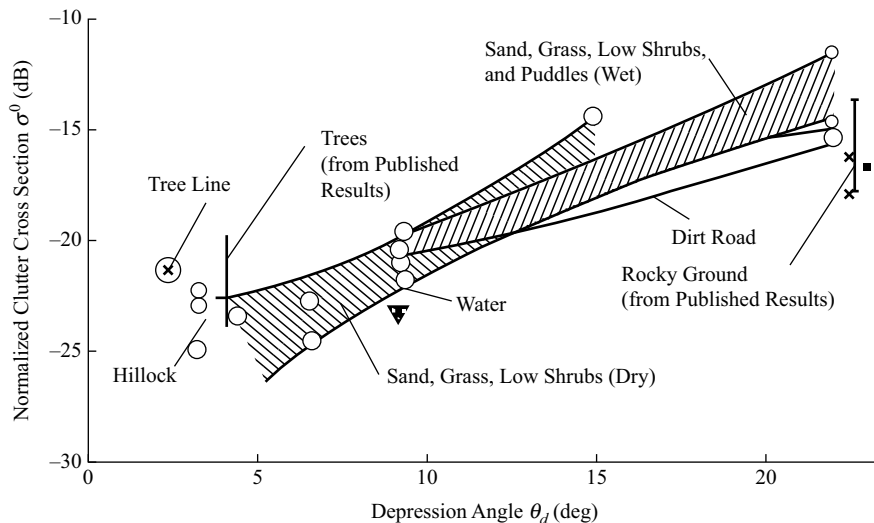


FIGURE 3-7 ■ Illustration of Increase in Clutter Reflectivity with Depression (or Grazing) Angle.

3.4 | ANTENNA BEAMWIDTH CONSIDERATIONS

One of the most obvious reasons for employing millimeter wave wavelengths is the small antenna beamwidth achieved for a given aperture size. Table 3-3 shows the approximate beamwidth and gain for three antenna sizes: at 34-GHz, 94-GHz, and, for

TABLE 3-3 ■ Antenna Beam Characteristics – Comparison with X-Band

Antenna Diameter	34 GHz	94 GHz	10 GHz
	Beamwidth	Beamwidth	Beamwidth
10 cm (4 inch)	0.1 rad (5.9 deg)	0.037 rad (2.13 deg)	0.36 rad (20.7 deg)
15 cm (6 inch)	0.075 rad (4.5 deg)	0.029 rad (1.6 deg)	0.29 rad (15.2 deg)
20 cm (8 inch)	0.05 rad (3.0 deg)	0.019 rad (1.07 deg)	0.18 rad (10.4 deg)

comparison, 10-GHz wavelengths. For seeker-sized radomes, in the range from 0.1 m to 0.2 m in diameter, the conventional microwave frequencies would produce a relatively wide beamwidth, such that the cross-range resolution in the scene would be poor. The millimeter wave frequencies produce a relatively narrow beam.

3.5 | MMW PERFORMANCE LIMITATIONS

In general, high-power sources are still not available at MMW for small packaging. Tube-based transmitters have been used in larger packages to support long-range requirements. For an MMW seeker application, tube transmitters and large power supplies are simply not appropriate for small airframe volumes, so only solid-state devices are typically used.

Two of the key performance parameters that are determined by existing technology are transmit power and receiver noise figure. Tables 3-4 and 3-5 illustrate examples of output power for solid-state and tube-type transmitters, and Table 3-6 shows some receiver noise figure values available commercially in the Ka- and W-band regions.

A signal-to-noise ratio (S/N) calculation is presented for an MMW continuous wave (CW) seeker example to illustrate the typical range performance of these types of systems. The MMW seeker parameters are given in Table 3-7.

TABLE 3-4 ■ Typical Ka Band Transmitter Power – Solid-State Devices

Manufacturer	Description	Frequency	Power
QuinStar Technology	QIC Series CW IMPATT Diode amplifier	34–36 GHz	1 W
Millitech, LLC	IDA Series CW Injection-Locked IMPATT Diode Amplifier	30–40 GHz	0.7 W
QuinStar Technology	QTI Series CW Injection-Locked GUNN Diode Amplifier	26.5–40 GHz	0.3 W
Marconi Applied Technologies	GUNN Diode Oscillator Model DC-1276G	26–40 GHz	0.5 W

TABLE 3-5 ■ Typical MMW Transmitter Power – Thermionic Devices

Manufacturer	Description	Frequency	Power	Bandwidth	Duty
CPI	CW EIO	35 GHz	1,200 W		
		95 GHz	50 W		
CPI	Pulsed EIK	35 GHz	2,000 W pk	800 MHz	15%
		95 GHz	1,000 W pk	1,000 MHz	10%

TABLE 3-6 ■ Typical Ka Band Noise Figures – Solid-State Devices

Manufacturer	Bandwidth	Noise Figure
QuinStar Technology QMB series balanced mixers	26.5 to 40 GHz	6.5 dB
Millitech series MXP balanced mixers	33 to 50 GHz	5.0 dB (DSB)
	26.5 to 40 GHz	
	33 to 50 GHz	

TABLE 3-7 ■ MMW CW Seeker Performance Parameters – Example

Symbol	Description	Value	Units	Value (dB)
P_t	Peak transmit power	2.5	Watts	4.0 dBw
G_t	Transmit antenna gain	17,647		42.5
G_r	Receive antenna gain	17,647		42.5
λ^2	Wavelength (squared)	$(0.0086)^2$	Meters squared	-41.3
σ	Target RCS	0.01	Meters squared	-20.0
$(4\pi)^3$	Constant	1,984		-33.0
R^4	(Range) ⁴	$(1,000)^4$	Meters ⁴	-120.0
k	Boltzmann constant	1.38e-23	Watts/Hz K	228.6
T_0	Standard temperature	290	Degrees K	-24.6
B	Instantaneous bandwidth	88.2	kHz	-49.5
F	Noise figure	4.47		-6.5
L	System losses	5.50		-7.4
L_a	Atmospheric attenuation	1.02		-0.1
S/N	Resulting signal-to-noise ratio			15.2 dB

Plugging these data into the radar range equation (equation 3-1) allows computation of S/N performance as a function of range for the -20 dBsm target. The resulting curve is shown in Figure 3-8.

$$\frac{S}{N} = \frac{P_t G_t^2 \lambda^2 \sigma}{(4\pi)^3 R^4 k T_0 B_n F_n L} \quad (3.1)$$

Notice that robust detection performance is on the order of 1 km.

A similar result illustrating short-range operation (based on signal-to-clutter ratio) is illustrated in Figure 3-9. The calculations were performed over different clutter types as a function of MMW airborne seeker parameters with the following specifications shown in Table 3-8. In this illustration, coded waveforms are used to achieve a significant level of pulse compression (or signal-processing gain).

As the figure illustrates, the additional waveform duration to allow higher levels of pulse compression (signal-processing gain) can extend the range performance somewhat but at the cost of increased data-collection time and lower effective data rate (updates) by the radar.

Available transmit power, noise figure (S/N), and clutter return (S/C) limitations, combined with increased atmospheric and external propagation effects, tend to restrict MMW applications to shorter ranges compared to lower-frequency systems.

FIGURE 3-8 ■ S/N for an MMW Seeker versus Target Range at Antenna Boresight.

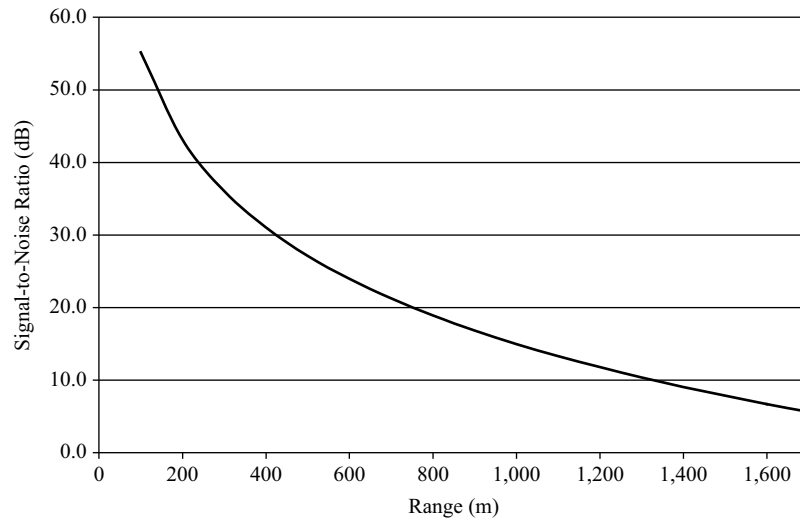


FIGURE 3-9 ■ Illustration of MMW Seeker Performance.

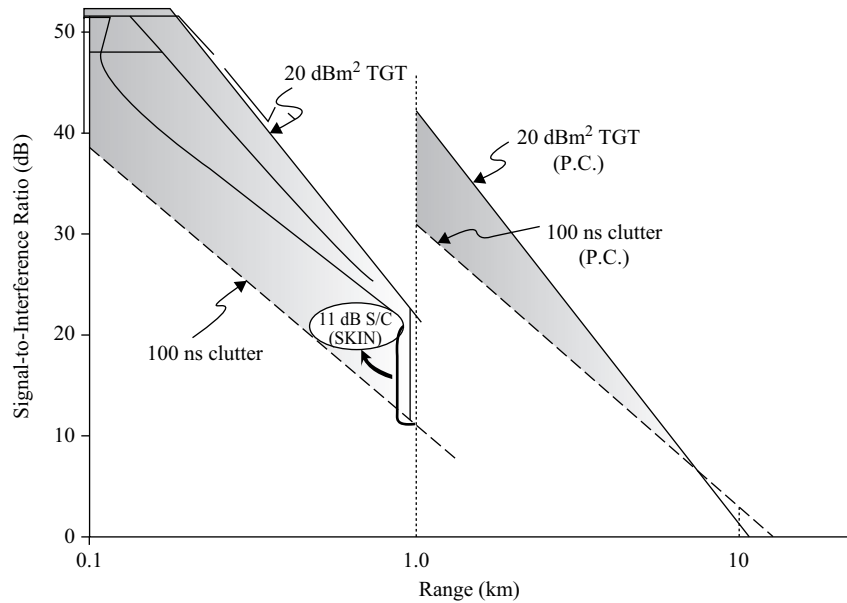


TABLE 3-8 ■ MMW Airborne Seeker Typical Specifications

Parameter	Value
Frequency	95 GHz
Waveform compression (long range)	100:1 (10- μ s pulse equivalent)
Waveform compression (short range)	10:1 (100- μ s pulse equivalent)
Antenna	6" diameter Cassegrain
Peak power	10 Watts
Noise figure	8 dB
Target RCS – nominal	20 dBm ²
Clutter reflectivity – nominal	-8 dBm ² /m ²
Clutter reflectivity – @ 10° grazing	-15.6 dBm ² /m ²

TABLE 3-9 ■ MMW Compares Well with Other Systems

Sensor Capability	Microwave (3–30 GHz)	MMW (30–300 GHz)	Optical (0.4–14 microns)
Volume search	3	2	3
Classification, identification	1	2	3
Tracking accuracy	1	2	3
Adverse weather performance	3	2	1
Smoke performance	3	3	1
Covert capability	1	3	3
Day/night performance	3	3	2
Total	15	17	16

Relative performance key: 1 = poor, 2 = fair, 3 = good

3.5.1 MMW Comparison with Other Systems

Even with all the issues discussed related to power, relative component costs, clutter returns, and atmospheric losses, MMW still offers the best compromise for high resolution with potential imaging capability in many applications compared to systems at different spectral regions. As a comparison, a simple subjective ranking system from 1 to 3, with 3 being the best, can be used to illustrate this compromise. Since a radar must perform many functions (search, detect, acquire, recognize) in a wide variety of conditions (targets, clutter, atmospheres), the values shown in Table 3-9 illustrate how MMW may still be the best choice for a selected system application as long as power budget considerations can be maintained.

3.5.2 MMW for Advanced Imaging Technology

The MMW spectrum can be combined in a “quasi-optical” common optics system with IR and visible sensors. The radar offers high-range resolution (inches) and object dimensionality measurements. As such, the basic implementation in the 3-D camera for radar would be for reflectance sensing (concealed “hard” objects and object classification), gross object geometry (except for range), and gross-and-point materials type electromagnetic (EM) properties. Radar also offers the ability to “see through” denser obstacles than higher wavelength sensors.

The MMW radar (active and passive) can also provide some level of imaging without controlled motion (Narrow Field of View (NFOV) implementation) on its own. As previously discussed, millimeter wave radar usually serves as a trade-off technology between microwaves and infrared. As such, it has imaging characteristics of both technologies, both good and bad. These trade-offs (and real-life applications) have been realized in many of today’s critical security locations and in military target discrimination and classification approaches. Some of the advantages of MMW radar, compared to electro-optical sensors and microwave radar for imaging, include:

- the ability to directly measure range, azimuth angles, and elevation angles;
- the ability to penetrate many nonmetallic surfaces;
- high spatial resolution (as compared to microwaves) and extension to 3-D with controlled geometry changes; and

- low resolution (relative to electro-optical), which means less scanning is required to fill a given search volume.

Some of the disadvantages of MMW radar for imaging include:

- nonoptical-quality images due to specular reflections, multipath, and the large difference in reflectance of various shapes (in some ways, this is an advantage in that it is another way to look at things);
- a relatively short range because near-field focusing of antennas is used to obtain high angular resolution; and
- the need for a larger aperture size for NFOV without controlled object motion.

More information on MMW advanced imaging technology (AIT) utilization is provided in the applications section of this chapter.

3.6 | TYPICAL SEEKER OR SMART MUNITION CONFIGURATION

One of the key thrusts for the U.S. military is the use of MMW in smart weapons. These smart weapons relate to warhead or penetrator munitions that carry a “seeker” onboard. The seeker represents the “eyes” of the missile. For the case of an MMW radar seeker, the missile contains an MMW radar (with or without a companion sensor) that is used to search, detect, classify, and guide the munition to its intended target. The seeker must be accurate and reliably discriminate the targets from the clutter and fit in a very small volume.

A smart weapon can be generally described as a *precision guided munition* (PGM). The PGM implementations relate to:

- hit-to-kill or guide-to-impact weapons,
- contact- or proximity-fusing weapons,
- direct-fire and kinetic-energy weapons (hypervelocity rods), and
- sensor-fused munition (SFM) weapons.

These weapons can be direct line of sight (LOS) or standoff non-line of sight (NLOS) fired. Both engagement types can apply to each weapon and seeker platform. In some cases, the MMW seeker will use high-resolution SAR or Doppler beam sharpening (DBS) techniques to form improved cross-range resolution and enhance target decisions. In these cases, the munition must fly a shaped trajectory before going into a terminal hit or fire mode. These requirements can be significant for motion compensation systems onboard the seeker munitions platform that must account for nonlinear motion of the airframe over a coherent-processing interval.

3.6.1 Smart Weapon Configurations

A smart weapon that contains MMW radar includes a number of key component items. The seeker is generally the MMW radar (including the antenna gimbal system) and frequency down-conversion systems of the analog data to be digitized for the signal

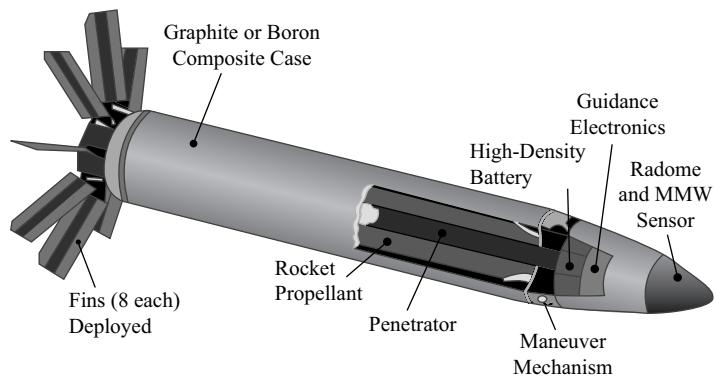


FIGURE 3-10 ■ Illustration of Single-Mode MMW Seeker on a Powered Munition.

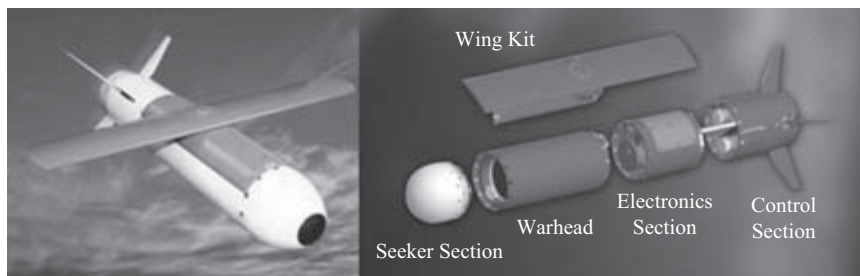


FIGURE 3-11 ■ Glide Munition Illustration with Discrete Sections of the System.

and data processors. An illustration of a kinetic energy smart weapon, sometimes called a *rod* or *penetrator munition* is shown in Figure 3-10.

The weapon or munition depicted in the figure is powered; that is, it contains a propellant to advance its progress in the flight timeline after launch. For a glide munition, there is no propellant. This allows more space for the warhead but reduces the available kinetic and potential energy of the platform. Depending on the design, this type of munition often leaves a “hole” in the center for electronics in front of a shaped charge warhead to allow minimal disturbance to the blast as it propagates toward the point of collision. Glide munitions contain “wings” much like airplanes to allow for stabilization and guidance throughout the flight profile.

A good illustration of a glide munition is the Scorpion system developed by Lockheed Martin Systems [10], which includes an option for an MMW seeker head as illustrated in Figure 3-11.

The seeker compartment contains the major MMW radar components, including:

- the antenna and RF transmit-and-receive section,
- the IF section,
- a digitizer, and
- the signal data processor.

Figure 3-12 shows a generic block diagram of the MMW seeker component.

In the seeker itself, many discrete components are required to perform open- and closed-loop tracking functions. In modern systems, many of the discrete functions are combined into solid-state transceivers. Since the wavelength is small, microstrip components have matured that embed “waveguide” materials directly onto substrates, thus allowing higher levels of component integration into single devices.

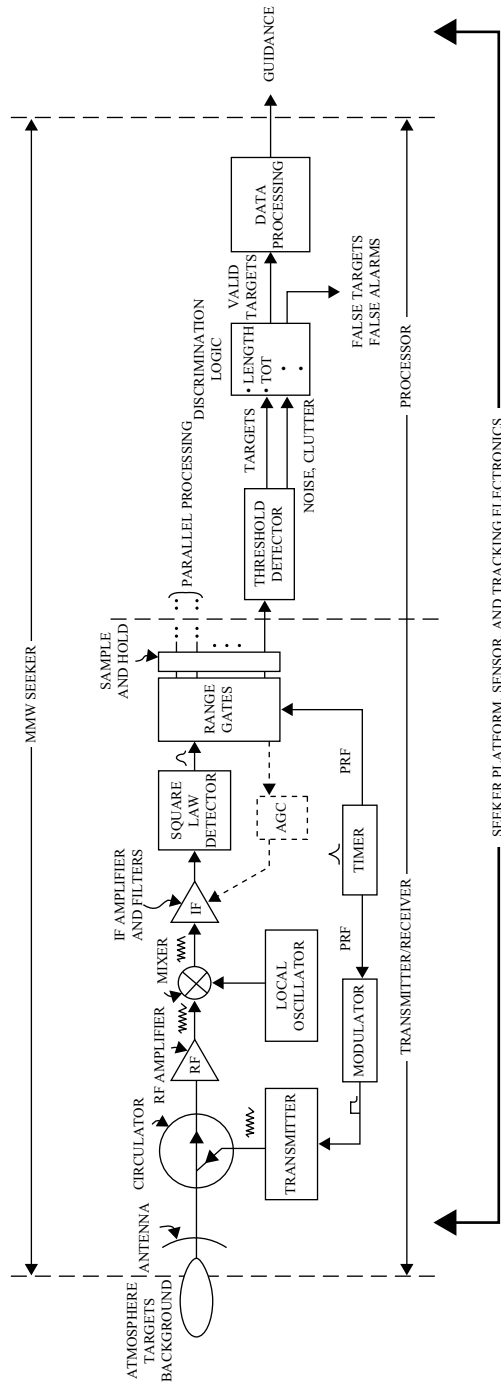


FIGURE 3-12 ■ Block Diagram of Generic MMW Seeker.

3.6.1.1 Components

Each key component in the MMW seeker is discussed in the following sections.

Radomes While generally not part of the MMW radar compartment, one key platform item for all seekers relates to the radome. The radome material must be strong for high g (acceleration) and velocity operations while providing minimal impact (loss or distortion) on the MMW waves passing through the material.

The fundamental radar system in the munition must “see” through the radome. The radome is there to protect the antenna and electronics from weather and potential high-velocity atmospheric impacts while preserving good transmission properties for the MMW signals. In many cases, the antenna inside the radome scans the field of view (either electronically or mechanically). Thus, the radome material must preserve good transmission properties under hostile conditions over all incidence angles in the scanned (and signal return) fields.

Radomes must maintain a high level of “transparency” over all the operating modes of the seeker (scan, frequency, polarization, etc.). In addition, they must be easily and reliably manufacturable at the lowest cost. Guidelines for materials selection and radome performance are shown in Table 3-10. Note that more than transmittance and reflectance must be considered in the selection of an adequate radome [11].

Table 3-11 lists some good materials candidates and their properties for MMW use.

Note that the table also provides a separate set of columns for the material properties at IR. MMW has mated with IR systems on a number of defense programs – mostly seekers – due to the natural complement of MMW and IR (and optical) performance and single-mode countermeasure rejection capability.

Antennas The transduction of the wave to and from the monostatic radar source in the seeker is accomplished by the antenna. For seeker applications, the antenna must be very lightweight to allow low inertial resistance for rapid scanner electronics. A number of antenna approaches are applicable to MMW sensing [12, 13], including:

- a parabolic dish,
- lenses,
- Cassegrain geometries,
- spirals,
- loops,
- wires,
- horns,
- phased (electronically scanned) arrays, and
- many other classical approaches.

A number of MMW antenna types and support and feed structures are illustrated in the following figures. Probably the most common are parabolic dishes and Cassegrain geometry types although two-dimensional array systems such as electronically scanned arrays (ESAs) are maturing rapidly for many applications [14–16]. Figures 3-13 and 3-14 are photographs of MMW parabolic “dish” and Cassegrain antennas, respectively, which are currently available from Deh-Ron Ltd.

Figure 3-15 depicts a microstrip antenna, in which the elements are made much like a printed circuit board, on a low-dielectric stable substrate [17, 18].

TABLE 3-10 ■ MMW Radome Performance Guidelines

Parameter	Units	Performance Requirement
Transmission	Percent	>85
Reflection	Percent	<0.5
Beam deflection	mrad	0.05–0.3
Beam deflection error rate	mrad/mrad	0.005–0.01
Change in 3-dB beamwidth	Percent	<5
Sidelobe increase		
–20-dB level	dB	<1
–25 dB level	dB	<2
–30 dB level	dB	<4
Axial ratio	dB	>40 (algorithm driven)
Hardness	Knoop	600–800

TABLE 3-11 ■ Radome Material Performance Summary (MMW and IR)

Material Type	IR Band	IR X-Mission	MMW Band	MMW X-Mission	Comments
Magnesium fluoride	3–5 μm	85–90%	Ka and W	>90%	MMW $\alpha = 5.3$
Fused silica	3 μm	90%, falling to opaque at 5 μm	Ka and W	>90%	MMW $\alpha = 3.05$
CVD zinc sulfide	3–5 μm	70%	Ka and W	>90%	MMW $\alpha = 8.3$ (higher loss tangent .0017)
Monochloro-trifluoroethylene (TFE)	3–5 μm	90%	Ka and W	>90%	MMW $\alpha = 2.2$
Fluorinated ethylene propylene (FEP)	3–5 μm	90%	Ka and W	>90%	MMW $\alpha = 2.2$
ZnSe	3–5 μm , 8–12 μm	64%, 96%	W	92%	
Ge	3–5 μm , 8–12 μm	48%, 47%	W	6%	
Si	3–5 μm , 8–12 μm	58%, 53%	W	10%	
CsI	3–5 μm , 8–12 μm	47%, 72%	W	80%	
KBr	3–5 μm , 8–12 μm	89%	W	85%	
AMTIR-1	3–5 μm , 8–12 μm	69%, 68%	W	55%	
IRTRAN-1	3–5 μm , 8–12 μm	90%, 14%	W	81%	
IRTRAN-2	3–5 μm , 8–12 μm	72%, 71%	W	39%	



FIGURE 3-13 ■
35-GHz MMW
Antenna (Parabolic
Dish).



FIGURE 3-14 ■
MMW Cassegrain
Reflector Antenna.

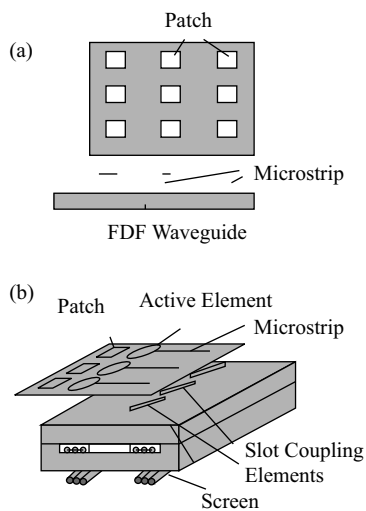


FIGURE 3-15 ■
Microstrip Patch
Antenna.

FIGURE 3-16 ■
Feed System for a
Ka-Band
Multibeam Antenna.

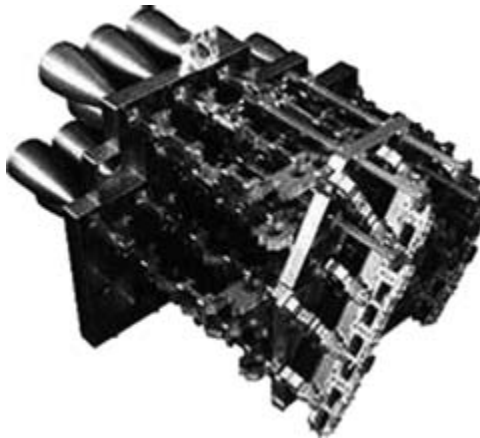


FIGURE 3-17 ■
Ka- Band MMW
Two-Dimensional
Electronically
Scanned Array
Antenna.

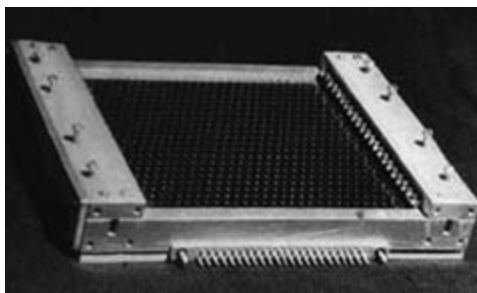


Figure 3-16 depicts a feed structure for use with a parabolic reflector antenna in a multibeam application. There are several feed horns, one of which can be selected at a given time. Since the horns are somewhat displaced from the parabolic focal point, the beam is scanned by electronic selection of the feed channel [19]. It is easy to see the complexity of a discrete component approach to beam steering at MMW frequencies.

Figure 3-17 shows a two-dimensional array of antenna elements in which the phase of the RF signal into the rows and columns can be individually controlled [18]. By controlling the row and column phases, the beam is electronically scanned in two planes. Note the significantly reduced complexity of the ESA approach.

In some cases, to reduce cost and inertial for mechanical scanning, the reflector design can be made of “stamped plastic” formed to a parabolic dish and then coated with a high surface roughness tolerance metal surface to preserve the electromagnetic properties at MMW.

Transceivers The key transceiver functions relate to (1) wave transduction, (2) wave generation, (3) wave reception, (4) wave down-conversion, and (5) digitization for signal-processing electronics.

Most of these functions can now be implemented on very small size hosts. A number of millimeter wave integrated circuit (MMIC) and microstrip technologies allow large-scale integration and miniaturization of MMW RF/IF and digital signal-processing devices. The short wavelength allows for entire “radars” being “grown” on single wafers. Figure 3-18 depicts an MMW MMIC device that integrates whole radar transceivers into single modules [20].

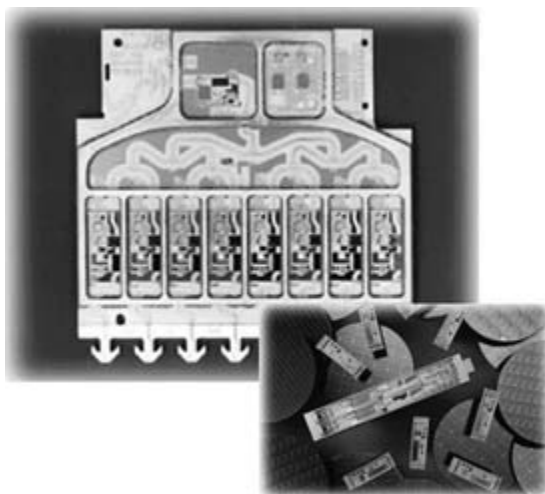


FIGURE 3-18 ■
MMW MMIC
Devices Integrate
Whole Radar
Transceivers into
Single Modules.

3.6.1.2 Seeker Spectra and Modes

A smart weapon or munition may contain either a single sensor or multiple sensors, depending on the application and mission complexity. When only a single sensor type is used, the seeker is considered *single spectral*. When multiple sensors are used in an application, the seeker is considered *multispectral*. The current thrust in the military is toward multispectral integration of MMW sensors with optical (IR, laser) to provide good search, terminal, and countermeasure performance across multiple firing platforms (e.g., shooters); each sensor provides its strengths to the application while other sensors compensate for its weaknesses.

For a single-spectral implementation, multiple radar modes are possible. These modes can include active, semi-active, or passive implementations. Each one is described below:

Active – The term *active* implies the radar is transmitting and receiving its own signal from a common location. From the point of view of a missile seeker, this is sometimes called a *fire-and-forget missile*.

Semi-active – The term *semi-active* implies there are separate transmitter and receiver locations in the radar configuration. A typical implementation is a surface-based illuminating radar and missile with a tracking receiver onboard.

Passive – The term *passive* implies detection of MMW radiometric noise either emitted or reflected from the source patch.

In some cases, all of the above may be used by the seeker onboard the munition during the engagement timeline. When a seeker uses multiple modes it can be called *multimode*. Unfortunately, in some communities the use of *multimode* implies multispectral seeker implementation. For this chapter, a seeker that contains only one sensor can operate in multiple modes.

The combinations of modes in the use of the seeker during the engagement timeline have traditionally included:

- active-only mode,
- active-and-passive MMW mode,

- passive radiometer only,
- semi-active mode, and
- beamrider mode.

Each mode is fairly self-explanatory. In general, the active modes are preferred in environments with high EM interference. Passive mode operation is generally preferred if the interference levels are low. In most cases, passive modes are confined to satellite platforms, although recent work on concealed-weapon detection indicate passive modes can be used in this application at very short range.

3.6.1.3 Multispectral Implementations

While MMW itself can do a good job with target detection and discrimination, in some cases an optical system can be used for terminal phases in the timeline due to its very narrow beamwidths. The terminal phase requires precise hit-point estimation on complex objects (tanks, buildings, etc.). The MMW system provides broader beams in the common aperture, allowing for efficient search in the timeline. The optical systems can get fine resolution of the target but only at very short ranges and under good weather. Thus, the MMW system is generally onboard to provide efficient target search along with bad weather operations. Current multispectral munitions are focused on integrating the following:

- dual mode MMW and infrared (MM/IR);
- dual mode MMW and laser radar (LADAR);
- tri-mode MMW, LADAR, and IR; and
- combinations of the above.

Figure 3-19 illustrates an MMW and IR system processing configuration.

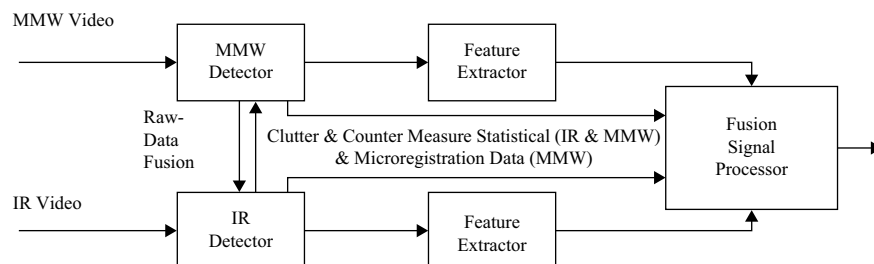
Each sensor provides unique – uncorrelated – information on the object (and clutter) of interest in a scene. As illustrated, the data from any sensor suite can be combined at multiple levels, each with a unique performance and cost impact.

The three basic levels of sensor fusion are:

- sensor and pixel level,
- feature level, and
- decision level.

At the sensor level, the raw data from both radar front ends are combined to form a composite data stream to subsequent processes. A good example of this is when the radar sensor provides excellent range measurement while the IR or optical sensor provides excellent azimuth and elevation information. The combination of these pixels can

FIGURE 3-19 ■
Generic Dual Mode
(MMW/IR) Radar
Processing.



form a 3-D image (r, θ, ϕ) in the relative spherical coordinate system afforded by the multispectral seeker. Pixel-level fusion is probably the most costly to implement but has the highest potential performance in the required mission.

In all cases, the two sensors must be microregistered to ensure that the data provided for in subsequent processes are based on the same physical point in 3-D space.

Feature-level fusion of the information is based on feature extraction from the sensor channels. The features can be “target size” or one of many other possible characteristics afforded by the individual sensors. Here the data are fundamentally convolved by each of the sensor channel front ends and the features extracted for combination algorithms. Feature-level fusion is somewhat costly to implement and has a higher performance potential than decision-level fusion.

Decision-level fusion essentially makes a target decision based on the decision made by the onboard sensors. Simple Boolean algorithms such as *and* and *or* can be used at this level. Decision-level fusion also is more robust than higher levels in the event of a single sensor failure or degradation. As you might imagine, decision-level fusion is the least costly to implement – from a target-detection algorithm perspective – but probably has the lowest performance potential for the multispectral smart weapon.

The use of MMW components in multispectral (optical) combinations exploits the fact that the wave optics more closely match IR and visible than lower frequency. The aperture tolerances are similar, and common aperture approaches become feasible. The component size reduction for the MMW radar sensor also allows more use of restricted volumes in smart weapons.

The combination of multisensor data into a common platform has two distinct advantages:

- false targets and real targets are decorrelated, and
- single-mode countermeasures are easily discriminated.

Each of the MMW radar complements are discussed in this chapter. In some cases, even multispectral seekers must rely on a single spectrum for complete operation. For example, in bad weather or obscurant engagements, the MMW radar may carry the primary load for sensor functions when combined with optical sensors.

3.6.1.4 Typical Waveforms

In general, active MMW radar systems will use either modulated CW or pulsed-type waveforms. For CW waveforms, the key advantages are:

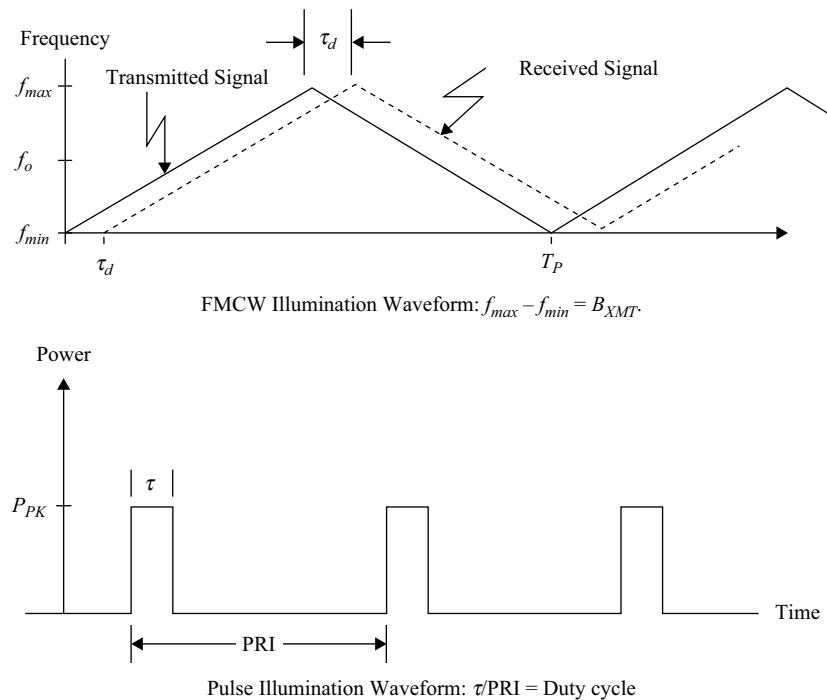
- high average power,
- good clutter smoothing with frequency modulation (FM) (e.g., FMCW), and
- high-range resolution in the frequency domain with FM.

Conversely, pulsed waveforms offer:

- high peak power,
- high-range resolution in time domain, and
- excellent transmit / receive (T/R) isolation for monostatic radar.

Many modulation options are available for either CW or pulsed waveforms. These include variations of frequency modulation, phase modulation, amplitude modulation,

FIGURE 3-20 ■
Illustration of Single-
Mode MMW Seeker
Waveforms.



and interleaved waveforms with complex parameters changing on a pulse-to-pulse basis. Phase modulation variations such as phase-shift keying (PSK) or binary phase codes have also shown promise for very-high-range resolution in military tracking applications.

The basic waveform types discussed are depicted in Figure 3-20.

Pulsed waveform generation can be difficult in some implementations due to requirements on rise and fall time and pulse shape. For FMCW implementations, the frequency sweep linearity is often the key limitation in some applications. Both types of waveforms are in use by the military and commercial markets today for MMW applications.

With the increased availability of high-rate digital encoders, phase-coded waveforms such as PSK have also become feasible for MMW waveform use but are not prevalent (yet) in current systems.

3.7 | MMW RADAR APPLICATIONS

As components become smaller and more efficient, MMW systems and use of the frequency bands have propagated into many areas. Many of these can be seen or used every day. This section briefly discusses a number of MMW applications that have been or currently are in use by both commercial and military markets.

3.7.1 Weapons

The military has implemented MMW technology into several different weapon systems as both a seeker component and as a standoff radar with different mission requirements. These include the following.

Sense and destroy armor (SADARM): This smart fire-and-forget, top-down attack, multisensor, proximity-fuse submunition was deployed from a mobile launcher such as the multiple launch rocket system (MLRS), which included a sensor equipped with MMW radar, a passive MMW radiometer, and an infrared telescope. A magnetometer was also used as an aid in arming and aiming. Tanks were the primary targets of this weapon [21].

XM1111 midrange munition (MRM): This precision-guided munition was developed for the Rheinmetall 120-mm gun (known as the M256 in the U.S. military) and used by several Western tanks. MRM was also known as the tank extended range munition (TERM) in previous programs. It was also intended to fulfill a requirement for a long-range, line-of-sight (LOS) and beyond-line-of-sight (BLOS) tank munition as a high-velocity penetrator for LOS and BLOS shots. In LOS, it would operate using laser guidance or an MMW seeker. In BLOS, the shell would be fired in a ballistic arc and seek out its own targets. The primary target of this weapon was tanks and other armored vehicles [21].

Longbow (AN/APG-78): This helicopter-mounted fire-control radar (FCR) married with the RF Longbow Hellfire fire-and-forget missile for the Apache helicopter. The Longbow MMW radar performs target acquisition and fire control for the 18 Hellfire missile payload. The fire-control radar dome is mounted above the helicopter rotor blades. The MMW radar searches for targets of interest, hands off the coordinates to the Hellfire missile seeker, and launches a missile. The rotor-mounted MMW antenna and radome scans over wide areas and is designed to rapidly and automatically search, detect, locate, classify, and prioritize multiple moving and stationary targets on land, air, and water in all weather and battlefield conditions to the maximum range of the missile with low probability of intercept [22].

Hellfire: This hit-to-kill missile can be deployed from rotary- and fixed-wing aircraft, naval assets, and land-based systems against a variety of targets. The missile uses an MMW seeker with characteristics similar to the AN/APG-78 Longbow Fire-Control Radar. It can lock onto to the target detected by the Longbow and provide seeker aim-point and target-type information for the missile to engage the target in fire-and-forget modes [21].

3.7.2 Intruder Detection and Tracking

The MMW radar at the U.S. Army's Reagan Test Site (RTS) on Kwajalein Atoll is a dual-frequency (Ka- and W-band) monopulse tracking radar used for intruder detection and tracking. The system is characterized by high-range and Doppler resolution, high sensitivity, precise pointing and tracking, waveform flexibility, and a high degree of computer control for real-time operation and signal processing [23].

3.7.3 Full-Body Imaging Systems

Full-body imaging (or advanced imaging technology, AIT) systems have made their way into our everyday lives. Many of these systems are based on MMW active and passive approaches and are currently in operation at many major locations in the United States and around the world. Typical uses for this technology include detection of items for commercial loss prevention, smuggling, and screening at government buildings and

airport security checkpoints. Perhaps the most prominent of these are the active MMW systems developed by ProVision. The Transportation Security Agency began testing state-of-the-art AIT in 2007 and began deploying units to airports in 2008. This technology can detect a wide range of threats to transportation security in a matter of seconds to protect passengers and crews [24–27].

3.7.4 Automotive MMW Radar

The automotive industry has realized the importance of radar in improving highway safety, and it is taking advantage of the technology that has been developed by the military. Automotive applications for radar include collision avoidance, speed control, cruise control, telecommunications, and attitude control, among many others. Automatic braking systems have been investigated and implemented by a number of manufacturers on higher end cars. Other than the military, automotive applications have been the most prominent applications maturing MMW technology in the past decade. All variations of automotive radar are active systems.

Adaptive cruise control (ACC) works by detecting the presence of other automobiles. When there are no vehicles ahead, the system keeps a steady speed controlled by the driver; when the car approaches other vehicles, the speed is controlled to keep a safe distance away. When another vehicle is detected, the system maintains a safe speed with a specific 1-, 2-, or 3-second gap. Radar-based ACC often feature a “pre-crash” system that warns the driver or provides brake support if there is a high risk of a collision. Also certain cars incorporate it with a lane-maintaining system that provides power steering assist to reduce steering input burden in corners when the cruise control system is activated [28].

Integrated collision warning uses similar technology to ACC but is designed to provide higher levels of obstacle avoidance and prioritize collision threats imposed by road objects. Collision warning systems also offer more control of vehicle systems such as speed, steering, braking, and gear position. Collision warning systems often provide a number of driver cues, which can include an audio warning via the sound system and a visual warning via a heads-up display (HUD) in higher-end cars. Collision warning and obstacle avoidance systems often use multiple beams that are mechanically scanned. Multiple and radar channels are used to survey and discriminate road objects; these are designed to operate at ranges out to 200 meters [29–31].

3.7.5 Automated Landing Guidance

Automated landing guidance (ALG) provides a clear real-time view of the runway and ground, even in the worst visibility conditions, through the use of a HUD. To achieve this virtual reality, Lear Astronics has selected Adaptive Solutions’s CNAPS massively parallel coprocessor technology. CNAPS is used in the image processor, where all sensor information is combined, to run several algorithms and process them in real time. The resulting images are then displayed on a heads-up display, providing the pilot with a detailed image of the approach and landing environment. Tackling this very computation-intensive task are four CNAPS chips that contain 256 processors to merge and enhance all MMW sensor information in real time.

Any airplane equipped with the ALG system could land in low visibility conditions (CAT III) at unmodified runways around the world. Only 41 U.S. airports are modified for CAT III landings. The ALG system enables airports to decrease landing delays and diversions due to weather, estimated at more than 2,000 per month in the United States, without having to invest further in low-visibility runway equipment at taxpayers' expense [32, 33].

3.7.6 Atmospheric Sensing

MMW has long been used by the atmospheric-sensing community due to its ability to resolve small scatterers suspended in the air. MMW has also been used to detect the presence of wind shear and turbulence in the atmosphere. Two of these atmospheric sensing systems are the CloudSAT and ProSensing cloud profile radars. In this section a number of atmospheric-sensing systems are discussed.

CloudSat: This cloud-profiling radar (CPR) uses a 94-GHz nadir-looking sensor that measures the power backscattered by clouds as a function of distance from the radar. The CPR will be developed jointly by NASA/JPL and the Canadian Space Agency. The overall design of the CPR is simple and well understood, and it has strong heritage from many cloud radars already in operation in ground-based and airborne applications. Most of the design parameters and subsystem configurations are nearly identical to those for the Airborne Cloud Radar, which has been flying on the NASA DC-8 aircraft since 1998 [34, 35].

ProSensing 94 GHz Cloud Profile Radar: This FMCW system, manufactured by ProSensing, represents a cost-effective alternative to ProSensing's high-power W-Band Polarimetric Cloud Radar Systems. The W-FMCW is a single-polarization system with same range resolution and slightly less sensitivity than the high-power radars. The W-FMCW is comprised of (1) a transceiver enclosure, (2) a data-acquisition and -control unit, (3) host PC computer, and (4) an elevation over azimuth (EL-AZ) scanning positioner. The transceiver is housed in a waterproof, thermally stabilized aluminum enclosure. The W-FMCW is offered with an EL-AZ scanning positioner that is completely integrated into the system. Scanning patterns or joystick control of the positioner is possible through the host software. A field-programmable gate array-based digital receiver /signal processor computes range profiles of reflectivity and pulse-pair-derived velocity products at PRFs up to 14 kHz [36].

3.7.7 Active Protection Systems

An active protection system (APS) is a system (usually for a military application) designed to prevent sensor-based weapons from acquiring or destroying a target. Typically, the MMW APS either senses the waveform of an incoming threat or actively detects its presence and provides target and tracking information to an intercept system. Once the incoming threat is established, the APS can then deploy directional countermeasures to fool the threat or shoot an interceptor at it [37–39].

3.7.8 Terrain Following/Obstacle Avoidance

The purpose of terrain following (TF) or obstacle avoidance (OA) for aircraft is to use the protection from enemy sight afforded by terrain masking. TF and OA systems can be

considered as similar collision avoidance technology but with the platform airborne rather than ground based. A usual requirement is to remain as close as possible above a given distance, the “set clearance height,” from the ground. Conventionally, a forward-looking TF and OA radar is used to provide range and angle information of points on the ground for processing into a TF pitch plane command. These techniques improve the accuracy of the aircraft’s primary dead reckoning system, typically an inertial navigation system, by using additional information obtained from radar altimeter returns and a stored digital terrain map.

The system works by transmitting a radar signal toward the ground area in front of the aircraft. The radar returns can then be analyzed to see how the terrain ahead varies, which can then be used by the aircraft’s autopilot to maintain a reasonably constant height above the earth. The TF and OA radar computer considers many factors in determining the flight path for the aircraft, including distance to the forward terrain, aircraft speed and velocity, angle of attack, and quality of signal being returned [40, 41].

3.7.9 Wireless Communications Systems

With the commissioning of portions of the MMW spectrum for communications by the FCC, a number of wireless communications systems have become available for the military and commercial markets. These include wireless USB systems, metro network systems, and cellular distributed antenna systems. Many of these systems are point-to-point systems in which MMW offers very high potential operating bandwidth along with broadband connectivity. Other implementations, also driven by the demand for high data rates, include gigabit wireless personal area networks, high-speed wireless local area networks, wireless USB transports, and high-speed wireless metropolitan area networks [42].

3.7.10 Combat Identification Systems

The battlefield target identification device (BTID) is an updated version of the battlefield combat identification system (BCIS). In 2003, the RDECOM Communications and Electronics Research, Development and Engineering Center teamed with Joint Forces Command to evaluate the BTID as part of the Coalition Combat ID Advanced Concept Technology Demonstration. Developed by Raytheon, the system is designed to distinguish whether a vehicle is friend or foe using advanced MMW technology. The NATO-compliant BTID integrates with a vehicle’s onboard weapons system, allowing the operator to make engagement decisions instantly using real-time identification data.

The BTID has question-and-answer, all-weather capabilities, and it offers real-time point-of-engagement target ID. The device has 98-percent positive identification and provides NATO interoperability verification and mature technology for next-generation MMW combat ID applications [43, 44].

3.8 | MMW FUTURE TRENDS

In general, the current trends for MMW application are oriented toward the FMCW lower-cost transmitter architectures. MMIC technologies are also maturing at a rapid pace, allowing for much smaller system packaging and high levels of signal

stability. MMIC is replacing older (larger) waveguide approaches for the following reasons:

- compact packaging size,
- low DC power requirements,
- higher level of repeatability, and
- higher level of reliability.

MMIC chip development is improving system performance with multiple function applications as higher power output specifications are obtained with lower receiver noise figures and ever-increasing operating frequency. This is largely due to the creation of new MMIC materials that result in improved performance at lower cost such as indium phosphide and silicon germanium. Of course, as MMW systems become smaller and cheaper, they will reap increased use in commercial areas, which further drives chip cost down with focus on the following application areas:

- MMW wireless and communication applications for ground and space,
- transportation (air and ground),
- collision avoidance and automatic cruise control,
- RF tags,
- parachute ground ranging, and
- velocity measurements.

3.9 | FURTHER READING

This chapter introduces key aspects of MMW radar applications. Many additional resources are available for further reading on the topic of MMW radar.

In addition to the books on MMW radar systems, techniques, and phenomenology listed in the reference section, several additional texts are recommended for further reading and investigation for readers both new and old to the subject. Each has many strong points to recommend it, and, depending on readers' specific interests, should provide a good starting point for getting into the literature of MMW radar characteristics and applications for military and commercial markets.

Currie, N.C., Hayes, R.D., and Trebits, R.N., *Millimeter-Wave Radar Clutter* (Artech House, 1992), is recommended for those needing a detailed background in propagation and clutter associated with MMW air-to-ground and ground-to-ground sensing geometries. It is more specific and provides a much deeper level of detail than some of the other books listed here.

Piper, S.O. [45] provides a good overview of how MMW seekers operate and some of the challenges they face when using FMCW waveforms.

Bruder, J.A., and Saffold, J.A. [46] is a complete reference on measurements with a calibrated MMW system and impacts of multipath on MMW low-angle tracking systems and attempts to correlate measurements with simulated data in these geometries.

Green, Hunton, *et al.* [47] is a good treatise on signal-processing techniques applicable to MMW seekers (a primary use of MMW for the military) and provides easy to read and understand approaches for pulses and FMCW waveform implementations.

3.10 | REFERENCES

- [1] Currie, N.C., and Brown, C.E., Editors, *Principles and Applications of Millimeter Wave Radar*, Artech House, December 1987.
- [2] Richards, M.A., Scheer, J.A., and Holm, W.A., *Principles of Modern Radar – Basic Principles*, Scitech Publishing, Raleigh, NC, 2012.
- [3] Richards, M.A., Scheer, J.A., and Holm, W.A., *Principles of Modern Radar – Basic Principles*, Scitech Publishing, Raleigh, NC, 2012, Chapter 4.
- [4] Knott, E.F., Shaeffer, J.F., and Tuley, M.T., *Radar Cross Section*, 2nd Edition, Scitech Publishing, Raleigh, NC, 2004.
- [5] Frisvad, J., Christensen, N., and Jensen, H. “Computing the Scattering Properties of Participating Media Using Lorenz-Mie Theory.” *ACM Transactions on Graphics - TOG*, 26(3), 2007.
- [6] Button, K.J., and Wiltse, J.C., *Infrared and Millimeter Waves, Millimeter Systems*, Academic Press, 1981.
- [7] <http://www.resrchnet.com/products/mrsim/>
- [8] Matkin, B.L., Mullings, J.H., *et al.*, “Bistatic Reflectivity Measurements at X, Ku, Ka and W-Band Frequencies,” Radar Conference, 2001. *Proceedings of the 2001 IEEE*, 2001.
- [9] Long, M.W., *Radar Reflectivity of Land and Sea*, Artech House, 15 April 2001.
- [10] Gunsten, B., *An Illustrated Guide to Modern Airborne Missiles*, Salamander Books, 1983.
- [11] Alexander, H., and Lamm, S., “Investigation of Dual-Mode Sensor Fusion Technology,” GTRI Final Tech Report A-8952, Hercules Defense Electronic Systems, June 1991.
- [12] Skolnik, M.I. *Radar Handbook*, 2nd Edition, McGraw Hill, New York, NY, 1990.
- [13] Barton, D.K., *Modern Radar System Analysis*, Artech House, 1988.
- [14] Rausch, E.O., Sexton, J., and Peterson, A.F., “Low Cost Compact Electronically Scanned Millimeter Wave Antenna,” Aerospace and Electronics Conference, 1996. NAECON 1996, *Proceedings of the IEEE 1996 National*, Vol. 1, May 1996.
- [15] Tokoro, S., Kuroda, K., Kawakubo, A., and Fujita, K., “Electronically Scanned Millimeter-Wave Radar for Pre-Crash Safety and Adaptive Cruise Control System,” Intelligent Vehicles Symposium, 2003. *Proceedings IEEE*.
- [16] Xing, S., and Peng, X.L., “Design and Implementation of Millimeter-Wave Active Phased Array Radar,” IEEE Radar Conference, 2006. CIE '06.
- [17] Bhartia, P., *Millimeter-Wave Microstrip and Printed Circuit Antennas*, Artech House.
- [18] Zaitsev, E.F., Gousskov, A.B., Cherepanov, A.S., and Yufit, G.A., “Low Profile, 2D-Scanning MMW Antenna Controlled by Two Currents,” *Microwave Symposium Digest*, 1998. IEEE MTT-S International.
- [19] World Technology Evaluation Center (WTEC) at Loyola College, WTEC Panel Report on Global Satellite Communications Technology and Systems, Workshop on Global Assessment of Satellite Communications Technology and Systems, National Science Foundation, 21 March 1997.
- [20] Yamano, S., *et al.*, “76 GHz Millimeter Wave Automobile Radar Using Single Chip MMIC,” *FUJITSU TEN Technical Journal*, 2004.
- [21] *Jane's Ammunition Handbook*, Jane's Information Group, 2003–2004.
- [22] “Boeing AH-64 Apache,” *Jane's All the World's Aircraft*. Jane's Information Group, 2010. Subscription article, 1 February 2010.

- [23] Abouzahra, M.D., and Avent, R.K., “The 100 kW Millimeter-Wave Radar at the Kwajalein Atoll,” *Antennas and Propagation Magazine, IEEE*, 36(2), 1984.
- [24] “TSA Imaging Technology,” *The TSA Blog*, tsa.gov.
- [25] Appleby, R., “Passive Millimetre-Wave Imaging and How It Differs from Terahertz Imaging,” *Philosophical Transactions of the Royal Society. A: Mathematical, Physical and Engineering Sciences*, 362(1815): 379–393, 2004.
- [26] Laskey, M., “An Assessment of Checkpoint Security: Are Our Airports Keeping Passengers Safe?,” House Homeland Security Subcommittee on Transportation Security & Infrastructure Protection, 2010.
- [27] Khajone, B., and Shandilya, V.K., “Concealed Weapon Detection Using Image Processing,” *International Journal of Scientific & Engineering Research*, 3(6), June 2012.
- [28] Kuroda, K., Kawakubo, A., and Fujita, K., “Electronically Scanned Millimeter-Wave Radar for Pre-Crash Safety and Adaptive Cruise Control System,” Intelligent Vehicles Symposium, 2003. *Proceedings IEEE*.
- [29] W.D. Jones, “Keeping Cars from Crashing,” *IEEE Spectrum*, September 2001, pp. 40–45.
- [30] Schumacker, R.W., Olney, R.D., Wragg, R., Landau, F.H., and Widman, G., “Collision Warning System Technology,” Automotive Electronics Development, Delco Electronics Corporation, 3011 Malibu Canyon Road, Malibu, CA 90265, USA.
- [31] Belohoubek, E.F., “Radar Control for Automotive Collision Mitigation and Headway Spacing,” *IEEE Transaction on Vehicular Technology*, VT-31(2), May 1982.
- [32] Bui, L.Q., Alon, Y., and Morton, T. “94 GHz FMCW Radar for Low Visibility Aircraft Landing System,” *IEEE MTT-S International Microwave Symposium Digest*. IEEE MTT-S International Microwave Symposium, August 1991.
- [33] Shoucri, M., Davidheiser, R., Hauss, B., Lee, P., Mussetto, M., Young, S., and Yujiri, L., “A Passive Millimeter Wave Camera for Aircraft Landing in Low Visibility Conditions,” *IEEE AESS*, Issue 5, May 1995.
- [34] Stephens, G.L., and Vane, D.G., “The CloudSat Mission,” Geoscience and Remote Sensing Symposium, 2003. IGARSS '03. *Proceedings*. 2003 IEEE International.
- [35] Durden, S.L., Tanelli, S., and Dobrowalski, G., “CloudSat W-Band Radar Measurements of Surface Backscatter,” *Geoscience and Remote Sensing Letters, IEEE*, 8(3).
- [36] Pazmany, A.L., and Wolde, M., “A Compact Airborne G-Band (183 GHz) Water Vapor Radiometer and Retrievals of Liquid Cloud Parameters from Coincident Radiometer and Millimeter Wave Radar Measurements,” *Microwave Radiometry and Remote Sensing of the Environment*, 2008. MICRORAD 2008.
- [37] Ogorlkiewicz, R.M., and Hewish, M., “Active Protection Systems for AFVs,” *International Defense Review*, pp. 31–38, 23 July 1999.
- [38] Pappert, G.W., Schlueter, K., and Koch, V., “General System Aspects of Active Armored Vehicle Protection,” *Proceedings of SPIE*, pp. 415–425, Vol. 4718, 2002.
- [39] Pappert, G.W., Schlueter, K., and Koch, V., “Anti-Tank Munitions Detectability and Interceptability.” *Proceedings of SPIE*, pp. 356–368, Vol. 4718, 2002.
- [40] Lefevre, R.J., Kirk, J.C., Jr., and Durand, R.L., Technology Service Corp, Santa Monica, CA, “Obstacle Avoidance Sensors for Automatic Nap-of-the-Earth Flight,” November 1994, *Proceedings of the 1994 IEEE/AIAA 13th Digital Avionics Systems Conference (DASC)*.
- [41] Starling, R.J., and Stewart, C.M., “The Development of Terrain Following Radar: An Account of the Progress Made with an Airborne Guidance System for Low Flying Military

- Aircraft,” *Aircraft Engineering and Aerospace Technology*, 1971, Vol. 43, Issue 4, pp. 13–15.
- [42] Xiao, S.-Q., and Zhou, M.-T., “Millimeter Wave Technology in Wireless PAN, LAN, and MAN (Wireless Networks and Mobile Communications).”
- [43] Baldwin, T., Ginther, J., Dere, T., and Nelson, P., “Digital Data Link (DDL) Through Battlefield Combat Identification System (BCIS),” *Proceedings of the 1996 Tactical Communications Conference*.
- [44] Nesbit, G., Dere, T., English, D., Purdy, V., and Parrish, B., “Ka-band MMIC-based transceiver for battlefield combat identification system,” *Tactical Communications Conference*, 1996.
- [45] Piper, S.O., “FMCW Range Resolution for MMW Seeker Applications,” *Southeastcon '90. Proceedings IEEE*, 1990.
- [46] Bruder, J.A., and Saffold, J.A., “Multipath Effects on Low Angle Tracking at Millimeter Wave Frequencies,” *IEE Proceedings – Radar and Signal Processing*; Special Issue on “Radar Clutter and Multipath Propagation,” May 1990.
- [47] Green, A.H., Hunton, A.J., *et al.*, “Methodology for Assessment and Evaluation of Signal Processing Techniques for Millimeter Wave Seekers,” *Tactical Weapon GACIAC SR-85-01*, January 1985.

Fire-Control Radar

William G. Ballard, GTRI, and Stéphane Kemkemia, THALES

Chapter Outline

4.1	Introduction	117
4.2	Airborne Fire-Control Radar	123
4.3	Surface-Based Fire-control Radar	160
4.4	Electronic Counter Countermeasures	170
4.5	The “AN” Equipment-Designation System	172
4.6	References.	173
4.7	Further Reading	173

4.1 | INTRODUCTION

4.1.1 Radar and Weapon Systems

The concept of a *weapons system* is a generalized term encompassing a broad spectrum of components and subsystems. These components range from simple devices directed or fired manually by a single individual against one specific class of target to a complex array of components or subsystems that are interconnected via data buses to onboard computers, and data communication links that are capable of performing multiple functions or engaging numerous targets or target classes simultaneously. Although each subsystem may be specifically designed to solve a particular part of the fire-control problem, it is these components operating in seamless concert that allows the whole system to achieve its ultimate goal – the destruction or neutralization of the designated target.

Modern weapons systems, regardless of the medium they operate in (land, sea, or air) or the type of weapon they employ (missile, bomb, or projectile), are composed of specific components that allow the system to detect, track, and engage the target. These sensors must be designed for the anticipated environments in which the weapons system and the target operate. A weapons system must employ at least one sensor but quite often has multiple sensors integrated to provide an optimal choice and redundancy, depending on the actual situation. These sensors ideally must also be capable of dealing with widely varying target characteristics, including target range, bearing, altitude, speed, size, heading, aspect, maneuvering, and countermeasures.

The main advantages of radar with respect to other sensors are:

- long detection and long tracking ranges that enable the firing of long-range weapons;
- all-weather operation, day and night; and
- full 3D localization and tracking (range, angles, and velocities).

Therefore, the majority of fire-control systems use radar as their main sensor. This chapter presents an overview of the radar technology and radar system concepts required to satisfy the fire-control mission.

The following is a list of abbreviations used in this chapter.

Δ_{az} and Δ_{el}	azimuth and elevation difference (channels)
Σ	sum (channel)
AACQ	auto-acquisition
ABF	adaptive beam forming
ACM	air-combat mode
ACQ	acquisition
AESA	active electronically scanned array
AGR	air-to-ground ranging
AI	air interception
AIM	air-interception missiles
AMRAAM	advanced medium-range air-to-air missile
AMSAR	airborne multirole solid-state active array radar
ASCM	antiship cruise missiles
ASIC	application-specific integrated circuit
BVR	beyond visual range
CAS	close air support
CCIP	constantly computed impact point
CCRP	constantly computed release point
CFAR	constant false alarm rate
CIWS	close-in weapons system
CNI	communication, navigation, and identification
COTS	commercial off-the-shelf
CPA	closest point of approach
DBS	Doppler beam sharpening
DPCA	displaced phase-center antenna
DRA	driver amplifier
DTM	digital terrain model
EA	electronic attack
ECM	electronic countermeasures
ECCM	electronic counter-countermeasurements
ELINT	electronic intelligence
EOTS	electro-optical targeting system

EP	electronic protection
E-SCAN	electronically scanned
EW	electronic warfare
EWS	electronic warfare system
FAC	forward air controller
FCC	fire-control computer
FCR	fire-control radars
FCS	fire-control systems
FFR	forward-firing rocket
FLIR	forward-looking infrared
FPGA	field-programmable gate array
GaAs	galium arsenide
GaN	galium nitride
GMTI	ground-moving target indicator
GMTT	ground-moving target tracking
GPS	Global Positioning System
HMD	helmet-mounted display
HMI	human-machine interface
HPRF	high-pulse repetition frequency
HRRP	high-range resolution profiling
HPA	high-power amplifier
HUD	heads-up display
IFF	identification friend or foe
IMM	interacting multiple model
INS	inertial navigation system
IRST	infrared search and track
ISAR	inverse synthetic aperture radar
IVVQ	integration, verification, validation, and qualification
JDAM	joint direct attack munition
JEM	jet-engine modulation
Joint STARS	Joint Surveillance Target Attack Radar System
JSOW	joint standoff weapon
JSTARS	Joint Surveillance Target Attack Radar System
LNA	low-noise amplifier
MFD	multifunction display
MPRF	medium-pulse repetition frequency
M-SCAN	mechanically scanned
MSL	mean or medium sea level
NCTR	noncooperative target recognition
NM	Nautical miles
OODA	observe, orient, decide, and act

PRF	pulse repetition frequency
RA	raid assessment
RABFAC	radar forward-air-controller beacon
RADFAC	radar beacon forward air controller
RAT	ram air turbine
RBGP	real beam ground mapping
RCS	radar cross section
RGPO	range gate pull-off
ROR	range-only radar
RWR	radar warning receiver
RWS	range while search
SAM	surface-to-air missiles
SAR	synthetic aperture radar
SLC	sidelobe canceller
SLS	sidelobe suppression
STAP	space-time adaptive processing
STT	single target track
TA	terrain avoidance
TF	terrain following
TOF	time of flight
TWS	track while scan
TVM	track via missile
TWT	traveling wave tube
VGPO	velocity gate pull-off
VS	velocity search
WAS	wide area search
WQT	weapon-quality track

When possible, radar measurements may be refined by those coming from other sensors – data fusion, for instance, with the electro-optical targeting system (EOTS), Forward-Looking Infrared (FLIR), and the infrared search-and-track (IRST) system. For effective fire-control applications, the radar must have a number of specific characteristics. The main features are the following.

- Detection and tracking ranges: They should be higher than those of the weapons unless the system efficiency is limited by the sensor.
- Sufficient tracking accuracy (in range, angle, and velocity vector) occurs with respect to the guidance requirements of the weaponry.
- Adequate discrimination occurs during both the detection and tracking phases. Indeed, the targets within a raid can be close to each other (both in position and velocity). These targets should be individually detected and properly localized, and then the tracking system should be able to maintain a given track on a given target without swapping or merging the tracks.

- Efficient electronic counter-countermeasurements (ECCM). The presence of these ECCM techniques is one specificity of fire-control radar.
- Fire-control systems include fire-control radar (FCR) as well as electronic warfare systems (EWS). The ability of both FCR and EWS to work together efficiently is an important feature of a fire-control system.

4.1.2 Kill Chain and Fire-Control Radar Functionality

Typical FCR characteristics include high-range resolution, high-pulse repetition frequency (HPRF) for efficient Doppler processing, and a very narrow beamwidth. The goal is to define the attributes of the designated target (location, motion data) so as to allow the weapons system to place the available weapon's proximity to the target within a lethal radius at detonation. These characteristics, while providing extreme accuracy, limit the range and make initial target detection difficult.

The next generation of fighters are adapting active electronically scanned array (AESA) for their radar sensors. In addition to expanding the functionality of the sensors, the potential for including some electronic warfare (EW) capabilities is being explored. Increasingly powerful onboard processors and advances in software make it possible to take advantage of the new arrays for electronic intelligence on in-band signal detection as well as some active EW jamming with modified radar transmissions. Examples of cooperative systems, also called *multifunction systems*, are described in [1].

The FCR operates according to a sequence of operations called the *kill chain*. These operations are carried out sequentially in the case of mechanically scanned radars. However, the new AESA radars provide the possibility of simultaneously carrying out several functions within the kill chain. For example, multifunction radars operating in an air-to-air engagement will perform a search-through-kill assessment of the kill chain. A kill chain example is shown in Figure 4-1.

Regarding the radar system itself, two configurations are usually encountered:

1. *Single sensor but dual-function system* (e.g., *searching and tracking*). This configuration is especially important for airborne platforms in which multiple radar sensors for separate tasks are normally not available. For example, the F-22 fighter AN/APG-77

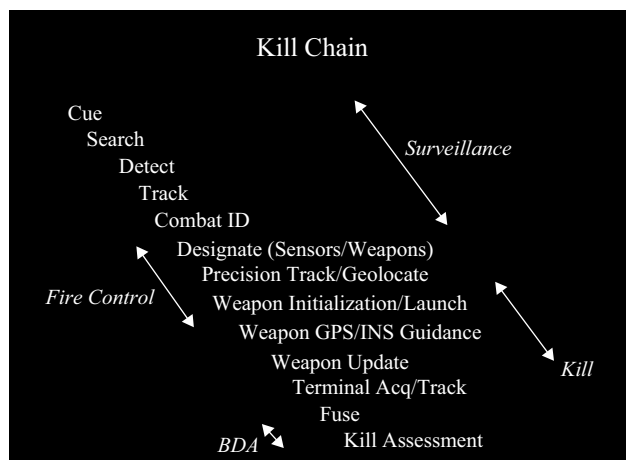


FIGURE 4-1 ■ Kill Chain [HQ AFDC/DR, "Air Force Doctrine Document 2-1.9 Targeting," (2006): p. 49].

multifunction radar operating in an air-to-air engagement will perform a search-through-kill assessment of the kill chain.

2. *Dual-sensor systems in which search and tracking radars are separate devices.* For instance, a search radar, with wide coverage but not necessarily high accuracy, can be used to cue a tracking radar (for weapon guidance) having high angle resolution. The search radar and the tracking radar may operate on distinct frequency bands; for instance, a search radar rather in a “low frequency band” for having a wide coverage without having scanning issues and a tracking radar rather in “high-frequency band” (Ku, Ka) for having high angular accuracy. This dual system may be also extended to a network of search radars, tracking, and weapon guidance. The networking may use interoperable tactical data links or ad-hoc ones.

4.1.3 The Four Fire-Control Scenarios

Fire-control radar can be found in the following platform-target combinations:

1. air to air,
2. air to ground,
3. surface to air, and
4. surface to surface.

The first two scenarios involve airborne radars, while the last two involve surface-based radar. Airborne radars are installed on moving platforms. Surface radars can be fixed or mobile, such as aboard a ship.

4.1.4 Organization of the Chapter

Airborne fire-control radar is described in section 4.2. Then surface-based fire-control radar is described in section 4.3. Both in the case of airborne FCR and surface-based FCR, the focus is on the following three specific steps in the design of such radars.

1. *The past:* Mechanically scanned FCR developed about one or two decades ago and constitutes the most important part of the systems currently in operational use. Their production goes on without continued development.
2. *The present:* Electronically scanned (E-SCAN) FCR have been or are being deployed for operational use. Indeed, the instantaneous agility of E-SCAN, especially using AESA, provides much improved capabilities of these kinds of radars with respect to older ones.
3. *The future:* Improved AESA FCR has three areas in which improvements are being done:
 - In *sensor improvement*, the future AESA will be fitted with more than the four traditional quadrants which serve to form the sum channel and the two difference channels. In particular, these multiple subarrays will allow Adaptive Beam Forming (ABF) for efficient cancellation of multiple jammers and space-time adaptive processing (STAP) for clutter cancellation and detection improvements. All these improvements, made possible by the subarrays processing, will enable a better protection against attacks, a better detection of difficult targets, and so on.
 - With *multifunction sensor*, the radar is now a multipurpose cooperative sensor. In conjunction with the EWS, the EOTS is part of a system of cooperating sensors. For example, the radar’s AESA can be used to perform more efficient EW

functions in its band of operation. In another area, the powerful AESA of the radar, in conjunction with a modem, can carry out ad-hoc data links at long range and very high speed.

- With a *network of cooperative sensors*, the combat platforms in the theater of operation that are fitted with multifunctional sensor systems are now networked. A global tactical situation is established through the contribution of each individual platform and then shared by all platforms thanks to interoperable data links.

For each generation of radars, the improvements in terms of capabilities and enabling technologies will be presented both in terms of hardware (RF technologies, antenna technologies, digitalization, processing machines, etc.) and in terms of algorithms for signal and data processing (adaptive processing, improved tracking on maneuvering and multiple targets, terrain imagery for navigation or targeting, smart scheduling of resources, etc.).

After analyzing the radar sensor itself, the different types of weapons at stake and their methods of guidance on target will be reviewed.

4.2 | AIRBORNE FIRE-CONTROL RADAR

Almost all of these radars operate in X-band. Indeed, this choice results in trade-offs between:

- The need for fine angle resolution and accurate angle measurement for target tracking, while available space is limited in aircraft's nose, which leads to use high operating frequencies.
- The need for all weather operation at long range (so, low propagation losses), which leads to use low operating frequencies.

Until about the 1980s, the platforms and FCR were mostly dedicated to specific missions: either air-to-air or air-to-surface. Advances in both platform technologies and electronic technologies have made the fire-control systems multirole systems. However, for the sake of clarity, the air-to-air and air-to-surface missions will be considered successively.

4.2.1 M-SCAN FCR

Typically, the most recent generations of such radars share the following characteristics:

- High-gain, flat-slotted antennas are divided into four quadrants for accurate monopulse angle measurements¹ both in elevation and azimuth. The reader is referred to Volume 1, Chapter 9 of *Principles of Modern Radar, Basic Principles*, for a description of monopulse principles. Such an antenna is light and compact and has low sidelobes in order to avoid being too hampered by the ground clutter or by intentional or unintentional interferences. At reception, the antenna provides three signals:
 - the sum channel (Σ) to detect the targets,
 - the difference channel in azimuth (Δ_{az}), and
 - the difference in elevation (Δ_{el}) for monopulse measurements in tracking.

¹Accurate angle measurements are a key feature for FCR (accurate target tracking).

- An auxiliary antenna (A) with low directivity (called a *guard* antenna) may also be present on some systems. The role of this guard antenna is to cancel false alarms caused by ground clutter or by jamming when viewed from the antenna's sidelobes. This processing is called *sidelobe suppression*. It aims to compare the signal issued from the sum antenna with respect to the signal issued from the guard antenna. If $\Sigma > A$, the detection is accepted; otherwise, it is rejected.
- A traveling wave tube (TWT) transmitter combines the following interesting features:
 - good power efficiency (about 40%),
 - coherent operation without adding spurious signals,
 - relatively wide bandwidth, and
 - good reliability.²
- A high dynamic range receiver, which is required to achieve good performance at low altitude or look-down configuration in the Doppler modes (high-pulse repetition frequency, or HPRF, and medium-pulse repetition frequency, or MPRF) that use both range-ambiguous waveforms, usually has two or three channels. The most common configurations are the following:
 - Two channels (most cases): (1) sum channel (Σ) and auxiliary channel (A) in search phase; and (2) sum channel (Σ) and two multiplexed difference channels (Δ_{az} and Δ_{el}) for monopulse measurements in tracking.
 - Three dedicated channels: Σ , Δ_{az} , and Δ_{el} (this configuration provides better performance in angle tracking and more robust ECCM).
- High spectral purity exciter for good performance at low altitude or in look-down configurations using Doppler modes. The exciter should be able to generate:
 - a wide range of pulse-repetition frequency (PRF), generally from low PRF (look-up configuration in air-to-air operations and most of the waveforms used in air-to-surface operations) to MPRF and HPRF (look-down configuration in air-to-air operations);
 - several intrapulse modulations intended for pulse compression (e.g., from no pulse compression in HPRF to large pulse compression factors in LPRF mode – for instance, in imagery modes); and
 - many carrier frequencies over some hundreds of megahertz; in particular, this capability enables (1) the use of frequency diversity to reduce the fluctuations of a target's RCS and (2) the ability to operate multiple radar systems simultaneously without interference and improved ECCM capabilities.
- Powerful programmable signal and data processors, which are key enablers for multimodes and multirole radars.

Finally, a very important element is the radome. It should be as transparent as possible to radar waves without degrading the radiation pattern of the antenna, have a proper aerodynamic shape, be shock resistant (to birds, hail, etc.), and of course protect the radar.

²The main cause of failure of the transmitter is from the high-voltage generators, not the tube.

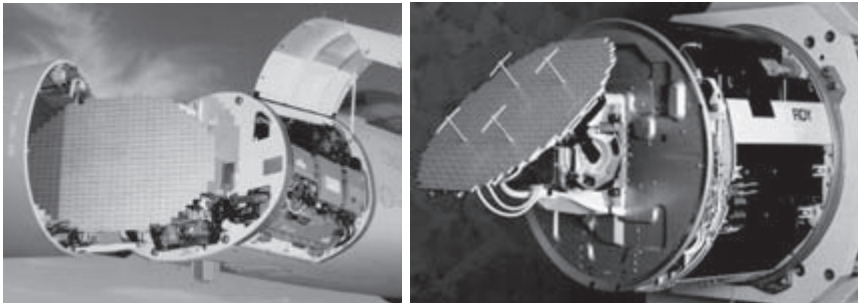


FIGURE 4-2 ■ Left: APG-68 for F-16 [Courtesy Northrop Grumman http://www.northropgrumman.com/MediaResources/Pages/Photo.aspx?pid%3DAN-10134_001%26rel%3D%2F%26name%3DPhotos + own work (Kemkernian)] Right: RDY for Mirage 2000 [Courtesy Thales Airborne Systems].

Two examples of the latest generation of M-SCAN fire-control radar are shown in Figure 4-2.

4.2.1.1 Air-to-Air Modes

Air superiority, air interception, and air combat are the main tasks of the air-to-air mission, which can also include:

- the air policing mission, which is a peacetime mission and aims to visually identify a doubtful aircraft; and
- the escort mission, which is the protection of friendly aircraft.

Air superiority is an offensive task that aims to destroy all enemy aircraft. The weaponry used mainly consists of missiles with seekers. The method for long-range air-to-air missile guidance will be discussed in the “Principles of Missile Guidance” section. The combat takes place at short distance (< 10 nm). It uses short-range missiles and even cannon.

The typical air-to-air modes of M-SCAN FCR are:

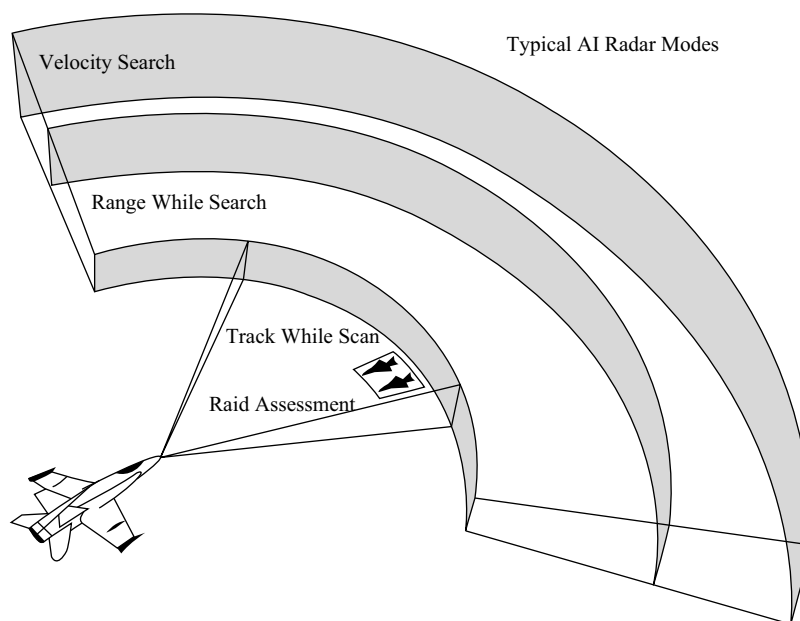
- velocity search (VS),
- range while search (RWS),
- track while scan (TWS),
- single-target track (STT),
- acquisition (ACQ), and
- air-combat mode (ACM).

Two subsidiary modes mainly triggered in TWS and before firing the weapons are:

- raid assessment (RA) and
- noncooperative target recognition (NCTR).

In all these tasks, especially in the air-to-air mission, the enemy will try to jam the FCR using electronic attack (EA) (formerly known as *electronic countermeasures* or ECM) techniques. The specificity of the FCR is to deploy all modes and techniques to

FIGURE 4-3 ■ AI Radar Modes
[Jane's Defence: Air & Space].



mitigate the effects of such EA. These means are called *electronic protection techniques* (formerly *electronic counter-countermeasures*).

The sequence of these modes in air interception (AI) is shown in Figure 4-3.

Velocity Search The VS mode provides long-range, forward-sector (nose-on), look-up, look-down target detection. The HPRF waveform is used to ensure that the target Doppler frequencies are unambiguously detected, but it causes the target return to be highly ambiguous in range. No ambiguity removal is performed in order to obtain the highest possible sensitivity. Since this method provides only velocity and azimuth information without any range measurement, it is often used cued by an early warning system.

Range While Search The RWS mode provides all-aspect (nose-on, tail-on) and all-altitude (look-up, look-down) target detection. RWS provides range and angular data without stopping the normal antenna search pattern. This mode can use different waveforms, depending on the configuration (look-up or look-down) and whether forward-sector target detection or all-aspect (nose-on, tail-on) target detection (see Figure 4-4) is desired using the following waveforms:

- look-up, all-aspect detection (LPRF);
- look-down, focus on nose-on target (HPRF); and
- look-down or low-altitude operation, all-aspect target (MPRF waveforms).

The reader is referred to [2] for more details.

An automatic waveform management is often used to help the pilot. The reader is referred to Chapter 5 in this volume for a description of methods of ambiguity removal and details on the related waveforms.

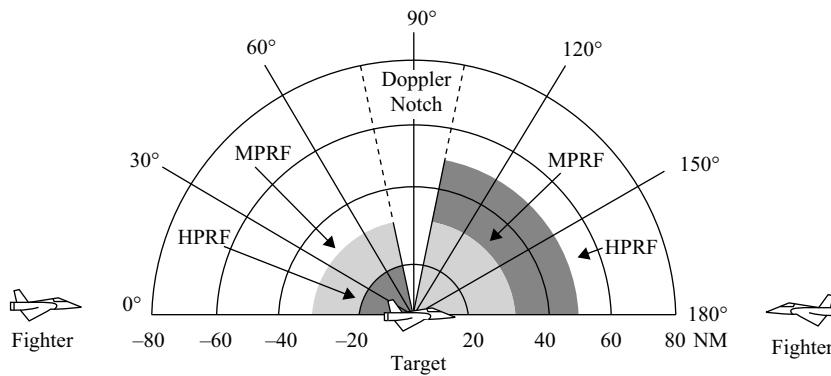


FIGURE 4-4 ■ HPRF and MPRF Range Comparison [Copy from “Air and Space borne Radar Systems – Ph. Lacomme, J.Ph Hardange, J.C. Marchais, E. Normant. SCITECH Publishing” (Lacomme)].

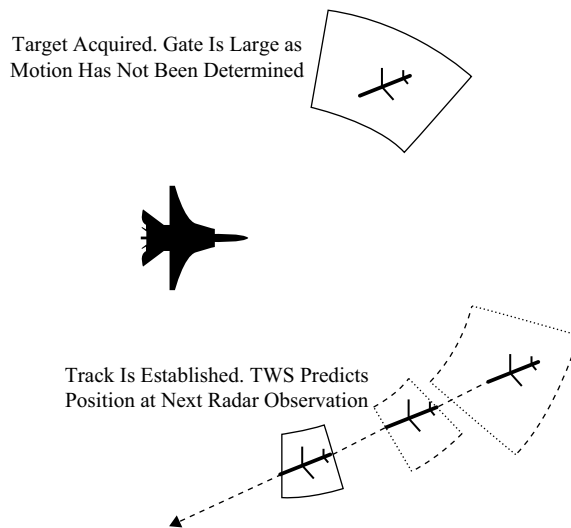


FIGURE 4-5 ■ Target Tracking and Acquisition Gates with TWS [Self-Developed Graphic (Ballard)].

Track While Scan The TWS mode can track and display multiple target tracks to the pilot. The track-while-scan system maintains the search function, while a data processor performs the tracking functions. The TWS system is capable of tracking many targets simultaneously. Furthermore, the TWS system can also perform a variety of other automated functions such as collision or closest-point-of-approach (CPA) warnings. The TWS system manages targets using gates as depicted in Figure 4-5. A TWS system may use range, angle, Doppler, and elevation gates in order to sort out targets from one another. When a target is first detected, the data processor will assign it an *acquisition gate*, which has fixed boundaries of range and bearing (angle), and possibly other parameters such as Doppler in coherent modes. When the radar sweeps by the target again, if the return still falls within the acquisition gate, the computer will initiate a track on the target.

By following the history of the target positions, the course and speed of the target can be found. The combination of range, bearing, course, and speed at any one time is known as the target's *solution*. It is used to predict where the target will be at the next observation. Once a solution has been determined, the computer uses a *tracking gate*

about its predicted position. If the target falls within the predicted tracking gate, then the computer will refine its solution and continue tracking.

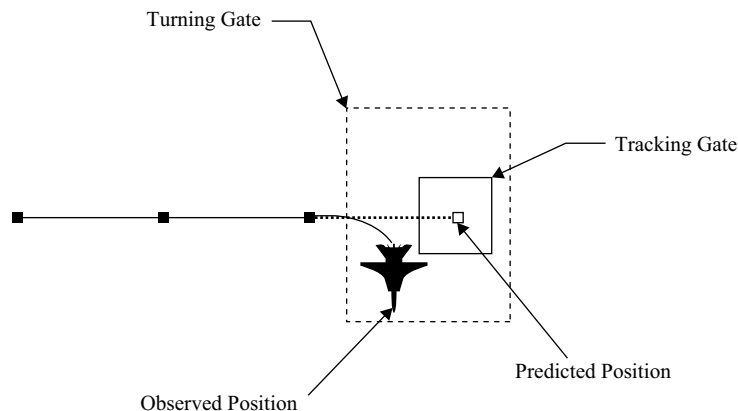
Typically, the pilot manually designates the targets to be tracked from the RWS mode. On some modern systems having a large number of tracking estimators, RWS is an embedded part of TWS: The detections automatically trigger tracks. In some multi-target fire-control systems, the tracks on targets to be fired are prioritized, and the scanning domain is automatically adjusted to maintain the tracking on these targets according to the prioritization. When these targets are too widely spread in angle, the M-SCAN is no longer capable of maintaining the multiple target tracking and a choice between the targets to track needs to be done by the system. The E-SCAN provides a huge improvement over the M-SCAN on this point.

Tracking Filters The first TWS systems used so-called α - β filters. There are multi-axis (angle, distance, Doppler velocity) recursive filters with filtering coefficients that are predetermined and based on various parameters (age of the track, update rate, error on innovation,³ etc.). The target model used to predict the position of the target at the next scan is a constant velocity model. In the case where the target is turning, the target will probably not be within the tracking gate at the next observation and the tracking system will check to see if the target is within a turning gate (Figure 4-6) that surrounds the tracking gate. (The reader is referred to Volume 1, Chapter 19 for more details.)

Given a maximal turn rate, the turning gate encompasses all the area that the target could be in since the last observation. If the target is within the turning gate, the computer starts over to obtain the new target-vector solution. If the target falls outside the turning gate, the track will be lost. The system will continue to predict tracking gates in case the target reappears. Depending on the system, the track file may contain other useful information, such as the classification of the target. This information may be used by the computer when determining the track and turning gates. The operator may also be required to drop the track.

More modern TWS systems often use a Kalman with a “Singer” target model. This model states that the residual error component on each axis (range, angle, etc.) is a

FIGURE 4-6 ■ Use of a Turning Gate to Maintain Track on a Maneuvering Target [Self-Developed Graphic (Ballard)].



³Innovation is the difference between the predicted position at scan k and the target position measured at the same scan k . The innovation is a multidimensional parameter (range error, angle errors, and Doppler velocity error).

random process with an exponential autocorrelation function. A Kalman filter continuously computes the covariance matrix of the position estimation, so it adaptively manages the tracking gate and the filtering coefficients provided that the errors' variances of the “raw” measurements have been correctly estimated. A single target's model cannot be optimal for all possible target trajectories. This is why, more performing estimators have been developed over the last 15 years.

The state of art in tracking systems (for TWS or other tracking modes) relies on the interacting multiple model (IMM) filter or its improved derivatives. Simply speaking, IMM uses several Kalman filters that run in parallel, each using a different model of target motion. Likelihoods with respect to the target path are computed for each model. Using these likelihoods, the IMM forms an optimal weighted sum of the output of all the filters and then rapidly adjust to target maneuvers. Although they were unrealizable before for multitarget-tracking systems because of the computing power requirements, these complex algorithms are now accessible thanks to advances in real-time computing. The description of the IMM algorithm can be found in Volume 1, Chapter 19.

Multitarget Tracking Issues The process of assigning observations with established tracks is known as *correlation*. During each sweep, the system will attempt to correlate all returns with existing tracks.

If the return cannot be correlated, it is assigned a new acquisition gate, and the process begins again. On some occasions, a new target may fall within an existing tracking gate. The system will attempt to determine which return is the existing target and which is the new target, but it may fail to do so correctly. External or not kinematic information can also be used, such as identification of friend or foe (IFF) info if available, the type of target if an NCTR mode is implemented, or data entered by the operator or an external system. Anyway, it is common for TWS systems to have difficulty when there are multiple targets in close proximity or when existing tracks cross each other (Figure 4-7).

On recent systems, efficient correlation algorithms are used in dense multitargets situations. The reader is referred to Volume 2, Chapter 15 for more details. On FCR, quick reactions are often mandatory: An important thing for choosing one method rather another is the delay before providing a decision of correlation (thus, a track estimate update) and especially in TWS modes where the refresh rate may be slow.

Track Files The TWS system uses a computed track file for each established target it tracks. The track file contains all of the observations that are correlated with that particular target: for example, the range, bearing and time of observation. The track file is given a unique name known as the *track designation*. This is usually a simple

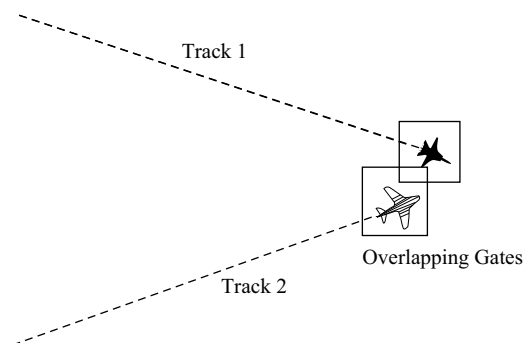


FIGURE 4-7 ■
Crossing Tracks
[Self-Developed
Graphic (Ballard)].

number such as “track 42.” Finally, the track file also contains the current solution to the track’s motion.

It is a natural extension of the track-while-scan system to create a system that shares tracking information between users: Single radar cannot see the entire tactical situation. All that is required is to transmit the contents of the track file, since it contains all of the observations and the current solution. The sharing of tracking information has been incorporated extensively into modern combat platforms. There are now global command and control networks such as Link 16 that are capable of sharing this information between units all over the world.

Single Target Track In STT, the radar antenna and range gates are continuously kept on the target, keeping a continuous record of the target position. The radar tracks a single target and performs no other function during the time it is tracking. It may be “cued” from another (search) radar, or it may initially find the target in a search mode. The STT mode provides accurate tracking of a single target and can function automatically by engaging auto-acquisition (AACQ) in combat mode or manually by designating a target on the VS, RWS, or TWS displays.

Raid Assessment The goal is to get a reliable count of the number of targets within a raid and their relative positions. This task takes place before the targets are engaged. The waveform used has a better range or Doppler resolution than the resolution used, for instance, in the RWS, TWS, or STT modes. The RA is triggered briefly just for the raid analysis from a tracking mode.

Noncooperative Target Recognition The ideal goal is to recognize the target type, whether, for example, an F-16, a MiG-29, an Su-30, or a civilian aircraft. In addition to the IFF interrogation, the NCTR has become essential before firing the weapons to avoid fratricide or civilian kills.

The current methods rely on high-resolution spectral analysis of the signal from the target. Indeed, the rotating parts of engines – namely, the low-pressure compressor blade – induce periodic modulations on the returned signal. This effect is called *jet-engine modulation* (JEM).⁴ It does not identify the target directly, only its engine(s). Similar effects occur with aircraft propellers, ram air turbine (RAT) devices used to power various aircraft pods, and helicopter main and tail rotors; all provide a chopped reflection of the impinging radar signal. The high-resolution spectrum is analyzed, and the result is compared with a library of signatures. A limitation to JEM NCTR techniques, though, is that if the aspect angle is too far from head-on or tail-on and the engine intake or exhaust ducts provide shielding for the jet engine, then there may be no JEM to detect. On the other hand, JEM increases when with an orthogonal orientation to the axis of blade rotation.

Another method of NCTR is to make a range profile of the target and compare it with a library of profile (by using a waveform having sufficient range resolution).

Acquisition and Air-Combat Mode There are four modes of AACQ with a nominal range of 10 nm (Figure 4-8):

- *Wide acquisition* (WACQ) displays the target nearest the aircraft after a wide azimuth scan. Typically, the radar scans several horizontal bars (about $\pm 30^\circ$) centered on the aircraft’s longitudinal reference axis.

⁴Moving or rotating surfaces on the target will have the same Doppler shift as the target: The modulation is “carried” by the Doppler line of the airframe.

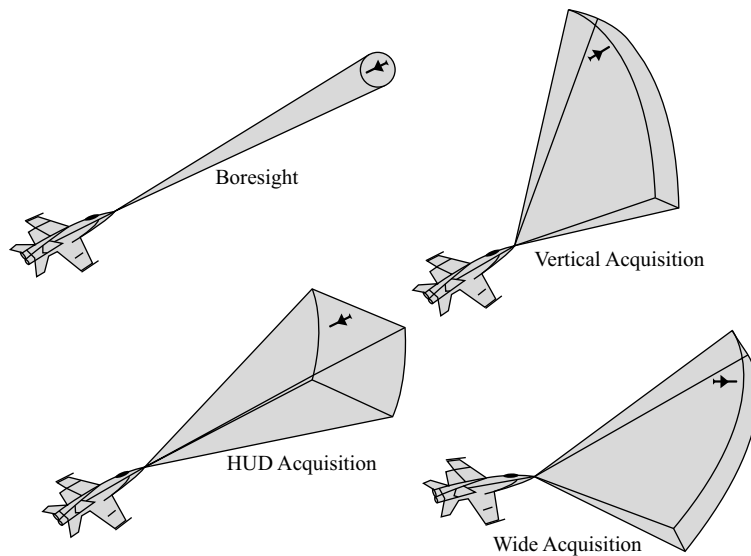


FIGURE 4-8 ■ Typical Auto-acquisition Modes for ACM [Jane's Defence: Air & Space].

- In *vertical acquisition* (VACQ), the radar scans about $\pm 50^\circ$ vertically, centered on the longitudinal axis, and automatically acquires and tracks the first target detected within the specified range. The scan pattern is referenced to own ship axis. This mode is employed when a large altitude separation between the fighter and the target aircraft is anticipated.
- *Heads-up display acquisition* (HACQ) displays the target nearest the aircraft after a scan of volume projected off the heads-up (HUD) field of view. This is typically used in the close-in, auto-acquisition, and gun scenario.
- *Boresight acquisition* (BACQ) displays the target nearest the aircraft. The HUD shows the antenna beam limits, and the pilot maneuvers to bring a visible target within this circle. This is a very selective acquisition mode since only targets within the antenna beam can be acquired.

Once acquired, the target is tracked in STT mode.

4.2.1.2 Air-to-Ground Modes

The main missions of an FCR in air-to-ground operation are:

- tactical support,
- ground attack, and
- interdiction.

All these missions aim to destroy or neutralize surface targets such as bridges, airfield runways, tank formations, and surface-to-air defense system. These tasks require:

- prior knowledge of the tactical situation provided by other means,
- high-performance navigation systems,
- sophisticated countermeasures,
- adapted weaponry, and
- air protection (escort).

It may be noted that the M-SCAN radars cannot simultaneously perform efficient air-to-ground tasks and efficient air protection. Thanks to the antenna's beam agility, the platforms equipped with new E-SCAN radars are now able to carry out air-ground missions while ensuring their own air protection.

The main radar modes involved in air-to-surface operation are:

- real-beam ground mapping (RBGP);
- high-resolution ground mapping, which occurs in Doppler beam sharpening (DBS) and synthetic aperture radar (SAR) modes;
- update of the inertial navigation system (INS) if the Global Positioning System (GPS) is not available;
- ground-moving target indicator (GMTI) and ground-moving target tracking (GMTT);
- air-to-ground ranging (AGR) for bombing by using radar telemetry;
- bombing using ground mapping; and
- assistance to low-altitude navigation through terrain avoidance (TA) and terrain following (TF).

Note that all air-to-surface modes use LPRF waveforms, sometimes with Doppler processing.

Real-Beam Ground Mapping RBGM provides a map of the ground with coarse resolution but over a large area. The quality of the map can be improved on contrasted echoes by using monopulse sharpening. The interest of RBGM is to provide a broad view of the environment. Unlike DBS and SAR modes, it can provide a view along the axis of the velocity vector.

Doppler Beam Sharpening and Synthetic Aperture Radar Modes DBS and SAR modes provide high- and very-high-resolution maps of the ground (only on fixed echoes). Both modes use the same principle for the lateral resolution – that is, the movement of the platform for getting a large virtual (synthetic) antenna.

- The DBS is a simplified version of SAR in which the antenna's beam sweeps the area to be mapped. The resolutions are on the order of tens of meters in DBS.
- In the strip SAR mode, the antenna remains steered in a constant azimuth. This mode displays a continuous map along a strip. The resolutions are usually less than a few meters. The length of the synthetic antenna, and thus the resolution, is limited by the duration of the crossing of a target in the main lobe.
- In the spot SAR, the antenna is slaved to illuminate a small area within the antenna's beam footprint. This slaving enables very long synthetic antennas. Resolutions as fine as four inches have been successfully achieved.

The reader is referred to Chapter 1 in Volume 1 and Chapters 6, 7, and 8 in Volume 2 for more details. These modes are used for navigation update, detection and accurate localization of fixed targets, and damage assessment after a strike. They may be also used for bombing purposes with GPS- or INS-guided weapons.

Update of the Inertial Navigation System Modern INS are tightly coupled with a GPS unit, making it possible to avoid position and velocity drifts and greatly improving navigation. However, the GPS signal may be unavailable or corrupted due to various

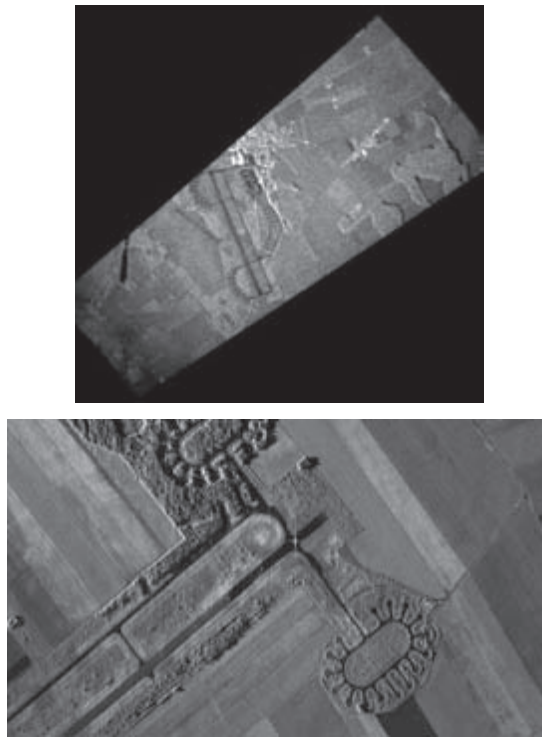


FIGURE 4-9 ■ Top: DBS Map. Bottom: SAR Map [(Courtesy THALES and [2]) Thales Airborne Systems + own work (Kemkemia)].

reasons. In this case, the update of the INS from radar is automatically obtained in modern systems by correlating radar images with a digital terrain model (e.g., map or terrain profiles). In older systems, the update was obtained thanks to manual designation of landmarks with known coordinates (Figure 4-9).

Ground Moving Target Indicator Ground targets of interest sometime fall into the mobile vehicle category. Their radar signature is at a level that they normally would be masked by ground clutter. If they are moving, though, the difference between the Doppler return of the target and the surrounding clutter can be exploited. In each range gate, a spectral analysis allows separation of the ground clutter area from the thermal noise area where the moving targets can be detected. The detected targets can be accurately localized in azimuth thanks to the monopulse processing. These ground-moving targets can then be tracked (GMTT). Two kinds of GMTI modes are used:

- Wide area search (WAS) uses a search domain of about $\pm 45^\circ$ in azimuth. The WAS method is easier to use if the detections are superimposed on a digital map. Figure 4-10 shows a typical display, with the concentration of vehicles on main roads clearly visible.
- In the mode known as SAR/GMTI, GMTI detections are superimposed on a SAR map. Both SAR mode and GMTI mode are performed by the radar so that they appear as a single mode. The SAR mode provides high-resolution images whose size is necessarily reduced. Thus, the SAR/GMTI operates on a small area. A typical display is shown in Figure 4-11. On the aircraft display, the dots indicate the moving targets. In urban, wooded, or hilly areas, the number of ground-moving targets is not visible.

FIGURE 4-10 ■
 Typical WAS GMTI
 Display
 [(Courtesy THALES)
 Thales Airborne
 Systems + own
 work (Kemkemia)].

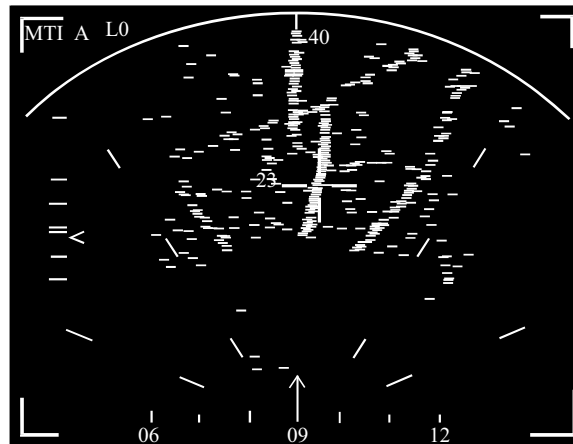


FIGURE 4-11 ■
 Typical SAR/GMTI
 Display
 [(Courtesy THALES)
 Thales Airborne
 Systems + own
 work (Kemkemia)].



Figure 4-12 illustrates the use of both types of GMTI. On the aircraft display, the dots are the moving vehicles.

Detection of Slow-Moving Targets When viewed by a moving radar platform, fixed targets on the ground lie within a particular Doppler bandwidth. Expressed in terms of radial velocity, the Doppler extent of these fixed targets is

$$\Delta V_R = V_P \sin \theta \bullet \Delta \theta_{clut}$$

where

θ = angle of fixed target relative to the aircraft velocity vector,

$\Delta \theta_{clut}$ = azimuth beamwidth that returns a clutter level exceeding the thermal noise level,

V_P = velocity of the platform, and

ΔV_R = change in radial velocity.



FIGURE 4-12 ■
 “WAS” GMTI
 Superimposed on
 Digital Map and
 SAR/GMTI
 [(Courtesy THALES)
 Thales Airborne
 Systems + own
 work (Kemkernian)].

Generally, $\Delta\theta_{clut} \cong 20_{-3dB}$. These considerations show that detection of slow targets is difficult, even impossible, for directions far from the direction of the platform’s velocity vector.

A better-performing approach can suppress fixed ground clutter that interferes with the moving-target returns by employing an antenna system divided into multiple subapertures and thus multiple phase centers. These multiple subapertures act as independent antennas to form a so-called displaced phase-center antenna (DPCA). The basic concept is to keep pairs of phase centers motionless from pulse to pulse, simulating an antenna that stays motionless in space. This has the effect of driving the Doppler bandwidth of clutter to zero so it can be canceled on subtraction of the data from these pulse pairs. With the background “removed,” all that remains are moving objects and noise. Moving targets, however, will suffer some amount of loss on subtraction, depending on their range rate and the difference in time between observations.

Still, after detection, the location in azimuth of the target remains unknown. Multiple phase centers along the horizontal axis can solve this problem, in an approximate sense, by means of monopulse techniques. With a minimum of three phase centers, both the DPCA technique of clutter cancellation and monopulse techniques for location of targets can be combined to detect and locate targets on the ground.

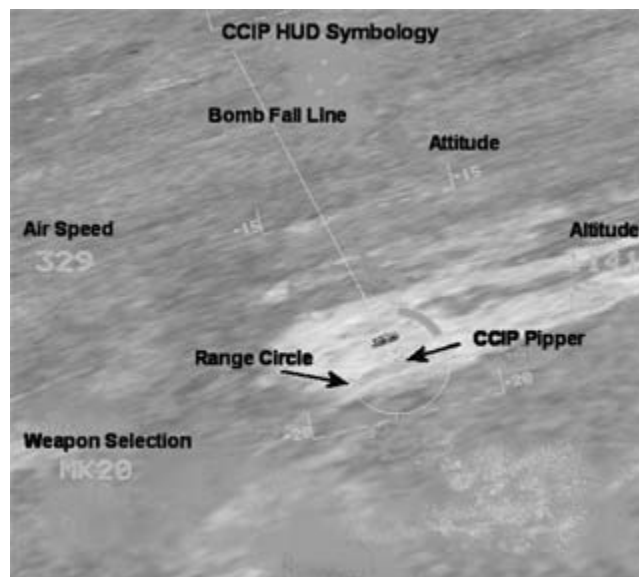
Surveillance radars designed for GMTI typically implement the DPCA technology and have three or more antenna phase centers in azimuth. An adaptive version of DPCA – STAP – is most often used. The reader is referred to Volume 2, Chapter 10 for more details.

Such an antenna’s arrangement is difficult to implement on existing multirole FCR (air-to-air and air-to-surface) with M-SCAN antenna. However, this technique will be commonly used on future AESA radars with multiple subarrays.

Air-to-Ground Ranging AGR provides the fire-control computer (FCC) the slant range of ground along the antenna's beam axis – that is to say, the range where the monopulse ecartometry in elevation is null. The AGR is used for bombing in two manners:

- In the first mode, *constantly computed impact point (CCIP)*, the air-to-ground ranging function of the radar measures the area in the vicinity of the CCIP HUD symbol so the FCC can interpret the correct range and elevation of the target. The impact point is indicated via HUD symbology (Figure 4-13). The FCR can provide ranging information to the target area, allowing impact point symbology to be displayed to the pilot on the HUD. In the CCIP mode, the pilot visually acquires the target but uses HUD CCIP information to determine when to release the designated weapon. The CCIP delivery is appropriate for strafing, forward-firing rocket (FFR), or free-fall bomb deliveries. The CCIP delivery is not an all-weather delivery even though radar information is used to assist in the fire-control solution because target acquisition and designation are done visually.
- In the second mode, *constantly computed release point (CCRP)*, the primary “full system” delivery of unguided and many guided weapons is summarized in the CCRP attack. Delivery parameters vary, depending on the tactical situation. Examples include (a) low-altitude, unaccelerated (1-G), delivery of high-drag, general-purpose (GP) weapons; (b) low-altitude, accelerated (> 1 G), toss or dive toss of GP and precision-guided weapons; and (c) medium- to high-altitude level or dive or dive toss maneuvers. The onboard FCR gives the option of all-weather day or night delivery. The radar provides range, bearing, and depression angle information to the FCC. Steering information presented to the pilot via the HUD or appropriate multifunction display (MFD) symbology includes prescribed heading and pull-up information for accelerated maneuvers. In general, when the down-range travel for the selected weapon is equal to the radar slant range, a release pulse

FIGURE 4-13 ■
CCIP Heads-Up
Display [Annotated
Simulation Screen
Capture. Lock-on
Modern Air Combat
[http://lockon.co.uk/
en/modern_air_
combat/](http://lockon.co.uk/en/modern_air_combat/)].



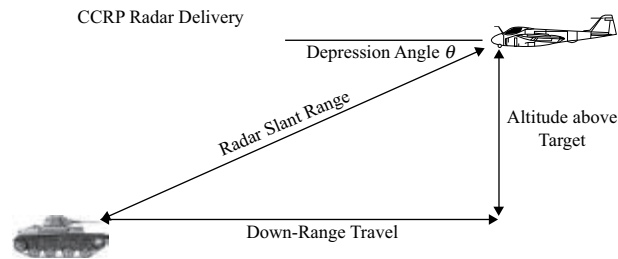


FIGURE 4-14 ■ CCRP Radar Delivery [Self-Developed Graphic (Ballard)].

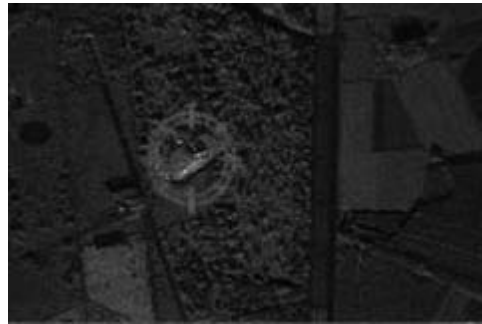


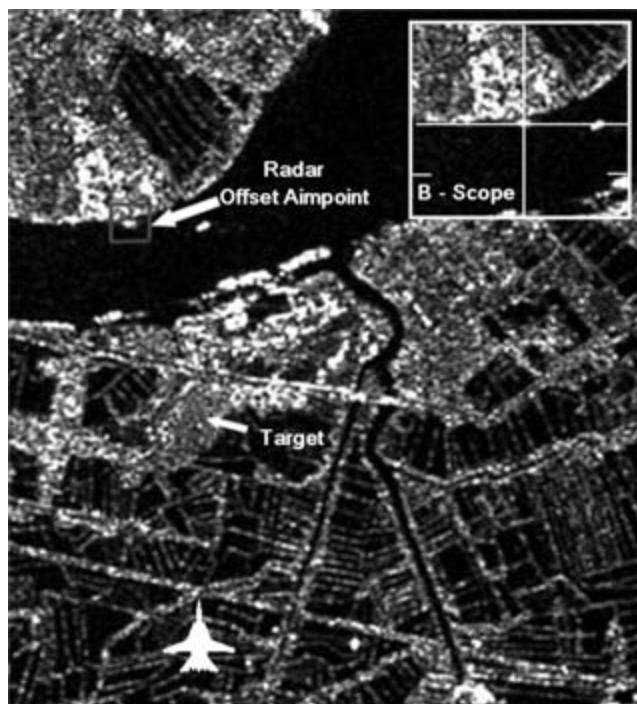
FIGURE 4-15 ■ Target Designation in Geodesic Coordinates with SAR [(Courtesy THALES) Thales Airborne Systems + own work (Kemkemia)].

is generated to the weapon's store (Figure 4-14). For a precision-guided weapon such as a laser-guided bomb, radar information is used to provide aircrews with weapons envelope information to allow selection of release parameters. Derived altitude information from the radar elevation array can also be used to compute minimum safe altitudes (blast avoidance) or minimum time-of-flight (TOF) information to allow for appropriate weapon arming.

Bombing Using Ground Mapping These modes are used with a weapon utilizing precise target location data based on coordinates defined by the World Geodetic System of 1984 (WGS 84).

- *INS- and GPS-guided weapons:* Precision standoff weapons such as the GBU-31 joint direct attack munition (JDAM), the AGM-154 joint standoff weapon (JSOW), or the French AASM, which all use accurate target designation, require high-resolution SAR modes for precision target identification and location (Figure 4-15).
- *Radar-offset aim point:* In some cases, the target level is not sufficient with respect to surrounding ground clutter and thus cannot be localized on the radar map. In fact, the target (e.g., underground bunker, maritime mine splash point) may be completely obscured. Often, though, unique radar-identifiable offset aim points are in the target vicinity, enabling accurate weapon delivery. Mission planning for radar-offset, aim-point delivery requires a radar-significant aim-point selection along the desired attack heading that is beyond the designated target. This allows the radar offset to be tracked through weapon release. Precise range, bearing, and differential altitude between the aim point and the target are calculated for entry into the fire-control computer. For low-altitude deliveries, consideration should first be given to cultural features with significant vertical development (tall buildings) for enhanced reflectivity and minimum masking. Medium to high-altitude attacks require radar offsets

FIGURE 4-16 ■
Offset Aim-Point
Bombing [Self-
Developed Graphic
(Ballard)].



far enough from the target to not be masked by limited depression angles of the fire-control radar at release. If EO or IR sensors are also available, the offset aim-point attack may provide initial cueing information to the target area with final target designation and weapon release being accomplished through the sensor fusion process in the fire-control system. Figure 4-16 depicts a typical offset scenario with a radar-significant pier on a river serving as the offset. The typical B-scan radar scope used by the pilot or weapon system operator is depicted in the inset.

- *Radar forward air controller beacon (RABFAC)*: Offset aim-point radar bombing can be used in close air-support (CAS) missions by use of a ground-based, radar beacon forward air controller (RADFAC) AN/PPN-18, which allows the identification of targets that are not radar significant to the supporting aircraft by a ground forward air controller (FAC). The FAC provides the offset range, bearing, and differential altitude info to the aircrew. The ground beacon provides the radar-significant offset on the radar ground-mapping display (Figure 4-17).

Terrain Avoidance and Terrain Following (TA and TF) Terrain avoidance is a mode in which the aircraft radar continuously sweeps the ground area directly in front of the aircraft in order to avoid mountains. This is particularly useful when clouds, haze, or darkness obscure visibility. Two horizontal bars are generally used, with a maximum range of 10 nm. Below 3 nm, the ground generally is no longer visible, but previously detected echoes are stored and displayed according to the aircraft's progression.

Such a mode is used at low altitude (typically 500 to 2,000 feet). Indeed, in enemy territory, safety is increased when the plane flies at low altitude to take benefit of masks formed by land relief. The pilot chooses the clearance altitude h_1 and then must navigate so that the ground echoes are located between h_1 and h_2 and appear in green on the radar

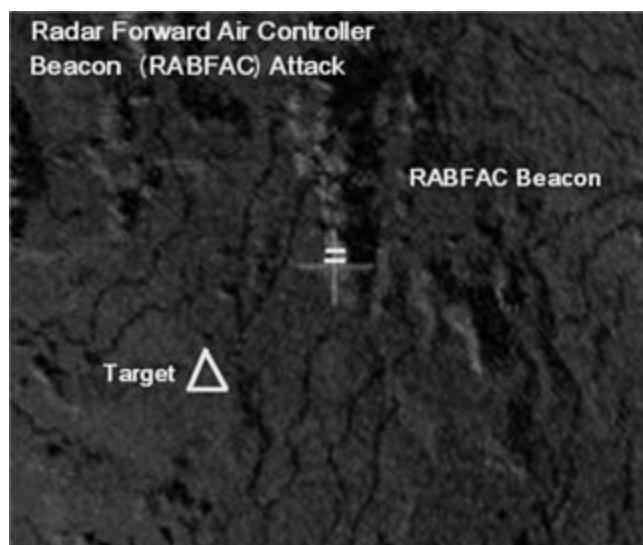


FIGURE 4-17 ■ RABFAC Beacon CAS [Self-Developed Graphic (Ballard)].

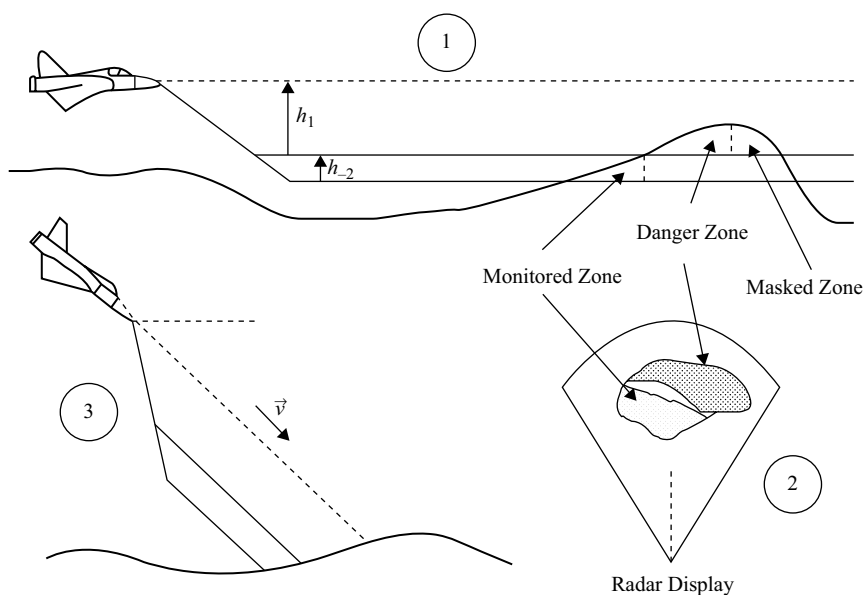


FIGURE 4-18 ■ Terrain Avoidance [(from [2]) Manuscript of “Air and Space borne Radar Systems – Ph. Lacomme, J.Ph Hardange, J.C. Marchais, E. Normant. SCITECH Publishing” (Lacomme with permission)].

display. Echoes above the clearance level appear in red (danger zone). Two types of TA are utilized:

1. contour mapping stabilized in the horizontal plane (Figure 4-18, 1) and
2. contour mapping slaved to the aircraft’s velocity vector (Figure 4-18, 3); this allows perfectly safe blind penetration.

A typical radar display is shown in Figure 4-18, 2.

Low-altitude navigation (>500 ft) cannot be used to penetrate safely far into enemy territory: The aircraft should fly as low as possible between 200 and 300 ft. Very-low-altitude navigation requires an automatic TF system. Such a mode is very demanding as

FIGURE 4-19 ■ Terrain-Following Profile [Self-Developed Graphic (Ballard)].

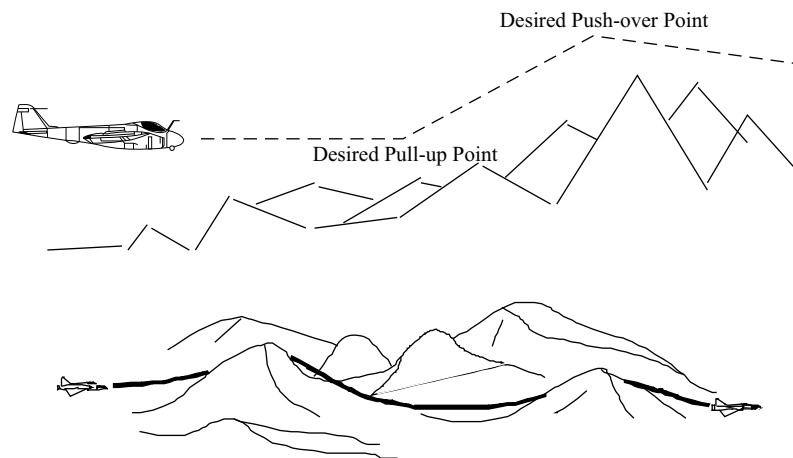


FIGURE 4-20 ■ Simultaneous Terrain Avoidance and Terrain Following for Very-Low-Altitude Navigation [(from [2]) Manuscript of “Air and Space borne Radar Systems – Ph. Lacomme, J.Ph Hardange, J.C. Marchais, E. Normant. SCITECH Publishing” (Lacomme with permission)].

not only all “normal” ground echoes must be detected but also particular vertically extended echoes such as tops of pylons and cliffs. Ideally, such a mode should work within rain without detecting it as obstacle. It should also detect power line cables, among other obstacles. To carry out this task, a vertical scanning mode is used (about $\pm 15^\circ$) with a few vertical bars since the revisit rate should be of the order of 1 second to provide sufficient reactivity. TF alone only allows navigation at very low altitude in the vertical plane (Figure 4-19).

Simultaneous TA or TF is difficult – even unachievable – with M-SCAN because a wide angular area must be swept in a limited time. E-SCAN overcomes these scanning issues and allows the full simultaneity of TA and TF, enabling a very-low-altitude navigation both in vertical plane and horizontal plane (Figure 4-20).

Precision Velocity Update and Doppler Navigation In this mode, the radar again tracks ground features using Doppler techniques to precisely predict aircraft ground speed and direction of motion. Wind influences are taken into account so that the radar can also be used to update the aircraft’s inertial navigation system when the GPS signal is unavailable or corrupted.

4.2.1.3 Air-to-Sea Modes

There are three primary air-to-sea modes:

- *Sea 1* is designed to detect and track at long range large vessels (large RCS) whether fixed or mobile. In a low sea state, it can also detect small targets at shorter range. An LPRF is used without Doppler processing. A target shall be detected if it is sufficiently contrasted with respect to the surrounding clutter, which increases with the sea state. Because the sea clutter is not a Gaussian noise but has a long-tailed probability density function, a special CFAR is required.
- *Sea 2* is designed to detect and track at medium range moving vessels by high sea states. An LPRF is used with Doppler processing. Small targets are detected if they are sufficiently moving to be located on the thermal noise region after Doppler processing.

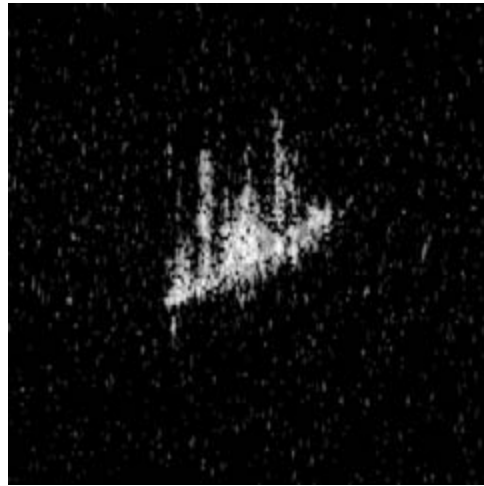


FIGURE 4-21 ■ ISAR Display [US Navy <http://www.nrl.navy.mil/research/nrl-review/2002/electronics-electromagnetics/lipps/>].

- *Inverse synthetic aperture radar* (ISAR) is a well-established technique to identify the reflectivity centers of the target with high spatial resolution. It jointly uses high-range resolution profiling (HRRP) and high-resolution Doppler analysis of the received signal. Indeed, a vessel has periodic motions around its center of gravity (roll, pitch, and yaw). Simply speaking, these motions create a Doppler effect proportional to the height of a given reflectivity center:

$$F_D = \frac{2\omega h}{\lambda} \sin \varphi$$

where F_D is the instant Doppler frequency, ω is the instantaneous rotation rate, φ is the angle between the line of sight and the rotation vector, and h is the height of the given reflector. A fine two-dimensional reflectivity map (range – Doppler) of the target is generated. After having estimated the instantaneous rotation rate ω , the range – Doppler map can be converted in a display such as Figure 4-21. ISAR is normally used to classify and designate targets to be attacked with antiship missiles such as the AGM-84C. Target information is relayed to the missile via the MILSTD 1760D interface and the missile acquires the target with its self-contained active radar missile-control system after launch.

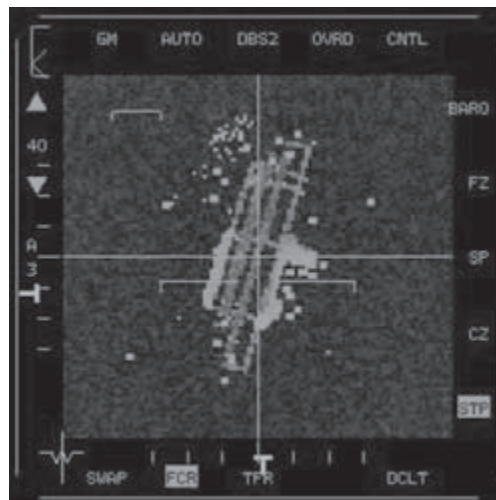
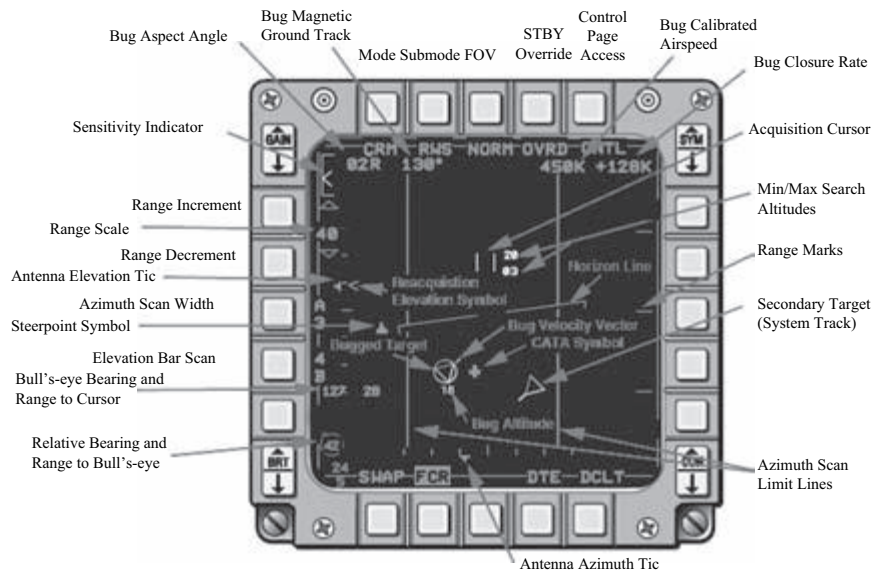
4.2.2 Radar Displays

The information issued from the radar can be displayed on both MFD and HUD.

4.2.2.1 Multifunction Displays

The multifunction displays are CRT-based displays that sit in the front of the cockpit (Figure 4-22). They are used primarily to display weapons system management functions, in particular, weapons stores information, radar information, and weapons electro-optical displays. The MFDs are also used to display HUD, radar warning receiver (RWR), and navigation information. The MFDs provide an integrated method of accessing the data required to perform a mission. Around the screen there are several control buttons. They are programmed to perform specific single or multiple functions for each MFD format. Each function is identified by a mnemonic displayed adjacent to the control buttons.

FIGURE 4-22 ■
 Top: Typical Air-to-Air MFD Display.
 Bottom: Air-to-Ground Display in DBS Mode [F-16 Block 52 Fighter Lead-In School Manual V 3.0].



4.2.2.2 Heads-Up Displays

Regarding information coming from the radar, the typical HUD shows the tracked target, velocity vector, maximum and minimum range, missile launch limits, an allowable steering error circle, and an aim dot. A typical display for STT is shown in Figure 4-23. This mode is highly recommended to reduce distraction as the pilot closes to optimal medium-range missile range.

4.2.3 Weapon Modes

4.2.3.1 Air-to-Air Missile Modes

Long ago, the weapons and sensors were short range, to the role of fire-control radar was mainly to guide cannon fire (dogfight). Although the cannon mode is still used as a last

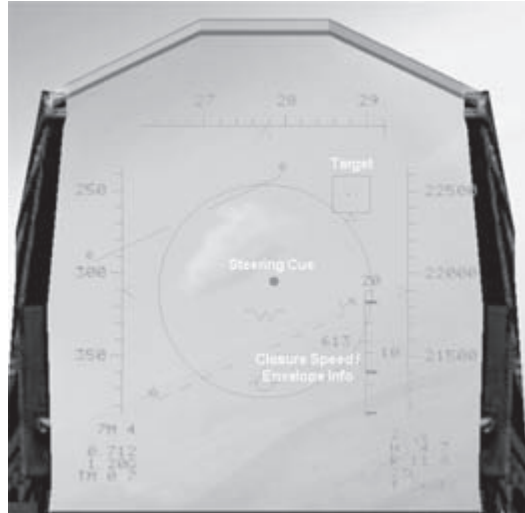


FIGURE 4-23 ■ Semi-active Missile Symbology with STT [Annotated Simulation Screen Capture. Lock-on Modern Air Combat http://lockon.co.uk/en/modern_air_combat/].

resort, most weaponry now consists of air-interception missiles (AIMs), which enables strikes from a distance. Currently, the following two types of missiles are in use.

1. *Missiles with electromagnetic seekers* (EM or radar missile) are intended for beyond-visual-range (BVR) strikes. Current inventory includes two basic types:
 - those with semi-active guidance such as the AIM-7 Sparrow (the target must be continuously illuminated by the FCR because the missile seeker is a receive-only system without a transmitter) and
 - those with active and autonomous guidance such as the advanced medium-range air-to-air missile (AMRAAM); in fact, the seeker is a small radar.
2. *Missiles with passive infrared seeker* are used for short to medium distances.

The missiles with autonomous seekers – that is, those that do not require illumination from the FCR – allow the engagement of multiple targets (in TWS mode or in search while track, or SWT, mode with E-SCAN). It can, however, also be fired in STT mode or in visual mode. In contrast, semi-active missiles only allow a mono-target fire control. Indeed, the radar must be locked in continuous STT mode or must be in flood mode.

In the case of an active seeker, the SNR at reception is proportional to

$$\text{SNR} \propto \frac{\text{ERP}_{\text{Seeker}}}{R_2^4} A_{\text{Seeker}} \sigma_M$$

where

ERP = equivalent radiated power (*Pe.Ge*) by the seeker's transmitter,

A_{Seeker} = antenna's seeker surface,

σ_M = monostatic RCS of the target, and

R_2 = distance between the target and the seeker.

In the case of a semi-active missile, the FCR and the seeker form a bi-static radar. The signal-to-noise ratio at the seeker's receiver level is now proportional to

$$\text{SNR} \propto \frac{\text{ERP}_{\text{FCR}}}{R_1^2 \cdot R_2^2} A_{\text{Seeker}} \sigma_B$$

where

ERP = equivalent radiated power from the FCR,

R_1 = distance between the FCR and the target,

A_{Seeker} = antenna's seeker surface,

σ_B = bi-static RCS of the target, and

R_2 = distance between the target and the seeker.

For the sake of simplicity, suppose the reception sections have the same characteristics in both cases and $\sigma_M = \sigma_B$. At launch, $R_1 \approx R_2 \approx R$, but the ERP of an FCR is much higher than those of an active seeker FCR. All things being equal, at minimum SNR allowing correct tracking:

$$\frac{R_{\text{semi-active}}}{R_{\text{active}}} \approx \left(\frac{\text{ERP}_{\text{FCR}}}{\text{ERP}_{\text{Seeker}}} \right)^{0.25}$$

The ratio $\text{ERP}_{\text{FCR}}/\text{ERP}_{\text{Seeker}}$ is about 10 to 20 dB, depending on the systems. So the tracking range ratio is about 2 to 3. At first glance, one might think that the semi-active guidance offers a longer engagement range. In fact, this analysis is not true: As the active radar seeker has a short range, an active missile such as AMRAAM performs most of its flight in inertial navigation mode guided by the tracking data coming from the FCR and using a particular data link. When it is close enough to the target, it locks its seeker and becomes active and autonomous (fire-and-forget concept).

On the one hand, the engagement envelope of a semi-active missile is limited by both:

- he tracking range of the bi-static radar range formed by the FCR and the seeker and
- the propulsion system of the missile and its aerodynamic features.

On the other hand, the engagement envelope of an active missile depends mainly on the missile's propulsion system and aerodynamic features. Nevertheless, the longer the active seeker range, the more "fire and forget" the missile is, so the less vulnerable the launcher is to an enemy riposte.

Figure 4-24 shows the relative envelopes of active and semi-active EM missiles. Three areas are displayed for the active missile:

1. The *seeker-only area* is the engagement envelope when the missile is fired with its seeker locked (no need of external guidance).
2. The *aim point + seeker area* is the engagement envelope when the missile is fired with a predicted target trajectory without data update during the inertial phase.
3. The *FCR tracking + seeker* is the usual engagement mode of an active missile: inertial navigation mode guided by the tracking data coming from the FCR, then final guidance by the active seeker.

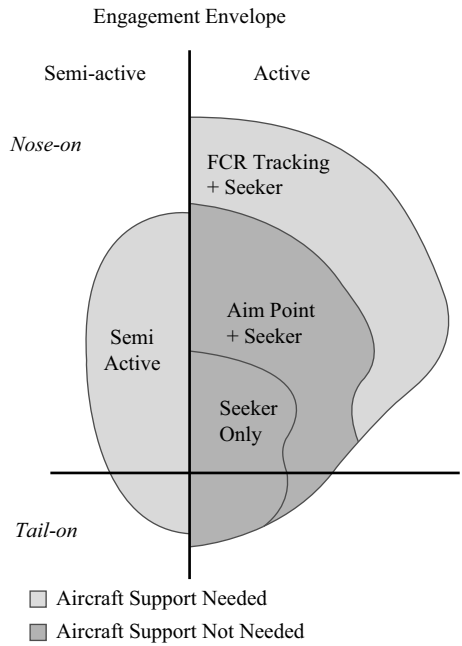


FIGURE 4-24 ■ Relative Comparison of Active vs. Semi-active Missiles Envelopes [http://www.fas.org/man/dod-101/sys/missile/aim-120.htm + own work (Kemkemian)].

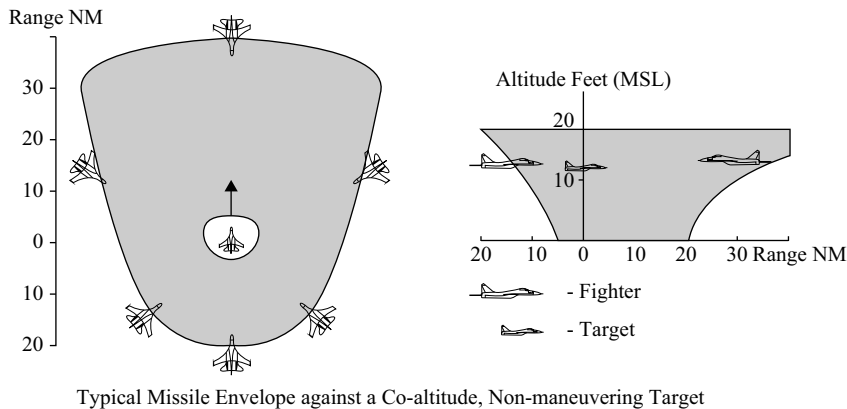


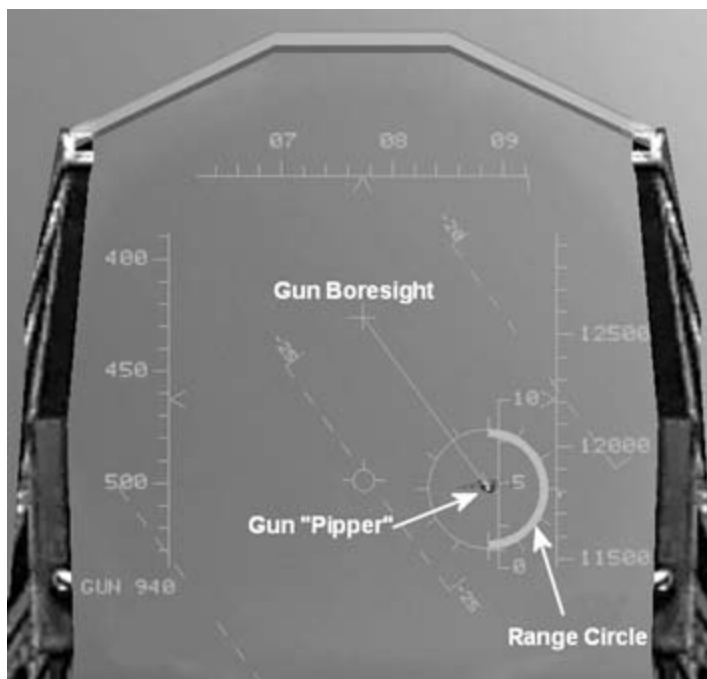
FIGURE 4-25 ■ Air-to-Air Missile Envelope [Jane's Defence: Air & Space].

Another example of AIM envelopes is at Figure 4-25. The fire range is greater in a nose-on configuration than in a tail-on configuration. Indeed, the relative closing velocity (between the missile and the target) is greater in nose-on configuration than in tail-on configuration. The missile envelope is wider at high altitude than at low altitude because air density (and thus aerodynamic drag on the missile) decreases with the altitude.

Two types of missile envelopes can be calculated by the FCC: the envelope for a nonmaneuvering target and the envelope with escape maneuver. When a target is engaged, a symbol is attached to it. This symbol represents all positions where the target may be after the missile's flight. When the symbol attached to the target is totally enclosed in the missile's envelope, the missile can be fired without the target's ability to normally avoid it.

The pilot will usually prosecute using HUD symbology for intercept and launch info. Figure 4-23 shows a typical STT semi-active missile scenario.

FIGURE 4-26 ■
 Typical HUD Air-to-Air Cannon
 Symbology
 [Annotated
 Simulation Screen
 Capture. Lock-on
 Modern Air Combat
http://lockon.co.uk/en/modern_air_combat/].



4.2.3.2 Cannon Mode

Automated air-to-air gunnery fire control requires sensor inputs that can define the target in 3D space (azimuth, elevation, range) and calculate the target's relative velocity vector with input of the ballistic characteristics of the round being fired. The solution results in the prediction of a point in space that the enemy aircraft will occupy after the predicted time of flight of the cannon round and providing the pilot a visible indicator (gun sight or HUD) by which to aim the cannon.

Most fighter aircraft aim the cannon by maneuvering to superimpose the HUD generated pipper with the designated target (Figure 4-26). Gun accuracy is typically limited by recoil and barrel dispersion but not radar accuracy.

4.2.3.3 Air-to-Ground Missile Mode

Unlike air-to-air missiles designed to hit highly maneuverable targets, air-to-ground missiles are designed for strikes on fixed targets or not very mobile targets. This is why the modern air-to-ground missiles use INS or GPS as their main guidance on geodetic coordinates. This guidance principle enables precision strikes at relatively low cost. Indeed, no seeker is needed for strikes against fixed targets. These weapons fired from standoff distance by day or night and in all-weather conditions offer a range exceeding tens of kilometers.

4.2.3.4 Air-to-Sea Missile Mode

Like ground targets, sea targets are not very maneuverable. These targets are large and robust; they require a powerful warhead to be destroyed and thus a large missile. The sea targets are often detected at very long range, so the weapon shall also be long range. A typical air-to-sea missile operates as follows.

After its launch, the missile stabilizes in the direction of its target at its first cruising altitude, which is low enough to avoid detection by its target yet high enough to allow its active radar seeker head to acquire the target. This acquisition may be assisted by a target's course corrections coming from the FCR via a suitable link.

Midcourse guidance is by an INS or GPS navigation system and a radio altimeter, allowing the missile to fly a sea-skimming trajectory to its target. This sea-skimming trajectory prevents radars on board the ship to detect the missile too early.

Then it descends to its second cruise altitude for the terminal phase, with a final approach at an altitude determined by prevailing sea conditions, sometimes as low as 3 m. Terminal guidance is provided by an active radar seeker. An ISAR image of the target (from the FCR) may be transferred into the missile computer. During the terminal phase, the missile seeker performs target imaging, comparison with the prestored ISAR image, and aim-point selection.

4.2.4 E-SCAN FCR

Two kinds of electronic scanning are seen worldwide:

1. The passive electronically scanned antenna (PESA) radar and
2. AESA radar.

The common feature of all E-SCAN radars, whether they are passive or active, is there are no motors or gimbals to point an antenna dish to search for or point at targets. The transmit-and-receive signal is steered electronically. Only the method for beam forming and the method for controlling the electronic scanning are different between PESA and AESA radars.

E-SCAN allows very rapid changes in the signal direction and shape, making it possible to do things nearly impossible with physically pointed antennas.

PESA Radars PESA radars were developed before AESA radars. Indeed, the technologies required for AESA have only been affordable over the last decade or so. The first PESA FCR was Zaslon aboard the MIG-31 aircraft. This radar entered service in the early 1980s in the former Soviet Union. The radiation of the antenna takes place through about a thousand ferrite phase shifters that control the direction of the wave front. Although the concept and the technology of radar (mainly analog signal processing) have become outdated, this PESA enabled a multitarget radar without limiting the angular spacing of the targets traditionally encountered even with more modern M-SCAN radars. This E-SCAN based on ferrite phase shifters continues to be used on newly designed modern Russian FCRs.

The first series of RBE2 radars installed on the French Rafale fighter are also fitted with PESA. E-SCAN is not performed by using ferrite phase shifters but is carried out by two electronically controlled deflection lenses located in front of a fixed illuminator (Radant technology). One lens controls azimuth steering, and the other controls elevation steering.

PESA has also been used on other kinds of radars than FCR.

AESA Radars AESA technology has been an important development for the radar industry. AESA radars are being procured in increasingly large numbers, for ground-based, sea-based, and airborne uses. In some early cases, operational radars

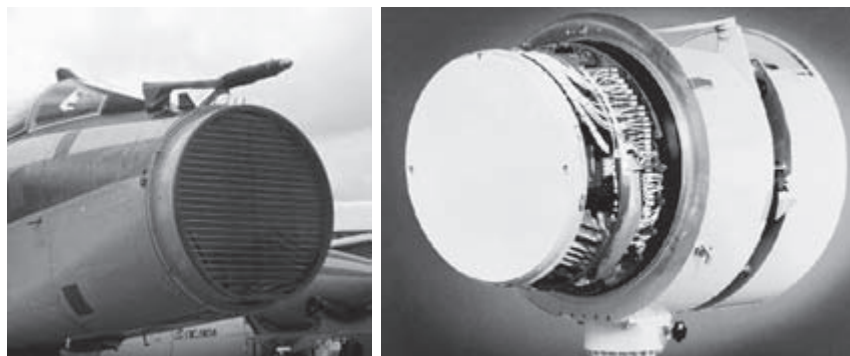


FIGURE 4-27 ■ Examples of PESA – Left: Russian ZASLON [<http://www.airforce-technology.com/projects/mig-31/images/2-mig-31-foxhound.jpg> + own work (Kemkemian)], Right: RBE2-PESA [(Courtesy THALES) Media resources Thales Airborne Systems].

were upgraded with new AESA antennas. But newer radars are being designed from scratch with AESA technology as a key part of the architecture.

AESA radars have fixed, flat antennas made up of a large number of transmit-and-receive modules (Figure 4-27). The transmit-and-receive signal is steered electronically by controlling the phase of the signal at each of hundreds – even thousands – of modules to cause the wave front to add or subtract in space in such a way as to shape and point the beam.

Compared to systems using M-SCAN or passive E-SCAN (PESA) where the transmit signal is generated by a separate source and applied to the antenna, the active array generates the transmit power and receive capability in each individual module. This distributed arrangement significantly reduces RF losses compared to systems with central transmitter and receiver. At a given overall power consumption, a figure of merit of the RF part (and thus performance in terms of detection range and tracking) is found to be much better than achieved by centralized systems. Because there are no moving parts to wear out and the antenna remains operational even if some modules have failed (graceful degradation), the antenna lifespan can run into the thousands of hours. Another advantage of such a distributed transmit-and-receive scheme is the ability to reconfigure the antenna's subarrays according to the modes. This capability will be leveraged with the upcoming generation of AESA radars with multiple subarrays.

AESA technology is most prevalent with airborne radars. While the operating techniques described for the various modes remain essentially the same, they can often be accomplished more quickly and the information obtained can be more accurate and more useful. Multiple modes can operate at the same time, something not possible with conventional pointed systems. The cost of producing the antennas and price of the powerful processors needed is such that AESA is not always cost-effective for many ground sensors. Airborne systems, however, are another story. Designers are finding the price worth the increase in capability; however, the reliability of the radar being significantly improved by the AESA, the cost of ownership is reduced.

Table 4-1 summarizes the main features of AESA radars compared to older ones.

All major air forces are adopting AESA radars for their next-generation aircraft. In addition to vastly improved radar performance, the radars can be adapted to be an important part of an overall situational awareness and electronic combat electronics suite.

TABLE 4-1 ■ Comparison of M-SCAN, PESA, and AESA

	M-SCAN	Passive E-SCAN	Active E-SCAN
Motors, gimbals	Yes	No	No
Transmission, reception	Centralized	Centralized	Distributed
Reliability	Reference	+	+++
RF losses	Reference	–	+++
Instant beam agility	No	Yes	Yes
Simultaneous modes ability	No	Yes ^a	Yes
Multiple beam shapes ability	No	Yes ^a	Yes
Reconfigurable array	No	No	Yes

^aDepending on available computational power.

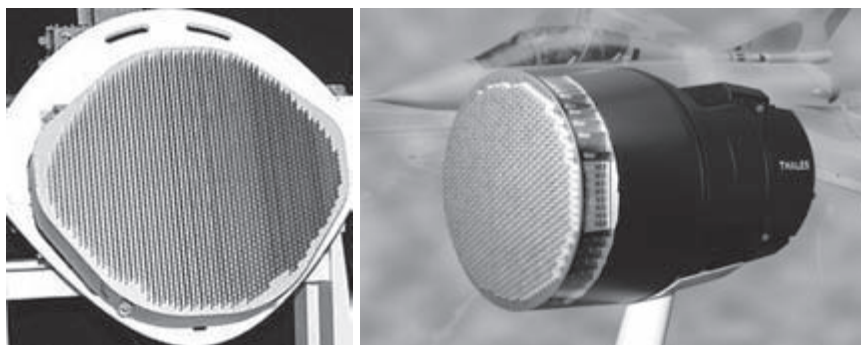


FIGURE 4-28 ■ Examples of AESA – Left AN/APG77 [(Courtesy Northrop-Grumman) <http://132.228.182.15/solutions/f22aesaradar/assets/apg77.jpg>], Right RBE2-AESA [(Courtesy THALES) Media resources Thales Airborne Systems].

The United States is not the only country working on airborne AESA radars. At the time of this writing, Russia and other European countries already have operational systems or planned systems for their new, frontline fighters. Figure 4-28 displays two examples of AESA.

4.2.4.1 Technological Aspects

A typical transmit-and-receive module's architecture is displayed in Figure 4-29.

A transmit-and-receive module (TRM) contains mainly three parts:

1. a transmission stage,
2. a low-noise reception stage, and
3. a core chip that is controlled by either an FPGA or an ASIC.

At transmission, the low-level incoming signal passes successively through:

- an attenuator and phase shifter,
- a driver amplifier (DRA),
- a high-power amplifier (HPA), and
- a circulator before finally reaching the radiating element.

FIGURE 4-29 ■ Synopsis of a Transmit-and-Receive Module [(Courtesy THALES) Thales Airborne Systems (Lacomme)].

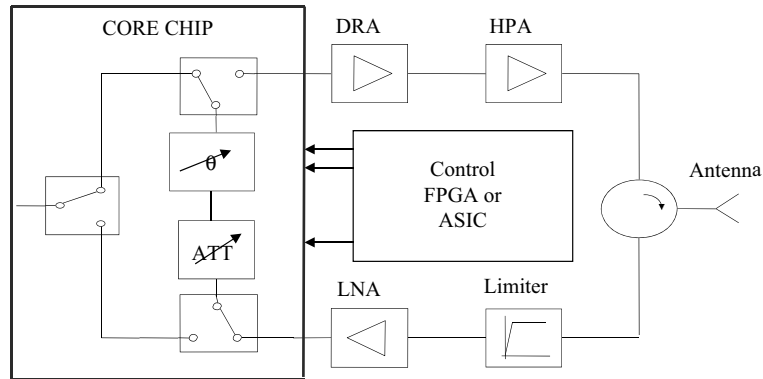
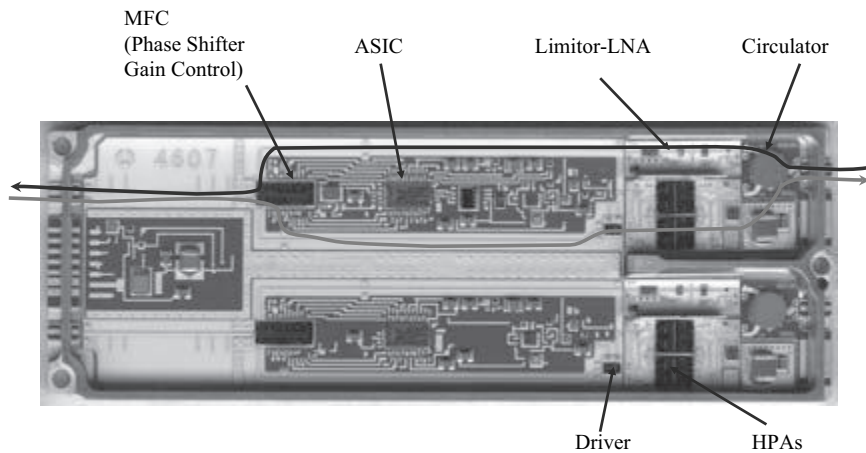


FIGURE 4-30 ■ Example of First-Generation TRM (late 90s) [(Courtesy THALES) Thales Airborne Systems (Lacomme)].



At the reception, the signal from the radiating element is applied to the Low Noise Amplifier (LNA). A limiter is placed before the LNA to protect it against strong signals and to prevent its destruction. After the LNA, the signal passes through the attenuator and the phase shifter.

The TRM currently in use relies on GaAs technology (Figure 4-30). The current trend is to ultimately replace GaAs by the following [3]:

- GaN technology for transmitting and receiving will allow better efficiency of the active antenna by allowing:
 - more peak power so that waveforms are easier to implement for a given RF average power or more average RF power if a supply power is available;
 - a higher supply voltage (typically 32V), which simplifies the DC wiring of the antenna and the power supplies (lower DC intensity) as well as the impedance matching to attack the radiating element; and
 - improved robustness of the LNA against strong signals so that a protective device will be easier to realize.
- SiGe technology for the core chip that will allow miniaturization and lower cost.

4.2.4.2 New Modes Enabled by E-SCAN and AESA

Two kinds of new modes and functions are present on the latest generation of AESA radars:

1. Modes and functionalities that can be implemented only because E-SCAN is present.
2. Modes and functions that do not directly depend on the presence of E-SCAN but whose feasibility is now made possible at affordable cost by the availability of some new technologies. These technologies, mainly driven by the explosion of civilian digital electronic market (mobile telecoms, the Internet, powerful computing servers, personal computing, etc.), are now available “off the shelf” and offer:
 - high-power real-time computing;
 - digital signal synthesis with high spectral purity;
 - Digital receivers, high speed Analog to Digital Converters (ADC), and so on; and
 - efficient and powerful simulation tools that dramatically reduce the duration and the cost of integration, verification, validation, and qualification (IVVQ) process of complex modes, complex system architectures, and so on.

In the United States and many European countries, the active antenna for FCR is now fully mature and can take advantage of these technologies from the civilian market to operate radar with more performing modes than were possible a few years ago.

Typically, the new modes and functionalities available on the current generation of AESA are described hereafter.

4.2.4.3 E-SCAN-Only Functionalities

E-SCAN-only functionalities are mainly:

- the search while scan air-to-air mode and
- the ability to carry out simultaneous modes – for instance, air-to-air mode while an air-to-surface task is being performed.

Search While Track (SWT) As previously discussed, to carry out an air interception, the M-SCAN radars have several air-to-air modes, which are successively used (VS, RWS, and TWS, and then STT). The SWT mode, which requires a fast beam-steering agility (thus E-SCAN), merges all these previous modes into a single mode (SWT). A typical SWT mode is represented in Figure 4-31.

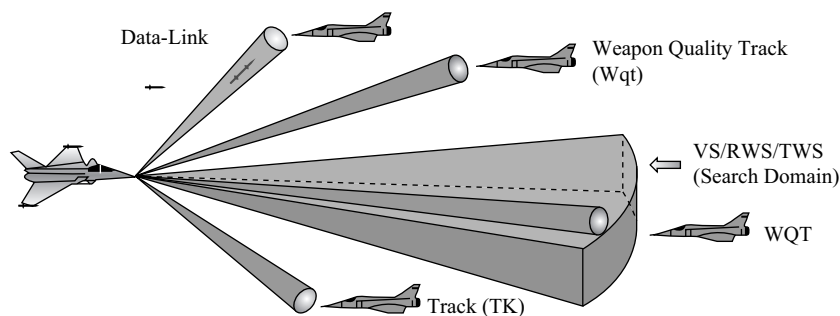


FIGURE 4-31 ■ Search While Track Mode for E-SCAN Radar [(Courtesy THALES) Thales Airborne Systems + own work (Kemkemia)].

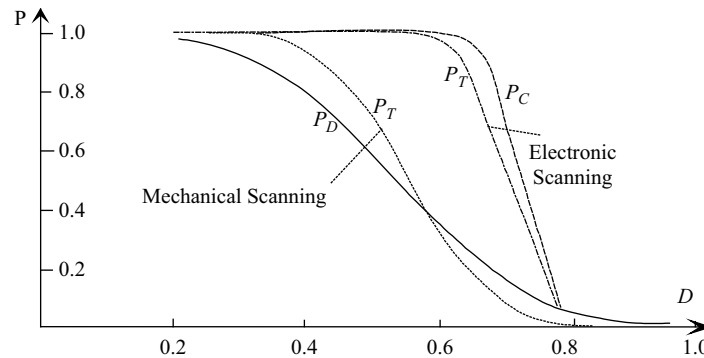


FIGURE 4-32 ■ Two Steps Detection Gain [(from [2]) Manuscript of “Air and Space borne Radar Systems – Ph. Lacomme, J.Ph Hardange, J.C. Marchais, E. Normant. SCITECH Publishing” (Lacomme with permission)].

• **Principle of SWT:** If no target is yet tracked, SWT operation performs the following:

1. The radar periodically sweeps a given search domain (in blue) like an M-SCAN radar. The waveform may be a VS mode if the focus is on the detection range (but without range information at this step) or of an RWS mode if range information is desired.
2. Once a target is detected at least once, there are two options: (a) The system decides the target has a high priority and triggers a fast opening sequence of a new track (TK) or new weapon-quality track (WQT). Thanks to the E-SCAN, a dedicated beam steering is associated with this track that can be afterward tracked regardless of its angular position provided it is within the whole AESA coverage. (b) The system decides this target has a low priority and it opens a new TWS track just as an M-SCAN would do. In this case, the target should remain within the search domain to be tracked. No particular antenna pointing is associated with this track, and it is refreshed each time the antenna’s scanning passes over it.

In the case of the first option (high-priority target, TK, or WQT), the tracking initiation sequence consists of N successive repointings. The track is confirmed if it is detected at least K times out of N repointings.

Figure 4-32 shows this detection strategy in two steps, providing, through the E-SCAN, a tracking range with a given probability $P_T(D)$ almost equal to the detection range with a cumulative probability $P_C(D) = P_T(D)$.⁵

Returning to Figure 4-32, we see that a given M-SCAN radar reaches $P_C = 0.5$ at the normalized distance 0.75. At this distance, the single-scan probability of detection is only 0.1, which is not sufficient to initiate a track with a conventional TWS scheme. A probability of tracking equal to 0.5 is reached at the normalized distance of 0.55.

Regarding the “double-step” strategy of track opening permitted by the E-SCAN, $P_C(0.75) = 0.5$ and $P_T(0.75) = 0.4$. In this example, this means that the conditional probability of confirming a track at $D = 0.75$, if a detection was obtained in the search phase, is $0.4/0.5 = 0.8$. In the case of E-SCAN, resulting in $P_T = 0.5$ at $D = 0.72$.

⁵The cumulative probability $P_C(D)$ is the probability for a closing target to have been detected at least one time at ranges greater than D .

This example highlights a very significant improvement provided by the double-stage strategy of track initialization. Comparing the TWS scheme and the SWT scheme, the tracking range's ratio is $0.72/0.5 = 1.44$. This tracking range's improvement is equivalent to 6 dB. The increase of the figure of merit of the AESA radar's RF front end compared to older M-SCAN or PESA radars and the processing gain provided by this detection strategy are the keys to the dramatic increase in operation ranges provided by these new AESA radars.

- **Target tracking strategy in SWT:** When several targets are being tracked, an efficient management of time's resources needs to be set up for the targets tracked with dedicated repointing. Indeed, without an efficient allocation of the time for the tracking and the time for the search phase, this tracking's scheme loses its efficiency. Indeed, the time spent to update the tracks (TK or WQT) slows down the period of the search phase, thus reduces its efficiency. However, the system is able to track as many TWS targets as desired without these numerous tracks impact overall performance. The only limit to this is the computing power, but it is no longer a major problem with modern radars. Regarding the tracks that use dedicated repointing (TK and WQT), there are two main parameters to manage:
 - **The dwell time on each target** direction during a repointing. The dwell time is mainly driven by the required signal-to-noise ratio. A distant target will require a long dwell time, but a close one will require only a short dwell time.
 - **The update rate.** This parameter impacts mainly the track quality. Distant targets, far from the weapon range envelope (TK), do not need fast update rates. Conversely, a target close or within the firing envelope (WQT) requires accurate tracking even in the presence of evasive maneuvers on the part of the target. At constant track quality, the new trajectory estimation algorithms (IMM, etc.) enable relaxing the constraints on the update rate.

Simultaneous modes and functions An impossible thing to do with M-SCAN radar is to have, viewed from the operator, two radars in one: one air-combat radar and one Surface Combat radar. With the E-SCAN and now available processing capabilities, this old dream is now possible with a single radar and so a single platform.

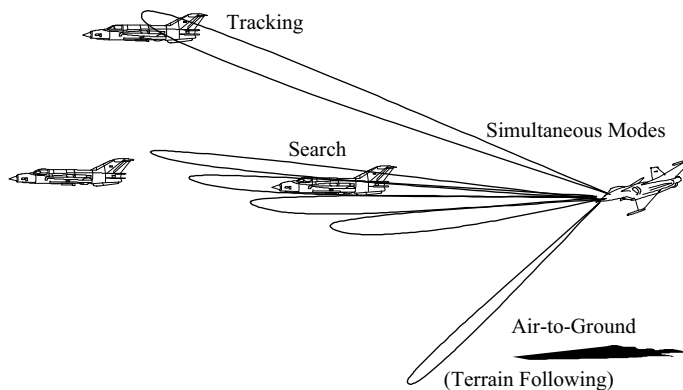
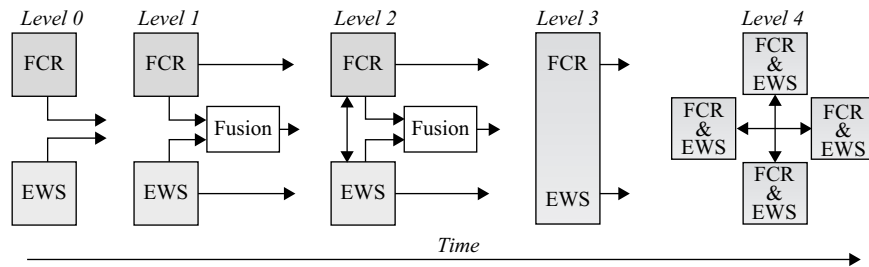


FIGURE 4-33 ■ Simultaneous Modes and Functions Enabled by E-SCAN [(from [2]) Manuscript of “Air and Space borne Radar Systems – Ph. Lacomme, J.Ph Hardange, J.C. Marchais, E. Normant. SCITECH Publishing” (Lacomme with permission)].

FIGURE 4-34 ■ From Set of Sensors to Multifunction Sensors [Own work (Kemkemian, Nouvel, Chamouard) also published in IEEE papers].



A time sharing between tasks is established and the antenna beam is instantaneously switched from a direction for a task to another direction for another task (Figure 4-33). As trade-offs must be made, according to the mission objectives, the “system” manages the scheduling (for instance air-to-air and air-to-ground task with priority to the air-to-ground or conversely).

4.2.4.4 Other Modern Functionalities Not Directly Related with E-SCAN

System Integration The next generation of AESA long-range radar and integrated sensors suite are designed from the beginning as a system of sensors and not as a set of stand-alone sensors. The successive steps are summarized in Figure 4-34. This figure (ref. [1]) illustrates the evolution of a set of sensors (radar & EWS) toward a multifunction system of sensors. It can obviously be extended to the electro-optical sensors (radar & EWS & EOTS), even to the communication means of each platform.

Radars discussed in this section correspond to “level 2”:

- data fusion at system level and
- close exchange of data/signals between sensors *via* ad hoc links for mutual enhancement.

The targeting sensors are designed to assure that the pilot concentrates on the combat environment, not on the onboard systems. Functions are heavily automated. Designers concentrated on a high level of systems integration and data fusion with targeting data developed from the AESA radar, E/O targeting system, Electronic Warfare suite, and the communication, navigation, and identification suite. This long-range sensor provides all-weather, standoff target detection, minimizing threat exposure. The radar will probably be the first onboard sensor to identify a target, but the entire suite will be used to prosecute whatever mission is called for.

New Capacities in Air-to-Air For air-to-air operations, up to date radars, like APG-81 and other modern AESA radars support such features as passive search and multitarget, and beyond-visual-range tracking and targeting. It also will support a cued search feature, in which the radar is cued toward another sensor’s line of sight. That other sensor can be on-board, off-board or pilot-directed. An example of cued radar’s search by the ESM part of the EWS is shown in Figure 4-35.

New Capacities in Air-to-Ground These new AESA radars come with a SAR terrain mapping function for air-to-surface surveillance and targeting. It is said to be comparable to the terrain mapping radar used in reconnaissance aircraft, unmanned air vehicles, and the E-8C Joint Surveillance Target Attack Radar System (Joint STARS) aircraft.

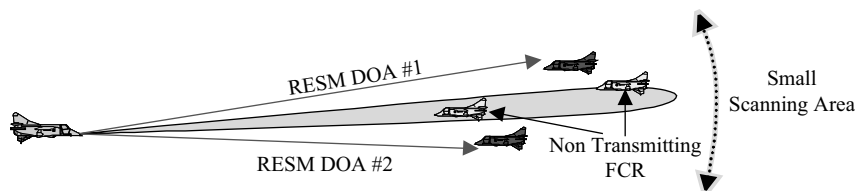


FIGURE 4-35 ■ Cued Search in Air-to-Air [Own work (Kemkemian, Nouvel, Chamouard) also published in IEEE papers].



FIGURE 4-36 ■ SAR Image Produced by Modern AESA Radar [(Courtesy THALES) Thales Airborne Systems + own work (Kemkemian)].

Designers worked to provide these new radars with higher resolution for easily recognizable features on the ground and to have the radar look at three or four times more terrain than previous radars (Figure 4-36).

New Capacities at the Level of Human Machine Interface (HMI) and System Automation By activating buttons around the aircraft's panoramic MultiFunction Display (MFD) the pilot can select from the radar's many software-driven modes: target identification and tracking, air-to-air, air-to-ground, air-to-sea surface target detection and electronic warfare, as well as SAR ground mapping. It can designate both ground targets and airborne targets simultaneously (thanks to the ability to carry out both air-to-air and air-to-ground tasks enabled by the AESA).

Describing a possible mission, as the tactical aircraft enters the combat zone, an indication of a potential target pops up on the pilot's MFD. Flying toward the area of interest, the pilot presses his or her finger against the touch-screen display and views a much clearer, close-up image of the target, which is identified as an enemy ground vehicle. The pilot presses the screen again, and target designation and weapons status imagery appears on the visor of his helmet-mounted display (HMD). Closer in, he views the target, now being automatically tracked; the crosshairs in the visor lock on to the

target; and the pilot fires a missile that follows a laser beam to its destination. The pilot again views the MFD and notes that the target has been destroyed.

The idea is to simplify the pilot's mission, making for easy target detection and destruction of ground vehicles, ships, or enemy aircraft. The complexity lies in the sensors, displays, and massive processing power that make up the automatic targeting capabilities of a 21st-century, multibranch, multinational, multimission supersonic fighter. The fused targeting data can be overlaid onto a battlefield situation display that the pilot has uplinked from a ground base or another aircraft. The intent is to produce battle scene awareness to support an Observe, Orient, Decide and Act (OODA) sequence for pilots.

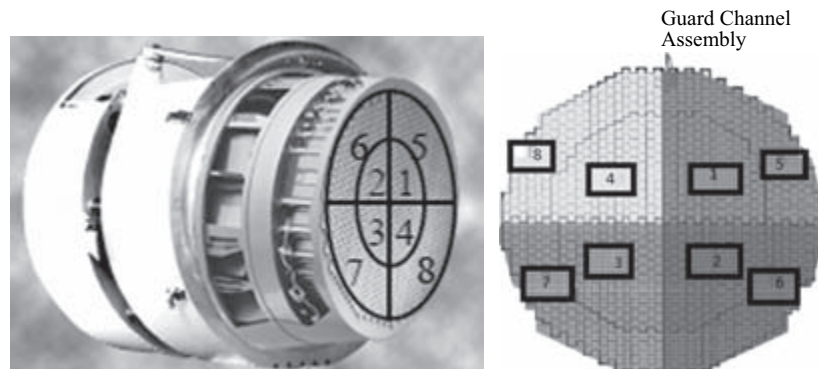
4.2.5 The Future of FCR

Sensor Improvement The future AESA will be fitted with more than the four traditional quadrants. These multiple subarrays will allow ABF for efficient multiple jammers cancellation, space-time adaptive processing for clutter cancellation and detection improvements. In Europe, such AESA were pioneered by the tri-national AMSAR program (Airborne **M**ultirole **S**olid-state **A**ctive array **radar**) [4] involving SELEX (formerly BAe Systems) for the United Kingdom, CASSIDIAN (formerly EADS Defense) for Germany, and THALES for France. The latest AMSAR's AESA configuration was made up of eight subarrays (Figure 4-37).

By using multiple subarrays, the processing enables better protection against attacks, better detection of slow moving targets in GMTI while keeping accurate angle localization. The number of subarrays determines the degrees of freedom's number for interference cancellation. In the worst case, to clean the Sum channel and the two Difference channels (for monopulse measurements), it is required that: $N_{SA} \geq N_J$, where N_{SA} and N_J are respectively the number of subarrays and the number of jammers.

- **Adaptive beam forming for multijammers cancellation** – This processing is described in section 4.4.2.
- **STAP for clutter cancellation** – STAP consists in forming a two-dimensional filter (Angle-Doppler) so that for each Doppler frequency (corresponding to a possible moving target), the antenna pattern has a null in the direction of fixed clutter having the same Doppler. An example is given in Figure 4-38. The clutter locus in 2D is represented by the oblique black ridge. The targets are in grey. Some of them (the slowest ones) can only be visible in a 2D representation since they are hidden by

FIGURE 4-37 ■
AMSAR Subarrays
[Thales Airborne
Systems + own
work (Kemkemian)].



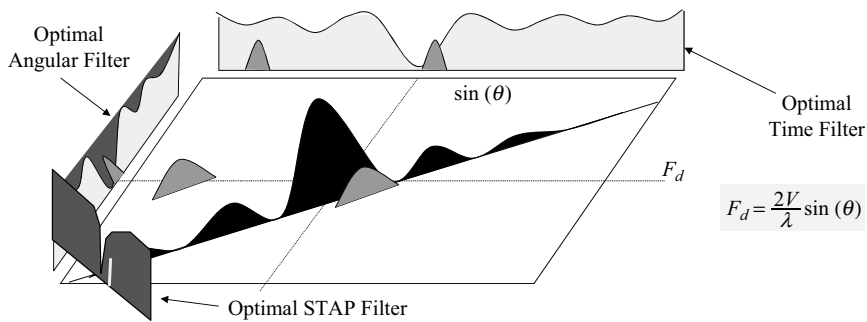


FIGURE 4-38 ■ STAP Filter (Side Looking Radar) [Thales Airborne Systems + own work (Lacomme)].

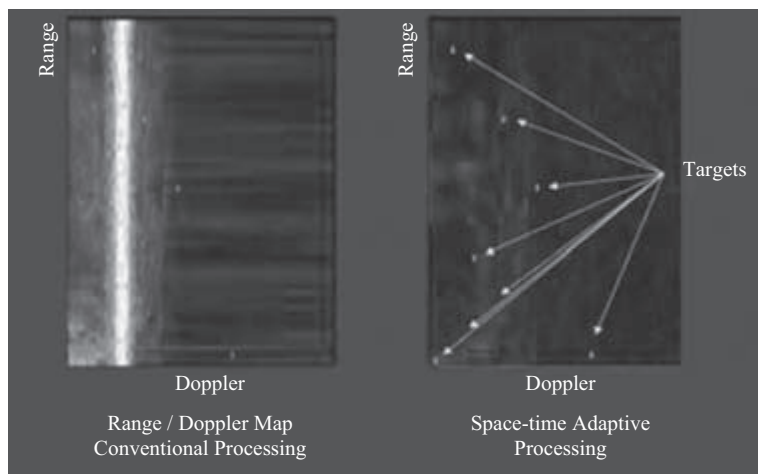


FIGURE 4-39 ■ STAP Benefit in GMTI [(from [4]) AMSAR – A European Success Story in AESA Radar – J.L. Millin, S. Moore, W. Bürger, P.Y. Triboulloy, M. Royden, J. Gerster. IEEE international Radar Conference, October 2009].

the clutter in 1D optimal filter (either in time/frequency domain or in space/angle domain):

- To detect only these targets, two degrees of freedom are needed (two subarrays) if there is no range/Doppler ambiguity.
- To localize these targets in azimuth (GMTI case), three degrees of freedom are needed (always without range/Doppler ambiguity).
- To localize these targets both in azimuth and elevation (air-to-air case), it is nice to have six degrees of freedom.
- Waveforms with range or Doppler ambiguities require extra degrees of freedom.

More details on STAP can be found in Volume 2, Chapter 10.

An example of STAP benefit in GMTI is given in Figure 4-39. The slow targets, not detectable with conventional Doppler processing, are visible after STAP.

Another example of STAP application is given for MPRF mode in air-to-air (Figure 4-40). Due to the Range and Doppler folding, the whole Range-Doppler domain is desensitized by the clutter returns. With STAP processing the clutter + noise level in the target's domain (excluding very slow velocities with respect to the ground) is now about the thermal noise only level.

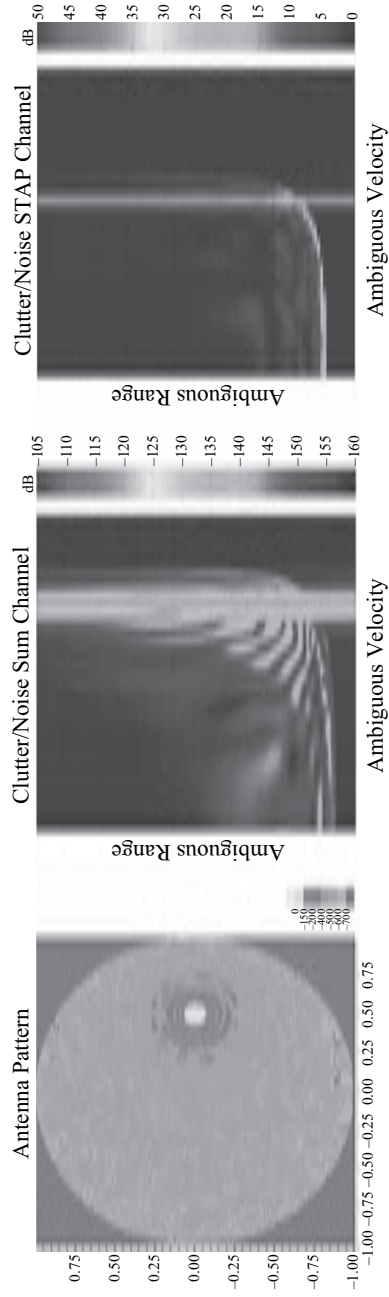


FIGURE 4-40 ■ STAP Benefit with MPRF Waveform [Thales Airborne Systems].

- *Multifunction sensor*: The radar is now a multipurpose cooperative sensor. In conjunction with the EWS and the electro-optical targeting system, it is part of a system of cooperating sensors. For example, the radar AESA can be used to perform more efficient EW functions in its bandwidth. In another area, the powerful AESA of the radar, in conjunction with a modem, can carry out “*ad-hoc*” data-links at long range and very high speed.

Key to the futuristic fighter’s targeting capability is sensor integration and data fusion. Mission system software fuses data from:

- the electronically scanned array radar,
- EOTS with FLIR and IRST system,
- the electronic warfare suite, and
- the communication, navigation, and identification (CNI) suite, providing identification friend or foe (IFF) and off-board data delivered via a high-speed data link.

All these sensors are arranged as a set of distributed apertures, both EM and Electro-Optical (Figure 4-41).

- **Smart management of the system of sensors** – The goal is for the pilot to receive unprecedented situational awareness from a mission systems package that incorporates modular open systems architecture, object-oriented design and common commercial off-the-shelf (COTS) processors. Combined with onboard precision weaponry—missiles, smart bombs, and a cannon, the future fighter will “compress the kill chain,” and have the ability to destroy targets “within single-digit minutes” of their detection.

In a typical scenario, the pilot would first detect a beyond-eyesight target in a predominantly radar image on the MFD. As the target gets closer, the EOTS imagery automatically creates a clearer picture of the target on the MFD. At this point, the pilot assesses an operational picture of the battle space, evaluates the threat responses, and rapidly plans a route to secure minimum exposure and maximum weapon effectiveness, as well as determining the best choice of weapon.

Once the decision is made to attack the target, the pilot would switch from the head-down to the head-up display in his or her helmet-mounted visor. In addition to presenting a center cross that locks onto the target for a point-and-shoot capability, the

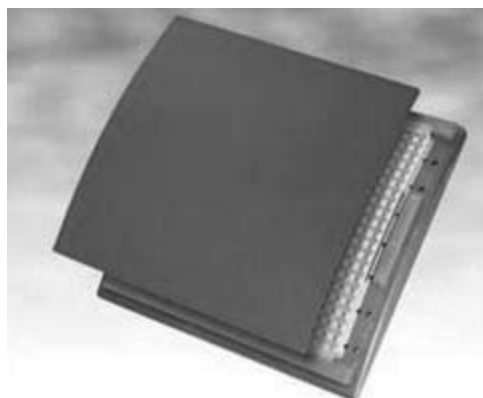


FIGURE 4-41 ■
Example of a
Conformal
Broadband
Multifunction Array
(radar, ESM, COM)
[Thales Airborne
Systems].

HMD also presents the status of available weapons, a symbol for IFF and indication of the target's range, closure, and velocity. With most of the target detection and presentation achieved automatically, the OODA process, from acquisition to destruction, can be done within a few minutes. The targeting sensors and processors will make these fighters not just a combat aircraft firing weapons, but a first-day-of-the-war, multi-mission aircraft able to perform autonomously, cooperatively or remotely, using information from off-board sources. In a cooperative mission, the integrated sensor suite would package and format targeting data to form a waveform for delivery by the CNI to a ground base or other aircraft via data link.

- **Network of cooperative systems of sensors** – The combat platforms present in the theater of operation, fitted with multifunctional sensor systems are now networked. A global tactical situation is established through the contribution of each individual platform, and then is shared by all platforms thanks to interoperable data-links. The theater of operation contains many platforms. Some of them operate in active mode (radar), the others may be operated in passive mode (Multistatic receive only radars sensors, ESM sensors, Electro-Optical sensors, etc.). Such a network has many advantages:
 - Difficult to neutralize: the loss of a node does not mean the loss of the whole network (same concept as Internet).
 - Diversity of observation: a target is observed from many angles of aspect. The traditional weaknesses of radar no longer exist, such as the Doppler notches.
 - Reduction of the exposure to threats of manned and costly platforms: UCAV and UAV may be sent to hazardous areas without endangering crews.
 - Difficulty for the enemy to identify the origin of the imminent threat for him.
 - Spectral resources saving: the minimal number of platforms is in active mode. The other ones remain in silent mode.

An example of networked system of cooperative platforms is shown in Figure 4-42. It is obvious that the key elements for deploying such a network of sensor are:

- high-speed, long range communication systems; and
- very accurate synchronization means.

4.3 | SURFACE-BASED FIRE-CONTROL RADAR

Technological developments of surface-based FCR are similar to those of airborne FCR. This particularly concerns electronics and signal processing. Depending on the implantation of these radars, space constraints are more or less critical.

4.3.1 Surface-to-Air Fire-Control Radar

4.3.1.1 Antiaircraft Artillery (AAA)

AAA can be employed as either unguided “barrage fire” or sensor guided “directed fire.” One of the earliest uses of radar as an AAA aid was by the German air defense in World War II when the altitude of incoming Allied bomber formations was measured to allow accurate setting of Flak projectile fuses.

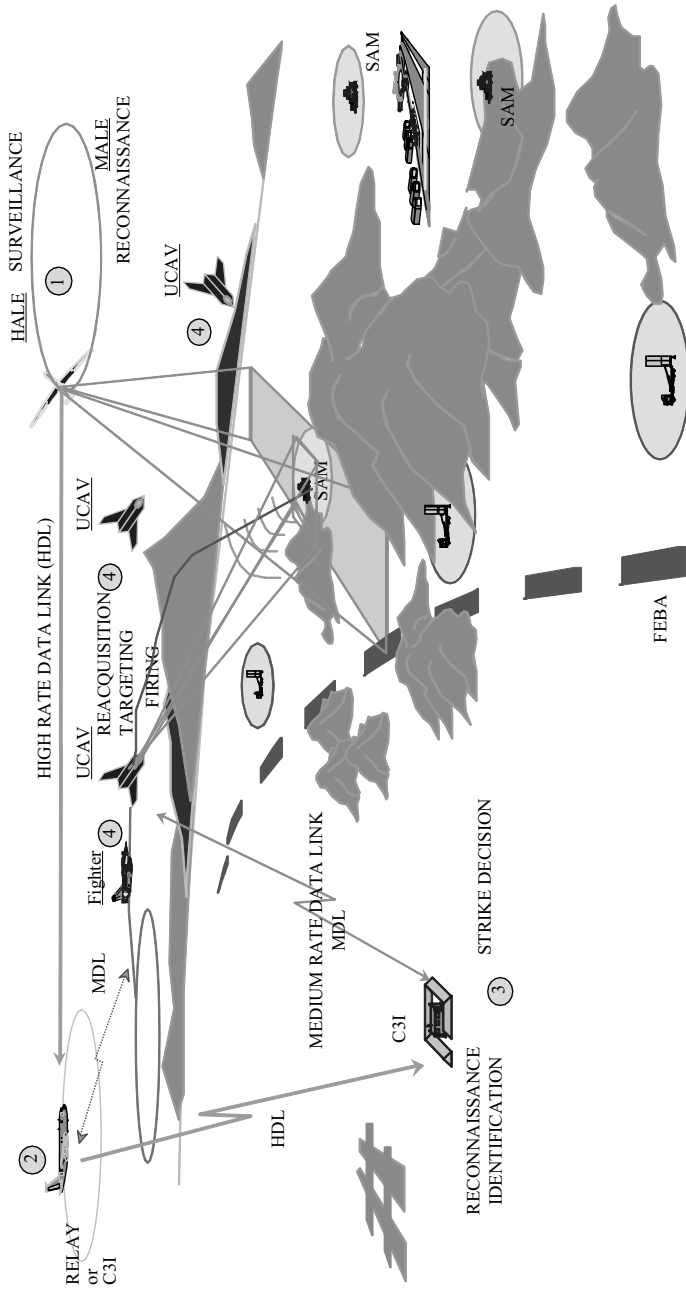
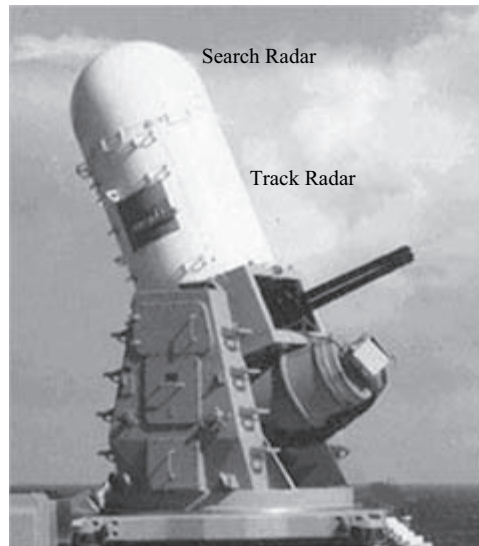


FIGURE 4-42 ■ Cooperative Network of Platforms [Thales Airborne Systems (Lacomme)].

FIGURE 4-43 ■
MK-15 CIWS.



More modern AAA systems employ radar sensors allowing accurate track predictions. The weapon system will fire at a point in space that the target is predicted to occupy after a predetermined time of flight of the projectile. As an example, the MK 15 Phalanx (RAYTHEON) “Close-In Weapons System” or CIWS (Figure 4-43) is a fast-reaction, rapid-fire 20-millimeter gun system that provides US Navy ships with a terminal defense against antiship cruise missiles (ASCM) that have penetrated other fleet defenses. This system is designed to engage ASCM and fixed-wing aircraft at short range. The Phalanx automatically enables “kill chain” functions usually performed by separate, independent systems such as search, detection, threat evaluation, acquisition, track, firing, target destruction, kill assessment, and cease fire.

The fire-control assembly is composed of a search radar (Ku-band, digital Moving Target Indicator: MTI) for surveillance and detection of hostile targets and a track radar (Ku-band, pulse Doppler monopulse) for aiming the weapon while tracking a target. The unique closed-loop fire-control system that tracks both the incoming target and the stream of outgoing projectiles gives CIWS the capability to correct its aim to hit very fast-moving targets. The monopulse beam design enables the azimuth and elevation tracking accuracy required in the AAA environment [5].

Another defense system against antiship cruise missiles is the “Goalkeeper” (Figure 4-44, THALES Nederland). As the Phalanx system, the Goalkeeper is constituted of a search radar and a tracking radar. The X-band search radar can handle up to 18 targets at once. The tracking radar operates both in X and Ka bands. This dual-band operation ensures:

- good robustness against CME, and
- double beamwidth (the Ka band beam performs an accurate angle tracking while the X-band beam allows a fast acquisition [from the search radar data] or a fast reacquisition).



FIGURE 4-44 ■ Goalkeeper System [http://fr.wikipedia.org/wiki/Goalkeeper_CIWS].

4.3.1.2 Surface-to-Air Missile Systems

These systems, designed to engage and destroy airborne threats, are generally made of two subsystems:

1. **A first subsystem fitted with a search radar** having a large coverage in elevation and a coverage of 360° in azimuth. Comparing the requirements of the search function of an airborne FCR and the requirement of the search function of a surface-based FCR, the following differences are noted:
 - The required coverage in azimuth is 360° , while an airborne FCR covers the front area. This requirement is not really an issue with mechanically scanned systems. However, the evolution toward AESA systems requires either an extra mechanical rotation axis in azimuth or a set of faceted AESA. In the future, systems with cylindrical AESA (i.e., non planar arrays) are being studied.
 - The angular domain in elevation is often quite large. Generally, the requirement is to provide oversight of a “quasi” cylindrical area whose cut is shown in Figure 4-45

It is interesting to note, if θ is the elevation angle, the required detection range is: $R_D = AB \cdot \csc\theta < RA$. That is why the first air-surveillance systems were using an antenna whose radiation gain pattern (called “cosecant”) varied with elevation in order to adjust the sensitivity according to the required detection range. It is a simple solution, but it does not allow very accurate localization in elevation. Also, new modern E-SCAN radars are adopting another strategy:

- A quick elevation E-SCAN is achieved during the antenna’s rotation in azimuth.
- The antenna gain does not vary during the quick scan; however, the dwell time on target decreases with elevation according to a cosecant law.

Thanks to E-SCAN, this method provides a fast refresh time while providing a good angular accuracy.

2. **A second subsystem equipped with a tracking radar** with more accurate azimuth and elevation accuracy. The tracking radar is cued by the search radar when it detects a target, then it tracks the target while providing the missile guidance. The second subsystem contains also the missiles battery. Again, tracking systems with M-SCAN antenna

FIGURE 4-45 ■ Typical Search Domain of Surface-to-Air Systems [Own work (Kemkemian)].

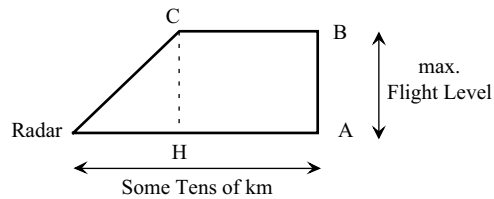


FIGURE 4-46 ■ HAWK System. Left: PAR, Right Top: HIPIR, Right Bottom: Missile Battery [(from Wikipedia) http://en.wikipedia.org/wiki/MIM-23_Hawk + own work (Kemkemian)].



only allow to engage one target at a time. A tracking system with E-SCAN radar, combined with active homing missiles (active radar seekers), allows multiple targets engagement.

These subsystems can be made up of separate units or be grouped on a single platform. Two representative systems are the HAWK system and the CROTALE system:

Improved HAWK (I-HAWK) System A Hawk unit uses several different ground radars and control systems. A typical I-Hawk battery mainly consists of (Figure 4-46):

- 1 × I-PAR: Improved Pulse Acquisition Radar (AN/MPQ-64) – A search radar with a 20 rpm rotation, for high-, medium-, or low-altitude target detection.
- 2 × HIPIR: High Power Illuminator Doppler Radar (AN/MPQ-61) – Which tracks designated targets and provides target illumination for the missile’s semi-active seeker.

Note: The old HAWK versions have an extra “Range Only Radar” (ROR) which is a K-band pulse radar intended to provide ranging data when the other radars are jammed by countermeasures.

I-PAR is a Doppler (MTI) radar that helps separate targets from ground clutter. It operates in the C-band frequency range with a peak operating power of 1,000 watts. It is



FIGURE 4-47 ■ Crotale NG [<http://www.spyworld-actu.com/spip.php?article8685> (original image: French Mod but no longer available)].

fitted with a rotating antenna in azimuth but electronically steered in elevation. The detection range is about 100 km versus 3 m² target.

HIPIR is an X band CW system which is used to illuminate targets in the Hawk Missile Battery. The unit comes mounted on its own mobile trailer. Unit automatically acquires and tracks designated targets in azimuth elevation and range rate. The CW operation requires simultaneous transmission and reception, so two separate antennas provide sufficient isolation.

Crotale NG System The whole set (search radar, tracking radar, and missiles battery) is grouped and mounted on a single trail (Figure 4-47). This system is composed of:

- A pulse-Doppler search radar operating in S-band able to operate in motion.
- A pulse-Doppler tracking radar operation in Ku-band with a narrow beam.
- An Infrared Camera.
- A visible Camera.
- An infrared localizer intended for missile tracking.

4.3.2 Surface-to-Surface Fire-Control Radar

These surface-to-surface systems are quite similar in their principles to the surface-to-air systems. This is essentially the nature of the targets which differentiates them.

4.3.2.1 Maritime Surface-to-Surface Fire-Control Systems

Radar is a primary sensor in maritime surface-to-surface engagements. Sensors are only required to provide a 2D input (range and azimuth) to the fire-control system to produce a viable solution as targets are mainly subsonic or supersonic sea-skimming missiles. The elevation can usually be assumed to be 0 feet Medium Sea Level (MSL).

Radar inputs can be used for providing fire-control solutions for surface-to-surface gunnery or to provide targeting information to antiship cruise missiles which have onboard radars for active homing guidance.

FIGURE 4-48 ■ AN/TPQ-47 Fire-Finder Radar [www.fas.org].



4.3.2.2 Fire-Finder Radar

Fire-Finder radar systems detect and backplot the fire of adversary weapons, artillery, rockets, and mortars to provide pinpoint targeting information for the counterattack. The systems also correct and improve the delivery of friendly fire.

Fire-Finder radars are tri-dimensional radars with 2D E-SCAN (Figure 4-48). The stationary antenna sweeps a rapid sequence of beams along the horizon, forming an electronic radar curtain over a 90° area. Any target penetrating the curtain triggers an immediate verification beam. Upon verification, an automatic tracking sequence begins.

While tracking any single target, the radar continues scanning, locating, and tracking others. Signal and data processors test each track to filter out birds, aircraft, and other unwanted returns, giving Fire-Finder radars an extremely low false-location rate and a very high probability of location rating. Once the computer establishes a target's validity, it "smooths" the measured track data, deriving a trajectory that it extrapolates to establish the target's firing position and impact location. Those data are displayed on a visual map and printed out in map coordinates.

4.3.3 Principles of Missile Guidance

Only the principles that are used in modern systems are discussed here.

4.3.3.1 Surface-to-Air Missile Engagement Envelopes

A surface-to-air missile (SAM) is neither guided after a target nor pursues or chases an aircraft. Instead, the fire-control computer predicts an intercept point on some future part of the target flight path based on the known flight parameters from the target tracking radar and the known maneuverable envelopes of both the target and the missile (Figure 4-49). The missile is accelerated for the brief initial phase of its flight (the boost phase) after which it can never again speed up: It is accelerated toward the predicted intercept point, after which it is only capable of slight course corrections to keep it pinpointed on the point of impact.

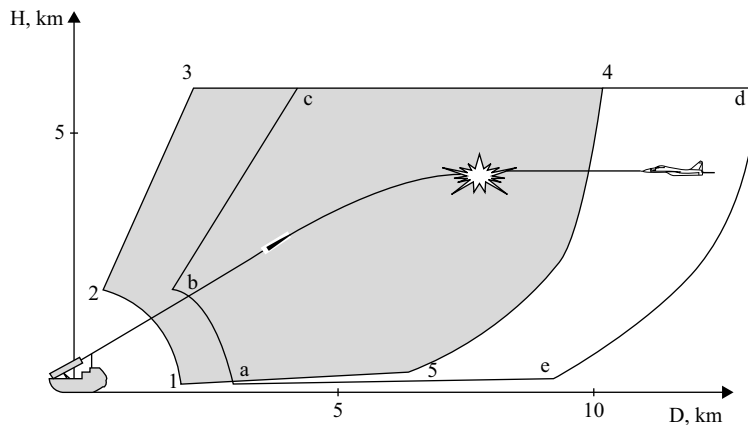


FIGURE 4-49 ■ Nominal SAM Engagement Envelope [(from [6] <http://www.scribd.com/doc/69703675/18/AIR-COMBAT-BASICS>)].

The effective engagement envelope of a nominal SAM system is determined by the location and speed of the airborne target. Maximum engagement ranges vary from a high-speed nonmaneuvering closing target to a high-speed crossing target, generating the highest miss distance due to required missile maneuvering. Minimum range is usually determined by the end of the missile's boost phase when missile guidance is initiated.

SAMs have specific engagement envelopes. Firing at targets within the heart of the envelope increases the likelihood of a hit. Just like air-to-air missiles, the envelope varies based on the target's range, altitude, and aspect. In the preceding engagement diagram, the area defined by numbers 1 through 5 represents the missile's effective area (assuming that the objective is motionless). This envelope shifts if the target is moving toward the launcher, in the area defined as a through e. In this case, the missile must be fired at longer range since the target will fly part of the way into the missile. If the missile is fired too late (once the target has crossed the a–b–c line), it passes out of the envelope before the missile arrives.

4.3.3.2 Missile Guidance Modes

The different types of missile guidance used in SAM systems include:

Command Guidance The target is tracked by an external radar (see Figure 4-50). However, a second radar tracks the missile itself. The tracking data from both radars are fed into a ground-based computer that calculates the paths of the two vehicles. This computer also determines what commands need to be sent to the missile-control surfaces to steer the missile on an intercept course with the target. These commands are transmitted to a receiver on the missile that allows the missile to adjust its course. An example of command guidance is the Russian SA-2 surface-to-air missile.

Semi-Active Homing Guidance The target needs to be continuously tracked by the FCS, but no guidance data is directly sent from the FCS to the missile. The energy reflected by the target is intercepted by a receive-only radar (seeker) located in the missile's nose (Figure 4-51). An onboard computer receives data from the seeker to determine the target's relative trajectory and sends correcting commands to control surfaces so that the missile will intercept the target. This system is also sometimes referred to as *bi-static*, meaning that the radar waves that intercept the target and those reflected back to the missile are at different angles (and at different ranges) to one another.

FIGURE 4-50 ■ SA-2 Command Guidance System [Self-Developed Graphic (Ballard)].

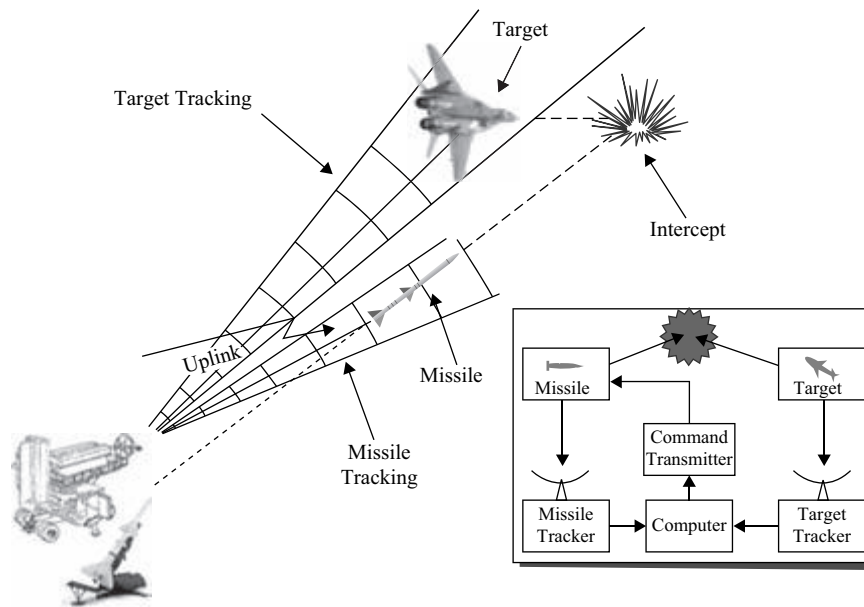
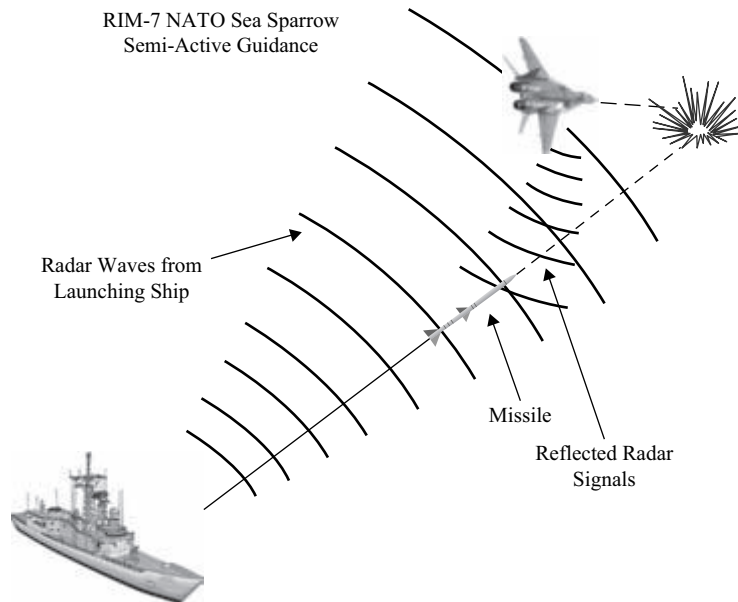


FIGURE 4-51 ■ Sea Sparrow Semi-Active Guidance [Self-Developed Graphic (Ballard)].



Active Homing Guidance Active homing missiles typically use radar seekers to track their target. Once the seeker is locked onto the target, the missile becomes autonomous: the fire-control system does not need to continue illuminating the target or transmit guidance data to the missile. For this reason, active homing missiles are often called *fire and forget*. The advanced medium-range air-to-air active homing missile has been adopted for use in the surface-to-air role by mounting it on a high-mobility multipurpose wheeled vehicle (HMMWV) and integrating it into various air-defense networks for target cueing. The Norwegian advanced surface-to-air missile system and the U.S. Marine Corps' complementary low-altitude weapon system (Figure 4-52) are two examples.

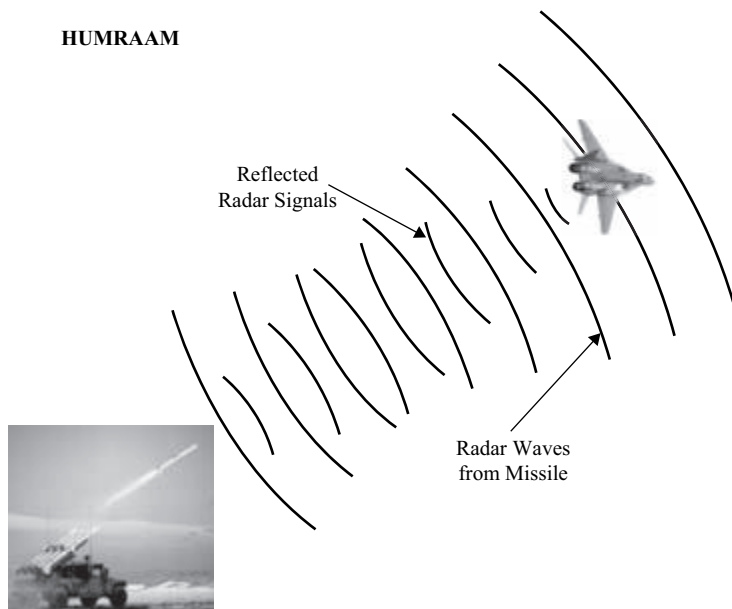


FIGURE 4-52 ■ HMMWV AMRAAM Launcher [Self-Developed Graphic (Ballard)].

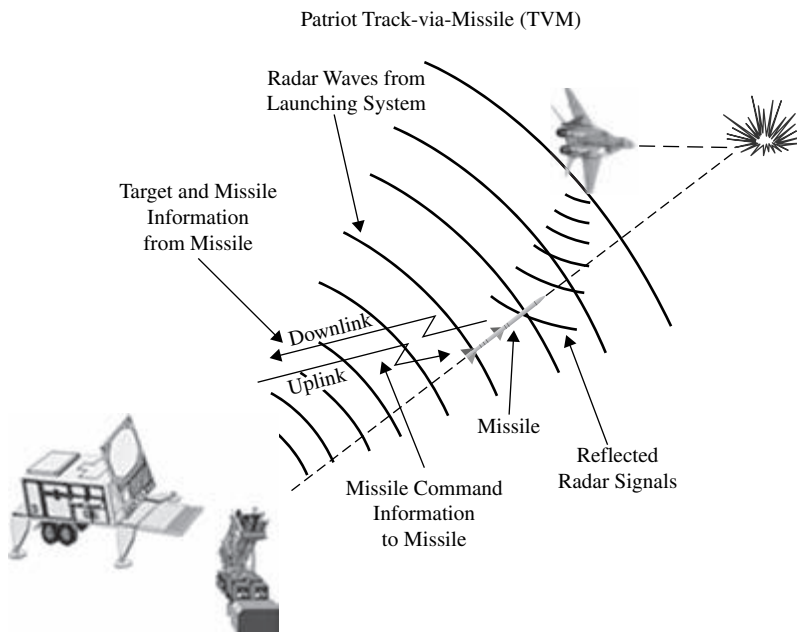


FIGURE 4-53 ■ Patriot Track-via-Missile TVM Tracking [Self-Developed Graphic (Ballard)].

Retransmission Homing Guidance A more unusual example of homing guidance is the retransmission method (Figure 4-53). This technique is very similar to command guidance but with a unique twist. The target is tracked via an external radar, but the reflected signal is intercepted by a receiver onboard the missile as in semi-active homing. However, the missile has no onboard computer to process these signals. The signals are instead transmitted back to the launch platform for processing. The subsequent

commands are then retransmitted back to the missile so that it can deflect control surfaces to adjust its trajectory.

This method is also sometimes called *track via missile* (TVM) since the missile acts as a conduit for tracking information from the target back to the ground control station. The advantage of TVM homing is that most of the expensive tracking and processing hardware is located on the ground, where it can be reused for future missile launches rather than be destroyed at missile detonation. A downside, though, is that the TVM method also requires robust high-speed communication data links between missile and control station, limiting the system to rather short ranges. Retransmission homing guidance is used on the Patriot surface-to-air missile system.

4.4 | ELECTRONIC COUNTER COUNTERMEASURES

The objective of ECCM techniques is to allow the accomplishment of the radar mission while countering the effects of the enemy's ECM [7]. The main jamming techniques to be countered are described hereafter.⁸ These ECM – and thus also ECCM – apply to both airborne and surface-based FCR. Some ECM techniques are intended more against airborne FCR whereas others are aimed against surface-based FCR. So, some ECCM will be more prevalent on airborne systems and others will be encountered more on surface-based systems.

4.4.1 Noise Jamming

This jamming aims at reducing the signal-to-noise ratio to prevent the target detection:

- **Barrage Noise** – This jamming is carried out by a powerful jammer onboard a “stand-off” platform. It attacks the victim radar by its antenna's sidelobes: the lower they are, the more difficult is the jamming.
- **Escort Jamming** – This jamming is performed by an escort A/C and attacks the victim radar by its antenna's main lobe or by its first sidelobes.
- **Self-Protection Jamming** – The jamming is issued from the target itself and attacks the victim radar by its antenna's main lobe. There is no possible angular discrimination between target and jamming.

4.4.2 ECCM against Noise Jamming

The first ECCM consists in using an unpredictable frequency agility sequence to force the jammer to transmit over a broadband (the jamming power within the instant radar bandwidth is reduced).

The jamming noise enters the victim radar through its sidelobes. It can be reduced by a Side Lobe Canceller (SLC). The SLC takes advantage of a “guard” antenna to form a “cleaned” sum channel. The SLC computes: $\Sigma' = \Sigma - \lambda A$, where “ Σ ” and “ A ” are

⁸Note: Only the main techniques that are efficient against modern radars have been discussed.

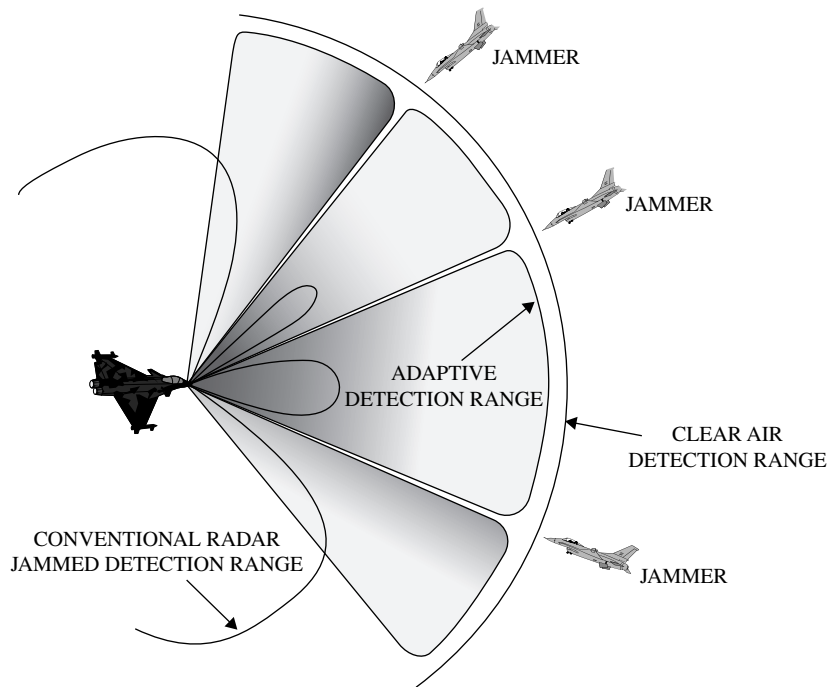


FIGURE 4-54 ■ Adaptive Beam Forming for Multiple Jammers Cancellation [Thales Airborne Systems].

respectively the sum channel and the guard channel. The coefficient λ is adaptively determined to maximize the signal-to-noise ratio. The auxiliary antenna's gain needs to be greater than the sidelobes gain otherwise the processing is not efficient. So far, SLC is mostly used on ground-based radars, but it will be extensively used to counter multiple jammers in future airborne radar with active arrays and multiple subarrays by using ABF (Figure 4-54).

In the case of jamming entering through the edges of the mainlobe or through the first sidelobes, the SLC is no longer helpful as the auxiliary antenna's gain is not sufficient. On future AESA radars with multiple subarrays, the solution will be to use ABF (Figure 4-54). Adaptive beam forming is a generalization of the SLC: its principle is to adaptively form, by linear combinations of subarrays, "cleaned" channels for detection and angle measurements of the target.

In the case of self-protection jamming, the previous ECCM are not very efficient, especially the cancellers using SLC or ABF which do not work at all. The target can no longer be detected and the distance of the target can no longer be measured (except at short-range where the Signal to Jamming Ratio becomes favorable to the radar, or by using a "Burn Through" look onto the target). However, the target remains localizable in angle by its jammer transmission (jammer strobe) and can be tracked in a degraded mode; moreover, a co-operative system with strobes from two or three spatially separated radars allows the jammer to be localized.

4.4.3 Gated Noise Jamming

A noise area is generated around or near the target echo (in range and/or Doppler). This kind of jamming requires the synchronization of the jammer on the radar's waveform.

Such synchronization is quite difficult with non-Doppler radar waveforms with pulse to pulse frequency/PRI agilities.

4.4.4 Range and Velocity Deception

This jamming consists of creating false targets around the true target to affect tracking:

- *Multiple false-target generation* – Multiple false targets are generated to saturate the display and mislead tracking initialization on the “good” target or to overwhelm the processing. The ECCM prevents overloading of the processing. It should also be noted that all false plots have the same direction as the “true” target, so angle only tracking remains feasible.
- *Range gate pull-off (RGPO) and velocity gate pull-off (VGPO)* – First, a false strong echo is superimposed on the target’s skin echo. This false echo is then progressively moved away from the target either by distance (RGPO) or by Doppler (VGPO). The purpose of this jamming is to capture the tracking on the real target. When the track is moved far enough away from the target, the false echo is stopped, which leads to lost tracking.

4.4.5 Angle Deception

These techniques aim to disrupt the angle measurements in order to lose the angular tracking:

- *Cross-eye* – This jamming employs two spatially separated jamming sources. Each source acts as a repeater-type jammer transmitting the same signal at the same time but with a phase shift of about 180° to create a wave-front distortion at the victim radar’s antenna level; as a result, a strong “glint effect” occurs in the angle.
- *Cross-polarization* – First, the jammer measures the polarization of the victim radar’s antenna. Jamming then consists of transmitting a strong signal in cross-polarization; the Σ and Δ patterns are so altered that they seem to have been exchanged. However, the gain is reduced by 20 dB to 40 dB, depending on the antenna’s quality. As a jammer is unable to transmit a perfect cross-polarized signal, a high-quality antenna will not be vulnerable to such jamming.

4.5 | THE “AN” EQUIPMENT-DESIGNATION SYSTEM

It is useful to review the designation of U.S. military electronics and communications equipment that allows a quick recognition of fire-control radar when referenced by its designation number. The Joint Electronics Type Designation System (the *AN system*) consists of a three-letter designation followed by a number. The first letter designates the type of platform: “A” for piloted aircraft, “S” for surface ship, “T” for ground transportable, and “M” for ground mobile. The second letter designates the type of equipment: “P” is always for radar. The third letter designates the purpose of the equipment:

“G” for fire control and “Q” for special or a combination of two or more functions. Several examples of the AN system are listed below:

- AN/APG-77 – Pulse Doppler X-band multimode radar used on F-22 aircraft,
- AN/SPG-62 I – J-band fire-control radar used on Aegis-class combatant ships,
- AN/TPQ-37 – mobile ground artillery locating radar, and
- AN/MPQ-53 – multifunction phased array radar used with the Patriot SAM.

4.6 | REFERENCES

- [1] Radar and Electronic Warfare Cooperation. How to Improve the System Efficiency? S. Kemkemian, M. Nouvel-Fiani, E. Chamouard. *IEEE/AESS Magazine*, August 2011, Vol. 26, number 8.
- [2] Air and Spaceborne Radar Systems. P. Lacomme, J.P. Hardange, J.C. Marchais, E. Normant. William Andrew; 1 edition (Dec 17, 2007) Norwich NY.
- [3] Thales Components and Technologies for T/R Modules. Y. Mancuso. IEEE International Radar Conference, October 2009.
- [4] AMSAR: A European Success Story in AESA Radar. J.L. Millin, S. Moore, W. Bürger, P.Y. Triboulloy, M. Royden, J. Gerster. IEEE International Radar Conference, October 2009.
- [5] <http://www.fas.org/man/dod-101/sys/ship/weaps/mk-15.htm>
- [6] <http://www.scribd.com/doc/69703675/18/AIR-COMBAT-BASICS>
- [7] Introduction to Electronic Defense Systems, Second Edition. Dr. Filippo Neri. Artech House Boston MA.

4.7 | FURTHER READING

Boyd: The Fighter Pilot Who Changed the Art of War. R. Coram. Little, Brown & Co. ISBN-10:0316796883

Fire-Control Radar Fundamentals Naval Education and Training October 1, 2007 ISBN-10:1466310766

Airborne Pulse-Doppler Radar

Aram Partizian, Georgia Tech Research Institute

Chapter Outline

5.1	Introduction	175
5.2	Geometry	177
5.3	The Doppler Shift and Motivation for Doppler Processing	181
5.4	Range and Doppler Distribution of Clutter	185
5.5	Contours of Constant Doppler and Range	196
5.6	Example Scenario	199
5.7	Pulse-Doppler Conceptual Approach	203
5.8	Ambiguities, Folded Clutter, and Blind Zones	216
5.9	Overview of PRF Regimes	226
5.10	High PRF Mode	228
5.11	Medium PRF Mode	235
5.12	Low PRF Mode	246
5.13	Summary	248
5.14	References	249

5.1 | INTRODUCTION

Airborne pulse-Doppler radar is used to provide detection and tracking of airborne moving targets in the presence of clutter. The pulse-Doppler waveform consists of a coherent burst of pulses, generally with constant pulse width and pulse repetition frequency (PRF). The returns from the environment are received, range-gated, and coherently integrated to form a Doppler spectrum for each range gate. The receiver–signal processor divides the Doppler spectrum into narrowband Doppler filters to isolate the moving target from competing clutter on the basis of their differences in Doppler shift and, therefore, radial velocity. Two other radar modes – continuous wave (CW) Doppler and moving target indicator (MTI) – also exploit the difference in Doppler shift between the target and clutter in order to improve detection. Pulse-Doppler radar, however, offers several advantages relative to these modes. Compared to unmodulated CW Doppler, the pulsed mode of operation offers much better transmit–receive isolation, especially for a monostatic radar, and the potential for significantly better range estimation. Compared to MTI, the narrowband Doppler filtering offers superior

clutter-rejection capability, especially given the wide Doppler extent of the clutter interference that results from the high speed of the radar platform itself, a major consideration for airborne pulse-Doppler radar that is not present in surface variants.

The benefits of pulse-Doppler radar are not without cost. Pulse-Doppler radar measurements are generally ambiguous in either range or velocity or both. In fact, pulse-Doppler waveforms are classified based on the nature of their ambiguities: high PRF (HPRF) is unambiguous in velocity but generally highly ambiguous in range; low PRF (LPRF) is unambiguous in range but generally highly ambiguous in velocity; and medium PRF (MPRF) is moderately ambiguous in both range and velocity. This ambiguous nature results not only in uncertainty of the target's true position or velocity but also in the folding of the clutter energy in the ambiguous dimension(s) and in the creation of range or velocity blind zones. These complications are particularly troublesome in search and acquisition modes, during which there is little or no prior information regarding target position and velocity. The pulse-Doppler radar generally circumvents these problems through the use of multiple pulse bursts at different PRFs, thereby resulting in increased radar timeline, a penalty that can be very costly when multiplied by many beam positions associated with a search pattern.

The main objective of this chapter is to describe how an airborne pulse-Doppler radar isolates targets of interest from clutter and measures target range and velocity. Related topics such as pulse compression, automatic detection, target tracking, and target and clutter statistics are described in [1]. The intent is to present basic principles and concepts. Although some of the approximations used sacrifice generality and rigor for the sake of clarity, they are otherwise fairly accurate for most conditions of interest. The material in this chapter is drawn largely from [2]. Table 5.1-1 lists many of the symbols used in this chapter for subsequent reference.

The remainder of the chapter is organized as follows. Section 5.2 defines the geometry and coordinate system used to describe the relative position and motion of the radar, targets, and clutter. Section 5.3 presents an approximate derivation of the Doppler shift and illustrates why airborne radars might need Doppler processing to detect targets in the presence of clutter. Section 5.4 derives expressions for the range and Doppler extents of the three main clutter components: mainlobe clutter, sidelobe clutter, and the altitude return (the vertical-incidence return). Section 5.5 shows how specific range and Doppler values of clutter map onto Earth's surface through iso-range and iso-Doppler contours. Section 5.6 presents an example scenario that illustrates the relative range-Doppler distribution of clutter and several different types of targets. Section 5.7 presents a top-level description of the operation of the pulse-Doppler radar, including the transmit-waveform characteristics and the formation of range gates and Doppler filters. Section 5.8 describes the ambiguities that arise due to sampling at the PRF rate that is intrinsic to pulse-Doppler waveforms, and the resulting implications of clutter folding (aliasing) and blind zones. Section 5.9 provides an overview of the three different PRF regimes – high, medium, and low – and summarizes their relative strengths and limitations. Section 5.10 describes the HPRF mode in additional detail, including methods of measuring range and the nature of range eclipsing. Section 5.11 describes the MPRF mode in additional detail, including blind zone charts, cumulative probability of detection and false alarm, ambiguity resolution, and sidelobe blanking. Section 5.12 relates the LPRF Doppler beam sharpening mode

TABLE 5.1-1 ■ Definition of Symbols

Symbol	Definition	Symbol	Definition
A	Area	α	Azimuth angle
B	Waveform bandwidth	ϵ	Elevation angle
c	Speed of light in vacuum (3×10^8 m/s)	ϵ'	Depression angle ($\epsilon' \equiv -\epsilon$)
d	Duty factor	ϵ_v	Aircraft climb angle
f_c	RF carrier frequency	ϵ_h	Elevation angle to the radar horizon
f_D	Doppler frequency	ϕ	Phase
f_p	Pulse repetition frequency (PRF)	γ	Grazing angle
G	Antenna gain	η	Angle of incidence
h	Height above Earth's surface	ψ	Angle relative to velocity vector
h_r	Radar aircraft height	λ	Wavelength
h_t	Target height	θ	Beamwidth (general)
M_R	Number of range bins	θ_{3dB}	Half-power beamwidth
N_b	Number of pulses in a burst	θ_{null}	Null-to-null beamwidth
N_D	Number of Doppler bins	δ_C	Cross-range resolution
N_p	Number of pulses processed	δ_D	Doppler resolution
R	Slant range	δ_R	Range resolution
R_C	Cross range	δ_v	Velocity resolution
r_e	Radius of Earth	σ	Radar cross section
R_G	Ground range	σ°	Backscatter coefficient
R_h	Range to radar horizon	τ	Uncompressed pulse width
R_U	Unambiguous range	τ_C	Compressed pulse width
T_{cpi}	Coherent processing interval	ω	Angular frequency
T_p	Pulse repetition interval (PRI)	ξ	Linear frequency modulation rate
v_R	Radial velocity, or range rate	ζ	Angle relative to $-z$ direction
v_r	Radar aircraft velocity	Δf_{bin}	Doppler bin, or Doppler filter, width
v_t	Target velocity	ΔR_{bin}	Range bin, or range gate, width
v_U	Unambiguous velocity		

to synthetic aperture radar (SAR). Section 5.13 provides a brief summary. References are listed in Section 5.14.

5.2 | GEOMETRY

5.2.1 Coordinate System

The geometry illustrated in Figure 5.2-1 will be used throughout this chapter. The radar is located at the origin of a Cartesian coordinate system, whose axes are body-fixed with respect to the radar platform. The z -axis corresponds to the vertical direction, with negative z being the direction of acceleration due to gravity (down). The unit vectors in the x , y , and z directions are denoted by \hat{x} , \hat{y} , and \hat{z} , respectively. The notation used for any three-dimensional vector \vec{u} is summarized in Table 5.2-1.

The radar is at height h_r above Earth's surface. The point directly below the radar on Earth's surface has coordinates $(0, 0, -h_r)$. The radar velocity is

$$\vec{v}_r = v_{rx}\hat{x} + v_{ry}\hat{y} + v_{rz}\hat{z} \quad (5.2-1)$$

FIGURE 5.2-1 ■ Coordinate System.
Coordinate System.

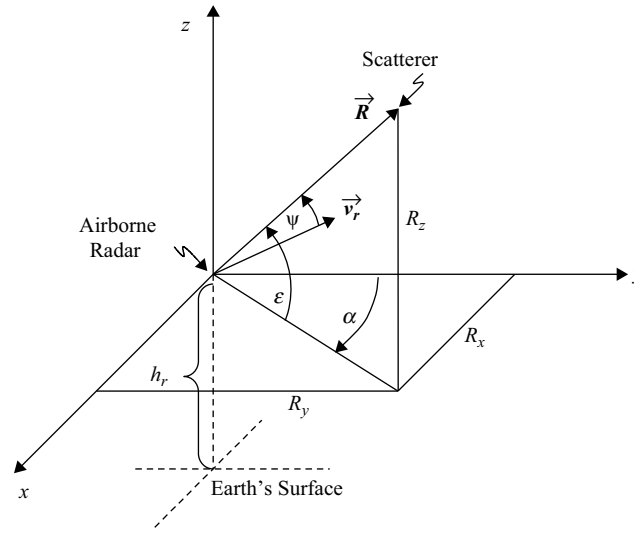


TABLE 5.2-1 ■ Notation for a Vector in Cartesian Coordinate System

Symbol	Definition
\vec{u}	Three-dimensional vector of some parameter u
u	Magnitude of \vec{u} ; i.e., $u = \vec{u} = \sqrt{\vec{u} \cdot \vec{u}}$
\hat{u}	Unit vector in the direction of \vec{u} ; i.e., $\hat{u} = \vec{u}/u$
u_x, u_y, u_z	Components of \vec{u} in the $x, y,$ and z directions; i.e., $u_x = \vec{u} \cdot \hat{x}$, etc.

The position of an object, or scatterer, in the environment relative to the radar is denoted by

$$\vec{R} = R_x \hat{x} + R_y \hat{y} + R_z \hat{z} \tag{5.2-2}$$

The object's position can also be described in terms of the slant range R , azimuth angle α , and elevation angle ϵ , relative to the radar. The slant range to the object is

$$R = |\vec{R}| = \sqrt{\vec{R} \cdot \vec{R}} = \sqrt{R_x^2 + R_y^2 + R_z^2} \tag{5.2-3}$$

The azimuth angle is the clockwise angle between the y -axis and the projection of \vec{R} onto the xy plane. The elevation angle is the angle of \vec{R} relative to the xy plane, defined as positive for scatterers above the xy plane and negative for scatterers below it, such as terrain clutter. It is often convenient to use the depression angle ϵ' , defined as the negative of the elevation angle, to provide an implicitly positive quantity for directions below the xy plane. The x -, y -, and z -components of \vec{R} are related to α , ϵ , and ϵ' through

$$R_x = R \cos(\epsilon) \sin(\alpha) = R \cos(\epsilon') \sin(\alpha) \tag{5.2-4}$$

$$R_y = R \cos(\epsilon) \cos(\alpha) = R \cos(\epsilon') \cos(\alpha) \tag{5.2-5}$$

$$R_z = R \sin(\epsilon) = -R \sin(\epsilon') \tag{5.2-6}$$

5.2.2 Angle Relative to the Radar Velocity Vector

The angle, ψ , between the radar velocity vector \vec{v}_r and the line-of-sight (LOS) direction of a scatterer at point \vec{R} is found through the relationship

$$\vec{v}_r \bullet \vec{R} = v_r R \cos(\psi) \quad (5.2-7)$$

Using the preceding expressions for R_x , R_y , and R_z , from Equations 5.2-4 through 5.2-6, we can express ψ in terms of the velocity vector and the azimuth and elevation angles:

$$\begin{aligned} \cos(\psi) &= \frac{\vec{v}_r \bullet \vec{R}}{v_r R} = \frac{v_{rx}R_x + v_{ry}R_y + v_{rz}R_z}{v_r R} \\ &= \frac{v_{rx} \cos(\varepsilon) \sin(\alpha) + v_{ry} \cos(\varepsilon) \cos(\alpha) + v_{rz} \sin(\varepsilon)}{v_r} \end{aligned} \quad (5.2-8)$$

Without loss of generality, we define the positive y direction to be that of the horizontal component of radar velocity, that is, $v_{rx} = 0$. The preceding expression becomes

$$\cos(\psi) = \frac{v_{ry} \cos(\varepsilon) \cos(\alpha) + v_{rz} \sin(\varepsilon)}{v_r} \quad (5.2-9)$$

The radar aircraft climb angle, ε_v , is related to the velocity x -, y -, and z -components through

$$\varepsilon_v = \tan^{-1}(v_{rz}/v_{ry}) = \sin^{-1}(v_{rz}/v_r) = \cos^{-1}(v_{ry}/v_r) \quad (5.2-10)$$

We can then alternatively express the angle ψ through

$$\cos(\psi) = \cos(\varepsilon_v) \cos(\varepsilon) \cos(\alpha) + \sin(\varepsilon_v) \sin(\varepsilon) \quad (5.2-11)$$

For the simple case in which the radar is flying entirely in the horizontal direction ($\varepsilon_v = 0$), the expression for angle relative to the radar velocity reduces to

$$\cos(\psi)|_{\varepsilon_v=0} = \cos(\varepsilon) \cos(\alpha) \quad (5.2-12)$$

For the case in which there is vertical motion, but we constrain the position vector to be in the yz plane, that is, $\alpha = 0$ or $\alpha = \pi$, the expression becomes

$$\cos(\psi)|_{\alpha=0} = \cos(\varepsilon_v) \cos(\varepsilon) + \sin(\varepsilon_v) \sin(\varepsilon) = \cos(\varepsilon_v - \varepsilon) \quad (5.2-13)$$

$$\cos(\psi)|_{\alpha=\pi} = -\cos(\varepsilon_v) \cos(\varepsilon) + \sin(\varepsilon_v) \sin(\varepsilon) = -\cos(\varepsilon_v + \varepsilon) \quad (5.2-14)$$

where we use the trigonometric identity $\cos(a + b) = \cos(a) \cos(b) - \sin(a) \sin(b)$.

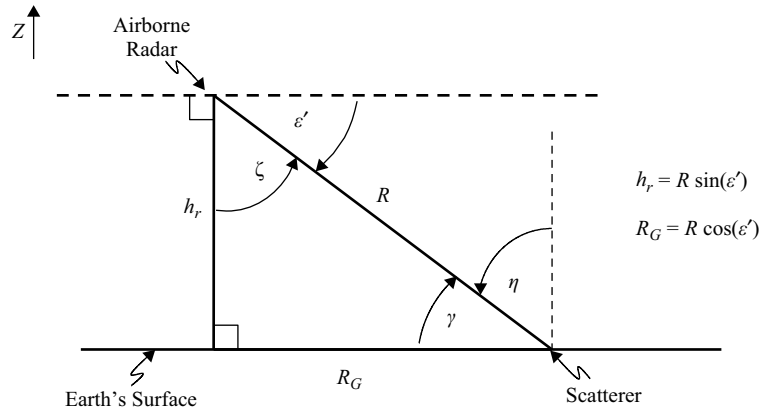
5.2.3 Range and Elevation Angle to a Point on the Earth Surface

5.2.3.1 Flat-Earth Approximation

We can approximate the slant range R and elevation angle ε to a point on Earth's surface by assuming a flat earth as shown in Figure 5.2-2. With this simplified model, the range and elevation (or depression) angle for a given radar height are related through

$$h_r = -R \sin(\varepsilon) = R \sin(\varepsilon') \quad (5.2-15)$$

FIGURE 5.2-2 ■
Geometry for
Flat-Earth
Approximation.



The grazing angle, γ , is the LOS angle relative to Earth's surface at the reflection point. The angle of incidence, η , is the LOS angle relative to the normal to Earth's surface at the reflection point. For the flat-earth model, these are given by

$$\gamma = \varepsilon' \quad (5.2-16)$$

$$\eta = \pi/2 - \varepsilon' \quad (5.2-17)$$

The projection of \vec{R} onto the flat-earth surface is referred to here as the ground range, R_G , given by $R_G = R \cos(\varepsilon')$. The flat-earth assumption is sufficiently accurate to convey most of the important concepts relevant to airborne pulse-Doppler radar and will be implicitly used in this chapter unless otherwise noted.

5.2.3.2 Spherical-Earth Approximation

One limitation of the flat-earth approximation is that it does not provide a means for estimating the range and elevation angle to the radar horizon. For this purpose, we employ a spherical-earth model as shown in Figure 5.2-3, where r_e is the radius of Earth, and the angle ζ is the LOS angle relative to the negative z -axis.

From the law of cosines and the fact that $\zeta = \pi/2 - \varepsilon'$ (implying $\cos(\zeta) = \sin(\varepsilon')$), we can relate range, height, and depression angle through

$$R^2 + (r_e + h_r)^2 - 2R(r_e + h_r) \sin \varepsilon' - r_e^2 = 0 \quad (5.2-18)$$

The depression angle in terms of slant range and height can therefore be found from

$$\sin(\varepsilon') = \frac{h_r}{R} \left(1 + \frac{R^2 - h_r^2}{2h_r(r_e + h_r)} \right) \quad (5.2-19)$$

The maximum range of any point on Earth's surface visible to the radar occurs at the radar horizon where the LOS angle is tangential to Earth's surface, that is, $\eta = \pi/2$ in Figure 5.2-3. From the Pythagorean theorem, the range to the radar horizon, R_h , is

$$R_h = \sqrt{(r_e + h_r)^2 - r_e^2} = \sqrt{2r_e h_r + h_r^2} \cong \sqrt{2r_e h_r} \quad (5.2-20)$$

The approximation of $R_h \cong \sqrt{2r_e h_r}$ is valid for $h_r \ll r_e$; and since Earth's radius is approximately 6,378 km while the height of an airborne radar is at most several tens

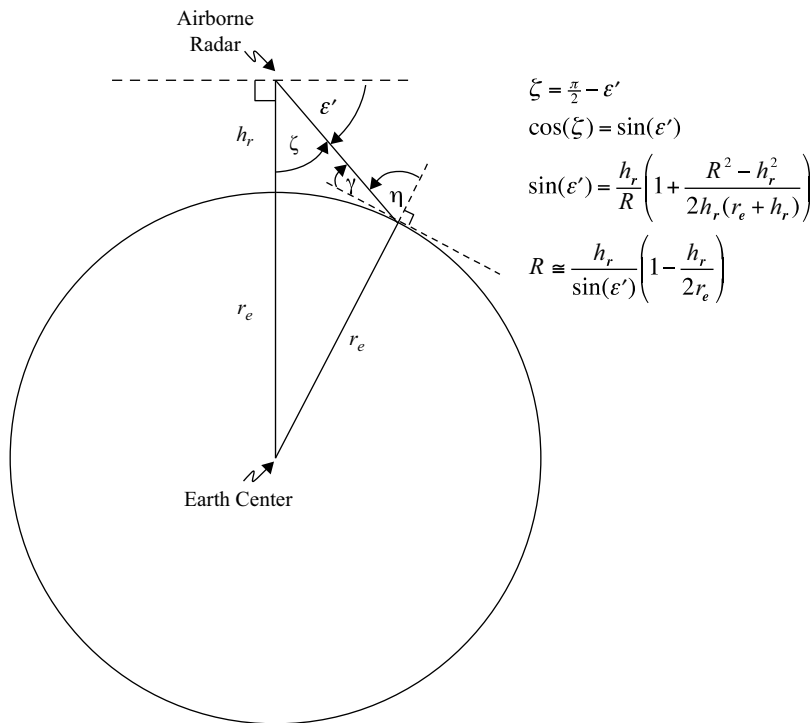


FIGURE 5.2-3 ■
Geometry for
Spherical-Earth
Approximation.

of kilometers, this condition is met for all cases of interest to us. Atmospheric refraction can sometimes extend the radar horizon beyond the visual (geometry-derived) horizon.

Comparison of Equations 5.2-15 and 5.2-19 reveals that the flat-earth approximation of depression angle, given by $\sin(\varepsilon') = h_r/R$, becomes less accurate relative to the spherical-earth approximation as the range increases from h_r to R_h . At the maximum range of $R = R_h \cong \sqrt{2r_e h_r}$, the spherical-earth approximation is $\sin(\varepsilon') \cong 2h_r/R_h$, while the flat-earth approximation is half this value. Thus, the flat-earth approximation of depression (or elevation) angle has a worst-case relative error of approximately 50 percent.

5.3 | THE DOPPLER SHIFT AND MOTIVATION FOR DOPPLER PROCESSING

5.3.1 The Doppler Shift

We can obtain an approximate (nonrelativistic) expression for the two-way Doppler shift by considering a radar that operates at frequency f_c , corresponding to wavelength $\lambda = c/f_c$, and a scatterer at range R from the radar. The round-trip distance between the radar and scatterer is $2R$. This distance corresponds to a round-trip phase delay, ϕ , equal to the number of wavelengths ($2R/\lambda$) multiplied by the number of radians (2π) per wavelength: $\phi = 4\pi R/\lambda$. A received signal from the target is of the form $s(t) = \cos(2\pi f_c t - \phi(t))$.

A time rate of change of range produces a proportional time rate of change of phase:

$$\frac{d\phi}{dt} = \frac{4\pi}{\lambda} \frac{dR}{dt} = \frac{4\pi}{\lambda} \dot{R} = \frac{4\pi}{\lambda} v_R \quad (5.3-1)$$

where $\dot{R} = v_R$ is the range rate, or radial velocity, defined to be positive for increasing range with time. The received signal can be rewritten as

$$s(t) = \cos\left(2\pi\left(f_c - \frac{2v_R}{\lambda}\right)t - \phi_0\right) \quad (5.3-2)$$

where ϕ_0 is some initial phase. The result of the time variation of range is to produce an apparent change in frequency from f_c to $\left(f_c - \frac{2v_R}{\lambda}\right)$ – namely the Doppler shift, f_D :

$$f_D = -\frac{2v_R}{\lambda} = -\frac{2f_c v_R}{c} \quad (5.3-3)$$

The radial velocity (range rate) v_R is the component of the relative velocity between the radar and scatterer in the direction of the radar-to-scatterer LOS:

$$v_R = (\vec{v}_t - \vec{v}_r) \cdot \hat{R} = \vec{v}_t \cdot \hat{R} - \vec{v}_r \cdot \hat{R} = v_t \cos(\psi_t) - v_r \cos(\psi_r), \quad (5.3-4)$$

where \vec{v}_r and \vec{v}_t are the radar and scatterer velocity vectors, respectively, and ψ_r and ψ_t are the angles between the unit vector \hat{R} in the direction of the radar-to-scatterer LOS and the radar and scatterer velocity vectors, respectively.

Expressed in terms of its x -, y -, and z -components, the range rate is

$$v_R = \frac{(v_{tx} - v_{rx})R_x + (v_{ty} - v_{ry})R_y + (v_{tz} - v_{rz})R_z}{R} \quad (5.3-5)$$

The radar and scatterer are said to be closing in range if the range is decreasing with time; this corresponds to a negative range rate and a positive Doppler shift. The radar and scatterer are said to be opening in range if the range is increasing with time; this corresponds to a positive range rate and negative Doppler shift. The two-way Doppler shift is approximately -6.67 Hz per m/s range rate per GHz radio frequency (RF). For example, the Doppler shift, f_D , from a stationary clutter return ($v_t = 0$) that is at an angle of 60 degrees (ψ_r) relative to the velocity vector of an airborne radar traveling at 300 m/s (v_r) and operating at 10 GHz ($\lambda = 0.03$ m) is equal to 10 kHz:

$$f_D = [-6.67 \text{ Hz}/(\text{m/s})/\text{GHz}] \times (-300 \text{ m/s}) \times [\cos(60^\circ)] \times (10 \text{ GHz}) = 10,000 \text{ Hz}$$

5.3.2 Motivation for Doppler Processing

To better appreciate the need for Doppler processing in airborne radar, consider an example of a conventional, pulsed (non-Doppler) radar and estimating the potential signal-to-clutter (S/C) ratio it may encounter.

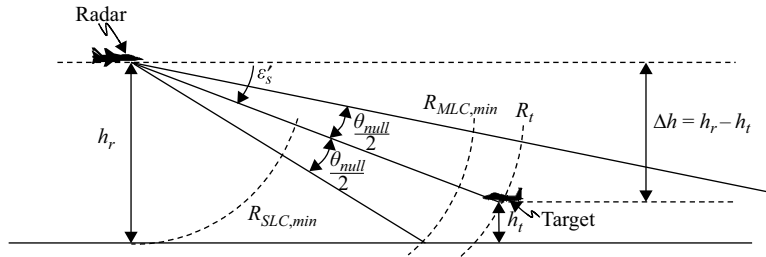


FIGURE 5.3-1 ■
Conditions of
Co-Range Clutter.

5.3.2.1 Conditions of Co-Range Mainlobe Clutter

Figure 5.3-1 depicts a radar at height h_r with an antenna beam that is steered toward a target at height h_t and slant range R_t , with $\Delta h = h_r - h_t$. Assuming that the target is at antenna boresight (beam center), the antenna depression scan angle ϵ'_s is related to the preceding parameters by

$$\sin(\epsilon'_s) = (h_r - h_t)/R_t = \Delta h/R_t \quad (5.3-6)$$

The nearest clutter is from the terrain directly below the aircraft; therefore, the minimum sidelobe clutter range is $R_{SLC,min} = h_r$: any mainbeam target with a range that is less than h_r does not have to compete with clutter in the same range cell.

Mainlobe clutter occupies an angular extent corresponding to the null-to-null beamwidth θ_{null} , which is typically approximately 2.5 times the half-power beamwidth, θ_{3dB} . The minimum range of mainlobe clutter, $R_{MLC,min}$, occurs at the lower edge of the elevation beam:

$$R_{MLC,min} = h_r/\sin(\epsilon'_s + \theta_{null}/2) \quad (5.3-7)$$

where θ_{null} is the null-to-null beamwidth in elevation. Any target in the mainbeam whose range is between h_r and $R_{MLC,min}$ will compete with sidelobe clutter but not mainlobe clutter. Any target in the mainbeam whose range is greater than $R_{MLC,min}$ (as shown in the figure) will compete with both mainlobe and sidelobe clutter.

The range $R_t = R_{MLC,min}$ represents the maximum range at which a radar at height h_r and with beamwidth θ_{null} can detect a target at height h_t without mainlobe clutter interference.

Using Equations 5.3-6 and 5.3-7 and applying the trigonometric identities $\sin(a + b) = \sin(a)\cos(b) + \sin(b)\cos(a)$ and $\cos(a) = \sqrt{1 - \sin^2(a)}$, we can express $R_{MLC,min}$ in terms of h_r , $\Delta h (= h_r - h_t)$, and θ_{null} :

$$R_{MLC,min} = \frac{h_r}{\sin(\theta_{null}/2)} \sqrt{1 - 2\cos(\theta_{null}/2)(\Delta h/h_r) + (\Delta h/h_r)^2} \quad (5.3-8)$$

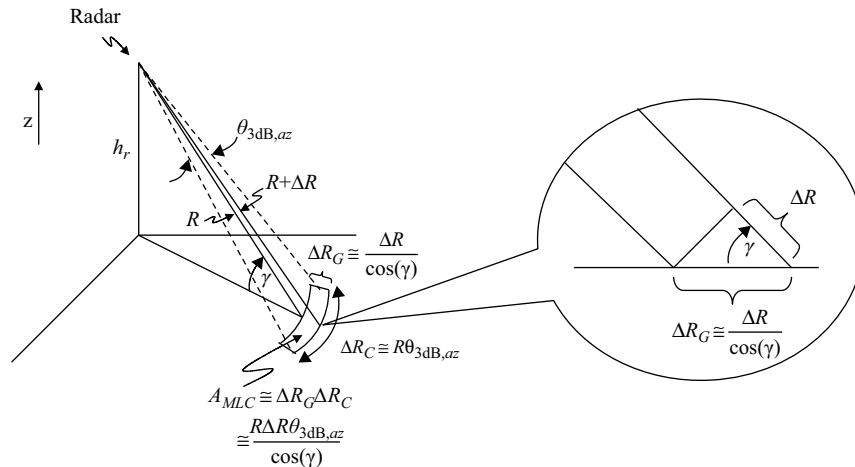
Table 5.3-1 lists $R_{MLC,min}$ for different values of radar height and target height assuming a radar half-power beamwidth of 3° , resulting in a null-to-null beamwidth of approximately 7.5° . Most of the mainlobe clutter-free ranges are too short to be of value. For example, a target 200 m above ground level (AGL) will not emerge from mainlobe clutter in a 2,000-m AGL radar until it reaches a range of 3.6 km, whereas generally it is desirable to detect and track such targets at many tens of kilometers range. Thus, for most cases of interest in look-down geometries, the target must compete with mainlobe clutter.

TABLE 5.3-1 ■ Maximum Range of Mainbeam Target without Mainlobe Clutter Interference

Radar Height (m)	Maximum Mainlobe Clutter-Free Range (km) versus Target Height, h_t				
	$h_t = 100$ m	$h_t = 200$ m	$h_t = 500$ m	$h_t = 1,000$ m	$h_t = 2,000$ m
200	1.5	3.1	–	–	–
500	1.6	3.1	7.6	–	–
1,000	1.8	3.2	7.7	15.3	–
2,000	2.5	3.6	7.8	15.4	30.6
5,000	5.2	5.8	9.0	15.9	30.8
10,000	10.1	10.4	12.4	18.0	31.9

*(assumes $\theta_{null} = 7.5^\circ$)

FIGURE 5.3-2 ■
Approximate Area of
Mainlobe Clutter.



5.3.2.2 Estimate of Signal-to-Clutter Ratio for Co-Range Mainlobe Clutter

We can obtain a rough estimate of the order of magnitude of the S/C ratio for a target competing with mainlobe clutter by first approximating the physical area of the co-range mainlobe clutter, A_{MLC} , as a rectangle of dimensions ΔR_G and ΔR_C . The ground range extent, ΔR_G , is the projection of the radar range resolution cell $\Delta R = \delta_R$ onto Earth's surface as shown in Figure 5.3-2. (The figure depicts a pulse-limited mainlobe clutter geometry in which the mainlobe clutter extends for multiple range bins. A less common condition is a beam-limited geometry in which the entire mainlobe clutter range extent is contained within a single range cell.) The cross-range extent, ΔR_C , is the arc described by the slant-range vector rotated through an angular extent equal to the azimuth beamwidth $\theta_{3dB,az}$. (We use the half-power beamwidth instead of the null-to-null beamwidth to estimate clutter power because it contains most of the mainlobe energy.) The approximate mainlobe clutter area in a range bin is thus

$$A_{MLC} \cong \left(\frac{\Delta R}{\cos(\gamma)} \right) (R\theta_{3dB,az}) = \frac{\delta_R R \theta_{3dB,az}}{\cos(\gamma)} \quad (5.3-9)$$

The effective RCS of the mainlobe clutter, σ_{MLC} , is estimated by multiplying the physical area by some representative average backscatter coefficient σ° within the mainbeam at that range:

$$\sigma_{MLC} \cong \sigma^\circ A_{MLC} = \sigma^\circ \frac{\delta_R R \theta_{3dB,az}}{\cos(\gamma)} \quad (5.3-10)$$

The signal-to-clutter ratio is the ratio of the target RCS σ_t to the mainlobe clutter RCS σ_{MLC} :

$$(S/C)_{MLC} \cong \frac{\sigma_t \cos(\gamma)}{\sigma^\circ \delta_R R \theta_{3dB,az}} \quad (5.3-11)$$

As an example, take $\sigma_t = 0$ dBsm; $\sigma^\circ = -20$ dB; $\delta_R = 150$ m; $\theta_{3dB,az} = 3$ degrees (0.052 radians); $\gamma = 5$ degrees; and $R = 50$ km. The S/C ratio for these assumptions is -35.9 dB:

$$\begin{aligned} (S/C)_{MLC} &= (+0 \text{ dBm}^2 - 0.02 \text{ dB}) - (-20 \text{ dB} - 12.8 \text{ dB} + 21.7 \text{ dBm} + 47 \text{ dBm}) \\ &= -35.9 \text{ dB} \end{aligned}$$

A noncoherent pulsed radar has virtually no chance of detecting the target at 50 km under such conditions because of the strong mainlobe clutter interference. The radar needs a positive S/C ratio of at least 12 to 15 dB for reliable detection, implying a deficit of 48 to 51 dB. Even with an improvement in range resolution from 150 m (1-MHz bandwidth) to 15 m (10-MHz bandwidth), the S/C ratio for mainlobe clutter is still tens of dB too low. Another method is therefore needed to separate the target from mainlobe clutter, and this is where Doppler processing becomes valuable.

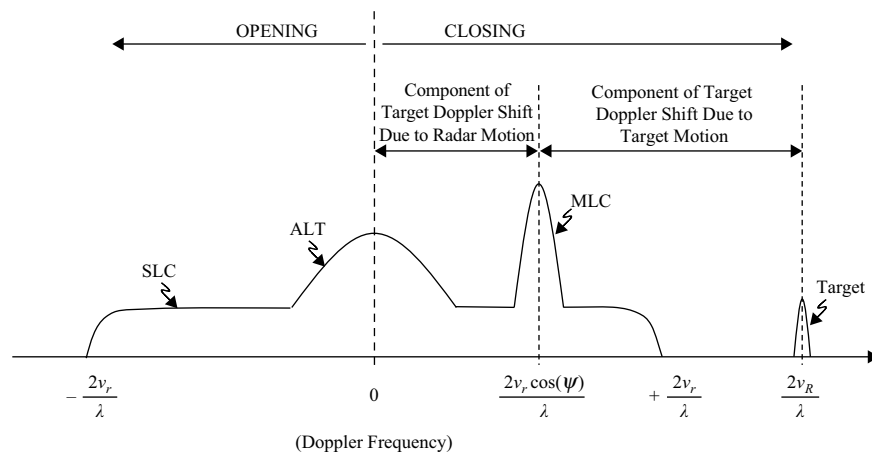
5.4 | RANGE AND DOPPLER DISTRIBUTION OF CLUTTER

5.4.1 Overview of Clutter Spectrum

The clutter Doppler spectrum seen by an airborne CW Doppler radar has three prominent components as illustrated in Figure 5.4-1: sidelobe clutter (SLC), mainlobe clutter (MLC), and the altitude return (ALT).

The sidelobe clutter Doppler spectrum results from the fact that the radar antenna is imperfect and therefore some sidelobe leakage occurs for both transmit and receive paths in all directions in space. (Low sidelobes and long range may, however, suppress parts of the sidelobe clutter spectrum below the radar noise floor.) Each sidelobe direction has a different LOS angle ψ relative to the velocity vector and therefore a different Doppler shift $f_D = \frac{2v_r}{\lambda} \cos(\psi)$. The sidelobe clutter extent is bounded by plus and minus the aircraft velocity: The highest (most positive) clutter Doppler shift possible under any circumstances, $+2v_r/\lambda$, occurs if the aircraft is flying directly toward the clutter; and the lowest (most negative) shift possible, $-2v_r/\lambda$, occurs if the aircraft is flying directly away from the clutter. By definition, the mainlobe clutter and altitude return Doppler frequencies also fall within these bounds.

FIGURE 5.4-1 ■ CW Doppler Spectrum Clutter Components.



The mainlobe clutter Doppler return is centered at $\frac{2v_r}{\lambda} \cos(\psi_s)$, where ψ_s is the mainbeam scan angle relative to the velocity vector. The spread of the mainlobe clutter Doppler return results from the variation of the LOS angle within the mainbeam relative to the velocity vector. The altitude return is a part of the sidelobe clutter that is coming from points on the terrain directly below the aircraft. This return can be significant because of its close range and highly specular backscatter condition. For an aircraft flying horizontally, the altitude return is centered at zero Doppler because it is directly orthogonal to the aircraft velocity vector.

The figure shows conditions of opening and closing target radial velocities. The total range rate of a mainbeam target is the sum of the radar's range-rate component plus the target's range-rate component. The former quantity is essentially equivalent to the range rate of mainlobe clutter at beam center. Thus, the difference in Doppler frequency between the center of mainlobe clutter and the return from a mainbeam target represents the Doppler shift due to the target motion itself, or equivalently, the target speed toward the radar. Factors such as clutter motion, radar acceleration, Doppler filter sidebands, finite dwell time, and radar oscillator noise contribute to additional spreading of these components.

The CW Doppler spectrum combines the contributions from all ranges into a single spectrum. In fact, each component (SLC, MLC, and ALT) actually occupies some range extent across which the Doppler spectrum may vary as a function of range. Figure 5.4-2 depicts a notional range profile of the received clutter. We will look at the range and Doppler extents of each of the three main clutter components to set the stage for interpreting the clutter spectrum seen by a pulse-Doppler radar. For simplicity, we will use the flat-earth approximation in this discussion.

5.4.2 Sidelobe Clutter Range and Doppler Extent

5.4.2.1 Sidelobe Clutter-Range Extent

The nearest-range sidelobe clutter return is from the point directly below the aircraft, at $R = h_r$. (A very small range interval at $R = h_r$, corresponding to the altitude return, is treated separately in Section 5.4.4.) The farthest range return is from the radar horizon, $R = R_h$. From Section 5.2.3, R_h is

$$R_h = \sqrt{2r_e h_r + h_r^2} \cong \sqrt{2r_e h_r} \quad (5.4-1)$$

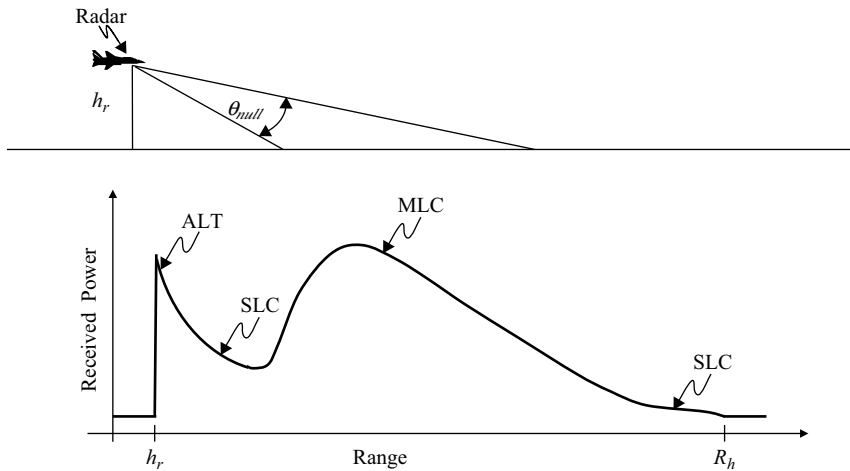


FIGURE 5.4-2 ■ Notional Range Profile of Received Clutter.

where the approximation is valid for $h_r \ll r_e$, as is the case for all airborne radar conditions. The sidelobe clutter range extent is therefore

$$\Delta R_{SLC} = R_h - h_r \cong \sqrt{2r_e h_r} - h_r. \tag{5.4-2}$$

Table 5.4-1 shows a few examples of the radar horizon range and the sidelobe clutter range extent for different values of radar height, assuming an Earth radius of 6,378 km. (An effective Earth radius such as $4/3 r_e$ is sometimes used to account for atmospheric refraction, but we will use the preceding value of r_e throughout this chapter for simplicity.)

TABLE 5.4-1 ■ Examples of Sidelobe Clutter Range Extent

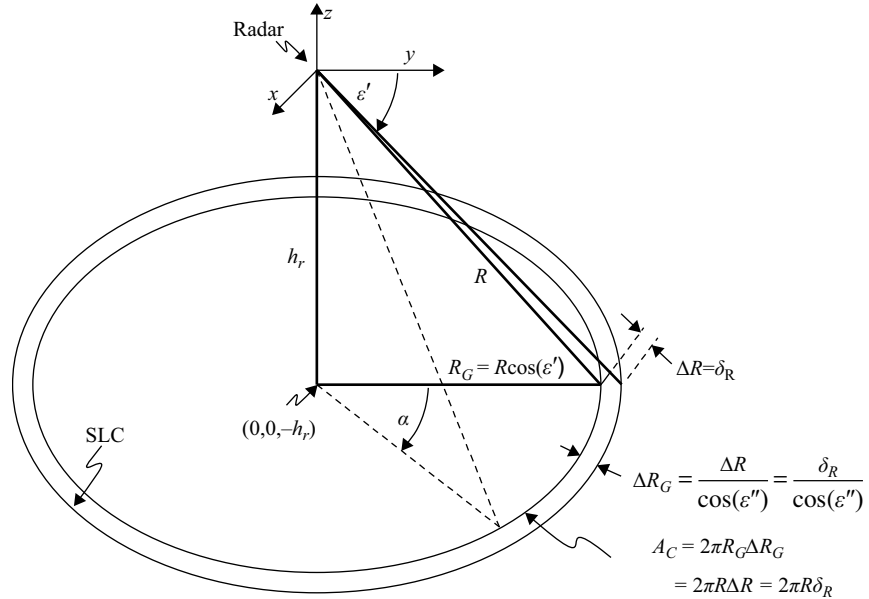
h_r (m)	h_r (ft)	R_h (km)	ΔR_{SLC} (km)
200	656	50.5	50.3
500	1,640	79.9	79.4
1,000	3,281	112.9	111.9
3,000	9,843	195.6	192.6

From Figure 5.4-3, the area of the circular band of sidelobe clutter contained within range interval $\Delta R = \delta_R$ at range R is proportional to range: $A_c = 2\pi R \delta_R$. The sidelobe clutter return power then is proportional to $\sigma^\circ A_c / R^4$, or $\sigma^\circ 2\pi \delta_R / R^3$. This decreases a little more rapidly with range than suggested by the explicit R^{-3} term because σ° also tends to decrease with decreasing grazing angle and therefore increasing range.

5.4.2.2 Sidelobe Clutter Doppler Extent

Sidelobe clutter in a range-resolution cell at range R occurs at all points on Earth's surface contained within a circular band of width $\delta_R / \cos(\epsilon')$ and radius $R \cos(\epsilon')$ centered around the point directly below the radar $(0, 0, -h_r)$, as illustrated in Figure 5.4-3. (The figure depicts a flat-earth geometry in which depression angle ϵ' equals the grazing angle γ .) The depression angle ϵ' is constant at all points for a given range R , defined by $\sin(\epsilon') = h_r / R$. The sidelobe clutter returns potentially occur from all azimuths over the

FIGURE 5.4-3 ■
Circular Band of
Sidelobe Clutter at
Range R .



full 360 degrees (except for the very narrow region occupied by mainlobe clutter if present at the same range).

Applying Equations 5.2-9 and 5.2-11 and noting that we have defined $\epsilon' = -\epsilon$, the Doppler shift of a clutter return at angle ψ relative to the velocity vector is

$$\begin{aligned} f_D &= \frac{2v_r}{\lambda} \cos(\psi) \\ &= \frac{2}{\lambda} \left(v_{ry} \cos(\epsilon') \cos(\alpha) - v_{rz} \sin(\epsilon') \right) \\ &= \frac{2v_r}{\lambda} \left(\cos(\epsilon_v) \cos(\epsilon') \cos(\alpha) - \sin(\epsilon_v) \sin(\epsilon') \right) \end{aligned} \quad (5.4-3)$$

The highest and lowest Doppler shifts at a given range (or equivalently, at a given ϵ') occur at $\alpha = 0$ and $\alpha = \pi$, respectively, that is, in the plane containing the z -axis and the velocity vector, defined in our coordinate system to be the yz plane (ignoring possible aircraft crab angle). Applying Equations 5.2-13 and 5.2-14,

$$f_D|_{\alpha=0} = \frac{2v_r}{\lambda} \cos(\epsilon_v - \epsilon) = \frac{2v_r}{\lambda} \cos(\epsilon_v + \epsilon') \quad (5.4-4)$$

$$f_D|_{\alpha=\pi} = -\frac{2v_r}{\lambda} \cos(\epsilon_v + \epsilon) = -\frac{2v_r}{\lambda} \cos(\epsilon_v - \epsilon') \quad (5.4-5)$$

Using the relationship $\sin(\epsilon') = h_r/R$ and the identity $\cos^2(a) = 1 - \sin^2(a)$, we can express the upper and lower bounds of the sidelobe clutter Doppler extent at a given range as

$$\begin{aligned} f_{D,SLCmax,R} &= \frac{2v_r}{\lambda} \cos(\epsilon_v + \sin^{-1}(h_r/R)) \\ &= \frac{2}{\lambda} \left(v_{ry} \sqrt{1 - \frac{h_r^2}{R^2}} - v_{rz} \frac{h_r}{R} \right) \end{aligned} \quad (5.4-6)$$

$$\begin{aligned}
f_{D,SLCmin,R} &= -\frac{2v_r}{\lambda} \cos(\varepsilon_v - \sin^{-1}(h_r/R)) \\
&= -\frac{2}{\lambda} \left(v_{ry} \sqrt{1 - \frac{h_r^2}{R^2}} + v_{rz} \frac{h_r}{R} \right)
\end{aligned} \tag{5.4-7}$$

The sidelobe clutter Doppler extent at a given range becomes

$$\Delta f_{D,SLC,R} = \pm \frac{2v_{ry}}{\lambda} \sqrt{1 - \frac{h_r^2}{R^2}} = \pm \frac{2v_r \cos(\varepsilon_v)}{\lambda} \sqrt{1 - \frac{h_r^2}{R^2}}, \tag{5.4-8}$$

centered at

$$f_{D,SLCtr,R} = -\frac{2v_{rz}h_r}{\lambda R} = -\frac{2v_r \sin(\varepsilon_v)h_r}{\lambda R} \tag{5.4-9}$$

Sidelobe clutter returns from 360 degrees of azimuth provide a continuum of values between the preceding bounds.

If the aircraft is flying approximately horizontally, then the maximum and minimum sidelobe clutter Doppler shifts over the entire range extent occur at the radar horizon, $R = R_h$. If, however, the descent (or climb) angle is such that the aircraft is flying directly toward (or away from) some point on Earth's surface, then the maximum (or minimum) sidelobe clutter Doppler shift occurs at some range $R < R_h$. This occurs if $|\varepsilon_v| > |\varepsilon'_h|$, where ε_h is the elevation angle to the horizon, given by $\varepsilon_h \cong -\sin^{-1}(h_r/R_h)$ for the flat-earth model. (See Section 5.2.3 for the accuracy relative to a spherical-earth model.) The ranges of the maximum and minimum sidelobe clutter Doppler shifts are

$$\begin{aligned}
R_{f_{D,SLCmax}} &= R_h \quad [\varepsilon_v \geq \varepsilon_h] \\
&= -\frac{h_r}{\sin(\varepsilon_v)} \quad [\varepsilon_v < \varepsilon_h]
\end{aligned} \tag{5.4-10}$$

$$\begin{aligned}
R_{f_{D,SLCmin}} &= R_h \quad [\varepsilon_v \leq -\varepsilon_h] \\
&= \frac{h_r}{\sin(\varepsilon_v)} \quad [\varepsilon_v > -\varepsilon_h]
\end{aligned} \tag{5.4-11}$$

The maximum and minimum Doppler shifts over all ranges are therefore

$$\begin{aligned}
f_{D,SLCmax} &= \frac{2v_r}{\lambda} \cos(\varepsilon_v - \varepsilon_h) \quad [\varepsilon_v \geq \varepsilon_h] \\
&= \frac{2v_r}{\lambda} \quad [\varepsilon_v < \varepsilon_h]
\end{aligned} \tag{5.4-12}$$

$$\begin{aligned}
f_{D,SLCmin} &= -\frac{2v_r}{\lambda} \cos(\varepsilon_v + \varepsilon_h) \quad [\varepsilon_v \leq -\varepsilon_h] \\
&= -\frac{2v_r}{\lambda} \quad [\varepsilon_v > -\varepsilon_h]
\end{aligned} \tag{5.4-13}$$

Figure 5.4-4 illustrates the notional shape of the sidelobe clutter range and Doppler bounds assuming purely horizontal motion ($\varepsilon_v = 0$). Table 5.4-2 lists the sidelobe clutter Doppler extent as a function of range for different ranges and heights, with $v_{ry} = 300$ m/s, $v_{rz} = 0$, and the radar frequency equal to 10 GHz ($\lambda = 3$ cm). The Doppler extent for each height rapidly approaches 40 kHz (± 20 kHz), corresponding to the upper and lower bounds of $\pm 2v_r/\lambda$.

FIGURE 5.4-4 ■ Sidelobe Clutter Range-Doppler Distribution.

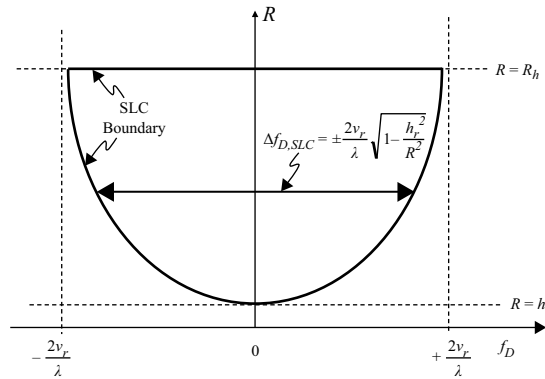


TABLE 5.4-2 ■ Example of Sidelobe Clutter Doppler Extent versus Range and Altitude

R (m)	Doppler Extent (Hz) per Aircraft Height h_r			
	$h_r = 500$ m ($R_h = 79.9$ km)	$h_r = 1,000$ m ($R_h = 112.9$ km)	$h_r = 2,000$ m ($R_h = 159.7$ km)	$h_r = 3,000$ m ($R_h = 195.6$ km)
600	22,111	0	0	0
1,100	35,629	16,664	0	0
2,100	38,850	35,174	12,196	0
3,100	39,476	37,862	30,562	10,078
5,000	39,799	39,192	36,661	32,000
10,000	39,950	39,799	39,192	38,158
20,000	39,987	39,950	39,799	39,547
50,000	39,998	39,992	39,968	39,928

* ($v_r = 300$ m/s; $v_z = 0$; $f_c = 10$ GHz)

The power in the sidelobe clutter spectrum at a given range is not uniformly distributed across all Doppler filters, being, of course, highly dependent on the radar antenna sidelobe pattern. We also note that the physical area of a clutter patch contained in a given Doppler bin increases in the vicinities of $\alpha = 0$ and $\alpha = \pm\pi$. To illustrate this, consider the variation in Doppler frequency Δf_D resulting from a small variation in azimuth $\Delta\alpha$:

$$\Delta f_D \cong \left| \frac{\partial f_D}{\partial \alpha} \Delta\alpha \right| = \left| \frac{\partial}{\partial \alpha} \left(\frac{2v_r}{\lambda} \cos(\epsilon) \cos(\alpha) \right) \Delta\alpha \right| = \left| -\frac{2v_r}{\lambda} \cos(\epsilon) \sin(\alpha) \Delta\alpha \right| \quad (5.4-14)$$

Rearranging terms, we see that the azimuth extent, and therefore the physical area, contained within a fixed Doppler interval is greatest in the regions near $\alpha = 0$ and $\alpha = \pm\pi$:

$$\left| \frac{\Delta\alpha}{\Delta f_D} \right| \cong \left| \frac{\lambda}{2v_r \cos(\epsilon) \sin(\alpha)} \right| \quad (5.4-15)$$

5.4.3 Mainlobe Clutter Range and Doppler Extent

5.4.3.1 Mainlobe Clutter-Range Extent

The mainlobe clutter extends in range from the intersection of the lower edge of the beam with the terrain to either the corresponding intersection of the upper edge of the

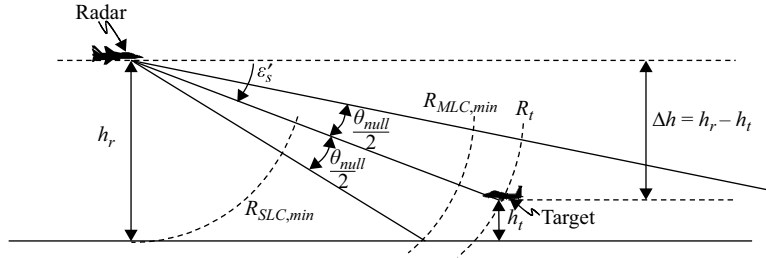


FIGURE 5.4-5 ■ Mainlobe Clutter Range Extent.

beam, if the entire beam illuminates the terrain, or the radar horizon, if the upper portion of the beam does not illuminate the terrain. Figure 5.4-5 illustrates the former condition.

The minimum mainlobe clutter range is

$$R_{MLC,min} = \frac{h_r}{\sin(\varepsilon'_s + \theta_{null}/2)} \quad (5.4-16)$$

The maximum mainlobe clutter range is

$$\begin{aligned} R_{MLC,max} &= \frac{h_r}{\sin(\varepsilon'_s - \theta_{null}/2)} \quad [(\varepsilon'_s - \theta_{null}/2) \geq \varepsilon'_h] \\ &= R_h \cong \sqrt{2r_e h_r} \quad [(\varepsilon'_s - \theta_{null}/2) < \varepsilon'_h] \end{aligned} \quad (5.4-17)$$

where from Equation 5.2-15, ε'_h is the depression angle to the radar horizon, $\varepsilon'_h = \sin^{-1}(h_r/R_h)$. The mainlobe clutter range extent is therefore

$$\begin{aligned} \Delta R_{MLC} &= \frac{2h_r \sin(\theta_{null}/2) \cos(\varepsilon'_s)}{\sin^2(\varepsilon'_s) - \sin^2(\theta_{null}/2)} \quad [(\varepsilon'_s - \theta_{null}/2) \geq \varepsilon'_h] \\ &= \sqrt{2r_e h_r} - \frac{h_r}{\sin(\varepsilon'_s + \theta_{null}/2)} \quad [(\varepsilon'_s - \theta_{null}/2) < \varepsilon'_h] \end{aligned} \quad (5.4-18)$$

(The form of the denominator in the preceding first equation is obtained by using the substitution $\cos^2(\theta_{null}/2) = 1 - \sin^2(\theta_{null}/2)$.) As an example, consider a radar at an altitude of $h_r = 3,000$ m, with a null-to-null beamwidth of $\theta_{null} = 7.5$ degrees, and an elevation scan angle of $\varepsilon_s = -15$ degrees. The range extent for this case (the entire mainbeam illuminates the terrain) is approximately 6,044 m, extending from 9,333 m to 15,377 m.

5.4.3.2 Mainlobe Clutter Doppler Extent

The Doppler shift of mainlobe clutter at the center of the mainbeam for a specific antenna scan angle ψ_s relative to the velocity vector is

$$f_{D,MLCctr} = \frac{2v_r \cos(\psi_s)}{\lambda} \quad (5.4-19)$$

To a first approximation, the mainlobe clutter Doppler extent is

$$\Delta f_{D,MLC} \cong \frac{2v_r}{\lambda} \left(\cos(\psi_s - \theta_{null}/2) - \cos(\psi_s + \theta_{null}/2) \right) \quad (5.4-20)$$

assuming a circular beam and $\psi_s > \theta_{null}/2$. Applying the identity $\cos(a+b) = \cos(a)\cos(b) - \sin(a)\sin(b)$ and using the approximation $\sin(\theta_{null}/2) \cong \theta_{null}/2$ for $\theta_{null}/2 \ll 1$ radian (as is always the case for this class of radar), we have

$$\Delta f_{D,MLC} \cong \frac{2v_r \sin(\psi_s) \theta_{null}}{\lambda} \quad (5.4-21)$$

(The same result may be obtained by multiplying the partial derivative of the Doppler shift with respect to scan angle by the mainlobe clutter angular extent in the plane of the scan angle.)

Note that the preceding expression yields zero extent for $\psi_s = 0$. Although the Doppler extent is indeed smaller for $\psi_s = 0$, it is not actually zero. For scan angles less than half the angular extent of the mainbeam, that is, $\psi_s < \theta_{null}/2$, the maximum Doppler shift does not occur at either edge of the beam but within the beam at angle $\psi = 0$, that is, the direction of the velocity vector. To account for this condition, the Doppler extent is more accurately expressed as

$$\begin{aligned} \Delta f_{D,MLC} &\cong \frac{2v_r \sin(\psi_s) \theta_{null}}{\lambda} \quad [\psi_s \geq \theta_{null}/2] \\ &\cong \frac{2v_r (1 - \cos(\psi_s) + \theta_{null}/2)}{\lambda} \quad [\psi_s < \theta_{null}/2] \end{aligned} \quad (5.4-22)$$

The preceding approximation is adequate for most conditions of interest and will be used in subsequent sections of this chapter.

In some cases, additional detail may be required to account for conditions in which the beam is not circular or does not fully illuminate the terrain or to capture the variation of Doppler extent with range. Such issues can be addressed by first modeling the mainbeam as an ellipse, using beamwidths $\theta_{null,az}$ and $\theta_{null,el}$, and scan angles α_s and ϵ'_s :

$$\frac{(\alpha - \alpha_s)^2}{(\theta_{null,az}/2)^2} + \frac{(\epsilon' - \epsilon'_s)^2}{(\theta_{null,el}/2)^2} = 1 \quad (5.4-23)$$

This allows us to express the azimuth extent, $\Delta\alpha$, at any depression angle within the beam as

$$\Delta\alpha \equiv 2|\alpha - \alpha_s| = \theta_{null,az} \sqrt{1 - \frac{(\epsilon' - \epsilon'_s)^2}{(\theta_{null,el}/2)^2}} \quad (5.4-24)$$

We can then determine the Doppler shift at each azimuth edge of the beam, $\alpha = \alpha_s \pm \Delta\alpha/2$, to determine the Doppler extent at a given depression angle. Finally, we use the relationship between range and depression angle, $\sin(\epsilon') = h_r/R$, to express the Doppler extent as a function of range rather than depression angle. This process yields a minimum mainlobe clutter Doppler shift at a given range of

$$f_{D,MLCmin,R} = \frac{2}{\lambda} \left(v_{ry} \sqrt{1 - (h_r/R)^2} \cos\left(|\alpha_s| + \frac{\Delta\alpha}{2}\right) - (v_{rz} h_r/R) \right) \quad (5.4-25)$$

and a maximum mainlobe clutter Doppler shift of

$$\begin{aligned}
 f_{D,MLCmax,R} &= \frac{2}{\lambda} \left(v_{ry} \sqrt{1 - (h_r/R)^2} \cos \left(|\alpha_s| - \frac{\Delta\alpha}{2} \right) - (v_{rz} h_r/R) \right) \quad \left[|\alpha_s| \geq \frac{\Delta\alpha}{2} \right] \\
 &= \frac{2}{\lambda} \left(v_{ry} \sqrt{1 - (h_r/R)^2} - (v_{rz} h_r/R) \right) \quad \left[|\alpha_s| < \frac{\Delta\alpha}{2} \right]
 \end{aligned} \tag{5.4-26}$$

where

$$\Delta\alpha = \theta_{null,az} \sqrt{1 - \frac{\left(\sin^{-1}(h_r/R) - \epsilon'_s \right)^2}{\left(\theta_{null,el}/2 \right)^2}} \tag{5.4-27}$$

It turns out that for most of the geometries and pulse-Doppler waveforms that we are considering, the potential benefits of such a detailed model are essentially negated by the effects of range folding of the mainlobe clutter, to be described in Section 5.8.

5.4.4 Altitude Return Range and Doppler Extent

5.4.4.1 Altitude Return Range Extent

The altitude return is a sidelobe clutter return from directly below the aircraft. It may be significant for low-flying aircraft because of the close proximity in range and the highly specular backscatter reflection path. The return is strongest at the point directly below the aircraft, where $R = h_r$. It turns out that even a small range extent $\Delta R = R - h_r$ (where $R > h_r$) encompasses a very large area on Earth's surface whose return may be much greater than targets of interest at longer range [3]. Although we treat it as a separate component to simplify the discussion, in fact it is generally part of a continuum of strong sidelobe returns that may occur along the elevation principle sidelobe plane between the mainbeam and the nadir direction (below the aircraft).

Figure 5.4-6 illustrates the geometry for the altitude return, assuming the flat-earth model. The ground range, R_G , is related to slant range through $R_G^2 = R^2 - h_r^2$ and to ΔR

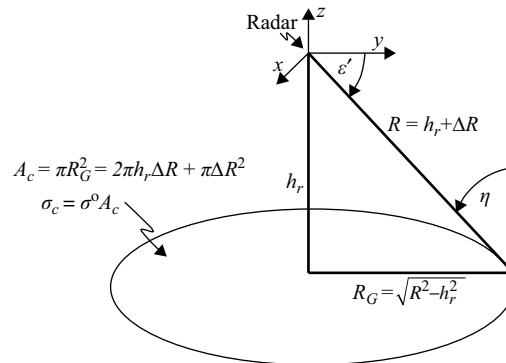


FIGURE 5.4-6 ■ Geometry of Altitude Return.

through $R_G^2 = 2\Delta R h_r + \Delta R^2$. The area on Earth's surface encompassed by the range extent ΔR is

$$A_c = \pi R_G^2 = 2\pi h_r \Delta R \left(1 + \frac{1}{2} \Delta R / h_r\right) \quad (5.4-28)$$

For $\Delta R / h_r \ll 1$, $A_c \cong 2\pi h_r \Delta R$. For example, at a radar height of 1,000 m, a range interval of 50 m (a nominal 3-MHz bandwidth), corresponding to $\Delta R / h_r = 5 \times 10^{-3}$, produces an area of +55.1 dBsm (approximately 300,000 m²). The backscatter coefficient for a given clutter type is highest at the near-zero angle of incidence geometry of the altitude return [4]. Values of σ° may be near 0 dB at such angles, for example. Thus, even with the two-way sidelobe antenna pattern attenuation of this return, the large RCS and close range cause the received power to be very strong relative to targets of interest.

With our flat-earth assumption, the angle of incidence, η , is related to the radar height and slant range through

$$\cos(\eta) = h_r / R \quad (5.4-29)$$

Since by definition $R = h_r + \Delta R$, we can also relate η to ΔR through

$$\cos(\eta) = (1 + \Delta R / h_r)^{-1} \quad (5.4-30)$$

The preceding expressions indicate that the greatest change of η for a given change of R occurs in the vicinity of $R = h_r$, or equivalently, $\eta = 0$, as relatively large changes in η result in relatively small changes in $\cos(\eta)$ in that region [3]. Another way of reaching this conclusion is by noting that the derivative of η with respect to R is maximum in the vicinity of $R = h_r$:

$$\frac{d\eta}{dR} = \frac{d}{dR} \left(\cos^{-1}(h_r / R) \right) = - \frac{1}{\sqrt{1 - (h_r / R)^2}} \frac{d}{dR} (h_r / R) = \frac{h_r}{R^2 \sqrt{1 - (h_r / R)^2}} \quad (5.4-31)$$

Continuing the preceding example, the 50-m range interval corresponds to an angle of incidence of $\eta = 17.8^\circ$. Thus, even a relatively small range interval begins to include scattering angles that depart significantly from the peak- σ° specular condition [4].

The nominal range extent of the altitude return is taken to be the radar range resolution:

$$\Delta R_{ALT} \cong \delta_R \quad (5.4-32)$$

This is the smallest range interval achievable by the radar, and contains the range-Doppler region in which the clutter power is most concentrated. As range increases beyond this region, the clutter energy is spread over a greater number of Doppler filters, σ° declines from its peak value at $\eta = 0$, and the range loss of R^{-3} (see Section 5.4.2.1) eventually becomes significant.

5.4.4.2 Altitude Return Doppler Extent

The range extent $\Delta R_{ALT} \cong \delta_R$ has associated with it a Doppler spread due to the variation in depression angle within that interval. We can determine the Doppler extent

and center frequency of the altitude clutter return through an analogous approach to that used for sidelobe clutter in Section 5.4.2. The Doppler extent within range interval ΔR_{ALT} is

$$\Delta f_{D,ALT} = \pm \frac{2v_{ry}}{\lambda} \sqrt{1 - \frac{h_r^2}{(h_r + \Delta R_{ALT})^2}} \quad (5.4-33)$$

centered at the Doppler frequency from the point directly below the aircraft

$$\Delta f_{D,ALT,ctr} = -\frac{2v_{rz}}{\lambda} \quad (5.4-34)$$

Using the approximation $\Delta R_{ALT} = \delta_R$ from the preceding discussion and assuming $\delta_R \ll h_r$, the Doppler extent can be written as

$$\Delta f_{D,ALT} = \pm \frac{2v_{ry}}{\lambda} \sqrt{\frac{2h_r\delta_R + \delta_R^2}{(h_r + \delta_R)^2}} \cong \pm \frac{2v_{ry}}{\lambda} \sqrt{\frac{2\delta_R}{h_r}} \quad (5.4-35)$$

Table 5.4-3 lists values of the altitude Doppler extent for different combination of range resolution and aircraft altitude, assuming the radar is flying horizontally at 300 m/s and is operating at a frequency of 10 GHz. (The values are computed from the exact expression in 5.4-35 rather than the approximation.) A 50-m resolution and 1,000-m aircraft height, as in the preceding example, results in a Doppler spread of $\pm 6,098$ Hz. This is fairly significant, considering the relatively narrow range bin chosen. Even a very small range extent produces a large variation in depression angle, as the slope of $\cos(\epsilon')$ in the expression for Doppler shift is at a maximum for $\epsilon' = 90^\circ$ [3]. The Doppler spectrum power is at a maximum for $f_{D,ALT,ctr}$ and falls off over the Doppler extent $\pm f_{D,ALT}/2$.

TABLE 5.4-3 ■ Altitude Return Doppler Extent versus Range Resolution and Altitude*

δ_R (m)	Doppler Extent (Hz) versus Radar Height					
	300 m	500 m	1,000 m	2,000 m	3,000 m	5,000 m
30	$\pm 8,332$	$\pm 6,633$	$\pm 4,792$	$\pm 3,426$	$\pm 2,807$	$\pm 2,181$
50	$\pm 10,302$	$\pm 8,332$	$\pm 6,098$	$\pm 4,390$	$\pm 3,607$	$\pm 2,807$
150	$\pm 14,907$	$\pm 12,779$	$\pm 9,876$	$\pm 7,339$	$\pm 6,098$	$\pm 4,792$
300	$\pm 17,321$	$\pm 15,612$	$\pm 12,779$	$\pm 9,876$	$\pm 8,332$	$\pm 6,633$

* $v_{ry} = 300$ m/s; $f_c = 10$ GHz.

5.4.5 Summary of Range-Doppler Clutter Distribution

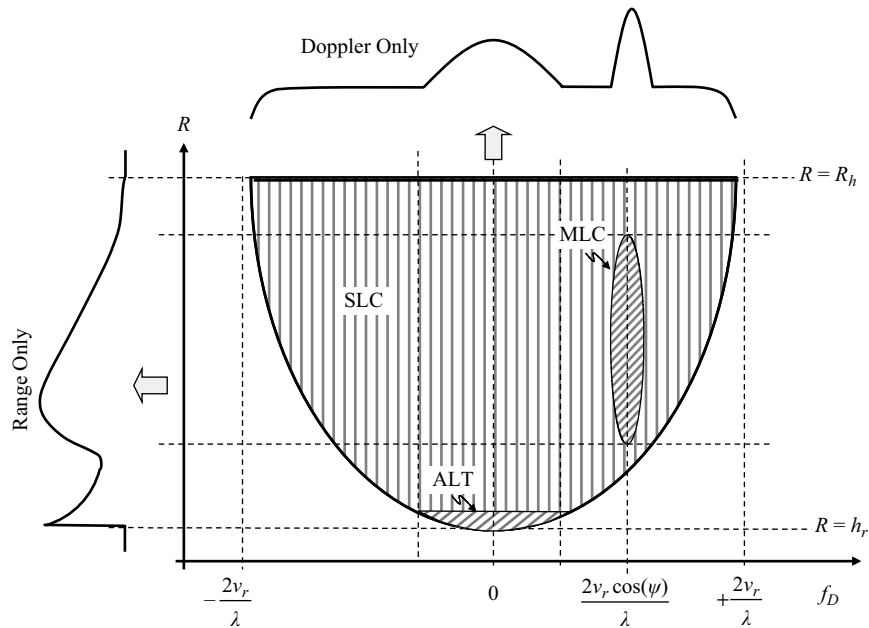
The approximate range and Doppler extents of the various clutter components for the case of purely horizontal flight are summarized in Table 5.4-4. From these relationships, we are able to plot the range-Doppler boundaries of each clutter component, as illustrated conceptually in Figure 5.4-7. Collapsing the two-dimensional plot into either the range or Doppler axis yields the familiar one-dimensional clutter profile for either a range-only or Doppler-only radar.

TABLE 5.4-4 ■ Approximate Range and Doppler Extents of Clutter Components

	Minimum Range (R_{min})	Maximum Range (R_{max})	Center Doppler ($f_{D,ctr}$)	Doppler Extent (Δf_D)
SLC	h_r	$R_h (\cong \sqrt{2r_e h_r})$	0	$\pm \frac{2v_r}{\lambda} \sqrt{1 - \frac{h_r^2}{R^2}}$ (1) $\pm \frac{2v_r}{\lambda}$ (2)
MLC	$\frac{h_r}{\sin(\epsilon'_s + \frac{\theta_{null}}{2})}$	$\frac{h_r}{\sin(\epsilon'_s - \frac{\theta_{null}}{2})}$ (3) $R_h (\cong \sqrt{2r_e h_r})$ (4)	$\frac{2v_r \cos(\psi_s)}{\lambda}$	$\frac{2v_r \sin(\psi_s) \theta_{null}}{\lambda}$ (2)
ALT	h_r	$h_r + \delta_R$	0	$\pm \frac{2v_r}{\lambda} \sqrt{\frac{2\delta_R}{h_r}}$

Notes: (1) Shows variation with range; (2) over entire range extent; (3) entire beam illuminates terrain; (4) upper edge of beam above horizon.

FIGURE 5.4-7 ■ Range-Doppler Distribution of Clutter Components.



5.5 | CONTOURS OF CONSTANT DOPPLER AND RANGE

5.5.1 Iso-Doppler Contours

The Doppler shift from a stationary clutter return at angle ψ relative to the radar velocity vector is proportional to $\cos(\psi)$. Any stationary scatterer at the same angle will have the same Doppler shift. This condition is satisfied for all points on the surface of a right circular cone of half-angle ψ whose vertex is located at the radar and whose axis is coincident with the velocity vector. (More precisely, a cone has two nappes, and the

preceding condition is satisfied by the nappe that projects forward.) The intersection of such a cone with Earth's surface for our flat-earth model is a conic section; this defines a locus of points with constant Doppler shift. Expressing this formulaically, every stationary scatterer whose position vector \vec{R} satisfies the equation $\vec{v}_r \bullet \vec{R} = v_r R \cos(\psi)$ will have the same Doppler shift $f_D = -2v_r \cos(\psi)/\lambda$, for a given angle ψ . Writing \vec{R} and \vec{v}_r in terms of their x -, y -, and z -components, this condition is

$$\vec{v}_r \bullet \vec{R} = \sqrt{v_{rx}^2 + v_{ry}^2 + v_{rz}^2} \sqrt{R_x^2 + R_y^2 + R_z^2} \cos(\psi) = v_{rx}R_x + v_{ry}R_y + v_{rz}R_z \quad (5.5-1)$$

Our coordinate system is defined such that the direction of motion is in the yz plane ($v_{rx} = 0$), and we use the flat-earth approximation with the radar at height h_r ($R_z = -h_r$). Squaring both sides of the preceding equation and rearranging terms yields

$$\frac{\left(v_{ry}^2 - v_r^2 \cos^2(\psi)\right)R_y^2 - 2v_{ry}v_{rz}h_rR_y - v_r^2 \cos^2(\psi)R_x^2}{h_r^2 \left(v_r^2 \cos^2(\psi) - v_{rz}^2\right)} = 1 \quad (5.5-2)$$

This is a quadratic relationship that allows one of the two unknown parameters, R_x or R_y , to be expressed in terms of the other. If we apply a further constraint that the aircraft is flying horizontally, that is, $v_{rz} = 0$, then the preceding expression simplifies to

$$\frac{R_y^2}{h_r^2 \cot^2(\psi)} - \frac{R_x^2}{h_r^2} = 1. \quad (5.5-3)$$

The conic section in this special case is a hyperbola whose positive branch ($R_y > 0$) corresponds to positive Doppler frequencies ($-90^\circ < \psi < +90^\circ$), and whose negative branch ($R_y < 0$), negative Doppler frequencies ($+90^\circ < \psi < 270^\circ$). The vertex of the positive branch is at $[0, h_r \cot(\psi), -h_r]$, and the focus is at $(0, h_r/\sin(\psi), -h_r)$.

Figure 5.5-1 illustrates contours of constant Doppler, or iso-Doppler contours, corresponding to hyperbolas formed by the intersection of various conic surfaces with a

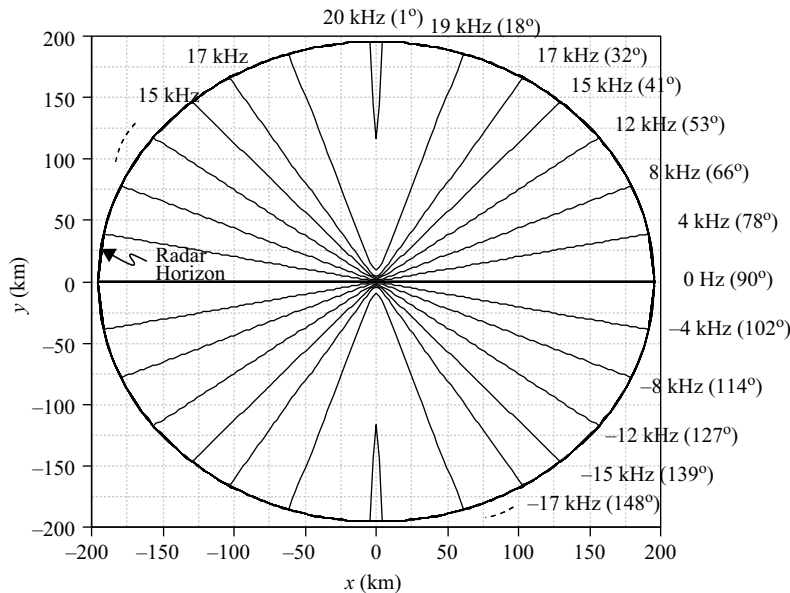
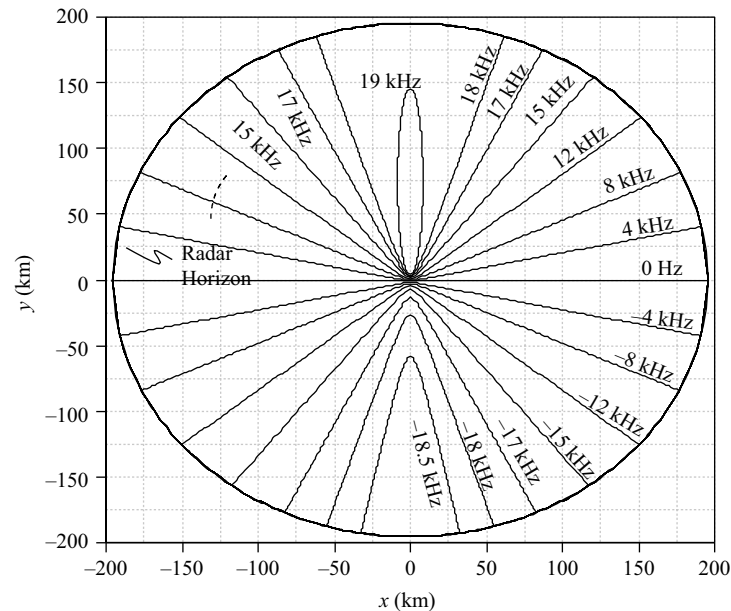


FIGURE 5.5-1 ■ Iso-Doppler Contours for Purely Horizontal Velocity ($v_{ry} = 300$ m/s; $v_{rz} = 0$; $f_c = 10$ GHz).

horizontal (flat-earth) surface for a 10-GHz radar flying with a purely horizontal velocity $v_{ry} = 300$ m/s. The broader the hyperbola, the lower the Doppler shift. Notice that the surface area per unit frequency increases as the frequency gets further from zero. This is most evident near the edges of the spectrum where the area contained in the 1-kHz interval between 19 kHz and 20 kHz (or -19 kHz and -20 kHz) is much greater than the 4-kHz interval between 0 Hz and 4 kHz (or 0 Hz and -4 kHz).

The Doppler contours are symmetric about the $y = 0$ line for the purely horizontal velocity shown in figure. This symmetry is not preserved if there is a vertical component to the velocity, however. Figure 5.5-2 shows an example of this in which the 300 m/s radar velocity includes both a horizontal component, $v_{ry} = 283$ m/s, and a vertical component, $v_{rz} = -100$ m/s. The curves are no longer hyperbolas because the velocity vector is no longer parallel with Earth. The 19-kHz contour results from the entire cone, of half-angle 18 degrees, intersecting Earth's surface.

FIGURE 5.5-2 ■ Iso-Doppler Contours for Velocity with a Vertical Component ($v_{ry} = 283$ m/s; $v_{rz} = -100$ m/s; $f_c = 10$ GHz).



5.5.2 Iso-Range Contours

Contours of constant range are more intuitively obvious. All points on the surface of a sphere centered at the radar are by definition equally distant from the radar. The locus of points corresponding to the intersection of such a sphere with the surface of Earth describes a contour of constant range. For the flat-earth approximation, the iso-range contours correspond to concentric circles on the $z = -h_r$ plane, centered at the point directly below the aircraft $(0, 0, -h_r)$, with radius $R_G = \sqrt{R^2 - h_r^2}$, where R_G is the ground range. Figure 5.5-3 adds iso-range contours to the iso-Doppler contours of Figure 5.5-1. The range rings in the figure correspond to integer multiples of 30-km slant range.

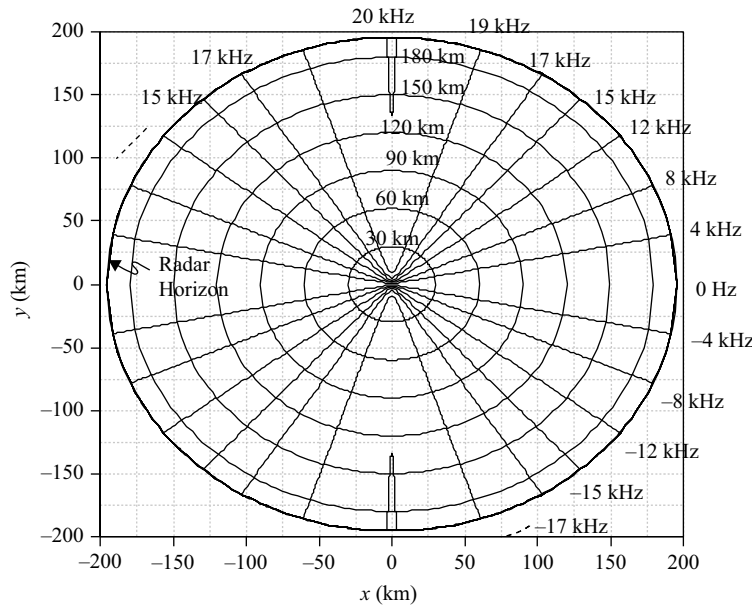


FIGURE 5.5-3 ■ 30-km Iso-Range Contours with Iso-Doppler Contours ($v_{ry} = 300$ m/s; $v_{rz} = 0$; $f_c = 10$ GHz).

5.6 | EXAMPLE SCENARIO

We will consider an example scenario to illustrate the range-Doppler distribution of clutter in relation to various types of targets. The scenario is a variation of that used in [1]. An airborne radar is at a height of $h_r = 3,000$ m and is flying with a purely horizontal velocity of $v_r = 300$ m/s. Its operating frequency is $f_c = 10$ GHz, corresponding to a wavelength of $\lambda = 0.03$ m, and its range resolution is $\delta_R = 150$ m, corresponding to a pulse width (or compressed pulse width if applicable) of $\tau = 1$ μ s. The antenna beam has a 3-dB width of $\theta_{3\text{dB}} = 3^\circ$ and is steered to azimuth $\alpha_s = 45^\circ$ and elevation $\epsilon_s = -2^\circ$, resulting in a scan angle relative to the velocity vector of $\psi_s \cong 45^\circ$ [since $\cos(\psi_s) = \cos(\epsilon_s) \cos(\alpha_s)$].

We can estimate the boundaries of the sidelobe clutter, mainlobe clutter, and altitude return through the expressions derived in the Section 5.4 and summarized in Table 5.4-4. Table 5.6-1 contains the results of the clutter extent computations. The sidelobe clutter begins at the radar height and extends to the radar horizon; for the 3,000-m radar height, the radar horizon is approximately $R_h = (2 \times 6,780 \text{ km} \times 3 \text{ km})^{1/2} = 195.6$ km. The sidelobe clutter Doppler extent is within the bounds of ± 20 kHz. The mainlobe clutter lies within the null-to-null beamwidth $\theta_{null} \cong 2.5 \times \theta_{3\text{dB}} = 7.5^\circ$. The

TABLE 5.6-1 ■ Summary of Clutter Extents for Example Scenario

Clutter Component	Range (m)				Doppler (Hz)			
	Minimum	Maximum	Center	Extent	Minimum	Maximum	Center	Extent
SLC	3,000	195,622	99,311	192,622	-20,000	20,000	0	40,000
MLC	29,815	195,622	84,906	165,807	13,207	15,059	14,133	1,852
ALT	3,000	3,150	3,075	150	-6,325	6,325	0	12,649

boundary of the null-to-null mainlobe footprint on the terrain begins at a range of approximately 30 km and extends to the radar horizon, as the upper portion of the mainbeam is above the horizon. The total mainlobe clutter Doppler extent is 1.85 kHz. The altitude return is assumed to fall within the first range-resolution cell and has a Doppler extent of ± 6.3 kHz.

Let us add to the scenario six objects, referred to generically as targets. Target 1 is a fast inbound aircraft; Target 2 a slow inbound aircraft; Target 3 a slow outbound aircraft; Target 4 a fast outbound aircraft; Target 5 a ground-moving vehicle; and Target 6 a large clutter discrete such as a water tower. Targets 1–5 are conveniently arranged to all fall in the mainbeam simultaneously, while Target 6 is in the radar antenna sidelobe. To keep things simple, all motion is parallel to the y direction.

Table 5.6-2 lists the target positions, velocities, and derived parameters. The table lists height above Earth's surface instead of the z coordinate; the two are related through $z = h - h_r$, with $h_r = 3,000$ m in this case. The range to each target relative to the radar is found from its Cartesian coordinates:

$$R = \sqrt{R_x^2 + R_y^2 + R_z^2} = \sqrt{x^2 + y^2 + z^2} \quad (5.6-1)$$

The range rate of each target includes the contribution from the radar motion, $-\vec{v}_r \cdot \hat{\mathbf{R}}$, and the contribution from the target motion, $\vec{v}_t \cdot \hat{\mathbf{R}}$, where $\hat{\mathbf{R}} \equiv \mathbf{R}/R$:

$$\begin{aligned} v_R &= \vec{v}_t \cdot \hat{\mathbf{R}} - \vec{v}_r \cdot \hat{\mathbf{R}} = \frac{(v_{tx}x + v_{ty}y + v_{tz}z)}{R} - \frac{(v_{rx}x + v_{ry}y + v_{rz}z)}{R} \\ &= \frac{(v_{tx} - v_{rx})x + (v_{ty} - v_{ry})y + (v_{tz} - v_{rz})z}{R} \end{aligned} \quad (5.6-2)$$

For example, the range to Target 1 is $[(35 \text{ km})^2 + (35 \text{ km})^2 + (3 \text{ km} - 1.25 \text{ km})^2]^{1/2} = 49.5$ km. The range rate of Target 1 is $(-400 \text{ m/s} - 300 \text{ m/s}) \times (35 \text{ km}/49.5 \text{ km}) = (-700 \text{ m/s}) \times (0.707) = -495$ m/s.

The corresponding Doppler shift is $-2 \times (-495 \text{ m/s})/(0.03 \text{ m}) = +32,978$ Hz.

Figures 5.6-1 and 5.6-2 depict the projection of the scenario onto the xy plane, with the aircraft moving in the positive y direction. The outline of the mainbeam footprint on the flat-earth surface is also shown. Figure 5.6-3 depicts the corresponding true range-Doppler map of the scenario.

The figures and tables indicate that neither mainlobe clutter nor the altitude return overlaps with any of the airborne targets (Targets 1–4) in both range and Doppler simultaneously. As these are the strongest sources of clutter interference, this suggests that each target has the potential to be detected in some pulse-Doppler mode. Only Target 1, the fast, inbound aircraft, is completely outside the sidelobe clutter Doppler region, however. Although Target 2 is also an inbound target, its Doppler shift is within the sidelobe clutter bounds because of its slower velocity (100 m/s versus 400 m/s for Target 1) and the relatively large scan angle (45°); its range rate is less than that of sidelobe clutter returns, which are more in line with the radar direction of motion.

Target 3, the slow outbound aircraft, has a positive Doppler shift because its velocity is less than the radar's (100 m/s versus 300 m/s for the radar), and, therefore, the radar is overtaking the target: the range is decreasing with time, and the Doppler shift is positive. Target 4, the fast outbound target, has a negative Doppler shift because its

TABLE 5.6-2 ■ Parameters of Targets in Example Scenario

Object	x (km)	y (km)	h (km)	v_x (m/s)	v_y (m/s)	v_z (m/s)	ε (°)	α (°)	ψ (°)	R (km)	v_R (m/s)	f_D (Hz)
Target 1 (fast inbound)	35.0	35.0	1.25	0	-400	0	-2.0	45.0	45.0	49.5	-495	32,978
Target 2 (slow inbound)	40.0	40.0	1.00	0	-100	0	-2.0	45.0	45.0	56.6	-283	18,844
Target 3 (slow outbound)	45.0	45.0	0.75	0	100	0	-2.0	45.0	45.0	63.7	-141	9,422
Target 4 (fast outbound)	50.0	50.0	0.50	0	400	0	-2.0	45.0	45.0	70.8	71	-4,711
Target 5 (ground vehicle)	60.0	60.0	0.00	0	-30	0	-2.0	45.0	45.0	84.9	-233	15,547
Target 6 (water tower)	0.0	5.0	0.00	0	0	0	-31.0	0.0	31.0	5.8	-257	17,150

FIGURE 5.6-1 ■ Example Scenario with Five Mainlobe Targets Plus Sidelobe Clutter Discrete.

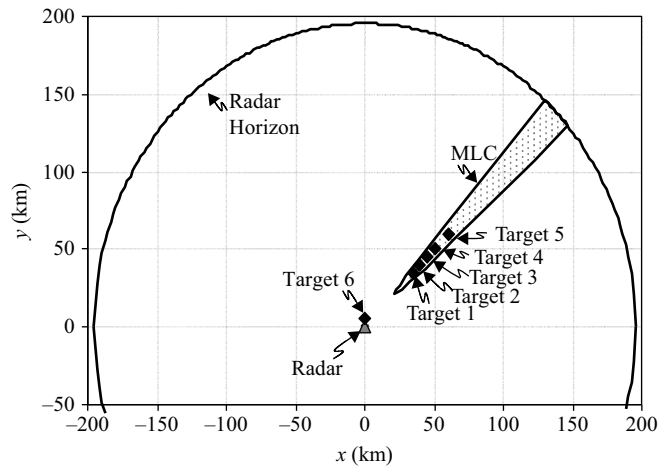


FIGURE 5.6-2 ■ Close-up of Example Scenario Geometry.

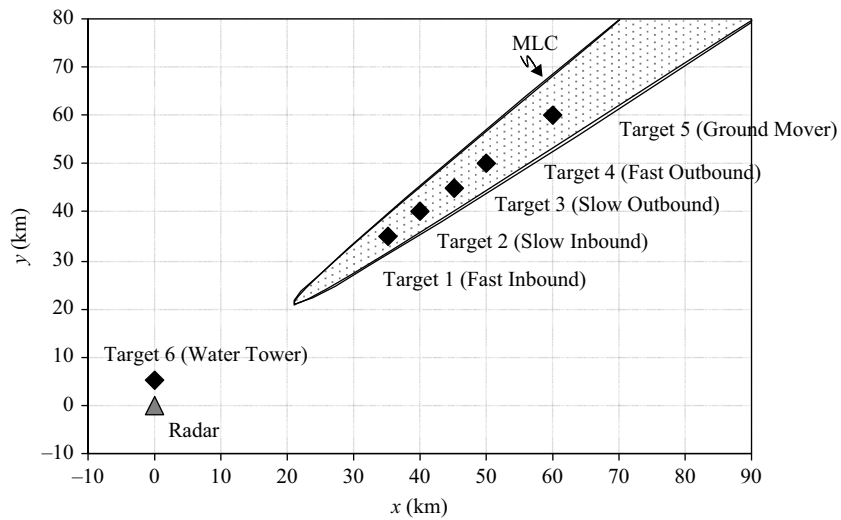
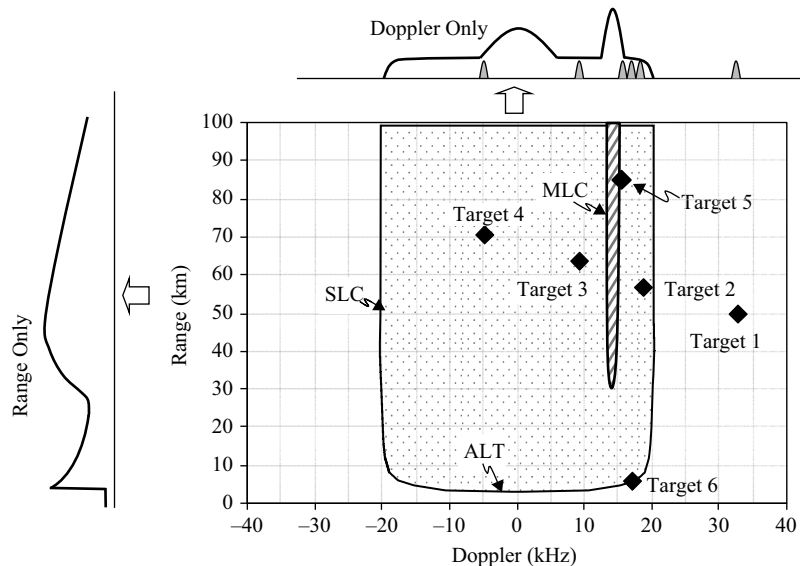


FIGURE 5.6-3 ■ Example Scenario of True Range-Doppler Map.



speed is greater than the radar's, and the radar is therefore losing ground to it: the range and range rate are increasing, and the Doppler shift is negative. Target 5, the ground-moving vehicle, is just off the edge of the mainlobe clutter; its velocity of 30 m/s (approximately 67 mph) produces a Doppler shift of $2 \text{ kHz} \times \cos(45^\circ) = 1.4 \text{ kHz}$, slightly more than half the nominal mainlobe clutter Doppler extent.

The water tower in the sidelobe, Target 6, lies along the sidelobe clutter boundary because it is at the same azimuth ($\alpha = 0^\circ$) as the aircraft velocity vector. At any given sidelobe clutter range, the 0° azimuth corresponds to the right-hand (most positive) Doppler boundary of the sidelobe clutter. As the magnitude of the azimuth increases, the Doppler moves to the left. At $\pm 90^\circ$ azimuth, the Doppler is exactly in the center, that is, at zero. As the magnitude of the azimuth increases beyond 90° , the Doppler continues moving toward the left, producing negative Doppler, until it reaches the left-hand boundary at 180° , corresponding to the most negative Doppler. Positions within the mainlobe clutter can be interpreted in a similar manner.

5.7 | PULSE-DOPPLER CONCEPTUAL APPROACH

5.7.1 Pulsed versus CW Operation

One of the main reasons that pulse-Doppler is used instead of CW Doppler for airborne radar applications is to improve transmit–receive (T/R) isolation. The target-clutter Doppler spectrum shown in Figure 5.4-1 suggests that a CW Doppler radar could potentially detect moving targets of sufficiently high range rate. Such a conclusion presumes that the radar can receive and transmit simultaneously, however. To determine the limits of such operation, suppose that a radar requires a minimum received signal power of S_{min} to achieve the necessary SNR for detection and that it has a requirement to detect a target of RCS σ at range R . The minimum received signal power is

$$S_{min} = \frac{P_{t,min} G^2 \lambda^2 \sigma}{L_s (4\pi)^3 R^4} \quad (5.7-1)$$

where $P_{t,min}$ is the minimum transmitter power, G is the radar antenna gain (assumed equal for transmit and receive), and L_s represents system losses that are not present in the transmit-leakage path. This expression can be solved for $P_{t,min}$ to determine the transmitter power required to produce S_{min} .

The minimum isolation needed to reduce the leakage power to S_{min} is the ratio of $P_{t,min}/S_{min}$:

$$I_{min} = \frac{P_{t,min}}{S_{min}} = \frac{L_s (4\pi)^3 R^4}{G^2 \lambda^2 \sigma} \quad (5.7-2)$$

Let us consider an example corresponding to a fairly modest requirement: $G = 35 \text{ dBi}$, $\lambda = .03 \text{ m}$ ($f_c = 10 \text{ GHz}$), $L_s = 2 \text{ dB}$, $\sigma = 10 \text{ m}^2$, and $R = 50 \text{ km}$. The isolation needed for this case is approximately 173 dB. Isolation in a CW radar can be achieved either spatially or spectrally. Spatial isolation achieved through the use of separate transmit and receive antennas is not an attractive option for most airborne radars (especially tactical size) due to limited space. For monostatic operation, a good circulator can provide approximately 25 dB isolation at best, leaving another 148 dB to be achieved spectrally.

Aside from the receiver dynamic range implications, which are also a limiting factor, this requires heroic filtering and extremely low oscillator phase noise, both well beyond the limits of available technology. To circumvent this problem, a pulse-Doppler radar achieves the requisite isolation temporally, using pulsed transmissions and performing the receive function only during the transmitter-off intervals.

In addition to the isolation improvement, pulse-Doppler modes typically provide superior range accuracy and resolution than CW radar, particularly in medium PRF mode.

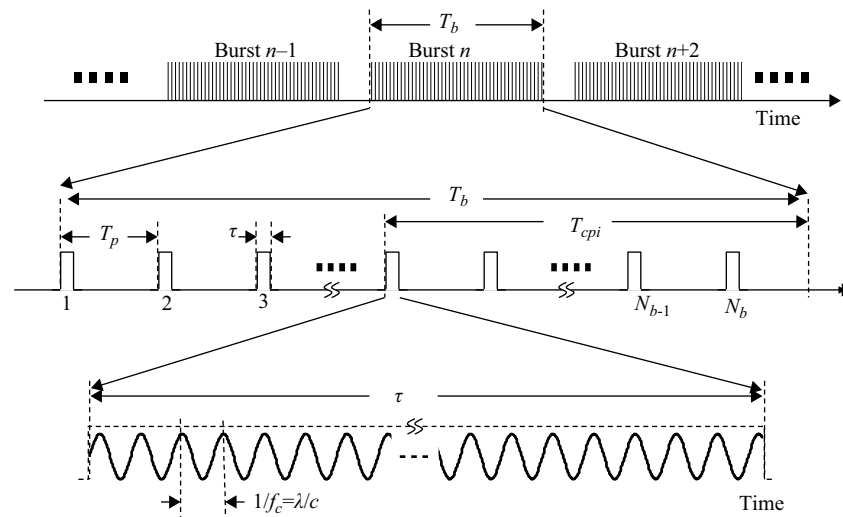
5.7.2 Pulse-Doppler Waveform

The pulse-Doppler waveform consists of a burst of N_b pulses with a constant pulse width of τ and a constant PRF of f_p , or, equivalently, a constant pulse repetition interval (PRI) of $T_p = f_p^{-1}$, as illustrated in Figure 5.7-1. This pulse modulation provides an envelope of an underlying RF carrier of frequency f_c and wavelength λ that is coherent over the duration of the pulse burst. (The figure shows a simple pulse without any intrapulse modulation.)

The radar receives and processes N_p PRIs, with $N_p < N_b$. The duration of the transmit burst is $T_b = N_b T_p$; the duration of the received and processed portion of this burst is $T_{cpi} = N_p T_p$, with T_{cpi} referred to as the coherent-processing interval (CPI). The radar receiver–signal processor divides all or a portion of the time between successive transmit pulses into M_R range gates, or range bins, as illustrated in Figure 5.7-2. The range bins have a nominal width of the radar range resolution, that is, $\Delta R_{bin} \cong \delta_R \cong c/2B$, where B is the waveform bandwidth, and, in the absence of pulse compression, $B \cong \tau^{-1}$. The received signal in each range gate is integrated over the N_p pulses of the CPI to form some number N_D of narrowband Doppler filters. The signal processor thus forms an $M_R \times N_D$ range-Doppler matrix, or map, of the received signals for subsequent processing.

Figure 5.7-3 illustrates the time domain and frequency domain of a coherent pulse train. The spectral characteristics are directly related to the temporal characteristics. The

FIGURE 5.7-1 ■
Pulse-Doppler
Waveform.



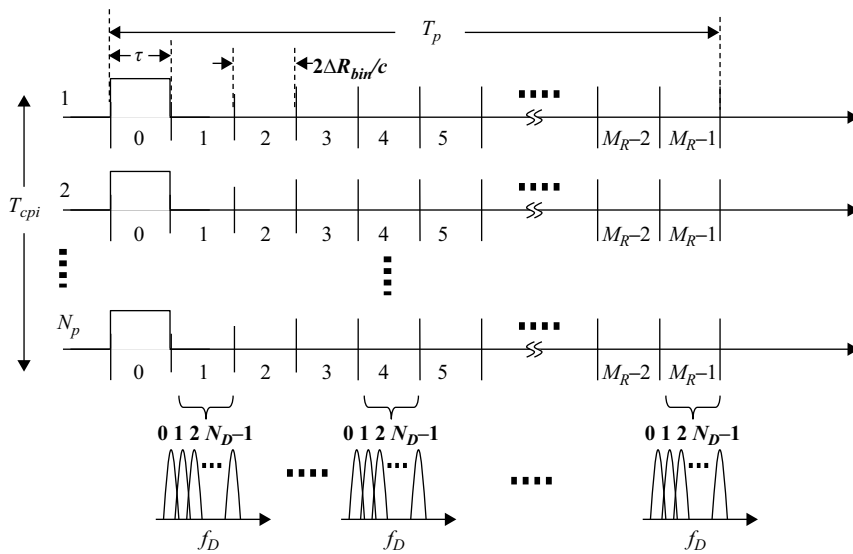


FIGURE 5.7-2 ■ Range Gates and Doppler Filters.

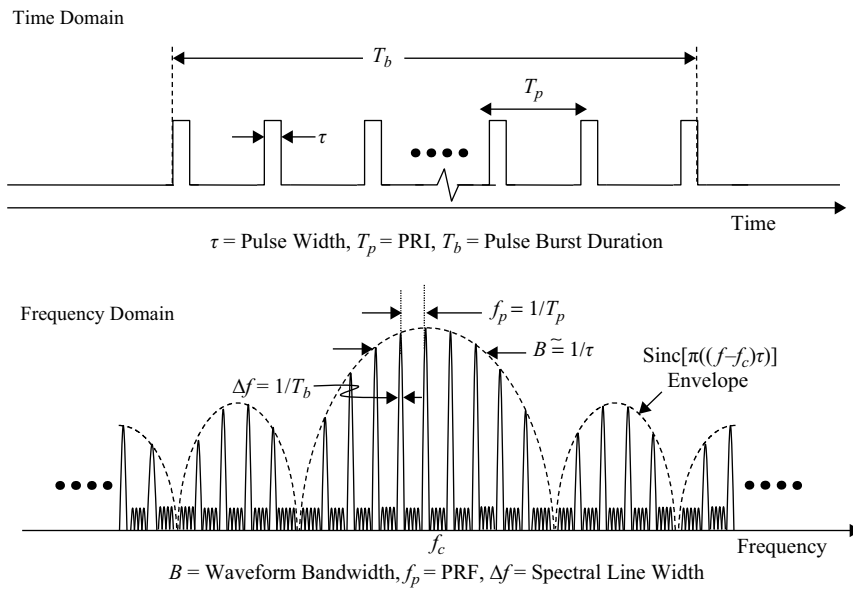
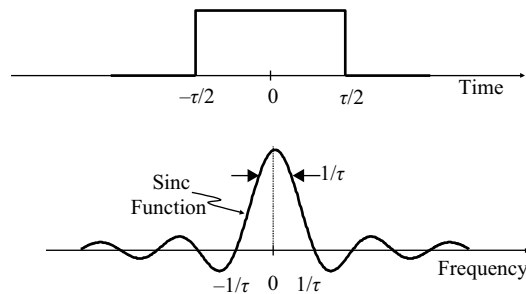


FIGURE 5.7-3 ■ Coherent Pulse Train Spectrum.

entire spectrum falls within an envelope whose half-power (actually -4 dB) width is approximately the inverse of the pulse width. This relationship is seen by taking the Fourier transform of a rectangular pulse of duration τ , illustrated in Figure 5.7-4, resulting in a $\sin(a)/a$, or $\text{sinc}(a)$, spectrum. For a duty cycle of $d = \tau/T_p = \tau f_p$, the bandwidth of the spectrum is approximately $\tau^{-1} = f_p/d$.

The spectrum in Figure 5.7-3 contains multiple peaks that are located at integer multiples of the PRF, or the inverse of the PRI. Each peak has a Doppler extent as well, with a half-power width approximately equal to the inverse of the duration of the coherent pulse train. There are approximately $1 + d^{-1}$ such peaks within the half-power width f_p/d of the spectrum. For example, a 25-percent duty factor implies five PRF lines within that interval.

FIGURE 5.7-4 ■
The Sinc-Shaped
Spectrum of a
Rectangular Pulse.

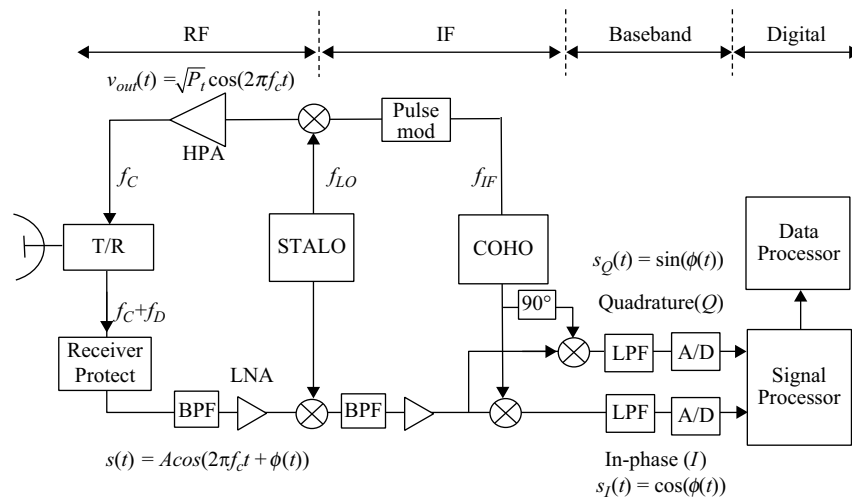


(a) Rectangular Pulse Time and Frequency.

$$\begin{aligned}
 F(\omega) &= \int_{-\tau/2}^{\tau/2} A e^{-j\omega t} dt \\
 &= \frac{A}{-j\omega} (e^{-j\omega\tau/2} - e^{+j\omega\tau/2}) \\
 &= \frac{A}{-j\omega} (-2j \sin(\omega\tau/2)) \\
 &= A\tau \left[\frac{\sin(\omega\tau/2)}{(\omega\tau/2)} \right]
 \end{aligned}$$

(b) The Fourier Transform of a
Rectangular Pulse.

FIGURE 5.7-5 ■
Pulse-Doppler
Radar Conceptual
Block Diagram.



5.7.3 Overview of Operation

Figure 5.7-5 depicts a conceptual block diagram of a pulse-Doppler radar. A *coherent oscillator* (COHO) provides a reference signal at frequency f_{IF} that is upconverted to the radar transmit frequency f_c by mixing with a *stable local oscillator* (STALO) at frequency f_{LO} such that $f_c = f_{IF} + f_{LO}$. Although the figure shows a single *intermediate frequency* (IF), it is common for a pulse-Doppler radar to employ multiple IF stages for the frequency translation. The carrier frequency is pulse modulated to provide the desired pulse width and PRI, amplified by a high-power amplifier to a transmit power of P_t , and radiated out the antenna after passing through a T/R switch or duplexer. The figure depicts a centralized transmit amplifier, such as a traveling wave tube amplifier for simplicity, but many modern systems employ active electronically scanned arrays in which the amplifier and T/R functions are implemented at the array element level. The transmitter configuration shown in Figure 5.7-5 is referred to as a *master oscillator power amplifier* implementation: The high power output is generated by amplifying an independently generated RF signal that is phase coherent from pulse to pulse. Traveling wave tube, klystron, and solid-state amplifiers provide this capability, in contrast to

magnetron transmitters for which RF is generated during the pulsing excitation and that lack interpulse phase coherence.

A signal received through the antenna from a particular scatterer has a frequency $f_c + f_D$ due to the Doppler shift imparted by the relative motion of the scatterer, where $\phi(t) = 2\pi f_D t$ in the figure. The RF signal is down converted using the same STALOs and COHO that were used for up-conversion of the transmit signal. Because these oscillators maintain phase coherence over the entire pulse burst, the variation in relative phase between the transmit and receive signals contains information about the relative motion between the radar and the target.

The received signal is eventually split and mixed with two different samples of the COHO, one having a 90° insertion phase ($\pi/2$ radians) relative to the other. (Alternatively, one of the signal paths may be subjected to the 90° phase shift, and the COHO samples would be in phase with each other.) The two channels, one in phase (I) and the other quadrature phase (Q), are then mixed to a baseband frequency at which point any residual phase variation with time is attributable to the Doppler shift of the received signal. The I and Q channels are low-pass filtered to eliminate LO leakage and higher-frequency mixing products. The filtered signals are sampled by an analog-to-digital (A/D) converter, and the digital samples are passed to the digital signal processor (DSP) for Doppler processing. Although we are considering the most common case in which range gating and Doppler filtering are performed by the A/D sampling and DSP, these functions have also been performed through analog means in some older pulse-Doppler systems. On the other hand, many newer radars do not use analog I and Q channels. Instead A/D conversion takes place at the final IF with the subsequent I/Q baseband conversion and low-pass filtering being performed digitally.

5.7.4 Synchronous Detection

The combination of the final mixer and low-pass filter (LPF) is referred to as a *synchronous detector* because it detects the relative phase, ϕ_{rcv} , between the input signal and reference oscillator. (We are ignoring thermal noise and other interference in this discussion.) The output of the final mixer in the I channel, $s_I(t)$, can be approximated as the product of the input signal with the COHO reference:

$$\begin{aligned} s_I(t) &= \cos(2\pi f_{IF}t + \phi_{rcv}) \cos(2\pi f_{IF}t) \\ &= \frac{1}{2} [\cos(\phi_{rcv}) + \cos(4\pi f_{IF}t + \phi_{rcv})] \end{aligned} \quad (5.7-3)$$

where we have applied the trigonometric identities $\cos(a+b) = \cos(a)\cos(b) - \sin(a)\sin(b)$ and $\cos^2(a) = \frac{1}{2}(1 + \cos(2a))$. Use of the identity $\cos(a - \pi/2) = \sin(a)$ in the preceding equation readily yields an analogous expression for the Q channel output:

$$\begin{aligned} s_Q(t) &= \cos\left(2\pi f_{IF}t + \phi_{rcv} - \frac{\pi}{2}\right) \cos(2\pi f_{IF}t) \\ &= \frac{1}{2} [\sin(\phi_{rcv}) + \sin(4\pi f_{IF}t + \phi_{rcv})] \end{aligned} \quad (5.7-4)$$

Each channel has a term whose argument, $(4\pi f_{IF}t + \phi_{rcv})$, that corresponds to a frequency that is twice the final IF. This component and any LO leakage are rejected by

the low-pass filter. Choosing the gain of the LPF to equal 2 for the sake of simplicity, the resulting filtered I- and Q-channel outputs are

$$s_{I,LPF}(t) = \cos(\phi_{rcv}) \quad (5.7-5)$$

$$s_{Q,LPF}(t) = \sin(\phi_{rcv}) \quad (5.7-6)$$

The LPF bandwidth is generally in the video-frequency region – on the order of 1 MHz to a few tens of MHz – to support the range-resolution requirements of the waveform, that is, $B_{LPF} \cong \frac{c}{2\delta R}$. This is approximately equal to the inverse of the pulse width (or compressed pulse width if applicable), that is, $B_{LPF} \cong \tau^{-1}$. From Section 5.7.2, the spectrum of the pulse-Doppler waveform is contained within a sinc envelope with a half-power width that is approximately equal to the inverse of the pulse width. Thus, the final band-limiting filter is approximately matched to the transmit spectrum width.

The synchronous detector outputs are said to be at baseband, that is, there is no underlying carrier, and all the available information in each channel is contained in the video amplitude. As a result, although the magnitude of the Doppler shift can be extracted from either channel alone, both channels are needed to determine the sign, thereby allowing approaching targets to be distinguished from receding targets on the basis of their Doppler shift.

5.7.5 Extracting Doppler Frequency

The relative phase, ϕ_{rcv} , between the received signal and the reference oscillator includes some unknown phase offset, ϕ_{unk} , plus the total phase delay of the radar-scatterer round-trip propagation path:

$$\phi_{rcv} = \phi_{unk} - \frac{4\pi R(t)}{\lambda} \quad (5.7-7)$$

Let us define $t = 0$ to be the start of the CPI, R_0 to be the range at time $t = 0$, and the CPI to be short enough such that the radial velocity, v_R , is approximately constant over that period. The radar-to-scatterer range during the CPI is $R = v_R t + R_0$, resulting in a relative phase of

$$\phi_{rcv} = \phi_{unk} - \frac{4\pi v_R t}{\lambda} - \frac{4\pi R_0}{\lambda} = \phi_0 - \frac{4\pi v_R t}{\lambda} \quad (5.7-8)$$

where we define $\phi_0 = \phi_{unk} - \frac{4\pi R_0}{\lambda}$. The first time derivative of ϕ_{rcv} is the angular frequency, ω_D :

$$\omega_D = \frac{d\phi_{rcv}}{dt} = -\frac{4\pi v_R}{\lambda} \quad (5.7-9)$$

The filtered I- and Q-channel signals from Equations 5.7-5 and 5.7-6 are then

$$s_{I,LPF}(t) = \cos(\omega_D t + \phi_0) \quad (5.7-10)$$

$$s_{Q,LPF}(t) = \sin(\omega_D t + \phi_0) \quad (5.7-11)$$

The Doppler frequency f_D is obtained by dividing the angular frequency ω_D by 2π to convert radians per second to cycles per second (Hz), yielding

$$f_D = -\frac{2v_R}{\lambda} \quad (5.7-12)$$

Neither $s_{I,LPF}(t)$ nor $s_{Q,LPF}(t)$ alone contains sufficient information to determine the sign of the Doppler shift because of the unknown phase offset ϕ_0 . A received in-phase signal of $s_{I,plus}(t) = \cos(\omega_D t + \phi_0)$ cannot by itself be distinguished from a hypothetical, oppositely signed frequency counterpart $s_{I,minus}(t) = \cos(-\omega_D t - \phi_0)$. Similarly, a received quadrature signal of $s_{Q,plus}(t) = \sin(\omega_D t + \phi_0)$ cannot by itself be distinguished from $s_{Q,minus}(t) = \sin(-\omega_D t - \phi_0 - \pi) = -\sin(-\omega_D t - \phi_0)$. The use of both channels, however, allows the frequency to be determined unambiguously, as the $s_{Q,minus}(t)$ hypothesis at any given time is the negative of that implied by the associated $s_{I,minus}(t)$ hypothesis, and therefore, invalid.

The preceding discussion is for a traditional I/Q receiver. With the advances made in A/D converter technology, many modern radars use a direct sampling approach, whereby rather than sampling a baseband signal that passes through an LPF, a high-speed A/D converter samples a band-pass-filtered signal at some higher IF. If the sampling rate is sufficiently high – for example, four times the signal bandwidth – the equivalent I/Q operation can be performed through digital processing. This avoids the problem of I/Q channel imbalances in which a direct current (DC) bias in either channel or a mismatch in gain or phase between channels will introduce spurious signals at Doppler frequencies other than ω_D .

5.7.6 The Sampled Waveform

The pulse modulation at PRF f_p and pulse width τ provides a periodic sampling of the environment over the N_p -pulse CPI. The I- and Q-channel video signals from a scatterer with a range that is R_0 at the beginning of the CPI are

$$s_{I,LPF}(t) = \cos(\omega_D t + \phi_0); \quad \left[\left(\frac{2R_0}{c} + kT_p \right) \leq t \leq \left(\frac{2R_0}{c} + kT_p + \tau \right), \quad k=0, 1, \dots, N_p-1; \right] \\ = 0 \quad [otherwise] \quad (5.7-13)$$

$$s_{Q,LPF}(t) = \sin(\omega_D t + \phi_0); \quad \left[\left(\frac{2R_0}{c} + kT_p \right) \leq t \leq \left(\frac{2R_0}{c} + kT_p + \tau \right), \quad k=0, 1, \dots, N_p-1; \right] \\ = 0 \quad [otherwise] \quad (5.7-14)$$

where $t = 0$ is the start time of the CPI and k is the pulse number in the CPI.

The video I and Q signals are sampled by the A/D converters at a high enough rate to ensure that at least one sample is obtained within a received pulse, for example, at a rate of τ^{-1} . The A/D timing is synchronized very precisely to the PRF over the entire pulse burst.

The signal duration at the input to the A/D converter is actually longer than that of the original pulse due to the temporal response of the preceding band-limiting IF or video filter. The convolution of the rectangular received pulse with the impulse response

of a matched filter is approximately a triangle of base 2τ . This allows an achievable time resolution of τ , using the Rayleigh criterion for resolution, namely, that two objects of equal amplitude are resolvable when the peak of one coincides with the first null of the other.

Let us say that each A/D sample corresponds to one range bin, ΔR_{bin} . Each range bin is sampled by the A/D converter once per PRI, resulting in successive samples of a given range bin being separated in time by T_p . The I- and Q-channel digital samples for a given range bin each produce a sequence of N_p samples over the CPI:

$$S_I(k) = \cos(\omega_D k T_p + \phi_0), \quad k = 0, 1, \dots, N_p - 1 \quad (5.7-15)$$

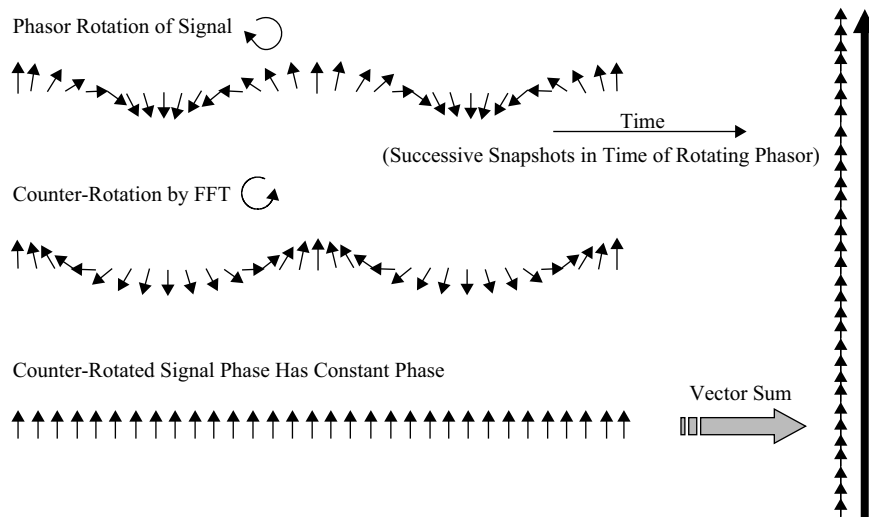
$$S_Q(k) = \sin(\omega_D k T_p + \phi_0), \quad k = 0, 1, \dots, N_p - 1 \quad (5.7-16)$$

5.7.7 Coherent Integration of Digital Samples

The digital signal processor performs a discrete Fourier transform on the sampled data to generate the Doppler spectrum present at range bin m . A computationally efficient implementation of this process that is commonly used is called the fast Fourier transform (FFT). An FFT with N_p samples obtained at a rate f_p generates N_p Doppler filters equally spaced by f_p/N_p .

We can gain insight into the FFT by representing an input signal of a certain Doppler shift f_D as a rotating phasor with angular frequency $\omega_D = 2\pi f_D$. The sampled I and Q channels provide periodic snapshots of the phasor rotation in range bin m over the CPI. For a given Doppler filter n with corresponding center frequency ω_n , the FFT counter-rotates the signal phasor by an amount $\omega_n k T_p$. The magnitude of the signal at frequency ω_n is taken as the vector sum of the N_p counter-rotated phasors. If $\omega_D = \omega_n$, the signal phasor rotation is exactly offset by the FFT counter-rotation, effectively freezing the phasor at one position, resulting in the maximum possible vector sum, as shown in Figure 5.7-6. If ω_D does not equal ω_n , there will be some residual rotation of the counter-rotated phasor, causing the vector sum to be lower, possibly zero, as shown in Figure 5.7-7.

FIGURE 5.7-6 ■ Counter-Rotation of Signal Phasor Matches Signal Frequency.



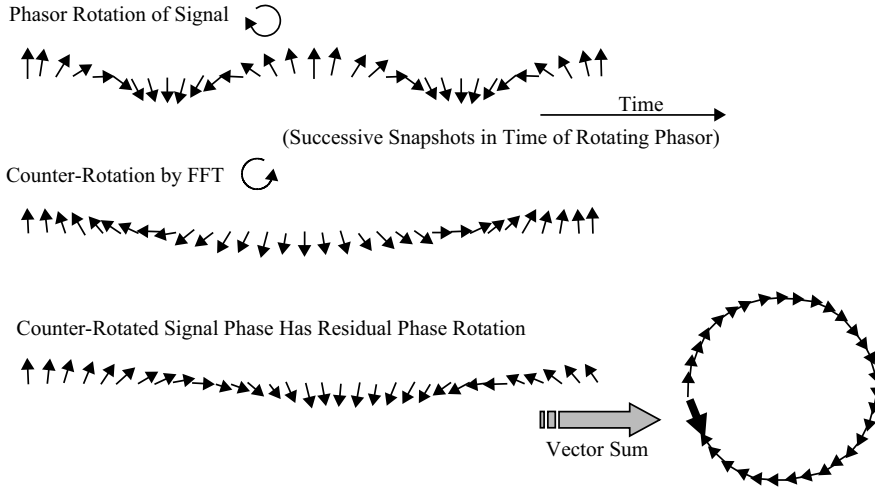


FIGURE 5.7-7 ■ Counter-Rotation of Signal Phasor Does Not Match Signal Frequency.

The signal processor computes the counter-rotated phasor, $U(k) = U_I(k) + jU_Q(k)$, from the real samples, $S_I(k)$ and $S_Q(k)$, through an operation that is equivalent to multiplying the complex signal $S(k) = S_I(k) + jS_Q(k)$ by $e^{-jk\omega_n T_p}$:

$$U_I(k) = S_I(k) \cos(k\omega_n T_p) + S_Q(k) \sin(k\omega_n T_p) \quad (5.7-17)$$

$$U_Q(k) = -S_I(k) \sin(k\omega_n T_p) + S_Q(k) \cos(k\omega_n T_p) \quad (5.7-18)$$

Using the identities $\cos(a+b) = \cos(a)\cos(b) - \sin(a)\sin(b)$ and $\sin(a+b) = \sin(a)\cos(b) + \cos(a)\sin(b)$ (where, in this case, $a = \omega_D k T_p + \phi_0$ and $b = \omega_n k T_p$), we see that this is equivalent to

$$U_I(k) = \cos(\Delta\omega_n k T_p + \phi_0) = \cos(2\pi\Delta f_n k T_p + \phi_0) \quad (5.7-19)$$

$$U_Q(k) = \sin(\Delta\omega_n k T_p + \phi_0) = \sin(2\pi\Delta f_n k T_p + \phi_0) \quad (5.7-20)$$

where $\Delta\omega_n = (\omega_D - \omega_n)$ and $\Delta f_n = \Delta\omega_n / (2\pi)$. The quantity Δf_n is the difference between the Doppler frequency of the signal and the center frequency of filter n .

The vector sum is achieved by taking the sum of the N_p complex samples of $U(k)$:

$$\sum_{k=0}^{N_p-1} U(k) = \sum_{k=0}^{N_p-1} (U_I(k) + jU_Q(k)) = \sum_{k=0}^{N_p-1} U_I(k) + j \sum_{k=0}^{N_p-1} U_Q(k) \quad (5.7-21)$$

Making use of the relationships $e^{ja} = \cos(a) + j\sin(a)$ and $\sum_{k=0}^{N-1} a^k = \frac{1-a^N}{1-a}$, as outlined in Table 5.7-1, we can express the sum of the U_I samples, defined as V_I , and the sum of the U_Q samples, defined as V_Q , as

$$V_I \equiv \sum_{k=0}^{N_p-1} U_I(k) = \left(\frac{\sin(N_p \pi \Delta f_n T_p)}{\sin(\pi \Delta f_n T_p)} \right) \cos((N_p - 1)\pi \Delta f_n T_p) \quad (5.7-22)$$

$$V_Q \equiv \sum_{k=0}^{N_p-1} U_Q(k) = \left(\frac{\sin(N_p \pi \Delta f_n T_p)}{\sin(\pi \Delta f_n T_p)} \right) \sin((N_p - 1)\pi \Delta f_n T_p) \quad (5.7-23)$$

TABLE 5.7-1 ■ Steps Used to Obtain the Complex Sum of N_p Digital Samples

Step	Approach	Result
1	$u \equiv \pi\Delta f_n T_p$	$\sum_{k=0}^{N_p} U(k) = \sum_{k=0}^{N_p} e^{j\phi_0} e^{jk2u} = e^{j\phi_0} \sum_{k=0}^{N_p} e^{jk2u}$
2	$(1-a) \sum_{k=0}^{N-1} a^k$ $= (1+a+\dots+a^{N-1})$ $-(a+a^2+\dots+a^N)$ $= 1-a^N$ $\Rightarrow \sum_{k=0}^{N-1} a^k = \frac{1-a^N}{1-a}$	$\sum_{k=0}^{N_p-1} U(k) = e^{j\phi_0} \frac{(1-e^{jN_p 2u})}{(1-e^{j2u})}$
3	$1-e^{ja} = e^{j\frac{a}{2}}(e^{-j\frac{a}{2}} - e^{j\frac{a}{2}})$ $= e^{ja/2}(-2j\sin(a/2))$	$\sum_{k=0}^{N_p-1} U(k) = e^{j\phi_0} \frac{e^{jN_p u}(-2j\sin(N_p u))}{e^{ju}(-2j\sin(u))}$ $= \left(e^{j((N_p-1)u+\phi_0)} \right) \frac{\sin(N_p u)}{\sin(u)}$
4	$e^{ja} = \cos(a) - j\sin(a)$	$\sum_{k=0}^{N_p-1} U(k) = \frac{\sin(N_p u)}{\sin(u)} [(\cos((N_p-1)u + \phi_0)$ $+ j\sin((N_p-1)u + \phi_0)]$ $\sum_{k=0}^{N_p-1} U_I(k) = \frac{\sin(N_p u)}{\sin(u)} \cos((N_p-1)u + \phi_0)$ $\sum_{k=0}^{N_p-1} U_Q(k) = \frac{\sin(N_p u)}{\sin(u)} \sin((N_p-1)u + \phi_0)$

This corresponds to a complex signal $V = V_I + jV_Q$ that is the result of the coherent integration of the N_p samples in Doppler filter $\omega_n = 2\pi f_n$.

5.7.8 Doppler Filter Response

From the preceding section, we see that the energy, V^2 , in a Doppler filter of a signal that has a frequency that is offset by Δf_n from the filter's center frequency is

$$V^2(\Delta f_n) = V_I^2 + V_Q^2 = \left(\frac{\sin(N_p \pi \Delta f_n T_p)}{\sin(\pi \Delta f_n T_p)} \right)^2 \quad (5.7-24)$$

(This presumes that the signal is of unity amplitude and is sampled N_p times; when referenced to the level of the input signal prior to the LPF, we must also apply the LPF filter response as a complex factor to the preceding.)

We define the parameter u as

$$u \equiv \pi \Delta f_n T_p = \pi \Delta f_n T_{cpi} / N_p \quad (5.7-25)$$

This represents half the phase rotation of the signal in Doppler filter n during each PRI. The energy V^2 can then be written as

$$V^2 = \left(\frac{\sin(N_p u)}{\sin(u)} \right)^2 = \left(\frac{\sin(\pi \Delta f_n T_{cpi})}{\sin(\pi \Delta f_n T_{cpi} / N_p)} \right)^2 \quad (5.7-26)$$

Both the numerator and denominator equal zero for $u = 0$, or $\Delta f_n = 0$. Their ratio is found by taking the ratio of their respective limits as u approaches zero:

$$\lim_{u \rightarrow 0} \left[\frac{\sin(N_p u)}{\sin(u)} \right]^2 = \left(\frac{N_p u}{u} \right)^2 = N_p^2 \quad (5.7-27)$$

The resulting magnitude of $V^2 = N_p^2$ corresponds to the coherent integration gain of N_p pulses for a signal that is exactly centered in the Doppler filter.

Equal magnitude peaks also occur at $u = m\pi$, or $\Delta f_n = m/T_p = mf_p$, where m is any integer, as this also results in both the numerator and denominator being zero. The peaks thus occur at any frequency offset that is an integer multiple of the PRF from the center of the Doppler filter. This is the phenomenon of *Doppler ambiguity*, or *aliasing*, caused by the PRF sampling inherent in the pulse-Doppler waveform. (Ambiguities are discussed in Section 5.8.) Figure 5.7-8 plots an example of $V^2(\Delta f_n)$ where $N_p = 32$.

Since the spectrum is periodic with the PRF, we focus our attention on the region of ($0 < f_D \leq f_p$) to gain insight into the response of the filter. The numerator of V^2 , $\sin^2(N_p u)$, varies at a rate that is N_p times faster than the denominator, $\sin^2(u)$, causing the former to pass through zero N_p times between successive zeros of the latter. This creates $N_p - 1$ sidelobes, or sidebands, between successive PRF peaks. The amplitudes of these sidelobes are much lower than that of the PRF peaks because the denominator of V^2 is nonzero over this interval. A sidelobe peak occurs whenever $\sin^2(N_p u) = 1$, with the i th sidelobe peak occurring at $N_p u = (I + 1/2)\pi$ (for $i \neq 0$), or

$$\Delta f_{n,peak,i} = \frac{(i + \frac{1}{2})f_p}{N_p} = \frac{(i + \frac{1}{2})}{T_p N_p} = \frac{(i + \frac{1}{2})}{T_{cpi}} \quad (5.7-28)$$

The sidelobe nulls occur whenever $\sin^2(N_p u) = 0$, with the i th null occurring at $N_p u = i\pi$ (for $i \neq 0$), or

$$\Delta f_{n,null,i} = \frac{if_p}{N_p} = \frac{i}{T_p N_p} = \frac{i}{T_{cpi}} \quad (5.7-29)$$

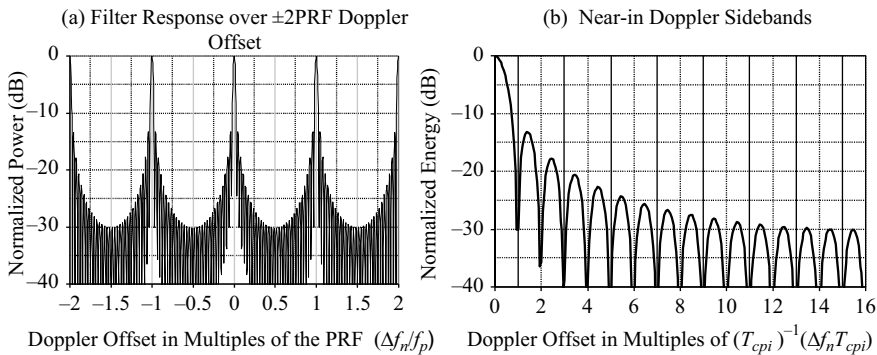


FIGURE 5.7-8 ■ Energy in Doppler Filter versus Signal Frequency Offset for 32-Pulse FFT.

The first null occurs at $u = \pi/N_p$, or $\Delta f_n = 1/T_{cpi}$, yielding a null-to-null mainlobe width of $2/T_{cpi}$. The nulls occur whenever there are an integer number of 360-degree phase rotations within the integration period, resulting in an average voltage of zero. Thus, the first null corresponds to one 360-degree rotation, the second to two 360-degree rotations, and so on.

For typical values of N_p used in practice, the approximation of $\sin(u) \cong u$ is valid out to at least the first few sidelobes. (For example, for $N_p = 16$, the approximation is within 6 percent of the correct value out to the third null, where $u = 3\pi/N_p$.) Thus, we can approximate the near-in filter response, normalized to the peak response at $u = 0$, by the familiar sinc function:

$$\frac{V^2}{N_p^2} \cong \left(\frac{\sin(N_p u)}{N_p u} \right)^2 = \left(\frac{\sin(\pi \Delta f_n T_{cpi})}{\pi \Delta f_n T_{cpi}} \right)^2 \quad (5.7-30)$$

The half-power point of the filter occurs for $N_p u = 0.443\pi = 1.391$; it is common, however, to approximate the half-power point as $N_p u = \pi/2$ for convenience, corresponding to a single-sided filter bandwidth of

$$\Delta f_{n,3dB} \cong \frac{1}{2T_{cpi}} \quad (5.7-31)$$

(This actually corresponds to the -4 -dB point rather than the -3 -dB point.) Thus the two-sided half-power width of the Doppler filter is

$$\Delta f_{bin} = 2\Delta f_{n,3dB} \cong \frac{1}{T_{cpi}} = \frac{f_p}{N_p} \quad (5.7-32)$$

An N_p -point FFT creates a bank of N_p such filters that span the PRF, with adjacent filters separated by $\Delta f_{bin} = f_p/N_p = 1/T_{cpi}$, and with the center frequency of filter n being $f_n = (n-1)/T_{cpi}$ ($n = 0, 1, 2, \dots, N_p - 1$). This causes the null of one filter to coincide with the peak of the next adjacent filter, corresponding to a Doppler resolution of

$$\delta_D \cong \Delta f_{bin} = f_p/N_p = 1/T_{cpi} \quad (5.7-33)$$

If, for example, the desired Doppler resolution is $\delta_D = 200$ Hz, then it is necessary to integrate over a coherent processing interval of at least $T_{cpi} = 5$ ms.

5.7.9 Reduction of Doppler Sidelobes

The FFT-generated Doppler filter has near-in sidelobes that begin at -13.2 dBc (dB below carrier or center frequency) and only gradually decrease to the minimum level at $\Delta f_n = f_p/2$. For the example shown in Figure 5.7-8, the sidelobes never fall below -30 dBc. High Doppler sidelobes are undesirable when detecting small targets in the presence of strong clutter. Suppose, for example, that a radar uses a 32-point FFT ($N_p = 32$) with a 64-kHz PRF and that the mainlobe clutter and target Doppler frequencies are 10 kHz and 25 kHz, respectively. The 15-kHz separation between the target and mainlobe clutter corresponds to a frequency difference of $7.5f_p/N_p = 7.5 \Delta f_{bin}$, which places the clutter at the peak of the seventh sidelobe of the target Doppler filter, at a level of -27.2 dBc. If the radar requires, say, $+15$ dB of signal-to-interference ratio for reliable detection, then any 10-kHz mainlobe clutter return that is 12 dB or more above

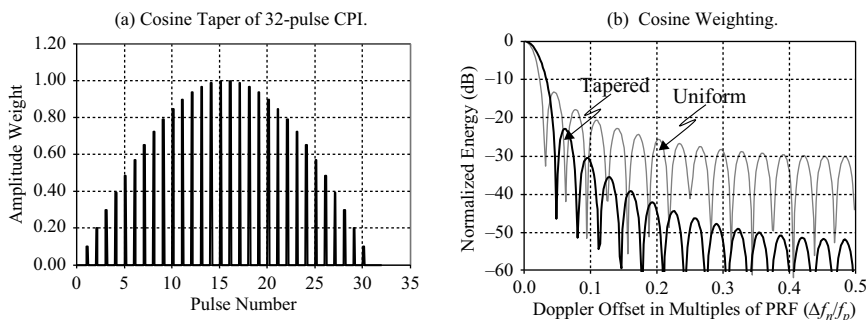


FIGURE 5.7-9 ■ Example of Cosine-Weighted CPI to Reduce Doppler Sidelobes.

the target will certainly begin to impact detection. The rough order of magnitude S/C ratio estimate of Section 5.3.2.2 suggests that such a power level is certainly within the realm of possibility.

Doppler sidebands are mitigated by amplitude weighting, or windowing, across the CPI prior to performing the FFT. This is analogous to the amplitude taper of an antenna aperture. The tapering of the edges of the sample window reduces the higher-frequency components of the spectrum at the expense of a slight broadening of the filter width and decrease in SNR. Various windowing functions – such as Kaiser, Taylor, Hamming, and Dolph-Chebyshev – may be used for the amplitude taper as discussed in [5]. The peak sidelobe levels associated with some of these weighting functions are less than -40 dBc, with an accompanying SNR loss of approximately 1.5 dB and filter-broadening factor of approximately 1.5.

Figure 5.7-9 shows a simple cosine taper across a 32-pulse CPI and the weighted filter response, using the function

$$\Omega(k) = \cos\left(\frac{k\pi}{N_p - 1} - \frac{\pi}{2}\right) = \sin\left(\frac{k\pi}{N_p - 1}\right) \quad (5.7-34)$$

where $\Omega(k)$ is the amplitude weight of the k th pulse of an N_p -pulse CPI, $0 < k < N_p - 1$. The argument of the cosine varies from $-\pi/2$ to $+\pi/2$ over the N_p pulses, producing zeros at each end. Even this simple taper reduces the first sidelobe by approximately 10 dB and subsequent sidelobes to below -30 dBc. For the 15-kHz target-clutter frequency difference in the preceding example, the sidelobe level is approximately -45 dBc – an improvement of almost 18 dB over the untapered level of -27.2 dBc.

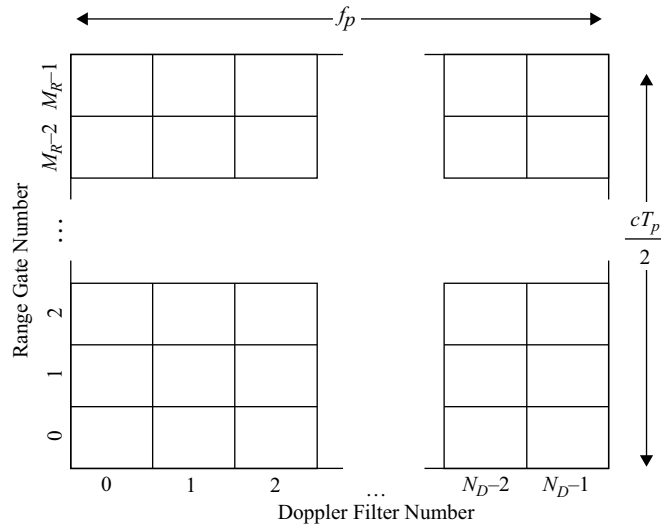
5.7.10 Range-Doppler Map

The M_R range bins and N_D Doppler filters per range bin form an M_R by N_D range-Doppler map of the environment. For our discussions, we will assume $N_D = N_p$, as would be the case for an FFT, and that the entire PRI is divided equally into M_R range gates, spaced in time by $\Delta t_{bin} = T_p/M_R$, corresponding to a range separation of $\Delta R_{bin} = c\Delta t_{bin}/2$, such that range bin m corresponds to an apparent range of

$$R_{app}(m) = \frac{mc\Delta t_{bin}}{2} = m\Delta R_{bin}, \quad m = 0, 1, \dots, M_R - 1 \quad (5.7-35)$$

(We use the term *apparent* to indicate that the value does not account for possible ambiguities and is therefore not necessarily the true value.)

FIGURE 5.7-10 ■
Notional Range-
Doppler Map.



The N_p Doppler filters span the PRF with an equal spacing of f_p/N_p such that Doppler bin (filter) n corresponds to an apparent Doppler frequency and radial velocity of

$$f_{D,app}(n) = \frac{nf_p}{N_p}, \quad n = 0, 1, \dots, N_p - 1 \quad (5.7-36)$$

$$v_{R,app}(n) = -\frac{n\lambda f_p}{2N_p}, \quad n = 0, 1, \dots, N_p - 1 \quad (5.7-37)$$

Figure 5.7-10 depicts the notional range-Doppler map.

During search mode, the radar performs automatic detection on all or a portion of the map using *constant false alarm rate* (CFAR) detection algorithms on a cell-by-cell basis. Each cell is tested relative to a detection threshold that is set based on an estimate of noise in that cell derived from the noise contained in nearby, but not adjacent, range-Doppler cells of presumably similar characteristics. During target-track mode, the range, velocity, and angle-track error signals are obtained from the specific range-Doppler cell(s) containing the target under track.

5.8 | AMBIGUITIES, FOLDED CLUTTER, AND BLIND ZONES

The preceding sections have shown that targets and clutter are often separable in either range, Doppler, or both, and that a pulse-Doppler radar can divide the interpulse period into M_R range bins and form N_D narrowband Doppler filters for each range bin by performing an FFT. On the surface, this seems to have solved the problem: The resulting $M_R \times N_D$ range-Doppler map ostensibly allows a target to be separated from clutter and its range and velocity to be determined by the range bin and Doppler filter in which it appears. This would be true except that for most conditions relevant to airborne

pulse-Doppler radar, there are inherent ambiguities in the measurements of at least one of the two parameters. The ambiguities not only cause uncertainty about the true target range and velocity but also result in clutter folding and blind zones in both dimensions. These adversely affect radar performance by limiting the ability to separate targets from clutter and reducing the probability of detection.

5.8.1 Range and Velocity Ambiguities

5.8.1.1 Range Ambiguity

The time it takes for a transmitted pulse to travel to a scatterer at range R and return to the radar is $T_R = 2R/c$. The range at which the round-trip transit time equals one PRI is the maximum unambiguous range, designated R_U :

$$R_U = \frac{cT_p}{2} = \frac{c}{2f_p} \tag{5.8-1}$$

Scatterers at ranges greater than R_U arrive in the same range bins as those whose ranges are less than R_U . Figure 5.8-1 illustrates the concept with two targets: Target 1 is within R_U , and Target 2 is between R_U and $2R_U$.

A detection in range bin m indicates an apparent range of $R_{app} = m\Delta R_{bin}$, but the true range is ambiguous and could be one of M_{amb} possible ranges:

$$R_{amb}(i) = R_{app} + icT_p/2, \quad i = 0, 1, \dots, M_{amb} - 1 \tag{5.8-2}$$

where M_{amb} is defined as the lowest integer for which the product $M_{amb}R_U$ exceeds the maximum range of any detectable target. Stated another way, the apparent range, R_{app} , is the remainder when the true range, R , is divided by the unambiguous range, R_U :

$$R_{app} = R \bmod R_U \tag{5.8-3}$$

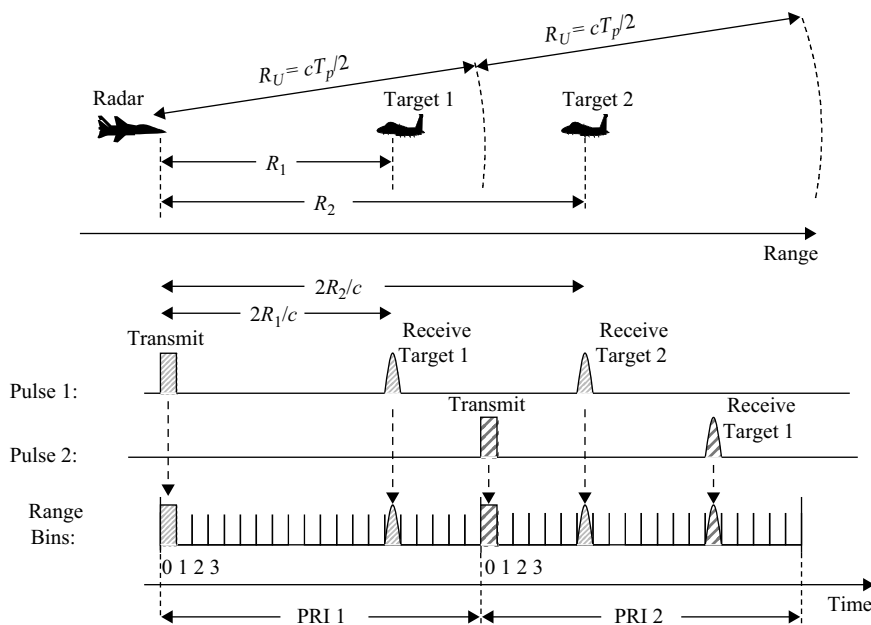


FIGURE 5.8-1 ■ Range Ambiguity Example.

The coherent integration needed to form the Doppler filters, described in Section 5.7, requires that the radar transmit a phase-coherent pulse train so that the only variation in relative phase of the received signal is due to the range rate of the target. As a result, each transmitted pulse in the burst is essentially identical to all the others, and the received pulses from a given scatterer are therefore indistinguishable. The radar cannot detect the first occurrence of a return in a specific range bin to resolve this ambiguity because it cannot detect target returns on a pulse-by-pulse basis. Rather, it must collect a full CPI worth of pulses and perform Doppler processing to separate the target from clutter before it is able to make a detection. (Conditions that allow the radar to detect a target on a single-pulse basis do not require the use of pulse-Doppler waveforms in the first place.)

5.8.1.2 Velocity Ambiguity

The PRF modulation of the pulse burst causes the measurement of Doppler frequency, and therefore radial velocity, of a received signal to be ambiguous. The Doppler ambiguities occur at integer multiples of the PRF. This is evident in the spectrum of the transmitted signal, described in Section 5.7.2, with the energy concentrated at the PRF harmonics. The signal received by the radar from a target of radial velocity v_R has exactly the same power spectrum as the transmitted signal, except shifted in frequency by $-2v_R/\lambda$. As long as each range bin is sampled at a rate greater than or equal to the PRF, the ambiguities of the digitized signal presented to the digital signal processor are no worse than those inherent in the transmitted and received RF signal.

To gain additional insight into the aliasing effect of the PRF, consider the sampled output of the I-channel synchronous detector described in Section 5.7.6 for a received signal of Doppler frequency f_D :

$$S_I(k) = \cos(2\pi f_D k T_p + \phi), \quad k = 0, 1, \dots, N_p - 1 \quad (5.8-4)$$

The A/D samples for Doppler processing occur at the PRF rate, or once per PRI, T_p . The sampled values for a received signal of Doppler frequency $f_D + n f_p$, where n is an integer, are

$$\begin{aligned} S_I(k) &= \cos(2\pi f_D k T_p + \phi + 2n\pi f_p T_p) \\ &= \cos(2\pi f_D k T_p + \phi) \end{aligned} \quad (5.8-5)$$

since $f_p T_p = 1$ and $\cos(a + 2n\pi) = \cos(a)$. Thus, a signal at Doppler frequency f_D will appear to have the same frequency as any other signal in the radar passband with a Doppler frequency that is an integer multiple of PRFs ($n f_p$) away from f_D . The same holds for the Q channel. Figure 5.8-2 illustrates the concept: The same voltages are obtained when sampling three different Doppler frequencies, separated by integer multiples of the PRF.

The unambiguous Doppler extent is thus one PRF. The corresponding unambiguous velocity extent, v_U , is given by

$$v_U = \frac{\lambda f_p}{2} = \frac{c f_p}{2 f_c} \quad (5.8-6)$$

Because the velocity can be either positive or negative, the unambiguous velocity actually ranges between $\pm v_U/2$, corresponding to a Doppler extent of $\pm f_p/2$. Thus, for

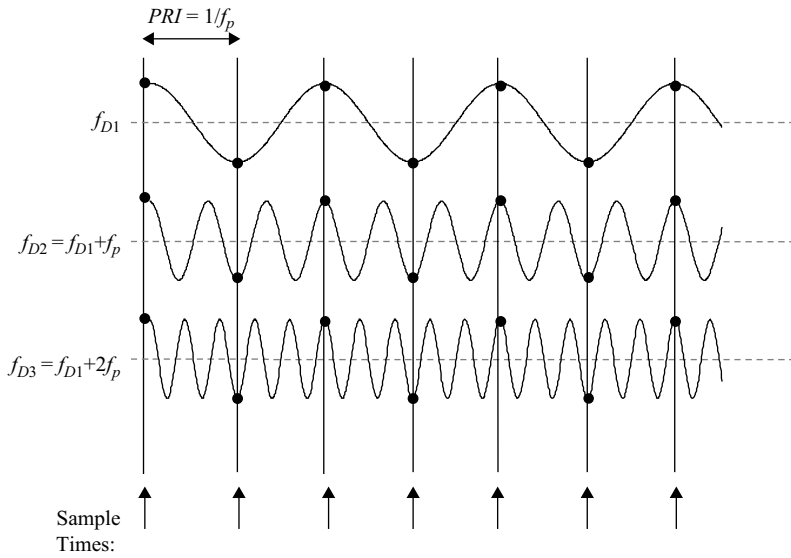


FIGURE 5.8-2 ■ PRF Aliasing of Doppler Frequency.

an apparent range rate of $v_{R,app}$, the true range rate may be any one of N_{amb} possibilities, where N_{amb} is the lowest integer for which $N_{amb}v_U \geq v_{R,max} - v_{R,min}$, and $v_{R,max}$ and $v_{R,min}$ are the maximum (most positive) and minimum (most negative) radial velocities of any potential target that has a Doppler shift within the radar detection passband. The apparent velocity of a scatterer that has a true velocity of v_R is, using the preceding $\pm v_U/2$ convention for the unambiguous velocity extent,

$$v_{R,app} = \left(v_R + \frac{v_U}{2} \right) \text{mod } v_U - \frac{v_U}{2} \tag{5.8-7}$$

and the corresponding apparent Doppler frequency is

$$f_{D,app} = \left(-\frac{2v_R}{\lambda} + \frac{f_p}{2} \right) \text{mod } f_p - \frac{f_p}{2} \tag{5.8-8}$$

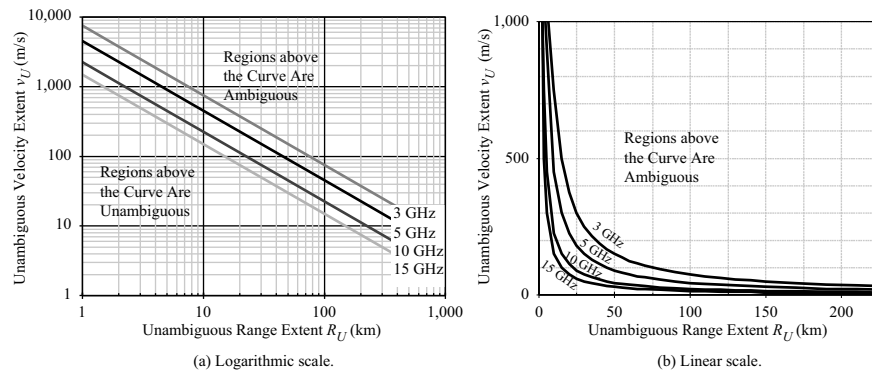
5.8.1.3 Interdependence of Unambiguous Range and Velocity

The unambiguous range extent and unambiguous velocity extent are both a function of the PRF and therefore cannot be chosen independently. The latter is proportional to f_p , and the former is inversely proportional to f_p . Thus, an increase in one dimension forces a proportional decrease in the other dimension, with their product constant for a given wavelength:

$$R_U v_U = \left(\frac{c}{2f_p} \right) \left(\frac{cf_p}{2f_c} \right) = \frac{c^2}{4f_c} = \frac{c\lambda}{4} \tag{5.8-9}$$

Figure 5.8-3 plots v_U as a function of R_U for 3 GHz, 5 GHz, 9 GHz, and 15 GHz. Any point on or below the curve of a specific frequency corresponds to a combination of range and velocity extent for which it is possible to find a PRF that is simultaneously unambiguous in both dimensions. Any point above the curve indicates that the measurement is ambiguous in at least one dimension. Part (b) of the figure uses a linear scale to underscore the vast region of range-velocity space for which unambiguous operation is impossible.

FIGURE 5.8-3 ■
Unambiguous
Range and Velocity
Extents for 3, 5, 10,
and 15 GHz.



To illustrate the difficulty in finding a totally unambiguous PRF, consider the example of an X-band airborne radar operating in an environment where the maximum target range is 100 km. An unambiguous range extent of 100 km corresponds to a maximum PRF of 1,500 Hz. Assuming a frequency of 10 GHz, the unambiguous velocity extent is only 22.5 m/s, or ± 11.25 m/s. This is far too limited a velocity extent for typical airborne radar applications where the radar platform itself is moving at many times this speed.

Although the product $R_U v_U$ is proportional to wavelength, it is not possible in practice to circumvent the ambiguity problem by descending to ever-lower frequencies. One reason is that any decrease in frequency requires a corresponding increase in antenna aperture size in order to achieve the same angle-track accuracy, a daunting prospect given the volume and weight constraints on most tactical aircraft. Another possible reason is that the CPI time required to achieve a given velocity resolution, δ_v , might become prohibitively long for longer wavelengths ($T_{CPI} = \lambda/2\delta_v$), given issues such as resource time allocation and target acceleration.

5.8.2 Folding of the Range-Doppler Spectrum

The ambiguities resulting from the PRF sampling of the environment cause all apparent measured ranges and velocities to fall within the intervals $0 - R_U$ and $0 - v_U$. This is equivalent to the time interval of one PRI and the frequency interval of one PRF. A detected target with an apparent range and velocity of R_{app} and $v_{R,app}$ has a true range and velocity that is one of approximately $N_{amb}M_{amb}$ possibilities. This is illustrated conceptually in Figure 5.8-4. The environment consists of five objects – for example, four targets and extended clutter. The radar measures apparent values of range and Doppler that are bounded by R_U and the PRF, respectively. Each apparent range-Doppler measurement is ambiguous, corresponding to numerous possible range-velocity values for each object, only one of which is true.

5.8.3 Folded Clutter

One of the consequences of range and Doppler ambiguities is that clutter may fold (alias) into the same range-Doppler region as a target and thereby impede detection. This is illustrated conceptually in Figure 5.8-4 from the preceding section: The clutter patch is isolated from the targets in true range and Doppler (velocity) but overlaps one of the

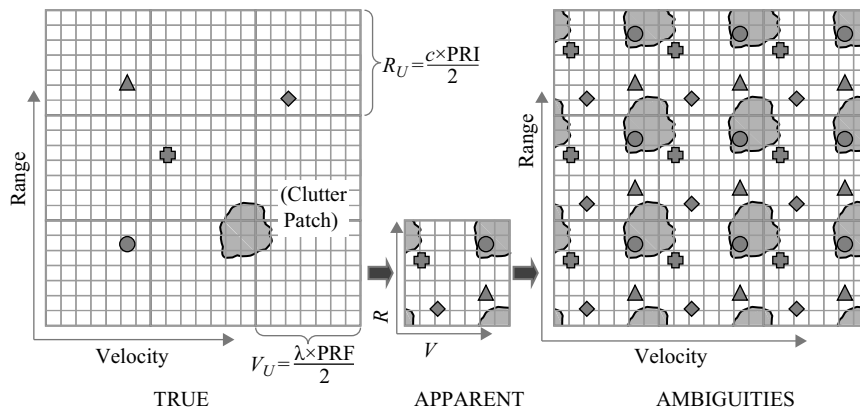


FIGURE 5.8-4 ■
Folded Range-
Doppler Spectrum.

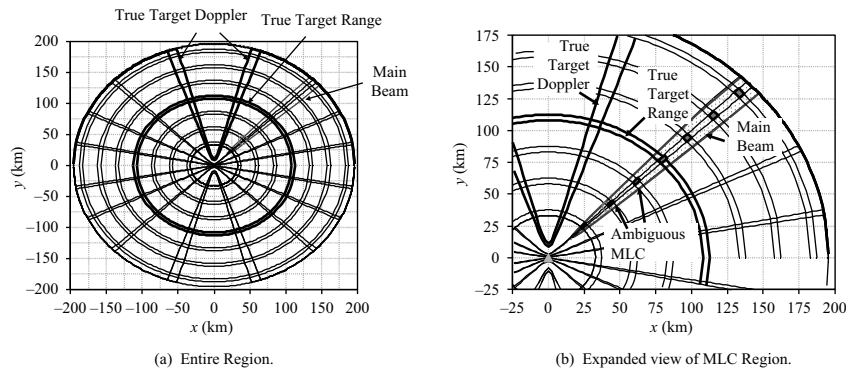


FIGURE 5.8-5 ■
Iso-Range and Iso-
Doppler Contours
for 6-kHz PRF.

targets after the spectrum is folded into the $R_U f_p$ region. The total clutter return in a given range-Doppler cell is the sum of the returns from all of the ambiguous range-Doppler cells.

Figure 5.8-5 illustrates iso-range and iso-Doppler contours for an X-band radar traveling at 350 m/s and using a 6-kHz PRF. The range cell and Doppler filter corresponding to the true range and Doppler of a target are highlighted. The other iso-range and iso-Doppler contours are separated from the target range and Doppler by integer multiples of R_U (25 km) and the PRF, respectively. The total clutter in the target range-Doppler cell is the sum of the returns from each patch of area defined by the intersection of a range gate and a Doppler filter. The return from a given patch depends on its physical area, the backscatter coefficient at the corresponding angle of incidence, the round-trip range, and the two-way radar antenna pattern gain in the corresponding direction. Folded clutter returns may come from ranges that are much closer to the radar than the target with which they are competing. Of particular concern is the case in which mainlobe clutter folds into the same range-Doppler cell as the target, as shown in the figure. Figures 5.8-6 and 5.8-7 illustrate the concept of clutter folding in range and Doppler.

5.8.4 Clutter-Fill Pulses

Range-folded clutter may require that the radar transmit some number of pulses at the beginning of its pulse burst before it begins its CPI. These pulses are sometimes referred to as *clutter fill* pulses. To confine a given clutter return to as narrow a region in the

FIGURE 5.8-6 ■ Clutter Folding in Range.

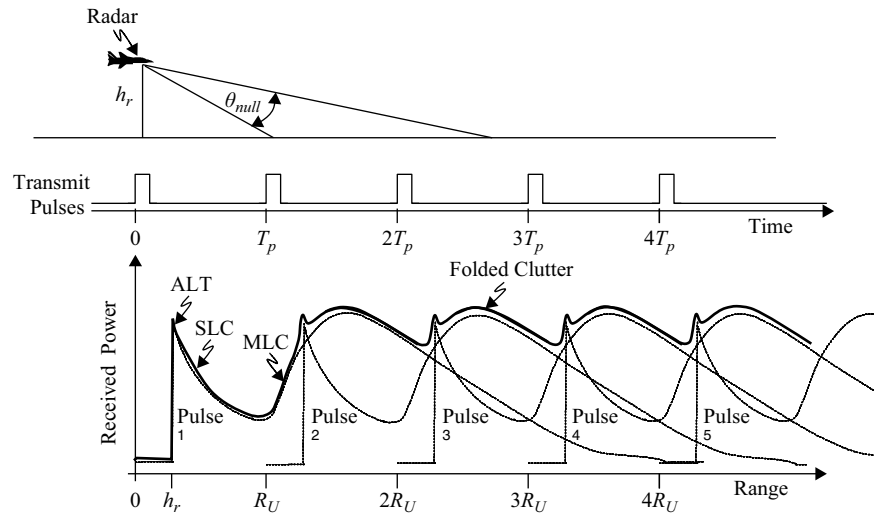
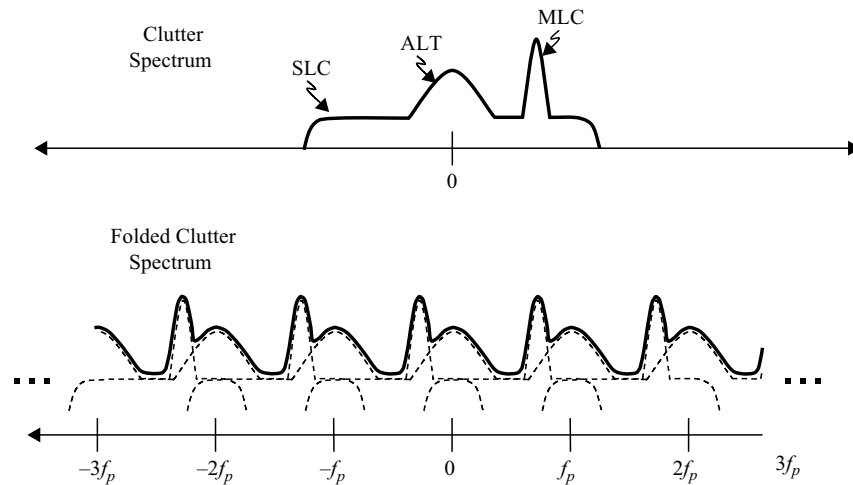


FIGURE 5.8-7 ■ Clutter Folding in Doppler.



Doppler spectrum as possible, the radar requires a full-CPI worth of pulses. The spectral width of a given return is inversely proportional to the Doppler integration time. If the clutter is present for only a portion of the CPI, then by definition its integration time is less and its spectral extent is greater. The resulting spreading increases the extent to which clutter will overlap with the target in Doppler. Although the total clutter energy is reduced due to the partial fill of the CPI, this benefit may be greatly outweighed by the increase in clutter–target overlap.

The degradation is even more pronounced when one considers the impact of a partially filled CPI on the amplitude-weighted Doppler filter sidelobes, described in Section 5.7.9. If the CPI begins before the long-range clutter starts to arrive, that is, without the use of clutter-fill pulses, the first returns from the clutter are attenuated less than those at the end of the CPI. This asymmetric weighting of the clutter results in very high Doppler sidebands of the clutter spectrum, largely negating the low-sidelobe benefit otherwise provided by the amplitude taper. Figure 5.8-8 illustrates the sidelobe

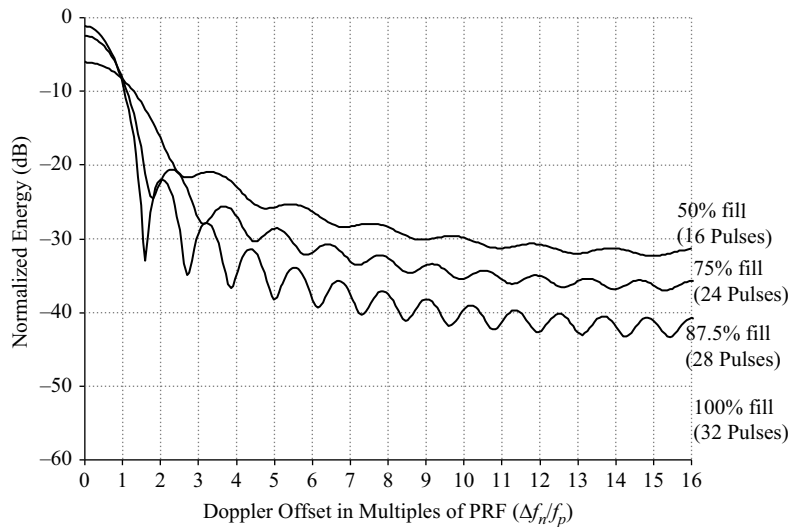


FIGURE 5.8-8 ■ Effect of Partially Filled CPIs on Doppler Filter Sidelobes.

degradation resulting from a CPI that is only partially filled. The plots are for a 32-pulse FFT with a cosine taper, as in Section 5.7.9, for cases of 100 percent (32 pulses), 87.5 percent (28 pulses), 75 percent (24 pulses), and 50 percent (16 pulses) of the CPI containing the signal.

The clutter-fill time, $T_{c,fill}$, is determined from the maximum range of significant clutter, $R_{c,max}$:

$$T_{c,fill} = \frac{2R_{c,max}}{c} \quad (5.8-10)$$

In the worst case for the radar, significant clutter (clutter that is strong enough to interfere with target detection) may occur as far as the radar horizon, $R_{c,max} = R_h$. The number of clutter-fill pulses is the product of the fill time and the PRF:

$$N_{c,fill} = T_{c,fill}f_p = \frac{T_{c,fill}}{T_p} \quad (5.8-11)$$

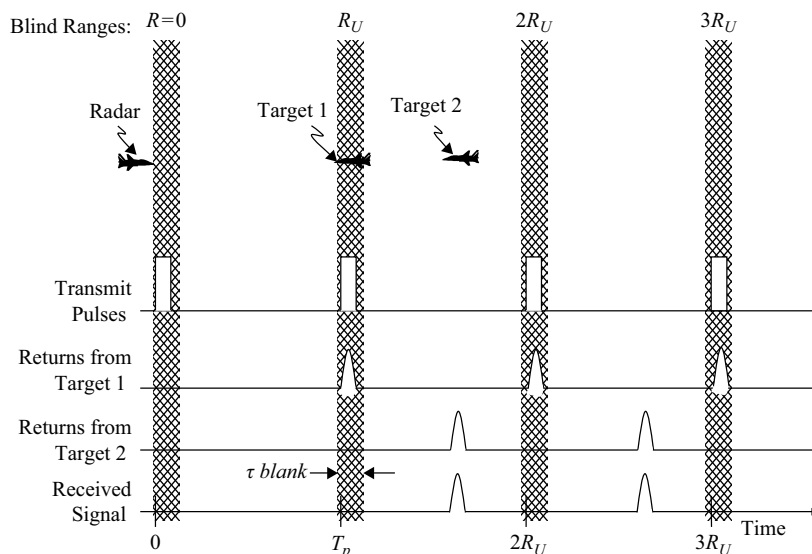
The clutter-fill pulses are wasted in the sense that no processing can be done during the corresponding PRIs, and therefore, more pulses must be transmitted during the burst, N_b , than are ultimately used by the radar, N_p . The pulses transmitted during the beginning of the pulse burst become the first returns from the long-range clutter. The pulses transmitted at the very end of the pulse burst never make the round-trip journey to the long-range clutter but are needed for short-range clutter and targets. This translates into an overhead on radar resource time incurred by pulse-Doppler operation. If, for example, $R_{c,max} = 150$ km and the CPI time is $T_{cpi} = 5$ ms, then the clutter fill time is $T_{c,fill} = 1$ ms, a 20-percent pulse-Doppler tax, so to speak, on radar resource time.

5.8.5 Blind Zones

5.8.5.1 Range Blind Zones

The pulse-Doppler radar is blind to any targets with returns that arrive during the time a pulse is transmitted. The radar receiver is blanked during transmission, at least for the

FIGURE 5.8-9 ■ Target Eclipsing Occurring at Integer Multiples of the Radar Unambiguous Range.



duration of the pulse (τ) and generally slightly longer to allow transients and near-in multipath to dissipate. Any target return that arrives during the transmit period will also be blanked, at least partially. The minimum range at which a complete pulse can be received from a target is therefore $R_{min} = c\tau_{blank}/2$, where τ_{blank} is the transmit blanking time. This target blanking, or eclipsing, occurs for ranges that are integer multiples of the unambiguous range, as illustrated in Figure 5.8-9. The blind ranges are therefore

$$nR_U \leq R_{blind} \leq nR_U + \frac{c\tau_{blank}}{2} \quad (5.8-12)$$

where n is a non-negative integer. Since R_U is a function of the PRF, we can also express the blind ranges as

$$\frac{nc}{2f_p} \leq R_{blind} \leq \frac{nc}{2f_p} + \frac{c\tau_{blank}}{2} \quad (5.8-13)$$

For radars with pulse compression, the blanking time corresponds to the uncompressed pulse width, not the compressed pulse width. The fraction of time during which the radar is blind is $\tau_{blank}f_p$, which approximately equals the transmit duty factor (as $\tau_{blank} \cong \tau$). Thus, although high duty factor helps improve probability of detection by increasing average power and therefore SNR, this benefit is partially offset during search mode by an accompanying increase in target eclipsing.

5.8.5.2 Velocity Blind Zones

Certain regions of the Doppler spectrum may be so dominated by clutter or other forms of interference that detection of targets within these regions is impossible. The radar filters out or ignores these contaminated Doppler regions in order to preserve dynamic range and limit false alarms. The most prominent source of interference in the Doppler spectrum is usually the mainlobe clutter; its center frequency varies with antenna scan angle. Another source of interference is the altitude return, which has a peak at zero-Doppler for horizontal flight and nonzero during climbs and descents. Other potential

forms of interference at the zero-Doppler region are transmitter leakage and video DC bias. Transmitter leakage may occur even if the high-power amplifier is gated off if the oscillators providing the low-power RF drive are left on continuously. A video DC bias in either the I- or Q-channel detectors manifests as strong zero-Doppler components following the FFT.

One factor that potentially limits dynamic range in modern radar is the resolution (number of bits) of the A/D converters. Receiver gain control can prevent saturation of the A/D converters but not without desensitizing the radar. A possible alternative approach is to filter out the interfering frequencies prior to the A/D converter. In past radar designs, this was sometimes accomplished with an analog notch filter located at a receiver IF or video stage [3]. The filter itself is at a fixed frequency – zero, for example – and the received signal is frequency translated to tune the interfering signal, such as mainlobe clutter, to the notch filter frequency, as shown in Figure 5.8-10. The filtered signal might then be translated back to the original IF before continuing through the remaining receiver path. The notch filtering can potentially be performed in stages to reject, for example, both the mainlobe clutter and altitude return.

This process must be preceded by a band-limiting filter that has a bandwidth narrow enough to select only one of the PRF ambiguities in the spectrum, generally the central line or carrier; otherwise, Doppler ambiguities of the interference would still be passed. Such a filter essentially removes the pulse modulation of the incoming signal since the filter bandwidth must be less than the PRF. This factor limits such an approach to HPRF modes where there is often no range gating, as described in Section 5.10.

Provided that the receiver and A/D converter are not saturated, it is possible to mitigate the interference digitally in the signal processor. Once the received signal has been digitized, the radar may employ a delay-line canceller in the signal processor to cancel strong interference such as clutter. The delay-line canceller employs the same approach used in the MTI radar to filter out stationary clutter. The MTI processing helps minimize the amount of signal-processing gain experienced by the clutter through the pulse compression and Doppler integration processes. Unlike typical MTI used on

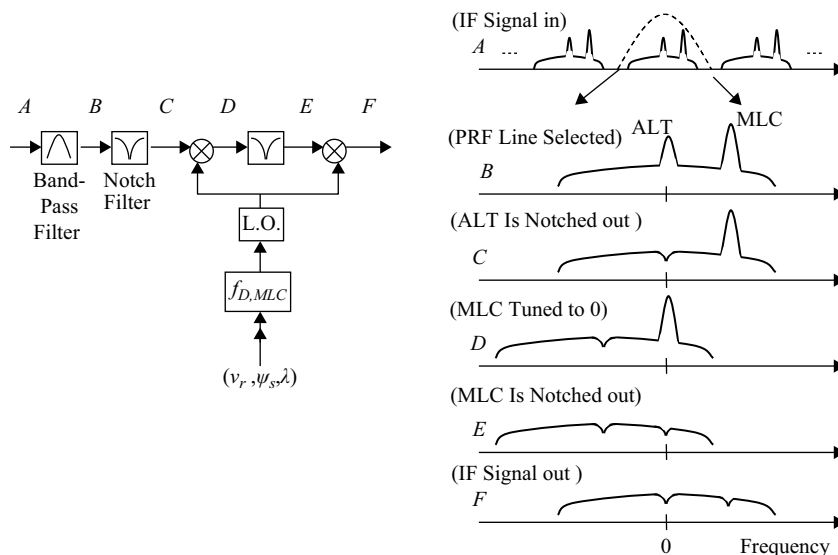
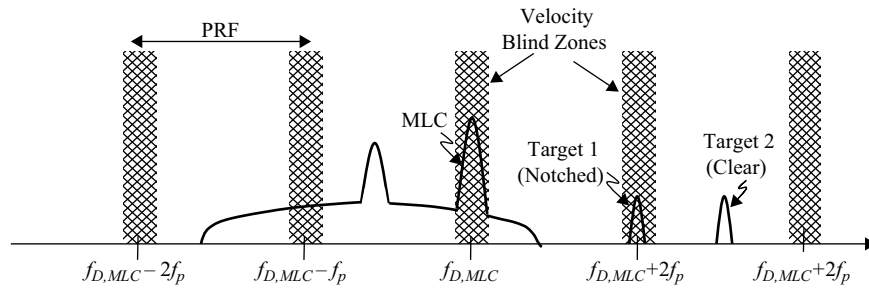


FIGURE 5.8-10 ■
Notch Filtering
Altitude Return and
Mainlobe Clutter.

FIGURE 5.8-11 ■
Velocity Blind Zones
Resulting from
Notching out
Mainlobe Clutter.



surface-based radar, however, the clutter encountered by airborne radar has a wide Doppler extent, and the mainlobe clutter is generally far from zero Doppler. The MTI notch can be tuned to cancel nonzero mainlobe clutter or other interference by adding an interpulse phase offset to either the delayed or undelayed pulse to compensate for the Doppler-induced, interpulse phase difference. The interpulse phase offset, $\Delta\phi_{notch}$, needed to generate a notch at Doppler frequency $f_{D,notch}$ is

$$\Delta\phi_{notch} = 2\pi f_{D,notch} T_p \quad (5.8-14)$$

The Doppler ambiguity associated with the PRF aliasing causes Doppler blind zones to occur at integer multiples of the PRF. Figure 5.8-11 depicts a notional Doppler spectrum and shows how a target that is apparently separated from mainlobe clutter may fall in a blind velocity region if mainlobe clutter is being notched out. The blind Doppler frequencies, $f_{D,blind}$, are given by

$$(f_{D,notch} - \frac{1}{2}\Delta f_{notch}) + nf_p \leq f_{D,blind} \leq (f_{D,notch} + \frac{1}{2}\Delta f_{notch}) + nf_p \quad (5.8-15)$$

where $f_{D,notch}$ is the center Doppler frequency of the notched region, Δf_{notch} is the frequency extent of the notched region, f_p is the PRF, and n is an integer in the range $\frac{2v_{R,min}}{\lambda f_p} \leq n \leq \frac{2v_{R,max}}{\lambda f_p}$, with $v_{R,min}$ and $v_{R,max}$ defined as the most negative and positive range rates, respectively, that the radar can potentially encounter.

5.9 | OVERVIEW OF PRF REGIMES

Pulse-Doppler radar modes are typically categorized as being either high PRF (HPRF), medium PRF (MPRF), or low PRF (LPRF), depending on the ambiguities in the range-Doppler spectrum. High PRF is unambiguous in Doppler (velocity) but is generally highly ambiguous in range. Low PRF is unambiguous in range but generally highly ambiguous in velocity. Medium PRF is moderately ambiguous in both range and velocity. Typical PRF values for an X-band airborne pulse-Doppler radar are 100–300 kHz for HPRF, 5–30 kHz for MPRF, and 0.3–2 kHz for LPRF. The blind zone incidence corresponds directly to the ambiguities: HPRF has many range blind zones, LPRF has many velocity blind zones, and MPRF has a moderate amount of range and velocity blind zones.

Figures 5.9-1, 5.9-2, and 5.9-3 illustrate conceptually the nature of the ambiguities for LPRF, HPRF, and MPRF, respectively. Each figure subdivides a notional range-Doppler spectrum consisting of clutter and a single target according to the unambiguous

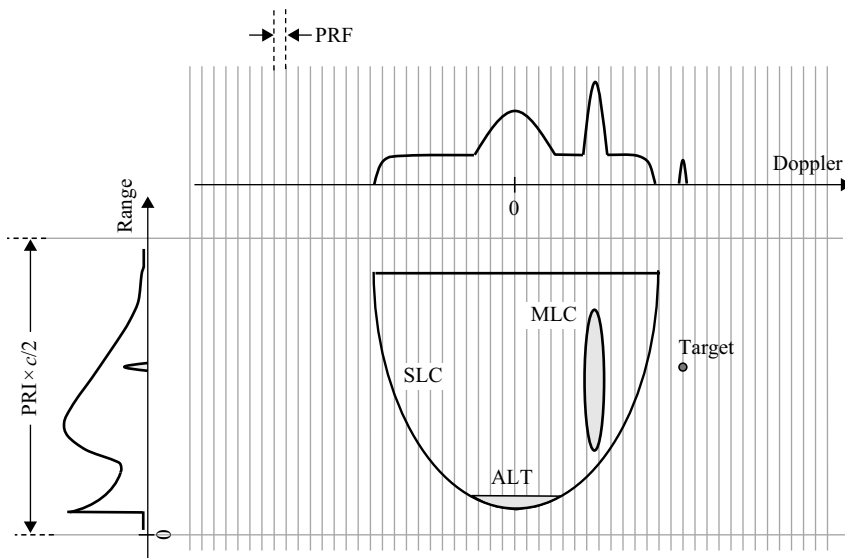


FIGURE 5.9-1 ■ Low-PRF Range-Doppler Ambiguities.

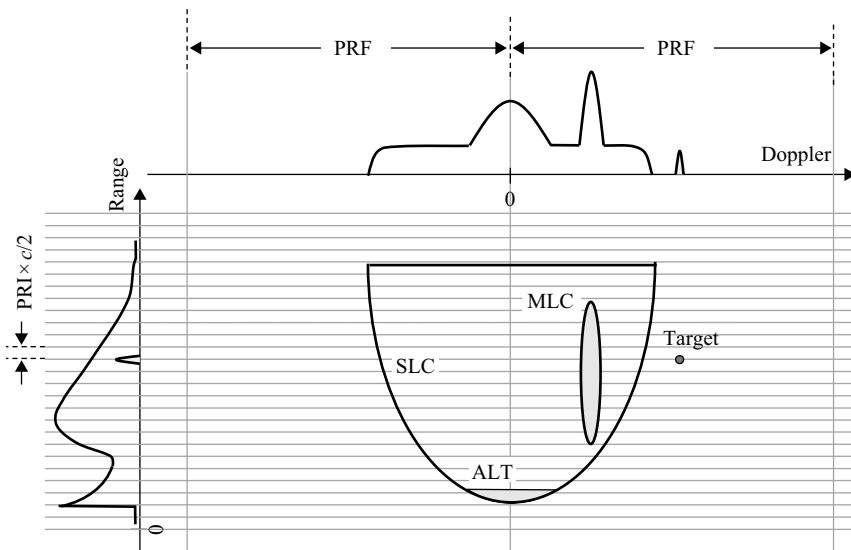
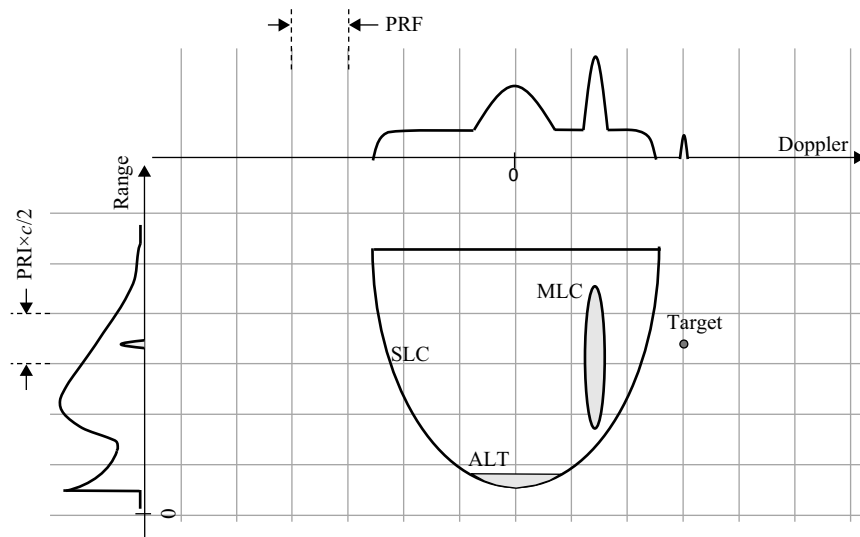


FIGURE 5.9-2 ■ High-PRF Range-Doppler Ambiguities.

range, that is, the PRI and the unambiguous Doppler, or PRF. The figures are not drawn to scale, but conceptually each unambiguous range-Doppler region has the same area (range \times Doppler) regardless of the PRF, as the area is proportional to the product of the PRF and its inverse, the PRI.

Each of the three PRF modes has a different capability in terms of separating targets from clutter. Low PRF is limited in its ability to separate airborne targets from mainlobe clutter because the mainlobe clutter Doppler extent is greater than or a significant fraction of the PRF. As mainlobe clutter is generally range coincident with targets of interest, there is little hope of isolating airborne targets from mainlobe clutter in either range or Doppler dimensions. Low-PRF waveforms are more applicable to air-to-ground modes, specifically ground-moving target indicator (GMTI) and synthetic aperture radar (SAR) modes.

FIGURE 5.9-3 ■
Medium-PRF
Range-Doppler
Ambiguities.



High PRF offers excellent capability against inbound targets in a nose-aspect geometry because this condition produces a high Doppler shift that falls in the exo-clutter (outside the clutter) region of the spectrum. Detection under such conditions is limited primarily by thermal noise and eclipsing rather than clutter. High PRF is less effective in other geometries, however. As the radar and target aspect angles get further away from the nose-on type of geometry, the target Doppler shift decreases and eventually falls within the bounds of sidelobe clutter. Sidelobe clutter is troublesome in HPRF modes because of the severe range folding of the clutter, as close range sidelobe clutter and the altitude return fold into the same range cell as longer range targets.

Medium PRF mode largely mitigates the sidelobe clutter limitation of HPRF by using both the range and Doppler dimensions to reduce the clutter-to-signal ratio in a target cell. The unambiguous Doppler frequency for MPRF is wide enough to provide a significant region that is free of mainlobe clutter. The unambiguous range is long enough to provide a significant region that is free of strong, near-in sidelobe clutter and the altitude return. The main disadvantage of MPRF relative to HPRF is in detecting high radial velocity targets. Doppler-folded sidelobe clutter still competes with target returns under such conditions for MPRF, whereas for HPRF, the same target is likely to be in an exo-clutter region.

Table 5.9-1 summarizes some of the characteristics of the three PRF regimes. Additional detail is provided in the subsequent sections.

5.10 | HIGH PRF MODE

High PRF provides a large clutter-free Doppler region in which to detect targets with high closing velocities. It provides an unambiguous velocity measurement and very good velocity resolution. We will consider three variants of HPRF: velocity search HPRF, which provides no range information; linear frequency modulation (LFM) ranging HPRF, which provides coarse range resolution; and range-gated HPRF, which provides good range resolution and ambiguous range estimates.

TABLE 5.9-1 ■ Representative Characteristics of High, Medium, and Low PRFs for an X-Band Radar

	HPRF	MPRF	LPRF
PRF (kHz)	100–300	5–30	0.5–2.0
R_U (km)	0.5–1.5	5–30	75–300
$v_U/2$ (m/s)	750–2,250	37.5–225	3.75–15
Applications	Air-to-air search, track; illumination	Air-to-air search, track	Air-to-ground SAR, GMTI
Strengths	<ul style="list-style-type: none"> * High average power for long-range detection * Large clutter-free region for detection of nose-aspect, high-speed targets * Unambiguous velocity measurement 	<ul style="list-style-type: none"> * Subdividing SLC in range improves detection of off-nose aspect, low-speed targets * Altitude return can be isolated by range-gating * Simultaneous range and velocity measurement 	<ul style="list-style-type: none"> * Unambiguous range measurement * Good range resolution * SAR processing provides images of terrain * GMTI processing allows detection of ground movers
Limitations	<ul style="list-style-type: none"> * MLC, SLC, and possibly ALT present at all ranges * Severe range eclipsing * Coarse or highly ambiguous range measurement * SLC limits detection for low- or medium-speed targets 	<ul style="list-style-type: none"> * MLC and SLC generally present at all ranges * Ambiguities in both range and Doppler * Strong SLC discretizes may cause false alarms * Ground movers' ambiguous range, velocity similar to airborne targets 	<ul style="list-style-type: none"> * MLC occupies much or all of unambiguous Doppler extent resulting in poor detection of airborne targets * Highly ambiguous velocity measurement of high-speed targets

5.10.1 Velocity Search HPRF Mode

The simplest form of HPRF consists of a high duty factor chopped CW waveform implementing a single range gate. This is referred to as the velocity search mode in the AN/APG-63 radar of the F-15, for example. The high duty factor provides high average power, thereby maximizing SNR, but at the expense of high range eclipsing. The duty factor cannot exceed 50 percent because there is no benefit to having a receive interval that is shorter than the transmitted pulse it is intended to capture. In practice, the duty factor must be somewhat less than 50 percent – for example, 40 percent – to allow for switching transients and close-range reflections to die down before processing any input signals. The receive interval between consecutive transmit pulses consists of a single range gate.

The HPRF clutter spectrum looks like that of a CW Doppler radar except that it is repeated at multiples of the PRF due to the Doppler ambiguity. The overall spectrum is contained within the envelope of the spectrum of a single pulse. The number of PRF intervals contained within the half-power points of the spectrum is approximately equal to the inverse of the duty factor. Since the duty factor never exceeds 50 percent, there are always at least two PRF intervals, or equivalently, three PRF lines (including the carrier) within the half-power bandwidth.

Figure 5.10-1 shows a notional HPRF Doppler spectrum. The clutter-free Doppler region is equal to the PRF (f_p) minus the sidelobe clutter Doppler extent ($4v_r/\lambda$). Ideally, the PRF is chosen to ensure that the target with the highest expected velocity, $v_{t,max}$, will fall in a clutter-free Doppler region, that is, its Doppler frequency does not overlap with the sidelobe clutter Doppler region of the adjacent PRF ambiguity:

$$\frac{2v_r}{\lambda} + \frac{2v_{t,max}}{\lambda} < f_p - \frac{2v_r}{\lambda} \tag{5.10-1}$$

$$\Leftrightarrow f_p > \frac{4v_r}{\lambda} + \frac{2v_{t,max}}{\lambda} \tag{5.10-2}$$

Figure 5.10-2 illustrates the Doppler spectrum of the example scenario, using a 250-kHz PRF and a 1.5- μ s pulse width. The highest magnitude Doppler shift in the example scenario is approximately 33 kHz for Target 1; the total Doppler extent of the sidelobe clutter is approximately 40 kHz; the PRF must therefore be greater than 73 kHz in order ensure that Target 1 is in the clutter-free region, a condition that is easily met by the selected value of 250 kHz. The unambiguous velocity for the 250-kHz PRF is 3,750 m/s. The unambiguous range is 600 m, indicating that all unclipped range returns are folded into a 600-m interval.

The other airborne targets (2, 3, and 4) are all in the sidelobe clutter region. Detection of these targets in HPRF mode is difficult because of the high degree of range folding of the clutter in each target’s Doppler filter. From Equation 5.4-8 we can infer

FIGURE 5.10-1 ■ Notional HPRF Doppler Spectrum.

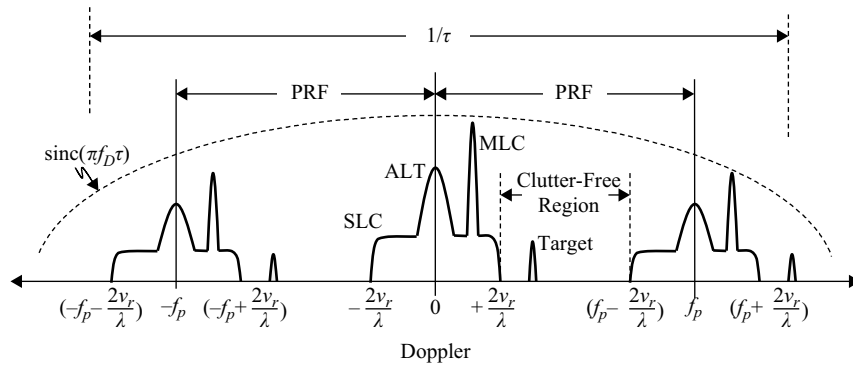
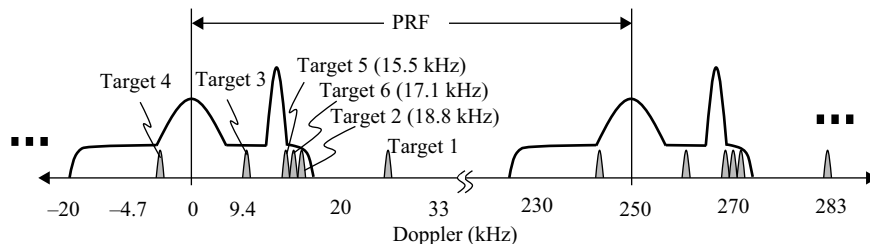


FIGURE 5.10-2 ■ HPRF Doppler Spectrum of the Example Scenario for a 250-kHz PRF.



that a Doppler filter centered at frequency f_n may contain sidelobe clutter returns from ranges as close as

$$R_{min,f_n} = \frac{h_r}{\sqrt{1 - \left(\frac{f_n \lambda}{2v_r \cos(\epsilon_v)}\right)^2}} \quad (5.10-3)$$

where ϵ_v is the aircraft climb angle. Consider, for example, the slow outbound aircraft, Target 3, in the example scenario. The radar is closing in on the target in a tail-chase type geometry. From Table 5.6-2, the range of Target 3 is 63.7 km, and the Doppler frequency is 9.4 kHz. The Doppler filter that contains this target therefore also includes sidelobe clutter from ranges as close as $R_{min,f_n} = 3.4$ km, a factor of 18.7 times closer than the target. Since received power is proportional to R^4 , this corresponds to a 51-dB disadvantage for the target, offsetting much of the two-way sidelobe antenna pattern attenuation that works in favor of the mainlobe target versus the sidelobe clutter. The target must compete with clutter returns from many ambiguous or folded ranges between the preceding minimum range and the radar horizon. With a 600-m unambiguous range, there are approximately 320 ambiguous range cells between R_{min,f_n} and the radar horizon, of which more than 100 are at ranges closer than Target 3. (Each range cell actually includes two clutter patches – one at positive azimuth and one at negative azimuth.)

The overall clutter interference is the sum of the contributions from each range-folded clutter patch within the Doppler filter. Associated with each patch k is its own physical area A_c , backscatter coefficient σ° , two-way antenna pattern gain $G_t G_r$ (where G_t and G_r are the transmit and receive antenna gains, respectively), and range-dependence R_c^{-4} . The impact of the folded clutter on target detection is assessed through the resulting signal-to-clutter ratio:

$$\frac{S}{C} \cong \left(\frac{\sigma_t}{R_t^4}\right) \div \left(\sum_k \frac{A_c(k) \sigma^\circ(k) G_t(k) G_r(k)}{R_c^4(k)}\right) \quad (5.10-4)$$

5.10.2 Linear FM Ranging HPRF

5.10.2.1 Linear FM Ranging Concept

One method of obtaining range information with an HPRF waveform is to use LFM ranging. This is referred to as range-while-search mode in the F-15 radar. The radar linearly varies the RF carrier frequency by a relatively small amount over the course of the transmitted pulse burst. The LFM is generated in one of the local oscillators that is common to both transmit and receive paths. Without any LFM, the frequency of a signal received from an object in the environment differs from the radar's instantaneous transmitter frequency by an amount equal to the object's Doppler shift $f_{D,v_R} = -2v_R/\lambda$. With the application of LFM, an additional frequency difference, $f_{D,LFM}$, is imparted to the object due to the change in transmitter (and receiver) frequency between the time the signal was originally transmitted and the time the reflection is received.

Let us represent the transmitter (and receiver) carrier frequency by $f_c(t) = f_{c,0} + \xi t$, where $f_{c,0}$ is the frequency at the beginning of the burst ($t = 0$), and ξ is the LFM rate

during the burst, expressed in units of frequency per unit time. The additional frequency shift of an object at range R that is induced by the LFM is therefore

$$f_{D,LFM} = f_c(t - 2R/c) - f_c(t) = [f_{c,0} + (\xi t - 2R\xi/c)] - [f_{c,0} + \xi t] = -2\xi R/c \quad (5.10-5)$$

The total frequency shift of a return from range R is

$$f_D = f_{D,v_R} + f_{D,LFM} = -\frac{2v_R}{\lambda} - \frac{2\xi R}{c} \quad (5.10-6)$$

Two bursts at LFM rates ξ_1 and ξ_2 produce two different shifts, f_{D1} and f_{D2} . The frequency difference between f_{D1} and f_{D2} allows the range of the object to be determined:

$$\Delta f_{12} \equiv f_{D2} - f_{D1} = \left(-\frac{2v_R}{\lambda} - \frac{2\xi_2 R}{c} \right) - \left(-\frac{2v_R}{\lambda} - \frac{2\xi_1 R}{c} \right) = \frac{2(\xi_1 - \xi_2)R}{c} \quad (5.10-7)$$

$$\Rightarrow R = \frac{c\Delta f_{12}}{2(\xi_1 - \xi_2)} \quad (5.10-8)$$

The concept of LFM ranging is illustrated in Figure 5.10-3. The figure illustrates three bursts: the first without LFM, the second with a positive LFM, and the third with a negative LFM. In general, more than two LFM rates are desirable to avoid ambiguities that arise due to multiple targets in the environment.

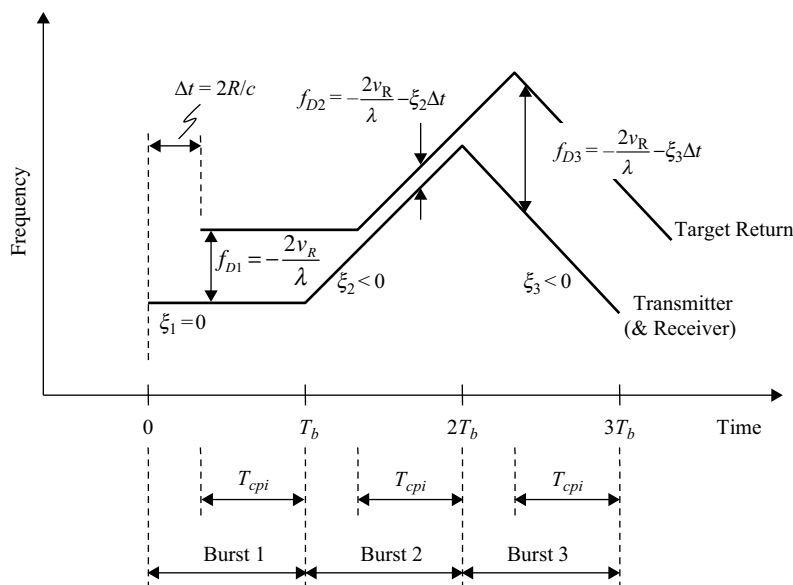
Two objects separated by ΔR can be resolved in range if the frequency displacement experienced by each differs by at least one Doppler filter:

$$|\Delta f_{12}(R) - \Delta f_{12}(R + \Delta R)| \geq \Delta f_{bin} \quad (5.10-9)$$

where Δf_{bin} is the Doppler filter width. If we approximate the Doppler filter width as $1/T_{cpi}$, where T_{cpi} is the CPI time, we can estimate the achievable range resolution, δ_R :

$$\Delta R = \frac{c(\Delta f_{12}(R) - \Delta f_{12}(R + \Delta R))}{2(\xi_1 - \xi_2)} \geq \frac{c\Delta f_{bin}}{2|\xi_1 - \xi_2|} \quad (5.10-10)$$

FIGURE 5.10-3 ■
Concept of LFM Ranging.



$$\Rightarrow \delta_R = \frac{c\Delta f_{bin}}{2|\xi_1 - \xi_2|} = \frac{c}{2|\xi_1 - \xi_2|T_{cpi}} \tag{5.10-11}$$

The product ($|\xi_1 - \xi_2|T_{cpi}$) in the denominator is actually the bandwidth, B , separating the two returns separated by range δ_R . This leads to the familiar result for range resolution in terms of signal bandwidth: $\delta_R = c/2B$. Suppose that an HPRF mode employs a 10-MHz/s LFM rate and a 5-ms CPI. The resulting bandwidth is 50 kHz, corresponding to a range resolution of approximately 3 km.

The requirement for multiple CPIs potentially impacts either radar timeline or sensitivity. Either the total time on target must increase to preserve the same single-CPI SNR, thereby impacting search frame time, or the CPI time per burst must decrease, thereby impacting probability of detection.

5.10.2.2 Clutter Spreading Due to LFM Ranging

One consequence of using LFM ranging in the HPRF mode is that the clutter is spread over a wider portion of the Doppler spectrum. In Section 5.4.3.2, we found that the Doppler shift of sidelobe clutter at a given range, R , falls within the bounds of

$$f_{D,SLCmin,R} = -\frac{2v_r}{\lambda} \sqrt{1 - \frac{h_r^2}{R^2}} \tag{5.10-12}$$

$$f_{D,SLCmax,R} = +\frac{2v_r}{\lambda} \sqrt{1 - \frac{h_r^2}{R^2}} \tag{5.10-13}$$

assuming horizontal flight. The square-root term is just the cosine of the depression angle under the flat-earth approximation. With LFM ranging, each of the preceding terms is offset by the addition of $-\frac{2\xi R}{c}$ to account for the range-dependent frequency shift induced by the LFM. This imparts a small frequency shift to close-range sidelobe clutter and a large frequency shift to long-range sidelobe clutter. The result is therefore not simply a shifting of the entire spectrum, but both a shifting and a spreading of the spectrum. This spreading cuts directly into the clutter-free region of the HPRF spectrum.

Figures 5.10-4a and 5.10-4b illustrate the spreading effect for the example scenario, using LFM slopes of +10 MHz/s and -10 MHz/s, respectively. The Doppler extents of

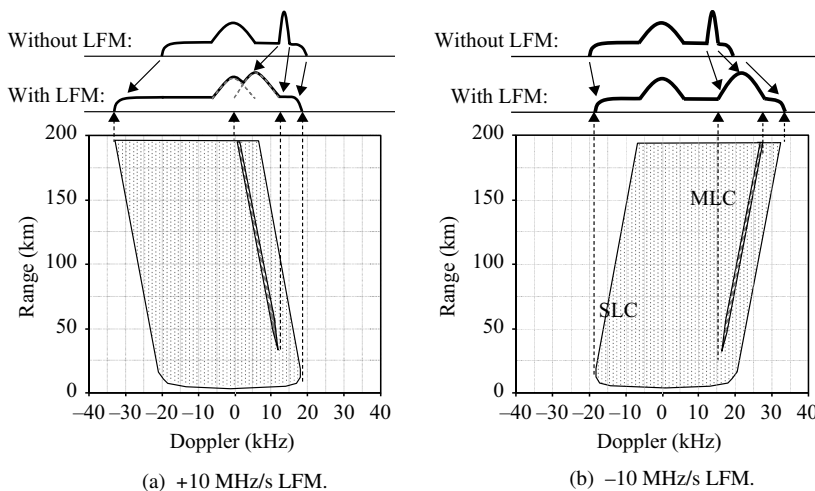


FIGURE 5.10-4 ■ Spreading of Clutter Spectrum Due to LFM Ranging in HPRF.

TABLE 5.10-1 ■ Example of Clutter Doppler Spread from LFM Ranging HPRF*

	Without LFM			With -10 MHz/s LFM			With +10 MHz/s LFM				
	$f_{D,min}$ (kHz)	$f_{D,max}$ (kHz)	Δf (kHz)	$f_{D,min}$ (kHz)	$f_{D,max}$ (kHz)	Δf (kHz)	Spread (kHz)	$f_{D,min}$ (kHz)	$f_{D,max}$ (kHz)	Δf (kHz)	Spread (kHz)
SLC	-20.0	+20.0	40.0	-18.6	33.4	51.0	11.0	-33.4	+18.6	51.0	11.0
MLC	+13.2	+15.1	1.8	15.8	28.0	12.2	10.4	0.3	12.3	12.0	10.2

* $f_c = 10$ GHz, $v_r = 300$ m/s, $h_r = 3,000$ m.

sidelobe clutter and mainlobe clutter are listed in Table 5.10-1 for the two LFM slopes as well as for the non-LFM case. The selected LFM rates cause the sidelobe clutter to spread by 11 kHz, or by approximately 27 percent, relative to the non-LFM extent of 40 kHz. The mainlobe clutter spreads by 10.2 or 10.4 kHz, or approximately 560 percent relative to its non-LFM extent of 1.8 kHz.

5.10.3 Range-Gated HPRF

Range-gated HPRF mode allows the PRI to be subdivided into range gates, providing improved range resolution and range measurement relative to conventional HPRF. The range gates may be achieved through lower duty cycle (shorter pulse widths or longer PRI or both) and low time-bandwidth product pulse compression. The range gates provide a highly ambiguous range measurement that can be resolved through a combination of LFM ranging, as previously described, and ambiguity-resolution methods similar to those employed in medium PRF modes, described in Section 5.11. The improved range resolution has two benefits. First, it improves situation awareness by allowing detection of multiple targets flying at the same radial velocity but at different ranges. Second, it allows the clutter within a Doppler filter to be subdivided in the range dimension. This may improve performance against targets with Doppler frequencies within the bounds of sidelobe clutter. Strong returns that are highly localized in range, such as the altitude return and close-range sidelobe discretets, can be isolated from the target through the range resolution.

5.10.4 HPRF Range Eclipsing

One disadvantage of high duty cycle HPRF waveforms is the range eclipsing, illustrated in Figure 5.10-5. The probability is high (approximately twice the duty factor) that the return signal from a target will be at least 50 percent eclipsed at any given time during search mode (prior to initial detection). For a given PRF, a target of radial velocity v_R will fly in and out of the eclipsing condition over a period of

$$T_{eclipse} = \frac{R_U}{|v_R|} = \frac{cT_p}{2|v_R|} = \frac{c}{2f_p|v_R|} \quad (5.10-14)$$

For example, if the radial velocity is $v_R = -600$ m/s and the PRF is $f_p = 250$ kHz ($T_p = 4$ μ s), then the eclipsing period is $T_{eclipse} = (3 \times 10^8 \text{ m/s}) / (2 \times 250 \times 10^3 \text{ Hz} \times 600 \text{ m/s}) = 1.0$ s.

Rather than merely waiting for the target to fly out of an eclipsed region, the radar can actively change the eclipsing condition by varying the PRF. The amount of PRF

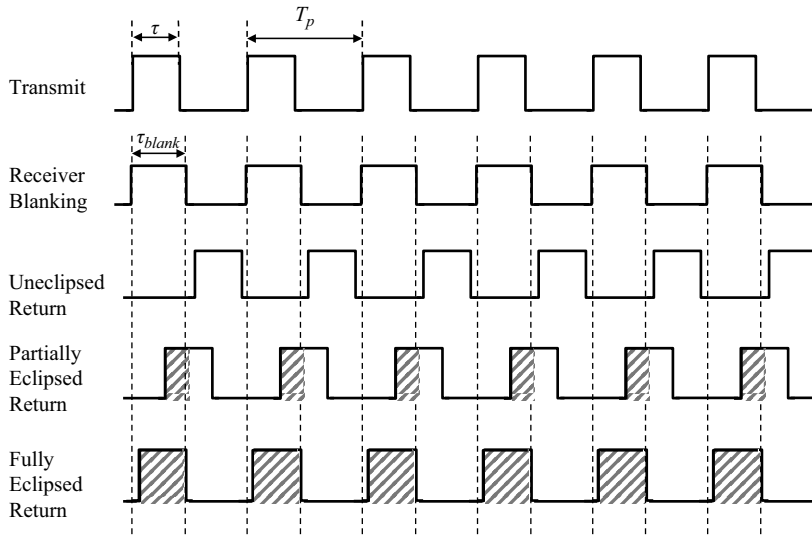


FIGURE 5.10-5 ■
HPRF Target
Eclipsing.

variation needed to move an eclipsed target into an uneclipsed region is relatively small. Suppose a target at range R_t is fully eclipsed with PRI T_{p1} . The total number of PRIs that correspond to range R_t for this PRI is

$$k_1 = \frac{R_t}{R_{U1}} = \frac{2R_t}{cT_{p1}} = \frac{2R_t f_{p1}}{c} \quad (5.10-15)$$

The nearest PRI that would also produce an integer multiple of PRI intervals to R_t is T_{p2} :

$$k_2 = k_1 + 1 = \frac{R_t}{R_{U2}} = \frac{2R_t}{cT_{p2}} = \frac{2R_t f_{p2}}{c} \quad (5.10-16)$$

The relative change in PRF is therefore

$$\frac{f_{p2} - f_{p1}}{f_{p1}} = \frac{c}{2R_t f_{p1}} = \frac{R_{U1}}{R_t} \quad (5.10-17)$$

For a 30-km target and a 250-kHz PRF ($R_{U1} = 600$ m), the relative PRF change needed to move the target through one complete eclipsing cycle is $(600/30,000) = 2$ percent. Thus, a 1-percent change, or approximately 2.5 kHz, would be sufficient to move the target half a PRI into the clear.

5.11 | MEDIUM PRF MODE

Medium PRF mode provides good capability under a wide range of conditions. Although MPRF waveforms are ambiguous in both range and Doppler, the ambiguities are sufficiently few that they can be resolved through the use of multiple PRFs, allowing both range and velocity measurements to be made of the target. The radar divides the PRI into many range gates, often using pulse compression to achieve good range resolution while maintaining reasonably high duty cycle. For example, a radar that uses

a 10-kHz PRF (100- μ s PRI), a 6.5- μ s pulse width, and a 13-bit Barker code pulse compression, has a 6.5-percent duty cycle and approximately 200 range gates over the PRI ($13 \times 100/6.5 = 200$), with a range resolution of approximately 75 m ($\tau_c = 6.5 \mu\text{s}/13$). A 32-pulse CPI at this PRF would be 3.2-ms long and would allow the 10-kHz folded Doppler spectrum to be divided into 32 Doppler filters (assuming FFT-type processing). Its main disadvantage relative to HPRF is that it does not provide a clutter-free region of the Doppler spectrum for optimum detection of high closing-rate targets.

5.11.1 Examples of Different PRFs

Figures 5.11-1, 5.11-2, and 5.11-3 illustrate the range-Doppler spectrum for three different PRFs in the MPRF range: 5 kHz, 10 kHz, and 18 kHz. The figures show the range-Doppler map of the example scenario divided into the corresponding ambiguous range and Doppler intervals (a) and the resultant folded spectrum (b). The range extent of both mainlobe clutter and sidelobe clutter exceeds the unambiguous range for each PRF; therefore, mainlobe clutter and sidelobe clutter are present at all ranges in the folded spectrum. The 40-kHz sidelobe clutter Doppler extent exceeds each PRF, and therefore sidelobe clutter is present at all Doppler frequencies in the folded spectrum. The 5-kHz PRF places Targets 2 and 3 in mainlobe clutter, indicating they would be in a velocity blind zone for this PRF. The 10-kHz PRF results in all targets being in the clear.

FIGURE 5.11-1 ■
Range-Doppler
Folding of Example
Scenario for 5-kHz
MPRF.

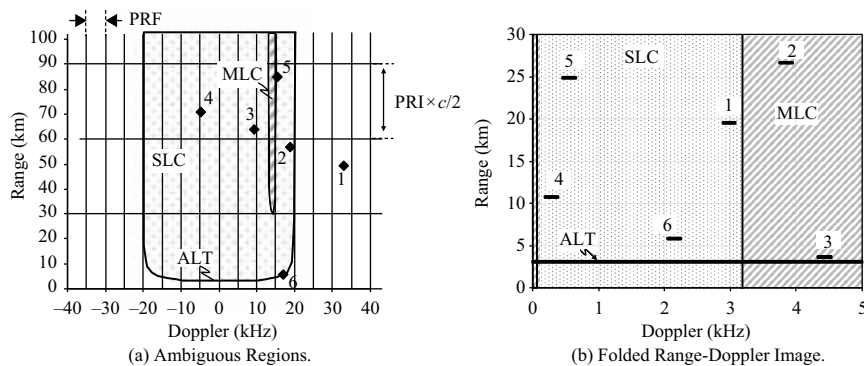
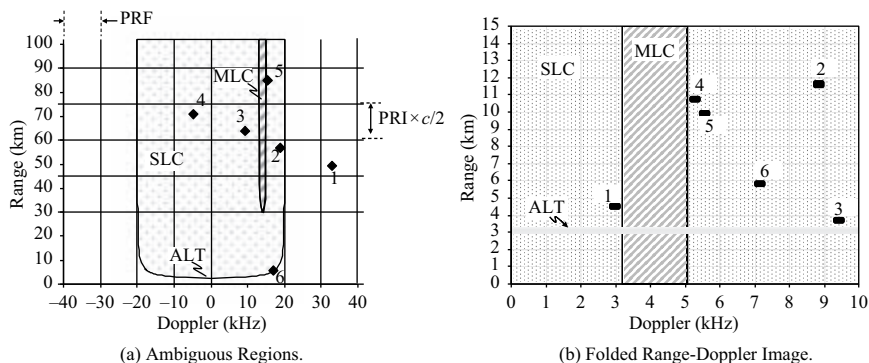


FIGURE 5.11-2 ■
Range-Doppler
Folding of Example
Scenario for 10-kHz
MPRF.



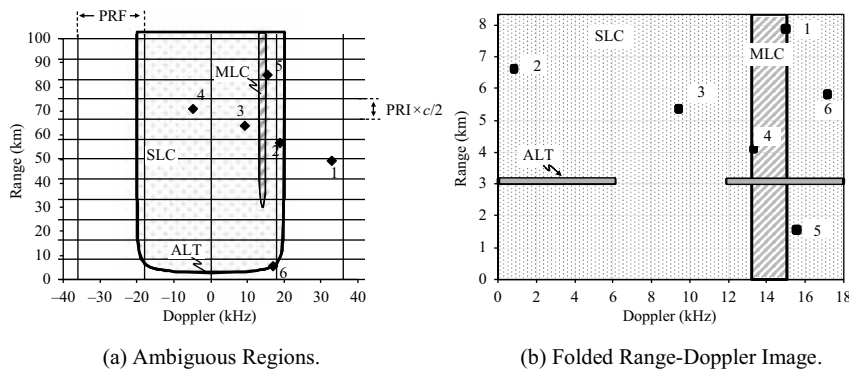


FIGURE 5.11-3 ■ Range-Doppler Folding of Example Scenario for 18-kHz MPRF.

The 18-kHz PRF puts Targets 1 and 4 at the edges of mainlobe clutter. The altitude return clutter spectrum is nominally ± 6 kHz, and therefore does not occupy the entire Doppler extent for this PRF. Notice that there is no way of distinguishing the various target types, including ground mover and sidelobe discrete, based on their location in the folded range-Doppler image for any given PRF. Thus, for a single CPI, they are all potentially valid target detections.

5.11.2 Blind-Zone Charts

Medium PRFs have blind zones in both range and Doppler that impact target detection in search mode. (In contrast, during track mode, the PRF can be chosen to keep the target in the clear because the target range and velocity have already been determined.) One way of illustrating the effect of waveform selection on target visibility is with a blind-zone chart. Figure 5.11-4 illustrates a blind-zone plot for a 10-kHz PRF, a 10- μ s pulse width, and a 2-kHz mainlobe clutter Doppler extent (Doppler blind zone), with the mainlobe clutter tuned to zero Doppler. The left and right vertical scales are in time delay and range, respectively, and the top and bottom horizontal scales are in velocity and Doppler shift, respectively, assuming a 10-GHz frequency. The chart covers the region of 0–60 km range (0–400 μ s time) and 0–600 m/s velocity (0–40 kHz Doppler). The range blind zones occur at integer multiples of the unambiguous range ($cT_p/2$), 15 km. Each range blind zone extends for at least the equivalent range of the transmit pulse width, $c\tau/2$, or 1.5 km. The velocity blind zones occur at integer multiples of the unambiguous velocity ($\lambda f_p/2$), 150 m/s. Each velocity blind zone extends for \pm half the velocity extent of the mainlobe clutter ($\pm \lambda \Delta f_{MLC}/4$), or ± 15 m/s. A radar that employs this waveform in a search mode is blind to approximately 28 percent of the potential targets in the environment [$1 - (90 \mu\text{s} \times 8 \text{ kHz}) / (100 \mu\text{s} \times 10 \text{ kHz}) = 1 - 0.72 = 0.28$].

Suppose the radar maintains the same pulse width but switches to a slightly different PRF of 11 kHz, as shown in Figure 5.11-5. Although the range blind zone at the minimum range and the velocity blind zone at zero Doppler remain in the same positions, the 11-kHz PRF produces blind zones that are otherwise at generally different locations than for the 10-kHz PRF. (The 10-kHz blind zones are outlined with the dashed lines for comparison.) A third PRF of 12 kHz would yield yet a different set of blind zones.

FIGURE 5.11-4 ■ Blind-Zone Chart for 10-kHz PRF ($f_c = 10$ GHz, $\tau = 10$ μ s, $\Delta f_{D,MLC} = 2$ kHz, Mainlobe Clutter Tuned to 0).

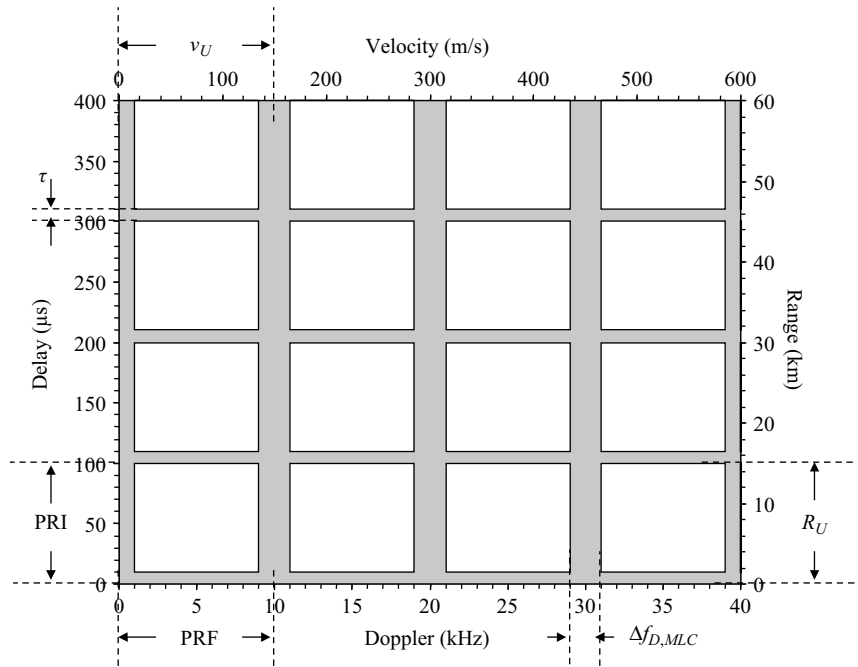


FIGURE 5.11-5 ■ Blind-Zone Chart for 11-kHz PRF ($f_c = 10$ GHz, $\tau = 10$ μ s, $\Delta f_{D,MLC} = 2$ kHz, Mainlobe Clutter Tuned to 0).

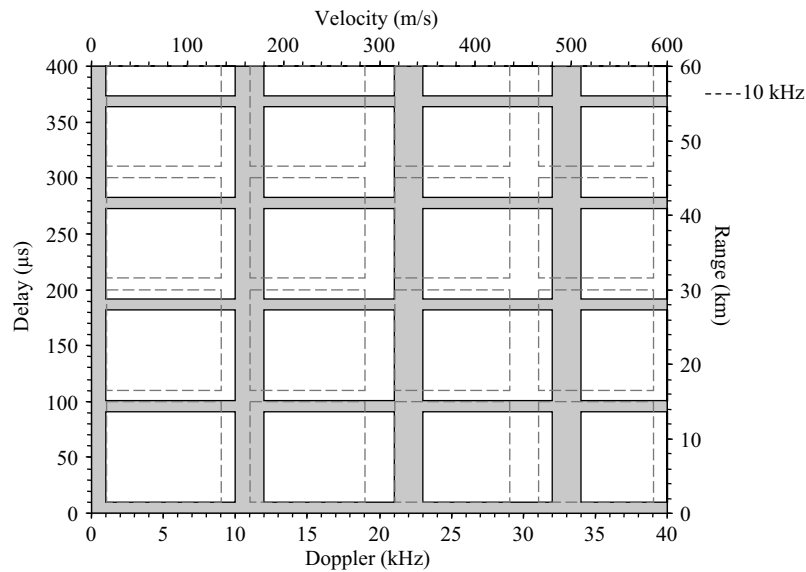


Figure 5.11-6 depicts a blind-zone chart illustrating the regions for which a target is in the clear for none, one, two, or all three of the above PRFs. The darkest regions are those for which the target is in a blind zone for all three PRFs. The lightest regions represent those for which the target is in the clear for all three PRFs. The probability that a target is in the clear for at least one of the three PRFs is much greater than it is for any one PRF alone.

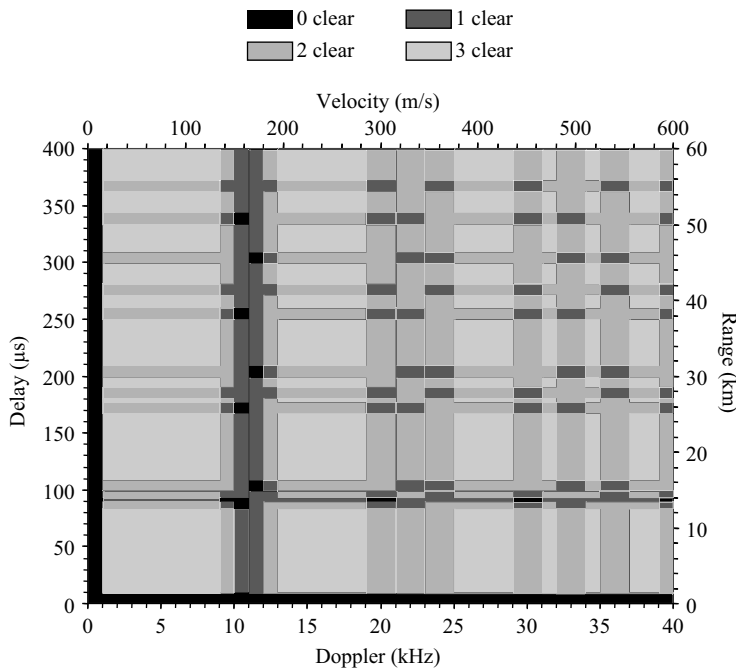


FIGURE 5.11-6 ■ Composite Blind-Zone Chart for 10-, 11-, and 12-kHz PRFs ($f_c = 10$ GHz, $\tau = 10$ μ s, $\Delta f_{D,MLC} = 2$ kHz, Mainlobe Clutter Tuned to 0).

5.11.3 Cumulative Probability of Detection and False Alarm

A radar using MPRF during a search mode may cycle through several PRFs in order to overcome blind zones and to resolve range ambiguities. At least two PRFs are needed to resolve the range ambiguity of a detected target (see Section 5.11.4). Since it is not guaranteed that the target will be in the clear for every PRF that is selected, the radar must generally use more PRFs than the minimum number needed for ambiguity resolution. Therefore, three might be considered a minimum number of PRFs. Increasing the number of PRFs increases the probability of the target being in the clear for the minimum number needed for detection.

One approach to PRF variation is referred to as an M -out-of- N criterion, whereby M detections are required out of N PRFs ($M < N$) in order to consider the detection valid. Consider the example of $M = 3$ and $N = 8$, in which the target must be detected in at least three out of the eight PRFs used. We are interested in the cumulative probability of detection P_d and cumulative probability of false alarm P_{fa} . Note that the cumulative P_d discussed here is different from the cumulative P_d resulting from successive scans in a search mode. In this case, P_d is the probability that a target will be detected in at least three PRFs, and P_{fa} is the probability that a false alarm will occur at the same range and velocity in at least three PRFs. Let $p_{d,1}$ be the single-CPI probability of detection for each PRF for which the target is in the clear. Let $p_{fa,1}$ be the single-CPI probability of false alarm for each PRF. (In practice, the single-CPI probability of detection and probability of false alarm may vary with different PRFs, depending on duty factor and CPI time. For the sake of discussion, we assume that the total energy per CPI is constant for each PRF. This can be achieved by using the same pulse width and total number of pulses per CPI, for example.) In the case of a pulse-Doppler radar, there is one detection opportunity for each range-Doppler cell.

Suppose that the target is in the clear for N_c of the N PRFs ($N_c \leq N$). If N_c is less than M , the minimum number required for a valid detection, then by definition the cumulative probability of detection P_d is zero. If $N_c \geq M$, there is a nonzero probability that the target will be detected in at least M out of the N_c clear PRFs given by

$$P_d = \sum_{m=M}^{N_c} \left(\frac{N_c!}{m!(N_c - m)!} \right) p_{d,1}^m (1 - p_{d,1})^{N_c - m} \quad (5.11-1)$$

The preceding index m indicates the number of PRFs out of the N_c clear PRFs in which detections occur. The summation adds the individual probabilities of getting m detections out of the N_c PRFs: first $m = M$ PRFs (the minimum), then $m = M + 1$, and so on until reaching the maximum possible of $m = N_c$. The product $p_{d,1}^m (1 - p_{d,1})^{N_c - m}$ is the probability of detection for a given set of m PRFs out of N_c , that is, the probability that detections occur on m PRFs, $p_{d,1}^m$, multiplied by the probability that a detection does not occur on the remaining $(N_c - m)$ PRFs, $(1 - p_{d,1})^{N_c - m}$.

The expression $\left(\frac{N_c!}{m!(N_c - m)!} \right)$ is the binomial coefficient, denoted by $\binom{N_c}{m}$. It represents the number of possible combinations of N_c PRFs taken m at a time [6]. A common approach to deriving this term is first to consider the total number of ways of forming an ordered sequence of m PRFs out of a set of N_c distinct PRFs without repeating a given PRF. Any of the N_c PRFs can be chosen for the first in the sequence. The pool from which to select the second is reduced by the first choice to $N_c - 1$ PRFs. This continues until reaching the m th PRF of the sequence, by which time the selection pool is reduced to a set of $N_c - m + 1$ remaining PRFs. Thus, the total number of ordered sequences, or permutations, $P_{N_c:m}$, is

$$\begin{aligned} P_{N_c:m} &= (N_c)(N_c - 1) \dots (N_c - m + 1) \\ &= \frac{(N_c)(N_c - 1) \dots (N_c - m + 1)(N_c - m)(N_c - m - 1) \dots (2)(1)}{(N_c - m)(N_c - m - 1) \dots (2)(1)} \\ &= \frac{N_c!}{(N_c - m)!} \end{aligned} \quad (5.11-2)$$

We are not interested in the specific order of selection of a given set of PRFs, however, so we must divide the preceding quantity by the number of different ways of ordering each unique set of m PRFs. Using the same approach, there are m choices for the first in the sequence, $m - 1$ choices for the second, and so on, until there is only one choice for the m th in the sequence (the remaining $m - 1$ having already been selected). The total number of ways of ordering a set of m PRFs is thus m factorial: $m! = m(m - 1)(m - 2) \dots (1)$. The total number of unique sets of m PRFs out of a set of N_c PRFs is therefore the binomial coefficient:

$$\frac{P_{N_c:m}}{m!} = \frac{N_c!}{m!(N_c - m)!} = \binom{N_c}{m} \quad (5.11-3)$$

We can also find an expression for the cumulative probability of false alarm using an analogous approach. In this case, however, we are not restricted to selecting from a set of N_c clear PRFs but instead may select from the entire set of N PRFs because a false

alarm is equally likely for both clear and blind PRFs. Thus, the cumulative probability of false alarm in at least M out of N PRFs is

$$P_{fa} = \sum_{m=M}^N \left(\frac{N!}{m!(N-m)!} \right) P_{fa,1}^m (1 - P_{fa,1})^{N-m} \tag{5.11-4}$$

Let us continue with the preceding example of requiring $M = 3$ detections out of $N = 8$ total PRFs and assume that the probability of detection on a single clear PRF is $p_{d,1} = 0.5$ and the probability of false alarm on any single PRF is $p_{fa,1} = 10^{-3}$. Table 5.11-1 shows the resulting values for P_d and P_{fa} . Each row represents the contribution to the cumulative probability from the condition of having exactly m detections. The probability of detection is a function of the number of clear PRFs listed in columns $N_c = 3$ through $N_c = 8$. Notice that the requirement of having a minimum of three detections results in a much lower cumulative probability of false alarm ($<10^{-7}$) than for a single PRF (10^{-3}). For the cumulative probability of detection to meet or exceed that of a single PRF (0.5), there must be at least five clear PRFs out of the eight used. Figure 5.11-7 plots cumulative P_d versus N_c for the example. The actual

TABLE 5.11-1 ■ Example of Cumulative P_d and P_{fa} for M out of N Detection*

PRFs with Detections	Probability of False Alarm	Probability of Detection					
		$N_c = 3$	$N_c = 4$	$N_c = 5$	$N_c = 6$	$N_c = 7$	$N_c = 8$
$m = 3$	5.6×10^{-8}	0.125	0.25	0.3125	0.3125	0.2734375	0.21875
$m = 4$	7.0×10^{-11}	N/A	0.0625	0.15625	0.234375	0.2734375	0.2734375
$m = 5$	5.6×10^{-14}	N/A	N/A	0.03125	0.09375	0.1640625	0.21875
$m = 6$	2.8×10^{-17}	N/A	N/A	N/A	0.015625	0.0546875	0.109375
$m = 7$	8.0×10^{-21}	N/A	N/A	N/A	N/A	0.0078125	0.03125
$m = 8$	1.0×10^{-24}	N/A	N/A	N/A	N/A	N/A	0.0039063
Cumulative:	5.6×10^{-8}	0.125	0.3125	0.5	0.65625	0.7734375	0.8554688

* $M = 3, N = 8, p_{d,1} = 0.5, p_{fa,1} = 10^{-3}$.

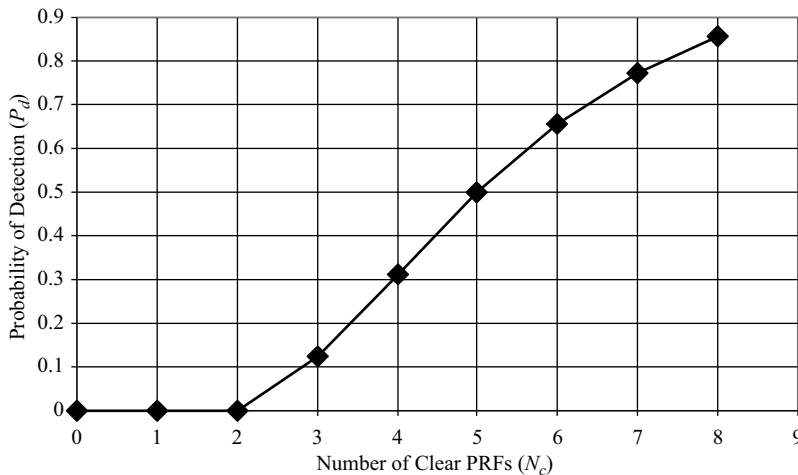


FIGURE 5.11-7 ■ Example of Cumulative P_d for M out of N Detection ($M = 3, N = 8, p_{d,1} = 0.5, p_{fa,1} = 10^{-3}$).

probability of detection for the eight PRFs is the sum of the individual cumulative P_d values, each weighted by the probability that there are exactly N_c clear PRFs for the target in question.

Increasing the number of CPIs used for detection implies that either the time on target must be increased, adding to search-frame time, or the time of each CPI must be decreased, potentially reducing SNR and single-CPI probability of detection. Fortunately, the impact is not quite as dramatic as it first appears. Because the cumulative probability of false alarm is so much lower than that for a single CPI, a relatively high single-CPI probability of false alarm, $p_{fa,1}$, can be tolerated. This allows the single-CPI detection threshold to be lowered, thereby increasing the single-CPI probability of detection for a given SNR.

5.11.4 Resolving Ambiguities

The measurements obtained in MPRF mode are generally ambiguous in both range and velocity. The radar varies PRFs to resolve these ambiguities. The ambiguity in each dimension may be resolved independently, or the radar may resolve the range ambiguity first and then use the range rate from the range tracker to resolve the velocity ambiguity. In either case, multiple PRFs are needed to obtain an unambiguous measurement. These PRFs must be chosen properly to minimize the possibility of ghosting (discussed in Section 5.11.4.2) and to provide a very large extent in range (or velocity) over which the combined measurement is unambiguous.

5.11.4.1 Correlation of PRF Detections

Consider a radar with a PRI of T_{p1} consisting of M_{R1} range bins, with each range bin corresponding to a range increment of ΔR_{bin} (nominally the range resolution). The unambiguous range interval for this PRI is $R_{U1} = cT_{p1}/2 = M_{R1}\Delta R_{bin}$. Suppose a detection occurs in bin number m_1 . The apparent range of the target is approximately $m_1\Delta R_{bin}$. The ambiguities resulting from this detection correspond to the set of values $R_1 = m_1\Delta R_{bin} + k_1R_{U1}$, where k_1 is any integer between zero and some maximum value for which k_1R_{U1} corresponds to the maximum expected range of any detectable returns.

The radar attempts to resolve the ambiguity by using a second PRI, T_{p2} , which consists of M_{R2} range bins and an unambiguous range of $R_{U2} = cT_{p2}/2 = M_{R2}\Delta R_{bin}$. We assume that the range bin size ΔR_{bin} is the same for both PRIs, or, equivalently, that the radar is maintaining a constant waveform bandwidth during this mode. Suppose that a detection occurs in range bin m_2 using the second PRI; this results in the set of ambiguous ranges $R_2 = m_2\Delta R + k_2R_{U2}$, where k_2 is defined similarly to k_1 . Since the true range must be included in the set of ambiguous ranges for both PRIs, the range ambiguity can potentially be resolved by finding the ambiguous range that is common to both PRIs. This is equivalent to finding integers k_1 and k_2 that satisfy the condition

$$m_1\Delta R_{bin} + k_1R_{U1} = m_2\Delta R_{bin} + k_2R_{U2} \quad (5.11-5)$$

The same process holds for multiple targets and a greater number of PRIs: We determine all possible ambiguous range values for the set of detections for each PRI, and then we determine which of the ambiguous values are correlated over all (or a sufficient number) of the multiple PRIs.

multiples of what is referred to as the *coambiguous range* for that set of PRFs. The coambiguous range is the smallest nonzero range that contains exactly an integer number of unambiguous range intervals (PRIs) for each PRF in the selected set. Once the coambiguous range is reached, the pattern of the different PRIs walking through each other, so to speak, begins to repeat itself as if starting again from range zero.

Let us consider the case in which the range bin size ΔR_{bin} is constant for all N PRFs in the set and each PRI consists of exactly an integer number of range bins [7]. To find the coambiguous range, we want to find the set of the smallest positive integer values k_i ($i = 1$ to N) that satisfy the equation

$$k_1 M_{R1} = k_2 M_{R2} = \dots = k_N M_{RN} \quad (5.11-6)$$

where M_{Ri} is the number of range bins in PRI number i . A candidate solution to the preceding equation is

$$k_i = \left(\prod_{j=1}^N M_{Rj} \right) / M_{Ri} \quad (5.11-7)$$

where

$$\prod_{j=1}^N M_{Rj} \equiv M_{R1} \times M_{R2} \times \dots \times M_{RN} \quad (5.11-8)$$

This solution does not ensure that the resulting values of k_i are the smallest positive integer values, however. To ensure the correct solution, we first factor each M_{Ri} into its constituent integer components. We then find the greatest common divisor for the N values of M_{Ri} , that is, the product of those factors that are common to all values of M_{Ri} . We can then rewrite each M_{Ri} as the product of the greatest common divisor, denoted by M_{GCD} , with the remaining factors of M_{Ri} that are not common to all N PRFs:

$$M_{Ri} = M_{GCD} \times (M_{Ri}/M_{GCD}) \quad (5.11-9)$$

We now seek solutions k_i to the equation

$$k_1 M_{GCD} \frac{M_{R1}}{M_{GCD}} = k_2 M_{GCD} \frac{M_{R2}}{M_{GCD}} = \dots = k_N M_{GCD} \frac{M_{RN}}{M_{GCD}} \quad (5.11-10)$$

or, equivalently, factoring out the greatest common divisor,

$$k_1 \frac{M_{R1}}{M_{GCD}} = k_2 \frac{M_{R2}}{M_{GCD}} = \dots = k_N \frac{M_{RN}}{M_{GCD}} \quad (5.11-11)$$

The solution

$$k_i = \left(\prod_{j=1}^N M_{Rj} / M_{GCD} \right) / (M_{Ri} / M_{GCD}) \quad (5.11-12)$$

is now certain to provide us with the smallest possible positive integer values. The coambiguous range can then be written, for example, as

$$R_{Coamb} = k_1 R_{U1} = k_1 M_{R1} \Delta R_{bin} = \left(M_{R1} \prod_{j=2}^N M_{Rj} / M_{GCD} \right) \Delta R_{bin} \quad (5.11-13)$$

The quantity in parentheses is referred to as the *least common multiple* for the set of N M_{Ri} values. Ideally, we would like the coambiguous range to be longer than the maximum anticipated detection range for any target to be encountered. Therefore, it is desirable to choose a set of PRIs that have a small greatest common divisor and, as a result, a least common multiple that is large.

As an example of the coambiguous range, suppose we had three PRIs of lengths 6, 8, and 10 range bins, respectively (again, using unrealistically low values for convenience). The greatest common divisor of these PRIs is $M_{GCD} = 2$, and the coambiguous range is therefore $6 \times (8/2) \times (10/2) = 120$ range bins. Now suppose that the set of PRIs is instead chosen to be 6, 7, and 10. The greatest common divisor in this case is $M_{GCD} = 1$, and the coambiguous range is 420 range bins. From the perspective of coambiguous range, the latter set of PRFs is clearly the superior of the two.

5.11.5 Sidelobe Blanking

Although the MPRF mode generally provides little or no clutter-free region in the Doppler spectrum, there is a significant portion of the folded spectrum that contains only sidelobe clutter and not mainlobe clutter. This is the region in which targets must be detected. Therefore, high RCS clutter discretizes – clutter that occupies only one or a few range bins – that are in the radar sidelobes will appear within the same ambiguous range-Doppler region as airborne moving targets. This is evident in Figures 5.11-1 through 5.11-3 of the example scenario: Target 6, the water tower in the radar sidelobe, is not distinguishable from any of the other targets on the basis of its apparent range and Doppler in the folded MPRF spectrum.

Suppose that the water tower at range $R = 5$ km in the example scenario has an RCS of +50 dBsm; that the radar has a mainlobe antenna gain of 35 dBi and a sidelobe gain toward the tower of -5 dBi; and that the radar has adequate sensitivity to detect a mainlobe target with a +5-dBsm RCS at a range of 50 km. The net two-way antenna gain toward the tower in the sidelobe relative to the target in the mainlobe is $2 \times (-5 \text{ dBi} - 35 \text{ dBi}) = -80 \text{ dB}$. The sidelobe target has an RCS that is $(50 \text{ dBsm} - 5 \text{ dBsm}) = 45 \text{ dB}$ greater than the mainlobe target and is at a range that is $(5/50) = 1/10$ the range of the target. As return power varies with R^{-4} , the range difference translates to a $10 \log(10^4) = 40 \text{ dB}$ advantage to the sidelobe return. Thus, the received power from the sidelobe discrete relative to that of the target is

$$45 \text{ dB (RCS)} + 40 \text{ dB (range)} - 80 \text{ dB (sidelobe)} = +5 \text{ dB}$$

Thus, even with the two-way sidelobe attenuation, the clutter power may be comparable to that of targets of interest.

It is desirable to reject such returns as early as possible in the radar receiver and signal-processing chain to minimize their impact on radar timeline. One method that is used is that of a sidelobe blanker. The radar employs a broadbeam auxiliary antenna, sometimes referred to as a *guard antenna*, that covers the sidelobe clutter region. The guard antenna has much lower gain than the main antenna in the direction of the latter's mainbeam, but it has higher gain than the main antenna in the direction of the latter's sidelobes. The radar receives through both the main antenna and the guard antenna in separate receiver channels. A potential sidelobe clutter false alarm will generally have higher amplitude in the guard channel than in the main channel. In contrast, the return

from a target in the mainlobe will be higher in the main channel than in the guard channel. A main-to-guard power ratio is formed on candidate detections obtained during a CPI. If the ratio exceeds some threshold (or there is no detection in the guard channel), then the detection is considered valid, that is, a mainlobe target. If the ratio is below the threshold, then it is rejected as a sidelobe clutter false alarm.

5.12 | LOW PRF MODE

Low PRF is generally not effective for detecting airborne targets. The percentage of the folded Doppler spectrum that is occupied by mainlobe clutter is too high, possibly 100 percent, to provide a useful probability of detecting the target. In the example scenario of Section 5.6, the mainlobe clutter has a Doppler extent of approximately 1.8 kHz. A radar with a 2-kHz PRF, corresponding to an unambiguous range of 75 km, would have only approximately 200 Hz of Doppler spectrum free of mainlobe clutter, or approximately 10 percent of the PRF space. As the objective of pulse-Doppler processing is to spectrally separate moving targets from co-range mainlobe clutter, such conditions do not portend success in detecting airborne targets.

Low-PRF waveforms find their greatest application in air-to-ground modes such as GMTI and SAR. These modes are similar to LPRF pulse-Doppler in their coherent, repetitive pulse transmissions, but they differ from pulse-Doppler in the way in which the returns are processed. The GMTI mode employs multiple antenna apertures and space-time adaptive processing (STAP) to help generate a narrow notch at the angle-Doppler location of mainlobe clutter in a given range cell, thereby allowing co-range ground-moving vehicles just outside the notched region to be detected. This mode is described in Chapter 9. The SAR mode employs very long coherent-processing intervals and narrow-range resolution to subdivide the mainlobe clutter much more finely than in pulse-Doppler. As a result, with the benefit of significant additional signal processing, it is possible to not only image the terrain but also to detect targets, as the target RCS may be significantly greater than the highly subdivided background clutter. The SAR mode is described in [8].

An LPRF pulse-Doppler air-to-ground imaging mode that provides a very coarse SAR-like capability is Doppler beam sharpening (DBS). In this mode, the radar scans the mainbeam over an azimuth extent of the terrain being imaged and displays a two-dimensional image showing amplitude versus range and cross range. The range resolution is achieved with pulse compression. The cross-range resolution $\delta_{C,real-beam}$, achievable at range R with a real beam of width θ_{3dB} , is

$$\delta_{C,real-beam} \cong R\theta_{3dB} \quad (5.12-1)$$

For a beamwidth of 3 degrees (0.053 radians), the cross-range resolution at a range of 20 km is only 1.05 km – quite coarse for imaging purposes. In order to improve the cross-range resolution, the radar exploits the fact that different LOS angles within the beam have different Doppler frequencies. By subdividing the beam into Doppler filters, it can essentially provide a finer angular, and hence cross-range, resolution proportional to the Doppler filter width.

Consider the conceptual LPRF pulse-Doppler implementation of Figure 5.12-1. Linear FM or phase-coding pulse compression with bandwidth B is used to achieve the range resolution of $\delta_R = c/2B$, subdividing the mainlobe clutter into many narrow slices in the range dimension. Doppler processing subdivides the mainlobe clutter into a large

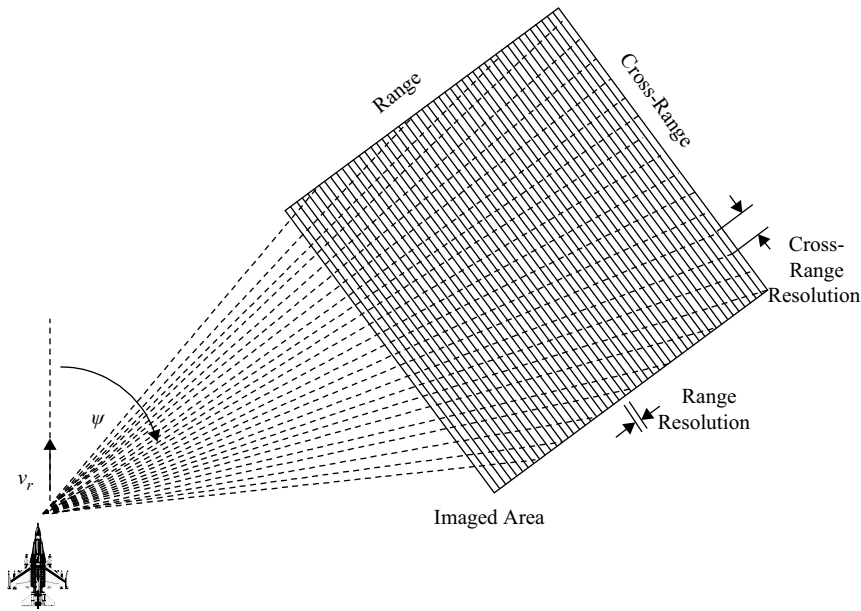


FIGURE 5.12-1 ■ Concept of Forming an Image through Range and Doppler Resolution.

number of Doppler filters at a given range. The center frequency of each Doppler filter corresponds to a slightly different scan angle relative to the radar velocity. Thus, the Doppler spectrum of a given range cell roughly corresponds to the cross-range clutter distribution at that range.

The change in Doppler frequency associated with a small change in scan angle ψ_s for a given radar velocity v_r is

$$\begin{aligned}\Delta f_D &= \frac{\partial f_D}{\partial \psi_s} \Delta \psi_s = \frac{\partial}{\partial \psi_s} \left(\frac{2v_r}{\lambda} \cos(\psi_s) \right) \Delta \psi_s \\ &= -\frac{2v_r}{\lambda} \sin(\psi_s) \Delta \psi_s\end{aligned}\quad (5.12-2)$$

The cross-range extent ΔR_C defined by the angular extent $\Delta \psi_s$ is $\Delta R_C = R \Delta \psi_s$. Therefore, the cross-range resolution $\delta_{C,DBS}$, achievable by DBS for a given Doppler resolution $\Delta f_D = \delta_D$, or equivalently, a given CPI time T_{cpi} , is

$$\begin{aligned}\delta_{C,DBS} &\cong \frac{\lambda R}{2v_r \sin(\psi_s)} \delta_D \\ &\cong \frac{\lambda R}{2v_r \sin(\psi_s) T_{cpi}}\end{aligned}\quad (5.12-3)$$

For example, $\lambda = 0.03$ m, $v_r = 200$ m/s, $\psi_s = 45$ degrees, and $T_{cpi} = 20$ ms ($\delta_D = 50$ Hz), the achievable cross-range resolution at 20 km is approximately 106 m, approximately a 10:1 improvement relative to the real-beam image.

As a bridge to understanding SAR from the DBS perspective, we instead approach the subject by determining the minimum CPI time, or aperture time, needed to satisfy a given cross-range resolution requirement:

$$T_{cpi} \cong \frac{\lambda R}{2v_r \sin(\psi_s) \delta_C} \quad (5.12-4)$$

For example, if $\lambda = 0.03$ m, $v_r = 200$ m/s, $\psi_s = 45$ degrees, $R = 20$ km, and the cross-range resolution requirement is $\delta_C = 3$ m, the SAR must coherently integrate for approximately $T_{cpi} = 0.7$ s, corresponding to a Doppler filter bandwidth of approximately $\Delta f_D = 1.4$ Hz. This is an increase of approximately two orders of magnitude in CPI time relative to typical pulse-Doppler dwells for this medium-resolution SAR capability. In addition, the signal processing required for SAR is considerably more involved than conventional pulse-Doppler, as effects such as the quadratic range variation with time must be accounted for to produce a well-focused image.

5.13 | SUMMARY

This chapter endeavored to introduce some of the key concepts associated with airborne pulse-Doppler radar. Pulse-Doppler waveforms are used to help separate airborne moving targets from strong clutter returns that are range coincident with the targets. Such clutter returns might be orders of magnitude greater than those of the targets. The radar achieves the target-clutter separation by taking advantage of the difference in range-rate that generally exists between the target and the clutter. The difference in range rate results in a difference in Doppler shift; this allows the radar to separate the two returns in the Doppler-frequency domain.

The primary clutter components are mainlobe clutter, sidelobe clutter, and the altitude return. The mainlobe clutter typically has a narrow Doppler extent but a wide range extent. The sidelobe clutter has both a wide range extent, from the radar altitude to the radar horizon, and a wide Doppler extent, increasing with range to a maximum that is equivalent to twice the radar velocity. The altitude return, a specific component of sidelobe clutter, typically has a wide Doppler extent but a narrow range extent located at the range equal to the radar altitude.

The pulse-Doppler waveform typically consists of a constant-PRF, phase-coherent burst of pulses. The radar processes returns from these pulses obtained within a time interval referred to as a *coherent-processing interval*. The receive interval in each PRI within the CPI is divided into range bins, or range gates, that are nominally equivalent to the radar range resolution. The complex voltages for each range gate are collected for all the PRIs in the CPI and processed through an FFT to obtain a Doppler spectrum for each range gate. This forms a two-dimensional range-Doppler map that potentially allows separation of the target in both range and Doppler domains.

The pulse-Doppler waveform is ambiguous in its measurement of range and Doppler due to the necessarily repetitive nature of the coherent pulse burst. This inherent ambiguity introduces measurement uncertainties and blind zones in both dimensions. Depending on the engagement geometry, the radar operates in one of three broad PRF regimes – high PRF, medium PRF, and low PRF – each with different properties related to ambiguities.

High PRF ensures an unambiguous Doppler measurement, but it is highly ambiguous in range. This mode is ideally suited for nose-aspect geometries where the target radial velocity exceeds the radar platform velocity and therefore has a Doppler shift that is higher than any clutter return. Variations of high PRF include velocity search, which is essentially a Doppler-only mode; linear FM ranging, which provides coarse range information through linear variation of the carrier frequency over the CPI; and range-gated high PRF, which employs a lower duty cycle waveform and pulse compression to

obtain improved range-measurement capability. High PRF performance typically suffers when the target Doppler falls within the bounds of the sidelobe clutter Doppler; this occurs, for example, under tail-chase or wide-aspect angle geometries.

Medium PRF is moderately ambiguous in both range and Doppler dimensions. The resulting range-Doppler map contains sidelobe clutter everywhere but has large Doppler regions that are free of mainlobe clutter and large range regions that are free of altitude returns. As a result, through low sidelobes, range gating, and Doppler filtering, the radar is able to detect airborne moving targets despite folded sidelobe clutter. Multiple PRFs are used to circumvent range and velocity blind zones and to resolve measurement ambiguities in each dimension.

Low PRF is unambiguous in range but highly ambiguous in Doppler. It is typically not as effective as high and medium PRFs for detecting airborne moving targets because most or all of the ambiguous Doppler extent – equal to the radar PRF – is consumed by the spread of the mainlobe clutter in Doppler. Low-PRF waveforms are more commonly used in air-to-ground modes, such as GMTI, Doppler beam sharpening, and SAR.

One penalty associated with pulse-Doppler is the consumption of radar timeline. Long CPIs consisting of many pulses, the overhead associated with clutter-fill pulses, and the use of multiple pulse bursts at different PRFs to overcome blind zones and ambiguities are all factors that increase the required time on target for pulse-Doppler operation. Despite the timeline penalty and the various design complications resulting from the ambiguous nature of the waveforms, the pulse-Doppler modes still provide the best choice for airborne radar to detect moving targets under most operational conditions of interest.

5.14 | REFERENCES

- [1] N.C. Currie, M.A. Richards, and B.M. Keel, Chapters 5, 7, 16, and 20, *Principles of Modern Radar: Basic Principles*, M.A. Richards *et al.*, Editors, SciTech Publishing, Inc., North Carolina, 2010.
- [2] G. Morris and L. Harkness, Editors, *Airborne Pulsed Doppler Radar*, Second Edition, Artech House, Inc., Massachusetts, 1996.
- [3] G.W. Stimson, *Introduction to Airborne Radar*, Second Edition, SciTech Publishing Inc., New Jersey, 1998.
- [4] R.K. Moore, “Ground Echo,” Chapter 12, *Radar Handbook*, Second Edition, Merrill Skolnik, Editor, McGraw-Hill, Inc., New York, 1990.
- [5] M.A. Richards, “Digital Signal Processing Fundamentals for Radar,” Chapter 14, *Principles of Modern Radar: Basic Principles*, M.A. Richards *et al.*, Editors, SciTech Publishing, Inc., North Carolina, 2010.
- [6] S. Ross, *A First Course in Probability*, Third Edition, Macmillan Publishing Company, New York, 1988.
- [7] G.A. Showman, “Medium PRF Selection,” Lecture 12 from the Georgia Tech short course, *Principles of Pulse-Doppler Radar*, March 2006.
- [8] D.A. Cook and G.A. Showman, Chapters 6 and 7, *Principles of Modern Radar, Vol. II: Advanced Techniques*, W.L. Melvin, J.A. Scheer, Editors, SciTech Publishing, New Jersey, 2013.

Multifunction Phased Array Radar Systems

Melvin L. Belcher, Jr., Georgia Tech Research Institute, Atlanta, GA

Chapter Outline

6.1	Introduction	251
6.2	Operational Concepts and Military Utilities	254
6.3	MPARS Sizing and Performance Evaluation	257
6.4	ESA Overview	262
6.5	Radar Control and Resource Management	268
6.6	MPARS Technologies	276
6.7	MPARS Testing and Evaluation	280
6.8	Netcentric MPARS Applications	281
6.9	References	283
6.10	Further Reading	283

6.1 | INTRODUCTION

This chapter provides an overview of modern Multifunction Phased Array Radar Systems (MPARSs). The distinguishing feature of a modern MPARS is element-level control of the antenna array directed by an automated resource management process providing:

- dwell-to-dwell beam agility enabling complex functional multiplexing and
- arbitrary antenna pattern synthesis, including tailored sidelobe suppression.

The two principal application areas of this class of radar currently are:

- ground-based and shipboard sensors for supporting air and missile defense and
- airborne radars onboard combat and surveillance platforms supporting a mixture of air-to-air and air-to-ground operations.

The scope of phased array radar applications is illustrated in Table 6-1 according to frequency operating band. As an important caveat, only a fraction of the depicted band allocations are actually available for radar applications, and any new radar application must address severe spectral compatibility constraints. Life-critical services, telecommunications, and personal communication system applications are increasingly constraining microwave radar applications at C-band and below.

TABLE 6-1 ■ Phased Array Radar Systems Grouped by Band and Application

Band	Frequency	Principal Applications	Selected Examples
HF	3–30 MHz	Over-the-horizon radar	Land: ROTH, JORN
VHF	30–300 MHz	Long range search	Land: Daryal (Pechora) and Voronezh Large Phased Array Radars, NEBO
UHF	300–1,000 MHz	Long range surveillance	Land: FPS-85, PARCS, PAVE PAWS, BMEWS; MEADS surveillance
L	1–2 GHz	Long range surveillance	Land: Cobra Dane Air: PHALCON, MESA (Wedgetail)
S	2–4 GHz	Surveillance; long range tracking	Land: G/ATOR Sea: Aegis SPY-1; Cobra Judy, VSR, Sampson, CEAFAAR Air: APY-1/2, Erieye
C	4–8 GHz	Fire control; instrumentation tracking	Land: PATRIOT, MOTR Sea: EMPAR
X	8–12 GHz	Fire control, missile seeker; target identification; airborne sensing	Land: S-300/S300V and descendants, TOR, MEADS fire control, TPY-2, XBR Sea: SPY-3, APAR Air: APQ-164, APY-7, APG-79, APG-80, APG-81, MP-RTIP
Ku	12–18 GHz	Short-range fire control; remote sensing	Air: APQ-181

Legacy surface-based MPARS integrating autonomous search and track functions tend to be concentrated in S-band and C-band as a compromise between search and track performance, as exemplified by the Aegis AN/SPY-1 B/D and PATRIOT AN/MPQ-53/65. Consolidation of diverse functions into a single radar may also force compromise on polarization optimization for competing functions, such as sensing weather versus maximizing noise-limited range. Radar resource demands associated with increasing degrees of consolidated functionality challenge the radar control process, as addressed subsequently. These considerations are motivating interest in constructing next-generation air and missile defense systems around highly integrated low-band and high-band multifunction radar systems, providing more optimized search and track performance as well as enhancing air and missile defense performance.

In general, performance/cost trades favor lower frequencies (UHF through L-band) for long-range air and missile defense and space surveillance. The costs of generating radio frequency (RF) transmit power and constructing the RF aperture area tend to fall with decreasing frequency. The relatively large beamwidth provided by a given aperture size at lower frequencies facilitates search by reducing the number of beams required to cover a specified angular extent. Operation at this band provides favorable target radar cross sections for typical aircraft and missile sizes. Propagation losses due to tropospheric attenuation fall with decreasing frequency, but the ambient noise environment increases with decreasing frequency due to the combination of sky noise and human-generated interference degrading very high frequency (VHF) and potentially ultrahigh frequency (UHF) detection performance. Susceptibility to ionospheric propagation effects also increases significantly with decreasing frequency, further impacting space surveillance and missile-warning performance.

Precision tracking, target identification, and low-elevation/short-range operations favor higher frequencies (C-band and above). Range resolution (achievable waveform bandwidth) and Doppler resolution (for a given coherent processing interval) both improve with increasing frequency. Metric accuracy similarly improves with increasing frequency, as the beamwidth is finer for a given aperture extent, as well as enhancing range and Doppler resolution. Operating at higher frequencies generally enhances low-elevation search and tracking by mitigating clutter and multipath effects and enabling a narrow beamwidth to provide sidelobe rejection of surface clutter. Multipath fades decorrelate over a shorter interval as the frequency increases. Doppler filtering resolution for clutter rejection is enhanced by increasing frequency. Both multipath mitigation and clutter rejection benefit from the use of a narrower beamwidth enabled by increasing the frequency for a given aperture extent enabling sidelobe rejection of returns. Ionospheric propagation effects, which are important in missile defense and space situational awareness, decrease markedly as the carrier frequency increases through the microwave band.

A great deal of military MPARS development is at X-band due to the associated advantages of RF aperture compactness, weapon guidance support, and enhanced resolution and accuracy, as well as relatively generous international frequency allocation. X-band radars are particularly well suited for two military applications:

- detection and tracking of small targets masked by strong surface clutter and
- precision tracking of long-range targets to support weapon guidance along with high-resolution noncooperative target identification.

Examples of modern X-band MPARSs include the F-18 E/F AN/APG-79, F-35 AN/APG-81, the AN/TPY-2/Terminal High Altitude Area Defense (THAAD) radar, and the U.S. Navy AN/SPY-3 ship self-defense radar. All these radars employ active electronically scanned arrays (AESAs) where each radiating element is supported by dedicated transmit and receive amplifiers employing solid-state technology.

The number of phased array elements required to support a given field-of-view increases with the square of the carrier frequency for a given array area, as elements must be linearly spaced at a specified fraction of a wavelength to avoid spatial under-sampling on the antenna aperture. Recurring array cost tends to trend with the number of elements. Array component costs also tend to increase with frequency. Hence, there is a corresponding affordability penalty as the carrier frequency is increased.

A key feature shared by all MPARSs is an automated software process to manage the phased array antenna and other subsystems in order to schedule and execute dwells. A dwell is a radar action resulting in transmission or reception of a beam into a specific angular coordinate so as to collect target returns over a given range interval. Exploitation of a phased array radar's full capabilities are critically dependent on this control process to utilize duty cycle and timeline resources effectively, as the associated computational decision rate demands far outstrip the capabilities of human operators. MPARSs employ a repertoire of single- and multiple-pulse waveforms to enable efficient resource management.

6.1.1 Organization

The enabling systems concept generally common to Multifunction Phased Array Radars is described in the following sections. Sizing issues and performance analysis are then

addressed as a means of relating the suitability of MPARSs to perform specific missions in terms of their composite search and track capabilities. Overviews of two key implementation issues are provided – the electronically scanned array (ESA) antenna and the resource management software – with emphasis on a systems engineering perspective. A brief account of key technologies is then provided. The chapter concludes with some pragmatic observations on the test and evaluation of MPARSs and some speculative considerations about anticipated MPARS evolution to support netcentric warfare.

6.1.2 Acronyms

AESA	– active electronically scanned array
AMD	– air and missile defense
DBF	– digital beamforming
ESA	– electronically scanned array
HPA	– high-power amplifier
LNA	– low-noise amplifier
MPARS	– Multifunction Phased Array Radar System
RCS	– radar cross section
T/RM	– transmit/receive module
TDS	– track during scan
TWS	– track while scan
TWT	– track while track

6.2 | OPERATIONAL CONCEPTS AND MILITARY UTILITIES

An MPARS employs an electronically scanned array (ESA) composed of individually controlled radiating elements directed by an automated resource management process. The phase and potentially amplitude of these individual elements are systemically controlled to provide electronic beam scanning and antenna pattern synthesis on both transmit and receive. Modern ESA designs can potentially change beam-pointing direction and overall antenna pattern within microseconds constrained typically by the beam-steering system that commands and controls the individual elements. The MPARS transmits a dwell into each beam position with tailored waveform characteristics and performs a corresponding receive dwell to collect returns. While electronic beam agility significantly increases the cost of a given antenna aperture area over that of a mechanically scanned array, the resulting capability enhancement has motivated extensive development and deployment of phased array radars in demanding mission areas.

Radar development for surface applications has been driven by the continuing trend in air and missile defense toward engaging multiple targets along with decreasing target radar cross section (RCS) and shorter timelines due to advances in threat velocity, low-altitude entry, and countermeasures. This mutually reinforcing set of offensive capabilities has grossly degraded the effectiveness of defensive systems employing an ensemble of specialized mechanically scanned radar for search/acquisition, target

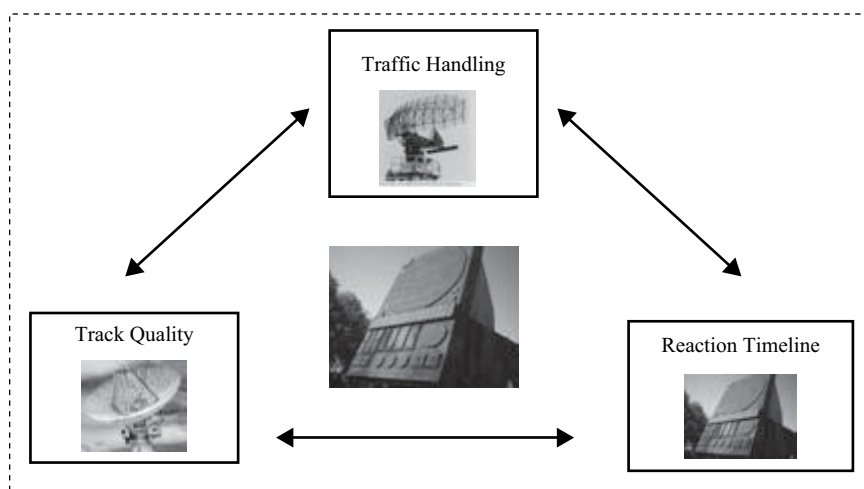


FIGURE 6-1 ■
MPARS Support of
Critical Air and
Missile Defense
Requirements.

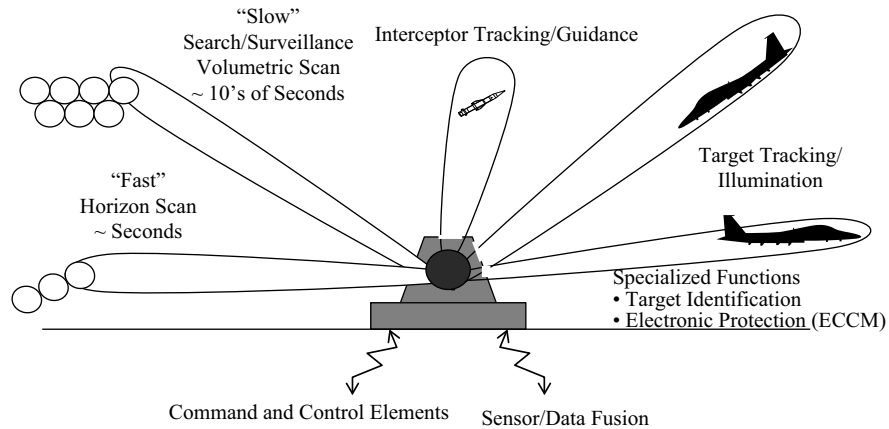
tracking, and weapon guidance. Mechanically scanned search/acquisition radars typically conduct track while scan (TWS) operation with repetitive 360° azimuthal rotation sweeps at periods of 5 to 10 seconds over fixed elevation extents. Track initiation under TWS requires target detection and correlation over several successive scans. Established tracks are then updated at the relatively slow rotation rate using coarse-resolution surveillance waveforms. The associated measurement accuracy and track update rate are generally inadequate to support fire control. Track firmness can be problematic in dense multiple-target environments.

Dedicated target track radars or semi-active illuminators must be used to support engagements when using mechanically scanned systems. These fire-control radars typically depend on handover from the TWS surveillance radars. The resultant timeline required for establishing, handing over, and acting on tracks is excessively long for conducting air and missile defense (AMD) engagements against modern threats. In addition, the necessity for dedicated fire-control radar operation against each target under engagement imposes significant susceptibility to saturation attacks.

MPARSs support the interacting AMD requirements for traffic handling, fire-control track quality, and quick reaction as depicted in Figure 6-1. A TWS surveillance radar generally possesses superior track capacity and coverage extent required to generate the “air picture.” However, TWS radars do not generally produce “fire-control quality” tracks of sufficient accuracy, timeliness, and confidence to support weapon commit and guidance. A mechanically scanned tracking radar generally provides the best quality track, since its “staring” mode of operation produces a high data rate but it is essentially a single-target tracker. The quick reaction enabled by automated beam agility enables MPARSs to enforce a track initiation range that is virtually synonymous with the initial detection range, as track can be initiated within a few hundred milliseconds of the initial detection. MPARSs can immediately verify a target detection report by revisiting that beam position and then implementing a dedicated track-initiation dwell sequence.

MPARS usage enables all three operational needs to be met with a single sensor. Track during scan (TDS) capability is critical to enforcing low-latency engagement against low-flying/small targets and meeting other AMD challenges. The capability to

FIGURE 6-2 ■
Surface-Based
Multifunction
Phased Array Radar
Operations.



put dedicated track dwells on a detected target at significantly higher data rates than the search frame rate enables an MPARS to provide fire-control quality tracks on multiple targets. Subject to sizing, as addressed subsequently, the automated resource manager can support multiple near-simultaneous engagements, varying measurement quality and update rates according to weapon system needs.

A key architectural imperative for affordability is to minimize the RF aperture sizing through aggressive trade analysis in deriving system requirements and implementing efficient resource management. The radar-control process is implicitly designed to minimize the resources allocated to any function subject to provide a specified minimum performance level. So, while an MPARS providing unique quick reaction capabilities, it may be designed to meet minimum military utility requirements in such areas as search volume refresh and track accuracy.

An MPARS multiplex dwells among track and interceptor guidance functions while continuing to conduct search and surveillance, as illustrated in Figure 6-2. This mixture of spatially diverse dwells tailored to specific search and track tasks is known as track during scan (TDS) operation. The capability to dynamically allocate radar resources between search and track increases resilience to saturation attacks, as well as enabling detection and track of stressing targets. Automated beam agility enables coverage volume, waveforms, and update rates to be optimized for individual functions and target characteristics. For example, horizon scans may be conducted frequently using waveforms optimized for clutter rejection to ensure timely detection of threatening targets. These horizon scan dwells can be interleaved with a slower volumetric scan using single-pulse waveforms intended to maintain a surveillance air picture. Other dwells can be inserted as needed to support specialized functions such as electronic protection or noncooperative target identification.

MPARS onboard aircraft and ships can support a dynamic mixture of offensive, defensive, and navigation functions, replacing multiple mechanically scanned radars formerly employed to perform specialized applications. For example, the AN/SPY-3 ship self-defense radar can replace legacy acquisition; tracking, illuminator, navigation, periscope detection, surface surveillance/engagement, and aircraft operations support radars depending on the specific type of ship [1]. This consolidation of mechanically scanned antennas into a single RF aperture improves signature control, as well as enabling more

compact radar mechanization. Modern MPARSs incorporating face-mounted inertial measurement units can also effectively compensate in the electronic beam-steering process for rotational motions of the host platform.

Modern MPARSs employed in combat and surveillance aircraft enable concurrent air-to-air and air-to-ground operations such as supporting multiple target engagements while maintaining situational awareness surveillance scans [2]. A modern combat aircraft MPARS of adequate capability can employ TDS techniques to simultaneously:

- maintain situational awareness via surveillance scans while tracking multiple airborne targets and
- interleave low-update-rate/long-duration radar air-to-ground functions such as synthetic aperture radar imaging and ground-moving target indicator tracking.

Maintaining situational awareness scans during engagements is of such significant military utility that MPARSs are sometimes referred to as search while track (SWT) sensors. The enhanced resolution and target performance of the interleaved air-to-ground modes are achieved by tailoring waveform parameters and signal processing on a beam-to-beam basis while coherently processing data across multiple noncontiguous dwells.

An MPARS can also provide significantly enhanced weapon guidance accuracy over dedicated mechanically scanned sensors that individually track the target and the interceptor to provide command guidance or in-flight updates. An MPARS can track both the target and engaging interceptor(s) so as to suppress bias-like error components from the guidance process since such error will be highly correlated between the target and interceptor tracks. The resultant guidance error should be dominated by the root-sum-square of the random errors associated with the target and interceptor tracks. The reduction in guidance error in conjunction with improved track firmness enables more energy-efficient fly-outs so as to enable the interceptor to fully exploit its kinematic capabilities.

6.3 | MPARS SIZING AND PERFORMANCE EVALUATION

The beam agility, waveform repertoire, and automated control of a modern MPARS enable exceptional mission flexibility. However, sizing the operational capabilities of MPARS is problematic due to this flexibility. While performance constraints imposed by the resource management process are addressed subsequently, the fundamental search and track performance bounds can be assessed using variants of the radar range equation as introduced in Chapter 2 of Volume 1. Performance under clutter-limited and inference-limited conditions is beyond the scope of this chapter, but the following analysis of noise-limited search and track capabilities provides an upper performance bound.

A modern representation of the radar range equation can be defined as

$$\frac{S}{N} = \frac{PGA\sigma T_p N_p}{(4\pi)^2 R^4 L_s k T_s L_o} \quad (6-1)$$

where

S/N = signal-to-noise ratio referenced to signal processor output,

P = peak transmitter power output,

G = directivity of the transmit antenna (nominally $4\pi A_t/\lambda^2$),

A = effective aperture area of the receive antenna,

σ = radar cross section (RCS),

T_p = pulse duration,

N_p = number of coherently integrated pulses,

R = range to target,

L_s = system loss,

k = Boltzmann's constant,

T_s = system noise temperature, and

L_o = operational loss factor.

This form of the radar range equation is applicable to radar systems employing pulse compression or pulse Doppler waveforms as well as the unmodulated single-pulse case. The system loss is referenced to the composite S/N loss from transmit losses and receive non-ohmic losses relative to the ideal matched filter response to the transmitted waveform. The system loss factor as defined here presupposes “matched filter” conditions corresponding to beam, range gate, and Doppler filter centered on the target without propagation or other external losses included. The system loss factor is typically verified via a combination of analysis, factory testing, and calibration measurements along with the other radar range equation parameters and ultimately anchored with end-to-end measurements from field testing using calibrated targets. System noise temperature captures the cumulative impact of external and internal noise sources interacting with the receive gain chain and associated ohmic receive losses [3].

The operational loss factor associated with specific search, track, and other functions is used to capture the incremental application-specific losses. Classical radar analysis procedures, such as Blake charts, developed without benefit of modern simulation capabilities, estimate the composite mean operational losses and insert them into the radar range equation to assess performance. Many high-fidelity radar simulations that evaluate dwell-by-dwell performance attempt to directly model specified target scenarios and environmental conditions so that the operational loss is effectively set to zero in estimating radar sensitivity. A classical radar analysis of sensitivity in conjunction with the following sizing estimation is a useful check to ensure that a high-fidelity radar simulation is representing the full span of operational loss sources in its truth models and functional representations of radar operation.

Environmental losses include attenuation due to tropospheric and ionospheric propagation, as well as multipath, where applicable, and are a key component of operational loss. Both search and track operational losses should include elevation-dependent propagation losses due to tropospheric effects under representative meteorological conditions. Ionospheric losses are a function of elevation, frequency, and polarization, varying with the total electron count encountered according to radar-target geometry and the state of the ionosphere. Multipath fading loss should be estimated for low-elevation applications according to the antenna pattern, polarization, surface characteristics, frequency, and elevation angle.

Search operational loss is typically 3–5 dB larger than track operational loss since it includes the effects of target positional uncertainty prior to detection and track initiation.

Operational losses should also include provision for scan loss and hardware degradation, as addressed in Section 6.4.2. In general, the average loss is estimated across the span of relevant operational conditions to assess impact on radar performance. Operational losses due to target positional uncertainty include:

- *Beamshape roll-off*: target position is assumed to be uniformly distributed within any beam position comprising a search raster so the average loss in two-way gain must be estimated.
- *Range gate mismatch*: target position is assumed to be uniformly distributed within a range gate so corresponding average straddle loss must be according to the range-mismatch response.
- *Doppler filter mismatch*: target range-rate is assumed to be uniformly distributed within a Doppler filter so the average straddle loss must be estimated according to the Doppler filter response.
- *Eclipsing loss*: in the event of pulse Doppler waveforms, the target range is assumed to be uniformly distributed within a pulse repetition interval so that the average eclipsing loss must be estimated.

Strictly speaking, the average loss should be computed by assessing the impact on detection probability and then computing the equivalent loss in S/N [4]. Operational losses can also be inferred from the Monte Carlo exercise of high-fidelity radar simulations.

Operational losses due to target positional uncertainty are largely eliminated in TDS tracking where each track dwell is “matched” to the estimated target position and velocity. The radar centers the beam and range/Doppler tracking gate on the target from one dwell to the next. Decreasing operational loss increases S/N so that if an MPARS is successful in initially detecting and initiating track on a target, it should be capable of maintaining a firm track under nominal conditions.

6.3.1 Search Sizing

In order to define a suitable performance metric, it is convenient to group relevant radar design parameters on one side of the equation while grouping operational and threat parameters on the other side of the equation. The solid angle over which search is conducted can be defined as

$$\Omega = \Delta AZ \cdot (\sin(EL_{max}) - \sin(EL_{min})) \quad (6-2)$$

where

ΔAZ = the azimuth search extent and

EL = the maximum and minimum elevation search extent, depending on the subscript [5].

The solid angle extent of a single transmit beam is $\sim \frac{4\pi}{G}$. Hence, the number of beams required to fill the search volume is $\sim \frac{\Omega \cdot G}{4\pi}$. The corresponding beam rate required for search can be estimated as the required number of beams divided by the search frame time T_{fs} . The search frame time is the maximum time interval allowed to scan through a given volume. The value is estimated on the basis of the minimum time estimated for a

target to transit through the angular extent of the search volume divided by the number of observations desired on each target during search.

This operationally specified beam rate can be related to the radar design by specifying the pulse repetition frequency (PRF) to be equal to the beam rate. The PRF is defined in terms of radar design parameters as

$$P_a = P \cdot PRF \cdot T_p = d \cdot P \quad (6-3)$$

where

P_a = average power and
 d = the duty cycle.

Pulse duration is determined by the S/N required on a per-beam basis for an operationally specified level of detection performance against a target of specified radar cross section, fluctuation model, and range.

Substituting the relation for average power in place of peak power in the radar range equation and inserting an incremental operational loss term representative of specific search functions L_{os} results in

$$\frac{S}{N} = \frac{P_a G A \sigma N_p}{(4\pi)^2 R^4 L_s L_{os} k T_s PRF} \quad (6-4)$$

Now, substitute in the operationally required beam rate in place of PRF while setting N_p to unity without loss of generality, resulting in

$$\frac{S}{N} = \frac{P_a G A \sigma 4\pi T_{fs}}{(4\pi)^2 R^4 L_s L_{os} k T_s \Omega G} \quad (6-5)$$

Rearranging the terms and denoting S/N by the quantity required for detection results in the following sizing metric:

$$\frac{P_a A}{L_s L_{os} T_s} \geq \frac{S}{N} \Big|_r \cdot 4\pi k \frac{R_{max}^4 * \Omega}{\sigma * T_{fs}} \quad (6-6)$$

where the newly introduced terms are

P_a = average transmitter power output,
 $S/N|_r$ = signal-to-noise ratio required for specified detection and false-alarm probabilities and RCS fluctuation model,
 Ω = solid angle over which search must be performed (steradians),
 T_{fs} = frame time allowed to search Ω by operational requirements.

As indicated, the left side of the equation contains radar design parameters while the right side is determined by target characteristics and operational requirements. In the event that the radar supports multiple concurrent search modes, such as volumetric and horizon search, the composite radar requirements are calculated by summing the right side across the requisite combinations of S/N requirement, maximum range, RCS, search extent, and search frame time corresponding to concurrent searches such that

$$\frac{P_a A}{L_s T_s} \geq 4\pi k \cdot \sum_{i=1}^N \frac{S}{N} \Big|_{r_i} \cdot \frac{R_{max_i}^4 * \Omega_i \cdot L_{osi}}{\sigma_i * T_{fs_i}} \quad (6-7)$$

Note that the operational term has been moved to the right side of the equation, signifying that it may vary with different search scenarios.

6.3.2 Track Sizing

Track, discrimination (target identification), signature collection, and other target-oriented radar functions can often be characterized by the capability to maintain a given measurement rate at a requisite single-measurement S/N across some number of targets. Using the previous expression for the radar range equation incorporating PRF explicitly and substituting in track requirements results in the following expression for a track set:

$$\frac{S}{N} = \frac{P_a G A \sigma}{(4\pi)^2 R^4 L_s L_{ot} k T_s N_t r} \quad (6-8)$$

where

r = single-target track rate (measurements per second) and
 L_{ot} = operational loss for track.

There is an implicit lower bound on S/N corresponding to that required to reliably maintain adequate detectability for the target track (say, >12 dB). Target positional uncertainty is minimized by TDS closed-loop tracking so as to result in the beam being pointed at the target under track and the return being approximately centered in the range gate/Doppler filter. An operational loss term for track is included to account for external propagation effects such as multipath fade and atmospheric absorption, as well as residual target uncertainty, if significant.

Assuming equivalent transmit and receive antenna areas, these substitutions result in the following sizing relationship to be summed across the N_t TDS tracks:

$$\frac{P_a A^2}{\lambda^2 L_s T_s} \geq 4\pi k \cdot \frac{S}{N} \bigg|_r \cdot \sum_{i=1}^{N_t} \frac{r_i R_i^4 L_{oti}}{\sigma_i} \quad (6-9)$$

where

N_t = number of targets under track.

As in the search radar range equation, operational losses have been moved to the right side of the equation to accommodate variation in losses due to elevation, scan angle, and other variations.

Since an MPARS must multiplex search and track, the left sides of the search and track equations represent performance bounds, with the entire radar resources allocated to search and track, respectively. Unlike mechanically scanned radars, automated beam agility enables an MPARS to dynamically allocate resources among search and track so as to maximize operational utility subject to the sizing metric bounds. Accordingly, the RF aperture should be sized to simultaneously satisfy the search and track sizing requirements metrics such that

$$\frac{d_s P A}{L_s T_s} \geq 4\pi k \cdot \sum_{i=1}^{N_t} \frac{S}{N} \bigg|_{r_i} \cdot \frac{R_{max_i}^4 \Omega_i \cdot L_{osi}}{\sigma_i T_{fs_i}} \quad (6-10a)$$

and

$$\frac{d_t P A^2}{\lambda^2 L_s T_s} \geq 4\pi k \cdot \frac{S}{N} \bigg|_r \cdot \sum_{i=1}^{N_t} \frac{r_i R_i^4 L_{oti}}{\sigma_i} \quad (6-10b)$$

where

d_s and d_t = the duty cycle allocations to search and track, respectively, such that $d = d_s + d_t$ in the absence of other radar functions.

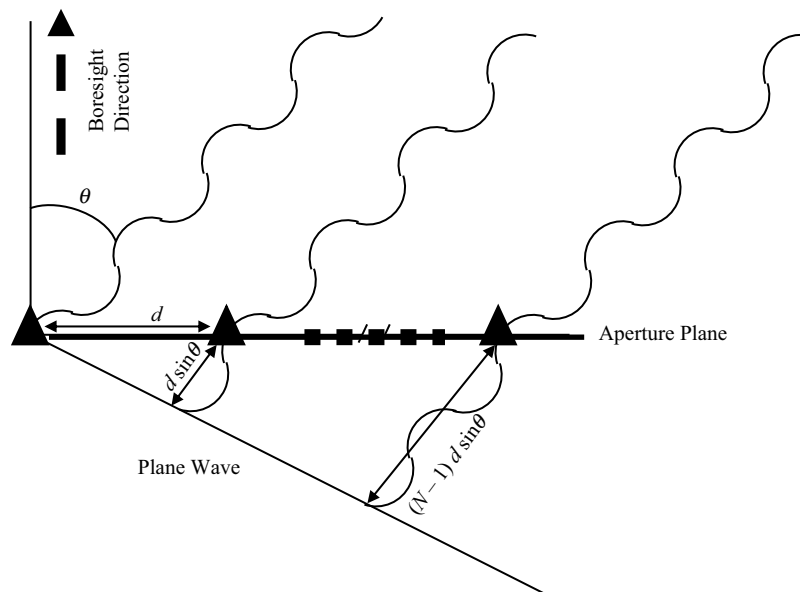
In order to exercise this functionality, the MPARS must employ a resource management process as described subsequently that schedules waveforms and beam rates to meet the operational search and track requirements. In addition to meeting the nominal sizing requirements, resource management can enable the radar to shift resources between search and track in response to time-varying loading demands. For example, volumetric search can be slowed in order to divert resources to horizon search or heavy track loading.

6.4 | ESA OVERVIEW

6.4.1 Array Principles

The principles of ESA beam scanning are summarized in Figure 6-3 using the one-dimensional case of a narrowband N -element array for ease of understanding. An electromagnetic plane wave impinging along the linear array imposes an element-to-element phase differential proportional to the element separation projected along the angle-of-arrival (AOA). The element-to-element phase differential $\Delta\varphi$ imposed by AOA

FIGURE 6-3 ■
Relationship
between Phase
Taper Geometry and
Beam Steering.



θ_{AOA} for an element spacing d and carrier wavelength λ along the plane of the scan is given by

$$\Delta\varphi = 2\pi \frac{d}{\lambda} \sin \theta_{AOA} \quad (6-11)$$

Hence, an impinging plane wave imposes a linear phase taper across the array with a cumulative run-out of $(N - 1) \Delta\varphi$ rad.

A beamformer with fixed-phase weights applied to each element would encounter destructive interference when summing samples of a plane wave received from outside the near-boresight region where $\Delta\varphi \rightarrow 0$. The narrow angular extent over which constructive interference occurs is the antenna mainlobe, while the region of destructive interference corresponds to the antenna sidelobes. The only way to scan the beam with an antenna employing a fixed-element phasing is to mechanically steer the boresight of the antenna.

An ESA scans by commanding element-level phase shifters to the conjugate plane-wave phase taper for a commanded AOA, the steering angle. The resulting element signals are then summed in a beamformer to produce the antenna output. The ESA effectively serves as a spatial filter matched to an element-sampled plane wave propagating along the designated AOA with a resultant gain proportional to the number of contributing elements N . On transmit, the contributions of each radiating element coherently sum in free space along the AOA corresponding to the commanded beam-pointing direction.

The individual elements possess phase shifters with settings computed and commanded by a beam-steering computer that implements the real-time pointing commands of a central data processor executing the radar control program. Hence, the beam can steer to another position as rapidly as the phase shifters can be reset. Beam-steering times in modern arrays employing PIN diode phase shifters are typically less than 10 μs as determined largely by the period required for beam-steering computations. In a modern AESA, the beam-steering computer typically maintains and implements compensation tables for errors measured during the array calibration process. Hence, the commanded setting of a given phase shifter takes into account the composite measured error of that element path through the array as a function of frequency and array temperature in order to closely approximate the desired element-level taper.

The far-field pattern of an aperture antenna possesses a Fourier transform relationship with the excitation function (current distribution) across the aperture [6]. The antenna elements are intended to represent samples of the ideal excitation function subject to hardware errors. The discrete Fourier transform of the element amplitude and phase samples is termed the array factor. If the aperture is undersampled by spacing the elements too far apart relative to the wavelength, grating lobes form analogous to aliased mainlobes. Suppressing all grating lobes within 90° of the mainlobe would mandate that the elements be spaced at $\lambda/2$ in the designated scan plane.

From the Fourier transform relationship, we can infer that amplitude weighting across the aperture can suppress the far-field sidelobes. Since weighting introduces mismatch relative to spatial matched filtering of an impinging plane wave, there is a corresponding S/N loss and mainlobe broadening. Weighting does not significantly suppress grating lobes, as they are aliased replications of the mainlobe. In addition, amplitude and phase errors – deviations from the desired excitation function – produce

spurious-angle sidelobes that are not mitigated by weighting and that impose a corresponding “floor” on achievable sidelobe suppression, as addressed in the next subsection.

Phased array antennas are constructed of directive radiating elements so that the actual far-field antenna pattern is the product of the array factor pattern and the element pattern [7]. Elements are generally designed to possess identical electrical characteristics so that the element pattern may be generally represented as corresponding to that of a single radiator embedded in the array electrical environment as a function of AOA, neglecting slight variations due to manufacturing tolerances as well as proximity to the array edge. The element pattern is fixed in angle and centered on boresight, the direction orthogonal to the plane of the aperture. The element pattern’s extent determines the effective scan extent of the array.

The gain of the array at a given AOA is then the corresponding gain of the element pattern multiplied by that of the array factor. Assuming that the radiating element is designed to support a full field of view (FFOV), the maximum element pattern gain can be approximated as $10 \cdot \log(\pi) \approx 5$ dB. The maximum gain on boresight, the direction perpendicular to the plane of the array, for a uniformly excited array of N FFOV elements is then approximately $10 \cdot \log(\pi N)$ corresponding to the directivity of the aperture as described later.

As the ESA beam is steered off boresight, the projected aperture extent decreases, resulting in beam broadening and loss in gain. The two-way transmit/receive element gain of a conventional array can generally be approximated as rolling off with the cosine cubed of AOA. This approximation includes consideration of the element pattern roll-off as well as the projected antenna aperture area. The element pattern extent defines the field-of-view over which the antenna can electronically steer the beam. The element pattern suppresses grating lobes outside this extent [8].

The polarization of the element pattern determines that of the array antenna for a given AOA. Hence, the polarization of a phased array varies with scan angle according to the element pattern characteristics. Polarization agility or diversity requires a switchable radiator at each element, which tends to motivate fixed polarizations for ESAs to minimize RF aperture costs and losses.

Parallel beamformers are typically used to provide monopulse difference channels as well as the sum channel described earlier. The monopulse difference channels, commonly termed the delta channels, enable the position of a resolved target to be estimated to within a fraction of a beamwidth in azimuth and elevation. Neglecting correlated errors, the noise-limited AOA estimation precision standard deviation σ_{AOA} can be estimated using typical design parameters in a given dimension by the expression

$$\sigma_{AOA} \approx \frac{\beta_o}{k_m \sqrt{2S/N} \cos(\theta)} \quad (6-12)$$

where

- β_o = beamwidth defined by the 3-dB roll-off mainlobe resolution on boresight,
- k_m = the monopulse slope of the antenna based on its design and calibration (typically 1.2–1.8), and
- θ = commanded scan angle in that dimension.

6.4.2 Antenna Impacts on MPARS Performance

As indicated in the previous section, the mainlobe extent, β_θ – the antenna beamwidth – of an ESA is commonly estimated as the on-boresight beamwidth divided by the cosine of the aperture extent projected along the commanded AOA. The boresight beamwidth is broadened from the Rayleigh resolution limit according to a weighting factor α_w imposed by a sidelobe weighting function. While this beam broadening can be derived through interaction of the array factor and element pattern, it also can be visualized as a consequence of the foreshortening of the projected antenna extent with increasing scan angle. This relationship can be summarized as

$$\beta(\theta) = \frac{\beta_o}{\cos(\theta)} = \frac{\alpha_w \lambda}{(N \cdot d \cdot \cos(\theta))} \quad (6-13)$$

From Equation (6-12), there is a corresponding degradation in angle measurement precision with increasing scan angle.

The gain of an FFOV ESA can be calculated on boresight as

$$G = 10 \cdot \log\left(\frac{4\pi A}{\lambda^2}\right) = 10 \cdot \log\left(\frac{4\pi \left(N_x \frac{\lambda}{2}\right) \left(N_y \frac{\lambda}{2}\right)}{\lambda^2}\right) = 10 \cdot \log(N\pi) \text{ dB} \quad (6-14)$$

for the case of a uniformly illuminated planar aperture with each orthogonal scan plane composed of N_x and N_y elements uniformly spaced at $\lambda/2$.

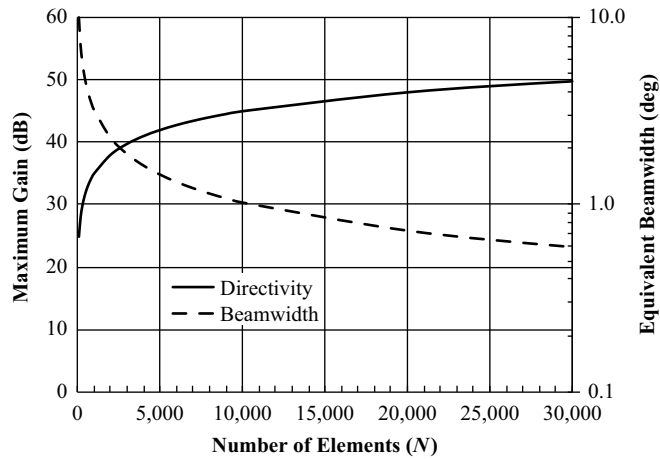
The implicit relationships of Equations (6-13) and (6-14) are depicted in Figure 6-4 as a function of the number of elements in an FFOV array. The maximum gain denotes the boresight directivity, so sidelobe weighting, electronic scanning, or aperture losses would reduce this value accordingly. The equivalent beamwidth approximation presupposes the elements are implemented as a symmetric array producing a pencil beam. Heavy sidelobe weighting or electronic scanning would broaden the depicted beamwidth. For context, several radar systems are slotted below the figure corresponding to their number of elements and organized by frequency band. The number of elements indicates the electrical size of an RF aperture such that the physical extent has been normalized to wavelength.

As noted earlier, the composite ESA directivity at a specified AOA is the product of the element pattern and array factor pattern. The resultant scan loss in directivity for FFOV arrays is calculated as a two-way value corresponding to the composite transmit/receive impact on sensitivity, typically using the element factor approximation

$$L_s \approx -30 \cdot \log[\cos(\theta)]. \quad (6-15)$$

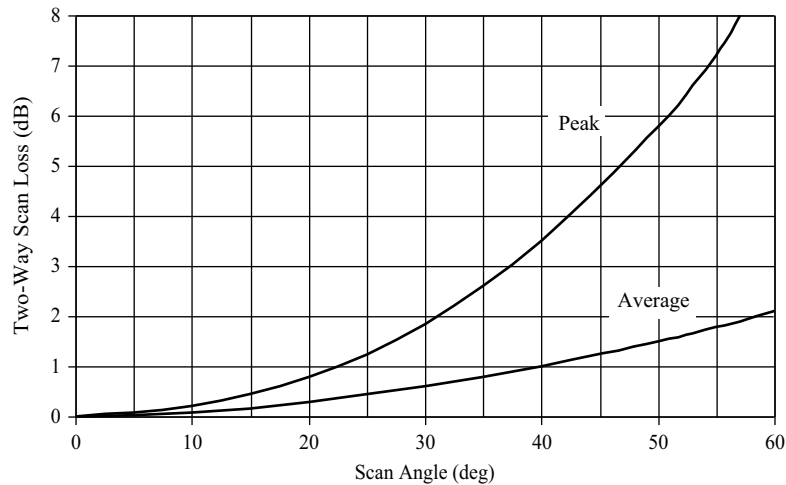
The resultant scan loss is plotted in Figure 6-5 along with the corresponding average loss taken between the designated scan angle and boresight. Since the scan losses are well defined, the radar control program may command longer pulses or additional pulses for beam positions at large scan angles to compensate for this loss in order to maintain requisite sensitivity. The peak loss indicates performance at a given scan angle, while average loss should be used to estimate impact on long-term duty cycle usage to support

FIGURE 6-4 ■ Antenna Gain and Equivalent Beamwidth with Exemplar Radar Systems.



VHF	Daryal	
UHF	BMEWS	
S-band	Aegis	
C-band	PATRIOT	
X-band	Fighter Radars	TPY-2

FIGURE 6-5 ■ Peak and Average Scan Loss Presupposing \cos^3 Roll-off.



uniform search performance across the field-of-view. The scan loss must be included in estimating search and track operational losses as well as high-fidelity, beam-by-beam simulations.

Distribution of the RF beamforming and amplification process offers graceful degradation of radar sensitivity as a function of component failure. A single-channel module failing on transmit would cost the RF aperture its contribution to transmit power generation and transmit gain, while a module failing on receive would detract from the

effective receive antenna aperture area. Thus, the S/N loss in dB from N_{fail} element-level failures of a uniformly illuminated array is given by

$$L_{fail} = -10i \cdot \log\left(\frac{N - N_{fail}}{N}\right) = -10i \cdot \log(1 - P_{fail}) \quad (6-16)$$

where

- P_{fail} = corresponding probability of an element-level failure,
- $i = 1$ corresponds to receive-only T/RM failure,
- $i = 2$ corresponds to transmit-only T/RM failure, and
- $i = 3$ corresponds to joint transmit and receive T/RM failure.

This relation presupposes a uniformly illuminated array, so it should be modified to accommodate aperture weightings. Outage loss should be computed according to anticipated failure statistics and included in the nominal system loss factor.

As plotted in Figure 6-6, assuming a worst-case failure mechanism in an AESA where a given T/RM fails on both transmit and receive and uniform illumination distribution, some 20 percent of the modules would have to fail before radar sensitivity is reduced by ~ 3 dB. In addition to this inherent graceful degradation due to the effective parallelism of transmit and receive chains, the attendant long life-times of solid-state components compared to tubes as well as the superior reliability of solid-state low-voltage supplies over the high-voltage power supplies required for transmitter tubes provide high mean times to failure at the component level.

As previously noted, the excitation current distribution on the antenna aperture and the resulting far-field pattern are related by the spatial Fourier transform so that aperture tapering can be used to suppress sidelobes. More generally, amplitude/phase illumination patterns can be computed to synthesize arbitrary antenna pattern characteristics while simultaneously steering the mainlobe. In addition, deviation from the commanded illumination pattern due to amplitude and phase errors or outages imposes a corresponding error sidelobe floor that cannot be reduced with array tapering. Wang provides a useful approximation formula for estimating the sidelobe error floor as a function of residual element-level error and probability of randomly distributed failures, as well as

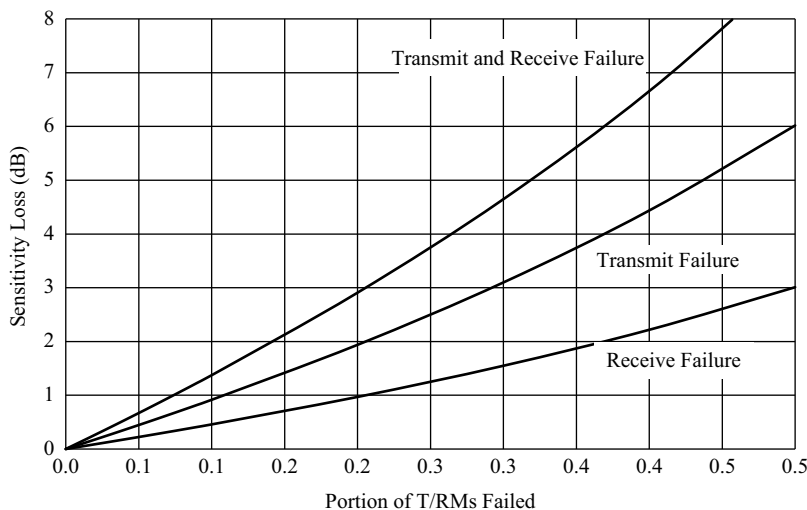


FIGURE 6-6 ■
Outage Losses Due to Failures within Uniformly Illuminated AESA.

addressing a number of systematic aperture error effects on sidelobe performance [9]. His expression for random error includes mechanical errors in element placement as well as amplitude and phase error due to residual calibration errors. Adopting Wang's notation for consistency and employing the assumption of small residual errors results in characterizing sidelobe error in dBi as

$$SLL_i \approx 10 \cdot \log[\pi(P_{fail} + \sigma_a^2 + \sigma_\theta^2 + k^2\sigma_m^2)] - 10 \cdot \log \left[1 - P_{fail} + \frac{P_{fail} + \sigma_a^2 + \sigma_\theta^2 + k^2\sigma_m^2}{\frac{2}{\pi}} \right] \quad (6-17)$$

where

$$k = 2\pi d/\lambda,$$

σ_a = standard deviation of element-level amplitude error,

σ_θ = standard deviation of element-level phase error, and

σ_m = root sum square of standard deviation of random element placement error.

By way of an example, in order to attain an error sidelobe floor of -15 dBi in the absence of any mechanical error or element failures, it would be necessary to jointly hold amplitude and phase error to 0.1 dB and 0.1 rad, respectively, in the absence of any mechanical fabrication error. A 2 percent failure rate would raise the error floor to ~ -10 dBi.

The amplitude, phase, and mechanical errors represent residual values after calibration and compensation techniques have been utilized to eliminate systemic bias-like errors. The associated error budget depends on the accuracy of antenna characterization, the stability of the errors over time, temperature, frequency, and the fidelity of the compensation process implemented by the beam-steering subsystem. The beam-steering fidelity is largely determined by the number of bits available for amplitude and phase element-level control as well as the adequacy of array characterization data to address the span of array operational conditions. An AESA aperture will likely be constructed from line-replaceable units that drive adjoining blocks of elements so that failures may be highly correlated rather than randomly distributed, as presupposed in Wang's expression. Such correlated failures tend to manifest as increases in the sidelobes near in to the mainlobe, and are of particular concern in rejecting clutter and external interference. In principle, the element-level control of an AESA enables arbitrary pattern synthesis, but in practice, this capability must be supported by alignment and calibration techniques that maintain performance after deployment.

6.5 | RADAR CONTROL AND RESOURCE MANAGEMENT

Resource management is implemented via a radar control program that plans and schedules the MPARS operations. Planning consists of formulating a course of action to achieve specified objectives while meeting operational and technical constraints. Mission requirements and resource constraints generally dictate cascading levels of action

decisions with interactions among them. In some implementations, radar action planning is conducted at the weapon system or platform level as a component of mission-level processing tasks. However, implementing an organic planner within the MPARS software is desirable to accommodate long-term or complex operations such as integrated electronic and mechanical beam steering, interleaving resource-intensive data collection to support target identification or electronic protection functions, and interceptor support during an engagement. The planner provides a coarse sequence of radar operations to be executed over a specified time period that is assessed to be within the radar resource capacity.

Scheduling is essentially the assignment of radar resources to implement the planner tasks. The scheduler operates according to optimization criteria and constraints dictated by platform and human safety, mission requirements, and radar technical characteristics. Priority-based approaches are used in modern MPARSs, in contrast to some legacy systems, which sometimes used a round-robin-type scheduler that essentially assigned search and track actions to fixed time slots. The scheduler typically provides a precise sequence of action commands for the radar hardware and application software to implement over an action interval or resource period that is significantly shorter than the planning interval. There should also be a means of the scheduler providing feedback to the planner when tasks must be deferred due to resource constraints or preemption.

Multiple algorithmic means for implementing planning and scheduling have been investigated that include template techniques, dynamic programming, auctioning, and neural networks. The computational complexity of planning and scheduling combined with the need to support real-time radar operations generally dictate a suboptimal approach that incorporates heuristic elements. Extensive software testing must be conducted under a span of target loading and environmental conditions to establish stability and reliability in a real-time processing environment.

The radar control program is also responsible for diverse functions, including health and status monitoring of the radar and coordination with higher-echelon entities, such as weapon system control programs and netcentric operations. While the interaction of a human operator can potentially enhance operational configuration management, countermeasure mitigation, and performance monitoring, the composite decision rate imposed by transmitting and receiving hundreds to thousands of dwells per second while maintaining track on tens to hundreds of targets grossly exceeds the human capacity to participate directly in the control process. The radar control program must define waveform characteristics, carrier frequency, beam-pointing coordinates, time slot allocation, and signal processing parameters for each dwell.

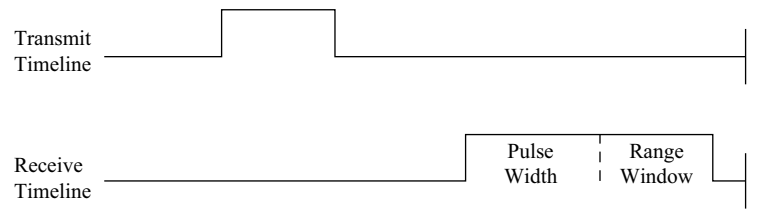
6.5.1 Radar Resources and Constraints

The principal radar resources managed by the radar control program are

- timeline occupancy,
- long-term duty cycle, and potentially
- signal/data processing capacity.

Timeline occupancy refers to the portion of the radar operating timeline that is occupied by transmit or receive actions and attendant supporting functions such as calibration pulse injection. The occupancy O for a transmit and receive dwell pair using

FIGURE 6-7 ■
Radar Transmit and
Receive Occupancy.



a pulsed waveform of duration τ , range window ΔR , and pulse repetition interval T , assuming sequential dwells, can be defined as

$$O = \frac{(\tau)_{\text{transmit}} + \left(\tau + 2 \cdot \frac{\Delta R}{c}\right)_{\text{receive}}}{T} = \frac{2 \cdot \tau + 2 \cdot \frac{\Delta R}{c}}{T} = 2d + \frac{2\Delta R}{Tc} \quad (6-18)$$

As indicated in Figure 6-7, the radar must operate for an interval corresponding to the sum of the transmitted pulse duration, received pulse duration, and range window extent over which target detections are accepted for each dwell. The achievable occupancy with a heterogeneous mixture of waveforms and functions is generally less than unity, as there is “dead time” imposed by the inability to avoid timing conflicts among transmit and receive actions. The inverse of the search beam rate imposes an upper bound on sequential transmit/receive dwell duration. If the search rate must increase corresponding to enlarging angular extent of surveillance or responding to an operational need to reduce search frame time, the resource manager may be unable to support the pulse duration required for the specified sensitivity or the full range window extent. Interleaved transmit and receive dwells can partially mitigate this constraint.

Dedicated pulse Doppler radar operation may result in near-unity occupancy since the transmitter and receiver operation are continually alternated within a coherent-processing interval (CPI) over each dwell. The dwells may be nearly contiguous, with fixed repetitive time slots assigned to specific search and track operations. However, the composite dwell rate and operational flexibility of such dedicated pulse Doppler phased array radars is generally less than an MPARS employing a diverse waveform repertoire.

MPARSs may be constrained by timeline occupancy in practice. Their inherent flexibility and adaptability enable the designer to support multiple users and functions, but as loading increases, time-critical tasks can no longer be executed as promptly as desired. In particular, conducting volumetric surveillance or horizon search at frequent update intervals imposes onerous timeline occupancy demands. Specialized measurement dwells to support semi-active guidance, extended detection range, electronic protection, or noncooperative target identification are used infrequently but tend to dominate short-term radar resource usage when they are utilized.

Long-term duty cycle denotes the portion of time over which the transmitter operates as computed across many dwells. Long-term duty cycle is ultimately constrained by the RF aperture cooling capability, as well as prime supply limits. The radar transmitter design may determine the short-term duty cycle by constraining maximum pulse duration due to associated energy storage demands required to maintain the transmitted pulse shape.

Signal/data processing resources include computational rate, memory storage, and data transfer among subsystems. Signal processing generally denotes high-throughput/low-latency functions such as pulse compression, Doppler filtering, and detection

processing that typically operate dwell to dwell. Data processing generally denotes software processes that operate over a relatively long duration and over many dwells, including radar control, tracking, and user support functions. Depending on the radar architecture, signal and data processing functions may be integrated in a common software/hardware environment or assigned to separate processing subsystems. Designers generally intend MPARS to operate virtually unconstrained from processing limits. However, growth in mission requirements and evolving software complexities often force processing performance limits over the life cycle of the radar.

Since search and track performance metrics are proportional to average power radiated, the radar scheduler attempts to attain the full long-term duty cycle to maximize radar performance, but may be constrained by timeline occupancy. Occupancy constraints are particularly severe for AESA architectures that often employ large long-term duty cycles, say 20 percent to 30 percent, to compensate for the relatively low peak power of solid-state high-power amplifier (HPAs). As implied in Figure 6-7, the maximum range window extent must decrease as the pulse duration increases for a fixed dwell repetition interval. However, operational requirements may mandate a minimum acceptable range window and maximum dwell repetition interval in order to sweep a specified search volume in the requisite period to prevent an unobserved target transit. Increasing the aperture size to improve search and track performance increases search occupancy demands, as more beams are required to cover the requisite search volume as the beamwidth decreases.

Occupancy constraints may be mitigated by techniques that include:

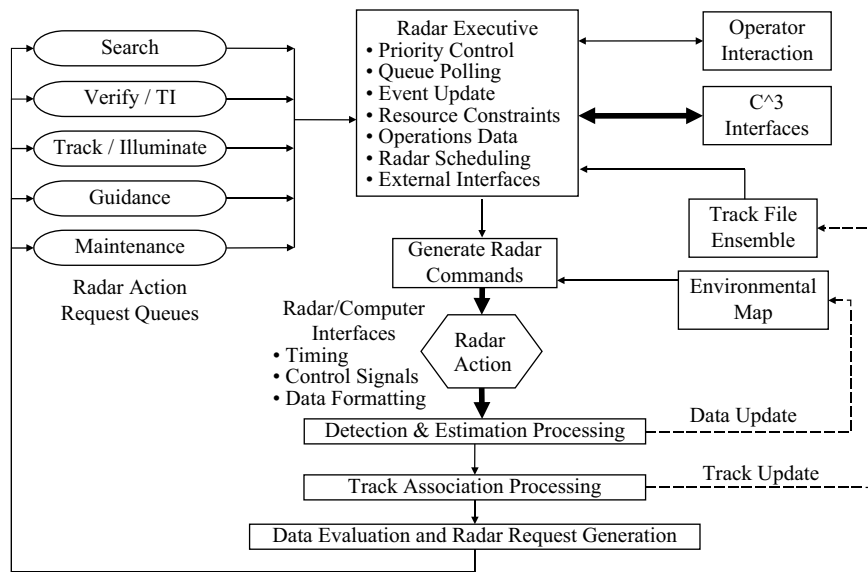
- parsing search and surveillance functions up to assure that time-critical search is implemented only in specified regions using narrow fence rasters,
- defocusing or rapidly re-steering the transmit beam to cover multiple beam positions while maintaining receive coverage by generating multiple simultaneous beams using digital beamforming (DBF) or a specialized analog beamformer, and
- dividing surveillance among multiple radars or other sensors so as to off-load search demands.

This resource management process must be conducted under operational constraints as well as hardware limitations. The transmit duty cycle may be sharply constrained in specified angular sectors due to RF exposure safety limits. Transmission may also be inhibited in order to avoid own-platform detection and targeting by adversary passive sensors. The transmitter design may constrain maximum pulse duration so that the scheduler must compensate by utilizing burst waveforms in order to achieve the requisite sensitivity in a given beam position. Beam-steering computation and subsystem/control processing may also impose latency that detracts from the achievable occupancy.

6.5.2 Resource Management Implementation

The purpose of the automated radar control process is to efficiently allocate resources to fulfill specified mission requirements while conforming to operational and technical constraints. Modern MPARSs generally employ some manner of priority-based scheduling process that adaptively allocates radar resources to competing demands, such as supporting search and track operations. Figure 6-8 provides a means of visualizing this control process as a cyclic decision and execution flow. A radar action corresponds to

FIGURE 6-8 ■
Resource
Management
Process.



the transmission or reception of a given dwell so it involves the highly synchronized operation of the transmitter, receiver, exciter, and digital signal acquisition subsystems. The rest of the radar control and processing process is generally conducted within a general-purpose processor hosting the radar control program and supporting application software such as track filtering and performance/environment monitoring.

The radar control program polls an ensemble of action request queues corresponding to multiple search plan execution, verification, and track initiation (TI) requests; track updates; and weapon guidance uplinks, as well as various housekeeping functions supporting test and calibration as indicated in Figure 6-8. As described earlier, the radar control program iteratively schedules the radar actions to be performed over a specific time slot. The request queues are updated during each interval to reflect search and track processing updates. The priority of any given request can be dependent on a number of factors, but some general considerations follow.

Weapon guidance and functions critical to ownship survival/safety are given the highest priority. Weapon guidance includes illumination dwells to support semi-active homing, as well as uplink/downlink operations to support interceptor tracking and midcourse guidance updates. Ownship survival/safety tasks may include navigation functions such as support of low-altitude terrain following onboard an aircraft.

As noted previously, MPARSs can be designed to immediately verify the presence of a target with a confirmation dwell injected into the estimated position of target detection. Radar search sensitivity can be improved 1–2 dB under typical conditions by lowering the initial detection threshold and depending on the verification dwell to achieve adequate false-alarm suppression. This two-stage sequential detection process is also termed alert-confirm processing. Upon the target returns successfully passing both the search and verify dwell detection thresholds, the radar control program schedules a track initiation (TI) sequence. Typically, this is a high dwell rate of limited duration intended to produce a stable track filter initiation and provide high-confidence measurement-to-track assignment during the initial few updates when the track is relatively coarse.

Track firmness mandates that the radar tracker accurately predict the position of the target to well within a beamwidth at the time of the next track update. This prediction requirement mandates the need for target velocity estimation. The estimated velocity error standard deviation is inversely proportional to the square root of the time in track so that initial track accuracy is relatively poor in motivating the TI sequence.

Verification and track initiation dwell sequences typically represent the second tier of priority since maximizing track initiation range is a critical performance parameter to the operational community. Upon completion of the track initiation sequence, the target track is maintained by periodic track updating at a lower rate typically of no more than a few measurements per second. Position and velocity estimation error generally decreases over the track until attaining a level determined by measurement quality, track filter characteristics, and target maneuvering.

Track updates may be assigned a priority depending on identification, maneuver behavior, engagement status, and range. In environments featuring heavy aircraft traffic, only targets of a specified level of priority may be assigned dedicated TDS track beams. In order to conserve radar resources, low-priority targets may be coarsely tracked using TWS techniques collected from one search frame to the next.

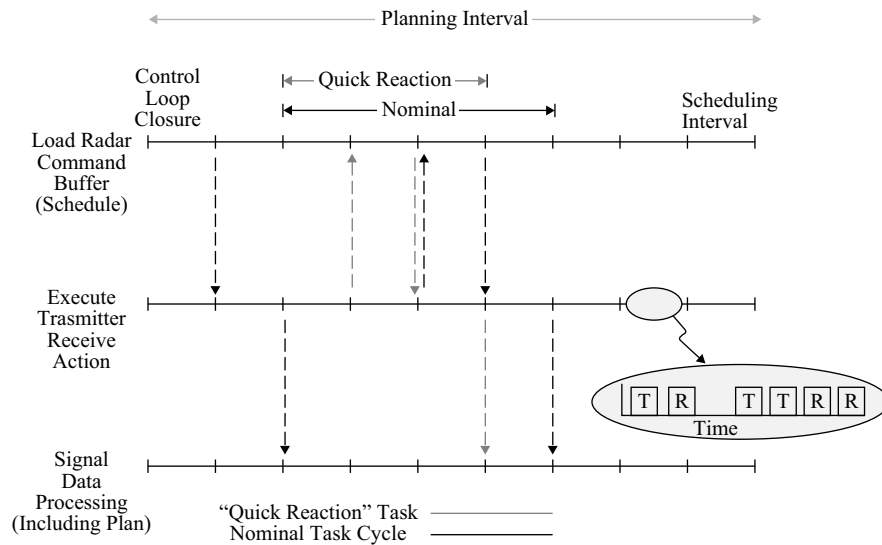
Search tends to be given less priority than TDS track, as any given search dwell is not time critical in contrast to the process of maintaining track with requisite confidence and accuracy. Unlike mechanically scanned radars with fixed transmit/receive beam patterns, the search pattern of an MPARS can be divided into multiple segments with independent waveforms and revisit rates to enhance performance to provide some degree of adaptivity to threat characteristics and local environmental conditions. As noted, an MPARS may employ a relatively slow volumetric search requiring hundreds of beam positions to cover the range and angular sector, potentially containing targets over a period of tens of seconds. In contrast, the horizon region, where targets enter the radar field-of-view, will likely be searched over briefer intervals on the order of seconds. If the interval required to search through a designated volume threatens to exceed the minimum estimated period required by a target to transit that region, the radar control program may be designed to increase search priority at the cost of decreasing target update rates or even dropping low-priority targets from TDS tracking.

The radar may be designed to maintain maps of interference sources, such as clutter compiled from processing search returns. These interference maps may support waveform selection and signal processing control. For example, pulse Doppler waveforms would be used where required for clutter rejection.

Adaptive resource management encourages usage of sophisticated track filtering. Simple fixed-coefficient polynomial smoothing filters have been successfully used in legacy MPARSs. However, alpha-beta filtering and other simple polynomial smoothers mandate fixed update intervals and do not provide indications of track quality. From the resource management perspective, one would prefer to be able to advance or retard the track update interval in order to accommodate the scheduling process and achieve higher occupancy. In addition, a real-time estimate of track quality can be useful in the prioritization process of the radar control program. Updates on firm accurate tracks can be deferred, while the update interval should be decreased on unstable tracks or in the event of a missed update detection.

Kalman filtering techniques are often used in MPARS tracking. This technique accommodates variable update intervals. The associated covariance matrix also provides a means of estimating track quality, as the diagonal axis terms denote the track filter's

FIGURE 6-9 ■
Resource
Management
Distributed over
Action Intervals.



estimate of the state vector variance. Based on the current covariance matrix and estimated measurement variance, the difference between the predicted target position and the update measurement assigned to that track is adaptively weighted to update the tracker state estimate.

Maneuvering characteristics that cannot readily be represented in the track filter typically limit the degree of position and velocity smoothing attainable. Since Kalman filtering performance is susceptible to measurement bias errors and target state model misrepresentations, the degree of smoothing is deliberately constrained by introducing plant noise into the update process. Track filters designed for tracking nonmaneuvering targets can reduce the variance of the radar position measurement by over an order of magnitude over a long-duration track. Improving performance against maneuvering targets is motivating more robust track filtering techniques that may fuse multiple models of target motion in the track update process.

The control and execution process is depicted from a timeline perspective in Figure 6-9. The radar timeline has been divided into arbitrary slots to facilitate the common use of non-real-time operating systems to support the radar control program. On the top line, transmit and receive dwells are scheduled for the next time slot and then used to command the radar hardware on the second level, which corresponds to real-time radar hardware operation. The third level corresponds to signal and data processing that result in updated radar action requests for subsequent scheduling.

The artifice of scheduling radar actions over finite time slots reduces the computational requirements that would be imposed by optimally scheduling radar actions from dwell to dwell. The scheduler efficiency generally increases and the requisite computation demands decrease with increasing time slot duration. However, the latency of the radar – the time required for it to react to new target detection and other significant events – increases with increasing time slot duration. The scheduling processing efficiency can potentially be improved within these constraints by utilizing scheduling intervals of variable duration. The scheduler may be designed to support “quick reaction” tasks where high-priority dwell requests, such as verifies, are inserted into the next scheduling interval as depicted earlier.

An MPARS typically implements a repertoire of waveforms matched to specific functional and energy needs. Waveform characteristics consist of modulation format, bandwidth, and duration, as well as pulse repetition interval for burst waveforms. The waveform bandwidth determines the range resolution, while the duration determines signal-to-noise ratio for a given target RCS and range. Burst duration determines Doppler resolution, as it defines the coherent-processing interval. In general, the radar control process chooses the waveform characteristics to minimize dwell time on target so as to enable resource availability for other tasks. For example, a surface-based radar system may restrict use of pulse Doppler waveforms to low-elevation search and track operations where clutter rejection requirements mandate this capability. Single-pulse or moving target indicator (MTI) waveforms would be used at higher elevation angles where the transmit/receive sidelobe suppression is adequate to attenuate surface clutter or the surveillance space is beyond the nominal clutter horizon.

While MPARS development emphasizes the RF aperture and the radar control and application software, the need for dwell-to-dwell agility in waveform, frequency, and signal processing parameters also significantly impacts subsystem design. The exciter and waveform generator must be capable of changing pulse duration, bandwidth, and carrier frequency within the beam-steering interval without attendant loss in stability to avoid generating spurious signal components. The signal processor must be capable of efficiently accommodating a heterogeneous series of computations, as waveforms vary from dwell to dwell. Finally, the timing and control interface must be capable of distributing the subsystem commands and maintaining strict synchronization throughout the radar system under all possible dwell sequences.

6.5.3 Multiple Target Tracking Considerations in Radar Control

Legacy MPARS may track multiple targets by essentially decomposing the high-priority target set into an ensemble of individual noninteracting track tasks subject to the resource management process. Under this approach, each target under dedicated track is serviced with an injected TDS transmit/receive dwell at a fixed update interval. However, this approach can lead to both performance degradation and inefficient resource usage in dense target environments or other stressing conditions. MPARS control and operation inherently present multiple target tracking challenges in the context of both measurement resolution and measurement-to-track data association [10].

In order to obtain measurements of suitable quality for supporting track or identification tasks, it is imperative that the targets – and sometimes the composite primary scatterers – must be well resolved from other returns in range, Doppler, or angle. In practice, the range and Doppler resolution capabilities are much finer than that afforded by angular resolution. As a general rule, the practical resolution achieved between targets or scatterers of comparable RCS is about twice that predicted by the Rayleigh limit [11]. Joint resolution in range, Doppler, or angle may be required to ensure that returns from strong target scatterers or clutter do not mask weak target scatterers. Waveform design and hardware performance bound the achievable rejection of returns outside the range/Doppler mainlobe, as commonly described in terms of range sidelobe and Doppler sideband suppression, which delineate rejection of resolved returns.

Air and missile defense often imposes scenarios where targets are poorly resolved from one another or from clutter for significant durations. In order to preserve radar tracking performance in these circumstances, it may be necessary to utilize waveforms

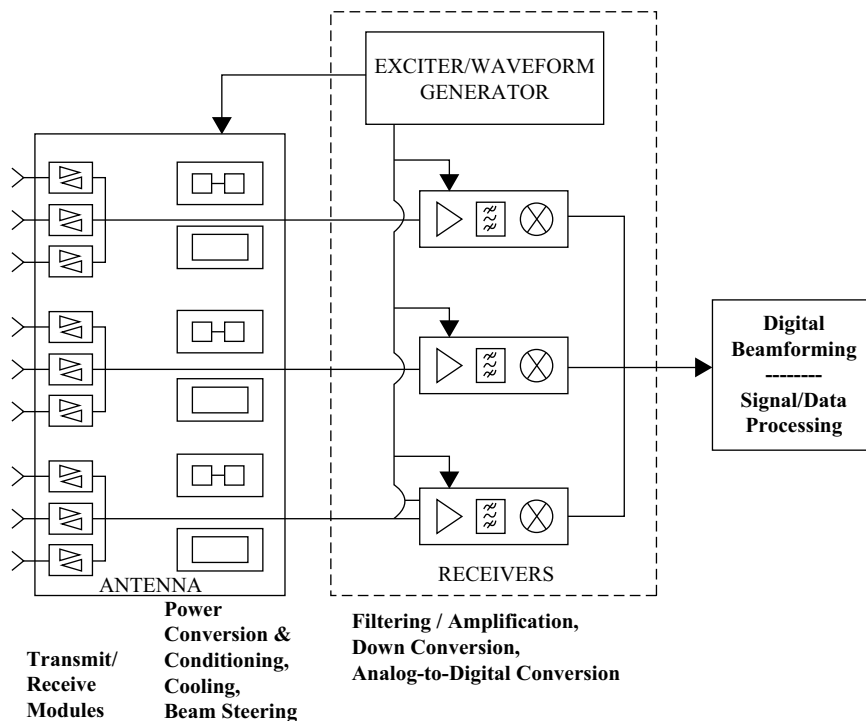
with superior range (wider bandwidth) or Doppler (longer duration) resolution. Even in the presence of adequately resolved target returns, measurement-to-track data assignment may challenge the radar processing. Mechanically scanned single-target tracking radars effectively “stare” at targets with a resultant high data rate. MPARSs update tracks at lower rates – but still much higher rates than rotating surveillance radars – so that an update dwell could produce multiple measurements that could potentially be associated with a given track. Robust data assignment techniques have been developed that significantly improve track stability at the cost of additional processing demands.

Ideally, the tracking process should be highly integrated with the resource management routines, including track file management subprocesses such as initiation, updating, and termination, as well as collateral functions such as redundant track detection and elimination and target counting functions. For example, the data assignment process should be capable of updating multiple independent tracks with a single transmit/receive dwell if there are multiple detection reports within the mainlobe. This capability can mitigate the impact of clutter and countermeasures, as well as enable tracking in dense target environments. The term track while track (TWT) denotes the capability to collect independent measurements and update multiple independent tracks with a single transmit/receive dwell.

6.6 | MPARS TECHNOLOGIES

Modern MPARSs generally employ active electronically scanned arrays (AESAs) due to associated benefits of performance, availability, technology base leverage, and life cycle affordability. As illustrated in Figure 6-10, AESAs employ an array of element-level

FIGURE 6-10 ■ RF Aperture Depicting AESA with Digital Beamforming.



solid-state transmit/receive modules (T/RMs). Each radiating element is supported by a dedicated channel, which includes a transmit high-power amplifier (HPA), receive low-noise amplifier (LNA), transmit/receive protection circuitry, and common transmit/receive components such as a phase shifter and attenuator [12]. In practice, multiple T/RM channels may be integrated into a single assembly to reduce production costs. The T/RMs are supported by an RF aperture infrastructure to provide distributed direct current (DC) power conversion and conditioning, cooling, and beam steering as well as mechanical housing. The cost of this infrastructure is typically on the same order as the total T/RM cost in modern systems [13]. While modern AESAs impose lower life cycle costs than functionally equivalent tube-based mechanically scanned radars, initial affordability is a continuing concern.

The peak power output of solid-state HPAs is multiple orders of magnitude below that of tube transmitters. For example, off-the-shelf products currently provide in excess of 50 W at S-band and 10 W at X-band. AESAs compensate for this component peak power disparity as follows:

- Element-level HPA mechanization provides a free-space power combining gain of $\sim 10 \times \log(N)$ dB, where N is the number of AESA elements;
- HPAs and LNAs directly feed the associated radiating element, with a circulator/receiver-protector typically being the only significant intervening component, so that the losses associated with an ESA passive beamformer are eliminated; and
- Solid-state HPAs can generally be operated at substantially higher duty cycles than high-power tubes so that extended-duration waveforms – longer pulses or pulse integration – can be used to maintain single-measurement sensitivity.

AESAs provide improved reliability and availability over mechanically scanned radars, readily increasing mean time between critical failures by over an order of magnitude. The dominant failure mechanisms for legacy radars are commonly transmit tubes, associated high-voltage power supplies, and antenna positioning servos. All three of these mechanisms are eliminated by a fixed-mount AESA, which uses distributed low-voltage power supplies to support its long-life solid-state amplifiers. Moreover, AESA architectures generally minimize single-point critical failure opportunities since performance is relatively insensitive to the loss of individual transmit/receive modules or power supplies, as delineated later.

A passive ESA is composed of an array of element-level phase shifters without active amplification on transmit or receive. A passive ESA beamformer is fed by a tube-based centralized transmitter and receiver, so it offers the advantages of beam agility but without significant improvements in reliability over mechanically scanned systems. However, a number of currently fielded MPARSs employ passive ESAs typically using space-fed phased array antennas to reduce beamformer cost over that of corporate feed designs. Modern AESA radars provide superior sensitivity (range) over passive ESA radars for a given aperture area, total system weight, and prime power consumption.

Both acquisition and life cycle costs of a modern AESA for given level of system performance have generally declined below that required when using a passive ESA of equivalent system performance. AESA characteristics also lend themselves to flexible form-fit-factor – supporting specialized implementations that mandate low radar cross section, light weight, platform compatibility, and conformal aperture applications. In many mobile applications, installing fixed-mount AESAs is a less complex and costly

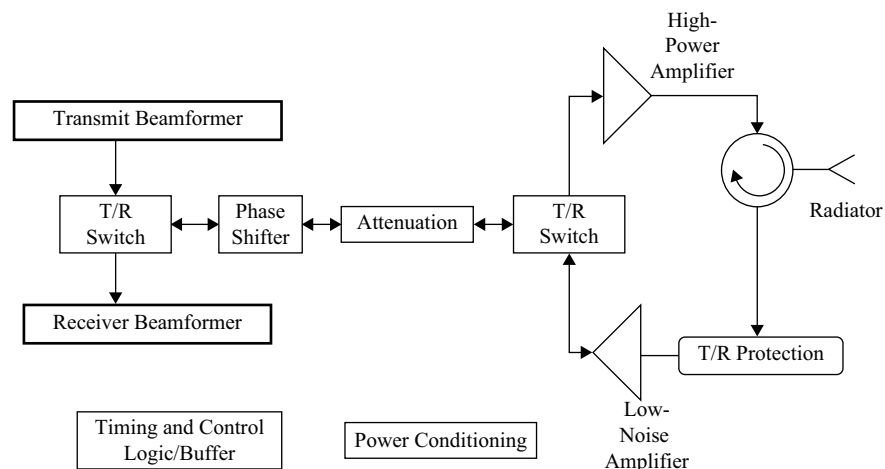
undertaking than attempting to mount a mechanically scanning antenna. These considerations are illustrated by airborne early warning radar providers that mate low-cost AESAs with user legacy airframes. The progress in AESA cost reduction can be assessed by the affordability of multiple-function fighter radars being marketed for both new and retrofit aircraft procurements, offering significant performance enhancement at comparable acquisition cost to legacy mechanically scanned radars. Development of air, artillery, and tactical missile self-defense radars employing low-cost AESA technology also represents a major application opportunity exploiting TDS capabilities to multiplex search and track. The trend toward reduced ownership cost may enable MPARS technology to be applied to civilian applications such as integrated air traffic control and weather sensing, where they can offer enhanced performance and reliability.

At present, bipolar silicon (Si) technology tends to dominate low-frequency AESA applications at L-band and below, while gallium arsenide (GaAs) component technology dominates microwave AESA applications at S, C, and X. Gallium nitride (GaN) technology appears very promising to provide increased power, bandwidth, and efficiency subject to establishing an adequate production base for integrated devices to achieve affordability. Current and future AESA component affordability depends heavily on leveraging commercial foundry operations, as radar applications are dwarfed by commercial communication markets for solid-state RF technology [14].

The key components of a T/RM are depicted in Figure 6-11. Amplitude and phase control are typically combined in a common transmit/receive circuit, while the HPA and the LNA are dedicated to the transmit and receive paths, respectively. Power conversion/conditioning and beam-steering mechanization are typically distributed across multiple elements. In contrast to a passive ESA, which performs element-level phase shifting but does not support transmit or receive element-level amplification, the AESA elements are fed directly by transmit and receive amplifiers, minimizing associated losses and system noise contribution. T/RMs may be integrated into a single multiple-channel assembly feeding two or more individual radiating elements in order to reduce production cost.

Taking into account respective losses, cooling requirements, and prime power conversion efficiencies, a modern AESA provides superior sensitivity to an ESA system for a given aperture area, weight allocation, and prime power input for less life cycle

FIGURE 6-11 ■
Elements of a
Transmit/Receive
Module.



cost. The AESA may subsume on the order of three-fourths of the radar recurring cost in a modern MPARS, so this motivates technology to reduce RF aperture costs through increasing component integration and other means. There are extensive efforts to develop “radar-on-a-chip” technologies integrating transmit/receive RF and digital functions. However, this technology is currently limited to low-power applications [15]. Designing the RF aperture to resist damage-induced failure is also a major imperative, as the high-cost AESA components are relatively exposed in the RF aperture with limited protection against physical or electromagnetic damage.

AESA designs facilitate digital beamforming (DBF) since received signals are amplified at the element level. Modern DBF implementations can aggressively leverage commercial technology performance and affordability while enhancing MPARS performance and improving resilience. DBF effectively distributes the receiver subsystem across the array, with individual elements or small groups of elements, termed sub-arrays, feeding individual receive chains as depicted in Figure 6-10 [16]. The composite antenna pattern is formed digitally within the signal processing subsystem.

Unlike a conventional analog beamformer, digital processing enables multiple beams to be generated by iteratively summing a given received signal set while preserving the full gain of the array for each beam. DBF offers significant operational utility from its inherent capability to flexibly generate multiple simultaneous receive beams with arbitrary weighting schemes. Timeline occupancy demands can be potentially mitigated by transmitting over a small angular sector that can be covered by a cluster of receive beams to collect returns in parallel. Adaptive digital beamforming (ADBF) incorporates adaptive interference suppression by integrating sidelobe cancellation and sidelobe blanking while providing a limited mainlobe cancellation capability. DBF is critical in airborne radar applications that must meet stressing subclutter visibility requirements using space-time adaptive processing. The inherent parallelism of DBF mitigates single-point failure mechanisms within the RF aperture. Integrated AESA/DBF apertures enable modular architectures that can potentially be scaled for multiple applications while offering the economy-of-scale benefits of a common technology base.

AESA RF apertures generally dominate the recurring cost of a modern radar system, but software development, updating, and sustainment are major concerns in life cycle cost. While previous military software initiatives have provided mixed results, the present trend toward increased use of commercial digital hardware and software development tools and practices appears promising. Emerging open system architecture standards for software should enable graceful rehosting across different generations of hardware and even different computer architectures. In addition, the use of modular and loosely coupled programming practices promises to ease software maintenance and potentially enable code reuse. Extending these techniques to support real-time operation remains a major challenge for MPARS applications.

The high development and acquisition costs of high-performance sensors encourage spiral development practices, where incremental capabilities are implemented over the lifetime of the system as adversary capabilities evolve and enabling technologies mature. In the specific instance of AESA radar systems, the high cost of the RF aperture dictates that it will not be modified over the life cycle of the radar system, other than occasional refurbishment of line-replaceable units containing failed components. However, multiple generations of software-based capability enhancement can be anticipated along with supporting processor upgrades. DBF can extend spiral development practices

into the beamforming regime by enabling hardware upgrades to increase throughput and bandwidth as well as algorithmic enhancements.

In the face of this trend toward using AESA technology for radar applications, the historical Russian success in low-cost space-fed passive arrays employing centralized transmitter/receiver chains is noteworthy [17]. Over the course of the Cold War, the Soviet Union deployed one to two orders of magnitude more phased array radars than did the United States despite the military technology leadership of the latter. While this comparative emphasis on ESA radars was partially due to asymmetric air defense strategies, Russian industry developed antenna architectures and components designed to minimize acquisition cost while delivering acceptable system-level performance. In addition, they constructed integrated air defense systems composed of multiple ESA radar designs optimized for search, battle management, and fire control, as opposed to the single multiple-function radar approach exemplified by the U.S. PATRIOT system.

6.7 | MPARS TESTING AND EVALUATION

MPARS development and testing are far more complex than that for legacy single-function radar systems. This complexity is imposed by the interleaving of multiple search and track task sequences, as well as the challenges of fully exercising the full performance range of the ESA and supporting subsystems.

A mechanically scanned target-tracking radar can be well tested by a series of tracks conducted against a span of representative targets. In contrast, the tracking performance of an MPARS must be evaluated under realistic resource management conditions that include interleaving of multiple target tracks and search operations and associated verification and track initiation. Data association may be more important in determining track performance than in dedicated mechanically scanned radar systems since MPARSs tend to employ significantly lower track update rates than “staring” sensors, which can only track a single target. Graceful interaction between dedicated TDS tracks and coarse TWS tracks generated from surveillance measurements is also desirable to support load shedding as well as suppress misassociation and wasted verification/track-initiation dwells on targets already under track. In addition to these considerations, testing of MPARS target-tracking capabilities must address the interaction of waveform selection and electronic scanning with measurement quality.

Some manner of simulation-based testing is necessary in order to establish MPARS performance. At a minimum, the radar control program and application software should be tested on representative data processing hardware to verify and validate performance. It may also be highly desirable to employ some manner of hardware-in-the-loop implementation that drives the digital processing software/hardware in a real-time environment while emulating radar subsystem interfaces and simulating target/environment returns. As introduced in Section 6.3, high-fidelity simulation efforts are challenged to capture the full span of operational losses due to target positional uncertainty and environmental effects. Simulations of lesser fidelity may entirely neglect the radar measurement modeling process so as to not capture the performance impacts of merged measurements and measure-to-track data misassociation. MPARS simulation accreditation efforts should strive to ensure that radar performance is not represented as excessively optimistic through a combination of targeted analyses and test data anchoring.

At a major increment in cost, the MPARS hardware-in-the-loop configuration may also incorporate a full-size or subscale RF aperture to conduct testing in which the RF aperture participation is critical. At a minimum, incorporation of a subscale aperture should enable the exercise of the beam-steering system and, if present, DBF subsystem. Motivating imperatives for including RF aperture and the attendant transmission and reception operations include determining performance in clutter-limited conditions and investigating susceptibility to electromagnetic interference and electronic attack.

6.8 | NETCENTRIC MPARS APPLICATIONS

Historically, the cost of developing and deploying MPARSs has been motivated by their military utility in the context of a specific weapon system or platform. AMD systems such as PATRIOT and Aegis illustrate this legacy. The MPARS enhances and accelerates the kill chain sequence of detection, track, weapon guidance, and kill assessment against a given target, as well as supporting simultaneous engagements against multiple targets. MPARS cost was somewhat mitigated by subsuming the roles of multiple mechanically scanned radars that would otherwise be required.

Future MPARS development and deployment costs will be largely motivated by netcentric applications, particularly for high-cost implementations. Netcentricity denotes the exploitation of a robust, globally interconnected network environment in which data is shared seamlessly among users, applications, and platforms [18]. MPARS military utility will increasingly be evaluated in terms of the capabilities that it brings across multiple platforms and in a system-of-systems context, as exemplified in Figure 6-12. Netcentric data sharing is performed among application domains as well as within a given domain, as denoted by the netcentric data products depicted as examples.

The availability of high-reliability, low-latency, broadband data-links among sensors and users is a necessary but not sufficient condition for netcentric operations. The MPARS can potentially provide multiple data products that are all referenced to a distributed tracking network that assimilates inputs from multiple sensors to generate a

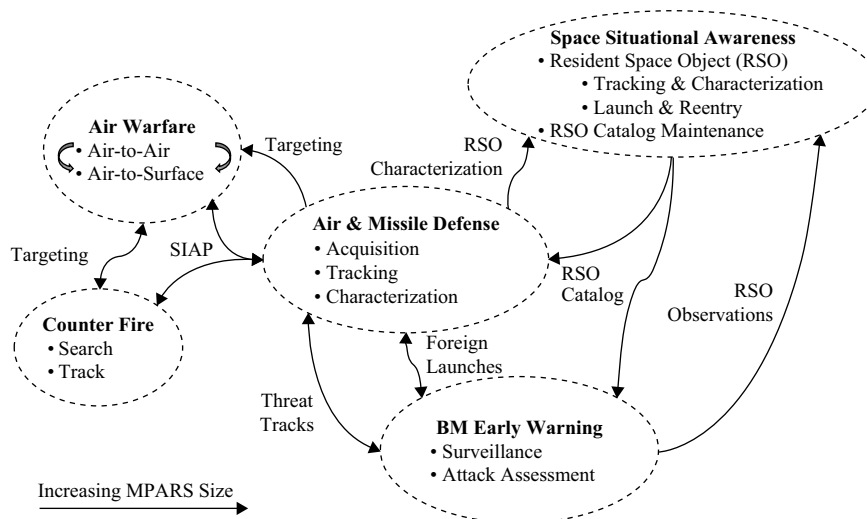


FIGURE 6-12 ■ Interacting MPARS Missions and Data Sharing.

single integrated air picture (SIAP). Tracks must be assigned global identifiers that are reliably correlated with local tracks generated by participating sensors.

MPARSs can contribute significant netcentric military utility in the context of this global track ensemble. Netted data processing from multiple TWS radars can increase composite surveillance performance in terms of coverage and track continuity. However, netcentric MPARSs potentially offer markedly improved capabilities in the context of situational awareness and distributed fire control. MPARSs possess the advantages of relatively high data rate and waveform optimization to assure high signal-to-interference ratio and precision measurements subject to accommodating the TDS tracking load. TDS precision tracking against high-priority or stressing targets enhances both accuracy and firmness over that achievable with TWS surveillance radars. Enhanced tracking combined with high-resolution target identification significantly increases situational awareness. Augmented with the capability to rapidly multiplex and tailor search scans, this multiple-target track/identification capability enables an MPARS to develop high-quality situational awareness. Transferring this situational awareness to a distributed user base is the foundation of MPARS netcentric military utility.

These fire-control-quality tracks can be accessed by external weapon systems to support netcentric engagement modes. For example, a weapon system can use externally provided fire-control-quality tracks to support commit-on-remote, where an interceptor is launched against an incoming threat before the organic fire-control sensor establishes track. Similarly, engage-on-remote utilizes externally provided tracks to conduct the entire engagement. The capability to rely on coarser, less costly sensors for surveillance enables MPARS resources to be focused on these high-value tracking tasks. Contributions from other sensors may also mitigate MPARS coverage gaps due to line-of-sight blockage, multipath fades, external interference, or other degradations.

MPARS netcentric implementation mandates incremental design requirements that can be set in the context of netcentric precepts as summarized in Table 6-2. A key netcentric operational challenge is tasking and prioritization procedures that enable distributed users to modify the behavior of the MPARS in response to their individual needs. The high data quality afforded by an MPARS can readily lead to it being overtaxed by external requests.

TABLE 6-2 ■ Netcentric Data Characteristics for MPARS

Netcentric Data Characteristic	MPARS Design and Operational Impacts
Visible	Both TDS and TWS track data must be integrated into a global track database. Environmental data, such as interference mapping and detection statistics, should also be visible on the network, as well as radar health and status reporting.
Accessible	In addition to accessing global track data, MPARS should respond to external tasking for both radar actions and data products: <ul style="list-style-type: none"> ● Radar actions: track prioritization, and special data collection ● Data products: measurement reports, tracks, specialized measurement, and reporting outputs
Usable	MPARS data should be synchronized with global timing reference and referenced to an external coordinate system. Data products must conform to global track data structures.

6.9 | REFERENCES

- [1] W.J. Fontana and K.H. Krueger, “AN/SPY-3: The Navy’s Next-Generation Force Protection Radar System,” *2003 IEEE International Symposium on Phased Array Systems and Technology*, Waltham, MA, 14–17 October 2003.
- [2] J.K. Green, “F/A-18E/F Active Electronically Scanned Array (AESA) Radar: Lessons Learned from System Development and Integration,” *2007 Military Radar Symposium*, 27 June 2007.
- [3] L. Blake, *Radar Range Performance Analysis*, Munro Publishing Co., Silver Spring, MD, 1991.
- [4] R.J. Galejs and C.E. Muche, “Beam and Filter Straddle Losses in an ESA Search Radar,” Lincoln Laboratory Technical Report, 31 March 1992.
- [5] P.J. Kahrilas, *Electronic Scanning Radar Systems (ESRS) Design Handbook*, Artech, 1976.
- [6] N. Fourikis, *Advanced Array Systems, Applications, and RF Technologies*, Academic Press, 2000.
- [7] R. Mailloux, *Phased Array Handbook*, Second Edition, Artech House, 2005.
- [8] W. Wirth, *Radar Techniques Using Array Antennas*, IEE, 2001.
- [9] H. Wang, “Performance of Phased-Array Antennas with Mechanical Errors,” *IEEE AES Transactions*, April 1992.
- [10] S. Blackman and R. Popoli, *Design and Analysis of Modern Tracking Systems*, Artech, 1999.
- [11] F. Daum, “A System Approach to Multiple Target Tracking,” *Multitarget-Multisensor Tracking: Applications and Advances*, Y. Bar-Shalom, Artech, 1992.
- [12] B. Kopp, M. Borkowski, and G. Jerinic, “Transmit/Receive Modules,” *IEEE Transactions on Microwave Theory and Techniques*, Vol. 50, No. 3, March 2002.
- [13] Y. Mancuso, P. Gremillet, and P. Lacomme, “T/R-Modules Technological and Technical Trends for Phased Array Antennas,” *2005 European Microwave Conference*, Elancourt, France, 4–6 October 2005.
- [14] B. Kopp, “S- and X-band Radar Transmit/Receive Module Overview,” *2007 IEEE Radar Conference*, 17–20 April 2007, pp. 948–953.
- [15] E. Brookner, “Phased-Array Radars: Past, Astounding Breakthroughs and Future Trends,” *Microwave Journal*, Vol. 51, No. 1, January 2008.
- [16] V. Chernyak, I. Immoreev, and B. Vovshin, “70 Years of Russian Radar Industry,” *2004 International Conference on Radar Systems*, Philadelphia, 26–29 April 2004.
- [17] D.K. Barton, “Design of the S-300P and S-300V Surface-to-Air Missile Systems,” Located at www.ausairpower.net/APA-Russian-SAM-Radars-DKB.html#mozTocId832616, March 2009.
- [18] “Data Sharing in a Net-Centric Department of Defense,” Department of Defense Directive, Number 8320.02, 2 December 2004.

6.10 | FURTHER READING

- T. Jeffrey, *Phased-Array Radar Design: Application of Radar Fundamentals*, SciTech Publishing, 2009.
- S. Sabatini and M. Tarantino, *Multifunction Array Radar: System Design and Analysis*, Artech, 1994.
- N. Fourkis, *Advanced Array Systems, Applications, and RF Technologies*, Academic Press, 2000.

Ballistic Missile Defense Radar

Melvin L. Belcher, Jr., Georgia Tech Research Institute, Atlanta, GA, USA

Chapter Outline	
7.1 Introduction	285
7.2 BMD Radar System Requirements	292
7.3 Radar Development for Ballistic Missile Defense	298
7.4 BMD Radar Design	307
7.5 BMD Radar Performance Estimation	312
7.6 References.	321
7.7 Further Reading	322

7.1 | INTRODUCTION

A class of radar systems has been developed and deployed to detect, track, and identify targets that are in excess of an order of magnitude greater in range, smaller in radar cross section, and faster than conventional air-breathing targets. These radars perform inter-related missions consisting of ballistic missile defense (BMD), ballistic missile warning (MW), and space situational awareness (SSA). Full field-of-view (FFOV) electronically scanned arrays (ESAs) are employed to interleave search and track functions within a given mission as well as tailor operations across multiple missions. This class of radar can be defined by large physical size, exceptional sensitivity, and high cost. Mechanically scanned reflector-antenna radars are employed to provide affordable sensitivity for niche missions such as test instrumentation and tracking resident space objects but are fundamentally constrained by lack of organic surveillance and target traffic handling.

The principal U.S. radars composing this class are listed in Table 7-1. While this chapter is focused on BMD, the MW and SSA missions are also addressed in the introduction because a given sensor may perform aspects of all three missions. In the United States, the Integrated Tactical Warning and Attack Assessment (ITWAA) system detects and tracks strategic ballistic missile threats to the United States. The current generation of early warning radars (EWRs) supporting the ITWAA mission employs active electronically scanned arrays (AESAs) operating in the ultrahigh frequency (UHF) band. While the United States has deployed geosynchronous satellites to detect missile launches from the short-wave infrared (SWIR) signature of the boost phase, EWRs are critical to verifying and characterizing the attack as well as estimating the impact points of the individual *reentry vehicles* (RVs). The first generation of missile

TABLE 7-1 ■ U.S. ESA Radars for BMD, Missile Warning, and Space Situational Awareness

Radar Name and Siting	Description	Missions	Capabilities
Eglin (AN/FPS-85) Radar; Eglin Air Force Base, Florida	UHF FFOV dual transmit–receive aperture ESA	SSA	Primary near-Earth sensor Metric and narrowband signature collection
Perimeter Acquisition Radar Attack Characterization System (PARCS); Cavalier Air Force Station, North Dakota	UHF FFOV ESA	Missile warning, SSA	Metric and narrowband signature collection
Ballistic Missile Early Warning System (BMEWS); Clear Air Force Station, Alaska; Thule Air Force Base, Greenland; and Royal Air Force Station, Fylingdales, United Kingdom	UHF FFOV AESA: Two faces at Clear and Thule Three faces at Fylingdales ~2,560 AESA elements per face	Missile warning; BMDS upgraded early warning radars: Fylingdales, Thule, and Clear (planned) SSA	Metric and narrowband signature
PAVE Phased Array Warning System (PAVE PAWS); Cape Cod Air Force Station, Massachusetts, and Beale Air Force Base, California	UHF FFOV AESA; Two faces per site ~1,800 AESA elements per face	Missile warning; BMDS Upgraded Early Warning Radar: Beale and Clear (planned) SSA	Metric and narrowband signature collection
COBRA DANE; Eareckson Air Force Station on Shemya Island, AK	L-band FFOV ESA	BMDS; SSA	Metric and signature collection
Sea-Based X-Band Radar (SBX): Based on mobile floating platform	X-band LFOV AESA on mechanical mount: ~45,000 AESA elements	BMDS	Metric and narrowband and wideband signature collection
AN/TPY-2; transportable; currently deployed in Shariki, Japan, and in Israel as forward-based radar; > 10 planned	X-band FFOV AESA ~25,300 AESA elements	BMDS: two roles-forward-based radar THAAD	Metric and narrowband and wideband signature collection
Aegis BMD SPY-1; Aegis cruisers and destroyers; > 30 planned for BMD	S-band FFOV ESA four faces per ship	BMDS; naval air defense	Metric and signature collection

warning radars employed fixed-beam search radars and mechanically scanned dish radars and was one of the first billion-dollar development projects undertaken by the U.S. defense establishment. The current generation of AESA EWRs provides superior traffic handling and reliability.

BMD radars are integrated into the Ballistic Missile Defense System (BMDS) which includes radars in the major elements of Ground-Based Midcourse Defense (GMD), Aegis BMD (ABMD), and Terminal High Altitude Area Defense (THAAD). The confluence between missile warning and missile defense is obvious as both missions require:

1. detection of incoming ballistic missile threats near maximum line-of-sight range;
2. characterization of ballistic missile complexes into major associated components – booster, reentry vehicle, and associated objects as well as supporting target identification functions; and
3. tracking of individual targets with sufficient accuracy to predict their trajectories even in the event of a raid comprised of multiple ballistic missile launches.

BMD enforces a more demanding mission on the supporting radar systems. The fidelity of MW characterization and tracking must only be adequate to provide situational awareness to support political and strategic military responses. BMD radars must precisely identify and track RVs so as to support fire control. BMD fire control requires trajectory prediction of the identified target to support long-range interceptor acquisition, which exerts onerous requirements for sensitivity, resolution, and accuracy.

Space situational awareness provides comprehensive knowledge of the space object population, including threats, event prediction, and object status as well as tactical picture generation. This mission requires metric data from tracking to support conjunction analysis among resident space objects (RSOs) so as to provide warning of potential collisions. Characterization data are required to aid in identifying objects and assessing their operational state. A global network of radars forms the backbone of the U.S. Space Surveillance Network (SSN) that provides the requisite metric and signature data for SSA. The SSN radars are augmented by ground-based and spaceborne platforms employing optical sensors. Optical sensors can provide superior range against typical space objects but are constrained by requisite solar illumination conditions that limit their utility against the low-altitude regime where RSOs are often in Earth's shadow. SSN ground-based telescopes are only able to detect solar-illuminated space objects, with the observation sites in darkness. Ground-based radars generally dominate SSA coverage of RSOs at altitudes below 2,000 km, which is why the coverage is termed the low Earth orbit (LEO) regime. The LEO regime is heavily populated by RSOs, including operational satellites, defunct satellites, miscellaneous launch hardware, and primarily orbital debris.

Table 7-2 lists the principal fixed-beam and mechanically scanned radar systems currently supporting SSA. Data from these radars as well as optical sensors are integrated with operational and space environment data to provide status, current and future positions, and characterization of the space object population and associated risks and threats. The current very-high-frequency (VHF) fixed-beam continuous wave (CW) Space Fence was fielded in 1961 and was originally known as the Naval Space Surveillance (NAVSPASUR) before it was transferred to the U.S. Air Force in 2004. There is currently an ambitious effort underway to develop a next-generation Space Fence consisting of a modular S-band beam-agile radar system. The SSN also includes a number of mechanically scanned reflector-antenna radars deployed around the world to

TABLE 7-2 ■ U.S. Detection Fence and Mechanically Scanned Radars Currently Used for SSA

Radar Name and Siting	Description	Capabilities	Year Fielded
Air Force Space Surveillance System (AFSSS): three transmit antennas and six receive antennas geographically located along the 33rd parallel of the United States from Georgia to California	VHF fixed beam pattern using bistatic continuous wave	Detection	1961
Globus II: Vardø, Norway	X-band dish radar	Metrics and narrowband and wideband signature Deep space capability	1999
Ascension radar: Ascension Island, South Atlantic Ocean	C-band dish radar	Metrics and narrowband signature	1971
Haystack radar: Westford, Massachusetts	X-band dish radar	Metrics and narrowband and wideband signature Deep space capability	1963
Haystack auxiliary radar: Westford, Massachusetts	Ku-band dish Radar	Metrics and narrowband and wideband signature	1993
Millstone Hill radar: Westford, Massachusetts	L-band dish radar	Metrics and narrowband signature Deep space capability	1957
Advanced Research Projects Agency (ARPA) Lincoln C-Band Observables Radar (ALCOR): Kwajalein Atoll, Marshall Islands	C-band dish radar	Metrics and narrowband and wideband signature	1970
ARPA Long-Range Tracking and Instrumentation Radar (ALTAIR): Kwajalein Atoll, Marshall Islands	VHF and UHF dish radar	Metrics and narrowband signature Deep space capability	1970
Target Resolution and Discrimination Experiment (TRADEX): Kwajalein Atoll, Marshall Islands	L- and S-band dish radar	Metrics and narrowband signature	1963
Millimeter wave (MMW) radar: Kwajalein Atoll, Marshall Islands	Ka- and W-band dish radar	Metrics and narrowband and wideband signature	1983

provide precision metric tracking to support orbital element estimation and to collect signature measurements to support characterization, identification, and monitoring of individual space objects. As noted in Table 7-1, a number of the large UHF phased array radars are dominant contributors to SSA.

The first generation of missile warning (MW) sensors deployed in the 1950s employed a similar architecture of fixed-beam detection radars and a small number of mechanically scanned precision tracker but target traffic handling and associated tracking accuracy requirements drove the replacement of these radars with the multiple-function phased array radars listed in Table 7-1. Mechanically scanned radars are not currently used for BMD or MW due to their limited target traffic handling. BMD

metric (prediction accuracy) and signature (number of independent observations) performance benefits from extended observation intervals at moderate measurement rates to assure track firmness and adequate signature sampling to support discrimination. Multiple-function phased array radars provide this mixture of adaptive traffic handling, variable data rates, and extended observation by tracking objects across their FFOV extent. Mechanically scanned radars are effectively staring sensors that are well suited for collecting continuous high-update rate metric and signature data on a single target or closely spaced target set. The superior sensitivity for a given cost of mechanically scanned radars over phased array radars provides them with enduring mission effectiveness for high-altitude orbit and deep-space SSA applications. The SSA community is migrating toward beam-agile radar systems for LEO surveillance as exemplified by the legacy AN/FPS-85 which tracks some 95 percent of the current Satellite Catalog. While most of the MW/BMD radars are located at northerly latitudes and boresighted to view near trans-polar ballistic missile trajectories, the AN/FPS-85 is located in the southern United States and is southerly boresighted. This arrangement significantly increases the number of potential RSO observations. Concerns over improving SSA timeliness, track quality across the space object population, orbital conjunction analysis accuracy to predict potential collisions, and detection of small space objects all motivate the SSA community interest in developing and deploying phased array radars such as the next-generation Space Fence.

Table 7-3 provides a summary of the mission characteristics of missile warning, BMD, and SSA. In general, SSA sensors must support a larger operational range span to cover the orbital regimes than required for BMDS or MW operations. In the absence of anomalous propagation or major geographical features such as mountains, ground-clutter returns typically fall below the radar horizon beyond 50 km or so. MW, BMD, and SSA applications share the common attribute that they are designed to attain noise-limited performance since their minimum range of interest is typically well beyond this point. However, at frequency bands below UHF, electromagnetic interference can become a major sensitivity constraint.

All three missions impose similar requirements such as mitigating propagation effects. As the radar line of sight is transiting the entire atmosphere, it is necessary to suppress tropospheric refraction effects at low elevation, including diurnal and seasonal variations. Radars operating at L-band and below tend to be susceptible to ionospheric propagation effects, including amplitude and angle scintillation. A nuclear bust in the atmosphere would create an extended region of dense ionization that would more severely block, attenuate, and degrade radar propagation with severity increasing with decreasing frequency [1].

All three mission sets motivate accurate tracking that must produce precise estimates of target position and velocity in an inertia-based coordinate system. In turn, this requires that the radar systems must be well registered in a geodetic coordinate system and correct propagation-refraction effects so as to prevent bias-like errors from degrading system-level performance. This capability is critical to extrapolating ballistic target trajectories as well as performing conjunction analyses of space objects to project potential collisions. While the SSA community must deal with ~20,000 resident space objects, these are distributed throughout the immense spatial volume of Earth's orbital regime, so the primary tracking challenge is correlation of observations (measurements and tracks) with predicted passes of cataloged RSO entries based on their associated ephemeris data. In contrast, ballistic missiles may impose the challenge of closely spaced objects (CSOs) where the booster, RV, or other objects are in close proximity, challenging resolution and

TABLE 7-3 ■ Comparison of Mission Requirements for Sensors

Mission Characteristic	Missile Warning	BMD	LEO SSA
Sensitivity drivers	<ul style="list-style-type: none"> • threat complex > 0 • targets < 0 • 1,000–4,000 	<ul style="list-style-type: none"> • threat complex > 0 • targets < 0 • 500–4,000 	<ul style="list-style-type: none"> • Satellites > 0 • orbital debris < 0 • Altitude < 2,000 km at low-Earth orbits
Nominal performance limit	Noise-limited detection: Operating range generally beyond maximum ground-clutter range		
Environment effects	Tropospheric refraction Ionospheric propagation; Nuclear burst effects		Tropospheric refraction Ionospheric propagation
Metric accuracy (referenced to external coordinate system)	Launch-point estimation Impact-point prediction	Launch-point estimation Impact-point prediction Track and discrimination Interceptor designation	Satellite catalog RSO correlation Conjunction analysis (orbit prediction)
Signature	<ul style="list-style-type: none"> • Target classification • None 	<ul style="list-style-type: none"> • Target classification • Target identification • Countermeasure and clutter rejection 	<ul style="list-style-type: none"> • Object classification; Debris size estimation • Range-Doppler imaging
Target traffic handling	Hundreds of simultaneous ballistic missile threats	Tens of ballistic missiles under engagement	~20,000 objects currently tracked in Earth orbits

measurement-to-track data association. Tracking in CSO environments may motivate high-resolution tracking waveforms to ensure firm tracks on individual objects.

Narrowband measurements – meaning that individual scatterers comprising a given target are unresolved – can be used to classify the type of object under track. Observed narrowband radar cross-section (RCS) statistics in conjunction with track characteristics can coarsely classify targets. Narrowband data are used for SSA characterization of RSOs as well. For example, empirical relationships have been developed to estimate space debris size from its RCS.

Target identification or discrimination within a class is essential to distinguishing between RVs and decoys. Decoys may be deployed from the same launcher as the RV and designed to emulate RV metric and signature characteristics so as to force the missile defense system to waste interceptors against nonlethal objects. Discrimination may require high-resolution measurements such that a given target is resolved into component scatterers. Wideband measurements provide resolved scatterer measurements across the

target range extent while coherent processing across a train of wideband pulse can be used to generate a two- or three-dimensional image of a target [2]. High-resolution radar imaging enables shape and dimensional estimation of the target as well as providing indication of its rotational motion characteristics. Moreover, resolution of individual scatterers can enhance the fidelity of RCS and polarization feature extraction.

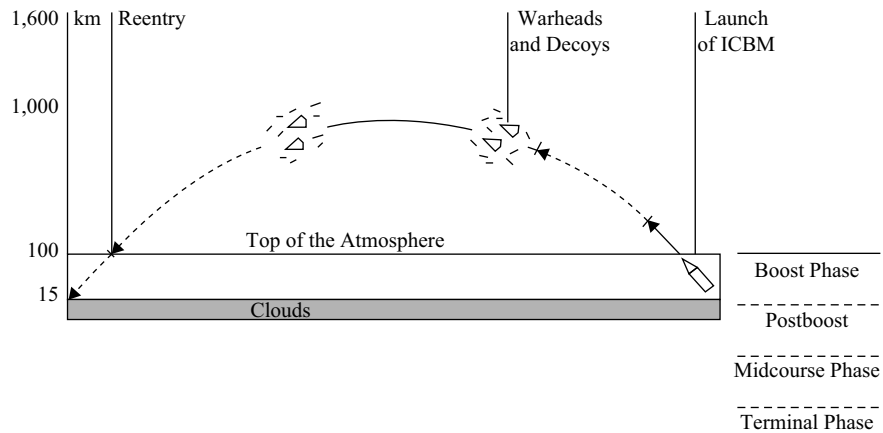
7.1.1 Organization

This remainder of this chapter expands the description of BMD radars as this sector is currently the focus of extensive development, deployment, and testing efforts as well as posing a number of technical challenges. A brief overview of ballistic missile characteristics and associated defensive architecture concerns are provided for context. The BMD engagement sequence and kill chain are then delineated with focus on the radar roles. A brief account of U.S., Russian, and other international BMD radar-deployment efforts is then provided because upgrading legacy sensors with new software and technology insertion is critical to modern BMD radar efforts. Radar functional requirements and supporting technology considerations are then addressed. The chapter concludes with an account of selected BMD performance metrics.

7.1.2 Acronyms

ABMD	Aegis ballistic missile defense
AESA	active electronically scanned array
BMDs	Ballistic Missile Defense System
BMEWS	Ballistic Missile Early Warning System
CEP	circular error probability
CSO	closely spaced objects
ESA	electronically scanned array
FFOV	full field of view
GMD	Ground-Based Midcourse Defense
ICBM	intercontinental ballistic missile
IR	infrared
ITWAA	Integrated Tactical Warning and Attack Assessment
LDS	launch-detection satellite
LEO	low-Earth orbit
LFOV	limited field of view
MDA	Missile Defense Agency
MW	missile warning
RSO	resident space object
RV	reentry vehicle
SSA	space situational awareness
SWIR	short-wave infrared
THAAD	Terminal High Altitude Area Defense System
UHF	ultrahigh frequency
VHF	very-high frequency

FIGURE 7-1 ■
Ballistic Missile
Flight Regimes.



7.2 | BMD RADAR SYSTEM REQUIREMENTS

7.2.1 Overview of the Ballistic Missile Threat

Ballistic missiles of varying degrees of capability are available to any established or emergent power as the critical technologies are widely proliferated [3]. The nominal flight path and associated atmospheric regimes of a long-range ballistic missile are depicted in Figure 7-1. A single- or multiple-stage booster is used to launch the ballistic missile according to its range. Short-range tactical ballistic missiles with ground ranges of less than 300 km typically use an integrated warhead and booster. The World War II V-2 and the variants of the descendant Russian Scud exemplify this single-stage class. Multiple-stage, long-range ballistic missiles package the weapon payload into a reentry vehicle designed to protect it as it transits the atmosphere. An accurate RV generally requires an exoatmospheric deployment orientation followed by spin stabilization to minimize atmospheric drag effects upon reentry. Associated debris may be produced from separating launch hardware, expended solid fuel, and other sources that manifest as volumetric clutter. The composite ensemble of the upper stage, RV, and associated volumetric clutter such as debris is termed the *threat complex*.

Ballistic missiles exhibit three kinematic phases corresponding to their flight regimes. The first is during boost when the missile is accelerating at least several g 's due to the axial thrust. This boost phase can employ several booster stages to accelerate the missile to a desired velocity and may include a low-acceleration stage for deployment of the RV. The second kinematic phase is when the RV or missile is flying a ballistic trajectory in the exoatmospheric. Only gravitational forces are significantly affecting the trajectory at this stage. The third phase initiates as the RV or missile reenters the atmosphere and drag forces contribute to shaping the trajectory. Both the boost and reentry phases contain acceleration and jerk terms that cannot be readily estimated a priori by the defense. The boost phase also imposes sudden changes in acceleration as burnout and staging events occur.

Table 7-4 denotes representative details of the flight regimes for various ballistic range classes [4]. As indicated, the missile transitions from a relatively short boost period into ballistic motion through the midcourse regime. The altitude above about 100 km is commonly termed *exoatmospheric* to denote that atmospheric effects are

TABLE 7-4 ■ Representative Ballistic Missile Parameters

Ground Range (km)	Burnout Velocity (km/s)	Burn Time (s)	Burnout Altitude (km)	Apogee (km)
100	1.0	30–40	10–15	< 30
300	1.7	60–70	25–35	< 100
600	2.4	60–90	40–60	< 150
1,000	2.9	70–110	50–80	230
3,000	4.9	80–140	100–120	650
10,000	7.2	170–300	180–220	1,300

minimal while the region below that altitude is denoted endoatmospheric. Entry into the atmosphere introduces drag that diverts the missile from the nominal ballistic flight path as well as introducing significant aerodynamic and thermal stresses. Endoatmospheric entry also induces low-mass, high-drag volumetric clutter to “strip out” while potential threatening targets such as warheads continue on a ballistic trajectory.

The accuracy of ballistic missiles is generally characterized by their circular error probability (CEP). The CEP is defined as the radius of the projected area within which the missile is expected to have a 0.50 probability of impacting. The CEP of modern ballistic missiles typically ranges from tens of meters to kilometers. The CEP decreases with decreasing guidance error and increasing mass–drag ratio. The improving accuracy of tactical ballistic missiles from advances in guidance and control technology significantly increases their potential lethality over the relatively inaccurate Soviet-era Scuds and third-party nation variants. While a number of currently deployed ballistic missiles utilize liquid fuel, there is an anticipated trend toward solid fuel systems as this latter approach decreases launch preparation requirements and can enable improved launcher mobility [5].

Ballistic missile payloads range from conventional high explosives to nuclear weapons. Tactical and theater ballistic missile may be designed to support multiple types of warheads, including chemical and biological weapons as well as submunitions. The intercept lethality of fragmentation warheads against this span of possible payloads is problematic. Achieving adequate lethality while avoiding the usage of interceptors armed with nuclear warheads has motivated the development and deployment of hit-to-kill interceptors that depend on high closing velocities to effectively incinerate the ballistic missile payload upon collision. The kinetic energy released by high-speed collisions is significantly greater than could be achieved with an explosive warhead of equivalent mass to the interceptor. BMD radars identify and designate the warhead and RV to the interceptor to enable its endgame homing.

There is typically a minimum acceptable intercept altitude specified for defense of “soft targets” such as population centers that drives the engagement timeline and battle space that must be supported by the BMD radar. Nuclear warheads must be intercepted sufficiently high to prevent their detonation from imposing damaging blast overpressure or thermal effects on the Earth’s surface. Chemical and biological payloads must be intercepted at sufficient altitude as to prevent their dispersion through the troposphere. In addition, interceptor design features may limit the minimum engagement altitude. BMD infrared seekers are largely confined to exoatmospheric operation due to sensitivity needs and atmospheric friction effects. Since the interceptor must possess sufficient

fly-out time to reach this minimum engagement altitude, modern BMD radars must acquire and track targets at long range in the exoatmospheric regime.

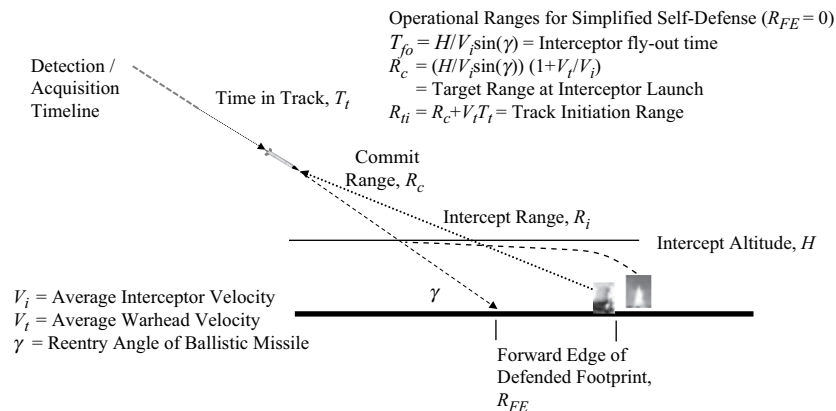
7.2.2 BMD Engagement Implementation

The BMD battle space can be characterized as the spatial volume encompassing the earliest and latest intercept opportunity for a given threat scenario and operational context. In general, the engagement sensor should be sized to operate significantly beyond this battle space, which should be ideally determined by interceptor kinematic capabilities. The maximum intercept range increases with the commit range of the target at which track accuracy is sufficient to support launching the interceptor since the interceptor has more time for fly-out. Ballistic trajectories can be accurately predicted using high-fidelity representation of the equations of motion from extrapolating the track position and velocity.

The extent of the defended footprint on Earth's surface protected by the BMD system correspondingly increases with the fly-out time available to the interceptor. A co-located engagement sensor must operate over a significantly longer range than the interceptor to provide adequate fly-out time to support exoatmospheric engagements and defend large areas. As illustrated in Figure 7-2, the engagement radar will require sufficient time in track to achieve the prediction commit accuracy and discrimination confidence necessary for commit. Using the expressions given for this simple linearized example, assume self-defense against a ballistic missile attacking at 3,000 m/s with a 30° reentry angle targeted directly at the BMD site. The exoatmospheric interceptor is assumed to engage the warhead at an altitude of 100 km with an average fly-out velocity of 1,500 m/s. This scenario corresponds to an intercept range of 200 km with a time of flight of ~133 s. The corresponding commit range is 600 km due to the 2:1 velocity advantage of the threat missile over the interceptor. Allowing for 30 s time-in-track precommit, the engagement radar must initiate track at a range of 690 km against the threat missile. The required commit range will increase with increasing defended footprint extent to provide the interceptor additional fly-out time.

BMD radars that provide early commit-quality tracks enable long fly-out times and large defended footprints. An early commit enables a large area, such as a nation, to be defended from long-range ballistic missiles using a single exoatmospheric interceptor

FIGURE 7-2 ■
Simplified
Engagement
Geometry with Self-
defense Parametric
Expressions.



site. Area defense motivates usage of an engagement sensor system that can achieve commit accuracy at the maximum target range congruent with the kinematic capability of the interceptor. The commit range can be extended by increasing the sensitivity and operational range of the radars, but this is ultimately constrained by *radar line of sight* (RLOS) and likely the incremental sensitivity cost. For example, the horizon-constrained range against an intercontinental ballistic missile (ICBM) with a ground range of 8,000 km is on the order of 4,000–5,000 km from the defended area. Forward basing radars nearer the ballistic missile launch area mitigates RLOS constraints and enables early acquisition and track. If there is an associated reduction in range requirements, forward basing enables usage of a smaller, less expensive radar. The AN/TPY-2, which was developed originally to support theater missile defense, demonstrates the utility of a transportable radar system in this context.

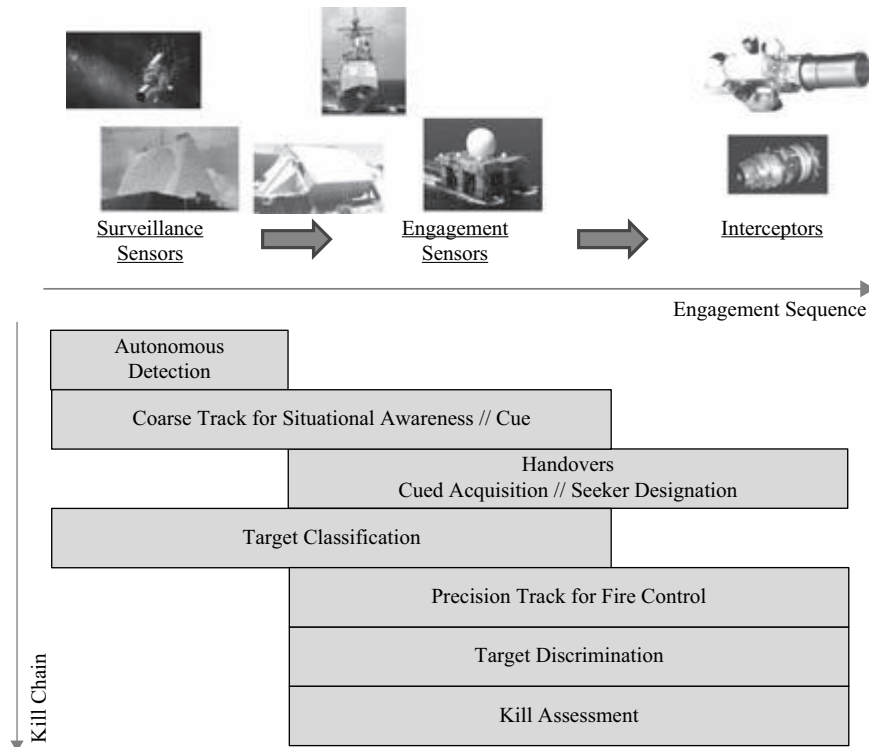
The engagement sensor system and resultant trend in forward-edge radius of the defended footprint, R_{FE} , can be coarsely divided into two cases from system analysis considerations [6]. Both the time of flight and burnout velocity of a ballistic missile with flight path ground range G_T are proportional to $\sqrt{G_T}$. So, the potential fly-out time available to the interceptor increases with increasing ballistic missile ground range, but the corresponding threat velocity increases proportionately. It follows that we can parameterize BMD engagements into two classes such that:

1. effective sensor range significantly less than maximum threat ground range due to RLOS or sensitivity constraints – that is, $R_{FE} \sim 1/\sqrt{G_T}$ corresponding to terminal defense with co-located radar and interceptors; and
2. effective sensor range enables early target detection and tracking corresponding to short-range *theater ballistic missile defense* (TBMD) scenarios or the use of networked forward-based radars for long-range fire control – that is, $R_{FE} \sim \sqrt{G_T}$.

As indicated, this parameterization derives from considering the increase in burnout velocity and time-of-flight with increasing threat ground range as delineated in Table 7-4 in conjunction with a simple linear representation of the interceptor fly-out. The effective engagement sensor coverage and threat missile trajectory drive the achievable defended footprint. This case analysis motivates usage of forward-based engagement radars to counter long-range/high-speed threats that would otherwise contract the defended footprint. A BMD system track may require support from a network of sensors to cover midcourse as well as ascent phases of the threat missile flight to provide high-quality fire control.

The canonical BMD engagement sequence and kill chain are depicted in Figure 7-3. The engagement sequence among BMD elements is depicted horizontally, while the functional sequence of the kill chain is depicted vertically in alignment with the corresponding BMD elements. The kill chain initiates with the autonomous detection of either launch events via *launch-detection satellite* (LDS) or ballistic missiles in flight via early warning and forward-based radars and subsequent reporting to the BMD command-and-control system. Metric and signature data from these sources are used to classify and characterize the threat. Ballistic missiles are tracked by multiple sensors with composite system track fidelity adequate to derive situational awareness, which includes launch-point estimation, impact-point prediction, and attack characterization. Using this tracking and classification data, the trajectories of threatening missiles are then predicted for handover to midcourse and terminal-engagement radars.

FIGURE 7-3 ■
BMD Kill Chain and
Engagement
Sequence.



After achieving target acquisition, the engagement radars perform two critical functions – precision track and discrimination. Precision track consists essentially of tracking the desired target with sufficient accuracy to designate it to the *kill vehicle* (KV). This designation must be generated on the predicted trajectory and translated into Earth-centered inertial coordinate system accessible by the kill vehicle so that it is within the field of view of the seeker with high confidence. In parallel with the precision tracking, the engagement sensor identifies the primary target(s), discriminating the RV from other launch components, debris, or decoys using a combination of an extended-observation metric and high-resolution signature data. Maintaining correct measurement-to-track association and well-resolved measurements is an implicit requirement for both the precision track and discrimination processes since these operations require an extended sequence of measurements for a given target.

Modern BMD interceptors employ a separating KV that essentially consists of an infrared (IR) focal plane array sensor and some manner of lateral maneuvering capability. The postcommit midcourse phase of an exoatmospheric engagement consists largely of the interceptor flying to a point in space where the KV will be deployed from its single- or multiple-stage launcher. During the fly-out, the engagement radar may refine and uplink its track and discrimination estimates to the interceptor, taking advantage of both additional observation time and an increasing *signal-to-noise ratio* (SNR) due to decreasing range. A *target object map* (TOM) may be generated by the radar and uplinked to the interceptor to aid seeker acquisition of the designated target when multiple objects are assessed to be present in its field of view. The TOM is essentially the state vectors of the proximate target set mapped into seeker coordinates.

The KV autonomously conducts the endgame transitioning through target acquisition using the engagement sensor designation, target identification, homing track, and aimpoint selection [7]. The seeker acquires the target as the KV enters endgame and performs final target identification, terminal tracking, and aimpoint selection to maximize lethality against the target. Hit-to-kill KVs are designed to destroy the target through body-to-body impact as the high closing-velocity collision releases much more energy against the target than could be achieved with conventional fragmentation warhead for a given KV mass. The operation and survivability of the IR seeker mechanism as well as maneuverability constraints generally limit KVs to exoatmospheric intercepts. Interceptors have been developed to engage short-range ballistic missiles endoatmospherically but intercept of long-range ballistic missiles is generally conducted exoatmospherically. The determinism – corresponding to the absence of unknown accelerations – of an exoatmospheric trajectory enables ballistic target to be engaged by interceptors, which may only have a comparable or even lesser velocity than the target as long as they possess sufficient endgame maneuverability to correct for the radar-prediction commit error and close out onboard guidance errors.

The depicted overlap of the kill chain functions between engagement sequence elements in Figure 7-3 indicates that the function can be allocated to any element or shared among them for increased robustness. For example, if the engagement radar is challenged by sensitivity or resolution requirements, precision track and discrimination can potentially be off-loaded or shared with the KV. The national missile defense architecture that developed into the GMD element of BMDS initially allocated the kill chain functions solely between the surveillance sensor and interceptor elements. Under this concept, the existing early warning radars were modified to directly designate targets to the KV via the GMD fire-control and interceptor data-link elements mitigating the expense of developing and deploying new X-band engagement radars [8]. The reliable measurement performance, extended observation capabilities, and robust integration of acquisition and multiple-target track functions have ensured that radars remain as the principal BMDS engagement sensors. Enhancing resolution and accuracy performance as well as enabling transportability motivated development and deployment of X-band radars such as the SBX and THAAD radars for engaging ICBMs and theater ballistic missiles, respectively.

Launch-detection satellites provide earlier detection but are incapable of precision tracking and attack assessment as they only observe the ballistic missile during boost. Future spaceborne sensors employing passive multiple-spectrum electro-optical sensors capable of tracking discrete objects will increasingly supplement this long-range surveillance mission. The generation of “stereoscopic tracks” can significantly improve accuracy by fusing angle-only measurements from multiple sensors with diverse viewing geometries to generate three-dimensional tracks. Even with this approach, electro-optical sensors will be limited in tracking and discrimination by their lack of range resolution and modest cross-range resolution. (Cross-range resolution can be approximated by the product of the sensor angular resolution in radians and the range to the target.)

The complex of objects deployed from a single booster may contain intentional countermeasures designed to degrade BMD effectiveness as well as unintentional debris [9]. Countermeasures may include decoys of various degrees of sophistication ranging from simple balloons to replicas of the actual RV [10]. Other countermeasures

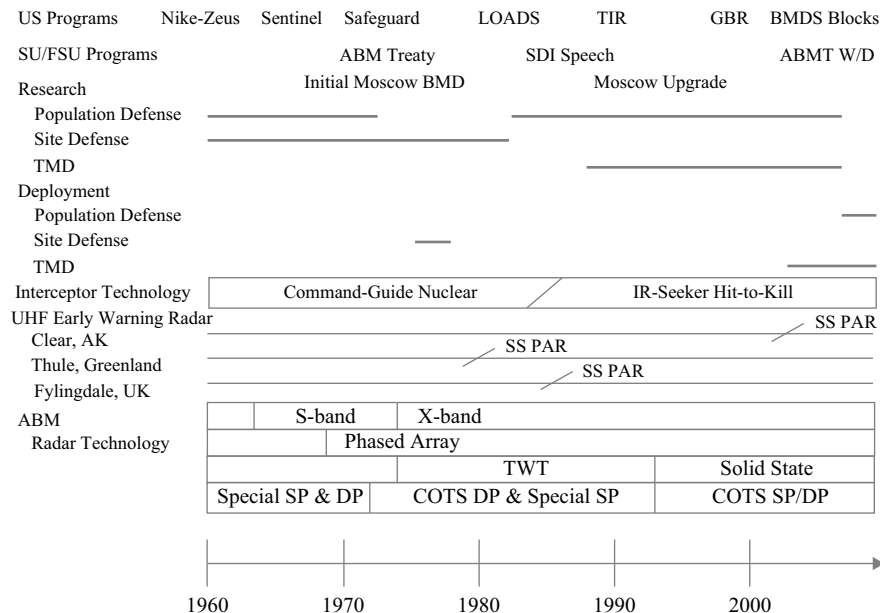
could be designed to mask the RV from BMD sensors by inducing volumetric clutter via chaff deployment or employing electronic attack. Finally, the RV design could be modified to distort or suppress key signature aspects, such as reducing RCS so as to degrade defensive radar effectiveness [11].

Discrimination of the RV from countermeasures and associated objects has long been viewed as problematic [12]. This challenge is particularly acute in the exoatmospheric midcourse regime where there are no atmospheric effects to separate heavy objects like RVs from light decoys. Entry into the atmosphere effectively serves as bulk filter against relatively lightweight countermeasures and debris. Some legacy BMD systems employed an overlay of long-range interceptors for high-altitude intercepts as well as an underlay of high-acceleration interceptors for endoatmospheric engagements of RVs that had leaked past the initial battle space or had been protected by countermeasures until reentry. However, defense of large areas and soft targets, such as population centers, mandates interceptor launch well before reentry in order to enforce high-altitude intercepts and defend large areas on Earth’s surface. Unless the BMD radar can reliably discriminate the RV from other objects, the BMD system must incur the wastage of committing an excessive number of interceptors against a given ballistic missile complex. Conversely, if the BMD system has a limited interceptor inventory, leakage will occur when the RV is not engaged due to incorrect discrimination or inaccurate designation to the KV.

7.3 | RADAR DEVELOPMENT FOR BALLISTIC MISSILE DEFENSE

The history of BMD with focus on radar aspects is summarized in Figure 7-4. While much attention has focused on successive generations of interceptor technology progressing from exoatmospheric and endoatmospheric missiles armed with nuclear

FIGURE 7-4 ■ BMD Development Timeline.



warheads to the present emphasis on kinetic kill vehicles, the progressive development and deployment of unique radar systems has been critical to advancing capabilities. Early research supporting BMD efforts was critical to developing the first generation of phased array radars for air defense. Later BMD research was critical to the emergence of AESA and high-throughput processing technologies. The large sunk cost required by this class of radars strongly motivates spiral development where new capabilities are inserted largely via new software builds as well as processing and communications hardware upgrades. The high cost of upgrading the radio-frequency (RF) apertures of large phased array radars has historically precluded that option. The primary source of situational awareness data for BMDS is the large phased array radars that were initially designed and deployed to support Cold War MW but later upgraded to support BMD. The COBRA DANE radar initiated operations in 1977, and the UHF early warning radars were developed in the 1980s.

In addition to utilization of advanced technologies such as solid-state phased array radars, their operational sizing and attendant physical extent is also a distinguishing characteristic of BMD radar systems. As defined in Chapter 6, the noise-limited search capability of a radar system is ultimately determined by the product of its average transmit power and receive antenna aperture divided by the product of its system noise temperature and system loss factor. BMD search requirements lead to the necessity for large antenna aperture fed by high average power. U.S. and Russian early warning radars are integrated into the sides of multiple-story buildings that also house the operations center, transmitter, receiver, and processing subsystems. Even TBMD radars designed to counter short-range theater missiles are large in comparison to their air-defense counterparts. For example, the X-band THAAD radar system antenna was designed to be transportable but is more than an order of magnitude larger and several orders of magnitude more capable than X-band AESAs used in airborne-fighter radars [13].

The modern generation of BMD radars addressed in this chapter is somewhat arbitrarily defined as those employed since the cessation of the Cold War in the 1990s, but all of the systems in use now were designed or initially deployed during that period under the constraints of the Anti-Ballistic Missile (ABM) Treaty as addressed shortly. Current BMD radars consist primarily of multiple-function phased array radar systems that were originally built to support early warning and attack assessment, TBMD, and area air defense. MDA is developing the BMDS composed of sensors, weapons, and command-and-control networks intended to provide increasing defense capabilities over a series of block upgrades and phased deployments as adversarial offensive capabilities grow and defensive technologies mature. The objective goal of the BMDS is provide the global capability to engage ballistic missiles of all ground-range classes throughout their entire flight regimes.

The ABM Treaty of May 1972 sought to ensure the stability of strategic competition based on mutually assured destruction such that neither the United States nor the Soviet Union (USSR) could instigate a first strike without fear of suffering a devastating retaliatory strike from the adversary's surviving strategic forces. Toward this end, the ABM Treaty limited deployment of BMD systems to the defense of two areas for each country; this was later amended to a single protected area. The USSR chose to develop a BMD system to defend Moscow, while the United States developed and briefly deployed a system to defend ICBM launch complexes. The United States activated the Safeguard BMDS system in North Dakota in 1975, but it was shut down within months.

This system employed the UHF Perimeter Acquisition Radar (PAR) and S-band Missile Site Radar (MSR) to support an overlay defense of exoatmospheric Spartan interceptors and an underlay defense of endoatmospheric Sprint interceptors. The PAR and MSR were both multiple-function phased array radars employing tube-based transmitters driving passive phased array antennas integrated into hardened building structures. Both classes of interceptors employed tailored nuclear warheads so that radar-uplinked command guidance provided adequate engagement accuracy. Perceiving value in a limited defensive capability for their national capital regions, the Soviet Union deployed and later upgraded a Moscow BMD system that remains operational in current-day Russia.

The principal constraints imposed by the ABM Treaty and subsequent interpretations of it on radar system and technology development are:

- bans on developing, testing, or deploying ABM systems or components that are “sea-based, air-based, space-based, or mobile land-based”;
- constraints on deployment of future early warning radars to the periphery of national territory with outward orientation;
- implicit definitions of ABM radar as phased array having average transmitted power – aperture area product in excess of 3 million; and
- interpretations that ban testing of air-defense components in “ABM mode,” including radar tracking of “strategic ballistic missiles” or operating “in conjunction with the test of . . . an ABM radar at the same test range.”

As delineated in Chapter 6, the search form of the radar-range equation indicates that noise-limited performance is proportional to the product of average transmit power and receive-antenna aperture area. The implicit definition of an ABM/BMD radar in terms of average power – aperture area product in excess of 3 million $\text{w}\cdot\text{m}^2$ – appears motivated by estimation of the search capability required to perform the strategic BMD surveillance mission along with assumed system noise temperature and loss characteristics likely based on the technologies of the time. The ABM Treaty is the only international agreement known to the author that makes implicit reference to the radar-range equation.

Under the ABM Treaty, BMD system development efforts in the United States subsequent to Safeguard were largely directed toward defense of strategic force assets in recognition of the technical challenges of defending dispersed and highly vulnerable population centers in contrast to hardened ICBM launching facilities and associated command-and-control installations. Research efforts produced the fixed S-band Site Defense Radar followed by the transportable X-band Sentry radar system concepts. Both radar systems were intended to support low-altitude engagements against counterforce attacks on hardened ICBM sites using high-acceleration command-guided interceptors intended to conduct endoatmospheric engagements. These radars intended to take advantage of the endoatmospheric battle space to ease the discrimination requirements and aggressively utilized nuclear hardening technology to enable survivability in the event of conflict. The associated BMD interceptors all employed command guidance with nuclear warheads, which imposed a significant lethality radius but presented the operational and technical challenges of operation in a nuclear environment. Substantial effort was expended on research and development, but the associated BMD systems

were never fabricated and deployed due to concerns over cost, effectiveness, and impacts on strategic stability.

President Ronald Reagan announced in March 1983 that he was initiating development of a BMD system that would provide high-confidence protection of the entire United States population. This system was anticipated to make extensive use of space-based sensors and weapons to provide global protection against ballistic missiles, leading to the appellation of “Star Wars” for this conceptual system. The anticipated transition from ground-based radar systems to spaceborne electro-optical sensors encountered a number of technical and affordability challenges leading to the present emphasis on spiral development of legacy radar systems to support BMDS and continued research efforts to develop spaceborne electro-optical sensors.

In parallel with the increased interest in radar for strategic BMD, Iraqi military operations using modified Scud theater ballistic missiles (TBMs) motivated new interest in TBMD. Research and demonstration efforts led to ongoing modifications in the U.S. Patriot and Aegis air-defense systems to detect, track, classify, and engage TBMs. The Russians also developed extended air-defense systems such as the S-300(V), which incorporated upgraded radars and interceptors to destroy TBMs.

While regarded by some as the cornerstone of strategic arms agreements, the ABM Treaty significantly constrained the development and deployment of radar systems with BMD-like characteristics. Upgrades of early warning systems and the development of mobile TBMD systems were, in principle, subject to bilateral adjudication to ensure compliance with the treaty. U.S. efforts to deploy a national missile defense appeared significantly constrained by the treaty. The constraints on U.S. BMD development led the United States to abrogate the ABM Treaty in June 2002. However, all the American and Russian BMD radar systems currently deployed were developed under its constraints. The great achievement of the BMDS effort is arguably accomplishing strategic missile defense with sensors that were designed expressly under treaty obligations to not possess this capability. Through innovative BMD system architectures, modern networking constructs, and advanced interceptor development, these radars support military utilities far beyond their original design intent.

Advancing the timeline of launch detection is precious to tactical attack warning as well as to BMD. The United States developed the Defense Support Program series of launch-detection satellites, which used infrared sensors to warn of ICBM and SLBM launches. Recent Russian writings indicate that the Russian LDS program was far less successful than that of the United States, leading to the deployment of over-the-horizon radar (OTHR) systems for early warning as well as construction of a network of large phased array radar systems around the periphery of the USSR to provide attack assessment and support their BMD system. The United States did not deploy OTHR systems for early cueing likely because of concerns over data reliability and availability constraints imposed by solar events and diurnal cycles on ionospheric propagation performance.

7.3.1 U.S. BMD Radar Deployment

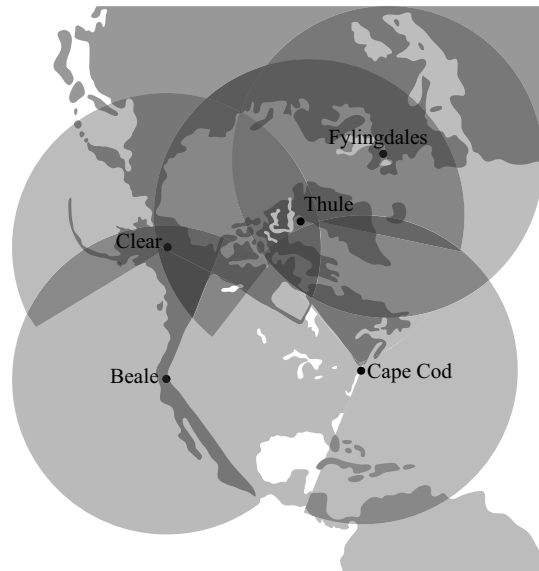
For decades, the United States has maintained a network of large UHF radar systems sited and oriented to provide tactical warning and attack assessment of ICBM attacks on the United States. This mission imposes search and track sizing requirements that also

make these radar systems well suited to support BMD operations. Upon deactivation of the Safeguard BMD system, the PAR surveillance sensor near Cavalier, North Dakota, was converted into an attack assessment MW role as the Perimeter Acquisition Radar Characterization System (PARCS). However, since PARCS is located in the northern United States, it cannot provide early warning due to its horizon-limited range constraints.

The United States deployed the Ballistic Missile Early Warning System (BMEWS) radars at locations near Clear, Alaska; Thule, Greenland; and Fylingdales Moor in the United Kingdom. These radar systems were sited to provide for the detection and assessment of Soviet ICBM attack on the United States. The initial deployments consisted of an ensemble of UHF switched-fan-beam radar systems and mechanically scanned single-target tracking radars. The BMEWS deployment was supplemented by a series of mechanically scanned radars sited to detect SLBM launches against the continental United States. This original BMEWS deployment circa 1960 was deemed inadequate due to incomplete coverage of possible Soviet attack trajectories, coarse resolution, inadequate accuracy, and limited target-handling capacity. The BMEWS and primary SLBM detection systems were all eventually upgraded to multiple-faced UHF multiple-function AESA radars integrated into the building structure that houses operations and supporting systems. There are currently two active PAVE PAWS radar systems sited in Massachusetts (Cape Cod Air Force Station) and north California (Beale Air Force Base). While these radars were developed and sited to address the Soviet threat to the United States, they have been adapted to provide coverage against emerging threat states as depicted in Figure 7-5.

The BMEWS and PAVE PAWS operate in the 420- to 450-MHz UHF band and employ circular polarization according to spectrum allocation data. The PAVE PAWS each use two transmit-and-receive apertures covering a composite azimuth extent of 240° . Each 22-m aperture possesses about 1,800 active elements reportedly generating about 340 watts each of peak RF power [14]. The BMEWS radar apertures possess about 2,560 elements each and are some 26 m across [15]. While the BMEWS radars at Thule,

FIGURE 7-5 ■ U.S. BMD and MW Surveillance Radar Coverage.



Greenland, and Clear, Alaska, are two-sided, the one near Fylingdales Moor in the United Kingdom employs three RF apertures for 360° coverage. These arrays are thinned designs that sacrifice aperture efficiency and sidelobe control in exchange for decreased beamwidth. This design also enables potential sensitivity growth by fully populating the RF aperture with active elements. These radars are sized to detect and track threat complexes at the maximum RLOS range of beyond 4,000 km against long-range ballistic missiles.

COBRA DANE was activated in 1977 on Shemya Island, Alaska, and has performed key roles in missile warning, BMD, and SSA as well as enforcing strategic arms control treaties by monitoring Russian missile testing. This multiple-function phased array radar employs 96 traveling wave tube transmitters distributed across the 30-m diameter corporate-feed antenna. The resulting spatial power combining enables very high peak power operation on the order of 15 MW and an average transmit power of 0.9 MW [16]. This L-band system operates in the 1,215- to 1,400-MHz band. COBRA DANE supports a wideband *linear frequency modulation* (LFM) waveform of some 200-MHz extent, which should provide a range resolution of about 1 m, taking into account broadening from weighting to suppress range sidelobes.

The Sea-Based X-Band (SBX) radar system utilizes a limited field-of-view (LFOV) AESA on a mechanical mount to provide adequate field of regard as illustrated in Figure 7-6. The ensemble is protected by a radome. About 65 percent of the 384-m² aperture is populated with active transmit-and-receive modules driving radiating horn elements. The X-band radar system is mounted on a self-propelled semisubmersible platform that was originally designed to support oil drilling. The platform measures 73 m wide by 118 m long and contains the power plant, control room, living quarters, and other infrastructure to support the SBX mission. The similar but smaller Ground-Based Radar-Prototype (GBR-P) at the Ronald Reagan Ballistic Missile Defense Test Site on Kwajalein Atoll in the Marshall Islands was used to retire the associated risk

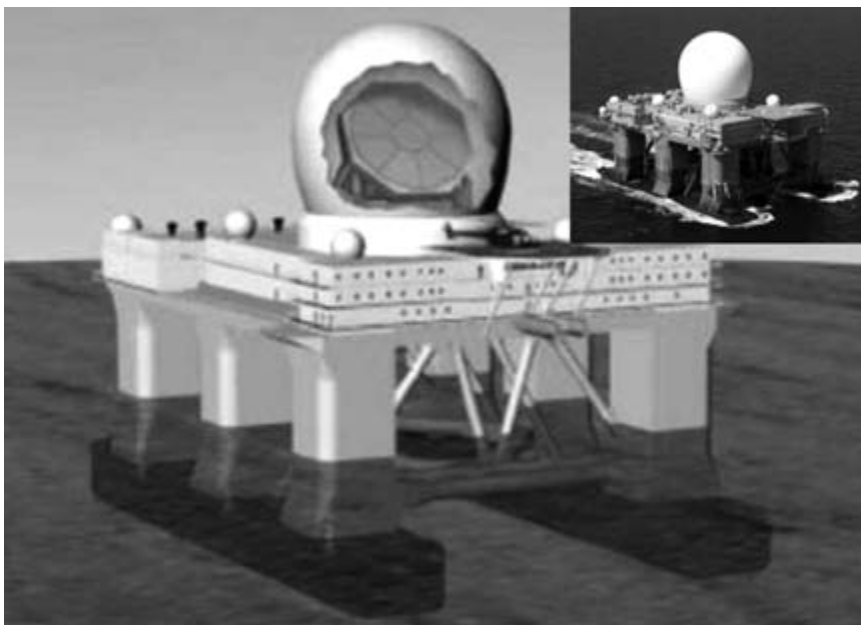


FIGURE 7-6 ■ SBX Radar and Platform.

with discrimination, electromechanical scanning, target object map generation, and hit assessment as well as support of GMD flight testing.

The AN/TPY-2/THAAD radar shares a significant degree of common technology with the SBX radar but is a full field-of-view design. Both radar systems were developed by Raytheon; this firm also constructed the BMEWS, PAVE PAWS, and COBRA DANE radar systems. The THAAD radar is an X-band AESA with a rectangular 9.2-m² antenna aperture supporting 25,344 transmit–receive modules [17]. This radar performs surveillance, tracking, and discrimination against tactical and theater ballistic missiles in support of BMDS as well as the THAAD TBMD system. The radar system is transportable via either C-5 or C-17 and consists of the antenna unit, electronics unit housing the receiver and digital-processing subsystems, cooling and power distribution unit, and a prime power diesel-generator unit.

7.3.2 Russian BMD Radar Deployment

The Russians began development of their BMD systems with supporting large ground-based radar systems during the 1960s. Their first-generation BMD system defending the Moscow region included mechanically scanned fire-control radars as well as large UHF battle-management and early warning radar systems [18]. These two Dunay-class battle-management radars were located in Moscow and known to Western analysts as Dog House and Cat House. They reportedly provided a 3,000-km detection and tracking range against RVs using frequency-scanned continuous wave techniques [19]. The Russians developed several variants of VHF azimuthally frequency-scanned early warning radars, including the Denestr, Dnestr-M, and Dnepr systems featuring antenna apertures approximately 200 m wide by 20 m tall. These radar systems were known collectively in the West as the Hen House series. These were reportedly multiple-face sites to achieve the requisite azimuth coverage. The UHF Volga variant of this architecture was intended to provide surveillance against intermediate range ballistic missiles and SLBMs [20].

Beginning in the 1970s, the USSR began deployment of the large Daryal-series VHF phased array systems featuring separate transmit and receive arrays in independent structures separated by 2–3 km. As depicted in Figure 6, these systems were known in the West as the Pechora-class Large Phased Array Radars, named for the location of an early installation. These systems reportedly employ phase-coded extended-duration waveforms and advanced signal-processing and electronic-protection features. Their operational flexibility is sufficient to support a mixture of early warning, BMD system support, and space surveillance. A significant innovation of these radars is that either the transmit or receive array could be reportedly paired with an existing Hen House frequency-scanned radar system, though obviously with degraded performance from the full dual-aperture configuration. These systems were physically massive, with the Krasnoyarsk installation being described as possessing a 30-story radar receiver and an 18-story transmitter [21]. These systems likely provided superior target handling and tracking accuracy to the previous generations of frequency-scanned arrays, but their relatively low frequency of operation likely imposed operational limits due to ionospheric propagation effects and electromagnetic interference.

Several of the key Soviet-era early warning radars were emplaced in territory that became independent nations with the end of the Cold War, resulting in their subsequent

destruction or operational compromise. As a result, the Hen House network continued to shoulder onward decades past its initial deployment. Podvig lists ten surviving early warning radar sites, with some supporting several radar systems of different generations or azimuthal coverage [22]. At the peak of the Soviet early warning radar, these systems collectively provided almost total coverage of potential ballistic missile attack trajectories.

Recent Russian press accounts have announced deployment of the new class of Voronezh early warning radars. The Voronezh radars can reportedly be rapidly constructed from factory-manufactured modular components. These radars are also reportedly far less expensive to construct and operate than predecessor systems. Efforts are currently underway to develop and deploy a new generation of surveillance radar systems around the periphery of Russia to support missile warning, missile defense, and SSA.

Russian sources have claimed maximum tracking range against ballistic targets and satellites of some 6,000 km from their early warning network radars. In parallel with the VHF line-of-sight early warning radars, the USSR also developed and deployed sky wave over-the-horizon radar capability that reportedly would provide launch-detection capability against U.S. ICBMs [23]. This work may have been motivated by the Soviets' reported difficulties in developing and operating launch-detection satellites. The OTHR effort was not without setbacks either: One site was reportedly located next to the Chernobyl nuclear plant. It is likely that the sky-wave propagation channel necessary to detect a U.S. ICBM launch suffers frequent outages as the radar must operate through the polar ionospheric region. The Daryal-class LOS early warning radars would have been crucial in detecting and assessing a strategically threatening ballistic missile attack that might have been launched against the USSR and likely did prevent military escalation from false attack indications that arose from less reliable sensors.

The early warning radar network and the Dunay battle-management radars supported the mechanically scanned fire-control radars of the initial Moscow BMD system termed the "A-35" [24]. The system reportedly employed command-guidance interceptors armed with high-yield nuclear warheads. The A-35 reportedly achieved some measure of operational capability in 1972 but with limitations well recognized by the Soviet leadership. It appears to have been extremely limited in its ability to accommodate multiple engagements and to mitigate countermeasures.

The USSR in 1989 reportedly developed and deployed the successor A-135 BMD system to defend Moscow with an initial operational capability as illustrated in Figure 7-7 [25]. This system employed both exoatmospheric overlay and endoatmospheric underlay interceptors. Battle management and fire control are integrated into the multiple-function Don-2N radar system deployed north of Moscow near Pushkino. This radar system is built into a four-sided truncated pyramid some 40 m tall with equal length and width sides of some 100 m extent [26]. Each face reportedly has a circular phased array aperture about 16 m in diameter and a square phased array aperture of about 10 m extent. The radar reportedly operates in the mid-microwave band and possesses significantly improved resolution capabilities over the predecessor system in addition to multiple target-handing and electronic-protection features. This radar has reportedly tracked 5-cm-diameter spherical satellites at some 2,000-km range [27].

FIGURE 7-7 ■
Russian Don-2N
("pillbox") Radar.



Like their counterparts in the United States, Russian BMD developers probably were challenged by discrimination of targets from debris and countermeasures. Some recent Russian writings suggest that the Soviets may have attempted to address this challenge by utilizing a precursor high-yield nuclear burst to destroy or mitigate low-mass countermeasures [28]. The resultant deviation in target-trajectory and target-polarization characteristics would reportedly have served as a basis of discrimination for the fire-control radar. However, this approach would have mandated that the radar operate in a nuclear environment, thus imposing severe challenges.

7.3.3 International BMD Radar Deployment

The enormous investment of resources required for BMD against ICBM attack has limited research, development, and deployment to the United States and Russia to date. However, the diffusion of ballistic missile and weapons of mass destruction technology has given regional peer competitors the capability to strategically threaten each other with theater ballistic missile weapons. In addition, the increasing accuracy of TBMs and the availability of more lethal conventional warheads have markedly increased their significance in tactical warfare. There will likely be increasing interest in warning sensors and BMD radar systems capable of supporting defense against TBM attack but within the budgets and operational capabilities of emerging regional powers.

A number of radar systems offering some degree of TBMD capability have been developed, deployed, or purchased in the international arena. There appears to be significant interest in upgrading exported Aegis and Patriot systems to support TBMD. Citing legacy development efforts to counter TBMs, Russia is offering updated area air-defense system variants with TBMD capability such as the Antei-2500. Israel developed the Arrow TBMD system, which includes the L-band Green Pine multiple-function AESA [29]. The new generation of European multiple-function radar systems developed to support area air defense may be upgraded to support TBMD operation in conjunction with weapon system enhancement. India and Japan are integrating internationally procured and domestically developed elements to develop BMD capabilities.

7.4 | BMD RADAR DESIGN

7.4.1 Frequency Considerations

As a general rule, the United States has historically tended to choose higher bands for BMD radars than optimal from consideration of target RCS and cost-constrained noise-limited sensitivity. This trend has been motivated by the combination of mitigating propagation effects, the desire for enhanced resolution to mitigate the effects of dense object environments and countermeasures on the engagement process, and enhanced track accuracy for reliable interceptor guidance. The USSR chose VHF for its early warning and battle-management radar systems, which is nominally optimal for detection as RV-sized targets are near their resonant peak RCS value. Small debris are in the Rayleigh region, resulting in decreased RCS so as to suppress volumetric clutter returns. The resonance enhancement and Rayleigh suppression RCS regions are both easily evident in Figure 7-8, which depicts the normalized RCS of a conducting sphere. (In comparison, microwave radars such as those used as engagement sensors and in forward-based surveillance operate in the optical RCS region against typical targets.) U.S. designers chose UHF for surveillance radars to mitigate ionospheric propagation degradation in the natural environment and severe blackout effects anticipated in nuclear environments while retaining some low-band advantage in target RCS enhancement and debris suppression. In addition, the UHF radar spectrum generally suffers less severe electromagnetic interference than often encountered at VHF.

Similarly, the United States migrated from S-band to X-band for BMD engagement radars to improve operation in a nuclear environment and to achieve finer range and range-rate resolution for enhanced discrimination. Moreover, interest in developing transportable BMD radars motivated interest in X-band as higher frequency enables a

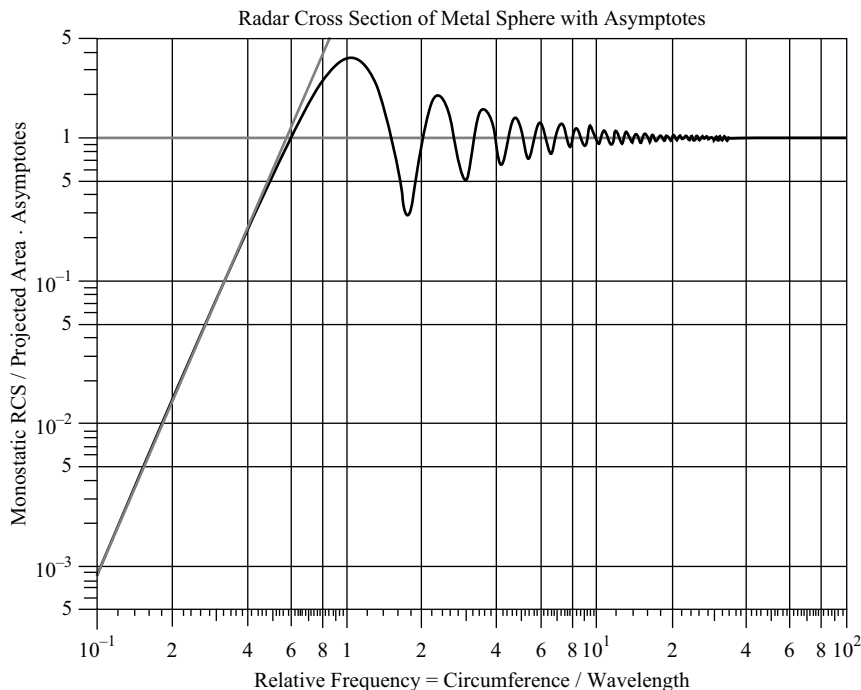


FIGURE 7-8 ■
Normalized RCS of
Conducting Sphere.

smaller antenna aperture for a given level of sensitivity and tracking accuracy. While AESA technologies promise the prospect of increasing the technically achievable bandwidth to at least 20 percent of the carrier frequency, the usable bandwidth below X-band is tightly constrained by spectrum allocation regulations. Above X-band, the cost of high-power RF generation increases markedly as does atmospheric attenuation. Hence, X-band has come to be viewed as the most desirable frequency band of operation by the U.S. BMD community. Affordability of large X-band BMD-class radar systems is a continuing challenge.

Radar operation in a nuclear environment is required if nuclear busts occur near surveillance zones or battle space. The ionized region of the fireball and immediately surrounding atmosphere tend to be relatively small. However, beta radiation emitted by the radioactive debris of high-altitude nuclear bursts can raise ionospheric electron densities by orders of magnitude over an extended region. The D-region of the ionosphere centered at an altitude of about 65 km has been assessed as exhibiting the most significant prolonged effects [30].

Ionization effects can be parameterized on the basis of the corresponding free-electron density, which determines the plasma frequency. RF waves at frequencies below this value are reflected from regions of elevated ionization. RF waves above this frequency penetrate but suffer attenuation that decreases with the increasing square of the frequency. The effects of this total reflectance or high degrees of attenuation on radar operation is termed *nuclear blackout* as it masks the surveillance volume and battle space beyond the ionized region [31]. BMD radar system designers may mitigate nuclear environmental effects by designing their systems at the highest practical radar frequency for the specified functionality. However, even X-band systems will be subject to attenuation, refraction, and phase dispersion in regions of high ionization.

7.4.2 Implementation

7.4.2.1 Search and Acquisition

Surveillance to achieve autonomous detection is typically performed by long-range VHF or UHF radar systems such as previously noted. Depending on capability and siting, these long-range radars may also perform battle-management functions generating handoffs for engagement radars and providing situational awareness tracks. Early warning against ICBMs mandates some manner of forward basing to mitigate RLOS limitations on detection range. Radars located within national boundaries can offer surveillance against SLBM or TBM attacks as well as support attack characterization, long-range interceptor engagement support, and target designation to engagement radars. However, the range resolution at these bands is inadequate to reliably resolve CSOs or discriminate individual targets.

Autonomous search for exoatmospheric ballistic missiles mandates large radar systems with capabilities far exceeding that encountered in air-defense applications. For example, published technical data indicate that the PAVE PAWS possesses an average power – aperture product of about 6×10^7 w-m², neglecting aperture efficiency and other losses [32]. While meeting the ABM Treaty threshold of BMD capability, this system is sized for SLBM detection, which demands less sensitivity than required by BMEWS to detect and characterize ICBM attacks due to the shorter range of operation. In addition to these noise-limited sensitivity demands, modern BMD AESA systems must jointly support high duty cycle and large range windows, which challenges

timeline occupancy. The radar planning and scheduling process must interleave search and track processes within the timeline required by mission requirements.

Based on a priori knowledge of threat launcher location and ballistic missile flight characteristics, a series of search fences may be devised that enable the radar system to focus its surveillance resources along anticipated threat trajectories. Targets detected in a search fence can then be tracked throughout the radar's field of view. In addition to supporting early target detection, this technique also enables efficient timeline usage.

A surveillance radar system can cue an engagement radar system, both extending its track-initiation range and increasing its target-handling capability by offloading autonomous search operations. Cueing from broad area sensors such as space-based infrared sensors can potentially extend radar acquisition and track-initiation range [33]. As noted previously, increasing track-initiation range can extend the intercept commit range and hence the extent of the defended footprint. In practice, the propagated error from a coarse cue may demand substantial search capability on the part of the engagement radar.

The military utility of tailoring the placement, extent, dwell sensitivity, and revisit rates search fences for specific autonomous operation and cued acquisition applications motivate the usage of multiple-function phased array radar systems for surveillance. In addition to beam agility, these systems typically employ energy-management techniques in their control process so that individual beam-position transmissions are of durations appropriate for a target class of specified RCSs at a corresponding maximum range.

7.4.2.2 Tracking and Discrimination

BMD imposes unique tracking challenges, including high degrees of measurement-error smoothing, multiple target tracking in the presence of closely spaced objects, and registration in an absolute coordinate system. Successfully meeting these challenges requires specialized radar design features such as high-resolution tracking and enhanced calibration and alignment techniques as well as sophisticated algorithms for measurement-to-track data association and track filtering.

The tracking and discrimination processes must be closely integrated. Any robust discrimination process requires multiple measurements over an extended interval on a given target, mandating firm track as a necessary condition. Having expended radar timeline and energy on target to identify the target, it must be kept in track to support subsequent designation to the interceptor.

To attain the accuracy required for midcourse intercept support, BMD engagement radars must and do attain significantly superior track-filtering performance than that of sensors tracking maneuvering air-breathing targets. Given that gravitational forces are the only significant effectors on target trajectory in the exoatmospheric regime, the track filter can be designed to attain a very high degree of smoothing. A six-state Kalman filter or batch-processing technique optimized to exploit the low process noise and replicate equations of motion is appropriate for this purpose. The states under estimation are simply the position and velocity vectors.

During reentry, a Kalman filter with an additional state to account for drag is generally utilized. Nine-state filters with terms to account for more complex aerodynamic forces may be used to optimize tracking performance for a maneuvering reentry body or other target anticipated to exhibit significant lift or aerodynamic control capability.

A nine-state filter with an acceleration vector in addition to position and velocity for state estimation may be employed against boosting targets. However, tuning the filter

plant noise (error model) terms for targets that transition almost instantaneously between boost and coast states is problematic and imposes significant performance compromises. The *interacting multiple model* (IMM) track filters performs well in this application [34]. This technique incorporates parallel state models, updates them in parallel with new measurements, and then blends the composite output and update variables. The IMM filter can accommodate boost and coast state model representations that accommodate booster burnout [35].

Successful track filtering presupposes that measurements of sufficient quality have been successfully extracted from the target under track. Data-association performance decreases with increasing update intervals, target maneuvering, and measurement error. The challenge of correctly associating measurements with the proper target in a CSO environment has been well documented in the academic literature. This problem can be particularly severe in an exoatmospheric environment since there is no drag to dissipate concentrations of CSOs. While exoatmospheric track filtering can achieve excellent smoothing performance the lack of dissipative forces enables the persistence proximity of CSOs challenging the capability of observing sensors to produce individually resolved measurements. BMD radars must resolve CSOs in range or Doppler to support the tracking and discrimination processes.

7.4.3 BMD Radar Technologies

7.4.3.1 RF Aperture

The RF aperture can be defined to include the antenna, integrated RF components, beam-forming network, and structurally integrated mechanical and electrical components. Beam agility is required to support integrated search and multiple-target track. The primary performance challenges imposed on RF aperture technology by BMD applications are sensitivity, bandwidth, and metric accuracy. Sensitivity denotes the need to achieve an adequate SNR and measurement rate on small targets at long ranges. The need for fine range resolution drives the RF aperture to be designed for wideband operation since the inverse of the waveform bandwidth bounds resolution in the range dimension. Designation of discriminated targets to the BMD battle manager or weapons system requires precise tracking. The requisite accuracy must often be attained in an absolute coordinate system so that coordinate misregistration can be a dominant BMD system track error source.

From the perspective of the acquisition community, cost is the driving concern typically associated with BMD radar systems. Modern BMD radar systems employ RF apertures constructed using AESA technologies as opposed to centralized or tube-based transmitters driving passive phased arrays or mechanically scanned antennas. The AESA RF aperture includes supporting power conversion and conditioning subsystems, beam-steering processor, and cooling and mechanical support structures in addition to the AESA transmit–receive module (TRM) assemblies and radiating elements. The RF aperture can impose in excess of 70 percent of the recurring cost, which is typically several hundred million dollars for a modern BMD radar system. The inherent redundancy and anticipated low component-failure rates of AESAs in surveillance and engagement radars are critical to overall BMD system reliability.

The noise-limited sensitivity that determines a radar’s capability to collect measurements in support of tracking and discrimination is determined by the product of

average transmit power and the square of the antenna aperture area for a given frequency, system loss, and system noise temperature as delineated in the track version of the radar-range equation. Through a simple application of optimization theory, it can be shown that this relationship dictates that the aperture should cost twice as much as the transmitter to maximize performance for a given total cost. Conventional AESA architectures are generally biased toward power relative to the optimal design point.

AESA architectures that implement lower power density than currently practiced promise reduced acquisition costs but impose larger antenna apertures. While a single TRM could be employed to drive multiple elements to achieve low power density, this would degrade the low-loss transmission and reception path afforded by AESA technology. Both American and Russian developers have investigated usage of LFOV electronically scanned arrays to reduce RF aperture cost. Hybrid systems that incorporate both electronic scanning and mechanical scanning provide expanded field of regard at the cost of increased mechanical complexity and restricted transportability associated with the requisite antenna mounts required to accommodate the mass and size of BMD-class RF apertures. The American SBX/XBR design utilizes high-gain horns as radiating elements so that the number of modules is reduced by more than an order of magnitude for a given aperture area. As addressed in Chapter 6, an ESA is restricted to scanning its beam within its element pattern, which decreases with increasing element gain and thus limits the field of view.

BMD radars may have to survive electromagnetic pulse (EMP) effects originating from high-altitude nuclear bursts and operate in an environment when such a burst has occurred. A high-altitude electromagnetic pulse (HEMP) can induce a sufficient level of EM energy to disrupt or destroy electrical systems and electronic components over a large surface of potentially thousands of miles extent [36]. HEMP bursts would occur above 30 km so that there is no appreciable blast or thermal effects at Earth's surface, eliminating the need for hardening modern BMD radars to these effects. The gamma radiation from such a burst induces a large-scale disposition of electrons across a broad extent of hundreds to thousands of km of the upper atmosphere, inducing EMP generation. While only a small portion of a nuclear burst is converted into EMP, this can result in very-high-peak electric field intensity on Earth's surface. A high-altitude burst of high yield could impose peak intensity of 100,000 v/m [37]. The EMP possesses multiple phases occurring over a time scale of microseconds to a second. Most of the energy would be concentrated at low frequencies relative to those used for LOS radar operation. While HEMP is a national concern due to the potential vulnerability of unprotected communication and power grids as well as specific devices, hardening and mitigation techniques applicable to radar systems and supporting subsystems are well established though potentially expensive.

7.4.3.2 Signal and Data Processing

As described previously, the exoatmospheric BMD environment does not impose the drag effects that eliminate volumetric clutter upon reentry. Identification of threatening objects from decoys and debris is problematic under these conditions motivating interest in high-resolution measurement techniques. Wideband linear frequency modulation on pulse is an attractive waveform for high-resolution BMD applications. The Doppler tolerance of LFM is attractive given the long pulses that may be required for adequate sensitivity and the large mean and spread of target range-rates. LFM supports active correlation or stretch processing whereby the pulse compression is effectively divided

between an initial down-conversion with an LFM reference signal matched to the transmitted waveform within the receiver followed by a Fourier transform in the signal processor to provide range-gated outputs across a broad range swath. In addition to decreasing analog-to-digital conversion bandwidth demands by several orders of magnitude, this technique also significantly decreases signal-processing throughput and memory requirements.

BMD radars employ an ensemble of waveforms of different bandwidth and durations that are scheduled by a real-time resource management process according to operational needs and radar capabilities. Like the radar community at large, BMD radar developers typically rely on commercial-off-the-shelf signal and data processing subsystems. BMD tends to be a high-throughput application space compared to the larger radar community. The usage of high-resolution waveforms over large range windows motivates significant signal-processing throughput and memory sizing. The potential presence of volumetric clutter also motivates sizing the computational capacity of the radar data processor to accommodate large numbers of simultaneous tracks. The long operational lives and evolving missions of BMD radars should strongly motivate investment in modular open system architecture practices for software to enhance software maintenance, mission growth, and software/hardware platform rehosting.

7.5 | BMD RADAR PERFORMANCE ESTIMATION

BMD radars are often designed and evaluated in terms of their noise-limited performance. This practice is in contrast to air-defense applications where performance is often determined by the radar capability to detect small targets in the presence of strong ground clutter. The emphasis on optimizing the radar design for noise-limited performance is a consequence of the BMD battle space typically being well beyond the maximum clutter range due to surface or atmospheric volumetric returns. This condition may not be met for short-range BMD applications in geographical areas where high-relief surface features or anomalous propagations are present. Electronic protection techniques such as sidelobe cancellation or sidelobe blanking may be required to mitigate intentional and unintentional electromagnetic interference.

The noise-limited search and track performance of BMD radars can be roughly estimated using the radar-range equation metrics presented in Chapter 6 but high-fidelity dwell-by-dwell simulation is required to fully assess performance. It is imperative that simulation tools adequately represent operational and environmental loss sources that impact radar performance. The extended range windows required for BMD search in conjunction with the long operational ranges present challenging timeline occupancy demands. Under some BMD scenarios, the radar may exhaust timeline for scheduling transmit and receive dwells before they reach their maximum long-term duty cycle. Hence, simulation tools must “keep book” of both duty cycle and timeline occupancy when estimating BMD radar resource usage.

Figure 7-9 depicts the nominal cross-range resolution of selected BMD radars taking into account their estimated angular resolution (beamwidth) as well as typical operational ranges. In contrast to anticipated range resolutions of <100 m for tracking and <1 m for identification function, the cross-range resolution defined by the product of angular resolution and range is on the order of kilometers. Accordingly, one would anticipate the bulk of an exoatmospheric threat complex to be confined to within a single beam.

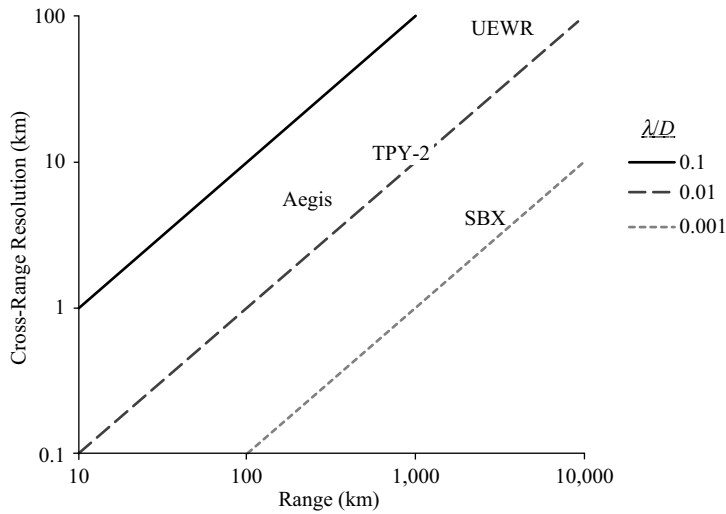


FIGURE 7-9 ■ Cross-Range Resolution of BMD Radars.

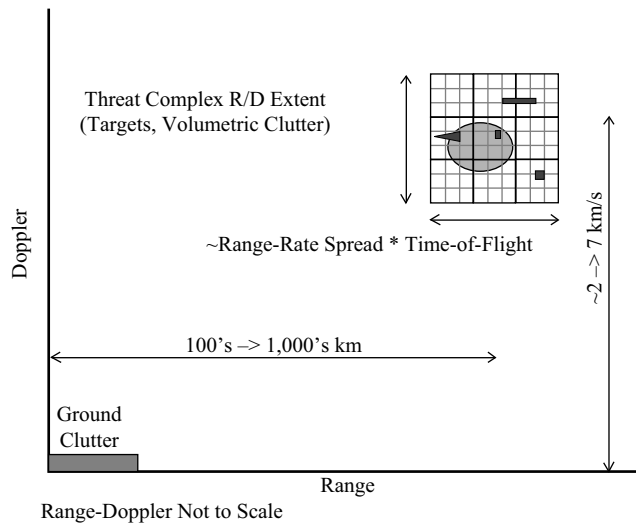


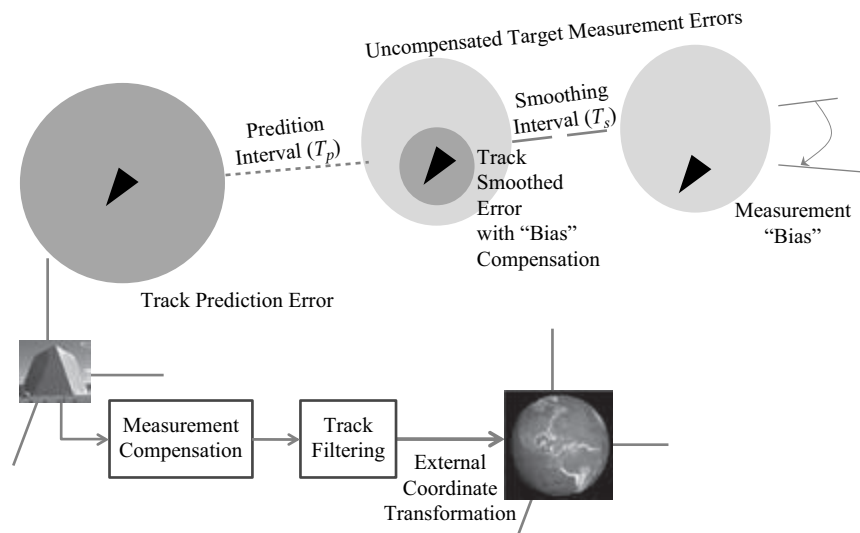
FIGURE 7-10 ■ BMD Radar View of a Threat Complex.

The exoatmospheric threat complex can be characterized as an ensemble of ballistic targets possibly accompanied by volumetric clutter. BMD radars are expected to resolve the threat complex in range and Doppler as depicted in Figure 7-10. The coarse grid over the threat complex corresponds to the notional resolution of surveillance radar, while the fine grid corresponds to that of an engagement sensor that must perform precision tracking and discrimination. The dark shapes correspond to discrete objects, while the shading denotes volumetric clutter that may be masking the discrete objects.

7.5.2 Track Prediction Performance

Prediction accuracy is a critical performance metric for BMD sensors. Predicted impact-point estimation is obviously critical to characterizing an attack as well as distinguishing between ballistic missiles and space-vehicle launchers. Prediction accuracy is critical to

FIGURE 7-11 ■
BMD Tracking
Process.



handover and system-level track correlation among the surveillance and engagement sensors that observe different portions of the threat trajectory. Designation of the target from these sensors to the interceptor to support fly-out trajectory planning as well as seeker acquisition by the kill vehicle at endgame requires prediction based on precision track data. Target tracking must also support a prediction interval adequate to compensate for latencies in the BMD-level command, control, and communications process. High-fidelity simulations anchored on test data are required for definitive performance assessment, but the expressions in this section provide some useful rules of thumb as well as analytical insight.

This BMD tracking process is depicted in Figure 7-11. Returns are collected over the smoothing interval for subsequent measurement compensation and track filtering. At the end of the smoothing interval over which the target is tracked, its position is estimated from track filtering the sequence of measurements, resulting in sufficient reduction of the random error relative to that associated with a single measurement. The predicted target position is extrapolated over a specified prediction interval so that the resultant error is typically dominated by the velocity error at the end of the smoothing interval as delineated shortly.

Measurement compensation is the correction process to remove bias-like errors, including both instrumentation errors due to the design of the radar as well as tropospheric refraction errors imposed by atmospheric propagation. True bias error would be spatially and temporally invariant such that it should be eliminated from a well-calibrated radar system. More properly speaking, these are systematic residual errors that remain after nominal alignment and calibration but tend to be spatially or temporally correlated. Such errors tend to vary “slowly” relative to the track update rate and so manifest as bias-like error components that cannot be effectively smoothed by the track filtering process. These systematic residual errors can contribute to coordinate system misregistration and degrade system track performance.

Modern error computation techniques supported by extensive reference target tracking and other calibration measures can reduce systematic residual error due to hardware sources to the same order as the nominal random error component. While the

Global Positioning System provides excellent positioning and timing data, it cannot directly characterize orientation error that manifests as angle error in the subject radar system. The sensitivity of BMD radars enables usage of satellites with precision ephemeris data as reference targets to characterize radar measurement error to support subsequent compensation. Frequent collection of calibration data also supports health and status reporting needs for BMD radar systems. Lookup table techniques that plot refraction bias versus elevation angle that are supplemented to account for diurnal and seasonal variations can eliminate roughly 90 percent of the mean tropospheric error. Computationally intensive model-based techniques anchored on local meteorological conditions can further suppress residual tropospheric error.

The compensated measurements are processed by a track filter to suppress random measurement error due primarily to additive thermal noise. In addition, the filter is typically designed to estimate velocity to support track prediction. Track filter design must generally bound the degree of smoothing to accommodate unanticipated target maneuvers. However, exoatmospheric track filters designed for the ballistic missile coast phase benefit from the associated deterministic trajectory to achieve order-of-magnitude improvement in smoothing performance over that feasible with a conventional track filter that must accommodate maneuvering targets.

Evaluating tracking performance requires high-fidelity simulation tools anchored on test data to characterize the random and systematic residual accuracy of a given sensor. However, the following procedure can be used to coarsely assess track performance. As a point of departure, we will look at noise-limited performance (random error smoothing) as that is the fundamental bound remaining if alignment and calibration procedures are sufficient to suppress systematic residual and coordinate registration errors.

Angle error effects dominate those of range error in measurement positions. Modern radars can readily measure range to a precision of meters or tens of meters. The effective cross-range measurement accuracy can be represented as the product of the azimuth and elevation angle errors in radians multiplied by the target range in meters. Neglecting such effects as radar line-of-sight rotation over the track interval [38] and detailed design parameters such as monopulse slope and antenna taper weighting [39], we can coarsely represent the standard deviation, σ_c , of the dominant one-dimensional cross-range error as

$$\sigma_c \approx \frac{\lambda R}{D \sqrt{2} \cdot \frac{S}{N}} \quad (7-1)$$

where

λ = wavelength,

R = range to the target,

D = antenna diameter, and

$\frac{S}{N}$ = signal-to-noise ratio of the measurement referenced to the output of the signal processor.

Assuming that the angle measurement error is on the order of a tenth of a beamwidth and approximating beamwidths and operational ranges from Figure 7-9 suggests effective cross-range measure errors will be orders of magnitude larger than the range measurement error. Hence, the effective cross-range accuracy should dominate the composite track accuracy.

Assuming N measurements are taken at fixed intervals of T over the smoothing period T_s such that $N > 1$, the standard deviation of the smoothed cross-range at the end of the tracking interval can be approximated as

$$\sigma_{cs} \approx \frac{2\sigma_c}{\sqrt{N}} \quad (7-2)$$

The corresponding standard deviation, σ_{cp} , of the predicted cross-range for prediction interval T_p where $T_p \gg T_s$ can be estimated as

$$\sigma_{cp} \approx \frac{\sqrt{12}\sigma_c T_p}{\sqrt{N} T_s} \quad (7-3)$$

Note that prediction error can be decreased by extending the smoothing interval even while keeping the number of measurements constant by increasing the measurement interval. While these expressions are based on theoretical bounds, they should be representative of the tracking performance of an optimal track filter matched to a target with a deterministic trajectory such as an exoatmospheric ballistic missile [40].

The composite two-dimensional cross-range error standard deviation can be estimated as the root-sum-square of cross-range standard deviation computed for azimuth and elevation. If the beamwidth is roughly symmetric, then the two-dimensional effective cross-range error can be estimated simply as the product of $\sqrt{2}$ and the one-dimensional values given previously. This value can be appropriately inflated to account for systematic residual errors [41].

As an example of the utility of this calculation, the lateral delta velocity, ΔV , required by the KV to compensate for the radar prediction error, can be roughly estimated as [42]

$$\Delta V = \frac{\sigma_{cp} N'}{(N' - 1) T_f} \quad (7-4)$$

where

N' = Effective Navigation Ratio of the KC guidance system and

T_f = time-of-flight of the homing interval.

This expression enables the radar prediction error to be traded against the homing interval and hence the effective range of the KV seeker. Assuming a lower bound of $N' = 3$ to ensure that endgame errors are closed out by the KV guidance process and a homing time of 10 s indicates that the composite radar prediction error must be kept to within ~330 m to keep the required ΔV requirement less than 50 m/s.

7.5.3 BMD CSO Performance

As previously addressed, BMD radars are typically evaluated in terms of their noise-limited performance. This practice is in contrast to air-defense applications where performance is often determined by the radar capability to detect small targets in the presence of strong ground clutter. As described previously, the absence of drag in the exoatmospheric midcourse regime enables “fly along” volumetric clutter that may include debris as well as intentional masking countermeasures such as chaff. At long ranges, this ensemble of CSOs associated with a given ballistic missile launch will be contained within a single beamwidth of a BMD radar. The RV may be embedded in an

extended volumetric clutter field composed of these multiple sources. In addition to distributed clutter, multiple discrete targets, such as decoys, may be closely spaced with respect to each other and the RV, further challenging the track and discrimination processes. High-resolution range and tracking waveforms may be required to support tracking and discrimination as well as resilient algorithms. This section formulates performance measures to characterize CSO and volumetric clutter performance impacts.

In air-defense applications, measures of surface clutter rejection indicate the radar's capability to detect small, low-flying aircraft and cruise missiles. The clutter improvement factor (CIF), the ratio of signal-to-clutter ratio (SCR) at the signal processor output referenced to the SCR at the signal processor input for a given target range rate is commonly used to characterize this performance. CIF performance can be accurately modeled and substantiated with hardware measurements so it can be used to anchor anticipated radar-system performance. An implicit condition of CIF and similar performance measures is that target returns can be resolved in Doppler from the near-stationary surface clutter. CIF does not seem a general metric for evaluating BMD radar performance under volumetric clutter conditions since the clutter is not necessarily Doppler resolved from targets of interest.

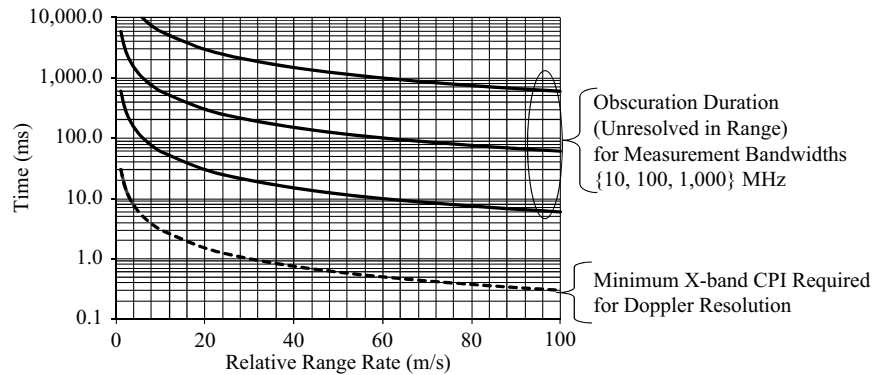
The total integrated RCS of such volumetric clutter is likely orders of magnitude less than near-in surface clutter so CIF requirements do not drive RF dynamic range in BMD as they do in air defense. CIF estimation could be used to characterize the signal-processing benefits of "thinning out" clutter thru extended coherent integration under a given scenario. In BMD applications, the measurements must be compensated for the estimated target velocity to maintain the target in a given range gate to enable pulse integration. Objects with dissimilar range-rates will "fly through" multiple range gates over the integration interval so that their returns are correspondingly "smeared." This condition occurs whenever the product of the object's range-rate offset from the target under track and the pulse integration interval exceeds the range-gate extent, which should be on the order of the radar-range resolution.

The challenge of volumetric clutter is its proximity in range and Doppler to targets of interest, which challenges resolution and measurement-to-track data association. In contrast to surface clutter, the range and Doppler distribution of BMD volumetric clutter cannot be delineated a priori since the birthing and distribution are determined by the design and operation of the ballistic missile threat. Moreover, volumetric clutter may vary dynamically over the engagement interval due to discrete events such as booster breakup or chaff release. The range or range-rate spread in the dispersion of the threat complex may include "crossing targets" where the radar must maintain track on individual CSOs that overtake each other in range, resulting in merged measurements and misassignment of measurements to tracks.

Resolution under crossing target conditions is parameterized in Figure 7-12. These curves compare performance achievable with range and Doppler processing in the case of a given target overtaking another as a function of differential range rate. The depicted time interval is defined as

1. the period over which the two objects are obscured (unresolved) in range for a radar employing a given waveform bandwidth, or
2. the required coherent-processing interval required to achieve continual Doppler resolution of the objects.

FIGURE 7-12 ■
Obscuration Interval
and Coherent
Processing Interval
for Crossing
Targets.



In both cases, the resolution was calculated as twice the Rayleigh limit to account for broadening factors such as tapering to suppress range sidelobe or Doppler sidebands, RF band limiting, and signal-processing artifacts. Hence, the following pragmatic relationships will be used:

$$\text{Pragmatic range resolution} = 2C/(2W) = C/W$$

$$\text{Pragmatic Doppler resolution} = 2/T_{ci}$$

where

W = waveform bandwidth and

T_{ci} = coherent pulse integration interval.

As depicted, coherent processing across a pulse train to achieve Doppler resolution of a pair of targets with a given range-rate differential reduces the obscuration interval relative to what can be achieved with single-pulse range-only processing. This result is somewhat intuitive as Doppler resolution derives from the time required for the differential range to change on the order of a wavelength while the range-only processing for a given obscuration interval is predicated on a relative motion of tens or hundreds of wavelengths. Moreover, the coherent processing maintains continual Doppler resolution of the crossing targets; tracking on range-only measurement processing mandates extrapolating or “coasting” the tracks through the obscuration interval until the composite targets can be resolved again.

Tracking performance in volumetric clutter is highly dependent on the clutter distribution and density as well as the radar waveforms, signal processing, and data-association implementation. Data association is the process of assigning M measurements from a given dwell to update N tracks, where M and N may differ due to missed detections, false alarms, clutter detection, and track-management artifacts. The track-management process may inadvertently create redundant or merged tracks as well introduce spurious track artifacts through track initiation and deletion operations [43]. A number of algorithmic approaches to data association have been suggested across a wide span of effectiveness and computational demands.

At a fundamental level, tracking requires well-resolved measurements that are correctly associated. The composite probability of both resolving and correctly associating measurements is termed *purity*. Anticipated purity can be estimated from target

density, measurement characteristics, and tracking accuracy. While actual performance verification must be anchored using high-fidelity simulation tools, a number of analytical expressions are useful for coarse performance estimation [44]. Conventional tracking algorithms need a composite purity of ~ 0.9 to maintain firm tracks. Estimating purity in a BMD context can be useful for coarse performance assessments.

Exoatmospheric track filter design can exploit the deterministic knowledge of a ballistic trajectory to achieve a much higher degree of smoothing than is achievable in air-defense applications where target maneuvers must be accommodated. The position of a ballistic target can be predicted to the next update measurement opportunity to well within a range gate. The probability of correct measurement association is correspondingly enhanced since the track-update acceptance gates for measurements decrease as the track prediction error decreases, which reduces the probability of misassociation in dense target environments.

Data-association performance is further improved when tracking adjacent objects as well as specific targets of interest. Blackman has shown that a given level of data-association performance can be maintained at $\sqrt{2}$ to 4 times the tracked target density relative to a target embedded in an equivalent false alarm density, depending on the measurement dimensionality [45]. However, this requirement can result in significant computational loading on the data processor. Multiple object.

As an illustrative analysis metric, we shall exploit the simplified scenario depicted in Figure 7-13 of a notional upper-stage fragmentation that produces N_o objects randomly distributed across a spherical surface expanding at a constant rate and producing multiple crossing targets with a warhead under track.

Assuming that the fragments are all contained within the radar beam, the mean number of objects in a given range-gate extent equivalent to the range resolution, n_r , is given simply by

$$n_r = \frac{N_o \cdot \delta_r}{2r} \quad (7-5)$$

where

δ_r = range resolution and

r = radius of the fragment sphere, which can simply be parameterized as the product of the expansion velocity and time after fragmentation.

The probability of resolution is defined here as the probability of a given range gate containing 0 objects such that a target under track at that range would be

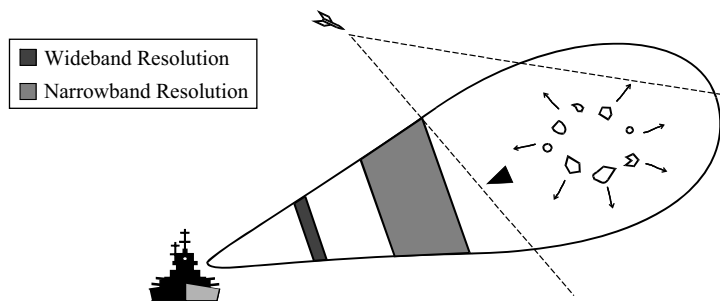


FIGURE 7-13 ■ Spherical Fragmentation Example for Evaluating Purity.

unimpaired. The number of objects in a given range gate is represented by a Poisson probability density function so that the probability of resolution, P_{res} , can be calculated as [46]

$$P_{res} = P\{x = 0\} = e^{-n_r} \frac{n_r^x}{x!} = e^{-n_r} \quad (7-6)$$

Under the same scenario, the probability of correctly data association, P_{ca} , can be derived as

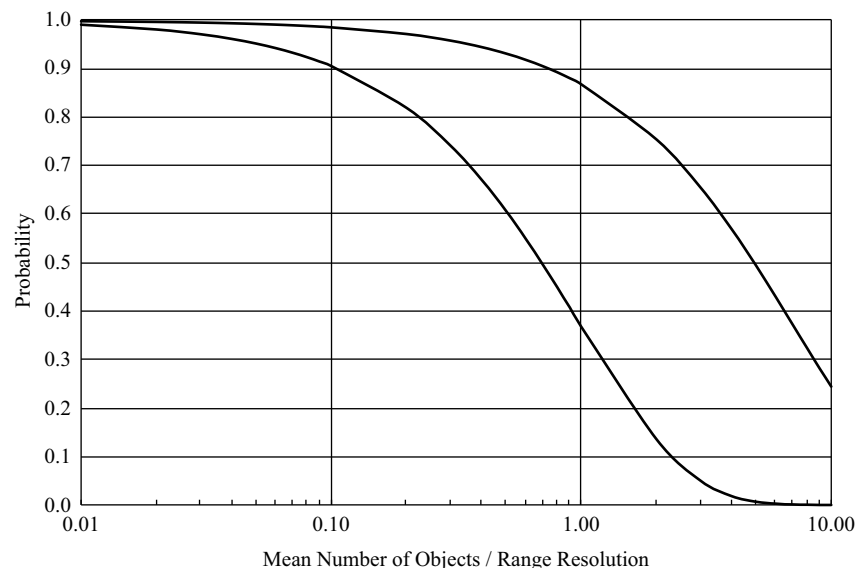
$$P_{ca} = e^{-\frac{n_r}{\sqrt{\pi}\epsilon}} \quad (7-7)$$

where

ϵ = ratio of the range-gate extent to the standard deviation of the estimated range predicted at the time the measurement was taken.

This expression corresponds to the mean number of objects within a one-sigma prediction-update volume for the one-dimensional case applicable to this example. As depicted in Figure 7-14, the purity of a mature track is dominated by resolution performance rather than data association for established tracks, even assuming conservative track filter smoothing with $\epsilon = 4$. The composite purity appears inadequate to maintain track when the mean number of objects in the range gate exceeds ~ 0.1 , corresponding to the objects spaced in range at ten times the range resolution. Canonical analysis shows that probability of resolution should be consistently lower than the probability of correct association under BMD tracking conditions [47]. Resolution is also a prerequisite to initiating tracks in a stressing CSO environment. Both resolution and data-association performance can be improved by decreasing δ_r , corresponding to increasing tracking waveform bandwidth.

FIGURE 7-14 ■ Probability of Resolution and Probability of Correct Association for Spherical Fragmentation Example.



7.6 | REFERENCES

- [1] J. Constant, *Introduction to Defense Radar Systems Engineering*, Spartan Books, New York - Washington 1972.
- [2] D. Ausherman, A. Kozma, J. Walker, H. Jones, and E. Poggio, "Developments in Radar Imaging," *IEEE Transactions AES*, 20, no 4, July 1984.
- [3] J. Spencer, *The Ballistic Missile Threat Handbook*, Heritage Foundation, Washington, 2000.
- [4] R. Braham, "Ballistic Missile Defense: It's Back," *Spectrum*, Vol 31, No 9, September 1997.
- [5] Spencer, *ibid*.
- [6] P. Mantle, *The Missile Defense Equation: Factors for Decision Making*, AIAA, Reston VA, 2004.
- [7] P. Zarchan, "Ballistic Missile Defense Guidance and Control Issues," *Space & Global Security*, 1998, 8, pp. 99–124.
- [8] B. Graham, *Hit to Kill: The New Battle over Shielding America from Missile Attack*. Public Affairs, New York, 2001.
- [9] Y. Velikhov et al., *Weaponry in Space: The Dilemma of Security*. MIR Publishers, Moscow, 1986.
- [10] T. Lin, "Development of U.S. Air Force Intercontinental Ballistic Missile Weapon Systems," *Journal of Spacecraft and Rockets*, 40, no. 4, July–August 2003.
- [11] G. Lewis and T. Postol, "Future Challenges to Ballistic Missile Defense," *Spectrum*, Vol 34, No 9, September 1997.
- [12] Sessler et al., "Countermeasures: A Technical Evaluation of the Operational Effectiveness of the Planned U.S. National Missile Defense System," Union of Concerned Scientists, M.I.T., April 2000.
- [13] M. Sarcione et al., "The Design, Development and Testing of the THAAD (Theater High Altitude Area Defense) Solid State Phased Array," IEEE Symposium on Phased Array Systems and Technology, Boston, 1996.
- [14] J. Tomay, "Warning and Assessment Sensors," *Managing Nuclear Operations*, A. Carter et al., editors, Brookings Institution, 1987.
- [15] "Visit to Fylingdale Moor BMEWS," <http://www.subbrit.org.uk/rsg/sites/f/fylingdales/>.
- [16] E. Filer and J. Hartt, "Cobra Dane Wideband Pulse Compression System," EASCON, 1976.
- [17] M. Sarcione, *ibid*.
- [18] S. Boyev, "Shrewd Eyes and Mind of the Missile and Space Defense High-Potential Radars: Past, Present and Future," *Military Parade*, September 2001.
- [19] P. Podvig, editor, *Russian Strategic Nuclear Forces*, M.I.T. Press, Cambridge, MA, 2001.
- [20] P. Podvig, "History and the Current Status of the Russian Early-Warning System," *Science and Global Security*, 10, pp. 21–60, 2002.
- [21] *Soviet Military Power 1988*, U.S. Government Printing Office.
- [22] Podvig, *ibid*.
- [23] Podvig, *ibid*.
- [24] Podvig, *ibid*.
- [25] P. Podvig, editor, *Russian Strategic Nuclear Forces*, M.I.T. Press, Cambridge, MA, 2001.
- [26] http://www.globalsecurity.org/wmd/world/russia/pill_box.htm.

- [27] Boyev, *ibid.*
- [28] Podvig, *ibid.*
- [29] B. Naveh and A. Lorber, editors, *Theater Ballistic Missile Defense*, AIAA, 2001.
- [30] S. Glasstone and P. Dolan, *The Effects of Nuclear Weapons*, U.S. Government Printing Office, 1977.
- [31] Constant, *ibid.*
- [32] *Radiation Intensity of the PAVE PAWS Radar System*, National Academy of Science, 1979.
- [33] B.-Z. Naveh and A. Lorber, editors, *Theater Ballistic Missile Defense*, AIAA, Reston, VA, 2001.
- [34] Y. Bar-Shalom and X.-R. Li, *Multitarget-Multisensor Tracking: Principles and Techniques*, YBS, 1995.
- [35] A.H. Register, W.D. Blair, and G. Brown, “Improved Radar Revisit Time Control to Observe Ballistic Missile Mode Transitions,” *Proceedings of the Thirty-Fourth Southeastern Symposium on System Theory*, 2002.
- [36] C. Wilson, *High Altitude Electromagnetic Pulse (HEMP) and High Power Microwave (HPM) Devices: Threat Assessments*, Congressional Research Service August 20, 2004.
- [37] R. Ghose, *EMP Environment and System Hardness Design*, Interference Control Technologies, Gainesville, VA, 1984.
- [38] F. Daum and R. Fitzgerald, “Decoupled Kalman Filters for Phased Array Radar Tracking,” *IEEE Transactions on Automatic Control*, 28, no. 3, March 1983.
- [39] D. Barton and H. Ward, *Handbook of Radar Measurement*, Artech, Dedham MA, 1984.
- [40] J. Minkoff, *Signals, Noise, and Active Sensors: Radar, Sonar, Laser Radar*, Wiley, 1992.
- [41] D. Hsu, *Spatial Error Analysis: A Unified Application-Oriented Treatment*, IEEE Press, New York, 1998.
- [42] P. Zarchan, *Tactical and Strategic Missile Guidance*, Third Edition, AIAA, Reston, VA, 1997, p. 292.
- [43] K. Manson and P. O’Kane, “Taxonomic Performance Evaluation for Multitarget Tracking Systems,” *IEEE Transactions*, 28, no. 3, July 1992.
- [44] F. Daum, “A System Approach to Multiple Target Tracking,” Y. Bar-Shalom, editor, *Multitarget-Multisensor Tracking: Applications and Advances*, Volume II, Artech, Dedham MA, 1992.
- [45] S. Blackman and R. Popoli, *Design and Analysis of Modern Tracking Systems*, Artech, Dedham MA, 1999, p. 885.
- [46] M. Belcher, “Tracking Unresolved Targets in Theater Ballistic Missile Defense,” *Proceedings of the 29th Southeastern Symposium on System Theory*, March 1997.
- [47] Blackman and Popoli, *ibid.*

7.7 | FURTHER READING

- S. Weiner and S. Rocklin, “Discrimination Performance Requirements for Ballistic Missile Defense,” *Lincoln Laboratory Journal*, 7, no. 1, 1994.
- T. Jeffrey, *Phased-Array Radar Design: Application of Radar Fundamentals*, SciTech Publishing, Raleigh, NC, 2009.

Ground-Based Early Warning Radar (GBEWR): Technology and Signal Processing Algorithms

*A. De Maio, Università degli Studi di Napoli “Federico II”, Italy,
A. Farina and L. Timmoneri, Selex ES - A Finmeccanica Company, Italy
and M. Wicks, University of Dayton (OH), US*

Chapter Outline

8.1 Introduction	323
8.2 Phased Array Antenna	335
8.3 Transceiver	342
8.4 Waveforms and Signal Processing	348
8.5 Tracking	352
8.6 Electronic Counter-Countermeasures (ECCM) Capabilities	357
8.7 Special Functions	359
8.8 Conclusions and Further Reading	376
8.9 References	377

8.1 | INTRODUCTION

Radar systems can be classified into two main families according to their application: defense and civilian. Defense radars include air-defense and battlefield radars, whereas civilian radars include weather radars, radars for remote sensing, and others. Air traffic control (ATC) radars can be either defense or civilian.

Air defense radars are also subdivided into two more categories: two-dimensional (2-D) and three-dimensional (3-D). The former can measure the target range and azimuth. The latter can determine the target’s height as well.

Since air-defense radars can detect targets at great distances (hundreds of kilometers), they can be used as early warning radars (EWRs). A classification of EWRs can be provided based on the platform where the radar is installed. Then, it is possible to distinguish between airborne and ground-based (GB) EWRs. In this chapter, GBEWRs will be discussed.

A GBEWR is used primarily for the long-range detection of targets, i.e., allowing defenses to be alerted as early as possible before the intruder reaches its objective, giving

the defenses the maximum time in which to operate [1]. The most challenging targets for a GBEWR are ballistic targets (BTs) because of their small radar cross section (RCS) and the great ranges (hundreds and sometimes even thousands of kilometers) where they are required to be detected. The GBEWRs have a low-measurement resolution, work with low-pulse repetition frequency, and use low-carrier frequencies. The choice of low frequency is supported by the low propagation loss and by the high power that can be transmitted. On the other hand, the resolution and accuracy are limited because a lower frequency requires very large physical antennas. In particular, they work at L- and S-bands (1–2 GHz/2–4 GHz) [2]. The best advantage for choosing these bands over very high frequency (VHF) is related to the smaller size of antenna that allows a better compromise between performance and deployability. In addition, the GBEWR can guarantee timely and reliable detection of a high number of targets, which are generally embedded in heavy natural (clutter) and man-made (electronic countermeasures (ECM)) interferences. The target RCS can range from very low to relatively high figures. Discriminating false detections from true targets and high accuracy in position finding, even in a multitarget environment (e.g., mass raid), are additional requirements. Finally, target classification, threat assessment, and efficient dissemination of processed data to computer and display systems are facilities that shall be implemented.

This chapter is organized as follows. Section 8.1 introduces the GBEWR and its main characteristics. Section 8.2 introduces the phased array antenna and illustrates its main characteristics, with a special focus on some beam-scanning techniques. Classic and modern architectures of the transceiver and its main parameters are presented in Section 8.3. Section 8.4 provides an overview of several signal-processing algorithms used in GBEWRs. Section 8.6 describes the issue of tracking, with emphasis on the evolution of both filtering and correlation logics. Section 8.7 provides a description of the ECCM capabilities and, in particular, of the sidelobe blanking technique. In Section 8.8, several GBEWRs' special functions are reported. Specifically, this section deals with the problem of radar detection and tracking of a BT, of the low probability of intercept, and of the denial of bistatic hosting by waveform design. Finally, conclusions are drawn in Section 8.9.

The following is a list of abbreviations and acronyms used in this chapter.

8.1.1 Acronyms/Abbreviations

2-D	two-dimensional
3-D	three-dimensional
ABT	air-breathing target
ACCS	Air Command and Control System
ACE	Allied Command Europe
ADC	analog-to-digital converters
AEGIS	Airborne Early Warning Ground Environment Integration Segment
AFS	automatic frequency selection
AGARD MSP	Advisory Group for Aerospace Research & Development Mission System Panel
ALTBMD	active layered theater ballistic missile defense
AMS	Alenia Marconi Systems
AMTI	adaptive moving target indicator

ARM	anti-radiation missile
ATC	air traffic control
BFN	beam-forming network
BITE	built-in test equipment
BM	ballistic missile
BMD	ballistic missile defense
BMEWS	ballistic missile early warning system
BST	beam-scanning technique
BT	ballistic target
CA-CFAR	cell averaging constant false alarm rate
CAD	computer-aided design
CFAR	constant false-alarm rate
COHO	coherent oscillator
CUT	cell under test
CW	continuous waveform
C3	Command and Control Center
DAC	digital-to-analog converter
dB	decibel
DDC	digital down conversion
DOA	direction of arrival
DUC	digital up conversion
ECM	electronic countermeasures
ECCM	electronic counter-countermeasures
EKF	extended Kalman filter
ESM	electronic support measures
EuRAD	European Radar Conference
EW	early warning
EWR	early warning radar
FA	false alarm
FFT	fast Fourier transform
FPGA	field programmable gate array
GaAs	gallium arsenide
GBEWR	ground-based early warning radar
GIS	geographic information system
GO-CFAR	greatest of constant false-alarm rate
HF	high frequency
HMI	human machine interface
HPRF	high pulse repetition frequency
Hz	Hertz
ICBM	intercontinental ballistic missile
IEE	Institution of Electrical Engineers

IEEE	Institute of Electrical and Electronics Engineers
IET	Institution of Engineering and Technology
IF	intermediate frequency
IFF	identification friend or foe
IFFT	inverse fast Fourier transform
ILDC	incremental length diffraction coefficients
IMM	interactive multiple model
ISL	integrated sidelobe level
ITRS	International Technology Roadmap for Semiconductors
JPDA	joint probabilistic data association
KB	knowledge-based
KF	Kalman filter
LFM	linear frequency modulation
LNA	low-noise amplifier
LO	local oscillator
LP	linear programming
LPI	low probability of intercept
LPRF	low-pulse repetition frequency
MESFET	metal semiconductor field effect transistor
MHT	multiple hypothesis tracking
MHz	MegaHertz
MIS	multiple independently scanned
MM	multiple model
MMIC	monolithic microwave integrated circuit
MMSE	minimum mean square error
MTI/MTD	moving target indicator/moving target detector
MW	moving window
NADGE	NATO Air Defense Ground Environment
NAEW	NATO Early Warning
NAI	not automatic initialization
NF	noise figure
NLFM	nonlinear frequency modulation
NN	nearest neighbor
ONS	original NADGE sites
OS-CFAR	ordered statistic constant false alarm rate
OTHB	over-the-horizon backscatter
OTHR	over-the-horizon radar
PAAM	phase and amplitude adjustment modules
PDA	probabilistic data association
PIN-diode	P-type/intrinsic/N-type (doped semiconductor diode)
PO	physical optics
PRF	pulse repetition frequency

PRT	pulse repetition time
PSL	peak sidelobe level
PTD	physical theory of diffraction
RAN	radar for naval surveillance
RAT	radar for terrestrial surveillance
RCS	radar cross section
RES	radar environment simulator
RF	radio frequency
RX	receiver
SoC	system on a chip
SFDR	spurious free dynamic range
SLB	sidelobe blanking
SLBM	sea-launched ballistic missile
SNR	signal-to-noise power ratio
SO-CFAR	smallest of constant false alarm rate
SOCP	second order cone programming
SR	shift register
SSC	scan to scan correlation
SSR	secondary surveillance radar
STALO	stable local oscillator
STC	sensitivity time control
TBM	tactical ballistic missile
ToT	time on target
TR	transmit/receive
TRM	transmit/receive module
TX	transmitter
UHF/VHF	ultrahigh frequency/very high frequency
VS IMM	variable structure interactive multiple model
WWII	Second World War

8.1.2 Historical Perspective

The first GBEWR was the British Chain Home, used during the Second World War (WWII) for the detection of the enemy's aircraft [2, 3]. It was composed of radars on top of towers to provide long-range detection. This system was designed by Sir Robert Watson-Watt and was established by 1939. The Chain Home worked in a range of frequencies between 20 and 55 MHz, and had a maximum detection range of 190 km. Because the British Chain Home could not detect low-flying aircraft, the United Kingdom created a second system of GBEWRs called Chain Home Low, with an operating frequency of 180–210 MHz and a maximum detection range of 160 km. As a result, the two GBEWR chains provided a good coverage of the space. In the same years, other important GBEWRs were developed: U.S. SCR-270 (Signal Corps Radio model 270), U.S. AN/CPS-6, U.S. CXAM, and German FREYA [4]. All these systems had a maximum detection range smaller than 190 km because of the propagation loss and the

limitation of the line of sight. The U.S. SCR-270 was the first long-range radar of the United States and was used for the first time in 1941 during the Pearl Harbor attack [5]. This EWR worked at an operating frequency around 100 MHz and had a maximum detection range from 120 to 190 km. There were two typologies of this radar: the mobile SCR-270 and the fixed SCR-271. Also the U.S. AN/CPS-6 was developed during WWII in 1945. Initially, the radar was designed to detect fighter aircraft for about 160 km; this radar operated at S-band frequencies from 2.7 to 3 GHz. The shipborne U.S. CXAM was used in 1941 in Australia and was positioned at the top of the ship's mast. It was able to detect single aircraft at 80 km and to detect large ships at 22 km. The German FREYA (a semi-mobile system), whose operating frequency was 120–130 MHz, had a maximum detection range of 160 km and could not determine the altitude. Japan developed its own systems, Mark-1 and Tachi-6, with detection ranges of 120 and 200 km, respectively. In 1942, the USSR installed RUS-2 radars with a maximum detection range between 95 and 145 km to aid the local defense of Moscow and Leningrad.

The use of GBEWRs grew during the Cold War. The United States and Canada in 1951 began the construction of more than 30 stations situated along their common border. Afterward, the Distant Early Warning Line (DEW Line), a series of radar stations, were installed along the Arctic Circle stretching from Alaska to Greenland. In 1985, the DEW Line was upgraded with new radars and was called the North Warning System. In the 2000s the U.S. Air Force upgraded operating software for long-range atmospheric GBEWR systems. During the 1970s, the U.S. Air Force had contracted with General Electric Aerospace to build a prototype over-the-horizon backscatter (OTHB) radar in Maine (AN/FPS-118). To counter the threat of surprise intercontinental ballistic missile (ICBM) attacks by the USSR, the United States also began the construction of the ballistic missile early warning system (BMEWS). Later, the United States replaced the BMEWS with the PAVE PAWS (developed by Raytheon Corp.), a long-range, solid-state phased array radar system [6] with the goal of assuring protection against sea-launched ballistic missile (SLBM) attacks.

Meanwhile, the USSR developed several EW and OTH radar (OTHR) systems against BM attacks and for air defense and developed systems for EW of cruise missile and bomber attacks. For BM detection, the USSR developed 11 large HEN HOUSE BMEWRs that were deployed to six locations along the Soviet borders. With the USSR's collapse in 1990, the missile warning radar system became too fiscally burdensome. In 2001, Russia announced its intention to scrap many of the fixed installations and rely on mobile stations.

In Australia, OTHRs were developed starting in 1950 [7]. The Jindalee radar network was the first Australian skywave OTHR system. In addition, several radar sets were produced to suit the particular operational and environmentally extreme conditions of the Pacific Theater during WWII. For example, 1,300 units of the British-designed ASV MkII were produced [8]. Indeed, the EW's capability of an OTH radar may be utilized to cue higher precision but more circumscribed surveillance and reconnaissance assets mounted on mobile platforms about areas where unauthorized activity has been detected. The complementary nature of such systems leads to more efficient use of defense resources for an effective response [9].

A series of NATO common-funded systems, called NADGE (NATO Air Defense Ground Environment) chain, are deployed in Europe [10].

8.1.2.1 The Evolution of NADGE

The NATO Air Defense Ground Environment (NADGE) was introduced in the late 1960s to provide a modernized, semi-automated air defense system, comprising new radars, new

ground-to-air communications, and computer-based control sites, with the ability to automatically exchange data between all the sites throughout Allied Command Europe (ACE). The software for the NADGE system was hosted on dedicated military computers.

Over the past 30 years, the various systems that comprise the overall NADGE system have been updated to account for both the changing air threat and more capable sensors and weapon systems. A major upgrade took place when the NATO Airborne Early Warning (NAEW) aircrafts were introduced. The NADGE system was enhanced with the airborne early warning ground environment integration segment (AEGIS), thereby providing interoperability with the NAEW aircraft.

An evolution of NADGE is represented by the Air Command and Control System (ACCS), which provides an in-place air command and control system scaled to accept air reinforcements and a deployable capability to enhance and augment the in-place facilities. ACCS provides services common to all sites supporting functions such as communications, information handling, data distribution, system management, interfaces, etc.

Some innovative aspects in ACCS surveillance with respect to old NADGE capabilities include:

- Multisensor tracker: All detections from all internetworked sensors are accounted for.
- One unique active/passive tracking (versus an active tracking and a concurrent passive tracking): Military and civilian radars, passive and active sensors, all feed the same tracker.
- High update rate.
- Online debiasing: Sensors and data-links are compensated for biases, so there is no need for manual intervention and calibration campaigns.
- Automatic identification data combining process: ACCS is the first system implementing this tool that will dramatically support air picture identification and track classification.

As a final remark, we mention that in 1998, NATO agreed to a program plan for an active layered theater ballistic missile defense (ALTBMD) capability to satisfy the military operational requirements. The objective is to defend NATO forces, deployed either within or beyond NATO's area of responsibility, against the threat posed by tactical BMs, with ranges up to 3,000 km. At the NATO Summit 2010 in Lisbon (http://en.wikipedia.org/wiki/2010_Lisbon_summit), heads of state and government approved the alliance's strategic concept and agreed to develop a BM defense capability with the aim of providing full coverage and protection for all NATO European populations, territories, and forces against the increasing threats posed by the proliferation of BMs.

8.1.3 Typical Characteristics

GBEWR coverage is typically obtained by scanning in elevation up to 20° or 30°, depending on the application, while mechanically rotating in azimuth. The antenna has a quite low rotational speed,¹ providing 360° azimuth coverage. Multiple independent and simultaneous pencil beams are often used in transmission and in reception. Accuracy of elevation angle measurement is guaranteed by monopulse technique. The receiver channel is linear in a wide

¹That is, 6 or 12 rounds per minute (rpm).

range, and it has a high dynamic on the order of 80 dB. (see Section 8.3). It uses digital pulse compression techniques to ensure a suitable average power with low-peak power to provide resistance against anti-radiation missile (ARMs) without a reduction in range resolution. The sensitivity time control (STC) avoids signal saturation when reflection is too high. The aforesaid features, when added to frequency agility, allow the radar to operate in an intense clutter environment and ECM. The ECCMs are assured by low sidelobe antenna, sidelobe blanking (SLB), the availability of a large number of different frequencies, frequency analysis on azimuth sector, automatic frequency selection (AFS), random selection, and jam strobe reporting.

Very low antenna sidelobes attenuate the interference outside the mainlobe. Fixed and adaptive moving target indicator/moving target detector (MTI/MTD) filters allow the operator to update suitable clutter maps, optimizing radar performances against the worst environmental conditions. The filters are generally enabled by continuously updated maps to optimize the performance for ground and sea clutter, rain, chaff, and clear conditions. The tracker manages several hundred 3-D tracks with the assistance during the plot-generation process of the false-alarm control function. EWR needs be easily integrated in all combat management systems, and it has generally to be completely remote controlled.

8.1.4 Platform

Usually, a radar classification on the base of the hosting platform is given. Thus, there are ground-based, shipborne, airborne, and spaceborne radars. In the next sections, ground-based radars are presented.

8.1.4.1 GBEWR: Some Commercial Systems

Ground-based radars do not suffer the problem of power limitation that shipborne or airborne radars do this feature enables them to cover large areas of space [11, 12]. Ground-based radars are characterized by a high antenna gain, which provides high incident power on the target, and a high effective antenna receiving area. The principal characteristics of a typical GBEWRs are presented in Section 8.1.6.

Actually, there are several commercial GBEWRs, both fixed and mobile. The following is a list of the principal commercial fixed ground-based long-range radars:

- Selex EX RAT 31 DL [13] is an advanced L-band, solid-state, phased array, 3-D surveillance radar. Figure 8-1 shows a picture of the system antenna.

Detection characteristics:

- Instrumented range: 500 km
- Elevation coverage: 20°

Beam-scanning techniques: Multiple simultaneous independently phase-controlled pencil beams. Each beam provides monopulse altitude measurements with excellent accuracy, even in the frequency agility mode.

Clutter suppression: The system presents an anti-clutter filter with adaptive notch MTI cancellers, fixed and real-time automatic clutter maps, with a moving window azimuth correlator and a digital modulus extractor for the amplitude detectors.

ECCM: Reduced peak power provides resistance against ARM and ECM. Excellent ECCMs are provided by very low sidelobe antenna, sidelobe blanking,



FIGURE 8-1² ■
 RAT 31 DL L-band,
 Solid-State, Phased
 Array, 3-D Air
 Surveillance Radar
 [Courtesy of
 Selex ES].

reduced peak power, frequency agility, jam strobe reporting, and a separate receiver for ECM monitoring.

Other characteristics: The RAT 31 DL has 42 transmitter/receiver modules and several simultaneous independent pencil beams in elevation, and a 5/6 rpm azimuth scan rate. It is also fully transportable. The receiver is a double-conversion, superheterodyne, dual-matched model, with a frequency selection that can be manual, random, or automatic.

- THALES RAYTHEON SYSTEMS GROUND MASTER 400 [14] is an S-band, fully digital, long-range, radar.
- LOCKHEED MARTIN FPS-117 [15] is an L-band, long-range, solid-state radar for both air surveillance and en route air traffic control.
- BAE SYSTEMS S743D MARTELLO [16] is an L-band, long-range, transportable/fixed-site, 3-D air defense surveillance radar.
- INDRA 3D LANZA [17] is an L-band, multiscenario, multithreat adaptive radar.
- BAE SYSTEMS COMMANDER SL [18] is an S-band, long-range, tactical air defense radar.

8.1.4.2 Mobile GBEWR: Some Commercial Systems

Here, an overview of the main commercial mobile ground-based long range radars is presented.

- Selex ES RAT 31DL/M [19] is an L-band, 3-D, fully solid-state, tactical long-range EWR and a tactical BM defense radar.

Detection characteristics:

- Elevation coverage: from -2° to 20°
- Instrumented range: 400 km
- Azimuth coverage: 360°

²This figure and those from 8-3 to 8-16 are either from references [23]–[26] and from the website <http://www.selex-es.com/>

Beam-scanning techniques: The radar architecture exploits multiple simultaneous pencil beams (MSPB). The multiple beams are electronically and independently steered in elevation, both in transmission and in reception. Monopulse technique is adopted for the elevation angle measurements.

Clutter suppression: The MSPB architecture provides a large number of transmitted pulses in each beam-pointing direction, guaranteeing high clutter suppression in adverse weather conditions in the whole instrumental coverage volume.

ECCM: The most advanced processing techniques are supported by flexible and state-of-the-art signal and data processors. These features, combined with the ultra-low antenna sidelobes, guarantee an outstanding jamming resistance. The MSPB technology allows innovative and dedicated war-fighting solutions against several threat sources such as tactical ballistic missiles (TBMs), ECMs, and mass raids.

Other characteristics: High mobility; transportability: aircraft (C-130), helicopter (CH-47), road (10 tons std); the radar is equipped with its own electrical power source and is self-sufficient for a long time. The system acts as an air defense stand-alone Command and Control Center (C3). It can be integrated in a cluster of some netted RAT 31 family systems reporting to a mobile C3, which ensures outstanding radar cooperation by means of robust radio link communications.

- THALES RAYTHEON SYSTEM MASTER-M [20] is an S-band, long-range, infrastructure 3-D surveillance radar.
- LOCKHEED MARTIN AN/TPS-77 [21] is an L-band, phased array, all-solid-state radar.
- BAE SYSTEMS AR327 COMMANDER [16] is an S-band, land-based mobile air defense radar.

8.1.4.3 Deployable GBEWR

Deployable GBEWRs are commonly referred to as tactical long-range radar, operating in the L- or S-band, specifically designed to support peacekeeping missions. They shall be deployed on the battlefield as a front-line system to protect and survey territories and assets against all air threats. To perform these tasks in a worldwide tactical environment, the deployable GBEWR shall be highly mobile and shall not require any special loading/unloading equipment, i.e., the radar is deployable with its own built-in means and tools, and including its self-installing devices not involving cranes or other tools. The whole system has to be housed in a few (say, two) 20-ft ISO containers mounted on two commercial cross-country trucks for land mobility. They are designed to provide users with the capability to move quickly for regrouping and are generally equipped with their own electrical power source and are autonomous for a long time.

These systems act as a stand-alone C3. They must be integrated in a cluster of other systems reporting to a mobile C3, which ensures outstanding radars cooperation by means of robust radio link communications.

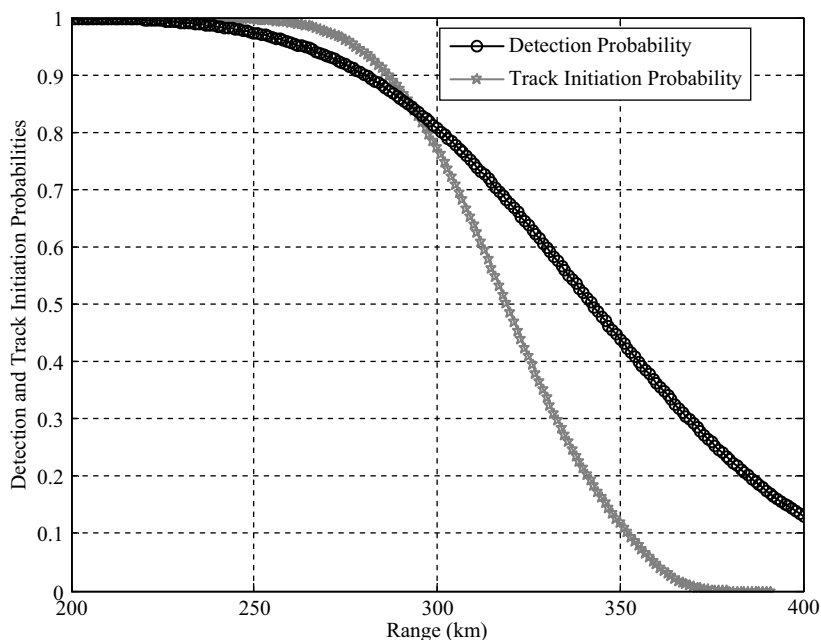
8.1.5 Requirements for GBEWR

Table 8-1 contains the main performance requirements of a fixed GBEWR.

In addition to the detection probability, the track initiation probability (P_{ii}) is of paramount importance for GBEWR. P_{ii} represents the probability that a firm track is

TABLE 8-1 ■ Requirements for fixed GBEWR

Coverage volume	Typical coverage volume is 360° in azimuth 20° in elevation 450 km instrumented range
Detection range	Assuming free space propagation, the typical required detection range of the primary radar is 300 km.
Measurement accuracies	The typical three-dimensional measurement accuracies of the primary radar are in range: ≤ 50 m in azimuth: $\leq 0.3^\circ$ in height: ≤ 400 m
Measurement resolutions	The typical three-dimensional measurement resolutions of the primary radar are in range: ≤ 300 m in azimuth: $\leq 3^\circ$ in height: $\leq 3^\circ$
Clutter cancellation	Typical requirement is 50 dB for ground clutter.

**FIGURE 8-2** ■ Detection Probability and Track Initiation Probability Versus Target Range for a Typical GBEWR.

established for a detected target at a certain distance. The P_{ii} is estimated starting from the detection probability, having fixed a certain N out of M logic, i.e., N independent detections should happen in a batch of M possibilities. The N out of M value defines the probability of false track, which is generally in the order of one per hour.

Let us consider a typical GBEWR and a 1 m^2 RCS target. Figure 8-2 reports the detection probability of the radar (blue curve) and the track initiation probability (red curve) when a 3 out of 4 logic is applied. Common requirements call for a P_{ii} of 90 percent, which is achieved at a distance of about 290 km.

TABLE 8-2 ■ Requirements for mobile GBEWR

Coverage volume	Typical coverage volume is: 360° in azimuth 30° in elevation 400 km instrumented range
Detection range	Assuming free space propagation, the typical required detection range of the primary radar is 250 km.
Measurement accuracies	The typical three-dimensional measurement accuracies of the primary radar are: in range: ≤ 50 m in azimuth: $\leq 0.4^\circ$ in height: ≤ 400 m
Measurement resolutions	The typical three-dimensional measurement resolutions of the primary radar are: in range: ≤ 300 m in azimuth: $\leq 4^\circ$ in height: $\leq 4^\circ$
Clutter cancellation	The typical requirement is 50 dB for ground clutter.

To achieve its mission and reach the performance requirements of Table 8-1, a GBEWR shall possess a number of unique characteristics, which will be discussed in the next sections.

Table 8-2 contains the main performance requirements that a mobile GBEWR should possess.

8.1.6 Distinctive Characteristics of a GBEWR

The GBEWR is typically a fully solid-state radar with transmitter modules distributed along the antenna array. The radar system is a self-contained unit of modular design to facilitate damage repair by rapid replacement of modular subsystems and subassemblies. The design of the radar shall allow both colocated and non-colocated installations with monitoring and control facilities.

The expected key features of GBEWR include:

- Fully solid-state radar with antenna-distributed transmitter modules.
- High modularity, redundancy, and reliability.
- Large “open” array antenna, permitting
 - a. very good angular resolution, both in azimuth and in elevation;
 - b. reduced emitted power with low power consumption and cooling requirements;
 - c. good resistance to wind, adverse climatic conditions, and easy access for maintenance.
- Electronic scanning in elevation.
- An accurate phase/amplitude control of the antenna distribution network.
- Multiple independent and contemporary beams for longer time-on-target without drawback on the track refreshing rate, allowing good azimuthal accuracy and optimum disturbance cancellation.

- Height measurement with excellent accuracy in all clutter environments; monopulse is often a desired feature.
- Signal processing based on a multichannel configuration with automatic or manual selection of the Doppler processing for optimum performances in changing environments.
- Staggered MTI filtering against stationary and/or moving clutter/chaff by using a cascade of fixed and adaptive notch MTI filters.
- Constant false-alarm rate (CFAR) circuit, which prevents false-target overload due to clutter residuals.
- High-quality construction and extensive built-in test equipment (BITE) for high reliability and maintainability.
- Multimicroprocessor and modular software configuration, which ensure growth capability for data processing.
- Secondary surveillance radar (SSR), which provides identification data within the same detection volume of the primary radar.
- Primary radar plots and secondary plots are compared to provide a single associated plot.
- Data processor is capable of handling a very high number of plots.

8.1.7 Selection of GBEWR Operative Frequency

L-band is the preferred frequency band (instead of S-band, for example) for the operation of long-range radar [2] mainly because [22]:

1. The effect of ground, sea, and rain clutter begins to become significant as the radar frequency is increased. L-band radar takes advantage of natural reduction of clutter mean reflectivity associated with lower frequencies. At center frequency, it results in a 5-dB advantage over S-band in land clutter and a 17-dB advantage in rain clutter.
2. The atmospheric loss increases with the frequency. The L-band has typically 1 dB less attenuation than S-band at 0° of elevation and at a range of 370 km.
3. The L-band is the most suitable for defense against intercontinental BMs due, for example, to large RCS values at lower frequencies.

8.2 | PHASED ARRAY ANTENNA

8.2.1 Introduction

The 3-D radar is replacing the 2-D one for military applications [23–26]. The improved performances in terms of detection capability, accuracy, and flexibility with respect to the 2-D alternatives are offered at an attractive manufacturing cost, especially when compared with the operational benefits. 3-D radar permits the measurement of the complete spatial position of each target at each antenna scan. This is a distinct advantage in systems (typically, early warning, air defense, and weapon control) where the complete knowledge of target position needs to be acquired as soon as possible. Other benefits are related to large antenna aperture and spatial filtering capability.

1. The vertical antenna size is not limited by the required elevation coverage [51]. As an example, a system devoted to naval point defense purposes requires detection and

measurement capability up to 80° in elevation. In 2-D architecture, this requires an antenna aperture with small vertical size, which results in an impairment of the radar detection range and height resolution. In 3-D, a narrow pencil beam can be aimed at the required elevation without reducing the antenna vertical length.

2. Larger antenna apertures permit a better control of the radiation patterns and better performances in terms of sharp cut-off at the horizon and elevation sidelobes.
3. The clutter interference is significantly reduced due to the attenuation produced by the pencil beam pattern. Rain at the upper elevation angles occurs only at short ranges: Targets not physically buried in the rain can be seen in the clear, which is not the case for 2-D.
4. The 3-D antenna pattern is affected by manmade disturbances only at small elevation angles where the interferences are impinging.

Examples of these systems have been developed by Selex ES, which has been active in this field for more than 30 years, with a number of defense radars like the MRCS403 (S-band medium range), RAT31SL (S-band long range), RAT31DL, RAN 40 L (L-band long range), 743D (L-band long range), AR327 (S-band long range), AWS-9 (S-band), and their derivations (see www.selex-es.com). These radars cover both the long and medium range for air and naval defense applications.

One important issue in designing 3-D radars is the selection of the beam-scanning technique (BST), which permits the acquisition of targets over the full elevation coverage in the frame time allowed by the antenna rotation speed and the azimuth beamwidth. This choice strongly determines the overall achievable performance. The L-band radars RAT31DL, RAT31DL/M, and RAN40L are the most recent members of the RAT31 family, which exploit a proprietary BST developed in SELEX Sistemi Integrati years ago and used on a number of SELEX Sistemi Integrati sensors with passive antennas (passive antennas are fed by one central high-power transmitter) [23]. Recent progress in active antennas (usually phased array antennas where, instead of a central high-power tube, every radiating element has a small power amplifier) has permitted designers to incorporate such BST into an architecture that combines the benefits of the technique with very competitive cost. In the coming years, such sensors will represent the backbone of the SELEX Sistemi Integrati NATO Class 1 product in the early warning and air defense roles, thus replacing the RAT 31SL. A number of RAT31DL radars are in service today in several countries, both within and beyond NATO borders. An evolution including ballistic missile defense (BMD) capability has been developed for the more recently acquired NATO sensors.

8.2.2 Overview of 3-D Beam-Scanning Techniques

3-D radar manufacturers mainly use three BSTs:

1. Single scanning beam: A single pencil beam (see Figure 8-3, where H stands for height and R for range; the dashed area represents the pencil beam) scans sequentially the full elevation sector to be covered both in transmission and reception.
2. Multiple stacked beams: A single transmission fan beam (see Figure 8-4 where E stands for elevation) radiates a single waveform over the whole radar coverage. N contemporary multiple pencil-stacked beams (see Figure 8-5) are used for reception over the whole elevation coverage.

3. Sequential scanning stacked beams: A single fan beam in transmission covers only a sector of the complete coverage area, and M (with $M < N$) contemporary multiple pencil-stacked beams cover the same sector for reception (see Figure 8-6). To explore the full coverage, both the transmission and reception beams are switched to sweep the sectors in which the full coverage has been split.

SELEX Sistemi Integrati has envisaged the multiple independent scanning (MIS) beam technique is shown in Figure 8-7 [21]. On transmission, multiple pencil beams illuminate

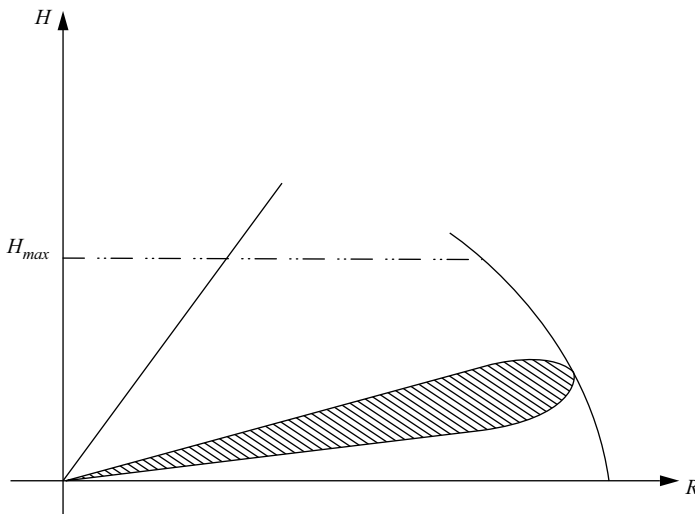


FIGURE 8-3 ■ Pencil Beam.

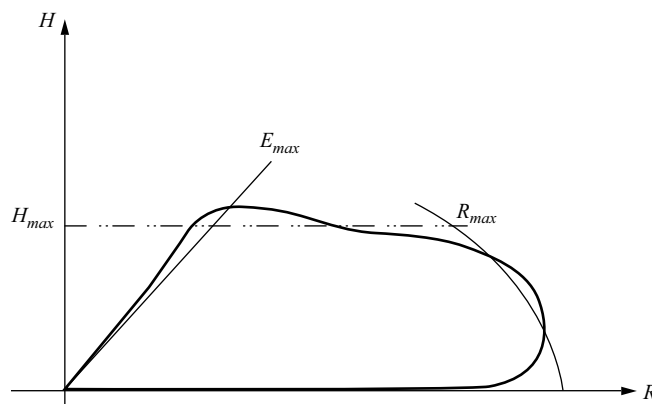


FIGURE 8-4 ■ Fan Beam.

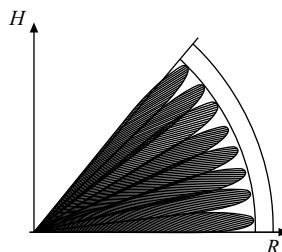


FIGURE 8-5 ■ Multiple Pencil-Stacked Beams.

FIGURE 8-6 ■
Sequential Scanning
Stacked Beams.

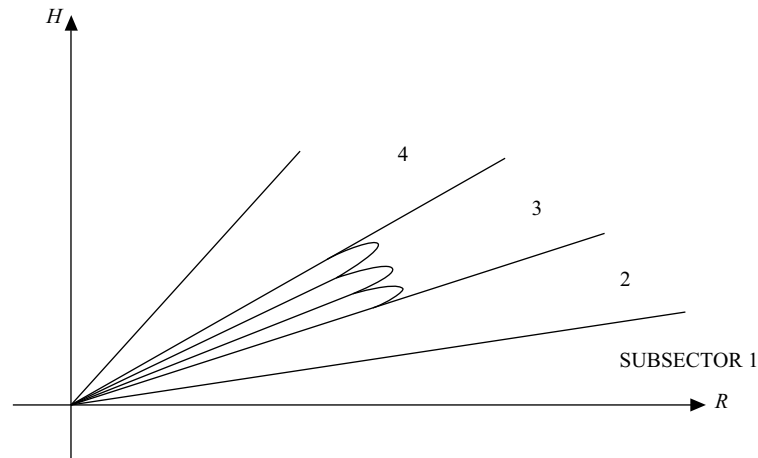
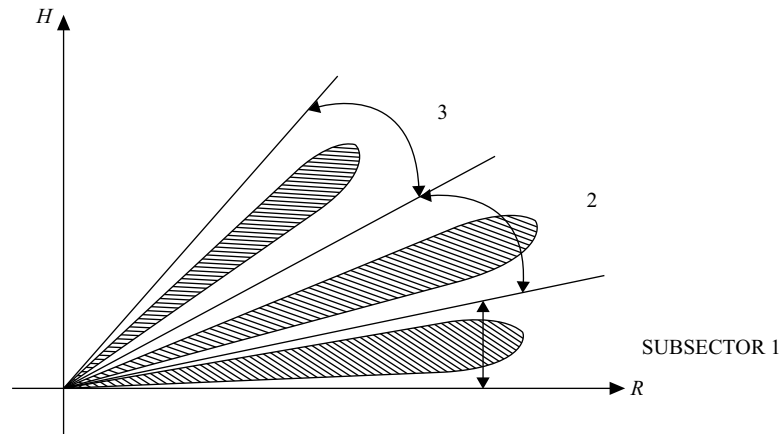


FIGURE 8-7 ■
Multiple
Independent
Scanning Beams.



M angular directions radiating in each direction a different waveform (pulse duration, code modulation, and frequency). On reception M , contemporary pencil beams acquire the signal coming from the directions where transmission occurred. The word “independent” is used here to indicate the following: (a) each beam can be pointed in any direction without limitation due to the pointing of other beams; and (b) the waveform to be used is not constrained to be coincident with the waveforms used in the other beams. The average power available from the transmitter is the only main issue to consider in the definition of the waveforms.

In a clear environment, no meaningful difference in radar range performance is related to the adopted scanning method. Thus, the comparison has to be done: (a) in clutter conditions where the time on target (ToT) is at its premium for efficient implementation of Doppler processing; and (b) under ECM where spatial filtering and waveform diversity are determinant.

1. Single pencil beam: This configuration suffers due to time shortage. Indeed, the single beam can dwell only a very short time in each beam position. As a consequence, such radar has to: (a) transmit very long pulses to reach the required range coverage, with a consequent higher vulnerability to ARM attack and a large range

interval around each target where the sensitivity is reduced by the presence of side-lobes generated by the pulse compression; and (b) use large azimuthal beamwidth to gain ToT, impairing the resolution and accuracy. To recover performance, a mono-pulse antenna is typically used in azimuth. The wider beam width is also more susceptible to jammers. (c) Doppler processing is not performed over the whole elevation coverage. On the other hand, this approach offers: (1) high spatial filtering due to the pencil beam shape, both in transmission and reception; (2) high flexibility in choosing different waveforms for different elevations to tightly match the radar coverage envelope; and (3) simplicity—in principle, only one sum and two (in azimuth and elevation) difference channels are necessary.

2. Multiple stacked beams: This permits the longest ToT with a more efficient Doppler filtering. The use of a transmitted fan beam and a single waveform implies the following: (a) the spatial filtering capability is reduced and the same Doppler processing is applied to all beams because the clutter return is present in any beams; (b) higher detectability by ARM in the elevation coverage; (c) the lack of flexibility in choosing waveforms results in energy that is often directed where not needed; (d) the need to use many different receiving channels if a wide elevation sector has to be covered (0° – 80°); (e) lower accuracy in target elevation measurement due to the use of sum channels of adjacent beams for angle estimation (difference channels are not available); (f) reduced ECCM capability in the presence of more than one smart jammer positioned at different elevations; and (g) lack of special functionalities such as “burn through” or “look down” (valley coverage) modes.³ Many manufacturers have used this configuration in the past because, in principle, phase shifters inside the antenna are not required to point the beams. But in many cases (as on board a ship or on ground, if terrain profiling or automatic leveling corrections are required), this advantage is lost.
3. Sequential scanning stacked beams: This approach typically uses a stack of four beams switched among two or three elevation sectors, together with the corresponding transmission fan beam. The number of receiving channels is reduced; the waveform can be optimized for each sector. The fan beam covers one sector at time, so clutter in high-elevation sectors is spatially filtered with respect to low-elevation sectors. More flexibility and simplicity are achieved in the antenna, but a lower ToT is available. The drawback caused by the use of the fan beam and single waveform applies at each elevation sector.
4. Multiple independently scanned (MIS) beams: This is an extension of the single scanning pencil beam with the addition of extra independent (not stacked) beams. Due to the use of pencil beams in transmission and reception, this solution retains all the benefits of the two-way spatial filtering with the addition of a longer ToT than the single pencil beam, allowing for good Doppler filtering over the full coverage area as well as in the presence of electromagnetic anomalous propagation. The use of different waveforms and carrier frequencies with independent agility criteria per beam strongly increases the separation between the different beams, reducing the possibility of false-target generation and improving radar robustness against multiple smart jammers. The

³These are operative modes required to enhance radar detection ranges in certain directions (burn through) or to point the beam at elevation angles lower than 0° (look down).

transmitted waveform is shared in different directions in a sequential fashion. With MIS, each beam is tailored to the assigned task; this is derived from the ability to freely choose among the beams the pointing direction, the beamwidth, and the waveform. The most relevant benefit is achieved when the elevation scanning profile is adapted to specific operational requirements occurring in limited azimuth sectors and changing in time (e.g. TBM tracking). As an example, in the TBM tracking role, the RAT31DL is able to dedicate one beam to illuminate the TBM while the other three beams are scheduled to cover the remaining coverage area. This guarantees the maximum ToT on the missile compatible with the antenna rotation speed. This capability can be exploited in adaptive fashion, applying it in the relevant azimuthal sectors only.

8.2.3 Overview of a GBEWR Family

The radar is composed of: (1) the antenna group, including a radiating array, the spine with transmit-receive modules (TRMs), an antenna cabinet with analogue receivers, and the mechanical base; (2) the equipment shelter containing the processing cabinet, the identification friend or foe (IFF), the radar environment simulator (RES), the human machine interface (HMI) and service monitors, UHF/VHF communication, modems, and time standard; and (3) the cooling unit consisting in an air cooler for the equipment shelter while the antenna group is cooled by natural air circulation.

8.2.3.1 Antenna

The active antenna architecture is the key for an easy and cost-effective implementation of the MIS technique. The radiating aperture of the RAT 31DL antenna shown on the left side of Figure 8-8 [25] has 42 row planks, each one supporting the horizontal beamformer. This is a strip line power splitter, distributing the signal to the radiating dipoles with a suitable amplitude and phase to achieve a horizontal pattern with the desired beamwidth and sidelobes. Each row is connected to a TRM that combines a transmit and receive channel. Placement of power and low-noise amplifiers at the antenna aperture eliminates transmit and receive losses. A filter and a coupler are used both in transmission and reception. The filter is used both to limit the radiated spectrum and to filter out electromagnetic disturbances during reception. The receiving chain includes a duplexer, a low-noise amplifier, and a set of four independent phase and amplitude adjustment modules (PAAMs). This last component uses gallium arsenide (GaAs) monolithic microwave integrated circuit (MMIC) technology and includes radio frequency (RF) and logical interface circuits. Each PAAM is devoted to a specific beam, and all together are combined into the sum and difference beamforming networks. The amplitude control of PAAM is mainly used to recover, via calibration, the gain change of the receiving chain. The transmission contains an RF power amplifier fed by a single PAAM; the latter is sufficient because the transmitted signal consists of a cascade of

FIGURE 8-8 ■ RAT 31DL, RAT 31DL/M, and RAN 40L Antennas [Courtesy of Selex ES].



four different pulses that can be controlled in time sequence. A single set of PAAMs is suitable both for sum and difference signals because the pointing directions of these two beams are always made coincident. To calibrate the antenna, a test signal is injected into each TRM through a coupler, so the performance (pointing accuracy and the vertical sidelobe levels at specified values) is unaffected by large temperature variations, aging components, and component replacement. To reach low sidelobes both in transmission and reception, suitable taperings have been used, except for the elevation transmission pattern, where a two 6-dB step taper has been adopted. Figure 8-8 also shows two more Selex ES radars built with the same technology and concepts.

The distributed power generation architecture has significant advantages compared to the solid-state bulk transmitter: (1) Power rotary joints are not needed. They are expensive and introduce mechanical constraints by their huge dimensions and weight. The connection between antenna group and equipment shelter is via intermediate frequency (IF) cable only because the front-end receiver is contained in the antenna cabinet, which is rotating with the antenna. This reduces cost and simplifies the cabling, permitting long connection paths. (2) The absence of insertion losses caused by power phase shifters and RF connections permits lower generated RF power. Thus, a lower number of active devices are used, a smaller prime power supply is needed, and less heat has to be removed from the array. Natural air circulation is sufficient because the dissipating surfaces on the antenna are large. (3) Growing capability: Beams can be added with a reasonable increase of modular components. Analyses have been done to compare the cost of a simple one-beam configuration with respect to an alternative four beams. There is a cost increase at the sensor level from 12 percent to 20 percent, depending on the specific application and the technology used for the receiver [26].

A relevant aspect of active array antennas is the accessibility of the components for removal and repair. This antenna is based on modular components that are easy to plug in and an elevator that is an integral part of the antenna spine, which allows for easy servicing. Furthermore, the distribution of the power source across the antenna aperture allows for graceful degradation.

8.2.3.2 TRM Technology

A notional transmit-receive module consists of three main sections: transmission, reception, and auxiliary. The transmit chain consists of power amplifiers that use GaAs [27] MMIC and silicon bipolar transistors in C class and a PAAM. The receive chain consists of a P-type/intrinsic/N-type (PIN) diode limiter, a very low-noise amplifier, a 1:4 RF divider; and four PAAMs. The complete high-power section is realized with a GaAs 10-W power and 40-dB gain amplifier and suitable cascade of C-class amplifiers to provide up to 2 kW. The same modular C-class power amplifier is used as a “brick” in a parallel configuration to achieve all the requested power values. The brick is made of two identical transistors connected in parallel to produce more than 500 W peak with 45 percent efficiency.

Typically, the PAAM (Figure 8-9) package includes hermetic multichip components with MMICs and a complete control circuit; it is plugged in a suitable number inside the TRM (typically, 4 RX plus 1 TX beam). The PAAM includes a phase shifter, an attenuator, switches, and amplifiers. The chip set, as well as the MMICs used in this system, are designed and produced using the SELEX Sistemi Integrati GaAs foundry. The metal semiconductor field effect transistor (MESFET) process was chosen based on cost and yield factors. The auxiliary section contains the power supply conditioner, a logic

FIGURE 8-9 ■
Brick and PAAM
[Courtesy of SELEX
Sistemi Integrati].

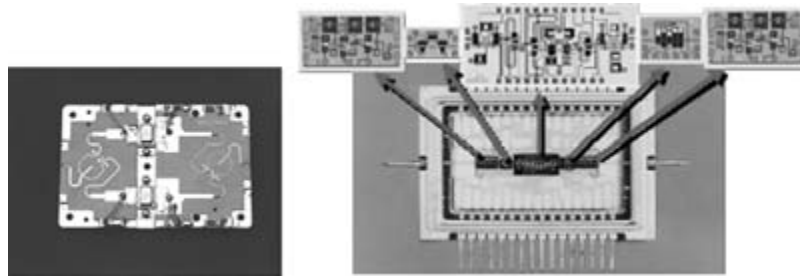


FIGURE 8-10 ■
TRM [Courtesy of
SELEX Sistemi
Integrati].



circuit realized with field programmable gate array (FPGA) technology for self- protection, byte, and external interface. Photos of TRM are shown in Figure 8-10.

8.2.3.3 Radiating Network Technology

Each radiating row plank is made of a high-power L-band, isolated divider with integrated radiating dipoles. The large antenna aperture requires the adoption of innovative technological solutions to guarantee electrical performance and mechanical robustness at a reasonable cost. Each row is subdivided into a central portion and two foldable wings. It houses 52 dipoles distributed along 11 m of length, with a weight of 25 kg and a total insertion loss <1 dB. The row network may use Wilkinson dividers with unbalanced coupling and a normalization of the impedances, permitting a reduction of the physical depth. The needs of weight reduction, low loss, and power handling call for the use of a strip-line sandwich of two metal skins, a tin fiberglass dielectric (for housing the network printed circuits), and dipoles. A special foam acts as a separator between the skin and the fiberglass. Figure 8-11 displays the horizontal network.

Some of the main parameters measured on the complete antenna system are: (1) maximum vertical steering angle equal to 30° without grating lobes, (2) vertical beam width of 2.2° , and (3) horizontal beam width of 1.5° . A peak power of about 60 kW is radiated with an overall efficiency of 20 percent [24]. Patterns in transmission and reception modes were measured on SELEX Sistemi Integrati near field facility. During the development phase, this facility was fundamental to set up the active phased array antenna. An example of measured performance is in Figure 8-12 depicting a typical azimuth pattern.

8.3 | TRANSCEIVER

Radar systems require one or more transceiver modules to generate and acquire the signals needed for target detection. In general conditions, the transceiver is set after the beam-forming network (BFN) of the antenna. On the generation side, the main purpose of the

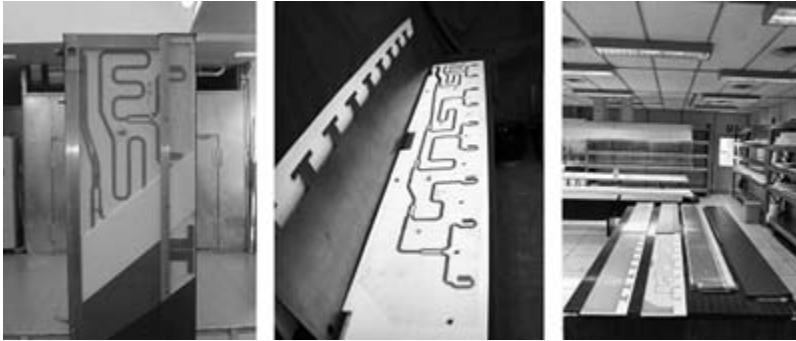


FIGURE 8-11 ■ Horizontal Radiating Network [Courtesy of SELEX Sistemi Integrati].

Rx Horizontal Pattern BFN 1. Punt = 5. Freq. = Central. Beamw = 1.467. Rms = -40.22 db

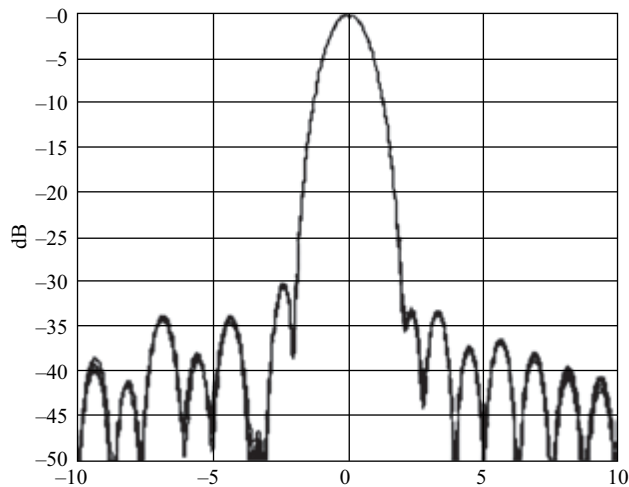


FIGURE 8-12 ■ Azimuth Pattern (dB vs. deg).

transceiver is to synthesize the signal and to shift it to the proper RF carrier before the transmission through the antenna. In addition, it has in charge to provide the proper power level to the BFN and to the input of each TR module. On the receiver side, the transceiver manages the signal coming from the BFN, providing a signal with the proper power level and carrier frequency to the digitizer. According to the specific architecture (e.g., number of beams, monopulse technique, etc.), one or more receiving chains can be employed.

Over the years, the transceiver architecture has been evolving in accordance with the technology improvement. In particular, the size of the analog section has been reduced for two main reasons: devices with increasingly smaller size, and advances in the digital section at the expense of the analog part. In particular, analog-to-digital converters (ADC) capable of sampling signals at a very high carrier frequency (700/800 MHz) while maintaining good resolution (12–14 bits) have permitted the replacement of most of the analog circuitry with digital processing (e.g., digital down conversion), thus reducing dimensions, complexity, and costs. A general description of the main capabilities of a typical transceiver and of its evolution over the last years is described in the following section. Without loss of generality, it will be considered a transceiver including only one transmitting and one receiving chain.

8.3.1 Classic Transceiver Architecture

This section describes the classic architecture of a transceiver. Its top-level block diagram is shown in Figure 8-13.

The transceiver is connected with the BFN and manages the signals from and to it. In Figure 8-13, the bottom and the top sections of the architecture refer to the generation and the receiving sides, respectively. For both transmitting and receiving sections, four zones are highlighted concerning four different frequency ranges where the circuitry works. There is the RF zone that treats the signals exchanged from and to the BFN, two different IF zones (IF1 and IF2), and finally the video section. In the literature, this scheme is frequently indicated as super-heterodyne solution. The number of the conversions depends on the technology employed and the desired transceiver performances (e.g., dynamic range). Typically, traditional architectures need two or three conversions before digitizing because ADCs and DACs (digital-to-analog converters) could only manage baseband signals. Conversion and digitizing are achieved by means of some reference sources:

- The STALO oscillator (stable local oscillator) is an agile source, and it is employed for RF conversion as well as RF channel selection. In general, the STALO source and distributor is one of the most complicated parts of the transceiver because of the contemporary requirements of agility, low phase noise, and low spurious levels.
- The LO (local oscillator) and COHO (coherent oscillator) are used to perform the other conversions needed to obtain video signal at the receiving side or to up-convert the signal at the generation side.
- The CLOCK is the signal employed to digitize at the receiving side and synthesize at the generation side the In-Phase and Quadrature (I-Q) baseband signals.

Some of the most important components in Figure 8-13 are briefly discussed next.

The circulator enables the monostatic operative mode because it permits the use of the same antenna for the transmission as well as the reception.

Regarding the amplifiers, although the circuitry employs different types at different points of the architecture, for the sake of clarity, in Figure 8-13, only two kinds of devices are indicated: the LNA (low-noise amplifier) and the driver. The requirements for the LNA are low-noise figure and high gain since it is typically placed at the beginning of the receiver chain to reduce the overall noise figure (NF) parameter. The driver amplifier is instead devoted to feed the TR modules properly, and it should be characterized by a suitable 1-dB compression point (1 dBcp⁴).

Filters perform different functions according to their position along the chain. The pre-selector filter placed at the RF level has a bandwidth equal to the operative band, and it is devoted to rejecting the input image frequency that would otherwise fall in band after down-conversion processing. The filters placed at the output of the mixers (in IF1 and IF2 zones) are devoted to cut the intermodulation products caused by the nonlinear

⁴1-dB compression point (1 dBcp): Practically, it characterizes the power-handling performance. Regardless of the theoretical definition, for the reception side, it is associated with the maximum input power, while for the transmission side, it refers to the maximum power level that can be provided to the TR modules.

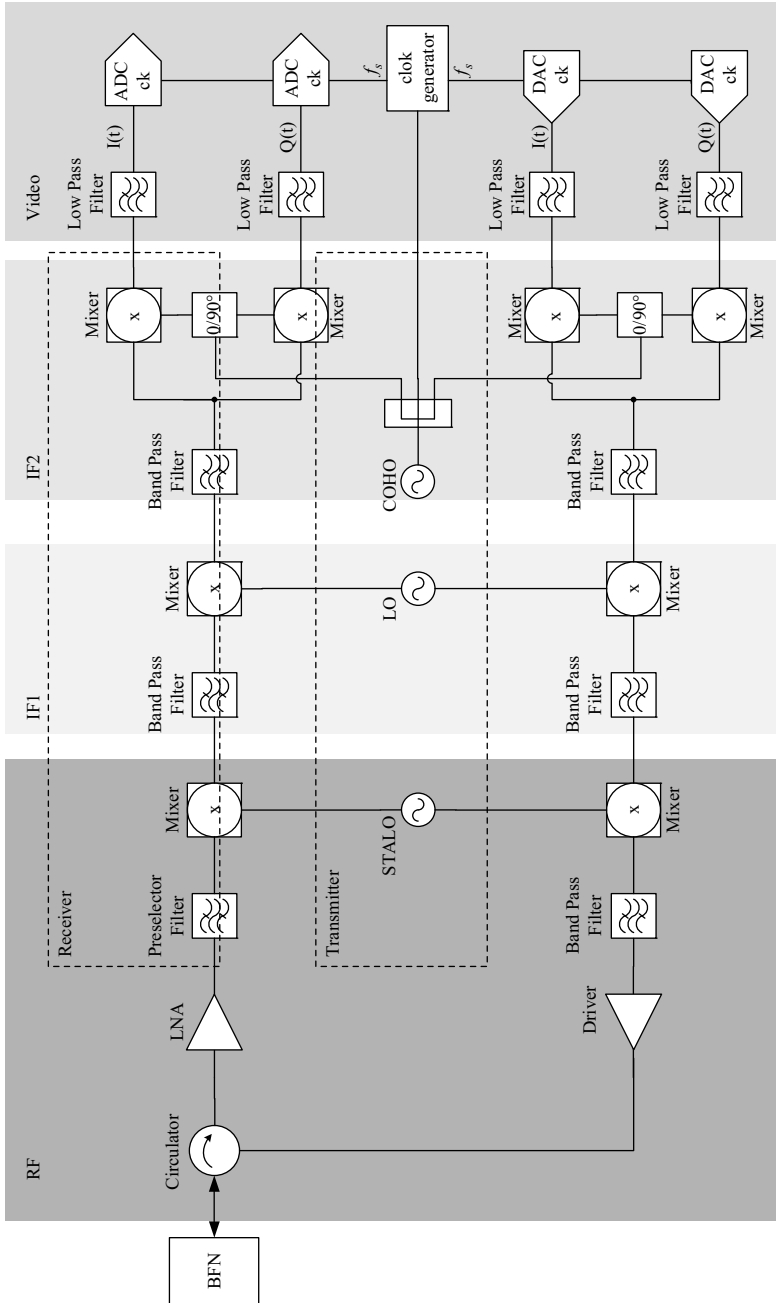


FIGURE 8-13 ■ Classic Transceiver Architecture.

FIGURE 8-14 ■ IF Receiving Board [Courtesy of SELEX Sistemi Integrati].



Dual Channel if Receiver
if Processing Circuit

behavior of the mixer. The low-pass filters set in front of the ADC are devoted to limit the band of the input signal.

An aspect associated with the filter selection is the design of the transceiver frequency plan, i.e., the definition of the frequency values employed at the different points of the architecture. The main scope of this plan is the reduction of interference effects (e.g., coupling and leakage) and of the intermodulation products.

Figure 8-14 shows an IF receiving board currently used in a radar system; the board includes part of the receiver section presented in Figure 8-13.

8.3.2 Modern Transceiver Architecture

Modern transceivers resort extensively to integrated devices and compact architectures. This chapter does not focus on technological solutions aimed at reducing the circuitry (like new devices, new material, etc.), but rather on compact architectures made possible by the market availability of ADCs and DACs operating at higher frequency ranges. In particular, these devices can sample and synthesize directly at carrier frequencies with the strong gain of the reduction of the analog components. In Figure 8-15, the basic architecture of a modern transceiver is described.

The analog conversions to baseband are removed, and the synthesis and the sampling of the signal occur directly at a carrier frequency by means of the so-called digital up-conversion (DUC) and digital down-conversion (DDC) processes. This architecture is made possible by ADCs and DACs operating at higher frequencies and maintaining a high number of bits (14/16 bits). Besides reducing costs and dimensions, this solution eliminates some distortions affecting the scheme shown Figure 8-13, such as phase and amplitude imbalance problems caused by the I&Q analog modulator.

Transceivers can sample carrier frequencies of about 100 MHz (or more) taking advantage of digitizers featuring 16 bits in this frequency range. Designers currently are investigating the possibility of transceivers with only one analog conversion, as represented in Figure 8-16.

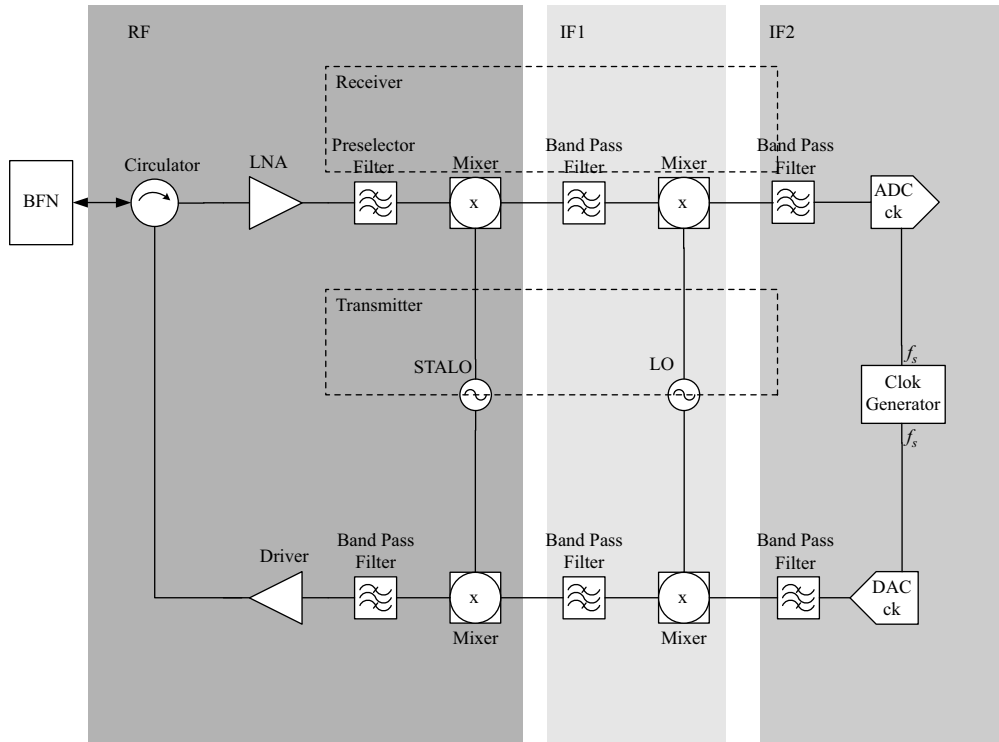


FIGURE 8-15 ■ Modern Transceiver Architecture.

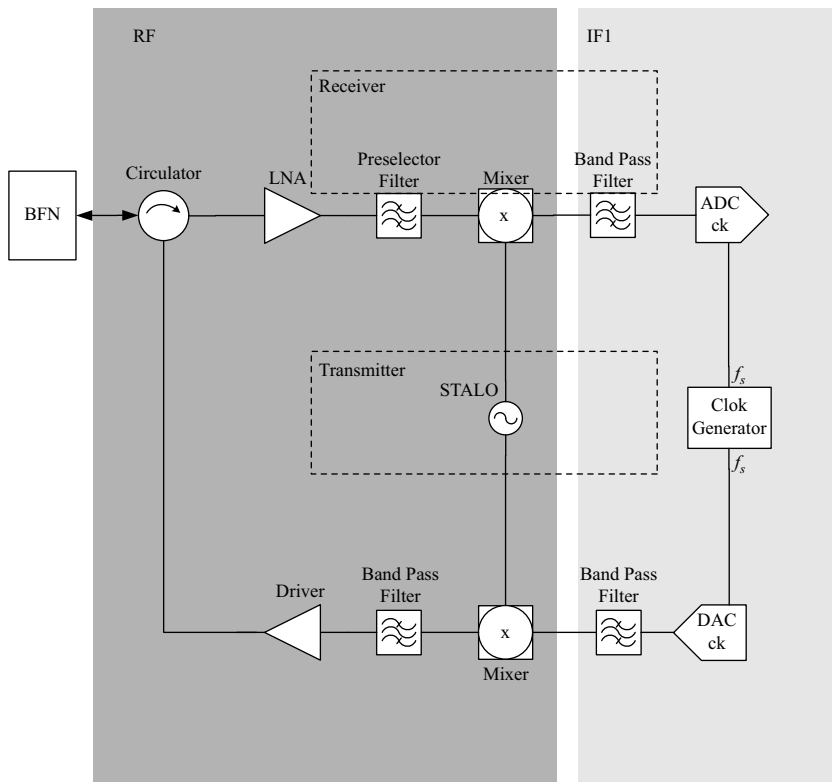


FIGURE 8-16 ■ Next Transceiver Architecture.

In this solution, ADC and DAC devices are required to manage signals with carrier frequencies around 700/800 MHz, where the state of the art features a resolution still equal to 12/14 bits. This scheme provides a further modification of the architecture with a reduction of dimensions and costs.

8.3.3 Transceiver Parameters

The main parameters of a transceiver are briefly discussed. Some concepts, such as band value, can be associated with both sides, transmission and reception; others (like NF) with only one side.

- **Operative band:** It is the band allocated for the radar service. Typical values are 1 GHz (for X-band applications), 500 MHz (C-band applications), 300 MHz (S-band applications), etc.
- **Instantaneous band:** The band value of the transmitted and received signals. For traditional radar applications, it can be 2 or 3 MHz.
- **Noise figure (NF):** Quantifies the sensitivity of the receiver and allows calculating equivalent noise spectral density at the input of the receiver. For a receiver with an NF equal to F , the input equivalent noise power spectral density is equal to KTF , where KT is the thermal noise density (-174 dBm/Hz).
- **Dynamic range:** It is the difference between the 1 dBcp and the receiver power noise within the instantaneous band. It is in general limited by the resolution (number of bits) of the ADC device.
- **Spurious free dynamic range (SFDR):** It defines the dynamic range free of spurious signals.
- **Phase stability affecting cancellation:** It regards the phase stability of the system. This is a very important value for primary coherent radars. In general, this value is limited by phase noise of the STALO source because it is the highest frequency value in the system.

8.4 | WAVEFORMS AND SIGNAL PROCESSING

This section is devoted to the description of waveform and signal processing algorithms for GBEWRs, and it assumes knowledge of the general radar basic principles [28]. The focus is on typical waveforms, pulse compression filters for sidelobe reduction, cancellation filter and insertion map, constant false-alarm rate (CFAR) techniques, and the moving window (MW) detector for the measurement of target azimuth.

8.4.1 Waveforms

Typical GBEWR detection range varies from 10 km to 500 km, and it is generally subdivided into two intervals where different waveforms are used:

- **Short range.** HPRF (high-pulse repetition frequency) waveforms are adopted for detection in a heavy clutter environment. The HPRF waveforms ensure radar coverage typically from 10 km to 250 km, which is the maximum range where clutter

returns are expected (as a function of the site height). Note that GBEWR is generally not ambiguous; thus, the pulse repetition time (PRT) is around 1.7 millisecc.

- **Long range.** LPRF (low-pulse repetition frequency) ensures the coverage of the remaining surveillance volume from 250 km up to the maximum unambiguous range. PRT is expected to be around 3.5 millisecc.

The use of NLFM (nonlinear frequency modulation) code is adopted for tracking waveforms because it permits the user to reach low sidelobes with very limited weighting loss: The hypothesis is that for a tracked target, the velocity is known and thus the compression filter can be adapted to compensate the target velocity; in this way, it is possible to increase the target SNR and thus probability of track maintenance.

For waveforms designed for the search function (which is the GBEWR main feature), where the target velocity is not known, it is preferable to adopt the LFM (linear frequency modulation) codes to preserve Doppler tolerance in case of fast targets, with the drawback of a bigger error in the target range measurement. Note also that it is possible to correct the target range position with a simple post-processing activity if the system gives the target velocity as a result of a tracking activity.

8.4.2 Pulse Compression Filters for Sidelobes Reduction

The design of optimized low sidelobe receive filters for pulse compression radar systems is a hot research topic among the radar signal processing community [2, 29]. While at the transmission side, the good sidelobes were attempted through waveform design, at the receiver side, the effort was focused on the development of suitable filters.

Some early approaches to the filter design can be dated to 1967–1968 [30, 31], with reference to the IEEE journals, and to 1970 [32, 33] in the context of Russian literature. In [34], a literary survey and a selected reference list on this interesting problem are provided, together with some new contributions concerning issues related to the filter length and the choice of the design criterion. According to [34], the receiving filters proposed over the years can be classified into two main categories. The former is a data-independent class of special interest for GBEWR and does not require any prior knowledge about the surrounding environment, whereas the latter is a data-dependent class and assumes the estimation of some parameters of the environment [35]. With reference to the former class, we quote [33], [36], and [37] where the minimum integrated sidelobe level (ISL) filter [33] and the minimum peak sidelobe level (PSL) filter [36, 37] are, respectively, designed. While the minimum ISL system shares a closed-form solution, the computation of the minimum PSL filter requires the solution of a linear programming (LP) problem [36, 37] with reference to real optimization variables and transmitted code sequence, or the solution of a convex optimization second-order cone programming (SOCP) problem [34] in the case of complex variables.

8.4.2.1 Typical Pulse Compression Scheme in GBEWR

The pulse compression is typically carried out in the frequency domain by means of the following steps:

- Complex valued fast Fourier transform (FFT) of the incoming signal;
- Complex product with the FFT of the reference signal; and
- Complex Inverse FFT (IFFT) of the obtained signal.

TABLE 8-3 ■ Code, PSLR, and ISLR

Code	PSLR (dB)	ISLR (dB)
HPRF	30 dB	25 dB
LPRF	40 dB	25 dB

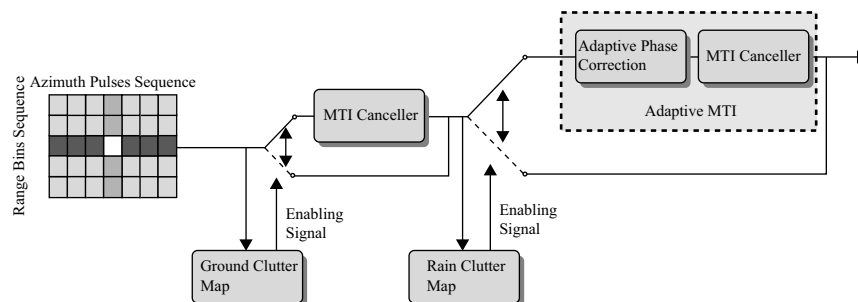
The time-bandwidth product is classically in the order of 100. The requirements for a notional system concerning the compressed pulse sidelobe level are reported in Table 8-3.

8.4.3 Cancellation Filter and Insertion Map

GBEWR signal processing usually exploits a number of static and dynamic maps for various functions. MTI (moving target indicator) or AMTI (adaptive MTI) filters are generally managed by maps, automatically including or excluding the MTI or AMTI based on the computed clutter (surface and volume) power, which can be larger or smaller than the receiver noise power. Fixed MTI filters are generally inserted after the digital pulse compression to cancel fixed clutter echoes. AMTI filters out moving clutter echoes, with a translation of the clutter spectrum around the zero Doppler frequency (adaptive phase correction) and a subsequent cancellation by means of a fixed MTI.

Specifically, fixed MTI is exploited when surface clutter intensity is above receiver noise, while AMTI is inserted when volume clutter (weather or chaff) is above the receiver noise. Figure 8-17 gives a pictorial view of this concept.

The MTI insertion map can be achieved by a two-step procedure. The first step is based on a geographic or site map defining the clutter presence and the type of environment surrounding the GBEWR. The second step requires a continuous updating of the map contents computing the GBEWR received power in each cell of the clutter map. If the power is greater than a predefined threshold, clutter presence is declared, and the corresponding characteristics are estimated and updated. Ideally, a map updating procedure has to be implemented under fair weather conditions. As a result, the AMTI insertion map is refreshed at each antenna rotation. Input data for this map are collected at the output of the MTI canceller device to avoid the map loading on fixed clutter returns.

FIGURE 8-17 ■ MTI/AMTI.

The use of the insertion maps is mandatory for GBEWR; the drawback is that MTI/AMTI devices introduce an SNR loss due to the shape of the filters and the reduction of the available number of pulses for target detection. As a trade-off, the insertion maps are used only where clutter is really present, thus giving remarkable advantages with respect to the use of filters in the whole radar sweep.

8.4.4 CFAR Techniques

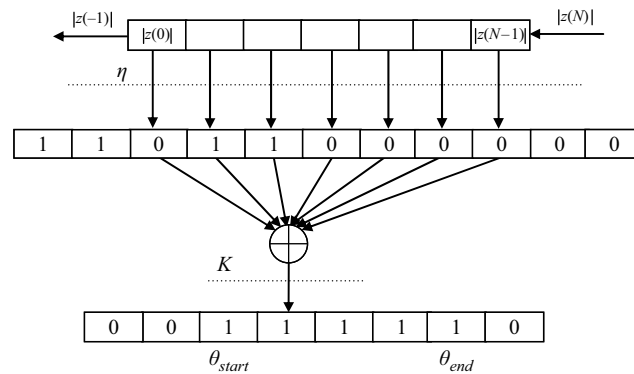
The detection performance is impaired by the presence of clutter returns due to reflections from buildings, trees, ground, the sea, etc. Since the clutter power is usually unknown, detection schemes with a fixed threshold may result in an excessive number of false alarms (FAs) and/or in poor target detection. A possible way to reduce this drawback relies on the use of processing devices with an adaptive threshold capable of ensuring the CFAR property.

Several strategies have been proposed in the literature and are implemented in modern GBEWR. Among them we mention the classic cell averaging CFAR (CA-CFAR) detector [38–40] that relies on secondary data (training data) from the range cells around the cell under test (CUT) to perform the threshold adaptation (notice that in a typical GBEWR, the number of reference data may be generally selected offline, from a minimum value of 8 up to a value of 128). However, training data are often contaminated by power variations over range (in addition to radar range equation effect), clutter discretets, and other outliers. Moreover, the strength of the clutter also fluctuates with terrain type, elevation, ground cover, and the presence of manmade structures. In these situations, training data may not be representative of the disturbance in the CUT, and the CA-CFAR exhibits strong degradations both in the detection performance and in the CFAR behavior [41]. This is especially true in regions containing varying ground cover, such as regions with land and sea.

To reduce the impact of a nonhomogeneous secondary data window, several modifications of the CA-CFAR detection scheme have been proposed during the last three decades. The greatest of CFAR (GO-CFAR) algorithm [42] tries to mitigate the impact of clutter discontinuities suitably choosing the reference window. As a result, the algorithm shows a CFAR behavior stronger than the CA-CFAR, but a detection probability (P_d) worse than the counterpart when interfering targets, and in general outliers, are present in the training window (masking effect). The smallest of CFAR (SO-CFAR) processor [43] reduces the masking effect, but it sacrifices the CFAR behavior in non-homogeneous clutter environments. A strong robustness can be obtained exploiting order statistic CFAR (OS-CFAR) schemes [44], which rely on the power ranking of the reference window samples. Nevertheless, the OS-CFAR processor is often unable to prevent an excessive FA rate in clutter transition regions [45]. Other algorithms, based on the excision of a predetermined number of reference cells and on clutter maps, have also been proposed and assessed [46–49].

A different approach that can aid the selection of training samples might be the real-time exploitation of a priori knowledge concerning the environment surrounding the radar. To this end, CFAR processors capable of exploiting a priori information provided by a geographic information system (GIS) about the observed radar scene are proposed in [50]. They are composed of two stages: the former is a knowledge-based (KB) data selector that suitably chooses the reference samples exploiting a priori information. The

FIGURE 8-18 ■
MW Scheme.



latter stage is a standard CFAR processor (for instance, a CA-CFAR, even if another system could also be exploited).

8.4.5 Moving Window Technique for Azimuth Estimation

In this section, we describe a multipulse algorithm working with only one channel for the estimation of the target azimuth. It is the MW technique [2] often implemented in many commercial radars. It exploits multiple detections in the same ToT, and its processing scheme is shown in Figure 8-18 [2].

The echoes collected by the radar during the scanning in the ToT are saved for each range cell into a shift register (SR) (first line in the scheme). The amplitude of each echo is compared with a first threshold η . By doing so, the string of amplitudes is converted into a string of bits “0” and “1”: “1” when the threshold is overcome, “0” conversely (second line in the scheme). The current N bits of this string are added and compared with a second threshold K . A target is declared present if this second integer threshold is overcome (K out of N detection rule). All the detections after the second threshold are saved in a second string⁵ (last line in the scheme) that is used by the radar processor for the target direction of arrival (DOA) estimation.

If θ_{start} is the angular position corresponding to the first detection (first bit “1” in the second string) and θ_{end} is the angular position of the last detection, then target DOA is estimated as the arithmetic average of θ_{start} and θ_{end} [2]. Notice that in picking θ_{start} and θ_{end} in the string, the processor checks for the continuity of the “1”s. If more than two consecutive “0”s are present, the estimation is not done and a “target split” is declared. The split corresponds to a possible presence of more than one target in the same range-azimuth cell.

8.5 | TRACKING

In a radar, the cascade of signal processor, data extractor, and data processor depicted in Figure 8-19 is ultimately a bandwidth compressor. It receives data at a high rate

⁵Bit “1” for detection, bit “0” for the alternative hypothesis.

(e.g., the bandwidth of radar signal, which is in the order of tens of MHz) and processes the signal in such a manner that a relatively low data rate (several Hz) is achieved. This feature is pictorially indicated by the narrowing of the arrows moving from the left to the right of the cascaded processors. At the same time, there is a progressive discrimination between useful and clutter/interference data by means of a stepwise decision process. The information handled by the processing chain is progressively manipulated into a form that allows easier decision making by the user. In fact, the raw video signal contains many false echoes. The data extractor isolates the useful target, and the data processor identifies the target (possibly labeled with a code) and determines the target velocity and additional parameters that are presented on a tabular display. A further observation can be made regarding the increase of the time span in which processing is performed through the cascade. The signal processor involves only few pulses, the data extractor some adjacent groups of pulses, and the data processor consecutive radar scans. In other words, the memory of the processing increases when moving from left to right in Figure 8-19 [53].

Tracking, from a classical point of view, can be defined as the set of algorithms that, when applied to the radar detections acquired during successive scans, allows

- recognition of a pattern of successive detections as pertaining to the same target;
- estimation of the kinematics parameters (position, velocity, and acceleration) of a target, thus establishing a so-called “target track”;
- extrapolation of the track parameters;
- distinguishing different targets, also on the basis of additional attributes (e.g., IFF, shape, electromagnetic signature) and thus establishing a different track for each target;

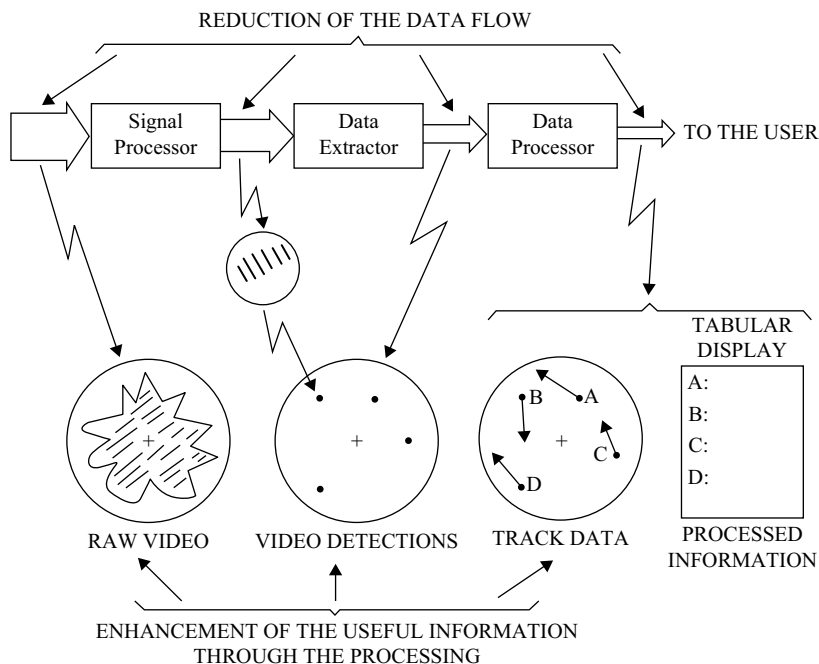


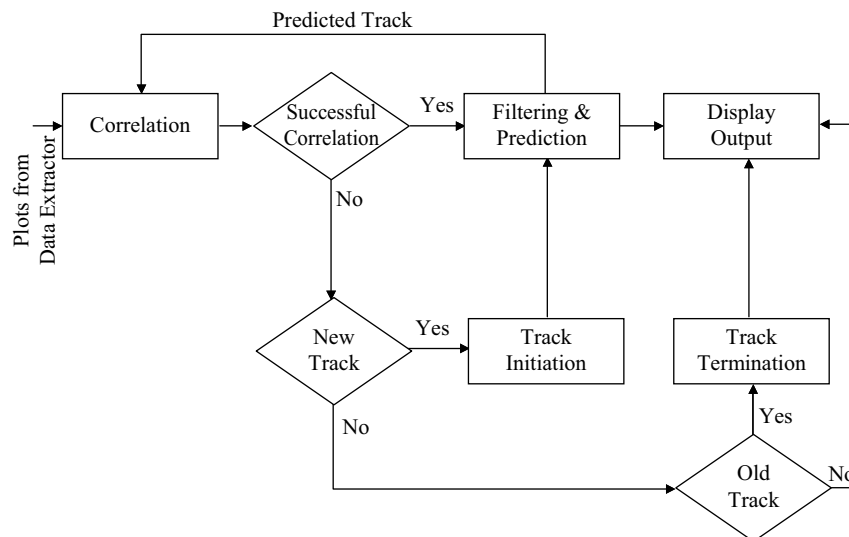
FIGURE 8-19 ■ Functions Performed During the Radar Receiving Phase [53].

- distinguishing false detections (caused by intentional or natural interference) from true targets;
- adaptive refinement of the threshold setting of the signal processor in order to make the radar more or less sensitive in the different spatial directions, depending on the content of a map of false detections refreshed on a scan-to-scan base;
- scheduling of the track dwells of a phased array radar in order to follow a maneuvering target with constant accuracy and to interleave in an optimum manner the tracking phases with search looks and other radar functions;
- efficient managing of the detections and/or the tracks provided by the different radar sets of a netted system looking at the same portion of the controlled space in order to provide a better picture of the latter.

The working principle of the classical tracking procedure is now explained. Tracking evolves through the following logic steps: track initiation, plot-track correlation, track prediction, track filtering, and track termination. The interconnections among these basic tracking functions are shown in Figure 8-20 [53].

First of all, a track must be established (track initiation). An estimation of the initial kinematics state of the target (say, its position and velocity) can usually be obtained from two consecutive target returns. The target velocity is obtained by the ratio of the position displacement to the radar scan time. This simple procedure is not reliable if false plots are present. It is then necessary to use for the track initiation only those sequences that are consistent with the expected behavior of the target. On the following scan, it is desirable to capture the return signal from the same target and associate it with the track (plot-track correlation logic). If the target is supposed to be moving with constant speed, then the position of the target on the next scan can be predicted (track prediction logic) using the current estimates of its position and velocity. However, there may be inaccuracies in these predictions, mainly due to the error on the measured plots.

FIGURE 8-20 ■
Basic Functions of
Tracking Procedure
[53].



Thus, in searching for the next target return, allowance for these errors must be made—for instance, by deploying a search area centered on the predicted position: A plot found within this search area will be associated with the established track. The size of the search area needs to be determined by estimating errors in position and velocity, as well as the antenna rotation time. The search area needs to be large enough to have a high probability of capturing the following target return, but needs to be kept minimal to reduce the probability of capturing false plots. This aggravates association problems since in the event that more than one plot falls inside the search area, it is not known which plot emanates from the target. This search procedure applies only to non-maneuvering targets. It is simply extended in principle to allow for target maneuvers. Some limits on the target's capacity to maneuver are assumed; in the simplest case, this may merely be its maximum acceleration. The maneuvering capability of the target can be expressed as a maneuver gate surrounding the predicted position such that, ignoring the effect of estimation and plot noise errors, the target must be found at some point inside this gate on the next scan. There are now two sources of discrepancy between the predicted position and the actual position of the next target plot, namely, that due to estimation errors and noise, and that due to possible maneuvers. The total search area should be formed allowing for the occurrence of the worst discrepancies from each of these sources—loosely speaking, the noise gate (i.e., the search area used for a non-maneuvering target) and the maneuver gate are “added” to obtain a final search gate. Assume that the next target plot is successfully associated with the established track. It now remains to update and improve the estimates of the target's position and velocity using the newly acquired plot (track filtering logic). This operation is accomplished by a digital filter that determines the error between the measured and predicted position of the plot and provides the smoothed position. The evolutions of smoothing and correlation logics run in parallel with and are motivated by the continuous increase in availability of computer processing power.

8.5.1 Evolution of Filtering Logics

A nonexhaustive list of techniques includes the following: α - β filter, fixed-weights filter, variable-weights filter, Kalman filter, and IMM (interactive multiple model) filter. The use of fixed-parameter filters avoids the necessity of iteratively calculating new coefficients at every scan and thus greatly reduces the computational load of the filter. This is the first algorithm employed to track a target and, because of its simplicity, is still used in practical applications; however, its performance might be poor. Variable-weight filters take into account the prediction uncertainty of the track in its different life stages and generally produce acceptable performance: Gains are pre-evaluated and stored in a look-up table so that computational requirements remain low. They assume a constant measurement error and a fixed update interval. The Kalman filter is a nonstationary filter in which both the estimate and its covariance are described by recursive equations. The Kalman filter can be suitably implemented by a feedback scheme embedding a replica of the system model. Weights are evaluated online and take into account measurement and prediction errors: The derived load is definitely higher than that of the previous techniques. Adaptivity to sudden changes in the system model (e.g., maneuvers, ...) is a fundamental quality of a filter, i.e., the capacity of providing good

filtering of measurement noise (which can be achieved with a narrowband filter) and simultaneously promptness in following sharp maneuvers (wide bandwidth). Adaptivity at this point requires some kind of maneuver detector to determine the onset time of the maneuver and heuristics to quickly accommodate the parameters of the filter to the sudden change. When the position displacement d ($|\text{associated plot} - \text{predicted state}|$) is larger than a threshold T (dependent on the noise level), the Kalman filter gain K is suitably increased by a quantity dependent on the displacement. The multiple model (MM) and its more powerful successor, the IMM filter, have intrinsic adaptivity. IMM is a variable-bandwidth filter that automatically adapts to target dynamics: It requires the selection of a set of models representative of target motion. The IMM algorithm selects each time the combination of the target models that best fits the measurement data, and by appropriate mixing of these different models, each of which is a Kalman filter, it produces the best representation of the target model. IMM was conceived by H. Blom and Y. Bar-Shalom [54]; further evolution of the theory has produced the variable structure (VS) IMM [55].

GBWER usually operates in a “dense” environment, i.e., in the presence of a number of different threats like air-breathing targets (ABTs), anti-radiation missiles, BMs, and others. Different KFs and EKFs can be designed for each type of target in the environment, and all together interact via IMM.

8.5.2 Evolution of Correlation Logics

A list of techniques includes the following: nearest neighbor (NN), local optimum, global optimum, PDA (probabilistic data association), JPDA (joint probabilistic data association), and multiscan correlation (MHT, or multiple hypothesis tracking). Nearest neighbor solutions are still widely used and attractive for their low computational requirements: A global optimum approach must certainly be preferred. However, they suffer from severe drawbacks in dense and noisy environments. JPDA was developed as a way of achieving acceptable performance in dense clutter environments. Miscorrelation is effectively contrasted by evaluating the probability of each plot-to-track association and then updating the track with a weighted sum of the plots. The approach is time consuming and so many suboptimal schemes have been developed to reduce its computational load. Multiscan approaches are certainly the most performant: They allow the user to defer the final association decision until data relative to subsequent scans are available. They are time consuming, since a set of hypotheses over several scans is maintained for each track. Combinatorial optimization and more powerful processors make multiscan approaches now feasible.

Most tracking systems in use today employ some type of nearest neighbor correlation and α - β adaptive or Kalman filtering with maneuver detection. These logics have been refined and improved through the years and produce a sound and consistent picture of the area under surveillance. In order to exploit the additional processing power now available, sophisticated though time-consuming algorithms have been investigated, benchmarked, and used in practice. IMM, JPDA, MHT, and combinations of these techniques represent the state of art. In air-defense applications, correlation is the greatest concern. Miscorrelation can completely invalidate the filtering process, and so resources should be focused on the data association problem. A computationally intensive MHT algorithm coupled with simple yet efficient dynamic modeling of target

motion has been extensively tested. Maneuvers are modeled by increasing the process noise of the target model. Several levels of gating are performed to cut down processing time. Results show that the load deriving from an MHT approach can be mastered [56, 57].

The performance of the combination of IMM and MHT solution [58, 59] has been investigated: The algorithm performance is more than simply the mere combination of the advantages of IMM and MHT, due to the tight coupling of the filtering and correlation components. The whole IMM + MHT solution provides a flexible framework that can be exploited in a civilian application reducing the depth of the multiscan technique and increasing the number and the modeling of targets. Also in a defense application the depth of the multiscan technique can be increased and the modeling made accurate as appropriate. The customization is also dependent on the available processing resources. IMM also plays a relevant role in the identification phase of surveillance; more precisely, tracking and identification can be jointly performed as explained, for instance, in [60].

8.5.3 Scan to Scan Correlator

GBEWR often exploits a “scan to scan correlation” (SSC) function in order to filter out plots due to noise or clutter residuals. It is based on the following main principles:

1. Construction of dynamic maps for stationary plots: The radar environment is divided into cells and it is dynamically checked if the cell is “clutter free” depending on the number of plots that are not confirmed as target after the track initialization step. A plot coming from a cell that is not clutter free shall be used just for the update of an already existing track and never for the creation of a new track.
2. Additional filtering techniques can be applied based on
 - Kinematics: if the plot velocity is below or above predefined thresholds, it is discarded.
 - Age: if the plots have not been used for a certain number of scans, they are discarded.
3. Track initialization: The track initialization logic can be properly set according to the expected number of clutter residuals, based on geographic maps and elevation beam pointing.
4. Definition of NAI (not automatic initialization) area where tracks are not initiated, regardless of their kinematics. This function is very helpful in the proximity of highways.

8.6 | ELECTRONIC COUNTER-COUNTERMEASURES (ECCM) CAPABILITIES

This section presents a list of the most conventional functions adopted in GBEWR to contrast ECM. The first column in Table 8-4 contains ECCM functions, while the

TABLE 8-4 ■ Conventional GBEWR ECCM features

Function	Note
Random frequency selection	Anti-radar localization and evasion of the missile guidance.
Automatic frequency selection	Radar has frequency agility capability, which permits both automatic selection of radar carrier frequency within the total radar operating frequency band (random selection) and automatic selection of the least jammed frequency (anti-radar localization, evasion of the missile guidance, and jammer avoidance).
High peak-to-sidelobe antenna ratio	Protection is provided against jamming sources impinging through the antenna sidelobes and thus entering into the receiver subsystem.
Sidelobe blanking	SLB channels are included to recognize the asynchronous interference and pulsed jamming entering via the sidelobes and to provide blanking commands of the detected video outputs.
CFAR and AMTI	The receiver subsystem has a potential capability to separate the moving targets in chaff by an adaptive MTI and adaptive thresholding.
Narrow pencil beam	It reduces the volume where an impinging jammer cannot be blanked.
Coded waveforms	It reduces the radar range cell enhancing the signal-to-noise ratio; it decreases ESM receiver ability to detect radar signals, and it reduces the emitted peak power.
Wide bandwidth	It decreases ESM receiver ability to detect radar signals.
High dynamic range	It prevents masking of the target in the presence of jamming.
Stagger	It decreases the synchronization ability of the ESM receiver.
Binary azimuth integration	It prevents asynchronous interference and pulsed jamming entering via the mainlobe.
Coherent processing	It provides the capability to filter out interference (e.g., chaff) on a Doppler basis.
Jamming detection	The jammer is detected and its direction and power are measured sweep by sweep in order to provide it to the Command and Control Center for triangulation purposes.
Emission control	A sector control of the transmitter is provided to combat the ARM threats.
Burnthrough	This operational mode allows an improvement in dwell time on targets in sectors selected by the operator.
Decoys control	The sensors control some decoy antennas at the side to deceive the ARMs.
Sidelobe canceler	It reduces the interferences received through the sidelobes by modifying the receiving pattern of the radar antenna to place nulls in the jammer's direction.
Mainbeam cancellation	It reduces the interferences received through the mainlobe by modifying the receiving pattern of the radar antenna to place nulls in the jammer's direction.
Frequency agility	The transmitted frequency is changed on a pulse to pulse or a batch to batch basis.
PRF jitter and PRF stagger	They contrast some deception jamming.

second column refers to the benefits of the function in an ECM environment ([2] Chapter 24).

8.6.1 Sidelobe Blanking (SLB)

In this subsection, we will focus on the SLB as it is widely used in GBEWR. SLB devices are used to inhibit the radar receiver output when any unwanted signals (jammers, strong target echo, clutter echoes, etc.) appear in the radar antenna sidelobes. The classic SLB architecture has been introduced in [61] (see Figure 8-21) and is equipped with two antennas (main and guard antenna), mounted close so that they

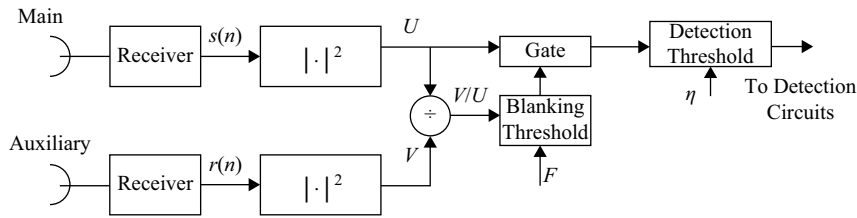


FIGURE 8-21 ■
Block Scheme of
Classic SLB Device.

receive the same interfering signals, and with their own receivers, referred to as the main and the auxiliary channels.

The guard antenna is designed to have a mainlobe gain higher than the sidelobe gain of the radar main antenna. Furthermore, the width of the guard antenna mainlobe is sufficient to encompass the entire region illuminated by the main antenna sidelobes. This implies that any impulsive interference that enters the radar antenna sidelobes will produce a stronger output from the auxiliary channel than that from the main channel. On the contrary, any target in the radar antenna mainlobe will produce a stronger output from the main channel than that from the auxiliary channel [62].

Consequently, comparing the outputs of the two receivers and inhibiting the main receiver when the auxiliary output is stronger, any targets or impulsive jammers that are in the sidelobes of the main antenna are prevented from entering the signal analysis circuits, thus avoiding false detections and angle errors. The SLB logic works independently for each range/azimuth bin and determines whether or not to blank the main radar channel: The blanking signal is generated each time the ratio V/U between the outputs of the square law detectors is greater than a suitable blanking threshold F . On the contrary, if the radar signal is not blanked, the main channel output is then conventionally processed—namely, it is compared with a detection threshold to decide if the presence of a target should be declared. Generalizations of the conventional SLB [61] have been proposed in [63], where a more complex blanking logic is discussed, and in [64], where a processing configuration incorporating CFAR devices in the two channels is introduced and assessed.

The performance of the Maisel SLB [61] has been thoroughly studied in [65] with reference to Rayleigh fluctuation, in [66] for the case of an arbitrary number of integrated pulses and in the presence of fluctuation that is modeled as a gamma distribution with integer shape parameter, and in [67] to account for the presence of correlated Gaussian clutter in addition to thermal noise. Finally, in [68], the performance of the conventional SLB in the presence of Swerling Chi [69] and Shadowed Rice [70] amplitude fluctuations has been examined.

The joint use of SLB and sidelobe canceller has been considered in [71].

8.7 | SPECIAL FUNCTIONS

8.7.1 Antiballistic Missile (BM)

This section deals with the problem of radar detection and tracking of a BM, which is a key issue in GBEWR, and some basic and unclassified concepts are included. Two

models of BMs are mentioned: (1) an EM (electromagnetic) model, and (2) a kinematic model:

1. The RCS plays a fundamental role in computing the target detection probability, and the EM model allows the user to predict the BM RCS versus the radar-target line of sight.
2. The BM kinematic is required to develop a successful tracking filter: Since the motion equations are highly nonlinear, the techniques based on the Kalman filter KF are widely exceeded if an accurate BM kinematic model is implemented by an extended Kalman filter EKF. The insertion of the EKF filters in interacting multiple models (IMMs) [72] guarantees a robust implementation in case of unknown target motion or unknown target parameters.

8.7.1.1 Prediction of BM RCS

To compute the RCS, the following steps must be executed [73–75]:

- Set up powerful software tools to speed up the EM calculation versus the frequency sweep and target aspect angle; this activity has taken many years of continuous R&D effort.
- Develop the computer-aided design (CAD) model of the BM reference target.
- Represent the target surface with triangular planar facets (mesh).
- Conduct accurate EM analysis: RCS predictions in the required frequency band and viewing angles.
- Validate the model by computing range profile curves and images by emulating high-resolution radar modes.

The CAD model of a typical BM missile is shown in Figure 8-22, while the patch model (with 10,000 planar triangular patches) is depicted in Figure 8-23.

FIGURE 8-22 ■
CAD Model of the
Reference Target.

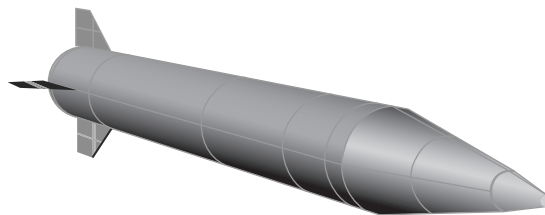
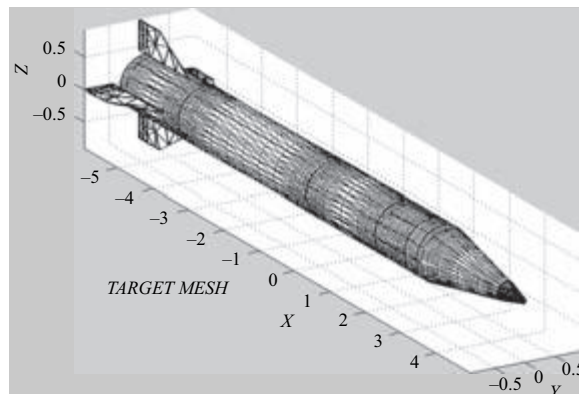


FIGURE 8-23 ■
Patch Model for the
Reference Target.



Some of the EM techniques used in RCS calculations are:

- Physical optics (PO)
- Physical theory of diffraction (PTD).

These techniques, based on the *EM equivalent principle*, start from the distribution of the electric and magnetic currents induced on the surface. PTD takes into account the fringe wave currents, perturbation currents introduced by the edge diffraction of the finite size structure, and a method called incremental-length diffraction coefficients (ILDC), which extends the applicability of Ufimtsev's diffraction theory [76] to arbitrary scattering aspect angles. The global field is obtained by an integration of the electric and magnetic currents induced on the objects (the so-called radiation integral). Figure 8-24 depicts the reference target RCS (in dB per m²) predicted by averaging the RCS obtained in four different frequencies of a generic L-band radar.

The next section applies the results of Figure 8-24 to predict the RCS during a generic BM flight.

8.7.1.2 BM Kinematic Model

Three main forces affect the BM motion: thrust, drag, and gravity [55, 77, 78]. The thrust and the drag deserve a more accurate modeling, which is reported later. The thrust acceleration depends on missile body mass M_b , fuel mass M_f , burn-out time t_{BO} , specific impulse I_{sp} , number of burn-out steps, gravity acceleration $g_0 = 9.8 \text{ m/s}^2$, and the rate with which the propellant is consumed during time. The thrust acts along the longitudinal axis of the rocket and, therefore, it is aligned with its velocity vector, whose direction is \mathbf{u}_v :

$$\mathbf{a}_{th} = \|\mathbf{a}_{th}\| \mathbf{u}_v \quad (8.1)$$

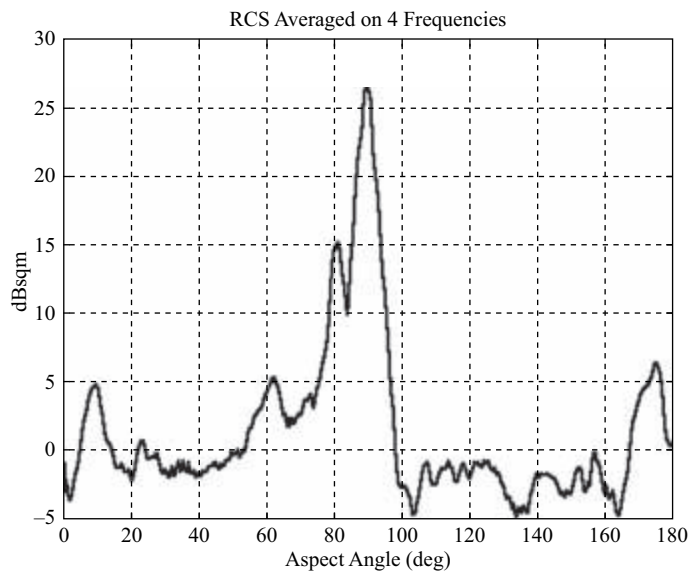


FIGURE 8-24 ■ Reference Target Prediction of RCS (L-band).

where $\|\cdot\|$ denotes the norm of the vector. The rocket can be assumed as single-stage, i.e., the propellant is consumed during the burn time (t_{BO}) in a linear fashion; to simplify the analysis, the specific impulse I_{sp} can be assumed to be known. Under these hypotheses, the norm of the thrust acceleration is

$$\|\mathbf{a}_{th}\| = g_0 I_{sp} \frac{M_{fuel}}{t_{BO} M(t)} \quad (8.2)$$

where $M(t)$ is the instantaneous time-varying mass of the rocket expressed in kg, which is a linear function of time:

$$M(t) = (M_b + M_f) \left(1 - m_f \frac{t}{t_{BO}} \right) \quad (8.3)$$

with M_b (kg) the empty missile mass and M_f (kg) the initial mass of the propellant. m_f is the fuel mass fraction given by

$$m_f = \frac{M_f}{M_b + M_f} \quad (8.4)$$

which represents a parameter of the propellant efficiency. The missile mass expression of Equation (8.3) is a linear function of time whose angular coefficient is $(-M_f/t_{BO})$ and whose initial value is $(M_b + M_f)$; sometimes it is used as a variable of the BM state vector. It is not necessary that the initial value of a variable of the filter state vector be unknown; however, its time evolution has to be correctly known to describe the transition in the tracking filter equations. The choice of the missile mass as a state vector component is not appropriate, and a new variable can be defined as the *normalized time* t_N :

$$t_N = \left(\frac{M_f}{t_{BO} M(t)} \right)^{-1} = t_{BO} \frac{M_b + M_f}{M_f} \left(1 - \frac{M_f}{M_b + M_f} \frac{t}{t_{BO}} \right) = t_{BO} \frac{M_b + M_f}{M_f} - t \quad (8.5)$$

whose initial value $t_{BO}(M_b + M_f)/M_f$ is still unknown, but the time evolution of the variable is linear with unitary slope. Hence, the norm of thrust acceleration can be expressed as a function of the normalized time as follows:

$$\|\mathbf{a}_{th}\| = \frac{g_0 I_{sp}}{t_N} \quad (8.6)$$

The thrust components are obtained by multiplying the total thrust acceleration by the components of the unitary vector of the velocity, obtaining the components of the vector \mathbf{a}_{th} :

$$\mathbf{a}_{th} = \begin{bmatrix} a_{th_x} \\ a_{th_y} \\ a_{th_z} \end{bmatrix} = \|\mathbf{a}_{th}\| \mathbf{u}_v = \frac{\|\mathbf{a}_{th}\|}{\sqrt{\dot{x}^2 + \dot{y}^2 + \dot{z}^2}} \begin{bmatrix} \dot{x} \\ \dot{y} \\ \dot{z} \end{bmatrix} = \frac{g_0 I_{sp}}{t_N} \frac{1}{\sqrt{\dot{x}^2 + \dot{y}^2 + \dot{z}^2}} \begin{bmatrix} \dot{x} \\ \dot{y} \\ \dot{z} \end{bmatrix} \quad (8.7)$$

Also, the drag acts on the missile motion; the corresponding acceleration expression is [77–79]:

$$\mathbf{a}_{drag} = \begin{bmatrix} a_{drag \ x} \\ a_{drag \ y} \\ a_{drag \ z} \end{bmatrix} = -\frac{1}{2} \frac{\rho(z) g_0}{\beta} \sqrt{\dot{x}^2 + \dot{y}^2 + \dot{z}^2} \begin{bmatrix} \dot{x} \\ \dot{y} \\ \dot{z} \end{bmatrix} \quad (8.8)$$

where β is the ballistic coefficient (N/m^2) and $\rho(z)$ is the air density (function of the height) [79]:

$$\begin{cases} \rho(z) = 1.21907e^{-z/9146.64} & \text{for } z < 9146.64 \text{ m} \\ \rho(z) = 1.754e^{-z/6707.536} & \text{for } z \geq 9146.64 \text{ m} \end{cases} \quad (8.9)$$

$\dot{x}, \dot{y}, \dot{z}$ are the velocity components of the BM along the three axes of a Cartesian reference system. Note that the Cartesian reference system is centered on the radar location and the three principal axes are directed as shown in Figure 8-25. This assumption is retained for all of the following simulations.

8.7.1.3 BM Detection

The dynamic model described in Section 8.8.1.2 has been used to generate a number of BM trajectories to test the detection and tracking procedures of a typical radar. An example of such trajectories is reported in Figure 8-25 for a BM with the following characteristics: $\beta = 30,000 \text{ N/m}^2$, $I_{sp} = 320 \text{ s}$, $M_b = 3,000 \text{ kg}$, $M_f = 2,900 \text{ kg}$, $t_{BO} = 65 \text{ s}$, single-stage BM, and linear consumption of propellant vs. flight time.

The BM trajectory is used to derive the RCS values along the missile flight time as depicted in Figure 8-26: From the target trajectory relative to the sensor, the radar-target aspect angle can be computed to feed Figure 8-24 and to get the RCS of the BM versus the BM flight time. Thus, the corresponding radar detection probability can be found by means of the radar equation as a function of a number of system parameters such as transmitted power, waveform, losses, and so on.

8.7.1.4 BM Tracking

This section describes the procedure to derive the EKF starting from the equations describing the forces acting on a BM (see Section 8.8.1.2). For sake of simplicity, the

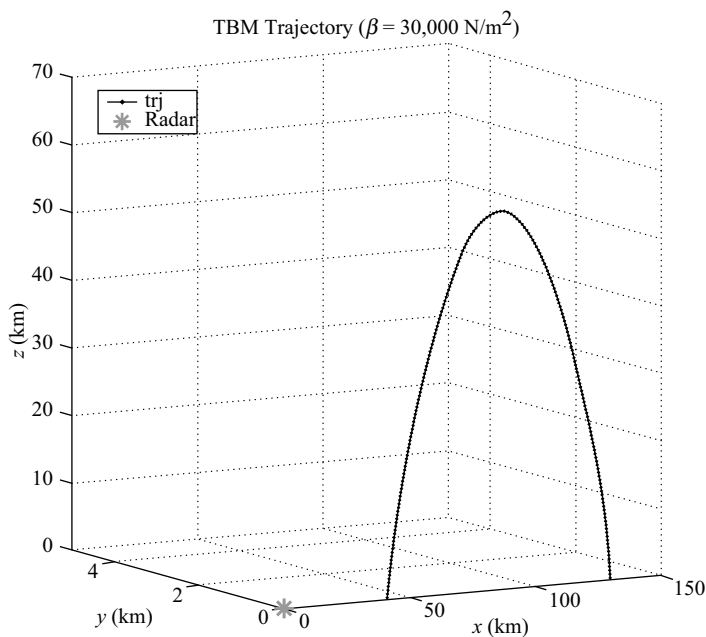


FIGURE 8-25 ■ An Example of a BM Trajectory.

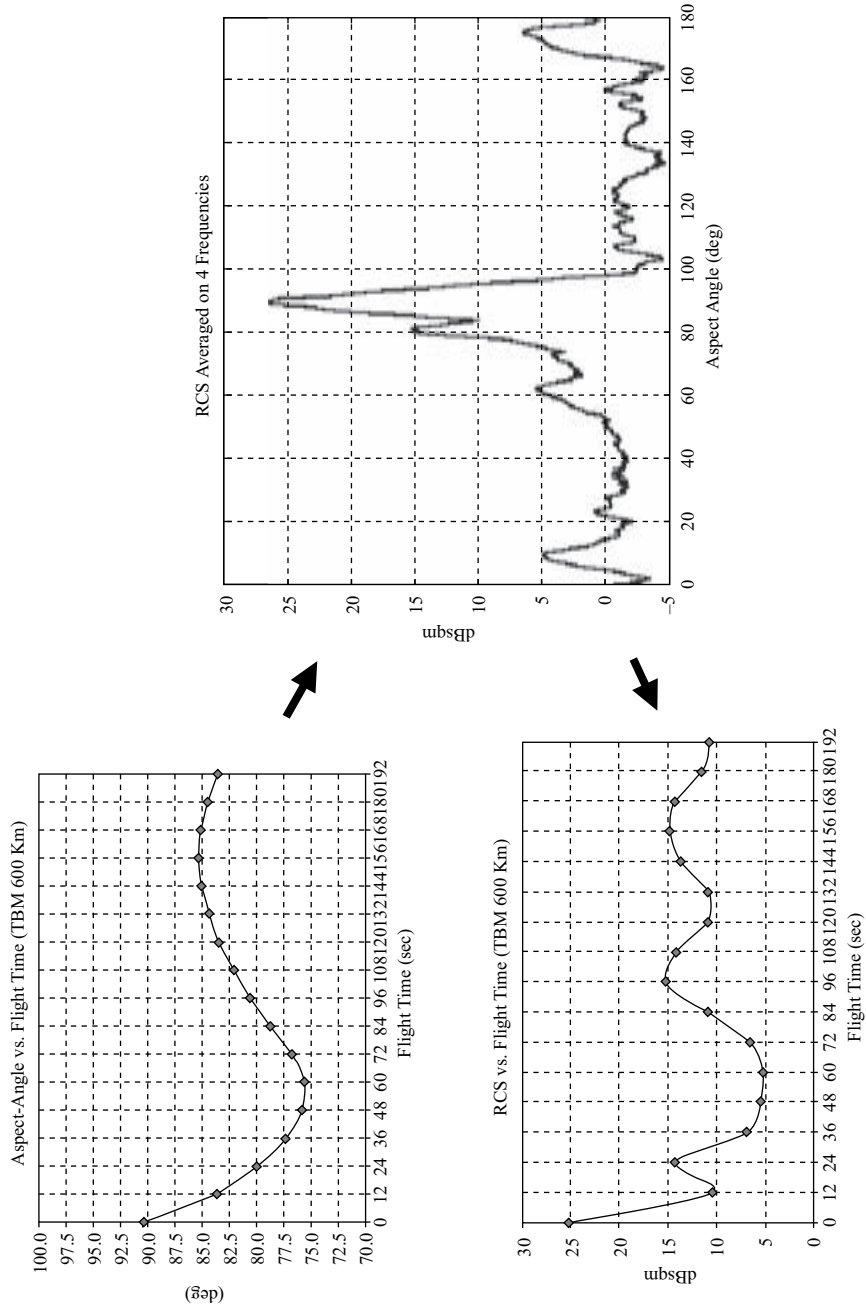


FIGURE 8-26 ■ Computed RCS vs. BM Flight Time.

hypothesis of flat earth is done and all the mathematical details connected to the change of coordinate system are not reported here. The theory of EKF is widely detailed in [53]. The EKF is used to account for the nonlinear target-state equation due to the presence of thrust acceleration and drag. At the k -th time instant, the state vector \mathbf{s}_k contains the position, the speed, and acceleration components of the target with respect to the Cartesian axes, the normalized time, and the ballistic coefficient:

$$\mathbf{s}_k = [x_k \quad \dot{x}_k \quad y_k \quad \dot{y}_k \quad z_k \quad \dot{z}_k \quad t_{Nk} \quad \beta_k]^T \quad (8.10)$$

The evolution of the state in time is

$$\mathbf{s}_{k+1} = \Phi \mathbf{s}_k + \mathbf{G}[\mathbf{a}_g + \mathbf{a}_{drag} + \mathbf{a}_{thrust}] + \mathbf{w}_k = \Phi \mathbf{s}_k + \mathbf{G}\mathbf{a}_g + \mathbf{f}_k(\mathbf{s}_k) + \mathbf{g}_k(\mathbf{s}_k) + \mathbf{w}_k \quad (8.11)$$

where Φ is the 8×8 state transition matrix:

$$\Phi = \begin{bmatrix} 1 & T & 0 & 0 & 0 & 0 & 0 & 0 \\ 0 & 1 & 0 & 0 & 0 & 0 & 0 & 0 \\ 0 & 0 & 1 & T & 0 & 0 & 0 & 0 \\ 0 & 0 & 0 & 1 & 0 & 0 & 0 & 0 \\ 0 & 0 & 0 & 0 & 1 & T & 0 & 0 \\ 0 & 0 & 0 & 0 & 0 & 1 & 0 & 0 \\ 0 & 0 & 0 & 0 & 0 & 0 & 1 & 0 \\ 0 & 0 & 0 & 0 & 0 & 0 & 0 & 1 \end{bmatrix} \quad (8.12)$$

\mathbf{G} is a 8×3 matrix where T is the radar scan time:

$$\mathbf{G} = \begin{bmatrix} T^2/2 & T & 0 & 0 & 0 & 0 & 0 & 0 \\ 0 & 0 & T^2/2 & T & 0 & 0 & 0 & 0 \\ 0 & 0 & 0 & 0 & T^2/2 & T & 0 & 0 \end{bmatrix}^T \quad (8.13)$$

The column vectors \mathbf{a}_g , \mathbf{a}_{drag} , and \mathbf{a}_{thrust} contain, respectively, the gravity, the drag, and the thrust acceleration components along the axes x , y , and z :

$$\mathbf{a}_g = \begin{bmatrix} a_{gx} \\ a_{gy} \\ a_{gz} \end{bmatrix} = \begin{bmatrix} 0 \\ 0 \\ -g_0 \end{bmatrix} \quad (8.14)$$

$$\mathbf{a}_{drag} = \begin{bmatrix} a_{drag_x} \\ a_{drag_y} \\ a_{drag_z} \end{bmatrix} = -\frac{1}{2} \frac{\rho(z)g_0}{\beta} \sqrt{\dot{x}^2 + \dot{y}^2 + \dot{z}^2} \begin{bmatrix} \dot{x} \\ \dot{y} \\ \dot{z} \end{bmatrix} = \quad (8.15)$$

$$\mathbf{f}_k(\mathbf{s}_k) = -\frac{1}{2} \frac{\rho(s_{k5})g_0}{s_{k8}} \sqrt{s_{k2}^2 + s_{k4}^2 + s_{k6}^2} \begin{bmatrix} s_{k2} \\ s_{k4} \\ s_{k6} \end{bmatrix}$$

$$\mathbf{a}_{thrust} = \begin{bmatrix} a_{thrust_x} \\ a_{thrust_y} \\ a_{thrust_z} \end{bmatrix} = \frac{g_0 I_{sp}}{t_N} \frac{1}{\sqrt{\dot{x}^2 + \dot{y}^2 + \dot{z}^2}} \begin{bmatrix} \dot{x} \\ \dot{y} \\ \dot{z} \end{bmatrix} = \quad (8.16)$$

$$\mathbf{g}_k(\mathbf{s}_k) = \frac{g_0 I_{sp}}{s_{k7}} \frac{1}{\sqrt{s_{k2}^2 + s_{k4}^2 + s_{k6}^2}} \begin{bmatrix} s_{k2} \\ s_{k4} \\ s_{k6} \end{bmatrix}$$

$f_k(s_k)$ is the nonlinear function that accounts for the drag contribution; $g_k(s_k)$ is the nonlinear function that models the thrust; both of them depend on the state components. w_k is the process noise: It has Gaussian pdf, with zero mean and nonsingular covariance matrix:

$$\mathbf{Q} = q \begin{bmatrix} \theta & 0 & 0 & 0 \\ 0 & \theta & 0 & 0 \\ 0 & 0 & \theta & 0 \\ 0 & 0 & 0 & \sigma_{t_N}^2 & 0 \\ & & & 0 & \sigma_\beta^2 \end{bmatrix} \quad (8.17)$$

with

$$\theta = \begin{bmatrix} T^3/3 & T^2/2 \\ T^2/2 & T \end{bmatrix} \quad (8.18)$$

and q is a scalar quantity accounting for the uncertainty on the target model; the variances $\sigma_{t_N}^2$ and σ_β^2 express the uncertainty on the normalized time and on the ballistic coefficient. The range of values assumed by β is wide: from about 4,000 N/m² to about 400,000 N/m², and it has a relevant impact on the trajectory shape.

The measurements collected by the radar are range ρ , azimuth, and elevation angles (θ, φ) . The error standard deviations of these measurements are, respectively σ_ρ , σ_θ , and σ_φ . The relationship between the target position in the Cartesian reference and the measurements is given by the polar coordinate transformation:

$$\begin{cases} x = \rho \cos \varphi \cos \theta \\ y = \rho \cos \varphi \sin \theta \\ z = \rho \sin \varphi \end{cases} \quad (8.19)$$

which is nonlinear; to make the relationship linear, we consider the coordinates $(x, y, \text{ and } z)$ as a new measurement vector. For all practical purposes, this is a good approximation that greatly simplifies the filtering implementation [80]. The measurement equation is

$$\mathbf{z}_k = [x_k \quad y_k \quad z_k]^T + \mathbf{v}_k = \mathbf{H}\mathbf{s}_k + \mathbf{v}_k \quad (8.20)$$

with

$$\mathbf{H} = \begin{bmatrix} 1 & 0 & 0 & 0 & 0 & 0 & 0 & 0 \\ 0 & 0 & 1 & 0 & 0 & 0 & 0 & 0 \\ 0 & 0 & 0 & 0 & 1 & 0 & 0 & 0 \end{bmatrix} \quad (8.21)$$

\mathbf{v}_k is the measurement error referred to Cartesian coordinates; it has a Gaussian pdf with zero mean and covariance matrix:

$$\mathbf{R}_k = \begin{bmatrix} \sigma_x^2 & \sigma_{xy} & \sigma_{xz} \\ \sigma_{xy} & \sigma_y^2 & \sigma_{yz} \\ \sigma_{xz} & \sigma_{yz} & \sigma_z^2 \end{bmatrix} \quad (8.22)$$

whose elements are [53]:

$$\begin{cases} \sigma_x^2 = \cos^2\theta (\sigma_\rho^2 \cos^2\varphi + \rho^2 \sigma_\varphi^2 \sin^2\varphi) + \rho^2 \sigma_\theta^2 \sin^2\theta \cos^2\varphi \\ \sigma_y^2 = \sin^2\theta (\sigma_\rho^2 \cos^2\varphi + \rho^2 \sigma_\varphi^2 \sin^2\varphi) + \rho^2 \sigma_\theta^2 \cos^2\theta \cos^2\varphi \\ \sigma_z^2 = \sigma_\rho^2 \sin^2\varphi + \rho^2 \sigma_\varphi^2 \sin^2\varphi \\ \sigma_{xy} = \frac{1}{2} \sin 2\theta \left[(\sigma_\rho^2 - \rho^2 \sigma_\theta^2) \cos^2\varphi + \rho^2 \sigma_\varphi^2 \sin^2\varphi \right] \\ \sigma_{xz} = \frac{1}{2} \cos\theta \sin 2\varphi (\sigma_\rho^2 - \rho^2 \sigma_\varphi^2) \\ \sigma_{yz} = \frac{1}{2} \sin\theta \sin 2\varphi (\sigma_\rho^2 - \rho^2 \sigma_\varphi^2) \end{cases} \quad (8.23)$$

Given the state $\hat{s}_{k/k}$ at the k -th time instant, with the corresponding estimation covariance matrix $\mathbf{P}_{k/k}$, the prediction at time instant $k+1$ is

$$\hat{s}_{k+1/k} = \Phi \mathbf{s}_k + \mathbf{G}[\mathbf{a}_g + \mathbf{f}_k(\mathbf{s}_k) + \mathbf{g}_k(\mathbf{s}_k)] \quad (8.24)$$

and the covariance matrix of the predicted state is

$$\mathbf{P}_{k+1/k} = (\Phi + \mathbf{G}\mathbf{J}_k)\mathbf{P}_{k/k}(\Phi + \mathbf{G}\mathbf{J}_k)^T + \mathbf{Q} \quad (8.25)$$

where \mathbf{J}_k (3×8 matrix) is the sum of the Jacobian of the nonlinear functions $\mathbf{f}_k(\mathbf{s}_k)$ and $\mathbf{g}_k(\mathbf{s}_k)$ calculated at the state $\hat{s}_{k/k}$ estimated at the previous step. The Jacobian is

$$\mathbf{J}_k = \mathbf{F}_k + \mathbf{G}_k = [\nabla_{s_k} \mathbf{f}_k^T(\mathbf{s}_k)]^T + [\nabla_{s_k} \mathbf{g}_k^T(\mathbf{s}_k)]^T \quad (8.26)$$

The previously described EKF model can be used to track targets with ballistic models, even with an initially unknown ballistic coefficient, but if inserted in an IMM architecture (Figure 8-27), it provides additional advantages:

1. The radar system operates in a “dense” environment, i.e., in the presence of a number of different threats, like air-breathing targets (ABTs), anti-radiation missiles, BMs, and others. A different EKF filter can be designed for each type of target in the environment and all together interact via IMM.
2. BMs may in general change their dynamics as a function of the flight time; the boost is present in the first part of the trajectory and it is followed by the cruise and the re-entry phases. Thus, it is required to account for the target maneuvers starting at some

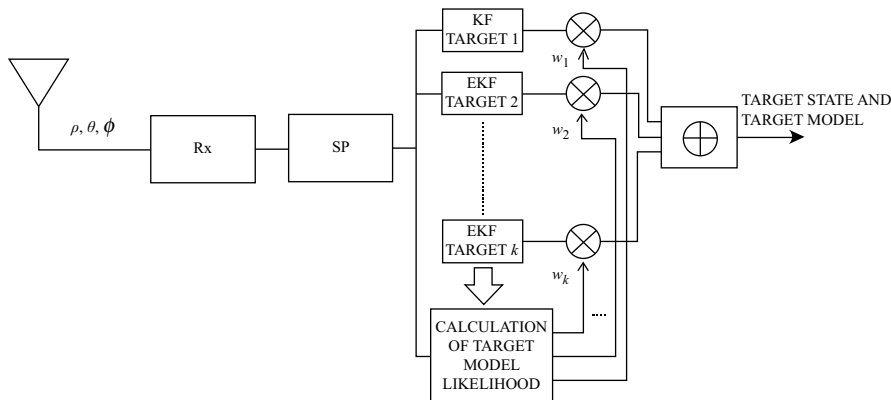


FIGURE 8-27 ■ Typical Block Scheme of an MM Filter. Weights w_k Related to the Probability of Model k given the Measurements.

time during the estimation interval, in which case a model change occurs. The changing of the target model is controlled by the computation of the IMM mixing probabilities and the interactions among the implemented target models.

3. The BM characteristics are not generally a priori known; thus, it is required to estimate online the BM parameters to improve the track accuracies. The IMM mixes the outputs of a bank of different filters designed for different BMs, each one adapting its estimated parameters to the tracked target, thus permitting the best tracking of BMs pertaining to different “classes.”
4. The IMM likelihood provides for each filter in the bank a clear indication of the confidence of the tracker on the type of target under analysis; this is an intrinsic capability of non-cooperative target classification available “for free” by the IMM.

Multiple model MM approaches (IMM, MMFM [multiple model for fixed model], and others) have an intrinsic capability of target classification. Through the MM filter development, in fact, it is possible to extrapolate classification information from the model probability of the different filters selected. The principal purpose in this case is to have some hooks into the system to deliver some preliminary ABT or BM flag and, therefore, use that early information to determine successive radar functions (i.e., imaging for refined identification).

Discrimination calculations are based on the weight assigned to each filter implemented into MM. Let’s say that the filters into MM are of two different families:

- Kalman filters (KF) to estimate the threats with kinematics typical of an ABT and more generally for highly maneuvering target, and
- Extended Kalman filters (EKF) designed to track threats with ballistic nonlinear kinematics (i.e., the BM in reentry phase).

8.7.1.5 Simulated Scenarios and Results

Three simulated scenarios are presented here. The following radar parameters have been maintained constant for the scenarios: range accuracy = 25 m, azimuth accuracy = 0.15° , elevation accuracy = 0.2° , and the $P_d = 0.9$. The IMM for scenarios 1 and 3 is designed as follows: a KF with the state vector equal to $(x, \dot{x}, y, \dot{y}, z, \dot{z})$ matched to ABTs with constant velocity (6 degrees of freedom); a KF with the state vector equal to $(x, \dot{x}, \ddot{x}, y, \dot{y}, \ddot{y}, z, \dot{z}, \ddot{z})$ matched to maneuver ABTs (9 degrees of freedom); an EKF with the state vector equal to $(x, \dot{x}, y, \dot{y}, z, \dot{z}, \beta)$ matched to “multistage” BM (initial value of the ballistic coefficient equal to $40,000 \text{ N/m}^2$); an EKF with the state vector equal to $(x, \dot{x}, y, \dot{y}, z, \dot{z}, \beta)$ matched to “one-stage” BM (initial value of the ballistic coefficient equal to $200,000 \text{ N/m}^2$). For scenario 2, the IMM is slightly different and it will be detailed later. The BM under track is described in Section 8.8.1.3.

Scenario no. 1. This simulation has the purpose of illustrating the working principle of the IMM showing the update probability model of a tracking architecture constituted by two KFs: The first KF has been designed for ABT with a constant velocity, while the second KF is pertinent to a maneuvering ABT. The simulated ABT trajectory is shown in Figure 8-28 in the xy plane, while the IMM probabilities are reported in Figure 8-29. In Figure 8-29 the transitions from one filter to the other are shown: The IMM selects the filter matched to the ABT kinematics, i.e., the update probability of the KF matched to

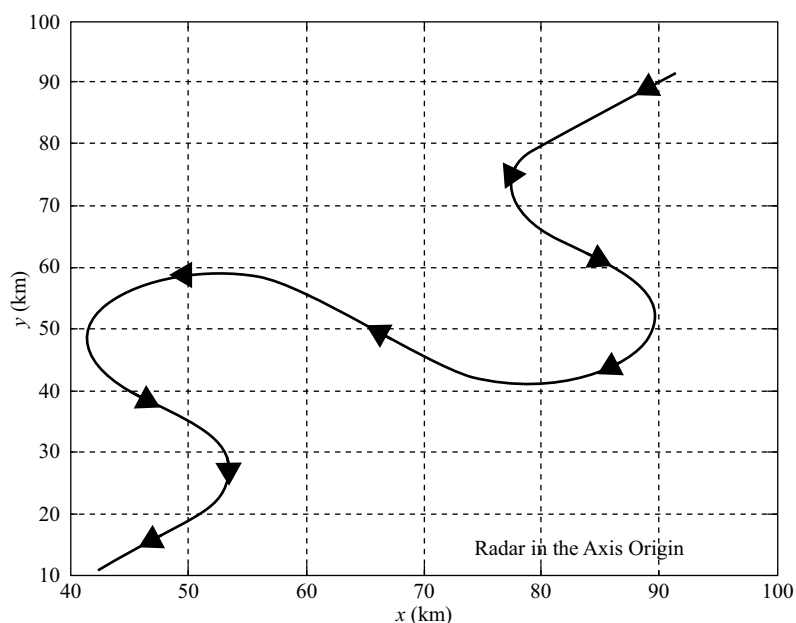


FIGURE 8-28 ■
ABT Reference
Trajectory.

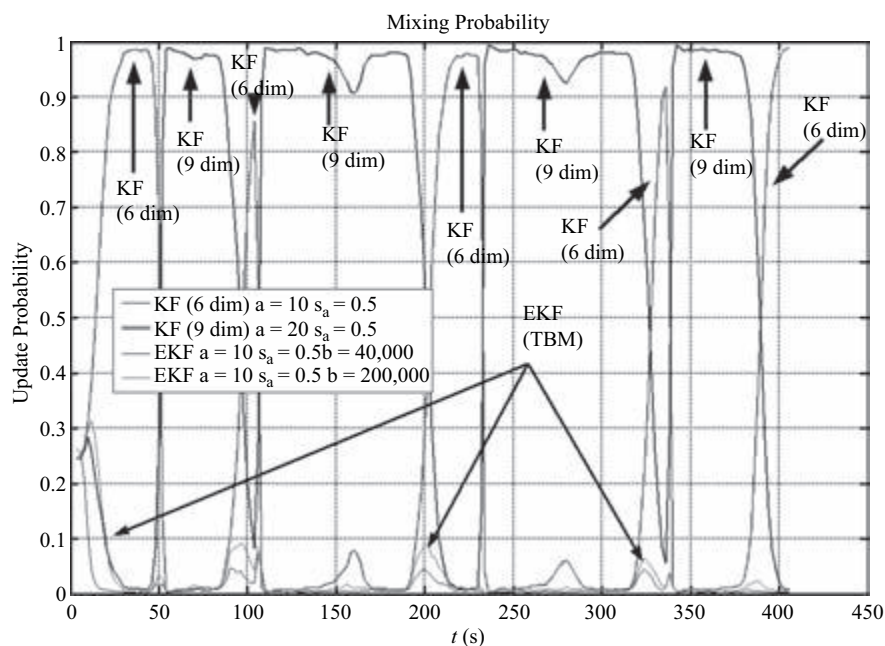


FIGURE 8-29 ■
Update Probability of the IMM Filters. (KF: Kalman filter, EKF: Extended Kalman Filter, $b = \beta$ = Ballistic Coefficient Starting Value, a = Reciprocal of the Expected Target Maneuver Time Duration, s_a = Standard Deviation of Acceleration).

the ABT model is practically equal to 1, while the analogous probability of the filters mismatched to the ABT kinematics is practically 0.

Scenario no. 2. This scenario has been considered to demonstrate the benefit of including a suitable boost acceleration filter in the IMM. The BM described in Section 8.8.1.3 (see also Figure 8-25) is adopted in the simulation. Figure 8-30 presents the

FIGURE 8-30 ■ Mean Value and Standard Deviation Along z-axis; No boost filter used.

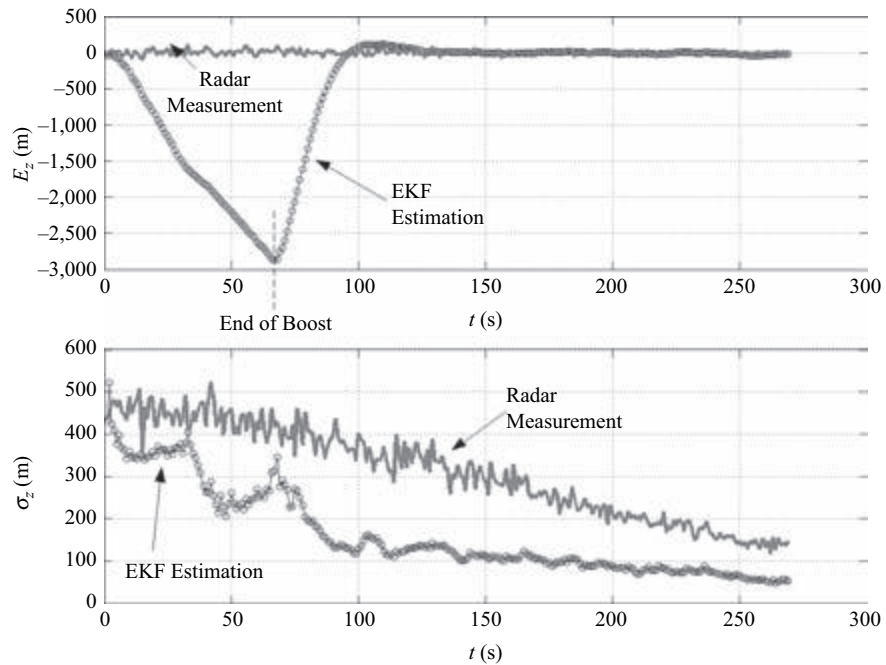
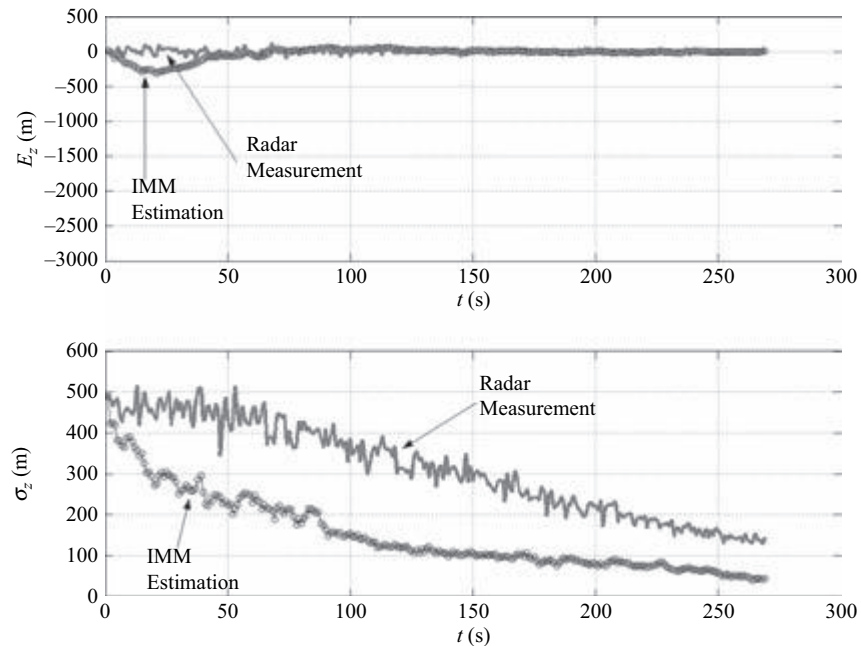


FIGURE 8-31 ■ Boost Filter Included in the IMM.



accuracy results along the z -axis achieved with an EKF designed for a cruise and re-entry phases of the BM. The upper curves are related to the mean value of the position error; lower curves are related to the error standard deviation. The EKF is not matched to the boost phase of BM; thus, the error in the mean value is evident. Figure 8-31 refers

to the same simulation, but the tracker is an IMM with two EKFs; the first is matched to the BM cruise and re-entry phases, while the second is designed for the boost phase; the benefit of the boost phase filter appears in the reduced mean value of the tracker error. For this scenario, it is assumed an a priori knowledge of the BM characteristics.

Scenario no. 3. This simulation shows the capability of the IMM architecture to be adaptive to the unknown BM characteristics. Consider the case of absence of knowledge of β , I_{sp} , and the other BM parameters of the BM under tracking. The IMM architecture is constituted by a number of EKFs matched to the BM dynamics (see Section 8.8.1.4), each filter having the capability of estimating online the BM characteristics (for instance, the β as a value).

Figure 8-32 reports the mean value and the standard deviation of the estimated error along the z -axis before and after the tracker filtering for the BM presented in Figure 8-25.

For the sake of simplicity, only the cruise and re-entry phases of the BM have been filtered. Note that the IMM is capable of tracking the BM by adaptively adjusting the EKF parameters during the BM flight time. The accuracy reported along the z -axis of Figure 8-32 is similar to the same quantity presented in Figure 8-31 that was achieved, assuming a perfect knowledge of the ballistic target characteristics. The lesson learned is to design EKFs filter matched to “general” BM motion equations and develop a tracking architecture based on the IMM that allows the user to maintain under track BMs with unknown “kinematic parameters.” It is also important to note that the conceived tracking architecture has an intrinsic classification capability.

Figure 8-33 reports the internal behavior of the four filters previously described and includes one KF with 6 degrees of freedom, one KF with 9 degrees of freedom, and two EKFs with initial β value equal to b in the picture (while a is related to the injected plant noise). The internal behavior is fully described by the mixing probability: In this case, the EKFs have been selected after few seconds from the track initialization, and the confidence of the IMM is practically equal to 1. This constitutes reliable information about the type (either BM or ABT) of target under tracking.

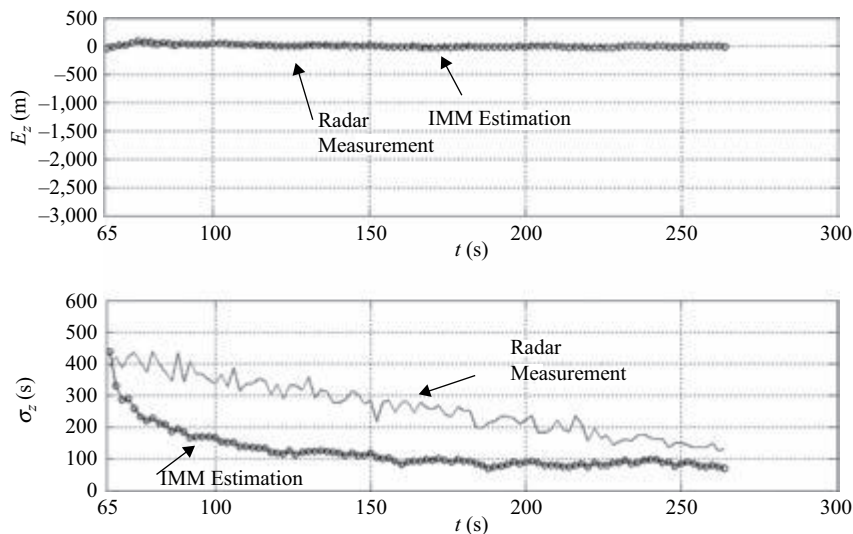
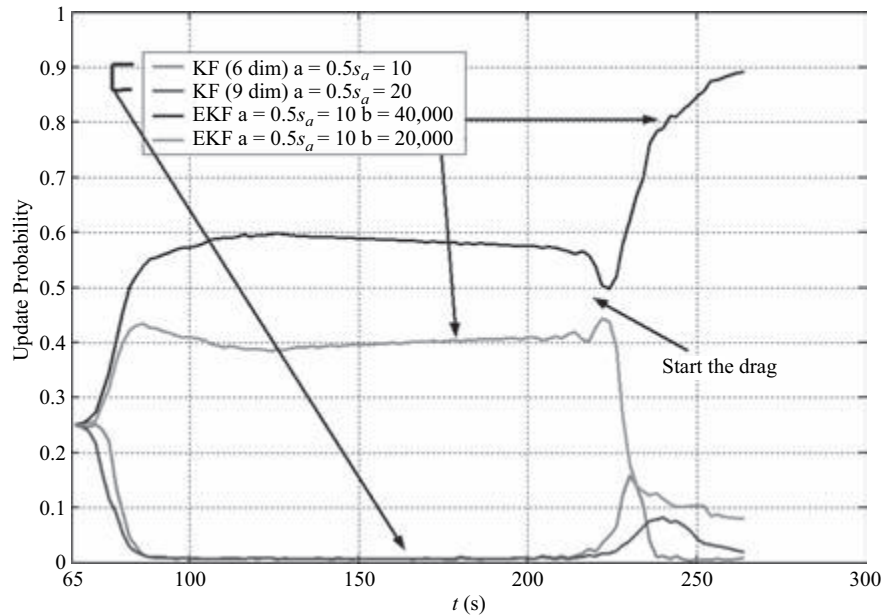


FIGURE 8-32 ■ Accuracy of the IMM in the Presence of an Unknown BM.

FIGURE 8-33 ■ Update Probability of the IMM (KF: Kalman Filter, EKF: Extended Kalman Filter, $b = \beta$ = Ballistic Coefficient Starting Value, a = Reciprocal of the Expected Target Maneuver Time Duration, s_a = Standard Deviation of Acceleration).



8.7.1.6 Anti-Radar Missile (ARM) Detection and Alert

GBEWR exploits several techniques to prevent detection by an intercept receiver, thus making it difficult for an ARM to lock on the radar emission.

1. The used transmitted waveform spreads the energy spectrum of the radar over the widest possible band. The use of a pseudo-random code prevents the intercept receiver from performing a matched filter to the radiated waveform. In fact, the transmitted frequency of the GBEWR can be selected either in a random fashion or under the control of the AFS device, among, say, hundreds frequency values within hundreds of MHz in the radar band. The GBEWR also adopts irregular modulation types of the transmitted waveform, such as pulse trains with nonuniform and staggered PRFs; it also uses variable dwell time and it changes the waveforms during the operation.
2. Most intercept receivers are designed to detect short radar pulses; coherence between radar pulses in a pulse train is generally ignored. Also, there is a little capability against pulse compression or noise-like radar waveforms. The time-bandwidth product of the radar code within the transmitted pulse should be as large as possible. In fact, this product expresses the relative mismatch between the transmitted radar waveform and the intercept receiver.
3. An ultra-low sidelobe antenna reduces the radiation level through the radar's sidelobes. This follows, since most ARMs are designed to attack through the radar's sidelobes where the signal is continuously available. The GBEWR looks for sidelobe level better than 45 dB down to the peak of the antenna main beam, thus making it difficult for an intercept receiver to detect and locate the EM radiation source.

4. A narrow beam in azimuth and in elevation reduces the volume of the space where the radar energy is radiated. This is important against that ARM that is sensitive to the flashes of energy radiated by the radar mainbeam. The lower beam in elevation of the GBEWR, which is the one that may be intercepted by a far ESM (electronic support measures) platform from which the ARM could be launched, has typical width values around 2° for the azimuth and elevation, respectively.
5. The GBEWR has a low-peak power combined with a multiple beam in elevation. This is advantageous with respect to another system solution built around a single beam with a high-peak power transmitter.
6. A typical GBEWR may have an elevation coverage up to, say, 30° . This means that an ARM that is approaching the radar flying, say, at 20,000 m altitude, is within the radar coverage up to approximately 60 km from the radar site. This means that the GBEWR has many opportunities to detect the ARM before the threat penetrates within the zenithal hole region above the radar where its detection capability is minimal.
7. When a track is radial toward the radar and a suspect rises that the ARM is locking on to the radar, then the natural defense of GBEWR is simply either to turn off the transmission or to activate suitably located transmitting decoys. In fact, any interruption of the radar's radiations leads to a complete loss of guidance information to the ARM.

8.7.2 Low Probability of Intercept (LPI)

It is generally accepted [81] that a quantitative measure of the radar efficiency in the presence of an ESM receiver is computed via the following equation:

$$\alpha^4 = \frac{1}{4\pi} \left(\frac{E_T}{\eta_I} \right) \left(\frac{T_R}{T_I} \right) \left(\frac{1}{\tau B_I} \right)^2 \left(\frac{L_R}{L_I^2} \right) \left(\frac{\lambda^2}{\sigma} \right) \left(\frac{S_R(n)}{S_I^2(1)} \right) \left(\frac{G_{TI}^2 G_I^2}{G_T G_R} \right) \quad (8.27)$$

where

$\alpha = R_I/R_m$,

R_I = ESM detection range,

R_m = radar detection range,

E_T = energy transmitted by the radar,

η_I = ESM system noise spectral density, i.e., KT_I , K = Boltzman constant,

T_I = ESM system noise temperature,

T_R = radar system noise temperature,

τ = radar pulse time duration,

B_I = ESM bandwidth,

L_R = radar losses,

L_I = ESM losses,

λ = radar wavelength,

σ = target radar cross section,

$S_R(n)$ = single-pulse useful signal to system noise power ratio (SNR) for the radar having fixed P_d (detection probability), P_{fa} (false alarm probability), and n pulses to be integrated,

$S_I(1)$ = single-pulse SNR for the interceptor having fixed P_d and P_{fa} ,
 G_{TI} = radar antenna gain along the interceptor direction of arrival,
 G_I = interceptor antenna peak gain,
 G_T = radar antenna transmission peak gain, and
 G_R = radar antenna receiving peak gain.

A value for α lower than 1 indicates an advantage for the radar being able to detect the ESM at a higher distance with respect to the ESM detection range being the radar the target to be revealed. If α is higher than 1, then the ESM has an advantage with respect to the radar. The distance corresponding to $\alpha = 1$ is called the *quiet range*. For ranges higher than the quiet range ($\alpha > 1$), the ESM detects the radar before the radar detects the ESM; on the contrary, before the quiet range ($\alpha < 1$), the radar detects the ESM before being detected by the ESM.

8.7.2.1 Discussion on the Evaluation of the Radar LPI Capability

Equation (8.27) has been obtained by combining the two equations that give the SNR value in correspondence of the radar antenna (produced by the echo reflected by the ESM) and the SNR in correspondence of the ESM antenna (produced by radar emission). The two equations are

$$\begin{aligned}
 S_R(n) &= \frac{P_T G_T}{4\pi R_m^2} \frac{\sigma}{4\pi R_m^2} \frac{G_R \lambda^2}{4\pi} \frac{1}{L_R} \frac{\tau}{KT_R} \\
 S_I(1) &= \frac{P_T}{4\pi R_I^2} G_{TI} \frac{G_I \lambda^2}{4\pi} \frac{1}{L_I} \frac{1}{KT_I B_I}
 \end{aligned} \tag{8.28}$$

The following considerations are in order:

1. Radars transmitting very high peak power are most easily detectable by the ESMs because E_T increases α .
2. The lower the ESM RCS, the higher the radar difficulty to detect it; in fact, σ increases α . RCS equal to 1 m² is generally selected for the evaluation.
3. G_{TI} represents the radar antenna gain along the ESM direction of arrival. If the ESM is in the antenna mainbeam, then G_{TI} is the radar antenna peak gain usually determined by other factors than the LPI capability. If the interceptor is in the antenna sidelobes, then G_{TI} is the sidelobes' value itself. Low-antenna sidelobes are clearly advantageous.
4. The (τB_I) product is a measure of the matching between the radar waveform and the receiver bandwidth. The radar objective is to increase the product as much as possible to minimize α ; the ESM objective is $\tau B_I = 1$. For the purpose of this section, B_I is approximated following the procedure (assuming a square law detection) suggested in [81]:

$$B_I = \sqrt{2B_{RF}B_V} \tag{8.29}$$

where B_{RF} is called “pre-detection bandwidth” and B_V “post-detection bandwidth.” If we hypothesize that the ESM does not exactly know the radar carrier frequency, then B_{RF} is considerably larger than the minimum required. B_V is, in general, selected such that very short pulses can be transmitted (τ_{min}); a common

choice is $B_V = 0.5/\tau_{min}$. A mismatching factor is defined as $M = \tau/\tau_{min}$, and the ESM bandwidth becomes

$$B_I = \sqrt{MB_{RF}/\tau} \quad (8.30)$$

After all, (τB_I) can be rewritten as

$$(\tau B_I)^2 = MB_{RF}\tau = M^2 B_{RF} \tau_{min} \quad (8.31)$$

Let us consider the case of a coded pulse. The ESM computes the envelope of the radar signal, regardless of the coded modulation; this means that the coded pulse appears to the ESM as a longer uncoded pulse. Let us denote by β the compression ratio of the coded pulse fired by the radar and by $M_P = \tau_{EFF}/\tau_{min}$ the ratio between the time duration of the compressed pulse (τ_{EFF}) and τ_{min} defined earlier; then the product $(\tau B_I)^2$ is equal to

$$(\tau B_I)^2 = \beta^2 M_P^2 B_{RF} \tau_{min}$$

From this new expression of the τB_I product, it stems that α is inversely proportional to β ; the radar should have very large β to be effective from the LPI perspective.

In conclusion, we can claim that a radar firing a long coded pulse with low peak power is advantageous for the “radar quietness”; this generally occurs in the radar of the class described in this chapter.

8.7.3 Denial of Bistatic Hosting by Waveform Design

Many countries have heavily invested in the development of advanced surveillance systems and technologies. An increasing concern is that potential adversaries may use bistatic technologies to gain capability versus significant investments in advanced sensors [82]. Indeed, with relatively inexpensive receiver systems, an adversary can use other signals as bistatic “illuminators of opportunity.”

The bistatic radar needs to acquire the illuminator signal and to correlate it as coherent reference signal versus the received signals acquired on the targets directions of arrival (TDoA). As illustrated in Figure 8-34, a coherent reference is typically obtained by measuring a direct path signal via the sidelobes of the illuminator [83].

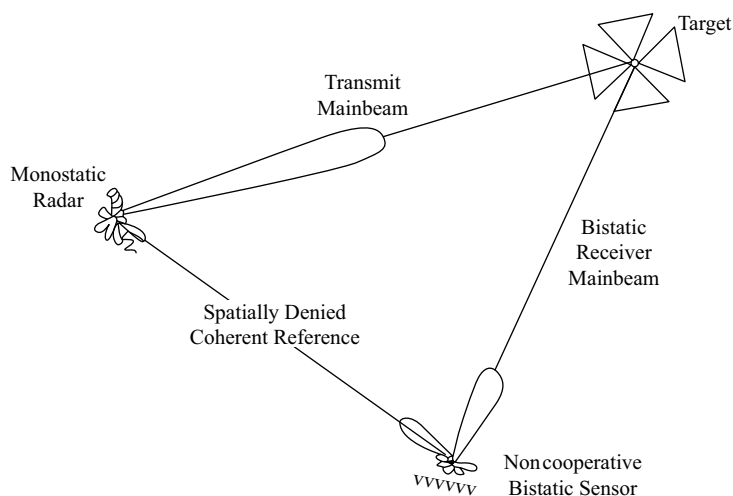
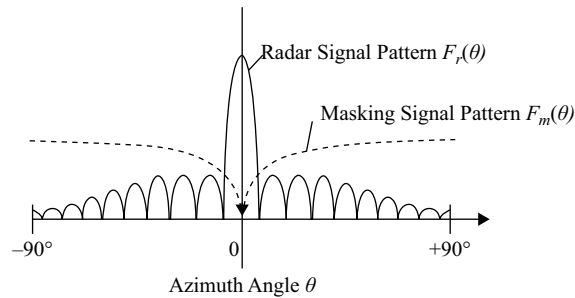


FIGURE 8-34 ■ Noncooperative Bistatic Receivers Require Coherent Reference from the Host Illuminator.

FIGURE 8-35 ■
Radar and Masking
Signal Radiation.



If conventional methods to prevent the interception of the direct path signal include low sidelobe antennas, physical isolation, and the use of spread spectrum waveforms, in [82], a number of theoretical techniques have been introduced and evaluated to prevent a radar being used by an adversary as a bistatic illuminator of opportunity. All of these techniques are based on the idea of radiating a so-called “masking signal” (Figure 8-35), which is arranged to be approximately orthogonal, both in a spatial sense and in a coding sense, to the radar signal, and on the idea of a sufficient level to mask the radar signal to an adversary, and hence, to deny a reference for bistatic operation.

Therefore, the solution needs to find a radar waveform $u_r(t)$ with suitable ambiguity function and a masking waveform $u_m(t)$ that is approximately orthogonal to the radar waveform over the full range and Doppler domain. So if the radar waveform is radiated via a pattern $F_r(\theta)$ and the masking waveform $u_m(t)$ is radiated via a pattern $F_m(\theta)$, then $F_r(\theta)$ and $F_m(\theta)$ need to be approximately spatially orthogonal over the full bandwidth of the radar.

A number of waveform coding techniques have been analyzed in [82], and among those considered, Costas codes appear to offer the best performance and flexibility. Two spatial coding techniques have been devised and analyzed—one based on an interferometer, and one based on a Butler matrix.

Expressions as a function of the system parameters have been derived for the degree of hiding of the radar signal by the masking signal, and for the suppression of the masking signal in the host radar echo. Evaluation and plotting of these expressions have demonstrated that it is possible to obtain adequate masking of the radar signal, while at the same time achieving suppression of echoes from the masking signal of the order of 30 or 40 dB: with respect to this capability, the performance given by the interferometer and by Butler matrix schemes are comparable.

8.8 | CONCLUSIONS AND FURTHER READING

In this chapter, we have described GBEWR, providing some historical, theoretical, and technological details.

Specifically, we first introduced the concept of GBEWR and emphasized its importance. Then, we traced back the history of EWR up to the current days, also providing an overview of some commercial products. Then, we focused on transmitter-receiver as well as antenna technology, with an emphasis on the SELEX Sistemi Integrati state of the art.

We also discussed advanced signal and data processing techniques exploited in GBEWR—for instance, the important function of BM tracking.

For further reading, the authors recommend some classic textbooks on the story of EWR and in general radar systems such as [84–87].

The chapter is focused on GBEWR, and in order to complete an understanding of EWR, a text on airborne EWR is necessary. In this context, we recommend [88]. In addition, an overview of OTHR is fundamental and, to this end, we suggest [9].

Finally, the seminal paper [89] represents an interesting contribution to the topic of upgrading obsolete GBEWRs for homeland security protection.

8.9 | REFERENCES

- [1] Wikipedia, http://en.wikipedia.org/wiki/Early_warning_radar.
- [2] M. Skolnik, *Radar Handbook*, McGraw-Hill, 3rd Ed., 2008.
- [3] R. W. Sturdevant, “Radar, Long-Range Early Warning Systems,” *Encyclopedia of 20th-Century Technology*, <http://www.bookrags.com/tandf/radar-long-range-early-warning-tf/>.
- [4] H. Griffiths and N. Willis, “Klein Heidelberg – The First Modern Bistatic Radar System,” *IEEE Trans. on Aerospace and Electronic Systems*, Vol. 46, No. 4, pp. 1571–1588, October 2010.
- [5] S. N. Stitzer, “Reverberations – The SCR-270 Radar,” *IEEE Microwave Magazine*, Vol. 8, pp. 88–98, June 2007.
- [6] E. Brookner, *Practical Phased Array Antenna Systems*, Artech House, 1991.
- [7] D.H. Sinnott, “The Development of Over-the-Horizon Radar in Australia,” 1988, http://www.dsto.defense.gov.au/attachments/The_development_of_over-the-horizon_radar.pdf.
- [8] D. H. Sinnott, “Defense Radar Development in Australia: 1939 to the Present,” *IEEE Intern. Radar Conference*, pp. 5–9, 2005.
- [9] G. A. Fabrizio, *High Frequency Over-the-Horizon Radar – Fundamental Principles, Signal Processing, Practical Applications*, McGraw-Hill Professional, San Francisco, CA, 2013.
- [10] “NADGE”, http://www.namsa.nato.int/gallery/ws_nadge_e.htm.
- [11] C. P. Satterthwaite, “Space Surveillance and Early Warning Radars: Buried Treasure for the Information Grid,” <http://www.dtic.mil/cgi-bin/GetTRDoc?Location=U2&doc=GetTRDoc.pdf&AD=ADA468199>.
- [12] A. Odile, “Modular Design Principles for Missile Defense Early Warning Radar,” *International Radar Conference - Surveillance for a Safer World*, October 2009.
- [13] http://www.selex-es.com/IT/Common/files/SelexSI/brochure_datasheet/2008/Data_Sheet/RAT_31DL.pdf.
- [14] http://www.thalesraytheon.com/fileadmin/tmpl/Products/pdf/111058_GM400_Paris_Update_v3_LR.pdf.
- [15] <http://www.lockheedmartin.com/data/assets/7152.pdf>.
- [16] JANE’S: www.janes.com (*Defense Equipment and Technology Section*).
- [17] <http://www.maquina-de-combate.com/articulo/3d-lanza-family-radars.pdf>.
- [18] http://www.baesystems.com/BAEProd/groups/public/documents/bae_publication/038035.pdf.

- [19] http://www.selex-es.com/IT/Common/files/SelexSI/brochure_datasheet/datasheet_terrestri/LR/RAT31DLM.pdf.
- [20] http://www.raytheon.com/capabilities/rtnwcm/groups/ncs/documents/content/rtn_ncs_products_mastern_pdf.pdf.
- [21] <http://www.lockheedmartin.com/data/assets/8408.pdf>.
- [22] R. J. Galejs, "Volume Surveillance Radar Frequency Selection," *Proc. of IEEE Intern. Radar Conference*, Alexandria (Va), pp. 187–192, 7–12 May 2000.
- [23] B. Palumbo, "Some Example of Systems Developments in Italy Based on Phased-Array Technology," *IEEE Intl. Symposium on Phased Array Systems and Technology*, Boston (Ma), pp. 444–449, 15–18 October 1996.
- [24] M. Cicolani, A. Farina, E. Giaccari, F. Madia, R. Ronconi, and S. Sabatini "Some Phased Array Systems and Technologies in AMS," *IEEE Intl. Symposium on Phased Array Systems and Technology*, Boston (Ma), 14–17 October 2003.
- [25] A. Fiorello, M. Grossi, and S. Pagliai, "Advances in Radar Systems by SELEX Sistemi Integrati: Today and Towards the Future," *6th European Radar Conference (EuRAD 2009)*, Rome, Italy, 30 September–2 October 2009.
- [26] A. Cetronio, M. D'Urso, A. Farina, A. Fiorello, L. Timmoneri, and M. Teglia, "Phased Array Systems and Technologies in SELEX-Sistemi Integrati: State Of Art and New Challenges," Invited Aasplenary talk, *Phased-Array 2010 Symposium*, Boston (USA), October 2010.
- [27] "ITRS International Technology Roadmap for Semiconductors – System Drivers," 2007, http://www.itrs.net/links/2007itrs/2007_chapters/2007_SystemDrivers.pdf.
- [28] M. A. Richards, J. A. Scheer, and W. A. Holm, "Principles of Modern Radar: Basic Principles," Vol. 1, *SciTech*, May 2010.
- [29] C. E. Cook and M. Bernfield, *Radar Signals: An Introduction to Theory and Application*, New York, Academic Press, 1967.
- [30] D. F. DeLong, and E. M. Hofstetter, "On the Design of Optimum Radar Waveforms for Clutter Rejection," *IEEE Trans. on Inform. Theory*, Vol. 13, No. 3, pp. 454–463, July 1967.
- [31] C. Stutt, and L. Spafford, "A Best Mismatched Filter Response for Radar Clutter Discrimination," *IEEE Trans. on Inform. Theory*, Vol. 14, No. 2, pp. 280–287, March 1968.
- [32] Y. I. Abramovich, and M. B. Sverdlik, "Synthesis of a Filter Which Maximizes the Signal-to-Noise Ratio Under Additional Quadratic Constraints," *Radio Eng. Electron. Phys.*, Vol. 15, No. 11, pp. 1977–1984, November 1970.
- [33] V. T. Dolgochub, and M. B. Sverdlik, "Generalized-Filters," *Radio Eng. Electron. Phys.*, Vol. 15, pp. 147–150, January 1970.
- [34] P. Stoica, J. Li, and M. Xue, "Transmit Codes and Receive Filters for Radar," *IEEE Signal Processing Magazine*, Vol. 25, No. 6, pp. 94–109, November 2008.
- [35] S. D. Blunt, and K. Gerlach, "Adaptive Pulse Compression via MMSE Estimation," *IEEE Trans. on Aerospace and Electronic Systems*, Vol. 42, No. 2, pp. 572–584, April 2006.
- [36] Y. I. Abramovich, and M. B. Sverdlik, "Synthesis of Filters Maximizing the Signal-to-Noise Ratio in the Case of a Minimax Constraint on the Sidelobes of the Crossambiguity Function," *Radio Eng. Electron. Phys.*, Vol. 16, pp. 253–258, February 1971.
- [37] S. Zoraster, "Minimum Peak Range Sidelobe Filters for Binary Phase-Coded Waveforms," *IEEE Trans. on Aerospace and Electronic Systems*, Vol. 16, No. 1, pp. 112–115, January 1980.

- [38] H. M. Finn, "Adaptive Detection in Clutter," *Proc. of the National Electronics Conference*, Vol. 22, pp. 562–567, 1966.
- [39] B. O. Steenson, "Detection Performance of a Mean Level Threshold," *IEEE Trans. on Aerospace and Electronic Systems*, Vol. 4, No. 4, pp. 529–534, July 1968.
- [40] H. M. Finn, and R. S. Johnson, "Adaptive Detection Mode with Threshold Control as a Function of Spatially Sampled Clutter-Level Estimates," *RCA Review*, Vol. 29, pp. 414–464, September 1968.
- [41] R. Nitzberg, "Constant-False-Alarm-Rate Signal Processors for Several Types of Interference," *IEEE Trans. on Aerospace and Electronic Systems*, Vol. 8, No. 1, pp. 27–44, January 1972.
- [42] V. G. Hansen, and J. H. Sawyers, "Detectability Loss Due to Greatest-Of-Selection in a Cell Averaging CFAR," *IEEE Trans. on Aerospace and Electronic Systems*, Vol. 16, No. 1, pp. 115–118, January 1980.
- [43] G. V. Trunk, "Range Resolution of Targets Using Automatic Detectors," *IEEE Trans. on Aerospace and Electronic Systems*, Vol. 14, No. 5, pp. 750–755, September 1978.
- [44] H. Rohling, "Radar CFAR Thresholding in Clutter and Multiple Target Situations," *IEEE Trans. on Aerospace and Electronic Systems*, Vol. 19, No. 4, pp. 608–621, July 1983.
- [45] P. P. Gandhi, and S. A. Kassam, "Analysis of CFAR Processors in Nonhomogeneous Background," *IEEE Trans. on Aerospace and Electronic Systems*, Vol. 24, No. 4, pp. 427–445, July 1988.
- [46] J. T. Rickard, and G. M. Dillard, "Adaptive Detection Algorithms for Multiple Target Situations," *IEEE Trans. on Aerospace and Electronic Systems*, Vol. 13, No. 4, pp. 338–343, July 1977.
- [47] H. Goldman, and I. Bar-David, "Analysis and Application of the Excision CFAR Detector," *IEE Proc. on Radar and Signal Processing*, Vol. 135, No. 6, pp. 563–575, December 1988.
- [48] E. Conte, M. Longo, and M. Lops, "Two-Sided Censored Mean-Level Detector for CFAR in Multiple Target Situations and Clutter Edges," *Alta Frequenza*, Vol. LVIII, No. 2, pp. 165–173, March–April 1989.
- [49] S. D. Himonas, and M. Barkat, "Automatic Censored CFAR Detection for Nonhomogeneous Environments," *IEEE Trans. on Aerospace and Electronic Systems*, Vol. 28, No. 1, pp. 286–304, January 1992.
- [50] A. De Maio, A. Farina, and G. Foglia, "Design and Experimental Validation of Knowledge-Based Constant False Alarm Rate Detectors," *Proc. IET Radar, Sonar and Navigation*, Vol. 1, No. 4, pp. 308–316, August 2007.
- [51] D. K. Barton, *Modern Radar System Analysis*, Artech House, 1988.
- [52] M. Skolnik, *Radar Handbook*, McGraw-Hill, 2nd Ed., 1990, page 20.14, eqn 20.2.
- [53] A. Farina, and F.A. Studer, *Radar Data Processing. Introduction and Tracking*, Vol. 1, Researches Studies Press., England (Editor P. Bowron), John Wiley & Sons (USA), May 1985. Translated into Russian (Radio I Sviyaz Moscow in 1993) and into Chinese (China Defense Publishing House in 1988).
- [54] H. Blom and Y. Bar-Shalom, "The Interacting Multiple Model Algorithm for Systems with Markovian Switching Coefficients," *IEEE Trans. on Automatic Control*, Vol. AC-33, No. 8, pp. 780–783, August 1988.

- [55] X. R. Li, "Engineer's Guide to Variable-Structure Multiple-Model Estimation for Tracking. Ch. 10," <http://ece.engr.uno.edu/isl/PublicationsBySubjects.htm>.
- [56] M. De Feo, A. Graziano, R. Miglioli, and A. Farina, "IMMJPDA Versus MHT and Kalman Filter with NN Correlation: Performance Comparison," *IEE Proc. on Radar, Sonar and Navigation (Pt. F)*, Vol. 144, No. 2, pp. 49–56, April 1997.
- [57] R. Graziano, R. Miglioli, and A. Farina, "Multiple Hypothesis Tracking vs. Kalman Filter with Nearest Neighbor Correlation. Performance Comparison," *AGARD MSP 3rd Symposium on "Tactical Aerospace C3I in Coming Years."* Lisbon, Portugal, 15–18 May 1995, published in CP-557, pp. 25–1, 25–11
- [58] R. Torelli, A. Graziano, and A. Farina, "IM3HT Algorithm: A Joint Formulation of IMM and MHT for Multitarget Tracking," *Invited Paper, Proc. of European Control Conference, ECC97*, Vol. 3 "Estimation," Pt.1 WE-A F1, p. 750, Bruxelles, 1–4 July 1997.
- [59] R. Torelli, A. Graziano, and A. Farina, "IM3HT Algorithm: A Joint Formulation of IMM and MHT for Multi-Target Tracking," *European Journal of Control*, Vol. 5, pp. 46–53, 1999.
- [60] A. Farina, P. Lombardo, and M. Marsella, "Joint Tracking and Identification Algorithms for Multisensor Data," *IEE Proc. on Radar, Sonar and Navigation*, Vol. 149, No. 6, pp. 271–280, December 2002.
- [61] L. Maisel, "Performance of Sidelobe Blanking System," *IEEE Trans. on Aerospace and Electronic Systems*, Vol. 4, No. 2, pp. 174–180, March 1968.
- [62] A. Farina, *Antenna-Based Signal Processing Techniques for Radar Systems*, Artech House, Boston, 1992.
- [63] D. H. Harvey, and T. L. Wood, "Designs for Sidelobe Blanking Systems," *Proc. of the IEEE Int. Radar Conference*, Washington D.C., USA, pp. 410–416, April 1980.
- [64] M. R. O'Sullivan, "A Comparison of Sidelobe Blanking Systems," *Proc. of the IEE Int. Radar Conference*, London, UK, pp. 345–349, April 1987.
- [65] A. Farina, and F. Gini, "Calculation of Blanking Probability for the Sidelobe Blanking for Two Interference Statistical Models," *IEEE Signal Processing Lett.*, Vol. 5, No. 4, pp. 98–100, April 1998.
- [66] D. A. Shnidman, and S. S. Toumodge, "Sidelobe Blanking with Integration and Target Fluctuation," *IEEE Trans. on Aerospace and Electronic Systems*, Vol. 38, No. 3, pp. 1023–1037, July 2002.
- [67] A. Farina and F. Gini, "Interference Blanking Probabilities for SLB in Correlated Gaussian Clutter Plus Noise," *IEEE Trans. on Signal Processing*, Vol. 48, No. 5, pp. 1481–1485, May 2000.
- [68] A. De Maio, A. Farina, and A. Gini, "Performance Analysis of the Sidelobe Blanking System for Two Fluctuating Jammer Models," *IEEE Trans. on Aerospace and Electronic Systems*, Vol. 41, No. 3, pp. 1082–1091, July 2005.
- [69] P. Swerling, "Radar Probability of Detection for Some Additional Fluctuating Target Cases," *IEEE Trans. on Aerospace and Electronic Systems*, Vol. 33, No. 2, pp. 698–709, April 1997.
- [70] A. De Maio, A. Farina, and G. Foglia, "Target Fluctuation Models and Their Applications to Radar Performance Prediction," *IEE Proc. on Radar, Sonar and Navigation*, Vol. 151, No. 5, pp. 261–269, October 2004.
- [71] A. Farina, L. Timmoneri, and R. Tosini, "Cascading SLB and SLC Devices," *Journal Signal Processing*, Vol. 45, No. 2, August 1995.

- [72] Y. Bar-Shalom, X. R. Li, and T. Kirubarajan, *Estimation with Applications to Tracking and Navigation*, John Wiley & Sons, 2001.
- [73] R. D. Graglia, P. L. E. Uslenghi, R. Vitiello, and U. F. D'Elia, "Electromagnetic Scattering for Oblique Incidence on Impedance Bodies of Revolution," *IEEE Trans. on Antennas and Propagation*, Vol. 43, No. 1, pp. 1126, January 1995.
- [74] U. F. D'Elia, M. G. Del Gaudio, and D. Pistoia, "Electromagnetic Modelling of Complex Targets in the Near Zone and Comparison with Experimental Results," *IEE Int. Radar Conference*, Edinburgh, 14–16 October 1997.
- [75] U. F. D'Elia, "Target Modelling for High Resolution Radar in the New Wide Band Seeker Applications," *Multinational Ballistic Missile Defense (BMD) Conference*, Dallas, Texas USA, 3–6 June 2002.
- [76] P. Ya. Ufimtsev, "Fundamentals of the Physical Theory of Diffraction," 2007, Reviews and Abstracts *Antennas and Propagation Magazine*, IEEE, Vol. 50, No. 1, pp.159–161, February 2008.
- [77] P. Zarchan, *Tactical and Strategic Missile Guidance*, 3rd ed. AIAA Inc., 1997.
- [78] A. Farina, B. Ristic, and D. Benvenuti, "Tracking a Ballistic Target: Comparison of Several Non Linear Filters," *IEEE Trans. on Aerospace and Electronic Systems*, Vol. 38, No. 3, pp. 854–867, July 2002.
- [79] B. Ristic, A. Farina, D. Benvenuti, and S. Arulampalam, "Performance Bounds and Comparison of Non-Linear Filters for Tracking a Ballistic Object on Re-Entry," *IEE Proc. on Radar, Sonar and Navigation*, Vol. 150, No. 2, pp. 65–70, 2003.
- [80] A. Farina, M. G. Del Gaudio, U. D'Elia, S. Immediata, L. Ortenzi, L. Timmoneri, and M. R. Toma, "Detection and Tracking of Ballistic Target," *IEEE Radar Conference*, Philadelphia (USA), pp. 26–29, April 2004.
- [81] D. C. Schleher, "Low Probability of Intercept Radar," *IEEE Int. Radar Conference*, Arlington (VA), pp. 346–349, May 6–9, 1985.
- [82] D. C. Schleher, *Introduction to Electronic Warfare*, Artech House, p. 59, 1986.
- [83] S. Ertan, H. D. Griffiths, M. C. Wicks, P. Antonik, D. Weiner, R. Adve, and I. Fotinopoulos, "Bistatic Radar Denial by Spatial Waveform Diversity," *IEE Int. Radar Conference*, Edinburgh UK, pp. 17–21, October 15–19, 2002.
- [84] H. D. Griffiths, and S. M. Carter, "Provision of Moving Target Indication in an Independent Bistatic Radar Receiver," *The Radio and Electronic Engineer*, Vol. 54, No. 7/8, pp. 336–342, July/August 1984.
- [85] C. Dobinson, *Building Radar: Forging Britain's Early-Warning Chain, 1935-1945*, Methuen Pub Ltd, January 2008.
- [86] R. C. Watson, Jr., *Radar Origins Worldwide: History of Its Evolution in 13 Nations Through World War II*, Trafford Publishing, November 2009.
- [87] R. Morenus, *Dew Line: Distant Early Warning. The Miracle of America's First Line of Defense*, Rand McNally, New York, 1957.
- [88] R. Wells, *Early Warning: Electronic Guardians of Our Country*, Prentice-Hall, 1962.
- [89] G. W. Stimson, *Introduction to Airborne Radar*, Second Edition, Scitech Publishing, USA, 1998.

Surface Moving Target Indication

*William L. Melvin, Ph.D., Georgia Institute of Technology,
Georgia Tech Research Institute, Atlanta, GA, USA*

Chapter Outline	
9.1	Introduction 383
9.2	SMTI Radar Operation 390
9.3	Signal Models. 393
9.4	SMTI Metrics 400
9.5	Antenna and Waveform Considerations 405
9.6	Clutter-Mitigation Approaches 410
9.7	Detection Processing 418
9.8	Angle and Doppler Estimation 421
9.9	Other Considerations 424
9.10	Summary 426
9.11	Further Reading 427
9.12	References. 427

9.1 | INTRODUCTION

Surface moving target indication (SMTI) involves searching Earth’s surface for moving objects using a dedicated radar mode. *Ground-moving target indication* (GMTI) is a subordinate, commonly referenced mode implying the detection, location, and discrimination of vehicles and personnel (dismounts) against rural, suburban, and urban land settings. The general class of SMTI radar modes also includes searching for vessels against sea, lake, and riverine backgrounds. An SMTI platform can be an aircraft, an *unmanned aerial system* (UAS), a satellite, an aerostat, or a tower.

Typically, SMTI refers to object detection on Earth’s surface from airborne or spaceborne radar systems. In such aerospace radar configurations, the Doppler spread of mainbeam clutter is a fundamental limiting factor that impedes target detection and tends to drive system requirements and complexity. The use of side-looking, extended, along-track antennas; multichannel receive apertures; *space–time adaptive processing* (STAP); and low-pulse repetition frequency waveforms are common SMTI design choices to be described further in this chapter. SMTI interrogation strategies include *wide area search* (WAS); selective search, also sometimes called *small area ground* (SAG) mode; and persistent area search. Legacy system development focused on

WAS-SMTI, but newer capabilities deployed on UASs and smaller platforms generally employ SAG or persistent search modes in addition to wider search capability.

In a typical SMTI system, the primary challenge centers on mitigating the impact of mainlobe clutter on slow-moving-target detection. The returns from stationary clutter objects exhibit a distinct angle-Doppler region of support, since the specification of angle to a point on Earth's surface also specifies its Doppler frequency shift. The objective of SMTI is to discriminate the target's angle-Doppler response from that of the clutter background, assuming the target signal power is sufficiently strong relative to the receiver noise strength.

SMTI has a number of military and civilian applications. Military applications include detection of troop movements, monitoring cordoned areas, and searching for time-critical targets in remote areas. Civilian applications include support for emergency management, such as evacuation of cities and towns, border surveillance, and highway safety.

The Joint Surveillance Targeting Attack Radar System (Joint STARS) is an example of an airborne GMTI radar system; it carries the AN/APY-3/-7 military designation. The Joint STARS system, shown in Figure 9-1, houses a 7.3-meter-long, X-band antenna system mounted along the fore section of the fuselage in the readily identified, canoe-shaped radome. The antenna is electronically scanned in azimuth and mechanically scanned in elevation. Three receive channels are adaptively combined to mitigate clutter and enhance detection performance. The Boeing 707 airframe supports long mission times, long-range search, and wide area coverage. The radar system outputs "dots" that represent the location and temporal appearance of detections. Figure 9-2 is an example of a GMTI display. The GMTI dots correspond to radar measurements of target position, range rate, *signal-to-interference-plus-noise ratio* (SINR), and other important attributes. An overview of Joint STARS and the field of GMTI radar is given in [1]. Another example is the AN/APY-9 UHF radar on the E2-D Advanced Hawkeye; this radar system incorporates a multichannel antenna and STAP to provide SMTI capability.

Deploying GMTI on UAS platforms is one area of significant current interest. The Global Hawk UAS is an ideal GMTI platform; this system is shown in Figure 9-3. Global Hawk carries a substantial payload on the order of 900–1,400 kg (depending on model), flies at an altitude of 18 km at a speed of 160–175 m/s, and provides exceedingly long endurance [2]. The Multi-Platform Radar Technology Insertion Program

FIGURE 9-1 ■ Joint STARS, AN/APY-3/-7 GMTI system [after <http://www.af.mil/information/factsheets/>].





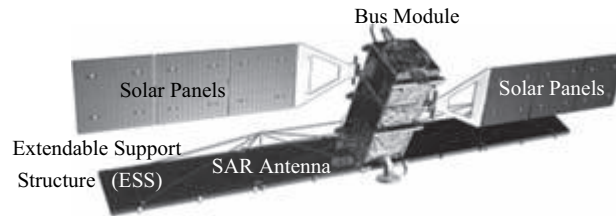
FIGURE 9-2 ■ GMTI “Dots” shown in Local, Plan View Coordinates [after http://en.wikipedia.org/wiki/Joint_STARS].



FIGURE 9-3 ■ Global Hawk UAS Payloads Include Radar Capability [after <http://www.af.mil/information/factsheets/>].

(MP-RTIP) is a scalable payload approach to GMTI and forms a basis for the Global Hawk GMTI mode. MP-RTIP became an option after publication of [1], hence its omission therein. The MP-RTIP architecture for Global Hawk employs multiple channels as required to produce an effective GMTI payload. The Vehicle and Dismount Exploitation Radar (VADER) developed by the Defense Advanced Research Projects Agency (DARPA) is designed for deployment on a Warrior UAS or similar platform. VADER provides the ability to “monitor a road, track a vehicle to a stop, observe dismount motion near the vehicle, characterize certain motions (like someone carrying a heavy load), and measure a ground disturbance after the vehicle departs” [3]. The AN/APY-8 Lynx radar provides *synthetic aperture radar* (SAR) and GMTI capability in a

FIGURE 9-4 ■ Canadian RADARSAT-2. [after <http://www.radarsat2.info/about/construction/index.asp>].



lightweight package less than 37 kg. The AN/APY-8 provides GMTI detection range out to 23 km using a 44-cm by 16.5-cm Ku-band antenna at 320-W peak power [4]. The AN/APY-8 is specially designed for UAS platforms.

There has also been considerable interest in deploying SMTI capability from satellites. The space radar program included high-performance GMTI as a primary mission goal, with target characterization and persistent tracking of keen interest [5]. Typical satellite-borne GMTI modes are dependent on STAP to cope with limited along-track aperture relative to the satellite velocity (exceeding 7 km/s at low-Earth orbit, LEO). A STAP-based, spaceborne GMTI processing architecture is discussed in [6]. The Canadian RADARSAT-2 performs remote sensing using a C-band SAR; RADARSAT-2 builds on the legacy of the RADARSAT-1's 15-m along-track aperture, push-broom SAR, with the addition of enhanced imaging modes and two along-track channels providing the necessary degrees of freedom to suppress clutter and detect moving targets [7] (see Figure 9-4). The RADARSAT-2 SMTI capability is called *moving object detection experiment* (MODEX) [8]. RADARSAT-2 uses, among other experimental approaches, a technique called *along-track interferometry* (ATI) to detect moving targets. In ATI, the processor compensates for the relative effects of motion between the two channels compared to the fixed scene; a conjugate multiply of one channel against the other zeros the phase response of the clutter background; a nonzero phase indicates the presence of moving targets [8].

Due to the importance of GMTI/SMTI, North Atlantic Treaty Organization (NATO) nations have agreed upon a standard GMTI format, called Standard NATO Agreement (STANAG) 4607. Details on STANAG 4607 are readily found in the public domain and available from NATO.

9.1.1 Organization

This chapter aims to familiarize the reader with the tenets of SMTI radar. With this goal in mind, the remainder of this chapter is organized as follows.

We describe SMTI radar operation in Section 9.2, including basic system issues, as well as target and clutter phenomenology that are driving system design and signal-processing choices. We also consider SMTI radar search strategies.

An understanding of surface clutter, target, and *radio-frequency interference* (RFI) signal characteristics is central to a discussion of SMTI radar. We describe multi-channel, multipulse, SMTI signal models in Section 9.3. Measured data are included to validate the ground-clutter model.

A primary objective of SMTI radar is to detect a target of a given *radar cross section* (RCS), with a specified minimum velocity, at a given range and with a desirable *area coverage rate* (ACR). Clutter, RFI, and receiver noise impede this process. The

SMTI radar interrogates the scene and then must decide between two primary models that generated the observations in the radar receiver: (1) the null hypothesis (H_0), or the case of target absence; or, (2) the alternative hypothesis (H_1), which denotes target presence in addition to receiver noise, clutter returns, and RFI. Calculating and evaluating SMTI radar performance metrics is thus a critical undertaking. We discuss important SMTI metrics in Section 9.4.

Exploiting the radar measurement space is the essence of radar detection. With the appropriate supporting hardware, the radar can collect measurements over fast-time, slow-time, spatial, polarimetric, and multiple-pass domains. Applying a matched filter to the fast-time samples yields range information, while the Fourier transform of slow-time samples yields Doppler. Each measurement accessible to the signal processor is called a *degree of freedom* (DoF). The SMTI processor combines those DoFs that best differentiate the target from clutter and RFI signals. Ground-clutter returns exhibit a well-defined angle-Doppler region of support that differs from the moving target response. The goal of SMTI is to discriminate the angle-Doppler offset of the target relative to the ground-clutter response. Section 9.5 describes SMTI antenna and waveform considerations.

We consider a number of clutter-mitigation approaches in Section 9.6, starting with the one-dimensional, nonadaptive Doppler processing method, and then varying the DoFs and use of adaptive or deterministic signal processing to include discussion of adaptive Doppler processing, *displaced phase-center antenna* (DPCA) processing, adaptive DPCA, and STAP.

Sections 9.7 and 9.8 describe the details of SMTI detection processing and target parameter estimation. In Section 9.7, we consider the practical matter of clutter filter normalization, *constant false alarm rate* (CFAR) processing, and postdetection integration. Section 9.8 develops a maximum likelihood approach to angle and Doppler estimation.

Section 9.9 discusses additional considerations, including the impact of spatially varying, heterogeneous clutter on SMTI performance; detection of moving targets in SAR phase history data; bistatic or multistatic radar topologies; and dismount detection.

9.1.2 Key Points

Key SMTI points the reader should identify in this chapter include the following:

- SMTI radar attempts to detect moving vehicles, ships, boats, and dismounts (people) on Earth's surface against strong clutter backgrounds. SMTI targets typically fall within the Doppler spread of mainlobe clutter and hence are referred to as being *endo-clutter*.
- The along-track length of the antenna subsystem relative to the platform velocity is a critical factor determining the *minimum detectable velocity* (MDV) of the radar.
- Exploiting the radar's angle and Doppler measurements are essential to effective SMTI radar performance. Deriving angle information requires a multichannel radar system. Discriminating slight differences in the target's angle-Doppler response relative to that of the fixed clutter background is an important concept.
- Effective SMTI systems require sophisticated signal processing to achieve performance requirements. STAP is a preeminent approach to mitigate the effect of ground clutter and RFI signals on performance, thereby maximizing detection capability.

- STAP is related to the class of super-resolution methods and thus provides an MDV that a nonadaptive radar can only achieve by significantly increasing the along-track length of the radar antenna by a factor of 2 to 5. This is an important consideration when implementing SMTI from UAV or satellite-borne platforms.
- Challenges in SMTI include operation in complex, heterogeneous clutter environments and detecting and characterizing dismount targets. Advanced signal-processing methods are critical to achieve the best possible system performance.

9.1.3 Notation and Acronyms

Basic Notation

Frequently used variables are given below.

f_0 = center frequency (Hz);

f_d = Doppler frequency (Hz);

ϕ, θ = azimuth and elevation (rads);

ψ_g = grazing angle (rads);

λ = wavelength (m);

M = number of channels;

N = number of pulses;

L = number of available range bins;

K = number of range bins used in covariance estimate;

T = pulse repetition interval (s);

c = velocity of propagation (speed of light, m/s);

δ_r = range resolution, ground plane (m);

δ_{cr} = cross-range resolution (m);

s_s = spatial steering vector;

v_s = hypothesized spatial steering vector;

s_t = temporal steering vector;

v_t = hypothesized temporal steering vector;

s_{s-t} = space-time steering vector;

v_{s-t} = hypothesized space-time steering vector

$x_{s/k}(n)$ = spatial data snapshot, k th range cell, n th pulse;

$x_{t/k}(m)$ = temporal data snapshot, k th range cell, m th channel;

x_k = space-time data snapshot, k th range cell;

c_k = clutter space-time snapshot, k th range cell;

j_k = RFI space-time snapshot, k th range cell;

n_k = uncorrelated noise space-time snapshot, k th range cell;

t_k = target space-time snapshot, k th range cell;

R_k = null-hypothesis covariance matrix, k th range cell;

$R_{c/k}$ = clutter covariance matrix;

R_{RFI} = RFI covariance matrix;

\hat{R}_k = null-hypothesis covariance estimate, k th range cell;

w_k = space-time weight vector;

\hat{w}_k = adaptive space-time weight vector;

y_k = filter output for k th range bin and selected angle and Doppler;

P_D = probability of detection;
 P_{FA} = probability of false alarm.

Acronyms

A/D	analog-to-digital (converter)
ACR	area coverage rate
AMF	adaptive matched filter
CFAR	constant false alarm rate
CMT	covariance matrix taper
CNR	clutter-to-noise ratio
CPI	coherent processing interval
DoF	degree of freedom
DPCA	displaced phase-center antenna (processing)
FAD	false alarm density
GMTI	ground-moving target indication
HRR	high-range resolution
ICM	intrinsic clutter motion
iid	independent and identically distributed
I/Q	in-phase and quadrature (voltages)
MDV	minimum detectable velocity
MLE	maximum likelihood estimate
MVDR	minimum variance distortionless response
NCA	noncoherent addition
PDI	postdetection integration
PRF	pulse repetition frequency
PRI	pulse repetition interval
RCS	radar cross section
RDM	range-Doppler map
RFI	radio frequency interference
RMS	root mean square
ROC	receiver operating characteristic
Rx	receiver
SAG	small area ground (search)
SAR	synthetic aperture radar
SINR	signal-to-interference plus noise ratio
SMI	sample matrix inversion
SMTI	surface moving target indication
SNR	signal-to-noise ratio
STANAG	Standard North Atlantic Treaty Organization Agreement
STAP	space-time adaptive processing
WAS	wide area search

9.2 | SMTI RADAR OPERATION

The SMTI radar system searches an area on Earth's surface, generally using a pulsed, *linear frequency modulated* (LFM) waveform. The *coherent-processing interval* (CPI) is comprised of the transmission and reception of N pulses at a common center frequency, f_0 . The pulse repetition interval (PRI) is T . A collection of M subapertures comprise the receive antenna. Each receiver channel down-converts and digitizes the receive waveform. The resulting data are conceptually organized into the radar data cube shown in Figure 9-5.

To mitigate target fading effects – an aspect-dependent phenomenon resulting from the coherent summation of the many scatterers comprising the target – the radar frequency must hop several times within the dwell. Each hop corresponds to a CPI at the new center frequency. The radar generally will keep the waveform bandwidth constant. It is the waveform bandwidth that determines the radar-range resolution. The dwell time is given by NTP , where P is the number of CPIs in the dwell.

Figure 9-6 shows the basic SMTI processing steps. The pulse compressor operates on each of the M channels, demodulating the waveform coding. Targets, clutter signals, receiver noise, and RFI may comprise the $NM \times 1$ space-time data vector corresponding to the k th range bin, x_k . Receiver noise is temporally and spatially uncorrelated; it results

FIGURE 9-5 ■ Coherent Radar Data Cube [after [25], © 2004 IEEE].

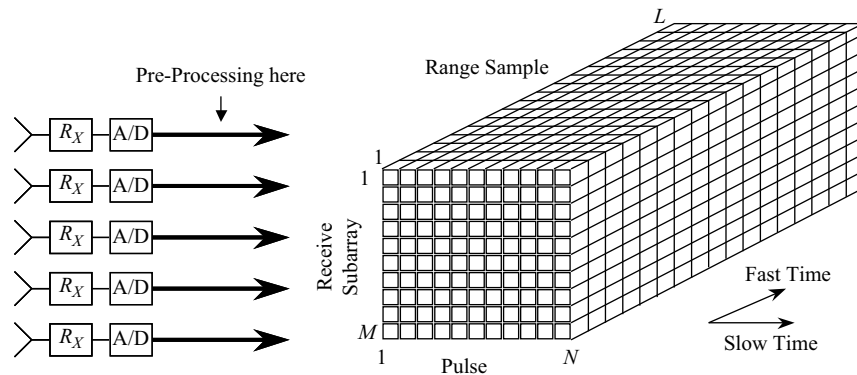
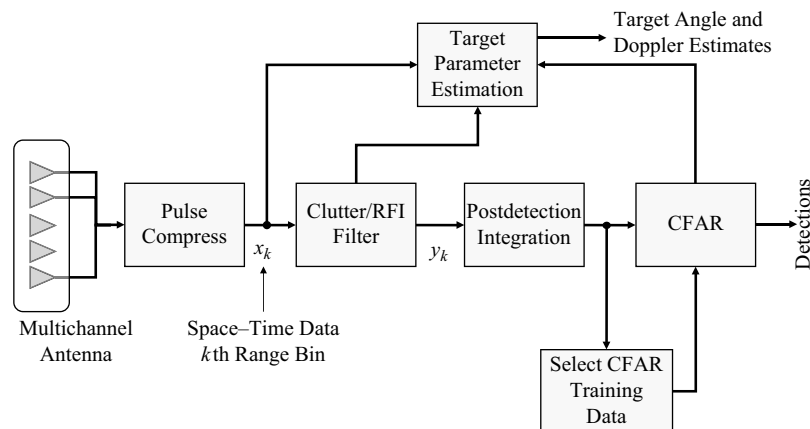


FIGURE 9-6 ■ Generic SMTI Processing Architecture.



from thermal agitation of electrons within the receiver. Clutter signals and RFI, however, exhibit some degree of correlation and filtering mitigates their effects on detection performance. It is common to apply the linear filter, $y_k = \mathbf{w}_k^H \mathbf{x}_k$, where \mathbf{w}_k are the filter weights. This linear filter formulation provides the framework needed to discuss Doppler processing, adaptive Doppler processing, DPCA, adaptive DPCA, STAP, and STAP variants, all methods used to suppress clutter. Adaptive digital beam forming also fits within this framework and is used to suppress RFI. We subsequently discuss these different methods in this chapter.

The clutter/RFI filter step of Figure 9-6 is applied to each of the P CPIs. Generally, the processor selects a single receive direction and then generates the y_k for all Doppler frequencies of interest. The result is a *range-Doppler map* (RDM). The processor then noncoherently sums the P RDMs for each of the CPIs in a step known as *postdetection integration* (PDI) to mitigate target fading. A detection threshold is then applied to the composite range-Doppler image. It is common to use a constant false alarm rate (CFAR) algorithm to set the detection threshold. CFAR algorithms estimate the varying residual interference power and scale the result in an attempt to keep the false alarm rate as constant as possible. After the processor detects a target, it then estimates bearing angle and Doppler frequency, sometimes also refining the range estimate. Bearing angle, Doppler, and range are then supplied to the analyst or an automatic tracker.

The SMTI radar may switch to a different waveform to collect a *high-range resolution* (HRR) profile to facilitate target characterization and association. The HRR collection step is not shown in Figure 9-6.

Figure 9-7 depicts several common SMTI collection modes. The wide area search mode involves searching large swaths of Earth's surface using the bar-scanning strategy shown in the figure. Each beam position corresponds to a dwell, with P CPIs comprising each dwell as previously discussed. In the small area ground mode, the radar still searches a specified though smaller area. Usually in SAG mode, the radar increases the dwell time. SAG is used to look for more challenging target sets, like small vehicles. In the persistent search mode, the radar spotlights a designated area for an extended period. Usually, the radar uses significantly longer dwells in the persistent mode, generating

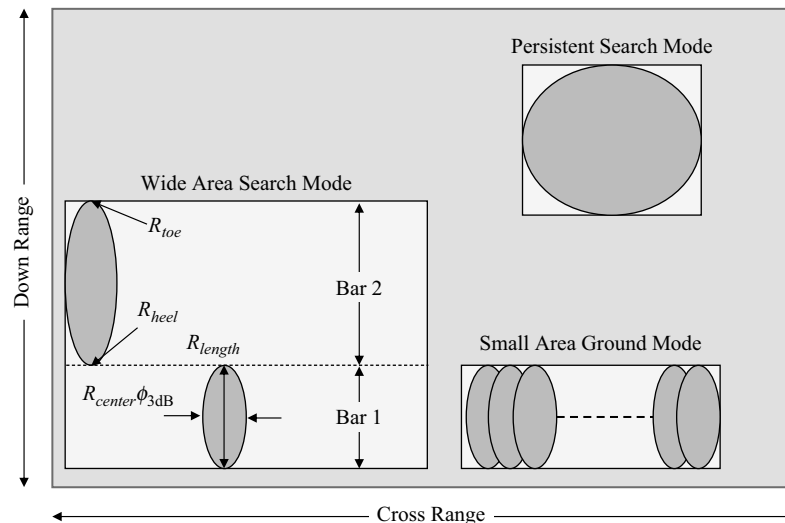


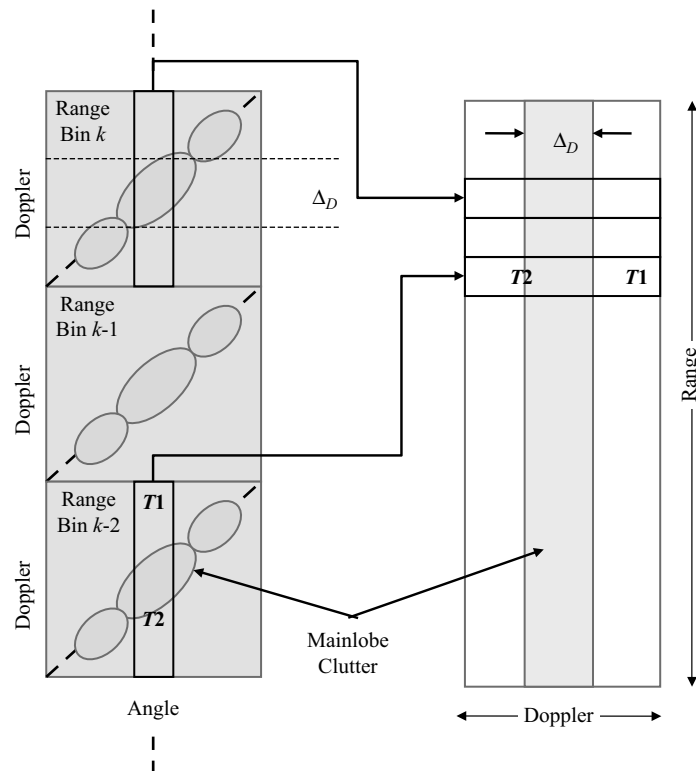
FIGURE 9-7 ■
SMTI Search
Modes.

SAR and SMTI products concurrently. The WAS and SAG modes are very similar in design and are the underlying focus of the discussion in this chapter.

The primary requirement of an SMTI radar is to detect a target of a specified RCS at a maximum range and minimum velocity while maintaining a desired area coverage rate. Unlike *airborne moving target indication* (AMTI) radar systems, SMTI radars usually do not operate in the noise-limited condition where receiver noise is the limiting factor. Rather, most SMTI radars are clutter limited. Developing a radar system meeting the SMTI requirements involves careful platform selection, antenna design, waveform selection, and signal-processing design and implementation. Key SMTI requirements are quantified using *probability of detection* (P_D), *false alarm density* (FAD), *minimum detectable velocity* (MDV), area coverage rate, and bearing and Doppler *root mean square* (RMS) error. It is also common to characterize SMTI performance using SINR loss, a measure of the performance degradation relative to some other condition, usually the noise-limited capability or the difference between the optimal and adaptive filter. We consider SMTI metrics in detail in Section 9.4.

As just mentioned, SMTI radar systems generally operate in the clutter-limited condition. This should not be a surprise, since the radar antenna is pointed toward Earth's surface, generating strong surface reflections that mask the detection of moving targets of interest. Figure 9-8 depicts SMTI clutter-limited detection. To the left is shown angle-Doppler images for each range bin; clutter lies along a ridge, as given in the figure. The vertical boxes in two of the angle-Doppler images correspond to a particular transmit-and-receive angle. The Doppler spread across the main beam is Δ_D . Antenna along-track length and platform velocity determine the magnitude of Δ_D . Exoclutter

FIGURE 9-8 ■ Clutter-Limited Detection Performance.



target, $T1$, and endocutter target, $T2$, are shown in range bin $k - 2$. Each vertical Doppler slice at the transmit–receive angle forms a horizontal slice at the corresponding range in the RDM to the right. Target $T1$ maps away from main beam clutter and is easily detected, whereas target $T2$ maps to the clutter edge. SMTI design – platform, aperture, signal-processing algorithms – focuses on improving the detectability of $T2$.

As shown in Figure 9-8, targets $T1$ and $T2$ reside off of the clutter ridge, since their angle-Doppler coupling differs from that of the stationary clutter. A two-dimensional notch filter, with the null aligned along the clutter angle-Doppler region of support, is the ideal approach to enhance detection performance. Accessing angle information requires a multichannel antenna. The various antenna channels sample the direction of arrival of the propagating electromagnetic wave. The radar processor also requires access to the multipulse data to build the space-and-slow-time (angle-Doppler) filter. Note that clutter is generally white (uncorrelated) in range. Improved performance comes at the cost of additional receivers, more complex antenna array design, and more capable embedded computing systems.

The following sections expand on the key elements of SMTI radar operation.

9.3 | SIGNAL MODELS

We first discuss the space–time response of a point scatterer. The point-scatter model provides insight into the ground clutter, target, and RFI signal models.

Consider the LFM transmit signal,

$$s_{tx}(t, n) = a_0 \text{rect}\left(\frac{\hat{t}}{\tau_u}\right) e^{j2\pi f_0 t} e^{j\pi \gamma_{LFM} \hat{t}^2} \quad (9.1)$$

where

t is time,

n is pulse number,

a_0 is the signal amplitude,

$\hat{t} = t - nT$ is fast time,

T is the PRI,

τ_u is uncompressed pulse width,

f_0 is the carrier frequency in Hertz,

γ_{LFM} is the LFM chirp rate in Hz/s, and

$$\text{rect}(t) = \begin{cases} 1 & \text{for } |t| \leq \frac{1}{2} \\ 0 & \text{otherwise} \end{cases} \quad (9.2)$$

Next, consider the case of transmit energy reflected from a target or source of point clutter. The received signal is a scaled, time-delayed replica of the transmit signal in (9.1), appearing as

$$s_r(t, n) = a_1 \text{rect}\left(\frac{\hat{t} - t_d}{\tau_u}\right) e^{j2\pi f_0 (t - t_d)} e^{j\pi \gamma_{LFM} (\hat{t} - t_d)^2} \quad (9.3)$$

with a_1 a complex gain term proportional to the square root of the object's RCS, and t_d the round-trip time delay from transmit phase center to the object and back to the receive antenna. Note that t_d typically varies with pulse number, n . After conversion to baseband and discrete-time sampling, (9.3) appears as

$$\bar{s}_r(k, n) = a_1 \text{rect}\left(\frac{(kT_s - nT) - t_d(n)}{\tau_u}\right) e^{-j2\pi f_0 t_d(n)} e^{j\pi \gamma_{LFM} (kT_s - nT - t_d(n))^2} \quad (9.4)$$

k is the sample index and T_s is the sample rate. The options for conversion to complex baseband include the use of synchronous detection [separate *in-phase* and *quadrature* (I/Q) receive channels] or digital I/Q, the latter involving data oversampling, low-pass filtering, and decimation [9]. We explicitly show the dependence of t_d on the pulse index, n . Further, assume M receive channels comprise the receive aperture. The signals in each channel are generally similar, with a spatial time delay being the predominant difference as a result of the signal's direction of arrival. The multichannel form of (9.4) is then

$$\tilde{s}_r(k, n, m) = a_1 \text{rect}\left(\frac{(kT_s - nT) - t_d(n, m)}{\tau_u}\right) e^{-j2\pi f_0 t_d(n, m)} e^{j\pi \gamma_{LFM} (kT_s - nT - t_d(n, m))^2} \quad (9.5)$$

where m is the channel index.

Examining (9.5), we observe a_1 is the amplitude-modulation term resulting from the interaction of the waveform and scattering object; the first exponential term incorporates a phase modulation varying in space and time, $2\pi f_0 t_d(n, m)$; and we identify the quadratic, time-varying phase modulation corresponding to the LFM waveform in the argument of the latter exponential. [Equation (9.5) is easily generalized to other types of transmit waveforms. The LFM waveform is the most popular.] The linearly varying phase modulation, $2\pi \gamma_{LFM} t_d(n, m)$, encodes the object's Doppler frequency and direction of arrival information. It is this space-time measurement the SMTI processor exploits to mitigate clutter and cohere the target's return signal.

The range resolution, determined by the bandwidth of the LFM waveform, is chosen to restrict the target to a single range bin over the coherent dwell. Pulse compression, applied on a pulse-by-pulse basis, removes the LFM modulation; the typical output of the pulse-compression stage appears as a weighted sinc function. Common range resolutions of tens of meters to single meter accuracy lead to sample intervals, T_s , on the order of tenths to hundredths of microseconds. The analog-to-digital converters in each receive channel provide this sampling mechanism. In contrast, the pulse-repetition interval is ordinarily on the order of milliseconds and is chosen to balance the trade-off between range and Doppler ambiguity. The time delay across elements of the multichannel array can be on the order of tenths to hundredths of nanoseconds for angles approaching end-fire.

Pulse compressing (9.5), simplifying by grouping complex gain terms, and considering the peak range sample, k_p , yields

$$\widehat{s}_r(k_p, n, m) = \widehat{a}_1(k_p) e^{-j2\pi f_0 t_d(n, m)} \quad (9.6)$$

where $\widehat{a}_1(k_p)$ is a complex gain. A coherent space-time aperture for a typical system involves integrating tens to hundreds of pulses (e.g., $64 \leq N \leq 512$) and usually several

to a dozen receive channels ($2 \leq M \leq 12$). Section 9.5 further considers coherent dwell length and design of spatial channels.

It is common to describe the SMTI observation as a space–time data vector for the k th range bin of interest. The space–time data vector for the point scatterer follows from (9.6) as

$$\begin{aligned} \mathbf{x}_k &= \widehat{a}_1 \left(e^{-j2\pi f_0 t_d(n,m)} \right)_{\substack{m=1:M \\ n=1:N}} \\ &= \widehat{a}_1 [e^{-j2\pi f_0 t_d(1,1)} \quad e^{-j2\pi f_0 t_d(1,2)} \quad \dots \quad e^{-j2\pi f_0 t_d(N,M-1)} \quad e^{-j2\pi f_0 t_d(N,M)}]^T \end{aligned} \quad (9.7)$$

where the superscript T denotes the transpose operation. Doppler frequency is given as the time derivative of $-2\pi f_0 t_d(n, m)$, where m is fixed; normalizing the derivative by $1/2\pi$ yields Doppler in Hertz. Analogously, the spatial derivative of $-2\pi f_0 t_d(n, m)$, for n fixed, yields spatial frequency, the indicator of signal direction of arrival. Equation (9.7) is expressible as

$$\mathbf{x}_k = \widehat{a}_1 \mathbf{s}_s(\phi, \theta) \otimes \mathbf{s}_t(f_d) = \widehat{a}_1 \mathbf{s}_{s-t}(\phi, \theta, f_d) \quad (9.8)$$

with \otimes denoting the Kronecker product [10]; ϕ is azimuth angle, θ is elevation angle, f_d is Doppler frequency, \mathbf{s}_s is the spatial steering vector describing the signal response across the receive array, \mathbf{s}_t is the Doppler steering vector, \mathbf{s}_{s-t} is the space–time steering vector, and \widehat{a}_1 is the peak complex gain.

The expression in (9.8) forms a basis for the following clutter, target, and RFI models.

9.3.1 Surface Clutter

Surface clutter is the most significant impediment to SMTI detection performance. Ground clutter exhibits a distinct angle–Doppler coupling: small changes in angle result in small changes in Doppler, with knowledge of angle uniquely specifying Doppler frequency (assuming a smooth Earth). In a side-looking radar configuration, clutter lies along a ridge in the angle–Doppler plane; the ridge opens up into an ellipse when platform yaw is present and into a circle in the forward-looking collection geometry. The reflectivity of ground and sea clutter typically appear spatially varying. The motion of vegetation blowing in the wind or the rise and fall of the ocean’s surface leads to partial decorrelation of the clutter signal over the temporal aperture.

The surface clutter space–time snapshot is the aggregate of the clutter returns from the various scatterers distributed in azimuth along the iso-range contour, including returns from ambiguous ranges. These scatterers include trees, grassy terrain, roadways, buildings, fence lines, etc. Dividing the azimuth interval into small angular extents representing a fraction of the lesser of the system spatial or Doppler resolution cells yields N_c clutter patches for each of N_a range ambiguities. Each clutter patch incorporates a number of unresolvable, subscatterers whose composite return assures the received clutter voltage is random and independent among patches. The randomness of the composite return leads to clutter speckle, or fading: voltages from each of the

subscatterers comprising the clutter patch add coherently to yield a constructive (strong) or destructive (weak) clutter voltage response. The surface clutter space–time snapshot takes the form

$$\mathbf{c}_k = \sum_{m=0}^{N_a} \sum_{n=1}^{N_c} \boldsymbol{\alpha}_{s-t}(m, n; k) \odot \mathbf{s}_{s-t}(\phi_{m,n}, \theta_{m,n}, f_{d/m,n}; k) \quad (9.9)$$

where

- $(\phi_{m,n}, \theta_{m,n})$ is the azimuth and elevation to the m th patch;
- $f_{d/m,n}$ is the corresponding Doppler frequency;
- $\boldsymbol{\alpha}_{s-t}(m, n; k) \in C^{NM \times 1}$ is the vector containing the space–time voltages for each channel-pulse-range sample, with each element proportional to the square root of the patch clutter-to-noise ratio (CNR);
- $\mathbf{s}_{s-t}(\phi_{m,n}, \theta_{m,n}, f_{d/m,n}; k)$ is the space–time steering vector; and
- \odot is the Hadamard product operation [10].

The space–time steering vector is given as the Kronecker product of the temporal and spatial steering vectors, $\mathbf{s}_{s-t}(\phi, \theta, f_d) = \mathbf{s}_t(f_d) \otimes \mathbf{s}_s(\phi, \theta)$.

The voltage vector can be written as

$$\boldsymbol{\alpha}_{s-t}(m, n; k) = v_{k/m,n} \left(\mathbf{d}_t(\phi_{m,n}, \theta_{m,n}; k) \otimes \mathbf{d}_s(\phi_{m,n}, \theta_{m,n}; k) \right) \quad (9.10)$$

where

- $v_{k/m,n}$ is the complex voltage of the m th patch for the k th range,
- $\mathbf{d}_t(\phi_{m,n}, \theta_{m,n}; k)$ is a random taper vector characterizing the voltage fluctuation over the temporal aperture, and
- $\mathbf{d}_s(\phi_{m,n}, \theta_{m,n}; k)$ is a random spatial taper describing the voltage decorrelation over the spatial aperture.

We recognize both \mathbf{d}_t and \mathbf{d}_s as covariance matrix taper (CMT) components [11]. Let $v_{k/m,n}$ be zero mean, complex normal, with variance $\sigma_{k/m,n}^2$, i.e., $v_{k/m,n} \sim CN(0, \sigma_{k/m,n}^2)$. The covariance matrix of (9.10) then follows as

$$\begin{aligned} \mathbf{D}_k(m, n) &= E[\boldsymbol{\alpha}_{s-t}(m, n; k) \boldsymbol{\alpha}_{s-t}^H(m, n; k)] = \sigma_{k/m,n}^2 \mathbf{D}_t(\phi_{m,n}, \theta_{m,n}; k) \otimes \mathbf{D}_s(\phi_{m,n}, \theta_{m,n}; k); \\ \mathbf{D}_t(\phi_{m,n}, \theta_{m,n}; k) &= E[\mathbf{d}_t(\phi_{m,n}, \theta_{m,n}; k) \mathbf{d}_t^H(\phi_{m,n}, \theta_{m,n}; k)]; \\ \mathbf{D}_s(\phi_{m,n}, \theta_{m,n}; k) &= E[\mathbf{d}_s(\phi_{m,n}, \theta_{m,n}; k) \mathbf{d}_s^H(\phi_{m,n}, \theta_{m,n}; k)]. \end{aligned} \quad (9.11)$$

The expected value of the two outer products corresponds to temporal and spatial CMTs. Also, the superscript, H , denotes conjugate transpose. Plausible functions characterizing the elements of \mathbf{D}_t , suitable for modeling intrinsic clutter motion, include the Gaussian autocorrelation [12] and Billingsley model involving an exponential autocorrelation [13]. Gaussian fits best for regions with seawater or freshwater because it fully decorrelates, whereas exponential is more appropriate for wooded regions or fields. A sampled sinc or “angle dither” is appropriate for the elements of \mathbf{D}_s and used to model wavefront dispersion [11].

The clutter covariance matrix, $\mathbf{R}_{c/k} = E[\mathbf{c}_k \mathbf{c}_k^H]$, follows from the prior discussion as

$$\mathbf{R}_{c/k} = \sum_{m=0}^{N_a} \sum_{n=1}^{N_c} \sigma_{k/m,n}^2 \mathbf{D}_{s-t}(\phi_{m,n}, \theta_{m,n}; k) \odot \mathbf{s}_{s-t}(\phi_{m,n}, \theta_{m,n}; k) \mathbf{s}_{s-t}^H(\phi_{m,n}, \theta_{m,n}; k); \quad (9.12)$$

$$\mathbf{D}_{s-t}(\phi_{m,n}, \theta_{m,n}; k) = \mathbf{D}_t(\phi_{m,n}, \theta_{m,n}; k) \otimes \mathbf{D}_s(\phi_{m,n}, \theta_{m,n}; k).$$

The clutter covariance matrix is unknown in practice. Many SMTI signal-processing architectures estimate the unknown clutter-plus-noise covariance matrix using training data. Observe that (9.12) is a function of range bin, k , thus acknowledging the potential for spatially varying clutter properties.

As discussed in [14], the model in (9.12) provides a good match to measured data. Figure 9-9 shows *minimum variance distortionless response* (MVDR) spectra (super-resolution views, see [10]) of the clutter angle-Doppler behavior for measured data taken from the Multi-Channel Airborne Radar Measurements (MCARM) program; the spectra in Figure 9-9 use estimated covariance matrices that average data over the range bins identified in the figure. Figure 9-10 shows the simulated response using the model of (9.12) and the radar parameters corresponding to the CPI shown in Figure 9-9.

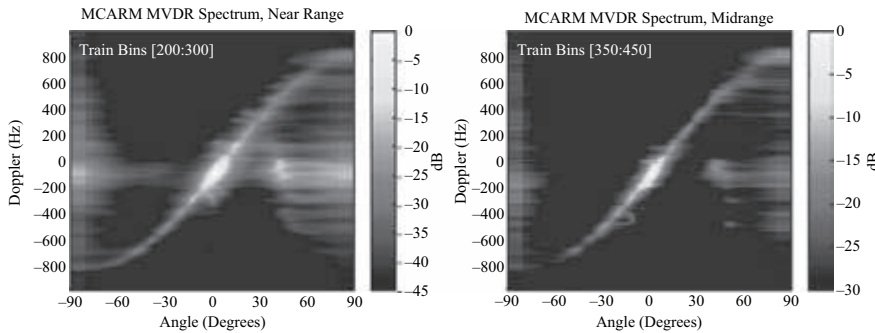


FIGURE 9-9 ■ Measured MCARM MVDR Spectra with Training Data Selected Over (a) Bins 200 to 300 and (b) Bins 350 to 450 [after [14], © 2006 IEEE].

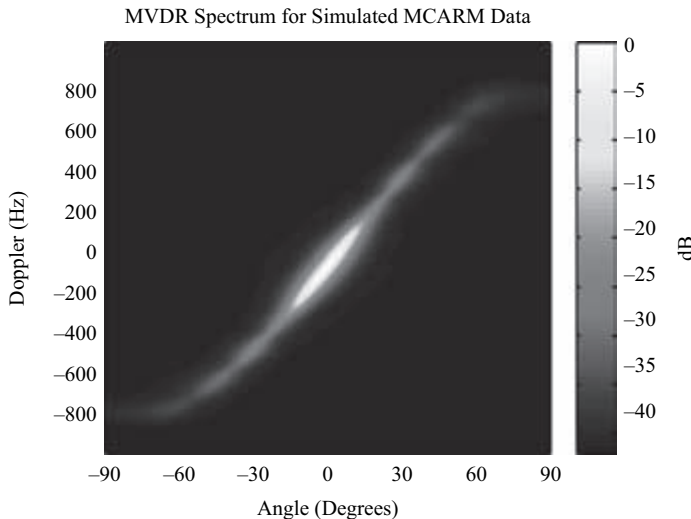


FIGURE 9-10 ■ MVDR Spectrum for MCARM Simulation [after [14], © 2006 IEEE].

Comparing Figure 9-10 with Figure 9-9, we see a very good match between the clutter responses. The primary difference is the end-fire clutter power spread observed in the measured data results due to multipath from the wing and radome struts corresponding to the port-mounted antenna system. Equation (9.12) does not model these multipath effects, which appear very near the system noise floor and have virtually no bearing on detection performance. Moreover, typical field deployments mount the antenna system under the fuselage to avoid such anomalous characteristics.

9.3.2 Targets

A description of different SMTI target models is given in Table 9-1. It is commonplace to use the fluctuating Swerling models to characterize SMTI targets [12]. The definitions in Table 9-1 differ slightly from [12] to account for modern radar operation.

In the Swerling 1 model, the target voltage is circular Gaussian as a result of the interaction of similarly sized subscatterers adding coherently and yielding, for certain aspects, a strong return, while for others a weak response. Otherwise, the target voltage is assumed perfectly correlated over the CPI. The weak response is called *target fading*. A Swerling 2 target exhibits decorrelated voltage responses from sample to sample. In the Swerling 2 case, the samples are target pixels taken from the RDMs generated for each of P CPIs, with each CPI corresponding to an offset and nonoverlapping transmit frequency. Frequency hopping purposely leads to target decorrelation and overcomes target fading effects.

To avoid the deleterious impact of fading, the SMTI radar employs offset center frequencies for each of the CPIs comprising the dwell. For example, an X-band SMTI radar might combine five 100-millisecond CPIs using a 30-MHz LFM waveform at center frequencies of 10 GHz, 10.03 GHz, 10.06 GHz, 10.09 GHz, and 10.12 GHz. The processor outputs from each CPI are then noncoherently combined to enhance detection performance. The envelope probability density function (PDF) is chi-squared for Swerling 3 and Swerling 4, with correlation properties matching Swerling 1 and Swerling 2; the presence of a dominant scatterer leads to the chi-squared envelope.

It is rare to assume the target is nonfluctuating. In the nonfluctuating model, the SNR is fixed, since the RCS is constant for all aspects. Sometimes the nonfluctuating target model is used in simulations to test and evaluate signal-processing algorithms.

TABLE 9-1 ■ SMTI Target Models

Target Type	Complex Envelope PDF	Temporal Correlation
Swerling 1	Rayleigh	Perfectly correlated over the CPI, RCS fluctuates due to changes in target aspect from CPI to CPI.
Swerling 2	Rayleigh	Uncorrelated from CPI to CPI, RCS fluctuates mainly due to frequency hopping between CPIs.
Swerling 3	Chi-squared	Same as Swerling 1.
Swerling 4	Chi-squared	Same as Swerling 2.
Nonfluctuating ("Swerling 0")	Delta function	Perfectly correlated over CPI, RCS is a constant value, yielding fixed SNR.

Most radar-system analyses exclusively rely on the Swerling 1–Swerling 2 model set. The target snapshot for Swerling 1 and Swerling 2 targets is

$$\mathbf{t}_k = \alpha_t \mathbf{s}_{s-t}(\phi, \theta, f_d) \quad (9.13)$$

where $\alpha_t = \sqrt{SNR \cdot P_n \zeta}$; P_n is the uncorrelated, receiver noise power; and ζ is a zero mean, unity variance complex Gaussian variate, viz. $\zeta \sim CN(0,1)$. With each frequency hop, ζ is redrawn to model the Swerling 1–Swerling 2 model.

9.3.3 Interference

RFI generally results from the reception of an in-band waveform generated by another electronic device, such as a communication system. The RFI waveform is uncorrelated with the radar waveform. The RFI data snapshot is

$$\mathbf{x}_J(nT) = w(nT) \mathbf{s}_s(\phi, \theta) \quad (9.14)$$

The RFI waveform, $w(t)$, exhibits noiselike characteristics, abiding for discrete times nT and qT by

$$E[w(nT)w^*(qT)] = \sigma_J^2 \delta((n - q)T) \quad (9.15)$$

where $\delta(nT)$ is the digital delta function and σ_J^2 is the RFI power.

In this model, the RFI exhibits spatial correlation, as it emanates from a specific angle relative to the radar, but the RFI waveform is white over the temporal aperture. The resulting space–time covariance matrix is

$$\mathbf{R}_{RFI} = \mathbf{I}_N \otimes \left(\sigma_J^2 \mathbf{s}_s(\phi, \theta) \mathbf{s}_s^H(\phi, \theta) \right) \quad (9.16)$$

In (9.16), \mathbf{I}_N is the $N \times N$ identity matrix. The space–time covariance matrix of the RFI is block diagonal as a result of (9.15); each block corresponds to a spatial covariance matrix identified within the parentheses of (9.16) that characterizes the RFI direction of arrival and power.

9.3.4 Space–Time Snapshot

Two models characterize the SMTI radar space–time snapshot. Under the null hypothesis, the snapshot for range bin k is

$$H_0 : \mathbf{x}_{s-t/k} = \mathbf{c}_k + \mathbf{j}_k + \mathbf{n}_k \quad (9.17)$$

whereas under the alternative hypothesis of target presence the snapshot appears as

$$H_1 : \mathbf{x}_{s-t/k} = \mathbf{t}_k + \mathbf{c}_k + \mathbf{j}_k + \mathbf{n}_k \quad (9.18)$$

\mathbf{n}_k is the uncorrelated receiver noise component, $\mathbf{n}_k \sim CN(\mathbf{0}, \sigma_n^2 \mathbf{I}_{NM})$, where σ_n^2 is the receiver noise power, \mathbf{I}_{NM} is the NM by NM identity matrix, and $\mathbf{0}$ is the zero vector (of length NM by 1, in this case). The snapshot is organized by stacking each spatial snapshot for a given pulse one on top of the other.

Since clutter, interference, and noise signals are independent, the null-hypothesis covariance matrix is

$$\mathbf{R}_k = \mathbf{R}_{c/k} + \mathbf{R}_{RFI} + \sigma_n^2 \mathbf{I}_{NM} \quad (9.19)$$

The SMTI radar signal processor manipulates the space–time snapshot at each range to determine which of the two hypotheses is most likely valid. Each of the elements of the space–time snapshot are coherently combined to ideally provide acceptable probability of detection at a required false alarm density.

9.4 | SMTI METRICS

9.4.1 Probability of Detection

The objective of the SMTI radar is to maximize probability of detection while maintaining an acceptable false alarm rate. The *receiver operating characteristic* (ROC) describes detection performance as a function of the *probability of false alarm* (P_{FA}) and output SINR. Figure 9-11 shows the ROC curves for nonfluctuating (denoted Swerling 0) and Swerling 1 targets in circular Gaussian disturbance. SINR is shown using the target RMS power. (A ROC curve more commonly plots probability of detection versus probability of false alarm for varying SINR.) The difference between the Swerling 1 curve relative to the nonfluctuating case for a fixed probability of detection and false alarm rate is known as *fluctuation loss*.

Figure 9-11 reveals that probability of detection increases monotonically with output SINR for a fixed probability of false alarm [15]. In addition, the figure shows that small changes in output SINR generally lead to large changes in probability of detection. Thus, it is critical the radar signal processor maximize output SINR to achieve best performance.

Over the CPI, the target RCS is assumed constant. The constant RCS value, however, is a random variable with a Rayleigh-distributed complex envelope (or exponentially distributed power). This randomness describes the Swerling 1 fluctuating target model. According to the curve in Figure 9-11, the *fluctuation loss*, $L_{fluctuate}$, between the nonfluctuating (Swerling 0) target and the Swerling 1 target is about 8 dB at $P_D = 0.9$

FIGURE 9-11 ■ Receiver Operating Characteristic (ROC) Curve.

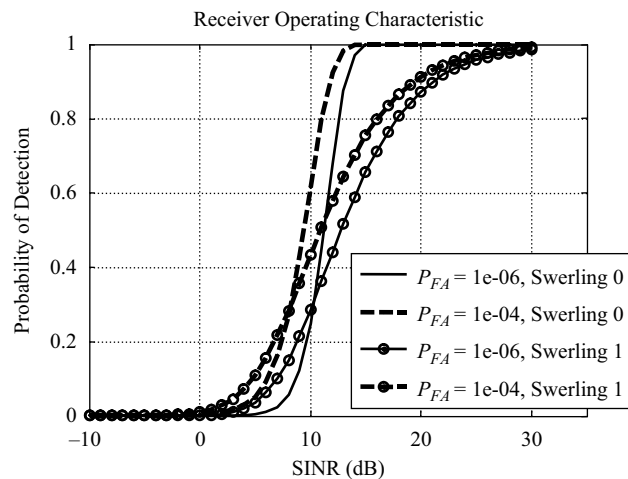


TABLE 9-2 ■ Postdetection Integration Performance Gains, $P_{FA} = 1E - 6$

NCAs	$I(n)$ (from [12])	$P_D = 0.9, L_{fluctuate} = 8$ dB		$P_D = 0.5, L_{fluctuate} = 1.25$ dB		
		Required Input SINR Fluctuating (dB)	Required Input SINR Nonfluctuating (dB)	$I(n)$ (from [12]) (dB)	Required Input SINR Fluctuating (dB)	Required Input SINR Nonfluctuating (dB)
1	0	21.2	13.2	0	12.75	11.5
2	7.5	13.7	10.2	4	8.75	8.5
3	10	11.2	8.4	5.5	7.25	6.7
4	11.5	9.7	7.2	6.5	6.25	5.5
5	13	8.2	6.2	7.5	5.25	4.5

and $P_{FA} = 1E - 6$ and 1.25 dB at $P_D = 0.5$ for the same false alarm rate. To enhance performance against target fluctuation (or, equivalently, target fading), the SMTI radar system commonly frequency hops to decorrelate the target voltage from CPI to CPI, thus inducing Swerling 2 target behavior. Through noncoherent addition (NCA) of the voltage outputs from CPI-level processing, the radar achieves integration gain. This latter step is called *postdetection integration*.

Table 9-2 describes the detection performance gain resulting from PDI. The first column gives the number of CPIs noncoherently summed. The table is then broken into halves: desired $P_D = 0.9$ and desired $P_D = 0.5$. The false alarm rate is $P_{FA} = 1E - 6$. $I(n)$ is the integration gain resulting from the NCA of the uncorrelated, Swerling 2 target voltages relative to the single CPI case; these values are taken from [12]. The column labeled “Required input SINR fluctuating” is the required single CPI SINR input to the PDI process to achieve the desired detection probability. The column labeled “Required input SINR nonfluctuating” is the single CPI SINR required when the *coherent* integration time is increased by a factor equal to the number of NCAs and the target RCS does not fluctuate (Swerling 0).

The required input SINR is always lower for the nonfluctuating case since there is no fading loss and the coherent integration is optimal. The required input SINR for the fluctuating case is given as the required Swerling 1 SINR from Figure 9-11 (the value when the number of NCAs is unity) minus the integration gain, $I(n)$. The “Required input SINR fluctuating” is the requirement at the output of all coherent-processing steps, prior to PDI, to achieve the desired detection probability. As seen from Table 9-2, there is only slight performance loss between the fluctuating and nonfluctuating cases for $P_D = 0.5$. However, PDI provides substantial gain at the more useful, higher detection probabilities, with only a few decibels of SINR separating the performance between coherently integrated nonfluctuating and PDI fluctuating cases.

9.4.2 False Alarm Density

In SMTI radar, it is desirable to specify the number of false alarms per area. This false alarm density is calculated by converting the probability of false alarm to number of false reports per area under surveillance,

$$\text{FAD} = P_{FA} \left(\frac{\text{Number of Decisions}}{\text{Beam Area}} \right) \quad (9.20)$$

The beam area is approximately given by

$$\text{Beam Area} \cong \frac{\pi}{4} \left((R_{toe} - R_{heel}) \sec \psi_{toe} \right) (R_{center} \phi_{3dB}) \quad (9.21)$$

where

R_{toe} and R_{heel} are slant ranges corresponding to the 3-dB points of the antenna elevation beam pattern intersecting Earth's surface,

ψ_{toe} is the grazing angle at the toe,

R_{center} is the slant range to scene center, and

ϕ_{3dB} is the antenna's 3-dB beamwidth in azimuth (see Figure 9-7).

A suitable SMTI false alarm density is on the order of 0.1/km². A high FAD masks targets of interest and makes target associations very difficult.

9.4.3 Signal-to-Interference-Plus-Noise Ratio Loss

Signal-to-interference plus noise ratio (SINR) directly affects probability of detection, as discussed in Section 9.4.1. The output SINR of the linear filter,

$$y_k = \mathbf{w}_k^H \mathbf{x}_{s-t/k} = \sum_{m=1}^{NM} [\mathbf{w}_k]_m^* [\mathbf{x}_{s-t/k}]_m \quad (9.22)$$

where $\mathbf{w}_k \in C^{NM \times 1}$ is the complex weight vector and $*$ denotes the conjugation operation, is

$$\begin{aligned} \text{SINR} &= \frac{\text{Target Signal Power}}{\text{Interference} + \text{Noise Power}} = \frac{E[y_{k/t} y_{k/t}^*]}{E[y_{k/H_0} y_{k/H_0}^*]} \\ &= \frac{E[\mathbf{w}_k^H \mathbf{t}_k \mathbf{t}_k^H \mathbf{w}_k]}{E[\mathbf{w}_k^H \mathbf{x}_{k/H_0} \mathbf{x}_{k/H_0}^H \mathbf{w}_k]} = \frac{\sigma_t^2 |\mathbf{w}_k^H \mathbf{s}_{s-t}(\phi_t, \theta_t, f_{d/t})|^2}{\mathbf{w}_k^H \mathbf{R}_{k/H_0} \mathbf{w}_k} \end{aligned} \quad (9.23)$$

$y_{k/t}$ and y_{k/H_0} are filter outputs for cases of target-only and the null hypothesis; ϕ_t , θ_t , and $f_{d/t}$ are target azimuth, elevation, and Doppler frequency; σ_t^2 is the target power; and, \mathbf{x}_{k/H_0} and \mathbf{R}_{k/H_0} are the null-hypothesis snapshot and covariance matrix, respectively.

SINR loss compares the performance degradation between a given processor implementation and an ideal. The most commonly used SINR loss term is defined as

$$L_{s,1} = \frac{\text{SINR}}{\text{SNR}} = \frac{\left(\frac{\sigma_t^2 |\mathbf{w}_k^H \mathbf{s}_{s-t}(\phi_t, \theta_t, f_{d/t})|^2}{\mathbf{w}_k^H \mathbf{R}_{k/H_0} \mathbf{w}_k} \right)}{\left(\frac{\sigma_n^2}{\sigma_t^2} NM \right)} = \frac{\sigma_n^2 |\mathbf{w}_k^H \mathbf{s}_{s-t}(\phi_t, \theta_t, f_{d/t})|^2}{NM \mathbf{w}_k^H \mathbf{R}_{k/H_0} \mathbf{w}_k} \quad (9.24)$$

Equation (9.24) is sometimes called *clairvoyant* SINR loss, since its calculation requires knowledge of the null-hypothesis covariance matrix; it must be approximated when using real-world data. Factors influencing the SINR loss in (9.24) include the

severity of the clutter and interference environment, the system design, and the particular algorithm defined by the selection of \mathbf{w}_k .

Another commonly used SINR loss metric is called *adaptive* SINR loss. It compares the difference in performance between an adaptive filter and its optimal implementation. The adaptive filter must estimate unknown quantities in its implementation, viz., the null-hypothesis covariance matrix and the target space–time steering vector, and the adaptive SINR loss captures the impact of estimation error. Adaptive SINR loss is given by

$$L_{s,2} = \frac{\text{Adaptive SINR}}{\text{Clairvoyant SINR}} = \frac{\left(\frac{|\widehat{\mathbf{w}}_k^H \mathbf{s}_{s-t}(\phi_t, \theta_t, f_{d/t})|^2}{\widehat{\mathbf{w}}_k^H \mathbf{R}_{k/H_0} \widehat{\mathbf{w}}_k} \right)}{\left(\frac{|\mathbf{w}_k^H \mathbf{s}_{s-t}(\phi_t, \theta_t, f_{d/t})|^2}{\mathbf{w}_k^H \mathbf{R}_{k/H_0} \mathbf{w}_k} \right)} \quad (9.25)$$

$\widehat{\mathbf{w}}_k$ is the adaptive weight vector, an estimate for \mathbf{w}_k computed using known quantities. For example, STAP employs $\widehat{\mathbf{w}}_k$ in its implementation. $L_{s,2}$ is a random variable and is described in further detail in [16]. In the case where $\widehat{\mathbf{w}}_k = \mathbf{w}_k$, it is seen $L_{s,2} = 1$ in (9.25).

In [16], it is shown that when the training data used to estimate the covariance matrix in $\widehat{\mathbf{w}}_k$ (to be described subsequently) are *independent and identically distributed* (iid) and the data are complex Gaussian, then the adaptive losses are roughly 3 dB on average when the processor uses a training data interval of roughly twice the processor's degrees of freedom (e.g., *NM* for STAP). This is sometimes called the *Reed-Mallett-Brennan rule* after the authors of [16].

The SINR loss terms are all bound between zero and unity. Since the SINR loss terms are all applied directly as numerator terms to the radar-range equation, negative-valued losses in decibels are indeed losses. This might seem like an oxymoron, but it is standard convention in the SMTI and STAP communities.

An example of SINR loss, $L_{s,1}$, is shown in Figure 9-12. This figure compares estimated SINR loss using data taken from the MCARM system against simulated loss using the clutter model from the prior section and the calculation in (9.24). The numbers in the legend correspond to the range bins used to estimate the clutter-plus-noise covariance matrix. While the MCARM system used a side-looking antenna, the clutter null in Figure 9-12 is shifted from 0 Hz due to a few degrees of yaw. The match between the simulated and measured data results is very good.

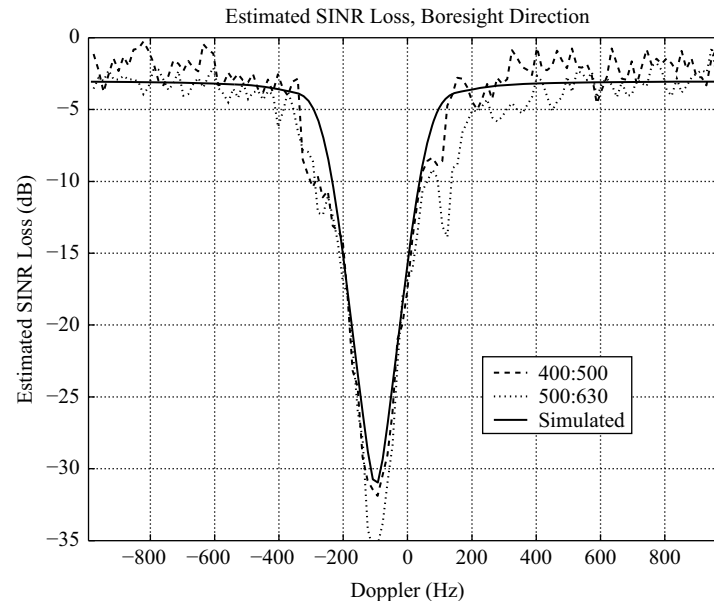
9.4.4 Minimum Detectable Velocity

The *minimum detectable velocity* is a critical SMTI performance metric that drives aperture, platform, and algorithm selection. Minimum detectable velocity is defined as the minimum target velocity where the radar system provides an acceptable, specified probability of detection at the desired false alarm rate. The severity of the clutter environment affects MDV. ICM is a fundamental, limiting factor on radar MDV.

MDV is approximated as follows:

- Calculate, or estimate, the target SNR;
- calculate, or estimate, the aggregate SINR loss, e.g., $L_{s,1} \cdot L_{s,2}$;

FIGURE 9-12 ■
Example SINR loss,
measured and
simulated data [after
[14], © 2006 IEEE].



- estimate SNR enhancement resulting from noncoherent addition; and, finally,
- determine the lowest target velocity where the product of SNR, SINR loss, and noncoherent gain exceeds the SINR required to achieve the desired probability of detection for the specified probability of false alarm or FAD.

Usually, high-fidelity numerical simulation is used to calculate $L_{s,1} \cdot L_{s,2}$. Estimating $L_{s,1} \cdot L_{s,2}$ requires a good estimate of the radar noise floor and an excellent estimate of the array response relative to the ideal steering manifold.

9.4.5 Area Coverage Rate

A common SMTI specification is: cover a specified area in a minimum allowable time, while providing a desired MDV against a certain target class at a maximum range designation.

Figure 9-7 depicts the radar search in WAS mode. The beam area for a chosen bar is specified by (9.21). The total time in each beam is called the *dwell time* and is the sum of the CPI lengths corresponding to each fixed beam position. Factors influencing the CPI length include the desired integration gain, target acceleration, and required Doppler resolution. Then the area coverage rate is given in straightforward fashion by

$$ACR = (\text{Area/Beam}) / (\text{Dwell/Beam}) \quad (9.26)$$

The ACR is spatially varying. In this case, it makes sense to specify an average value. Equation (9.26) must consider beam overlap to provide the most accurate estimate.

9.4.6 Parameter Estimation Accuracy

After detecting a target, the radar system generally attempts to estimate target location and speed. The radar first determines the target bearing (in antenna coordinates) and then, using knowledge of the platform location and antenna state, the radar processor maps the bearing estimate to a location within a fixed coordinate system. This coordinate system may be local – such as *north–east–down* (NED) – but given knowledge of the origin and orientation, is easily relatable to an Earth-centered framework, such as *latitude–longitude–altitude* (LLA) with World Geodetic System (WGS) standards. WGS-84 is the current standard.

The processor further estimates the target range–rate through the Doppler frequency estimate and *inertial navigation unit* (INU) data coupled to a Global Positioning System (GPS) receiver. The INU/GPS provides estimates of the platform-velocity vector and antenna-pointing direction; this information is needed to map the measured Doppler frequency shift, comprising both target and platform motion, to the target range–rate.

It is common to assess position and range–rate accuracy using root mean square error estimates. The RMS error is the square root of the square of the difference between the components of the actual parameter value and the estimate. When characterizing position error, it is common to report the total error. It is also common to specify the *elliptical error probable* (EEP) for 50-percent or 90-percent levels. EEP-50 is the ellipse projected onto Earth’s surface characterizing the accuracy of half the measurements. For example, a 1-m by 1-m EEP-50 indicates that 50 percent of the estimates are within a circle at least 1 m from the true location. (When the ellipse defaults to a circle, this measure is called the *circular error probable*, or CEP.) Similarly, EEP-90 indicates 90 percent of the targets fall within an ellipse on Earth’s surface with specified semi-major and semiminor axes.

9.5 | ANTENNA AND WAVEFORM CONSIDERATIONS

This section briefly overviews antenna and waveform issues important in SMTI radar operation.

9.5.1 Antenna

The along-track length (horizontal array dimension), height, frequency, number of channels, and subarray design are important SMTI antenna design choices.

9.5.1.1 Along-Track Antenna Length

The along-track antenna length determines the azimuth beamwidth. Coupled with the platform velocity, the azimuth beamwidth determines the spread of mainlobe clutter. Assume a side-looking array configuration, since the Doppler spread is greatest in this case. Let ϕ_c be the cone angle from the platform center line – and, hence, platform-velocity

vector – to a particular point of interest. The Doppler frequency at the antenna 3-dB point closest to the velocity vector, and on Earth's surface, is

$$f_{d/1} = \frac{2v_p}{\lambda} \cos(\phi_c - \Delta_B) \quad (9.27)$$

where v_p is the platform velocity, λ is wavelength, and $2\Delta_B$ is the 3-dB antenna azimuth beamwidth. The corresponding Doppler at the 3-dB point farthest from the velocity vector is

$$f_{d/2} = \frac{2v_p}{\lambda} \cos(\phi_c + \Delta_B) \quad (9.28)$$

The total mainbeam Doppler spread is the difference between (9.27) and (9.28); this spread has a profound impact on MDV. Usually, techniques like STAP can reduce the MDV from the diffraction-limited spread given by the difference between (9.27) and (9.28) by a factor of 2 or more. For nonadaptive methods, the radar dwell must increase substantially to reduce the MDV. This latter approach is not as efficient as increasing the along-track antenna length.

9.5.1.2 Antenna Height

In SMTI radar, antenna height determines the elevation beamwidth and, hence, the footprint length (in range) on Earth's surface. The footprint size impacts the highest selectable pulse repetition frequency (PRF) if the radar is to avoid range ambiguities within the antenna mainlobe. It is desirable to ensure that only one pulse traverses the footprint at any given time, since clutter fold-over increases the CNR and can appear spectrally divergent when the antenna normal and velocity vector are nonorthogonal.

Given the platform height, h_p , and the effective Earth radius, R_{EM} , both in meters, the relationship between the angle from nadir, θ_{nadir} , and the slant range, R_{slant} , is

$$R_{slant} = (R_{EM} + h_p) \cos \theta_{nadir} - \sqrt{\left((R_{EM} + h_p) \cos \theta_{nadir} \right)^2 - h_p(2R_{EM} + h_p)} \quad (9.29)$$

To determine the range to the antenna footprint toe and heel, take the antenna elevation beam-pointing angle and the antenna elevation beamwidth, convert the antenna elevation 3 dB points into nadir angles, and then substitute into (9.29). Next, the grazing angle, ψ_g , follows as

$$\psi_g = -\arcsin\left(\frac{R_{slant}^2 - h_p(2R_{EM} + h_p)}{2R_{EM}R_{slant}}\right) \quad (9.30)$$

As (9.21) shows, the footprint length is $(R_{toe} - R_{heel}) \sec \psi_{toe}$. The unambiguous ground range is given by

$$R_{amb} \approx \frac{cT}{2} \sec \psi_{toe} \quad (9.31)$$

with c being the speed of light. To avoid ambiguities within the footprint, we require

$$R_{amb} \geq (R_{toe} - R_{heel}) \sec \psi_{toe} \quad (9.32)$$

The PRF is then constrained as

$$PRF \leq \frac{c}{2(R_{toe} - R_{heel}) \sec \psi_{toe}} \quad (9.33)$$

Increasing the height of the antenna decreases the 3-dB elevation beamwidth and the length of the footprint, thereby allowing radar operation at a higher PRF. The higher PRF is useful to mitigate Doppler ambiguity and reduce the number of receive channels.

9.5.1.3 Subarray Design Considerations

There are several approaches to design a multichannel radar: form subapertures from the elements of a phased array antenna, employ reflector antennas offset in elevation baseline and mechanically squinted in azimuth, or use horn antennas squinted to form multiple beams in azimuth and elevation. Forming multiple subapertures from a phased array antenna is generally the preferred approach, since the phased array radar most readily supports wide area search and other radar modes.

A digital subarray is usually a collection of radiating elements, electronically combined to form a receive beam in a specified direction, and including a receiver and analog-to-digital converter. The SMTI radar will use M subarrays, or channels, to spatially sample propagating electromagnetic waves impinging on the array. In some cases, especially for lower frequency applications, the system combines a column of radiating elements into a single along-track channel. Figure 9-13 shows these example subarray configurations for $M = 4$.

Grating lobes (or high-peak sidelobes) are spatial ambiguities occurring for uniformly sampled arrays when the separation between spatial sample points exceeds $\lambda/2$. Specifically, grating lobes occur in a uniform linear array at *cone angles*

$$\phi_c = \arccos\left(\cos\phi_{scan} + \frac{n\lambda}{d}\right) \quad (9.34)$$

where

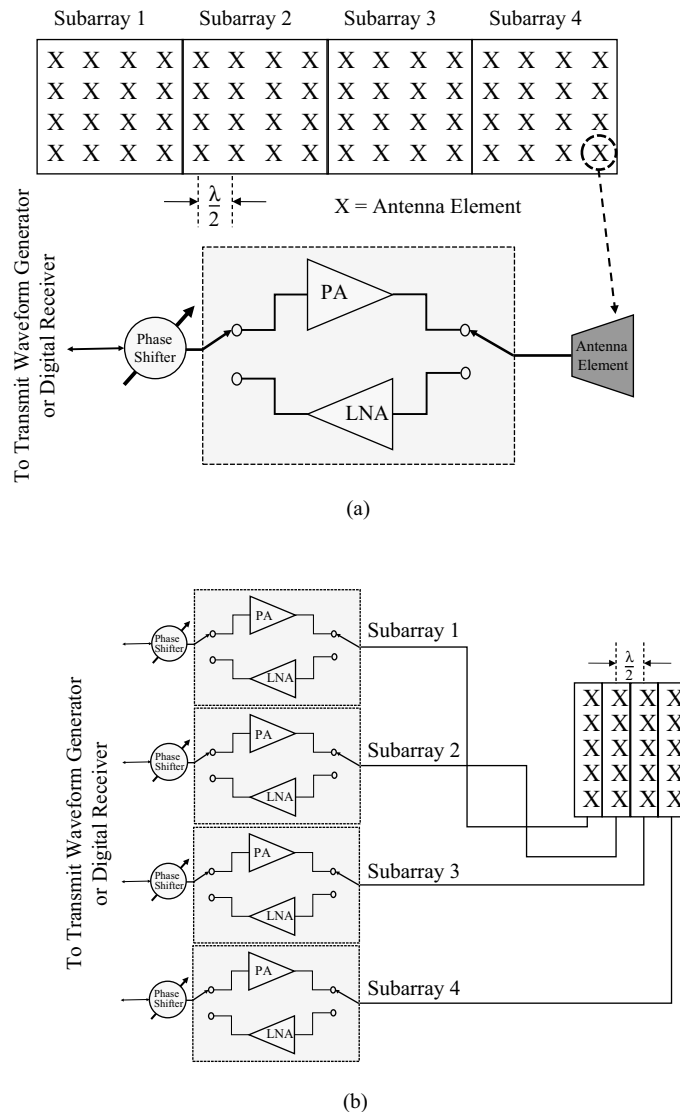
ϕ_{scan} is the scan cone angle,

d is the subarray channel spacing, and

n is an integer chosen to yield a real solution,

thereby satisfying $-1 \leq \cos\phi_{scan} + \frac{n\lambda}{d} \leq 1$. (Note: A ULA measures cone angle, and this cone angle generally differs from the Doppler cone angle previously defined, depending on the antenna mounting. The Doppler and antenna cone angles are the same when the ULA is oriented along the platform-velocity vector. The difference between the two cone angles is evident from context in our discussion.) Grating lobes are problematic in SMTI for two main reasons. First, if beam spoiling is used on transmit, then care should be taken to ensure the mainlobe transmit pattern does not extend into the angle ambiguous receive region; otherwise, the processor suffers significant clutter loss in the look direction – but at Doppler frequencies away from the unambiguous clutter ridge extent. The appearance of additional clutter ridges intersecting the look direction lead to target-blind Dopplers. A secondary concern is the presence of RFI in the vicinity of a spatial ambiguity. Adaptive spatial nulling suppresses the RFI source at the expense of a distorted gain pattern in the desired look direction and higher sidelobes.

FIGURE 9-13 ■
Examples of Subarray Configurations: (a) Nonoverlapped, 4×4 Subarray Configuration, with Each Antenna Element Tied to its Own Power Amplifier (PA), Low Noise Amplifier (LNA), Switches, and Phase Shifter; (b) a Column of Antenna Elements Called a Stick Summed Together and Fed to a Transmit-Receive Module.



Overlapped subarrays represent another design option. In the overlapped subarray design, antenna elements are shared among receive channels. In this approach, phase centers are moved closer, thereby pushing grating lobes out toward the invisible region (beyond $\pm 90^\circ$). Sharing subarray elements results in the correlation of receiver noise. The impact of element reuse and receiver noise correlation is generally minor.

As shown in [17], M spatial channels support $M - 1$ nulls. As a general rule, an SMTI radar system requires at least three channels ($M = 3$) to simultaneously null clutter and form a beam in the target search direction. This is the case for the Joint STARS radar, as mentioned in Section 9.1. Referring to Figures 9-8 through 9-10, when the clutter ridge is unambiguous in Doppler within the mainlobe, a single spatial null is

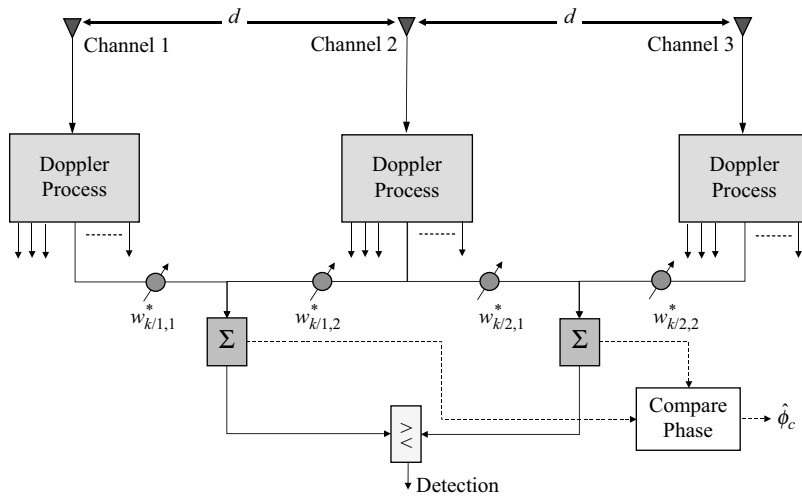


FIGURE 9-14 ■ Three-channel SMTI Processing Architecture.

sufficient to suppress clutter, assuming the target Doppler is adequately separated from the clutter coming from the look angle. Figure 9-14 highlights one approach to combine three channels to mitigate clutter and derive an estimate of the target bearing. In this case, the system cancels clutter between channel pairs, summing the results prior to making a detection decision. Once a target is identified, and assuming a uniform linear array, the system provides an estimate of target cone angle, $\hat{\phi}_c$, through a phase comparison of the clutter-canceled channel pairs. A Doppler-ambiguous clutter response requires additional spatial channels for effective operation.

9.5.2 Waveforms

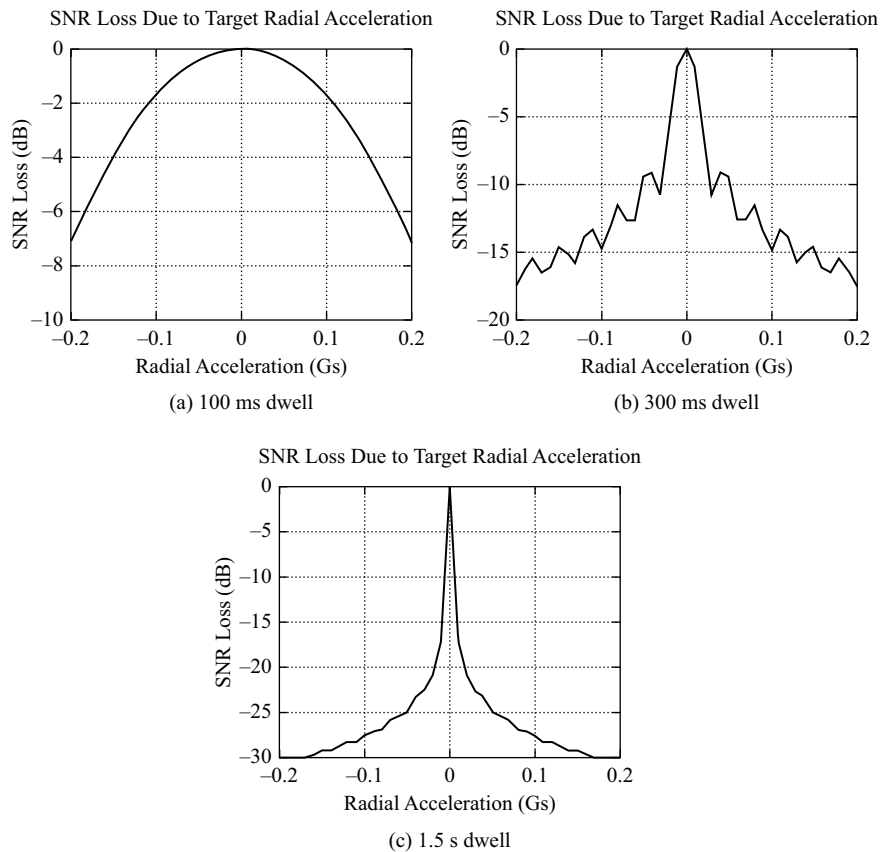
SMTI radar systems generally employ pulse-compression waveforms to achieve desired range resolution [18]. Use of the LFM waveform is most common.

The typical range resolution of an SMTI radar system varies from a few meters to a dozen meters, depending on the target of interest. This suggests waveform bandwidths from roughly 10 MHz up to 50–60 MHz.

After the SMTI radar detects a target, it may collect a high-range resolution profile to facilitate target feature discrimination. HRR profiles aid target association and tracking.

A typical SMTI dwell consists of a series of CPIs offset in frequency to enhance performance against fading targets. Target acceleration is a primary consideration when selecting the dwell time. When left uncompensated, target acceleration significantly degrades performance. Figure 9-15 shows signal-to-noise ratio (SNR) loss as a function of acceleration for varying coherent dwells and a typical X-band radar configuration; from this figure we see that losses due to 0.1 G acceleration are roughly 2 dB for a 100 ms dwell, 15 dB for a 300 ms dwell, and excessive for a 1.5 s dwell. Thus, target acceleration limits dwell times to 200–300 ms, perhaps organized as four or five 64 ms CPIs. Selection of longer dwells is certainly possible if either target acceleration is not a significant concern or the processor compensates for acceleration.

FIGURE 9-15 ■ SNR Loss due to Acceleration for Different Coherent Dwells.



9.6 | CLUTTER-MITIGATION APPROACHES

In this section we consider strategies to mitigate the impact of ground-clutter returns on detection performance. In each case, we describe the method and then benchmark its performance using a standard radar example. This allows for a fair comparison of the different algorithms.

The methods considered include Doppler processing, adaptive Doppler processing, DPCA, adaptive DPCA, STAP, and post-Doppler STAP. This progression moves from one-dimensional (temporal) nonadaptive processing, incorporates adaptivity, and then moves to two-dimensional (space–time) nonadaptive and then adaptive processing. It is seen that space–time processing provides the necessary DoFs to suppress the clutter power distributed over angle and Doppler. Moreover, STAP provides the best performance potential by a significant margin.

9.6.1 Nonadaptive and Adaptive Doppler Processing

Starting with the space–time data of (9.17) and (9.18), the beam-space transformation, T_B , collapses the spatial DoFs,

$$\mathbf{x}_{t/k} = T_B^H \mathbf{x}_{s-t/k}; \quad T_B = I_N \otimes s_s(\phi, \theta), \quad (9.35)$$

yielding the length N temporal snapshot, $\mathbf{x}_{t,k}$, for the k th range bin. For example, considering the case where $N = 3$,

$$\mathbf{T}_B = \begin{bmatrix} \mathbf{v}_s(\phi, \theta) & \mathbf{0}_M & \mathbf{0}_M \\ \mathbf{0}_M & \mathbf{v}_s(\phi, \theta) & \mathbf{0}_M \\ \mathbf{0}_M & \mathbf{0}_M & \mathbf{v}_s(\phi, \theta) \end{bmatrix} \quad (9.36)$$

with $\mathbf{0}_M$ the length M zero vector. In this case, \mathbf{T}_B is NM by N .

The output of the Doppler processor for the k th range and Doppler frequency f_d is

$$y_k = \left(\mathbf{a}_t \odot \mathbf{v}_t(f_d) \right)^H \mathbf{x}_{t/k}, \quad (9.37)$$

where \mathbf{a}_t is a real weighting (e.g., Hanning, Chebyshev) and $\mathbf{v}_t(f_d)$ is a hypothesized steering vector (since the actual Doppler frequency of the target is unknown in practice). In (9.37), the weight vector is nonadaptive and the same for every range bin: $\mathbf{w}_k = \mathbf{a}_t \odot \mathbf{v}_t(f_d)$.

The temporal clutter covariance matrix follows from (9.19) as $\mathbf{R}_{t/k} = \mathbf{T}_B^H \mathbf{R}_k \mathbf{T}_B$. Benchmark assessment requires the temporal covariance matrix.

Doppler processing improves detection performance by increasing the system resolution so that the target RCS exceeds that of the background clutter by an acceptable margin. The Doppler resolution is β_{dop} , which equals the inverse of the coherent dwell time. Applying a real weighting to control sidelobes, such as a Chebyshev weighting, leads to degraded Doppler resolution. The Doppler resolution has a corresponding angular extent, called the *Doppler beamwidth*, that subtends points on Earth's surface that contribute clutter power to the Doppler filter of interest. The Doppler beamwidth, θ_{DBS} , follows by taking the difference between (9.27) and (9.28) over an angular extent identified by the Doppler spread across the Doppler filter output, setting the result equal to the Doppler resolution, and simplifying,

$$f_{d/1} - f_{d/2} = \frac{2v_p}{\lambda} (2\sin\phi_c \sin\Delta_D) \approx \left(\frac{2v_p}{\lambda} \sin\phi_c \right) 2\Delta_D = \beta_{dop} \quad (9.38)$$

where $\Delta_D = \theta_{DBS}$ is the Doppler half-beamwidth and DBS refers to ‘‘Doppler beam sharpening.’’ From (9.38) we find

$$\theta_{DBS} = 2\Delta_D \approx \frac{\lambda\beta_{dop}}{2v_p \sin\phi_c} \quad (9.39)$$

It is seen from (9.39) that as the Doppler resolution improves (gets smaller or finer), the Doppler beamwidth gets narrower or sharper. The signal-to-clutter ratio (SCR) is

$$\frac{\text{Target Signal Power}}{\text{Noise Power}} \times \frac{\text{Noise Power}}{\text{Clutter Power}} = \frac{\text{Target Signal Power}}{\text{Clutter Power}} = \frac{\sigma_{target}}{\sigma_{clutter}} \quad (9.40)$$

where σ_{target} is the target RCS and $\sigma_{clutter}$ is the clutter RCS. The clutter RCS equals the clutter reflectivity, σ_0 , times the clutter cell area, A_c ,

$$\sigma_{clutter} = \sigma_0 A_c = \sigma_0 (\delta_r \delta_{cr}) \quad (9.41)$$

The range resolution in the ground plane is δ_r , and the cross-range resolution is δ_{cr} . The range resolution is

$$\delta_r = \left(\frac{c\tau_c}{2}\right)\sec\psi_g, \quad (9.42)$$

with τ_c the compressed pulse width, whereas

$$\delta_{cr} = \theta_{DBS} \times r = \frac{\lambda\beta_{dop}r}{2v_p\sin\phi_c} \quad (9.43)$$

is the cross-range resolution. As the Doppler resolution, β_{dop} , gets finer, the cross-range extent lessens in accord with (9.43). Thus, the clutter cell area halves with each doubling of the coherent dwell. In this manner, the SCR improves by a factor equal to the increase in dwell time, as seen from (9.43). The increased resolution enhances detection performance. Target motion places a natural limit on coherent dwell time, as discussed in Section 9.5.2. Adaptive Doppler processing overcomes diffraction-limited beamwidths using shorter dwells.

Given $\mathbf{x}_{t/k}$, the weight vector maximizing output SINR is

$$\mathbf{w}_k = \mu_t \mathbf{R}_{t/k}^{-1} \mathbf{s}_t(f_d), \quad (9.44)$$

where μ_t is an arbitrary scalar and $\mathbf{s}_t(f_d)$ is the target steering vector [19]. Equation (9.44) is optimal in the maximum SINR sense. The adaptive Doppler weight vector follows from (9.44) after replacing $\mathbf{R}_{t/k}$ with the covariance matrix estimate, $\hat{\mathbf{R}}_{t/k}$, and the precise target Doppler steering vector, $\mathbf{s}_t(f_d)$, with the hypothesized steering vector, $\mathbf{v}_t(f_d)$. The covariance estimate is

$$\hat{\mathbf{R}}_{t/k} = \frac{1}{K} \sum_{\substack{m=1 \\ m \neq k}}^K \mathbf{x}_{t/m} \mathbf{x}_{t/m}^H, \quad (9.45)$$

which is a maximum likelihood estimate when the training data, $\mathbf{x}_{t/m}$, are iid relative to the null hypothesis of the cell under test and otherwise Gaussian distributed [16]. Generally, $2N \leq K \leq 5N$, where K is the number of samples used to calculate the covariance matrix estimate given in (9.45).

Using the clutter and noise signal models and covariance matrices described in Section 9.3 to generate synthetic data, a relative comparison of the performance of the following processing methods is shown in Figure 9-16: optimal space–time processor (described in Section 9.6.3); the standard STAP implementation using sample matrix inversion (SMI) (again, see Section 9.6.3), which is a data domain implementation of the optimal processor; the Doppler processor, using a Hanning amplitude weighting to control sidelobe levels; and the adaptive Doppler processor. This scenario corresponds to a representative, side-looking airborne radar with a CNR of approximately 60 dB, $N = 24$ pulses, and $M = 11$ spatial channels. A complete space–time-range data cube is simulated, and then *digital beam forming* (DBF) is applied to collapse the 11 channels to one receive beam focused in the transmit direction, thus reducing the data DoFs to temporal only.

Figure 9-16 shows the composite SINR loss, $L_{s,1} \cdot L_{s,2}$, in the transmit direction for each of the algorithm implementations. Noise-limited performance aligns with 0 dB on

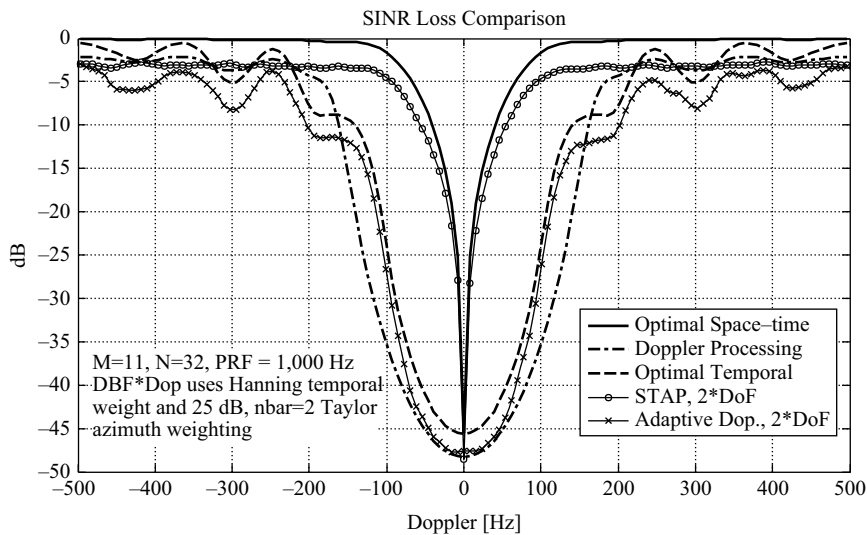


FIGURE 9-16 ■ SINR Loss Comparison of Doppler Processing and Adaptive Doppler Processing Relative to the Space-time Optimal and STAP Performance Characteristics.

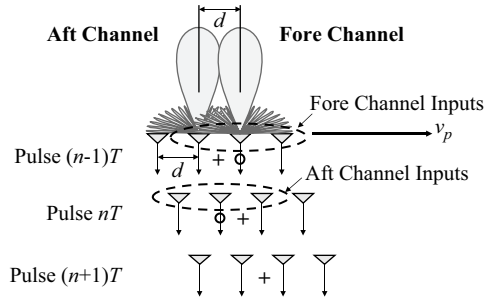
the loss axis. Note the results correspond to the same collected data processed in different ways. It is seen from the figure that the optimal processor provides the best performance, exhibiting a very tight null in the vicinity of the mainlobe clutter centered at 0 Hz Doppler. The SMI-STAP performance, using 2 NM training samples, closely tracks the optimal performance, with slight loss due to the finite training data set and corresponding covariance matrix estimation error. The Doppler processing performance is generally poor, as it is diffraction limited; the size of the space-time aperture limits its achievable capability. Adaptive Doppler processing shows only slight improvement; this is the case, since the adaptive Doppler processor can only null in the temporal (Doppler) domain, whereas clutter distributes along a two-dimensional region of support covering both angle and Doppler measurement spaces. In the adaptive Doppler processing case, clutter from the same Doppler but a slightly different angle spills over and degrades detection performance.

9.6.2 Nonadaptive and Adaptive DPCA

As seen from Figure 9-16, one-dimensional Doppler processing yields poor performance potential relative to the space-time optimal result. As ground-clutter returns exhibit a region of support in space and time, two-dimensional filtering is necessary to null the clutter response. Adaptive Doppler processing can only null along a one-dimensional line corresponding to the Doppler dimension; clutter at the same Doppler frequency but with a different angle of arrival bleeds into the target filter, leading to degraded SINR (increased SINR loss) and reduced detection performance.

DPCA is a two-dimensional, nonadaptive filtering method [20, 21]. It applies to a side-looking, multichannel radar with precise pulse-to-pulse timing control. The essence of the DPCA concept is to arrest platform motion by timing the position of the aft receive channel on a given pulse to electronically align with the fore channel on the preceding pulse. In this manner, the ranges to all stationary scatterers remains constant and the processor can simply subtract the aft channel output on a given pulse from the

FIGURE 9-17 ■
Description of DPCA
Concept.



fore channel on the preceding pulse to precisely cancel the ground-clutter signal. The DPCA condition requires

$$v_p T = \frac{d}{2} \quad (9.46)$$

where d is the physical separation between fore and aft channel phase centers. In addition, DPCA requires very precise hardware matching among receive channels to achieve high degrees of clutter cancellation.

Figure 9-17 depicts the DPCA approach. The platform moves in the direction orthogonal to the array normal with velocity v_p . The fore and aft channels comprise the receive array. At time nT , the aft channel electronically aligns with the fore channel at the prior pulse time, $(n-1)T$. The “+” in the figure denotes the transmit phase center and the “o” identifies the location of the receive phase center for the pulse of interest. The transmit beam uses all elements. In this case, to create electrical alignment the aft channel has to move half the channel spacing, d , due to the balanced transmit phase center, as (9.13) indicates. As seen from the figure, the transmit and receive phase centers for pulse $(n-1)T$ and nT balance so that the round-trip delay to each of the stationary scatterers in the scene is fixed and the receive voltages match. The processor subtracts fore and aft channel outputs to cancel clutter. Assuming the DPCA canceler employs N_{dPCA} pulses ($N_{dPCA} = 2$ in our example), then the processor feeds the $N - N_{dPCA} + 1$ clutter-canceled pulses into a Doppler processor to achieve integration gain.

Additional DPCA characterization is given in [20].

As a result of a number of impractical constraints – such as stringent hardware matching, requirement for side-looking collection geometry, and precise waveform timing – adaptive variants of DPCA are preferable. Adaptive DPCA (ADPCA) is a pre-Doppler STAP technique [20–22]. Consider the three pulse canceler cases, $N_{adPCA} = 3$; the following discussion generalizes to other values of N_{adPCA} . The space–time subvector is

$$\mathbf{x}_{adPCA/k}(n-1:n+1) = \begin{bmatrix} \mathbf{x}_{s/k}(n-1) \\ \mathbf{x}_{s/k}(n) \\ \mathbf{x}_{s/k}(n+1) \end{bmatrix} \quad (9.47)$$

where $\mathbf{x}_{s/k}(n)$ is the spatial snapshot of length M for the n th pulse. The ADPCA weight vector is

$$\hat{\mathbf{w}}_{adPCA/k} = \hat{\mathbf{R}}_{adPCA/k,(n-1:n+1)}^{-1} \left(\left(\begin{bmatrix} 1 \\ -2 \\ 1 \end{bmatrix} \odot \begin{bmatrix} 1 \\ \exp(j2\pi\bar{f}_{adPCA}) \\ \exp(j2\pi 2\bar{f}_{adPCA}) \end{bmatrix} \right) \otimes \mathbf{v}_s(\phi, \theta) \right) \quad (9.48)$$

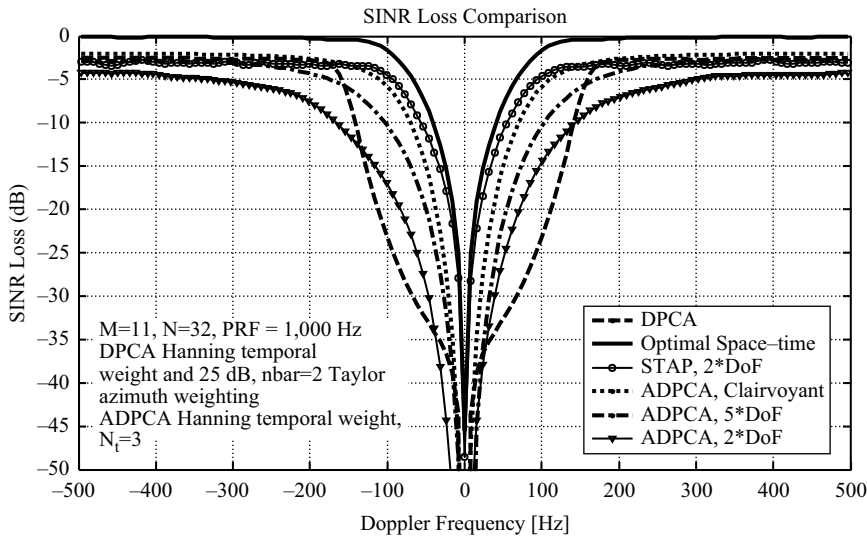


FIGURE 9-18 ■ SINR Loss Comparison of DPCA and ADPCA Relative to the Optimal Performance Bound and STAP; PRF is Not Set to the Precise DPCA Condition.

with \bar{f}_{adpca} the peak clutter Doppler times the PRI. The $3M \times 3M$ ADPCA covariance matrix estimate, $\hat{\mathbf{R}}_{adpca/k,(n-1:n+1)}$, is an approximation to

$$\mathbf{R}_{adpca/k,(n-1:n+1)} = E[\mathbf{x}_{adpca/k}(n-1:n+1)\mathbf{x}_{adpca/k}^H(n-1:n+1)] \quad (9.49)$$

The covariance inverse in (9.48) provides a dynamic response to whiten ground-clutter returns. The steering vector term in parentheses suppresses mainlobe clutter with the binominal weights, identified as $[1 \ -2 \ 1]^T$, while forming a beam in a specified angular direction; the steering vector incorporates an additional vector with linear phase variation over the aperture to steer the null in cases where clutter is not centered at 0 Hz.

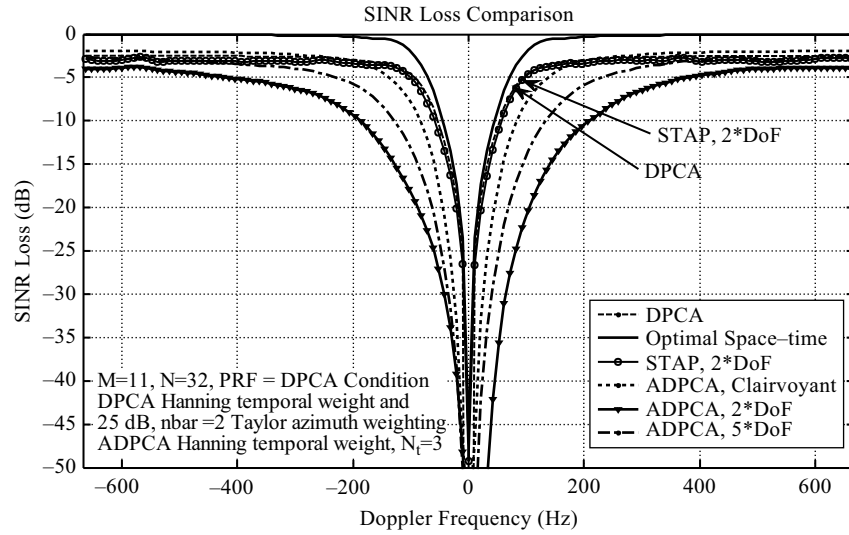
As in the DPCA case, the $N - N_{adpca} + 1$ clutter-canceled pulses pass through a Doppler processor to achieve integration gain.

A benchmark comparison of the performance potential of DPCA and ADPCA applied to the example shown in Figure 9-16 is given in Figure 9-18 and Figure 9-19. We modify the PRF between Figure 9-18 and Figure 9-19. Otherwise, the system is simulated without array errors and platform yaw, the most favorable – but least realistic – situation for DPCA. As seen from Figure 9-18, DPCA's performance suffers considerably relative to the bound set by the optimal processor when the specific DPCA conditions are not met (in this case, the PRF does not precisely satisfy (9.46)). ADPCA performance is not much better in this case. In contrast, Figure 9-19 shows capability when the DPCA conditions are precisely met (exact PRF, no system errors, no yaw, etc.). Figure 9-19 indicates DPCA closely aligns with the STAP results; ADPCA performance suffers relative to the optimal, STAP, and DPCA results but outperforms Doppler processing and adaptive Doppler processing.

9.6.3 STAP and STAP Variants

Detailed discussion on STAP is given in [11, 20, 21, 23–25]. The results in Figure 9-16, Figure 9-18, and Figure 9-19 indicated the vastly superior performance potential of STAP relative to competing methods. This section provides a brief overview.

FIGURE 9-19 ■
SINR Loss
Comparison of
DPCA and ADPCA
Relative to the
Optimal
Performance Bound
and STAP, PRF Set
to DPCA Condition.



The optimal space–time filter combines data from the range bin of interest to maximize SINR, thereby equivalently maximizing the probability of detection in the multivariate, colored Gaussian case for a fixed probability of false alarm. The optimal filter weights are given by

$$\mathbf{w}_k = \mu_{s-t} \mathbf{R}_k^{-1} \mathbf{s}_{s-t}(\phi, \theta, f_d) \quad (9.50)$$

where μ_{s-t} is a scalar [15]. Naturally, (9.50) compares to (9.44) but operates in the space–time domain for enhanced clutter-suppression capability. STAP is a data domain approximation of (9.50), where

$$\hat{\mathbf{w}}_k = \hat{\mu}_{s-t} \hat{\mathbf{R}}_k^{-1} \mathbf{v}_{s-t}(\phi, \theta, f_d) \quad (9.51)$$

are the STAP weights, $\hat{\mathbf{R}}_k$ is the space–time covariance estimate, and $\mathbf{v}_{s-t}(\phi, \theta, f_d)$ is the surrogate space–time steering vector. The spatial component of $\mathbf{v}_{s-t}(\phi, \theta, f_d)$ exhibits mismatch from the precise spatial steering vector due to uncompensated array errors; otherwise, straddle loss affects both spatial and temporal components. This approach is sometimes called *sample matrix inversion* (SMI) STAP, since the processor inverts the sample covariance matrix, $\hat{\mathbf{R}}_k$, to calculate the adaptive weights.

A calculation of the space–time covariance estimate, $\hat{\mathbf{R}}_k$, follows from (9.45) after replacing $\mathbf{x}_{t,m}$ with the space–time snapshot, \mathbf{x}_m . As discussed in [16], when using the estimator of (9.45), under the Gaussian iid assumption, $K \approx 2NM$ leads to $E[L_{s,2}] \approx 0.5$. With typical values of $64 \leq N \leq 512$ and $2 \leq M \leq 12$, a space–time product, NM , of several thousand is common. STAP training can thus potentially use 10,000 or more training samples, which is prohibitive for most applications, either because the samples are not available or the clutter environment is spatially heterogeneous. However, the real-time computation of $\hat{\mathbf{w}}_k$ is unrealistic, since the inversion of $\hat{\mathbf{R}}_k$ is $O(N^3M^3)$; each doubling of the space–time product leads to an increase in computational burden by a factor of eight.

For the aforementioned reasons, implementing the full space–time version of (9.51) is infeasible. Practitioners use *reduced-dimension STAP* (RD-STAP). RD-STAP

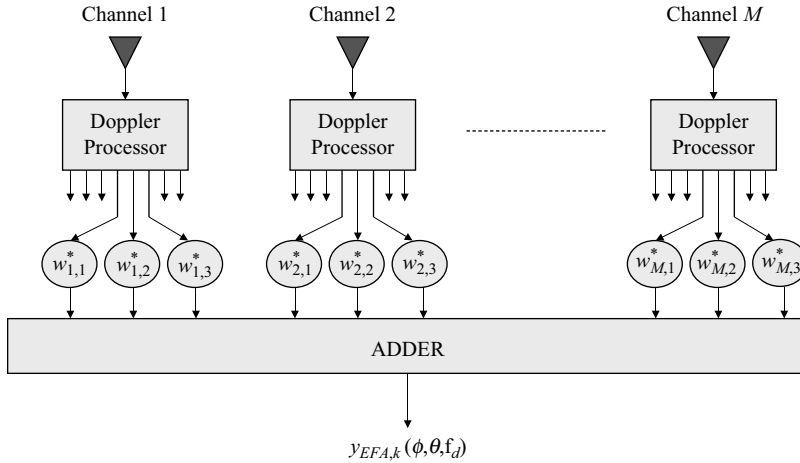


FIGURE 9-20 ■
EFA Processing
Flow.

involves linear transformation and subspace selection leading to reduced dimensionality. When properly applied, RD-STAP suffers only minor asymptotic loss relative to the optimal bound. The *extended factored algorithm* (EFA) is a popular approach [26]. EFA is a post-Doppler STAP method. In its standard implementation, it retains all M spatial DoFs and a subset, N_t , of the temporal DoFs. Typically, $3 \leq N_t \leq 5$. Figure 9-20 shows the EFA processing flow. Doppler processing is applied to each of the M channels. For each channel, the processor selects the specified number of adjacent Doppler filters; three are shown in Figure 9-20. The processor's adaptive DoFs are now $N_t M$; typically, DoFs for EFA are less than 30. The EFA output is

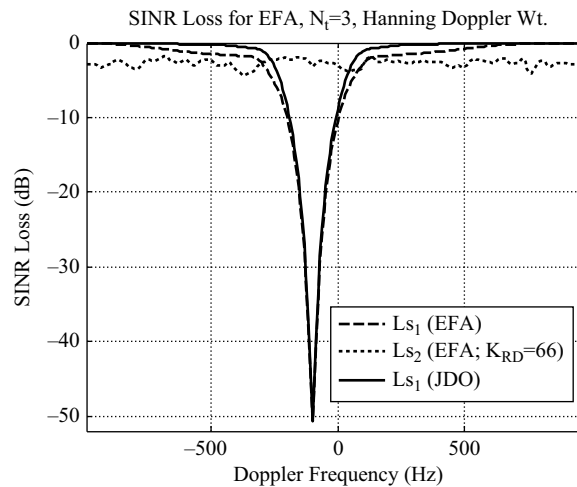
$$y_{EFA/k}(\phi, \theta, f_d) = \mathbf{v}_{EFA}^H(\phi, \theta, f_d) \widehat{\mathbf{R}}_{EFA/k}^{-1}(f_d) \mathbf{x}_{EFA/k}(f_d) \quad (9.52)$$

The transformation from space–time to space–Doppler is given by \mathbf{T}_{EFA} . Equation (9.52) follows from (9.51) using \mathbf{T}_{EFA} : $\mathbf{v}_{EFA}(\phi, \theta, f_d) = \mathbf{T}_{EFA}^H \mathbf{v}_{s-t}(\phi, \theta, f_d)$, $\widehat{\mathbf{R}}_{EFA/k}(f_d) = \mathbf{T}_{EFA}^H \widehat{\mathbf{R}}_k \mathbf{T}_{EFA}$, and $\mathbf{x}_{EFA/k}(f_d) = \mathbf{T}_{EFA}^H \mathbf{x}_k$. The practical implementation does not explicitly use \mathbf{T}_{EFA} , except to calculate the EFA steering vector. Rather, as Figure 9-20 suggests, the data are Doppler processed and then a covariance estimate is formed by training over the space–Doppler data.

There are a number of other RD-STAP methods discussed in further detail in [21].

Figure 9-21 shows the performance bound for the optimal space–time processor and EFA with a training window size equal to twice the processor's adaptive DoFs. In this case, the analysis uses a simulation of the MCARM system mentioned in Section 9.3.1, with the scenario matching that shown in Figure 9-9 and Figure 9-10. The Doppler offset shown in Figure 9-21 is a result of a yaw angle of approximately six degrees, and the CNR is on the order of 50–55 dB. Using the simulated data with known covariance matrix analysis, Figure 9-21 shows the performance of the optimal processor, denoted as *joint domain optimal* (JDO), along with the $L_{s,1}$ clairvoyant SINR loss and $L_{s,2}$ adaptive SINR loss for EFA. The EFA implementation uses $N_t = 3$ (three adjacent Doppler bins) and $M = 11$ receive channels, configured as a uniform linear array. As seen from the figure, the EFA performance potential given by $L_{s,1}$ closely approaches the theoretical bound given by JDO. The adaptive SINR losses, $L_{s,2}$, are consistent with a training support size of twice the processor's adaptive DoFs in a homogeneous environment – roughly 3 dB in

FIGURE 9-21 ■
Performance
Comparison of EFA
to Full-dimension
STAP.



this case [16]. The significantly reduced computational burden and reduced sample support size of EFA make it a practical approach to STAP implementation with performance approaching that of the full space–time processor.

9.6.4 Other Strategies

The progression of techniques in the prior sections suggests the substantial performance improvement of STAP over competing methods. STAP maximizes SINR for the given space–time aperture, thereby yielding superior detection performance. This is particularly compelling for the wide-area search mode.

With the advent of small area or persistent surveillance, SMTI may serve as a co-product to SAR outputs or the processor is able to dwell longer to potentially enhance detection performance. In this case, blending STAP and SAR techniques is of interest. References [27–31] provide a good introduction.

The previously discussed ATI method (see Section 9.1) falls into this category of nontraditional SMTI strategies.

Further comments are given in Section 9.9.2.

9.7 | DETECTION PROCESSING

Figure 9-22 shows the basic SMTI detection processing chain. The figure is broken into four main parts: pre-processed data cubes, STAP implementation, PDI and thresholding, and then post-processing.

The pre-processing steps generally involve digital I/Q and baseband down-conversion, decimation to one sample per range resolution cell, channel equalization, array manifold estimation, and pulse compression. Channel equalization attempts to match the channel transfer functions among the receivers over the instantaneous bandwidth; this is useful if the processor is to most effectively use the available adaptive DoFs. The array manifold is the span of the actual steering vectors characterizing the array response. The actual spatial steering vector is $s_s(\phi, \theta) = \epsilon(\phi, \theta) \odot \mathbf{v}_s(\phi, \theta)$, where $\epsilon(\phi, \theta)$ is the $M \times 1$

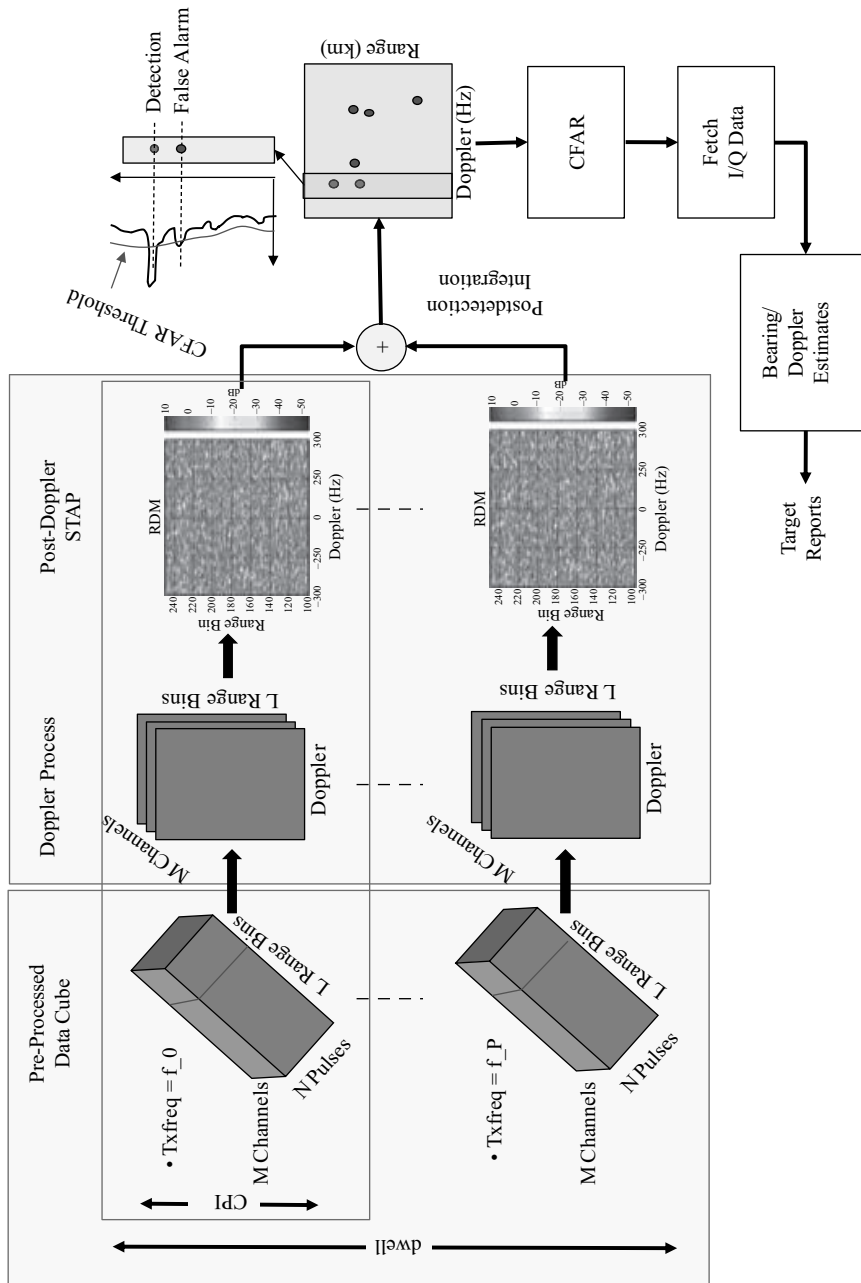


FIGURE 9-22 ■ SMTI Detection Processing.

complex vector of array errors. The elements of $\varepsilon(\phi, \theta)$ characterize the amplitude and phase errors between the presumed steering vector, $\mathbf{v}_s(\phi, \theta)$ (perfectly matched to the target angle), and the actual target spatial steering vector, $\mathbf{s}_s(\phi, \theta)$. Generally, array errors vary with receive angle. Uncompensated array errors lead to matched filter (SNR) loss and degraded bearing estimation performance. The common approaches to estimate the array errors include using a dedicated test manifold or exploiting the background clutter, the latter being known as “cal-on-clutter” (see the appendix in [14]). In some cases, pre-processing might include motion compensation (not shown in Figure 9-22).

A complex baseband, pulse-compressed, compensated data cube of dimension M channels by N pulses by L range bins is the result of the pre-processing steps described previously. Post-Doppler STAP is a typical approach to mitigate the impact of clutter on detection performance. The processor applies weighted Doppler processing to each channel, in accord with (9.37), yielding a data cube of M channels by \tilde{N} Doppler bins by L range bins. EFA is next applied by creating space/post-Doppler data vectors, as described by $\mathbf{x}_{\text{EFA}/k}(f_d) = \mathbf{T}_{\text{EFA}}^H \mathbf{x}_k$, training over range to form a covariance matrix estimate, and applying the adaptive weight vector to the range bin of interest to generate a complex scalar output, as given in (9.52). The weight vector steers the data to the receive angle and Doppler bin of interest. The scalar output forms one pixel in the RDM shown in Figure 9-22. The processor repeats the weight calculation and application process to create the remaining outputs corresponding to the many RDM pixels shown in Figure 9-22.

Normalizing the output of the STAP is an important consideration when multiple weights are applied to the data over range. For example, if the processor divides the range extent into six training and application regions, then a scalar offset in the weights between application regions can potentially lead to a step variation in the residual clutter and noise power. This step in power leads to threshold biases and false alarms.

The scalar, $\hat{\mu}_{s-t}$, in (9.51) does not affect output SINR, but is useful to prevent inadvertent modulation of the interference-plus-noise residue resulting from weight updating. (Note: this discussion also applies to the STAP variants, such as the post-Doppler EFA given by (9.52).) The most popular, and common, normalization leads to the *adaptive matched filter* (AMF) [32]. The AMF statistic is

$$\eta_{AMF} = \frac{|\mathbf{v}_{s-t}^H \hat{\mathbf{R}}_k^{-1} \mathbf{x}_k|^2}{\mathbf{v}_{s-t}^H \hat{\mathbf{R}}_k^{-1} \mathbf{v}_{s-t}} \quad (9.53)$$

The processor compares η_{AMF} to a detection threshold to determine the likely presence of a target for each range-angle-Doppler cell of interest. The purpose of the AMF is to set the interference-plus-noise residue to unity (0 dB). The corresponding scalar is

$$\hat{\mu}_{s-t} = \frac{1}{\sqrt{\mathbf{v}_{s-t}^H \hat{\mathbf{R}}_k^{-1} \mathbf{v}_{s-t}}} \quad (9.54)$$

Using (9.54) in (9.51) gives the AMF weight vector,

$$\mathbf{w}_{AMF} = \frac{\hat{\mathbf{R}}_k^{-1} \mathbf{v}_{s-t}}{\sqrt{\mathbf{v}_{s-t}^H \hat{\mathbf{R}}_k^{-1} \mathbf{v}_{s-t}}} \quad (9.55)$$

The output power under the null hypothesis is then

$$P_o = E[|y_{H_0}|^2] = E[\mathbf{w}_{AMF}^H \mathbf{x}_{H_0} \mathbf{x}_{H_0}^H \mathbf{w}_{AMF}] = E \left[\frac{\mathbf{v}_{s-t}^H \hat{\mathbf{R}}_k^{-1} \mathbf{x}_{H_0} \mathbf{x}_{H_0}^H \hat{\mathbf{R}}_k^{-1} \mathbf{v}_{s-t}}{\mathbf{v}_{s-t}^H \hat{\mathbf{R}}_k^{-1} \mathbf{v}_{s-t}} \right] \quad (9.56)$$

Observe that if $E[\hat{\mathbf{R}}_k] \approx \mathbf{R}_k$, then $P_o \approx 1$. Thus, if the clutter environment is homogeneous, the output power tends, on average, to unity.

After the AMF normalization, it is possible to apply a fixed threshold to the RDM. The AMF statistic compared to a detection threshold, T_1 , can be written

$$\eta_{AMF} = \frac{|\mathbf{v}_{s-t}^H \hat{\mathbf{R}}_k^{-1} \mathbf{x}_k|^2}{\mathbf{v}_{s-t}^H \hat{\mathbf{R}}_k^{-1} \mathbf{v}_{s-t}} \begin{matrix} >_{H_1} \\ <_{H_0} \end{matrix} T_1 \Rightarrow |\mathbf{v}_{s-t}^H \hat{\mathbf{R}}_k^{-1} \mathbf{x}_k|^2 \begin{matrix} >_{H_1} \\ <_{H_0} \end{matrix} T_1 \underbrace{(\mathbf{v}_{s-t}^H \hat{\mathbf{R}}_k^{-1} \mathbf{v}_{s-t})}_{\substack{\text{Estimate of} \\ \text{Interference} \\ \text{Power}}} \quad (9.57)$$

This expression applies to the post-Doppler case with the appropriate substitutions, as described in Section 9.6.3. To the right of the arrow, it is seen the AMF decision simplifies to the magnitude squared of the adaptive filter output compared to the equivalent of a threshold multiplier, T_1 , times an estimate of the local clutter power residue (to see this, consider (9.56) with $\hat{\mu}_{s-t} = 1$, rather than the AMF normalization). The AMF normalization is imperfect in heterogeneous environments, so other CFAR methods, like cell averaging CFAR, are used in practice [12].

The processor applies the aforementioned step to each of P CPIs, generating the RDMs for a common look direction. The transmit frequency hops for each CPI to mitigate target fading. It is possible to apply a detection threshold to each RDM and then implement M -of- N detection [12]. However, a preferable approach is to noncoherently add the RDMs in a step called postdetection integration. Section 9.4.1 describes the benefits of PDI. The processor applies a detection threshold to the noncoherently summed RDMs to determine target presence, as Figure 9-22 suggests. Either a fixed or CFAR threshold can be used; the fixed threshold tends, naturally, to suffer from a higher FAD.

After a threshold crossing, the processor fetches the corresponding I/Q data and estimates the target bearing and Doppler. Details of angle-Doppler estimation are given subsequently in Section 9.8.

The target range, Doppler, angle, and other characteristics – such as estimated SINR – are formatted and provided to postdetection processing. The STANAG 4607 is the common approach to format GMTI/SMTI data.

In some cases, additional processing is used to cope with the impact of heterogeneous clutter on detection performance. The details of this sophisticated processing are beyond the scope of this chapter. A brief overview is given in Section 9.9.1 for the interested reader.

9.8 | ANGLE AND DOPPLER ESTIMATION

Once the processor detects a target, a bearing estimate is necessary to initiate target tracking. A method seamlessly integrating with STAP processing is desirable [33–35].

Express the alternative hypothesis of (9.18) as

$$\mathbf{x}_k = \alpha s_{s-t}(\mathbf{p}) + \mathbf{n}_{\text{tot}}; \mathbf{p} = \begin{bmatrix} \phi \\ \theta \\ f_d \end{bmatrix} \quad (9.58)$$

where α is a complex constant, and $\mathbf{n}_{\text{tot}} = \mathbf{c}_k + \mathbf{j}_k + \mathbf{n}_k$ is the interference-plus-noise (total noise) vector. The basic problem is to estimate the true target parameters, \mathbf{p} , with $\hat{\mathbf{p}}$. If $\mathbf{n}_{\text{tot}} \sim CN(\mathbf{0}, \mathbf{R}_k)$, then the PDF is

$$p(\mathbf{x}_k | \mathbf{p}) = \frac{1}{\pi^M |\mathbf{R}_k|} \exp\left(-(\mathbf{x}_k - \alpha s_{s-t}(\mathbf{p}))^H \mathbf{R}_k^{-1} (\mathbf{x}_k - \alpha s_{s-t}(\mathbf{p}))\right) \quad (9.59)$$

Given (9.59) as a likelihood function, we first require an estimate for the complex constant. Equation (9.59) is maximal when

$$Q(\alpha, \mathbf{p}) = (\mathbf{x}_k - \alpha s_{s-t}(\mathbf{p}))^H \mathbf{R}_k^{-1} (\mathbf{x}_k - \alpha s_{s-t}(\mathbf{p})) \quad (9.60)$$

is minimal. Differentiating (9.60) and setting the result to zero yields

$$\hat{\alpha} = \frac{s_{s-t}^H(\mathbf{p}) \mathbf{R}_k^{-1} \mathbf{x}_k}{s_{s-t}^H(\mathbf{p}) \mathbf{R}_k^{-1} s_{s-t}(\mathbf{p})} \quad (9.61)$$

Next, substituting (9.61) into (9.60) leads to

$$Q(\hat{\alpha}, \mathbf{p}) = \mathbf{x}_k^H \mathbf{R}_k^{-1} \mathbf{x}_k - \frac{|\mathbf{x}_k^H \mathbf{R}_k^{-1} s_{s-t}(\mathbf{p})|^2}{s_{s-t}^H(\mathbf{p}) \mathbf{R}_k^{-1} s_{s-t}(\mathbf{p})} \quad (9.62)$$

Differentiating (9.62) with respect to \mathbf{p} and setting the result to zero yields the maximum likelihood estimate (MLE) of \mathbf{p} , given as $\hat{\mathbf{p}}$. Consequently, the estimator is [33]

$$\hat{\mathbf{p}} = \begin{bmatrix} \hat{\phi} \\ \hat{\theta} \\ \hat{f}_d \end{bmatrix} = \underset{\mathbf{p}=[\phi \ \theta \ f_d]^T}{\text{arg max}} \left(\frac{|s_{s-t}^H(\mathbf{p}) \mathbf{R}_k^{-1} \mathbf{x}_k|^2}{s_{s-t}^H(\mathbf{p}) \mathbf{R}_k^{-1} s_{s-t}(\mathbf{p})} \right) \quad (9.63)$$

Observe that (9.63) is very sensible, taking the form of the normalized magnitude of the STAP output. Implementing the estimator requires a very fine grid search to find the peak of the likelihood function (via the MLE approach). The grid search – which essentially amounts to stepping the space–time steering vector over potential target angles and Dopplers – is computationally burdensome and can be suboptimum. Specifically, if the step size is too large, the estimator can exhibit bias and increased variance. For this reason, numerical approximations to the MLE, which exhibit good practical performance, are commonly used [e.g., polynomial fits to the cost surface resulting from (9.63)].

Figure 9-23 shows an example of the minimum variance distortionless response spectrum from [34] for a generic X-band radar simulation. This figure shows the clutter ridge along the diagonal and an interference strobe in the vertical direction at a fixed angle. The angle is measured in the *antenna coordinate system* (ACS); the ACS definition is not important to the present discussion. Figure 9-24 shows the standard

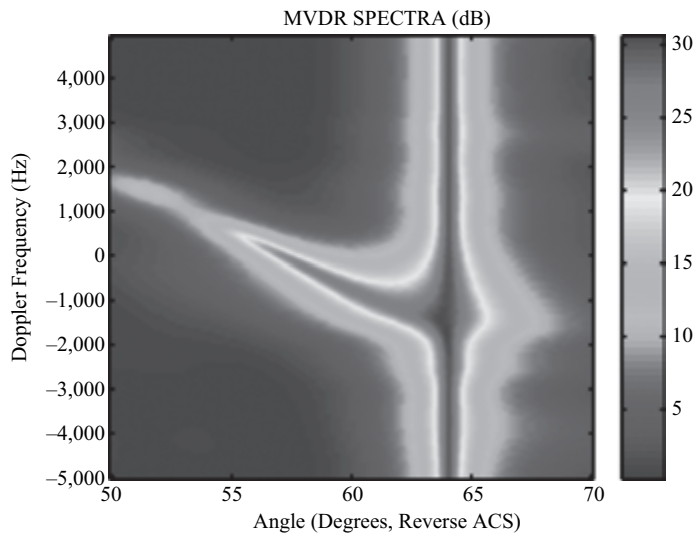


FIGURE 9-23 ■ Example Angle-Doppler Interference Spectrum for Airborne STAP, Where the Vertical Line Corresponds to RFI [after [34], © 2004 IEEE].

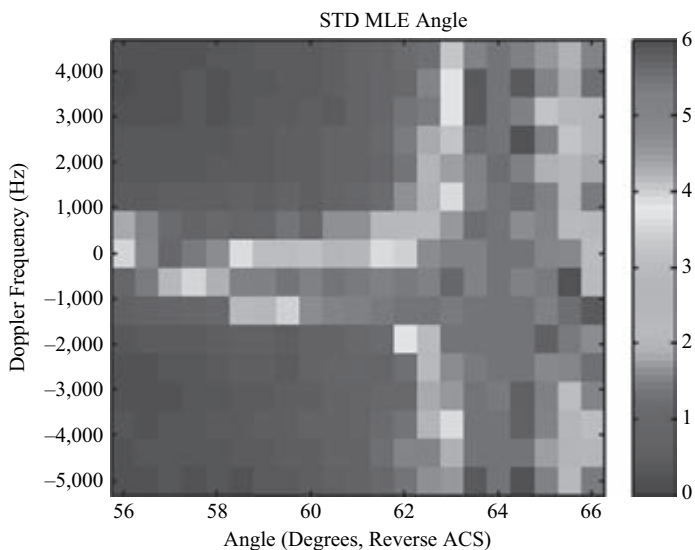


FIGURE 9-24 ■ Standard Deviation of Monte Carlo MLE Direction of Arrival Estimates, in Degrees [after [34], © 2004 IEEE].

deviation of the MLE of (9.63) through Monte Carlo analysis for each unambiguous angle and Doppler observable by the radar. As seen from Figure 9-24, the MLE gives very good estimation performance away from the clutter ridge and interference strobe; this makes sense, as we expect better performance in regions where the SINR is higher.

In the PDI case, it can be shown that the MLE amounts to summing the corresponding cost surfaces of the form of (9.63) for each CPI and then finding the peak. A similar derivation for the case of uncorrelated target voltages due to multistatic geometry is given in [35] and applies to the PDI case given in Figure 9-22, where frequency is instead used to decorrelate target voltages from CPI to CPI.

9.9 | OTHER CONSIDERATIONS

9.9.1 Heterogeneous Clutter

The severity of the surface clutter environment influences SMTI performance. As previously discussed, adaptive radar techniques provide significant advantage over their nonadaptive counterparts. STAP estimates clutter properties from a training interval. Similarly, CFAR algorithms estimate the residual clutter and interference power levels prior to applying a threshold multiplier. A common assumption of most adaptive algorithms is independence and statistical similarity among the elements of the training set and the null-hypothesis condition of the application region.

STAP uses training data to estimate the unknown, null-hypothesis covariance matrix, commonly using a sample covariance formulation similar to the calculation in (9.45) with the appropriately formatted data vectors. This approach is developed extensively in [16]. An underlying assumption of the approach is that the training data are multivariate Gaussian, as well as independent and identically distributed. When the iid assumption holds, the expected value of the covariance matrix tends to the actual covariance matrix. The real world, however, is generally not iid. The non-iid behavior is a result of the heterogeneous nature of the clutter environment. Sources of clutter heterogeneity include spatially varying clutter reflectivity, spatially varying clutter spectral spread, clutter discretets, moving targets corrupting the training data, extensive shadowing, and clutter-region boundaries.

The impact of heterogeneous clutter on adaptive radar performance is discussed at length in [14, 19, 36, 37]. Heterogeneous clutter leads to covariance matrix estimation error, and consequently, filter mismatch relative to the null-hypothesis condition of the cell under test (note, the covariance error is not due to finite amounts of training data but to the fact the training data are non-iid). Solutions to mitigate the impact of heterogeneous clutter on adaptive radar are available from a number of sources. The driver for the array of CFAR algorithms has been heterogeneous clutter. In the case of STAP, the solution space includes training techniques, constraints, and knowledge-aided implementations [14, 38].

9.9.2 SAR-GMTI

Spatial aperture is a major cost driver in radar-system design. In addition, the radar-bearing platform constrains the aperture dimensions. Extending the temporal dwell is a potential approach to enhance detection of slow-moving targets at extended range. Interest also exists in moving target detection as a coproduct to a typical SAR mode. As the dwell increases, however, uncompensated target motion effects lead to significant matched filter losses, as Figure 9-15 indicates. For this reason, an effective approach to detection blends multichannel processing to suppress stationary clutter with an estimate of the nonlinear target phase history to accomplish the linearly transformed matched filtering [27, 28].

Assuming the target motion is adequately given by the combination of radial and tangential velocities, with origin specified at the antenna, the time-varying range to the moving target is expressible as

$$r(t) = \sqrt{r_o^2 + (v_p^2 - 2v_p v_{T/t})t^2 + 2r_o v_{T/r} t} \approx r_o + \frac{1}{2} \frac{(v_p^2 - 2v_p v_{T/t})t^2 + 2r_o v_{T/r} t}{r_o} \quad (9.64)$$

where r_o is the starting range to the target from aperture center, v_p is the platform-velocity vector in the along-track direction, $v_{T/t}$ is the target's tangential velocity, and $v_{T/r}$ is the target radial velocity. The target phase history is then $\upsilon(t) = 4\pi r(t)/\lambda$, where the quadratic term defines a chirp slope due to the tangential target motion. This quadratic term results in target energy smearing across Doppler bins. The linear term in (9.64) defines the target range rate; this differs from typical SAR processing, where Doppler determines cross-range position. Rather, for moving targets, the system requires multiple receive channels to measure physical direction of arrival. Acceleration leads to higher-order phase terms, up to fourth order, that greatly complicate searching for a suitable match to the range of plausible target hypotheses.

9.9.3 Bistatic and Multistatic Configurations

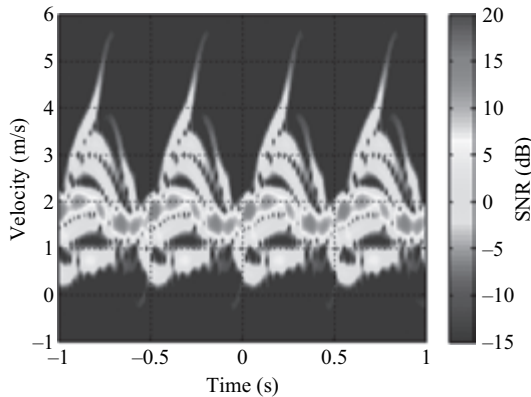
The bistatic configuration consists of a transmitter separately located a significant distance from the receiver. In the case in which both transmitter and receiver are airborne, substantial separation between the transmitter and receiver leads to distinct bistatic phenomenology. In SMTI, the predominant challenge centers on the spatially varying bistatic clutter properties induced by the sensor geometry. Specifically, the angle-Doppler properties of bistatic clutter can vary from range bin to range bin; the angle of arrival is a function of the receive platform orientation, but both transmitter and receiver contribute to the Doppler frequency. Details of bistatic clutter nonstationarity are given in [39–43].

Clutter nonstationarity violates the iid assumption fundamental to STAP implementation. The covariance estimate represents the average properties of the data comprising the training interval. The corresponding covariance error leads to filter mismatch and, in some cases, greatly degraded detection performance. Fortunately, a number of effective bistatic STAP methods are available, as [40] summarizes. The bistatic STAP methods generally fall into three categories: localized training, data warping, or time-varying weights. In the localized training method, the STAP implementation selects training data in the vicinity of the cell under test in an attempt to minimize clutter-range variation. The data-warping approach modulates the data in a pre-processing step to create a degree of similarity to a designated reference; the modulation can be in time [43] or space–time [39]. In the time-varying weight approach, the weights are expanded using a truncated Taylor series, typically to first order, to track range variation in the clutter properties [42].

9.9.4 Dismount Detection

Detecting personnel on Earth's surface is the objective of dismount radar [44]. Dismount detection at suitable ranges is a challenge. The dismount RCS is over an order of magnitude smaller than that of a typical vehicle target. In addition, the dismount energy smears across Doppler filters, as the spectrogram in Figure 9-25 indicates. The sinusoidal variation in Figure 9-25 corresponds to the torso motion, whereas the other frequency components are due to movement of the extremities. The spectrogram is generated from a series of overlapping, short time Fourier transforms; for the example shown, the single pulse SNR is strong. When clutter is present and the radar is searching for targets at greater range, the detection processor must better match to the dismount target phase history to boost the SINR to levels acceptable for a useful detection rate.

FIGURE 9-25 ■
 Simulated
 Spectrogram of a
 Dismount Taking
 Two Walking Steps
 at an Average Speed
 of 1.85 m/s [after
 [44], © 2008 IEEE].



9.10 | SUMMARY

SMTI radar design and implementation is an important component of modern radar. This chapter discussed the fundamentals of SMTI.

SMTI is a radar mode with a history that started in the early 1990s with Joint STARS. Since that time, interest in SMTI has grown considerably, with efforts to deploy SMTI on manned aircraft, UASs, and satellites. WAS-SMTI involves searching considerable areas of Earth's surface by rapidly scanning the transmit beam and receive subarrays, processing considerable amounts of data in short time periods, and displaying the evolving target dots to the operator. In contrast, selective search and persistent search SMTI focus the radar system on smaller surface areas, leveraging the additional radar timeline to enhance detection of specific targets of interest.

The impact of clutter returns on detection is a limiting factor in SMTI radar. Clutter mitigation requires careful system design and signal processing. In particular, the along-track length of the radar antenna, relative to the platform velocity, is a critical consideration. Longer arrays yield lower minimum detectable velocities for a fixed platform velocity. Sophisticated processing methods are further necessary to mitigate clutter effects. STAP provides the capability to see targets to within a fraction of the mainbeam clutter spread, with an improvement generally exceeding a factor of 2 to 5, depending on the circumstances. At its essence, SMTI radar attempts to discriminate the angle-Doppler response of a potential target from the background clutter. This chapter describes antenna, waveform, and signal-processing issues in considerable detail. In addition, the fundamental clutter, RFI, receiver noise, and target models are described and then used in benchmark analyses to compare the performance of varying methods.

The latter parts of this chapter describe the end-to-end detection processing chain and a standard approach to bearing and Doppler estimation. Discussion of some germane SMTI issues culminates the chapter: an overview of the impact of heterogeneous clutter on detection performance, long coherent dwell processing considerations (SAR-GMTI), bistatic and multistatic configurations, and dismount detection.

9.11 | FURTHER READING

SMTI is an application of modern radar technology. As this chapter describes, key SMTI elements include a detailed understanding of clutter and target phenomenology, multi-channel antenna design, and advanced signal processing. These topics are covered in multiple sources.

The interested reader should find this chapter's references to be very useful for further investigation. We highlight several of these references as good starting points.

We recommend that the interested reader spend a few moments reviewing [1] for historical reasons. Also, a perusal of the NATO STANAG 4607 format documents, found at the NATO website, is worthwhile.

STAP is an important SMTI enabling technology. The seminal paper by Brennan and Reed, given as [15], should be read by anyone interested in STAP, along with the companion paper by Reed, Mallett, and Brennan in [16] describing the most commonly used approach to estimate the unknown covariance matrix.

The report by Ward in [20] is a clear exposition on the basics of STAP, and the STAP overview by Melvin in [25] summarizes key STAP concepts and research trends. Both are worth spending some time reviewing and provide good foundational discussion on STAP technology. The book on STAP by Guerri in [17] should also be considered further reading; this book provides many important STAP insights. It is probably best to read these suggested texts chronologically as [25], [20], and then [17]. An in-depth understanding of STAP is critical to a detailed appreciation for SMTI radar.

9.12 | REFERENCES

- [1] J.N. Entzminger, C.A. Fowler, and W.J. Kenneally, "JointSTARS and GMTI: Past, present and future," *IEEE Trans. AES*, Vol. 35, No. 2, April 1999, pp. 748–761.
- [2] USAF official website, <http://www.af.mil/information/factsheets/factsheet.asp?id=13225>.
- [3] DARPA website, <http://www.darpa.mil/ipto/programs/vader/vader.asp>.
- [4] "Lynx SAR/GMTI radar: Increased capability for manned and unmanned missions," General Atomics Aeronautical factsheet, General Atomics Aeronautical Systems, Inc. 13322 Evening Creek Dr., N., San Diego, California 92128 USA.
- [5] Space Radar information, <http://www.losangeles.af.mil/library/factsheets/factsheet.asp?id=5308>.
- [6] D. Rabideau and S. Kogon, "A signal processing architecture for space-based GMTI radar," in *Proc. 1999 IEEE Radar Conference*, Waltham, MA, pp. 96–101.
- [7] "RADARSAT-2: A new era in synthetic aperture radar," RADARSAT-2 factsheet, Geospatial Services, 13800 Commerce Parkway, Richmond, BC Canada, V6V 2J3. See www.RADARSAT2.info.
- [8] C.H. Gierull and C. Livingstone, "SAR-GMTI concept for RADARSAT-2," Chapter 6, *The Applications of Space-Time Processing*, R. Klemm (Ed.), IEE Radar, Sonar, Navigation and Avionics 9, IEE Press, 2004.
- [9] C.M Rader, "A simple method for sampling in-phase and quadrature components," *IEEE Trans. AES*, Vol. AES-20, No. 6, November 1984.

- [10] D.H. Johnson and D.E. Dudgeon, *Array Signal Processing: Concepts and Techniques*, Prentice-Hall, Englewood Cliffs, NJ, 1993.
- [11] J.R. Guerci, "Theory and application of covariance matrix tapers for robust adaptive beamforming," *IEEE Trans. Signal Processing*, Vol. 47, No. 4, April 1999, pp. 977–985.
- [12] M.I. Skolnik, *Introduction to Radar Systems*, 2nd Ed., McGraw Hill, New York, NY, 1980.
- [13] J.B. Billingsley, *Low-Angle Radar Land Clutter: Measurements and Empirical Models*, William Andrew Publishing, Inc., Norwich, NY, 2002.
- [14] W.L. Melvin and G.A. Showman, "Knowledge-aided parametric covariance estimation," *IEEE Trans. AES*, July 2006, pp. 1021–1042.
- [15] L.E. Brennan and I.S. Reed, "Theory of adaptive radar," *IEEE Trans. AES*, Vol. 9, No. 2, March 1973, pp. 237–252.
- [16] I.S. Reed, J.D. Mallett, and L.E. Brennan, "Rapid convergence rate in adaptive arrays," *IEEE Trans. AES*, Vol. 10, No. 6, November 1974, pp. 853–863.
- [17] J.R. Guerci, *Space-Time Adaptive Processing for Radar*, Artech House, Norwood, MA, 2003.
- [18] B.M. Keel, "Fundamentals of pulse compression waveforms," Chapter 20, *Principles of Modern Radar: Basic Principles*, M.A. Richards et al. (Eds.), SciTech Publishing, Inc., North Carolina, 2010.
- [19] B.C. Armstrong, H.D. Griffiths, C.J. Baker, and R.G. White, "Performance of adaptive optimal Doppler processors in heterogeneous clutter," *IEE Proc.-Radar, Sonar, Navig.*, Vol. 142, No. 4, August 1995, pp. 179–190.
- [20] J. Ward, "Space-time adaptive processing for airborne radar," *Lincoln Laboratory Tech. Rept.*, ESC-TR-94-109, December 1994.
- [21] W.L. Melvin, "Clutter suppression using space-time adaptive processing," *Principles of Modern Radar: Advanced Techniques*, ed. W. Melvin and J. Scheer, Sci-Tech Publishing, Edison, NJ, 2011.
- [22] R. Blum, W.L. Melvin, and M.C. Wicks, "An analysis of adaptive DPCA," in *Proc. 1996 IEEE National Radar Conference*, Ann Arbor, Michigan, May 13–16, 1996, pp. 303–308.
- [23] R. Klemm, *Space-Time Adaptive Processing: Principles and Applications*, IEE Radar, Sonar, Navigation and Avionics 9, IEE Press, London, UK, 1998.
- [24] R. Klemm, *Principles of Space-Time Adaptive Processing*, 2nd Ed., IEE Radar, Sonar, Navigation and Avionics 12, IEE Press, UK, 2002.
- [25] W.L. Melvin, "STAP overview," *IEEE AES Systems Magazine – Special Tutorials Issue*, Vol. 19, No. 1, January 2004, pp. 19–35.
- [26] R.C. DiPietro, "Extended factored space-time processing for airborne radar," in *Proc. 26th Asilomar Conf.*, Pacific Grove, CA, October 1992, pp. 425–430.
- [27] J.H.G. Ender, "Space-time processing for multichannel synthetic aperture radar," *IEE Electronics & Comm. Eng. J.*, February 1999, pp. 29–37.
- [28] G.A. Showman and W.L. Melvin, "Multi-resolution processing to enhance knowledge-aided STAP", in *Proc. 2003 DARPA/AFRL KASSPER Workshop*, April 14–16, 2003, Las Vegas, NV.
- [29] M. Kirscht, "Detection and imaging of arbitrarily moving targets with single-channel SAR," *IEE Proc.—Radar Sonar Navig.*, Vol. 150, No. 1, February 2003, pp. 7–11.
- [30] R.P. Perry, R.C. DiPietro, and R.L. Fante, "SAR imaging of moving targets," *IEEE Trans. AES*, Vol. 35, No. 1, January 1999, pp. 188–199.

- [31] J.R. Fienup, "Detecting moving targets in SAR imagery by focusing," *IEEE Trans. AES*, Vol. 37, No. 3, July 2001, pp. 794–809.
- [32] F.C. Robey, D.R. Fuhrman, E.J. Kelly, and R. Nitzberg, "A CFAR adaptive matched filter detector," *IEEE Trans. AES*, Vol. 28, No. 1, January 1992, pp. 208–216.
- [33] R.C. Davis, L.E. Brennan, and I.S. Reed, "Angle estimation with adaptive arrays in external noise fields," *IEEE Trans AES*, Vol. AES-12, No. 2, March 1976, pp. 179–186.
- [34] G.A. Showman, W.L. Melvin, and D.J. Zywicki, "Application of the Cramér-Rao lower bound for bearing estimation to STAP performance studies," in *Proc. 2004 IEEE Radar Conference*, Philadelphia, PA, 26–29 April 2004, ISBN No. 0-7803-8235-8.
- [35] W.L. Melvin, R. Hancock, M. Rangaswamy, and J. Parker, "Adaptive distributed radar," in *Proc. 2009 Int'l Radar Conf.*, Bordeaux, France, October 2009.
- [36] W.L. Melvin, "Space-time adaptive radar performance in heterogeneous clutter," *IEEE Trans. AES*, Vol. 36, No. 2, April 2000, pp. 621–633.
- [37] W.L. Melvin, "STAP in heterogeneous clutter environments," in *The Applications of Space-Time Processing*, ed. R. Klemm, IEE Radar, Sonar, Navigation and Avionics 9, IEE Press, 2004.
- [38] W.L. Melvin and J.R. Guerci, "Knowledge-aided sensor signal processing: a new paradigm for radar and other sensors," *IEEE Tran. AES*, July 2006, pp. 983–996.
- [39] W.L. Melvin and M.E. Davis, "Adaptive cancellation method for geometry-induced non-stationary bistatic clutter environments," *IEEE Trans. AES*, April 2007, pp. 651–672.
- [40] W.L. Melvin, "Adaptive moving target indication," in *Advances in Bistatic Radar*, Chapter 11, ed. N. Willis and H. Griffiths, Sci-Tech Publishing, Rayleigh, NC, 2007.
- [41] B. Himed, J.H. Michels, and Y. Zhang, "Bistatic STAP performance analysis in radar applications," in *Proc. 2001 IEEE Radar Conf.*, Atlanta, GA, May 2001, pp. 198–203.
- [42] S.M. Kogon and M.A. Zatman, "Bistatic STAP for airborne radar systems," in *Proc. IEEE SAM 2000*, Lexington, MA, March 2000.
- [43] F. Pearson and G. Borsari, "Simulation and analysis of adaptive interference suppression for bistatic surveillance radars," in *Proc. 2001 ASAP Symp.*, Lexington, MA, 13 March 2001.
- [44] R.K. Hersey, W.L. Melvin, and E. Culpepper, "Dismount modeling and detection from small aperture moving radar platforms," in *Proc. 2008 IEEE Radar Conf.*, May 2008, Rome, Italy.

Space-Based SAR for Remote Sensing

Lee Blanton, General Atomics Aeronautical Systems, Inc., San Diego, CA

Chapter Outline

10.1	Introduction	431
10.2	Historical Perspective.	438
10.3	Orbits.	451
10.4	Design Considerations for the Spaceborne SAR.	457
10.5	Special Modes and Capabilities	473
10.6	Design Example: Germany's TerraSAR-X.	482
10.7	Summary	493
10.8	References.	494
10.9	Further Reading	498

10.1 | INTRODUCTION

Space, as with land, sea, and air, is now a well-established operating environment for radars. As in other environments, radars operating in space assume a wide variety of forms and span a wide range of applications. This chapter will focus on satellite-borne synthetic aperture radars (SARs) for remote sensing applications. This is an important and growing field with numerous applications in the areas of oceanography; land use; seismology; volcanology; disaster assessment; and the monitoring of sea ice, maritime economic zones, environmental conditions, etc.

10.1.1 Spaceborne SARs

Placing a SAR into orbit and operating it for many years involve considerable expense. To justify this expense, a spaceborne SAR must provide benefits that at least equal its cost. Spaceborne SARs have the following advantages over other types of sensors:

- Ability to make observations through clouds.
- Ability to make observations in darkness.
- Ability to sense phenomena that other types of sensors cannot sense.
- Near-global coverage repeated at regular intervals.
- Long-term temporal coverage.

TABLE 10-1 ■ Characteristics and Challenges of Spaceborne SARs

-
- Long range; high two-way spreading loss (path loss)
 - High platform velocity (large Doppler shift)
 - Large antennas, some requiring distributed RF amplification and control circuitry
 - Highly constrained PRF, often range-ambiguous
 - Large imaged area resulting in a large data volume
 - Image formation processing is usually done on the ground; system performance may be data-link-limited
-

Because the microwave wavelength is much longer than visible and infrared (IR) wavelengths, a SAR can observe phenomena that are either unobservable or much less evident to an electro-optic/infrared (EO/IR) sensor. Such phenomena include ocean wave patterns, surface roughness, soil moisture content, etc. The ability of a radar to sense the Doppler shift of the return signals also enables measurement of ocean and river currents and other phenomena involving motion.

As with other long-range radars, achieving an adequate signal-to-noise ratio (SNR) is a major challenge. For this reason, all remote sensing SARs flown to date have operated in low earth orbit (LEO). Even from LEO, the long range between the radar and the imaged area results in a high free-space spreading loss (aka path loss) requiring fairly large antennas and moderately high radiated powers (1–5 kW peak).

A high platform velocity imparts a large Doppler frequency shift to the surface returns. The Doppler bandwidth of the surface returns can be limited by using an antenna with a narrow azimuth beamwidth (i.e., an antenna that is long in the horizontal or along-track dimension). Both the azimuth and elevation beamwidths affect the choice of pulse repetition frequency (PRF) since the PRF is constrained by factors involving range ambiguities as well as the requirement to keep the Doppler shift of the mainlobe returns unambiguous. Because of these factors the PRF in a spaceborne SAR is likely to be comparable to the Doppler bandwidth of the mainlobe returns, making Doppler (azimuth) ambiguities a serious design issue. Waveform requirements (e.g., the PRF) and antenna beam requirements are therefore closely coupled and require careful trade-offs during the system design process. Table 10-1 lists some of the top-level characteristics and challenges of spaceborne SARs as compared with airborne radars.

10.1.2 Other Types of Spaceborne Remote Sensing Radars

Although the emphasis in this chapter is on spaceborne SARs, two other types of spaceborne radars—altimeters and scatterometers—are important in the field of remote sensing. These nonimaging instruments often share the same satellite bus with SAR instruments, providing measurements that are both complementary to and time-correlated with the SAR images, so they will be discussed briefly here.

Radar Altimeters. Satellite-borne radar altimeters have made important contributions to the fields of geodesy and oceanography. Since the satellite orbit is usually known with great precision, a satellite-borne altimeter can measure small variations in the height of the ocean surface resulting from various geophysical phenomena. In the absence of any other disturbances, the equipotential surface corresponding to the local

mean sea level is known as the geoid. Over the entire Earth the height of the geoid deviates from its mean value by -104 m to $+64$ m primarily as a result of density variations in Earth's mantle [1]. Superimposed on this “permanent” geoid topography are variations due to oceanic-scale circulation (currents), mesoscale circulation (eddies), regions of high or low atmospheric pressure, bathymetry (depth), wind, and tides. These variations range in magnitude from a few centimeters to a few meters. The effects of tides and wind are more pronounced in shallow water such as over continental shelves. Sea surface height variations due to tides and wind-driven waves must be averaged out of radar altimetric (range) measurements in order for variations due to other phenomena to be quantified. On the other hand, since wind waves increase the surface roughness and reduce the backscatter coefficient in the nadir direction, the amplitude of the nadir return can be used to infer the surface wind speed [1, 2].

Several design approaches have been used in spaceborne radar altimeters. Pulse-limited altimeters use the pulse width (usually the compressed pulse width, i.e., the range bin width) to limit the lateral extent of the nadir-centered clutter patch where the altimetric measurement is desired. Beam-limited altimeters rely on the beamwidth rather than the range bin width for this purpose. Whether a pulse-limited or beam-limited approach is more desirable depends on the hardware capabilities (waveform generator, A/D converter, etc.), the antenna size, and the operating frequency. Other approaches have also been proposed. A “synthetic aperture” altimeter uses Doppler processing to provide finer resolution in the along-track dimension, while resolution in the across-track direction is still limited by either the beamwidth or the range bin width. In some applications, particularly over land, a single nadir-looking beam does not provide sufficient coverage. In these cases the beam can be scanned in the across-track direction to cover a wider swath on either side of the satellite's ground track. Well-calibrated radar altimeter instruments can provide a measurement precision of a few centimeters [2]. A fairly high frequency (13 GHz) is often used in order to obtain a narrow beamwidth with a reasonably sized antenna.

Scatterometers. Scatterometers are relatively coarse-resolution, nonimaging radar instruments that measure the backscatter coefficient of the surface. They often employ long antennas producing fan beams that provide narrow angular resolution in one dimension. In other dimensions, fine resolution can be obtained either in range through the compressed pulse width or in Doppler through Doppler filtering.

Over oceanic areas, measurements of the backscatter coefficient in different, orthogonal directions from the radar can be used to infer the surface wind speed. Wind-driven waves produce a maximum backscatter return when they are viewed along the wind direction (i.e., perpendicular to the wave fronts) and a minimum return when viewed perpendicular to the wind direction (parallel to the wave fronts) [1, 2]. At incidence angles well away from nadir, the overall strength of the returns is proportional to the wind speed, which is opposite to the relationship observed in nadir-pointing altimeters. Surface wind speed is an important meteorological parameter that can be retrieved by scatterometers from mid-ocean areas where there are no surface instruments. Scatterometers designed for this purpose are often called “wind scatterometers,” although the wind measurement is indirect.

Scatterometers are also used to observe land areas. Since scatterometers have resolutions of tens of kilometers, the most consistent results are obtained from fairly homogeneous terrain types, such as tropical forests. Tropical forests exhibit volumetric

scattering, making the backscatter coefficient relatively independent of the incidence angle [2]. For surfaces in which soil is at least partially visible, the backscatter coefficient can be related to the soil moisture content, although it is also affected by many other factors. Observations of changes in the backscatter coefficient of a particular area over time can be correlated with changes in the soil moisture conditions from in situ measurements for calibration purposes. Changes in soil moisture content and sea surface salinity can also be detected by passive microwave radiometers. Scatterometers and radiometers can, therefore, provide complementary data and each instrument can aid in calibrating the other.

10.1.3 List of Symbols

a	= semi-major axis of the satellite orbit
A	= aperture area
B_d	= Doppler bandwidth
B_n	= noise bandwidth
B_0	= Earth's magnetic field strength ≈ 0.5 gauss near Earth's surface
B_x	= along-track phase center spacing
c	= propagation velocity $\approx 3.0 \times 10^8$ m/s
f	= frequency
f_d	= Doppler frequency shift
f_r	= pulse repetition frequency (PRF)
F	= noise figure
G_r	= receive antenna gain
g_s	= acceleration of gravity at Earth's surface ≈ 9.81 m/s ²
G_t	= transmit antenna gain
H	= antenna aperture height (vertical dimension)
h_{sat}	= height of the satellite above the mean Earth radius
i	= inclination of the orbital plane
k	= Boltzmann's constant = 1.38×10^{-23} J/K or W/(Hz·K)
k_{az}	= azimuth beamwidth coefficient
k_{el}	= elevation beamwidth coefficient
L	= antenna aperture length (horizontal or along-track dimension)
L_{SA}	= synthetic array (or synthetic aperture) length
L_{sys}	= system loss (total)
M_e	= mass of Earth = 5.972×10^{24} kg
m_{sat}	= mass of the satellite
P	= orbital period
P_{avg}	= average transmitted power

P_t = peak transmitted power

R_e = radius of Earth (mean) = 6,371.462 km

r_{sat} = radius of the satellite from Earth's center (instantaneous)

s = antenna element spacing

$R, R_s, R_{s(min)}, R_{s(max)}$ = slant range

T_r = pulse repetition interval (PRI)

T_{SA} = synthetic array (or synthetic aperture) time

T_0 = standard reference temperature = 290 K

v_r = radial ("line-of-sight") velocity

v_{sat} = satellite velocity

$\beta, \beta_{near}, \beta_{far}$ = angle at the target location on Earth's surface between the directions toward the satellite and the center of Earth

β_L = argument of latitude

$\gamma, \gamma_{min}, \gamma_{max}$ = angle at the center of Earth between the directions toward the satellite and the target location

δ_{CR} = cross-range ("azimuth") resolution

δ_R = range resolution

$\Delta\theta$ = change in target aspect angle during the synthetic array time

$\Delta\theta_0$ = shift in the beam position ("beam squint") with a change in frequency

ΔR_g = difference between the maximum and minimum ground (surface) ranges in the mainlobe footprint

ΔR_s = difference between the maximum and minimum slant ranges in the mainlobe footprint

φ = angle of propagation path from nadir

η_a = antenna aperture efficiency

θ = true anomaly (angular position of the satellite in its orbit, measured from the periapsis)

θ_b = one-way half-power beamwidth

$\theta_{b(Az)}$ = one-way half-power azimuth beamwidth

$\theta_{b(EI)}$ = one-way half-power elevation beamwidth

θ_B = angle between the propagation path and Earth's magnetic field

θ_g = angle of the first grating lobe from broadside

θ_i = angle of incidence of the wavefront at Earth's surface

$\theta_L, \theta_{L(min)}, \theta_{L(nom)}, \theta_{L(max)}$ = look angle from nadir

$\theta_s, \theta_{s(max)}$ = antenna beam scan angle

λ = wavelength

μ = gravitational parameter = 3.986×10^{14} m³/s² for Earth

σ = radar cross section (RCS)

σ_c = clutter RCS in a resolution cell

σ^0 = surface backscatter coefficient (area-normalized RCS)

σ_N^0 = noise-equivalent sigma zero (NESZ), also known as noise-equivalent sigma “naught” ($NE\sigma^0$) or additive noise coefficient (ANC)

τ = pulse width (uncompressed)

ψ = grazing angle

ω = argument of the perigee/periapsis

ω_e = Earth’s angular rotation rate

ω_{sat} = satellite angular rate

Ω = right ascension of the ascending node

Ω_p = polarization rotation angle

10.1.4 List of Abbreviations and Acronyms

ADC – Analog-to-Digital Converter

AESA – active electronically scanned array

AFB – Air Force Base

aka – also known as

ALOS – advanced land observation satellite

ANC – additive noise coefficient, also known as noise-equivalent sigma zero (NESZ)

ASAR – advanced synthetic aperture radar

ATI – along-track interferometry

BAQ – block adaptive quantizer

BFPQ – block floating point quantization

C-band – 4–8 GHz (typically ~5.3 GHz for spaceborne SARs)

COSMO – Constellation of Small Satellites for Mediterranean Basin Observation

DARPA – Defense Advanced Research Projects Agency

DC – direct current; also zero Doppler frequency

DEM – digital elevation measurement

DPCA – displaced phase center antenna

DTAR – distributed target ambiguity ratio

EO – electro-optic

ERIM – Environmental Research Institute of Michigan

ESA – European Space Agency

FBAQ – flexible block adaptive quantizer

FM – frequency modulation

GMTI – ground moving target indicator

HH – transmit using horizontal polarization, receive using horizontal polarization

HV – transmit using horizontal polarization, receive using vertical polarization

I – inphase

IR – infrared

ITU – International Telecommunication Union

JAROS – Japan Resources Observation System Organization

JERS – Japanese Earth Resources Satellite

JPL – Jet Propulsion Laboratory

L-band – 1–2 GHz (typically ~1.3 GHz for spaceborne SARs)

LEO – low earth orbit

LFM – linear frequency modulation

mrad – milliradians

MTI – moving target indicator

NASA – National Aeronautics and Space Administration

NASDA – National Space Development Agency of Japan

NESZ – noise-equivalent sigma zero

PALSAR – phased array type L-band SAR

PRF – pulse repetition frequency

PRI – pulse repetition interval

Q – quadrature

RCS – radar cross section

SAR – synthetic aperture radar

S-band – 2–4 GHz (typically ~3.1 GHz for spaceborne SARs)

SCR – signal to clutter ratio

SDNR – signal to distortion noise ratio

SIR-A – Shuttle Imaging Radar - A

SIR-B – Shuttle Imaging Radar - B

SIR-C – Spaceborne Imaging Radar - C

SNR – signal to noise ratio

SRTM – Shuttle Radar Topography Mission

STAP – space–time adaptive processing

STS – space transportation system

TanDEM-X – TerraSAR-X add-on for digital elevation measurements

TEC – total electron content

T/R – transmit/receive

TRM – transmit/receive module

TRMM – Tropical Rainfall Measuring Mission

U.S. – United States

VV – transmit using vertical polarization, receive using vertical polarization

VH – transmit using vertical polarization, receive using horizontal polarization

X-band – 8–12 GHz (typically ~9.5 GHz for spaceborne SARs)

X-SAR – X-Band synthetic aperture radar (shuttleborne)

10.2 | HISTORICAL PERSPECTIVE

10.2.1 Overview

The use of SARs for civil remote sensing began with the NASA/Jet Propulsion Laboratory (JPL) Seasat mission in 1978. Seasat carried three pioneering radar instruments for studying Earth's oceans: an L-band SAR, a precision radar altimeter, and a microwave scatterometer. Since Seasat many other SAR satellites have successfully flown. The later satellites have operated over a wider range of frequencies (L-band through X-band), have provided multipolarization measurements, and have implemented other capabilities, such as electronic scanning, that continue to evolve over time.

The U.S. Seasat mission of 1978 was followed by five short-duration shuttle imaging radar (SIR) missions of increasing sophistication between 1981 and 2000: SIR-A, SIR-B, SIR-C/XSAR (two flights), and the Shuttle Radar Topography Mission (SRTM). The United States has not launched a free-flying civil SAR satellite since Seasat.

In 1987 and 1991 the USSR orbited two large SAR spacecraft (Cosmos 1870 and Almaz-1). These satellites were both unmanned versions of the Salyut spacecraft carrying S-band (3.1 GHz) synthetic aperture radars. They functioned for 1.5 to 2 years, after which they were intentionally deorbited. Russia has not orbited any civil SAR satellites since that time but several new programs have reportedly been under consideration.

Between 1991 and 2006, spaceborne SARs were developed by the European Space Agency (ESA) and the space agencies of Japan and Canada. The European Remote Sensing satellite ERS-1 carried a C-band SAR and operated from 1991 through 2000. Follow-on missions ERS-2 and ENVISAT also carried SARs operating in the C-band. The Japanese Earth Resources Satellite JERS-1 operated in L-band from 1992–1998. Canada has operated the highly successful RADARSAT-1 carrying a C-band SAR since its launch from California in 1995 (still operating in early 2013). A more sophisticated follow-on satellite, RADARSAT-2, was launched for Canada by Russia in 2007.

Beginning in 2006 a new generation of advanced SAR satellites appeared, including RADARSAT-2, with the majority of the others being developed and operated by Germany and Italy. Germany placed its five-satellite SAR-Lupe constellation into orbit between 2006 and 2008 using Russian launch services. These satellites operate in X-band for the purpose of security-related reconnaissance. Germany also operates two civil remote sensing SAR satellites called TerraSAR-X, launched in 2007, and its near-twin TanDEM-X, launched in 2010. These satellites orbit in close formation, enabling the pair to produce highly accurate elevation maps through the use of interferometry. Italy's four-satellite SAR constellation, COSMO/SkyMed, was placed into orbit between 2007 and 2010 using U.S. launch vehicles from Vandenberg AFB, California. These X-band satellites form a dual-use system providing imagery for both security-related reconnaissance and civil remote sensing purposes.

Since 2008 India and Israel (using an Indian launch vehicle) have orbited their own SAR satellites—Israel’s TecSAR and India’s RISAT-1 and RISAT-2. ESA, Canada, and Japan continue to evolve their SAR remote sensing capabilities with future launches planned. In addition, China and Japan have spaceborne SAR programs supporting their national security. Several other countries, notably South Korea and Argentina, have SAR remote sensing satellites under development.

A timeline of SAR remote sensing missions since 1978 is presented in Figure 10-1. Table 10-2 presents technical characteristics of some of the more historically significant SAR missions, although space limitations prevented the inclusion of many other interesting programs. Brief descriptions of a few of the more significant and widely publicized missions are presented in the subsections that follow.

10.2.2 U.S. Spaceborne SARs

Seasat (1978). Seasat was the first civil spaceborne SAR. It was developed by the Jet Propulsion Laboratory under funding from NASA. Seasat was launched in June 1978 into a circular orbit with an altitude of 800 km and an orbital inclination of 108° , completing 14 orbits per day. Seasat carried three active radar instruments: an L-band synthetic aperture radar, a Ku-band radar altimeter, and a Ku-band scatterometer. It also carried two passive instruments: a visible and infrared radiometer and a scanning multichannel microwave radiometer. The Seasat SAR used horizontal polarization on transmit and horizontal polarization on receive (a combination designated HH) to monitor the global surface wave field and polar sea ice conditions. A low off-nadir look angle of only 20° provided adequate SNR and accentuated returns from ocean surface features. Seasat operated for 105 days until October 1978 during which approximately 42 hours of SAR data were collected, an average of about 24 minutes per day [3, 4]. There was no onboard recorder, so imagery and other data could only be collected when the satellite was within range of a ground station. An artist’s depiction of the Seasat satellite is shown in Figure 10-2.

Shuttle Imaging Radar SIR-A (1981). The Shuttle Imaging Radar A (SIR-A) was flown aboard the Space Shuttle *Columbia* in November 1981 on the second shuttle flight. SIR-A, as well as its successors SIR-B and SIR-C/X-SAR, operated from the shuttle payload bay and did not fly freely. SIR-A was largely assembled from spare parts from the Seasat program [5]. As compared with Seasat, SIR-A operated at a lower altitude of 259 km and a lower orbit inclination of 38° due to shuttle flight constraints. SIR-A had a narrower system bandwidth (6 MHz) than that of Seasat and a coarser resolution of 40 m in azimuth and range. The SIR-A swath width of 50 km was narrower, and the incidence angle of $50 \pm 3^\circ$ was considerably higher (i.e., the grazing angle at the surface was shallower) than that of Seasat [6]. The higher incidence angle was more suitable for imaging terrain with significant relief as opposed to the ocean surface. Radar data was recorded optically on film for later processing on the ground.

Shuttle Imaging Radar SIR-B (1984). SIR-B was an updated radar using newly designed hardware that was flown aboard the Space Shuttle *Challenger* on flight 41-G (shuttle flight 13) in October 1984. The orbit was nominally circular during radar data collection, although several different altitudes were used. The average altitude for the first 20 orbits was 360 km, for the next 29 orbits it was 257 km, and for the remainder of the mission it was 224 km. These altitudes were fairly comparable with those of the

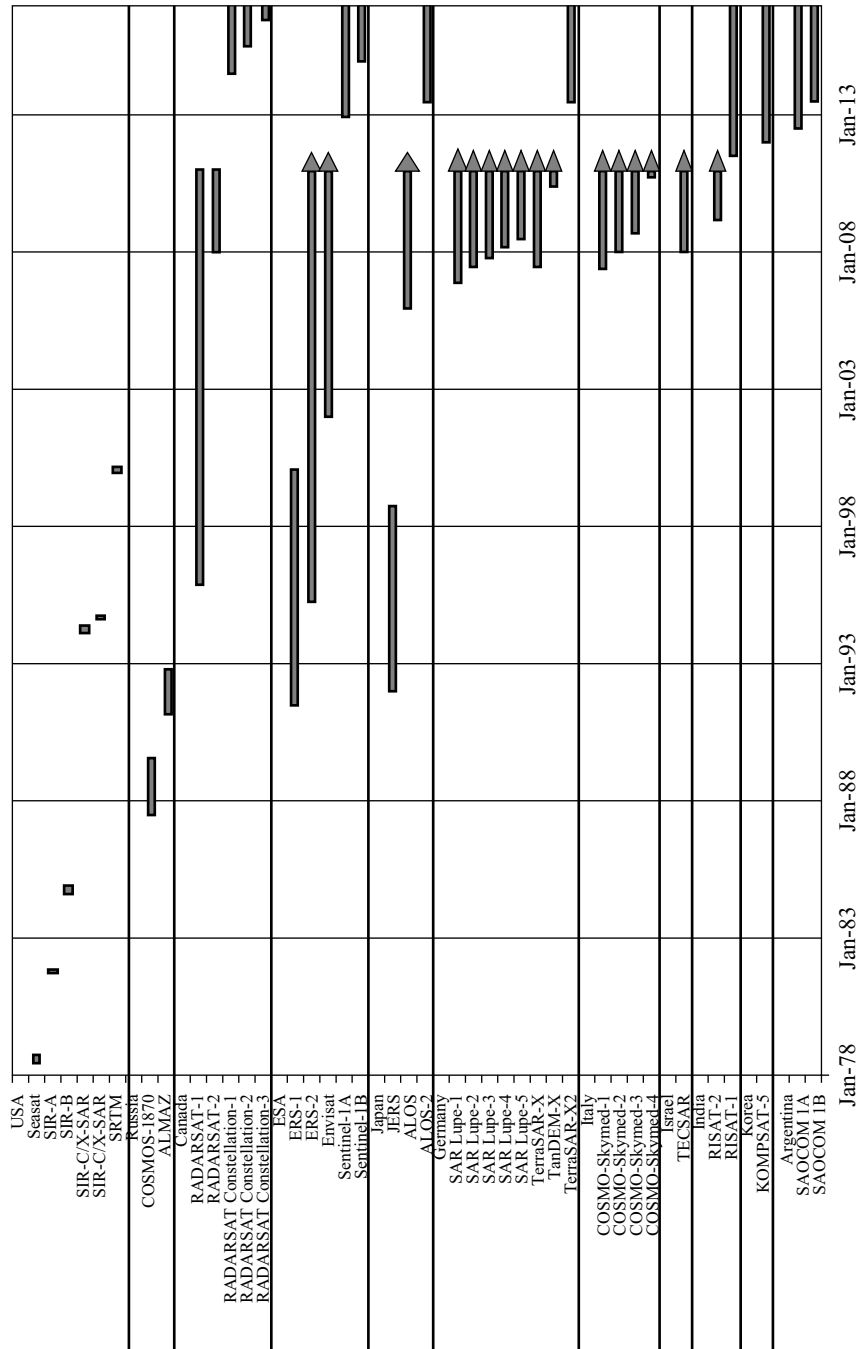


FIGURE 10-1 ■ Timeline of SAR Satellite Missions.

TABLE 10-2 ■ SAR Satellite and Radar Characteristics

Parameter	Seasat	Shuttle Imaging Radar A (SIR-A)	Shuttle Imaging Radar B (SIR-B)	Shuttle Imaging Radar C (SIR-C)/ X-SAR	ERS-1 and ERS-2	ENVISAT (ASAR instrument)	JERS-1	ALOS PALSAR	Radarsat-1	Radarsat-2
Nationality	U.S.	U.S.	U.S.	U.S.	Europe	Europe	Japan	Japan	Canada	Canada
Mission dates (and duration)	1978 (105 days)	Nov. 1981 (2 days)	Oct. 1984 (8.3 days)	Apr. and Oct. 1994	ERS-1: 1991–2000 ERS-2: 1995–2011	2002–2012	1992–1998	2006–2011	Nov. 1995–2013	Dec. 2007–2013
Orbit altitude	800 km	259 km	360, 257, and 224 km	225 km	782–785 km	800 km	568 km	690 km	793–821 km	793–821 km
Orbit inclination	108°	38°	57°	57°	98.5°	98.55°	97.7°	98.16°	98.6°	98.6°
Radar frequency	1.275 GHz (L-band)	1.275 GHz (L-band)	1.275 GHz (L-band)	1.277 GHz (L) 5.172 GHz (C) 9.677 GHz (X)	5.3 GHz (C-band)	5.331 GHz (C-band)	1.275 GHz (L-band)	1.270 GHz (L-band)	5.3 GHz (C-band)	5.405 GHz (C-band)
Antenna type	Passive array	Passive array	Passive array	AESA	Passive array	AESA	AESA	AESA	Passive array	AESA
Antenna dimensions	10.74 × 2.16 m	9.4 m × 2.16 m	10.7 m × 2.16 m	12 m × 4 m (overall)	10 m × 1 m	10 × 1.3 m	11.9 m × 2.2 m	8.8 m × 3.1 m	15 m × 1.5 m	15 m × 1.37 m
Beamwidths (Az × El)	1.26° × 6.24° (uniform wgt.)	1.27° × 6.24° (uniform wgt.)	1.26° × 6.24° (uniform wgt.)	El: 5.2–18.4°	0.29° × 5.4°	0.29° × 2.2° (uniform wgt.)	1° × 5.5°	1.36° × 3.87° (uniform wgt.)	0.19° × 1.92° (uniform wgt.)	Az: 0.21–0.63°
Swath width (in range)	100 km	50 km	20–40 km	15–90 km (L & C) 15–40 km (X)	100 km	100 km	75 km	40–70 km; 250–350 km using ScanSAR	45–170 km; 300–500 km using ScanSAR	18–170 km; 300–500 km using ScanSAR
Look angle from nadir	20°	47°	14°–56° (at 257 km alt.)	17°–63°	~20°	13°–39°	35° (typical)	9.9°–50.8°	20°–59°	9°–50°
Incidence angle at the surface	23° ± 3° across the swath	50 ± 3°	15°–65°	20°–65°	20.1°–25.9°	15°–45°	32°–38°	8°–60° (24° and 39° typ.)	20°–60°	10°–60°

(Continues)

Table 10-2 ■ (Continued)

Parameter	Seasat	Shuttle Imaging Radar A (SIR-A)	Shuttle Imaging Radar B (SIR-B)	Shuttle Imaging Radar C (SIR-C)/ X-SAR	ERS-1 and ERS-2	ENVISAT (ASAR instrument)	JERS-1	ALOS PALSAR	Radarsat-1	Radarsat-2
Polarization	HH	HH	HH	L & C band: HH, HV, VV, VH X band: VV	VV	HH, HV, VV, VH	HH	HH, HV, VV, VH	HH	HH, HV, VV, VH
Waveform bandwidth	19 MHz	6 MHz	12 MHz	10 and 20 MHz (L, C)	15.55 MHz	15 MHz	11.6, 17.3, 30 MHz	14 and 28 MHz	11.6, 17.3, 30 MHz	12–100 MHz
Range resolution (cross-track)	25 m (Theoretical)	40 m	58–16 m	9 and 19.6 MHz (X)	26.3 m	18 m	5 m (min.)	7–89 m (10–30 m typ.)	5 m (min.)	3 m (min.)
Azimuth resolution (along-track)	25 m (Theoretical)	40 m	20–30 m	30 m (L, C) 10 and 20 m (X)	30 m	18 m	8–100 m (30 m typical)	10 m	8–100 m (30 m typical)	1–100 m (25–40 m typical)
Number of looks	4	6	4	4	4	3	1–16	2	1–16	1–4
Transmitted pulse length	33.4 μ s	30.4 μ s	30.4 μ s	8.5–33.8 μ s (L, C) 40 μ s (X)	37.12 μ s	35 μ s	42 μ s	16 and 27 μ s	42 μ s	21 and 42 μ s
PRF (Hz)	1,463–1,640	1,464–1,824	1,464–1,824	1,395–1,736 (L, C) 1,240–1,860 (X)	1,640–1,720	1,506–1,606	1,270–1,390	1,500–2,500	1,270–1,390	1,300–3,800
Transmitted peak power	1.0 kW	1.0 kW	1.12 kW	3.3 kW (X)	4.8 kW	1.3 kW	5 kW	2 kW	5 kW	2.4–3.7 kW
Transmit duty factor	4.9–5.5% (est.)	4.5–5.5% (est.)	6.2%	5.6–6.9%	6.2%	5.3–5.6%	5.3–5.8%	2.4–6.8%	5.3–5.8%	10%
Data recorder bit rate	110 Mbits/s (on the ground)	Optical film recorder	Optical film recorder (30.4 Mbits/s on ground)	45–90 Mbits/s	105 Mbits/s	60 Mbits/s	74–105 Mbits/s	120 and 240 Mbits/s	400 Mbits/s	400 Mbits/s



FIGURE 10-2 ■
NASA Seasat
Satellite [Jet
Propulsion
Laboratory].

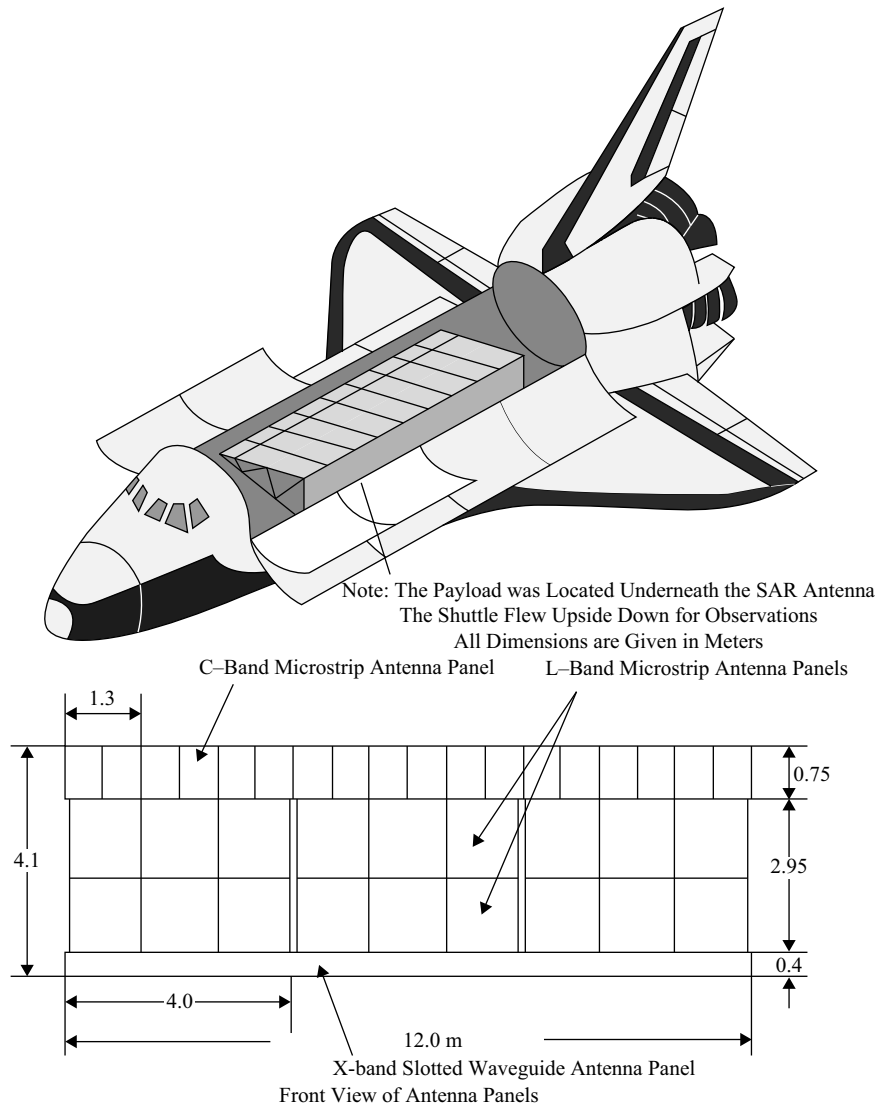
SIR-A mission. The 57° orbit inclination was greater than that used for SIR-A, providing greater coverage of Earth's surface. The system bandwidth of 12 MHz was twice that of SIR-A. A mechanically tiltable antenna provided a wide range of off-nadir look angles from 15° to 65° . This permitted observations of both oceans and land, as well as repeated observations of the same target area at multiple incidence angles [7].

SIR-C/X-SAR (1994). The Spaceborne Imaging Radar C/X-Band Synthetic Aperture Radar (SIR-C/X-SAR) was flown twice in 1994 on the Space Shuttle *Endeavour*, during April on flight STS-59 and during late September and early October on flight STS-68. (Note: The STS numbering did not follow a strict chronological sequence during this period.) The SIR-C portion of the system evolved from JPL's L-band SIR-A and SIR-B radars, while the X-SAR X-band radar subsystem was provided by Germany [8]. Figure 10-3 shows the general concept of the SIR-C/X-SAR installation in the shuttle payload bay along with the antenna layout and dimensions.

10.2.3 European Space Agency (ESA) Spaceborne SARs

ERS-1 and ERS-2. The European Remote Sensing satellites, ERS-1 and ERS-2, were launched in July 1991 and April 1995, respectively. Their near-polar sun-synchronous orbits had a mean altitude of approximately 780 km, an inclination angle of 98.5° , and an orbital period of 100 minutes. (A sun-synchronous orbit is an orbit in which the orbital plane maintains a relatively constant orientation with respect to the sun. With respect to the fixed stars, the plane of a sun-synchronous orbit precesses exactly 360° in one year, or slightly less than one degree per day. Sun-synchronous orbits will be discussed in greater detail in Section 10.3.) ERS-2 was initially placed into the same orbit as ERS-1 in a so-called tandem mission providing opportunities for SAR interferometry [9]. ERS-2 coverage of any particular point on the ground was phased one day behind

FIGURE 10-3 ■
SIR-C/X-SAR
Antenna Installation,
Dimensions,
and Layout
[eoportal.org].



that of ERS-1 [10]. The ground track of both ERS satellites repeated every 35 days. Both ERS-1 and ERS-2 SARs operated in C-band. Major instruments onboard ERS-2 included a synthetic aperture radar; a radar altimeter; a wind scatterometer; and several passive instruments covering microwave, IR, visible, and UV wavelengths. ERS-1 failed in March 2000 after operating for over nine years, which was over three times its design lifetime. ERS-2 operated for 16 years until September 2011 when it was taken out of service. Figure 10-4 shows the ERS-2 satellite; ERS-1 was very similar in appearance.

Envisat ASAR. ESA's Envisat satellite was launched in March 2002 and operated for ten years until April 2012. As shown in Figure 10-5, Envisat instruments included the advanced synthetic aperture radar (ASAR) with an active phased array antenna [11, 12]. At the 800-km orbit altitude, Envisat circled Earth every 100 minutes. For most instruments, global coverage was provided every 3 days, with exact repeat coverage occurring every 35 days, which was the same as for ERS-2. This repeat coverage

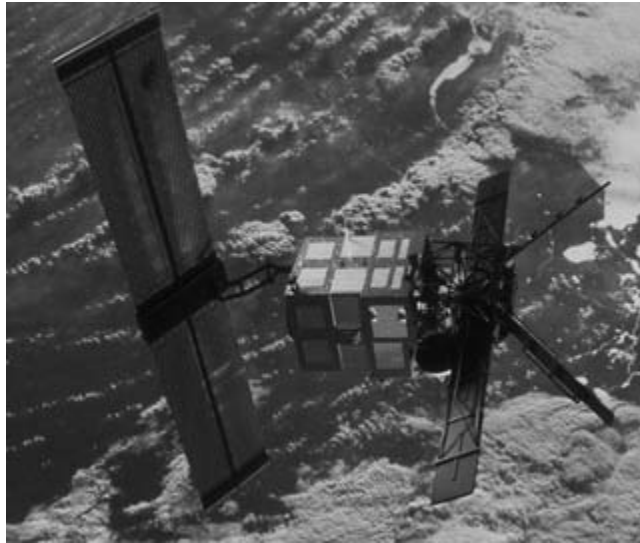


FIGURE 10-4 ■ ERS-2 Satellite. ERS-1 was Similar in Appearance. Major Components from Left to Right are the Solar Array, Spacecraft Body, SAR Antenna, and a Pair of Scatterometer Antennas. [European Space Agency].

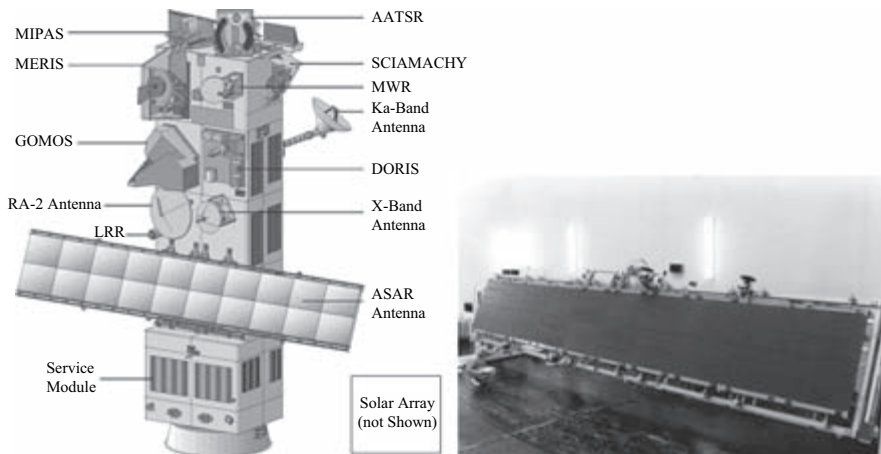
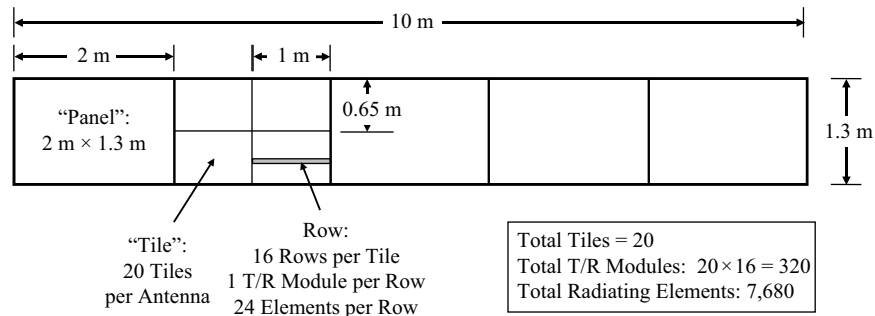


FIGURE 10-5 ■ Envisat Satellite and ASAR Antenna [European Space Agency].

provided images for multipass SAR interferometry, enabling interferometric image pairs to be taken at the same incidence angles. Envisat operated for double its original five-year design life.

Like ERS-2, the ASAR operated in C-band. While ERS-1 and ERS-2 used vertical polarization, ASAR had the capability to transmit either horizontal or vertical polarization, and to receive either horizontally or vertically polarized returns, or both, providing full coverage of the polarization matrix (HH, HV, VH, and VV). In the imaging and dual-polarization modes, the ASAR peak radiated power was 1,395 W.

FIGURE 10-6 ■
ENVISAT ASAR
Antenna Layout.



In contrast to ERS-1 and ERS-2, the Envisat ASAR used an active phased array antenna. This antenna was 10 m long by 1.3 m high and was composed of five “panels” that were each 2.0 m long by 1.3 m high. Each panel contained four “tiles” (antenna panel subassemblies) for a total of 20 tiles in the full array. Each tile was 1 m wide by 0.65 m high and was composed of 16 rows of 24 dual-polarized radiating elements. Each row was connected to a transmit/receive (T/R) module providing power amplification on transmit, low-noise amplification on receive, and amplitude and phase control at the subarray (row-in-tile) level. The ASAR antenna thus had a total of 320 transmit/receive modules driving 7,680 radiating elements, providing an electronic beam-steering capability in elevation and a more limited electronic beam-steering capability in azimuth [11, 13]. The ASAR antenna layout is shown in Figure 10-6.

ASAR was also equipped with a programmable digital waveform generator. Another improvement compared to ERS-1 and ERS-2 was an eight-bit analog-to-digital converter (ADC) with a flexible block adaptive quantizer (FBAQ). The FBAQ provided 8/4 (i.e., 8 bits in, 4 bits out) and 8/2 compression ratios that enabled the collection of input signals spanning a larger dynamic range while remaining within the data rate constraints of the downlink. Block adaptive quantization is discussed in greater detail in Section 10.4.6.

10.2.4 Japanese Spaceborne SARs

JERS-1. The Japanese Earth Resources Satellite (JERS) was launched in February 1992 into a 568-km circular orbit with a 97.7-degree inclination. It functioned for six years until October 1998 [14]. JERS-1 operated in L-band at an RF center frequency of 1.275 GHz with a peak transmitted power of 1.3 kW. The SAR resolution was 18 m. A 75-km range swath could be covered with three-look imagery. The corporate-fed antenna dimensions were 11.9 m by 2.2 m, and it was oriented to provide an incidence angle of approximately 35° at the surface. Most spaceborne SARs are able to operate for only a small portion of each orbit due to limitations in the data recording capacity and/or power storage (battery) capacity. The JERS-1 SAR could operate for up to 20 minutes per orbit. A total data rate of 60 Mbps was provided (30 Mbps per channel for I and Q channels), with three-bit quantization [15]. JERS-1 was a National Space Development Agency of Japan (NASDA) project. An illustration of the JERS-1 satellite is shown in Figure 10-7.

ALOS PALSAR. The Phased Array Type L-band Synthetic Aperture Radar (PALSAR) development is a joint project between the NASDA and the Japan Resources Observation System Organization (JAROS). PALSAR is a payload on the advanced land



FIGURE 10-7 ■ JERS-1 Satellite [Jet Propulsion Laboratory].

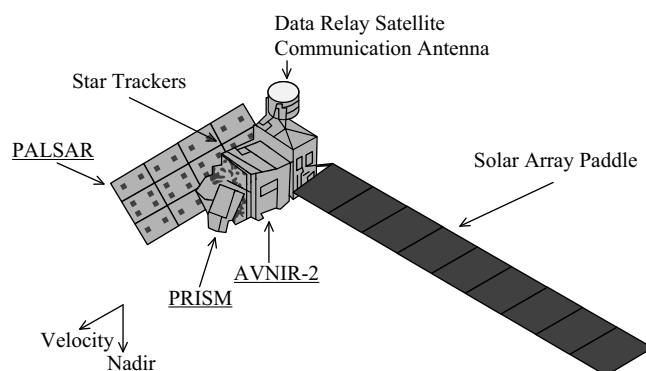


FIGURE 10-8 ■ Japanese ALOS with PALSAR [European Space Agency].

observing satellite (ALOS), which was launched in January 2006 and functioned until April 2011. ALOS was in a sun-synchronous orbit at an altitude of 690 km with an orbital period of 99 minutes. The ALOS spacecraft configuration is illustrated in Figure 10-8 [17].

PALSAR operated in L-band at 1.27 GHz with waveform bandwidths of 14 and 28 MHz. PALSAR provided 10-m resolution with dual-polarization capability [16]. Like the ENVISAT ASAR, PALSAR employed an active phased array antenna. The deployed antenna dimensions were 8.8 m wide by 3.1 m high. It was organized into four panels that were each 2.2 m wide by 3.1 m high containing a total of 80 T/R modules [16]. The T/R modules were at the subarray level, so each T/R module served multiple radiating elements. The PALSAR antenna was electronically steerable in elevation with an off-nadir look angle capability of 9.9° to 50.8°.

10.2.5 Canadian Spaceborne SARs

RADARSAT-1. Canada's first radar satellite, RADARSAT-1, was launched in November 1995 from Vandenberg, AFB, California, into an approximately 800-km-high orbit

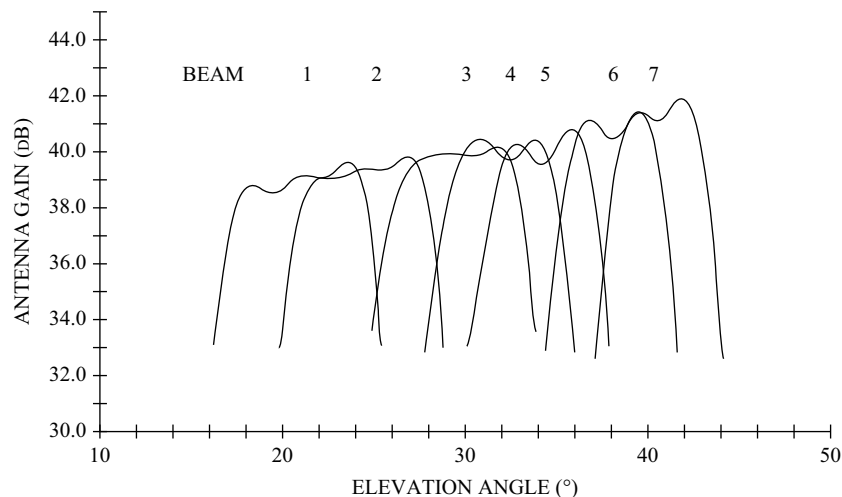
inclined 98.6° . Launch services were provided by NASA in exchange for data collected by the satellite. RADARSAT-1 is still operating in early 2013, far exceeding its five-year design lifetime. RADARSAT-1 was placed into a sun-synchronous “dawn–dusk” orbit in which the orbital plane remains approximately aligned with the terminator (the boundary between Earth’s sunlit and dark sides). This provides nearly continuous solar illumination for power generation except during brief eclipse periods around the June solstice that affect a portion of the orbit at far southern latitudes.

The radar normally looks toward the right of the satellite track in order to provide coverage of the region around the North Pole. Solar illumination is from the left. The satellite can occasionally be rotated 180° about its yaw axis to operate in a left-looking configuration providing temporary coverage of the South Pole. In that configuration, the radar looks toward the left of the satellite track and the solar illumination is still from the left.

The SAR operates in C-band at 5.3 GHz, a frequency that is well suited for monitoring and categorizing sea ice. The peak transmit power is 5 kW with an average transmit power of 300 W [18]. RADARSAT-1 uses a planar array antenna providing seven selectable shaped elevation beams as shown in Figure 10-9 [18]. These beam patterns have peak gains varying from approximately 39 dBi for beam 1 (the broadest elevation beam) to approximately 42 dBi for beam 7 (the narrowest). Elevation beam shaping and beam selection or scanning are becoming increasingly important in spaceborne SARs for expanding the processed range swath using the ScanSAR mode (discussed in Section 10.5.4).

The maximum RF bandwidth used by RADARSAT-1 is 30 MHz, providing a fine ground range resolution of about 9 m [18]. RADARSAT-1 also implements bandwidths of 17.3 MHz and 11.6 MHz providing coarser resolutions but with multilook capability and better image quality. The pulse repetition frequency (PRF) can be varied from 1,270 Hz to 1,390 Hz in 2-Hz steps [18]. The PRF is selected to avoid overlap between the desired mainlobe returns and the nadir sidelobe return (i.e., the “altitude return”), which may be in a different range ambiguity, as well as to avoid eclipsing of the mainlobe returns [19]. The pulse length is $42.0 \mu\text{s}$ [20] resulting in a 5.3 to 5.8 percent duty cycle.

FIGURE 10-9 ■
RADARSAT-1 SAR
Elevation Beam
Patterns [18].



RADARSAT-2. RADARSAT-2 was launched from Baikonur, Kazakhstan, in December 2007 and was placed into the same orbit as RADARSAT-1. RADARSAT-2 operates in C-band at a center frequency of 5.405 GHz and provides a resolution down to 3 m in its “ultra-fine” resolution mode.

The RADARSAT-2 SAR antenna, like the ASAR and PALSAR antennas, is an active phased array with electronic scan capability in elevation. It is 15 m long by 1.37 m high and is composed of a total of 512 subarrays arranged on two “wings.” This configuration allows the array to be partitioned into left and right halves to support along-track interferometry and other moving target detection modes. Each subarray is a row of 20 radiating elements associated with one transmit/receive (T/R) module providing amplification and phase control. Thirty-two subarrays are stacked to form a “column” or subpanel. Sixteen of these “columns” span the length of the antenna [21]. The horizontal center-to-center spacing between columns is 0.94 m, or 16.9 wavelengths. The center-to-center spacing between the subarrays (rows of elements) in the height dimension (aka “width” as opposed to “length”) is 0.77 wavelength, allowing the beam to be electronically scanned in elevation over a range of approximately 39° without incurring problems from grating lobes [20]. Figure 10-10 shows the layout of the RADARSAT-2 antenna along with the nomenclature used on that program.

Each subarray can transmit either horizontal or vertical polarization and can receive both polarizations. Aperture weighting can be applied using phase-only weighting on transmit and using amplitude and/or phase on receive. Any subset of columns can be enabled or disabled on transmit or receive. The radar receiver provides two independent receive channels that can either be used for dual-polarized (horizontal and vertical) reception or for separate reception on the leading and trailing antenna wings to support along-track interferometry (discussed in Section 10.5.6).

The linear frequency modulation (LFM) modulator can generate waveform bandwidths from 12 MHz to 100 MHz. The ultra-fine resolution mode provides approximately 3 m by 3 m resolution over 20-km swaths at incidence angles from 30° to 40° . To provide the additional aperture time required to achieve a 3-m cross-range resolution an azimuth beamwidth of approximately 0.5° is required. This can be achieved in the strip map mode either by using only a portion of the aperture or by slightly decollimating the beam in azimuth. In order to retain sensitivity, the T/R modules can be operated at a higher peak transmit power using a shorter pulse width in this mode as compared with other modes.

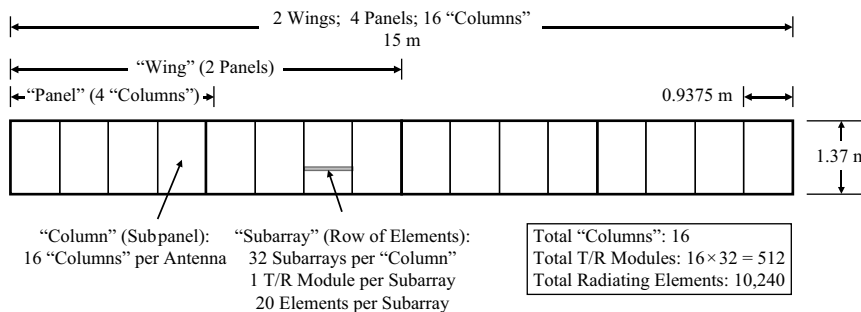


FIGURE 10-10 ■
RADARSAT-2
Antenna Layout.

TABLE 10-3 ■ COSMO-SkyMed Modes and Parameters [22]

Mode	Enhanced Spotlight	Himage Strip Map	PingPong Strip Map	ScanSAR Wide Region	ScanSAR Huge Region
Azimuth resolution	~1 m	~3 m	~10 m	~30 m	~100 m
Range resolution	~1 m	~3 m	~10 m	~30 m	~100 m
Azimuth frame extent	~11 km	~40 km	~30 km	~100 km	~200 km
Range swath extent	~11 km	~40 km (acq. time ~6.5 s)	30 km (acq. time ~5 s)	~100 km (acq. time ~15 s)	~200 km (acq. time ~30 s)
PRF	3,148.1 Hz to 4,116.7 Hz	2,905.9 Hz to 3,874.5 Hz	2,905.9 Hz to 3,632.4 Hz	2,905.9 Hz to 3,632.4 Hz	2,905.9 Hz to 3,632.4 Hz
Linear FM chirp duration	70 to 80 μ s	35 and 40 μ s	30 μ s	30 to 40 μ s	30 to 40 μ s
LFM chirp bandwidth – minimum	185.2 MHz (187.5 MHz sampling rate)	65.64 MHz (82.50 MHz sampling rate)	14.77 MHz (18.75 MHz sampling rate)	32.74 MHz (41.25 MHz sampling rate)	8.86 MHz (11.25 MHz sampling rate)
LFM chirp bandwidth – maximum	400.0 MHz (187.5 MHz sampling rate)	138.60 MHz (176.25 MHz sampling rate)	38.37 MHz (48.75 MHz sampling rate)	86.34 MHz (108.75 MHz sampling rate)	23.74 MHz (30.0 MHz sampling rate)

10.2.6 Italian COSMO/SkyMed System

The “Constellation of Small Satellites for Mediterranean Basin Observation” (COSMO)-SkyMed satellites were launched between 2007 and 2010 from Vandenberg AFB, California. All four COSMO-SkyMed satellites are in a single near-polar, sun-synchronous orbital plane at an altitude of approximately 620 km. Data from these satellites support both security-related reconnaissance and civil remote sensing activities. The COSMO-SkyMed SAR operates at a frequency of 9.6 GHz (X-band), which is well suited to the reconnaissance mission. An active phased array antenna is used. The antenna dimensions are 5.7 m by 1.4 m, organized into five panels. The antenna is divided into 40 tiles, each with 32 T/R modules, for a total of 1,280 T/R modules, with each T/R module serving multiple radiating elements.

Parameters for the COSMO-SkyMed modes are summarized in Table 10-3. In the enhanced spotlight mode, electronic beam steering increases the time on target to improve the cross-range resolution. The PingPong strip map mode employs alternating transmit and receive polarizations. ScanSAR is also supported [22–24].

10.2.7 German SAR Programs

SAR-Lupe. A constellation of five German SAR-Lupe reconnaissance satellites was launched between December 2006 and July 2008 from Plesetsk, Russia. These five satellites are in three orbital planes. The SAR-Lupe radar operates in X-band with a fixed 3.3 m by 2.7 m parabolic antenna. This contrasts with the active phased array antennas used on many other recent spaceborne SARs. In the strip map mode with 1-m resolution, SAR-Lupe can image a 60 km by 8 km area. The spotlight mode is implemented by rotating the satellite bus in the along-track direction, using reaction wheels to

enable the reflector antenna to dwell on the area of interest. This increases the integration time, enabling a resolution of less than 1 m to be achieved over a 5.5 km by 5.5 km image area.

TerraSAR-X. TerraSAR-X is a German X-band SAR satellite for civil remote sensing that was launched in 2007. TerraSAR-X will be described in detail in Section 10.6 as a design example of a spaceborne SAR.

TanDEM-X. Launched in 2010, TanDEM-X is nearly identical to TerraSAR-X and provides supplemental capabilities for making digital elevation measurements [25]. TerraSAR-X and TanDEM-X operate in formation in essentially the same orbit. To support interferometric SAR modes, a cold gas propulsion system on TanDEM-X permits maneuvering to achieve 200-m to 10,000-m cross-track baselines, with along-track baselines from zero to several hundred meters [26].

10.3 | ORBITS

Some of the characteristics of satellite orbits as they pertain to radar remote sensing satellites are discussed briefly in this section. Although this discussion applies to satellites in Earth orbit, the same principles and equations apply to spacecraft orbiting other planets when the appropriate planet radius, planet mass, and/or gravitational acceleration are substituted.

10.3.1 Definitions

Before proceeding further, some definitions are in order:

apogee or *apoapsis*: The highest point in a satellite orbit, i.e., the point where the satellite height (or orbit radius) is maximum. The term “apogee” refers specifically to Earth orbits, with the “gee” coming from “geo.” The more general term “apoapsis” refers to the highest point in an orbit around any celestial body.

argument of latitude: Angular position of the satellite in its orbit as measured from the ascending node (defined later). The argument of latitude is equal to the sum of the argument of the perigee/periapsis and the true anomaly, which are also defined later [27, 28]. Note that the argument of latitude does not correspond to the satellite’s latitude in Earth coordinates. As the satellite moves around its orbit, the argument of latitude takes on all values from 0 to 2π , regardless of the orbit inclination.

argument of the perigee/periapsis: Angle between the ascending node and the perigee or periapsis.

ascending node: The point at which the satellite crosses Earth’s equatorial plane from south to north.

descending node: The point at which the satellite crosses Earth’s equatorial plane from north to south.

inclination: Angle between the satellite orbital plane and Earth’s equatorial plane at the south-to-north equator plane crossing (ascending node). The orbit inclination can range from 0 to 180° and is always positive.

node: A point at which the satellite crosses Earth’s equatorial plane.

node line: Intersection of the orbital plane and Earth’s equatorial plane.

polar orbit: Strictly speaking, an orbit whose inclination is exactly 90° . The term “polar orbit” is often used loosely to refer to near-polar orbits with inclinations of roughly 70° to 110° .

perigee or *periapsis*: The lowest point in a satellite orbit, i.e., the point where the satellite height (or orbit radius) is minimum. The term “perigee” applies specifically to Earth orbits. The more general term “periapsis” refers to the lowest point in an orbit around any celestial body.

prograde orbit: An orbit in which a satellite has a velocity component in the direction of Earth’s rotation. Such orbits have inclinations between 0° and 90° . Many satellites are launched into prograde orbits to take advantage of Earth’s rotational velocity at launch, permitting a larger payload to be delivered to orbit with a given amount of fuel. Other factors can preclude the use of prograde orbits for some missions, however.

retrograde orbit: An orbit in which a satellite has a velocity component opposite to the direction of Earth’s rotation. Such orbits have inclinations between 90° and 180° . Many remote sensing satellites are placed into orbits that are near-polar and slightly retrograde (“sun-synchronous” orbits, to be discussed later).

true anomaly: The angular position of a satellite in its orbit as measured in the direction of satellite motion from the perigee/periapsis. The angle’s vertex is Earth’s center, which is also one of the two foci of the elliptical orbit.

vernal equinox direction: The direction defined by a line originating at the center of Earth and passing through the center of the sun at the time of the vernal equinox. This line points toward a specific direction in space beyond the sun, which slowly changes over the 26,000-year precession cycle of Earth’s rotational axis. Although the vernal equinox direction is currently in the constellation Pisces, it was in Aries when observations began over 2,000 years ago. It is, therefore, still referred to as the “first point of Aries” or sometimes simply “Aries.”

10.3.2 Circular Orbits

Circular orbits are a limiting case of elliptical orbits. Since many remote sensing applications prefer a circular orbit, this type of orbit will be discussed first. Although no satellite orbit is perfectly circular, many are sufficiently close to permit a circular orbit approximation to be used for top-level design calculations and trade-offs.

In a circular orbit, the speed of a satellite along its orbital path is

$$v_{sat} = \sqrt{\frac{\mu}{r_{sat}}} \quad (10.1)$$

where r_{sat} is the radius of the orbit from the center of Earth in meters and μ is a constant defined by

$$\mu = G(M_e + m_{sat}) \approx GM_e = g_s R_e^2 \quad (10.2)$$

where

G = universal gravitational constant (6.67×10^{-11} nt – m²/kg²)

M_e = mass of the Earth (5.983×10^{24} kg)

m_{sat} = mass of the satellite (kg)

g_s = acceleration of gravity at Earth's surface (9.81 m/s²)

R_e = radius of Earth ($\sim 6.370 \times 10^6$ m, assumed spherical)

The value of μ is 3.986×10^{14} m³/s². As an example, at an altitude of 800 km, the orbital velocity in a circular orbit is 7.456 km/s.

The orbital period is defined as the interval between successive passages of a reference point in the orbit, such as the ascending node. The satellite orbital period (in seconds) is

$$P = \frac{2\pi r_{sat}}{v_{sat}} = 2\pi \sqrt{\frac{r_{sat}^3}{\mu}} \quad (10.3)$$

Conversely, the orbit radius required for a specified orbital period is

$$r_{sat} = \left(\frac{\mu P^2}{4\pi^2} \right)^{1/3} \quad (10.4)$$

A satellite in an 800-km-high circular orbit would have an orbital period of 6,042 seconds, or 100.7 minutes.

Earth is not a perfect sphere, but rather is an oblate spheroid. It has an equatorial radius of 6,378.1 km and a polar radius of 6,356.8 km, making the radius at the poles 21.3 km less than the radius at the equator [29]. There are additional irregularities in Earth's shape that can be defined in terms of higher-order spherical harmonics, which are beyond the scope of the present discussion. Earth's oblateness imparts a torque to a satellite, causing its orbital plane to precess slowly about Earth's rotational axis. The rate of precession is given by

$$\frac{d\Omega}{dt} = -\frac{3}{2} J_2 \sqrt{g_s} \left(\frac{R_e^3}{r_{sat}^{7/2}} \right) \cos i \quad (10.5a)$$

or, equivalently,

$$\frac{d\Omega}{dt} = -\frac{3}{2} J_2 \sqrt{\mu} \left(\frac{R_e^2}{r_{sat}^{7/2}} \right) \cos i \quad (10.5b)$$

where i is the orbit inclination and Ω is the right ascension of the ascending node (i.e., the angular difference between the node line and the vernal equinox direction) [30]. (Right ascension is analogous to longitude in Earth-referenced celestial coordinates. It should not be confused with “celestial longitude,” which is defined in sun-referenced, or “ecliptic,” coordinates.) J_2 is a coefficient of the second zonal harmonic of the geopotential field. (Zonal harmonics are rotationally symmetric deviations in Earth's shape from a perfect sphere.) The value of the J_2 coefficient is approximately

1.08228×10^{-3} . All higher-order spherical harmonic coefficients for Earth are at least three orders of magnitude smaller than this value and can generally be neglected. It is evident by inspection that when the inclination is 90° , the orbit plane precession rate will be zero with respect to the fixed stars.

Of greater interest is the case where the orbit plane precesses by exactly one full rotation per year. This is termed a “sun-synchronous” orbit because the ascending or descending passes over a given point on Earth’s surface occur at approximately the same local solar time each day. (The word “approximately” is used here because there may not be an integer number of orbits per day and because the satellite orbit precesses at a constant rate while Earth moves at a variable rate in its elliptical orbit around the sun.)

Two types of sun-synchronous orbits are of interest in radar remote sensing. First, some sun-synchronous orbits are designed to ensure that the satellite will pass over a given point on Earth’s surface near a particular local time each day, such as 10:00 a.m. Such orbits are often used by remote sensing satellites employing EO/IR sensors to enable their data to be collected with consistent solar illumination. A satellite carrying both radar and EO/IR sensors may be placed in this type of sun-synchronous orbit for the benefit of the optical sensors. In the second type of sun-synchronous orbit, called a *dawn-to-dusk* or *dawn–dusk* orbit, the node line remains perpendicular to the solar illumination and the satellite flies approximately along the terminator. For a radar-only satellite, this type of orbit ensures consistency in power production from the solar panels since the satellite is nearly always sunlit except for brief eclipsed periods near the summer solstice. The Canadian RADARSATs use a dawn-to-dusk orbit.

Equation (10.5) infers that the inclination required to make a circular orbit sun-synchronous depends on the orbit radius or satellite height. The required inclination can be found by setting

$$\begin{aligned}\frac{d\Omega}{dt} &= \frac{2\pi \text{ radians}}{31,556,926 \text{ seconds}} \\ &= 1.99106 \times 10^{-7} \text{ radians/second} \\ &= 0.985647^\circ/\text{day}\end{aligned}$$

where 31,556,926 seconds represents one solar year (365.242199 days), and solving Equation (10.5) for i yields

$$i = \cos^{-1} \left\{ -\frac{d\Omega}{dt} \left(\frac{2}{3J_2\sqrt{g_s}} \right) \left(\frac{r_{sat}^{7/2}}{R_e^3} \right) \right\} \quad (10.6a)$$

or

$$i = \cos^{-1} \left\{ -\frac{d\Omega}{dt} \left(\frac{2}{3J_2\sqrt{\mu}} \right) \left(\frac{r_{sat}^{7/2}}{R_e^2} \right) \right\} \quad (10.6b)$$

For typical orbits used by remote sensing satellites, the inclination required for a sun-synchronous orbit is on the order of 97° to 103° , or slightly retrograde from a true polar orbit. Figure 10-11 plots the inclination required for a sun-synchronous circular orbit as a function of the orbit altitude together with the period of a satellite at that altitude (regardless of whether or not the orbit is sun-synchronous).

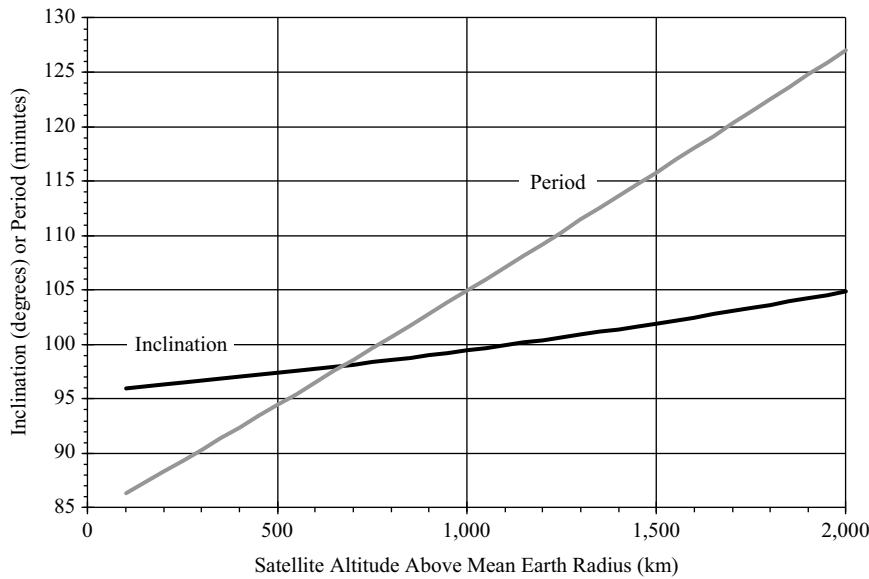


FIGURE 10-11 ■ Period and Inclination Required for a Sun-Synchronous Circular Orbit.

10.3.3 Elliptical Orbits

When the orbit is not sufficiently circular, equations for an elliptical orbit must be used. An ellipse is traditionally defined in terms of its semimajor axis a (i.e., half of the major axis) and its eccentricity e . The semimajor axis is

$$a = \frac{r_{sat(min)} + r_{sat(max)}}{2} = R_e + \frac{h_{min} + h_{max}}{2} \quad (10.7)$$

where

$r_{sat(min)}$ = orbit radius at perigee

$r_{sat(max)}$ = orbit radius at apogee

h_{min} = satellite height above mean Earth radius at perigee

h_{max} = satellite height above mean Earth radius at apogee

The orbit eccentricity is

$$e = 1 - \frac{r_{sat(min)}}{a} \quad (10.8)$$

and is zero for a circular orbit. Using these variables, the satellite radius at any point in the orbit is given by

$$r_{sat} = \frac{a(1 - e^2)}{1 + e \cos\theta} \quad (10.9)$$

where θ is the true anomaly (i.e., the angular coordinate of the satellite in its orbit as measured from the perigee) [30]. The satellite velocity in an elliptical orbit varies with the satellite radius [31] and is given by

$$v = \sqrt{\mu \left(\frac{2}{r_{sat}} - \frac{1}{a} \right)} \quad (10.10)$$

The orbital period (in seconds) is

$$P = 2\pi\sqrt{\frac{a^3}{\mu}} \quad (10.11)$$

and the flight path angle with respect to a local horizontal plane [31] is

$$\gamma_{sat} = \tan^{-1}\left(\frac{e \sin \theta}{1 + e \cos \theta}\right) \quad (10.12)$$

The rate of precession of the orbital plane [1] is

$$\frac{d\Omega}{dt} = -\frac{3}{2}J_2\sqrt{g_s}\left(\frac{R_e^3}{a^{7/2}(1-e^2)^2}\right)\cos i \quad (10.13a)$$

or, alternatively,

$$\frac{d\Omega}{dt} = -\frac{3}{2}J_2\sqrt{\mu}\left(\frac{R_e^2}{a^{7/2}(1-e^2)^2}\right)\cos i \quad (10.13b)$$

These expressions reduce to those of Equation (10.5) when $e = 0$. As with circular orbits, the precession rate of the orbital plane is zero when the inclination is 90° .

In addition to orbit plane precession, the angle ω between the perigee and the ascending node (the “argument of the perigee”) can also shift over time [1], as governed by

$$\frac{d\omega}{dt} = -\frac{3}{4}J_2\sqrt{g_s}\left(\frac{R_e^3}{a^{7/2}(1-e^2)^2}\right)(1-5\cos^2 i) \quad (10.14a)$$

or

$$\frac{d\omega}{dt} = -\frac{3}{4}J_2\sqrt{\mu}\left(\frac{R_e^2}{a^{7/2}(1-e^2)^2}\right)(1-5\cos^2 i) \quad (10.14b)$$

This angular rate is zero when the inclination is equal to a “critical angle” i_c that can be found by setting

$$1 - 5\cos^2 i_c = 0$$

and solving for i_c yielding

$$i_c = \cos^{-1}\left(\frac{1}{\sqrt{5}}\right) = 63.4^\circ \quad (10.15)$$

independent of the orbit altitude or eccentricity. An orbit with this inclination would be desirable if the perigee must remain over a specified latitude on Earth, such as when the maximum SNR is desired. Other mission requirements may dictate an orbital inclination different from i_c , however. If that is the case, the satellite’s orbit should be as nearly circular as possible to provide uniform SNR performance over the entire orbit.

10.3.4 Target Doppler Shift

Unlike the case of airborne SAR, the Doppler shift of a target or clutter patch observed by a spaceborne radar includes a contribution from Earth's rotation. The net two-way Doppler shift seen by a satellite in a circular orbit is given [32] by

$$f_d = \frac{2v_{sat}}{\lambda} \sin \theta_L \cos a \cdot \left\{ 1 - \left(\frac{\omega_e}{\omega_{sat}} \right) \cdot [\varepsilon \cos \beta_L \sin i \tan a + \cos i] \right\} \quad (10.16)$$

where

θ_L = look angle from nadir

a = azimuth squint angle (about the yaw axis) between the velocity vector and the target azimuth

ω_e = Earth's angular rotation rate

ω_{sat} = satellite angular rate = $2\pi/P$ radians/sec for a circular orbit

$\varepsilon = -1$ if the radar is left-looking; $+1$ if right-looking

β_L = argument of latitude (angular position of the satellite in its orbit as measured from the ascending node)

i = orbit plane inclination

The term in brackets is due to Earth's rotation. If ω_e is zero, the term in brackets vanishes and the equation reduces to the form used for airborne radars in which the radar moves in an Earth-referenced frame. Derivations for both circular and elliptical orbits are presented in Appendix B of Curlander and McDonough [33].

Based on Equation (10.16), the azimuth squint angle resulting in zero Doppler shift is

$$a_0 = \tan^{-1} \left\{ \varepsilon \left[\frac{N - \cos i}{\cos \beta_L \sin i} \right] \right\} \quad (10.17)$$

where N is the number of orbits per day ($N = \omega_{sat}/\omega_e$). This angle typically deviates by plus or minus a few degrees from 90° (side-looking) and varies sinusoidally during the orbit. The beam should ideally be pointed in this direction in strip map modes to center the surface returns at DC (zero Doppler). Some of the newer satellites have this capability, which reduces throughput requirements in the ground-based processor.

10.4 | DESIGN CONSIDERATIONS FOR THE SPACEBORNE SAR

This section addresses design issues and trade-offs that are unique to spaceborne SARs. More general aspects of SAR design are covered in many excellent references. In particular, Curlander and McDonough [33] thoroughly cover all issues associated with strip map SARs, both spaceborne and airborne. Carrara *et al.* [34] is a detailed and practical reference on spotlight SAR imaging from airborne platforms. Jakowatz *et al.* [35] and Cumming and Wong [36] provide greater detail on SAR processing. The Cumming and Wong book in particular emphasizes processing of SAR data from spaceborne radars.

10.4.1 Propagation Phenomena

10.4.1.1 Ionospheric Effects

Faraday Rotation. When a linearly polarized wave passes through the ionosphere, the plane of polarization rotates due to a phenomenon called Faraday rotation. This occurs because the phase delay through the ionosphere is different for different polarization components with respect to Earth's magnetic field. The amount of polarization rotation depends on the total electron content (TEC) along the path and the geometric relationship between the propagating wave and Earth's magnetic field.

Free electrons are present in the ionosphere as a result of ionization of upper atmospheric atoms by solar ultraviolet radiation. The degree of ionization varies with the time of day, season, the 11-year sunspot cycle, short-term solar activity (flares, etc.), and ionospheric dynamics. Thus, most ionospheric phenomena, including Faraday rotation, are highly variable.

The amount of Faraday rotation is given approximately [37] by

$$\Omega_P = \frac{2.365 \times 10^4 \text{ TEC } B_0 \cos \theta_B}{f^2 \cos \varphi} \quad (10.18)$$

where

Ω_P = rotation of the polarization plane (radians)

TEC = total electron content in a vertical column through the ionosphere with a cross-section of 1 m² (electrons/m²)

B_0 = magnetic field strength = 0.5×10^{-4} teslas (= 0.5 gauss)

θ_B = angle between the direction of propagation and the magnetic field

f = radar frequency (Hz)

φ = angle of the propagation path in the ionosphere from nadir (approximately equal to the off-nadir look angle θ_L)

The primary effect of Faraday rotation on linearly polarized radar returns is a loss in the return power due to the polarization mismatch between the radar returns and the receiving antenna. This loss can degrade the data quality in a single-polarization radar and can alter polarization measurements in dual-polarization radars.

Equation (10.18) shows that the magnitude of the Faraday rotation is proportional to $1/f^2$. At low frequencies (<100 MHz) during periods of high solar activity, the polarization plane of a linearly polarized wave can undergo dozens of complete rotations during its transit through the ionosphere. At L-band (1.3 GHz) the magnitude of the Faraday rotation is much lower, typically ranging from under one degree to a few tens of degrees, although it can be larger under extreme conditions. This amount of Faraday rotation can introduce significant errors in polarimetric measurements at L-band, so this phenomenon needs to be considered for L-band spaceborne SAR design and operation. Faraday rotation is not a major concern at frequencies above L-band.

Figure 10-12 plots the Faraday rotation versus frequency and total electron content for a representative path through the ionosphere (30° off nadir and 45° from the magnetic field direction). A value of 10^{17} electrons/m² is often used as a typical value for the total electron content.

Faraday rotation is a major impediment to the development of spaceborne radars in the VHF and UHF bands as is currently being considered by several research

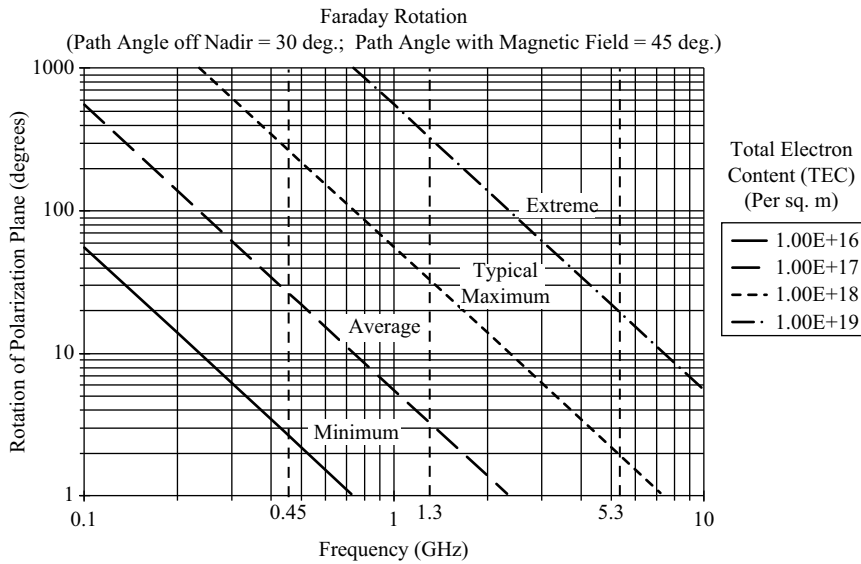


FIGURE 10-12 ■ Faraday Rotation versus Signal Frequency and Total Electron Content.

organizations. VHF and UHF radars would provide foliage-penetration capability and ground-penetration capability in dry areas.

Excess Range Delay. When a wave passes through the ionosphere, its group velocity is slowed, causing an increase in the apparent target range. This change in range as measured by a radar is approximately [2]

$$\Delta r = \frac{40 \text{ TEC}}{f^2 \cos \varphi} \tag{10.19}$$

with TEC values typically ranging from 10^{16} to 10^{18} electrons/m². A plot of the excess target range versus frequency (with TEC as a parameter) is presented in Figure 10-13.

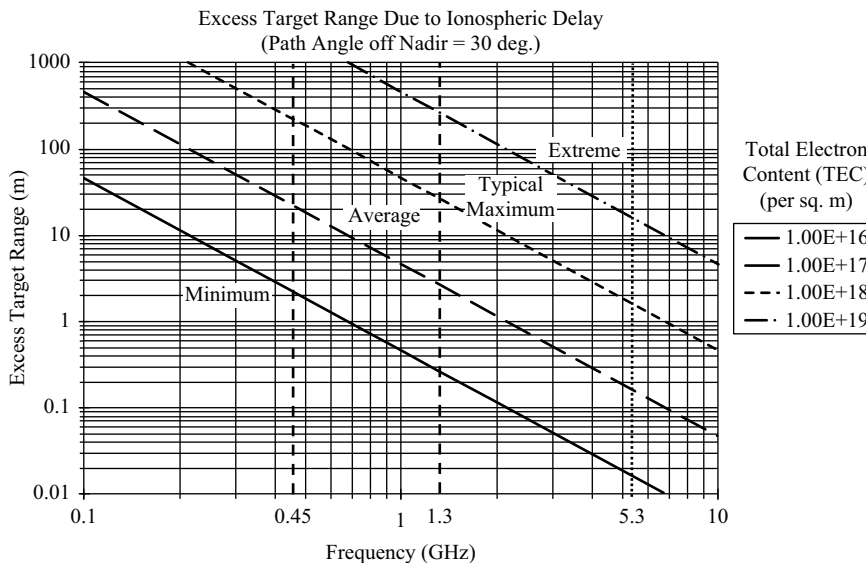


FIGURE 10-13 ■ Excess Target Range Due to Ionospheric Group Delay.

For most SARs operating in the 1–10 GHz range, the ionospheric range error is less than one range resolution cell and is generally not a concern. It can be a serious issue for radar altimeters, however. Even at 13–14 GHz, where many radar altimeters operate, the range error can sometimes be tens of centimeters. This is a problem for instruments designed to measure the sea surface height with centimeter precision [2].

Refraction (Elevation Error). Refraction occurs on oblique paths through the ionosphere, resulting in an error in the target elevation angle as seen from the radar. The amount of elevation error is related to the excess group delay (range error) and the path elevation angle. For L-band and higher frequencies, the elevation error is less than 1 mrad even at the extreme TEC value of 10^{19} electrons/m² [37]. Since most spaceborne radars do not measure the target elevation angle directly, the range error is of greater interest.

10.4.1.2 Tropospheric Effects

The primary tropospheric source of degradation for signals in the 1–10-GHz range is rain. Rain attenuation and backscatter increase markedly with increasing frequency, so these effects are most pronounced at the higher frequencies (e.g., X-band). Propagation paths from radar satellites typically use off-nadir look angles of 20°–50° while the rain height never exceeds about 5 km so the path length through rain is generally less than 10 km. Spaceborne radars may therefore experience less rain attenuation than airborne or ground-based radars that must look along shallower paths. There are many excellent references on rain attenuation (e.g., [38, 39]) so it will not be discussed further here.

Rain volumetric reflectivity is proportional to f^4 in the Rayleigh scattering region (below ~15 GHz for most rain) [38, 40]. Rain backscatter can appear in X-band SAR images as “foggy” patches, which can mask terrain or target returns. Rain can also depolarize the radar returns, although attenuation and backscatter are usually more serious problems. Rain attenuation and backscatter are generally not significant issues at C-band and below.

Clouds can produce attenuation at X-band comparable to that of light rain at equivalent rain rates of 1–10 mm/hr. Cloud thickness and condensed water content are highly variable, so this is a very rough approximation. Backscatter from clouds is lower than that of rain due to the smaller drop size and is not significant below 10 GHz. Ippolito [39] provides much more information on signal attenuation and depolarization on space–earth paths.

Atmospheric humidity can introduce excess propagation delay. The residual range error after correction using an atmospheric model and known environmental parameters ranges from a few centimeters on vertical paths under good conditions [2] to approximately 0.5 m on slanted paths under unfavorable conditions [41]. This error contributor is usually only significant in precise radar altimeters.

10.4.2 Radar Frequency Selection

The operating frequency of a spaceborne SAR is driven by several factors involving propagation and surface phenomenology. Most spaceborne SARs operate in the 1–10-GHz frequency range. Below 1 GHz, ionospheric effects, particularly Faraday rotation, can introduce significant measurement errors. These effects are evident at L-band (1.3 GHz) during periods of high solar activity. Above 10 GHz, rain can cause

serious attenuation of the radar signals and can contaminate SAR images with rain backscatter. Rain effects may be a major design consideration if the radar is required to observe regions where high rainfall rates are common, such as the tropics.

Within the 1–10-GHz frequency range, the preferred radar operating frequency is somewhat dependent on the surface properties to be sensed. Radars whose primary purpose is ocean observation typically operate at L-band (~1.3 GHz). The relatively long wavelength (23 cm) is responsive to large-scale wind waves and surface perturbations due to internal waves, but is less responsive to small-scale ripples (capillary waves) caused by local surface winds. L-band can also provide limited penetration of forest canopies [42].

C-band (~5 GHz) is a good compromise for observing other surface phenomena. C-band has been determined to be better than L-band for observing sea ice, for example, so C-band was selected for use in the Canadian RADARSAT satellites. C-band is also the least affected by propagation phenomena and can therefore provide relatively uncorrupted measurements of surface characteristics.

X-band (~9 GHz) is more responsive to smaller-scale surface roughness characteristics than the lower frequencies. X-band frequency allocations for remote sensing satellites provide wider operating bandwidths than the lower frequency bands, enabling spaceborne SARs to attain finer range resolution. The high frequency also allows finer cross-range resolution to be achieved during a given coherent dwell time. For these reasons, X-band has been the frequency of choice for reconnaissance missions (e.g., the German SAR-Lupe constellation, the Israeli TecSAR and Israeli-built Indian RISAT-2 reconnaissance satellites, and the dual-use Italian COSMO/SkyMed system). X-band has also been used for civil remote sensing missions such as the shuttle-borne X-SAR radar and the TerraSAR-X and TanDEM-X satellites (all German). X-band SAR images are subject to degradation by rain, however.

Frequencies specifically allocated by the International Telecommunication Union (ITU) for spaceborne radar remote sensing purposes are listed in Table 10-4 [43]. There are currently no frequency allocations for spaceborne radars below 1,000 MHz, although UHF (and even VHF) radar concepts are being considered by the remote sensing community. These low frequencies can provide foliage-penetration capability and possibly some surface-penetration capability under dry conditions, but are subject to pronounced ionospheric effects. The 13-GHz allocations have been used primarily by spaceborne radar altimeters and scatterometers and by one precipitation radar, the Tropical Rainfall Measuring Mission (TRMM). The W-band (94 GHz) allocation was used by a cloud-profiling radar on CloudSat and will likely be used for similar future missions.

10.4.3 Observable Characteristics

In addition to making visually pleasing images, imaging radars have a quantitative objective of measuring the equivalent radar cross section (RCS) or backscatter coefficient in every resolution cell. This requires an accurate knowledge of the radar's power output, antenna pattern, and internal gains and losses. These parameters must be remeasured on an ongoing basis to account for variations with temperature, aging, etc., in a process known as radiometric calibration. It is also useful to characterize the RCS in each resolution cell in terms of its polarization components. Many spaceborne remote sensing SARs now provide either a full or partial polarization measurement capability.

TABLE 10-4 ■ International Frequency Allocations for Active Earth Exploration Satellites Below 100 GHz [43]. (“Radiolocation” = Radar)

Frequency Band (MHz)	Services Allocated (International Allocations)
1,215–1,240	Earth exploration satellite (active), radiolocation, radionavigation-satellite (space-to-earth and space-to-space), space research (active)
1,240–1,300	Earth exploration satellite (active), radiolocation, radionavigation-satellite (space-to-earth and space-to-space), space research (active), amateur
3,100–3,300	Radiolocation, earth exploration satellite (active), space research (active)
5,250–5,255	Earth exploration satellite (active), radiolocation, space research, mobile except aeronautical mobile
5,255–5,350	Earth exploration satellite (active), radiolocation, space research (active), mobile except aeronautical mobile
5,350–5,460	Earth exploration satellite (active), space research (active), aeronautical radionavigation, radiolocation
5,460–5,470	Radionavigation, earth exploration satellite (active), space research (active), radiolocation
5,470–5,570	Maritime radionavigation, mobile except aeronautical mobile, earth exploration satellite (active), space research (active), radiolocation
8,550–8,650	Earth exploration satellite (active), radiolocation, space research (active)
9,300–9,500 (outside the United States)	Earth exploration satellite (active), space research (active), radiolocation, radionavigation
9,500–9,800	Earth exploration satellite (active), space research (active), radiolocation, radionavigation
9,800–9,900	Radiolocation, earth exploration satellite (active), space research (active), fixed
13,250–13,400	Earth exploration satellite (active), aeronautical radionavigation, space research (active)
13,400–13,750	Earth exploration satellite (active), radiolocation, space research, standard frequency and time signal satellite (earth-to-space)
17,200–17,300	Earth exploration satellite (active), radiolocation, space research (active)
24,050–24,250	Radiolocation, amateur, earth exploration satellite (active)
35,500–36,000	Meteorological aids, earth exploration satellite (active), radiolocation, space research (active)
94,000–94,100	Earth exploration satellite (active), radiolocation, space research (active), radio astronomy

Interferometric radars also compare the phases of the composite returns in corresponding resolution cells between two SAR images.

The RCS in a resolution cell is the complex sum of the returns from all scatterers in that cell. Manmade objects can produce large, discrete returns that may dominate the overall return from a given resolution cell. Natural surfaces, on the other hand, typically consist of a myriad of small scatterers whose returns add to produce a composite return characterized by an average backscatter coefficient. It is this type of return that is usually of interest in remote sensing applications.

The strength of returns from a surface depends on several basic factors:

- The dielectric properties of the surface material (which may be frequency-dependent).
- The surface roughness relative to the radar wavelength.

TABLE 10-5 ■ Penetration Depth for Various Surface Materials [45]

Material	Approximate Penetration Depth
Soil, moist (0.3 g/cm ³ water)	$\sim\lambda/8$ to $\sim\lambda/3$
Soil, dry (0.02 g/cm ³ water)	~ 1 to 3λ
Sand, dry	to $\sim 10\lambda$
Sea ice, first year	~ 1 to 3λ
Sea ice, multiyear	~ 4 to 9λ
Snow, wet (4% liquid water)	~ 1 to 2λ
Snow, dry (0.2% liquid water)	~ 30 to 100λ

- The orientation of complex scatterers (such as vegetation) relative to the polarization of the radar wave.
- The angle of incidence of the radar wavefront at the surface.

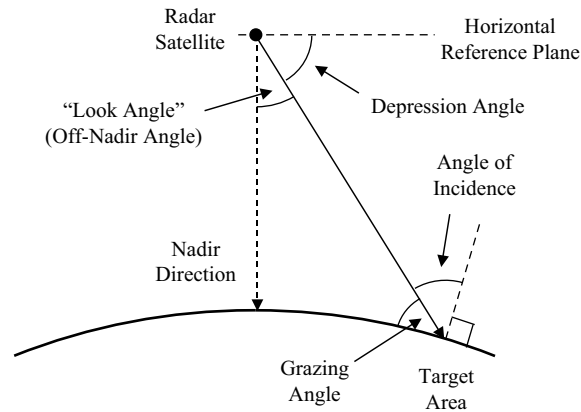
The first three of these factors depend, in turn, on a variety of other target-dependent parameters. For example, the backscatter characteristics of vegetation can depend on the vegetation type or species, moisture content, season, etc. The backscatter from ocean surfaces can vary with wind speed and/or wave height, swell height, and, at shorter radar wavelengths, by small-scale alteration of the surface characteristics due to rainfall or oil slicks.

In addition to surface phenomena, radar waves can penetrate beneath the surface to varying degrees. In some cases, ancient surface morphology buried under several meters of sand has been revealed [44]. A “penetration depth” can be defined as the depth at which the incident power density is reduced to $1/e$ (about 37 percent) of its value just below the surface. Table 10-5 lists approximate penetration depths for several types of surface materials.

10.4.4 Observation Geometry Nomenclature

The terminology applied to spaceborne SAR observation geometry is somewhat different from that used with airborne SARs. Spaceborne SARs typically view their target areas at much steeper depression angles than airborne SARs in order to minimize the slant range to the imaged area, thereby minimizing the power-aperture requirements and cost. Steep depression angles also provide a higher backscatter coefficient from water surfaces and may help to accentuate certain surface features such as ocean waves. In spaceborne SAR imaging, the “look angle” at the radar (i.e., the beam direction in elevation) is typically measured from the nadir direction rather than from a horizontal reference plane (i.e., “depression angle”), as is typical with airborne radars. Where the beam intersects the surface, the illumination direction is described in terms of the “angle of incidence” between the wavefront plane and the surface, or, alternatively, the angle between the illuminating ray and the zenith direction at the illuminated surface point. In airborne SAR operations, the complement of this angle, the grazing angle at the surface, is typically used instead. Figure 10-14 illustrates these definitions.

FIGURE 10-14 ■ Nomenclature for Spaceborne SAR Geometry. The Direction of Satellite Movement is Perpendicular to the Page.



10.4.5 SAR Ambiguities and Associated Trade-offs

10.4.5.1 Range Ambiguities, Aperture Height, and PRF Selection

A spaceborne SAR generally operates at a considerable distance from the area to be imaged. Every possible step toward maximizing the target SNR must be taken, including maximizing the transmit duty factor while maintaining the desired swath width and controlling range ambiguities. For this reason, the PRF is typically chosen to be range-ambiguous with respect to the desired target range in order to keep the duty factor (and the average transmitted power) as high as possible. That is, multiple pulses will be in flight during the round-trip delay time between the radar and the target area. The beam footprint on the surface must, therefore, be limited in range by the elevation beamwidth to ensure that target returns from undesired range ambiguities will be attenuated by the elevation beam pattern. The elevation beam pattern should be designed to provide the needed suppression of returns from undesired range ambiguities, especially any occurring at ranges closer to the radar than the desired range swath. Thus, there is a trade-off between the PRF and the elevation beamwidth, which is determined by the aperture height. (Note: In spaceborne SAR terminology, the aperture height is frequently referred to as the aperture “width,” as opposed to aperture “length,” which is the along-track aperture dimension.)

To determine how the PRF is constrained by range ambiguities, the slant range extent of the mainlobe footprint must be calculated. This will first be done using a spherical earth geometry, followed by a highly simplified and approximate solution based on a flat earth geometry.

Spherical Earth. The geometry for slant range calculations is shown in Figure 10-15. Two subcases can be considered: (1) the look angle is specified, and the incidence angle and other parameters are derived; and (2) the incidence angle or grazing angle is specified, and the look angle and other parameters are derived. In the first case, the minimum and maximum look angles can be expressed in terms of the elevation beamwidth as

$$\theta_{L(\min)} = \theta_{L(\text{nom})} - \frac{k_{el}\theta_{b(El)}}{2} \quad (10-20a)$$

$$\theta_{L(\max)} = \theta_{L(\text{nom})} + \frac{k_{el}\theta_{b(El)}}{2} \quad (10-20b)$$

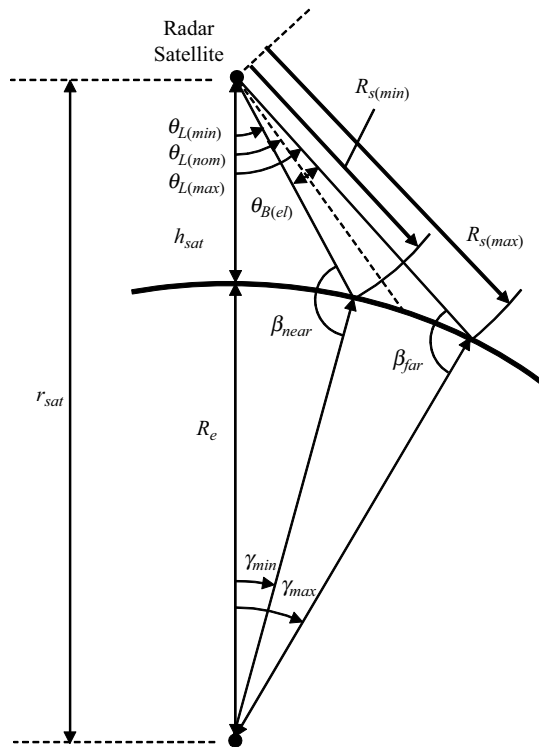


FIGURE 10-15 ■ Geometry for Range Footprint Calculation.

where

$\theta_{L(nom)}$ = nominal or specified look angle from nadir

$\theta_{b(EL)}$ = 3-dB elevation beamwidth

and k_{el} is a coefficient to provide margin. For PRF trade-offs, the minimum and maximum look angles are often chosen to correspond to the first nulls in the elevation pattern. If the null-to-null elevation beamwidth is used, $k_{el} \approx 2$. (The null-to-null beamwidth is a somewhat notional concept since some antenna patterns do not have well-defined first nulls.) The limits of the *processed* range swath correspond to a k_{el} value closer to unity.

First, the slant range at the near edge of the mainlobe footprint will be calculated. If the off-nadir look angle is specified, the law of sines establishes the following relationship between angles and their opposite sides:

$$\frac{\sin \beta_{near}}{r_{sat}} = \frac{\sin \theta_{L(min)}}{R_e} \tag{10.21}$$

where $\beta_{near} = \pi - \theta_{i(near)}$, with $\theta_{i(near)}$ being the angle of incidence at the near edge of the mainlobe footprint. Solving Equation (10.21) for $\sin \beta_{near}$ produces

$$\sin \beta_{near} = \frac{r_{sat}}{R_e} \sin \theta_{L(min)} \tag{10.22}$$

The sine function is unambiguous in the range $-\pi/2$ to $+\pi/2$. Since the angle β is always greater than $\pi/2$, the result from Equation (10.22) is used as

$$\beta_{near} = \pi - \arcsin(\sin \beta_{near}) \tag{10.23}$$

If instead the incidence or grazing angle is specified, the angle β_{near} is

$$\beta_{near} = \pi - \theta_{i(near)} \quad (10.24)$$

or

$$\beta_{near} = \frac{\pi}{2} + \psi_{near} \quad (10.25)$$

where ψ_{near} is the grazing angle at the near edge of the mainlobe footprint. If β_{near} is known, Equation (10.21) can be solved for $\theta_{L(min)}$ as

$$\theta_{L(min)} = \arcsin\left(\frac{R_e}{r_{sat}} \sin \beta_{near}\right) \quad (10.26)$$

The angle at the center of Earth can now be found from

$$\gamma_{min} = \pi - \theta_{L(min)} - \beta_{near} \quad (10.27)$$

Two sides of a triangle, r_{sat} and R_e , and their included angle γ_{min} are now known, so the law of cosines can be used to obtain the third side, which is the slant range:

$$R_{s(min)} = \sqrt{r_{sat}^2 + R_e^2 - 2r_{sat}R_e \cos \gamma_{min}} \quad (10.28)$$

Similarly, the slant range to the far edge of the mainlobe footprint $R_{s(max)}$ can be calculated by substituting β_{far} and $\theta_{L(max)}$ into Equation (10.21) and proceeding accordingly.

The two-way time delays to the near and far edges of the mainlobe footprint are

$$t_{d(min)} = \frac{2R_{s(min)}}{c} \quad t_{d(max)} = \frac{2R_{s(max)}}{c} \quad (10.29)$$

The PRI (T_r) is constrained to be greater than the difference between these two delays:

$$T_r > \frac{2}{c} (R_{s(max)} - R_{s(min)}) \quad (10.30)$$

or, more compactly,

$$T_r > \frac{2\Delta R_s}{c} \quad (10.31)$$

where $\Delta R_s = R_{s(max)} - R_{s(min)}$ [2]. Equivalently, the PRF (f_r) is constrained to be

$$f_r < \frac{c}{2\Delta R_s} \quad (10.32)$$

Since ΔR_s is related to the elevation beamwidth, a trade-off exists between the PRF and the aperture height. Aperture height also affects the two-way antenna gain and, in turn, the target SNR, so this trade-off has repercussions throughout the radar design.

Flat Earth Approximation. For rough calculations, a flat earth approximation can be used [2] as shown in Figure 10-16. In this geometry, the incidence angle θ_i is equal to the off-nadir look angle θ_L . The ground range extent of the mainlobe footprint is

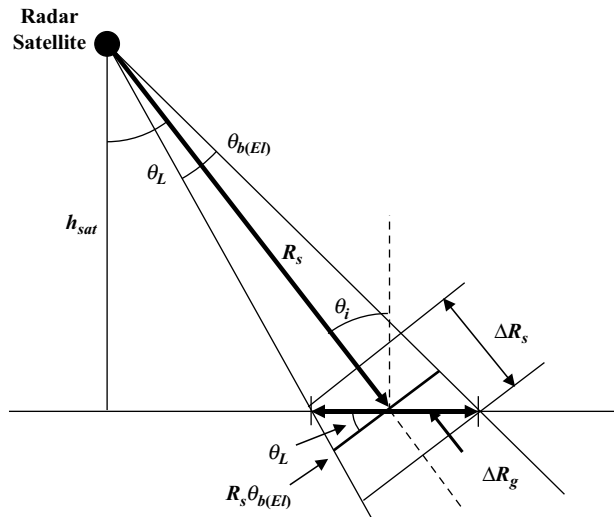


FIGURE 10-16 ■ Flat earth Approximation for Obtaining the Slant Range Extent of the Beam Footprint.

$$\Delta R_g = R_s \frac{k_{el} \theta_{b(El)}}{\cos \theta_i} \approx \frac{R_s k_{el}}{\cos \theta_i} \cdot \frac{\lambda}{H} \quad (10.33)$$

where

R_s = slant range on the beam axis

H = antenna height

and $k_{el} = 2$ is used for the null-to-null elevation beamwidth. The slant range extent of the mainlobe footprint is

$$\Delta R_s \approx \Delta R_g \sin \theta_i = \frac{R_s \lambda k_{el} \tan \theta_i}{H} \quad (10.34)$$

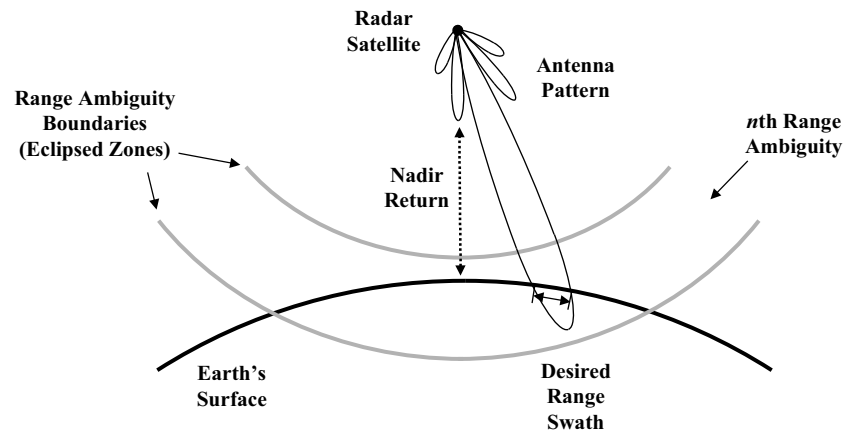
From Equation (10.32), the general PRF constraint is $f_r < c/(2\Delta R_s)$, so a more specific expression for the minimum PRF can be written as

$$f_r < \frac{cH}{2R_s \lambda k_{el} \tan \theta_i} \quad (10.35)$$

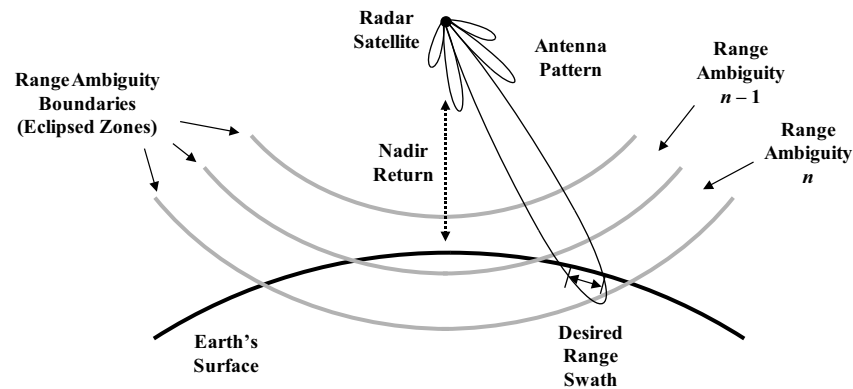
Additional discussion of these trade-offs can be found in [46].

In addition to the PRF constraint, another consideration is whether or not the desired target area and potential nadir sidelobe returns fall in the same range ambiguity. If so, as illustrated in Figure 10-17a, the nadir sidelobe return and the mainlobe returns are guaranteed not to overlap in time, so there can be no interference between the nadir return and the desired mainlobe returns. If the nadir return and the mainlobe return fall in different range ambiguities, as shown in Figure 10.17b, there is a possibility that the nadir sidelobe return could overlap with and corrupt the mainlobe returns. This is of concern over oceans, particularly at low frequencies where the sea return is more specular and the elevation sidelobe pattern may be less well controlled due to the limited aperture height in wavelengths. In these situations, the PRF and the elevation beam direction must be chosen carefully to keep the ambiguous nadir return away from the mainlobe return region in the time domain. This issue is discussed further in [2].

FIGURE 10-17 ■
Range Ambiguities
in Spaceborne SAR.



(a) Desired Range Swath and Nadir Return are in the Same Range Ambiguity. Nadir Return Cannot Interfere with Returns from the Desired Range Swath.



(b) Desired Range Swath and Nadir Return are in Different Range Ambiguities. Nadir Return May Interfere with Returns From the Desired Range Swath.

10.4.5.2 Doppler (Azimuth) Ambiguities and PRF Selection

Doppler or azimuth ambiguities result from undersampling in the “slow time” or pulse-to-pulse time frame, which can occur when the PRF is too low with respect to the mainlobe Doppler bandwidth. In that case, mainlobe return spectra from multiple PRF spectral lines can overlap in the PRF interval (the processed frequency range between DC and the PRF, or alternatively, between $-PRF/2$ and $+PRF/2$). To minimize image degradation due to Doppler ambiguities, the PRF line spacing should be greater than the mainlobe Doppler bandwidth, which is determined by the azimuth beamwidth. For ambiguity calculations, the null-to-null azimuth beamwidth is frequently used. Thus, another trade-off involving the PRF and the antenna characteristics arises, this time between the PRF and the azimuth beamwidth, which is determined by the aperture length in the along-track dimension. Because there is a close interrelationship between both the azimuth and elevation beam characteristics and the selected PRF, the waveform and antenna requirements must usually be defined together through an iterative process to arrive at an acceptable compromise.

Most spaceborne SARs for remote sensing employ some form of strip map mode as their primary operating mode. Since the high platform velocity produces a large Doppler shift, most imaging is done in the side-looking direction with an optional small crab angle to compensate for Earth's rotation, keeping the center of the mainlobe footprint near zero Doppler. This issue was mentioned briefly in Section 10.3.4. The discussion in this section will address basic Doppler/azimuth ambiguity trade-offs for strip map (as opposed to spotlight) mode design.

The one-way half-power (“3-dB”) beamwidth of a uniformly illuminated aperture is

$$\theta_b = 0.886 \frac{\lambda}{L} \quad (10.36)$$

where L is the antenna length and λ is the wavelength. The coefficient 0.886 applies to uniformly excited antennas. Many antennas employ an illumination taper for controlling sidelobes, which causes this beamwidth coefficient to increase to typically 1.1 to 1.2. For trade-off purposes, however, the beamwidth is frequently approximated as

$$\theta_b \approx \frac{\lambda}{L} \quad (10.37)$$

The cross-range resolution in a SAR is given by

$$\delta_{CR} = \frac{\lambda}{2\Delta\theta} \quad (10.38)$$

where $\Delta\theta$ is the change in the target aspect angle during the synthetic array time [47]. In a strip map SAR, this change is approximately equal to the along-track beamwidth, i.e., $\Delta\theta \approx \theta_{b(Az)}$. Making this replacement and then substituting from Equation (10.37) produces the classic relation for strip map SAR:

$$\delta_{CR} = \frac{L}{2} \quad (10.39)$$

That is, the best resolution obtainable in a side-looking strip map SAR is half the antenna length in the along-track direction. In reality, this is only an approximate result because it does not account for beam broadening due to aperture weighting and other factors. The synthetic array length (L_{SA}) for the finest attainable cross-range resolution is approximately equal to the cross-range beamwidth at the target range:

$$L_{SA} \approx R_s \theta_{b(Az)} = v_{sat} T_{SA} \quad (10.40)$$

where R_s is the slant range to the target and T_{SA} is the synthetic array time or “aperture time” (i.e., the time required to traverse the distance L_{SA}). This equation can be solved for T_{SA} yielding

$$T_{SA} = \frac{R_s \theta_{b(Az)}}{v_{sat}} = \frac{R_s \lambda}{v_{sat} L} = \frac{R_s \lambda}{2v_{sat} \delta_{CR}} \quad (10.41)$$

The synthetic array time will become a consideration in the discussion of multilook processing in Section 10.5.2.

A general expression for the target Doppler shift (neglecting Earth rotation) is

$$f_d = \frac{2v_{sat}}{\lambda} \cos \alpha \quad (10.42)$$

where α is the Doppler cone angle between the satellite velocity vector and the target or clutter element. The target is assumed to be stationary on Earth's surface. For side-looking strip map SAR, it is more convenient to reference angles from the broadside direction (or, more properly, the zero-Doppler direction). The Doppler shift at the leading edge of the beam is, therefore,

$$f_d = \frac{2v_{sat}}{\lambda} \sin \frac{\theta_{b(Az)}}{2} \quad (10.43)$$

assuming that the beam center corresponds to zero-Doppler shift. The 3-dB Doppler bandwidth corresponding to the 3-dB beamwidth is twice this value, or

$$B_d = \frac{4v_{sat}}{\lambda} \sin \frac{\theta_{b(Az)}}{2} \approx \frac{2v_{sat}\theta_{b(Az)}}{\lambda} \approx \frac{2v_{sat}}{L} \quad (10.44)$$

where the small angle approximation $\sin \theta_{b(Az)} \approx \theta_{b(Az)}$ has been invoked. Thus, for a given along-track aperture length L , the Doppler bandwidth is independent of the wavelength.

To prevent the mainlobe returns from aliasing in the PRF interval, the PRF must be greater than the mainlobe Doppler bandwidth, typically by a margin-of-safety factor k_{az} . That is, $f_r > k_{az}B_d$ where f_r is the PRF. A value of $k_{az} = 2$ corresponds approximately to the null-to-null beamwidth and is frequently used. Thus, the minimum PRF is

$$f_r > \frac{2k_{az}v_{sat}}{L} \quad (10.45)$$

This expression relates the minimum PRF to the antenna length in the along-track direction, an important trade-off in SAR design. Substituting $L = 2\delta_{CR}$ from Equation (10.39) produces

$$f_r > \frac{k_{az}v_{sat}}{\delta_{CR}} \quad (10.46)$$

which relates the minimum PRF to the required cross-range resolution, which is limited by the antenna length in the strip map mode. Clearly there is a complex interplay between the cross-range resolution requirement, the along-track antenna length, and the minimum PRF. When the relationship between the PRF and the elevation beamwidth is also considered, it is often difficult to arrive at a completely optimal design, although suboptimal designs have been flown very successfully. These issues are addressed in greater detail in [46].

10.4.5.3 Minimum Aperture Area Requirement for SAR

Solving Equation (10.35) for H yields the minimum antenna height for a given PRF based on range ambiguity considerations, i.e.,

$$H > \frac{2f_r R_s k_{el} \lambda \tan \theta_i}{c} \quad (10.47)$$

Similarly, solving Equation (10.45) for L provides the minimum antenna length for a given PRF based on azimuth ambiguity considerations, or

$$L > \frac{2k_{az}v_{sat}}{f_r} \quad (10.48)$$

When the product of Equations (10.47) and (10.48) is taken, the PRF cancels and the result is a minimum aperture area requirement for a given frequency, satellite velocity, and radar-target geometry:

$$A = HL > \frac{4R_s \lambda k_{az} k_{el} v_{sat} \tan \theta_i}{c} \quad (10.49)$$

This result is also given in [32] and [46]. It should be noted that this is not a hard limit. Through careful design, spaceborne SARs violating this criterion have flown successfully, realizing a cost savings through a reduced aperture area.

10.4.6 Block Adaptive Quantization (BAQ)

Most of the signal and image formation processing in spaceborne remote sensing radars is usually done on the ground. Also, many spaceborne radars have a limited downlink capacity. Since complex I/Q data are fairly noiselike, conventional data compression algorithms provide little benefit since they generally try to exploit correlations and redundancies in the data. One data compression approach that has been used fairly successfully involves reducing the number of ADC bits per sample that are transmitted to the ground. For example, an 8-bit quantizer may be used to digitize the IF or baseband return signals, but only a subset of the eight bits is sent to the ground. The specific bit range selected depends on the characteristics of the data, so this subset can vary over time. This approach to data compression is called block adaptive quantization (BAQ) or block floating point quantization (BFPQ). Block adaptive quantization is widely used in spaceborne radars, as it helps to maximize the utility of the spaceborne assets when the system is data rate limited.

BAQ takes advantage of the fact that the dynamic range of the raw samples is limited within restricted portions of the raw data set for an image. This is especially true when pulse compression is used (which is almost always the case) because the uncompressed returns from various scatterers in the scene overlap in time, reducing the overall variability in the samples. BAQ is usually done with buffered blocks of data rather than being applied “on-the-fly” to a continuous data stream. For BAQ to be effective, the variance of the samples within each block should be small compared with the variance across all blocks in the data set. The criteria for selecting an appropriate block size [33] are:

1. The block size should be >50–100 samples to ensure Gaussian statistics in the presence of speckle.
2. The block size should have a limited range extent to avoid power variation due to range (R^{-3} for distributed surface clutter) and elevation beam pattern roll-off. The variation due to these effects should be kept to <1–2 dB.
3. The block size should be <¼ to ½ the uncompressed pulse width in “fast time.”
4. The block size should be <¼ to ½ the synthetic array time in “slow time.”

Magnitudes of samples in the block are integrated or averaged to determine the mean magnitude in the block, which is used to set the reference level (also known as the “threshold” or “exponent” level). This level determines how many least significant bits are to be dropped from each sample before transmission. It is sometimes called an exponent because each bit represents a power of two.

The overall objective of BAQ is to maximize the signal-to-distortion ratio in the sample block, where distortion is the sum of the errors due to quantization and saturation. This issue, as pertaining to A/D converters in general, is addressed in a well-known short paper by Gray and Zeoli [48].

Typical steps in a BAQ/BFPQ process [33] are:

1. Calculate the standard deviation of samples in the block relative to the mean of the sample magnitudes (absolute values).
2. Scale all samples in the block by a threshold level that is set below the estimated standard deviation for that block.
3. Downlink the threshold value (i.e., “scale factor”) and all scaled sample values for that block.
4. Restore (i.e., “descale”) the samples in the ground-based processor.

An example of a BAQ/BFPQ implementation is the one that was used on the Magellan Venus Radar Mapper. In that radar, raw data were quantized at a resolution of eight bits in-phase (I) and eight bits quadrature (Q) and was compressed to two bits I and two bits Q for transmission to Earth. In BAQ/BFPQ nomenclature, this scheme is designated (8, 2) or (8/2). Each of the resulting two bit “words” represents one of four possible voltage levels—two positive and two negative. The resulting signal-to-distortion noise ratio (SDNR) is that of a two-bit quantizer, but it is maintained over an input range of nearly eight bits.

The block size used on Magellan was 16 range samples by eight pulses, or 128 complex samples per block. The threshold value calculated in the preceding block was used to scale the samples in the current block. This was possible in part due to the topography of Venus, which lacks land/water boundaries and other high-contrast features, limiting the expected variance in the data. Other radars use a threshold value calculated from the same block of data that is to be encoded.

In general, the SDNR due to the quantization process should be significantly larger than the signal-to-noise ratio (SNR) due to system noise. That is, the system (“thermal”) noise should be the dominant noise in the system and should set the range performance. Added “noise” due to quantization and saturation should not desensitize the radar relative to its thermal noise-limited performance. This objective becomes harder to achieve as the number of bits after BAQ encoding is reduced.

10.4.7 SAR Image Quality Metrics

SAR image quality can be characterized by several metrics, including the impulse response (IPR), peak sidelobe ratio (PSLR), integrated sidelobe ratio (ISLR), and multiplicative noise ratio (MNR). These metrics apply to all SAR systems and are not unique to spaceborne SARs, so they will only be mentioned briefly here.

The two-dimensional impulse response is the SAR’s response to a point target. It is analogous to the point spread function (PSF) in optical systems, although the dimensions in a SAR image are range and cross-range. The impulse response consists of two separable components: the range impulse response and the cross-range (or “azimuth”) impulse response. The range impulse response applies in the “fast time” (intra-PRI) domain and is generally determined by the hardware amplitude and phase response

across the waveform bandwidth. The cross-range impulse response applies in the “slow time” (pulse-to-pulse) domain and is dominated (at least in airborne radars) by motion compensation errors.

Since the SAR impulse response is essentially the result of a two-dimensional Fourier transform, amplitude and phase errors with low periodicity across the data set (e.g., quadratic, cubic, and low-frequency sinusoidal errors) produce image artifacts close to strong discrete scatterers. Amplitude and phase errors characterized by higher frequency “ripple” produce sidelobes farther removed from the associated strong scatterers.

The peak sidelobe ratio is the ratio of the mainlobe peak to the highest sidelobe of the two-dimensional impulse response. PSLR is an important metric when a SAR image contains strong isolated scatterers. The integrated sidelobe ratio is more relevant when the imaged scene consists of relatively uniformly scattering terrain without discrete scatterers. The ISLR is due to range and Doppler processing sidelobes, also known as “leakage” in signal processing terminology.

The multiplicative noise ratio defines a nonthermal noise level that is referenced to the terrain or target return power. It is essentially a contrast ratio. If the MNR is poor, low-backscatter regions such as lakes or shadows may be filled in with weak system-generated noise, degrading the image contrast. The MNR has many contributors, the dominant ones usually being the ISLR, range- and Doppler-ambiguous returns and quantization noise. Oscillator phase noise can also be a contributor to the MNR. These metrics are discussed in greater detail by Carrara *et al.* [34] and by Cook [71].

10.5 | SPECIAL MODES AND CAPABILITIES

There are a number of modes and capabilities that extend spaceborne SAR operation beyond the basic side-looking strip map mode. Many of these techniques are also used by airborne SARs, while some (e.g., ScanSAR) are used primarily by spaceborne radars. A few of these techniques are introduced in this section.

10.5.1 Spotlight Mode

It was shown in Equation (10.39) that the best cross-range resolution attainable in a side-looking strip map mode is equal to half the antenna length ($L/2$) because the synthetic array time (i.e., the coherent integration time) is limited by the beamwidth. Achieving a finer resolution requires increasing the synthetic array time and consequently the range of aspect angles over which the target is observed. That is, a synthetic array time greater than the transit time of the target through a nonsteered beam is required. In a strip map mode, finer cross-range resolution can be achieved by broadening the azimuth beamwidth through a reduction in the antenna length or by decollimating the beam in the along-track dimension. Such a resolution improvement would come at the expense of a lower two-way antenna gain and degraded target SNR, as well as requiring changes to the waveform. This dilemma can be avoided by steering the beam to keep it pointed at the target area as the radar moves past. In this way, the synthetic array time can be extended to obtain better cross-range resolution without reducing the antenna length and gain. This technique is known as spotlight mode SAR.

Since the beam must spend extra time on a particular target area, continuous coverage as provided by the strip map mode is no longer possible in the spotlight mode. Spotlight dwells providing a resolution finer than $L/2$ require more time than the beam transit time across the target in a strip map mode. Consequently, over a long swath, unavoidable gaps in coverage between the spotlight images would occur since the spotlight imaging wouldn't be able to keep up with the spacecraft motion. The spotlight mode is therefore used for imaging specific target areas rather than for continuous mapping.

Most spaceborne SAR antennas have an along-track length of approximately 5–15 meters. The desirable resolution in a spotlight mode is generally of the order of 1–3 meters for civil applications such as ship classification. This means that the beam typically needs to be scanned by only a few beamwidths during the synthetic array time to obtain the desired resolution. Resolutions finer than 1 meter, which are needed for some reconnaissance missions, require a larger azimuth scan range, particularly if multiple images of the same target area are desired for reducing speckle.

Azimuth beam steering in spaceborne radars can be accomplished in two ways. First, the entire spacecraft can be rotated by a small amount as it passes the target area. This rotation is accomplished using electrically driven momentum wheels so no fuel is consumed. Spacecraft rotation is used when the SAR satellite employs a non-scanned antenna such as a reflector. Examples of such satellites include the Israeli TecSAR and German SAR-Lupe satellites. The second azimuth steering method, electronic scanning, is more suitable for active phased array antennas as used by many other spaceborne SARs. Since the required azimuth scan range is very limited in civil applications, a phase center spacing of many wavelengths in the along-track dimension can be used, with grating lobes being suppressed by the subarray pattern. This allows phase control and amplification to be done at the subarray level rather than at each radiating element, reducing the antenna cost. A third azimuth steering approach, a gimballed antenna, is generally not used in spaceborne radars. Gimbaling a large antenna with respect to the spacecraft body would complicate the spacecraft dynamics, increase the spacecraft complexity and cost, and reduce the system reliability.

When the cross-range resolution is improved through spotlighting, a commensurate improvement in the slant range resolution is usually desired as well. This requires an increase in the waveform bandwidth. Wide waveform bandwidths (hundreds of MHz) are readily achievable using the “stretch” or dechirp technique [49], although the usable range swath width is limited with that approach. Waveform bandwidths of civil remote sensing SARs may be restricted by international frequency allocations, as was discussed in Section 10.4.2. As is evident, a great many trade-offs are involved in designing a spaceborne spotlight mode SAR.

There are several excellent references on spotlight SAR. Of particular note are the books by Carrara *et al.* of the Environmental Research Institute of Michigan (ERIM) [34] and Jakowatz *et al.* of Sandia National Laboratories [35]. Cook [71] provides a good introductory chapter in the second volume of the *Principles of Modern Radar* series, and Richards [50] also discusses spotlight SAR as part of an introductory chapter on SAR signal processing.

10.5.2 Multilook Processing

The synthetic array time required in the strip map mode was given in Equation (10.41). Recall that the minimum cross-range resolution in the strip map mode is at least half the

aperture length in the along-track dimension, i.e., $\delta_{CR} > L/2$. Section 10.4.5.2 discussed an ideal cross-range resolution δ_{CR} corresponding to $L/2$, which can be achieved using the full synthetic array time available in the side-looking strip map mode. Many remote-sensing SARs do not require this resolution in their final image products, however. Instead, they form multiple independent images (“looks”) of the same scene at a resolution coarser than $L/2$ during the synthetic array time. After co-registration, corresponding pixels are summed or averaged to form a final image with reduced effects of noise and speckle. For example, in the available beam transit time in a strip map mode, n independent images can be combined to form a final image product with a resolution $\geq nL/2$ but with better image quality than any of the individual images.

Achieving fine slant range resolution in a SAR requires a wide waveform bandwidth, which has a significant hardware impact. There is not always excess range resolution capability that would permit multilook processing in the range dimension. In the cross-range dimension, fine resolution requires a long synthetic array time, which is a challenge for motion compensation techniques in airborne SARs. Motion compensation is much more deterministic in spaceborne radars, however, since there are no unexpected motions due to wind gusts, etc. Spaceborne SARs, therefore, usually have a surplus of azimuth resolution capability, so multilook processing is most often implemented in the azimuth or Doppler dimension.

One approach to multilook processing involves forming the multiple independent looks simultaneously by dividing the mainlobe Doppler spectrum into subbands, which are processed into independent coarser-resolution images. This is done through digital band pass filtering of the Doppler spectrum after pulse compression and range migration correction but before azimuth compression, as illustrated in Figure 10-18 [33]. Each filter passband represents a portion of the mainlobe spectrum and hence an azimuth subsector of the beam with reduced time on target and coarser azimuth resolution. The band pass filters are sometimes called “look extraction filters.” Their passbands usually have a small degree of overlap to prevent gaps in coverage. After

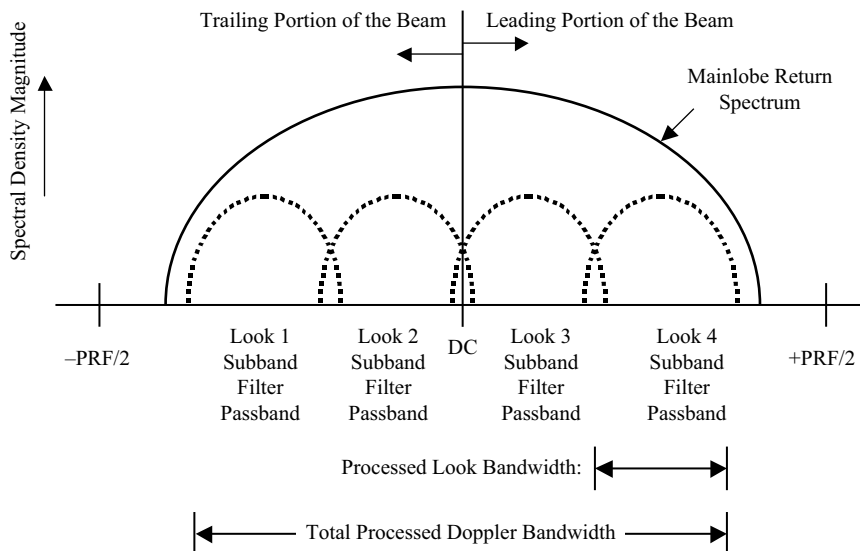


FIGURE 10-18 ■ Doppler Spectrum Filtering for Four-look Processing.

image formation, the images formed from the different filters at different times are co-registered and then the corresponding pixel magnitudes or powers (magnitudes squared) are added to form a better quality image. Other approaches to multilook image formation are also possible.

Ideally, the SNR of an N -look image improves by a factor of the square root of N , i.e.,

$$SNR_N = SNR_1 \sqrt{N} \quad (10.50)$$

where SNR_1 is the SNR of a single-look magnitude image. This expression is valid for high values of SNR_1 such that the dominant “noise” in the image is speckle. When SNR_1 is low and system noise (also called “thermal” noise) is a significant factor, the SNR improvement will be less than \sqrt{N} .

The use of multilook processing may raise the question, “If a resolution of $L/2$ is never really required, why not use a longer antenna to obtain a higher two-way gain?” A longer antenna (by a factor of two to four, for example) would greatly increase the cost and technical risk to the spacecraft. Large deployable structures are not completely rigid, so maintaining a planar phase front could be a problem in the presence of temperature changes, spacecraft attitude adjustments, etc. A longer structure could also affect spacecraft control and stability. Active, distributed amplification on transmit and receive would be required to offset transmission line losses in the feed network.

10.5.3 Burst Mode

In some applications, the required image resolution is far greater than $L/2$. For example, the Magellan Venus Radar Mapper antenna diameter was 3.7 m while the desired image resolution for global mapping was approximately 300 m [51]. Even with multilook processing, only a small portion of the available timeline was needed. Also, the radar hardware did not support the waveform bandwidth required for very fine range resolution and the downlink data rate capacity was severely limited. SAR data was therefore only collected in bursts occupying a fraction of the available timeline. Between bursts the radar was inactive. This provided two benefits: a reduction of the downlink data rate and a reduction of the average power consumption during the SAR imaging portion of the orbit. Both of these benefits were extremely important for the planetary mapping mission [52].

10.5.4 ScanSAR

If the finest strip map cross-range resolution ($L/2$) is not required, as is the case in many remote sensing applications, the available transit time of the beam across the target area can be used to obtain multiple looks (images) at a coarser resolution. Multiple looks at the same target area can then be combined to reduce speckle and improve the image quality, as was discussed in Section 10.5.2. Alternatively, the beam can be scanned in elevation to observe multiple target areas at different ranges at a reduced cross-range resolution during the available beam transit time. This mode of operation is called ScanSAR and it provides wider swath coverage for strip maps at a reduced resolution.

Figure 10-19 illustrates this concept from the standpoints of data collection timing and ground coverage. In Figure 10-19a, a coarse resolution image is acquired at a relatively short ground range during one-fourth of the along-track beam transit time

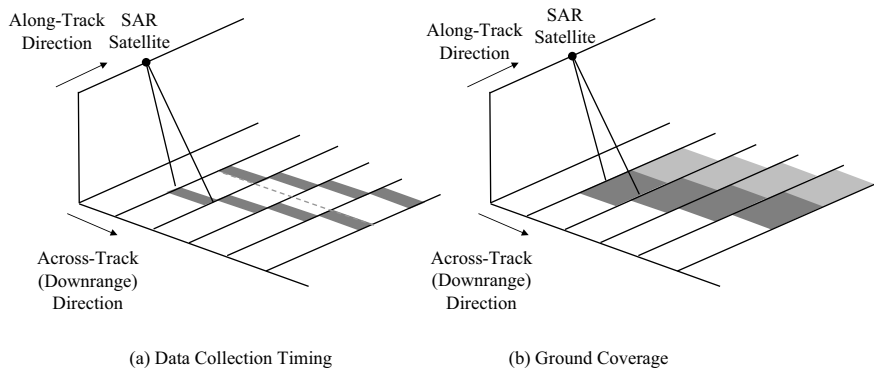


FIGURE 10-19 ■ ScanSAR Operation.

across the target area. The beam elevation angle and the radar waveform are then adjusted to illuminate a more distant area and another image is acquired, and so on. In this example, four coarse-resolution images are acquired during the time normally needed to acquire one fine-resolution image. Since the images have a coarser resolution than a single-look image, there are no gaps in the ground coverage and continuous wide swath strip map coverage can be achieved as shown in Figure 10-19b.

There are several ways in which the beam can be repositioned in elevation. Canada's RADARSAT-1 uses a planar array antenna that provides several selectable, shaped elevation beams. Similarly, the Israeli TecSAR satellite uses a 3-meter diameter reflector with multiple selectable feed horns providing a limited set of elevation beams. Satellites employing active electronically scanned arrays (e.g., RADARSAT-2, TerraSAR-X, TanDEM-X) with phase shifters in each T/R module can provide elevation pointing and beam shaping electronically. This approach permits a continuously variable elevation beam position and beam shape, as opposed to a limited set of fixed elevation beam positions and shapes provided by the other approaches.

This discussion has emphasized the trade-off between obtaining the finest available single-look cross-range resolution versus a coarser resolution with a wider swath width. Intermediate approaches are also possible, wherein a moderate swath width expansion with a moderate coarsening of the cross-range resolution is implemented with some degree of multilook processing to improve the image quality.

10.5.5 Terrain Observation by Progressive Scan (TOPS)

One drawback of ScanSAR is a considerable amplitude variation across the images, an effect known as scalloping. An approach to countering scalloping, called terrain observation by progressive scan (TOPS), has been developed [53]. In this approach, the beam is scanned in azimuth during the image data collection time (the synthetic array time) in the same direction as the platform motion such that the time on target is less than what it would be in a non-scanned strip map mode. Doing so enables all portions of the images to be illuminated by the central portion of the beam, reducing amplitude variation in the images. This manner of scanning is opposite to the spotlight mode concept; hence, the name TOPS is the opposite of SPOT. The TOPS mode has been developed by the European Space Agency and has been tested on the TerraSAR-X satellite [54]. It is planned to be used operationally on Europe's next radar satellite, Sentinel-1.

10.5.6 Across-Track Interferometric SAR (InSAR)

Across-track interferometric SAR, frequently called InSAR or IfSAR, has been developed extensively in recent decades, first using airborne platforms and later with satellites. This type of interferometry can be used to characterize topography fairly accurately, which is particularly useful in parts of the world that have not been well surveyed. Comparing topographic observations separated in time can also reveal information about ground deformation due to tectonic and volcanic activity, subsidence due to changes in ground water levels, the extent of flooding, changes in glaciers, etc.

Across-track interferometry requires reception and processing of signals from at least two antenna phase centers that have a component of their separation in a direction perpendicular to both the flight path and the line of sight to the target area. There are three principal approaches to accomplishing this. “Two-pass” or “repeat-pass” interferometry involves coherently imaging the same target area on different satellite passes with closely spaced flight paths. This approach requires only one radar and antenna, although the temporal separation between the images can introduce errors. A second approach employs two antennas on the same platform (aircraft or satellite). This approach was used for the Shuttle Radar Topography Mission (SRTM) in February 2000, which used a version of the SIR-C/X-SAR radar with a second antenna subsystem at the end of a 60-meter boom. The third and most complex approach involves two SAR satellites flying in close formation. This approach is being used with the TerraSAR-X and TanDEM-X satellites to obtain terrain elevation data with a finer resolution than that obtainable using two antennas on a single platform.

Across-track interferometric SAR is described in greater detail in the second volume of the *Principles of Modern Radar* series [72] and the related article by the same author [73], so it won't be elaborated upon any further here. Another useful reference from a signal processing perspective is Chapter 5 in Jakowatz *et al.* [35].

10.5.7 Along-Track Interferometry

Along-track interferometry (ATI) is a technique for estimating the aggregate range rate (radial velocity) of scatterers in each SAR resolution cell. ATI requires the receive aperture to be partitioned into two subapertures whose phase centers are displaced in the along-track dimension, i.e., a “forward” or “leading” receive subaperture and an “aft” or “trailing” receive subaperture. The signal outputs from these two subapertures are processed separately to form two SAR images. An interferogram (to be described later) between the two SAR images is formed and the phase difference between corresponding pixels in the two images is estimated, providing an estimate of the average radial velocity of the scatterers in each pixel.

Figure 10-20 shows the phase center relationships for a stationary antenna. Transmission uses the full aperture whose phase center is at point **A**. Reception can occur through either of the two subapertures whose phase centers are at points **B** and **C**. For a round-trip path, the composite transmit-receive (T/R) phase centers are located at points **AB** and **AC**. These points are nominally separated by one-fourth the antenna length for a uniformly weighted aperture when the antenna is stationary. The stationary T/R phase center separation between points **AB** and **AC** will be designated B_x .

The situation is a bit different when the antenna is in motion. Figure 10-21 shows the SAR antenna at points in time when pulses are transmitted and received. Between

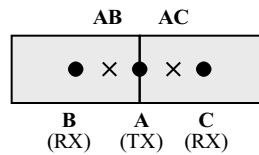


FIGURE 10-20 ■ Phase Center Relationships for a Stationary Antenna. **AB** and **AC** are the Composite Transmit-Receive Phase Centers, and the Distance Between them is B_x .

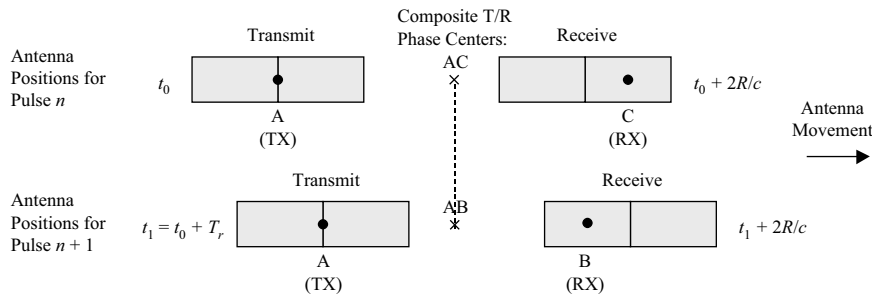


FIGURE 10-21 ■ Phase Center Relationships for a Moving Antenna. The Direction Toward the Target is Perpendicular to the Page [55].

transmission and reception, the antenna moves in the along-track direction (toward the right). For typical target ranges and antenna lengths, the antenna may move up to several times its length during the round-trip delay time. Since the waveform is typically range-ambiguous, the delay between transmission and reception for a particular pulse may be several PRIs.

At time $t = t_0$ a pulse is transmitted through the full aperture whose phase center is at the aperture midpoint (point **A**). After the round-trip range delay $2R/c$, return signals are received through the leading subaperture with its phase center at **C**. The composite T/R phase center for this transmit-receive aperture pair is point **AC**. At time $t = t_1$ the next pulse is transmitted through the full aperture. The returns in this case are received through the trailing subaperture whose phase center is at point **B**. The composite T/R phase center for this transmit-receive aperture pair is point **AB**. Ideally, the PRF is chosen such that points **AB** and **AC** are coincident in space for consecutive pulses. This is equivalent to choosing the PRF such that the distance the array traverses between t_0 and t_1 (i.e., during the PRI) equals the stationary T/R phase center spacing B_x . That is, $v_{sat}T_r = B_x$ where T_r is the “ideal” PRI. Operation using other PRIs is also possible through interpolation in the signal processing [56].

In reality, return signals are received through both subapertures on every pulse. The two sets of complex samples are processed separately to form two SAR images. Suppose that a SAR image requires m pulses. The first of the two complex SAR images is formed from samples collected through the leading receive phase center **C** (T/R phase center **AC**) for pulse times t_0 through t_{m-1} . The second complex image is formed from samples collected through the trailing receive phase center **B** (T/R phase center **AB**) for pulse times t_1 through t_m . For each pulse, composite T/R phase center **AB** is at the same location where T/R phase center **AC** was for the preceding pulse. Thus, two complete sets of samples are taken at the same phase center locations in space and one PRI apart in time. This type of operation is discussed further in [55] and [57].

The two sets of complex samples from the two receive subapertures may be processed in several ways [58], including:

1. “Pre-Doppler” displaced phase center antenna (DPCA) SAR. Corresponding samples in the two sample sets are subtracted and the resulting set of differenced samples is used to form a SAR image.
2. “Post-Doppler” DPCA SAR. The two sets of samples are used to form two SAR images. After image formation, the images are subtracted on a pixel-by-pixel basis.
3. Along-track interferometry (ATI). The two sets of samples are used to form two SAR images. The first image is multiplied by the complex conjugate of the second image on a pixel-by-pixel basis, producing an “interferogram.” This is simply a convenient way to separate the magnitude-squared (power) and the phase difference information contained in the two images.

These approaches are all limited to fairly slow target speeds since fast movers may be Doppler-shifted out of the SAR image, defocused, or both. In the two DPCA approaches, stationary clutter is theoretically canceled, permitting noise-limited detection of discrete moving targets, such as vehicles, against the stationary clutter background. The amount of clutter cancellation obtainable is limited by hardware errors. Very slow-moving targets will experience partial cancellation along with the stationary clutter, which is a drawback if these targets are of interest.

Due to the linear nature of SAR processing, methods (1) and (2) are equivalent [58]. Method (1) is not used in spaceborne SARs. Method (2), also known as SAR DPCA, and method (3) have been tested with RADARSAT-2 [59] and TerraSAR-X data [60, 61]. Most interest in the remote sensing community has focused on method (3), ATI.

ATI does not attempt to cancel stationary clutter, permitting detection of very low radial velocities. ATI performs best when all scatterers in the resolution cell have approximately the same velocity (i.e., there is no stationary “clutter”). This is frequently the case in remote sensing applications involving the observation of ocean and river surfaces. A more detailed comparison between DPCA and ATI performance can be found in [59]. The remainder of this section will focus on ATI. The term “interferometry” may be somewhat misleading since the phase difference is observed over time rather than space.

After the SAR interferogram is formed, the real part of the complex pixel value corresponds to the pixel return power, while the imaginary part is a measure of the phase change between the two images. The observable phase change is given by

$$\Delta\phi = \frac{4\pi B_x v_r}{\lambda v_{sat}} = \frac{4\pi T_r v_r}{\lambda} \quad (10.51)$$

where

B_x = spacing between the stationary composite (T-R) phase centers

T_r = ideal PRI

v_r = radial velocity of the scatterer(s) in the resolution cell [62]

Since the phase measurement is ambiguous (modulo 2π), the velocity estimate is also ambiguous with the ambiguity limit given by [62]

$$v_{ambig} = \frac{\lambda v_{sat}}{2B_x} = \frac{\lambda}{2T_r} \quad (10.52)$$

The unambiguously measurable velocity range is actually $-v_{ambig}/2 < v_r < v_{ambig}/2$ [62]. For example, if $v_{sat} = 7.6$ km/s with $B_x = 1.2$ m at a frequency of 9.65 GHz (approximate TerraSAR-X parameters), $v_{ambig}/2 = 49.2$ m/s, or 95.7 knots. This unambiguous velocity range seems reasonable for many moving target applications, but there are more restrictive criteria [62] that will be not be discussed in detail here. ATI is therefore applicable only to slowly moving scatterers.

Along-track interferometry estimates the net phase difference between corresponding pixels in two SAR images, with the pixel phase being a composite value from all scatterers in the pixel. If all scatterers are moving at approximately the same velocity, the phase estimates and therefore the velocity estimates for the pixel can be fairly accurate. Along-track interferometry has been used successfully for measuring ocean currents, for example, where velocity accuracies of the order of a few centimeters per second have been achieved. When both moving and stationary scatterers are present in the resolution cell, the phase estimate may not be as accurate for either class of scatterers.

Although there has been much interest in using ATI to detect ground-moving targets (e.g., vehicles), there has been only limited success in this area. ATI does not attempt to cancel clutter, as do other techniques such as DPCA, adaptive DPCA, and space-time adaptive processing (STAP). ATI therefore does not perform well as a detector of moving targets in high clutter environments unless the resolution cell size is small. In low-clutter environments, it provides better detection sensitivity against small targets due to the long coherent integration times used for SAR imaging, but it has disadvantages with regard to the more general problem of ground-moving target indication (GMTI). These drawbacks include:

1. ATI is limited to slow closing or opening rates. Fast-moving targets such as vehicles are likely to be Doppler-shifted to some other part of the image or out of the image entirely. Also, fast movers may not focus properly in the SAR processing.
2. Even relatively slowly moving scatterers may be Doppler-shifted by one or more pixels in azimuth. In remote sensing applications (e.g., ocean currents), this displacement may not be important, but it is of greater significance when attempting to geolocate ground-moving targets such as vehicles or people.
3. Velocity estimates are ambiguous due to the modulo- 2π characteristic of phase measurements. This restricts ATI to velocity measurement of fairly slowly moving targets or surfaces, or it requires phase unwrapping (a nontrivial task [63], particularly if the target velocity is unknown).

More detailed descriptions of SAR-ATI and comparisons with SAR-DPCA may be found in two Canadian reports describing RADARSAT-2 MTI modes [64, 65].

10.5.8 Summary of Mode and Capability Trade-offs

Often, the downlink data rate capacity is a principal limiting factor on the capability of a spaceborne SAR. When more modes or features are desired, some other capability must be forfeited in order to keep the downlink data rate within the communication system capacity. Typically what is forfeited is either image resolution or image quality. A top-level summary of some of the mode and capability trade-offs is presented in Table 10-6.

TABLE 10-6 ■ Summary of Mode/Capability Trade-offs

Mode or Capability	Obtains	By Forfeiting
Block adaptive quantizer	Reduced downlink data rate or added mode capabilities using a given downlink data rate	Instantaneous dynamic range in the raw I/Q data; image SNR
Spotlight mode	Improved cross-range resolution	Continuous strip coverage
Burst mode	Reduced downlink data rate; reduced average power consumption	Cross-range resolution
Multilook imaging	Improved image quality (reduced noise and speckle)	Cross-range resolution
ScanSAR	Increased range swath width	Cross-range resolution
TOPS	Increased swath width with improved image quality (reduced scalloping)	Cross-range resolution
Along-track interferometry	Surface radial velocity measurement capability	SNR (due to receiving on half the aperture)
Multipolarization processing	Better characterization of scenes or targets	Resolution or multiple looks (i.e., image quality) assuming a data link limited system

10.6 | DESIGN EXAMPLE: GERMANY'S TERRASAR-X

10.6.1 Overview

The German TerraSAR-X satellite for civil remote sensing was launched in June 2007 from Baikonur, Kazakhstan, aboard a Dnepr rocket. This satellite incorporates an active X-band phased array antenna instead of the reflector design used in the German SAR-Lupe reconnaissance satellites. An illustration of TerraSAR-X is shown in Figure 10-22 [66].

FIGURE 10-22 ■ TerraSAR-X satellite [66].

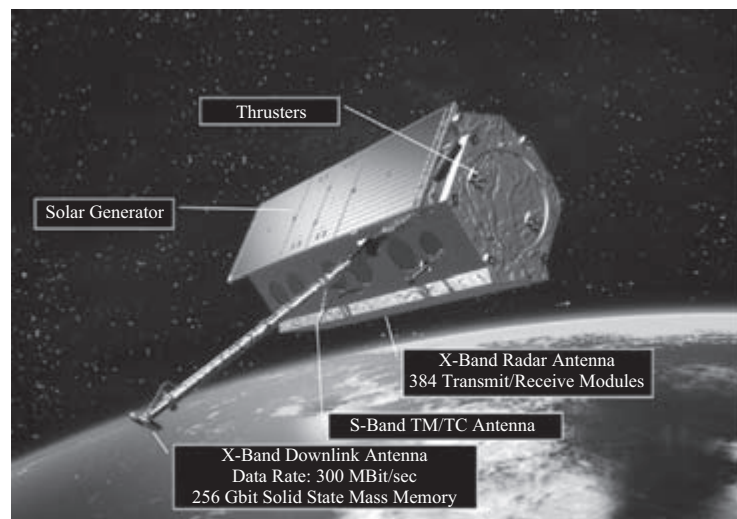


TABLE 10-7 ■ TerraSAR-X Parameter Summary

Orbit parameters	Value
Height at equator, altitude variation above GEM6	514.8 km, 505 km–533 km
Semi-major axis	6,883.513 km
Period	94.85 min
Orbits per day	$15 \frac{2}{11}$
Inclination	97.44°
Eccentricity	0.001
Argument of perigee	90°
SAR instrument parameters	Value
Center frequency	9.65 GHz
Wavelength at center frequency	3.11 cm
Antenna aperture dimensions	4.784 m × 0.704 m
Antenna aperture area	3.368 m ²
Phase centers for beam steering (azimuth × elevation)	12 × 32
Scan angle range (azimuth, elevation)	±0.75° Az, ±19.2° El
Incidence angle access range	15°–60°
Radiated peak output power	2,260 W
Transmit duty cycle (strip map mode and spotlight mode)	18%, 20%
System noise figure	5.0 dB
Operational PRF range	3,000–6,500 Hz
Chirp bandwidth range	5–300 MHz
ADC sample resolution	8 bits I and 8 bits Q
ADC sample rates	110, 165, 330 MHz
Maximum receive duty cycles	100%, 67%, 33%
Selectable block adaptive quantizer (BAQ) compression	8 to 6, 4, 3, 2, by-pass
Mass memory size, beginning of life (BoL), end of life (EoL)	320 Gbit, 256 Gbit
Absolute timing (along-track, across-track)	3.6 ms, 63 ns (1σ)

TerraSAR-X orbits in a sun-synchronous dawn–dusk orbit. This orbit allows the body-fixed solar array to remain pointed toward the sun, eliminating the need for a solar array pointing mechanism that would increase the satellite cost. This spacecraft configuration provides radar coverage primarily on one side of the ground track. Coverage on the opposite side can be achieved for short periods by rotating the satellite about its roll axis to point the radar beam toward the desired swath on the surface. In this attitude the solar arrays may be oriented at a less favorable incidence angle respect to the solar illumination so a greater reliance on battery power must be made.

Table 10-7 lists the orbit and radar parameters for TerraSAR-X, while Table 10-8 [67] lists the TerraSAR-X mode characteristics. In the high-resolution spotlight mode, an azimuth electronic steering angle of up to ±0.75° (approximately ±2.3 one-way beamwidths) extends the synthetic array time to obtain better azimuth resolution. TerraSAR-X accomplishes the azimuth scanning electronically rather than by rotating the satellite bus, as is done with SAR-Lupe.

10.6.2 TerraSAR-X Orbit

TerraSAR-X is in a nearly circular orbit at an altitude of 515 km with an orbital radius of 6,883 km. The resulting orbital period is approximately 94.8 min, and the satellite angle

TABLE 10-8 ■ TerraSAR-X Mode Summary [67]

Parameter/ Operational Mode	Spotlight HS Mode	Spotlight SL Mode	Experimental Spotlight	Strip Map Mode (SM)	ScanSAR Mode (SC)
Resolution, cross-track	2 m 1 m	2 m 1 m	1 m 1 m	3 m 3 m	16 m 16 m
Resolution, along-track					
Product coverage, (km) along- track × cross- track	5 × 10	10 × 10	5 × 10	≤1,500 × 30	≤1,500 × 100
Access range of incidence angles (full performance)	20–55° 2 × 463 km	20–55° 2 × 463 km	20–55° 2 × 463 km	20–45° 2 × 287 km	20–45° 2 × 287 km
Access range of incidence angles (data collection – reduced performance)	15–60° 2 × 622 km	15–60° 2 × 622 km	15–60° 2 × 622 km	15–60° 2 × 622 km	20–60° 2 × 577 km
Sensitivity NESZ: - typical - worst case	–23 dB –19 dB	–23 dB –19 dB	–20 dB –16 dB	–22 dB –19 dB	–21 dB –19 dB
Distributed target ambiguity ratio (DTAR)	<–17 dB	<–17 dB	<–17 dB	<–17 dB	<–17 dB
Source data rate (8/4 BAQ)	340 Mbit/s	340 Mbit/s	680 Mbit/s	580 Mbit/s	580 Mbit/s

rate (i.e., the true anomaly angle rate) is $0.063^\circ/\text{s}$. The angular rate of the rotating earth is approximately $0.004^\circ/\text{s}$, which is 7 percent of the satellite’s orbital angle rate. Because TerraSAR-X is in a slightly retrograde sun-synchronous orbit, the velocity relative to Earth is 7.68 km/s, or approximately 1 percent greater than the nominal orbital velocity of 7.61 km/s, varying by approximately ± 0.1 percent with the true anomaly.

10.6.3 TerraSAR-X Antenna

TerraSAR-X employs an active phased array antenna providing an electronic scan capability of approximately 38° in elevation and a much more limited electronic scan capability in azimuth. This antenna has 12 phase centers in azimuth and 32 phase centers in elevation for a total of 384 phase centers for beam-steering purposes. A transmit/receive (T/R) module at each phase center provides approximately 5.8 W peak and 1.2 W average radiated power per phase center. Figure 10-23 shows the general layout of the TerraSAR-X antenna. Although the antenna is physically constructed in three subsections, called “leaves,” it can be electronically partitioned into two halves to support MTI modes (e.g., SAR-ATI and SAR-DPCA).

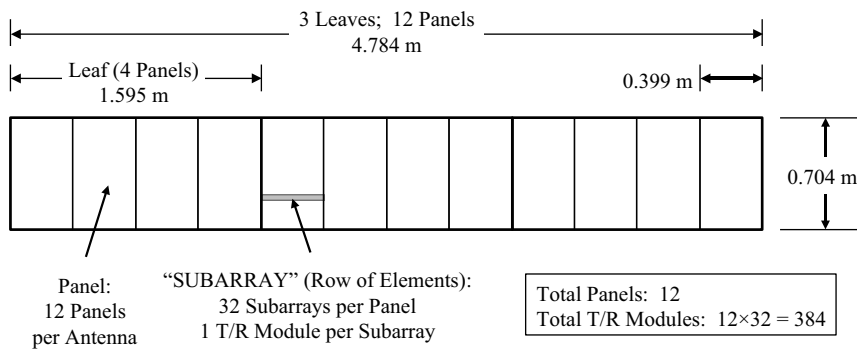


FIGURE 10-23 ■ TerraSAR-X Antenna Layout.

Polarization. The TerraSAR-X antenna is capable of transmitting and receiving horizontal polarization (HH) and transmitting and receiving vertical polarization (VV). In addition, it supports the cross-polarization modes of transmitting horizontal and receiving vertical polarization (HV) and transmitting vertical and receiving horizontal polarization (VH). These capabilities can extract all available polarization information from the radar returns.

Gain. The TerraSAR-X antenna gain is estimated to be 46.4 dBi based on a uniform aperture illumination and unity aperture efficiency for the radar parameters listed in Table 10-7. Gain is calculated from

$$G = \frac{4\pi A \eta_a}{\lambda^2} = \frac{4\pi(4.784 \text{ m} \times 0.704 \text{ m})}{(0.031 \text{ m})^2} = \frac{42.323}{0.00097} = 43,791 = 46.4 \text{ dBi} \quad (10.53)$$

where A is the aperture area and η_a is the aperture illumination efficiency (assumed here to be 1.0).

Beamwidth. The TerraSAR-X one-way half-power (3-dB) azimuth beamwidth is 0.33° , or 5.8 mrad, and the one-way elevation half-power beamwidth is 2.3° , or 40.1 mrad [68]. These beamwidths correspond closely to uniform aperture illumination with approximately 13-dB sidelobes. Assuming uniform illumination, the one-way half-power azimuth beamwidth can be found from

$$\theta_3 = \frac{\lambda}{L} 50.8^\circ = \frac{0.031 \text{ m}}{4.784 \text{ m}} 50.8^\circ = 0.33^\circ \quad (10.54)$$

The antenna boresight pointing accuracy provided by TerraSAR-X is 65 arcsec (3 sigma), corresponding to 0.018° (0.315 mrad) or 5.5 percent of the azimuth beamwidth and 0.78 percent of the elevation beamwidth.

Elevation Scan Range. In TerraSAR-X, as in many spaceborne SARs, the greater scan capability is provided in elevation. The maximum scan capability from broadside that avoids the appearance of grating lobes is related to the wavelength and the phase center spacing by

$$|\theta_s| < \arcsin\left(\frac{\lambda}{s} - 1\right) \quad (10.55)$$

where θ_s is the scan angle from broadside and s is the phase center spacing [69]. This equation is valid for phase center spacings between 0.5 and 1.0 wavelengths. At

spacings less than 0.5 wavelength, there are no grating lobes at any scan angle, while at spacings greater than 1.0 wavelengths, grating lobes are always present. The TerraSAR-X vertical phase center (i.e., row) spacing is 0.022 m, or 0.71 wavelengths, permitting a maximum elevation scan angle of $\pm 24^\circ$. The largest elevation scan range actually used is $\pm 19.2^\circ$, or about ± 8.2 broadside elevation beamwidths, keeping in mind that the elevation beamwidth will change slightly over this range of scan angles.

Azimuth Scan Range. In azimuth, the phase center spacing is 0.399 m, or 12.82 wavelengths, restricting the azimuth scan capability to a much more limited range. When the phase center spacing is greater than one wavelength and the beam scan angle is zero (or nearly zero), the angle of the first grating lobe from broadside is given [70] by

$$|\theta_g| = \arcsin\left(\frac{\lambda}{s}\right) \quad (10.56)$$

In TerraSAR-X, this places the first grating lobes at about $\pm 4.5^\circ$ from broadside. The actual azimuth scan range used is $\pm 0.75^\circ$, or ± 2.3 one-way azimuth beamwidths. Azimuth grating lobes are suppressed by the subarray azimuth beam pattern whose 3-dB width is about 4° .

Pointing Error versus Frequency. When constant-phase type phase shifters (in which the phase shift is independent of frequency) are used at each phase center, the phase distribution across the antenna array matches that of the desired radiated or incident phase front at only one frequency f_0 and for a particular off-broadside angle θ_0 . At a different frequency f_1 , the phase center spacing *in wavelengths* is different but the phase distribution across the antenna array remains fixed; hence, the array is phased for a different beam direction θ_1 . This change in the beam direction (or “beam squint”) $\Delta\theta_0$ with a change in frequency Δf is given by the following relationships [69]:

$$f_1 \sin\theta_1 = f_0 \sin\theta_0 \quad \text{or} \quad \frac{f_1}{f_0} = \frac{\sin\theta_0}{\sin\theta_1} \quad (10.57)$$

$$\theta_1 = \arcsin\left[\left(\frac{f_0}{f_1}\right) \sin\theta_0\right] \quad (10.58)$$

$$\Delta\theta_0 = -\left(\frac{\Delta f}{f}\right) \tan\theta_0 \quad (10.59)$$

Equation (10.59) indicates that under this set of assumptions, the beam angle decreases (i.e., shifts toward broadside) as the frequency increases. The amount of beam squint depends upon the original scan angle as well as on the percent frequency change, with the maximum beam shift occurring at the maximum scan angle from broadside. For TerraSAR-X with a 9.65-GHz RF center frequency, a 300-MHz maximum waveform bandwidth, and an azimuth scan angle range of $\pm 0.75^\circ$, the maximum azimuth beam squint over the waveform bandwidth is only 0.01° , which is approximately 4 percent of the azimuth beamwidth. For the $\pm 19.2^\circ$ elevation scan range, the maximum beam squint over the waveform bandwidth is 0.3° , which is 14 percent of the elevation beamwidth.

Radiated Power. The TerraSAR-X radiated peak output power is 2,260 W, or approximately 5.8 W per T/R module. The duty factor is 0.18 in the strip map mode and 0.20 in the spotlight mode, so the average output power is 407 W and 452 W in those modes, respectively.

10.6.4 Target, Terrain, and Noise Power

This section estimates the received target and terrain return signal powers, along with the receiver noise power for the TerraSAR-X radar.

10.6.4.1. Target Return Signal Power

The slant ranges of interest for TerraSAR-X vary from 532 km to 935 km, corresponding to incidence angles from 15° to 60° and grazing angles from 75° to 30°. The corresponding ground ranges from the subsatellite point vary from 127 km to 751 km. Table 10-9 summarizes the TerraSAR-X look geometry parameters.

The expected return power from a discrete scatterer is

$$P_r = \frac{P_t G_t G_r \lambda^2 \sigma}{(4\pi)^3 R^4 L} \quad (10.60)$$

The symbols in this equation are defined in Table 10-10 along with representative values for TerraSAR-X radar parameters, plus the result of this calculation. In this tabulation, the parameter values are converted to decibels in the right column, then the numerator terms are added, and the denominator terms are subtracted. The result is the target power that would be measured at the output port of a lossless passive receive antenna. This target power is not directly observable at any point in the active electronically scanned array (AESA) radar system, but it can still serve as a useful metric. Either the peak or average transmit power can be used, depending on the end use of the calculation, as long as consistency is maintained. The calculation in Table 10-10 assumes the ideal antenna gain with no aperture weighting and no losses.

10.6.4.2 Terrain Return Power

The return power from the terrain is also of interest. Terrain return depends on the terrain type, along with the polarization and incidence angle. The RCS of the terrain can be estimated as the product of the resolution cell area and the area-normalized backscatter coefficient, sigma zero (σ^0). In the TerraSAR-X high-resolution spotlight mode with an azimuth resolution of 1.1 m and a ground range resolution of 1.5 m

TABLE 10-9 ■ TerraSAR-X Look Geometry Parameters (Satellite Altitude = 515 km)

Angle of Incidence (Degrees)	Grazing Angle (Degrees)	Off-Nadir Look Angle (Degrees)	Slant Range (km)	Ground Range (km)
15	75	13.9	531.7	127.3
20	70	18.4	545.4	172.6
25	65	23.0	563.7	220.4
30	60	27.6	587.4	271.8
35	55	32.1	617.6	327.9
40	50	36.5	655.4	390.0
45	45	40.9	702.9	460.2
50	40	45.1	762.6	541.1
55	35	49.3	838.0	636.2
60	30	53.2	934.5	750.5

TABLE 10-10 ■ TerraSAR-X Spotlight Mode Received Signal Power Calculation

Parameter	Symbol	Value	Units	dB Value	dB Units
Numerator terms					
Transmit power (average*)	P_t	452	W	56.6	dBm
Transmit antenna gain	G_t	43,791		46.4	dB
Receive antenna gain	G_r	43,791		46.4	dB
Wavelength ²	λ^2	0.031	m ²	-30.1	dBsm
Target RCS	σ	10	m ²	10.0	dBsm
Denominator terms					
$(4\pi)^3$	$(4\pi)^3$	1,984		33.0	dB
(Slant range) ⁴	R^4	(935,000) ⁴	m ⁴	238.8	dB m ⁴
Losses affecting P_r (RF and beamshape losses)	L	1.00		0.0	dB
Result					
Received power (equivalent average power* at the output port of a lossless passive antenna)	P_r			-142.5	dBm

*The average transmit power is used here since our ultimate interest is in the target power after pulse compression and Doppler processing, referenced to the output of a lossless passive array.

(corresponding to a slant range resolution of 1.2 m at a 55° incidence angle), the resolution cell area on the ground is 1.65 m², or 2.17 dBsm. For short vegetation at a 55° incidence angle, the mean backscatter coefficient (σ_o) is approximately -12 dB, resulting in a resolution cell RCS of approximately -9.8 dBsm. Consequently, a discrete target with an RCS of +10 dBsm would have approximately 20 dB more return power than the -9.8-dBsm RCS of the short vegetation in the resolution cell.

10.6.4.3 Noise

Synthetic Array Time and Post-Processing Noise Bandwidth The required synthetic array time T_{SA} from Equation (10.41) and the approximate post-processing noise bandwidth (the inverse of T_{SA}) are shown as functions of slant range in Figure 10-24. The markers correspond to 5° increments in incidence angle from 15° to 60°. The minimum dwell time increases from approximately 1.1 s at the 532-km minimum range to 1.9 s at the 935-km maximum range, while the maximum post-processing noise bandwidth decreases from approximately 0.9 Hz to 0.5 Hz.

At the 935-km maximum slant range, the 0.33° azimuth beamwidth yields a footprint width of approximately 5.4 km. At the 7.68-km/s ground-referenced velocity, a target at that range takes approximately 0.7 s to transit a fixed side-looking beam, which is less than half of the required 1.9-s dwell time for 1.1-m cross-range resolution. The 0.7-s dwell time corresponds to a cross-range resolution of approximately 3.0 m. In order to achieve the desired 1.1-m cross-range resolution, the beam must be scanned in azimuth to extend the dwell time beyond that available in the strip map mode.

Effective Noise Power in the Post-Processing Noise Bandwidth The effective noise power referenced to the receive port of a lossless antenna is

$$N = kT_0BF \quad (10.61)$$

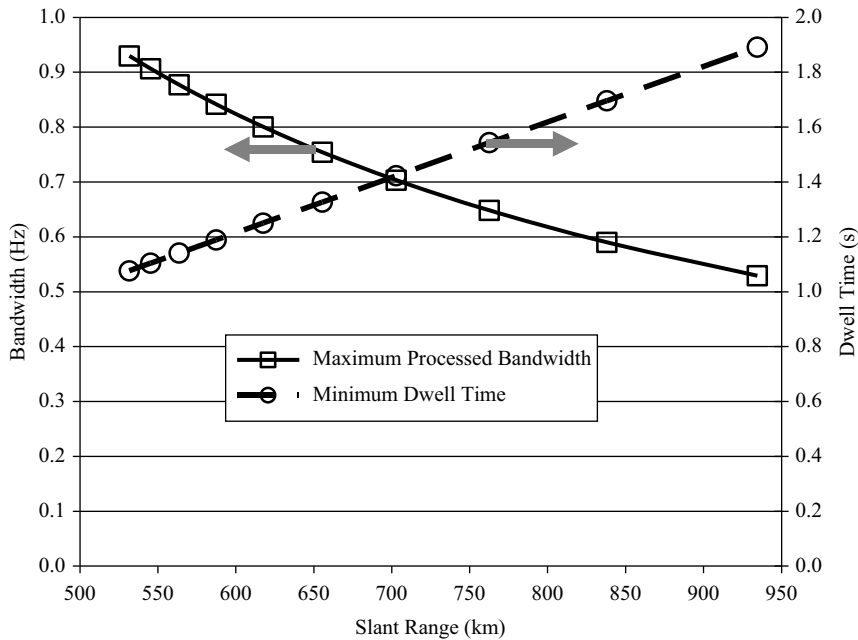


FIGURE 10-24 ■ Post-Processing Noise Bandwidth and Dwell Time as a Function of Slant Range.

TABLE 10-11 ■ TerraSAR-X Estimated Noise Power Calculation

Parameter	Symbol	Value	Units	dB Value	dB Units
Boltzmann's constant	k	1.38×10^{-23}	W/(Hz·K)	-228.6	dB W/(Hz·K)
Reference temperature	T_0	290	K	24.6	dB K
System noise bandwidth (post-processing)	B	0.5	Hz	-3.0	dB Hz
System noise figure	F	3.16		5.0	dB
Result					
Effective noise power	N			-202.0	dB W
				-172.0	dBm

where the symbol definitions and representative values are presented in Table 10-11. This calculation assumes a scene background noise temperature of 290 K, which is the worst case. Land and water surfaces generally have lower background noise temperatures due to their emissivities being less than 100 percent. The post-processing noise bandwidth is assumed to be 0.5 Hz, corresponding to a 2-second synthetic array time. The effective noise power of -172 dBm in this bandwidth (i.e., resolution cell) is 29.5 dB less than the 10-dBsm RCS target return power and 9.7 dB less than the -12-dB sigma zero terrain return power at the maximum range.

Noise Equivalent Sigma Zero The power in any resolution cell after processing can be converted into an equivalent radar cross section based on knowledge of the radar parameters and the slant range. This can be done even if the resolution cell contains only noise and no surface returns. Normalizing the equivalent RCS of a noise-only resolution cell by the resolution cell area produces an equivalent backscatter coefficient of a surface that returns the same power as the average noise power in the resolution cell. This

backscatter coefficient is known as the noise-equivalent sigma zero (NESZ), alternatively known as noise-equivalent sigma “naught” or the additive noise coefficient (ANC). Since the NESZ is a measure of the SAR sensitivity, it is sometimes simply referred to as “sensitivity.” This figure-of-merit includes the effects of transmitted power, two-way antenna gain, receiver noise figure, and all other RF and processing gains and losses. The NESZ can be found [47] from

$$NESZ = \frac{8\pi R^3 \lambda k T_0 F L_{sys} v_{sat} \cos \psi}{P_{t(avg)} A^2 \eta_a^2 \delta_R} \quad (10.62)$$

where

L_{sys} = all system losses (including processing losses)

ψ = grazing angle

$P_{t(avg)}$ = average transmit power

A = aperture area

η_a = aperture illumination efficiency

δ_R = range resolution

Calculation and/or prediction of the NESZ is described in greater detail by Sullivan [47] and Carrara *et al.* [34]. Typical NESZ values for a spaceborne SAR are -15 to -25 dB.

Table 10-12 shows a calculation of the NESZ for TerraSAR-X at the maximum slant range and at an incidence angle of 60° . With no system losses and 100 percent aperture illumination efficiency, the calculated NESZ is approximately -25 dB. Many

TABLE 10-12 ■ NESZ Calculation for TerraSAR-X at 60° Incidence Angle

Parameter	Symbol	Value	Units	dB value	dB units
Numerator terms					
Constants	8π	25.1327		14.00	dB
(Slant range) ³	R^3	$(935,000)^3 = 8.174 \times 10^{17}$	m ³	179.1	dB m ³
Wavelength	λ	0.031	m	-15.07	dB m
Boltzmann’s constant	k	1.38×10^{-23}	W/(Hz·K)	-228.60	dB W/(Hz·K)
Reference temperature	T_0	290	K	24.62	dB K
Noise figure	F	3.16		5.0	dB
System loss	L_{sys}	1.00*		0.0	dB
Satellite velocity relative to Earth	v_{sat}	7,680	m/s	38.85	dB m/s
$\cos(60^\circ)$	$\cos \psi$	0.5		-3.0	dB
Denominator terms:					
Average transmit power	P_{avg}	452	W	26.55	dBW
(Aperture area) ²	A^2	$(3,368)^2$	m ⁴	10.55	dB m ⁴
(Aperture efficiency) ²	η_a^2	1*		0.0	dB
Slant range resolution	δ_r	2.0	m	3.01	dB m
Result:					
Noise-equivalent sigma zero	$NESZ$			-25.2	dB

*This calculation was done with no system loss and 100% aperture illumination efficiency for illustrative purposes.

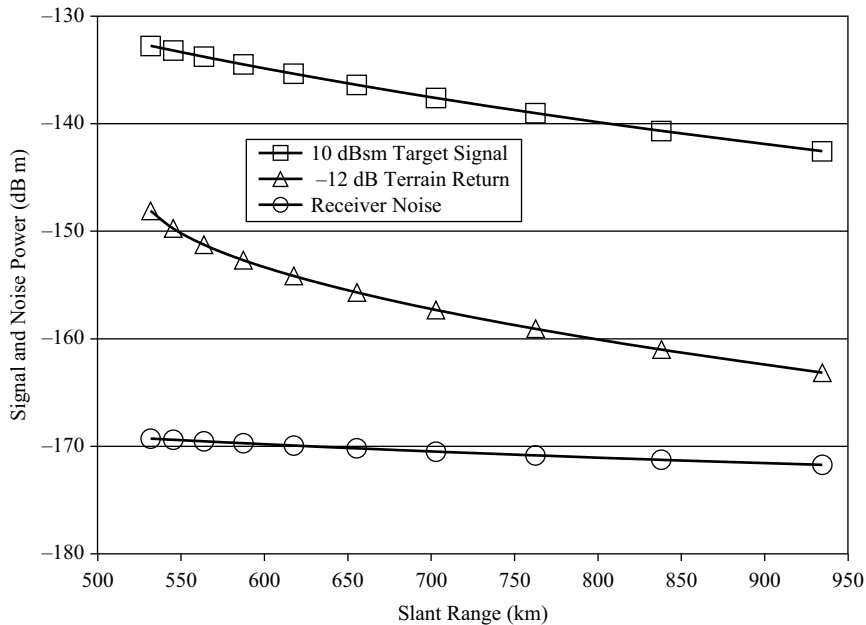


FIGURE 10-25 ■ TerraSAR-X Target, Terrain, and Noise Powers in a Resolution Cell as a Function of Slant Range in the Spotlight Mode. All Powers are Referenced to the Output Port of a Lossless Receive Antenna. The Receiver Noise Power Decreases Slightly with Increasing Range Due to the Longer Time on Target (Lower Noise Bandwidth after Processing) with Increasing Range.

radars have total system losses of approximately 5 to 10 dB, however, which will increase (i.e., degrade) the NESZ accordingly.

10.6.4.4 Return Power and Noise Summary

Figure 10-25 shows the effective target return power, terrain return power, and receiver noise power for the TerraSAR-X radar as a function of slant range from the 532-km minimum range to the 935-km maximum range. The markers correspond to 5° increments in incidence angle from 15° to 60°. Even at the maximum slant range, the signal-to-noise ratio for a 10-dBsm target is over 29 dB. This post-processing effective signal power calculation assumes negligible losses.

10.6.5 SAR Waveform

10.6.5.1 Maximum PRF and Maximum Unambiguous Range

TerraSAR-X implements PRFs from as low as 2.0 kHz to 6.5 kHz, with corresponding PRIs from 500 μ s to 154 μ s. The duty factor is 0.18 in the strip map mode and 0.2 in the spotlight mode. Figure 10-26 shows the slant range and the slant range extent of the mainlobe footprint as a function of the incidence angle, while Figure 10-27 shows the maximum PRF along with the slant range extent of the mainlobe footprint as a function of incidence angle. For a 55° incidence angle, the maximum PRF that avoids range ambiguities in the mainlobe footprint is 3 kHz. At incidence angles less than

FIGURE 10-26 ■ TerraSAR-X Slant Range and Antenna Footprint Range Extent as a Function of Incidence Angle.

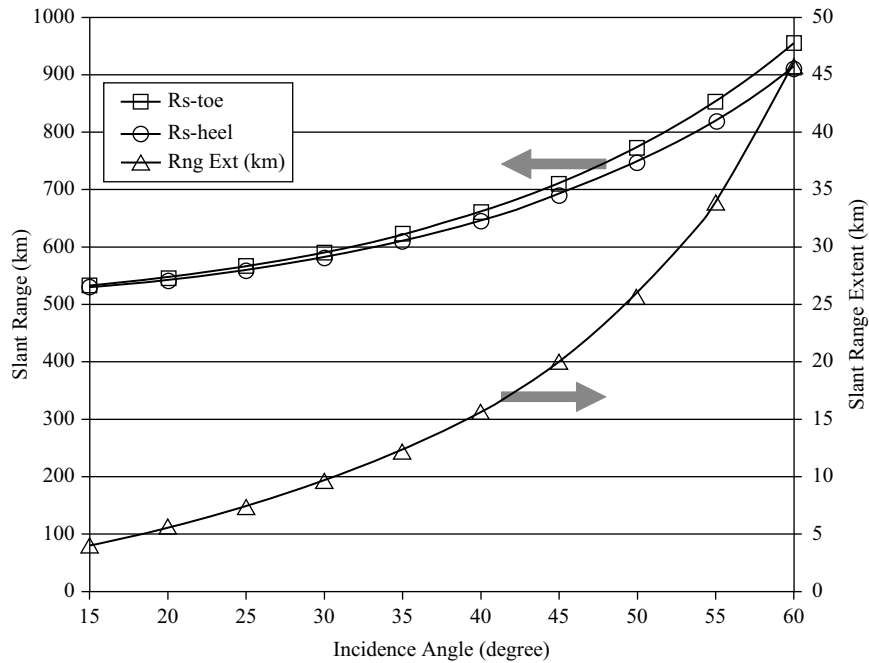
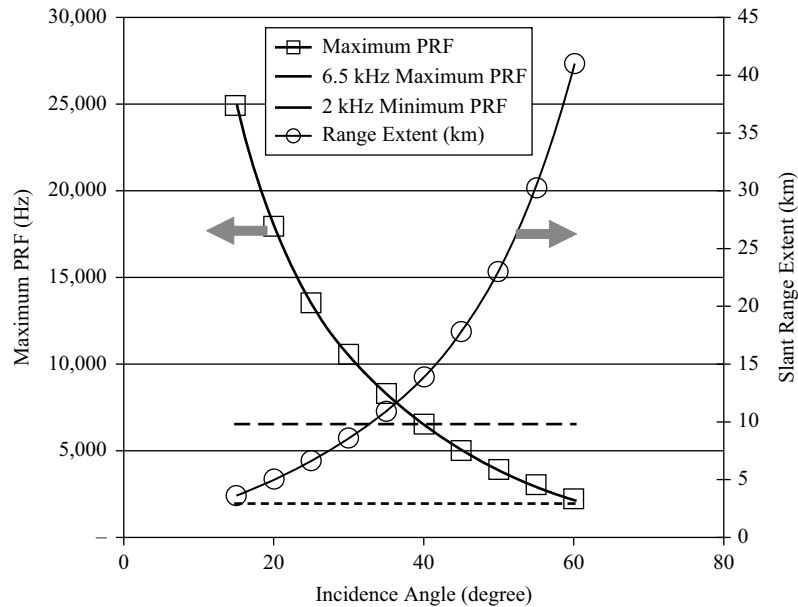


FIGURE 10-27 ■ Maximum PRF and Beam Footprint Range Extent as a Function of Incidence Angle.



approximately 40°, PRFs exceeding the maximum available PRF of 6.5 kHz could be used while avoiding mainlobe range ambiguities.

10.6.5.2 Minimum PRF and Doppler/Velocity/Azimuth Ambiguities

The Doppler bandwidth corresponding to a given azimuth beamwidth can be estimated using Equation (10.44). With a platform velocity of 7,682 m/s relative to the rotating Earth and the beam direction normal to the velocity vector, the half-power Doppler

bandwidth is approximately 3.2 kHz (± 1.6 kHz with respect to zero Doppler) and the velocity spread across the beam is 50 m/s (± 25 m/s from zero velocity). To avoid aliasing (i.e., Doppler or azimuth ambiguities) the PRF should be well above 3.2 kHz.

10.7 | SUMMARY

Radar remote sensing of Earth and other solar system bodies (the moon, Venus, Mars, and Titan) has become an established field. At the time of this writing (2013), there are approximately 19 operating SAR satellites in Earth orbit: seven German, four Italian, two Canadian, two Japanese, two Indian, one Israeli, and at least one Chinese. Of these, nine are primarily dedicated to security-related reconnaissance, five are dedicated to civil remote sensing, and five are dual-use. Some of the funding for Earth radar remote sensing programs is shifting from pure government sponsorship to consortia of national and regional governments, along with private industrial firms and other investors.

Implementation of a spaceborne SAR is challenging due to the long range to the target area, high-platform velocity, waveform ambiguities, and the level of precision required in the measurements. Spaceborne SARs have evolved a great deal since the single-polarization Seasat mission in 1978. Some SARs now have full polarization capability (HH, HV, VH, VV) and a variety of modes, including spotlight for high-resolution imaging and ScanSAR for wide swath coverage. Split-aperture modes such as along-track interferometry and other forms of moving target indication are being used to measure geophysical parameters such as ocean and river currents. These modes are also being tested experimentally for remotely monitoring vehicular traffic on highways. Nonimaging sensors such as radar altimeters and scatterometers also play an important role in remote sensing, particularly in oceanography.

Most spaceborne SAR satellites operate in high-inclination orbits, providing coverage of most of Earth's surface. One such orbit of particular interest is the sun-synchronous orbit, with typical inclinations of approximately 97° to 103° . The dawn–dusk sun-synchronous orbit maximizes illumination of the solar panels for power generation.

Spaceborne SARs typically operate in the 1–10-GHz frequency range (L-band through X-band). Frequencies below L-band are significantly affected by ionospheric phenomena, particularly Faraday rotation, while X-band and higher frequencies can be affected by clouds and rain. C-band is a good compromise that is least degraded by propagation effects.

The PRF in spaceborne SARs is usually range-ambiguous, with multiple pulses “in flight” during the round-trip target delay time. The elevation beam pattern must be designed to attenuate undesired range ambiguities, while the azimuth beam pattern must reject returns that are ambiguous in Doppler. One difference between spaceborne and airborne SAR operation is that a spaceborne SAR must take into account the Doppler shift due to Earth's rotation, while an airborne SAR operates in an Earth-referenced coordinate frame. In spaceborne SAR, because of Earth's rotation, the zero-Doppler direction is not always exactly perpendicular to the flight path. Some satellites provide a small time-varying yaw angle to compensate for this effect.

Since the SAR image formation processing is usually done on the ground, the downlink channel capacity is a frequent limitation on the potential capabilities and data products available from a SAR mission. Block adaptive quantization is often used to reduce the downlink data rate requirement or to permit more data to be sent to the

ground in a fixed-capacity communication channel (e.g., to support multiple receive subapertures, polarizations, etc.).

Multilook processing improves the image quality at the expense of poorer cross-range resolution. ScanSAR increases the swath width and the area coverage rate also at the expense of poorer cross-range resolution. When cross-range resolution is degraded, it is often desirable to coarsen the downrange resolution by the same amount in order to maintain square pixels and to reduce the required downlink data rate.

Several approaches to the detection and measurement of moving targets have been tried. Along-track interferometry has been of interest for measuring the radial velocity of geophysical phenomena such as surface currents in oceans and rivers. ATI, as well as other approaches to moving target indication, require that the receive aperture be split into two or more subapertures whose phase centers are separated in the along-track dimension. Outputs from these subapertures are processed through separate receiver channels. Many of the newer SAR satellites are being designed with this feature, opening up new possibilities for remote sensing of moving objects and phenomena.

Germany's TerraSAR-X is a recent X-band SAR satellite that was launched in 2007. It serves as a good example of a SAR satellite with a rich set of features and capabilities for remote sensing. Together with its near-twin TanDEM-X, it also supports two-satellite interferometric SAR for topographic mapping.

10.8 | REFERENCES

- [1] Stewart, R. H., *Methods of Satellite Oceanography*, University of California Press, Berkeley, CA, 1985.
- [2] Elachi, C., *Spaceborne Radar Remote Sensing: Applications and Techniques*, IEEE Press, New York, 1987.
- [3] NASA, "Seasat 1978," <http://southport.jpl.nasa.gov/scienceapps/seasat.html>.
- [4] Raney, R. K., "Space-Based Remote Sensing Radars," Chapter 18 in *Radar Handbook, Third Edition*, M. I. Skolnik, editor, McGraw-Hill, New York, 2008.
- [5] NASA, "20 Years of Shuttle Imaging Radar," <http://www.jpl.nasa.gov/news/features.cfm?feature=422>.
- [6] NASA, "SIR-A 1982," <http://southport.jpl.nasa.gov/scienceapps/sira.html>.
- [7] NASA, "SIR-B 1985," <http://southport.jpl.nasa.gov/scienceapps/sirb.html>.
- [8] NASA, "What Is SIR-C/X-SAR?," <http://southport.jpl.nasa.gov/desc/SIRCdesc.html>.
- [9] eoPortal, "ERS-2 (European Remote-Sensing Satellite-2)," http://www.eoportal.org/directory/pres_ERS2EuropeanRemoteSensingSatellite2.html.
- [10] Francis, C. R., Graf, G., Edwards, P. G., McCaig, M., McCarthy, C., Lefebvre, A., Pieper, B., Pouvreau, P.-Y., Wall, R., Weschler, F., Louet, J., Schumann, W., and Zobl, R., "The ERS-2 Spacecraft and Its Payload," <http://esapub.esrin.esa.it/bulletin/bullet83/fran83.htm>.
- [11] Desnos, Y-L., Buck, C., Guijarro, J., Suchail, J-L., Torres, T., and Attema, E., "ASAR – Envisat's Advanced Synthetic Aperture Radar," *ESA Bulletin* 102, May 2000, pp. 91–100, <http://crs.itb.ac.id/media/jurnal/Refs/Download/22Apr/Desnos102.pdf>.
- [12] Canadian Space Agency, "Canada and the ENVISAT Program," <http://www.asc-csa.gc.ca/pdf/envisat-en.pdf>.

- [13] ESA, “ENVISAT Tour: ASAR (Advanced Synthetic Aperture Radar) ASAR transmit tile,” http://envisat.esa.int/instruments/tour-index/asar/asar_transmit_tile.htm.
- [14] eoPortal, “JERS-1 (Japan Earth Resources Satellite),” http://www.eoportal.org/directory/pres_JERS1JapanEarthResourcesSatellite.html.
- [15] Nemoto, Y., Nishino, H., Ono, M., Mizutamari, H., Nishikawa, K., and Tanaka, K., “Japanese Earth Resources Satellite-1 Synthetic Aperture Radar,” *Proceedings of the IEEE*, Vol. 79, No. 6, June 1991, pp. 800–809.
- [16] Rosenqvist, A., Shimada, M., Ito, N., and Watanabe, M., “ALOS PALSAR: A Pathfinder Mission for Global-Scale Monitoring of the Environment,” *IEEE Transactions on Geoscience and Remote Sensing*, Vol. 45, No. 11, November 2007, pp. 3307–3316.
- [17] Norimasa Ito, “ALOS/PALSAR Characteristics and Status,” Committee on Earth Observation Satellites (CEOS) Work Group on Calibration and Validation (WGCV)-SAR Workshop 2001, 2–5 April 2001 NASDA/EORC, Tokyo, Japan.
- [18] Raney, R. K., Luscombe, A. P., Langham, E. J., and Ahmed, S., “RADARSAT,” *Proceedings of the IEEE*, Vol. 79, No. 6, 1991, pp. 839–849.
- [19] Luscombe, A. P., Furseth, D. A., Srivastava, S. K., and Jeffries, W. C., “Using the RADARSAT SAR Versatility to Enhance Fine Resolution Imaging Capabilities,” *Proceedings 1997 IEEE International Geoscience and Remote Sensing Symposium*, Figure 1, p. 1064.
- [20] Ahmed, S., Warren, H. R., Symonds, M. D., and Cox, R. P., “The Radarsat System,” *IEEE Transactions on Geoscience and Remote Sensing*, Vol. 28, No. 4, July 1990, pp. 598–602.
- [21] Luscombe, A., Fox, P. A., James, K., Thompson, A., and MacDonald Dettwiler and Associates Ltd., “In-Orbit Characterisation of the RADARSAT-2 Antenna,” Proceedings of the Committee on Earth Observation Satellites, Working Group on Calibration and Validation, Synthetic Aperture Radar Workshop 2004, Ulm, Germany, 27–28 May 2004, http://earth.esa.int/workshops/ceos_sar_2004/papers/16_luscombe.pdf.
- [22] Agenzia Spaziale Italiana (Italian Space Agency), *COSMO-SkyMed System Description & User Guide*, Doc. No: ASI-CSM-ENG-RS-093-A, Rev. A, 04-05-2007, http://www.eurimage.com/products/pdf/csk-user_guide.pdf.
- [23] Capece, P., Borgarelli, L., Di Lazzaro, M., Di Marcantonio, U., and Torre, A., “COSMO SkyMed Active Phased Array SAR Instrument,” *IEEE Radar Conference, 2008*, (RADAR ’08), Digital Object Identifier: 10.1109/RADAR.2008.4720773, pp. 1–4.
- [24] Mezzasoma, S., Gallon, A., Impagnatiello, F., Angino, G., Fagioli, S., Capuzi, A., Caltagirone, F., Leonardi, R., and Ziliotto, U., “COSMO-SkyMed System Commissioning: End-to-End System Performance Verification,” *IEEE Radar Conference, 2008*, (RADAR ’08), Digital Object Identifier: 10.1109/RADAR.2008.4720930, pp. 1–5.
- [25] NASA, “TanDEM-X Description,” <http://nssdc.gsfc.nasa.gov/nmc/spacecraftDisplay.do?id=2010-030A>.
- [26] DLR, “TanDEM-X Brochure,” http://www.dlr.de/hr/en/Portaldata/32/Resources/dokumente/broschueren/TanDEM-X_web_Brochure2010.pdf.
- [27] Bate, R. R., Mueller, D. D., and White, J. E., *Fundamentals of Astrodynamics*, Dover Publications, New York, 1971, p. 60.
- [28] Escobal, P. R., *Methods of Orbit Determination*, Krieger Publishing Company, Malabar, FL, 1976 (originally published by John Wiley & Sons, 1965), p. 80.
- [29] NASA, “Earth Fact Sheet,” <http://nssdc.gsfc.nasa.gov/planetary/factsheet/earthfact.html>.

- [30] Elachi, C., *Introduction to the Physics and Techniques of Remote Sensing*, John Wiley & Sons, New York, 1987.
- [31] Cantafio, L. J., ed., *Space-Based Radar Handbook*, Artech House, Boston, 1989, p.58.
- [32] Bickel, D. L., Brock, B. C., and Allen, C. T., "Spaceborne SAR Study: LDRD '92 Final Report," Sandia National Laboratories report SAND93-0731, March 1993, pp. 51–53.
- [33] Curlander, J. C. and McDonough, R. N., *Synthetic Aperture Radar: Systems and Signal Processing*, John Wiley & Sons, New York, 1991.
- [34] Carrara, W. G., Goodman, R. S., and Majewski, R. M., *Spotlight Synthetic Aperture Radar: Signal Processing Algorithms*, Artech House, Boston, 1995.
- [35] Jakowatz, C. V., Jr., Wahl, D. E., Eichel, P. H., Ghiglia, D. C., and Thompson, P. A., *Spotlight-Mode Synthetic Aperture Radar: A Signal Processing Approach*, Kluwer Academic Publishers, Boston, 1996.
- [36] Cumming, I. G. and Wong, F. H., *Digital Processing of Synthetic Aperture Radar Data: Algorithms and Implementations*, Artech House, Boston, 2005.
- [37] Davies, K., *Ionospheric Radio*, IEE/Peter Peregrinus, London, 1990, Chapter 8, "Earth-Space Propagation."
- [38] Ulaby, F. T., Moore, R. K., and Fung, A. K., "Microwave Interaction with Atmospheric Constituents," Chapter 5 in *Microwave Remote Sensing, Active and Passive, Volume 1: Microwave Remote Sensing Fundamentals and Radiometry*, Addison-Wesley Publishing Company, Reading, MA, 1981, pp. 256–343.
- [39] Ippolito, Jr., J. L., *Radiowave Propagation in Satellite Communications*, Van Nostrand Reinhold, New York, 1986.
- [40] Keeler, R. J. and Serafin, R. J., "Meteorological Radar," Chapter 19 in *Radar Handbook, Third Edition*, M. I. Skolnik, ed., McGraw-Hill, New York, 2008.
- [41] Schubert, A., Jehle, M., Small, D., and Meier, E., "Influence of Atmospheric Path Delay on the Absolute Geolocation Accuracy of TerraSAR-X High Resolution Products," *IEEE Transactions on Geoscience and Remote Sensing*, Vol. 48, No. 2, February 2010, pp. 751–758.
- [42] Imhoff, M., Story, M., Vermillion, C., Khan, F., and Polcyn, F., "Forest Canopy Characterization and Vegetation Penetration Assessment with Space-Borne Radar," *IEEE Transactions on Geoscience and Remote Sensing*, Vol. GE-24, No. 4, July 1986, pp. 535–542.
- [43] National Telecommunications and Information Administration (NTIA), *Federal Radar Spectrum Requirements*, NTIA Special Publication 00-40, U.S. Department of Commerce, May 2000.
- [44] Hurtak, J. J., "Subsurface Morphology and Geoarchaeology Revealed by Spaceborne and Airborne Radar," <http://www.affs.org/html/geoarcheology.html>.
- [45] Ulaby, F. T., Moore, R. K., and Fung, A. K., *Microwave Remote Sensing, Active and Passive, Volume 2: Radar Remote Sensing and Surface Scattering and Emission Theory*, Addison-Wesley Publishing Company, Reading, MA, 1982, pp. 848–852.
- [46] Freeman, A., Johnson, W. T. K., Huneycutt, B., Jordan, R., Hensley, S., Siqueira, P., and Curlander, J., "The Myth of the Minimum SAR Antenna Area Constraint," *IEEE Transactions on Geoscience and Remote Sensing*, Vol. 38, No. 1, January 2000, pp. 320–324.
- [47] Sullivan, R., "Synthetic Aperture Radar," Chapter 17 in *Radar Handbook, Third Edition*, M. I. Skolnik, ed., McGraw-Hill, New York, 2008.
- [48] Gray, G. A. and Zeoli, G. W., "Quantization and Saturation Noise Due to Analog-to-Digital Conversion," *IEEE Transactions on Aerospace and Electronic Systems*, January 1971, pp. 222–223.

- [49] Ducoff, M. R. and Tietjen, B. W., “Pulse Compression Radar,” Chapter 8 in *Radar Handbook, Third Edition*, M. I. Skolnik, ed., McGraw-Hill, New York, 2008, pp. 8.31–8.36.
- [50] Richards, M. A., “Introduction to Synthetic Aperture Imaging,” Chapter 8 in *Fundamentals of Radar Signal Processing*, McGraw-Hill, New York, 2005, pp. 385–459.
- [51] Jet Propulsion Laboratory, *Venus Radar Mapper System Requirements*, 22 February 1985.
- [52] Chang, C. Y., Jin, M. Y., Lou, Y. L., and Holt, B., “First SIR-C Scansar Results,” *IEEE Transactions on Geoscience and Remote Sensing*, Vol. 34, No. 5, September 1996, pp. 1278–1281.
- [53] De Zan, F. and Guarnieri, M., “TOPSAR: Terrain Observation by Progressive Scans,” *IEEE Transactions on Geoscience and Remote Sensing*, Vol. 44, No. 9, September 2006, pp. 2352–2360.
- [54] Meta, A., Mittermayer, J., Prats, P., Scheiber, R., and Steinbrecher, U., “TOPS Imaging with TerraSAR-X: Mode Design and Performance Analysis,” *IEEE Transactions on Geoscience and Remote Sensing*, Vol. 48, No. 2, February 2010, pp. 759–769.
- [55] Nohara, T., “Comparison of DPCA and STAP for Space-Based Radar,” *IEEE 1995 International Radar Conference*, IEEE Press, 1995, pp. 113–119.
- [56] Chiu, S. and Gierull, C., “Multi-Channel Receiver Concepts for RADARSAT-2 Ground Moving Target Indication,” <http://www.geo.uzh.ch/microsite/rsl-documents/research/SARlab/GMTILiterature/PDF/CG06.pdf>.
- [57] Moccia, A. and Rufino, G., “Spaceborne Along-Track SAR Interferometry: Performance Analysis and Mission Scenarios,” *IEEE Transactions on Aerospace and Electronic Systems*, Vol. 37, No. 1, January 2001, pp. 199–213.
- [58] Thompson, A. A. and Livingstone, C. E., “Moving Target Performance for RADARSAT-2,” *IEEE Geoscience and Remote Sensing Symposium, 2000 (IGARSS 2000)*, July 2000, pp. 2599–2601.
- [59] Chiu, S. and Livingstone, C., “A Comparison of Displaced Phase Centre Antenna and Along-Track Interferometry Techniques for RADARSAT-2 Ground Moving Target Indication,” *Canadian Journal of Remote Sensing*, Vol. 31, No. 1, pp. 37–51, 2005.
- [60] Suchandt, S., Runge, H., and Steinbrecher, U., “Ship Detection and Measurement Using the TerraSAR-X Dual-Receive Antenna Mode,” *IEEE Geoscience and Remote Sensing Symposium, 2010 (IGARSS 2010)*, pp. 2860–2863.
- [61] Romeiser, R., Suchandt, S., Runge, H., Steinbrecher, U., and Grunler, S., “First Analysis of TerraSAR-X Along-Track InSAR-Derived Current Fields,” *IEEE Transactions on Geoscience and Remote Sensing*, Vol. 48, No. 2, February 2010, pp. 820–829.
- [62] Chen, C. W. “Performance Assessment of Along-Track Interferometry for Detecting Ground Moving Targets,” *Proceedings of IEEE Radar Conference 2004*, 26–29 April 2004, pp. 99–104.
- [63] Ghiglia, D. C. and Pritt, M. D., *Two-Dimensional Phase Unwrapping: Theory, Algorithms, and Software*, Wiley-Interscience, New York, 1998.
- [64] Chiu, S., “An Analysis of RADARSAT-2 SAR-GMTI Performance for Standard Beam Mode,” Defense R&D Canada (DRDC), Defense Research Establishment Ottawa (DREO), Technical Report DREO TR 2000-088, December 2000.
- [65] Chiu, S., “Performance of RADARSAT-2 SAR-GMTI Processors at High SAR Resolutions,” Defense R&D Canada (DRDC), Defense Research Establishment Ottawa (DREO), Technical Report DREO TR 2000-093, November 2000.

- [66] Werninghaus, R. and Buckreuss, S., “The TerraSAR-X Mission and System Design,” *IEEE Transactions on Geoscience and Remote Sensing*, Vol. 48, No. 2, Digital Object Identifier 10.1109/TGRS.2009.2031062, pp. 606–614.
- [67] “TerraSAR-X Mission,” eoPortal, www.eoportal.org/directory/pres_TerraSARXMission.html.
- [68] Moreira, A. and German Aerospace Center (DLR), “TerraSAR-X Upgrade to a Fully Polarimetric Imaging Mode,” Workshop on Applications of SAR Polarimetry and Polarimetric Interferometry, POLinSAR 2003, 16 January 2003, <http://earth.esa.int/workshops/polinsar2003/participants/moreira72/TerraSAR-PolInSAR-16-01-2003.pdf>.
- [69] Bailey, C. D., “Radar Antennas,” Chapter 9 in *Principles of Modern Radar, Volume I: Basic Principles*, Mark A. Richards, James A. Scheer, and William A. Holm, editors, SciTech Publishing, 2010, pp. 331–336.
- [70] Kraus, J. D., *Radio Astronomy*, McGraw-Hill Book Company, New York, 1966, p. 172.
- [71] Cook, D. A., “Spotlight Synthetic Aperture Radar,” Chapter 6 in *Principles of Modern Radar, Vol. II: Advanced Techniques*, W. L. Melvin and J. A. Scheer, editors, SciTech Publishing, Edison, NJ, 2013.
- [72] Richards, M. A., “Interferometric SAR and Coherent Exploitation,” Chapter 8 in *Principles of Modern Radar, Vol. II: Advanced Techniques*, W. L. Melvin and J. A. Scheer, editors, SciTech Publishing, Edison, NJ, 2013.
- [73] Richards, M. A., “A Beginner’s Guide to Interferometric SAR Concepts and Signal Processing,” *IEEE Aerospace and Electronic Systems Magazine*, Vol. 22, No. 9, September 2007, pp. 5–29.

10.9 | FURTHER READING

- Boain, R. J., “A-B-Cs of Sun-Synchronous Orbit Mission Design,” NASA/JPL, <http://trs-new.jpl.nasa.gov/dspace/bitstream/2014/7885/1/03-2432.pdf>.
- Cloude, S., *Polarisation: Applications in Remote Sensing*, Oxford University Press, Oxford, UK, 2009.
- Hein, A., *Processing of SAR Data: Fundamentals, Signal Processing, Interferometry*, Springer-Verlag, Berlin, 2010.
- Richards, J. A., *Remote Sensing with Imaging Radar*, Springer-Verlag, Berlin, 2009.
- Ulaby, F. T., Moore, R. K., and Fung, A. K., *Microwave Remote Sensing, Active and Passive, Volume III: From Theory to Applications*, Artech House, Dedham, MA, 1986.
- van Zyl, J. J., *Synthetic Aperture Radar Polarimetry*, John Wiley & Sons, Hoboken, NJ, 2011.

Passive Bistatic Radar

*Hugh Griffiths, University College London, and
Chris Baker, The Ohio State University*

Chapter Outline

11.1	Introduction	499
11.2	Bistatic Radar	505
11.3	Passive Bistatic Radar Waveforms	509
11.4	The Signal Environment	519
11.5	Passive Bistatic Radar Techniques	524
11.6	Examples of Systems	527
11.7	Conclusions	536
11.8	References	537
11.9	Further Reading	540

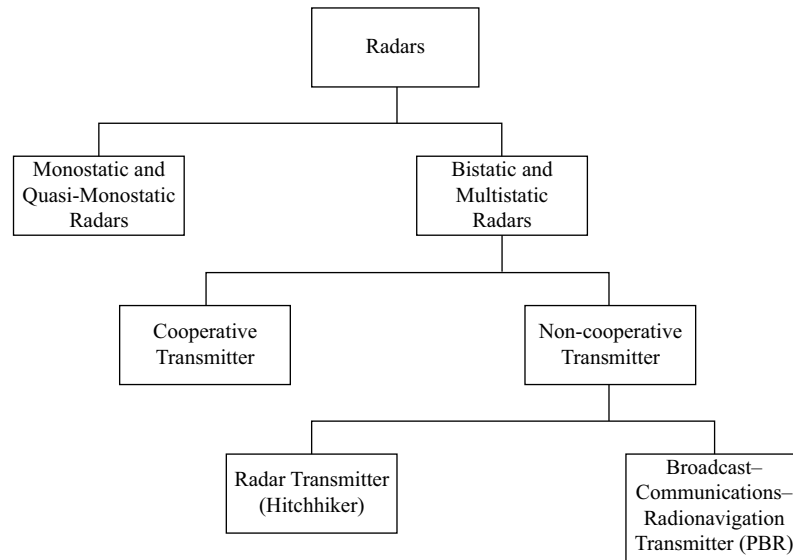
11.1 | INTRODUCTION

11.1.1 Definitions and Taxonomy

Passive bistatic radar (PBR) is the name given to a type of bistatic radar [1–5] in which the transmitting source is a broadcast, communications, or radionavigation signal. Figure 11-1 shows an attempt to classify bistatic and multistatic radar systems according to their properties. Bistatic radars may be defined as those in which the transmitter and receiver are at separate locations, sufficiently separated that the properties are significantly different to those of a monostatic radar. Radars that use separate but co-sited transmit and receive antennas (*quasi-bistatic* radars) are classified with monostatic radars. Bistatic and multistatic radars are classified into those that use cooperative transmitters under control of the user and those that use noncooperative transmitters. These are further divided into those for which the transmitter is a radar, in which case the system may be known as a *hitchhiker*, and those for which the transmitter is a broadcast, communications, or radionavigation signal, in which case the system is called a passive bistatic radar.

Other names that have been used include *passive coherent location* (PCL), *piggy-back radar*, *passive covert radar*, *parasitic radar*, *opportunistic radar*, *broadcast radar*, or *passive radar*. A discussion in [3], also reproduced in [6], concludes that none of

FIGURE 11-1 ■
How Passive
Bistatic Radar Fits
into the Overall
Taxonomy of
Radars.



these terms is entirely satisfactory but that passive bistatic radar is the most suitable of those on offer.

The distinction can also be drawn between *narrowband PBR*, in which only a portion of the signal spectrum is used, and *wideband PBR*, in which the whole signal spectrum is used. The former needs only modest digital sampling rates and makes use of Doppler and *direction-of-arrival* (DOA) information, while the latter can give range information as well.

11.1.2 Historical Perspective

Since many of the first radar experiments made use of broadcast transmitters, it can be argued that PBR dates back to the very earliest days of radar. We can note Appleton and Barnett's use toward the end of 1924 of a broadcast transmitter located at Bournemouth on the south coast of the United Kingdom and a receiver at Oxford to determine the height of the ionosphere (also the first FM radar) [7] and the celebrated Daventry Experiment on 26 February 1935, in which Watson Watt and Wilkins used the BBC Empire transmitter at a frequency of 6.1 MHz to detect a Heyford bomber aircraft at a range of 8 miles [8]. As a manifestation of a more modern interpretation of PBR, using television transmissions, Figure 11-2 shows a cutting from a popular science journal from 1938.

Quite evidently, the principles of detecting echoes from aircraft targets of broadcast signals had been realized more than 70 years ago. In addition, in WW2 German radar engineers had developed a sophisticated hitchhiker bistatic radar system called *Klein Heidelberg*, which used the British Chain Home radars as an unwitting (at least, initially) illumination source [10].

The first published description of a modern bistatic radar concept using a transmitter of opportunity appears to be a 1960 paper by Rittenbach and Fishbein [11], an annotated summary of which is as follows [3]:

This paper describes a semi-active radar system {the U.S. Army's preferred nomenclature, although the term bistatic had been coined by Siegel and Machol

[12] in 1952} in which the transmitter is carried in a [geosynchronous] satellite. The satellite transmits a randomly modulated signal [proposed at 100-W continuous wave, illuminating a ground area of 7,000 miles in diameter]. On the ground the radar has two antennas and receivers. One antenna points at the satellite, the other at the target [a ground vehicle]. The signal from the satellite-oriented receiver is delayed and [time-] correlated with the satellite signal reflected from the target. The delay corresponding to the peak of the correlation function is used to determine range [1,000 yds for a 1-m² target, 10,000 yds for 100 m²]. It is planned to test this system with various communications satellites [once they are orbited].

Probably the first modern PBR system to be built, in the 1960s, was Sugar Tree, an HF over-the-horizon system using short-wave radio broadcast illuminators to detect Soviet missile launches. This program has recently been declassified and is reported in a chapter in [3]. In the early 1980s, work at University College London led to some of the first experiments using analog television transmissions to detect air targets [13]. Subsequently, in 1996 Ogrodnik reported a “bistatic laptop receiver” [14] anticipating much of the PBR work that would follow, and in 1999 Howland published work showing detection and tracking of air targets at substantial ranges using echoes from analog television transmissions [15]. This interest prompted a special issue of *IEE Proceedings Radar, Sonar and Navigation* on Passive Radar in 2005 [16], in which numerous advances were reported. At the time of writing of this chapter, whole sessions at conferences – and, indeed, entire conferences – are devoted to PBR, and interest continues to grow.

269

PHYSICS

May Spot Airplanes With Television Receivers

“ENTIRELY possible” is the scientific verdict of radio engineers at the National Bureau of Standards to British dispatches citing the use of television receivers as “spotters” of airplanes.

While Army officials would not confirm reports that similar methods are being worked out for the military uses of the United States, it was admitted that secret research is underway to test other ways of spotting airplanes than by the present sound detection methods.

Since television broadcasts have been in progress over London it has been noted that when airplanes are flying in the vicinity there are produced “ghost” images in the television receivers. These “ghosts” are caused by reflection of the television waves from the metal airplane surface. Thus the reflected waves arrive at the television receivers at a slightly different time than the ordinary waves. The result is a dual image of the scene being transmitted. The image of the plane itself is not received.

According to British reports the displacement of the “ghost” image has been correlated with the distance of the plane away from the television receivers. A system has been worked out whereby television receivers on England’s eastern coast could thus serve as “spotters” for approaching enemy aircraft in time of war.

Whether the plan can be worked out in complete detail and serve a valuable military use is for the future to decide, but in principle the method is an almost exact counterpart of the system of determining airplane altitude by having the plane send down to the ground a beam of radio waves and then having the plane pick up the signals of the reflected waves. This method was announced by Dr. E. F. W. Alexanderson of the General Electric Company in 1928.

For the television case, in contrast, the waves go up, strike the plane, and are picked up by ground receivers. By multiple receivers and methods of triangulation it is believed the altitude of the plane and its approximate direction and distance could be worked out.

In another analogy the television spotting system for planes can be called “upside-down” geophysical prospecting. In geology, metallic masses are located by reflected radio waves.

Science News Letter, April 27, 1928

FIGURE 11-2 ■
Possibly the
First Published
Description of PBR
Using Television
Transmissions [9].

11.1.3 Applications

Passive bistatic radar has a number of obvious attractions. In common with all bistatic radars, the receiver is passive, and so it is potentially undetectable. This means it is immune to attack by antiradiation missiles (ARMs) and, because an adversary does not know the location of the receiver, any jamming must be nondirectional, which dilutes its effectiveness. Bistatic systems may offer a counterstealth advantage, since target shaping to reduce the monostatic radar cross section (RCS) of a target may not be effective in bistatic geometries. Bistatic radars may also be able to exploit the significant enhancement of a target RCS that occurs in forward scatter. PBR systems will often make use of VHF or UHF frequencies that are not normally available for radar use and where RCS reduction techniques may be less effective than at microwave frequencies, since target dimensions will often be of the same order as the radar wavelength. There are many illumination sources that can be used, many of them of high power and favorably sited, and the ever-greater congestion of the electromagnetic spectrum – which represents a problem for almost all radar applications – is actually an advantage for PBR. Finally, the receiver systems can often be rather simple and low cost, and there is no need for any license for the transmitter.

These factors, and particularly the latter two, have meant that PBR has been an ideal subject for research by university labs, and many such systems have been built and demonstrated. Despite this, there have been rather few examples where PBR systems have been able to offer a clear advantage over conventional radar approaches. Notable exceptions to this include low-cost scientific measurements of the ionosphere [17, 18], planets [19], wind [20, 21], and thunderstorms [22]. PBR has also been proposed as a “gap filler” where coverage of conventional air surveillance radars is compromised – for example, by wind turbines [23]. Two examples of commercially available PBR systems are Lockheed Martin’s Silent Sentry [24] and THALES’s Homeland Alerter [25]. Nevertheless, the challenge to PBR systems remains to identify and exploit applications where there is a clear advantage – in terms of performance or cost or both.

11.1.4 Objective, Scope, and Structure of Chapter

The objective of this chapter is therefore to describe the principles of PBR, highlighting the particular issues that come from using a waveform that is not explicitly designed for radar purposes and the processing techniques that need to be used. Section 11.2 provides a brief review of the properties of bistatic radar; Section 11.3 then reviews the properties of various types of waveforms that may be used for PBR, and Section 11.4 describes the signal environment. Section 11.5 describes specific processing techniques used in PBR, and Section 11.6 provides examples of a number of current systems, showing in each case the system architecture and examples of results. Finally, Section 11.7 draws some conclusions, particularly in respect to the challenges identified in this introduction. The following is a list of symbols and abbreviations used in this chapter.

11.1.4.1 Principal Symbols

A	target silhouette area
A_R	radial component of target acceleration
B	receiver effective bandwidth

d	target linear dimension
F	receiver effective noise figure
F_t	pattern propagation factor for transmitter-to-target path
f_D	Doppler shift of received echo
G_p	processing gain
G_r	receive antenna gain
G_t	transmit antenna gain
\mathbf{h}^T	vector of state equations
k	Boltzmann's constant (1.38×10^{-23} J/K)
$\mathbf{K}(t_n)$	Kalman gain
L	bistatic baseline
$\mathbf{M}(t_n)$	linearized measurement matrix
P_d	direct signal power
P_n	receiver noise power
P_r	received target signal power
P_t	transmit power
\mathbf{P}'_x	covariance of state prediction
\mathbf{P}_x	covariance of smoothed estimate
R_T	transmitter-to-target range
R_R	target-to-receiver range
$s(t)$	transmitted signal
T	update interval
T_0	noise reference temperature, 290 K
T_R	range delay
v	target velocity
(x_0, y_0)	target location
\mathbf{z}^T	vector of measurements
β	bistatic angle
δ	angle of target velocity with respect to bistatic bisector
θ_R	angle of arrival of received echo
λ	wavelength
σ_b	target bistatic radar cross section
σ_{FS}	forward scatter radar cross section
Φ	power density at target
$\Phi(t_n)$	linearized state equations
ψ	output of matched filter

11.1.4.2 Commonly Used Acronyms in This Chapter

AM	amplitude modulation
ARM	antiradiation missile

BBC	British Broadcasting Corporation
CAF	cross-ambiguity function
CDMA	code division multiple access
DAB	digital audio broadcasting
DBS	direct broadcast satellite
DOA	direction of arrival
DRM	Digital Radio Mondiale
DSI	direct signal interference
DSSS	direct sequence spread spectrum
DVB	digital video broadcasting
EIRP	effective isotropic radiated power
ESA	European Space Agency
FDMA	frequency division multiple access
FM	frequency modulation
GLONASS	GLObalnaya NAVigatsionnaya Sputnikovaya Sistema
GMSK	Gaussian minimum-shift keying
GNSS	global navigation satellite systems
GPS	Global Positioning System
GSM	Groupe Spéciale Mobile; Global System for Mobile Communications
LAN	local area network
LEO	low-Earth orbit
MAN	metropolitan area network
NTSC	National Television System Committee
OFDM	orthogonal frequency-division multiplexing
OVSF	orthogonal variable spreading factor
PAL	phase alternating line
PBR	passive bistatic radar
QAM	quadrature amplitude modulation
QPSK	quadrature phase-shift keying
RCS	radar cross section
SAR	synthetic aperture radar
SECAM	Séquentiel Couleur à Mémoire
SNR	signal-to-noise ratio
TDMA	time-division multiple access
UHF	ultrahigh frequency
UMTS	Universal Mobile Telecommunication System
VHF	very-high frequency
WiMAX	Worldwide Interoperability for Microwave Access

11.2 | BISTATIC RADAR

11.2.1 Bistatic and Multistatic Radar Geometry

Figure 11-3 shows the basic bistatic geometry [26]. The transmitter and receiver are separated by the baseline L . The angle subtended at the target by the transmitter and receiver is the bistatic angle, β . There are essentially three parameters that the bistatic receiver may measure: (1) the difference in range ($R_T + R_R - L$) between the direct signal and the transmitter–target–receiver path, (2) the angle of arrival θ_R of the received echo, and (3) the Doppler shift f_D of the received echo.

Contours of constant bistatic range ($R_T + R_R$) define an ellipse, with the transmitter and receiver at the two foci. If L is known, then the range sum ($R_T + R_R$) can be extracted from the observable quantity ($R_T + R_R - L$). If θ_R is measured, then the range of the target from the receiver may be found from

$$R_R = \frac{(R_T + R_R)^2 - L^2}{2(R_T + R_R + L \sin \theta_R)} \quad (11.1)$$

In the general case when transmitter, target and receiver are all moving, the Doppler shift on the echo is obtained from the rate of change of the transmitter–target–receiver path. If the transmitter and receiver are stationary, then the Doppler shift on the received echo is given by

$$f_D = \frac{2v}{\lambda} \cos \delta \cos (\beta/2) \quad (11.2)$$

where

v = target velocity and

δ = angle of the velocity with respect to the bisector of the bistatic angle β .

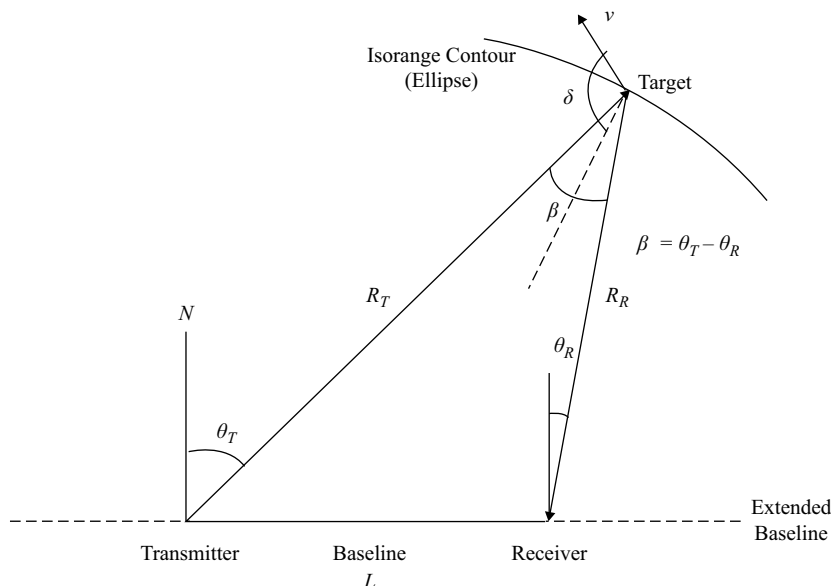


FIGURE 11-3 ■ Bistatic Radar Geometry: The Target Velocity Is v , Making an Angle δ with the Bisector of the Bistatic Angle β .

It can be seen that, if the target is crossing the bistatic baseline, then $\beta = 180^\circ$ and $f_D = 0$, no matter what the direction or magnitude of v . Physically this can be understood because at this point the transmitter-to-target range is changing in an equal and opposite way to the target-to-receiver range.

11.2.2 Radar Equation

The starting point for an analysis of the performance of a passive bistatic radar system is the basic form of the bistatic radar equation [27]:

$$\frac{P_r}{P_n} = \frac{P_t G_t}{4\pi R_T^2} \cdot \sigma_b \cdot \frac{1}{4\pi R_R^2} \cdot \frac{G_r \lambda^2}{4\pi} \cdot \frac{1}{kT_0 BF} \quad (11.3)$$

where

P_r = received signal power

P_n = receiver noise power

P_t = transmit power

G_t = transmit antenna gain

R_T = transmitter-to-target range

σ_b = target bistatic radar cross section

R_R = target-to-receiver range

G_r = receive antenna gain

λ = signal wavelength

k = Boltzmann's constant

T_0 = noise reference temperature, 290 K

B = receiver effective bandwidth

F = receiver effective noise figure

The factor $\left(\frac{1}{R_T^2 R_R^2}\right)$ in (11.3) means that the signal-to-noise ratio (SNR) has a minimum value for $R_T = R_R$ and is greatest when the target is either close to the transmitter or close to the receiver. Contours of constant values of $\left(\frac{1}{R_T^2 R_R^2}\right)$, and hence of SNR, define geometric figures known as *ovals of Cassini* [26].

The basic equation (11.3) is modified by the inclusion of losses, the pattern propagation factors on the transmitter-to-target and target-to-receiver paths, and appropriate integration gain. The noise figures of receivers at VHF and UHF will be of the order of a few dB at most, so the noise level will be dominated by external noise, most likely in the form of the direct signal, multipath, and other co-channel signals. Unless steps are taken to suppress these signals, the sensitivity and dynamic range of the system will be severely limited. This is considered in more detail in Section 11.4.

11.2.3 Target Signatures

Rather little has appeared in the unclassified literature on the bistatic signatures of targets [28]. In general, the bistatic RCS of a given target will not be the same as its monostatic RCS, though the values may be comparable for a nonstealthy target. Early in

the history of bistatic radar, the *bistatic equivalence theorem* [29] was put forward. This states that the bistatic RCS of a given target at a bistatic angle β is equivalent to the monostatic RCS measured at the bisector of the bistatic angle, reduced in frequency by the factor $\cos(\beta/2)$, provided that: (1) the target is sufficiently smooth, (2) there is no shadowing of one part of the target by another, and (3) retroreflectors persist as a function of angle. In practice, these conditions are not always met, so the theorem should be used with care.

Many practical targets will include dihedral and trihedral features that will result in a high-monostatic RCS but a reduced bistatic RCS. Measurements of the RCS of some ship targets as a function of bistatic angle [30] illustrate this. For the same reason, glint phenomena may be substantially reduced in bistatic geometries.

Three mechanisms have been put forward that enhance the bistatic RCS of a target: (1) resonant scatter, (2) specular scatter, and (3) forward scatter. The first two of these are also effective in monostatic geometries.

Resonant scatter occurs when physical dimensions of the target (such as the length of an engine, or the distance between nose and wing root of an aircraft) correspond to the multiples of half of the radar wavelength, and it can also be understood with reference to the classical frequency dependence of scattering from a conducting sphere. Such effects will be dependent on both frequency and target aspect.

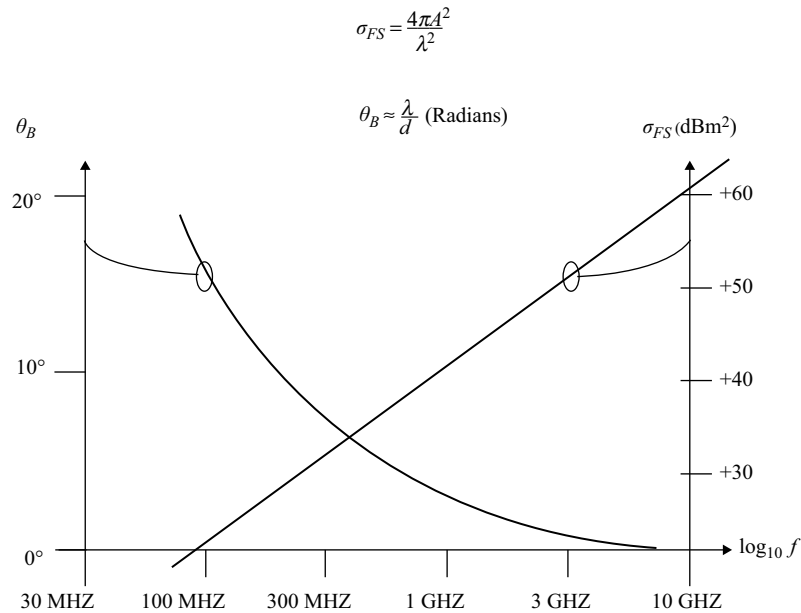
Specular scattering will occur if the target possesses flat features that happen to be oriented to give a specular reflection. However, such scattering depends on the specular condition being met, so it will be ephemeral in nature.

Forward scatter occurs when the target lies on or close to the baseline between the transmitter and receiver. According to Babinet's principle [31], the signal diffracted around a target of a given silhouette area will be equal and opposite to that diffracted through an equivalent target-shaped hole in an infinite screen perpendicular to the path between transmitter and receiver. The signal diffracted through an aperture of a given shape and area can be readily calculated, allowing the forward scatter RCS to be determined directly. For a target of silhouette area A and linear dimension d , the forward scatter RCS is approximately $\sigma_{FS} = \frac{4\pi A^2}{\lambda^2}$, and the angular width of the forward scatter is approximately $\frac{\lambda}{d}$ radians. These are plotted in Figure 11-4 for a target for which $A = 10 \text{ m}^2$ and $d = 10 \text{ m}$ (a medium-sized aircraft), and it can be seen that the forward-scatter RCS can be substantially greater than the equivalent monostatic RCS (which might be of the order of 10 m^2). However, it can be appreciated that while this geometry may give good detection performance, the target-location capability will be poor, since the range and Doppler resolution will both be poor when the target is near the baseline. This point is developed further in the next sections, which consider the bistatic ambiguity function.

11.2.4 Ambiguity Function for Bistatic Radar

Range and Doppler resolution are fundamentally important parameters in the design of any radar system as they govern the ability to distinguish between two or more targets by virtue of spatial or frequency (i.e., radial velocity) differences. The classical way of evaluating the behavior of a waveform for radar purposes is the *ambiguity function*, originated by Woodward in the 1950s [32]. This plots the resolution, the sidelobe levels, and the position and level of ambiguities, in both range and Doppler. In the case of PBR, the waveform and location and direction of its transmission are not under the control of the radar designer and may even be derived from a number of differing transmissions

FIGURE 11-4 ■
Forward Scatter RCS
 σ_{FS} and Angular
Width of Scatter θ_B
for an Idealized
Medium Aircraft
Target with
 $A = 10 \text{ m}^2$ and
 $d = 10 \text{ m}$.



and transmitters. The range and Doppler resolution is computed by match filtering the directly received transmitter signal. In a PBR system, this is the signal used to provide a “reference” waveform for correlation with the indirect target scattering. We term this the *self-ambiguity function* as it does not take into account the relative positions of the target, transmitter, and receiver and effectively mimics a monostatic geometry. This enables the best achievable resolutions to be evaluated and the time-varying properties to be investigated. These have an important bearing on overall range and Doppler resolution, as will be seen later.

The ambiguity function represents the output of a matched filter and may be written as

$$|\psi(T_R, f_d)|^2 = \left| \int_{-\infty}^{\infty} s_t(t) s_t^*(t + T_R) \exp[j2\pi f_d t] dt \right|^2 \quad (11.4)$$

where

$\psi(T_R, f_d)$ = ambiguity response at delay range T_R and Doppler f_d and
 $s(t)$ = directly received transmitted signal.

Computation of this function results in a three-dimensional plot for which one axis is time delay (or range), the second is Doppler frequency or radial velocity, and the third is the output power of the matched filter (usually normalized to unity and plotted either in linear form or in dB). The width of the ambiguity function peak in the T_R and the f_d dimensions determines the range and Doppler resolutions, respectively. As we are using the directly received signal only, we term this *self-ambiguity* as there is no inclusion of any system geometry dependence on the transmitter and receiver locations. Examples of the ambiguity function for a variety of candidate waveforms for PBR systems are demonstrated in Section 11.3.

In PBR, and more generally in bistatic radar, the relative positions of target, transmitter, and receiver govern the actual resolutions that can be achieved. Here we use the formulation derived by Tsao *et al.* [33] to compute the bistatic ambiguity function:

$$|\psi(R_{RH}, R_{Ra}, V_H, V_a, \theta_R, L)|^2 = \left| \int_{-\infty}^{\infty} s_t(t - \tau_a(R_{Ra}, \theta_R, L)) s_t^*(t + \tau_R(R_{RH}, \theta_R, L)) \times \exp[j2\pi f_{DH}(R_{RH}, V_H, \theta_R, L) - 2\pi f_{Da}(R_{Ra}, V_a, \theta_R, L)t] dt \right|^2 \quad (11.5)$$

where

R_{RH} and R_{Ra} = hypothesized and actual ranges (delays) from the receiver to the target,

V_H and V_a = hypothesized and actual target radial velocities with respect to the receiver,

f_{DH} and f_{Da} = hypothesized and actual Doppler frequencies, and

θ_R and L are as defined in Figure 11-3.

The expression assumes the reference point of the PBR geometry to be the receiver and is essentially a straight change of variables in (11.4). The important difference is that the geometrical layout of the transmitter, receiver, and target are now taken into account. This can have a significant effect on the form of the ambiguity function and hence on the resulting range and Doppler resolutions. The ambiguity function can lose all range and Doppler resolution if a target is on or close to the transmitter–receiver baseline. For targets at long ranges the form of the ambiguity diagram is much like that for the monostatic case. These cases represent the two extremes and practical cases lie in between the two. This needs to be carefully taken into account when determining the full performance of any candidate system design.

11.3 | PASSIVE BISTATIC RADAR WAVEFORMS

Quite evidently, PBR depends upon the use of waveforms that are not explicitly designed for radar purposes. It is therefore necessary to understand the effect of the waveform on the performance of the passive bistatic radar, so as to be able to choose the most appropriate illuminator and to process the waveform in the optimal way [34]. In this sense, PBR forms part of the subject of waveform diversity [35].

In the case of waveforms used for PBR, we will also be concerned with the way in which those quantities vary with the waveform as a function of time. In addition, though, it has been shown in the previous section that for bistatic radar the ambiguity performance depends not only on the waveform but also on the bistatic geometry, so that for targets close to the bistatic baseline the resolution in both range and Doppler will be very poor, no matter what the waveform. In what follows, the performance is presented in terms of the conventional ambiguity function, and the additional effects of the bistatic geometry must be added on top of these.

In this section, we look at a number of different types of waveform. In addition to the properties of the waveform, we also need to be concerned with the power density at the target and the temporal and spatial coverage of the illuminator.

11.3.1 VHF FM

VHF FM signals have been quite extensively used as a PBR illumination source. Almost all countries have a network of FM broadcast stations in the VHF band from 88 to 108 MHz, though in many the process has begun of switching over to digital (DAB) transmissions. VHF FM signals use broadband frequency modulation with a bandwidth of order 50 kHz, which corresponds to a monostatic range resolution of 3 km. The effective isotropic radiated power (EIRP) may be as high as 250 kW, and, of course, the transmitters are generally sited on high points to give wide coverage.

The power density Φ (in W m^{-2}) at a target at range R_T can easily be evaluated:

$$\Phi = \frac{P_t G_t}{4\pi R_T^2} F_t^2 \quad (11.6)$$

where F_t is the pattern propagation factor for the transmitter-to-target path. For $P_t G_t = 250$ kW, $R_T = 100$ km, and $F_t = 1$ (free-space propagation), this equates to $\Phi = -57$ dBW/m².

The ambiguity performance of broadcast and communications signals have been evaluated by several authors [36, 37] by capturing off-air samples of different transmissions and computing and plotting the ambiguity functions. In the following examples, a spectrum analyzer in zero-scan mode was used with a digitizer card connected to its IF output, giving a highly versatile and linear receiver testbed.

Figure 11-5(a) shows the ambiguity function for speech modulation (BBC Radio 4, 93.5 MHz), while Figure 11-5(b) shows the ambiguity function for fast-tempo jazz music (Jazz FM, 102.2 MHz). It can be seen that the ambiguity functions are quite different. In Figure 11-5(b), the broader spectral content of the modulation means that the peak of the ambiguity function is narrower, and the sidelobe structure also has greater high-frequency content for the same reason, though the sidelobe levels in the two cases are comparable. Furthermore, it is found that the ambiguity performance is time varying, since during pauses between words or passages of music the ambiguity function is very broad and the range resolution consequently very poor, and it depends on the program content, so (for example) a cacophony of rock music is likely to be better for PBR purposes than speech or music from a solo instrument.

11.3.2 Analog TV

The majority of analog television transmissions lie in the UHF band around 500–600 MHz. Some countries also use VHF bands for television. As with audio broadcasting, many countries are in the process of decommissioning their analog TV transmissions and switching over to digital TV (DVB), and in the United States this conversion has already happened.

As with VHF FM transmissions, analog TV transmitters use high power and are sited to give excellent coverage. The EIRP may be as high as 1 MW, which corresponds to a power density at a range of 100 km of $\Phi = -51$ dBW/m².

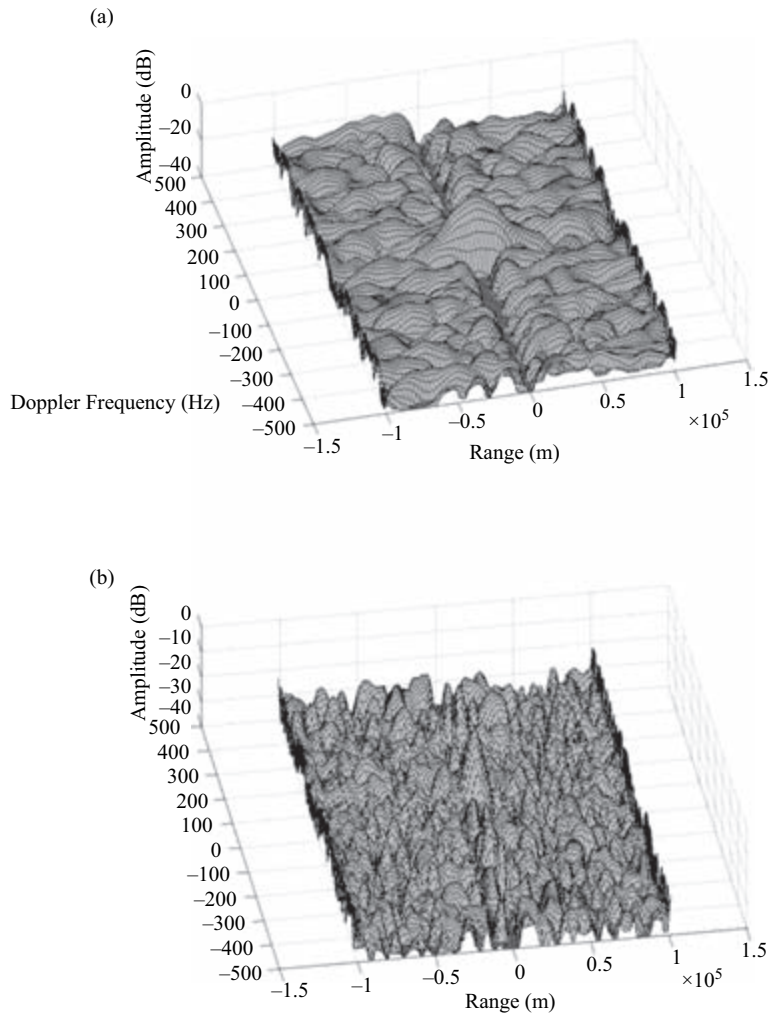


FIGURE 11-5 ■ Typical Off-Air Ambiguity Functions from (a) Speech (BBC Radio 4) and (b) Fast-Tempo Jazz Music (Jazz FM).

In the United Kingdom, the phase alternating line (PAL) modulation format is used in which the video information is coded as two interlaced scans of a total of 625 lines at a frame rate of 50 Hz. The start of each line is marked with a sync pulse, and the total duration of each line is 64 μ s. The video information is modulated onto a carrier as vestigial-sideband AM, coded as *luminance* (red + green + blue) and two *chrominance* signals (green – blue) and (red – blue). The two chrominance subcarriers are in phase quadrature so that they can be separately recovered. The sound information (including stereo information) is frequency modulated onto a second carrier. Variants of this basic scheme are used in different countries; in the United States, the NTSC (National Television System Committee) format was used; and in France and Eastern Europe, the SECAM (Séquentiel Couleur à Mémoire) format.

Figure 11-6 shows the measured spectrum of a PAL analog TV signal (right-hand side) and the corresponding digital TV signal (left-hand side). The different components of the analog signal spectrum are identified: The picture information is transmitted as vestigial-sideband AM. The color information is modulated onto the chrominance subcarrier, and the sound information is modulated both in analog and digital form.

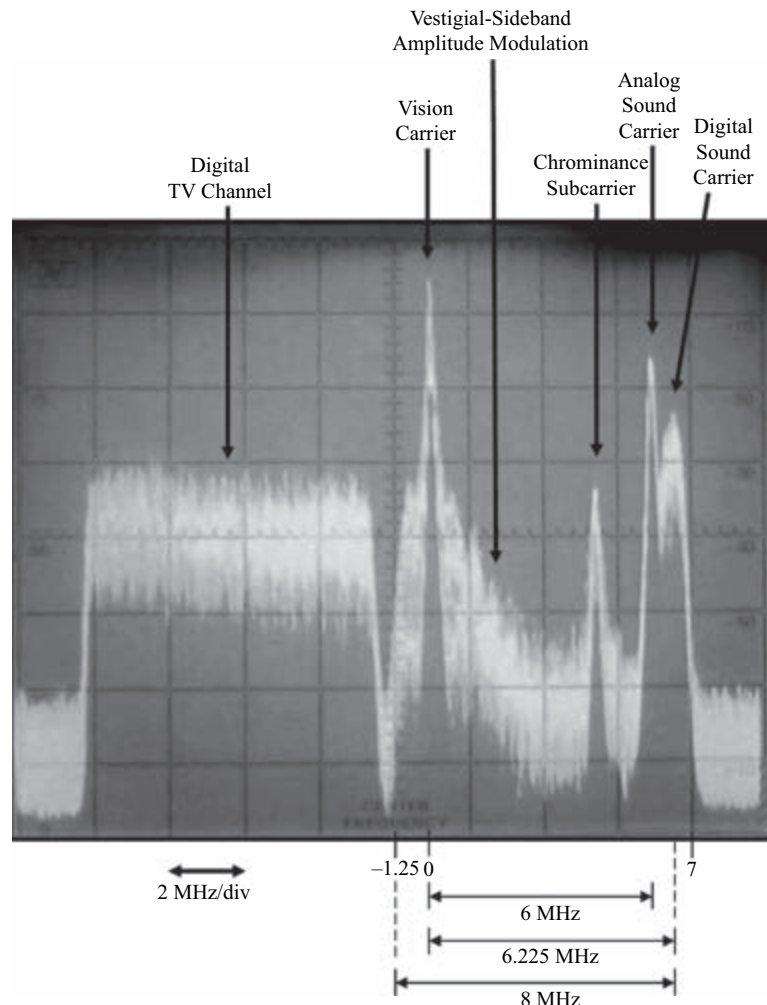
The picture is transmitted as successive 64- μ s lines with a sync pulse at the beginning of each line; this means that there are pronounced range ambiguities, corresponding to a bistatic range of 9.6 km. There are also ambiguities corresponding to the frame repetition rate of 50 Hz. The range resolution corresponding to the full signal bandwidth (5.5 MHz) is 30 m, which is substantially better than that of VHF FM.

11.3.3 Digital Radio/TV

In recent years, digital radio (DAB) and television (DVB) have been introduced in many countries. These transmissions use coded orthogonal frequency-division multiplex (COFDM) modulation in which all transmitters for a given station use the same frequency (so-called single-frequency networks). This provides much more efficient use of the spectrum and the ability to reject multipath.

In COFDM, the information is transmitted in synchronized frames [38]. Each frame contains a large number of orthogonally coded subcarriers that carry the modulation information. The receiver samples each frame only after a guard interval delay that has a

FIGURE 11-6 ■ Spectrum of Typical PAL Analog TV Signal (Right of Center) and Digital TV Signal (Left of Center): Horizontal Scale 501–521 MHz, Vertical Scale 10 dB/Division.



duration greater than the maximum delay of the propagation path. This means that any multipath or signal from another co-channel transmitter will be stationary. Poullin [39] gives typical parameters of a DAB modulation scheme as follows:

- symbols of 1-ms useful duration with a guard interval of 0.246 ms,
- 1,536 subcarriers transmitted simultaneously per symbol,
- quadrature phase shift keying (QPSK) modulation for each subcarrier,
- symbols are organized into frames of 77 symbols,
- the first symbol is null (with no frequency transmitted or only the center frequency), and
- the second symbol is a reference, where all the subcarriers are transmitted with reference code elements. This symbol is used for the propagation channel estimation, and hence equalization.

Since this type of modulation is more noiselike and does not show the same dependence on program content or variability with time as FM radio, it has potentially favorable PBR properties. Offsetting this advantage is the lower radiated power for DAB transmitters, which at about 1 kW is significantly less than the equivalent VHF FM transmissions.

11.3.4 Cell Phone (GSM, 3G)

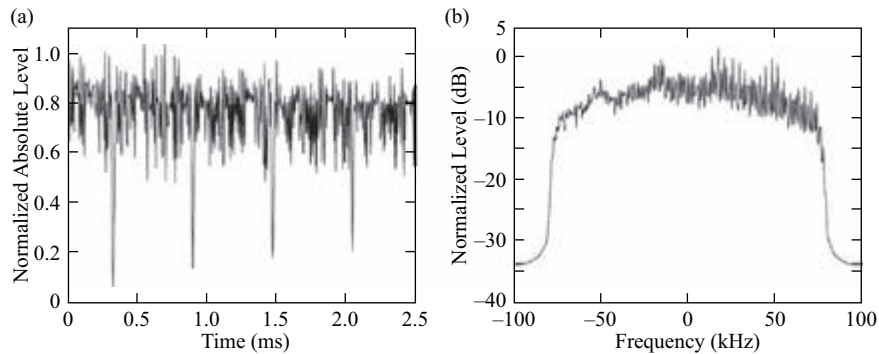
Another type of transmission that has been used as an illumination source for PBR is the cell-phone base station. These are ubiquitous in almost all countries, and although the transmit power is somewhat lower than for radio or television transmitters (from a few watts up to a maximum of perhaps 100 W) their separation is sufficiently close, particularly in cities, as to give good reception at a mobile receiver practically anywhere.

The GSM system uses bands centered on 900 MHz and 1.8 GHz, with 1.9 GHz used in the United States. The uplink and downlink bands are each of 25 MHz bandwidth split into 125 FDMA (frequency division multiple access) carriers spaced by 200 kHz. A given base station will use only a small number of these channels. Each of these carriers is divided into eight time-division multiple access (TDMA) time slots, with each time slot 577 μ s in duration. Each carrier is modulated with Gaussian minimum-shift keying (GMSK) modulation. A single bit corresponds to 3.692 μ s, giving a modulation rate of 270.833 kbits/s. Figures 11.7(a) and 11.7(b) show time-domain and frequency-domain representations of these signals.

The third-generation (3G) system uses a band in the region of 2 GHz. The Universal Mobile Telecommunication System (UMTS) is the main implementation of 3G and has the following characteristics [41].

- It uses two forms: frequency-division duplex (FDD) and time-division duplex (TDD). FDD requires two frequency bands – one for the uplink and one for the downlink; TDD requires a single band. A given band (or pair of bands) is allocated to a particular operator.
- FDD and TDD bands are of 5-MHz nominal width/channel spacing.
- The transmission is wideband CDMA (WCDMA) using Walsh–Hadamard coding. The transmission rate is 3.84 Mchips/s.

FIGURE 11-7 ■
 (a) Time-Domain Representation of Part of One TDMA-Modulated Carrier, Showing the 577- μ s Slots; (b) Frequency-Domain Representation, Showing the 200-kHz Channel [after Tan *et al.* [40]].



- The modulation used is QPSK. The null-to-null bandwidth is effectively 3.84 MHz, hence the 4.4-MHz minimum channel spacing. The signals are shaped with a 0.2 root-raised cosine filter.

The choice of frequency band for UMTS in Europe and Asia is consistent, but in the United States these bands were not available. At the World Radio Conference in Istanbul, Turkey, in May 2000, three bands were suggested for the implementation of UMTS in the United States: 806–890 MHz (used for cellular and other mobile services), 1,710–1,885 MHz (used by the Department of Defense), and 2,500–2,960 MHz (used commercially for instructional TV and for wireless data providers). However, the fact that these bands are already used for other purposes led to further consultation; as a result, 45 MHz of bandwidth in the 1,710–1,755 MHz band and 45 MHz of bandwidth in the 2,110–2,170 MHz were to be made available for 3G services.

The radiation patterns of cell-phone base station antennas are typically arranged in 120° sectors, with the vertical-plane radiation pattern shaped to avoid wasting power above the horizontal. Future trends will be in the direction of greater numbers of base stations, with lower transmit powers and the use of “smart antennas.”

Figure 11-8 shows typical ambiguity functions for three digital PBR transmissions: DAB, DBV-TV, and GSM. These functions are more favorable for PBR purposes than signals with analog modulation (Figure 11-5), since the peak of the ambiguity function is narrower and the sidelobes are lower. Also, they are much more constant with time.

11.3.5 WiFi and WiMAX

Another class of signal that has received considerable attention for short-range surveillance using PBR are the wireless transmissions for wireless fidelity (WiFi) local area networks (LANs) (IEEE Std 802.11 [42, 43, 44]) – and WiMAX metropolitan area networks (MANs) (IEEE Std 802.16 [45, 46, 47]). The WiFi standard is intended for indoor use and may therefore be suitable for surveillance within buildings for security purposes; the WiMAX standard provides broader coverage (up to several tens of km), so it may be useful for applications such as port or harbor surveillance. These applications are discussed more fully in Section 11.6.

Either direct sequence spread spectrum (DSSS) or orthogonal frequency division multiplexing (OFDM) are used within the overall IEEE 802.11 WiFi standard. Both 802.11b and 802.11g operate in the 2.4-GHz band, while 802.11a uses the 5-GHz band.

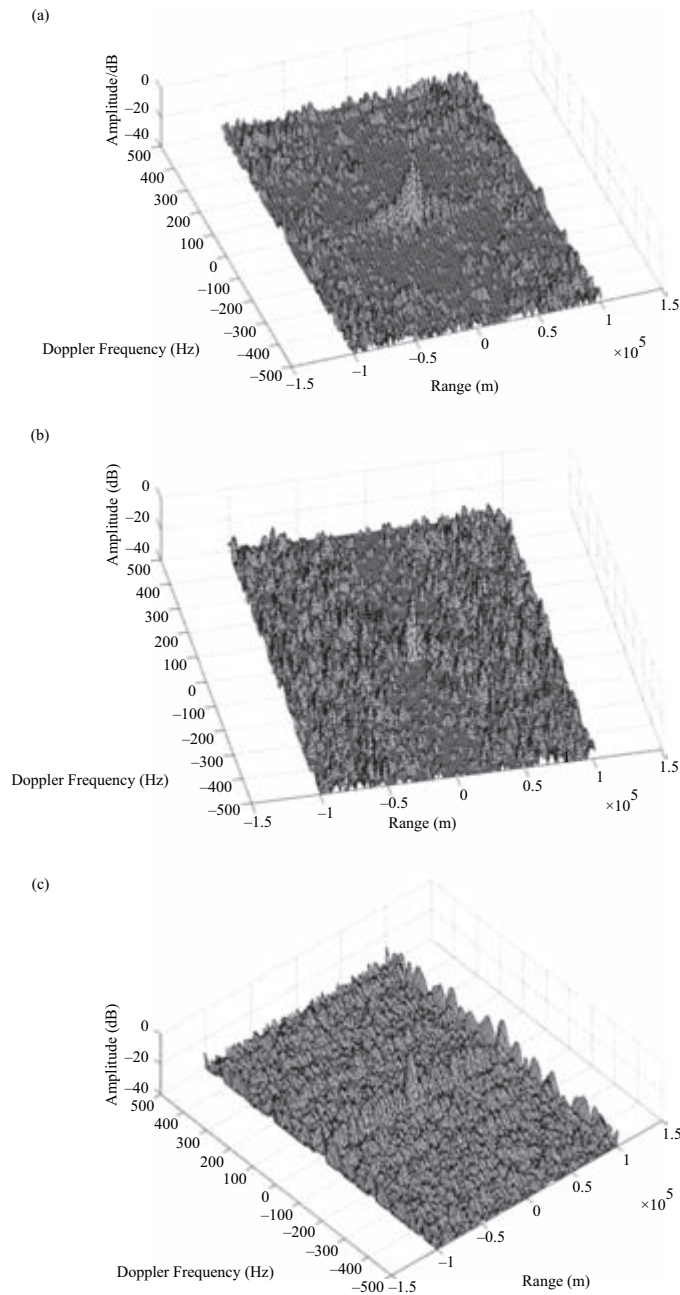
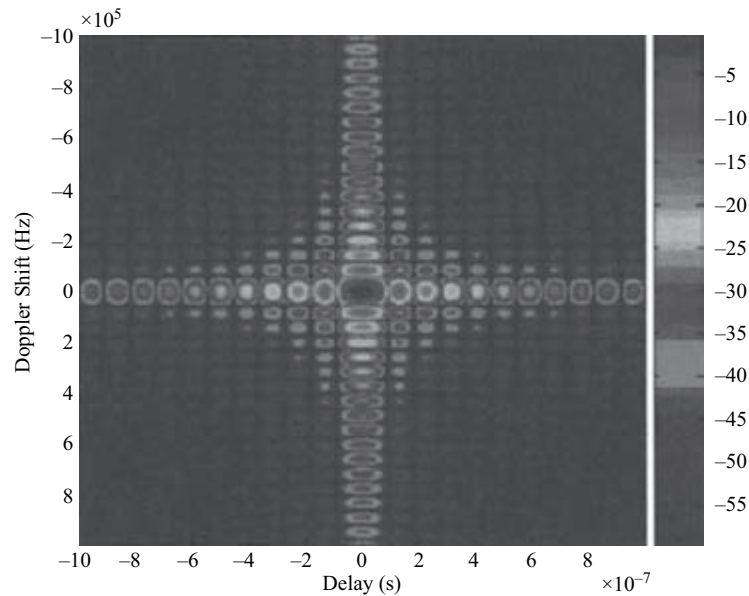


FIGURE 11-8 ■ Ambiguity Functions for Three Digital PBR Transmissions: (a) Digital Audio Broadcast (DAB) at 222.4 MHz; (b) Digital Video Broadcast (Terrestrial DBV-T) at 505 MHz; (c) GSM900 at 944.6 MHz.

The transmitters tend to use dynamic power management according to the number of users, but a maximum value for the transmit power might be 100 mW.

A typical ambiguity function, showing cuts at zero range and zero Doppler, is given in Figure 11-9. It can be seen that the ambiguity function is well behaved. The range resolution is of the order of 30 m, which is rather coarse for indoor applications, but the Doppler resolution can be quite good, particularly if long integration times are used, suggesting that micro-Doppler information on echoes from moving targets, such as walking humans, may be extracted and exploited.

FIGURE 11-9 ■ Ambiguity Function for WiFi 802.11b Preamble/Header Signal and Cuts at Zero Range and Zero Doppler [42].



The 802.16 WiMAX standards allow for fixed, portable, and mobile broadband access in a number of different bands, including 2.3 GHz, 2.5 GHz, 3.3 GHz, and 3.5 GHz. They also use orthogonal frequency division multiple access (OFDMA) modulation, with bandwidths ranging from 1.25 to 20 MHz. A maximum value for the transmit power might be 20 W. Several groups have examined the use of these signals as PBR sources [45, 46, 47] and concluded that they offer significant potential. Four examples of measured ambiguity functions are shown in Figure 11-10.

11.3.6 HF

HF (short-wave) broadcasting is another class of transmission that has been used since the 1960s for PBR illumination. A new, very-high-power type of HF broadcast signal is the Digital Radio Mondiale (DRM) format, which is of particular interest to PBR. In DRM, the digitized audio stream is source coded using a combination of advanced audio coding (AAC) and spectral band replication (SBR) to reduce the data rate before time-division multiplexing with two data streams (which are required for decoding at the receiver). A coded OFDM channel-coding scheme is then applied, nominally with 200

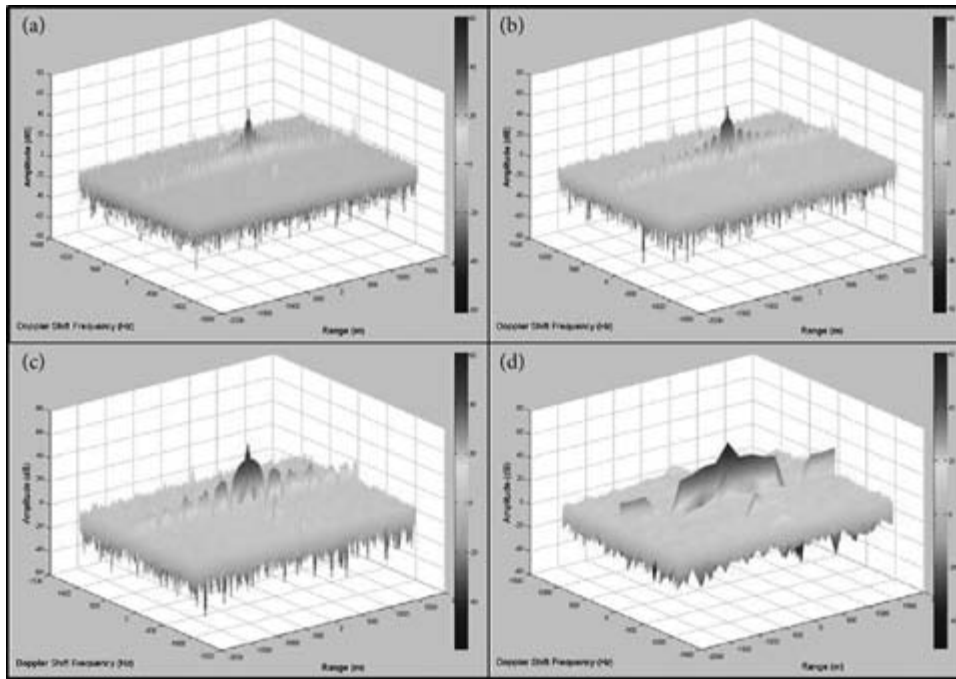


FIGURE 11-10 ■ Four Examples of Self-Ambiguity Plots of WIMAX Waveforms [47].

subcarriers and a quadrature amplitude modulation (QAM) mapping of these subcarriers is used to transmit the encoded data. The effective bandwidth is 10 kHz. This scheme is designed to combat channel fading, multipath, and Doppler spread, enabling reception of data in the most demanding of propagation environments [48].

11.3.7 Spaceborne Illuminators

The final class of illuminator to be considered are those from spaceborne platforms. These are classified first in terms of the satellite orbit and second in terms of the waveform. Satellites in geostationary orbit – a height of 36,000 km above the equator – provide relatively weak signals at Earth’s surface, but because the illuminator is effectively stationary, long integration times may be used. On the other hand, satellites in low-Earth orbit (LEO) are much closer to the target scene but are moving rapidly with respect to the target scene and so have limited integration time. However, the moving transmit source may allow the use of synthetic aperture techniques. The revisit time will depend on the particular orbit of the satellite. The waveforms may be associated with radar, radionavigation, or communications.

The following briefly reviews the properties of some spaceborne illuminators of opportunity.

11.3.7.1 GNSS

The GPS constellation of satellites can be used as illuminators for PBR, and the same is true of the Russian GLONASS (GLObalnaya NAVigatsionnaya Sputnikovaya Sistema) and the European Galileo systems, all of which operate in L-band. The GPS system consists of 24 satellites in six orbital planes at an orbit height of 20,200 km and uses CDMA modulation (GLONASS uses FDMA) with bandwidths between 1 MHz and 10 MHz. The power density on Earth’s surface depends on the elevation of the satellite

but is of the order of -134 dBW/m². The Galileo system has more favorable parameters, both in terms of bandwidth (and hence range resolution) and power level.

11.3.7.2 DBS TV

Satellite television (DBS TV) transmissions, in Ku-band (11–12 GHz) from geostationary orbit, provide a sufficient power density at Earth's surface to give an adequate signal-to-noise ratio with a small aperture antenna. The radiation patterns of the transmit antennas are shaped so as to give coverage of specific land areas, which means that the coverage of ocean areas is poor. The modulation may be either analog or digital (including high-definition digital television, or HDTV), with bandwidths up to several MHz. Although the power density is low in comparison with other sources, the geostationary satellite orbit means that long integration times can be used [49].

11.3.7.3 Maritime Communications (Inmarsat)

The Inmarsat service provides communications with ships and aircraft from satellites in geostationary orbit. The latest generation (Inmarsat-4) consists of three identical satellites. The downlink is at L-band, with 630 channels each of 200-kHz bandwidth (432 kbps), 228 spot beams, and an EIRP of +67 dBW. This is typical of satellite communications systems, and these could in principle also be used as illuminators for PBR purposes.

11.3.7.4 Low-Earth Orbit Synthetic Aperture Radar (SAR)

Several space Agencies have built and flown spaceborne SAR systems for Earth observation. These include NASA (SEASAT, SIR-A, SIR-B, SIR-C, etc.), the European Space Agency (ERS-1, ERS-2, and ENVISAT) and the Canadian Space Agency (RADARSAT-1 and RADARSAT-2). The antenna radiation patterns and orbit-repeat patterns of such systems mean that the target scene is only illuminated for a matter of a second or so and the revisit time may be several days, but because the waveform is explicitly designed for radar purposes (usually linear FM chirp signals) and because the transmit power and antenna gain are high, the signals are very suitable for PBR, particularly for bistatic SAR. The ASAR instrument carried by the ESA's ENVISAT satellite launched in 2002 is typical of a modern remote-sensing SAR. It operates at 5.331 GHz and uses a 320-element electronically scanned array, 10 m × 1.3 m, with a 20- μ s pulse of up to 15 MHz bandwidth, a PRF of 1,650 to 2,100 Hz, and a swath width of up to 100 km. The orbit pattern is sun synchronous, 800-km mean altitude, in a one-, three-, or 35-day repeat cycle.

In addition to SARs, other types of satellite-borne radars include scatterometers and radar altimeters, though no attempts thus far have been made to exploit them as sources for PBR purposes.

11.3.8 Summary

To summarize, there is a wide variety of different types of source that might be used for PBR purposes (Table 11-1). The parameters that need to be taken into account in assessing their usefulness are (1) their power density at the target, (2) their coverage (both spatial and temporal), and (3) the nature of their waveform. In general, digital modulation schemes are found to be more suitable than analog, since their ambiguity function properties are better (since the modulation is more noiselike), they do not depend on the program material, and they do not vary with time.

TABLE 11-1 ■ Summary of Typical Parameters of PBR Illuminators of Opportunity

Transmission	Frequency	Modulation, bandwidth	$P_t G_t$	Power Density* $\phi = \frac{P_t G_t}{4\pi R_T^2}$
HF broadcast	10–30 MHz	DSB AM, 9 kHz	50 MW	–67 to –53 dBW/m ² at $R_T = 1,000$ km
VHF FM	88–108 MHz	FM, 50 kHz	250 kW	–57 dBW/m ² at $R_T = 100$ km
Analog TV	~550 MHz	PAL, SECAM, NTSC, 5.5 MHz	1 MW	–51 dBW/m ² at $R_T = 100$ km
DAB	~220 MHz	Digital, OFDM, 220 kHz	10 kW	–71 dBW/m ² at $R_T = 100$ km
Digital TV	~750 MHz	Digital, 6 MHz	8 kW	–71 dBW/m ² at $R_T = 100$ km
Cell-phone base station (GSM)	900 MHz, 1.8 GHz	GMSK, FDMA/TDMA/FDD 200 kHz	10 W	–81 dBW/m ² at $R_T = 10$ km
Cell-phone base station (3G)	2 GHz	CDMA, 5 MHz	10 W	–81 dBW/m ² at $R_T = 10$ km
WiFi 802.11	2.4 GHz	DSSS/OFDM, 5 MHz	100 mW	–41 dBW/m ² ‡ at $R_T = 10$ m
WiMAX 802.16	2.4 GHz	QAM, 20 MHz	20 W	–88 dBW/m ² at $R_T = 10$ km
GNSS	L-band	CDMA, FDMA 1–10 MHz	200 W	–134 dBW/m ² at Earth’s surface
DBS TV	Ku-band	Analog and digital	55 dBW	–107 dBW/m ² at Earth’s surface
Satellite SAR†	11–12 GHz 5.3 GHz	Chirp pulse, 15 MHz	68 MW	–55 dBW/m ² at Earth’s surface

*Assuming free space line-of-sight propagation.

†Would be subject to additional attenuation due to propagation through walls.

‡Parameters from ASAR instrument carried by ESA’s ENVISAT satellite.

11.4 | THE SIGNAL ENVIRONMENT

11.4.1 Direct Signal Interference

The majority of illuminators exploited by PBR systems are omnidirectional. Scattered radiation is used to survey a scene or zone of interest. Directly received radiation provides a reference signal for coherent operation in a separate receive channel. However, the directly received signal will also enter the surveillance channel and can therefore represent a fundamental source of undesirable interference that will provide a basic limit on radar performance. We can formulate a simple expression for the required amount of direct signal suppression by calculating the ratio of the indirect received signal to the direct signal and requiring this to be at least the same value used to compute the maximum detection range. We make the simple assumption that a target can be seen above this level of direct signal breakthrough and hence approximate to the highest level of interference that is tolerable for single “pulselike” detection. There is, however, no benefit from integration as the direct leakage will also integrate up, and this may mean that a more stringent requirement needs to be set in practice. This places the direct leakage signal at the same level as the noise floor in the receiver and hence it has the attractive feature of proving equivalent performance to “single-pulse” detection. Thus, to achieve adequate suppression and hence maintenance of full-system dynamic range, the direct signal P_d must be canceled by an amount given by the magnitude of the ratio of the indirect and directly received signals – for example

$$\frac{P_r}{P_d} = \frac{L^2 \sigma_b}{4\pi R_T^2 R_R^2} > 1 \quad (11.7)$$

This expression is indicative only, and has assumed that the transmit and receive antenna patterns are omnidirectional. More strictly, the direct signal should be below that of the noise floor after integration, if integration is employed.

Taking the numerical example of a television transmitter located at Crystal Palace in the south of London, a receiver located at University College London in the center of London, and the assumptions that a target is 10 m^2 and has a maximum detection range of 100 km, equates to a requirement for suppression of direct signal leakage of some 120 dB. Note that as the detection range is reduced from the maximum, the amount of direct signal breakthrough compared to the indirect signal will fall sharply. In addition, the leakage signal will be time varying and subjected to multiple scattering paths. This behavior requires a thorough and detailed understanding to optimize the performance of a given design.

11.4.2 Direct Signal Suppression

Several techniques can be used to suppress this leakage: (1) physical shielding, (2) Fourier processing, (3) high-gain antennas, (4) sidelobe cancellation, (5) adaptive beamforming, and (6) adaptive filtering. The combination of high-gain antennas and adaptive beamforming also enables multiple simultaneous transmissions to be exploited.

Physical shielding might include anything from buildings through to using local geography or synthetic material such as radar absorbing material (RAM). These might be used individually or collectively to achieve an acceptable level of suppression when combined with techniques 2 to 6. A typical design aim would be to suppress interference to below the noise floor of the receiver. This would fully mitigate the interference. However, in practice this is not always possible, and the level of suppression must be determined in order to understand the performance bounds of the system. Digital waveforms can offer greater suppression than their analog counterparts due to the form of their dynamic coding.

For the detection of moving targets, Doppler or Fourier processing will automatically improve dynamic range, as the direct signal leakage will only occur at DC (with some spill over). However it should be noted that significant sidelobe leakage due to very strong directly received signals not being adequately suppressed will reduce the gain from Fourier processing and hence impair dynamic range.

If a linear array rather than an omnidirectional antenna is used, then techniques 3 to 5 can all be taken advantage of. This allows the directional gain of the antenna to provide suppression via control of the sidelobes. If a fully digital antenna is employed, then adaptive beamforming can be used to minimize sensitivity in the direction of the location of the directly received signal. If external noise such as multipath is present, then multiple nulls have to be formed. If the external noise environment is nonstationary, the cancellation will need to be adaptive, with a suitably rapid response time. The number of degrees of freedom, and hence the number of antenna elements and receiver channels, must be greater than the number of signal components to be suppressed. The antenna pattern factor, the transmitter and receiver locations, and the target trajectory for a given scenario will lead to “blind zones.” These are caused either by a loss of line of sight between the transmitter, target, and receiver or when the target traverses the bistatic baseline between the transmitter and receiver.

It may also be useful (technique 6) to use a stage of analog cancellation to reduce the dynamic range requirement of subsequent digital cancellation. In either case,

standard adaptive filtering techniques can be used. We can say that a combination of techniques (e.g. physical screening, Doppler processing, and adaptive cancellation) may be required, and these should yield suitably high levels of suppression. However, the use of an array antenna and adaptive cancellation processing does mean that the receiving system is not as simple as might originally have been supposed. Examples of the adaptive suppression algorithms are given in [6] and [50].

11.4.3 Processing

A PBR receiver requires at least two channels: one for the reception from the area of interest (surveillance channel) and the other to receive signals directly from the transmitter of opportunity (reference channel), which provides a reference for correlation-based matched filtering. A block diagram of a typical PBR receiver system is shown in Figure 11-11. A PBR receiver with multiple surveillance channels is often used in more expensive PBRs for operation with array antennas; the additional channels provide extra degrees of freedom for beam steering and placing nulls in the direction of the direct path interference.

The disadvantage of employing an array antenna in a PBR system is that it adds significantly to system complexity and is contrary to one of the stated advantages of PBRs as being inexpensive. Generally, when array antennas are used the objective is to excite the array elements into steering a (narrow) beam in a desired direction. In PBR applications, a proportion of the array elements would necessarily be employed to create a broadband null in the direction of the transmitters of opportunity. Therefore, the PBR array performance would be more distributed (than a conventional beam-steering array) into (1) reducing the direct signal interference (DSI) by nulling and (2) steering a (narrower) beam toward the area under surveillance. FM radio-based PBR receivers generally take two forms. They can be based on the traditional superheterodyne receiver that down-converts the RF signal to a convenient intermediate frequency (IF) prior to sampling. Alternatively, the receiver configuration can be based on the direct RF sampling approach. PBRs based on the direct RF sampling method have simpler receiver architecture, require fewer RF components, and are therefore generally less expensive.

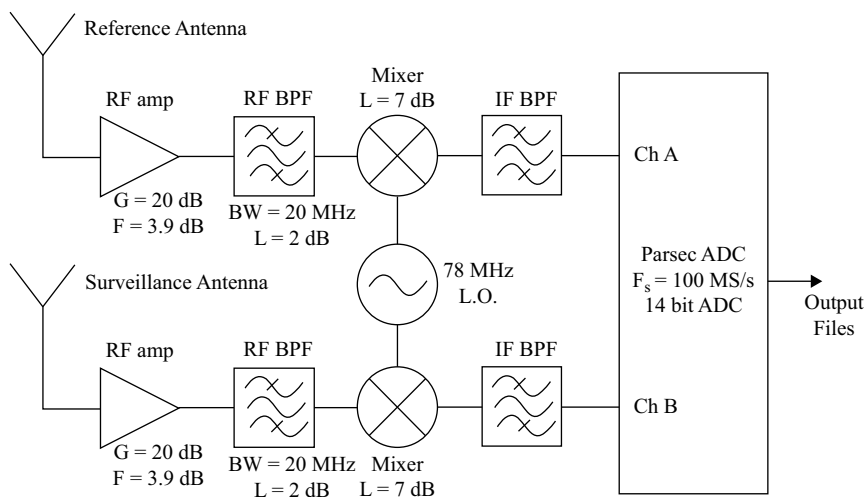


FIGURE 11-11 ■ Architecture of a Typical PBR Receiver.

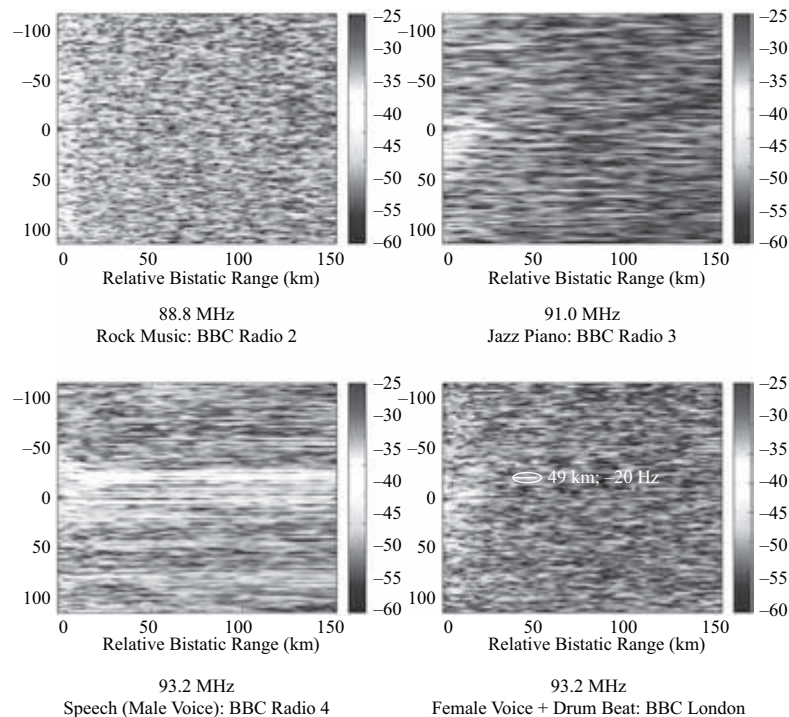
Both receiver types – the superheterodyne and the direct RF sampling receiver configurations – have been evaluated experimentally. As target detection relies on correlation-based matched filtering between the surveillance signal and a replica of the transmitted signal (reference signal), it is paramount that both the reference and surveillance channels are highly correlated.

11.4.4 Range-Doppler Plots and Their Properties

The detection process in passive radar is based on the evaluation of the delay-Doppler cross-correlation function between the surveillance and the reference signals. Generation of the two-dimensional (2-D) bistatic radar display plots is analyzed here as it is the typical means of display for the majority of experimental PBRs. Computation and display of PBR data in 2-D format of bistatic range versus Doppler is illustrative and insightful for observing the PBR operating environment and for identifying targets of interest, making it a useful tool for system characterization. In practice, the actual FM signal is corrupted with multipath and clutter as well as possible interference from adjacent FM stations, which sets a cancellation limit. To reveal targets that may be far from the receiver, cancellation must be performed over an extended range.

Figure 11-12 shows 2-D bistatic plots for FM radio stations transmitting from Crystal Palace. In each of the figures, the station frequency as well as the particular type of program material is listed – for example, rock music on BBC Radio 2 (88.8 MHz). Further examination of the 2-D search space corresponding to the 88.8-MHz stations does not reveal any prominent scattering features to suggest the presence of a target of interest. The composition of the 2-D plot is indicative of the random variation of the

FIGURE 11-12 ■
Typical Range-Doppler Plots for FM Radio-Based PBR.



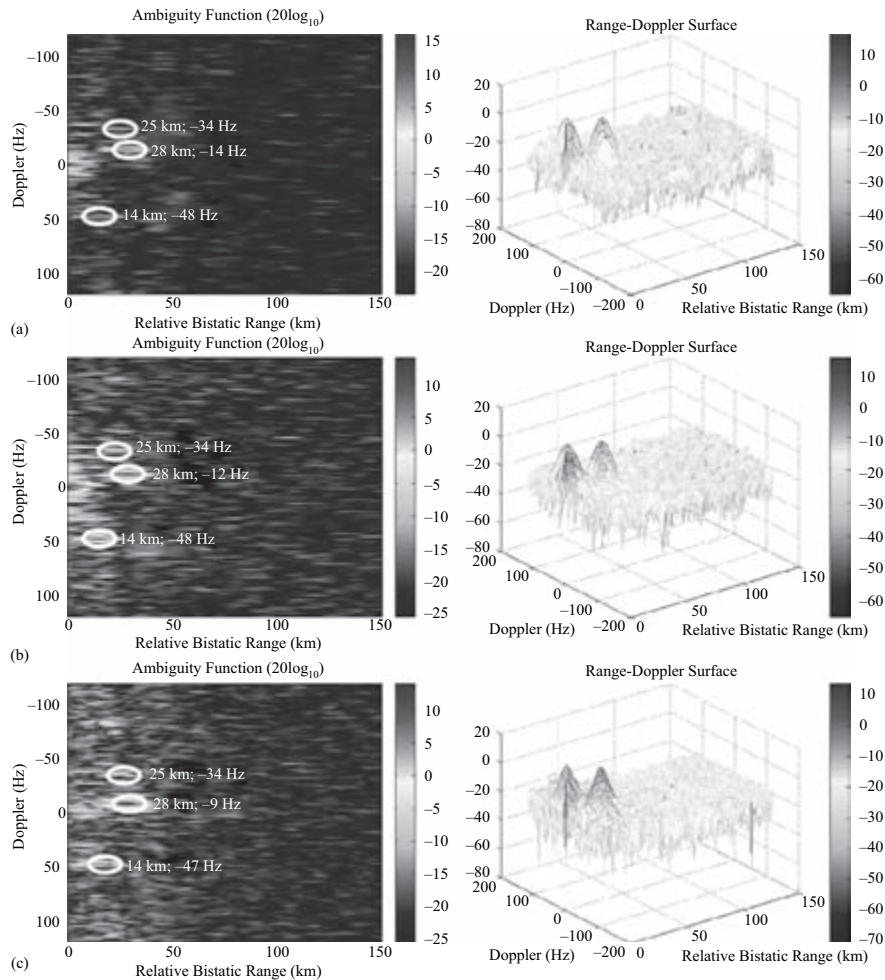


FIGURE 11-13 ■ Two-Dimensional Bistatic Display Plot for the 91.3-MHz Wrotham FM Transmitter; (a), (b), and (c) Show Three Successive 1-s Blocks of Data.

illuminating waveform. The region of highest intensity in the display plot occurs around 0 Hz, corresponding to strong DSI. The reason for the highest signal intensity at low Doppler frequencies is due to the DSI sidelobes and multipath that lie outside of the cancellation notch (rejection band) of the cancellation algorithm. The cancellation algorithm does, however, suppress the DSI at 0 Hz and low Doppler frequencies.

The 2-D detection plots in Figure 11-13 show each of the remaining 1-s blocks of PBR data for the 91.3-MHz BBC Radio 3 station. Figure 11-13 (a) shows the second sample of processed data, Figure 11-13 (b) shows the third sample, and Figure 11-13 (c) shows the fourth sample. The corresponding range/Doppler surface accompanies each of the 2-D display plots. It can be seen that the scattering feature that was observed at 68 km in the first processed data block for 91.3 MHz in Figure 11-12 does not appear in Figure 11-13 (a), (b), or (c). Therefore, the target-like feature in 91.3 MHz in the figure was declared a “false alarm” as it did not appear in any of the other processed stations. In this case, the system’s temporal diversity was used to authenticate an individual scattering feature.

To evaluate the performance achieved, it is possible to compare the 2-D bistatic display plots with air-truth data to further corroborate that the scattering features identified on each display corresponded to a civil aircraft target. The air-truth data may be

FIGURE 11-14 ■
Air Truth: Mode-S/
ADS-B Virtual
Radar Display
Corroborating PBR
Target Declarations.



obtained from a Mode-S/automatic dependent surveillance broadcast (ADS-B) receiver that decodes transponder signals from aircraft. The accompanying base-station software displays the decoded transponder information on a virtual radar screen. The bistatic range is defined as that from the target to the receiver, which is then converted to a monostatic equivalent range (in nautical miles) and highlighted on the virtual radar display. Figure 11-14 shows the 91.3-MHz FM station (also from Figure 11-13) and matches the three target declarations A, B, and C to their corresponding point on the Mode-S/ADS-B display. In this example, the good correspondence is clear.

11.5 | PASSIVE BISTATIC RADAR TECHNIQUES

There are a number of processing techniques that are particular to PBR. As noted in Section 11.2, the information provided by a PBR receiver from a given target can be (1) the differential range, obtained from the time difference of arrival between the echo signal and the direct signal from the transmitter; (2) the direction of arrival of the echo signal; and (3) the Doppler shift on the echo. This may come from a single transmission or a number of transmissions in different locations, and the system may consist of a single receiver or a number of receivers in different locations.

11.5.1 Triangulation

Probably the simplest way of combining measurements from PBR receivers is to use the differential range measurements. For a single transmitter–receiver pair, a measurement of the differential range locates the target on an ellipse defined by $(R_T + R_R) = \text{constant}$. If the direction of arrival of the echo can be measured, then the location of the target on the ellipse can be unambiguously located; if not, if there is a second receiver (or a second transmitter) there will be two such ellipses, and the target location must lie on one of the points where the ellipses intersect (Figure 11-15). If there are three or more transmit–receiver pairs, and hence three or more ellipses, there will be only one point where they all intersect and so the correct target location can be identified, but the process of identifying and excising the incorrect locations can be complicated.

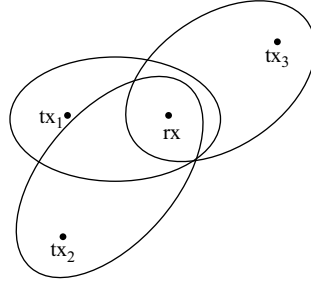


FIGURE 11-15 ■ Triangulation Using Three Transmit–receive Pairs; the Target Is Located at the Point Where the Three Ellipses Intersect. tx_n is a transmitter location and rx_n is a receiver location.

11.5.2 Tracking

A more rigorous approach to the problem of localization and tracking is to set up a target-state vector and use the radar measurements to estimate the vector components, in a process analogous to classical tracking theory. This process has been described by Howland in [15], and the essence of this is described in the following paragraphs, using the same notation for clarity.

Suppose that the receiver is located at the origin of a Cartesian coordinate system with the transmitter at $(0, L)$. A target is located at (x_0, y_0) at time t_0 and is moving with velocity components (\dot{x}, \dot{y}) . If the radar derives the Doppler spectrum at intervals of T seconds, then after n samples at time $t = (t_0 + nT)$ the Doppler shift and bearing of the target are

$$F(n) = -\frac{1}{\lambda} \left[\frac{(x_0 + nT\dot{x})\dot{x} + (y_0 + nT\dot{y})\dot{y}}{\sqrt{(x_0 + nT\dot{x})^2 + (y_0 + nT\dot{y})^2}} + \frac{(x_0 + nT\dot{x})\dot{x} + [L - (y_0 + nT\dot{y})]\dot{y}}{\sqrt{(x_0 + nT\dot{x})^2 + (L - (y_0 + nT\dot{y}))^2}} \right] \quad (11.8)$$

and

$$\theta(n) = \tan^{-1} \left(\frac{x_0 - nT\dot{x}}{y_0 - nT\dot{y}} \right) \quad (11.9)$$

respectively, where λ is the wavelength. The measurements of Doppler are therefore functions of the known parameters n , T , L , and λ and the unknown track parameters $(x_0, \dot{x}, y_0, \dot{y})$.

The unknown track parameters can be estimated from a sequence of measurements of Doppler $F_m(k)$ and DOA $\theta_m(k)$ for samples at times $k = 0, \dots, (m - 1)$ by a straightforward minimization process. Consider a vector of measurements $z^T = (F_m(0), \theta_m(0), F_m(1), \theta_m(1), \dots, F_m(m - 1), \theta_m(m - 1))$ and a corresponding vector of state equations $\mathbf{h}^T(x) = (F(0), \theta(0), F(1), \theta(1), \dots, F(m - 1), \theta(m - 1))$. The problem is then one of attempting to minimize the least square difference between the measurements and the state equations by selecting the best values of the track parameters, x . The difference is defined as

$$J_{LS} = \frac{1}{2} [z - \mathbf{h}(x)]^T [z - \mathbf{h}(x)] \quad (11.10)$$

This can be minimized by any of a number of standard algorithms, including steepest descent, Gauss–Newton, and Levenberg–Marquardt [51]. For these to work properly, the

least squares difference J_{LS} should have a unique and well-defined minimum. Because the information contained in individual measurements of Doppler and direction of arrival is low, relatively long integration periods, of the order of a minute in practice, are found to be necessary. In addition, a good initial estimate of the target state is required.

A more efficient approach, once the track has become established, is to use a Kalman filter. Because the measurements of Doppler and direction of arrival are related to the target track in a very nonlinear fashion, a nonlinear version of the Kalman filter, such as the extended Kalman filter (EKF), unscented Kalman filter (UKF) or particle filter (PF) [52], will be appropriate. The EKF estimates the target state from the Doppler and angle of arrival measurements as follows:

$$\hat{x}(t_n) = x(t_n) + \mathbf{K}(t_n)y(t_n) - \mathbf{h}(x(t_n), t_n) \quad (11.11)$$

where

$y(t_n)$ = vector of Doppler and DOA measurements at time t_n ,

$\mathbf{h}(x(t_n), t_n)$ = measurement that would be expected at time t_n given the predicted state $x(t_n)$, and

$\mathbf{K}(t_n)$ = Kalman gain at time t_n .

These are calculated from:

$x(t_n) = f(\hat{x}(t_{n-1}), t_n)$ predicted track state at time t_n given its state at time t_{n-1} and

$\mathbf{K}(t_n) = \mathbf{P}'_x(t_n)\mathbf{M}^T(t_n) \left[\mathbf{M}(t_n)\mathbf{P}'_x(t_n)\mathbf{M}^T(t_n) + \mathbf{P}_v(t_n) \right]^{-1}$ Kalman gain

where

$\mathbf{P}'_x(t_n) = \Phi(t_n)\mathbf{P}_x(t_{n-1})\Phi^T(t_n) + \mathbf{G}$ covariance of the state prediction $x(t_n)$,

$\mathbf{P}_x(t_{n-1}) = \mathbf{I} - \mathbf{K}(t_{n-1})\mathbf{M}(t_{n-1})\mathbf{P}'_x(t_{n-1})$ covariance of the previous smoothed estimate, $\hat{x}(t_{n-1})$,

$\mathbf{M}(t_n) = \frac{\partial \mathbf{h}(x(t_n), t_n)}{\partial x}$ linearized measurement matrix,

$\Phi(t_n) = \frac{\partial f(\hat{x}(t_n), t_n)}{\partial x}$ linearized state equations,

$\mathbf{P}_v(t_n)$ = covariance matrix representing the measurement errors, and

\mathbf{G} = covariance matrix representing errors in the state equations.

The measurement vector $\mathbf{h}(x(t_n), t_n)$ is defined as $(F, \theta)^T$ where F and θ represent the measurements of Doppler and DOA, respectively:

$$F = -\frac{1}{\lambda} \left[\frac{x\dot{x} + y\dot{y}}{\sqrt{x^2 + y^2}} + \frac{x\dot{x} - (L-y)\dot{y}}{\sqrt{x^2 + (L-y)^2}} \right] \quad (11.12)$$

$$\theta = \tan^{-1} \left(\frac{x}{y} \right) \quad (11.13)$$

and, assuming a simple linear model for target motion, the state equations are defined as

$$f(\hat{x}(t_{n-1}), t_n) = \begin{pmatrix} x(t_{n-1}) + \dot{x}(t_{n-1})\Delta t \\ y(t_{n-1}) + \dot{y}(t_{n-1})\Delta t \end{pmatrix} \quad (11.14)$$

where Δt is the coherent integration time, $t_n - t_{n-1}$.

11.5.3 Performance Prediction

The PBR radar eq. (11.3) derived in Section 11.2.2 can be cast in the form

$$(R_R)_{max} = \left(\frac{\Phi \sigma_b G_R \lambda^2 L G_p}{(4\pi)^2 (S/N)_{min} k T_0 B F} \right)^{1/2} \quad (11.15)$$

where

the appropriate value of Φ is used according to the illuminator source,

$(S/N)_{min}$ = minimum signal-to-noise ratio for adequate detection, and

G_p = processing gain.

The maximum value of this is set by the maximum time for which the target echo remains coherent, which in turn depends on the extent to which the target is maneuvering or accelerating. A rule of thumb value for this time is

$$T_{max} = \left(\frac{\lambda}{A_R} \right)^{1/2} \quad (11.16)$$

where A_R is the radial component of target acceleration. For a VHF FM waveform of bandwidth 50 kHz and an integration time of 1 second, this gives $G_p = 47$ dB.

It is also important to use the correct values of the other parameters in the equation. The factors governing the target bistatic RCS σ_b are discussed in Section 11.2.3. The discussion of the signal environment in Section 11.4 has shown that the level of direct signals, multipath, and other sources of noise can be severe, particularly in urban environments, and even with sophisticated suppression algorithms it is not possible to suppress the noise level right down to thermal noise. In practice, an effective value of the noise figure F of the order of 25 dB may be appropriate.

Equation (11.15) can be plotted to show coverage contours for particular system and target parameters. Figure 11-16 shows an example of one such plot – in this case, for a 10-kW DAB transmitter located at Crystal Palace in South London, a target of $\sigma_b = 100 \text{ m}^2$, and a receiver at University College London in central London at a range of about 12 km from the transmitter. The noise figure, including the effect of losses, has been taken as 30 dB. The contours take the form of ovals of Cassini.

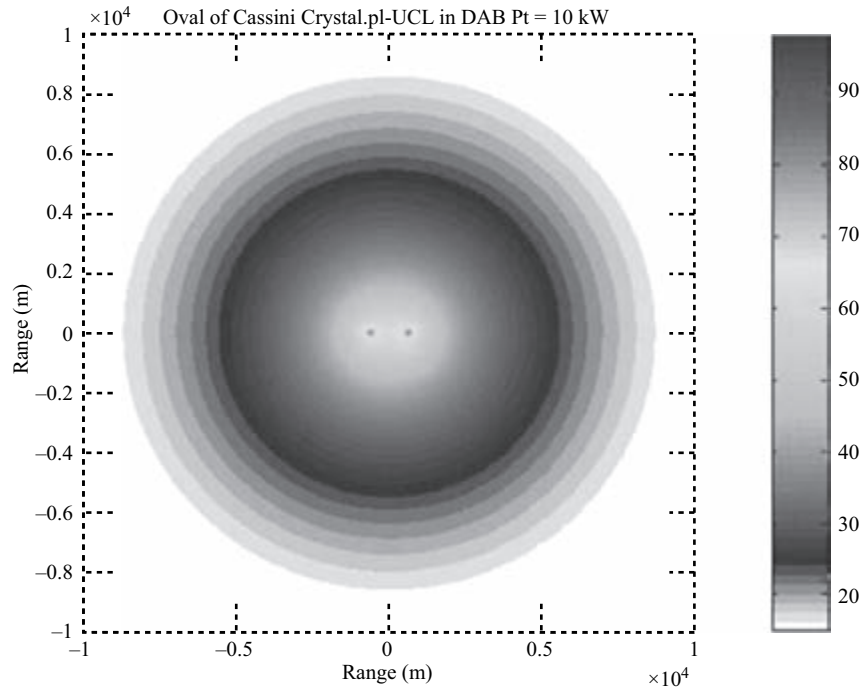
11.6 | EXAMPLES OF SYSTEMS

This section presents examples of practical systems and results to show how the principles described in the previous sections are used in practice as well as typical results.

11.6.1 VHF FM and Analog TV

Analog VHF FM and TV transmissions represent some of the highest-power sources for PBR use, with excellent coverage, and have been widely used in experiments. The performance prediction methods described in Section 11.5.3 can be used to derive the detection ranges as a function of system and target parameters and show that large aircraft targets should be detectable at ranges well in excess of 100 km.

FIGURE 11-16 ■ Predicted Coverage for a DAB Transmitter Located at Crystal Palace in South London and a Receiver at UCL in Central London.



One example of a practical system using an FM radio illuminator is the Manastash Ridge Radar, developed at the University of Washington in Seattle, the United States [17, 18]. The purpose of this system is to study plasma turbulence (auroral E-region irregularities) in northern latitudes at ranges in excess of 1,000 km, for which frequencies around 100 MHz are very suitable. The illumination source is a VHF FM transmitter in the Seattle area, and the receiver is located remotely, 150 km to the east, shielded from the transmitter by the Cascade Mountains. This provides an effective solution to the problem of direct signal interference. Synchronization between transmitter and receiver is achieved via GPS. This represents a notably elegant, low-cost example of the application of PBR techniques.

Another example is a low-cost experimental system assembled at the NATO C3 Agency in The Hague in the Netherlands [53]. This used a single FM radio transmitter located at Lopik, about 45 km inland. The transmitter ERP was 50 kW, vertically polarized, and mounted on a 375-m-high tower. The receiver used 14-bit digitization, adaptive cancellation of the direct signal and multipath, cross-correlation processing to estimate target range, and a simple phase interferometer to estimate direction of arrival (Figure 11-17). The state estimation processing is as described in Section 11.5.3, associating detections in range and Doppler space. Figure 11-18 shows an example of aircraft targets over the North Sea being tracked at ranges approaching 150 km.

Figure 11-19 shows one result from work undertaken at University College London [54]. In this case, the receiver is carried by an aircraft flying from Shoreham on the south coast of England. The receiver is able to use transmissions from several transmitters simultaneously (Wrotham, Guildford, Oxford, and so on) and to measure the differential range and the Doppler shift (which is due both to the motion of the target and of the receiver). The differential range defines an ellipse, and the target velocity derived from

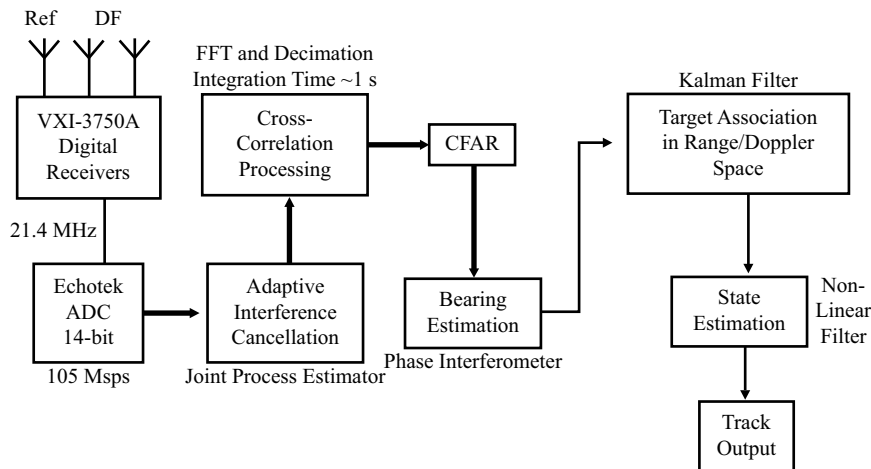


FIGURE 11-17 ■ Block Diagram of Processing Used in the NC3A FM-Based PBR.

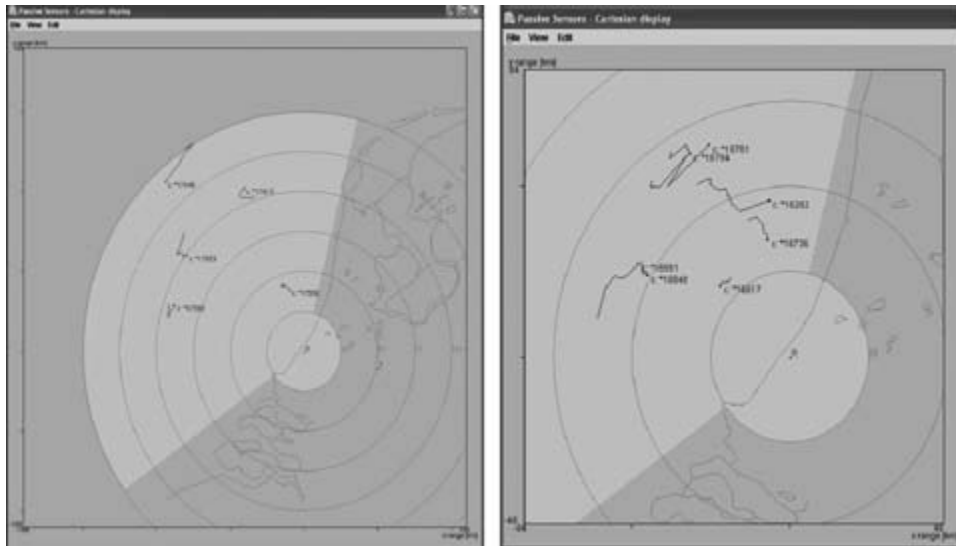


FIGURE 11-18 ■ Examples of Targets Detected and Tracked by NC3A FM-Based PBR at Ranges Approaching 150 km.

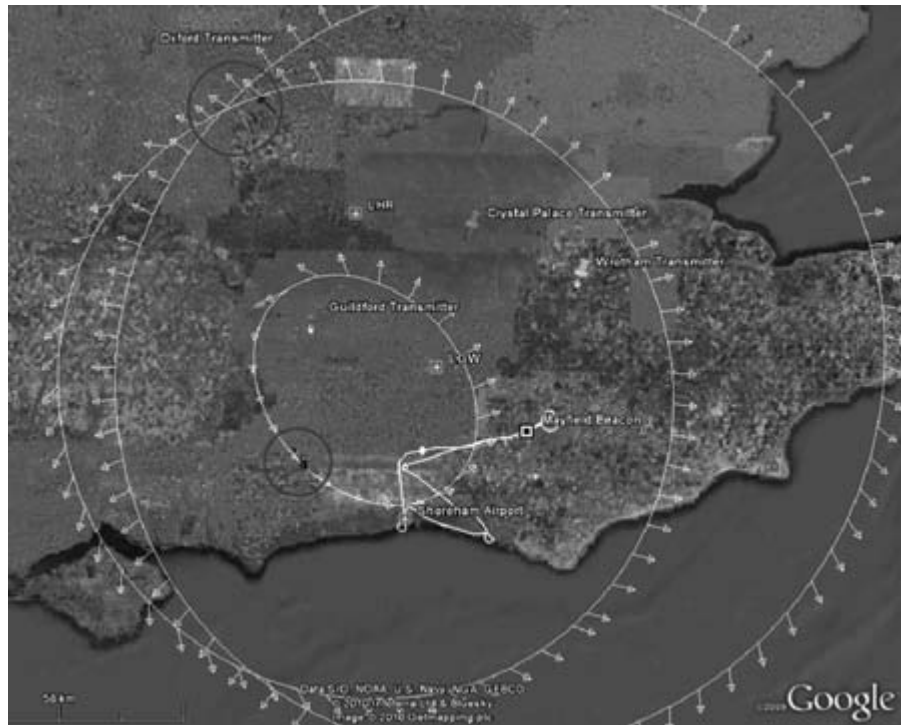
the measured Doppler is shown as a vector at a number of points around the ellipse in each case. It can be seen that the ellipses intersect at several places (as in Figure 11-15), but only at some of these intersections do the target velocity vectors agree. This allows the ambiguities associated with the multiple intersections of the ellipses to be resolved and hence the correct target locations to be identified.

Despite the advantages noted above, VHF FM and analog TV transmissions are not ideal in all respects. The time-varying nature of the ambiguity performance has been noted in Section 11.3. Furthermore, in many countries the analog radio and TV transmissions are scheduled to be phased out and replaced by digital transmissions; in some countries, this has already happened.

11.6.2 Digital Radio and TV

Available today are an increasing number of digital transmission sources that are attractive for use in passive bistatic radar configurations. Chief among these are HDTV,

FIGURE 11-19 ■ Results from UCL Aircraft-Borne PBR Receiver; the Ambiguities Associated with the Intersection of the Differential Range Ellipses Are Resolved Using the Target-Velocity Vectors.



digital video broadcasts, and digital audio broadcasts. These waveforms are being increasingly explored for PBR application as they have advantageous ambiguity function properties. In particular, the form of coding and the rate of modulation result in both range and Doppler resolution being much higher than for analog waveforms. However, on the negative side, transmission powers tend to be lower. The reason for this is that it is easier to exert processing gains in a receiver. This applies just as much in passive radar as it does for the originally intended usage; the effects of some of the reduction in overall power can be mitigated.

A number of systems have been constructed and tested [e.g. 39, 55], all using the same basic construct as described earlier in this chapter. The lower transmit power and the nature of the waveform modulation mean that the level of suppression required is much reduced. DAB has a modulation bandwidth of 1.5 MHz and DVB 7.6 MHz. An example of the ambiguity function was shown in Section 11.3.4. However, the waveform does possess deterministic structure due to the transmission of pilot tone components and so forth. Bongioanni *et al.* [56] propose a method based on using the cross-ambiguity function (CAF) in which these features are effectively removed. They show that this leads to more robust detection performance.

Overall, this form of PBR is receiving increasing attention from the research community; the desirable waveform properties suggest it is a very promising candidate for operational development.

11.6.3 Cell Phone

The use of cell-phone base stations as illuminators for PBR was first proposed in the late 1990s, and work was done at Roke Manor Research in the United Kingdom to develop

TABLE 11-2 ■ Experimental Parameters [57]

Transmit power	10 W
Transmit antenna gain (120° sector)	10 dB
Signal bandwidth	81.3 kHz
Receive antenna gain	25 dB
Coherent integration time	0.34 s
Processing gain	41.2 dB

the concept, which was named *CELLDAR* [57]. However, although a number of claims were made in press releases, nothing was published in the peer-reviewed technical literature.

The performance prediction methods described in Section 11.5.4 can be used to estimate the performance of such systems and show that they will be limited to relatively short-range applications. This is confirmed by Tan *et al.* [40], who reported experimental results with a 25-W GSM transmitter in Singapore. They note that the 81.3-kHz signal bandwidth provides only coarse range resolution (coarser than the expected maximum detection range), which meant that they were constrained to using Doppler-only processing. They reported detection and tracking of large vehicle targets at ranges up to 1 km and of human targets up to about 100 m.

Better results may be obtained with higher-power transmissions, greater receive antenna gain, and longer integration times. Work at the Fraunhofer FHR Institute in Germany has used a multiple-beam, multiple-channel array antenna with sufficient gain so it can exploit the transmissions from several base stations and hence track targets over a substantial area at ranges of up to 40 km. The main system parameters are given in Table 11-2. The base station transmissions in each case have a power of 10 W radiated over 120° azimuth sectors, giving 100-W EIRP. Figure 11-20 shows the cumulative probability of detection P_D overlaid on a map of the area for this system, as well as the locations and beam directions of the four base stations used in this calculation.

The key part of the processing is to fuse the detections from a sequence of transmitter–receiver pairs and hence to track targets. Quoting from [58]: “Selecting a good tx-rx configuration is a multi-objective optimization where the weights of the different criteria are not known *a priori*.”

While the performance of this system is impressive, and indicative of what can be done with adequate receive antenna gain and sophisticated processing, the system is certainly neither simple nor low-cost. Also, even with this level of sophistication, the coverage is not as great as with other types of illuminator.

11.6.4 WiFi and WiMAX

WiFi is freely available in increasingly numerous locations worldwide. It has very low transmission power but relatively wide bandwidths, so it offers possible short-range application. The first reported example of such a system is in [42], where an 802.11 wireless network was used as a transmitter in a simple configuration operated in an indoor environment. Table 11-3 shows the operating parameters of the system.

The results show power levels consistent with a simple application of the bistatic radar equation. This form of system, and in particular the type of waveform transmissions and their radar properties, have been analyzed in more detail in [59]. Here the

FIGURE 11-20 ■ Coverage of the FGAN PBR System Using GSM Illuminators; Four of the Seven Base Stations Are Shown, Each with Its 120° Illumination Sector [58].

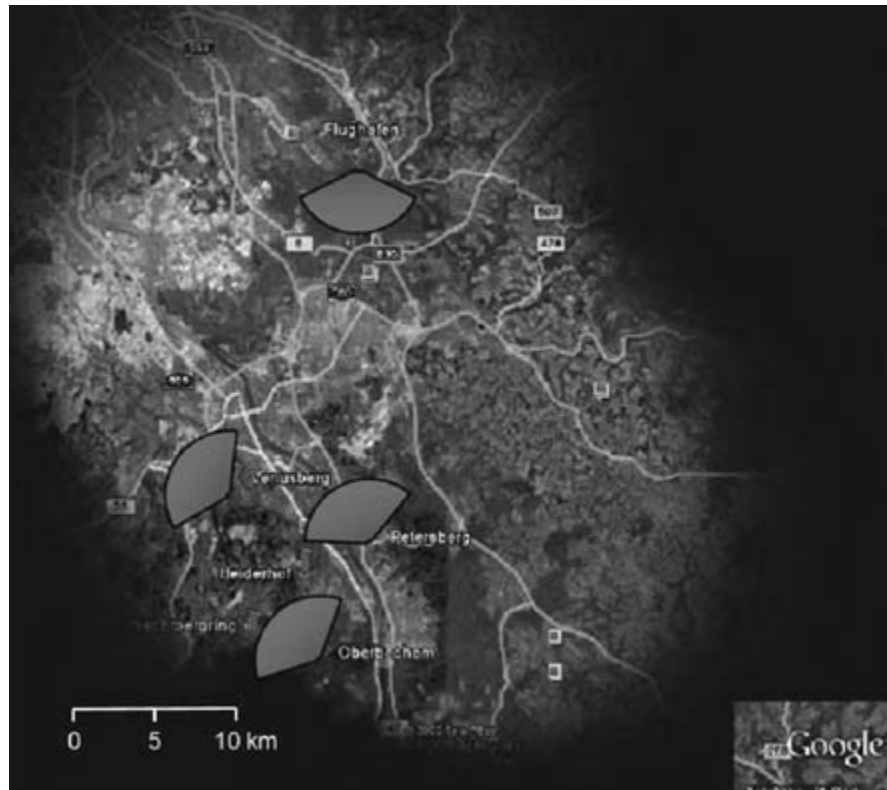


TABLE 11-3 ■ Experimental Parameters

Transmit power	+6 dBm
Transmit antenna gain	0 dBi
Receive antenna gain	18 dBi
Wavelength	0.123 m
Target RCS	Variable
Transmitter-to-target range	2.2 m
Target-to-receiver range	1–4 m
Total losses	11 dB
Effective bandwidth	11 MHz
Receiver noise figure	3 dB

WiFi transmission sequence has been found to be complex and dependent on the user environment, but is dominated by the direct sequence spread spectrum and orthogonal frequency-division multiplexing signals. Ambiguity function analysis of the DSSS-based WiFi shows range and Doppler performance is comparable with that expected based on theoretical predictions. Detection of moving human targets was demonstrated for the first time. This work shows that this technique has considerable promise for a low-cost and widely deployable short-range detection and tracking system.

Figure 11-21 shows a “raw” range Doppler map integrated over a time span of 300 ms in which a target is circled against quite a dense clutter background. The target is corroborated with ground truth and provides a sound basis for subsequent detection and

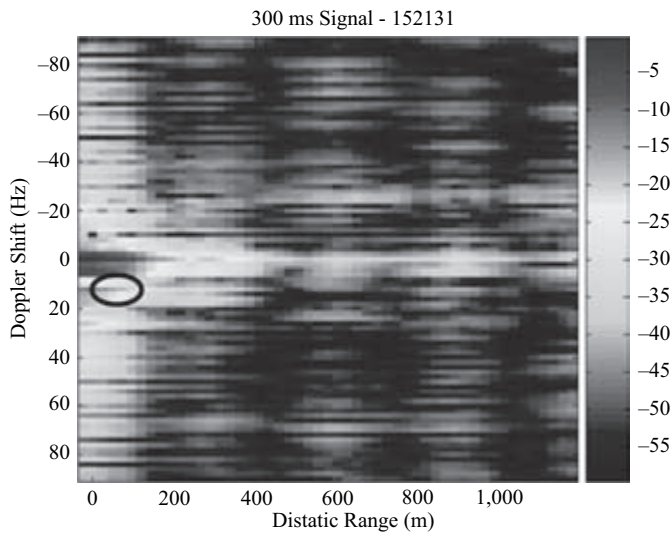


FIGURE 11-21 ■ “Raw” Range Doppler Map Integrated over a Time Span of 300 ms in Which a Target Is Circled Against Quite a Dense Clutter Background [59].

tracking. Detection and tracking techniques specifically designed to operate with passive bistatic radar data of this type are the subject of Chapter 17 in POMR volume 2.

This demonstrates the feasibility for developing a low-cost surveillance device utilizing WiFi networks as transmitters of opportunity. In [44], the passive bistatic WiFi radar approach is explored further to determine performance limits by examining the detection of targets in a dense clutter background. Through-wall detections of personnel targets moving at differing velocities within an indoor environment are presented for the first time in [44]. Figure 11-22 shows the geometry employed. The complexity of the clutter environment with multiple reflections occurring in the direct and indirect

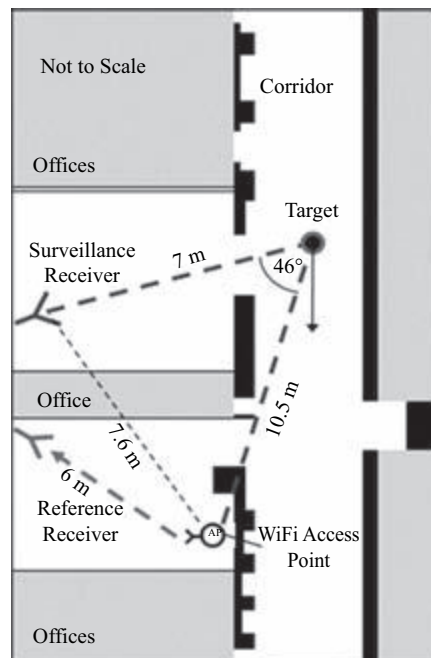


FIGURE 11-22 ■ Schematic of the Indoor Dense-Clutter WiFi Radar Experimental Setup [44].

channels can be appreciated. Overall, these papers demonstrate that it is feasible to use WiFi transmissions to make passive bistatic radar systems that can be used over short ranges in both indoor and outdoor scenarios.

As indicated in Section 11.3.5, the “big brother” to WiFi, WiMAX has considerably higher transmission power levels and represents a potentially attractive alternative to DAB and DVB. In the United Kingdom, two bands are currently licensed at 3.5 and 3.6 GHz. The bandwidth is variable from 1.25 MHz to 20 MHz and hence even higher-range resolutions are possible. This means that imaging techniques start to be more readily addressable, although no application has concentrated on detection to date.

In [47], Woodbridge *et al.* have considered WiMAX transmission to the problem of providing maritime radar-surveillance services. Their study shows that a 4,000-m² target should be detected out to a range of 45 km with a transmitter-to-receiver baseline of between 10 and 32 km. Coverage is predicted to be suitable for busy commercial areas such as that covered by the Port of London. Range and Doppler resolution are calculated to be 5 m and 3.5 Hz, respectively, which is consistent with parameters suited to the detection of marine vessels. They conclude by recommending field trials of an experimental system.

11.6.5 Global Navigation Satellite Systems

Of the spaceborne illuminators discussed in Section 11.3.7, the network of GNSS (GPS, GLONASS, or Galileo) satellites have significant attraction. Their coverage is such that there will always be several satellites of each network visible at any location on Earth’s surface. The signal bandwidth provides fair range resolution, and the digital modulation gives good ambiguity performance. Against this must be balanced the fact that the power density at Earth’s surface is relatively low – certainly in comparison with some of the other sources that may be used for PBR. Since the range of the transmitter to the target scene is more or less constant, this sets a limit on the range of the receiver from the target scene.

Some early work demonstrated the detection of various targets using GPS illuminators [60, 61]. These included military and civil aircraft, an antitank missile, and the Mir Space Station, and exploited forward-scatter geometries and significant integration gain. GPS signals have also been used for remote sensing of ocean surface winds [62, 63], where again advantage can be taken of relatively long integration times.

More recent work by Cherniakov and his coworkers at the University of Birmingham has used GPS signals as an illumination source for radar imaging, which Cherniakov *et al.* term *space-surface bistatic synthetic aperture radar (SS-BSAR)* [64, 65]. The synthetic aperture is formed by a moving receiver platform that, in their experiments, has used a rail, a vehicle, and ultimately a helicopter. In its final form, the system is intended as a passive, medium-range imaging system in which a compact receiver (the size of a conventional navigation receiver) can be mounted on a UAV and provide coarse, covert surveillance. Their most recent results [66] use the Galileo satellites, which give a factor of 2 better range resolution than GPS and GLONASS and a slightly better power budget. Another benefit is that all Galileo satellites transmit at the same frequency. Table 11-4 gives typical experimental parameters for the rail-mounted system, and Figure 11-23 shows typical image results obtained with a vehicle-mounted receiver moving at a speed of 8 m/s. The range to the target is on the order of 250 m. The receiver-to-target look angle in this example is close to 0°, and therefore only the front face of the building is being imaged.

TABLE 11-4 ■ Experimental Parameters [66]

Frequency channel	10 (1,607.625 MHz)
Satellite azimuth θ_A	178.4914°
Satellite elevation θ_E	11.3558°
Bistatic angle β	~11°
Satellite altitude	~23 000 km
Aperture length	26.78 m
Integration time	45 s
Receiver velocity	~0.6 m/s
Receive antenna gain	16 dBi, effective area 0.11 m ²

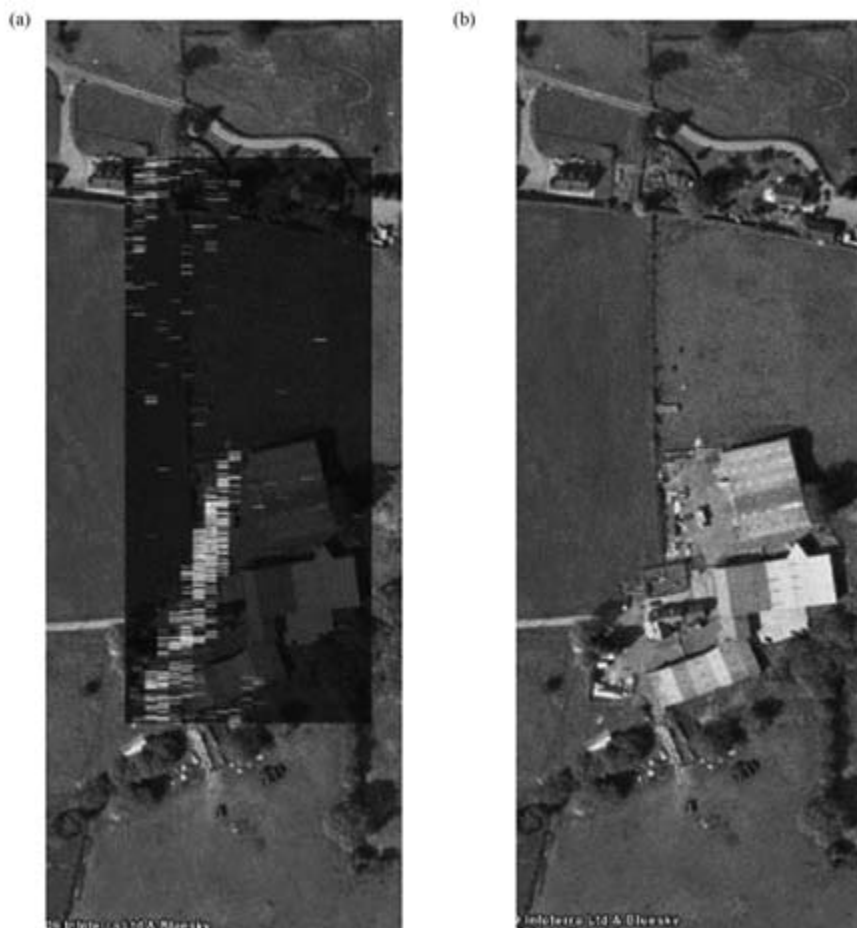
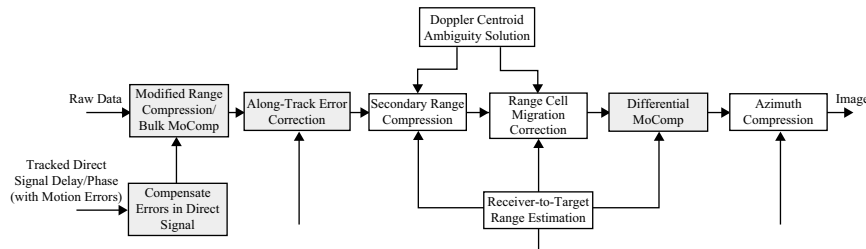
**FIGURE 11-23** ■
(a) SS-BSAR Image Superimposed on Satellite Photograph;
(b) Satellite Photograph [66].

Figure 11-24 shows a block diagram of the stages of processing. The key processes here are (1) synchronization and (2) characterizing and compensating for motion irregularities of the moving platform. This image-formation algorithm has been developed specifically for this type of radar configuration. Due to the altitude of the satellites, their contribution to the target Doppler (and hence, the azimuth resolution) is insignificant compared to that introduced by the motion of the receiver. Using a modified range-compression

FIGURE 11-24 ■
Stages of
Processing in
SS-BSAR [66].



approach, the algorithm suppresses unwanted satellite signal effects, such as the Doppler centroid and linear-range cell migration, and equalizes the range histories of targets at the same range. Thus, after this step, a range-Doppler algorithm can be adapted to provide the final imagery.

11.7 | CONCLUSIONS

To summarize, we can conclude that passive bistatic radar has come a long way since the first experiments in the early 1980s – and certainly since the first radar experiments using broadcast signals more than 50 years before that. Potentially, it offers covert operation with simple and low-cost equipment without the need for a transmitting license, and the ability to use parts of the electromagnetic spectrum not normally available for radar use. The wide variety of broadcast, communications, and radio-navigation sources and their excellent spatial coverage gives great scope for PBR. In common with all bistatic radars, it may allow mechanisms such as forward scatter, which enhances the radar signature of targets, to be exploited. The fact that PBR systems can be simple and low cost has meant that they have been very suitable for research by university groups, and there have been numerous publications on the subject.

Against this must be weighed the fact that PBR waveforms are not designed explicitly for radar, so their performance in radar applications is not optimal. Care must therefore be taken to understand how best to choose which transmissions to use and how best to process them. It is found that analog modulation formats give time-varying ambiguity performance, but more modern digital modulation formats are much better in this respect. In addition, as with all bistatic radars, the ambiguity performance depends on the bistatic geometry, so for targets on or close to the bistatic baseline, the range and Doppler resolution are both poor, no matter what the waveform.

Since most PBR modulation sources are continuous, high-powered, and operate in bands that are already congested, the level of direct signal and other noise sources is usually high, and considerable effort has to be expended to suppress these signals to allow the target echoes to be reliably detected.

The applications to which PBR systems may be put therefore need careful consideration. It is no good claiming to do “almost as well” as conventional radar approaches. It is important to understand very thoroughly the relationship between the desired application (surveillance, remote sensing, and so on) and the requirements that follow, and the properties of the illuminator source that might be used – for example, in terms of coverage (spatial and temporal), bandwidth (resolution), integration time (scene stationarity), and so on.

Applications that show promise are

- scientific measurements (remote sensing) where long integration times can be employed,
- border or perimeter surveillance (perhaps exploiting forward scatter) or protection of critical assets or both, and
- gap filling in areas where operation of conventional sensors is incomplete.

Finally, we may also comment that because the ambiguity functions of PBR illuminators depend fundamentally on geometry, there will always be regions where the performance of a bistatic sensor is compromised. It makes sense, therefore, to think in multistatic terms rather than purely bistatic.

11.8 | REFERENCES

- [1] N.J. Willis, *Bistatic Radar* (2nd ed.), Technology Service Corp., Silver Spring, MD, 1995, corrected and republished by SciTech Publishing, Inc., Raleigh, NC, 2005.
- [2] V.S. Chernyak, *Fundamentals of Multisite Radar Systems: Multistatic Radars and Multiradar Systems*, Gordon & Breach, Amsterdam, 1998.
- [3] N.J. Willis and H.D. Griffiths, *Advances in Bistatic Radar*, SciTech Publishing Inc., Raleigh, NC, 2007.
- [4] N.J. Willis, “Bistatic Radar,” Chapter 23 in *Radar Handbook*, third edition (M.I. Skolnik ed.), McGraw-Hill, New York, 2008.
- [5] M. Cherniakov (ed.), *Bistatic Radar: Principles and Practice*, (2007) and *Bistatic Radar: Emerging Technology*, Wiley, New York, ISBN 0470026308, 2008.
- [6] P.E. Howland, H.D. Griffiths, and C.J. Baker, “Passive Bistatic Radar,” chapter in *Bistatic Radar: Emerging Technology* (M. Cherniakov ed.), Wiley, New York, 2008.
- [7] E.V. Appleton and M.A.F. Barnett, “On some direct evidence for downward atmospheric reflection of electric rays,” *Proceedings of the Royal Society*, Vol. 109, pp. 261–641, December 1925.
- [8] S.S. Swords, *Technical History of the Beginnings of Radar*, Peter Peregrinus, Stevenage, 1986.
- [9] P.E. Judkins, *Making Vision into Power: Britain’s Acquisition of the World’s First Radar-Based Integrated Air Defence System 1935–1941*, PhD thesis, Cranfield University, 2007.
- [10] H.D. Griffiths and N.J. Willis, “Klein Heidelberg – the first modern bistatic radar system,” *IEEE Transactions on Aerospace and Electronic Systems*, Vol. 46, No.4, October 2010.
- [11] O.E. Rittenbach and W. Fishbein, “Semi-active correlation radar employing satellite-borne illumination,” *IRE Transactions on Military Electronics*, pp. 268–269, April–July 1960.
- [12] K.M. Siegel, “Bistatic radars and forward scattering,” *Proceedings of the National Conference of Aeronautical Electronics*, pp. 286–290, 12–14 May 1958.
- [13] H.D. Griffiths and N.R.W. Long, “Television-based bistatic radar,” *IEE Proceedings*, Vol. 133, Pt.F, No. 7, pp. 649–657, December 1986.
- [14] R.F. Ogrodnik, “Bistatic laptop radar: an affordable, silent radar alternative,” *Proceedings of the IEEE Radar Conference*, Ann Arbor, MI, pp. 369–373, May 1996.
- [15] P.E. Howland, “Target tracking using television-based bistatic radar,” *IEE Proceedings Radar, Sonar and Navigation*, Vol. 146, No. 3, pp. 166–174, June 1999.

- [16] P.E. Howland (ed.), *IEEE Proceedings Radar, Sonar & Navigation on Passive Radar Systems* (Special Issue), Vol. 152, No. 3, June 2005.
- [17] J.D. Sahr and F.D. Lind, "The Manastash Ridge radar: a passive bistatic radar for upper atmospheric radio science," *Radio Science*, Vol. 32, No. 6, pp. 2345–2358, 1997.
- [18] J.D. Sahr, "Passive radar observation of ionospheric turbulence," Chapter 10 in *Advances in Bistatic Radar* (N.J. Willis and H.D. Griffiths eds.), SciTech, Raleigh, NC, 2007.
- [19] R.A. Simpson, "Spacecraft studies of planetary surfaces using bistatic radar," *IEEE Transactions on Geoscience and Remote Sensing*, Vol. 31, No. 2, March 1993.
- [20] J. Wurman, M. Randall, C. L. Frush, E. Loew and C. L. Holloway, "Design of a bistatic dual-Doppler radar for retrieving vector winds using one transmitter and a remote low-gain passive receiver," *Proceedings IEEE*, Vol. 82, No. 12, pp. 1861–1871, December 1994.
- [21] S. Satoh and J. Wurman, "Accuracy of wind fields observed by a bistatic Doppler radar network," *Journal of Oceanic and Atmospheric Technology*, Vol. 20, pp. 1077–1091, 2003.
- [22] E.F. Greneker and J.L. Geisheimer, "The use of passive radar for mapping lightning channels in a thunderstorm," *Proceedings of the IEEE Radar Conference*, Huntsville, AL, pp. 28–33, 5–8 May 2003.
- [23] D.J. Bannister, "Radar in-fill for Greater Wash area: feasibility study – final report," Department for Business, Enterprise and Regulatory Reform, UK, 31 August 2007.
- [24] J. Baniak, G. Baker, A.M. Cunningham and L. Martin, "Silent Sentry passive surveillance," *Aviation Week and Space Technology*, 7 June 1999.
- [25] <http://www.air-defense.net/forum/index.php?topic=11376.0>
- [26] M.C. Jackson, "The geometry of bistatic radar systems," *IEE Proceedings*, Vol. 133, Part F., No. 7, pp. 604–612, December 1986.
- [27] H.D. Griffiths and C.J. Baker, "Passive Coherent Radar systems – part I: performance prediction," *IEE Proceedings Radar, Sonar and Navigation on Passive Radar Systems* (Special Issue), Vol. 152, No. 3, pp. 153–159, June 2005.
- [28] G.W. Ewell, "Bistatic radar cross section measurements," Chapter 7 in *Techniques of Radar Reflectivity Measurement*, (N.C. Currie ed.), Artech House, Dedham, MA, 1989.
- [29] R.E. Kell, "On the derivation of bistatic RCS from monostatic measurements," *Proceedings IEEE*, Vol. 53, pp. 983–988, 1965.
- [30] G.W. Ewell and S.P. Zehner, "Bistatic radar cross section of ship targets," *IEEE Journal of Oceanic Engineering*, Vol.OE-5, No. 4, pp. 211–215, October 1980.
- [31] M. Born and E. Wolf, *Principles of Optics* (sixth edition), Pergamon Press, London, p. 559, 1980.
- [32] P.M. Woodward, *Probability and Information Theory, with Applications to Radar*, Pergamon Press, London 1953; reprinted by Artech House, Dedham, MA, 1980.
- [33] T. Tsao, M. Slamani, P. Varshney, D. Weiner, H. Schwarzlander, and S. Borek, "Ambiguity function for a bistatic radar," *IEEE Transactions on Aerospace and Electronic Systems*, Vol. 33, No. 3, pp. 1041–1051, July 1997.
- [34] C.J. Baker, H.D. Griffiths, and I. Papoutsis, "Passive Coherent Radar systems – part II: waveform properties," *IEE Proceedings Radar, Sonar and Navigation on Passive Radar Systems* (Special Issue), Vol. 152, No. 3, pp. 160–168, June 2005.
- [35] M.C. Wicks, E.L. Mokole, S.D. Blunt, R.S. Scheible, and V.J. Amuso (eds), *Principles of Waveform Diversity and Design*, SciTech Publishing Inc., Raleigh, NC, 2010.
- [36] M.A. Ringer and G.J. Frazer, "Waveform analysis of transmissions of opportunity for passive radar," *Proceedings ISSPA '99*, Brisbane, Australia, pp. 511–514, 22–25 August 1999.

- [37] H.D. Griffiths, C.J. Baker, H. Ghaleb, R. Ramakrishnan, and E. Willman, "Measurement and analysis of ambiguity functions of off-air signals for passive coherent location," *Electronics Letters*, Vol. 39, No. 13, pp. 1005–1007, 26 June 2003.
- [38] M. Alard, R. Halbert, and R. Lassalle, "Principles of modulation and channel coding for digital broadcasting for mobile receivers," *EBU Technical Review*, Vol. 224, pp. 3–25, 1987.
- [39] D. Poullin, "Passive detection using digital broadcasters (DAB, DVB) with COFDM modulation," *IEE Proceedings Radar, Sonar and Navigation on Passive Radar Systems* (Special Issue), Vol. 152, No. 3, pp. 143–152, June 2005.
- [40] D.K.P. Tan, H. Sun, Y. Lu, M. Lesturgie, and H.L. Chan, "Passive radar using Global System for Mobile communication signal: theory, implementation, and measurements," *IEE Proceedings Radar, Sonar and Navigation on Passive Radar Systems* (Special Issue), Vol. 152, No. 3, pp. 116–123, June 2005.
- [41] B. Walke, *Mobile Radio Networks; Networking, Protocols and Traffic Performance*, Wiley, New York, 1998.
- [42] H. Guo, S. Coetzee, D. Mason, K. Woodbridge, and C.J. Baker, "Passive radar detection using wireless networks," *Proceedings IET of the Radar Conference RADAR 2007*, Edinburgh, pp. 1–4, September 2007.
- [43] F. Colone, K. Woodbridge, H. Guo, D. Mason, and C.J. Baker, "Ambiguity function analysis of wireless LAN transmissions for passive radar," *IEEE Transactions on Aerospace and Electronic Systems*, Vol. 47, No. 1, pp. 240–264, January 2011.
- [44] K. Chetty, G. Smith, H. Guo, and K. Woodbridge, "Target detection in high clutter using passive bistatic WiFi radar," *IEEE Radar Conference 2009*, Pasadena, CA, pp. 1–5, 4–8 May 2009.
- [45] Q. Wang, Y. Lu, and C. Hou, "Evaluation of WiMax transmission for passive radar applications," *Microwave and Optical Technology Letters*, Vol. 52, No. 7, pp. 1507–1509, 2010.
- [46] F. Colone, P. Falcone, and P. Lombardo, "Ambiguity function analysis of WiMAX transmissions for passive radar," *Proceedings of the IEEE International Radar Conference RADAR 2010*, Washington DC, pp. 689–694, 10–14 May 2010.
- [47] K. Chetty, K. Woodbridge, Guo, Hui, and G.E. Smith, "Passive bistatic WiMAX radar for marine surveillance," *Proceedings of the IEEE International Radar Conference RADAR 2010*, Washington DC, 10–14 May 2010.
- [48] J.M. Thomas, H.D. Griffiths, and C.J. Baker, "Ambiguity function analysis of Digital Radio Mondiale signals for HF passive bistatic radar," *Electronics Letters*, Vol. 42, No. 25, pp. 1482–1483, 7 December 2006.
- [49] H.D. Griffiths, A.J. Garnett, C.J. Baker, and S. Keaveney, "Bistatic radar using satellite-borne illuminators of opportunity," *Proceedings RADAR-92 Conference*, Brighton; IEE Conf. Publ. No. 365, pp. 276–279, 12–13 October 1992.
- [50] F. Colone, R. Cardinali, and P. Lombardo, "Cancellation of clutter and multipath in passive radar using a sequential approach," *Proceedings of the IEEE Radar Conference*, Verona (NY), USA, pp. 393–399, 24–27 April 2006.
- [51] R. Fletcher, *Practical Methods of Optimization* (2nd ed.), Wiley, New York, 1981.
- [52] B. Ristic, S. Arulampalam, and N. Gordon, *Beyond the Kalman Filter: Particle Filters for Tracking Applications*, Artech House, Dedham, MA, 2004.
- [53] P.E. Howland, D. Maksimiuk, and G. Reitsma, "FM radio based bistatic radar," *IEE Proceedings Radar, Sonar and Navigation on Passive Radar Systems* (Special Issue), Vol. 152, No. 3, pp. 107–115, June 2005.

- [54] J. Brown, K. Woodbridge, A. Stove, and S. Watts, “Air target detection using airborne passive bistatic radar,” *Electronics Letters*, Vol. 46, No. 20, pp. 1396–1397, 30 September 2010.
- [55] C.J. Coleman, R.A. Watson, and H. Yardley, “A practical bistatic passive radar system for use with DAB and DRM illuminators,” *Proceedings of the International Conference RADAR 2008*, Adelaide, Australia, pp. 1–7, 2–5 September 2008.
- [56] C. Bongioanni, F. Colone, D. Langellotti, P. Lombardo, and T. Bucciarelli, “A new approach for DVB-T Cross-Ambiguity Function evaluation,” *Proceedings of the EuRAD 2009 conference*, Rome, pp. 37–40, 30 September–2 October 2009.
- [57] <http://www.roke.co.uk/sensing/radar.html>
- [58] U.R.O. Nickel, “Extending range coverage with GSM passive localization by sensor fusion,” *Proceedings of the International Radar Symposium*, Vilnius, 14–18 June 2010.
- [59] Guo, Hui, K. Woodbridge and C.J. Baker, “Evaluation of WiFi beacon transmissions for wireless based passive radar,” *Proceedings of the IEEE Radar Conference*, Rome, Italy, pp. 1–6, 26–30 May 2008.
- [60] V. Koch and R. Westphal, “A new approach to a multistatic passive radar sensor for air defense,” *Proceedings of the IEEE International Radar Conference RADAR 1995*, Washington DC, IEEE Conf. Publ No.95CH3571-0, pp. 22–28, 8–11 May 1995.
- [61] V. Koch and R. Westphal, “New approach to a multistatic passive radar sensor for air/space defense,” *IEEE AES Magazine*, Vol. 10, No. 11, pp. 24–32, November 1995.
- [62] V.U. Zavorotny and A.G. Voronovich, “Scattering of GPS signals from the ocean with wind remote sensing application,” *IEEE Transactions on Geoscience and Remote Sensing*, Vol. 38, No. 2, pp. 951–964, March 2000.
- [63] H. You, J.L. Garrison, G. Heckler, and V.U. Zavorotny, “Stochastic model and experimental measurement of ocean-scattered GPS signal statistics,” *IEEE Transactions on Geoscience and Remote Sensing*, Vol. 42, No. 10, pp. 2160–2169, October 2004.
- [64] He, X., M. Cherniakov and T. Zeng, “Signal detectability in SS-BSAR with GNSS non-cooperative transmitters,” *IEE Proceedings Radar, Sonar and Navigation on Passive Radar Systems* (Special Issue), Vol. 152, No. 3, pp. 124–132, June 2005.
- [65] M. Cherniakov, R. Saini, R. Zuo, and M. Antoniou, “Space-surface bistatic synthetic aperture radar with global navigation satellite system transmitter of opportunity – experimental results,” *IET Radar, Sonar and Navigation on EMRS DTC* (Special Issue), Vol. 1, No. 6, pp. 447–458, December 2007.
- [66] M. Antoniou, R. Zuo, and M. Cherniakov, “Passive space-surface bistatic SAR imaging,” *7th EMRS DTC Technical Conference*, Edinburgh, 13/14 Jul 2010.

11.9 | FURTHER READING

A number of books, book chapters, and review papers have been published on bistatic radar in general and PBR in particular. The following are recommended:

- N.J. Willis, *Bistatic Radar*, 2nd ed., Technology Service Corp., 1995, corrected and republished by SciTech, 2005 (given as [1] above).
- V.S. Chernyak, *Fundamentals of Multisite Radar Systems: Multistatic Radars and Multiradar Systems*, Gordon & Breach, 1998 (given as [2] above).
- N.J. Willis and H.D. Griffiths, *Advances in Bistatic Radar*, SciTech, 2007 (given as [3] above).

N.J. Willis, “Bistatic Radar,” Chapter 23 in *Radar Handbook*, third edition (M.I. Skolnik ed.), McGraw-Hill, 2008 (given as [4] above).

M. Cherniakov (ed.), *Bistatic Radar: Principles and Practice*, (2007) and *Bistatic Radar: Emerging Technology*, (2008) Wiley (given as [5] above).

Advances in Bistatic Radar covers a number of recent developments, including descriptions of some systems whose details have only recently been declassified. *Fundamentals of Multisite Radar Systems* provides a thorough review of the theoretical aspects of multistatic radar systems. There is a chapter in Cherniakov’s *Bistatic Radar: Emerging Technology* book devoted to passive bistatic radar.

In addition, two journal special issues contain valuable and topical material:

C. Pell and E. Hanle (eds.), *IEE Proceedings Part F on Bistatic Radar*, *IEE Proceedings* (Special issue), Vol. 133, Pt.F, No. 7, December 1986.

P.E. Howland (ed.), *IEE Proceedings Radar, Sonar & Navigation on Passive Radar Systems* (Special issue), Vol. 152, No. 3, June 2005 (given as [16] above).

Air Traffic Control Radar

*John C. Porcello, Georgia Tech Research Institute (GTRI),
Atlanta, Georgia, U.S.A*

Chapter Outline

12.1	Introduction – The Task of Air Traffic Control (ATC)	543
12.2	System Requirements/Mission	552
12.3	Design Issues.	558
12.4	The Future of ATC Radar	582
12.5	Summary	585
12.6	Further Reading	585
12.7	Acknowledgments	585
12.8	References.	585

12.1 | INTRODUCTION – THE TASK OF AIR TRAFFIC CONTROL (ATC)

In order to understand how radar is utilized for air traffic control (ATC), a brief introduction to aviation is provided in the following paragraphs. Modern aviation involves large numbers of commercial, private, and military flights each day. The safe and efficient coordination of such a large number of flights is possible by the work of ATC. ATC, both commercial and military, relies on a system based on two important principles. First, that the air traffic controller has real-time knowledge of all flights (aircraft, helicopters, balloons, etc.) operating in a given volume of airspace, and second, that a system of communicating instructions between pilots and air traffic controllers is mutually understood by all who use the airspace. The air traffic controller has the life-critical task of coordinating safe and efficient flight in a specific volume of airspace by providing airspace usage instructions to pilots. These instructions from ATC to pilots provide both horizontal and vertical separation of each aircraft from takeoff, through the use of navigational waypoints in the airspace, up to and including approach and landing instruction, as well as other safety-related communications. Pilots operating in this selected airspace must understand and follow ATC instructions in order to maintain safe and efficient flight. It is this pilot–controller relationship that provides the safety and efficiency of aviation that we have come to expect from modern aviation. Air traffic control radar is the tool that ATC uses to obtain real-time, independent surveillance of all flying craft operating in a given volume of airspace. Furthermore, ATC radar also

provides ATC with real-time knowledge of specific types of severe and/or hazardous aviation weather (hail, wind shear, etc.) occurring within a given volume of airspace such that ATC can vector aircraft around these events to maintain aviation safety.

In the United States there are two general types of airspace: controlled and uncontrolled. ATC manages controlled airspace. Controlled airspace is a general term that refers to many airspace types defined by the Federal Aviation Administration (FAA). For our discussion, controlled airspace is everything within a given radius of specific airports, specific air routes, all airspace between 18,000 ft and 60,000 ft mean sea level (MSL), and any area that ATC provides service to. Other specific areas may be designated as controlled airspace. Essentially, most of the airspace east of the Mississippi River is controlled airspace. The majority of uncontrolled airspace exists west of the Mississippi River. Furthermore, commercial aviation may be described by two sets of flight rules. Visual flight rules (VFR) allow for operation of flying craft within certain areas of controlled airspace at specific altitudes when meteorological conditions permit safe flight based on the pilot being able to see and avoid other craft. Instrument flight rules (IFR) allow for flight into instrument meteorological conditions (IMC) in which the pilot is unable to see out of the cockpit and avoid other flying craft. ATC services in controlled airspace provide horizontal and vertical separation of aircraft, both IFR to IFR aircraft separation as well as IFR to VFR aircraft separation [31, 38]. ATC may also provide VFR traffic advisories in both controlled and uncontrolled airspace. Flying craft operating in both controlled and uncontrolled airspace operate a wide range of groundspeeds (a few knots to greater than supersonic flight) and cover a wide range of radar cross section (small flying craft to large commercial and transport aircraft).

ATC provides safe and efficient flight by guaranteeing that a particular volume of controlled airspace is free of other aircraft during a given period of time, or otherwise providing vectors to aircraft to maintain safe operating distances. ATC provides clearances to pilots to operate in a particular volume of airspace. Most often, this protected airspace originates at the departure airport, includes specific air routes, and concludes at a destination airport. The controlled airspace at both the departure and destination airports is referred to as the *terminal phase* of flight. The controlled airspace along air routes is referred to as the *en route phase* of flight. The two phases of flight, terminal and en route, make up the two largest types of controlled airspace. We will neglect other types of airspace for simplicity of this discussion. Additional details on ATC can be found in [67].

In the United States, the FAA performs the vast majority of ATC. The FAA operates not only a significant number of air traffic control radars, but also uses an entire system of systems to maintain safe and efficient air travel. This system of systems covers a wide variety of facilities and equipment used in aviation and is known as the National Airspace System (NAS). Due to the nature of aviation, and particularly requirements for safe air travel, NAS components such as ATC radar typically have challenging requirements for high reliability, maintainability, and availability (RMA).

As stated earlier, ATC radar is used by controllers to maintain real-time knowledge of the airspace and issue appropriate clearances to pilots for coordinating safe and efficient use of controlled airspace. Not surprisingly, ATC facilities, equipment, and air traffic controllers' tasks are generally divided along the two phases of flight. Likewise, ATC radar design is largely based on these two phases of flight. ATC radar supporting the terminal phase of flight is referred to as airport surveillance radar (ASR). ASRs are

S-band radars operating over a range 0.5 to 60 nmi. ATC radar supporting the en route phase of flight is referred to as air route surveillance radar (ARSR). ARSRs are L-band radars typically operating over a range of 5 to 250 nmi. Many NAS components, operations, and responsibilities are, in fact, divided between terminal and en route flight. A terminal radar approach control (TRACON) facility versus an air route traffic control center (ARTCC) is an example of ATC facilities that contrast terminal ATC versus en route ATC, respectively. It should also be noted that while the FAA operates all of the terminal radars, the FAA and the United States Air Force (USAF) jointly operate the en route radars along the periphery of the U.S. border.

The use of radar in ATC began after World War II, and up to the late 1950s and early 1960s generally provided only two-dimensional information of aircraft operating in a given airspace. This early use of radar provided only azimuth and range of aircraft, and the controller relied on the pilot to provide altitude information. The radar derived this information solely from the radar return off the skin of the aircraft. Information derived from conventional radar in the classic sense (an aircraft skin return) is referred to as *primary surveillance radar* (PSR).

The early 1960s began to see widespread use of an enhancement to radar known as *secondary surveillance radar* (SSR). SSR was derived from the military's identification of friend or foe (IFF) system. That is, when a cooperative airborne target is illuminated (also called an interrogation pulse) by a radar, it can transmit a known reply to let the radar know it is a friendly target. Lack of a reply in an IFF system indicates a potentially hostile target. SSR applies the beacon radar concept to enhance ATC by equipping aircraft with a beacon called a transponder. SSR has several important advantages that enhance PSR for ATC. First, because the aircraft is now using an onboard transmitter called a beacon to reply to the radar interrogation pulse, the aircraft can be detected at longer ranges than a conventional radar skin return. Second, ATC can assign aircraft-specific transponder reply codes (referred to as squawk codes) and can discriminate between aircraft based on the squawk code. Finally, the aircraft reply to the radar interrogation pulse can be encoded with additional information (Mode C transponders encode altitude information from sensors onboard the aircraft). The concept of SSR was originally applied to aviation using the air traffic control radar beacon system (ATCRBS). We will discuss the technical performance of both PSR and SSR in detail further in this chapter. It should be noted here that the use of a beacon radar return is not limited to ATC radar, but has been successfully used in other radar applications such as range instrumentation radar (RIR).

Figure 12-1 shows the antenna of the ASR-9. The ASR-9, like all modern ASR radars, implements PSR and SSR. The classic FAA-orange PSR and SSR reflector antennas are easily identified. ATC radar typically use a cosecant-squared reflector (as opposed to a purely parabolic reflector) to produce a fan beam pattern appropriate for 2-D surveillance radar [33]. Note the dual feed associated with the PSR allows for two antenna patterns: a high beam and a low beam. The low beam performs transmit and receive and is called the mainbeam. The high beam is receive-only; is referred to as the passive beam; and is used for near-range, high-angle coverage. This dual-beam system helps ATC radar to discriminate relatively close range surface clutter that occurs at very low elevation angles [10]. Detection and discrimination of aircraft in clutter is one of the most significant challenges in ATC radar design. The SSR interrogator antenna (the rectangular antenna at the top) is a monopulse beacon antenna mounted above the PSR reflector.

FIGURE 12-1 ■ ASR-9 Antenna Showing Collocated PSR Antenna and SSR Antenna [http://en.wikipedia.org/wiki/File:ASR-9_Radar_Antenna.jpg].



Currently in the NAS, ASRs in operational service include the ASR-7, ASR-8, ASR-9, and ASR-11 for terminal radars. ARSRs currently in operational service include Air Force long-range radars (LRRs) such as the AN/FPS-66/67 series, as well as dedicated FAA en route radars such as the ARSR-1/2, ARSR-3, and the ARSR-4 (AN/FPS-130). Since the ASRs are terminal radar, they are generally located on or very close to airports. The FAA requirements for improving terminal radar have been consistent for decades, resulting in continuous development and improvement of airport surveillance radar for many years. The ASR-9 was operationally deployed during the late 1980s. Air route surveillance radars, on the other hand, experienced development up to the deployment of the ARSR-4 during the 1990s. ARSR-4s were primarily deployed along the border of the continental United States (CONUS). ARSRs (and ASRs) can detect cooperative and noncooperative radar targets. With the exception of the ARSR-4, ASRs and ARSRs are 2-D radar and can generate slant range and azimuth information. The ARSR-4 is capable of determining azimuth, elevation, and range (a 3-D radar). With the increasing use of automatic dependent surveillance (ADS), which is simply cooperating equipment onboard the aircraft to support ATC (i.e., an operating transponder for SSR), the FAA had planned to decommission the en route radars located in the interior of the United States (all en route radar except the ARSR-4). In the aftermath of the terrorist attacks of September, 11, 2001, the U.S. government determined that the capability to detect and track noncooperating targets (i.e., anything airborne with a nonoperating SSR transponder) in the interior of the United States using only PSR (aircraft skin track) is essential. A Service Life Extension Program (SLEP) for these interior en route radars was implemented [3]. Operational SSR systems currently in use by the NAS include the air traffic control beacon interrogator (ATCBI) system such as the ATCBI-4, ATCBI-5, ATCBI-6, and Mode S.

Finally, it should also be noted that weather has a very significant impact on aviation in terms of safety and air travel capacity within a given airspace. Because weather is natural phenomena, it can impact very small to very large geographic

regions. Dangerous aviation weather (such as thunderstorms, ice, fog, etc.) remains a significant common factor in many fatal and nonfatal aircraft accidents, with severe weather responsible for air travel delays in terms of delayed departures or landings, as well as changes to the route of flight. Modern ATC radar systems detect and categorize precipitation intensity to provide real-time, coarse weather information for both the terminal and en route environment. The term “coarse weather information” is used here to refer to precipitation reflectivity measurements from the radar. The primary purpose of the radar design is for ATC, not to obtain specific meteorological information. The signal processing of radar echoes for coarse weather detection looks at weather as a distributed target, as opposed to signal processing weather as precipitation clutter for detection of point targets such as aircraft. The ASR-9 was the first ASR to be designed with dedicated coarse weather detection based on precipitation reflectivity. Modern ATC radar is capable of distinguishing six standardized levels of precipitation reflectivity in both the terminal and en route environment. The real-time, coarse weather information detected by ASRs and ARSRs is used by ATC to vector aircraft to support safe and efficient ATC operations. Aviation weather forecasting is provided by other dedicated weather sensors, such as the Next-Generation Weather Radar (NEXRAD) WSR-88D. The relatively recent past of aviation includes an additional meteorological radar to NAS dedicated to detecting the potentially catastrophic condition when weather phenomena known as a microburst produces wind shear in the terminal environment. Microburst phenomena, which can be invisible during a dry microburst, for example, can produce very significant low-level wind shear, resulting in an unrecoverable drop in aircraft altitude and potentially fatal aircraft accidents. It should be noted that detection of microburst phenomena by current ATC radar represents a significant technical challenge, primarily due to the low reflectivity of this weather phenomena combined with the limited number of pulses transmitted in a given direction due to the scan rate requirements for surveillance. The FAA meteorological radar designed to alert ATC of dangerous aviation weather is known as the Terminal Doppler Weather Radar (TDWR) and also provides real-time weather information to ATC. The FAA examined upgrading ATC radar for this same purpose, and the result was the weather systems processor (WSP), a bolt-on digital signal processor for the ASR-9 that provides dedicated wind shear detection equipment in the terminal environment. The WSP is deployed at medium-density air traffic airports where a TDWR is not present. Furthermore, nonradar weather sensor and processing systems are in the NAS to provide specific weather sensor information in real-time, such as the Low Level Windshear Alert System (LLWAS). Developing systems that optimize aviation weather sensors and aviation weather information for safe and efficient use of airspace remains an important priority in aviation. In this chapter, we are concerned with ASR or ARSR requirements that impact ATC radar, including precipitation detection requirements. Meteorological radar is discussed in detail in another chapter of this text, and radar used for terminal approach guidance, such as precision approach radar (PAR), will not be covered in this chapter.

12.1.1 Organization

Section 12.2 of this chapter discusses ATC radar system requirements and mission issues. The section begins with an overview and covers PSR and SSR. Section 12.3 looks at ATC radar design in detail. Specifically, Section 12.3 looks at PSR design

considerations such as radar transmitters, antennas, energy-on-target for detection, waveform design, clutter, dynamic range, and radar system stability. Section 12.3 continues by examining SSR design issues such as the SSR link calculation. This section also considers PSR design issues for weather radar detection. Finally, Section 12.3 considers ATC radar design issues for reliability, maintainability, and availability, as well as other operational performance issues. Section 12.4 looks at the future of ATC radar and air traffic surveillance. Chapter 12 concludes with a summary, further reading, acknowledgments, and references.

12.1.2 Key Points

- The air traffic controller has the life-critical task of coordinating safe and efficient flight in a specific volume of airspace by providing airspace usage instructions to pilots.
- Pilots operating in selected airspace must understand and follow ATC instructions in order to maintain safe and efficient flight.
- ATC provides safe and efficient flight by guaranteeing that a particular volume of controlled airspace is free of other aircraft during a given period of time, or otherwise providing vectors to aircraft to maintain safe operating distances.
- Air traffic control radar is the tool that ATC uses to obtain real-time, independent surveillance of all flying craft operating in a given volume of airspace.
- ATC radar also provides ATC with real-time knowledge of specific types of severe and/or hazardous aviation weather (hail, wind shear, etc.) occurring within a given volume of airspace such that ATC can vector aircraft around these events to maintain aviation safety.
- ATC radar employs both PSR (skin track) and SSR (aircraft transponder) for the terminal radar environment, which is serviced by ASRs, and the en route radar environment, which is serviced by ARSRs.
- Advancements in DSP technology, such as FPGAs, significantly increase the precision and complexity of signal-processing algorithms that can be implemented in real time for ATC radar.
- When we begin to consider ATC radar design, we should realize that ATC radar is a class of surveillance radar and, as such, PSR design is based on the principles of surveillance radar.
- SSR design is based on the military IFF system and relies on communications link budget principles to provide cooperative surveillance.
- ATC radars, and surveillance radars in general, have only a few pulses to tens of pulses of energy available from an aircraft for radar signal processing.
- ATC radar system stability sets a performance limit on the accuracy and sensitivity that a radar can measure Doppler shift and thereby discriminate stationary versus non-stationary targets.
- High probability of detection of wind shear phenomena such as wet or dry microbursts and other weather phenomena represents a challenge to ATC radar since it is optimized for the surveillance mission.

- ATC radar operational performance is a true measure of effectiveness and can be used to quantify whether or not a system meets the mission for which it is intended.
- Future ATC radar, whether it remains the primary ATC surveillance tool or becomes an alternative means of surveillance to support ATC, will continue to contribute to aviation safety.
- The FAA and the NWS have been jointly investigating the viability of Multifunction Phased Array Radar (MPAR) technology.
- ADS-B has a proven track record improving ATM in both the radar and non-radar environments.

12.1.3 Notation

The following lists several of the variable names found within this chapter:

$d\theta_{ERR}/dt$ = instantaneous change in phase with respect to time

$d\theta_{PK}$ = peak phase deviation in radians

df_{PK} = peak frequency deviation in Hertz

dBZ = radar reflectivity

DR = dynamic range

E_0 = energy required for detection

f_D = Doppler shift

f_m = modulation frequency in Hertz

f_{RD} = residual Doppler

G_T = transmit antenna gain

G_R = receive antenna gain

INP = integrated phase noise power

$L(f)$ = SSB phase noise performance in dBc/Hz

$L_{SYS}(f)$ = cascaded system-level SSB phase noise performance in dBc/Hz

L_{Abs} = atmospheric absorption loss

L_{Rt} = atmospheric refraction loss

L_{RI} = anomalous propagation loss

m = modulation index

P_{ADC} = ideal ADC quantization noise power in dBW referenced to a 1-ohm load

$P_{AV}A_r$ = power-aperture product

P_C = carrier power

P_{SSB} = SSB sideband power density in a 1-Hertz bandwidth

P_T = transmitted power

P_R = received power

R_{max} = maximum detection range

R = range

$s(t)$ = time domain expression for the radar waveform

S = received power

t_{BEAM} = time that the aircraft is within the 3-dB beamwidth of the antenna in seconds

t_D = time delay offset

t_S = search time

ψ_s = the surveillance solid angle, which must be scanned

ϕ_{RMS} = total system rms phase jitter in radians

σ = target RCS

σ_C = standard deviation of the clutter power spectrum in Hertz

ω_{SCAN} = antenna angular scan rate in RPM

θ_B = 3-dB antenna beamwidth in degrees

$|A(t, f_D)|^2$ = ambiguity surface

λ = wavelength

12.1.4 Acronyms

Commonly used acronyms in this chapter include:

ADC	analog-to-digital converter
ADS	automatic dependent surveillance
ADS-B	automatic dependent surveillance-broadcast
AM	amplitude modulation
ARSR	air route surveillance radar
ARTCC	air route traffic control center
ASR	airport surveillance radar
ATC	air traffic control
ATCBI	air traffic control beacon interrogator
ATCRBS	air traffic control radar beacon system
ATM	air traffic management
CD-2	common digitizer-2
CFAR	constant false alarm rate
COHO	coherent oscillator
CONUS	continental United States
DABS	Discrete Address Beacon System
DAC	digital-to-analog converter
DFT	discrete Fourier transform
DHS	Department of Homeland Security
DME	distance measuring equipment
DOD	Department of Defense
DSB	double sideband
DSP	digital signal processing
EMI	electromagnetic interference
FAA	Federal Aviation Administration
FIS-B	flight information service-broadcast
FM	frequency modulation
FPGA	field programmable gate array
FRUIT	false replies uncorrelated in time
GPS	global positioning system
G/T	antenna gain-to-noise temperature ratio
HPA	high-power amplifier
IFF	identification friend or foe

IFR	instrument flight rules
IMC	instrument meteorological conditions
ISLS	interference sidelobe suppression
LFM	linear frequency modulation
LLWAS	Low-Level Windshear Alert System
MDS	minimum discernable signal
MOE	measures-of-effectiveness
MOP	measures-of-performance
MPAR	Multifunction Phased-Array Radar
MSL	mean sea level
MTBCF	mean time between critical failures
MTD	moving target detector
MTI	moving target indicator
MTL	minimum threshold level
MTTR	mean time to repair
NAS	National Airspace System
NEXRAD	Next-Generation Weather Radar
NEXTGEN	Next-Generation Air Transportation System
NLFM	nonlinear frequency modulation
NWS	National Weather Service
O&M	operations and maintenance
PAR	precision approach radar
PD	pulse Doppler
PDF	probability density function
PRF	pulse repetition frequency
PSR	primary surveillance radar
RCS	radar cross section
RFI	radio frequency interference
RMA	reliability, maintainability, and availability
RMMS	remote maintenance monitoring subsystem
RPM	revolutions per minute
RSP	radar signal processing
RSS	root-sum-square
SCR	signal-to-clutter ratio
SCV	subclutter visibility
SLEP	service life extension program
SNR	signal-to-noise ratio
SSB	single sideband
SSR	secondary surveillance radar
STALO	stabilized local oscillator
STC	sensitivity time control

TCAS	Traffic Collision Avoidance System
TDS	track during scan
TDWR	Terminal Doppler Weather Radar
TIS-B	traffic information service-broadcast
TWS	track while scan
UAT	universal access transceiver
USAF	United States Air Force
VFR	visual flight rules
WSP	weather systems processor

12.2 | SYSTEM REQUIREMENTS/MISSION

12.2.1 Overview

In the previous section, we briefly described the aviation environment and the use of radar by ATC to obtain real-time knowledge of all flying craft operating in a given volume of airspace. This includes both PSR and SSR. We described two classes of ATC radar: the ASR and the ARSR. We also mentioned the large operating range of groundspeeds and radar cross sections from various types of flying craft, as well as the significant impact of weather on aviation. Based on the previous section, we can now describe ATC radar in more detail and discuss some basic system requirements for ATC radar.

12.2.2 Primary Surveillance Radar (PSR)

For PSR, ATC radar must detect and track both slow- and fast-moving aircraft. ATC radar must also discriminate aircraft from non-aircraft in the radar environment. One of the most basic design considerations for ATC radar is clutter suppression. Clutter in the ATC radar environment refers to several clutter types, including land (ground, ground vehicles, etc.), sea, weather, birds, and any additional natural phenomena that generate strong reflections of the transmitted pulse but are not reflections from a flying craft. Clutter is such an important consideration in radar design that it has required a great deal of characterization in the past, and continues to do so. Because clutter echoes are the result of complex physical process that may change over various time periods (seconds to seasonal, etc.), good ATC radar design requires an understanding of the impact of each applicable type of clutter on radar performance. Large flocks of birds (angel clutter) impact the radar very differently than sea clutter. As pointed out in previous chapters in Volume 1 of the *Principles of Modern Radar* [32], ground clutter (largely stationary clutter) in particular is typically much stronger than the target return from the skin of an aircraft. Improvement factor (IF) is used to quantify the increase in signal-to-clutter ratio due to MTI filtering, and subclutter visibility (SCV) accounts for detection and false-alarm probabilities as well as the detector. These measures of performance are used to quantify the ability of ATC radar to detect and track objects in the presence of clutter. Weather clutter, or in the case of ATC radar, precipitation clutter, is particularly important to ATC. ATC radar has specific processing to detect precipitation clutter and process weather echoes into two or six levels of precipitation. The requirements of ATC

radar to detect and track aircraft over near range and far range, as well as the sensitivity and dynamic range needed to provide weather processing, are challenging requirements to ATC radar. ATC radar often uses sensitivity time control (STC) to balance these needs in the dynamic range. Furthermore, in order to reduce operating costs and increase reliability, microwave power tube transmitters have been replaced with solid-state radar transmitters when it is technically and operationally feasible. This reduction in peak power due to the conversion to solid-state transmitters has resulted in a need for more than one waveform in order to maintain detection and resolution performance of the instrumented range of the radar.

Although there is no single formula that quantifies ATC radar design, some important considerations and methodologies for radar design have been discussed [8, 9]. A good ATC radar design is achieved typically by coherent and noncoherent integration of several transmitted pulses such that the total target energy becomes sufficiently high enough to produce an SNR that meets the required probability of detection. Furthermore, radar signal processors use clutter maps to estimate the clutter level and control the false-alarm rate of the radar. Both en route radar (ARSR) and terminal radar (ASR) need to maximize the probability of detection (the probability that an aircraft is present) for a given target model. After the target is detected, the target detections must be correlated so that the aircraft can be tracked. ATC radars must have processing resources to maintain tracks of aircraft. Many other ATC radar specifications exist for an operational ASR or ARSR.

Historically, the ARSRs mission and requirements have been developed specifically for long-range ATC radar [10]. The ARSR-4 requirements are more of an exception and a significant improvement on previous ARSRs in the sense that the requirements for this system were based on a joint collaboration between the FAA and the USAF [7, 11]. The ARSR mission requirements are long-range surveillance, with a maximum range out to typically 200 nmi for an ARSR-3 prior to the last SLEP [3], and 250 nmi for an ARSR-4 with a service altitude of 100,000 ft. ARSRs are L-band radars (1.215–1.4 GHz) designed to detect relatively small targets on the order of 1 m^2 over the radar service volume. ASRs are shorter-range S-band radars (2.7–2.9 GHz), with a maximum range out to typically 60 nmi and a service altitude of around 24,000 ft. En route radar (ARSR) can be contrasted to terminal radar (ASR) in the sense that en route radars may be located based on strategic and/or geographic considerations such as border, coastal and mountainous regions, and overall en route coverage considerations, while ASRs are located on, or very near, airports to provide real-time detection and tracking of aircraft in the terminal area.

Table 12-1 contrasts some of the parameters between ASRs and ARSRs. Table 12-1 is based on information available in [1, 2, 4, 8, 10] as well as some published marketing material. Table 12-1 is not intended to be a comprehensive comparison, but rather to illustrate the performance and improvements made by generations of ATC radar. The original ASR-8 and original ARSR-3 were based on tube transmitter technology. The ASR-9 incorporated the first MTD architecture and a weather channel, and uses tube transmitter technology. The high output power of the ASR-9 provides enough transmit signal strength such that it can be enhanced with a WSP to detect microbursts. The ARSR-4 represents the last new ARSR design, which also fulfills the FAA and DOD long-range surveillance mission. The ASR-11, the ASR-12, and the ARSR SLEP radars [3] (not shown in Table 12-1) represent modern digital radar technology with solid-state transmitters. Note that the information for the original ARSR-3 in Table 12-1 is not based on the upgrade of the interior ARSRs from the SLEP [3].

TABLE 12-1 ■ Performance Characteristics of Some ASRs and ARSRs

Radar vs Parameter	ASR-8 (original)	ASR-9	ASR-11	ASR-12	ARSR-3 (original)	ARSR-4
<i>Frequency</i>	S-band	S-band	S-band	S-band	L-band	L-band
<i>Surveillance mission (range)</i>	2-D terminal (0.5–60 nmi)	2-D terminal (0.5–60 nmi)	2-D terminal (0.5–100 nmi)	2-D terminal (0.5–60 nmi)	2-D en route (5–200 nmi)	3-D en route (5–250 nmi)
<i>Antenna scan rate (RPM)</i>	12.8	12.5	12.5	10/12/15	5	5
<i>Peak power (kW)</i>	1,400 (tube)	1,200 (tube)	34 (solid-state)	22 (solid-state)	5,000 (tube)	60 (solid-state)
<i>Pulse width (µSec)</i>	0.6	1.05	89 (long) 1 (short)	55 (long) 1 (short)	2	150
<i>Pulse compression</i>	No	No	NLFM	NLFM	No	NLFM
<i>Ant. gain TX (dB)</i>	>33.5	>33.5	>33.5	>33.5	34	35
<i>Ant. gain RX (dB)</i>	33	33.5/32.5	33.5/32.5	33.5/32.5	34	40
<i>Polarization</i>	Linear, circular	Linear, circular	Linear, circular	Linear, circular	Horiz. and vert. circular	Linear

The development of ATC radar originated in the early foundations of radar using analog signal processing. Traditionally, ATC radar has primarily used the Doppler velocity of aircraft to discriminate between aircraft and significant stationary clutter. Additional signal processing techniques to improve detection and tracking performance have been successfully developed and implemented. ATC radar systems use pulsed radar along with coherent transmitter/receiver architectures such that the Doppler shift of the received pulse is used to determine the presence of a target. Often, this is performed using Doppler filtering. Later in the chapter we will discuss radar stability, the capability of the radar to detect true target Doppler from internally generated phase noise and other noise sources, which is a function of the transmitter and receiver components and system architecture.

Radar signal processing (RSP) for moving targets can be divided into two general classes based on the receiver signal processing techniques. Moving target indicator (MTI) and pulse Doppler (PD) represent these two broad types of RSP. MTI is a general class of radar signal processing that uses the Doppler shift of any moving target to separate it from relatively stationary clutter. Although the MTI transmitter and receiver are phase coherent, MTI signal processing may use coherent and non-coherent signal processing of the radar return in the receiver. ARSRs are typically coherent MTI. MTI RSP architecture is often based on the use of relatively simple filtering to suppress clutter. This MTI filtering operation typically produces blind speeds at specific PRFs, which are compensated by the use of staggered PRFs. PD radar is a class of radar signal processing that uses coherent integration in the receiver signal processing, typically via a discrete Fourier transform (DFT), to coherently integrate radar return energy in the receiver and implement a Doppler filter bank for discrimination. These definitions for MTI and PD RSP architectures should only be considered from a high-level and historical perspective. RSP architecture is often implemented to yield the best performance based on the radar system requirements and the radar environment.

Within ATC radar, a subclass of MTI processing is called moving target detection (MTD) [8]. MTD is a dedicated method of radar signal processing specifically for ASRs, and was developed by MIT Lincoln Laboratory for the FAA. MTD enhanced the MTI architecture by increasing the linear dynamic range of the signal processor followed by Doppler filtering, CFAR processing, and a clutter map to improve detection in the presence of clutter [1]. As described in [2], MTD is a specific type of RSP designed for a low-PRF, 2-D Doppler air surveillance radar in a heterogeneous clutter environment. MTD is designed to provide very reliable detection and tracking of aircraft when surface clutter, precipitation clutter, and angel clutter are present. It has been highly successful for ASR signal processing. Details of MTI, PD, and MTD architectures can be found throughout the literature [1, 2, 4–6, 8, 35, 36].

Radar system design often represents a performance trade-off based on system requirements for the radar mission. ATC radar is no exception, and ASRs and ARSRs have very different implementations in order to meet the demand of terminal radar and en route radar, respectively. Several radar texts listed in the reference section of this chapter contain a detailed performance analysis of various MTI, PD, and MTD processing configurations. The ASR and ARSR systems identified as currently operational in the NAS were originally designed and deployed many years ago. Perhaps the most important thing to remember when designing, developing, or improving ATC radar

systems and their processing techniques is that substantial increases in digital signal processing (DSP) have occurred since the initial deployment of these radars. Furthermore, the increasing capability of DSP allows us to increase ATC radar system performance by implementing radar signal processing algorithms of higher complexity. Some of the initial design and implementation trade-offs made by older systems may not be relevant to a new or upgraded system. Advancements in DSP technology such as field programmable gate arrays (FPGAs), as well as faster and higher-resolution ADCs and DACs, are examples of currently available DSP technology that significantly increase the precision and complexity of signal processing algorithms that can be implemented in real time for ATC radar. This relatively recent trend, termed by some engineers as the golden age of signal processing, is expected to continue and provide a larger design space for the engineer to meet increasingly demanding radar performance and multi-function mission requirements [57, 58].

12.2.3 Secondary Surveillance Radar (SSR)

We now look at SSR, where a cooperative aircraft has an operating transponder. For SSR, aircraft detection and tracking becomes significantly easier when a cooperative target is radiating a beacon. SSR works on the principle that a ground-based SSR transmits interrogation pulses at 1,030 \pm 0.2 MHz. The SSR is often, but not necessarily, collocated with PSR, as shown in Figure 12-1. The SSR interrogation pulses are received by the transponder on the aircraft. Since the transponder on the aircraft has a built-in receiver, the radar range equation is now reduced to a single one-way transmission path equivalent to a communications link budget. This fact significantly improves the performance of SSR, and reduces the cost of SSR over PSR. The transponder on the aircraft determines if the interrogation pulse was transmitted by the mainbeam of the SSR antenna or from a sidelobe of the SSR antenna. If the transmit pulse was from the mainbeam of an SSR antenna, the transponder transmits a coded reply on 1,090 \pm 3 MHz [12]. SSR operates at L-band, like ARSRs, and has sufficient pulsed energy in each path to operate over long distances. Given the SNR form of the radar range equation at the radar site from an aircraft:

$$\frac{S}{N} = \frac{P_T G_T G_R \lambda^2 \sigma}{(4\pi)^3 R^4 (kTB) L_{SYS}}$$

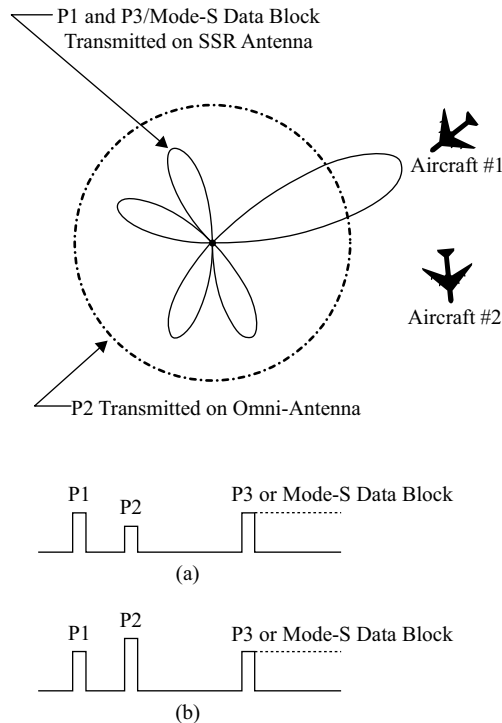
we can write the beacon form of a one-way radar range equation. Since we only have path loss in one direction, the SNR at the transponder on the aircraft is now only a function of the square of the range in the denominator, as opposed to the fourth power of the range in the denominator for a round-trip signal path. Also, note that the equation is obviously independent of the radar cross section, the L-band wavelength of the SSR will be longer than an S-band signal from an ASR system, and the noise power is a function of the receiver in the transponder. Finally, note also that the transponder on the aircraft will have a much smaller antenna gain than that of the radar antenna. The SNR seen at the transponder on the aircraft can be written as follows, representing a one-way transmission path from the radar to the transponder on the aircraft:

$$\frac{S}{N} = \frac{P_T G_T G_{Ri} \lambda^2}{(4\pi)^2 R^2 (kTB) L_{Ri}}$$

where B and T are the transponder receiver bandwidth and system temperature, respectively. L_{Rt} represents the transponder losses, R is the SSR antenna to transponder path distance, and G_{Rt} is the antenna gain of the transponder antenna. In practice, SSR can be a challenging environment, with high aircraft density generating strong interference from other aircraft replies and potentially strong multipath channel environment. Aircraft interrogation pulses and aircraft transponders have operating modes [13, 40]. The most common transponder operating modes are Mode A, Mode C, and Mode S. The FAA requires aircraft to have at least Mode C (altitude reporting) to enter all major terminal areas in the United States. Terminal areas are controlled airspace in the vicinity of major airports, which resemble an upside-down wedding cake centered around the major airport. The SSR ground transmitter may transmit a Mode A or Mode C interrogation pulse to an aircraft. Mode A transponder replies provide the transponder identification code, which is set in the cockpit by the pilot. The transponder identification code is coordinated by ATC for aircraft identification, or can be set by the pilot to indicate to ATC specific in-flight emergencies (loss of radio communications, hijack, etc.). Mode C transponder replies provide the encoded pressure altitude based on an altitude sensor onboard the aircraft. It should be noted here that Mode C provides aircraft altitude information necessary (in increments of 100 feet) along with SSR determination of azimuth and slant range to the aircraft and yields the aircraft 3-D position in space. Mode S provides selective interrogation of aircraft, monopulse processing, and a ground-air-ground data-link. A detailed discussion of Mode S can be found in [14, 40]. Originally started as the Discrete Address Beacon System (DABS), Mode S also supports the Traffic Alert and Collision Avoidance System (TCAS) [15]. A good discussion of the history behind SSR can be found in [40].

In this discussion of SSR, it was noted earlier that the aircraft transponder determines if the interrogation pulse was transmitted by the mainbeam of the SSR antenna or by an antenna sidelobe. Interrogation pulses are used by the transponder on the aircraft to make this determination. Figure 12-2 shows an SSR antenna pattern and a collocated omnidirectional antenna. The first interrogation pulse, P1, and third interrogation pulse, P3 (for Mode A/C) or the Mode S data block are transmitted by a rotating array antenna. The second interrogation pulse, P2, is transmitted by an omni-directional antenna. The gain and transmit power of the omni-directional antenna is adjusted such that the EIRP is just above the maximum sidelobe power level and below the mainbeam power level of the rotating array antenna. Therefore, when an interrogation pulse is transmitted by the SSR, the aircraft transponder can perform an amplitude comparison of P1 and P2 and determine if the interrogation was from the mainbeam or antenna sidelobe. If the received P1 has a higher amplitude than the received P2, the aircraft transponder generates a reply. In other words, the transponder will send a reply to any valid interrogation by the mainbeam of an SSR transmitter pulse. Other antenna configurations for SSR may be used, and monopulse antennas have improved azimuth estimation of the reply. Finally, we should note that since the transponder will reply to any valid SSR interrogation pulse, many of the early technical challenges that faced the ATCRBS are based on an SSR site reception of a transponder reply to interrogations from another SSR transmitter. Such replies in SSR terminology are called false replies uncorrelated in time (FRUIT). Various types of defruiting equipment have been employed to solve this issue, and other SSR issues have been addressed. However, assuming aviation security considerations are resolved, it is likely that the next major improvement to dependent surveillance will be the widespread implementation of automatic dependent surveillance-broadcast (ADS-B). We will take a closer look at SSR design issues later in this chapter.

FIGURE 12-2 ■ SSR Discrimination of Interrogation Pulse. (a) P1 Amplitude Greater than P2 Amplitude, a Valid SSR Interrogation Pulse, and the Aircraft Transponder Will Reply to This Interrogation Pulse. (b) P2 Amplitude Greater than or Equal to P1 Amplitude, an Invalid Interrogation, and the Aircraft Transponder Will Ignore the Interrogation Pulse.



12.2.4 Summary of System Requirements/Mission

In the previous sections we described the sole purpose of ATC radar – to support the ATC mission of providing safe and efficient flight. We also described ATC radar supporting two distinct ATC missions. The ASR provides real-time knowledge of aircraft and hazardous weather in terminal airspace, and the ARSR provides this capability in en route airspace. Design and development of ATC radar systems demand a thorough understanding of the ATC mission, ATC input to understand and improve radar service to ATC, and practical knowledge of radar in the NAS environment. During the development and modernization of NAS, instances of ATC systems development without an understanding of the ATC mission and controller input have occurred with poor results [24]. Having emphasized this point, the next sections will focus on basic ATC radar design issues.

A comprehensive explanation of ASR or ARSR radar performance requirements for an operational ATC radar system is beyond the scope of a single chapter. The goal of this section is to describe basic ASR and ARSR radar design issues. Operational ATC radar systems will have many basic requirements and derived requirements, as well as performance specifications at the system level, subsystem level, and component level.

12.3 | DESIGN ISSUES

12.3.1 Primary Surveillance Radar Design Issues

We shall discuss design issues for PSR in the following sections. The discussion that follows is based on currently operational ATC radar systems. The discussion applies to ground-based, fixed ATC radar that use an antenna rotating at a constant scan rate and

covering 360 degrees in azimuth at a fixed elevation angle. When we begin to consider ATC radar design, we should realize that ATC radar is a class of surveillance radar and, as such, PSR design is based on the principles of surveillance radar. Both Skolnik [8] and Barton [33] derive the *search radar equation*. Using Equation 7.2 in [33], we can express the detection performance of a search radar as

$$P_{AV}A_r = \frac{4\pi(R_{max})^4 E_0 \psi_s}{t_s \sigma}$$

where

- $P_{AV}A_r$ = product of average transmitter power and antenna aperture, also known as the power-aperture product,
- R_{max} = maximum detection range,
- E_0 = energy required for detection,
- ψ_s = surveillance solid angle that must be scanned during a given search time t_s , and
- σ = target RCS.

The search radar equation simply describes the fact that in order to perform radar surveillance over a fixed volume in a given time and collect a specific amount of energy for detection based on an RCS, there exists a minimum power-aperture product required for such a task. In other words, the system requirements for surveillance volume and detection metrics will typically drive the radar design to a minimum power-aperture product. It should be noted that the search radar equation is based on the radar equation using noise-limited detection. Furthermore, although the search radar equation is independent of frequency, there are frequency-dependent practical implications with respect to path losses, system losses, and power-aperture generation. It is also worth noting that the equation is not restricted to monochromatic or narrowband systems or the signal processing used in the radar, all of which factor into the value of E_0 . The search radar equation is very intuitive, defines radar parameters that can be traded to meet detection performance criteria, and provides initial design insight into surveillance radar. This is particularly true for radars with constant scan rates, such as ASRs and ARSRs. For ATC radar, ψ_s is fixed by the volume coverage requirements over 360 degrees in azimuth, and there is a relatively small range for the search time t_s for both ASRs and ARSRs. Given that target range and target RCS for ATC radar are also defined by the ATC mission requirements and aircraft characteristics, the remaining design space leaves power-aperture product and energy required for detection.

ATC radar discriminates between relatively stationary targets (clutter) with large echo power and moving targets (aircraft) with much lower echo power. The ability of the radar to perform its mission is a function of the ability of the radar to discriminate between these types of returns. Two major factors that determine the ability of the MTI radar to discriminate moving targets from clutter are stationary clutter filtering and radar stability [1]. As described earlier, one of the major challenges to ATC radar is the limited amount of energy-on-target that can be reflected from an aircraft and still maintain volume coverage for a given set of parameters from the search radar equation. This leaves a finite number of pulses available to filter stationary clutter from the radar echo data in order to observe moving targets. Furthermore, the spectral width associated with stationary clutter will be impacted by natural clutter motion phenomena (such as wind-blown trees) and antenna scan modulation effects (a product of antenna rotational motion). The radar designer must select the best MTI filtering that can perform this task.

References [1, 2] and Volume 1 of *Principles of Modern Radar* [32] introduced MTI pulse cancellation filters, also known as delay line cancellers or nonrecursive cancellers, that have the ability to notch-filter stationary clutter. Circuit diagrams and performance curves are provided in these references for analysis of two-pulse and three-pulse cancellers. This concept can be extended to *N-pulse MTI cancellers* to utilize this class of filtering. Furthermore, it was shown in the references that MTI pulse cancellation filters also have rejection regions at multiples of the PRF. This causes the filter to reject valid target velocities at integer multiples of the PRF, and hence the term *blind speeds* is applied to characterize the velocities at which the filter will reject desired signals. From [1] we have the following:

$$V_{BLIND} = k \cdot \frac{0.29 \cdot f_r}{f_{GHz}}$$

where

$$\begin{aligned} V_{BLIND} &= \text{blind speed in knots,} \\ f_r &= \text{PRF in Hertz,} \\ f_{GHz} &= \text{transmitted frequency GHz, and} \\ k &= \text{any integer } (k = \dots -3, -2, -1, 0, 1, 2, 3, \dots). \end{aligned}$$

Because of the blind speeds associated with the filtering, MTI radar typically staggers the PRF in order to observe the blind speeds from a single PRF. The references listed earlier also detail the procedure for staggered PRF design for MTI radar.

Not surprisingly, the earlier discussion of MTI filtering has some associated definitions for performance. If we consider the MTI filter as a singular process, strictly in terms of the change in signal-to-clutter ratio at the input of the MTI filtering to the signal-to-clutter ratio at the output of the MTI filtering, averaged over all Doppler frequencies of interest, we have the following definition for improvement factor:

$$I_C = \frac{SCR_{AVE_OUT}}{SCR_{AVE_IN}}$$

where

$$\begin{aligned} I_C &= \text{improvement factor expressed as a ratio,} \\ SCR_{AVE_IN} &= \text{average signal-to-clutter ratio (SCR) at the input of the MTI filtering, and} \\ SCR_{AVE_OUT} &= \text{average SCR at the output of the MTI filtering.} \end{aligned}$$

It should be noted that in ATC radar some definitions of MTI improvement factor are based on the broader metric of interference residue power in place of clutter power as the definition of improvement factor. Likewise, we can define the *MTI gain* based on the average ratio of output signal to input signal and the *clutter attenuation* ratio as the ratio of input clutter to output clutter. The *subclutter visibility* (SCV) is a measure of the ability of the radar to detect targets at the required P_{fa} and P_d in the presence of clutter. Details on these basic definitions are provided in [1, 2, 32] and most general radar texts that discuss MTI radar.

The topics of antenna scan modulation and radar stability will be addressed later in the chapter. Radar stability simply refers to the internal characteristics of the radar as a system to detect true target Doppler from internal noise in the radar for the purpose of discriminating moving targets from stationary clutter.

In Volume 1 of *Principles of Modern Radar* [32], the concept of *clutter mapping* was discussed. As a ground-based fixed radar site, ATC radar has the advantage of continuous mapping of clutter without any platform motion due to the radar. This allows the radar to exploit information from the clutter map to discriminate point targets (aircraft) and even maintain track when the radial velocity component is at or near zero. Clutter mapping, including adaptive clutter maps, has been a successful processing technique in ATC radar.

It should also be noted that all ATC radars must be interoperable with the existing NAS infrastructure. ATC radar detection reports are correlated into aircraft tracks for use by ATC. Tracking algorithms, such as track while scan (TWS), can be used to convert detections into aircraft tracks. The aircraft track information is often converted to a standard NAS data format to share with various users, such as the common digitizer-2 (CD-2) data format.

The following sections address some of the most significant design issues of ATC radar. It should be noted that each type of ASR and ARSR has architecture-specific characteristics that vary depending on the mission requirements and specifications. Furthermore, variations in radar architecture are often vendor dependent as well. Ultimately, verification of radar design choices and quantifying performance metrics of a given radar architecture require solid engineering practices in modeling and simulation, as well as testing and data analysis.

12.3.1.1 Design Issue – Radar Transmitter Considerations

Radar transmitters generate high levels of radio frequency (RF) and microwave power. The radar performance is not only a function of the output power level, but also the stability of the transmitted pulse. Transmitter stability can have a significant impact on radar system stability. ATC radars require substantial amounts of radiated power, and the resulting high-power transmitters tend to have reliability issues. Systems such as the ASR-9 require a high-power amplifier tube and high-voltage power supplies to operate the klystron tube. Tube voltage requirements can easily exceed 30-kV beam voltage. The design and construction of such a power supply requires close attention to details associated with cooling (to keep the electronic components within safe operating ranges); voltage isolation (to prevent arcing and corona, which can deteriorate insulating materials over time and eventually result in breakdown or arcing); and circuit designs required to generate the regulated, low-ripple, and low-noise voltages required by the tube for proper system operation.

The major reliability problems seen in current ATC radars are the result of either moving mechanical components or subsystems related to the high-power transmitters. This is not surprising, since these components are often the source of reliability issues in other similar systems for military applications. The most common failure modes are related to the high-power transmitter, high-power rotary joints, and the mechanical servo systems that control antenna rotation. ASRs and ARSRs are rotating antenna radars that require rotating joints to feed the RF signal (on transmit and receive) from the antenna to the transmitter or receiver subsystems.

The high-voltage power supply takes an input AC voltage and transforms the output to provide the higher voltage required by the microwave power tube. High-voltage step-up transformers are generally utilized to provide the step-up function. These circuits may operate at either 60 Hz or 400 Hz, or possibly at some higher frequency if a switch mode or resonant power supply architecture is used. On the primary or low-voltage side of the transformer, there are high currents and moderate voltages, and stresses on the

control components (silicon-controlled rectifiers, transistors, etc.) can be very high, especially as the switching frequencies increase. On the high-voltage side, the currents are lower, but the operating voltages are higher. Derating of the components that are used (such as rectifier diodes, filter capacitors, etc.) to account for parasitic inductances and capacitances is important, especially at higher switching frequencies.

Finally, many hazards to humans exist when working on RF and microwave power tubes. Extreme caution is required. Operating voltage levels above about 10 kV can generate X-rays and require sufficient shielding to protect personnel. Since an electron beam is sensitive to any magnetic field, care must be taken and nonmagnetic tools are required to work in close vicinity of klystrons, magnetrons, and other power tubes. Additional caution is required with any power tubes that have a broken vacuum envelope, as the inside of power tubes can contain hazardous materials.

12.3.1.2 Design Issue – Radar Antenna Aperture

The radar antenna is arguably the single most important component in radar performance. For ATC radar, this is typically a narrow beamwidth in azimuth with a large beamwidth in elevation, also called a fan beam, to sweep over a specific volume coverage pattern. In addition to antenna gain, antenna sidelobes are among the most important characteristics of the antenna with respect to the radar performance. Antenna sidelobes are an undesired source of transmission and reflection of radar energy, as well as an additional source of input noise (and jamming) for the radar receiver. In the ATC radar environment, where there is strong clutter in the presence of weak targets, performance can be substantially impacted by sidelobe energy, also known as *sidelobe clutter*. The radar receiver performance is adversely impacted by the addition of this unwanted sidelobe energy. For example, the ARSR-4 required very low sidelobe levels (–35 dB at all beams and all frequencies) to achieve the system performance requirements [11] and thus used a phased array feed in the antenna. Finally, for receiver system performance calculations, it is important to note that the G/T ratio (a figure of merit) of an antenna will set the initial SNR that will be seen in the radar receiver chain.

With the exception of the 3-D ARSR-4 antenna, all other ASR and ARSR antennas have a fan beam pattern for 2-D surveillance and do not have elevation data. This 2-D processing is performed in range and azimuth gates (RAGs). ASR and ARSR antennas have an azimuth beamwidth typically between 1 and 1.5 degrees. ARSRs typically have a maximum elevation coverage of about 40–45 degrees, while ASRs have a typical elevation coverage angle of about 30 degrees. As the antenna rotates, this upper limit on the elevation pattern produces the *cone of silence* over the top of the radar where it is blind to aircraft detection. Another characteristic of ATC radar is that the PSR antenna reflector is designed to provide a *cosecant-squared* coverage pattern. The ideal cosecant-squared coverage pattern is designed to provide sufficient power gain at high elevation angles such that a target approaching at constant height would provide a constant received signal. Details of the cosecant-squared pattern can be found in many texts on antenna design, as well as [33], with implementation typically performed by shaping the reflector to obtain the desired pattern. Finally, another characteristic of ATC radar aperture is the *dual-beam configuration* as shown in Figure 12-1. The upper beam is passive for receive only for near-range, high-angle coverage and the lower mainbeam operates on transmit and receive. As previously mentioned, this dual-beam system helps ATC radar to discriminate relatively close-range surface clutter, which occurs at very low elevation angles [10].

In addition to natural clutter motion phenomena, a rotating antenna in an MTI radar will introduce amplitude modulation (AM) on a return. This is known as antenna scanning modulation [1, 2, 8]. Antenna scanning modulation is the result of the relative motion between a scatterer and the two-way antenna pattern. It is observed when an antenna scans by clutter or a target and a transmitted pulse train of finite duration is echoed back to the radar. This phenomenon adds finite spectral width to stationary clutter. From [1], we can quantify antenna scan modulation as follows:

$$\sigma_C = \frac{6 \cdot \omega_{SCAN}}{3.77 \cdot \theta_B}$$

where

σ_C = standard deviation of the clutter power spectrum in Hertz,
 ω_{SCAN} = antenna angular scan rate in revolutions per minute (RPM), and
 θ_B = 3-dB antenna beamwidth in degrees.

For ATC radar, this only amounts to a few Hz. For example, an ATC radar with a scan rate of 15 RPM and beamwidth of 1.25 degrees yields a spectral smear due to antenna scan modulation of only about 19 Hz.

12.3.1.3 Design Issue – Energy-On-Target, P_d and P_{fa}

The most fundamental purpose of ATC radar is to accurately identify an aircraft present or not present in a given airspace. ATC radar design must maximize the probability of detection P_d and minimize the probability of false alarm P_{fa} . As the antenna rotates in azimuth, the radar transmits pulses to detect targets. In this situation, the design parameters at the radar that impact the amount of energy reflected by the aircraft include antenna scan rate, antenna gain (both transmit and receive), antenna beamwidth, the transmit waveform, and the PRF used to transmit the waveform. Note that the PRF may be constrained by design or requirements to provide an unambiguous range and/or Doppler frequency. These are very important initial design parameters for an ATC radar. The radar system requirements provide the necessary maximum detection range for a given minimum radar cross section of a target. As the main beam of the antenna sweeps through an azimuth containing an aircraft, a number of pulses will be reflected back to the radar site. The number of pulses echoed back by the aircraft is also a function of the relative velocity and range of the aircraft with respect to the radar site. All of these factors together determine the very important number of pulses (and hence, the total amount of energy) available for integration by the radar signal processor to provide aircraft detection. For an aircraft that has a relative velocity and range to a radar such that it remains in nearly the same azimuth and range cell during an antenna scan, we can make the following approximations for the number of pulses returned from a given aircraft. First, we can calculate the time the aircraft is within the 3-dB beamwidth of the antenna as

$$t_{BEAM} = \frac{Beamwidth_{3dB}}{\omega_{SCAN} \times 6}$$

where

t_{BEAM} = time that the aircraft is within the 3-dB beamwidth of the antenna in seconds,

$Beamwidth_{3dB}$ = 3-dB antenna beamwidth in degrees, and
 ω_{SCAN} = antenna angular scan rate in RPM.

Next, we can apply the PRF to calculate the number of pulses reflected by the aircraft:

$$N_{PULSES} = t_{BEAM} \times PRF$$

where

N_{PULSES} = number of pulses returned from the aircraft from a single scan and
 PRF = pulse repetition frequency of the radar.

Combining equations, we have a simple expression for the number of pulses returned from an aircraft when it is effectively stationary during the antenna scan:

$$N_{PULSES} = \frac{Beamwidth_{3dB}}{\omega_{SCAN} \times 6} \times PRF$$

As a numerical example, consider an ASR-8 with a 3-dB antenna beamwidth in azimuth equal to 1.35 degrees, an antenna scan rate of 12.8 RPM, and operating at a PRF equal to 1,200. A typical aircraft will have a $t_{BEAM} = 0.0176$ seconds and a total number of radar pulses returned from the aircraft equal to about 21. Consider the original ARSR-3 with a 3-dB antenna beamwidth in azimuth equal to 1.25 degrees, an antenna scan rate of 5 RPM, and operating at a PRF equal to 310. A typical aircraft will have a $t_{BEAM} = 0.0417$ seconds and a total number of radar pulses returned from the aircraft equal to about 13.

These examples demonstrate the very important fact that ATC radars, and surveillance radars in general, have only a few pulses to tens of pulses of energy available from an aircraft for radar signal processing. Based on the search radar equation and the preceding equations, we can see that transmitting additional pulses during t_{BEAM} at the same or additional frequencies, or transmitting at a higher power-aperture product, would increase the total target energy returned to the radar and improve detection performance. The cost associated with design choices such as these include increasing the cost and complexity to the radar.

In Chapter 3 of Volume 1 of the *Principles of Modern Radar* [32], the concept of radar target detection was discussed and included a discussion of the *probability density function* (PDF) of a known noise distribution, as well as the PDF of a signal present (aircraft) plus noise distribution. The overlay of these PDFs was considered, as well as the concept of a detection threshold used to declare the presence of an aircraft based on maximum likelihood estimation. Many references on radar [1, 5, 6, 33] and detection theory [34] cover radar target detection in detail. This classic issue in radar and communications design is referred to as a *binary hypothesis test*. The signal (a target echo, a communications preamble, etc.) is either present or not present. Note that these PDFs and their overlay contain SNR information. That is, the signal power to noise power ratio is the square of the difference between the mean of the noise PDF and the mean of the signal plus noise PDF divided by the variance of the noise PDF. The SNR information need not be based on a single radar pulse, but can be written to include the integration gain of several pulses in the radar signal processor [34]. This threshold setting determines the integration limits in order to integrate the PDFs to obtain the P_d and the P_{fa} . Furthermore, in Chapter 3 of [32], the concept of plotting threshold detection based on P_d and the P_{fa} values for a given SNR

to obtain the *receiver operating characteristic* (ROC) curve was also discussed. In Chapter 15 of [32], this concept was extended to radar detection algorithms using the *Neyman-Pearson criterion*. The Neyman-Pearson criterion is an optimization strategy for radar detection, where the P_{fa} is set to a constant value and P_d is maximized for a given SNR. It is important to note here that the SNR is determined by the radar system design (signal), operating parameters (number of pulses for integration), signal processing characteristics (integration gain), and the radar environment (noise PDF characteristics).

In practice, the ATC radar system requirements will set the required P_d and P_{fa} for a specific target RCS and target range under a given set of conditions. The ATC radar designer must then create a radar system architecture with operating parameters and radar signal processing that produces sufficient target SNR to meet the detection performance requirements for the specified radar environment. A typical value for ATC radar would specify a P_d greater than or equal to 0.80 and a P_{fa} less than or equal to 10^{-6} for a Swerling 1 target with an RCS of 1 m^2 (0 dBsm) during a single scan over the instrumented range of the radar. Other conditions are typically specified for a given P_d and P_{fa} performance, such as Doppler velocities, ground and/or sea clutter conditions, etc. In the ATC radar environment, clutter is a very significant performance issue, and meeting detection requirements mandates a design that provides sufficient SNR as well as sufficient SCR. The addition of clutter energy to the simple model of a noise-only PDF and a signal-plus-noise PDF changes the detection performance of the radar. This emphasizes the importance of SCV and IF performance specifications to ATC radar design. The ARSR SLEP, for example, indicates an average SCV of about 46 dB [3]. ATC will always desire the highest P_d achievable [7]; in practice, significant modeling and simulation are used to verify that a given radar design will meet all of the performance requirements in the presence of clutter, as well as in the presence of specified noise and interference conditions, and for a given physical implementation (phase noise, implementation loss, etc.). From an ATC radar detection requirements perspective, only the ARSR-4 reflects both the DOD and FAA missions [7, 11], while the ARSR SLEP met FAA, DOD, and DHS requirements [3]. Other operational ATC radar detection requirements reflect only the FAA mission requirements [4, 51].

12.3.1.4 Design Issue – Waveform Design

In order to increase system reliability and lower cost, ATC radar design shifted toward replacing high-power klystron tube transmitters with solid-state transmitters [3, 27, 49]. Solid-state technology could not produce the same level of output power as high-power microwave tubes. Currently, solid-state transmitters may produce only up to a few tens of kilowatts of peak power versus up to a megawatt or more of peak power for microwave power tubes. This requires a longer pulse for solid-state transmitters operating at a lower power level to get the same energy-on-target for detection. Furthermore, in order to maintain range resolution using the longer pulse, pulse compression is used with solid-state ATC radar such as the ARSRs, the ASR-11, and ASR-12 [51]. Specifically, a concatenated waveform was used in the ARSR SLEP and is described in [3]. Both the ASR-11 and ASR-12 have a dual waveform capability consisting of a CW short pulse and nonlinear FM (NLFM) long pulse. The short pulse is used for targets from the minimum instrumented range out to a given range, after which the NLFM long pulse is used to meet performance requirements out to the maximum instrumented range of the radar. Designing and implementing low sidelobe NLFM pulse compression waveforms

for radar has been studied [1, 33, 50, 53, 54] and successfully used in ATC radar [2, 3, 51]. The major disadvantage of NLFM is that it is a Doppler-intolerant waveform and requires careful Doppler filtering for implementation. However, digital technology for implementing radar waveforms has made very significant progress over the recent past, and performance improvements in this area are expected to continue.

For waveform design and analysis, it is the ambiguity function that is used to analyze the output of the matched filter in the presence of Doppler and time shifts. The ambiguity function can be defined from [6] as

$$A(t, f_D) = \left| \int x(\alpha) \cdot x^*(\alpha - t_D) \cdot \exp(j2\pi f_D \alpha) d\alpha \right|$$

where

$x(t)$ = radar waveform,
 f_D = Doppler shift, and
 t_D = time delay offset.

Analyzing the results of the ambiguity function of a given waveform can be performed with computer modeling of the three-dimensional plot of the waveform, known as the ambiguity surface. The ambiguity surface can be expressed with $|A(t, f_D)|^2$ along the z -axis. It can be used to model matched filter performance in the presence of Doppler shift and delay [52]. This analysis yields design insight into Doppler sidelobe levels for each radar waveform used by the system. The results of the ambiguity function are compared to the Doppler filtering for the system and other aspects of the radar signal processing to determine the magnitude and impact of Doppler sidelobes to the system. An analysis of both the peak and integrated sidelobe levels may be performed to identify conditions that will introduce false Doppler target information (artifacts) into the system. Careful waveform design is required in addition to system modeling to ensure all waveforms used by the radar will meet both aircraft surveillance and weather detection performance requirements.

12.3.1.5 Design Issue – Clutter and Clutter Processing

All ATC radar is ground-based fixed radar and, as such, the only perceived system motion is due to antenna scan modulation and the effects of radar system stability. This fact and the fact that surface clutter with the highest RCS remains relatively stationary represent an advantage for the MTI radar to filter stationary clutter using MTI filtering. Some significant types of stationary clutter for ATC radar include mountains, buildings, and relatively stationary sea clutter. Significant types of nonstationary clutter for ATC radar include angel clutter (birds), insects, and ground vehicles. Various models exist that describe different forms of clutter [1, 2, 5, 26, 32, 33, 37]. In the previous section, the Neyman-Pearson criterion and the concept of a detection strategy using a constant false-alarm rate were discussed. The context of the previous discussion included known noise PDFs and the addition of clutter energy from the radar environment. In Chapter 16 of Volume 1 of the *Principles of Modern Radar* [32], the concept of CFAR detection was discussed and detailed descriptions of several types of CFAR algorithms were presented. Of particular importance in the discussion in [32] was the fact that each CFAR algorithm has advantages and disadvantages in terms of performance and CFAR loss. Furthermore, the performance advantage of selecting a specific CFAR algorithm based on measured data rather than on assumptions of the clutter environment, known as

adaptive CFARs, as well as the concept of a *clutter map CFAR*, were also discussed. In the ATC radar environment, clutter is heterogeneous, and the ability of clutter map CFARs to process heterogeneous clutter on a cell-to-cell basis is an important advantage for this type of clutter processing. Additional details of clutter map CFAR processing are provided in [1, 5, 55, 56]. As an illustration here of the processing involved, Nathanson [5] provides an example of one type of clutter map CFAR analyzed in [55], which is based on a simple recursive equation performed for each clutter map cell:

$$y_i = (1 - w)y_{i-1} + wx_i$$

where y_{i-1} is equal to the last clutter map amplitude, y_i is the updated clutter map value, x_i is the output from the radar on the current scan, and w is simply a weighting factor, typically equal to one-fourth, one-eighteenth, or one-sixteenth. If a threshold for target presence k is established, then a target can be declared present when x_i is greater than $k \cdot y_{i-1}$. The integrations in this equation essentially act like a clutter memory. The recursion has an effective number of integrations based on w and an associated clutter map loss, based on some assumptions, of about 0.4 to 2 dB.

In ATC radar, clutter mapping is used to detect targets with little or no radial velocity with respect to the radar. It is a technique that finds application when it is possible to estimate clutter power in a given cell and then use it as a threshold to declare targets present when the echo power in that cell exceeds the estimated clutter power. For fixed, ground-based systems such as ATC radar, the use of clutter mapping has significant advantages. The estimation of clutter power in a given cell may be based on scan-to-scan averages, energy in nearby cells, or other criteria. Specifically for ATC radar, clutter maps are used in MTD processing and for weather detection. In MTD processing, clutter maps are used with a CFAR thresholding algorithm to track existing targets with tangential velocity (little or no radial velocity). This allows the radar to maintain tracks of aircraft flying at or near perpendicular, or that are very slow with respect to the radar. Weather phenomena can have little or no velocity at all, such as stationary weather. The ASR-9 weather processor, for example, uses a clear-day clutter map as a threshold for weather detection. Clutter mapping has replaced the older MTI technique of IF limiting, and future ATC radar signal processing will most likely improve adaptive clutter map techniques in order to improve on this concept.

12.3.1.6 Design Issue – Dynamic Range

In ATC radar, the term “dynamic range” refers to the capability of the radar to see both large and small targets, as well as weather phenomena. For large aircraft, the RCS can be on the order of 10 m^2 to 100 m^2 , while small aircraft may typically be on the order of 1 m^2 to 10 m^2 . Furthermore, the ATC radar environment includes significant stationary and nonstationary clutter such as birds (angel clutter) and insects at close enough ranges to the radar that they reflect significant amounts of radar energy. Likewise, surface ships have a very large range of RCS, from small craft to cargo ships. ATC radar must also operate over relatively short ranges to long ranges. For ASRs, a typical operating range is 0.5–60 nmi, and for ARSRs, a typical operating range is 5–250 nmi. It is this variation in RCS in the ATC radar environment, combined with the operating range of the radar, that determines the required dynamic range for the system.

Dynamic range is determined by several factors in ATC radar. Assuming we have sufficient power-aperture product for transmission, the radar receiver must have the

sensitivity to receive low-level signals from low RCS targets (weather, etc.) at long ranges, as well as the capability to receive high-level signals from large RCS targets (large aircraft, etc.) at close range. The dynamic range of the RF/microwave radar receiver is determined based on the operating range between the system noise floor and saturation of the components in the RF/microwave signal processing chain (typically, the 1-dB compression point from end to end). In place of the noise floor as an operating point, this is sometimes measured at the minimum discernable signal level in the receiver, which can be based on the radar signal processing, which includes integration gain. The radar range equation for a single pulse can provide an initial estimate of the dynamic range required in the RF/microwave receiver chain. Given a sequence of radar returns over a given range extent, and treating each return as a point target with a specific range and RCS, the dynamic range DR required by an RF/microwave receiver chain to receive the largest and smallest return without saturating the receiver is

$$DR = \frac{P_T G_T G_R \lambda^2}{(4\pi)^3} \left(\max_{R_{min} \leq R \leq R_{max}} \left(\frac{\sigma}{R^4} \right) - \min_{R_{min} \leq R \leq R_{max}} \left(\frac{\sigma}{R^4} \right) \right)$$

where the quantities in parentheses represent the maximum and minimum values of all of the RCS divided by the fourth power of the range to that object (σ/R^4) over the instrumented range of the radar. In other words, neglecting clutter and weather, the value of the $\max(\sigma/R^4)$ reduces to the largest aircraft RCS at the minimum instrumented range of the radar, and the value of $\min(\sigma/R^4)$ reduces to the smallest aircraft RCS at the greatest instrumented range of the radar. Of course, the equation also assumes $\min(\sigma/R^4)$ is at or above the minimum discernable signal (MDS) level for the system, including signal processing gain. This simplified estimate of dynamic range can be written as

$$DR = \frac{P_T G_T G_R \lambda^2}{(4\pi)^3} \left(\frac{\sigma_{max}}{R_{min}^4} - \frac{\sigma_{min}}{R_{max}^4} \right)$$

where σ_{max} and σ_{min} are the maximum RCS and minimum RCS of all targets, respectively. R_{max} and R_{min} are the maximum and minimum instrumented range of the radar, respectively. Note that each term in the parentheses determines the maximum and minimum operating points for the receiver chain. This equation can then be expanded via modeling and simulation to determine dynamic range accounting for clutter. Weather processing for ATC radar is often performed using a separate weather channel, and therefore dynamic range requirements will be different between an aircraft detection channel and a weather processing channel. As a comparison to ATC radar, NEXRAD has a receiver dynamic range on the order of 95 dB. It is interesting to note that weather radar signal processing channels often blank out cells that contain point targets due to the fact that the return energy in the cell is usually due to the aircraft. Significantly higher RCS from clutter and lower distributed RCS from weather can increase the required dynamic range for the radar receiver. In order to increase the dynamic range, variable gain devices (amplifiers, attenuators, etc.) are used to maintain a usable dynamic range in the receiver. In addition to the dynamic range of the receiver chain, the resolution of the ADC will impact the dynamic range. The number of bits from the ADC will determine the minimum and maximum signal levels that can be quantized. The designer's rule of thumb is 6 dB per bit, which can be derived from most texts on basic signal processing. In other

words, we can expect 48 dB of dynamic range from a 12-bit ADC. The waveforms used by the radar also impact dynamic range. The use of multiple waveforms on solid-state, transmitter-based systems, such as the ARSR SLEP and the ASR-11 and ASR-12, will have different design parameters for dynamic range versus a tube transmitter-based system using a high-power pulse. Other radar architecture factors will impact dynamic range, such as the amount of coherent and/or noncoherent integration for digital radar signal processing. Some work has been performed to increase instantaneous dynamic range in radar receivers, such as [16], and it is expected that continuing advances in microwave, RF, analog, and digital hardware will also improve radar performance.

In practice, ATC radars use sensitivity time control (STC) to settle for a usable operating point for dynamic range in the radar receiver. STC is a means to compensate for large clutter returns at close ranges. STC implements a time-varying receiver gain for the radar based on gain control curves. STC is implemented in the radar RF/microwave receiver chain; in addition, it can be applied in the IF receiver chain and digitally in the radar signal processor. Some STC implementations allow user-selectable RAGs. As described in [1], STC often requires an increase in gain in the high (passive) beam of the antenna to compensate for loss at higher elevation angles. The disadvantage of STC is that it can raise the energy level of range sidelobes [48], particularly near the vicinity of the radar. The resulting range sidelobe energy can generate false targets in the radar. Such artifacts in the signal processing chain can cause other issues as well. The STC analysis of the concatenated waveforms used in ARSR SLEP is described in [47]. Implementation of STC for ATC radar requires careful design consideration of the radar specifications and the radar system architecture in terms of both peak range sidelobe level and integrated range sidelobe level. This is particularly true with respect to processing weather returns at close range to the radar [27]. Careful consideration should be given to dynamic range requirements such that low echo power signals that represent dangerous aviation weather phenomena, such as a dry microburst, can be successfully detected with a very low P_{fa} and provide timely alerts to pilots via ATC.

Finally, it should also be noted that wind turbines may have an RCS on the order of 100,000 m² or greater, as well as significant Doppler due to the turbine blades. This can significantly impact ATC radar. Wind farm mitigation for surveillance radar is currently an ongoing area of research.

12.3.1.7 Design Issue – Radar System Stability

ATC radar uses the Doppler effect to discriminate between moving targets and relatively stationary clutter. Often, this is implemented using Doppler filtering. This requires a measurement by the radar system of the echo from the target and as a result determining the phase and/or frequency of the return signal. The radar is composed of physically realizable components and subsystems that have finite properties and performance characteristics. In a broad definition, radar system stability refers to any internal phenomena within the system that degrades performance, such as AM noise, FM noise, PM noise, and quantization noise. Thermal noise generated in the system adds to the performance impact of these phenomena. Radar system stability with respect to Doppler energy detection and Doppler measurement error will be discussed. It should be noted that Doppler energy detection is a more appropriate term for MTI radar using a Doppler filter bank, while Doppler measurement error is more appropriate for PD radar, which measures true target Doppler. We will discuss how to quantify radar system stability for both AM noise and phase noise, and it will be shown from modulation theory that FM noise and PM noise are related.

Increased radar stability reduces the system internal noise and improves the ability of the radar to discriminate between moving and stationary targets. For clarification, radar system stability has to do with the internal performance of the radar system. Although one of the products of system instability is that it adds residual Doppler to stationary clutter, radar system stability does not include Doppler from clutter motion, such as clutter motion caused by trees blowing in the wind, or the effects of the antenna, such as scan modulation and sidelobe effects. To put it another way, consider the equation for Doppler shift and system stability in terms of phase error that exists due to finite properties of the radar system. This phase error is the collection of transmit phase noise and receive phase noise within the radar and represents the total system phase error. The total system phase error can be considered a random vector, which is added to the true phase difference of the target return. Furthermore, because several types of physical phenomena generate phase noise, the magnitude of the phase noise decreases with increasing or decreasing frequency offset from the carrier. For a completely stationary target where the true phase difference is zero, phase noise from the system generates a small Doppler shift, a residual Doppler, without any contribution from the fixed target. Given that the time derivative of phase is frequency, the limit on the ability of the radar system to measure the Doppler velocity of targets due to system stability is

$$\frac{1}{2\pi} \left(\frac{d\theta_{ERR}}{dt} \right) = f_{RD} = \frac{2v_{ERR}}{\lambda}$$

where $d\theta_{ERR}/dt$ represents the instantaneous change in phase with respect to time. The residual Doppler generated by the radar system is f_{RD} and v_{ERR} represents the error in radial velocity measured by the radar caused by total system phase error. This equation also assumes that the return from the stationary target is not noise limited. In other types of radar systems, the measurement of residual Doppler and other echo data from a fixed target (such as a corner cube reflector) can be used as part of the calibration procedure or system diagnostics. For ATC radar systems that rely on Doppler velocity to identify moving targets, low phase noise is essential to minimize the amount of internal noise power generated in a given Doppler filter.

Chapter 12 in Volume 1 of *Principles of Modern Radar* [32] introduced the concept of phase noise. Phase noise is the result of small fluctuations in phase due to several physical phenomena. The magnitude of phase error will decrease with increasing frequency offset from the carrier until the magnitude of the phase error eventually falls below the thermal noise floor in the system. Phase noise and AM noise are typically defined in terms of power in a single sideband (SSB) power density in a 1-Hertz bandwidth at a given frequency offset from the carrier. The corresponding units for this metric are dB below the carrier per Hertz, written as dBc/Hz. Phase noise can also be expressed by more than one definition, and careful consideration is required when reviewing phase noise literature and specifications. For our purposes in this section, we can use the following definition:

$$L(f) = \frac{P_{SSB}}{P_C}$$

where

P_{SSB} = SSB sideband power density in a 1-Hertz bandwidth,

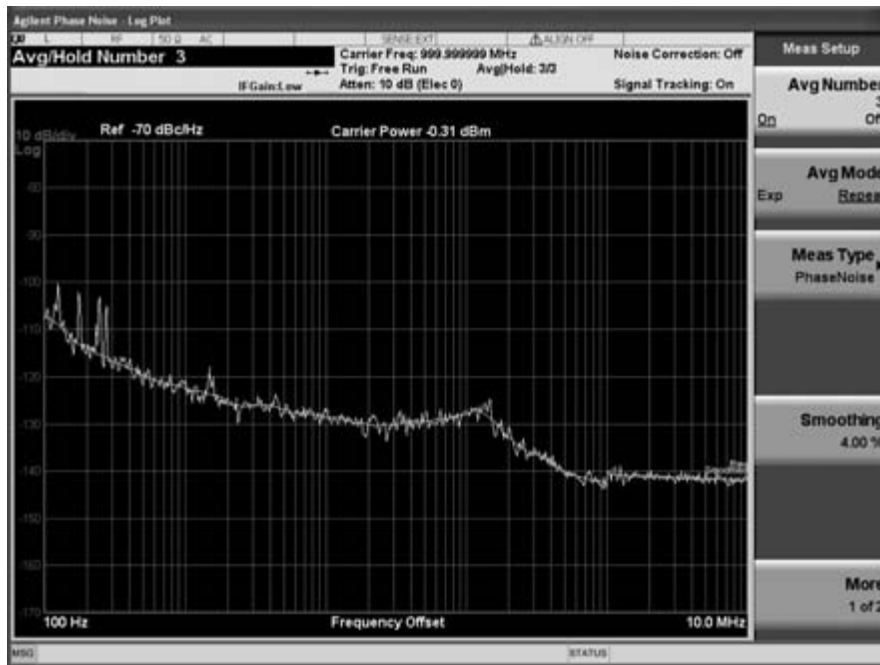


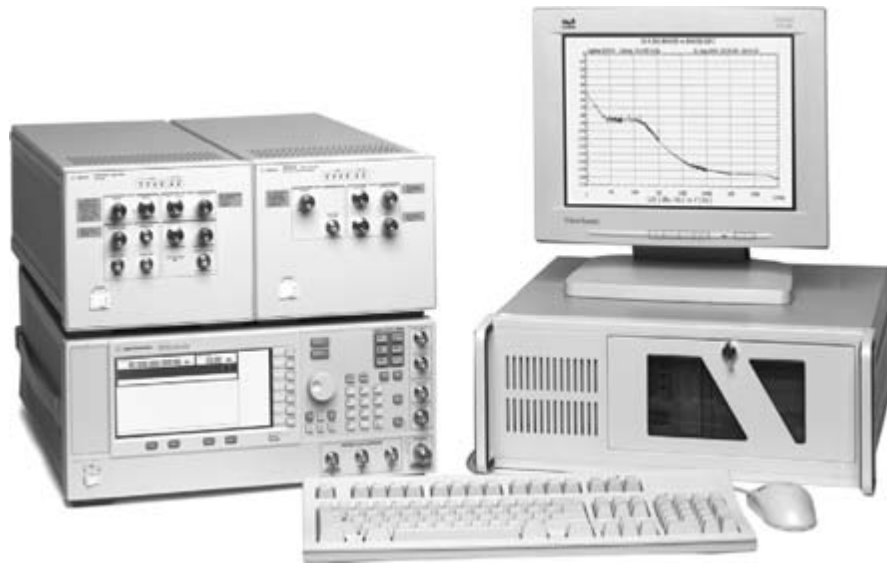
FIGURE 12-3 ■ An Example Plot of SSB Phase Noise Performance Curve $L(f)$ in dBc/Hz [Copyright © Agilent Technologies June 30, 2011. Reproduced with Permission, Courtesy of Agilent Technologies, Inc.].

P_C = carrier power, and
 $L(f)$ = SSB phase noise performance curve in dBc/Hz.

Figure 12-3 is an actual SSB phase noise plot using an Agilent PXA Spectrum Analyzer [68].

When we look at the physical phenomena contributing to total system phase error, oscillator phase noise is usually one of the first things to come to mind. However, other factors will also play a role in system phase error. In addition to generating phase noise and thermal noise, physically real systems will generate AM noise, FM noise, and quantization noise. Phase noise is a product of various sources of physical phenomena. These include random-walk FM noise, flicker FM noise, random-walk phase noise or white FM noise, flicker phase noise, and white noise. Other contributions to system phase error may come from individual components or subsystems in the radar due to a variety of other physical phenomena [65, 66]. These physical phenomena may ultimately manifest themselves as a contributor to phase noise simply via a modulation process. It should be noted here that phase noise phenomena and other noise phenomena types represent an area of ongoing research. We can often reduce system phase error to a lower magnitude by compensating for one or more types of physical phenomena, with an associated increase in cost for that component. This results in other physical phenomena becoming the dominant source of phase error at the now lower level of phase noise produced by that component. This process where phase noise is reduced but not completely eliminated, with a corresponding cost for each reduction in phase noise, forces the radar designer to settle for a low enough level of phase noise in the system that meets both the system performance and system cost. For example, in a typical radar system, the coherent oscillator (COHO) and stabilized local oscillator (STALO) represent critical components that set the initial level of phase noise in the transmitted pulse.

FIGURE 12-4 ■
 The Agilent E5500
 Phase Noise
 Measurement
 System Shown Here
 Is an Example of
 High-Performance
 Measurement
 Equipment Capable
 of Making Pulsed
 Phase Noise and AM
 Noise Measurements
 [Copyright © Agilent
 Technologies June
 30, 2011.
 Reproduced with
 Permission, Courtesy
 of Agilent
 Technologies, Inc.]



The stability of these sources can be increased using lower phase noise oscillators, but at increasing cost to the system. High-power amplifiers (HPAs), for example, require a power supply. HPA power supply variations such as ripple will typically create AM noise and FM noise, and result in added phase noise to the radar system. Furthermore, HPAs may also introduce significant intrapulse jitter during generation of a high-power transmit pulse, which results in an additional phase noise contribution to the system.

Constructing a system stability budget or performing a cascaded phase noise analysis for a radar system is a radar architecture-specific process that requires detailed component analysis and measurements in addition to applying modulation theory. Figure 12-4 illustrates the Agilent E5500 phase noise measurement system. This type of measurement system represents equipment capable of performing phase noise and AM noise measurements to quantify component, subsystem, and system-level noise performance for analysis and verification of radar system stability [69]. Correctly identifying and quantifying AM, FM, and PM noise sources that contribute to radar instability requires experience in radar art as well as theory. The basis for radar system noise analysis begins with the fact that if two uncorrelated signals are combined, their root-mean-square (RMS) powers may be added. If the two signals are correlated, then the RMS voltages of the signals may add or cancel in phase, depending on the correlation coefficient between the signals. Of course, the instantaneous voltages of any two signals may be directly added, but in noise analysis, the instantaneous voltages as a function of time are not usually known. System-level phase noise analysis is a process of identifying noise sources within a system architecture and then determining the phase noise associated with each source. This process then requires converting the magnitude of each of these noise sources to equivalent phase noise power level (referenced to a 1-Hz bandwidth). FM noise can be converted to phase noise based on the assumption of a small modulation index for FM. AM noise may be converted to phase noise when the device or subsystem couples amplitude changes with a phase change. In this case, a device, such as an amplifier, has an AM/PM conversion factor. AM/PM conversion values are often based on specific operating conditions. The results are combined in a system-level cascade of all of the

components into total values at specific offsets from the carrier. This process is repeated at specific offsets from the carrier over the entire range of frequencies. The system phase noise analysis includes the analysis of the thermal noise floor within the system in order to understand where corner frequencies for phase noise limited and thermal noise limited performance exists in the system.

Given two completely independent white noise sources, with RMS power levels P_{n1} and P_{n2} expressed in dB relative to a reference, the combined output power level of the two signals P_{total} is also expressed in dB relative to the same reference and can be written as

$$P_{total} = 10 \times \log\left(10^{\frac{P_{n1}}{10}} + 10^{\frac{P_{n2}}{10}}\right)$$

This equation simply converts the input signals to absolute power with respect to the reference in linear form, adds the two uncorrelated signals' RMS power levels, and converts them back to log form in dB relative to the same reference. This equation is valid for adding signal power as long as the sources are uncorrelated (independent). Consider two independent noise sources whose magnitude at 1-MHz offset from the carrier are -141 dBc (SSB) and -138 dBc (SSB). The total power from these two sources at 1-MHz offset from the carrier will be -136.2 dBc (SSB). Note that for physically real signals, phase noise, like other noise types, only increases. This is similar to physically real radar and communications receiver systems in which SNR only decreases along the RF/microwave receiver component chain due to thermal noise generated in physically real components. The previous equation emphasizes an important point about radar stability, which is that noise sources (AM, FM, PM, quantization, or thermal noise) will all contribute to degraded system performance. Good design practice is an exercise in minimizing these sources such that the system design meets required performance. The phase noise mask can be expressed as double sideband (DSB) or single sideband (SSB), but SSB is the most common. AM noise analysis is a similar process. AM noise is often measured in DSB and converted to SSB. It is often correctly assumed that all of the contributions to the system-level AM noise or phase noise spectrum have a mirror image about the carrier frequency f_c . When this is true, DSB power and SSB power are related as

$$DSB = SSB + 3\text{dB}$$

This reflects the fact that half the power is in each sideband. Care must be taken when interpreting phase noise specifications as SSB or DSB, as well as peak values versus RMS values for AM, FM, and PM. The phase noise mask is most often expressed with phase noise power along the y -axis expressed in dBc/Hz and frequency offset from the carrier along the x -axis expressed in Hz. The phase noise mask is normalized to energy in a 1-Hz bandwidth. The radar system architecture is then analyzed at specific offsets from the carrier, and the cascaded phase noise is calculated. Individual RF and microwave components have different phase noise properties. For example, a frequency multiplier with multiplication value M will introduce an increase in phase noise of $20 \log(M)$.

The cascaded phase noise analysis begins with the specified (or measured) oscillator inputs for phase noise at frequency offsets from the carrier, which determine the initial phase noise levels and have a significant impact on system phase noise. In addition to the obvious noise sources in the component chain such as mixers and amplifiers, other

sources need to be examined. Furthermore, AM noise sources may be observed as sources of phase noise and impact the system phase noise budget if the product of AM noise and AM/PM conversion coefficient for the component or subsystem is large enough. In addition, independent FM noise components may be combined via root-sum-square (RSS) analysis to provide a composite FM noise value for a component or subsystem. Consider an example HPA subsystem using a klystron transmitter. Given that at 100-Hz offset from the carrier an example klystron has a beam pushing factor of 0.01Hz/volt and a filament ripple of 10 volts, an FM noise component of 0.1 Hz (SSB) is generated in the transmitter. Furthermore, this FM noise component is added to another independent FM noise component at the same frequency offset from the carrier, whose RMS magnitude is 0.25 Hz (SSB). The total FM noise from these two sources at 100-Hz offset from the carrier will be the RSS of the two sources, or 0.269 Hz (SSB).

Both FM and PM are angle modulation. Likewise, the spectral energy relationship between FM noise and PM noise can be derived from modulation theory. From [43], we note that FM and PM are both angle modulation and are related as follows:

$$m = d\theta_{PK} = \frac{df_{PK}}{f_M}$$

where

$$\begin{aligned} m &= \text{modulation index,} \\ d\theta_{PK} &= \text{peak phase deviation in radians,} \\ df_{PK} &= \text{peak frequency deviation in Hertz, and} \\ f_M &= \text{modulation frequency in Hertz.} \end{aligned}$$

For small values of modulation index ($m \ll 1$), only the carrier and first upper sideband and first lower sideband contain significant energy. Based on [43], the magnitude of spectral energy offset from the carrier for small angle modulation such as FM noise becomes

$$\frac{P_{SSB}}{P_C} = 20 \cdot \log\left(\frac{df_{RMS}}{\sqrt{2} \cdot f_M}\right)$$

where df_{RMS} is the RMS frequency deviation in Hertz. By substituting this equation for modulation index in terms of df_{RMS} and dividing both sides of the equation by $1/2$, the expression for PM noise is similar and becomes

$$\frac{P_{SSB}}{P_C} = 20 \cdot \log\left(\frac{d\theta_{PK}}{2}\right)$$

P_{SSB}/P_C is the noise power in a 1-Hertz bandwidth relative to the carrier at a specific frequency offset from the carrier. Attention is required to performance or measurement data used for these equations to apply correct RMS values and peak values for frequency and phase deviation. Therefore, in our FM noise example earlier, an RMS FM noise component of 0.269 Hz at 100-Hz offset from the carrier yields a noise power of -54.41 dBc/Hz at 100-Hz offset from the carrier.

ADCs and DACs will also introduce noise into the radar system. For these sampling devices, aperture jitter due to the finite properties of the devices and their sampling clocks, as well as the physical quantization limits of the devices, will contribute to noise in the system, including phase noise. In theory, we can calculate DAC and ADC

quantization noise for an ideal converter. We can also estimate performance degradation due to jitter. For ideal ADCs, we can estimate the ideal quantization noise based on assuming a uniform distribution for the noise PDF over the quantization voltage interval q_V volts ($q_V = 1$ LSB); this provides an initial estimate for quantization noise of

$$P_{ADC} = 10 \cdot \log \left(\frac{(q_V)^2}{12} \right)$$

where P_{ADC} is the ideal ADC quantization noise power in dBW referenced to a 1-ohm load. In order to determine the contribution of the converter's aperture jitter to AM noise and phase noise, performance information about the oscillator used to clock the converter, as well as the converter specifications, are required. In practice, real DACs and ADCs exhibit both linearities and nonlinearities that impact performance. Actual converter performance measurements can verify AM noise and phase noise contributions to the system. The characteristics of noise from converters are both device dependent and application dependent. For example, operating DACs and ADCs in a higher Nyquist zone will increase phase noise. Furthermore, the analysis is also architecture dependent. For example, converter noise contributions are dependent on whether or not the receiver in-phase and quadrature components are derived in the digital domain from the output of a single ADC or in the analog domain using two ADCs. Printed circuit board (PCB) layout of the converter boards will also impact performance, particularly for high-speed converters. Specifications from the device manufacturers are required for system-level performance analysis, and testing details are beyond the scope of this section. The subject of phase noise measurements to verify system analysis is also beyond the scope of this chapter, but many good references are available on this subject. Caution is required when equating converter specifications to practical hardware. Similar to many DSP calculations, equations are often normalized to a 1-ohm load, while in practice RF and microwave components often use the characteristic impedance of 50 ohms.

The process of analyzing radar system stability for AM noise and phase noise proceeds based on the system architecture, and is performed end-to-end until a system-level budget for both noise types is completed. These system-level budgets may be based on theoretical or measured data or a combination of both. However, at some point, physical measurements for design verification should be performed to verify actual system performance. It is useful to note that an estimate of radar system-level stability for Doppler measurements can be performed by integrating the cascaded system SSB phase noise performance curve over the Doppler frequency range of interest and converting the value to RMS phase jitter. Integrating the system-level phase noise performance yields the total noise power over a given frequency range. We can express total integrated phase noise power as

$$INP = \int_{f_{MIN}}^{f_{MAX}} L_{SYS}(f) df$$

where

INP = total integrated phase noise power in dBc,

$L_{SYS}(f)$ = cascaded system level SSB phase noise performance curve in dBc/Hz,
and

f_{MIN} and f_{MAX} = minimum and maximum frequency offsets, respectively, from the carrier.

In practice, the integration can be performed numerically or by summing area from individual regions under the $L_{SYS}(f)$ curve. Skolnik [1] in Section 15.11 details an example oscillator calculation of integrated phase noise power. Data from the $L_{SYS}(f)$ performance curve is put into a system-level DSP model to determine actual I_C for the given radar architecture (MTI filtering, etc.). This approach yields design insight and can be used to quantify reductions in noise power in components and subsystems and the overall impact at the system level. In general, good radar receiver design will use low-noise components and reduce any significant noise contributions in the system with low-noise techniques. Therefore, the system oscillators will set the initial phase noise power level and have the greatest impact on $L_{SYS}(f)$. In order to get a quantitative metric for interpreting system stability in terms of phase, the following equation can be used to convert SSB phase noise data to RMS phase jitter over a given frequency range [45]:

$$\phi_{RMS} \approx \sqrt{2 \cdot 10^{\left(\frac{INP}{10}\right)}}$$

where ϕ_{RMS} is the total system RMS phase jitter in radians. The resulting RMS phase jitter then reflects an overall estimate of the system stability in a given frequency range. As a performance estimate, the integration limits f_{MIN} and f_{MAX} are determined based on the minimum and maximum Doppler values that the radar will observe. For ASRs and ARSRs operating at S-band and L-band, respectively, the integration is only performed out to a few KHz. An important point here is that the integration limits are performed on the region of the system-level phase noise curve $L_{SYS}(f)$, which is limited by the system noise performance (i.e., prior to reaching the corner frequency for the thermal noise floor). This point demonstrates the direct impact of phase noise on radar system stability. Assuming that all other noise sources in the system are substantially lower in magnitude, phase noise will be the limiting performance factor in the system. As f_{MIN} is increased, the integration is performed at a greater offset from the carrier where the phase noise is at a reduced level. Of course, the phase noise typically continues to reduce in magnitude at greater offsets from the carrier until the corner frequency with the thermal noise floor is crossed and noise power is essentially flat. This type of conversion from SSB phase noise to RMS phase jitter is often used to characterize stability of a signal source [45], often with much larger integration limits.

At this point, the system-level AM noise budgets and phase noise budget provide insight and design guidance in terms of where in the system to direct resources to improve radar stability. A cost can also be associated with each improvement. The system-level phase noise budget can be used with a radar system model to determine the greatest reduction in phase noise from each contribution in the system. As lower magnitudes of phase noise are required, more physical phenomena must be attenuated to achieve low-noise performance. This requires the use of low-noise design and measurement techniques. In many radar designs, it is not uncommon for the radar engineer to use low-noise DC sources such as batteries; perform noise testing in a Faraday cage for isolation; and deal with acoustic noise issues to design, test, and debug low-noise components and subsystems. It should be noted that there are many subtleties with testing, measuring, and analyzing phase noise and AM noise. It should also be noted in our discussion that we have neglected EMI and RFI, which can also generate internal noise in a radar system. It is assumed that the radar design must reduce these types of noise sources to where they are sufficiently below the thermal noise floor to have an

insignificant impact on stability. Reference [30] provides details on radar performance estimation. References [43] and [44] provide details on phase noise and AM noise measurements. It should also be noted that the aforementioned techniques can be applied to other areas of RF and microwave performance analysis [46].

12.3.2 Secondary Surveillance Radar Design Issues

An initial discussion of SSR and the ATCRBS was provided earlier in this chapter. The concept of the ATCBI, the ground-based transmitter that uplinks a 1,030-MHz interrogation pulse to the aircraft, and the aircraft transponder that responds with a coded reply at 1,090 MHz was also described. This exchange has several defined modes to communicate important information to ATC about aircraft, such as “who are you?” and “what is your altitude?” (Mode C). SSR also performs monopulse processing on transponder replies to achieve azimuth bearing accuracy [19, 40]. The previous discussion also described the performance advantage of the ATCRBS link, since received power is now a function of range as R^{-2} as opposed to R^{-4} for conventional PSR. This allows SSR to operate with transmit pulses on the order of a few hundred watts peak versus several kilowatts or greater than a megawatt for PSR. Aircraft transponders have a specific reply sequence composed of listening for an interrogation pulse above a specific trigger threshold level and transmitting an interrogation reply to an ATCBI, followed by a recovery period during which transmission to other interrogations is suppressed. The ATCRBS link allows SSR to achieve a high probability of detection, typically greater than 97 percent. Essentially, SSR has performance and redundancy advantages that complement PSR for all aircraft that have an operational transponder.

Given the advantage of the ATCRBS, there are many design issues surrounding operational SSR [25, 40]. Many of the design issues for SSR mirror that of PSR, such as interference, multipath, antenna pattern issues such as vertical lobing and null depths, anomalous propagation, etc. Other design issues are specific to SSR, such as detection and reply issues. For example, SSR is susceptible to fading when aircraft maneuvering shields the transponder antenna from the ATCBI interrogation pulse. Such aircraft maneuvers are typical in the terminal environment. SSR represents a dense communication environment in the terminal area, which can create other design challenges. This environment may allow the condition in which near-simultaneous ATCBI transponder interrogations from different locations may temporarily desensitize the aircraft transponder receiver. Likewise, multiple transponder replies from several aircraft may interfere with each other and garble the coded reply from transponders. Indeed, one of the limitations of SSR Mode A/C systems is that there is no provision for error detection in the transponder coded reply.

In light of the previous operational issues, SSR is a mature system and has been operational since the 1960s. Many of the operational challenges for SSR are mitigated by proper system design, proper antenna siting criteria, and careful spectrum management. For example, ATCBI sites are assigned unique PRFs (typically between 150 and 450 Hz) to allow the defruiting equipment to filter only transponder replies for that site and reject replies for other ATCBIs in the same vicinity [25]. Furthermore, cross-coupling to PSR systems and interference from other radiators, such as distance measuring equipment (DME), is also manageable. SSR systems employ interference sidelobe suppression (ISLS) to assist in sorting many transponder replies in a dense

environment. Typical ATCBI system requirements include processing as many as several hundred aircraft, dealing with up to several thousand FRUIT replies per second, discriminating multiple closely spaced aircraft in both range and azimuth via monopulse processing, and performing Mode A/C/S processing in real time. Similar to PSR, target detections require additional processing for conversion into real-time aircraft track data, which is then forwarded to other ATC systems.

12.3.2.1 Design Issue – SSR Link Calculation

We can now take a closer look at the link calculations for SSR. Both the uplink to the transponder and the downlink will exhibit atmospheric absorption, refraction loss, and sometimes anomalous propagation. The transponder will reply to an interrogation when the signal exceeds the minimum threshold level (MTL). We can rewrite the ATCRBS 1,030-MHz uplink equation in terms of received signal at the aircraft transponder:

$$S = \frac{P_T G_T G_{Rt} \lambda^2}{(4\pi)^2 R^2 L_{Rt} L_{Abs} L_{Rl}}$$

The ATCBI 1,090-MHz downlink equation is also derived from this equation by changing the wavelength and using the correct transmit power for the aircraft transponder, aircraft transponder antenna gain at 1,090 MHz, and ATCBI receive antenna gain. The losses in this equation must also be adjusted for 1,090 MHz. Figure 12-5 illustrates a MATLAB[®] program example that performs a simple SSR uplink calculation. The example code neglects atmospheric losses and assumes an MTL of -71 dBm. Figure 12-6 shows a

FIGURE 12-5 ■ An Example SSR Link Calculation in MATLAB[®].

```

%
% Example SSR Uplink Calculation
%
%
clear all; close all; clc;

% SSR Uplink Parameters (Neglecting Atmospheric Losses)
%-----
Pt           = 37;      % dBW - 5kW TX peak
G_rxant_dB   = -10;    % dB - Aircraft in a turn
G_txant_dB   = 27;     % dB
Range_NM     = 1:250;  % Radar to Aircraft distance in Nautical Miles
Freq         = 1030e6; % Hz
c_light      = 3E+08;  % Speed of light m/s

MTL          = -101;   % dBW - Minimum Threshold Level for Transponder
              % = (-71 dBm)

wavelength   = c_light ./ (Freq);

Free_Space_Path_Loss_dB = 20 * log10( (4*pi*Range_NM*1852.00) ./ ( wavelength ) );

Pr_dB = Pt + G_rxant_dB + G_txant_dB - Free_Space_Path_Loss_dB;

MTL_x = [ min(Range_NM), max(Range_NM)]; % Setup to plot MTL as a horiz. dashed line
MTL_y = [MTL, MTL];

figure(1)
plot( MTL_x, MTL_y, 'r--')
hold on;
plot( Range_NM, Pr_dB, 'b:')
grid on;

title(' Example SSR Uplink Calculation');
xlabel('Range (Nautical Miles)');
ylabel('Received Power (dBW) ');
legend('Aircraft Transponder MTL for Reply', 'Aircraft Transponder Received Power');

```

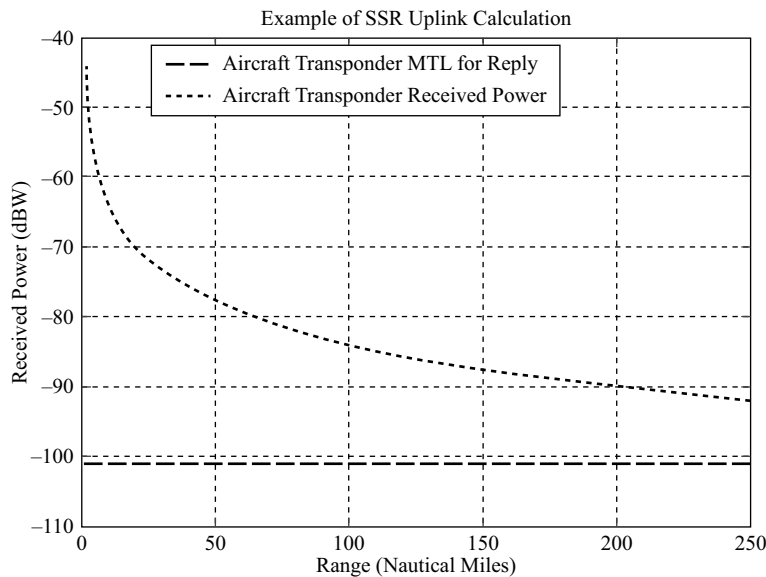


FIGURE 12-6 ■ Performance Plot of Range versus Received Power for the Example SSR Uplink Calculation.

performance plot of received signal power versus range from the example and indicates where the received signal power falls below MTL.

12.3.3 Primary Surveillance Radar Design Issues for Weather Radar Detection

In the introduction we described the need for real-time, coarse weather detection for ATC. Furthermore, with the exception of TDWR or an ASR-9 that has a WSP, real-time weather detection in ATC radar refers to real-time precipitation reflectivity measured by the radar to obtain rainfall reflectivity and categorize it into six standard levels as defined by the National Weather Service (NWS). Extracting weather information from a 2-D ATC radar can represent a challenge due to the antenna 2-D fan beam, available transmit power, and waveforms [63]. ATC radar looks at weather in two contexts: weather as a form of clutter and weather as a real-time product to ATC. In the former context, weather is considered a form of distributed clutter when detecting aircraft (point targets). Early ATC radar detected weather, but the design goal was to reject weather and only optimize detection of point targets. In the latter context, the ability to vector aircraft around potentially hazardous weather was realized as important for ATC, and the ASR-9 was the first ATC radar designed to provide real-time weather information for ATC. The ARSR-4, as well as the SLEP for the interior ARSRs, also incorporated weather detection into the radar design. ATC radar often use dedicated weather processing resources, in terms of dedicated weather channels and weather radar signal processing, to obtain real-time weather information and provide this information to ATC in the form of a weather contour map.

Table 12-2 shows the six NWS Standard Reflectivity levels that are typically used to display an ATC radar weather contour map. The six levels represent an estimate of the rainfall rate based on the equation for stratiform (widespread, relatively uniform) rain [1]:

TABLE 12-2 ■ NWS Standard Reflectivity Levels

NWS Level	Reflectivity (dBZ)	Category
1	18 to < 30	Light Mist
2	30 to < 41	Moderate
3	41 to < 46	Heavy
4	46 to < 50	Very Heavy
5	50 to < 57	Intense
6	57 and above	Extreme

$$dBZ = 10 \times \log(200 \times r^{1.6})$$

where dBZ is the reflectivity and r is the rainfall rate in units of mm/hr [27]. The estimate of reflectivity in dBZ is obtained by specific weather processing using dedicated weather processing resources in the radar signal processor. Although the specific weather processing used by an individual type of ATC radar (ASR-9, ARSR-4, ASR-11, etc.) may be different, the general approach to processing weather data has some commonality. Weather processing involves using the data collected from multiple scans. An initial step involves removing ground and sea clutter, anomalous propagation, and multiple-return echoes from the data used for processing. The ASR-9 uses a clear-day clutter map to support rejecting nonweather clutter. Furthermore, point targets (cells containing aircraft) are removed from the data and they are normalized based on any applicable settings for STC. The data are also calibrated based on the type of polarization (linear or circular) used for the pulse. Finally, multiple scans are averaged over several cells (spatial averaging) and also averaged over time to obtain a weather contour map. This processing also includes a correction for the beam fill loss adjustment, which accounts for the 2-D fan beam pattern [64]. This represents a process of creating a 2-D weather display for ATC based on 3-D weather phenomena. It should be noted that the resolution of the weather contour map is coarser than the resolution of the raw radar data.

The challenge in implementing weather detection in ATC radar is that surveillance radar is not optimized for weather detection, such as a meteorological radar. The surveillance antenna aperture as a fan beam was designed for broad volume coverage to detect relatively strong point targets as opposed to relatively weak distributed targets such as weather. The slower scan rates and pencil beam antenna patterns used by meteorological radar to dwell longer on low-reflectivity precipitation are not an option for an ATC radar, which must perform surveillance. In order for ATC radar to detect low-reflectivity precipitation, high sensitivity and high dynamic range are required. The dynamic range required for weather detection starts at a lower received power level than the dynamic range required for detecting aircraft. Typically, the required sensitivity may be as low as 10 dBZ and the dynamic range on the order of 76 dBZ or more [27]. The high dynamic range pushes challenging requirements not only onto the radar hardware, but also onto the radar waveforms used by ATC radar for weather detection. These challenges also include minimizing false output from sidelobe energy, which may cause the generation of false weather products. Waveform design is critical, and an ATC radar solution that meets all of the aircraft and weather detection requirements over the required dynamic range typically requires a multiple-waveform, multiple-frequency approach [3, 27, 63]. In addition to dynamic range and sidelobes, antenna scan

modulation may impact weather detection by an ATC radar. Rejection of weather precipitation echoes is accomplished, in part, by the use of circularly polarized (CP) transmission. Linear (vertical) polarization is more susceptible to rainfall. Typically, linear polarization would be used on a clear or light precipitation day, and ATC would switch to CP during inclement weather in order to maintain tracking of aircraft targets. Both linear and circular polarization may be used for weather detection.

12.3.4 ATC Radar System Reliability, Maintainability, and Availability (RMA)

The reliability, maintainability, and availability (RMA) of an ATC radar represent very important system-level requirements. Failures of critical systems to ATC can result in severe consequences to aviation safety and, therefore, human life. The FAA mandates that critical NAS components have very demanding RMA requirements to maximize aviation safety. ATC radar achieves these demanding RMA requirements through the use of redundant systems, specifying high mean time between critical failures (MTBCF) and low mean time to repair (MTTR). Both ASR and ARSR radars have only one antenna, but each system will have redundant transmitter subsystems, receiver subsystems, and signal processing subsystems. Although the antenna pedestal subsystem is composed of a single antenna, even this subsystem will have redundant pedestal drive motors and other redundancy built in to improve RMA. Redundant system design allows one channel to be operating while the other channel is in standby. Maintenance tasks can be performed on the standby channel to achieve high availability. Redundant system design to improve RMA of ATC radar is achieved at the expense of higher initial system cost due to purchasing additional radar subsystems and also requires a higher life cycle cost due to maintaining two sets of subsystems at each radar site. When the FAA procures a new ATC radar, it is considered a major acquisition, and RMA performance requirements are balanced between technical feasibility and life cycle cost for each type of ATC radar [39]. Modern ATC radars require system-level modeling and often demonstration to verify RMA performance. The RMA models for ATC radar are based on existing standards to determine RMA performance. General design guidance, RMA definitions, and methods used to create RMA models can be found in the references listed in [39]. Finally, NAS requirements call for the use of a remote monitoring subsystem (RMS) at the ATC radar site to provide remote access of radar system status information to FAA maintenance personnel. The RMS is a subsystem of the remote maintenance monitoring subsystem (RMMS) [4]. The RMS is designed to allow unattended operation by typically making radar system health, status, remote control, performance monitoring, and specific alarms available to ATC maintenance.

From an operational perspective, ATC radar systems require certification by the FAA prior to use by ATC. The FAA has the critical task of not only repairing and maintaining ATC radar, but also certifying each radar system can be put in service for use by ATC.

12.3.5 Other ATC Radar Design Considerations

ATC radar design includes other factors that need to be considered for large-scale operational deployment of safety-critical radar systems. Previous experience indicates that interference mitigation with other radio and microwave equipment, radar siting and

land acquisition, operational performance and effectiveness for ATC, and RMA represent some of the major considerations for ATC radar.

An ATC radar is a multimillion-dollar system that contains a high-power radar transmitter and a sensitive radar receiver. The radar must operate in a dense EM environment, which contains EMI, while operating in the vicinity of other radar systems, radio, cellular, and television transmitters. Many communications and radar systems are often located in close proximity to each other for coverage and propagation reasons. Spectrum management is required in the process of site selection. Furthermore, site-specific interference mitigation techniques are sometimes necessary as the only means to reach a successful outcome. In cases where modifications to an ATC radar system are performed, engineering is required to quantify that the system has not been degraded by any modifications. Reference [25] details older but still valuable insight into issues surrounding PSR and SSR site selection. These issues include antenna pattern estimation, facilities, site analysis, and coverage of airspace. While [25] provides an introduction to site selection, more advanced techniques exist today for site selection and analysis for ATC radar deployment, particularly with regard to computer modeling and the simulation of performance at a given location.

Operational performance and effectiveness of an ATC radar involve several criteria. An ATC radar can literally have several hundred system requirements in its specification. Measures-of-performance (MOPs) and measures-of-effectiveness (MOEs) represent significant metrics used to evaluate how well the ATC radar system is capable of meeting the needs of ATC and any other needs for which it was intended. Prior to placing a new or modified ATC radar into service for ATC, an evaluation of MOPs and MOEs is necessary to ensure the system does not negatively impact aviation safety or efficient management of airspace by ATC. As was noted in the previous section on RMA, an entire support structure must be in place to maintain and certify that an ATC radar system is operational for use in the NAS. Finally, it should be noted, as is often the case with many radar systems, that system enhancements and performance upgrades are expected to be implemented to meet changing user needs and/or to help recover the substantial investment required for a major systems acquisition and large-scale operational deployment.

12.4 | THE FUTURE OF ATC RADAR

Aviation has always faced the challenge of simultaneously improving safety and efficiency while increasing air traffic capacity. The Next-Generation Air Transportation System (NextGen) is the FAA vision for the future of air transportation in the United States. NextGen represents a vision forward not only in aircraft surveillance, but also in many other aspects of NAS (weather, communications, ground operations, etc.). With respect to airspace surveillance, NextGen will rely primarily on automatic dependent surveillance-broadcast (ADS-B), a technology based on the global positioning system (GPS), to provide air traffic management (ATM) benefits to ATC for improving efficiency, safety, and increasing capacity. ADS-B can provide many benefits to aviation, and currently the FAA intends to shift toward ADS-B as the primary means of aircraft surveillance. Future ATC radar, whether it remains the primary ATC surveillance tool or becomes an alternative means of surveillance to support ATC, will continue to contribute to aviation safety. GPS technology is susceptible to interference. Furthermore, ADS-B and SSR transponders, and avionics in general, can and do fail. Radar provides ATC with critical position information

about aircraft that have a nonoperating transponder, as well as noncooperative aircraft. Such redundancy in aviation provides an important safety margin to help prevent tragedy, particularly in high-density areas such as the terminal environment.

12.4.1 Radar Advancements for ATC

There has been considerable interest in recent years in the application of phased array radar technology to ATC. The increases in the performance envelope of digital radar signal processing technology support such a concept [62]. The main obstacle has been cost; phased array radars are considerably more expensive to develop and build than traditional dish-type rotating radars. For example, the defense industry has a hard time justifying the cost of phased array radars unless a newly developed system can replace a number of legacy systems by taking on their cumulative roles (low-elevation search, volume search, target track, target identification, weather detection and characterization, interceptor guidance, etc.). That way, the costs of those systems, to include their substantial logistics costs (which include training technicians and operators on the many individual systems), can be factored into a rationalization for the development, construction, and life cycle cost of the new phased array radar system.

There is a general consensus that long-term maintenance and operational costs will be lower for a solid-state active aperture phased array radar that has no rotating parts compared to existing ATC radar with high-voltage power supplies, high-power tubes, single point-of-failure transmitters, and multiple tube-based and dish-type rotating radars. Active aperture phased array radars should also require fewer major maintenance actions since they can degrade gracefully over time, as opposed to having to prevent or repair major failures. Such attributes of phased array radar makes them competitive in terms of life cycle costs with other systems that have lower initial costs for development and acquisition.

Therefore, in order to rationalize and justify the cost of phased array radar technology, the resulting radar will have to replace a large number of legacy systems (ASRs and ARSRs). In addition, it is hard to justify that such a radar would be practical in the context of affordability of the entire integrated system without also incorporating weather sensing capabilities as well so that it could also replace the NEXRADs and TDWRs. However, performing all of these functions in a single radar can increase the cost due to distinct requirements between aircraft and weather sensing functionality.

The FAA and the NWS have been jointly investigating the viability of Multifunction Phased Array Radar (MPAR) technology to solve the sensing functions of both agencies [59]. A multifunction radar could replace a large number of existing systems, as described earlier. Many of these systems are approaching the end of their life cycle. Future decisions will consider an SLEP for each system or undertake major acquisition(s) for replacement. It is challenging to meet the MPAR requirement to perform multiple missions yet meet aggressive cost targets. Significant benefits of an MPAR would include improved elevation angle accuracy due to the ability to form multiple pencil beams; faster update rates on point targets of interest (especially aircraft that appear threatening or with non-functioning transponders); faster update rates on weather cells of interest (of particular interest to the weather community, as it allows for improved forecasting and shorter warning times for severe weather events such as tornadoes [60]); and lower ongoing maintenance, training, and logistics costs across the radar “fleet.”

The faster update rates on either discrete targets or weather cells of interest stem from the capability of a phased array radar to interleave dedicated track beams while spending

most of the time in search mode. If a target is in track and the radar is accurately predicting the next location of the target based on target track file history, then the radar can put a dedicated beam at that location. If done properly, this dedicated track beam can be more precisely centered on the target, as opposed to a beam pointed in space as a result of a search raster. This “track during scan,” or TDS, mode results in less processing loss (beam shape loss, Doppler filter loss, range gate loss) as compared to the “track while scan,” or TWS, mode that is typical of a rotating dish-type radar, which means that less time needs to be spent on the target to maintain adequate signal-to-noise ratio.

A number of specific challenges are associated with multifunction radar development. To combine the functionality of a number of different radar types into one system increases the complexity of the radar waveform and beam-scheduling processes. Multifunctionality also challenges radar resources such as timeline, duty cycle, and occupancy. The resulting radar will require significant software architecture to manage radar resources so that adequate performance is maintained for the various functions under a variety of conditions (weather, aircraft track load, etc.). Experience indicates that the potential cost and cost growth of phased array radar software maintenance and updates across a large number of radar sites is an operations and maintenance (O&M) issue that requires careful consideration early in a program.

Some new technical challenges need to be addressed in an MPAR system. This can include a dual-polarization capability, which is of great interest within the weather community, as it allows for better characterization of precipitation type, which leads to better translation of volumetric reflectivity into precipitation rate [61]. The NEXRAD radars (WSR-88D) are currently being updated with a dual-polarization capability. Technical, cost, and complexity details for a dual-polarization capability for a phased array radar system need to be addressed, along with the corresponding technical challenges associated with alignment and calibration of both polarizations. Other challenges include the level of polarization purity required, as well as the level of polarization isolation required, which is dependent upon the switching scheme (i.e., simultaneous alternative transmission of the two polarizations) [61].

12.4.2 Other Surveillance Systems for ATC – ADS-B

ADS-B is a surveillance system in which aircraft position information received by GPS equipment on the aircraft is broadcast to ATC and other aircraft in real time. ADS-B also uses a data-link to exchange information with ground-based FAA equipment to provide increased situational awareness and services to pilots. ADS-B has a proven track record in improving ATM in both the radar and non-radar environments. The ability of ADS-B to also provide traffic information service-broadcast (TIS-B) and flight information service-broadcast (FIS-B) has the potential for significant benefits to aviation. ADS-B currently has two communications link architectures: the 1,090-MHz extended squitter (1090ES) and the 978-MHz universal access transceiver (UAT). The 1090ES is an extension of Mode S technology operating on the same 1090-MHz channel as the ATRCBS. The UAT offers relief for spectrum congestion with the additional data-link on a different frequency. In ADS-B terminology, “ADS-B Out” refers to the ability of an aircraft to transmit position information on an ADS-B data-link, but not process and display ADS-B traffic to the pilot. The ability to transmit ADS-B information as well as process and display real-time traffic information to the pilot is referred to as “ADS-B In.” The FAA will mandate an equipment installation deadline for each capability based

on aircraft operation in a given class of airspace. Certified ADS-B Out equipment will be mandated first on aircraft, followed by ADS-B In equipment. In a cooperative air traffic environment with high GPS signal integrity and availability, ADS-B represents remarkable capabilities. The rate of transition to ADS-B, the end state of ADS-B as a method of FAA surveillance, and the evolution of security or signal integrity enhancements for ADS-B remain as questions for the future.

12.5 | SUMMARY

In this chapter, an overview of ATC radar has been provided. ATC radar is the tool used by ATC to control airspace and provide safe and efficient air travel. Currently, there are two classes of ATC radar: ASRs and ARSRs. The S-band ASRs and L-band ARSRs are optimized to perform real-time monitoring of airspace in the terminal and en route environment, respectively. ATC radar employs both PSR (skin track) and SSR (aircraft transponder). A general discussion of PSR and SSR for these radar classes was provided. Weather detection design issues for ATC radar were also discussed. Finally, a look into the future of ATC radar was provided.

12.6 | FURTHER READING

This chapter has provided a brief look into some of the issues surrounding ATC radar. Other ATC radar design issues exist, such as atmospheric propagation, and the references listed in the following section provide additional material to explore in greater depth. The topic of ATC radar involves long-range ARSR for en route ATC, the shorter-range ASR for terminal ATC, and the development and implementation of SSR. Weather detection and processing for ATC radar is also of great importance for ATC, and additional reading is identified in the references. Each of these technologies has specific technical issues, as well as historical development, associated with the operational systems currently deployed within the NAS.

12.7 | ACKNOWLEDGMENTS

The author wishes to gratefully acknowledge the support of Mr. Tracy Wallace of Georgia Tech Research Institute (GTRI) and Mr. Paul Oesterle of Agilent Technologies, Inc.

12.8 | REFERENCES

- [1] M. I. Skolnik, *Radar Handbook*, 2nd Ed., McGraw-Hill, New York, NY, 1990.
- [2] D. C. Schleher, *MTI and Pulsed Doppler Radar with MATLAB*, 2nd Ed., Artech House, Norwood, MA, 2010.
- [3] J. Wang, M. Gerecke, E. Brookner, P. Cornwell, and J. Farr, "Design and Implementation of Long Range Radar Service Life Extension," in *Proceedings of the IEEE 2009 Radar Conference*, Pasadena, CA, May 4–8, 2009, pp. 1–6.

- [4] J. W. Taylor Jr. and G. Brunins, "Design of a New Airport Surveillance Radar (ASR-9)," in *Proceedings of the IEEE*, Volume 73, Issue 2, Feb. 1985, pp. 284–289.
- [5] F. E. Nathanson, *Radar Design Principles: Signal Processing and the Environment*, 2nd Ed., SciTech Publishing, Raleigh, NC, 1999.
- [6] M. A. Richards, *Fundamentals of Radar Signal Processing*, McGraw-Hill, New York, 2005.
- [7] R. J. Lay and J. W. Taylor, Jr., "ARSR-4: Unique Solutions to Long Recognized Radar Problems," in *Proceedings of the IEEE 1990 International Radar Conference*, Arlington, VA, May 7–10, 2009, pp. 6–11.
- [8] M. I. Skolnik, *Introduction to Radar*, 2nd Ed., McGraw-Hill, New York, NY, 1980.
- [9] M. L. Belcher and J. A. Scheer, *The Electronics Handbook*, 2nd Ed., Chapter 17, Section 2, CRC Press, Boca Raton, FL, 2005.
- [10] W. M. Shrader, "Radar Technology Applied to Air Traffic Control," in *IEEE Transactions on Communications*, Volume Com-21, No. 5, May 1973, pp. 591–605.
- [11] R. J. Lay, "Mission Determines Equality in Radar," in *IEEE 1995 International Radar Conference*, May 8–11, 1995, pp. 5–8.
- [12] Bendix King, KT76A/78A Transponder Manual, Rev. 1, March, 1977.
- [13] FAA TSO-C74c, "Airborne Transponder Equipment," Technical Standard Order (TSO), Department of Transportation, Federal Aviation Administration, Aircraft Certification Service, Washington, D.C., February 20, 1973.
- [14] J. L. Baker, V. A. Orlando, W. B. Link, and W. G. Collins, "Mode S System Design and Architecture," in *Proceedings of the IEEE*, Volume 77, Issue 11, Nov. 1989, pp. 1684–1694.
- [15] M. L. Wood, "Multilateration System Development History and Performance at Dallas/Ft. Worth Airport," in *Proceedings of the 19th Digital Avionics Systems Conference (DASC)*, Volume 1, pp. 2E1/1–2E1/8, 2000.
- [16] S. R. Duncan, V. Gregers-Hansen, and J. P. McConnell, "A Stacked Analog-to-Digital Converter Providing 100 dB of Dynamic Range," in *IEEE 2005 International Radar Conference*, May 9–12, 2005, pp. 31–36.
- [17] D. S. Crippen, "The Air Traffic Control Radar Beacon System," in *IRE Transactions on Aeronautical and Navigational Electronics*, Volume ANE-4, Issue 1, 1957, pp. 6–15.
- [18] S. H. Starr and J. E. Freedman, "The Effects of Defruiting on the ATCRBS," in *IEEE Transactions on Aerospace and Electronic Systems*, Volume AES-11, Issue 4, 1975, pp. 474–484.
- [19] G. Jacovatti, "Performance Analysis of Monopulse Receivers for Secondary Surveillance Radar," in *IEEE Transactions on Aerospace and Electronic Systems*, Volume AES-19, Issue 6, 1983, pp. 884–897.
- [20] D. L. Sengupta and J. Zatkalik, "On the Performance of Air Traffic Control Radar Beacon System," in *IEEE Transactions on Aerospace and Electronic Systems*, Volume AES-12, Issue 4, 1976, pp. 494–502.
- [21] M. C. Stevens, "New Developments in Secondary-Surveillance Radar," in *Electronics and Power*, Volume 31, Issue 6, 1985, pp. 463–466.
- [23] N. K. Shaw and A. A. Simolunas, "System Capability of Air Traffic Control Radar Beacon System," in *Proceedings of the IEEE*, Volume 58, Issue 3, 1970, pp. 399–407.

- [24] T. S. Perry, “In Search of the Future of Air Traffic Control,” in *Spectrum IEEE*, Volume 34, Issue 8, 1997, pp.18–35.
- [25] FAA Order 6310.6, *Primary/Secondary Terminal Radar Siting Handbook*, Department of Transportation, Federal Aviation Administration, Washington, D.C., July 20, 1976.
- [26] K. Roulston, “Angel Discrimination in the ARSR-4 Joint Use Radar,” in *Record of the 1993 IEEE National Radar Conference*, 1993, pp. 156–162.
- [27] M. Martineau and E.L. Cole, “Weather Detection Design Issues for a Solid State ASR,” in *Record of the 1995 IEEE National Radar Conference*, 1995, pp. 536–541.
- [28] F. H. Sanders, R. L. Hinkle, and B. J. Ramsey, *Measurement Procedures for the Radar Spectrum Engineering Criteria (RSEC)*, NTIA Report TR-05-420, U.S. Department of Commerce, March, 2005.
- [29] D. C. Schleher, *Electronic Warfare in the Information Age*, Artech House, Norwood, MA, 1999.
- [30] J. A. Scheer and J. L. Kurtz, *Coherent Radar Performance Estimation*, Artech House, Norwood, MA, 1993.
- [31] FAA Order JO 7110.65T, *Air Traffic Control*, Department of Transportation, Federal Aviation Administration, AJR-0, Washington, D.C., February 11, 2010.
- [32] M. A. Richards, J. A. Scheer, and W. A. Holm, *Principles of Modern Radar, Volume 1: Basic Principles*, 1st Ed., SciTech Publishing, Raleigh, NC, 2010.
- [33] D. K. Barton, *Radar System Analysis and Modeling*, Artech House, Norwood, MA, 2005.
- [34] S. M. Kay, *Fundamentals of Statistical Signal Processing, Volume 2: Detection Theory*, 1st Ed., Prentice Hall, Upper Saddle River, NJ, 1998.
- [35] L. Cartledge and R. M. O’Donnel, “Description and Performance Evaluation of the Moving Target Detector,” Report FAA-RD-76-190, *MIT Lincoln Laboratory, Project Report ATC-69*, March 8, 1977.
- [36] D. Carp and J. R. Anderson, “Moving Target Detector (Mod II) Summary Report,” Report FAA-RD-80-77, *MIT Lincoln Laboratory, Project Report ATC-95*, November 3, 1981.
- [37] J. Barrie Billingsley, *Low-Angle Radar Land Clutter, Measurements and Empirical Models*, 1st Ed., William Andrew Publishing (Acquired by Elsevier in 2009), Amsterdam, Netherlands, 2002.
- [38] G. Donohue, *Air Transportation Systems Engineering*, Chapter 34, Analysis of Aircraft Separation Minima Using a Surveillance State Vector Approach, AIAA, 2001.
- [39] FAA-HDBK-006A, *Reliability, Maintainability, and Availability (RMA) Handbook*, Department of Transportation, Federal Aviation Administration, Washington, D.C., January 7, 2008.
- [40] M. C. Stevens, *Secondary Surveillance Radar*, Artech House, Norwood, MA, 1988.
- [41] R. J. Doviak and D. S. Zrnic, *Doppler Radar and Weather Observations*, 2nd Ed., Academic Press, Inc., NY, 1993.
- [42] J. R. Probert-Jones, “The Radar Equation in Meteorology,” in *Quarterly Journal of the Royal Meteorological Society*, Volume 88, 1962, pp. 485–495.
- [43] A. L. Lance, W. D. Seal, and F. Labaar, *Phase Noise and AM Noise Measurements in the Frequency Domain*, Chapter 7, Infrared and Millimeter Waves, Volume 11, pp. 239–289, Academic Press, Waltham, MA, 1984.

- [44] D. Scherer, “The Art of Phase Noise Measurement,” Hewlett-Packard RF and Microwave Measurement Symposium and Exhibition, March, 1985.
- [45] W. Kessler, “Converting Oscillator Noise to Time Jitter,” Analog Devices Tutorial MT-008, October, 2008.
- [46] J. Porcello, “Scalar Measurement Error in Microwave and RF Test Configurations,” in *Microwave Journal*, Volume 38, No. 2, February 1995, pp. 100–108.
- [47] J. Wang, E. Brookner, and M. Gerecke, “Analysis of Concatenated Waveforms and Required STC,” in *IEEE Radar Conference*, Rome, Italy, 2008.
- [48] R. Nitzberg, “Effects of Particular Gain Changes Upon LFM Sidelobes” in *IEEE Transactions on Aerospace and Electronic Systems*, November 1974, pp. 870–872.
- [49] R. Baron and D. Shultheis, “The ARSR-4 High Fidelity Solid State Transmitter,” in *Microwave Symposium Digest*, IEEE MTT-S International, Volume 3, May 1994, pp. 1733–1736.
- [50] M. Labitt, “Obtaining Low Sidelobes Using Non-Linear FM Pulse Compression,” *MIT Lincoln Laboratory, Project Report ATC-223*, November 4, 1994.
- [51] E. Cole, P. DeCesare, M. Martineau, R. Baker, and S. Buswell, “ASR-12: A Next Generation Solid State Air Traffic Control Radar,” in *Proceedings of the 1998 Radar Conference*, May 1998, pp. 9–14.
- [52] B. R. Mahafza, *Radar Signal Analysis and Processing Using MATLAB*, CRC Press, Boca Raton, FL, 2008.
- [53] E. De Witte and H. D. Griffiths, “Improved Ultra-Low Range Sidelobe Pulse Compression Waveform Design,” in *Electronic Letters*, Volume 40, Issue No. 22, October 28, 2004, pp. 1448–1450.
- [54] S. Boukeffa, Y. Jiang, and T. Jiang, “Sidelobe Reduction with Nonlinear Frequency Modulated Waveforms,” in *IEEE 7th International Colloquium on Signal Processing and Its Applications (CSPA)*, March 2011, pp. 399–403.
- [55] R. Nitzberg, “Clutter Map CFAR Analysis,” in *IEEE Transactions on Aerospace and Electronic Systems*, Volume 22, Issue No. 4, July 1986, pp. 419–421.
- [56] N. Levanon, “Numerically Efficient Calculations of Clutter Map CFAR Performance,” in *IEEE Transactions on Aerospace and Electronic Systems*, Volume 23, Issue No. 6, November 1987, pp. 813–814.
- [57] J. Porcello, “Automation Techniques for Fast Implementation of High Performance DSP Algorithms in FPGAs,” in *NASA Military and Aerospace Programmable Logic Devices (MAPLD) Conference*, September 2005.
- [58] J. Porcello, “Design and Implementation of Multifunction SDR Algorithms in FPGAs,” in *NASA Military and Aerospace Programmable Logic Devices (MAPLD) Conference*, September 2006.
- [59] Weber, et al., “The Next-Generation Multimission U.S. Surveillance Radar Network,” in *Bulletin of the American Meteorological Society*, November 2007. pp. 1739–1751.
- [60] A. Smith, P. Heinselman, and P. Chilson, “Evaluation of Rapid Sampling Rates Using the National Weather Radar Testbed Phased-Array Radar,” in *The Sixth European Conference on Radar in Meteorology and Hydrology*, July 2010.
- [61] R. Doviak, V. Bringi, A. Ryzhkov, A. Zahrai, and D. Zrnica, “Considerations for Polarimetric Upgrades to Operational WSR-88D Radars,” in *Journal of Atmospheric and Oceanic Technology*, Volume 17, March 2000, pp. 257–277.

- [62] J. Porcello, “Designing and Implementing Time-Domain Interpolation Based Digital Beamforming in FPGAs,” in *56th Military Sensing Symposium (MSS) Tri-Service Radar Symposium*, June 2010.
- [63] R. Thompson, “Doppler-Weather Signal Processing for a Rapid RF- and PRF- Agile Airport Surveillance Radar,” in *Proceeding of the 19th Digital Avionics Systems Conferences (DASC)*, Volume 2, August 2000.
- [64] C. Engholm and S. Troxel, “Beam Filling Loss Adjustments for ASR-9 Weather Channel Reflectivity Estimates,” in *MIT Lincoln Laboratory, Project Report ATC-177*, October 22, 1990.
- [65] E. Rubiola, *Phase Noise and Frequency Stability in Oscillators*, Cambridge University Press, Cambridge, England, 2009.
- [66] U. Rhode, *Digital PLL Frequency Synthesizers, Theory and Design*, Prentice-Hall, Upper Saddle River, NJ, 1983.
- [67] S. Nolan, *Fundamentals of Air Traffic Control*, 5th Ed., Cengage Learning, Stamford, CT, 2010.
- [68] Agilent Technologies, Application Note, “Agilent Radar Measurements,” Literature Number E5989-7575EN, 2011.
- [69] Agilent Technologies, Application Note AN 1309, “Pulsed Carrier Phase Noise Measurements,” Literature Number E5968-2081EN, 2006.

Weather Radar

*J. Trostel, Director, Severe Storms Research Center,
Georgia Tech Research Institute, Atlanta, GA 30332-0857*

Chapter Outline

13.1	Introduction	591
13.2	Typical Weather-Radar Hardware.	595
13.3	The Radar-Range Equation for Weather Radar.	597
13.4	Doppler Processing	603
13.5	Hydrological Measurements.	609
13.6	Characteristics of Some Meteorological Phenomena	615
13.7	Sun Echoes and Roost Rings.	623
13.8	Advanced Processing and Systems	623
13.9	References.	632
13.10	Further Reading	634

13.1 | INTRODUCTION

13.1.1 A Short History of Weather Radar

The most common interaction many in the public have with radar on a daily basis is with weather radar. Most television meteorologists use the output of weather radar as a central part of their broadcasts. As a consequence, much of the general public has a passing familiarity with some elementary concepts of weather radar, such as the association of precipitation with areas of enhanced reflectivity and perhaps even morphological characteristics of some storms such as a tornadic “hook echo.” This familiarity and the ubiquity of commercial weather radar in broadcasting are testaments to the advanced state of weather radar in the current age.

The use of radar to investigate meteorological phenomena has a long history; nearly as long as the history of radar itself. During the formative years of radar during World War II, meteorological effects were generally seen as a nuisance. However, some air traffic and surveillance radars installed on the east and west sides of the Panama Canal were also used to look at weather as early as 1943. A second network was established in India in 1944. The AN/APQ-13 radar set was used in both airborne and ground-based configurations. Shortly after the war, interest in using radar to detect and track weather targets increased [1, 2]. The Air Weather Service (AWS) made great use of the APQ-13,

with a maximum of 60 in operation at one time. The last APQ-13 was removed from service in 1977 [3].

The National Weather Service (NWS) initially used modified APS-2F S-band radars – renamed the WSR-1, WSR-1A, WSR-3 and WSR-4, where WSR is an acronym for Weather Surveillance Radar) – between 1947 and the 1980s, when they were mostly replaced by the WSR-74C radars.

Figure 13-1 shows the first recorded image of a tornadic *hook echo*. A hook echo is often taken as a precursor of tornadic activity in a severe thunderstorm. It is a manifestation of the intense mesocyclone within the storm, pulling raindrop laden air around the potentially tornadic circulation. The photographic image was taken on April 9, 1953, from the screen of an APS-15 radar operated by the Illinois State Water Survey [4]. In this same year, Ian Browne and Peter Barratt first used Doppler techniques to measure vertical motions in a rain shower.

By the mid-1950s, the U.S. Weather Bureau, the predecessor of the National Weather Service, had convinced the Congress to fund a major initiative for improvement of hurricane and tornado warning services through the initial approval and funding for the purchase of first operational weather radars, the WSR-57s. The WSR-57, illustrated in Figure 13-2, was an S-band radar, chosen to minimize attenuation by rainfall, with a 2° beamwidth. The first WSR-57 was installed in June 1959 in Miami, Florida. The NWS operated 53 WSR-57s at the peak of their use.

Many WSR-57 radars were still in use well into the 1990s. In the mid-1970s, Enterprise Electronics Corporation (EEC) was funded to replace many aging local warning radars in the NWS with a C-band system, the WSR-74C. Several S-band radars were also produced, including the WSR-74S, to fill existing gaps in the national grid.

Research into the Doppler effect and its application to weather radar began as early as 1956. By 1961, the Air Force Cambridge Research Laboratory was using a 5-cm pulsed Doppler radar to investigate weather. The 1960s and 1970s saw much pioneering research in the application of Doppler processing, with the first mesocyclone detected by radar in 1968 and the first confirmed tornado vortex signature recorded in 1975. The Joint Doppler Operational Project (JDOP) was formed in 1977 as an effort to define a

FIGURE 13-1 ■
First Documented
Recording of a
Tornadic Hook
Echo. Credit:
Courtesy of the
Illinois State Water
Survey, Champaign,
Illinois; photograph,
Donald W. Staggs.

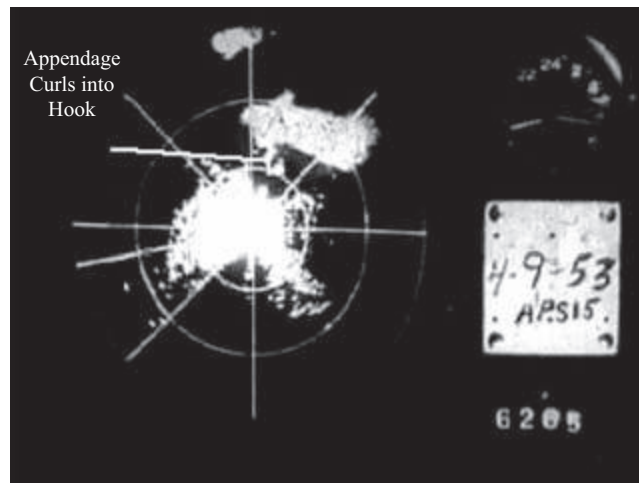




FIGURE 13-2 ■
WSR-57 Weather-
Radar Console.
[Source: [3]]

replacement radar system to aging Department of Defense (DoD) and NWS radar assets as well as to determine the benefits of a Doppler system.

The recommendations of JDOP directly led to the capabilities that would be required of the new Doppler weather-radar systems. These systems were code-named WSR-88D and more commonly known now as *next generation radar* (NEXRAD). The NEXRAD system is an S-band system with Doppler capability. The original design specifications for the NEXRAD systems included a 1° beamwidth, a maximum range of nearly 460 km, and detection Doppler motions of ± 50 m/s at distances up to 230 km [5, 6]. All NWS facilities have now been updated to the more modern, Doppler-capable WSR-88D units. An upgrade cycle, completed in 2013, added dual-polarization capabilities to the NEXRAD radar systems.

One of the uses of commercial weather radar in the broadcast media occurred in 1969 when EEC sent a C-band weather radar to a Tampa, Florida, TV station. Since the 1990s, many stations have added Doppler radar capability to their weather centers and raised public awareness of the ability to detect various weather types, including dangerous tornadoes with this technology.

13.1.2 Typical Applications of Weather Radar

Weather radars are used daily in a wide variety of applications. These uses include the day-to-day forecasting and weather warning tasks of the National Weather Service. The detection of severe local storms, dangerous winds, precipitation areas, and approximate rainfall amounts are several very useful additional functions provided by the NWS radars.

Commercial media outlets, particularly local television stations, have made great use of weather radar and often employ Doppler radars to warn their local listeners of potentially dangerous weather situations. The general public's most common interaction with radar is often the weather radar on local television stations and the radar speed-detection devices employed by law enforcement.

Commercial airlines, as well as a growing number of private pilots, employ smaller, airborne versions of weather radar to provide an immediate capability to detect potential weather hazards while in flight. These systems typically operate at a much shorter wavelength than ground-based weather radars and are therefore much more susceptible to attenuation by precipitation. Nevertheless, the timeliness of the information provided often greatly outweighs the shortcomings of the increased frequency.

Military use of radar was a driving force in the development of early weather radars, and the use of these systems in tactical situations remains important. Often size, weight, and power considerations require that tactical weather-radar systems operate at higher frequencies or over shorter ranges than fixed ground-based systems.

13.1.3 Current Innovations

Public, commercial, and military interest in weather-radar applications continue to drive innovation in this field. Improvements and advancements in electronics also have led to smaller, more powerful, and less expensive radar systems.

Between 2010 and 2013, the national network of NEXRAD radars were all upgraded to provide a dual-polarization capability [7]. Initially, the NEXRAD radars were configured to transmit and receive only horizontally polarized pulses. The upgrade added the ability to transmit and receive both horizontally and vertically polarized pulses. As will be seen in Sections 13.5 and 13.8, the ability of a radar system to transmit and receive both horizontal and vertical polarizations greatly enhances the ability to discriminate between different types of precipitation.

A single Doppler capable radar can detect the component of motion only along a radial from the radar, either directly toward or directly away from the radar. Components of the motion that are tangential to the radar beam produce no Doppler signal. The dual-Doppler method has been successfully used to produce a more complete description of the velocity field by combining information from two separate Doppler radar systems.

Phased array technology, in which a large array of smaller transmitters and receivers are controlled to produce directed transmit and receive beams, has been utilized in military radar systems for many years [8]. The advantage of using a phased array in controlling beam size, shape, and direction in these applications outweighed the higher costs and complexities of the phased array technology. The National Weather Service is currently evaluating the use of this technology to improve the detection and surveillance of severe weather [9].

Mobile meteorological radar platforms have been developed by both university and governmental agencies in order to rapidly deploy these scientific assets to study storm systems of interest. All of these innovative applications of weather radar will be discussed in Section 13.8.

13.1.4 Symbols and Abbreviations Used in This Chapter

CASA	Collaborative Adaptive Sensing of the Atmosphere
DCAS	Distributed Collaborative Adaptive Sensing
NOAA	National Oceanic and Atmospheric Administration
NEXRAD	next generation radar
Z_{DR}	relative reflectivity factor

dBZ	reflectivity factor expressed in dB
BWER	bounded weak echo region
NWS	National Weather Service
MPAR	multifunction phased array radar
PAR	phased array radar
PPI	plan position indicator
RHI	range height indicator
TDWR	terminal Doppler weather radar
Z	reflectivity factor

13.1.5 Organization of the Rest of This Chapter

The rest of this chapter begins by describing the general characteristics, specifications, and end uses of some of the common types of weather radar in use today. These radars include the NWS NEXRAD and terminal Doppler weather radar (TDWR) systems, as well as a description of airborne radars.

Next, a special form of the radar-range equation will be developed that is suited for describing the volume scattering found in weather-related echoes. The reflectivity factor, Z , will be introduced along with the more common measurement quantity, dBZ. This will be followed by a description of the application of Doppler processing for weather measurements, including several potential pitfalls in this processing, such as range folding and the so-called Doppler dilemma. The methods used to measure important meteorological phenomena will be discussed with an emphasis on the development of the relationship for measurement of rain. The characteristics of hail and snow, as well as clear air and non-meteorological targets, will also be discussed. Some basic radar characteristics of weather systems such as supercells, tornadoes, and hurricanes will be shown.

The chapter concludes with a short discussion of some of the most recent advances in weather-radar systems and processing, including dual-Doppler processing, various mobile weather-radar systems, and some radar systems and concepts currently still in development or on the drawing board.

13.2 | TYPICAL WEATHER-RADAR HARDWARE

13.2.1 NEXRAD

The primary weather-radar network covering the United States consists of 156 S-band WSR-88D (Weather Surveillance Radar, 1988 Doppler) radars. They are also commonly referred to as *NEXRAD*, for *next generation radar*. These radars are operated mostly by the National Weather Service, with some sites operated by either DoD or the Federal Aviation Administration (FAA). WSR-88Ds are the workhorse of the weather-radar system, providing data to both the NWS and the interested public. The NEXRAD sites have been chosen to provide overlapping coverage when possible and are typically chosen to be collocated with a NWS forecast office. The NEXRAD radars were originally klystron-based, single-frequency, polarization radar systems [10]. Most NEXRAD sites have been upgraded to a super-resolution mode in recent years. Additionally, all NEXRAD sites were upgraded to dual-polarization capability between 2010 and 2013 [11].

Specifications

- Transmit frequency 2.7–3.0 GHz
- Peak power 475 kW
- Pulse width 1.57 μ s to 4.57 μ s
- Antenna beamwidth 0.95 degrees
- PRF 320 Hz to 1,300 Hz (318 and 1,304 @ 1.57, 452 @ 4.7)
- Range resolution 236 m to 685 m
- Unambiguous range 115 km to 468 km
- Unambiguous Doppler 8 m/s to 32.5 m/s

The NEXRAD network is used daily by the NWS, as well as by commercial interests, to provide the general population with warnings about weather, including precipitation events and severe storms.

13.2.2 Commercial Weather Radar

A number of commercial vendors of weather radar, both in the United States and worldwide, supply weather-radar technology to commercial concerns, such as television and radio stations, as well as to governmental agencies around the world. Often these systems are tasked to be multiple-use systems, with some tracking and surveillance functions mixed in with weather applications. A typical system produced by the Vaisala Corporation is summarized as follows. The Vaisala WRK-200 system is a dual-polarization, klystron-based, C-band weather-radar system.

Specifications

- Operating frequency range 5.6–5.65 GHz
- Peak power 250 kW
- Modulator Solid State
- Antenna gain 45 dB
- Antenna diameter 4.5 m
- Beamwidth <1 degree
- PRF 200 to 2,400 Hz
- Range resolution 15 m or greater
- Pulse widths 0.5, 0.8, 1.0, 2.0 μ s

13.2.3 TDWR

The terminal Doppler weather radar (TDWR), was developed by the FAA in response to a number of aircraft encounters with downbursts and wind shear near airports. The TDWR systems are designed to detect these phenomenon and operate, therefore, at a shorter wavelength, in C-band, than the longer-range, general-purpose weather-surveillance NEXRADs. The TDWR systems are deployed at 45 of the largest airports in the

United States. While the TDWR systems are primarily used to detect hazardous wind events near these airports, the data from these systems have become generally available. Their increased resolution and added information can be valuable when severe weather threatens an area.

Specifications

- Transmit frequency 5.6–5.65 GHz
- Peak power 250 kW
- Antenna beamwidth <0.55 degree (pencil beam)
- Pulse width 1.1 μ s
- PRF 2,000 Hz (maximum)
- Range resolution 165 meters
- Maximum observation range
 - Doppler 90 km
 - Radial velocity 89 km
 - Reflectivity 460 km
- Maximum unambiguous Doppler 53.6 m/s

13.2.4 Aviation Radars

Aviation radars need to be both reliable and small in order to fit within the airframe that carries them. Often these systems are low-power, solid-state radars that have the primary mission of relatively close surveillance of weather in the immediate area of the aircraft. The Rockwell Collins weather radar, described as follows, is an X-band radar designed for medium-sized aircraft.

Example Specifications

- Weather detection
 - 320-nautical mile maximum selected range
- Wind-shear detection
 - Coverage area ± 30 degrees
 - Detection range 5 nautical miles
- Radar parameters
 - PRF 180 pps (up to 9,000 pps)
 - Pulse widths 1 to 20 microseconds
 - Frequency 9.33 GHz (X-band)
 - Peak power 150 watts
 - Beamwidth 3.5°
 - Antenna gain 34 dB

13.3 | THE RADAR-RANGE EQUATION FOR WEATHER RADAR

13.3.1 The Nature of Weather-Radar Measurements

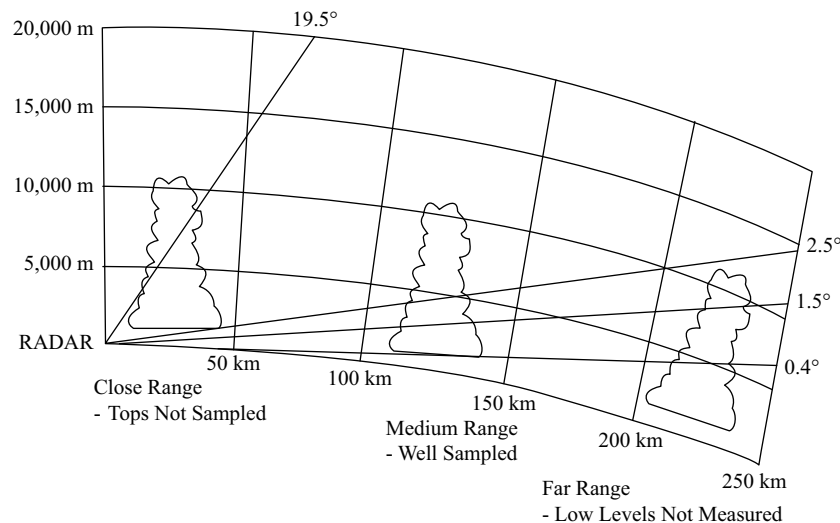
The measurement of weather by radar typically takes place over extended ranges, on the order of hundreds of kilometers. Aspects of the measurement such as the curvature of Earth and the spreading of the transmit beam are, therefore, significant factors to be considered. Figure 13-3 illustrates the effect of Earth's curvature on the height above the surface that the beam traverses. For a storm close to the radar transmitter, good sampling of even the lower levels of a storm cell may be possible. Storms that are located at greater distances will not be sampled well at lower levels and may be missed entirely.

A typical volume coverage pattern (VCP) used operationally with NWS NEXRAD radars is shown in Figure 13-4. In this scan strategy (VCP 11), which is optimized for storm-cell coverage, one can see the exceptional coverage afforded, even up to 40 kft, at a relatively short range of 20 nmi. A secondary effect at close ranges called the *cone of silence* can be seen at these short ranges. Echoes at height are not visible at extremely close ranges. At larger ranges such as 120 nmi, the radar is not sampling the lowest levels of the atmosphere. All echoes below 10 kft are missed in this scan strategy due to Earth curvature effects. This can cause problems in detecting low-level shear and rotation fields in distant storms.

13.3.2 Characteristics of Precipitation

The major use for weather radar is the detection and measurement of precipitation. In general, precipitation varies greatly spatially and temporally. The type of storm producing the precipitation has a great effect on the characteristics of the precipitation, ranging from highly variable thunderstorms and other small cellular events to large systems associated with frontal systems and synoptic scale (hundreds to thousands of km) weather systems. Precipitation may include liquid water ranging from fog, haze, and drizzle to very large droplets several mm in diameter. As storm clouds can reach tens of thousands of meters

FIGURE 13-3 ■
Effect of Earth's
Curvature on
Storm-Cell
Sampling.



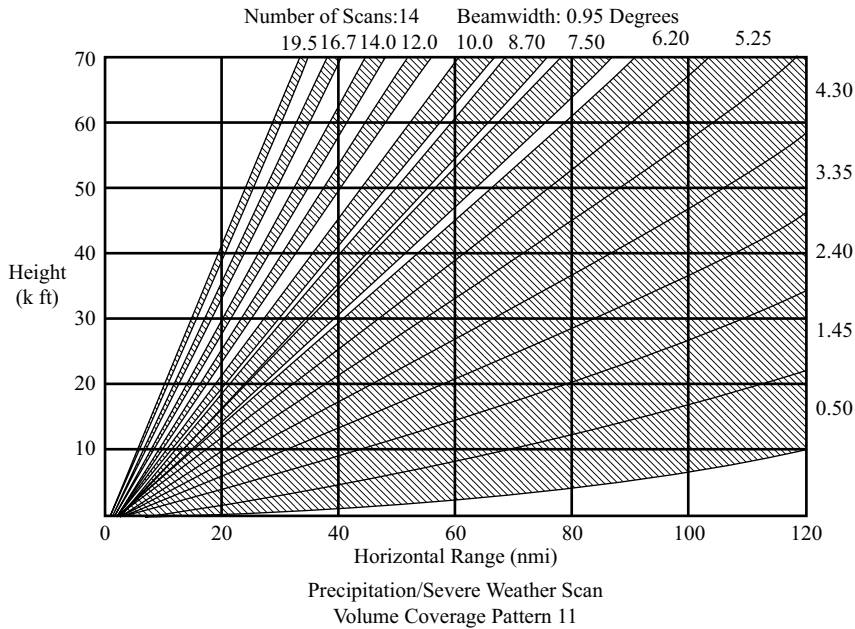


FIGURE 13-4 ■ NEXRAD Volume Coverage Pattern for Precipitation and Severe Weather. [Source: National Oceanic and Atmospheric Administration]

into the atmosphere, precipitation in a single storm may consist of liquid water, sleet or graupel, hail and snow, and ice particles. While each type of precipitation presents itself differently to the radar, by means of some simplifying assumptions, a generalized view of the radars response to the precipitation may be found useful in real-world applications.

13.3.3 Volume Scattering

Several basic assumptions are made in the derivation of the radar equation for meteorological targets. One main assumption is that the volume illuminated by the radar beam is uniformly filled with scattering targets. A second common assumption is that attenuation by and multiple scattering between these targets can be ignored. The received power then simply becomes the sum of the power scattered by all the individual scattering centers in the volume.

Recalling the radar equation for a single scatterer as

$$\bar{P}_r = \frac{P_t G^2 \lambda^2 \sigma}{(4\pi)^3 r^4} \tag{13.1}$$

where

- \bar{P}_r = average received power,
- P_t = transmit power,
- G = radar gain,
- λ = wavelength,
- σ = single target scattering cross section, and
- r = range to the scatterer (m).*

*Since capital “R” is used to denote rain rate, for the weather radar purposes, range is denoted with lower case “r.”

Summing over all the targets located within the pulse volume gives

$$\bar{P}_r = \frac{P_t G^2 \lambda^2}{(4\pi)^3} \sum_i \frac{\sigma_i}{r_i^4} \quad (13.2)$$

This equation can be further simplified by moving the r^4 back outside the summation, assuming that we are at a distance sufficiently large that all the ranges within a pulse volume are essentially equal. A second simplification is made by introducing a factor, η , defined as the backscattering cross section per unit volume:

$$\eta = \frac{1}{V} \sum_i \sigma_i \quad (13.3)$$

Solving (13.3) for $\sum \sigma$, and substituting back into (13.2) gives

$$\bar{P}_r = \frac{P_t G^2 \lambda^2 \eta V}{(4\pi)^3 r_i^4} \quad (13.4)$$

The illuminated volume, V , can be approximated as

$$V = \pi \left(r \frac{\theta}{2} r \frac{\phi}{2} \frac{c\tau}{2} \right) = \frac{\pi r^2 \theta \phi c\tau}{8} \quad (13.5)$$

where

- θ = azimuthal beamwidth,
- ϕ = elevation beamwidth,
- c = speed of light, and
- τ = pulse length.

The factor of $\frac{c\tau}{2}$ arises because of the two-way path the pulse takes between the radar transmitter, the target volume, and then back again to the radar receiver. We are interested in returns from a distributed volume that all arrive at the radar at the same time. In other words, the returns from the far end of the volume, illuminated by the start of the pulse, should arrive at the same time as the returns from the rear end of the volume illuminated by the end of the pulse. Since the front of the pulse must travel out to the far end *and back to the near end of the volume* by the time that the end of the pulse reaches the near end of the volume, the total illuminated volume is not $c\tau$, but rather half that, or $\frac{c\tau}{2}$.

In meteorological radars, the beam geometry is often symmetric, allowing us to replace $\theta\phi$ with θ^2 . This leaves a form involving only the backscattering cross section per unit volume as an unknown:

$$\bar{P}_r = \left(\frac{1}{2 \ln 2} \right) \frac{P_t G^2 \lambda^2 \eta \theta^2 c\tau}{512 \pi^2 r^2} \quad (13.6)$$

A factor of $1/(2 \ln 2)$ has been added to account for the nonuniform Gaussian beam-shape weighing [12].

13.3.4 Raindrop-Scattering Cross Sections

As demonstrated by Figure 13-5, when the particle circumference is on the order of half the wavelength of the interrogating radar, the Rayleigh approximation to scattering is quite valid, although often the Rayleigh approximation is used over all circumferences less than the wavelength. Above this region, the oscillatory nature of Mie scattering must be taken into account.

The normalized backscatter from water and ice spheres is somewhat more complex but follows the same pattern. Calculations performed by Herman and Battan [13] and reproduced in Battan [14] for normalized backscattering for water spheres between 1 and 10 cm and ice spheres between 1 and 30 cm at a λ of 3.21 cm is shown in Figure 13-6.

Operationally, the diameters of raindrops are often small compared to the incident wavelength of the radar beam. When the ratio of the circumference of the drops to the wavelength is much less than 1 – that is, $a \ll 1$ – we can assume that the drops act as Rayleigh scatterers; their individual scattering cross sections can be expressed as

$$\sigma_i = \frac{\pi^5 |K|^2 D_i^6}{\lambda^4} \tag{13.7}$$

In this equation, D_i , the drop diameter is given in millimeters and K is defined as

$$K = \frac{m^2 - 1}{m^2 + 1} \tag{13.8}$$

where m is the complex index of refraction. For wavelengths between 3 and 10 cm and temperatures between 0 and 20 °C, $|K|^2$ can be approximated as

$$|K|^2 \approx 0.93 \text{ (water)}$$

and

$$|K|^2 \approx 0.197 \text{ (ice)}$$

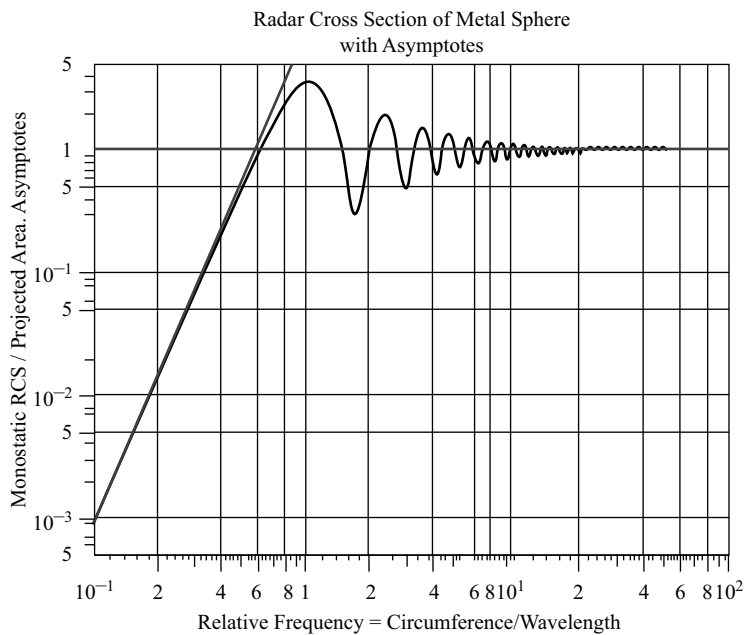
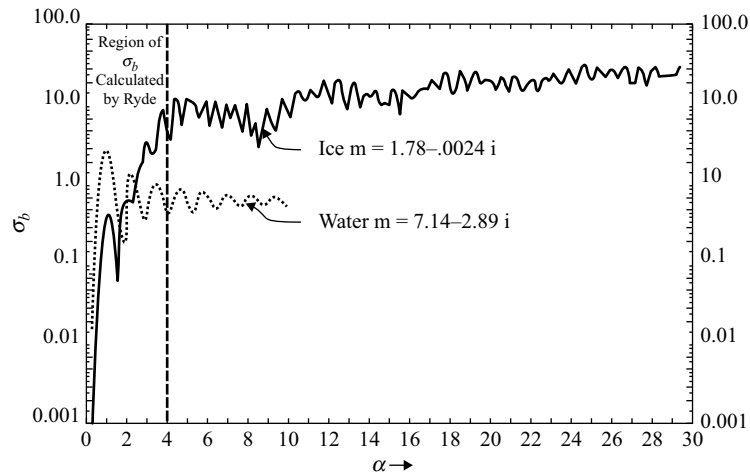


FIGURE 13-5 ■ Radar Cross Section of a Perfectly Conductive Sphere Showing Rayleigh and Mie Regions.

FIGURE 13-6 ■
 Calculated Values
 of σ_b for Water
 and Ice Spheres at
 0 °C for 3.21-cm
 Wavelength.
 [Source: [12]]



13.3.5 The Reflectivity Factor (Z)

A convenient term, the *reflectivity factor*, can now be introduced to relate the diameters of the scatters to the received backscatter. This factor is defined as

$$Z = \frac{1}{V} \sum_{vol} D^6 \quad (13.9)$$

Using the spherical backscattering equation for the drops previously developed, we can rewrite the definition of the backscattering cross section per unit volume, η , in terms of Z :

$$\eta = \frac{\pi^5 |K|^2}{\lambda^4} Z \quad (13.10)$$

Z has units of mm^6/m^3 and is usually expressed on a dB scale as “dBZ” due to the large range of variation encountered.

13.3.6 Final Form of the Radar-Range Equation for Weather Radar

The radar equation for meteorological targets can be further simplified by substituting in the formula for η in terms of Z , resulting in the following final form:

$$\bar{P}_r = (1/\ln 2) \frac{P_t G^2 \theta^2 c \tau \pi^3 |K|^2 Z}{1,024 \lambda^2 r^2} \quad (13.11)$$

Notice that if we assume either all water or all ice, then all the factors in the equation are known with the exception of Z , which is dependent on the spectrum of drop sizes found within the illuminated volume. Also, given equivalent drop-size distributions, the effect of $|K|^2$ is such that ice will scatter back a significantly lower power and, if the K for water is used, will appear to have a much lower effective reflectivity factor, Z_e . The

assumption of K as the value for water, K_w , is often made, and typically an effective reflectivity factor is the operationally measured and displayed value.

13.4 | DOPPLER PROCESSING

13.4.1 Development of the Doppler-Frequency Equation

If the distance between a radar and the target it is measuring is r , then the distance that a radar pulse travels to the target and back is $2r$. In terms of wavelengths at a frequency, f , with corresponding wavelength, λ , the distance can be expressed as

$$D = 2r/\lambda \quad (13.12)$$

where

$$\lambda = c/f$$

As there are 2π radians in a wavelength, the distance can be expressed in terms of radians as

$$D = \left(\frac{2r}{\lambda}\right)2\pi = \frac{4\pi r}{\lambda} \quad (13.13)$$

The phase of a pulse of initial phase θ_0 returned from a target at range, r , then becomes

$$\theta = \theta_0 + \frac{4\pi r}{\lambda} \quad (13.14)$$

The phase change of the returned pulse, due to movement by the target, is then

$$\frac{d\theta}{dt} = \frac{4\pi}{\lambda} \frac{dr}{dt} \quad (13.15)$$

In this equation, $\frac{dr}{dt}$ is simply the velocity, V , and $\frac{d\theta}{dt}$ is the resulting Doppler shift in radians per second. A corresponding Doppler frequency can be determined using the relationship:

$$f_d = \frac{1}{2\pi} \frac{d\theta}{dt} \quad (13.16)$$

This leads to the familiar expression for Doppler frequency as a function of target motion, V , and radar wavelength, λ :

$$f_d = \frac{2V}{\lambda} \quad (13.17)$$

It is important to remember that these equations were developed with the assumption that the motion of the target was completely along a radial from the radar. If the target has a direction of motion that is not completely toward or away from the radar, the Doppler frequency will only be representative of the radial component of that motion.

It is instructive to look at the magnitude of the Doppler frequency due to various radial velocities as a function of several radar frequency bands typically used in

TABLE 13-1 ■ Doppler Shift for Various Radar Bands

Radial Velocity	X-band (9 GHz)	C-band (5 GHz)	S-band (3 GHz)
1 m/s	60 Hz	33 Hz	20 Hz
10 m/s	600 Hz	333 Hz	200 Hz
30 m/s	1,800 Hz	1,000 Hz	600 Hz
50 m/s	3,000 Hz	1,667 Hz	1,000 Hz

meteorological radar systems. As Table 13-1 shows, the Doppler shift, even for fast targets at short wavelengths (high frequencies), is several orders of magnitude below the transmitted frequency. Therefore, Doppler radars must employ very stable transmitters and receivers to operate effectively.

13.4.2 Maximum Unambiguous Range and Velocity

Doppler radars, being pulsed radar systems, have a maximum unambiguous range that can be determined based on the pulse repetition frequency (PRF) of the radar. For the range to the target to be unambiguously measured, a pulse must travel out to the target and return before the next pulse is transmitted. This time period, τ , is just the inverse of the PRF. In terms of distance to the target, τ can be represented as

$$\tau = \frac{2r}{c} \quad (13.18)$$

Substituting for τ and solving for the maximum unambiguous target range, r_{max} , leads to

$$r_{max} = \frac{c}{2 * f_{PRF}} \quad (13.19)$$

Similarly, the Nyquist frequency for a given PRF determines the maximum unambiguous Doppler frequency that can be determined. Any higher frequency will be indeterminate as either a higher frequency or a wrapped negative frequency. The Nyquist frequency is written as

$$f_{Nyquist} = \frac{f_{PRF}}{2} \quad (13.20)$$

and represents the maximum unambiguous Doppler frequency that can be determined. This can be used to determine, using (13.17), a corresponding maximum unambiguous velocity, v_{max} :

$$f_{Nyquist} = \frac{2v_{max}}{\lambda} \quad (13.21)$$

Substituting back for the PRF and solving for v_{max} yields the following relationship between the PRF and the maximum unambiguous velocity:

$$v_{max} = \frac{f_{PRF}\lambda}{4} \quad (13.22)$$

13.4.3 The Doppler Dilemma

At a given radar operating frequency, maximum unambiguous range is inversely proportional to the system PRF, while maximum unambiguous velocity is directly proportional. Therefore, to measure higher Doppler velocities, a trade-off must be made to measure these velocities at shorter ranges. The equations developed for the maximum unambiguous range and velocity developed in the preceding section both involve the pulse repetition frequency and so can be combined and solved simultaneously to produce (13.23) to illustrate this point:

$$r_{max}v_{max} = \frac{c}{2 * f_{PRF}} \frac{f_{PRF}\lambda}{4} \quad (13.23)$$

$$r_{max}v_{max} = \frac{c\lambda}{8}$$

This trade-off is often called the *Doppler dilemma* and is shown graphically as a function of different radar wavelengths in Figure 13-7.

A typical method used to address the Doppler dilemma is to use two different PRFs. A set of pulses at a long PRF is used to measure reflectivity out to the maximum unambiguous range, while a second set of pulses at a shorter PRF is used to accurately measure Doppler velocity to a reasonable unambiguous velocity at shorter distances.

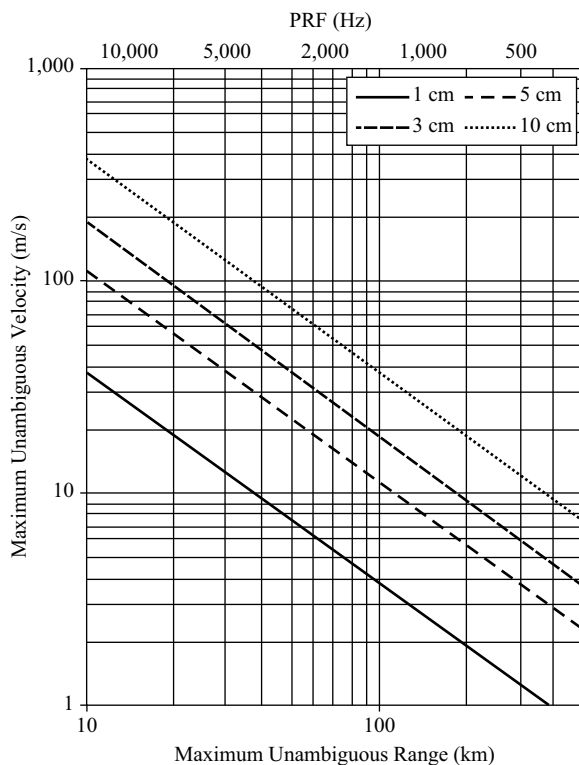


FIGURE 13-7 ■
The Doppler
Dilemma.

13.4.4 The Doppler Spectrum

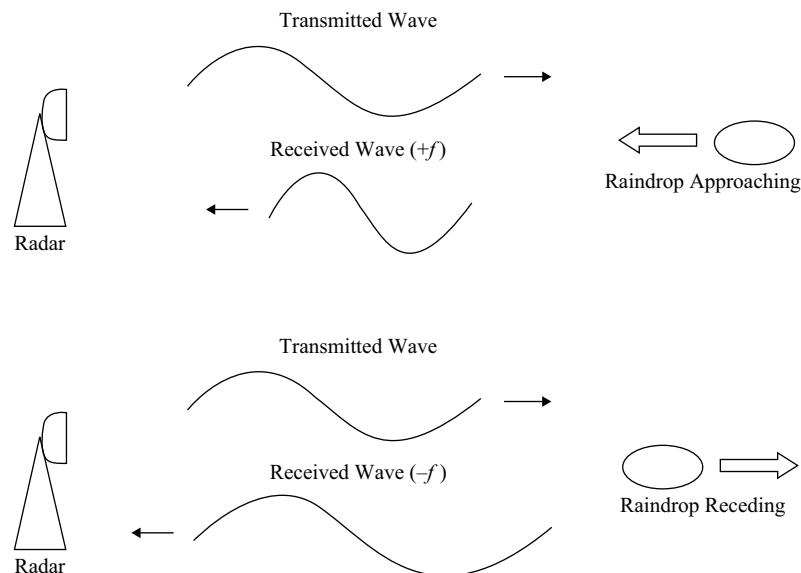
The preceding discussion of Doppler processing has assumed that only a single scatterer is present in the sampled volume reflecting the energy from the radar, as illustrated in Figure 13-8.

In reality, the radar pulse will intercept many droplets within the active volume. These raindrops will consist of a range of sizes, distributed across that range with larger numbers of small drops and smaller numbers of larger drops. Several drop-size distributions that closely resemble measured distributions are presented in Section 13.5.1 along with their effects on radar reflectivity. The existence of this distribution of droplets leads to a variety of reflectivities returned to the radar. Another complicating factor is the relatively large area encompassed by the radar beam, especially at longer ranges. These large sampling areas often include particles moving at different relative radial velocities with respect to the radar. The velocity differences can be due to turbulence, vertical wind shear (especially at higher elevation angles), differential drag effects on different-sized particles, or small-scale storm motions. These reflections at varying Doppler offsets combine to produce a complex waveform, as shown in Figure 13-9, and a corresponding spectrum of Doppler responses representative of the sum of the responses from all the droplets, as illustrated in Figure 13-10. Various components of this Doppler spectrum represent different characteristics of the precipitation.

The area under the curve in Figure 13-10 represents the total energy reflected from the full distribution of drops within the volume. The position of the peak of the distribution represents a reflectivity weighted mean radial velocity of the drops in the volume. Finally, the width of the distribution is a measure of the variability of radial velocities detected within the sample.

Weather radars use one of two major methods to extract this type of information about the distribution of particle sizes and motion included in the pulse volume: (1) pulse-to-pulse correlation methods or (2) Fourier transforms of the complex returned waveform. Both methods can lead to measurements of mean reflectivity and velocity of the raindrops within the volume as well as the variability of velocities within the volume.

FIGURE 13-8 ■
Doppler Scattering
from a Single
Particle.



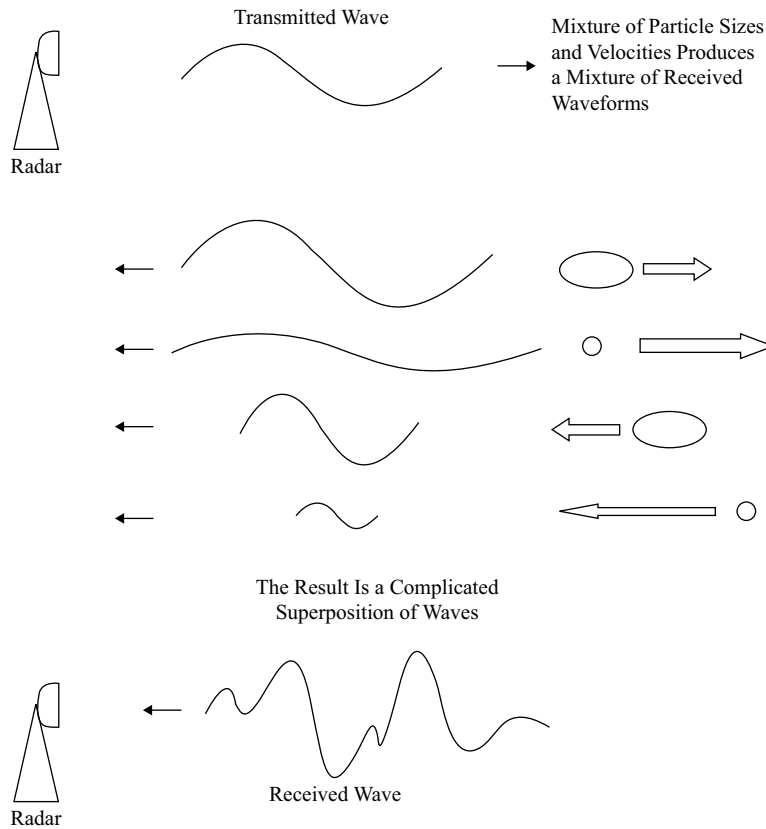


FIGURE 13-9 ■ Doppler Scattering from Multiple Drops.

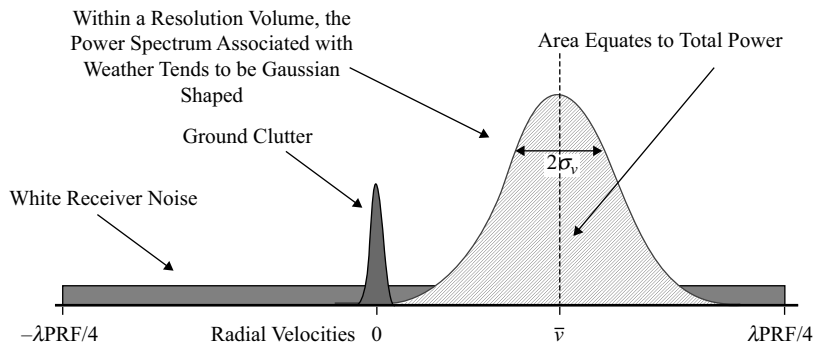


FIGURE 13-10 ■ Shape of the Doppler Spectrum.

The first method, commonly referred to as *pulse-pair processing*, is simpler and faster. This is important when considering the large number of range and azimuth bins over which data are collected and the corresponding short time period allowed for processing a pulse's data, especially when Doppler processing is desired. To accomplish pulse-pair processing, a series of pulses are emitted such that each pulse in the series interrogates the volume of interest. As shown in detail in Section 17.7 of Volume 1 in a full mathematical treatment of pulse-pair processing, three important parameters relating to the precipitation return can be estimated from successive pulses. The zeroth

autocorrelation lag, $\varphi_{yy}[0]$, can be shown to represent the average power of the precipitation return.

$$\hat{P} = \varphi_{yy}[0] = \sigma_n^2 + \sigma_w^2 = \left(1 + \frac{\sigma_n^2}{\sigma_w^2}\right) \sigma_w^2 \quad (13.24)$$

In this equation, σ_n^2 and σ_w^2 represent the noise power and weather component power, respectively. If we assume $\sigma_w^2 \gg \sigma_n^2$, then

$$\hat{P} = \varphi_{yy}[0] \cong \sigma_w^2 \quad (13.25)$$

Similarly, the velocity was shown in Chapter 17 in Volume 1 to be related to the first autocorrelation lag as the Doppler center frequency and is estimated as

$$\tilde{f}_0 = \frac{1}{2\pi T} \arg\{\varphi_{yy}[1]\} \quad (13.26)$$

Doppler velocity can be retrieved from this value by simply multiplying by $\lambda/2$.

Finally, spectrum width, in frequency space, was shown to be related to the ratio of the magnitudes of $\varphi_{yy}[1]$ and $\varphi_{yy}[0]$:

$$\hat{\sigma}_f^2 = \frac{-1}{2\pi^2 T^2} \left\{ \frac{|\varphi_{yy}[1]|}{|\varphi_{yy}[0]|} \right\} \quad (13.27)$$

In the second method, the complete Fourier transform (or the more likely fast Fourier transform, FFT) of the velocity spectrum received from each range bin is computed. This allows a direct measurement of the three spectral moments of interest, but it is much more computationally intensive and requires the collection and analysis of much larger amounts of raw data. The use of today's high-speed electronics and ever-larger memory capacities, however, make this more direct method more feasible.

13.4.5 Spectrum Width

The presence of many precipitation particles within each reflectivity volume leads to a natural spread in the Doppler velocities observed. Each particle contributes to the reflected radar spectrum with a Doppler frequency corresponding to its particular radial velocity with respect to the radar transmitter. This is illustrated in Figure 13-10 as the $2\sigma_v$ width of the velocity spectrum. Several factors contribute to the spread in velocities, including different drop sizes with correspondingly different aerodynamic drag and the inclusion of areas of different relative velocity within the reflectivity volume due to turbulence or rotation within the precipitation.

Large spectrum widths can also often be observed in the “debris balls” produced in extremely vigorous tornadoes. These severe storms can loft a multitude of objects, often including large human-made debris, which is then vigorously circulated by the tornado winds. The wide variety of sizes and shapes of debris contribute to an extremely large spread in observed Doppler velocities and corresponding large spectrum width.

13.4.6 Range Folding and Velocity Aliasing

The Doppler dilemma introduced in Section 13.4.3 can lead to several artifacts in Doppler weather-radar processing that need to be accounted for. The maximum unambiguous range leads to a phenomenon known as range folding while the maximum unambiguous Doppler velocity leads to a complementary phenomenon known as velocity aliasing.

Range-folded or range-aliased images can appear on the Doppler weather-radar output if the significant energy is reflected from distant tall storms. If the radar's PRI is short enough, then the radar receiver may process these reflections as if they were the result of a more recent transmitted pulse and therefore indicative of a closer storm. These reflections are called *multitrip echoes*. If the storms are strong enough reflectors, several reflections may be seen for these storms, appearing at ranges indicated by

$$r_{\text{apparent}} = r_{\text{actual}} - n r_{\text{max}} \quad (13.28)$$

Several characteristics common to range-aliased echoes can be used as clues to their existence. First, range-aliased echoes often occur as narrow wedge-shaped echoes pointed toward the radar location. As the storms should not have a shape preference based on the location of the radar, this orientation is a good clue that the echoes are false. Second, the aliased echoes are often of abnormally low height. The aliased reflections are likely from much higher in the real storm but are presented as a lower height due to their *apparent* closer range. Finally, the storm returns are often much weaker than would be expected based on other storm cells at the same apparent range. These echoes have traveled much farther ($n r_{\text{max}}$) and therefore are much weaker.

A simple method can be used to determine if an echo is the result of range aliasing. If the PRF of the transmitter is changed, the range of accurately detected storm cells will not change while the range of aliased cells will be modified as the maximum unambiguous range, r_{max} , changes in (13.25).

A similar phenomenon occurs due to the maximum unambiguous velocity available from a Doppler radar at a given PRI and wavelength. If measurements are made of scatterers that are moving with radial velocities above the maximum velocity, v_{max} , they will instead appear to be moving at an oppositely sensed but still nearly maximum velocity. These areas can often be seen as rapid changes in velocity along the radial to the radar transmitter in an area at the maximum detectable Doppler velocity. Modern Doppler radar systems often include sophisticated procedures to detect velocity ambiguities and apply Nyquist unfolding algorithms to present a corrected velocity to the end user. There are times where these algorithms break down. In these cases, the typical system will depict the velocities as purple, a color not usually on the velocity scale. These areas of ambiguous velocities are often referred to as *purple haze*.

13.5 | HYDROLOGICAL MEASUREMENTS

The major use of weather radar is to determine and characterize areas of precipitation and the storms that produce this precipitation. It is therefore useful to develop basic concepts and relationships relating to rain parameters that affect these measurements. In the following sections, the basic form of raindrop size and velocity distributions will be developed. When combined with scattering and absorption characteristics of rain, these

allow the development of fairly simple but very useful relationships that can relate rain rate to the radar reflectivity factor, Z .

Subsequent sections will look at variations of the scattering properties of liquid and frozen precipitation. These varying properties allow weather radar to distinguish several very important structures in typical thunderstorms as well as estimate precipitation types with some measure of success.

13.5.1 Rain Measurements

13.5.1.1 Drop Size Distributions

Recalling (13.11) the derivation of the radar equation for meteorological applications,

$$\bar{P}_r = (1/\ln 2) \frac{P_t G^2 \theta^2 c \tau \pi^3 |K|^2 Z}{1,024 \lambda^2 r^2}$$

we see that the received power is dependent on only three environmental factors: (1) the index of refraction $|K|^2$; (2) the range to the resolution cell, r ; and (3) the reflectivity factor, Z . The reflectivity factor was shown to be related to the sum of the drop sizes within the volume (13.9):

$$Z = \frac{1}{V} \sum_{vol} D^6$$

A simplified form for Z is obtained by assuming a summation over only a unit volume:

$$Z = \sum_{vol} D^6 \quad (13.29)$$

Theoretically, if we neglect attenuation, assume a beam filled with either all water or all ice, and know the complete distribution of drop sizes, D , within the volume, then we can calculate the received power, \bar{P}_r . The values encountered for Z can vary greatly from $0.001 \text{ mm}^6/\text{m}^3$ in fog to more than $30,000,000 \text{ mm}^6/\text{m}^3$ in storms containing very large hail. It is therefore often more convenient to refer to the logarithmic radar reflectivity factor, dBZ:

$$\text{dBZ} = 10 \log_{10} \left(\frac{Z}{1 \text{ mm}^6/\text{m}^3} \right) \quad (13.30)$$

This formulation produces ranges of dBZ from about -30 dBZ for fog to more than 75 dBZ for large hail.

Several different methods have been used to measure drop-size distributions. These range from simple methods to complex instruments. The simplest methods include allowing raindrops to fall on dyed filter paper and measuring the size of the spots formed and capturing the drops in an open-topped container of flour and measuring the sizes of the flour balls that form. More complex measurements may be made using more modern instrumentation often called *distrometers*. Some of these operate by measuring the acoustic signals produced when drops hit a membrane or solid sensing element and correlating those signals to calibrated values of drop sizes. The most common type of distrometers currently used measure the radii of drops using

collimated laser light. Both types of modern instruments are capable of continuous measurement of drop-size distributions. The distrometers typically measure the number of droplets contained within intervals of diameters, which leads to an alternate discrete form of the reflectivity factor:

$$Z = \sum_i N_i D_i^6 \quad (13.31)$$

where N_i is a count of the number of drops detected within diameter interval D_i , which spans the diameters $D_i - \frac{1}{2}\delta d$ to $D_i + \frac{1}{2}\delta d$.

Various studies have been made of the distribution of raindrop sizes and attempts have been made to relate those distributions to rainfall rates for various types of storms. A seminal paper in this series is the 1948 work of Marshall and Palmer [15]. The distribution presented in this work is often simply referred to as the *Marshall–Palmer distribution* and is characterized by a negative exponential distribution of the form

$$N_D = N_0 e^{-\Lambda D} \quad (13.32)$$

for the number of drops, N_D , of diameter D contained within a unit volume. In (13.32), the value of N_0 is $8,000 \text{ m}^{-3} \text{ mm}^{-1}$, D is the drop diameter in mm, and Λ defines the distribution as a function of rain rate R , in mm per hour, as follows:

$$\Lambda = 4.1R^{-0.21} \quad (13.33)$$

Figure 13-11 shows the Marshall–Palmer distribution at several rain rates (solid lines) compared with alternate distributions defined by Laws and Parsons (dashed lines) and observations made with dyed filter paper (dotted lines). It can be seen that generally good agreement is found between the three distributions except for smaller drop sizes.

13.5.1.2 $Z = aR^b$ Relationships

Radar has been used extensively to observe rainfall events in many localities and for many types of rain. Given the relationship between drop size distribution, rainfall rate, and radar reflectivity, many investigations have sought to discover relationships between the radar reflectivity, Z , and the rainfall rate, R . Indeed, if we assume a given raindrop size distribution and apply terminal velocity relationships such as those determined by Gunn and Kinzer [16], we should, in theory, be able to calculate relationships between rainfall rate and Z .

In general, empirical relationships between Z and R have been measured for a wide variety of rainfall types. It has been found that the relationships can usually be characterized relatively well by various variants of the form

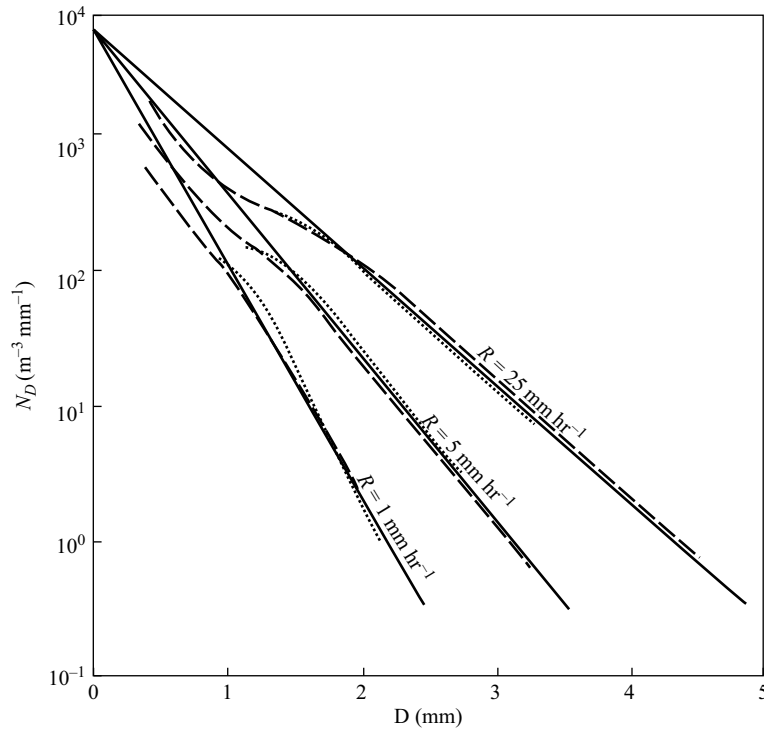
$$Z = aR^b \quad (13.34)$$

Four relationships are listed by Battan for “typical” types of rainfall:

$$\text{Stratiform rain } Z = 200R^{1.60} \quad (13.35)$$

$$\text{Orographic rain } Z = 31R^{1.71} \quad (13.36)$$

FIGURE 13-11 ■ Marshall–Palmer Raindrop Size Distribution (Solid Lines) Compared to Laws and Parson Results (Dashed Lines) and Observations (Dotted Lines).



$$\text{Thunderstorm rain } Z = 486R^{1.37} \quad (13.37)$$

$$\text{Snow } Z = 2000R^{2.00} \quad (13.38)$$

Many other relationships have been measured, including more complex forms.

Rainfall estimates can obviously be obtained from these relationships by solving for R instead of Z . The rainfall estimates for the basic stratiform relationship and the estimate commonly used operationally by the WSR-88D are

$$\text{Stratiform } (Z = 200R^{1.60}) \quad R_{strat} = 0.0365 Z^{0.625} \quad (13.39)$$

$$\text{WSR-88D } (Z = 300R^{1.40}) \quad R_{WSR-88D} = 0.0170Z^{0.714} \quad (13.40)$$

13.5.2 Hail Measurements

Hail often forms in vigorous thunderstorms and can be used as an indicator of severe weather. The dynamic forces required to produce the hailstones and then support them before they precipitate are present only in very vigorous thunderstorms. The presence of hail in a reflectivity resolution cell will usually be manifested as a very large return, often more than 55 dBZ. This is due to several factors, the major one being the large size of the hailstones. As reflectivity increases as D^6 , a large hailstone can provide quite a large contribution to the overall resolution cell return. The reflectivity of hailstones can be greatly affected by the presence of liquid water within the hailstone, a phenomenon known as *spongy hail* [17]. Another factor influencing the large reflectivities characteristic of hail can be the presence of a film of water coating the surface of melting hailstones. These hailstones then appear to be extremely large raindrops. As hailstones

can often approach or exceed the wavelength of the interrogating radar, effects can become nonlinear as the reflectivity enters the Mie scattering regime. Hailstones are also often irregular in shape and may tumble while falling, leading to both large returns and no preferential polarization characteristics.

13.5.3 Snow Measurements

Snow is often detected by weather radar during the winter months but tends to be less intense than rain and can be missed at times. Snow and snowstorms are less easily detected on weather radar than storms containing liquid water for several reasons. Because it is a frozen form, snow has a lower reflectivity than liquid precipitation of equivalent water content due to the large difference between $|K|^2$ for water (≈ 0.93) and ice (≈ 0.197). This leads to a reduction in return of about 7 dB. A secondary effect occurs due to the lower total equivalent liquid water content in snowstorms. Winter storms simply contain less water due to the lower temperature of the environment. Finally, snowstorms often do not develop to as great a height as equivalent storms during warmer months. All of the return from the snowstorm may then be hidden below the lowest scan angle of the interrogating radar [18].

13.5.4 Attenuation from Precipitation

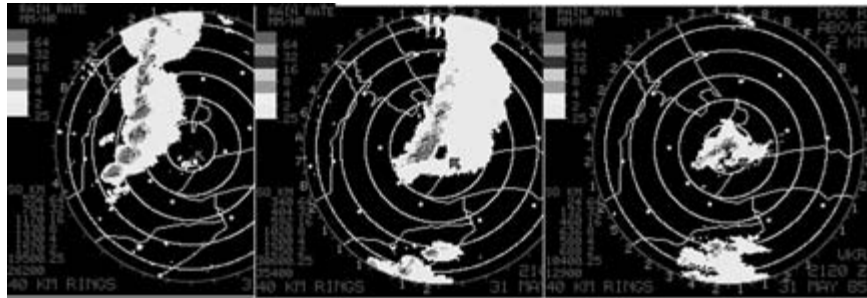
Attenuation along the path between the radar and the weather under interrogation has been ignored so far in this chapter. Attenuation is caused by the effects of both absorption and scattering of the radar pulse as it traverses the path to the primary scatter and back to the radar. Attenuation of weather-radar signals in the atmosphere can be divided into three general regimes: (1) water vapor effects, (2) the effects of cloud droplets and fog, and (3) the effects of liquid and frozen precipitation. Generally, the attenuating effects of water vapor in the air at the operating frequencies of weather radars is on the order of hundredths of a dB per km and is therefore usually ignored. Similarly, the attenuation due to cloud droplets and fog is generally considered to be due to the total liquid water content of the clouds and is very low. Gunn and East [19] showed that the attenuation in water clouds at X-band was quite small, ranging from 0.0483 dB/km per g/m^3 of liquid water at 20 °C to 0.112 dB/km per g/m^3 at -8 °C. Attenuation in ice clouds was much smaller, ranging from 2.46×10^{-3} at 0 °C to 5.63×10^{-3} at -20 °C. Attenuation at the longer and more commonly used C and S wavelengths would be correspondingly smaller.

Of more importance for weather radar is the attenuation caused by rain, sleet, hail, and snow. Weather radars are designed to operate at wavelengths that are significantly longer than the principal dimensions of the precipitation they are meant to detect. NEXRAD WSR-88D radar operates at S-band at a frequency of 3 GHz. This leads to a wavelength of about 10 cm, quite large compared to even the largest raindrops, which measure only about 9 mm in diameter. Above that size, the drops tend to break into smaller drops.

Hailstone sizes can often approach the weather-radar wavelengths, with stones of diameters on the order of an inch or two recorded in severe thunderstorms with some regularity. These hailstone sizes are about half the wavelength of the WSR-88D (about 4 inches). The largest of hailstones can exceed this size but are fairly rare. The largest recorded hailstone was discovered in Vivian, South Dakota, on July 23, 2010. It measured 8 inches (20.3 cm) in diameter and probably had melted some before measurement [20].

TABLE 13-2 ■ One Way Rain Attenuation in $\text{dB km}^{-1}/\text{mm hr}^{-1}$ as a Function of Rainfall Rate, R , for Various Drop Distributions

Wavelength (cm)	Marshall–Palmer (0°C)	Modified Marshall–Palmer (0°C)	Mueller–Jones (0°C)	Gunn and East (18°C)
1.24	$0.117R^{0.07}$	$0.13R^{0.07}$	0.18	$0.12R^{0.06}$
3.21	$0.011R^{0.15}$	$0.013R^{0.15}$	0.018	$0.0074R^{0.31}$
5.5	0.003 to 0.004	0.0031	0.0033	
5.7				$0.0022R^{0.17}$
10	0.0009 to 0.0007	0.00082	0.00092	0.0003

FIGURE 13-12 ■ Strong Attenuation of the Signal when Heavy Rain Is Passing on a 5-cm Wavelength Radar (Which Is Located at the Point of the Arrow). [Source: Environment Canada]**TABLE 13-3** ■ Calculated Attenuation due to Snow in $\text{dB km}^{-1}/\text{mm hr}^{-1}$ at Various Equivalent Rain Rates

Wavelength (cm)	$R = 1 \text{ mm/hr}$	$R = 10 \text{ mm/hr}$	$R = 100 \text{ mm/hr}$
1.8	0.0046	0.344	33.5
3.2	0.0010	0.040	3.42
10	0.00022	0.0026	0.057

Because the attenuation of the radar beam is due to both absorption and scattering, the Rayleigh approximation is generally only valid for drop sizes below about 1 mm for an illuminating wavelength of 10 cm. For larger droplets or shorter wavelengths, Mie scattering becomes important. For this reason, it has been common to determine the path attenuation using presumed raindrop size distributions. These raindrop size distributions and particle-dependent fall speeds can be combined to give various rainfall rates. Calculations of the one-way attenuation due to different rain rates expressed in terms of $\text{dB km}^{-1}/\text{mm hr}^{-1}$ were computed by Wexler and Atlas [21] for various common raindrop size distributions. Table 13-2 shows these values as extracted from [21].

As Table 13-2 shows, at the longer wavelengths used by NEXRAD – 10 cm – attenuation due to rain is very small. At shorter wavelengths, which are characteristic of commercial weather radar and airborne units, attenuation due to rain can become significant and must be considered when interpreting data. An example of this is shown in Figure 13-12.

Battan [14] calculated attenuation due to snow at various characteristic wavelengths. The one-way attenuations, in dB km^{-1} , for various equivalent rainfall rates, are shown in Table 13-3. These results indicate that attenuation due to snow is an order of magnitude less than that due to rain. Again, attenuation at 10 cm seems

negligible. Only at high equivalent rain rates and shorter wavelengths are the calculated attenuations very large.

Attenuation due to hail can be very complex and depends on the interior structure of the hailstone. Battan [14] reviews much of the fundamental research in this area. As mentioned by Rinehart [18], hail is usually not common or widespread in the beam path of the radar, so the effects are less overwhelming than the often accompanying heavy rain. The results shown in Battan do show that attenuation by wet hail, especially hail covered with a layer of liquid water, can be appreciable.

13.6 | CHARACTERISTICS OF SOME METEOROLOGICAL PHENOMENA

The operational use of weather-radar depends on their ability to detect different forms and rates of precipitation. The intensity, geometry, and spatial characteristics of that precipitation can be very important in the analysis of weather systems by forecasters and researchers. This section will examine some interesting characteristics of several different types of weather systems that are often examined by weather-radar systems.

13.6.1 Extratropical Storms and Stratiform Precipitation

13.6.1.1 Precipitation Estimation

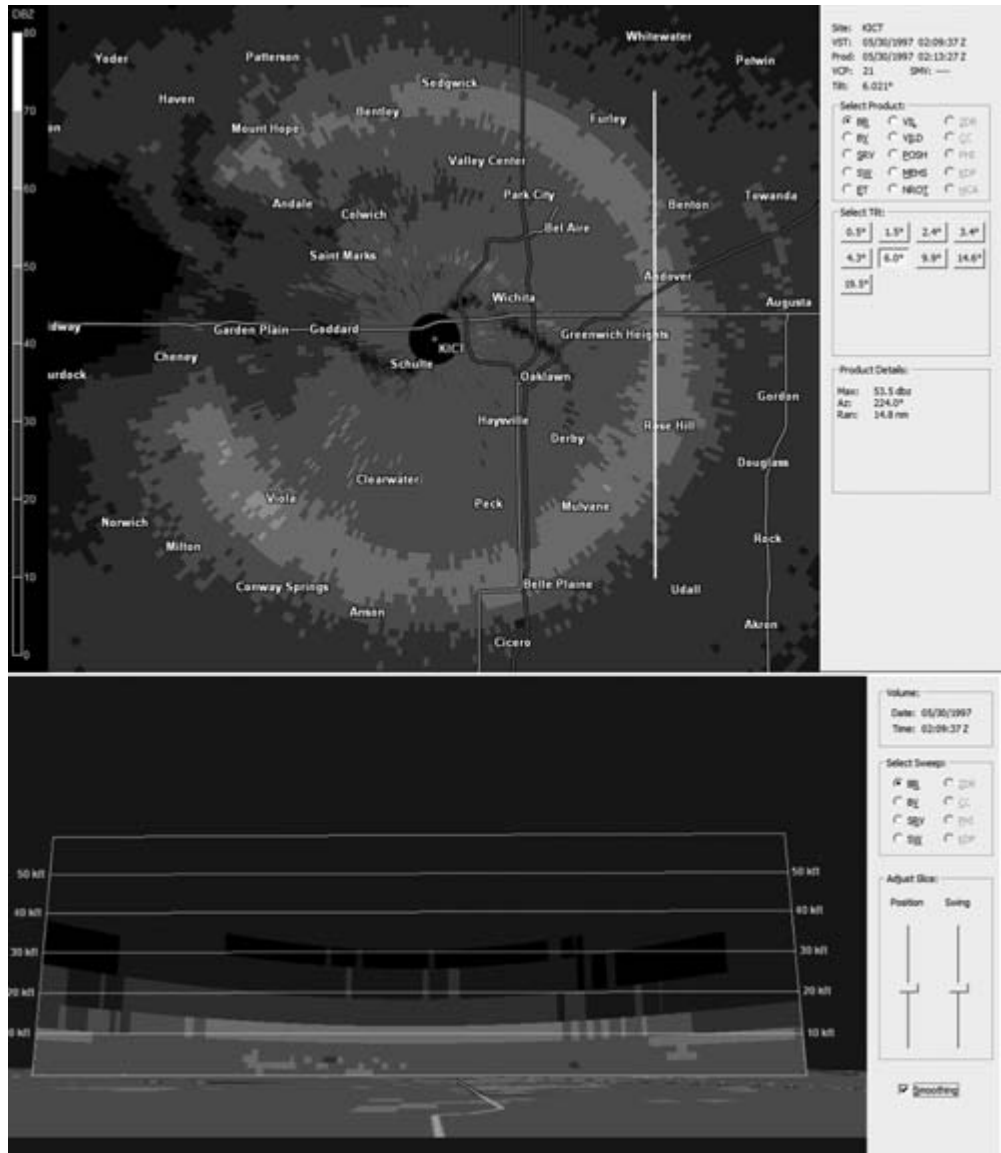
Much of the precipitation that affects us occurs as a result of frontal passages and is in the form of large rain areas associated with the passage of these fronts and their associated low-pressure areas. Radar is used to great effect to determine the edges of these large rain areas and therefore to predict their starting and ending times. Using the radar reflectivity relationships to rain rate, supplemented by on-the-ground real-time adjustment by rain-gauge networks, very good estimates of rainfall rates and totals can be made over large areas. These estimates can be used operationally to provide stream flow estimates and flood warnings to the general public.

13.6.1.2 Bright Band

When looking at the vertical structure of a precipitating storm, a layer of enhanced reflectivity called the *bright band* can often be seen at a level that corresponds to the melting level, 0 °C. This is a result of snowflakes falling through this transition region and melting to form raindrops; the phenomenon is well illustrated in Figure 13-13. The upper portion of the figure shows a plan position indicator (PPI) NEXRAD image at 6 degree elevation near Wichita, KS in May of 1997. A ring-shaped area of increased reflectivity can be seen surrounding the radar. The lower plot in the figure shows a range height indicator (RHI) plot of the same data along the white vertical line to the east of Wichita in the upper plot. At a height of about 10,000 feet in the RHI plot is an area of increased reflectivity, indicative of the melting of frozen precipitation and the formation of a bright band.

The area of enhanced reflectivity results from two effects that occur during this transition from frozen to liquid precipitation. The first effect is a consequence of the higher values of $|K|^2$ for water (≈ 0.93) compared to $|K|^2$ for ice (≈ 0.197). Above the bright band, the precipitation is all ice and snow, characterized by the lower value of $|K|^2$. As the flakes fall into the warmer air, they start to melt. The melting first causes

FIGURE 13-13 ■ Illustration of the Bright Band. Upper: PPI Image at 6 degree elevation. Lower: RHI cut along line indicated in PPI image



them to be covered in a thin film of water and appear to the radar as very large raindrops, also characterized by the higher values of $|K|^2$ typical of water. Both of these factors lead to correspondingly large reflectivities.

As the drops fall through the melting region and become completely liquid, their size then decreases, which leads to a corresponding reduction in reflectivity. A secondary effect due to changes in fall speed enhances this diminishing of reflectivity at the base of the bright band. Above the melting layer, the precipitation is composed of snowflakes, which have a low fall speed. As the flakes melt into water droplets, their surface area and corresponding aerodynamic drag decreases and their fall speed increases. As the drops accelerate near the bottom of the melting layer, the number concentration necessarily also decreases. This decrease in drop density enhances the reduction of reflectivity at the base of the bright band.

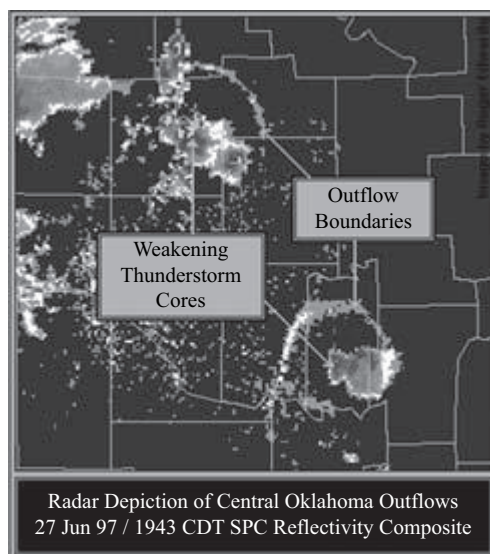


FIGURE 13-14 ■
Outflow Regions.
[Source: National
Severe Storms
Laboratory, or
NSSL]

13.6.2 Thunderstorms and Supercells

The detection and tracking of thunderstorms is a major use of weather radar. The NEXRAD system has been optimized to detect the presence of these storms and to measure their vital parameters. By carefully observing the genesis and development of storm cells, much can be inferred about their relative strength and potential for damage. Among the features that can indicate strong storm development are the development of a characteristic almond or triangular shape in the cell, the presence of inflow notches, and the splitting of the storm cell. Often the southern split cell will move to the right of the mean storm motion and develop into a more severe storm. The *Lemon technique* [22] can provide radar operators with methods to determine a storms' severity and to infer updraft strength and damage potential.

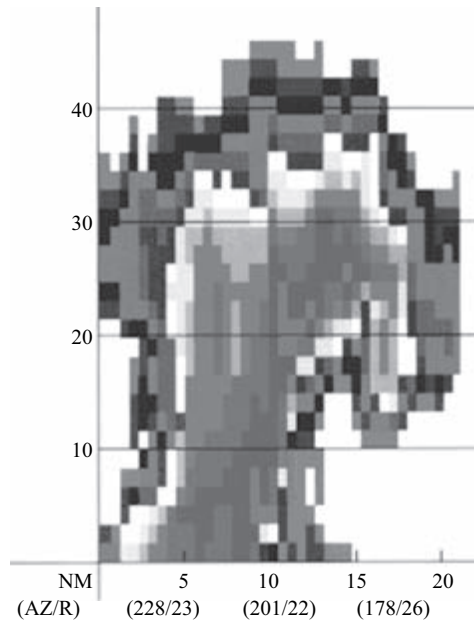
13.6.2.1 Gust Fronts and Outflow Regions

The rapid evolution of thunderstorms often produces gust fronts and outflow regions that can contain significant wind fields. Often these regions can be seen as concentric arcs radiating from the central storm location, as shown in Figure 13-14. As the gust fronts and outflow may often be rain free, the enhanced reflectivity is due to either suspended dust and insects or a sharp gradient in refractivity or both. The detection of these artifacts may be subtle due to their low reflectivity and coexistence with much larger returns from the parent storms, but their discovery can be very important in forecasting severe wind events.

13.6.2.2 Bounded Weak Echo Region

Another artifact related to the state of the precipitation is referred to as the *bounded weak echo region* (BWER). An example of a BWER is illustrated by the RHI image shown in Figure 13-15. BWERs can often be observed in the core of strong thunderstorms. They are formed when the intense updraft of the thunderstorm is sufficiently strong to support hail and large raindrops. The development of a BWER is indicative of a vigorous evolution of the storm and its circulation system. The collapse of the BWER often signals the final stages of a storm's evolution, but it can be accompanied by large wind gusts and copious rain and hail as the suspended precipitation is released.

FIGURE 13-15 ■
RHI of a Bounded
Weak Echo Region
in a Supercell
Thunderstorm.
[Source: National
Weather Service]



13.6.3 Tornadoes

Tornadic supercell thunderstorms and tornadoes embedded in mesoscale convective systems can cause widespread destruction, injury, and loss of life. One of the goals in the development of the current NEXRAD radar system across the continental United States has been to provide an early warning system to the population for these dangerous storms. Much has been learned about the characteristics of tornadic storms in the radar era. This section will only touch on a few major characteristics observable for these storms. An illustration of the major features of a tornadic supercell thunderstorm is presented in Figure 13-16 for reference.

13.6.3.1 Hook Echoes

As mentioned in Section 13.1.1 and illustrated in Figure 13-1, tornadoes and their characteristic hook echoes have been observed on radar since at least 1953. A dramatic illustration of a hook echo, captured by the NEXRAD radar in Oklahoma City, OK on May 20, 2013, is shown in Figure 13-17. This figure has been annotated to show many of the major tornadic characteristics that may be seen in a mature tornadic supercell. As noted in the illustration, the hook echo is a manifestation of the larger mesocyclone that supports the formation of the intense tornadic circulation. In the model presented by Lemon and Doswell [23], the hook echo is associated with rear-flank downdraft wrapping around the mesocyclone contained in the supercell. Note that hook echoes and appendages are not always associated with tornadoes and may appear after the formation of the tornadoes [24][25].

13.6.3.2 Velocity Couplets

Doppler weather radar's great advantage in detecting tornadic storms is its ability to discern the velocity of air parcels within the storm. The general public in regions where tornadic storms are common is now somewhat familiar with seeing the Doppler representation of the weather-radar data. When adjacent pixels, or small areas of pixels,

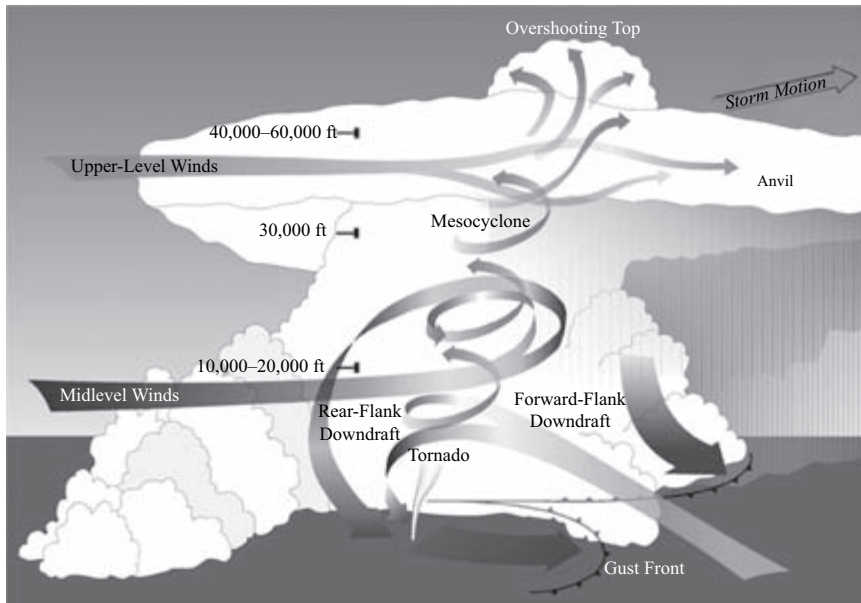


FIGURE 13-16 ■ Major Components of a Tornadic Supercell Thunderstorm. [Source: NSSL]

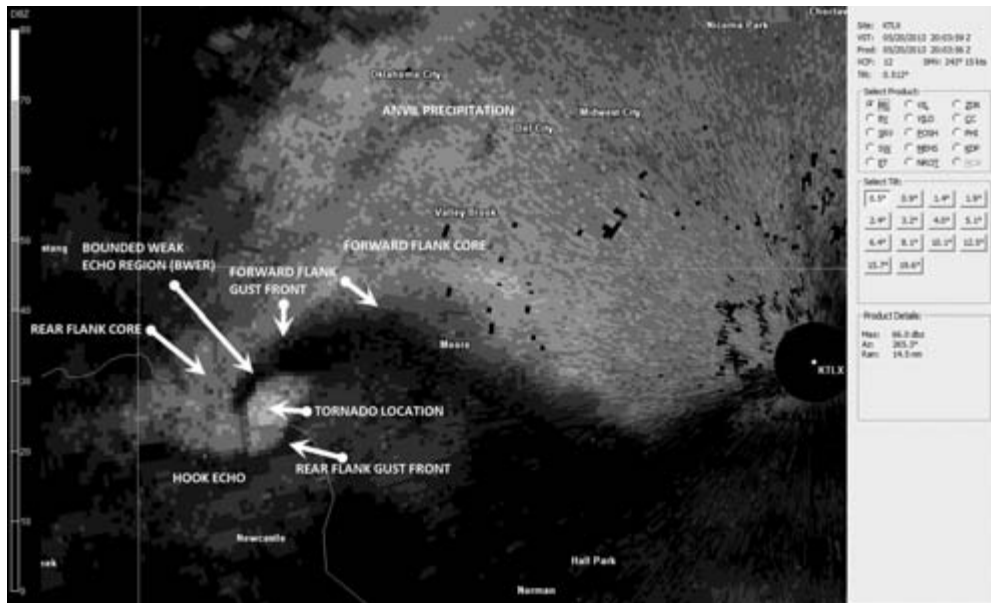


FIGURE 13-17 ■ A Radar Image of a Classic Supercell Containing a Violent Tornado Near Oklahoma City, Oklahoma, on May 20, 2013.

show significant differences in radial velocity, it can be taken as a sign of rotation in the storm. These adjacent areas are commonly referred to as *velocity couplets*.

Velocity couplets rarely image the actual tornado circulation itself. The tornado is a small, low-level phenomenon. If the storm is at any significant distance from the radar site, the lowest radar scan may be completely above the tornadic circulation. The tornadic circulation is also rarely large enough in width to be resolved by the radar at range. The NEXRAD beamwidth of 0.95 degrees means that, at a range of only 25 miles, the size of a resolution cell is nearly a half a mile. This does not mean that Doppler weather

FIGURE 13-18 ■
Mesocyclone
Associated with a
Tornado and Hook
Echo. [Source:
NSSL]

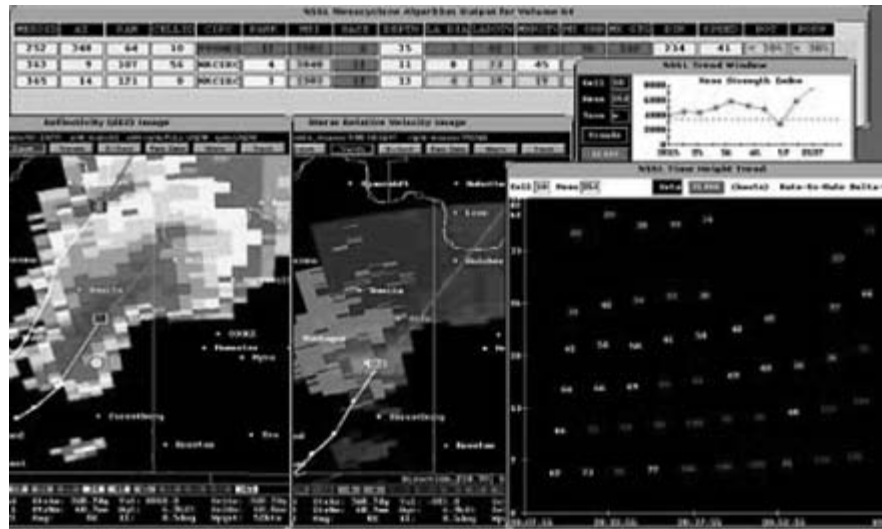
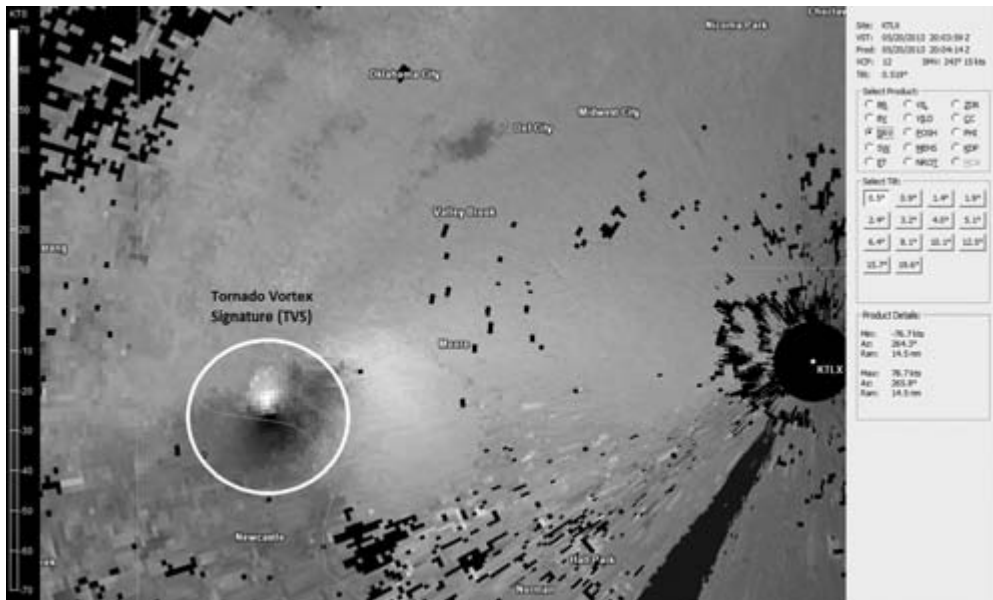


FIGURE 13-19 ■
Tornado Vortex
Signature (TVS).
[Source: NSSL]



radar is not useful in detecting tornadoes. Instead, the radar often detects, at relative high levels in the storm, the larger mesocyclone that supports tornado formation. If the tornadic storm is close enough, the lowest elevation scans of the radar may be able to detect a lower-level tornado vortex signature (TVS), which often precedes the tornado touchdown. An example of the large-scale mesocyclone detection and the detection of a low level, extremely intense TVS are shown in Figures 13-18 and 13-19, respectively.

13.6.3.3 Debris Balls

When large, violent tornadoes encounter urbanized areas, they are capable of pulverizing houses and lofting large human-made objects and debris into the tornado inflow.

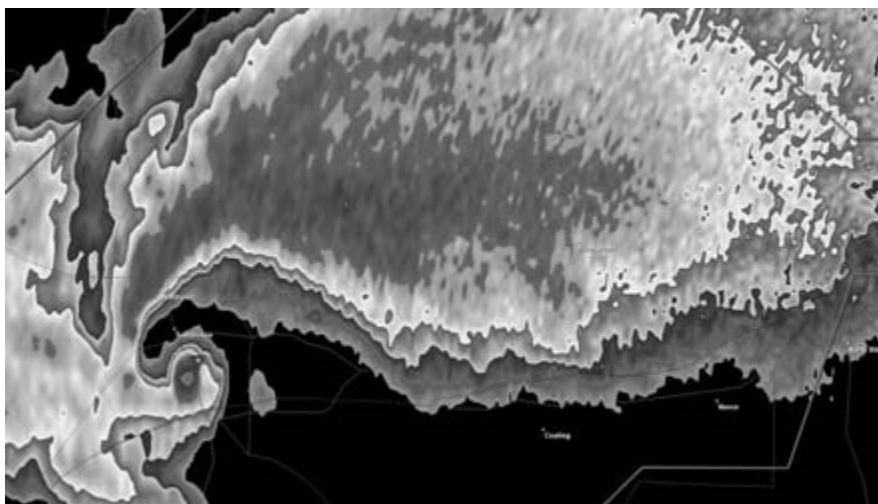


FIGURE 13-20 ■ Probable Debris Ball Formation Formation as Tornado Passes through Tuscaloosa, Alabama.

If the tornado is sufficiently close to the radar, this highly reflective area can sometimes be detected as a *debris ball*. Figure 13-20 shows a suspected debris ball which formed at the end of a very pronounced hook echo as a strong tornado passed through Tuscaloosa, Alabama on April 27, 2011. The existence of a debris ball can be inferred to a greater degree if dual-polarization capabilities are available to the forecaster. An area of debris should be indicated by high reflectivity collocated with a radial velocity couplet. As will be shown in Section 13.8.3 these features should be collocated with an area of low correlation coefficient and differential reflectivity, due to the large diversity of scatter shapes, sizes and orientations in the debris ball. (Heavy rainfall areas would be expected to have high reflectivity with a corresponding high value of differential reflectivity, due to the oblateness of the larger drops.)

13.6.4 Bow Echoes, Squall Lines, and Derechos

Not all severe storms develop as isolated pop-up or supercell thunderstorms. Lines of storms may form along the frontal boundaries associated with low-pressure areas and may travel long distances before dissipating. Radar is an important tool to determine areas within these squall lines that may contain areas of intense rainfall, large hail, strong winds, or tornadic storms. Very strong straight line winds are often associated with bow echoes. Doppler radar can be used to great advantage in imaging these areas of great velocity discontinuity.

Figure 13-21 depicts the evolution of a single thunderstorm cell into a potentially dangerous bow echo. The areas of cyclonic rotation (C) and anticyclonic rotation (A) are prime areas for tornado development. Derechos are distinguished from thunderstorms by the presence of sustained winds greater than 58 miles per hour combined with a rapid forward progress and a large geographical extent. Derechos have been observed to travel hundreds of miles and persist for many hours.

13.6.5 Hurricanes

In the Northern Hemisphere, hurricanes form during late summer over the warm waters of tropical oceans and can intensify to become major hazards to both shipping and

FIGURE 13-21 ■ Evolution of a Bow Echo. [Source: National Weather Service]

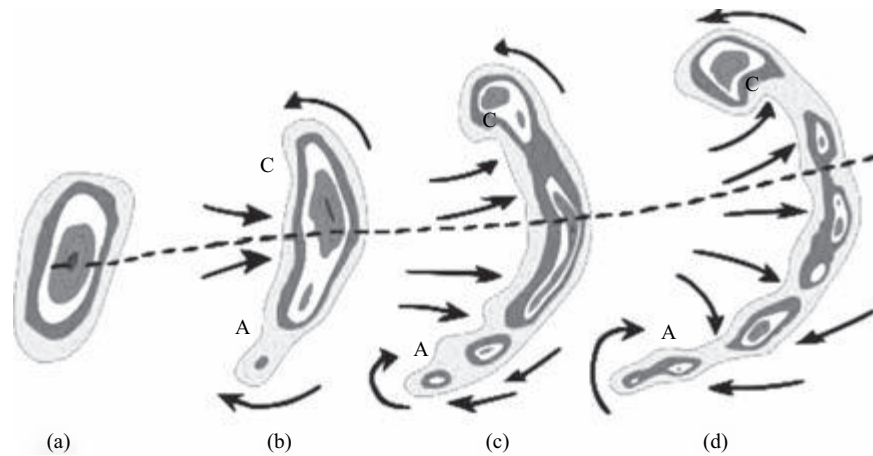
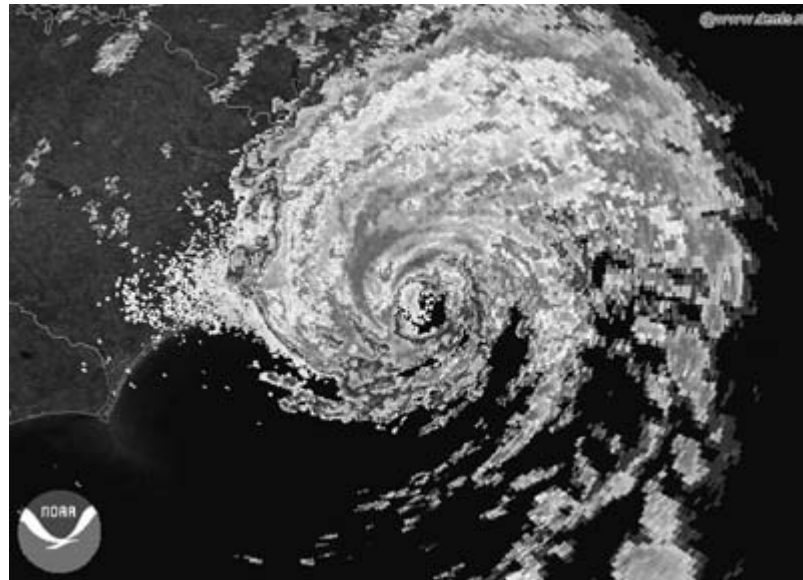


FIGURE 13-22 ■ Radar Mosaic of Hurricane Alex as it Nears the North Carolina Coast on August 3, 2004. [Source: NOAA]



coastal populations. Hurricanes are tracked by satellite and perhaps airborne or space radar when out to sea. When these storms get close to coastal areas or track inland, they have a potential to produce damaging winds and torrential rainfall. If the storms are within the range of NEXRAD systems, much warning information can be gathered. Figure 13-22 shows Hurricane Alex as it approached the North Carolina coast in August 2004. The large rain bands that encircle the hurricane eye are easily resolved. Tracking these rain bands and estimating storm rainfall totals can allow forecasters and emergency managers to determine which areas may be hardest hit by flooding during the event.

A secondary concern in hurricanes making landfall is the potential for embedded tornadoes, which are often small, low-topped, and rain wrapped, making them very difficult to see until they are very close. If the rain bands that contain the embedded tornadoes are close enough to NEXRAD facilities, they can be detected.



FIGURE 13-23 ■
Echoes Caused by
Sunset Energy.
[Source: NOAA/
SPC]

13.7 | SUN ECHOES AND ROOST RINGS

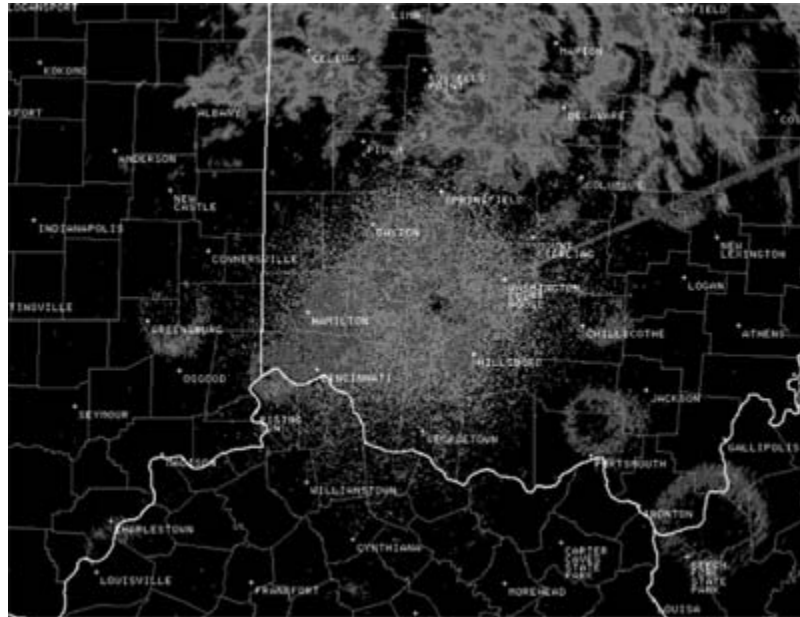
An interesting anomaly can be seen sometimes either in the morning when the sun rises or in the evening when it sets. As the sun reaches the angle that the NEXRAD radar is interrogating, it can introduce a large amount of radio-frequency energy into the receiver. These false returns show up at all expected ranges and appear as a spoke at the azimuthal angle that corresponds to the solar angle. These *sun echoes* are very prominent in Figure 13-23, showing up at six separate radar sites across the Midwest. Only those sites where the sun is low enough to be captured by the receiving antennas are affected, so the sites showing the effect are somewhat collocated along a north–south line.

Sometimes great numbers of concentric rings can be seen propagating radially from several separated locations within the radar field of view. These concentric rings grow both radially and in altitude until they fade out. Often the rings occur in the early morning hours. It has been determined that these rings can be caused as large flocks of birds, such as purple martins as they leave communal roosts at the same time to begin foraging for the day. Figure 13-24 shows a good example of these *roost rings* along with an echo caused by the dawning sun.

13.8 | ADVANCED PROCESSING AND SYSTEMS

The NEXRAD radar systems were developed in the late 1980s and have been in place for 25 to 30 years. While they have allowed for great advances in the detection and tracking of weather systems, several advanced techniques and technologies are now being used to great advantage in the weather-radar field. These include several varieties

FIGURE 13-24 ■
Roost Rings and
Solar Flare from
Sunrise.



of small, mobile, short-range radar systems; the use of several coordinating radar systems; and developments adapted from defense applications for weather.

13.8.1 Mobile Radar Systems

The current NEXRAD system consists of 169 large, fixed S-band radars located across the United States. While the coverage provided by these systems is rather good, there are gaps, especially at low altitudes. Storms are often located at large distances from the radar site, leading to fairly poor resolution in both range and cross-range. Mobile, truck-based weather-radar systems have been developed by a number of universities and the Center for Severe Weather Research (CSWR). The CSWR currently operates three X-band Doppler on wheels (DOW) systems. Two of these system are dual-polarization, dual-frequency radars using conventional antennas and rapidly scanning pedestals. An example of these vehicles is shown in Figure 13-25. These systems provide much greater resolution than is available from the NEXRAD system – on the order of $65 \times 65 \times 75$ meters – but at the expense of operating range.

The ability to rapidly scan large volumes is very important in order to characterize the quickly changing environment in severe storms. One solution to this problem is to use phased array technology to provide electronic steering for at least some of the necessary coverage. The DOW-5 at CWSR, shown in Figure 13-26, employs a phased array antenna to both provide a good beam shape as well as provide multiple steerable beams in elevation while mechanically scanning in azimuth.

13.8.2 Dual Doppler

A single Doppler radar site is only able to determine that component of velocity of precipitation that is directly along to the beam of the radar. Any component of motion perpendicular to the beam is undetected. This limitation can be overcome by using



FIGURE 13-25 ■
CSWR DOW with
Conventional
Antenna.
[Source: CSWR]



FIGURE 13-26 ■
Rapid Scan DOW.
[Source: CWSR]

multiple Doppler radars, separated by a distance and oriented to provide overlapping areas of coverage. By combining the radial velocities detected from two or more radars, a full two-dimensional wind field can be derived. Mobile radars such as the DOW mentioned in the previous section have been positioned to provide such overlapping coverage and have greatly increased the knowledge of low-level wind fields in severe storms.

13.8.3 Dual Polarization

The NEXRAD network of weather radars was upgraded to dual polarization capability between 2011 and 2013. Instead of simply transmitting and receiving horizontally

polarized beams, the systems were upgraded to transmit and receive both vertically and horizontally polarized beams. These upgrades took several weeks for each installation and were therefore staggered and planned for “climatologically inactive periods.” The advantages gained from upgrading the systems to dual polarization are now being exploited by NWS meteorologists.

The addition of dual-polarization capabilities greatly enhance the ability of the radar systems to differentiate between different precipitation types as well as enhance the ability to determine rainfall rates. Three derived parameters of interest in dual-polarization radars will be discussed in this section. These parameters, which will be described shortly, include the correlation coefficient, ρ_{HV} , differential reflectivity, Z_{DR} , and specific differential phase shift, K_{DP} .

13.8.3.1 Correlation Coefficient

The correlation coefficient, represented as ρ_{HV} , is a measure of the similarity of successive returns from an illuminated volume. It is most easily described on the basis of the vector, or phasor, representation of the radar returns. Highly correlated returns are illustrated in Figure 13-27. The top part of the illustration shows the phasors received for the first horizontal and vertically polarized pulses. The second and third rows represent the phasors from subsequent pulses, both of which show high correlation. In the case of the correlation between the first and second pulses, both the H and V returns on the second pulse are similar in both amplitude and phase angle difference to the original pulse and therefore have a high correlation coefficient. The correlation between the second and third pulses is also very high. In this case, while the amplitudes are different between the two pulses, the ratios between the H and V phasors are similar and the phase angles remain the same, once again leading to a high correlation. In both

FIGURE 13-27 ■
Examples of Highly
Correlated Phasors.

Pulse Number	Horizontal	Vertical
1		
2		
3		

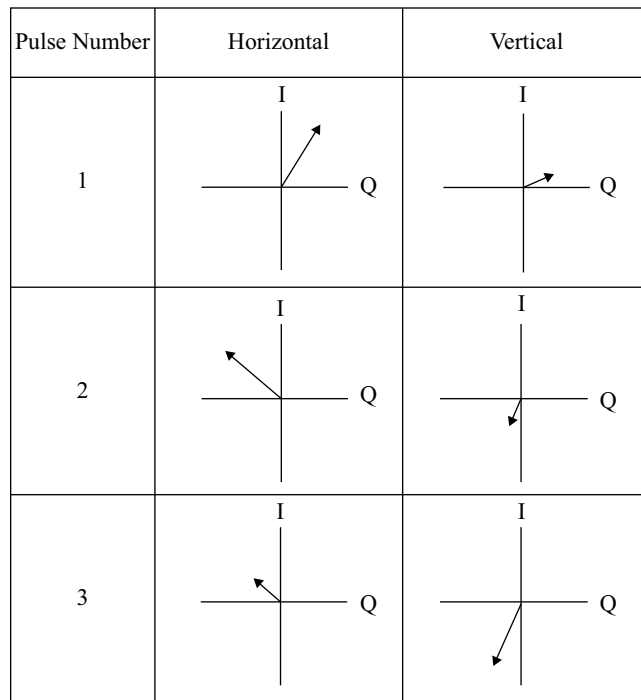


FIGURE 13-28 ■
Examples of
Phasors with
Low Correlation.

cases, the magnitude or the phase angle or both change in a similar manner between highly correlated pulses.

A contrasting illustration of the phasor relationships between subsequent pulses for low correlation coefficient cases is shown in Figure 13-28. Again, the received H and V phasors for the initial pulse are shown in the first row of the illustration. The second row shows the return for the next pulse with low correlation. In this case, although the amplitudes of the H and V phasors are similar, the phase angle differences from pulse to pulse are oppositely sensed between the H and V phasors. The third row shows another low-correlation case. Comparing the returns between pulses two and three, the phase angles remain the same but the amplitudes vary in opposite directions. A low correlation coefficient means that magnitude or phase angle or both change significantly between pulses.

The correlation coefficient is a good measure of the variety of scatters within a resolution volume. Typical values, which are unitless, vary from about 0.2 to 1. A low ρ_{HV} , below 0.8, typically represents scattering from nonmeteorological targets such as birds, insects, and human-made structures. A moderate ρ_{HV} , between 0.8 and 0.97, can be representative of a mixture of precipitation types, sizes, or states. This could include a wide spectrum of drop sizes, a mixture of rain and hail, or melting snow. High ρ_{HV} , above 0.97, represents areas of uniform rain or snow.

As is apparent from the preceding discussion, a somewhat lower value of ρ_{HV} , typical of melting snow and hail, can be used to good effect to discern both the melting layer and transition areas from rain to snow in radar returns.

13.8.3.2 Differential Reflectivity

A second very useful parameter available from dual-polarization systems is differential reflectivity, Z_{DR} . Differential reflectivity is simply defined as the difference between the

FIGURE 13-29 ■ Major Axis Orientations for Various Z_{DR} Values.




Spherical	Horizontally Oriented	Vertically Oriented
Drizzle, Small Hail, etc.	Rain, Melting Hail, etc.	Vertically Oriented Ice Crystals
		
$Z_H \sim Z_V$ $Z_H - Z_V \sim 0$	$Z_H > Z_V$ $Z_H - Z_V > 0$	$Z_H < Z_V$ $Z_H - Z_V < 0$
$Z_{DR} \sim 0$ dB	Z_{DR} is positive	Z_{DR} is negative

TABLE 13-4 ■ Z_{DR} as a Function of Raindrop Size

Major (H) Axis Dimension (mm)	Differential Reflectivity (dB)
< 0.3	0
1.35	1.3
1.75	1.9
2.65	2.8
2.90	3.3
3.68	4.1
4.0	4.5

horizontal reflectivity, Z_H , and the vertical reflectivity, Z_V , and is expressed in values of dB. Typical values observed range from about -8 dB to $+8$ dB and reflect the degree to which the reflecting particles are oriented in the horizontal or vertical.

Figure 13-29 shows the relative major axis orientations for Z_{DR} values, which are negative, near zero, and positive. Typically, small values of Z_{DR} represent uniformly shaped particles such as drizzle and small hailstones. Values of Z_{DR} greater than zero, representing reflections dominated by horizontal polarization, are typical of rain and melting hail. Table 13-4 shows typical values of Z_{DR} seen for different raindrop sizes. As the drop size increases, the drops become more oblate, with the major axis in the horizontal. Z_{DR} can be of utility in determining the approximate average drop size within a resolution cell. Values of Z_{DR} less than zero are not often seen but can be observed in areas of vertically oriented ice crystals. These areas are sometimes seen in thunderstorms where large electric fields can exert forces sufficient to orient the crystals.

Several special cases of Z_{DR} deserve to be mentioned. These special variations can be used to great advantage to discern precipitation types from polarimetric returns when combined with other data. Tumbling hail, regardless of its overall shape, often results in a large value of Z combined with a very small value of Z_{DR} , while small and completely water-coated hail can often stop tumbling and result in very large Z_{DR} values between 5 dB and 6 dB.

Snow and ice produce a wide variety of Z_{DR} values dependent on the wetness and density of the ice or snow. Ice and snow crystals can also become preferentially aligned by electrical forces within the storms. This is an area that needs more research to characterize the precipitation effects. Snow typically sees values of 0.2 dB to 0.3 dB for dry snow and 2 dB to 3 dB for wet snows. Ice Z_{DR} returned can vary from less than 1 dB for low-density, randomly oriented crystals to 4 dB to 5 dB for high-density crystals with a preferred horizontal orientation. High-density, vertically oriented ice crystal might produce Z_{DR} values between 0 and -2 dB.

Nonmeteorological targets typically produce returns that are highly variable from place to place and therefore have low values of Z_{DR} .

Other factors that need to be considered when analyzing Z_{DR} values include several effects arising from basic characteristics of Z itself. As Z is a function of the sixth power of the diameter, D^6 , so the Z_{DR} values will be also biased toward contributions from larger particles. The value of Z is also lower for ice than for water, leading to a dominance of Z_{DR} for liquid (or liquid-coated) particles over ice (frozen) particles.

For large particles, Mie scattering can become important. Some very large hail can have vertical dimensions on the order of 1 inch in the Rayleigh region for S-band, while the horizontal dimension can reach 2 inches bordering the Mie region. The oscillatory nature of the relationship between dimension and returned power can then reduce the value of Z_{DR} for these hailstones. Typically, regions with these particles are also characterized by values of correlation coefficient less than 0.95.

13.8.3.3 Specific Differential Phase

As radar pulses travel through areas containing precipitation particles, they slow as they pass through the medium. Horizontally and vertically polarized pulses are affected (slowed) preferentially by particles that are oriented in the horizontal or vertical direction, respectively. As most of the precipitation particles typically encountered by weather radar are raindrops, which have a major axis primarily in the horizontal dimension, the horizontal phase tends to lag the vertical phase. This differential phase shift can be written as

$$\varphi_{DP} = \varphi_H - \varphi_V \quad (13.38)$$

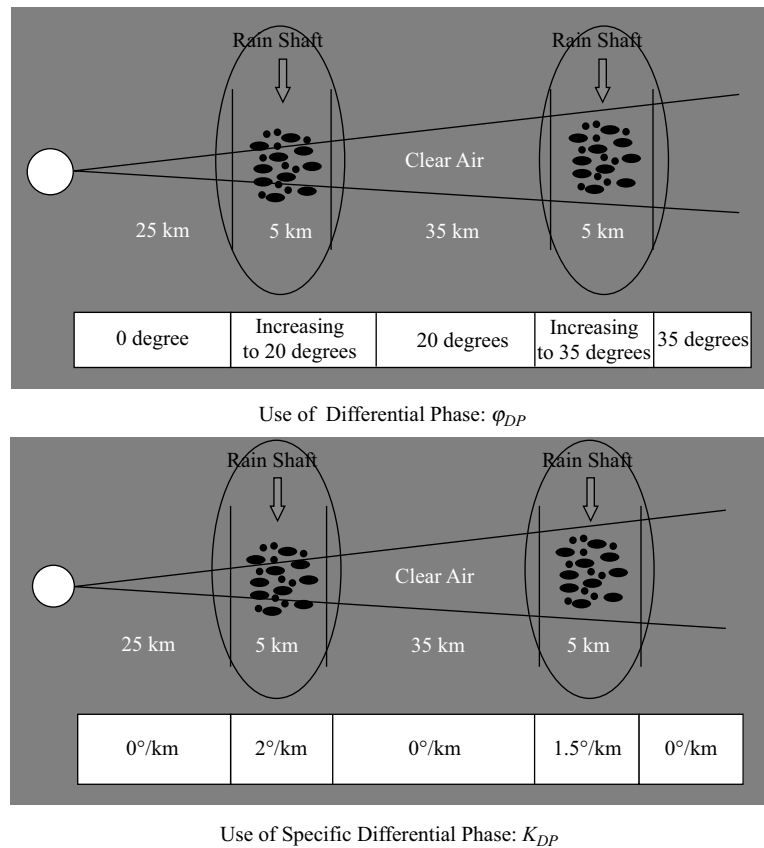
As φ_H tends to lag φ_V in meteorological environments and is therefore larger, φ_{DP} is typically positive and can reach values on the order of 10° or so.

As previously defined, differential phase change behaves in a similar manner as Z_{DR} . Particles that are small and uniformly shaped have little influence on φ_{DP} . Particles with horizontal orientations lead to positive values of φ_{DP} , while those with vertical orientations lead to negative values. Differential phase is highly affected by the concentration of oriented drops. One primary application of differential phase shift is discerning areas of heavy rainfall.

Most frozen precipitation exhibits very low values of differential phase. One exception to this rule is for small, nearly melted hail, which may appear as very large rain. A second exception is snow and ice affected by strong electric fields in thunderstorms. The orienting effect of the fields can then lead to large negative or positive values of φ_{DP} . Nonmeteorological targets tend to have variable and noisy values of φ_{DP} .

An operational difficulty in using φ_{DP} is that the quantity is cumulative. This leads to the development and use of a related, but more useful, quantity defined as

FIGURE 13-30 ■
Use of Differential
Phase and Specific
Differential Phase.



the specific *differential phase shift*, K_{DP} , expressed in units of degrees per kilometer ($^{\circ}/\text{km}$)[24]:

$$K_{DP} = \frac{\varphi_{DP}(r_2) - \varphi_{DP}(r_1)}{2(r_2 - r_1)} \quad (13.39)$$

K_{DP} is the change in differential phase shift between two specific range bins, divided by the distance over which the radar signal travels. (A factor of 2 is included to account for the round-trip travel of the pulse.) A schematic illustrating the differences in φ_{DP} and K_{DP} as the radar samples two distinct areas of precipitation is shown in Figure 13-30.

In the top part of the figure, using φ_{DP} , we see that the differential phase change remains at zero until it encounters the first area of precipitation. It then increases from zero to a value of 20 degrees. As the beam traverses the second area devoid of precipitation, the differential phase remains at 20 degrees. When the beam reaches the second area of precipitation, the differential phase again increases, this time from 20 degrees to 35 degrees while traversing the precipitation area. Finally, after emerging from the second precipitation area, φ_{DP} remains at the 40 degrees value.

The problem that arises using simple φ_{DP} is that high or low values do not indicate particular precipitation regimes. This problem is solved when looking at the behavior of K_{DP} , as illustrated in the lower part of Figure 13-30. Here we look at the behavior of K_{DP} over the same two distinct areas of precipitation. Again, before reaching the

precipitation, φ_{DP} is zero at all points, so the related quantity K_{DP} is also zero. When the beam traverses the first precipitation area, it experiences an increase of φ_{DP} from 0 degrees to 20 degrees over a distance of 5 km. Using (13.39) and accounting for the factor of 2 in the denominator, the value of K_{DP} within the precipitation area, assuming it is uniform, is $2^\circ/\text{km}$. As the beam traverses the empty region between the first and second precipitation areas, there is no change in φ_{DP} , so K_{DP} in this area is again zero. Finally, when the beam reaches and moves through the second precipitation area, the value of φ_{DP} increases from 20 dB to 35 degrees, or 15 degrees, over a distance of 5 km. Again, accounting for the factor of 2 in the denominator, the value of K_{DP} in this region can be shown to be $1.5^\circ/\text{km}$.

In operational use, higher values of K_{DP} are indicative of heavy rain areas. Hail is relatively undetected by K_{DP} and results in values near zero, as do snow and other forms of ice unless they are in highly preferred orientations. Frozen precipitation will generally exhibit higher values of K_{DP} as it grows wetter. Nonmeteorological targets typically appear quite noisy in K_{DP} .

13.8.4 Multifunction Phased Array Radar (MPAR)

The current network of weather radars in the United States has been operational for 25 to 30 years. Most of the aircraft surveillance radars in use are also aging and either nearing the end of their service lives or have become subject to service life extension programs to keep them operational. All of these systems rely on conventional rotating antenna systems. A program to devise a common replacement platform that would be able to perform weather, aircraft, and homeland defense functions simultaneously has been sponsored jointly by NOAA, the FAA, DoD, and the Department of Homeland Security. The replacement system has been called the Multifunction Phased Array Radar (MPAR) [26]. It is envisioned to be a phased array system at a band that would allow both aircraft tracking and weather monitoring. Several designs are under consideration, including multiple-faced phased arrays. It is expected that the MPAR system would be able to provide multiple independent beams to allow it to accomplish several simultaneous missions. As illustrated in Figure 13-31, a single network of

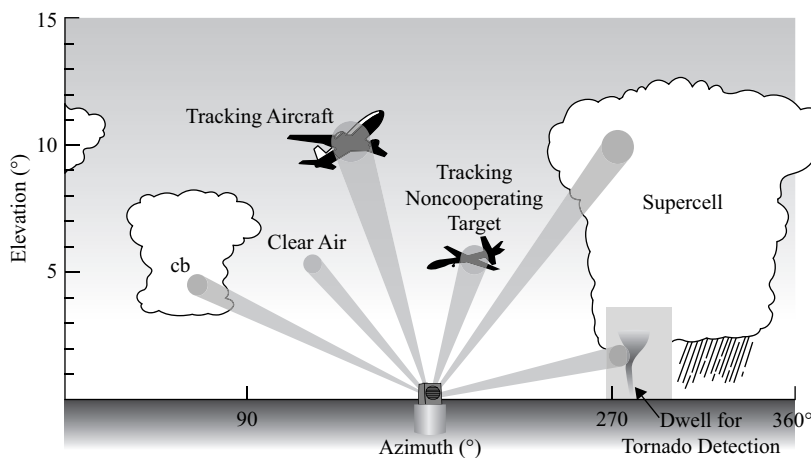


FIGURE 13-31 ■ MPAR Concept of Operation.

MPAR systems could replace multiple networks of NEXRAD weather radar, ASR-9 and ASR-11 air traffic control radar, terminal Doppler weather radar, and ARSR-4 air-route surveillance radar.

A demonstration phased array system, based on a SPY-1A panel formerly used on an Aegis-class guided missile cruiser, is currently deployed at the National Weather Radar Testbed (NWRT) at the National Severe Storms Laboratory (NSSL) in Norman, Oklahoma. The single panel has provided meteorologists the ability to compare the high temporal and spatial resolution data available from the NWRT with conventional NEXRAD data from nearby facilities. These experimental campaigns have proven the value of the increased resolution available from the phased array system.

13.8.5 CASA and DCAS Concepts

The wide spacing of NEXRAD sites, combined with a minimum elevation angle of 0.5 degrees leads to a lack of capability to interrogate the lowest portions of the atmosphere. Unfortunately, this is the area where much of the weather that most impacts us occurs. To address this need, an engineering center was established, sponsored by the National Science Foundation and led by the University of Massachusetts for the Collaborative Adaptive Sensing of the Atmosphere (CASA) [27]. One of CASA's goals is to develop Distributed Collaborative Adaptive Sensing (DCAS) networks of small, X-band phased array radars that can be used to scan the areas beneath the NEXRAD beam coverage as well as provide overlapping coverage patterns to avoid problems such as the so-called cone of silence [28], the area directly above the radar and above the maximum elevation angle, making radar coverage impossible. This area would be covered in a DCAS network by a neighboring system. Intelligent algorithms, as well as operator control, would allow the systems to focus on high-impact weather phenomena in the area.

An Oklahoma test bed has been established that consists of four closely spaced X-band dual-polarization radar systems. These systems have been used in recent years to simultaneously observe several severe storms and tornadoes and have proven ability to provide enhanced information on these storms.

13.9 | REFERENCES

- [1] R. H. Maynard, "Radar and Weather," *Journal of Meteorology*, vol. 2, no. 4, pp. 214–226, Dec. 1945.
- [2] A. E. Bent, "Radar Detection of Precipitation," *Journal of Meteorology*, vol. 3, pp. 78–84, Sep. 1946.
- [3] R. C. Whiton, P. L. Smith, S. G. Bigler, K. E. Wilk, and A. C. Harbuck, "History of Operational Use of Weather Radar by U.S. Weather Services. Part I: The Pre-NEXRAD Era," *Wea. Forecasting*, vol. 13, no. 2, pp. 219–243, Jun. 1998.
- [4] "CHILL history – CHILL." [Online]. Available: http://www.chill.colostate.edu/w/CHILL_history#The_First_Tornadic_Hook_Echo_Weather_Radar_Observations. [Accessed: 12-Dec-2010].
- [5] R. A. Brown and J. M. Lewis, "PATH TO NEXRAD: Doppler Radar Development at the National Severe Storms Laboratory," *Bulletin of the American Meteorological Society*, vol. 86, pp. 1459–1470, Oct. 2005.

- [6] T. D. Crum, R. E. Saffle, and J. W. Wilson, "An Update on the NEXRAD Program and Future WSR-88D Support to Operations," *Weather and Forecasting*, vol. 13, no. 2, pp. 253–262, Jun. 1998.
- [7] R. J. Doviak, V. Bringi, A. Ryzhkov, A. Zahrai, and D. Zrníc, "Considerations for Polarimetric Upgrades to Operational WSR-88D Radars," *Journal of Atmospheric and Oceanic Technology*, vol. 17, no. 3, pp. 257–278, Mar. 2000.
- [8] E. Brookner, "Phased Arrays and Radars – Past, *Present and Future. (Cover story)*," *Microwave Journal*, vol. 49, no. 1, pp. 24–46, Jan. 2006.
- [9] "Federal Research and Development Needs and Priorities for Phased Array Radar." [Online]. Available: <http://www.ofcm.gov/r25-mpar/fcm-r25.htm>. [Accessed: 07-Oct-2012].
- [10] R. C. Whiton and P. L. Smith, "History of Operational Use of Weather Radar by U.S. Weather Services. Part II: Development of Operational Doppler Weather Radars," *Wea. Forecasting*, vol. 13, no. 2, pp. 244–252, Jun. 1998.
- [11] "WSR-88D Dual Polarization Overview." [Online]. Available: <http://www.roc.noaa.gov/WSR88D/dualpol/DualPolOverview.aspx>. [Accessed: 07-Oct-2012].
- [12] Probert-Jones, J. R. (1962), The radar equation in meteorology. Q.J.R. Meteorol. Soc., 88: 485–495. doi:10.1002/qj.49708837810.
- [13] B. M. Herman and L. J. Battan, "Calculations of Mie Back-Scattering of Microwaves from Ice Spheres," *Quarterly Journal of the Royal Meteorological Society*, vol. 87, no. 372, pp. 223–230, 1961.
- [14] L. J. Battan, *Radar Observation of the Atmosphere*, Rev. ed. Chicago, IL, University of Chicago Press, 1973.
- [15] J. S. Marshall and W. M. K. Palmer, "The Distribution of Raindrops with Size," *Journal of Meteorology*, vol. 5, no. 4, pp. 165–166, Aug. 1948.
- [16] R. Gunn and G. D. Kinzer, "The Terminal Velocity of Fall for Water Droplets in Stagnant Air," *Journal of Meteorology*, vol. 6, no. 4, pp. 243–248, Aug. 1949.
- [17] L. J. Battan and B. M. Herman, "The Radar Cross Sections of "Spongy" Ice Spheres," *Journal of Geophysical Research*, vol. 67, no. 13, pp. 5139–5146, 1962.
- [18] Ronald Rinehart, *Radar for Meteorologists*, 4th ed. St. Joseph, MO, Rinehart Publications, 2004.
- [19] K. L. S. Gunn and T. W. R. East, "The Microwave Properties of Precipitation Particles," *Quarterly Journal of the Royal Meteorological Society*, vol. 80, no. 346, pp. 522–545, 1954.
- [20] "July 23rd Extreme Hail Event." [Online]. Available: <http://www.crh.noaa.gov/abr/?n=stormdamagetemplate>. [Accessed: 07-Oct-2012].
- [21] R. Wexler and D. Atlas, "Radar Reflectivity and Attenuation of Rain," *Journal of Applied Meteorology*, vol. 2, no. 2, pp. 276–280, Apr. 1963.
- [22] "Supercell Analysis: Using the Lemon Technique." [Online]. Available: [http://ww2010.atmos.uiuc.edu/\(Gh\)/guides/mtr/svr/comp/up/spr.rxml](http://ww2010.atmos.uiuc.edu/(Gh)/guides/mtr/svr/comp/up/spr.rxml). [Accessed: 07-Oct-2012].
- [23] L. R. Lemon and C. A. Doswell, "Severe Thunderstorm Evolution and Mesocyclone Structure as Related to Tornadogenesis," *Monthly Weather Review*, vol. 107, pp. 1184–1197, Sep. 1979.
- [24] P. M. Markowski, "Hook Echoes and Rear-Flank Downdrafts: A Review," *Monthly Weather Review*, vol. 130, no. 4, pp. 852–876, Apr. 2002.
- [25] D. S. Zrníc and A. Ryzhkov, "Advantages of Rain Measurements Using Specific Differential Phase," *Journal of Atmospheric and Oceanic Technology*, vol. 13, no. 2, pp. 454–464, Apr. 1996.

- [26] M. E. Weber, J. Y. N. Cho, J. S. Herd, J. M. Flavin, W. E. Benner, and G. S. Torok, “The Next-Generation Multimission U.S. Surveillance Radar Network,” *Bulletin of the American Meteorological Society*, vol. 88, pp. 1739–1751, Nov. 2007.
- [27] J. Brotzge, K. Hondl, B. Philips, L. Lemon, E. J. Bass, D. Rude, and J. Andra, “Evaluation of Distributed Collaborative Adaptive Sensing for Detection of Low-Level Circulations and Implications for Severe Weather Warning Operations.,” *Weather & Forecasting*, vol. 25, no. 1, pp. 173–189, Feb. 2010.
- [28] “P10R.5 Improved radar sensitivity through limited sector scanning: The DCAS approach (2005 - 32Rad11Meso_32radar).” [Online]. Available: https://ams.confex.com/ams/32Rad11Meso/techprogram/paper_96577.htm. [Accessed: 07-Oct-2012].

13.10 | FURTHER READING

- R. E. Rinehart, *Radar for Meteorologists*. Columbia, MO, Rinehart Publications, 482 pp., 2004.
- H. Sauvageot, *Radar Meteorology*. Norwood, MA, Artech House, 366 pp., 1992.
- R. J. Doviak and D. S. Zmic, *Doppler Radar and Weather Observations*. Mineola, NY, Dover Publications, 562 pp., 2006.
- L. J. Battan, *Radar Observation of the Atmosphere*. Chicago, IL, University of Chicago Press, 324 pp., 1973.

Foliage-Penetrating Radar

Mark E. Davis, Consultant Prospect, NY, USA

Chapter Outline

14.1	Introduction	635
14.2	History of Battlefield Surveillance	637
14.3	Foliage-Penetrating SAR Collection Systems	642
14.4	FOPEN Clutter Characteristics	645
14.5	Image Formation	654
14.6	Radio Frequency Interference.	665
14.7	Target Detection and Characterization	676
14.8	Summary	684
14.9	References.	685
14.10	Further Reading	688

14.1 | INTRODUCTION

Foliage-penetrating (FOPEN) radar is a relatively modern capability for surveillance and earth resource monitoring. It had been well known for several decades that radar could propagate efficiently through forests at frequencies below 1 GHz [1]. But it was not until the 1960s that the propagation loss and clutter scattering models were effectively developed to provide reasonable expectations that fixed and moving objects could be detected. More importantly, the technology for effective waveform design and signal processing was not available until the advent of coherent sources and high-speed digital processing.

The initial FOPEN radar systems were ground-based moving target indication (MTI) systems to detect troops moving through dense jungles [2]. The coherent processing was innovative for the time, but the systems suffered from interference from local radio and television transmitters and effects of wind-blown clutter. An early experiment to develop an airborne synthetic aperture radar (SAR) was successful, but never developed into an operational system [3].

FOPEN SAR systems were developed more thoroughly starting in the early 1990s, primarily with the objective of operation from a remotely piloted vehicle (RPV). To provide efficient detection on these RPVs, extensive data collections were needed to refine the foliage loss and clutter scattering models. Furthermore, algorithms for the ultra-wide bandwidth (UWB) waveforms for SAR were required to remove the radio

frequency interference (RFI), as well as to provide efficient target detection and characterization. By the end of that decade, high-performance computing was available to implement real-time, onboard processing.

14.1.1 Organization and Key Points

This chapter organization follows the history and development of UWB FOPEN radar with a technical progression of the following sections:

Section 14.2 – FOPEN history: early development of foliage-penetrating moving and fixed target detection systems, along with lessons learned

Section 14.3 – FOPEN SAR collection systems: experimental FOPEN SAR systems during the 1990s that established the feasibility and advanced subsystem capabilities to further FOPEN development

Section 14.4 – FOPEN clutter characterization: experimental data providing the impact of clutter backscatter, foliage loss, and external radio frequency interference effects on FOPEN SAR design

Section 14.5 – Image formation: summary of waveform and signal processing to form UWB SAR images with very fine resolution

Section 14.6 – Radio frequency interference: characteristics of the radio frequency spectrum and limitations in using that spectrum, which directly affect the ability to develop and operate airborne UWB systems

Section 14.7 – Target detection and characterization: critical developments in signal and image processing that provide the feasibility of semi-automated detection and characterization of manmade targets under dense foliage.

14.1.2 Acronyms

Commonly used acronyms used in this chapter include (in alphabetical order):

ADC – analog to digital converter

BPA – back projection algorithm

CARABAS – coherent all radio band system (by Swedish research institute FOA)

CNR – clutter-to-noise ratio

CPI – coherent processing interval

DARPA – Defense Advanced Research Projects Agency

DEM – digital elevation model

DTED – digital terrain elevation data

ERIM – Environmental Research Institute of Michigan

FCC – Federal Communications Commission

FEBA – forward edge of battle area

FFT – fast Fourier transform

FOLPEN – foliage-penetrating radar system (by SRI)

FOPEN – foliage-penetrating

GeoSAR – geographic synthetic aperture radar system (by Jet Propulsion Laboratory)

GMTI – ground moving target indication
IFSARE – interferometric synthetic aperture radar - elevation (by ERIM)
IFFT – inverse fast Fourier transform
JPL – Jet Propulsion Laboratory
JSTARS – Joint Surveillance and Target Attack Radar System
LWL – Land Warfare Laboratory
MDV – minimum detectable velocity
M-FOPEN – multipurpose – foliage-penetrating (by Syracuse University Research Corporation)
MIT – Massachusetts Institute of Technology
MTI – moving target indication
NTIA – National Telecommunications and Information Administration
PRI – pulse repetition interval
radar – radio detection and ranging
RCS – radar cross section
REFORGER – return of forces to Germany
RFI – radio frequency interference
RMA – range migration algorithm
RPV – remotely piloted vehicle
SAR – synthetic aperture radar
SINR – signal-to-interference-plus-noise ratio
SLAR – side-looking array radar
SNR – signal-to-noise ratio
SOTAS – stand-off target acquisition system
SRI – Stanford Research Institute
STAP – space-time adaptive processing
UHF – ultrahigh frequency
UWB – ultrawide bandwidth
VHF – very high frequency

14.2 | HISTORY OF BATTLEFIELD SURVEILLANCE

Battlefield surveillance radar was started in early 1960s with the development of the OV-1 APS-94 side-looking array radar (SLAR) by the U.S. Army for detecting military encampments and large groups of artillery and mechanized vehicles on the battlefield [4]. In the early 1970s, the Army determined that there was also a need for detecting large numbers of moving vehicles at a significant range from the forward edge of the battle area (FEBA). The first ground-moving target indication (GMTI) system for battlefield surveillance was developed as the stand-off target acquisition system (SOTAS). It was constructed using the APS-94 radar with a moving target mode and operated from a UH-1 helicopter. Operation from a helicopter was necessary to minimize platform motion and to provide wide area, low minimum discernable velocity (MDV) detections [5].

The battlefield surveillance capabilities of SLAR and SOTAS soon led to the development of the Joint Surveillance and Target Attack System (JSTARS) for use by the U.S. Army and Air Force [5]. The JSTARS stand-off battlefield surveillance capabilities could be integrated on a high-altitude, multiengine aircraft for longer endurance and significant stand-off range for survivability. The benefits of JSTARS combining SAR and GMTI on the battlefield are extensively documented, and have been reproduced and fielded on many international platforms. All of these early battlefield surveillance radar systems were developed in the microwave frequency band. Microwave frequencies were important to provide all-weather, long-range, high-probability detection of vehicles and structures, yet be small enough that they could be carried on tactical aircraft.

However, there was one important operational issue: The opposing combatants understood X-band radar's limitations to see through forest cover. Tactics were being developed to deny these radars the ability to image the movement and location of ground forces. Hiding in tree lines and using other forms of camouflage and concealment quickly countered microwave radar. This countering tactic became highly effective, as demonstrated against early optical surveillance. Thus, there was a need to develop detection of fixed and moving targets under foliage as a complement to the very capable microwave battlefield surveillance radar systems.

The first application for FOPEN radar was during the Vietnam conflict, where early systems were developed to detect and recognize ground-moving targets [6]. Specifically, there was a need to detect and locate insurgent soldiers walking through dense tropical forests. Two innovations were needed: coherent waveforms and the associated signal processing; and reduction of foliage attenuation via radar installation on major hills and tall towers or masts. These two features increased the coherent gain on targets and minimized the effects of clutter Doppler spread masking the small returns from personnel and vehicles. However, it did not provide the ability to detect stationary manmade objects. A parallel development of FOPEN synthetic aperture radar (SAR) was needed to detect manmade objects under the trees. The required innovation for foliage-penetrating SAR was wideband image processing and coherent discrimination of manmade objects from the background clutter [3].

Early analysis of propagation loss through forests had been very pessimistic about detecting personnel in dense woods. The losses quoted for 100-MHz propagation varied from 0.02 dB to 1.0 dB per meter, depending on the source of the radio wave and the density of the forest. However, radio tests for Vietnam showed radio propagation was not over a straight line, but by propagation over the tops of the trees and eventual diffraction into the forest. Subsequent tests were made in forests in Georgia, Puerto Rico, and Panama at VHF (30 MHz to 300 MHz) and UHF (300 MHz to 1,000 MHz). The results of these tests indicated that foliage loss was lower at VHF frequencies than at UHF, and significantly lower if the transmitter was elevated above the local foliage canopy. Based on these observations, the U.S. Army Land Warfare Laboratory (LWL) conducted a series of tests in a dense Georgia forest with light undergrowth, using a 140-MHz CW signal to quantify the propagation losses. Both horizontal and vertical polarizations were tested; horizontal polarization exhibited the lowest propagation loss [2].

DARPA and MIT Lincoln Laboratory undertook the development (under the Camp Sentinel program) of an operational area surveillance radar to detect insurgents moving under thick jungle canopy. The radar system shown in Figure 14-1 operated at a higher



FIGURE 14-1 ■
Camp Sentinel II
Radar Installed on
Hill in Vietnam.
[Source: MIT Lincoln
Laboratory [6]]



FIGURE 14-2 ■
Camp Sentinel
Radar Antenna [7].

frequency (435 MHz) than the earlier brassboard systems. The goal was to obtain a more accurate location of personnel at much longer ranges. Lincoln Laboratory developed an initial Camp Sentinel II service test system using a solid-state transmitter and a mechanically scanned antenna. This early system had a moderate detection range up to 200 meters [6].

In order to provide longer detection range and counter higher losses at UHF, the system was upgraded to Camp Sentinel III with a high power-aperture design. A 3.5-meter-diameter, 1-meter-high cylindrical antenna was developed through the Army Harry Diamond Laboratory. This antenna was mounted on a 33-meter-high tower along with a 2-kilowatt tube transmitter. The high tower was chosen primarily to extend the propagation range out to 2 kilometers. Stepped angle surveillance with 32 beam positions was provided by the cylindrical antenna, shown in Figure 14-2. This stepped scan

eliminates the mechanically scanned antenna, masking low Doppler targets by clutter modulation. The waveform used a coherent, range-gated pulse Doppler MTI dwell to provide relatively accurate location of the intruders. An automatic motion alarm processor was developed and installed in the remote operation shelter to alert the operators when a person came within detection range.

The Camp Sentinel radar was a very large system, weighing over 3,600 kg. For transportation to the theater, it was packaged on a tractor-trailer and carried in a C-130 or under a Chinook helicopter. This provided for defense around larger fixed encampments, where there was sufficient height above the surrounding terrain. However, it required mounting on a hill and atop a very tall tower; and as a result, it presented a very distinctive visual landmark.

The LWL developed a more mobile VHF radar system for use in forward deployed encampments. Called the multipurpose-FOPEN, or M-FOPEN, system, it could be carried by a single person, as shown in Figure 14-3, and be set up in the jungle in an hour [2]. The objectives were to have a system supporting remote operations where a large fixed installation was not feasible.

The characteristics of the M-FOPEN radar are given in Table 14-1. In contrast to the 435-MHz Camp Sentinel radar, this system operated at 140 MHz in an attempt to reduce the foliage loss and minimize the need for a heavy, high power-aperture design. Furthermore, the target should be enhanced with the wavelength close to target resonance. Figure 14-4 shows the radar antenna installed on the 13-meter tower as tested in Florida's light tropical forest environment, with the transmitter/receiver directly mounted to the antenna.

FIGURE 14-3 ■
M-FOPEN Man-
Transportable Radar
[8].

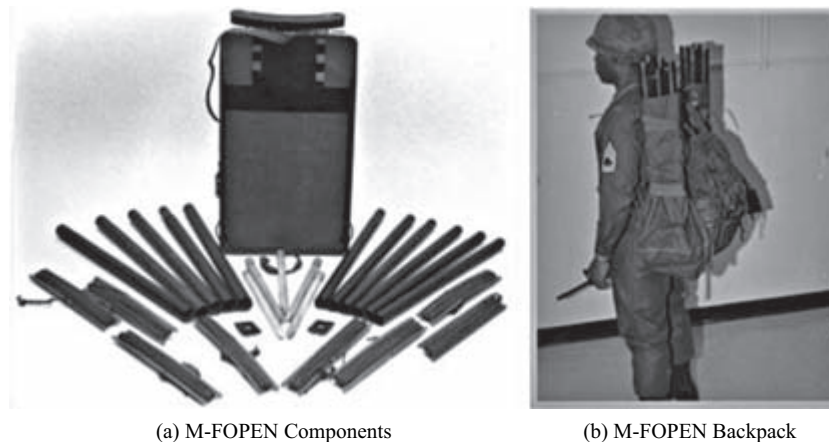


TABLE 14-1 ■ Characteristics of M-FOPEN Radar [7]

Frequency	140 MHz	Antenna gain	9 dB
Transmit power (peak)	50 watts	Azimuth beamwidth	45 degrees
Pulse length	0.1 μ sec	Polarization	Horizontal
PRF	15 KHz	Height	15 meters
Receiver	Homodyne	Detection	Kalman filter



FIGURE 14-4 ■
M-FOPEN for Tests
in a Florida
Environment [8].

These early development radars for foliage penetration were in response to the military's needs to find and locate insurgents in a severe tropical environment. Little quantitative data existed to characterize the clutter and propagation losses in this environment. Based on a series of data collections in tropical regions, the decision was made to rapidly develop experimental systems and get them into operational tests in a deployed war zone. Although some limited testing had been carried out prior to deployment, extensive system design and performance verification were not followed. These systems performed well, and both the technical and military communities learned from the experience.

Only the ground-moving target indication radars were taken to the theater. The development of SAR capabilities was attempted, but the military planners could not justify the development due to several factors. First, the resolution of FOPEN SAR was limited to tens of meters. Operational SAR systems were significantly better than this, and were not accepted due to the poor SAR resolution obtained and lack of image or object feature recognition. Second, the SAR systems were large and could not be carried on aircraft that would survive in a military environment. Finally, the state of the art in real-time signal processing was not mature enough to meet the needs of the military users.

No documented developments for peacetime use of FOPEN radar systems are found for the period from 1975 to 1985. Because of the lack of mature coherent subsystems in the FOPEN radar band, it required a major push by the military to re-energize the development of this new capability. It would take significant breakthroughs in the understanding of foliage-penetrating phenomenology, the concept of operations in a crowded electromagnetic spectrum, and algorithms for signal and image processing before FOPEN radar would become a viable system.

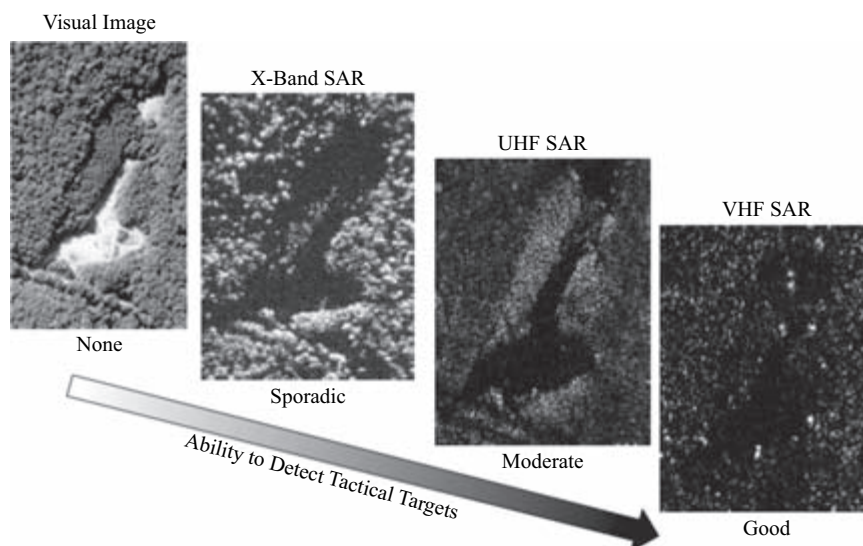
14.3 | FOLIAGE-PENETRATING SAR COLLECTION SYSTEMS

With the advances in critical radar technologies of wideband waveform generation and digital image formation, the community could start the task of understanding the capabilities and limitations of FOPEN SAR. Microwave SAR systems were just beginning to gain acceptance in the surveillance community, which had relied on high-resolution pictures for decades. Figure 14-5 presents the motivation for FOPEN SAR needs and an advanced look at what it provides the operational user – whether a military or commercial customer of the image products [9]. All four panes in the figure are of the same scene – a forested region with several vehicles parked under the foliage and in the tree lines – but collected with different imaging technologies. On the left is a moderate to high-resolution optical picture, but the vehicles cannot be observed until the sensor is nadir looking. The next image to the right is a typical 1-meter resolution X-band image of the scene taken on the same day. Sporadic detections were obtained, but only when the glint of targets could be captured in the image. Neither of these two image products would satisfy the user, especially when high area coverage rate is needed.

The next two SAR images, which are within UHF (235–445 MHz) and VHF (20–88 MHz), show a more optimistic ability to detect the fixed targets. The UHF panel shows images of many of the manmade targets, but high false alarms caused by the foliage clutter in the scene. The detection at VHF is higher where the foliage attenuation is significantly lower, and the target cross sections are larger than the clutter. However, these lower frequencies provide limited resolution (i.e., pixels on target) to characterize the objects in the image.

This realization of reliable imaging capabilities for FOPEN SAR was important. It started a five-year campaign to re-characterize the foliage clutter so better SAR system engineering could be designed. It was also realized at that time that a better understanding of the foliage scattering phenomenology would derive civilian uses for

FIGURE 14-5 ■
Comparison of
Optical and Several
Radar Image
Sources. [Source:
MIT Lincoln
Laboratory ©1998
IEEE [9]]



the FOPEN systems. In the early 1990s, there was a definite dual-use message in the development objectives.

The advantage of SAR systems is the improved cross-range resolution over that of a real beam antenna system obtained by flying a long synthetic aperture as shown in Figure 14-6. The cross-range resolution for SAR integration through an angle of θ_I is given by [10]:

$$\delta_{CR} = \frac{k_{CR} \lambda_c}{4 \sin(\theta_I/2)} \tag{14.1}$$

where

- k_{CR} = cross-range broadening factor due to aperture weighting
- λ_c = wavelength at the radar's center frequency
- θ_I = total azimuth integration angle during SAR image formation

For VHF and UHF frequencies, the angles needed to achieve fine cross-range resolution become very large. As a result, both the fractional bandwidth and the integration angle are *ultrawide* compared to the conventional microwave frequency SAR systems. Figure 14-7 shows the achievable cross-range resolution as a function of the frequency and integration angles for the frequency bands commonly chosen for FOPEN systems. For VHF, it is important to have integration angles in excess of 45 degrees to obtain 5 meters of cross-range resolution. This was a major development challenge in terms of the integration times, motion measurement, and motion compensation, as well as achieving the comparable range resolution.

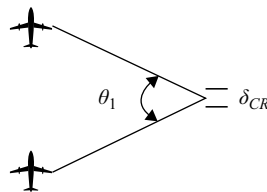


FIGURE 14-6 ■ SAR Geometry for Cross-Range Resolution.

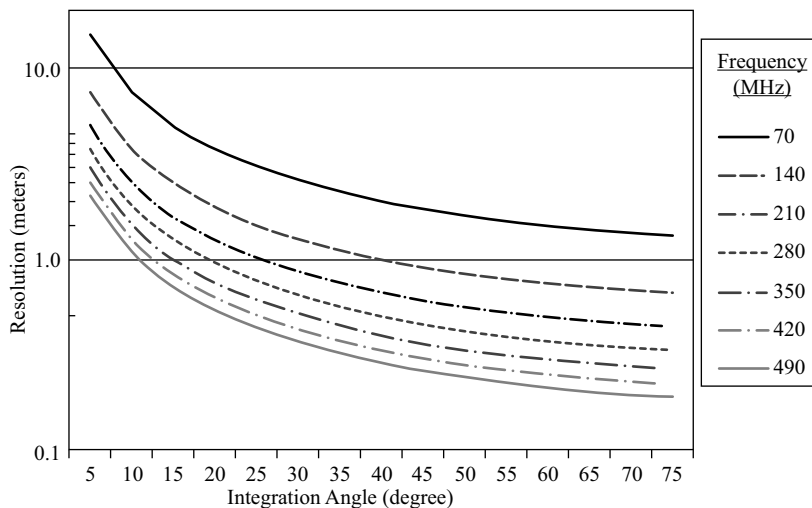


FIGURE 14-7 ■ SAR Resolution with Variable Integration Angle and Frequency.

TABLE 14-2 ■ Comparison of Technology from FOPEN SAR Experimental Systems

	FOLPEN II	CARABAS II	P3 UWB	GeoSAR	BoomSAR
Waveform	Impulse	Freq jump	Notched LFM	Notched LFM	Impulse
Frequency MHz	200–400	20–80	225–740	270–430	50–1100
Polarization	HH	HH	HH, HV, or VV	HH, HV, or VV	Full pol
Transmit RFI	N/A	Freq sequence	Notch	Notch	N/A
Image formation	Back projection	Back projection	RMA	INSAR	Back projection

Several FOPEN SAR systems were developed and flown in the early 1990s [11–15]. These FOPEN SAR data collection systems had to factor these issues into many aspects of the radar design. They represent significantly different approaches for image formation processing, the details of which will be presented in Section 14.5. Table 14-2 summarizes the critical technologies employed in the design and development of each of the systems. Significant publication of the design details and system performance results occurred in that decade. As a result, the lessons have been shared and formed the designs of more recent systems for the next decade.

The five radars illustrated in the following sections present a wide variation in frequency, transmit waveform design, image processing, and the use of polarization. Four of the systems were installed on fixed-wing aircraft, which varied widely in size and speed. Two were multiengine planes that allowed onboard signal processing and real-time observation of the data during a flight. And two were flown on small tactical aircraft with onboard data recording and subsequent image formation processing and analysis after the flight. Much had to be learned in order to formulate the eventual design objective of installation on unmanned air vehicles for operation over remote, and often hostile, environments. The fifth system to be examined was an instrumentation radar installed on a computer controlled “cart” that would provide performance verification of target characterization by allowing high dynamic range collection of both foliage and ground penetration data [15].

They also provided extensive data on the characterization of both the clutter and the detection of objects under and near the clutter. Each of these experimental FOPEN SAR systems embodied a new technology that had the potential to enable operational system design. Details of these technologies and their experimental results for clutter and target characterization will be covered in subsequent sections.

One of those collections included both an X-band and a UWB UHF collection over Camp Roberts California to evaluate both foliage penetration and digital elevation model (DEM) generation. The image is of a small segment of the wooded area shown in Figure 14-8. These images were collected on the same day that several military vehicles had been placed under the foliage area known as “Sherwood Forest.” It is apparent that only the tops of the trees were visible in the X-band image. The X-band image on the left was from the IFSARE system, built by ERIM to provide high area coverage rate DEM with fine elevation accuracy [16].

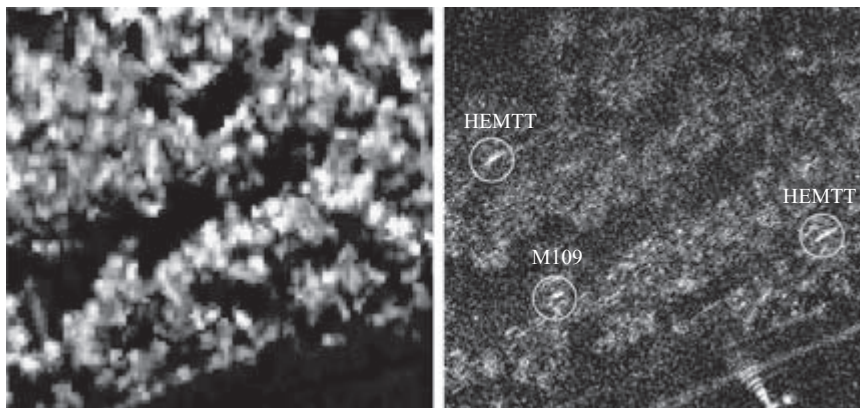
The image on the right was collected with the UWB P-3 FOPEN SAR, also built by ERIM [13]. The three tactical targets under the foliage were revealed only in the horizontally polarized UHF image. However, it is also clear that false-alarm rates are very high if only the horizontal polarization image were to be used. The strong return in the

foreground was from one of the instrumentation trihedrals deployed to calibrate the multiple polarization sensitivity. This comparison of X-band and UHF SAR provides sufficient evidence to many operational users of the importance of UWB SAR at VHF or UHF for detecting manmade objects under foliage. But it was important to quantify the performance with available technology prior to development of an operational system.

CARABAS I participated in the 1993 Maine FOPEN data collection, where several large vehicles were assembled in the open and under a tree-lined road to determine the effects of foliage on the detection of trucks [12]. The quantitative analysis of these factors will be presented in Section 14.4. However, it is illustrative to look at the same geometry and target array with two frequency bands: FOLPEN II at low UHF-band and CARABAS I at low VHF-band. Figure 14-9 provides a side-by-side comparison of the phenomenology at two collection frequencies [17].

14.4 | FOPEN CLUTTER CHARACTERISTICS

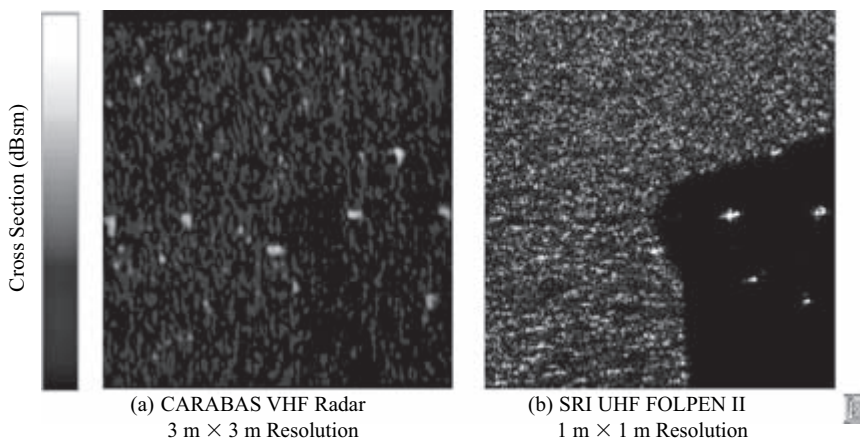
Scattering in a forest setting is a combination of many factors, as illustrated in Figure 14-10. This simple figure illustrates the process for multiple scattering and polarized returns from trees and vehicles. In general, all of the processes shown in the figure exist



X-band 2.5 m × 2.5 m, HH, IFSARE

UHF, 0.33 m × 0.66 m, HH, UWB P-3

FIGURE 14-8 ■ Comparison of X-Band and UHF SAR Image for a Forested Hide Position [©1998 IEEE [9]].

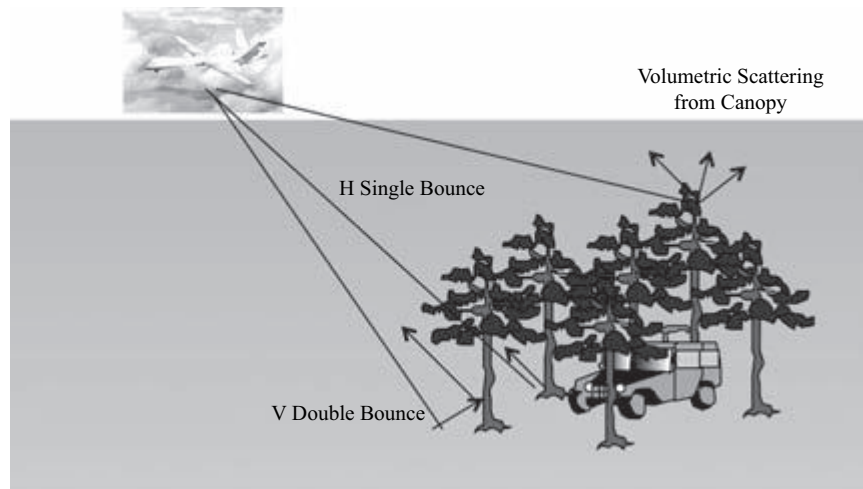


(a) CARABAS VHF Radar
3 m × 3 m Resolution

(b) SRI UHF FOLPEN II
1 m × 1 m Resolution

FIGURE 14-9 ■ Comparison of VHF and UHF Target Detection (1993 Maine Collection). [Source: MIT Lincoln Laboratory ©1995 IEEE [17]]

FIGURE 14-10 ■
Scattering of FOPEN
Radar Signals from
Forest and Targets.



for horizontal and vertical polarization, but with differing strengths of interaction. The basic effects that directly affect the detection and characterization of manmade objects and forests themselves are:

- The vertically polarized return is shown with a double bounce from the ground and the tree trunks. Both horizontal and vertical polarizations will exhibit the double-bounce phenomenon. However, the vertically polarized energy will penetrate the ground and interact more weakly with the tree trunk. Thus, the HH polarization double-bounce return will typically be stronger than the VV polarization return.
- The horizontal polarization is illustrated with a single bounce from the ground–tree interface. This resembles the return from a top hat over a conducting ground plane, and has similar characteristics at variable azimuth look angles. A departure from cylindrical-dihedral scattering will occur when the ground and tree trunks are not exactly perpendicular. As a result, the local terrain slope produces a strong influence on the magnitude of the return.
- Vertical polarization will react with thin vertical stems, which look like vertical dipoles. These show up strongly in VV polarization images, and are not observed in HH polarization images. When the branches are at an angle between horizontal and vertical, there will be returns with cross-polarization HV components.
- Vehicles will have more complex scattering depending on the number and orientation of panels. These scattering centers can also introduce cross-polarization effects, depending on the orientation to the radar. More importantly, the interaction of the surrounding trees and the ground-to-vehicle dihedral effect is important in the quantitative return from vehicles in dense foliage.
- Finally, the tops of the trees present random scattering to the radar depending on the number and orientation of the major branches. A significant effect is to depolarize the incident radiation and provide a component of cross-polarization. For low UHF band and VHF, the leaves have little effect on the principal polarization returns, but do provide a random phase fluctuation. These effects tend to be integrated out in SAR, but contribute to a defocus of the image in the presence of strong winds. This *internal clutter motion* is a major degradation of performance in GMTI operation.

14.4.1 Clutter Characterization

The data shown in Figure 14-11 are for variation of clutter backscatter versus frequency. The Panama rain forest data were collected with CARABAS I and FOLPEN II radar platforms. The Maine collection, which was carried out with the P-3 platform, obtained single-polarization data at UHF, L-band, and C-band. The clutter backscatter characteristics σ_0 in dB was obtained by dividing the measurement of RCS in a resolution cell by the area of the cell, i.e., dBm^2/m^2 . The mean clutter backscatter coefficients were obtained by averaging the log-scaled σ_0 values. The plots are exceedance curves giving the percentage of the data that exceed a clutter reflectivity level. The long tails in the curves are indicative of the strong returns from spiky clutter, especially in the bands that can penetrate the foliage canopy and scatter off of ground-trunk interactions [18].

The analysis of scattering data from Figure 14-11 indicates that the clutter is well represented by a lognormal distribution. The lognormal distributions are generated from the clutter backscatter magnitude statistics: mean (m) and standard deviation (sd). The lognormal probability density function is defined as [19]:

$$f(x) = \frac{1}{\sigma x \sqrt{2\pi}} \exp \left[-\frac{(\ln x - \mu)^2}{2\sigma^2} \right] \tag{14.2}$$

where

$\ln x$ = natural log of the scattering cross section

$$\mu = \frac{1}{2} [2 \ln(m) - \sigma^2] \tag{14.3}$$

$$\sigma^2 = \ln[(sd)^2/m^2 + 1] \tag{14.4}$$

The data in Figure 14-12, which is from the horizontally polarized P-3 UWB radar collection in Grayling, Michigan, illustrates the importance of examining FOPEN SAR clutter data. The data were taken at three grazing angles – 45, 30, and 20 degrees – and are plotted as the lognormal function $f(x)$ versus the clutter backscatter coefficient characteristics. It is difficult to compare the three grazing angle returns from just the lognormal function.

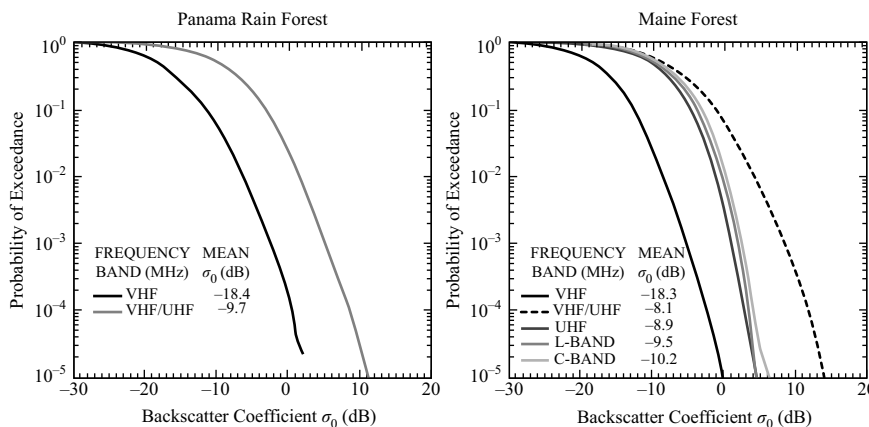


FIGURE 14-11 ■ Clutter Scattering Characteristics. [Source: MIT Lincoln Laboratory [18]]

FIGURE 14-12 ■
Lognormal
Distribution of UHF
Horizontal
Polarization Data
from P-3.

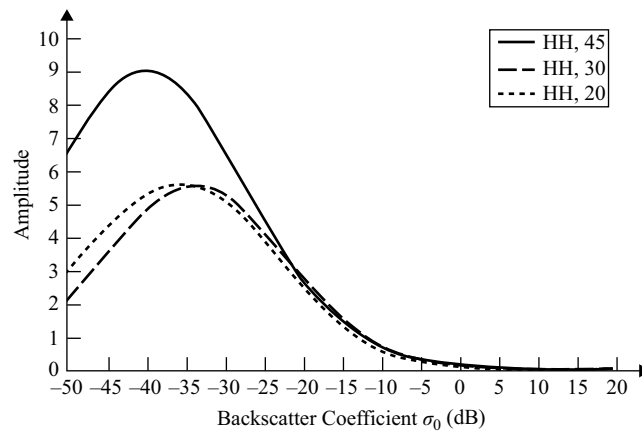
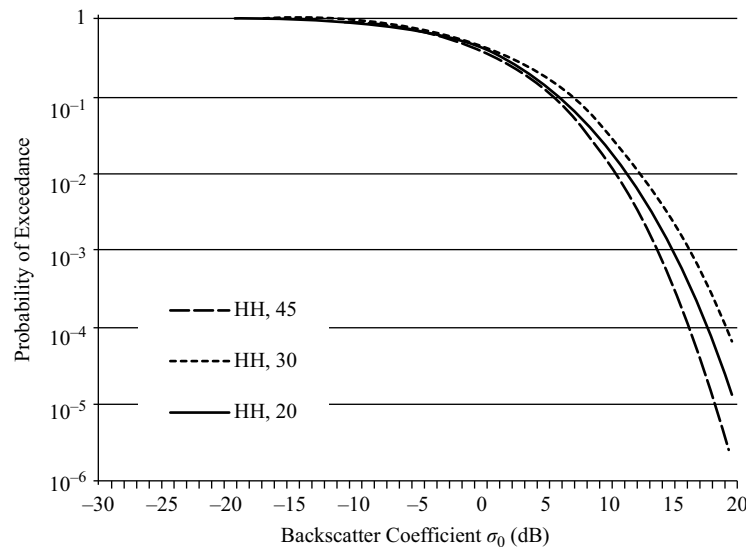


FIGURE 14-13 ■
Probability of
Exceedance of P-3
UWB Horizontal
Polarization.
[Source: MIT Lincoln
Laboratory ©2001
IEEE [19]]



However, when the probability of exceedance is examined, as in Figure 14-13, a better insight into the distribution of the clutter is obtained. The probability of exceedance in the data gives a measure of how strong the large scattering centers will contribute to the false-alarm density in the target detection. The statistics are obtained by determining the number of resolution cells containing a target backscatter coefficient above a particular threshold. A plot of the data is obtained from the clutter characteristics by computing the quantity (1 minus the cumulative density function). The difference in returns between the three grazing angles is due to a combination of the loss in signal through the foliage canopy and the interaction of the horizontally polarized energy from the ground–trunk interface. At a 20-degree grazing angle, the loss through the foliage is expected to be larger than at 45 degrees. In addition, the dihedral effect will be more pronounced at a 45-degree grazing angle than at 20 degrees.

The data collections were then needed to carefully examine the interdependencies on scattering due to frequency, polarization, foliage type, and interfaces between different types of clutter. These effects will be now presented using the probability of exceedance data graphs.

The effects of different foliage types will next be examined utilizing the fully polarimetric P-3 UWB SAR as shown in Figure 14-14. Fully polarimetric operation was critical to answer questions about the backscatter at fine image resolution. The data were calibrated against top hats and trihedrals, both in the open and under trees, to obtain accurate metrics on backscatter levels. The measurements were calibrated each day against the electromagnetic scattering model of a corner reflector in the open to determine the accuracy of the clutter reflectance estimation. A summary of the maximum measurement error for forest clutter versus grazing angle and polarization is given in Table 14-3.

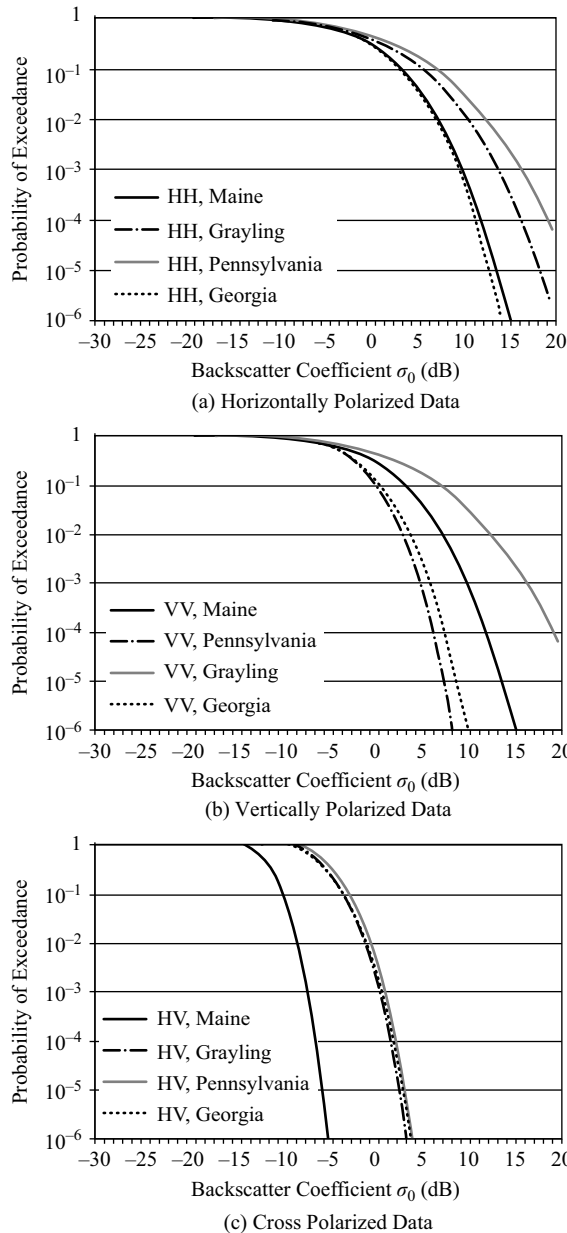
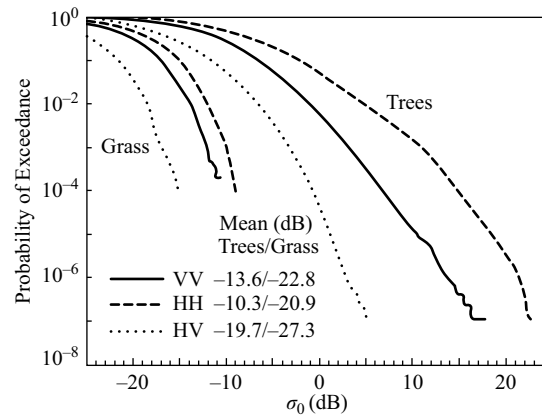
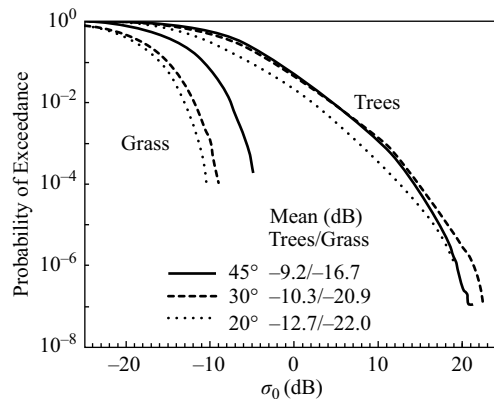


FIGURE 14-14 ■ UHF Polarization Backscatter Characteristics [dB] at Various Geographic Sites. [Source: MIT Lincoln Laboratory ©2001 IEEE [19]]

TABLE 14-3 ■ Maximum Error in Tree Backscatter Coefficient Measurement [dB] versus Depression Angle and Polarization [Source: MIT Lincoln Laboratory ©1999 IEEE [20]]

Channel	Depression Angle		
	20°	30°	45°
VV	0.6	0.5	1.5
HV	0.9	0.9	1.6
HH	0.7	1.3	1.0

FIGURE 14-15 ■ Clutter Backscatter Coefficient versus Polarization. [Source: MIT Lincoln Laboratory ©1999 IEEE [20]]**FIGURE 14-16** ■ Tree and Grass Clutter Backscatter Coefficient versus Grazing Angle. [Source: MIT Lincoln Laboratory ©1999 IEEE [20]]

Grassland areas were used to obtain a comparison of backscatter for open areas versus the trees. This is important to size the distributed clutter return within the scene. Figure 14-15 illustrates the data versus polarization and Figure 14-16 as a function of grazing angle. However, it should be noted that the cumulative scattering curves for forests have significant tails in the distribution. For horizontal polarization, the distribution is very pronounced due to the ground-trunk interaction. These strong localized returns will be very target-like at UHF.

The data represented in Figure 14-17 are shown superimposed on the lognormal distribution function for HH and VV polarization, and for interior trees and tree lines. Table 14-4 presents the values of mean and standard deviation for the four cases.

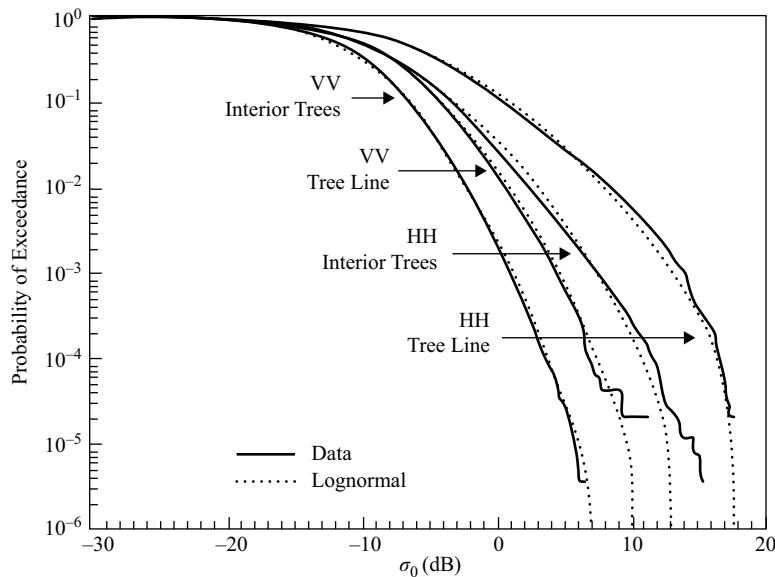


FIGURE 14-17 ■ Comparison of Tree Line and Interior Scattering versus Lognormal Model. [Source: MIT Lincoln Laboratory ©1999 IEEE [20]]

TABLE 14-4 ■ Clutter Backscatter Coefficient [dB] for Tree Lines and Interior Regions [Source: MIT Lincoln Laboratory ©1999 IEEE [20]]

	HH		VV	
	Mean	Std dev	Mean	Std dev
Interior region	0.22	0.48	0.11	0.13
Tree line	0.61	1.78	0.18	0.26

One of the important observations in the early FOPEN radar systems was the effect of tree lines on the clutter, and more importantly, the variation in both the size and Doppler signature of the clutter. These effects were a significant issue with both MTI radar and SAR systems, where stationary returns are important for coherent integration.

This set of data, presented in Figure 14-17, focuses on the difference in clutter return from the edges of the forest and the interior clutter. Horizontal polarization is significantly affected by the tree lines in both the mean and standard deviation of the returns. The tree line represents an elongated dihedral, enhancing the return for horizontal polarization. In addition, the ground–trunk interaction is not attenuated, giving much larger discrete scattering centers. What is not shown in the data is the temporal motion of the trees in a line. For SAR, this shows up as a smearing of the image. For GMTI radar, the internal clutter motion is expected to be a significant source of false alarms.

14.4.2 Foliage Attenuation

After the 1990–1992 FOPEN data collections, a database of attenuation statistics was published for horizontally polarized foliage attenuation for the Panama rain

forest (double canopy) and the Maine boreal forest (single canopy) collections (Figure 14-18). Significant conclusions provided from the analysis of these data include:

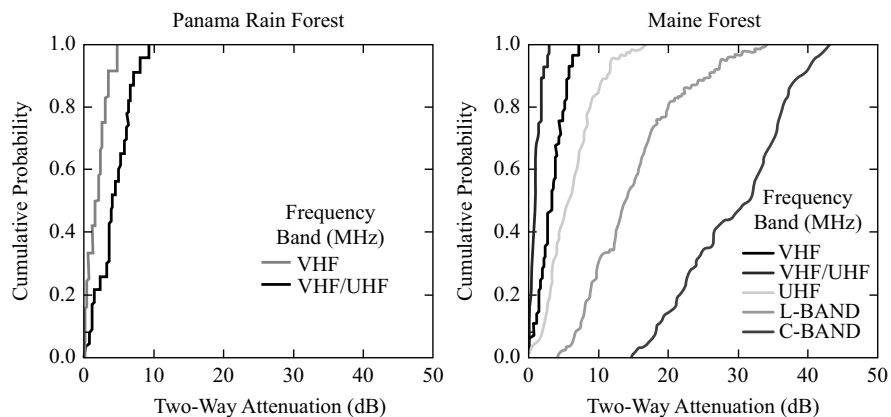
- VHF band (CARABAS I) attenuation was significantly less than at any other frequency tested in the FOPEN SAR characterization efforts. This is explained by the very long wavelength compared to the size of the tree branches and trunks.
- Rain forest attenuation was higher than the northern-latitude boreal forest attenuation. Again, the VHF-band attenuation was lower than the VHF/UHF data from the SRI FOLPEN II system. No higher-frequency data were collected in Panama.
- Microwave frequencies had such high attenuation that future FOPEN system development was mainly concentrated at the UHF band and below.

These data were also collected over several grazing angles for application to a system design. A distinction is made between single- and double-canopy forest, and is best differentiated by the height of the forest and the density of the tree canopy. Single canopy is most typical of new growth forests with heights of 15 meters or less, where the separation between trees allows for modest occlusion of the sky when observed from the forest floor. A typical range of occlusion is 40 to 70 percent, and is a first-order measure of the forest density. Double canopy is representative of old forests or tropical rain forests, where there is significant growth of smaller trees below the primary forest canopy. The height of these double-growth trees is over 15 meters, and the range of occlusion will be from 60 to 90 percent [19, 20].

The importance of foliage type can be understood by considering the propagation path length through the stand of trees, which will vary as $\sin^{-1}\gamma_g$, where γ_g is the grazing angle. At lower grazing angles, the propagation is through a significantly higher volume of trees. And for the double canopy, the density of the forest is significantly higher than with a single canopy. The factors of grazing angle, foliage type, and transitions between land cover will be developed later.

Bessette has characterized the losses from all of the FOPEN data collections [20]. A statistical analysis of the median two-way foliage loss versus grazing angle and frequency shows regular trends. A two-parameter model has been constructed for polarization and forest type (single or double canopy). The plots show the loss predictions for single and double canopy at horizontal and vertical polarization at a 450-MHz frequency.

FIGURE 14-18 ■ Attenuation of Foliage-Penetrating Radar Signal versus Frequency - Panama Rain Forest and Maine Pine Forest. [Source: MIT Lincoln Laboratory [18]]



In conducting system design, these factors should be considered to bound the expected performance on detecting tactical targets beneath the foliage. A two-parameter model has been constructed for polarization and forest type (single or double canopy) [20]:

$$L_{2-way} = \frac{(-\alpha_F)(freq)^{\beta_F}}{\sin(\gamma_g)} \tag{14.5}$$

where

- α_F = foliage attenuation scalar factor
- β_F = FOPEN radar center frequency exponential factor
- γ_g = grazing angle to the local clutter patch

Note that there are ranges of parameters for foliage loss, as shown in Table 14-5. These ranges can be indicative of foliage type (e.g., deciduous or conifer) or of the variations within a particular forest (e.g., heavy growth or light new growth).

The plots in Figure 14-19 show the two-way loss prediction for a signal at both horizontal and vertical polarizations, calculated from Equation (14.5) at a 450-MHz

TABLE 14-5 ■ Median Foliage Attenuation Model Parameters for Single and Double Canopy [Source: MIT Lincoln Laboratory ©2001 IEEE [19]]

Polarization	Single Canopy		Double Canopy	
	α_F	β_F	α_F	β_F
HH	0.18±0.045	0.53	0.34±0.085	0.53
VV	0.30±0.073	0.47	0.71±0.1775	0.47

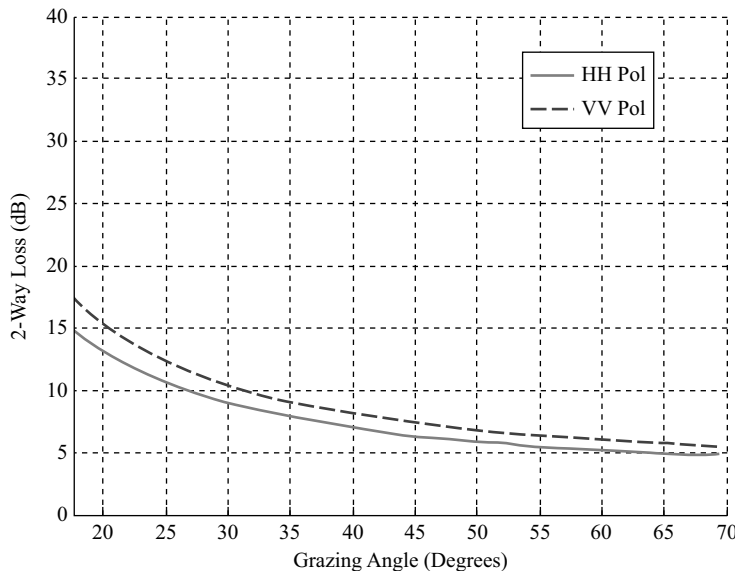


FIGURE 14-19 ■ Single-Canopy Foliage Loss (Maine Data - 450 MHz).

frequency. It can be seen that there is little difference in single-canopy loss between horizontal and vertical polarized propagation. However, there is a measureable increase in the loss at low grazing angles.

Figure 14-20 illustrates the two-way loss for double-canopy forests. These forests are more typical of the jungles near the equator. The horizontally polarized loss is significantly lower than for vertical polarization. Moreover, the low grazing angle losses are increased to above 20 dB for both propagation polarizations. These losses are a major design driver for any FOPEN radar that needs to operate in jungle environments.

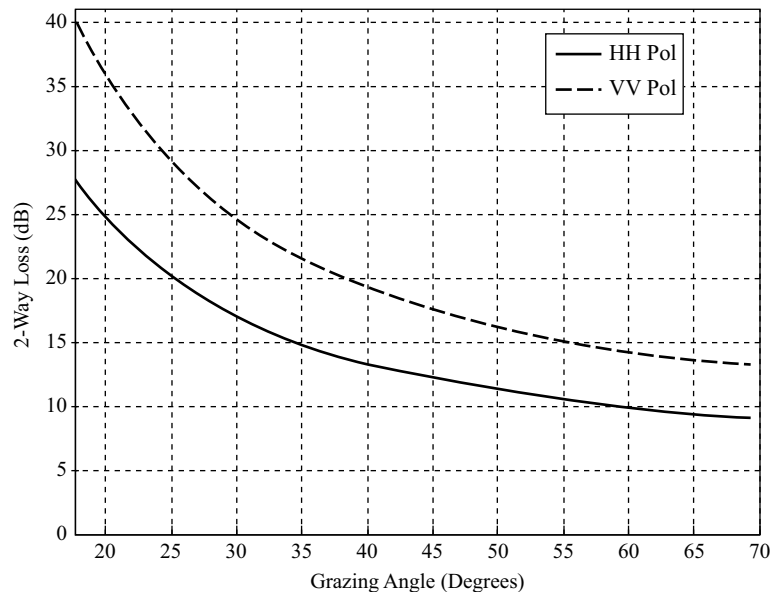
14.5 | IMAGE FORMATION

The integration angles required as a function of frequency and platform speed are an important system consideration for FOPEN SAR. They have been useful in explaining the concept of operations for VHF and UHF SAR platforms in comparison to the previous microwave SAR systems. If one needs to see below the tops of the trees, plans for operating the platform for lengthy collections during a single pass are required. Because of the long integration times for collecting fine image resolution, other areas of interest within the field of view of the airborne platform are unavailable for surveillance.

Section 14.3 developed the relationship between the integration angle θ_I and the cross-range resolution δ_{CR} . Because of the assumption on range to the scene being large compared to the SAR integration length, the cross-range resolution is independent on range and L_{SAR} . However, this assumption is not valid for UWB SAR, as seen in Figure 14-21. The more exact expression for cross-range resolution is given by [10]:

$$\delta_{CR} = \frac{\lambda_c k_{CR} R_C}{2 L_{eff} \sin \alpha_{DC} \cos (\theta_I/2)} \quad (14.6)$$

FIGURE 14-20 ■
Double-Canopy
Foliage Loss
(Panama Data - 450
MHz).



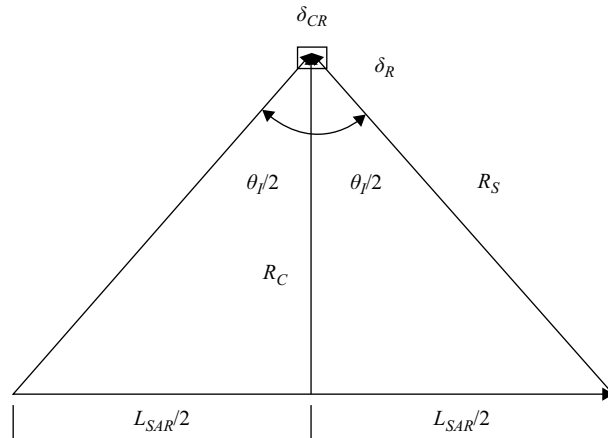


FIGURE 14-21 ■
Geometry for UWB
SAR Resolution
Calculation.

where

λ_c = wavelength at center frequency

k_{CR} = resolution spreading factor due to aperture weighting

α_{DC} = Doppler cone angle

θ_I = azimuthal SAR image collection angle

L_{eff} = effective SAR integration length

R_C = slant range from image point to center of SAR collection

In Figure 14-21, the imaging is assumed to be broadside with $\alpha_{DC} = \pi/2$. The $\cos(\theta_I/2)$ transforms the slant range to the center of the SAR image collection, and the L_{SAR} is changed to an effective SAR length L_{eff} , which can be solved from Equation (14.6), using the cross-range resolution from Equation (14.1) and trigonometric manipulations [21]:

$$L_{eff} = \frac{k_{CR} \lambda_c R_C}{2 \delta_{CR} \sqrt{1 - \left(\frac{k_{CR} \lambda_c}{4 \delta_{CR}} \right)^2}} \quad (14.7)$$

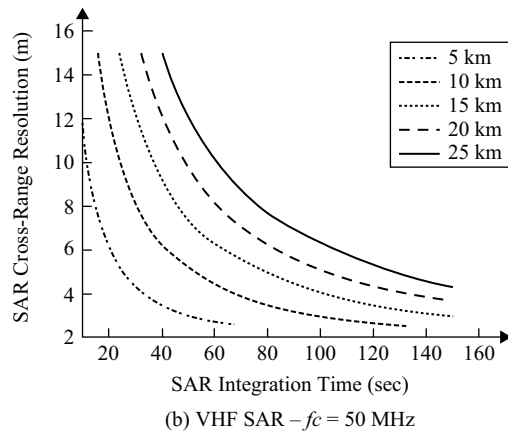
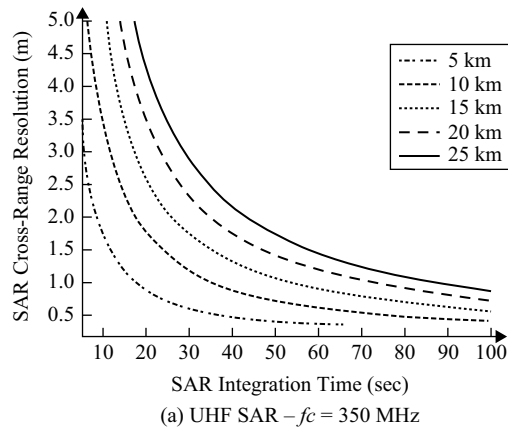
The SAR integration time t_I for a UWB SAR is now determined by the effective synthetic aperture length and the speed of the platform v_P , and can be approximated by

$$t_I = \frac{L_{eff}}{v_P} \quad (14.8)$$

Figure 14-22 compares the integration times at VHF and UHF at a variety of stand-off ranges when collected from a platform traveling at 150 m/s. For microwave-frequency SAR, a cross-range resolution of better than 1 meter can be easily obtained in less than 4 seconds at a range of 24 kilometers. This time is contrasted with 20 seconds with UHF FOPEN SAR. At VHF, it is a challenge to obtain a 3-meter cross-range resolution, and the required collection time will be greater than 60 seconds [22].

The impact on the system is major. First, an entire pass is consumed in collecting a single swath of data. In addition, the variation of the terrain can be large over this

FIGURE 14-22 ■
FOPEN SAR
Integration Time,
 $V_p = 150$ m/sec.



geographic area. The demands on the motion measurement system and motion compensation are amplified. As will be shown in the next section, there are limitations on the choice of algorithms for efficient and effective focus of the image.

Another aspect of UWB SAR is the effect of range curvature on the image. Figure 14-23 illustrates the impact of collection angle on swath width. Data must be collected from the beginning of the swath through to the end in order to support the resolution in the middle of the swath length. As a result, the slant range extent of the collected data must be larger than the maximum swath width so that the support data at the end of the swath coincide with the pixels in the middle. These considerations will now be quantified.

The integration angle and the range to the swath define the range curvature ΔR_0 . At broadside, the range to the edge of the swath is indicated as R_0 . However, at the edges of the integration angle, an additional slant range swath interval ΔR_0 must be collected, where

$$\Delta R_0 = \left[\frac{1}{\cos(\theta_I/2)} - 1 \right] R_0 \quad (14.9)$$

These additional range samples must be collected for the entire swath length L_S plus the SAR integration length L , to fully support the cross-range resolution.

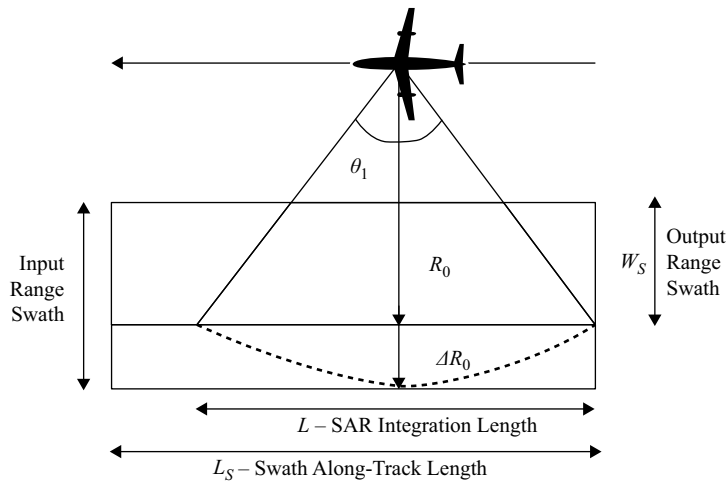


FIGURE 14-23 ■ Effect of Integration Angle on Range Swath Collection.

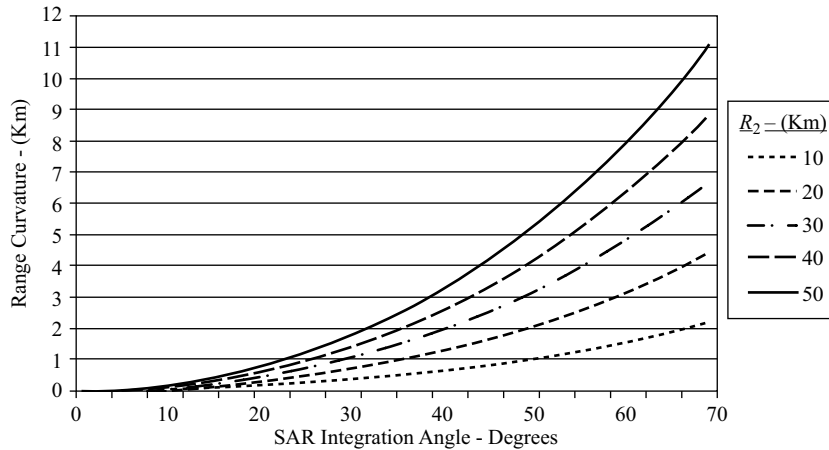


FIGURE 14-24 ■ Range Curvature as a Function of SAR Integration Angle.

Figure 14-24 quantifies the impact on additional range samples as a function of range to the edge of the swath. At a nominal 50-km stand-off range, an additional 2.4 km of range samples must be collected for a 33-degree integration angle at UHF and 9.8 km for 66 degrees at VHF. These must be factored into the design of the SAR waveform, the signal processing requirements, and the onboard memory storage.

The first aspect of UWB SAR to be considered is the swath length, where a sufficiently long integration aperture must be collected to form the desired cross-range resolution. The number of pulses to be integrated N_P , which can be approximated based on the range to the swath center R_C and the desired resolution δ_{CR} , is given by

$$N_P = \frac{k_S R_C \lambda_c}{2 \delta_{CR}^2} \quad (14.10)$$

where

- N_P = number of pulses in the synthetic aperture
- k_S = oversample ratio for data collection

R_C = range to swath center

λ_c = wavelength at UWB SAR center band

δ_{CR} = cross-range resolution

The minimum number of range cells N_R in the synthetic aperture can be expressed by the width W_S of the SAR swath and the added range ΔR_0 to provide for range curvature:

$$N_R = \frac{(W_S + \Delta R_0)}{\delta_R} \quad (14.11)$$

When there is an oversampling of the data in the fast-time dimension, Equation (14.11) needs to be multiplied by the oversampling factor. For UHF and VHF SAR, the number of pulses can be very large due to the long collection times. The along-track data collection is similarly determined by the resolution and the speed of the platform.

It should be noted in Figure 14-23 that the area in the swath is not fully covered by the SAR integration length L . Only the pixels at the minimum range to the swath have the full sample support for resolution. As a result, it is common to break the swath up into smaller along-track segments and form several subapertures, such as in stripmap SAR.

14.5.1 SAR Phase History

The SAR operates by collecting a series of pulses, as shown in Figure 14-23, yielding a phase history to be processed for image formation. This phase history changes continuously as a function of time along the SAR integration path, and it is normal to define a *reference point* at a range R_C to calibrate the coherent integration process. The round-trip delay to the antenna will be $2R_C/c$. For a stripmap SAR, R_C will be the constant range to the center of the stripmap, assuming a straight flight path. For a spotlight SAR mode, the central point of the image (x_c, y_c) will be constant, and the calibration, or motion compensation range, will vary as the SAR image is collected. In general, the reference phase function for SAR image construction is a constant of unity amplitude that is given by [10]:

$$S_{ref} = \exp \left[j \left(\omega_c (t - 2R_C/c) + \pi \gamma_p (\hat{t} - 2R_C/c)^2 \right) \right] \quad (14.12)$$

where

ω_c = radian frequency at the center of the SAR bandwidth ($\omega_c = 2\pi f_c$)

R_C = slant range to the center of the image

T = pulse repetition interval

$\hat{t} = t - nT$ = slow-time coordinate

n = pulse number in slow-time

γ_p = linear frequency modulation (LFM) modulation index in radians per second

The received signal is obtained from the return from each point $R_t(x_t, y_t, z_t)$ in the scene with a signal amplitude of $a_T = \sqrt{\sigma_T}$. Each point in the synthetic aperture has a

round-trip time delay from the transmitter to the receiver of t_d . Three factors make up the measurement of time delay: motion between successive transmit pulses, motion during transmission and reception of a pulse, and motion between transmission and reception of a pulse. Motion between and during pulses does occur and contributes to a space-invariant defocus of the image. However, this effect can be removed with autofocus, and is normally ignored in the image formation process. The two-way time delay to each point in the SAR image is given by

$$t_d = \frac{2R_t}{c} \quad (14.13)$$

The distance R_t varies during each point in the SAR collection path, as shown in Figure 14-27. This distance is given by the relation

$$R_t = \sqrt{(x_a - x_t)^2 + (y_a - y_t)^2 + (z_a - z_t)^2} \quad (14.14)$$

The coordinates $R_t(x_t, y_t, z_t)$ are the true three-dimensional location of the scattering points on the surface, and the points $R_a(x_a, y_a, z_a)$ are the measured locations of the antenna phase center on each received pulse. Note that R_a will have errors due to motion compensation inaccuracies, as well as geolocation errors in the exact position with respect to the image surface. Given these coordinate definitions, the received signal phase history is expressed by

$$S_R(n, t) = a_T \text{rect} \left[\frac{\hat{t} - 2R_t/c}{T_p} \right] \exp \left[j\omega_c \left(t - \frac{2R_t}{c} \right) + j\pi\gamma_p \left(\hat{t} - \frac{2R_t}{c} \right)^2 \right] \quad (14.15)$$

where

T_p = modulated pulse width

$\text{rect}()$ = function equal to 1 for $\hat{t} \in [-T_p/2, T_p/2]$, and 0 otherwise

a_T = signal amplitude

One should also note that the transmit amplitude a_T is assumed to be constant. This constancy is for an ideal system, where the transmit amplitude does not fluctuate from pulse to pulse or across the frequency band. For more exact image processing, the waveform model must take into account any changes or modulation of the transmit function caused by either intended amplitude changes or unintended changes due to transmit and antenna power-spectral characteristics.

14.5.2 Image Formation

The formation of UWB SAR images has been widely published. Two algorithms were applied to the early FOPEN SAR systems. The first successful FOPEN SAR imaging was accomplished with the back projection algorithm (BPA) [23, 24]. In this approach, each pulse is coherently integrated into the image plane by calculating the time delay from the imaging platform. BPA is a computationally intensive algorithm that requires $O(N^3)$ operations. An alternative algorithm is the range migration algorithm (RMA), which applies an approximation of the range and Doppler motion of each pixel during

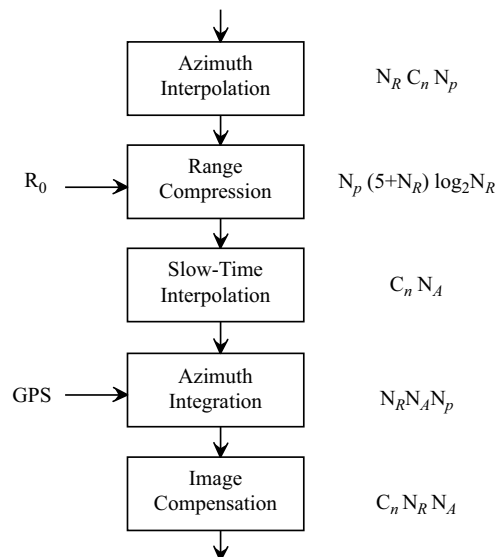
the SAR collection [10]. The RMA is a more efficient processing approach, but suffers from increased demands on motion compensation for realistic synthetic aperture lengths. RMA is an $O(N^2 \log_2 N)$ processing approach that was considered to be more practical for real-time operation during the 1990s. Only BPA will be presented to illustrate the generic FOPEN SAR signal processing approach.

BPA is a time domain convolution of each point on the image surface with the radar waveform in both slow and fast time. To form a SAR image, a time domain correlation is formed with each scatterer. This correlation step for an image of N_A pixels in along-track dimension and N_R pixels in the range dimension using N_P transmitted pulses requires $N_P N_A N_R$ complex operations. The advantage of this approach is there are no approximations to the range and Doppler contributions to the image formation, and it can be focused directly to a DEM. When the transmitter location and velocity are accurately known, and a geographically stabilized image plane can be maintained on Earth's surface, the image will be well focused. If these criteria can be maintained over the wide geometry, there is no theoretical degradation of the image focus.

However, the process of forming the image was computationally expensive, and was determined not to be suitable for real-time implementation in early FOPEN SAR systems. As the speed of computers and the combined GPS/INS systems have improved, the BPA has become a serious candidate for a real-time airborne FOPEN SAR system. Furthermore, research in fast BPA processing has yielded an approximation based on subapertures that reduce the computation by a factor of $\sqrt{N_P}$ [25, 26].

The processing flow for the BPA is shown in Figure 14-25, along with an estimate of the processing requirements for each stage. The first block is needed to compensate for nonuniform spacings of the transmitter locations during radar transmission. Each pulse is transmitted at a time determined by T , the pulse repetition rate of the radar. These points are nominally established to be on half-wavelength centers, and determined by the velocity of the aircraft and the center wavelength λ_c of the radar. Based on the inertial measurement system, the position and velocity of the aircraft are measured and compared with the desired transmit position.

FIGURE 14-25 ■ Computational Flow of Back Projection Algorithm Image Formation.



The SAR image is formed by correlating the transmit waveform with each pixel on the image surface:

$$s_M(t, u) = s(t, u) \otimes s_T(-t) \quad (14.16)$$

where \otimes is the convolution symbol. The time domain correlation image is given by

$$f(x_i, y_j) = \int_u s_M[t_{ij}(u), u] du \quad (14.17)$$

where the time delay from the SAR platform position u to each pixel in the image is given by

$$t_{ij} = \frac{\sqrt{x_i^2 + (y_j - u)^2}}{c} \quad (14.18)$$

Therefore, the time delay to each point on the surface must be calculated at each position along the synthetic flight path. It can be appreciated that knowledge of the position, velocity, and orientation of the SAR platform is needed at each point in the SAR map. In addition, the DEM of the SAR image surface needs to be known to correctly calculate the time delay to the surface. Otherwise, if the image is formed in a plane, there will be issues with focus and position for each voxel of the image.

Because the distance from the transmitter to each point on the ground varies with slant range and angle, it is important to interpolate the pulse-compressed data on a pulse-by-pulse basis along the slant range dimension to each point on the ground. Figure 14-27 shows the basic interpolation used for resampling data in a generic slant range and angle (i_{SR}, θ) coordinate system into the image coordinate system (X_0, Y_0). The interpolation is accomplished by up-sampling the phase history function from the nonuniform sample spacing to a uniform spacing coordinate system:

$$y(m) = \sum_{k=-\infty}^{\infty} \hat{x}(k) h(m - k) \quad (14.19)$$

where

$$\hat{x}(m) = \begin{cases} x\left(\frac{m}{M}\right) & m = 0, \pm M, \pm 2M, \dots \\ 0 & \text{otherwise} \end{cases} \quad (14.20)$$

$$h(m) = \sin c\left(\frac{m}{M}\right) \quad (14.21)$$

The along-track samples are shown as the solid circles along the u -axis for the phase history given by the unit vector i_{SR} at an angle θ with respect to the image coordinate system (X_0, Y_0). The open circles are the resampled values of the function $y(m)$ on the image Y_0 axis.

The operations complexity for data interpolation is given by [10]:

$$C_p = 0.5 N[(L_f - 1) DSR + 1] \quad (14.22)$$

where

N = number of output points

L_f = length of the resample filter

DSR = down-sample ratio of output-to-input sample

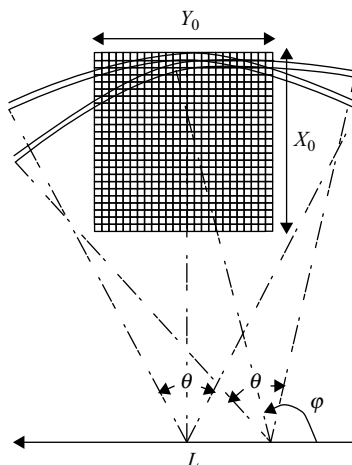
Next, the radar waveform in the fast-time dimension needs to be compressed so that the required range resolution is obtained. This requirement for early pulse compression differs from both stripmap and polar algorithm SAR processing [10]. But it is important to perform range compression prior to the time domain correlation of the transmit signal with the signal received from each point on the image surface. The pulse compression will be referenced to a range delay $2R_C/c$ corresponding to the central reference point in the image. The pulse-compressed signal $s_{PC}(x,t)$ is formed by the process of [27]:

$$\begin{aligned} S_{PC}(u, t) &= \sum_{N_R} s(u, t)^* \exp\left(-j\omega_c\left(t - \frac{2R_C}{c}\right) - j\gamma\left(t - \frac{2R_C}{c}\right)^2\right) \\ &= \sum_{N_R} s(u, t)^* s_0(u, -t) \end{aligned} \quad (14.23)$$

The process is accomplished through the use of an FFT in the range dimension on each pulse return, multiplying by the time delay of the slant range R_C to the center of the scene, and then taking an IFFT to return the spatial domain. The range-compressed returns from 15 spatially separated targets are shown in Figure 14-28. The amount of range curvature in the SAR signal collection is easily seen in the figure. Next, the pulse-compressed signals are coherently added at each image location on a pulse-by-pulse basis, as depicted in Figure 14-26, until the entire synthetic aperture has been collected. However, it is important to resample the input data $s_M(t,u)$ accurately to the individual image locations $[x_i, y_j]$ or image resolution and focus will be lost in the processing.

The third processing step is to up-sample the fast-time waveform to enable this alignment. Figure 14-26 illustrates the range resolution of the waveform transmitted from two points on the synthetic aperture within the image area of X_0, Y_0 . Depending on where the radar phase center lies along the aperture of length L , an accurate map of each pulse and range bin must be added to the appropriate pixels. Typically, the resampling

FIGURE 14-26 ■
SAR Range
Resolution
Superimposed on
Image x, y Plane.



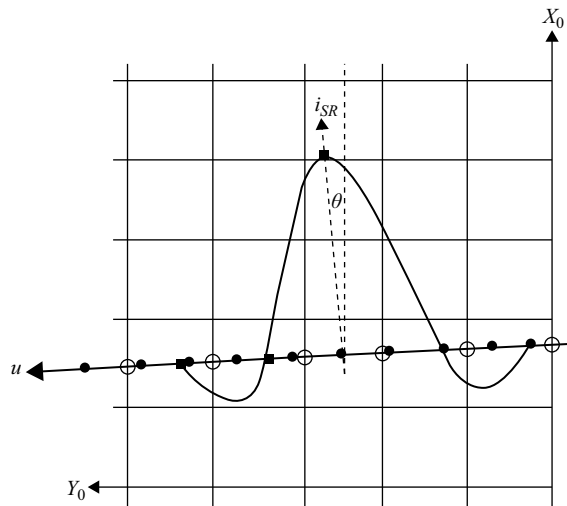


FIGURE 14-27 ■ Interpolation Function for Along-Track Samples [10].

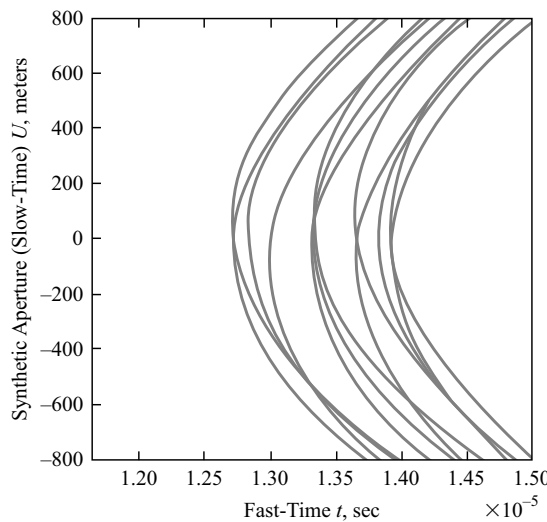
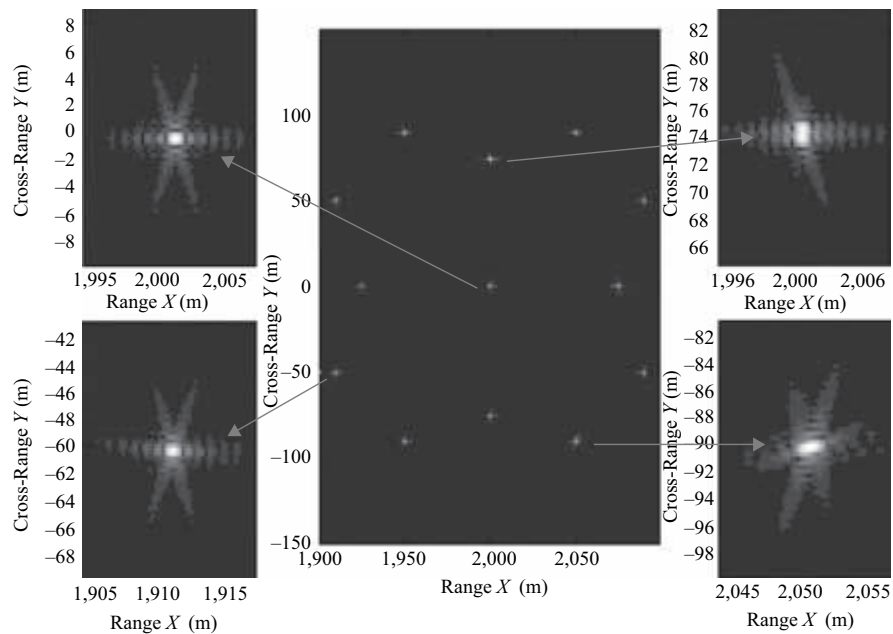


FIGURE 14-28 ■ Range Compression for 15 Target Examples.

process will utilize 10 to 20 samples on each side of the cell that is to be corrected. Next, the nearest point to the image resolution grid is chosen and the value is accumulated. This process is repeated for each pulse and location of the SAR platform.

Figure 14-29 illustrates the BPA image formation for the 15 target locations simulated in the SAR image. Two of the single targets (σ_1 and σ_{11}) are shown expanded, providing the image pulse response with no defocus of the image. This is as expected, since the motion compensation was exact and there were no spectral notches in the transmit pulse. Two additional expanded images are shown for the target pairs (σ_3 and σ_{14}) and (σ_8 and σ_{15}). The image points show the separation in resolution of target locations with three times the range and cross-range resolution. However, it should be noted that there has been no aperture weighting applied to the images. With either range or cross-range weighting, these resolutions will be degraded by the δ_R and δ_{CR} factor.

FIGURE 14-29 ■
Reconstructed UWB
Image with Back-
Projection
Algorithm.



The BPA processing requires accurate, detailed knowledge of the system characteristics. The range delay to each point in the antenna beam and for each pulse in the synthetic aperture depends on several variables:

- The amplitude and phase, in both the X and Y dimensions, affect the integration at each pixel in the scene.
- The focus will depend on accurate knowledge of the orientation and velocity of the aircraft and antenna, as well as the image plane on the surface of the earth.

Because of the wide antenna angles, especially for VHF SAR, Doppler ambiguities need to be characterized and compensated. If this is not done, the returns at wider angles or Doppler ambiguities will fold into the image as artifacts. If these factors can be properly accomplished, the back-projection algorithm will provide the largest depth of focus. This is due to the fact that each pixel is focused to the position, velocity, and propagation delay to the radar. Early in the development of FOPEN SAR, efficient algorithms were sought to lower this operations count.

Several development efforts on reducing the computational complexity of the BPA class of algorithms have been reported [24, 25]. The approaches are generally based on segmenting the apertures into subapertures and compensating for range curvature within the image by applying higher-order corrections. The algorithm reproduces images generated by standard back-projection pixel by pixel to any required tolerance, but it runs roughly $\sqrt{N_P}$ times faster for a, N_A -by- N_R pixel image. Furthermore, fast back-projection retains the advantages of standard BPA: perfect motion compensation for any flight path, low artifact levels, unlimited scene size, perfect and focus for arbitrarily wide bandwidths and integration angles.

14.6 | RADIO FREQUENCY INTERFERENCE

This section will cover the significant design factors that are needed to operate an FOPEN SAR under most operational conditions. Because of the worldwide regulation of the RF frequency spectrum for telecommunications and active sensing operation, it is necessary to accommodate the limitations on power spectral density for transmission of the SAR waveform. Equally as important is the need to remove the dense, high-power transmissions that will be intercepted by the wide beamwidth SAR antenna and that will affect the SAR receiver dynamic range and image formation processing. An example of this dense interference, along with the general sources of RF energy in the Adelphi, Maryland, area, is given in Figure 14-30 [28].

There are two parts to the RFI environment: 1) the bands that must be avoided due to U.S. federal regulations and 2) the frequencies that represent strong interference to the FOPEN SAR. It is evident that no part of the UWB spectrum is allocated for these radars. The proscribed transmit frequencies, which are regulated in the United States by the Federal Communications Commission (FCC) and the National Telecommunications and Information Administration (NTIA), have strict requirements on the bandwidth and power spectral density of any UWB system operating in the environment. There are similar regulatory bodies in the rest of the world, which must be considered when designing an FOPEN system for military or civilian use, for example, the International Telecommunications Union (ITU) and World Radiocommunication Conferences (WRC).

The radio and television transmissions are particularly detrimental to the SAR received signal, and hence, the image quality. As can be seen in Figure 14-30, the narrowband amplitude or frequency-modulated (AM and FM) transmissions are from 20 to 60 dB above the radar noise level. These interferences must be removed to provide the

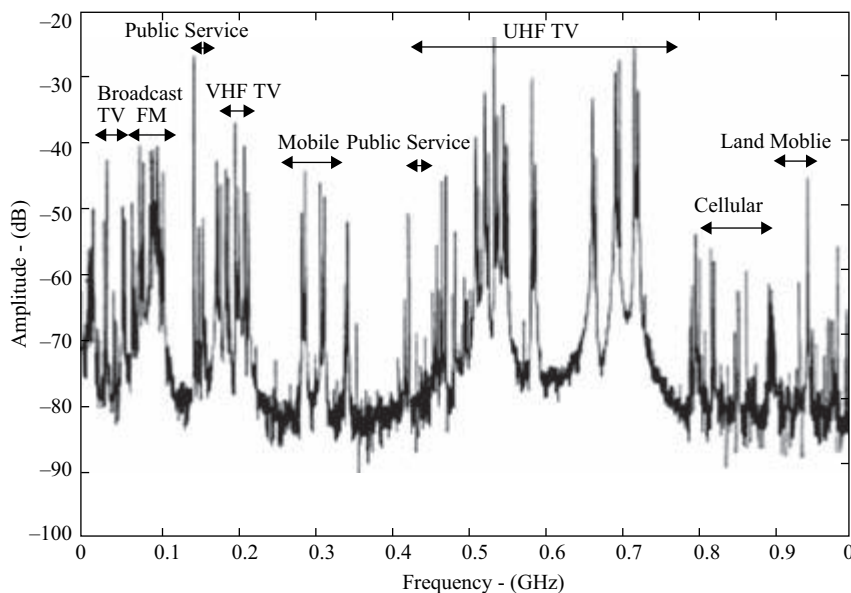


FIGURE 14-30 ■ Radio Frequency Spectrum Affecting FOPEN SAR Design [28].

necessary sensitivity for either characterization of terrain features or detection of targets under the foliage.

The mixture of FOPEN SAR experimental sensors and platforms illustrated the variation in design approach for transmit waveforms. Most of the early experimental FOPEN radars either ignored the issue of interfering with sensitive or emergency receiver frequencies, or avoided them by limiting bandwidth or segmentation of the frequency coverage. However, there was significant scrutiny of all UWB sensor operation during the growth in Wi-Fi system development in the late 1990s. As a result, the number of choices in UWB radar transmitter design was limited, and those few need to be incorporated into any new system development.

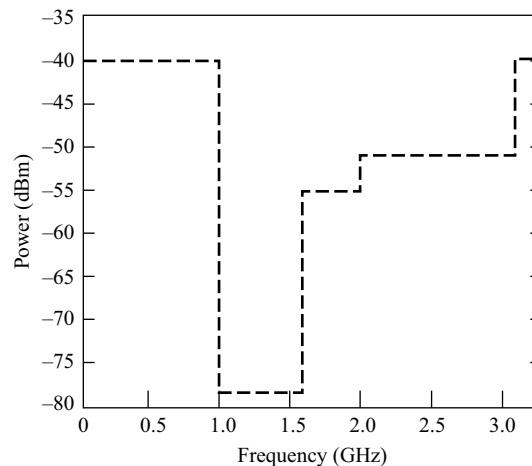
The NTIA regulations on UWB transmission specify the power density that can be transmitted by an unrestricted intentional radiator, within the fundamental frequencies, and at any out-of-band harmonics. The NTIA requires that any emissions from a UWB transmitter operating under the Part 15 provisions shall not exceed an equivalent isotropically radiated power (EIRP) density level over the frequency bands, as shown in Figure 14-31. The power density, which is specified at a 3-meter distance in a 1-MHz bandwidth, serves as the top-level requirement for qualifying the UWB device for unrestricted operation [29]. Since these power levels are significantly lower than required by any FOPEN radar, they should be used only as a first approximation for calculating the interference level at a remote receiver.

14.6.1 Transmit Waveform Design for the RFI Environment

In order to obtain a license to operate any UWB radar system, the NTIA is required to assess the amount of interference the radar will have on any existing system operating within the same frequency range. The NTIA requirements are expressed in terms of a frequency mask, shown in Figure 14-31. This is predominantly a case of radar intercept analysis by a sensitive receiver. The key parameter to be considered is the signal-to-noise ratio SNR_I at a victim (intercept) receiver [30]:

$$SNR_I = \frac{P_T G_{TI} G_I \lambda_T^2 L_I}{K_B T_0 N F_I B_I (4\pi R_{TI})^2} \left(\frac{G_{IP}}{G_{IPN}} \right) \quad (14.24)$$

FIGURE 14-31 ■
NTIA Frequency
Mask Required for
Part 15 Compliance
[29].



where the parameters are

P_T = peak radar-emitted power

G_{TI} = gain from the transmitter in the direction of the intercept receiver

G_I = gain of the victim receiver

λ_T = wavelength transmitted

L_I = loss between the radar and the victim receiver

$k_B T_0 N F_I B_I$ = noise power at the receiver

R_{TI} = range from the transmitter to the receiver

(G_{IP}/G_{IPN}) = receiver processing gain with respect to noise, plus any losses

The victim receiver sensitivity is related to the received power P_I and the antenna gain G_I :

$$S_I = \frac{P_I}{G_I} = \frac{P_T G_{TI} \lambda_T^2 L_I}{(4\pi)^2 R_{TI}^2} \left[\frac{B_I}{B_T} \right] \quad (14.25)$$

The system sensitivity represents the power received by a victim receiver at its location such that the received power density results in the required SNR to be detected. When there is a difference in the bandwidth of the receivers, the power density is reduced by the ratio (B_I/B_T) . If the system sensitivity levels from the Part 15 frequency mask are used, a first-order assessment of the interference ranges from a candidate SAR system can be calculated. It should be noted that the NTIA Part 15 as expressed in Equation (14.25) assumes the intercept receiver is coherent with the transmitted receiver. This is a much more conservative approach, as the intercept receivers will normally be incoherent. This assumption has been a contentious point between FOPEN SAR developers and the regulating bodies.

Given an FOPEN radar with 1,000-watt peak power, 200-MHz bandwidth, and a 10 percent duty factor, the sensitivity at a receiver can be calculated [31]. This is shown in Figure 14-32 where the antenna gain is assumed to be 6 dB and the antenna is pointed

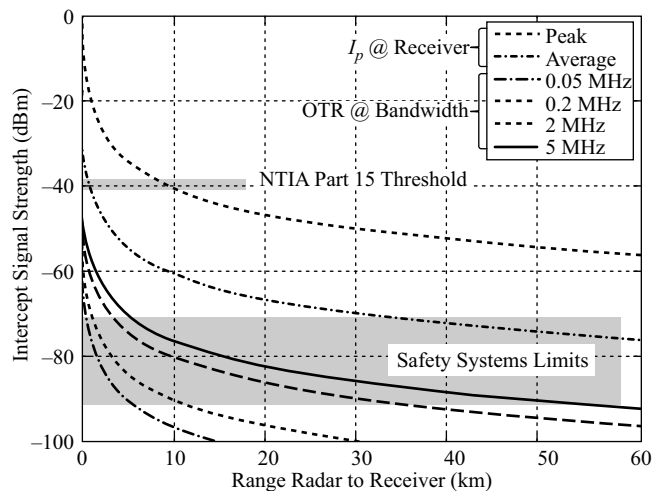


FIGURE 14-32 ■ Intercept Power of Radar Pulse Transmission as a Function of Range [31].

TABLE 14-6 ■ VHF/UHF Frequency Bands Requiring Transmitter Avoidance [29]

Function	Freq (MHz)	Function	Freq (MHz)
Radio astronomy	37.5–38.25	AIS (Automatic Identification System)	162.0125–167.17
Radio astronomy	73–74.6	Fixed mobile, public safety, forest fighting	167.72–173.2
Aeronautical radionavigation	74.8–75.2	Fixed mobile, emergency	240–285
Aeronautical radionavigation	108–121.94	Fixed mobile, radio astronomy	322–335.4
Aeronautical mobile location	123–138	Radio navigation satellite	399.9–410
Mobile satellite (earth to space)	149.9–150.05	Radio astronomy	608–614
Maritime mobile safety	156.52475–156.52525	Aeronautical radio navigation satellite	960–1240
Maritime mobile distress	156.7–156.9	Radio navigation satellite	1,300–1,427

directly at the victim receiver. Various bandwidths of intercept receivers are evaluated, between 50 KHz and 5 MHz. The power received is calculated based on the ratio of the victim receiver and the total bandwidth of the SAR LFM signal BW. If the plan for SAR collection is closer than 2.0 km for the 5-MHz receiver, the radar will violate the FCC Part 15 specification. Moreover, it is important to note that many of the sensitive receivers have EIRP avoidance thresholds lower than Part 15 – often as low as –90 dBm. Because of these receiver intercept requirements, a different model of the radar waveform is required.

Table 14-6 lists the frequency bands that require special avoidance in UWB operation. It is evident that there are few “empty” spaces in VHF or UHF bands where the freedom for complete operation can be achieved. Early in the FOPEN SAR development process, signal intercept collections and analyses were carried out to determine the extent of the problem. If the problem were one of removing RFI alone, there would not be a frequency allocation problem. In order to get a license to operate an FOPEN SAR in most of the developed world, however, there is a strict requirement to avoid frequencies that are sensitive to both civilian and government operation.

This section will treat the problems of avoiding transmitting signals at the prescribed frequencies. This is a very important part of FOPEN radar development, since most areas in the world will not provide frequency allocation for any UWB device unless it satisfies the NTIA guidelines on spectrum compliance, or the equivalent requirements in most developed nations [29].

14.6.2 Notched Linear FM Waveform

A number of approaches have been considered to achieve a notch in the transmit spectrum and avoid interfering with existing band users. These approaches are either implemented by the use of an analog waveform exciter or by digital waveform synthesis. The ERIM P-3 UWB SAR, which was the first system that confronted the need for notching on transmit, utilized an analog waveform synthesis approach [32].

Because the frequencies are known a priori, a notch in the transmit spectrum can be constructed deterministically. The performance impact on the waveform can be analyzed in terms of the LFM transmit waveform and the spectrum of the notch applied. The LFM waveform has a spectral response of [33]:

$$S(\omega) = \text{rect}\left[\frac{\omega}{2\pi B}\right] \exp\left(-j\frac{\omega^2}{4\pi\gamma}\right) \quad (14.26)$$

If there is a single notch at carrier radian frequency $\omega_1 = 2\pi f_1$ and bandwidth B_1 to be applied to the transmit signal, the matched filter in the spectral domain will be

$$H(\omega) = S^*(\omega) - \text{rect}\left[\frac{\omega - \omega_1}{2\pi B_1}\right] \exp\left(-j\frac{\omega^2}{4\pi\gamma}\right) \quad (14.27)$$

The output of the matched filter with a notch has two parts: the first is the desired signal, and the second is a perturbation to the signal. This latter part represents a high-frequency modulation of the waveform that can affect the clutter return. The influence on the system can be considered to be *clutter-like* with an impact on the signal-to-clutter ratio (SCR) of

$$SCR = 20 \log\left(\frac{B_1}{B}\right) \quad (14.28)$$

If multiple notches are required, the second term in Equation (14.27) is iterated at each frequency.

The performance impact on the radar is a function of the notch center frequency, bandwidth, and depth. In general, as long as the notches are random and the sum of all the notches $\Sigma B_1 \ll B$, there will be little impact on the range resolution. However, these notches will have a major impact on the waveform sidelobes.

A simple illustration of the notching process is provided. First, the specific frequency must be avoided in programming the LFM frequencies within the waveform generator. The narrowband waveform is represented by a single tone, such as [34]

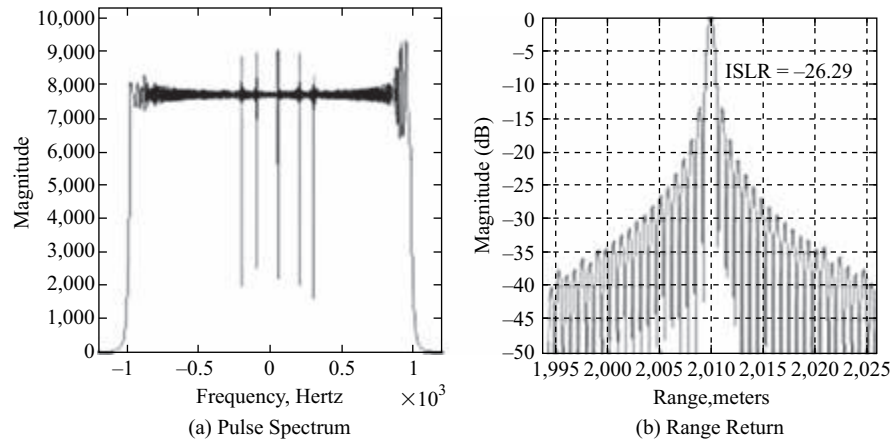
$$s_{\text{notch},j} = b_j \text{rect}\left(\frac{t}{T_P}\right) \sin(\omega_j t) \quad (14.29)$$

where $\omega_j = 2\pi f_j$ is the radian frequency to be avoided.

When this function is subtracted from the LFM waveform in the spectral domain, finite notches are formed. If multiple notches are required, one notching signal function from Equation (14.29) is derived for each frequency. The summation of these notching signals is then subtracted from the LFM waveform before transmission. Figure 14-33 illustrates an LFM waveform with five notches that comprise less than 0.6 percent of the signal bandwidth. As a result, the range sidelobes shown in Figure 14-33b are not significantly modified from the uniform weighting *sinc* function.

Notching a UWB SAR signal is effective in reducing the interference from the FOPEN SAR to most sensitive receivers, such as emergency communications and airport glide slope indicators, because the frequency is being swept at a rate significantly greater than the receiver can process within its bandwidth. In addition, the power spectral density at any one subband is reduced by the typically high-time bandwidth ($BT \gg 100$). If the FOPEN SAR is also going to be used for terrain mapping or

FIGURE 14-33 ■
Digitally Notched
SAR LFM Spectrum.



characterization, it is important that both the spectral and polarimetric characteristics be maintained. This may be accomplished by digital preselection or emphasis on transmit, or by compensation in the digital processing on receive. However, the primary effect of narrow notches on a transmitter is the multiple time constants to turn on and off the transmitter response. Depending on the design of the hardware, several MHz of bandwidth can be lost by forming a 100-KHz notch.

14.6.3 Cancellation of Radio Frequency Interference

It has been noted several times that radio frequency interference (RFI) will directly affect the background noise in the image, adversely impacting the ability to discern features of the SAR image and any target detection. A significant development effort was carried out to determine the most effective RFI removal technique [34, 35]. Two competing objectives are illustrated later for trade-off of an appropriate algorithm: 1) processing efficiency for real-time image formation, and 2) RFI removal effectiveness to restore the image quality.

The first approach for estimating the interference spectrum is used to digitally filter the signals prior to image formation. Depending on the number of interfering signals and the bandwidth of the interference, the power in the RFI removal can be effective. However, it is important to understand the stationary nature of the environment and the motion of these interferers in the SAR collection aperture.

One early method of removing the interference caused by narrowband radio and television transmissions was to sample the environment without the clutter return from the radar-transmitted waveform. A spectral filter measured the interference spectrum and determines the location and strength of the transmissions. Based on a straightforward CFAR technique, the interference peaks are identified and removed from the radar returns. This approach, although simple to implement, does not preserve the full characteristics of the image. Either the spectral lines are completely removed, or the radar signal energy is clipped prior to image formation. In the first case, the waveform spectral content is highly thinned and the image loses valuable resolution. In the second approach, residual RFI energy remains in the return and the image noise level is appropriately raised.

Significant progress was made in the late 1990s in understanding the effects of strong RFI and providing efficient RFI removal to enhance the FOPEN SAR image quality. The following sections illustrate several approaches for removing RFI from the SAR signal, along with an assessment of their processing complexity.

14.6.3.1 Deramp RFI Removal

The P-3 UWB SAR system utilized stretch (or deramp-on-receive) processing. It was necessary to develop an RFI mitigation algorithm that could correctly convert the SAR wideband signal and perform removal of RFI. Equally as important to reduction of RFI was the need to limit the number of computational operations. The parametric maximum likelihood algorithm was developed to estimate the narrowband, constant-frequency RFI and enable its subtraction from the SAR image [35].

Because the SAR signals are similar to wideband noise in their nature, it was determined that estimation of the RFI during the period when receivers were not receiving SAR signals was important. Even more important was determining that the RFI was stable during P-3 SAR signal collection. Hence, the RFI tones could be estimated early in the image collection, and therefore, did not need to be re-estimated. Specifically, for the P-3 range and velocity, the RFI was stable for a period of time on the order of 200 pulses.

The deramp RFI removal algorithm shown in Figure 14-34 consists of multiple stages. First, the received samples are band pass filtered and the tones for the highest interference sources are estimated. For the P-3, this was accomplished on a single pulse, using the N_K range samples collected in the dead time of the first pulse.

The incoming signal is then band pass filtered into several sub-bands to isolate the RFI tones, with an objective of one tone per sub-band. The amplitude, phase, and frequency of the interferer in each sub-band are estimated, and those signals are subtracted from the incoming data. This step was important to provide the accuracy of signal estimation on the smaller tones, which are masked by the stronger tone energy. An iterative estimation of RFI tones is conducted with multiple thresholds, each threshold covering success levels of signal strengths. For the P-3 data, six thresholds were used with up to 28 band pass filters.

The estimation of the frequency is provided using a forward-backward linear prediction model and based on the single pulse time series data of order N . Data records of

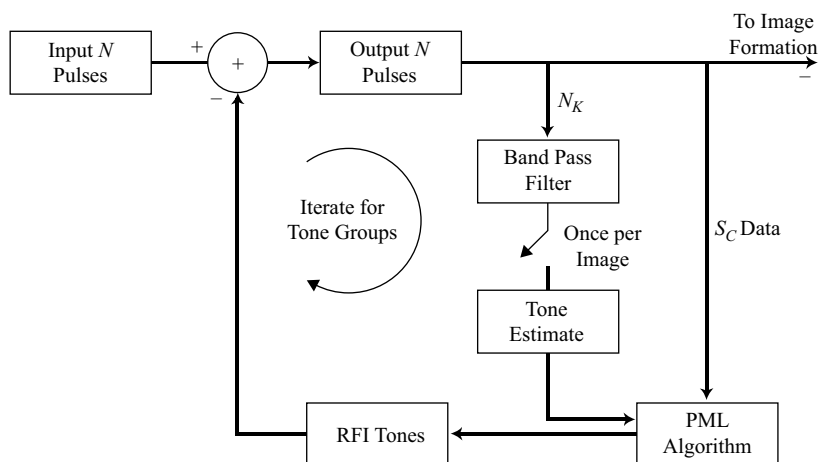


FIGURE 14-34 ■ Parametric Maximum Likelihood Algorithm Processing [35].

length L_D were constructed, and a correlation matrix of rank $2(N-L_D)$ is utilized. The improvement of the prediction estimate approaches the maximum likelihood estimate, but with a reduction in processing complexity. This was assured by limiting the number of interfering sinusoids in each sub-band filter [36].

Because of the use of stretch processing in SAR collection, it is important to have an RFI removal technique that can be effective with the deskew process [10]. In a deramp SAR, the receive signal is mixed with the frequency-shifted replica of the transmitted chirp waveform. Any RFI becomes a chirped signal when passing through the intermediate frequency amplifier. However, because the receiver has a band pass filter after the deskew mixing, not all of the RFI passes through the analog filter and into the processing chain.

Figure 14-35 shows the stretch processing on a SAR signal (with RFI present), as previously presented in Section 4.2.3. There are two key time periods depicted: T_P , the duration of the SAR pulse; and T , the delay of the chirp tone at the IF output. Since the SAR signal has a constant FM rate of γ , it will be deramped into constant tones within the IF bandwidth $B_{IF} = \gamma T$, as shown in Figure 14-35a. However, the RFI within the SAR bandwidth is spread out over a wide bandwidth during deramp, as shown in Figure 14-35b. As a result, the SAR signal after deramp and IF filtering has the following form [35]:

$$s(t) = A \exp \left[j\pi\gamma(t - t_0)^2 \right] \text{rect} \left[\frac{t - t_0}{T} \right] \quad (14.30)$$

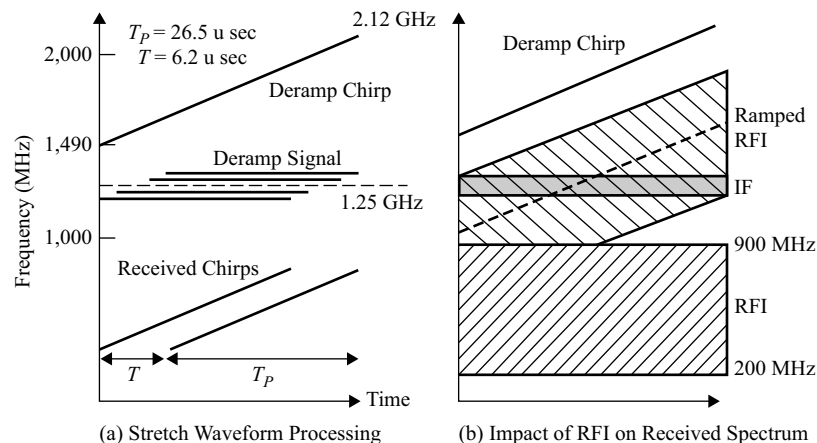
where t_0 is the delay from the start of the SAR chirp until the deramped tone frequency equals the IF center frequency.

After the deramp process, the signal history is digitally processed with a combination of deskew and removal of the residual video phase (RVP) history. The deramped signal s_0 is Fourier processed, multiplied by the residual phase function, and inverse Fourier transformed. The inverse Fourier transform recovers the SAR signal with frequency tones proportional to the range extent, as given by

$$\Phi_{RVP} = \exp \left[-j \frac{\omega^2}{4\pi\gamma} \right] \quad (14.31)$$

The same operations are applied to the RFI, causing them to appear as pulse-modulated signals whose parameters are a function of the product of a pulse waveform

FIGURE 14-35 ■ Deramp Process During UWB SAR Image Formation [35].



and a chirp waveform. The first FFT on the product of these two signals results in a convolution of the transforms of the two individual functions:

$$S(\omega) = \left(A \sqrt{\frac{j}{\gamma}} \exp \left[j \left(\frac{\omega^2}{4\pi\gamma} \right) \right] \exp(-j\omega t_0) \right) \otimes \left(T \operatorname{sinc} c \left(\frac{\omega T}{2} \right) \exp(-j\omega t_0) \right) \quad (14.32)$$

$$\approx A \sqrt{\frac{j}{\gamma}} \exp \left[j \frac{\omega^2}{4\pi\gamma} \right] \exp(-j\omega t_0)$$

The multiplication by Φ_{RVP} and the final IFFT results in a sinc function output in time:

$$s_0(t) = A \sqrt{\frac{j}{\gamma}} \frac{\sin[\pi B_{IF}(t - t_0)]}{\pi B_{IF}(t - t_0)} \quad (14.33)$$

Thus, after the first two steps of the deskew/RVP removal process, a single tone at ω remains, which corresponds to the time that the i -th tone is swept through the center of the IF bandwidth. This is the same form as a single complex sinusoid of radian frequency ω over the time period. Thus, the PML algorithm can be implemented to estimate the time of each of the tones through the IF over the period $-\pi B_{IF} < \omega < \pi B_{IF}$. It is also apparent that the compression of the RFI at the deskew/RVP removal output enables the processor to either clip the RFI impulse peaks or detect their presence and remove them later in the PML process. Figure 14-36 shows the FFT of the output of the deskew process and illustrates the single-frequency tone of the RFI. The stability of the RFI tones over time is verified.

The deramp RFI removal technique is applied in the time domain, based on the assumption that a significant portion of the RFI can be eliminated by the deskew process. It also counts on the use of stretch processing. For newer SAR systems that use direct digitization of the signal, a new approach was needed.

Figure 14-37 illustrates the recorded spectrum from a P-3 UWB collection in Grayling, Michigan. The image shown at the upper left was formed without removing the RFI from the image processing. It is apparent that the strong interference from radio and television transmissions severely degraded the noise level of the image. When the RFI spectrum was appropriately removed, the image at the right was obtained. In this example, the noise equivalent s_0 was improved from -6 dB to -18 dB [36].

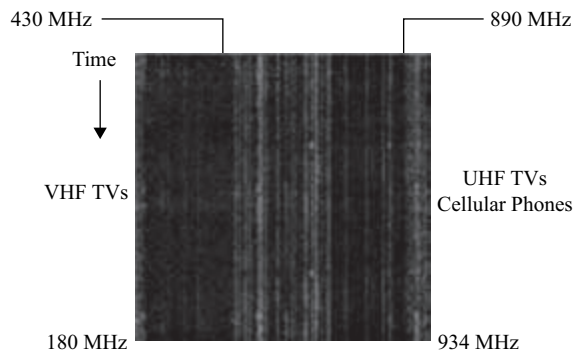


FIGURE 14-36 ■ RFI During Deramp Processing [35].

The processing complexity of the PML algorithm can be estimated in a straightforward manner. Because this is an iterative algorithm, one must specify the number of samples used to estimate the RFI tones N_K and the number of tones to be removed M . In addition, the number of band pass filters in the estimation process needs to be counted, along with the number of iterations N_I . A summary of the PML algorithm operations count is provided in Table 14-7.

The P-3 UWB SAR operated with a PRF of 300 Hz, with the number of samples per pulse being 4,096. The number of tones per pass per threshold was on the order of eight. Based on the operations in Table 14-7, the real-time operations for PML are estimated to be 80 Billion Floating Point Operations per Second (GFLOPS) [35].

14.6.3.2 Adaptive RFI Removal

An adaptive processing technique was developed for the GeoSAR system to enable RFI removal in the frequency domain rather than in the time domain. The bandwidth of GeoSAR was smaller than that of the UWB P-3; as a result, direct digital sampling at the intermediate frequency was used [38].

A technique that resembles adaptive array processing was developed for GeoSAR. By using a reference channel, the RFI environment was sampled and transformed into the SAR fast-time domain. A least means square (LMS) adaptive algorithm then correlated the reference signal to the primary input and subtracted the weighted signal. For each iteration of the pulse compression, an adaptive weight is calculated by the

FIGURE 14-37 ■ Radio Frequency Interference Removal Improvement in P-3 SAR. [Source: MIT Lincoln Laboratory [37]]

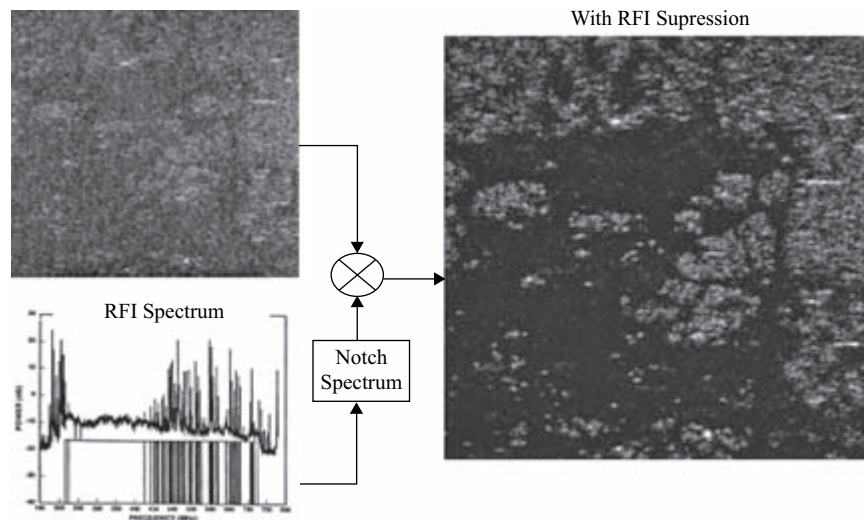


TABLE 14-7 ■ Operations Count Estimation for the Parametric Maximum Likelihood Algorithm [35]

Operation	Count
PML iteration	$(7/3)M^3 + 34M^2 + 6MN$
Total processing	$N_I N_T M(\text{PML})$

following process. A reference signal $x(n)$ is an L_F -dimension vector, constructed using the decorrelated Δ -delayed version of the input signal [39]:

$$\begin{aligned} x(n) &= [x(n), x(n-1), \dots, x(n-L+1)]^T \\ &= d(n-\Delta) \end{aligned} \quad (14.34)$$

The output signal $y(n)$ is formed by adaptively weighting the data:

$$y(n) = w^T(n) \cdot x(n) \quad (14.35)$$

The weights are iteratively calculated from the previous weights using a constant step-size parameter μ and the error vector $e(n)$, given by

$$w(n+1) = w(n) + \mu x(n)e^*(n) \quad (14.36)$$

where

- $d(n)$ = input signal
- $w(n)$ = complex filter weights of n th iteration
- $x(n)$ = reference signal
- $y(n)$ = filter output
- $e(n)$ = error vector from adaptive process
- μ = constant step size parameter
- Δ = constant decorrelation parameter
- L = filter length

Several techniques were explored using both temporal and frequency domains for the interference subtraction. Figure 14-38 illustrates LMS adaptive interference subtraction from the pulse compression filter in the frequency domain. The first spectrum plot shows the received signal, including the RFI and the transmitted waveform. It is impossible to detect the target or terrain feature in this representation. The adaptive filter helps in reducing the interference and enhancing the target visibility. The bottom graph in Figure 14-39 represents the ideal performance of the pulse compression without RFI.

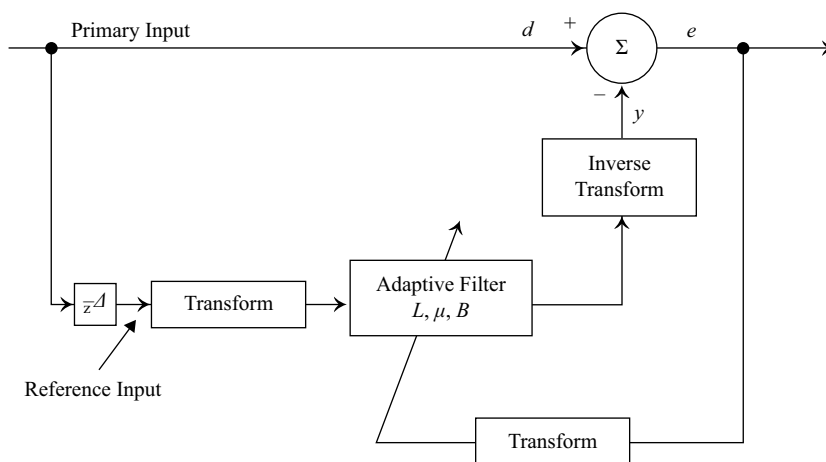
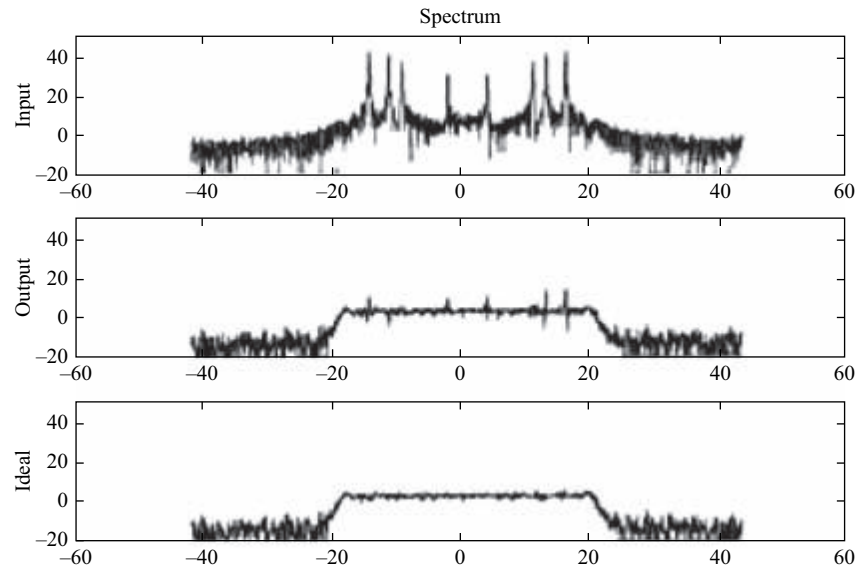


FIGURE 14-38 ■ Adaptive RFI Removal Process. [Source: NASA Jet Propulsion Laboratory [40]]

FIGURE 14-39 ■
RFI Removal from
GeoSAR Waveform.
[Source: NASA Jet
Propulsion
Laboratory [40]]



By comparing the middle and lower spectra, it is evident that a system sensitivity within 3 dB of ideal was achieved.

14.7 | TARGET DETECTION AND CHARACTERIZATION

This section will provide a summary of the major advances in the ability of radar to detect objects under foliage with sufficient characterization for scientific and tactical applications. Because of the spiky nature of foliage-penetrating clutter and the propagation losses through foliage, the concept of probability of detection and false alarm from microwave radars needs to be re-examined [41]. Specific areas of radar research to improve FOPEN SAR target detection include the uses of polarization diversity and change detection, along with their impact on the image formation processing. Target characterization includes techniques for using image morphological filtering in addition to polarization and to discriminate manmade from natural objects. It is highly instructional to look at the whole image formation, target detection, and feature characterization chain to understand the importance of polarimetry and change detection.

The results of FOPEN SAR collection campaigns and subsequent image processing analyses have shown three important advantages of a polarization diverse SAR system. The first is the ability to counter the speckle obtained from wide-collection-angle SAR image processing through the use of polarization whitening. The second is the effect of polarization on differentiating several target features. And third is the importance of polarization on image change detection.

Several benefits of polarization discrimination have developed in the SAR literature over the past decades. Specific to foliage-penetrating SAR, it is evident that the statistical distribution of clutter returns is very spiky in nature. In addition, the image segment transitions from one type of clutter to the next, providing strong specular returns at

discrete aspect angles. Having polarization diversity in the image provides the potential for reducing these strong returns, which can often resemble tactical targets [42].

Manmade objects exhibit returns that are strongly correlated at discrete angles. Thus, a physical object will provide similar returns when viewed at aspect angles or polarization within the target correlation angle. These features are usually attributed to large planar structures and the junctions between these structures that will reflect incident energy with enhanced radar RCS. By knowing the characteristics of manmade objects and applying a spatial filter over the SAR image, it is possible to reduce the false alarms due to strong clutter discretets [43].

It is also known that the polarization of the energy from various terrain types and/or slopes will have a characteristic return. If the terrain is flat, the sense of polarization will be returned with a predictable phase between orthogonal polarization senses [44].

14.7.1 Target Detection Processing

In order to detect targets under foliage, signal processing in UWB SAR includes several important image processing steps, as shown in Figure 14-40. First, the SAR image must be formed within each of the polarization channels in order to provide an image with pixels aligned within a common image frame. The processing steps and images are from a P-3 UWB collection at Grayling, Michigan, where the three polarization images are HH, VV, and HV. A common nomenclature convention for polarization channels uses *transmit* as the first letter and *receive* as the second. The figure summarizes the appropriate number of operations per pixel for each step in the process.

The first step in signal processing is to remove the RFI from the images, as covered in Section 14.6. An improvement in noise-equivalent sigma-0 (i.e., σ_{ne}^0) is visually illustrated in the second stage of the image processing. For the range migration algorithm used on the P-3 FOPEN SAR images, the operations count was approximately 2,000 operations per pixel per polarization. The RFI removal was carried out during the deskew image formation processing, requiring an additional 100 operations per pixel.

Because of the spiky polarization characteristics of FOPEN clutter, a whitening of the image is necessary to improve the target detection process. This polarization whitening filter (PWF) step provides a significant improvement in the target-to-clutter

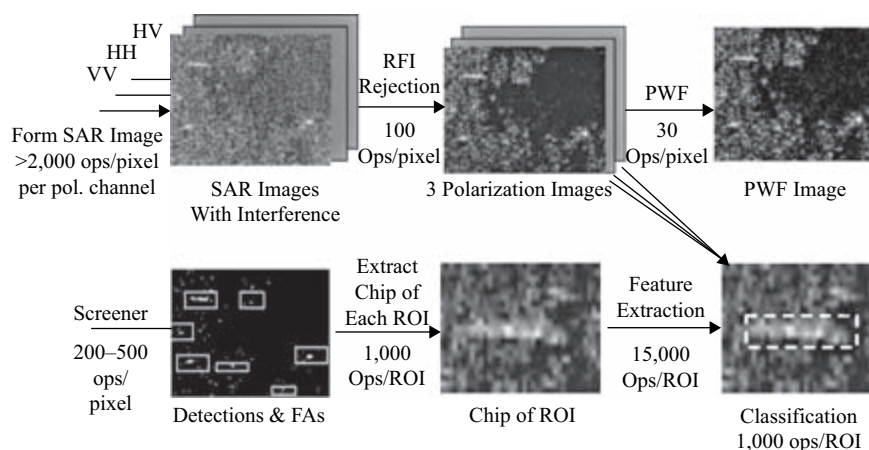


FIGURE 14-40 ■ FOPEN SAR Target Detection and Characterization Processing Flow. [Source: MIT Lincoln Laboratory [45]]

ratio and the subsequent ability to nominate areas of the image that are likely to contain manmade targets. Target detection is accomplished through an area CFAR on the image, providing a nomination of regions of interest (ROIs) for subsequent feature examination. These regions are then delineated as small areas of target and background clutter, called chips, and passed on for subsequent feature extraction. These “chips” will be examined finally for features that include size, shape, and polarization characteristics for final classification as a manmade target versus terrain artifact.

14.7.2 Polarization Whitening

Speckle has been recognized to be the cause of significant false alarms in SAR images [41]. As a result, the consideration of polarization diversity as a technique to reduce this speckle has been examined extensively, primarily for microwave frequency radars. The analysis of polarimetric returns from manmade targets and clutter provided verification of the benefit of using the independent degrees of signal polarization characteristics. Based on these results and the known spiky characteristics of clutter, it was straightforward to investigate applications to assist in the reduction of false alarms in foliage-penetrating SAR. The P-3 UWB SAR was specifically built to collect fully polarimetric clutter and target characteristics over a wide range of geographic and forested regions.

It was shown in Section 14.4 that the foliage clutter is non-Gaussian. With a Gaussian clutter model, each resolution cell of the SAR image will be spatially homogeneous and have the same average polarimetric power. However, with the foliage lognormal clutter model, this characteristic cannot be assumed. In fact, there is a significant inhomogeneity of the clutter distribution over a typical SAR scene.

A polarimetric FOPEN SAR system typically collects three polarization components by using two receiver channels. On successive pulses, horizontal and vertical transmit pulses illuminate the scene, and the co-polarization and cross-polarization returns are recorded. Because the two cross-polarization channels HV and VH have been observed and analyzed as being reciprocal, only three channels are typically recorded: HH, HV, and VV.

Polarization whitening is the process that combines the three input channels into a complex vector in order to equalize the energy in three polarization vector quantities. The polarization measurements of the signal return are collected into a complex vector [43]:

$$Y = \begin{bmatrix} HH \\ HV \\ VV \end{bmatrix} = \begin{bmatrix} HH_I + jHH_Q \\ HV_I + jHV_Q \\ VV_I + jVV_Q \end{bmatrix} \quad (14.37)$$

The vector Y is assumed to be the product of a complex Gaussian vector X (representing the speckle) and a spatially varying texture variable g :

$$Y = \sqrt{g}X \quad (14.38)$$

The probability density function of the complex speckle vector X is defined by

$$f(X) = \frac{1}{\pi^3 |\Sigma|} \exp(-X^* \Sigma^{-1} X) \quad (14.39)$$

where Σ is the polarization covariance matrix. It is common to express the clutter covariance matrices in terms of normalized linear-polarization bases in the form:

$$\Sigma = \sigma_{HH} \cdot \begin{pmatrix} 1 & 0 & \rho\sqrt{\gamma} \\ 0 & \varepsilon & 0 \\ \rho^*\sqrt{\gamma} & 0 & \gamma \end{pmatrix} \quad (14.40)$$

In Equation (14.40), the parameter γ is the ratio of the square of the expectation value of the VV to that of the HH return:

$$\gamma = \frac{E(|VV|^2)}{E(|HH|^2)} \quad (14.41)$$

Similarly, ε is the ratio of the HV cross-polarization to the HH return:

$$\varepsilon = \frac{E(|HV|^2)}{E(|HH|^2)} \quad (14.42)$$

Finally, ρ is the cross-correlation coefficient between the HH and VV returns:

$$\rho = \frac{E(HH \cdot VV^*)}{[E(|HH|^2)E(|VV|^2)]^{1/2}} \quad (14.43)$$

From the polarimetric measurements at each pixel, the objective is to construct a new image that minimizes the variance of speckle between the three channels. This is carried out by a transformation of the complex vector Y in the quadratic form:

$$y = Y^\dagger A Y = g X^\dagger A X \quad (14.44)$$

The measure of speckle in the image is expressed as the ratio of the standard deviation of the image pixel intensities to the mean of the intensities (s/m):

$$\frac{\sigma_y}{\mu_y} = \frac{\text{std.dev}(y)}{\text{mean}(y)} \quad (14.45)$$

A is the desired weighting matrix that minimizes the (s/m) in each channel. This has been shown to equal the inverse of the polarization covariance matrix. So the polarization vector Y from each pixel in the image is passed through the whitening filter $\Sigma^{-1/2}$ to obtain a new image function Y_W :

$$Y_W = \Sigma^{-1/2} Y = \sqrt{g} \Sigma^{-1/2} X \quad (14.46)$$

The whitened vector Y_W then forms a single SAR image with the requisite reduction in background clutter speckle, given by [41]:

$$Y_W = \left[HH, \quad \frac{HV}{\sqrt{\varepsilon}}, \quad \frac{VV - \rho^* \sqrt{\gamma} HH}{\sqrt{\gamma(1 - |\rho|^2)}} \right] \quad (14.47)$$

The scale factors in Equation (14.47) come from the three ratios of image polarization channel data given by γ , ε , and ρ in Equations (14.41) to (14.43).

Figure 14-41 shows the three P-3 FOPEN SAR polarimetric input channels from the Grayling, Michigan, collection [43]. It can be clearly seen that the HH and VV channels exhibit a spiky distribution of clutter discretets, representative of a lognormal distribution, as summarized in Section 14.4.

To characterize this clutter distribution, a set of 500 clutter chips was extracted from the images, each containing 200 pixels in range and 100 pixels in cross-range. The values of the parameters of the tree clutter polarization covariance matrix were then estimated. For this type of northern latitude forest clutter, the parameters are found to be approximately [42]:

$$\begin{aligned}\sigma_{HH} &= 0.08 \\ \varepsilon &= 0.25 \\ \gamma &= 0.5 \\ \rho\sqrt{\gamma} &= -j0.125\end{aligned}\tag{14.48}$$

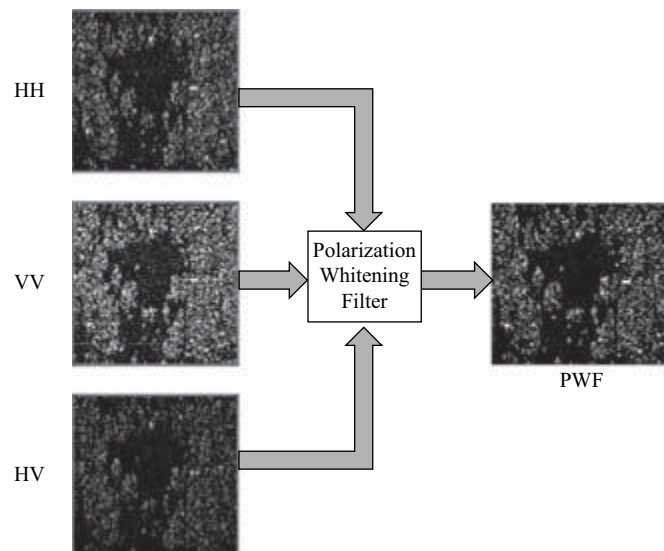
When the three channels were combined with the PWF, the clutter distribution of scatterers is modified significantly. This is evidenced in Figure 14-41 by the closer distribution of return amplitudes in the forested area and the reduction in speckle noise in the open field.

The SCR for targets under the foliage was also improved from 9 dB to 19 dB. More importantly, the targets suffered no loss of resolution. Thus, it is expected that after PWF processing, the target detection process will be greatly improved.

14.7.3 Target Characterization

With efficient image formation and RFI mitigation, the polarimetric FOPEN SAR presents an opportunity to improve the detection of tactical targets hidden under forest cover. However, the reduction of the target signature, due to both the foliage-penetrating

FIGURE 14-41 ■ Polarization Whitening of Grayling P-3 UWB Data. [Source: MIT Lincoln Laboratory [45]]



losses and the similarity of many natural objects in size to the desired targets, false-alarm rate remains high. Further image processing techniques were developed to discriminate returns that pass the CFAR test.

Polarization is one of many techniques developed to determine whether an individual object is manmade or natural. However, there has been an equally strong emphasis on increased image resolution in an attempt to segregate the scattering centers and to reduce the competing clutter volume. Both fine spatial resolution and polarization have been shown to improve target feature characterization [46]. Other strong image processing techniques, as outlined in Table 14-8, were examined to understand the geometric characteristics of tactical objects under the forest canopy, including determining the geometric and polarimetric features of targets versus terrain feature [47, 48].

Several data collections have been conducted to obtain sufficient clutter and target data to test the process of image segmentation and strength of target characterization for both false-alarm reduction and classification of manmade targets. It is not anticipated that FOPEN SAR will provide any useful automatic target recognition due principally to two factors. First, at the long wavelengths of UHF and VHF, there are insufficient pixels on a target to expect a good recognition performance. But more importantly, the few features that exist on manmade and tactical objects will be occluded by the propagation of the signal energy through large trees. These essentially mask many of the pixels and cause amplitude and phase perturbation of the radar returns. So the most that can be expected from FOPEN SAR automatic target detection and characterization (ATD/C) is to place objects in broad classes based on the features that do exist robustly in the measurements.

14.7.4 FOPEN Target Features

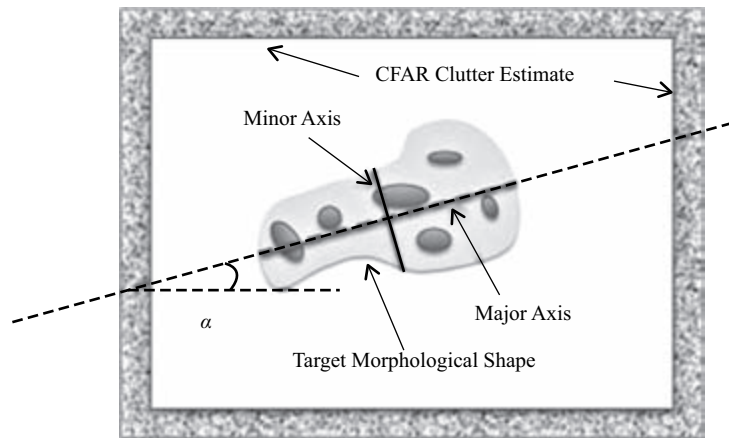
Four types of features have been employed in classification analyses, as summarized in Table 14-8 [46]:

- *Texture*: The spatial variation of the returns in the neighborhood or as part of the area being characterized. The returns for clutter and target within the CFAR box are examined for their particular statistical characteristics. The *standard deviation* of the

TABLE 14-8 ■ Image Processing Techniques for Detecting Manmade Objects [47]

Feature Types	Algorithm
Textural	Standard deviation
	Fractal dimension
	Ranked fill ration
Size	Mass
	Diameter
	Normalized square rotational inertia
Contrast features	Peak CFAR
	Mean CFAR
	Percent bright CFAR
Polarimetric features (Fully polarimetric only)	Percent pure (odd or even)
	Percent pure even
	Percent bright even

FIGURE 14-42 ■
Estimating Size and
Shape Features for
Target
Characterization.



returns in the area is a measure of the fluctuation of the intensity in an image. The *fractal dimension* measures the N brightest scatterers in the region and characterizes them in terms of geometric shape. A single bright pixel will have a dimension of 0, a line will have a dimension of 1, and a solid rectangle will have a dimension of 2. Finally, the *rank fill* feature measures the percentage of total energy contained in the N largest pixels. N is typically chosen as 5.

- *Size*: The grouping of strong scatterers and association with an object via a morphological filter for determination of length and width, as illustrated in Figure 14-42. The *mass* feature is obtained by counting the number of pixels in this morphological shape. The *normalized square rotational inertia* feature is the second mechanical moment of the shape around its center of mass, normalized by the inertia of an equal mass square.

The *center of mass* of the object within the image chip can be calculated by the weighted position of each pixel that exceeds the CFAR threshold. Given (x_i, y_i) as the position of the pixel, the centers of mass M_x and M_y are calculated by

$$M_x = \frac{\sum_i x_i}{N} \quad M_y = \frac{\sum_i y_i}{N} \quad (14.49)$$

The *second moment* of the image (i.e., its inertia) is now given in three dimensions, based on the distance between each detected image pixel and the center of mass of the image:

$$U_{xx} = \frac{1}{N} \sum_i (x_i - M_x)^2 \quad (14.50a)$$

$$U_{yy} = \frac{1}{N} \sum_i (y_i - M_y)^2 \quad (14.50b)$$

$$U_{xy} = \frac{1}{N} \sum_i (x_i - M_x)(y_i - M_y) \quad (14.50c)$$

Calculation of the critical parameters for target discrimination are next determined by estimating the *pose* (i.e., orientation) of the shape with respect to the x - and y -axes. Based on these measurements, the pose of the object is determined as

$$\alpha = \frac{1}{2} \tan^{-1} \left(\frac{2U_{xy}}{U_{xx} - U_{yy}} \right) \quad (14.51)$$

The coordinate system can now be transformed from (x, y) to (x', y') by an α -rotation in the image plane. The lengths of the major and minor axes are next determined by centering the locations of the N brightest pixels:

$$U_{Major} = \sqrt{\frac{1}{N} \sum (x'_i)^2} \quad (14.52a)$$

$$U_{Minor} = \sqrt{\frac{1}{N_C} \sum (y'_i)^2} \quad (14.52b)$$

- *Contrast*: The collection of features obtained from the statistics in the CFAR processing. The ratio and distribution of the scattering center returns in the target shape (shown in Figure 14-42) are compared to the background clutter statistics. The maximum statistic is the greatest intensity pixel in the target distribution. The mean feature is the average of the CFAR target returns within the morphological shape, while the percentage bright feature is the percentage of the pixels within the object that exceeds a CFAR threshold.
- *Polarization*: It has been found to provide a very effective method to discriminate between manmade and natural scatterers, as summarized in Section 14.4. *Odd-bounce* statistics are representative of flat-plate, linear (e.g., wires), or trihedral objects. *Even-bounce* returns are associated with the radar scattering from a dihedral. Thus, the polarimetric features are calculated from a transformation of the *HH-VV* data collection coordinates to even-bounce and odd-bounce images. These transformations are given by the following equations:

$$E_{even} = \frac{|S_{HH} + S_{VV}|^2}{2} \quad (14.53)$$

$$E_{odd} = \frac{|S_{HH} - S_{VV}|^2}{2} + 2|S_{HV}|^2 \quad (14.54)$$

The *percentage-pure* feature is the fraction of the pixels within the target shape for which at least a threshold of the scattered energy falls within either the even-bounce or odd-bounce metric. The *percentage-bright-even* feature is the fraction of the pixels within the target shape that exceed a threshold in the CFAR image, which are predominantly even-bounce scatterers.

Evaluating the pixels in a target chip after image segmentation or designation of ROIs provides additional quantitative scoring to the even- and odd-bounce features for additional image characterization. First, the S_{HH}/S_{HV} and S_{HH}/S_{VV} ratios are calculated for each pixel. Then the average and standard deviation of the measurements are

calculated for the number of pixels in the ROI. The six additional polarimetric features that need to be calculated are

$$\begin{aligned}
 P_1 &= \text{Average} \left(\frac{|S_{HH}|}{|S_{HV}|} \right) & P_4 &= \text{Average} \left(\frac{|S_{HH}|}{|S_{VV}|} \right) \\
 P_2 &= \text{Std.Dev.} \left(\frac{|S_{HH}|}{|S_{HV}|} \right) & P_5 &= \text{Std.Dev.} \left(\frac{|S_{HH}|}{|S_{VV}|} \right) \\
 P_3 &= \left(\frac{\text{Average}|S_{HH}|}{\text{Average}|S_{HV}|} \right) & P_6 &= \left(\frac{\text{Average}|S_{HH}|}{\text{Average}|S_{VV}|} \right)
 \end{aligned} \tag{14.55}$$

The final step in the target discrimination process combines the appropriate features from the aforementioned extensive list into a single discrimination statistic. The features can then be collected and examined in terms of a quadratic distance metric to identify classes of objects for either classification or elimination as false alarms. This discrimination statistic is calculated as a quadratic distance metric:

$$d_T(X) = \frac{1}{N} (X - \hat{M})^T \hat{\Sigma}^{-1} (X - \hat{M}) \tag{14.56}$$

where

- N = number of features used for discrimination
- M = estimate of the mean target vector class
- Σ = estimate of the standard deviation target vector class
- $d_T(X)$ = statistical distance of the unknown object from a class

The estimates of M and Σ are often collected on targets in the open to obtain a fundamental understanding of the target features. The measured quadratic distance $d_T(X)$ will be small for targets that are close to the correct class. For natural clutter, it is anticipated that the quadratic measure will be large for scattering that does not exhibit the dominant even- or odd-bounce characteristics of manmade objects.

The challenge in FOPEN ATD/C has always been the occlusion (i.e., shadowing) of the targets by dense foliage. If the target's statistics are collected for manmade objects in the open, there will be an inherent error in the mean and standard deviation of the target classes. These errors will be larger if the target SCR is low, or if there are very large natural objects in the direct path. As a result, any collection of data to test ATD/C capabilities need to be gathered in a variety of foliage conditions, including types of forests, terrain slope, and radar incident angles.

14.8 | SUMMARY

Foliage-penetrating radar has been in development for over 40 years. The early systems provided an important insight into the scattering characteristics of forest and jungle environments, as well as the requirements for coherent waveforms and signal processing. The attenuation of propagation of radar through foliage was not as severe as originally expected, but only as long as the propagation occurred at a grazing angle (to the top of the foliage) above approximately 20 degrees. However, the motion of foliage in

any wind conditions would mask the motion of moving targets and obscure any target features. As a consequence, the further development of FOPEN radar needed to wait for advances in compact VHF- and UHF-band components, as well as high-performance computing.

FOPEN SAR requires the use of UWB waveforms and a significant percentage of the spectrum. Two factors became an early limitation on FOPEN resurgence in the late 1990s. First, the large number of VHF and UHF transmitters for radio, television, and communications was a constant source of interference in the formation of high-quality FOPEN images. Second, the regulations on transmissions outside of the radar bands required significant advances in the low probability of intercept frequency operation. These conditions still exist, and acceptance of any new system requires comprehensive testing and verification that no disruption to emergency and safety support systems exists.

In order for efficient target detection, FOPEN SAR signal processing must consider the removal of RFI as well as maintaining high-quality images. Polarization features are shown to be important in the basic detection process, as well as discriminating manmade targets from cultural objects. Future systems will rely on the continued maturing of image processing as well as the steady improvement in real-time processing.

14.9 | REFERENCES

- [1] Gordon G. A. and Holt E., “An Estimate of the HF/VHF Surface-Wave Communications Wave Reaches in the West German Forest Environment,” Defense Nuclear Agency Report DNA-TR-82-07, January 1982, pp. 12–17.
- [2] Surgent L. V. Jr., “Foliage Penetration Radar: History and Developed Technology,” U.S. Land Warfare Laboratory Report AD/A000805, July 1974 (Publically released).
- [3] Centofanti J. J., “Synthetic Aperture Dual Frequency Radar (SADFRAD) – A Unique Airborne Sensor,” AFCRL-70-0676, Air Force Cambridge Research Laboratories, Hanscom Field Bedford, MA, AD515249, 9 December 1970 (Publically released 31 December 1982).
- [4] Fowler, C. A., “The Standoff Observation of Enemy Ground Forces: From Project PEEK to JointSTARS,” *IEEE Systems Magazine*, Vol. 12, No. 6, June 1997, pp. 3–17.
- [5] Entzminger J. N., Fowler C. A., and Kenneally W. J., “Joint STARS and GMTI: Past, Present, and Future,” *IEEE Transactions on Aerospace and Electronic Systems*, Vol. 35, No. 2, April 1999, pp. 748–761.
- [6] Bryant T. G., Morse G. B, Bovak L. M, and Henry J. C., “Tactical Radars for Ground Surveillance,” *MIT Lincoln Laboratory Journal*, Vol. 12, No. 2, Lexington, MA, 2000, p. 342.
- [7] Picture of Camp Sentinel Radar Antenna courtesy of Lee Moyer Technology Services Company, Silver Springs, MD.
- [8] Photographs and details of M-FOPEN radar provided by Mr. James Rodems, former Syracuse University Research Company division manager.
- [9] Davis M. E., “Technical Challenges in Ultra-Wideband Radar Development for Terrain Mapping,” Proc. IGARSS, 1998, Seattle, WA.
- [10] Carrara W. G., Goodman R. S., and Majewski R. M., *Spotlight Synthetic Aperture Radar Signal Processing Algorithms*, Artech House, Boston, MA, 1995, Chapter 2.

- [11] Vickers R. S., "Ultra Wideband Radar – Potential and Limitations," *Proc. 1991 IEEE MTT-S Conference*, June 1991, pp. 371–374.
- [12] Hellsten H., Ulander L. M. H., Gustavsson A., and Larsson B., "Development of VHF CARABAS II SAR," *Proc. Radar Sensor Technology, SPIE*, Vol. 2747, Orlando, FL, 8–9 April 1996.
- [13] Vandenberg N., Sheen D. R., Shackman S., Wiseman D., "P-3 Ultra Wide Band SAR: System Applications to Foliage Penetration," *SPIE*, Vol. 2757, Orlando, FL April 1996, p. 130.
- [14] Hensley S., Chapin E., Freedman A., Le C., Madsen S., Michel T., Rodriguez E., Siqueira P., and Wheeler K., "First P Band Results Using the GeoSAR Mapping System," *Proc. 2001 IEEE Radar Conference*, Atlanta, GA, May 2001, p. 126.
- [15] Ressler M., Happ L., Nguyen L., Tuan T., and Bennett M., "The Army Research Laboratory Ultra-Wide Band Testbed Radars," *Proc. IEEE International Radar Conference*, Arlington, VA, May 1995, pp. 686–691.
- [16] Adams G. F., Ausherman D. A., Crippen S. L., Sos G. T., and Williams B. P., Heidelberg R., "The ERIM Interferometric SAR: IFSARE," *Proc 1996 National Radar Conference*, Ann Arbor, MI, 13–16 May 1996, pp. 249–254.
- [17] Courtesy of M. Toups, MIT Lincoln Laboratory, Lexington, MA, June 1997.
- [18] Fleischman J., Toups M. F., and Ayasli S., "Summary of Results from a Foliage Penetration Experiment with a Three Frequency Polarimetric SAR," *Proc. SPIE*, Vol. 1693 Surveillance Technologies II, April 1992, p. 151.
- [19] Bessette L. A. and Ayasli S., "Ultra Wideband P-3 and CARABAS II Foliage Attenuation and Backscatter Analysis," *Proc. 2001 IEEE Radar Conference*, Atlanta, GA, May 2001, p. 357.
- [20] Bessette L. A., Crooks S. M., and Ayasli S., "P-3 Ultra Wideband SAR Grayling, Michigan, Target and Clutter Phenomenology," *Proc. 1999 IEEE Radar Conference*, Boston, MA, May 1999, p. 125.
- [21] Moyer L. R., private communication, Technology Services Corporation, Silver Springs, MD, February 2010.
- [22] Davis M. E., Tomlinson P. R., and Maloney R. P., "Technical Challenges in Ultra- Wideband Radar Development for Target Detection and Terrain Mapping," *Proc. 1999 IEEE Radar Conference*, Boston, MA, pp. 1–6.
- [23] Hellsten H., "CARABAS – a UWB Low Frequency SAR," *IEEE MTT-S International*, Vol. 3, 1–5 June 1992, pp. 1495–1498.
- [24] Vickers R., Gonzalez V. H., and Ficklin R. W., "Results from a VHF Impulse Synthetic Aperture Radar," *Proc. SPIE*, Vol. 1631, Bellingham, WA, 1992, pp. 219–226.
- [25] Yegulalp A. R., "Fast Backprojection Algorithm for Synthetic Aperture Radar," *Proc. 1999 IEEE Radar Conference*, Boston, MA, April 1999, pp. 60–65.
- [26] Hunter A. J., Hayes M. P., and Gough P. T., "A Comparison of Fast Factorised Back-Projection and Wavenumber Algorithms for SAS Image Reconstruction," *Proc. of the World Congress on Ultrasonics*, Paris, France, September 2003.
- [27] Soumekh M., *Synthetic Aperture Radar Signal Processing with MATLAB Algorithms*, Wiley, New York, 1999.
- [28] Miller T., McCorkle J., and Potter L., "Near Least Square Radio Frequency Interference Suppression," *Proc. SPIE*, Vol. 2487, Orlando, FL, April 1995, pp. 72–83.

- [29] FCC Part 15 Regulations July 10, 2008, from Federal Communications Commission Internet Site, http://www.fcc.gov/oet/info/rules/part15/PART15_07-10-08.pdf.
- [30] Lynch D. Jr., *Introduction to RF Stealth*, SciTech Publishing, Raleigh, NC, 2004, Chapter 2: Interceptability Parameters and Analysis.
- [31] Davis M. E., “Waveforms for Ultra Wideband FOPEN SAR,” *Proc. 2010 International Radar Conference*, Washington, DC, May 2010.
- [32] Goodman R., Tummala S., and Carrara W., “Issues in Ultra-Wideband, Widebeam SAR Image Formation,” *Proc. IEEE 1995 International Radar Conference*, Arlington, VA, May 1995, pp. 479–485.
- [33] Chang W., Cherniakov M., Li X., and Li J., “Performance Analysis of the Notch Filter for RF Interference Suppression in Ultra-Wideband SAR,” *Proc. 9th International Conference on Signal Processing (ICSP200)*, 2008, pp. 2446–2451.
- [34] Le C. T. C. and Hensley S., “Removal of RFI in Wideband Radars,” *Proc. 1998 IGARSS Symposium*, Seattle, WA, July 1998, p. 2032.
- [35] Golden A., Werness S. A., Stuff M., DeGraaf S., and Sullivan R., “Radio Frequency Interference Removal in a VHF/UHF Deramp SAR,” *Proc. SPIE*, Vol. 2487, Orlando, FL, April 1995, pp. 84–95.
- [36] Tufts D. W. and Kumaresan R. “Estimation of Frequencies of Multiple Sinusoids: Making Linear Prediction Perform Like Maximum Likelihood,” *Proc. IEEE*, Vol. 70, No. 9, September 1982, pp. 975–989.
- [37] Touns, M., unpublished images provided by MIT Lincoln Laboratory as part of DARPA/ Navy UWB P-3 Collection and Verification Program, 1997.
- [38] Hensley S. and Madsen S. N., “Interferometric Radar Waveform Design and the Effective Interferometric Wavelength,” *Proc. 2007 Waveform Diversity & Design Conference*, Kauai, HI, April 2007, pp. 287–291.
- [39] Le C. T. C., Hensley S., and Chapin E., “Adaptive Filtering of RFI in Wideband Radars Using the LMS Algorithms. Part I: The TDLMS Adaptive Filter,” *JPL Technical Symposium*, Pasadena, CA, 2002.
- [40] Hensley S., Le C. T. C., and Gurrola E., “A Rigorous Expression for the Amount of Interference from a Chirped Waveform Using Ideal Band Pass and Realistic Receiver Models,” NASA Jet Propulsion Laboratory GeoSAR Memo (unpublished), September 20, 1999.
- [41] Novak L. M., Burl M. C., and Irving W. W., “Optimal Polarimetric Processing for Enhanced Target Detection,” *IEEE Trans. on Aerospace and Electronic Systems*, Vol. 29, No. 1, January 1993, pp. 234–243.
- [42] Novak, L. M., “Effects of Various Image Enhancement Techniques on FOPEN Data,” *Proc. 2001 IEEE Radar Conference*, Atlanta, GA, May 2001, p. 87.
- [43] Nanis J. G., Halversen S. D., Owirka G. J., and Novak L. M., “Adaptive Filters for Detection of Targets in Foliage,” *IEEE AESS Magazine*, August 1995, p. 34.
- [44] Schuler D. L., Lee J.-S., and De Grandi G., “Measurement of Topography Using Polarimetric SAR Images,” *IEEE Trans. on Geoscience and Remote Sensing*, Vol. 34, No. 5, September 1996.
- [45] Davis M. E., Tomlinson P. G., and Malone R. P., “Technical Challenges in Ultra Wideband Radar Development for Target Detection and Terrain Mapping,” *Proc. 1999 IEEE Radar Conference*, Boston, MA, April 1999, p. 1.

- [46] Novak L. M., Halversen S. D., and Owirka G. J., “Effects of Polarization and Resolution on the Performance of a SAR Automatic Target Recognition System,” *MIT Lincoln Laboratory Journal*, Vol. 8, No. 1, January 1995.
- [47] MacDonald D., Chang C. F., Roman J., and Koesel R., “Automatic Target Detection and Cueing for Foliage-Concealed Targets,” *Proc. SPIE*, Vol. 2757, Orlando, FL, April 1996, pp. 152–162.
- [48] Gorman J. D. and Marble J. A., “A Low Complexity Multi-Discriminant FOPEN Target Screener,” *Proc. SPIE*, Vol. 3370, Orlando, FL, April 1998, pp. 307–317.

14.10 | FURTHER READING

Further details on the development and technology for foliage-penetrating radar can be found in the following:

Davis M. E., *Foliage Penetration Radar – Detection and Characterization of Objects Under Trees*, SciTech Publishing, Raleigh NC, 2011.

Several key papers that cover the essential elements of FOPEN phenomenology and radar design include:

FOPEN History

Surgent L.V. Jr., “Foliage Penetration Radar: History and Developed Technology,” U.S. Land Warfare Laboratory Report AD/A000805, July 1974 (Publically released).

Bryant T. G., Morse G. B., Novak L. M., and Henry J. C., “Tactical Radars for Ground Surveillance,” *Lincoln Laboratory Journal*, Vol. 12, No. 2, Lexington, MA, 2000, p. 342.

Phenomenology

Bessette L. A. and Ayasli S., “Ultra Wideband P-3 and CARABAS II Foliage Attenuation and Backscatter Analysis,” *Proc. 2001 IEEE Radar Conference*, Atlanta, GA, May 2001, p. 357.

RFI Removal

Le C. T. C. and Hensley S., “Removal of RFI in Wideband Radars,” *Proc. 1998 IGARSS Symposium*, Seattle, WA, July 1998, p. 2032.

Golden A., Werness S. A., Stuff M., DeGraaf S., and Sullivan R., “Radio Frequency Interference Removal in a VHF/UHF Deramp SAR,” *Proc. SPIE*, Vol. 2487, Orlando, FL, April 1995, pp. 84–95.

Waveform Processing

Carrara W. G., Goodman R. S., and Majewski R. M., *Spotlight Synthetic Aperture Radar Signal Processing Algorithms*, Artech House, Boston, MA, 1995.

Soumekh M., *Synthetic Aperture Radar Signal Processing with MATLAB Algorithms*, Wiley, New York, 1999.

Target Detection and Discrimination

Novak L. M., Halversen S. D., and Owirka G. J., “Effects of Polarization and Resolution on the Performance of a SAR Automatic Target Recognition System,” *MIT Lincoln Laboratory Journal*, Vol. 8, No. 1 January 1995.

MacDonald D., Chang C. F., Roman J., and Koesel R., “Automatic Target Detection and Cueing for Foliage-Concealed Targets,” *Proc. SPIE*, Vol. 2757, Orlando, FL, April 1996, pp. 152–162.

Ground-Penetrating Radar

Richard Liu, Wei Ren, Huaping Wang and Chen Guo, Department of Electrical and Computer Engineering, University of Houston, Houston, Texas 77004

Chapter Outline

15.1 Overview	691
15.2 Pulsed Ground-Penetrating Radar System Design	697
15.3 GPR System Implementation and Test Results	731
15.4 Conclusions	746
15.5 References	746

15.1 | OVERVIEW

Ground-penetrating radar (GPR) is a noninvasive electromagnetic geophysical survey device. GPR uses high-frequency electromagnetic (EM) wave propagation (generally, 10 MHz to 10 GHz) and scattering to image, locate and quantitatively identify changes in electromagnetic properties in materials, especially in the ground. GPR measurements may be conducted from the surface of the materials, from a small distance (0.5–2 m) above the material surface, in a borehole or between boreholes, and even from an aircraft. GPR offers a high spatial resolution in the subsurface imaging as a geophysical method. Depending on the antennas used, the spatial resolution can reach centimeters or even millimeters under the right conditions. The depth of investigation varies from less than a meter to more than tens of meters, depending on the material properties and antennas used [1].

The areas of application for the GPR are diverse [2–10] and include the detection or mapping of metallic features, which include utility lines, archeological sites, and subsidence in soil. The system has also been used successfully to determine the structural integrity of the ground underneath a road or runway. This results in applications involving the identification of defects within pavements and bridge decks, measuring moisture contents, detecting corrosion of reinforcing steel in concrete [3], and assessing the thickness of pavement layers [4–8]. GPR has also been used in many other areas as a nondestructive investigation tool, such as in geophysics to estimate the structure of Earth sediments and to find the depth of bedrocks and water tables [9]. In archeology, GPR has been used to locate buried structures before digging to prevent accidental damage [10–12]. Moreover, GPR is an effective tool to locate landmines [13–15]. Recently, GPR systems have also found applications in imaging through walls and life detection after disasters [16–20].

As a communication system, a GPR system is a complete system with a transmitter (TX) and a receiver (RX). A normal communication system has an information source, communication media, and a receiver. In wireless voice communication, the source is the voice or data that contains the information to be transmitted by the transmitter and recovered by the receiver. The media of the wireless voice communication system can be anything but is irrelevant to users. The sole purpose of the wireless voice communication system is to correctly send the voice or data to the receiver.

In a GPR system, the transmitted source signal is known and therefore contains no information. What is sought are the media characteristics that the GPR waves went through. From the received signal, the GPR system attempts to invert the communication media through which the GPR signals pass. As the media are more complex, GPR systems are also more challenging than voice communication systems.

15.1.1 GPR Operating Principle

Also known as material-penetrating radar (MPR), GPR uses electromagnetic radiation in the radio-frequency (RF) and microwave band of the radio spectrum and detects the reflected signals from subsurface structures. It can be used in a variety of media, including rock, soil, ice, freshwater, pavements, and various infrastructures. Detection vectors include anomalies in the soil and changes in material such as layers, voids, and cracks.

From a frequency-domain viewpoint, a GPR is an ultrawideband transceiver. A narrow pulse in a time domain contains a wideband frequency spectrum. The narrower the pulse is, the wider the frequency band it occupies. If a transmitter emits a narrow pulse, then it will propagate through the materials to be detected and reflected at the boundaries between different materials with different electrical properties (dielectric constant and conductivities). The time delay between the transmitted and reflected pulses is directly related to the spatial distance between layers as shown in Figure 15-1. The amplitude attenuation, pulse delay, and pulse width expansion are determined by the electrical properties of the materials near the GPR system. Therefore, in the ideal case, narrower pulses are preferred in a GPR transmitter for increased spatial resolution. However, when pulses are narrow, they contain more high-frequency energy and less low-frequency energy due to the limit of the system bandwidth, and therefore the penetration depth will be reduced. So, because the GPR are band limited, appropriate GPR center frequency must be selected in accordance to the application in which it is used.

The GPR system uses high-frequency EM waves to probe lossy dielectric materials to detect structures and changes within materials, depending on the waveforms transmitted from a radar transmitter, and can be divided into two categories based on the hardware implementation strategy: impulse [1–4] radar and continuous wave radar. An impulse radar transmitter transmits a high-speed pulse, whereas the continuous wave (CW) radar transmits a continuous wave sweeping frequency in either a linear or stepped mode. In this section, we discuss the impulse radar system, since it is the system used most in GPR.

In a pulse radar system, an impulse electromagnetic wave is transmitted from the transmitter antenna and is reflected at the boundaries between two materials with different electrical properties. These waves are received by a GPR receiver and digitized by the control and communication unit, and then finally the data are sent to the host computer for processing and display as shown in Figure 15-1.

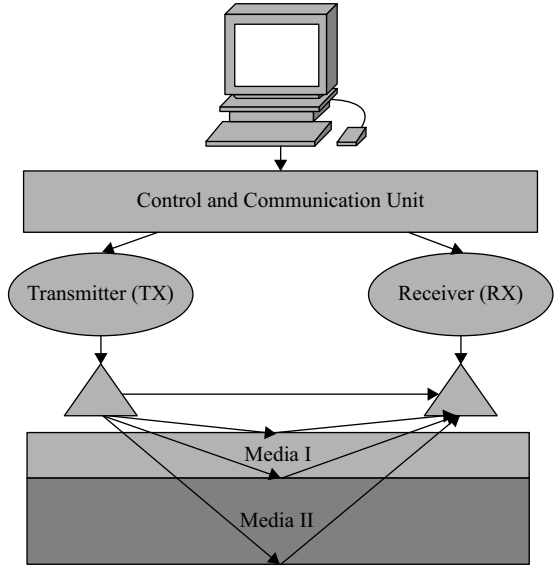


FIGURE 15-1 ■ Operating Principle of a Ground-Penetrating (or Material-Penetrating) Radar in a Three-Layer Environment.

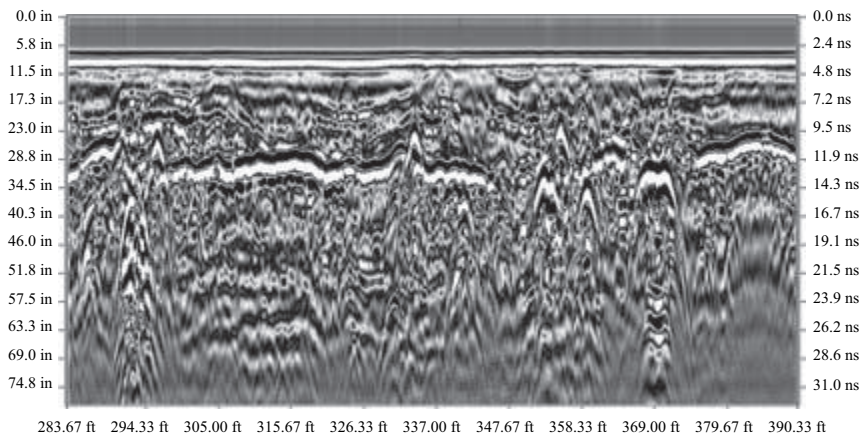


FIGURE 15-2 ■ Two-Dimensional Pseudocolor Display of Measured Radar Signals.

As the radar system moves along a designated survey line, an array of waveforms is received by the receiver and displayed in a two-dimensional pseudocolor fashion as shown in Figure 15-2.

From Figures 15-1 and 15-2 we can see that the depth range of GPR is limited by the electrical conductivity of the materials, the operating center frequency, and the radiated power of the GPR. As conductivity of the materials increases, the penetration depth decreases. This is because the electromagnetic energy is more quickly dissipated in the conductive materials and converted into heat, causing a loss in signal strength in the media. Higher frequencies do not penetrate as deeply as lower frequencies due to shallower skin depth (which is inversely proportional to the square root of the operating frequency and the conductivity of the materials) but give better spatial resolution. Maximum depth of penetration is achieved in ice and can reach several hundred meters. Good penetration is also achieved in dry sandy soils or massive dry materials such as granite, limestone, and concrete and could be up to 45 meters. In moist or clay-laden

soils and soils with high electrical conductivity, penetration depth is sometimes only a few centimeters.

Ground-penetrating radar antennas are generally in contact with the ground to couple more EM energy to the ground surface; however, air-launched GPR antennas can be used above the ground for shallow detection. Cross-borehole GPR has developed within the field of hydrogeophysics to be a valuable means of assessing the presence and amount of soil water.

As shown in Figure 15-1, a GPR system includes four main parts: a transmitter, a receiver, a control unit, and a host computer. The transmitter generates an electrical signal in the frequency band of interest, and the signal is then radiated into material in the form of EM waves by the transmitting antenna. Part of the transmitted wave – the *direct wave* – reaches the receiving antenna through the air; another part of the wave – the *surface reflection wave* – is reflected by the ground surface; and the other part of the transmitted wave penetrates the ground surface into the material and is absorbed, transmitted, and reflected back when it hits the interface between the layers. The travel time of each echo is proportional to the distance from the interface to the transmitting and receiving antennas as well as the electrical properties of the media. The receiver receives all these signals. The control unit controls the timing procedures of the transmitter and receiver. The host computer processes the received data and extracts and displays measured pavement information.

15.1.2 Hardware Architectures of GPR Systems

To increase spatial resolution, GPR systems have to be ultrawideband. Therefore, for CW radars, some forms of frequency modulation must be applied. Three major architectures have been employed to construct a GPR system: impulse radar, frequency-modulated CW (FMCW) radar, and stepped frequency CW (SFCW) radar. FMCW and SFCW GPRs are frequency-domain implementations of a pulsed GPR. These GPR architectures can be described by the waveform of the transmitted signals. Figure 15-3 shows the transmitted waveforms of different GPR architectures. In the following sections, we will briefly discuss each cited structure.

15.1.2.1 Impulse Radar

The transmitted signal of the impulse radar is a nanosecond monopolar or bipolar pulse [Figure 15-3(a)]. The reflected signal is usually a wavelet with a short duration. The delay time of the reflected signal with respect to the direct wave is proportional to the distance from the antennas to the reflection boundary. The impulse radar is the most used GPR architecture due to its hardware simplicity and low cost. However, it has shortcomings such as ultrahigh sampling rate (picosecond equivalent-sampling period), difficulty in accurate frequency band control, and pulse jittering noise.

15.1.2.2 Frequency-Modulated Continuous Wave Radar

The FMCW radar radiates a linearly frequency modulated wave [Figure 15-3(b)]. As the frequency of transmitted and received signals increases with the time, delay in the reflected signals is then translated into frequency differences between the transmitted reference signal and the received signals. When the received signal is mixed with the reference signal, which is synchronized with the transmitting signal, a *beat signal* or

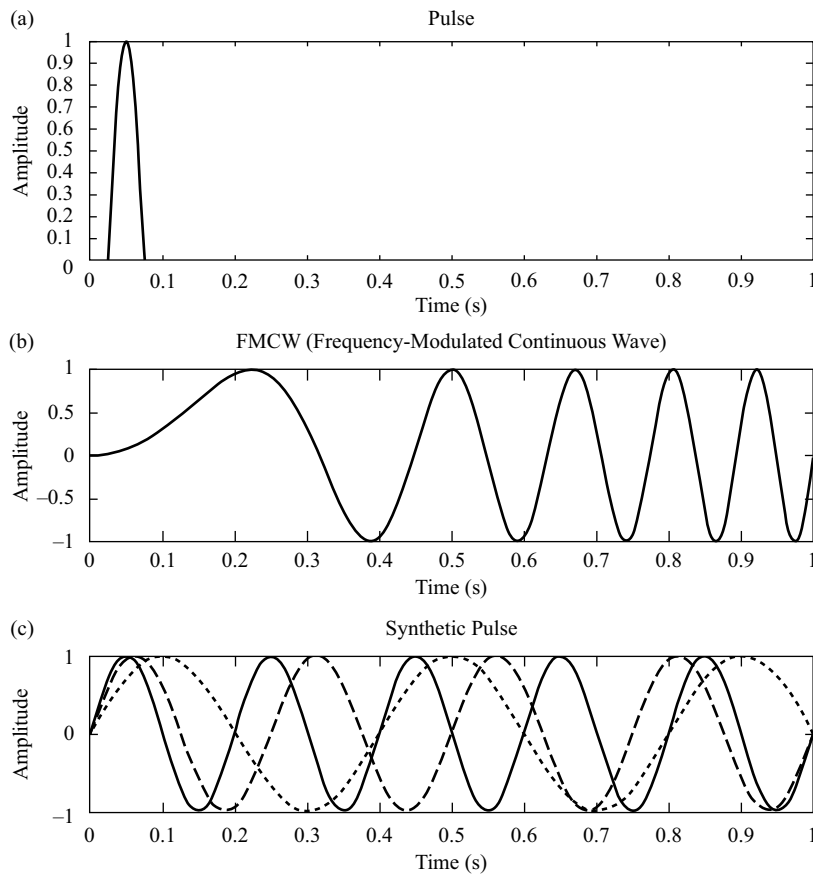


FIGURE 15-3 ■ The Transmitted Waveforms of Different Radar Methods Used in GPR Hardware Implementation.

frequency-difference signal will be formed. Since the beat frequency is proportional to the time delay and the amplitude is proportional to the strength of the reflected signal, the spectrum analysis of the received signal will determine the target distance and attenuation.

15.1.2.3 Synthetic Pulse Radar

Synthetic pulse radar is also called *stepped frequency continuous wave radar*. In FMCW radar, the frequency of the transmitting signal is linearly modulated and the beat signal spectrum is obtained as a received signal for analysis. Consider a pulsed-GPR transmitting signal: If the time-domain signal is Fourier transformed into the frequency domain, a wide frequency band can be found. This gives us a hint that the pulsed-GPR system can also be implemented in the frequency domain and then inversely Fourier transformed to the time domain, as long as we have enough frequency-domain samples. Therefore, another way to implement pulsed radar is to transmit a single frequency signal each time and step up at a small delta in frequency until the end of the frequency band as shown in Figure 15-3(c). The receiver receives both amplitude and phase at each frequency step. When the received signal is inversely Fourier transformed into time domain, a signal similar to the impulse radar can be obtained.

It is clearly seen that SFCW radar is a frequency-domain implementation of the impulse radar. However, SFCW radar has both benefits of FMCW radar and pulsed

radar. Theoretically, in a SFCW radar system, transmitter amplitude, phase, and frequency can be accurately controlled at each frequency step, so it is possible to compensate the nonideal frequency response of antennas to improve spatial resolution and penetration depth. However, the compromise of SFCW radar is its complicated hardware structure and high power consumption.

The other consideration is the transmitting power. Pulsed GPR can generate narrow pulses with large amplitude to increase instant power. Most pulsed GPR can reach 100 W of instant power easily. However, for continuous wave radars, the transmitting power is limited to a few watts.

15.1.3 The Pulsed-GPR System

As discussed in the previous sections, the GPR system uses pulse echoes to determine material boundaries and characteristics. In Figure 15-1, the directly coupled wave from the transmitter antenna to the receiver antenna is used as a time and amplitude reference since it is least affected by the change in the materials to be measured. The layer and material information is carried in the reflected signals (echoes). We will now discuss echoes in more detail.

Consider Figure 15-4, assuming the materials are lossless and the distance between the transmitter and receiver antennas is negligible, the travel distance along this path can be calculated by

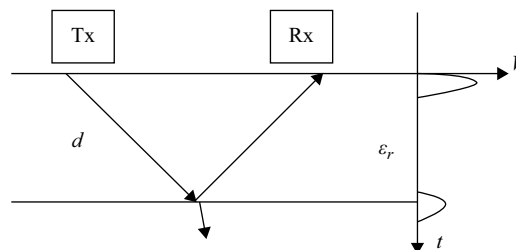
$$d = \frac{t \times c}{2\sqrt{\epsilon_r}} \quad (15.1)$$

where

- t = signal travel time between the transmitting and receiving antenna via the reflecting interface,
- c = speed of light in a vacuum, and
- ϵ_r = relative dielectric constant of the medium.

In the ideal case, the reflected signal is just a replica of the transmitted waveform. However, in real application, the received signal not only has the wave component that travels along the path shown in Figure 15-4 but also includes the direct wave and the surface-reflected waves described in Figure 15-1. Figure 15-5 shows a waveform of the received signal in a 400-MHz GPR system that uses a 2-ns pulse transmitter. A_0 in Figure 15-5 is the direct coupling between transmitting and receiving antennas, A_1 is the reflection from the ground surface, and A_2 and A_3 are caused by the boundaries between different materials under the ground. The positions of the peaks and the valleys in the

FIGURE 15-4 ■
A Path of Signal
Propagation in a
One-Layer
Structure.



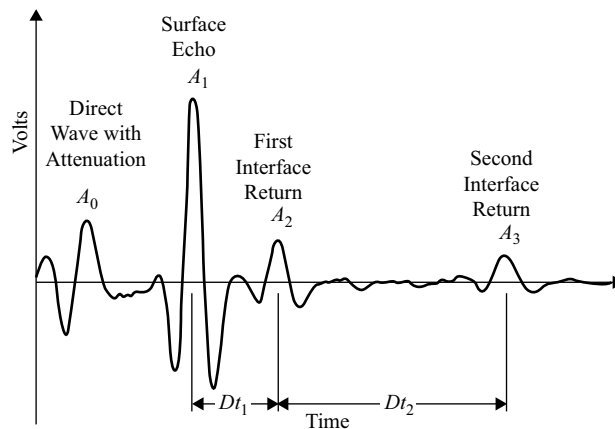


FIGURE 15-5 ■ The Waveform of Received Signals in an Impulse GPR System.

received signal represent the travel time of the reflected waves, which is proportional to the distance from the boundaries to the antennas. We also noticed that the actual waveforms transmitted from transmitter antenna, going through materials, and received by the receiver antenna is a typical Gaussian pulse going through a band-limited system. In addition, the actual directly coupled wave A_0 has a smaller amplitude because the GPR system has a nonlinear gain-control mechanism to intentionally suppress the directly coupled signal to enhance the reflected signal from layer surfaces. The detection resolution of the radar is determined by the high-frequency components of the received signal. The higher the system frequency, the easier it is to distinguish two closely spaced reflection events.

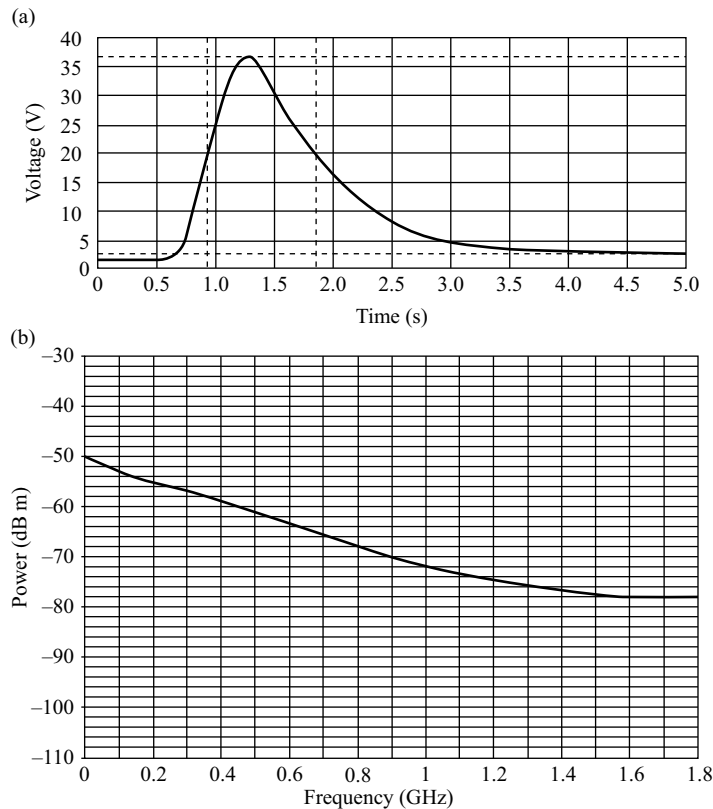
The transmitted signal is usually generated from an avalanche transistor circuit and shaped to a desired frequency band. A typical transmitter signal is shown in Figure 15-6(a). The spectrum of the transmitted signal is shown in Figure 15-6(b). The spectrum of the received signal is determined by the bandwidth of the transmitted signal, the bandwidth of the transmitting and receiving antenna, and the propagation paths. From Figure 15-6, we can see that the highest frequency of the signal reaches to 1.7 GHz, with attenuation of 30 dB from its peak at zero frequency or DC. To process these signals in computers, we need to convert the signals to digital form. Nyquist's theorem states that if we sample the complex waveform uniformly at a rate more than twice the highest frequency component sine wave contained within, then the samples obtained are sufficient information to reconstruct the waveform. Therefore, the sampling rate for this signal is at least 3.4 GHz to obtain a good time-domain waveform. Thus, a sampling period of at least 300 ps must be achieved.

15.2 | PULSED GROUND-PENETRATING RADAR SYSTEM DESIGN

15.2.1 GPR Design Consideration

The design of a GPR system is application specific. For different applications, different GPRs with different parameters must be used. Therefore, GPR manufacturing must be custom made for each case. For example, for a road-survey application, an air-launched

FIGURE 15-6 ■
The Frequency
Spectrum of the
Received Signal with
2-ns Transmitter:
(a) Transmitting
Pulse and (b)
Spectrum of the
Transmitted Pulse.



GPR is used to measure the thickness of the top layer and base layer. The center frequency of this radar should be high enough, usually more than 1 GHz in order to achieve required spatial resolution. The other issue is that the speed of GPR measurements must be high enough for fast data acquisition. The corresponding receiver and data processing should be designed to cope with the system design. The basic system design parameters of a pulsed-GPR system include center frequency, sampling rate, antennas, time window, and equivalent-sampling interval.

15.2.1.1 Center Frequency

Selecting the operating frequency for a GPR survey is the first step in the application process. There is a trade-off between spatial resolution, depth of penetration, and system portability. As a rule, it is better to trade off resolution for penetration depth since it is apparently useless to have a great resolution if the target cannot be detected. The best way to approach the problem is to define a generic target type (i.e., point target, rough planar target, or specula target) and specify a desired spatial resolution S . The initial frequency estimate is then defined by the empirical:

$$f = \frac{150}{S\sqrt{\epsilon_r}} \text{ (MHz)} \quad (15.2)$$

where ϵ_r = relative permittivity (dielectric constant) of the material.

A simple guide is the following table, which is based on the assumption that the spatial resolution required is about 10–40 percent of the target depth as indicated in Table 15-1. When the material is low loss, 10-percent spatial resolution can be achieved. For high-loss materials, upper boundary should be selected. These are values based on empirical data. Since every problem requires careful thought, the values in Table 15-1 should only be used as a quick guide and not as a replacement for thoughtful survey planning. In lighter materials (low loss) such as snow, ice, sand, and rocks, the penetration depth is deeper and the spatial resolution is higher. For a 100-MHz GPR, when used in coal mines, the penetration depth can reach as deep as 20 meters [21]. We should note that in (15.2) the contribution of conductivity of the materials is not shown. This is because the conductivity of the material is difficult to estimate. Actually, the conductivity plays a more important role in spatial resolution and penetration depth. High-conductivity material absorbs more EM energy and reduces penetration depth and spatial resolution. Equation (15.2) applies only to nominal attenuation cases.

15.2.1.2 Window Size

The GPR signal is a time-domain signal. The received signal is a time-domain waveform as shown in Figure 15-5. The number of display points is fixed, depending on the GPR clock speed and number of sampling points in one frame. To show the reflection signal from the deepest reflection layer, the GPR window must be set according to the dielectric constant of the material and the investigation depth. If the window is too wide, then the waveforms may be too narrow and detailed information of the subsurface may be lost. However, if the window is too narrow, then only a portion of the total waveform can be obtained. The way to estimate the time window required by a given application can be estimated by the following equation derived from (15.1):

$$W = 1.3 \times \frac{2 \times \text{MaxDepth}}{\text{Velocity}} = 8.7 \times \text{MaxDepth} \times \sqrt{\epsilon_r} \quad (15.3)$$

where

MaxDepth = maximum depth desired to investigate and

Velocity = wave propagation velocity in the media.

Usually, to avoid narrow window settings, the preceding expression increases the estimate time by 30 percent to allow for uncertainties in velocity and depth variations. If no information is available about the electrical properties of the subsurface, see

TABLE 15-1 ■ Investigation Depth, Spatial Resolution and Center Frequency of a GPR System in Soil ($\gamma = 4.3$)

Depth of Investigation (m)	Center Frequency (MHz)	Nominal Spatial Resolution (m)
0.5	1,000	0.07
1.0	500	0.14
2.0	200	0.35
5.0	100	0.70
10	50	1.41
30	25	2.83
50	10	7.07

Table 15-2, which provides a list of materials and their dielectric constant and conductivity ranges for initial estimation of the velocities of common geologic materials. Note that the attenuation of air is listed as zero, which does not necessarily mean that the wave will transmit in the air without attenuation. As EM wave propagates in the air as a function of distance, the amplitude will reduce inversely proportional to the distance it travels. In other words, the attenuation due to distance is not considered in Table 15-2.

15.2.1.3 Sampling Interval

One important parameter in designing a GPR system is the time interval between sampling points on a recorded waveform. The sampling interval is determined by the highest frequency desired in a GPR system. Based on the Nyquist sampling theorem, the sampling frequency of the GPR receiver should be at least twice the highest frequency components desired in the GPR system; in a practical system, it is usually three or more times higher than this minimum requirement. For most GPR antenna systems, the bandwidth to the center frequency ratio is typically about 1. What this means is that the pulse radiated contains energy from 0.5 times the center frequency to 1.5 times the center frequency. As a result, the maximum frequency is around 1.5 times the nominal center frequency of the antenna.

TABLE 15-2 ■ The Parameters of Different Geologic Materials

Material	Typical Relative Dielectric Constant	Conductivity (mS/m)	Velocity (m/ns)	Attenuation (dB/m)
Air	1	0	0.3	0
Distilled water	80	0.01	0.033	0.002
Freshwater	80	0.5	0.033	0.1
Seawater	80	0.01	0.01	1,000
Dry sand	3–5	0.01	0.15	0.001
Saturated sand	20–30	0.1–1.0	0.06	0.03–0.3
Limestone	4–8	0.5–2	0.112	0.4–1
Shale	5–15	1–100	0.09	1–100
Silts	5–30	1–100	0.07	1–100
Clays	5–40	2–1,000	0.06	1–300
Granite	4–6	0.01–1	0.13	0.01–1
Dry salt	5–6	0.01–1	0.13	0.01–1
Ice	3–4	0.01	0.16	0.01

TABLE 15-3 ■ Sampling Intervals versus Operating Frequency

Antenna Center Frequency (MHz)	Maximum Sampling Interval (ns)	Minimum Equivalent-Sampling Frequency (MHz)
10	16.7	60
20	8.3	120
50	3.3	300
100	1.67	600
200	0.83	1,200
500	0.33	3,000
1,000	0.17	6,000

Based on the assumption that the maximum frequency is 1.5 times the nominal antenna center frequency, data should be sampled at a rate twice this frequency. For good survey design, it is better to use a safety margin of 2. Therefore, the sampling rate should be approximately six times the center frequency of the antenna being utilized. Hence, the sampling frequency of the GPR receiver should be higher than the lower limit of

$$f_s \geq 6f_0 \quad (15.4)$$

where

f_s = sampling frequency and
 f_0 = center frequency of the GPR antenna.

The corresponding sampling interval t_s is

$$t_s \leq \frac{1}{6f_0} \quad (15.5)$$

Table 15-3 summarizes suitable sampling intervals versus operating frequency.

In modern GPR design, the sampling interval is software selectable and can be largely beyond the numbers listed in Table 15-3. The equivalent-sampling frequency can reach more than 10 times the GPR center frequency. Table 15-4 shows the requirements of GPR transmitter rise time for various GPR center frequencies.

15.2.2 GPR Hardware Block Diagram

As shown in Figure 15-7, a complete pulsed-GPR hardware system includes a transmitter antenna, a receiver antenna, a narrow-pulse generator, a sampling bridge, a GPR receiver, various timing and control circuits, a data-acquisition unit, a data-processing and data-communication system, and a data-storage and data-display device. Each block will be described in detail in the following sections.

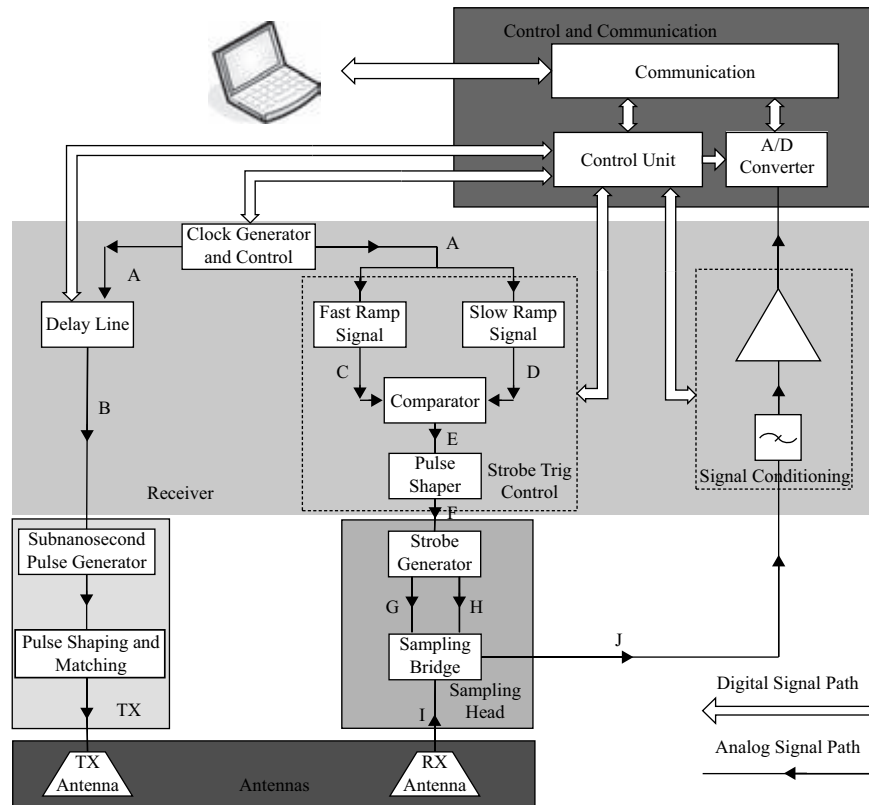
15.2.2.1 Antenna Selection

Consider Figure 15-5. GPR reflections are replicas of the transmitted signals separated by time intervals. The transmitted signal has a main pulse followed by a short tail. The short tail is caused by insufficient bandwidth of the system. Narrowband usually makes the tail of the transmitted signal and reflected signals rather long, resulting in the mix between waves, and therefore reduces the spatial resolution. In an ideal case, GPR system bandwidth should be as wide as possible. Practically, the GPR system bandwidth is about the same as the center frequency – that is, the relative bandwidth is about 100 percent. Although the GPR bandwidth is determined by many factors such as transmitter pulse width, antenna bandwidth, and sampling interval, antenna bandwidth is the most deterministic parameter that plays the bottle neck in a GPR system. Since the

TABLE 15-4 ■ GPR Center Frequency versus Transmitter Pulse Width

GPR center frequency (GHz)	0.1	0.2	0.4	0.6	1	1.2	2	2.5	3	3.5
Required transmitter pulse rise time (ns)	2.51	1.25	0.63	0.41	0.25	0.21	0.13	0.10	0.08	0.07
First zero crossing frequency in spectrum (GHz)	0.40	0.80	1.60	2.39	3.99	4.78	7.97	9.97	11.96	13.95

FIGURE 15-7 ■ Detailed Impulse GPR Hardware Block Diagram.



spatial resolution is determined by the characteristics of the GPR system bandwidth, antenna selection becomes critical in GPR development. Wideband requirements usually result in a relatively large antenna size to radiate the energy in the spectrum at the low-frequency end. To achieve small antenna dimensions and acceptable antenna performance, the antenna design must compromise between bandwidth and gain for a given application. An important consideration when choosing equipment for any particular application is to determine correctly the exact trade-off between spatial resolution, size of antenna, scope of signal processing, and ability to penetrate the material.

15.2.2.2 High Sampling Rates Data Acquisition

The GPR received signal is a high-frequency RF signal. Unlike frequency-domain receivers, the GPR receivers must recover the entire time-domain waveform without distortion. To sample this high-frequency signal, according to the Nyquist sampling concept, the sampling period should be at most half the period of the highest frequency signal in the record. Take the GPR with center frequency of 400 MHz as an example: The maximum spectrum is about 1.7 GHz (Figure 15-6), and therefore a minimum of a 3.4-GHz analog-to-digital (A/D) converter must be used. In circuit design, a 3.4-GHz A/D converter is difficult to implement with the wide dynamic range and low power consumption that a GPR system requires. A non-real-time sampling method is usually used in a GPR implementation to solve this problem.

A sample method called *equivalent time sampling* is used to sample the high-frequency signal without losing the information in the signal but with a relatively low

sampling rate. Equivalent time sampling, however, is based on the assumption that the received signal is repetitive in the time interval during the sampling period. Detailed discussions about the sequential-sampling method will be introduced in the following sections.

15.2.2.3 Microprocessor and Microcontroller

Timing in the GPR system is critical: All the parts – the transmitter, the sampling rates, and the receiver – must follow the sequential clock. A microcontroller is the best way to do this because it has rich peripheral devices such as a timer, a pulse-width modulation wave generator, and a counter, as well as control features necessary in the GPR system design such as filter selection, gain control, window size control, and transmission-delay control.

A modern GPR system is so complex that microprocessors become a necessity in the system and timing control. Powerful microprocessors such as the ARM processor and digital signal processor not only can provide control functions but also have additional peripherals such as an Ethernet port, LCD, USB ports, SDRAM drive, and a Flash controller. A microprocessor is generally used to accomplish system control, data acquisition, and data communication.

15.2.2.4 Digital Circuit and Analog Circuit

As previously mentioned, timing and control circuits are critical in a GPR system due to requirements for accurate timing and sampling. Logic-integrated chips such as the inverter, OR gate, AND gate, and XOR gate will be used.

When the RF signal is obtained from the sampling head, it is very small in amplitude and noisy. Low-noise amplifiers and filters are used to amplify the signal to a certain level and proper frequency band so that the subsequent A/D converters can reach their maximum dynamic range.

15.2.2.5 Communication and Synchronization

There are two kinds of communication in the radar system: One is between the transmit and receive antennas, and the other is the communication among the microcontrollers, microprocessors, and host computers. When the transmitter and receivers are located in the same enclosure, the communication and synchronization between the transmitter and receiver is relatively direct. However, in low-frequency GPR systems (100 MHz or lower), to increase detection range and reduce influence from the direct wave, the transmitter and receiver antennas are usually spatially separated. Timing synchronization between transmitter and receiver antennas is critical in such cases. The communication links inside GPR systems must be reliable and chronologically accurate.

Communication methods can be wired communication between the microcontroller and microprocessor or wireless communication between antennas and host computer and antenna box.

15.2.2.6 Signal Processing

Signal processing here refers to the hardware signal conditioning and software data processing inside the GPR system in real time, not post-processing. For hardware signal processing, it includes the amplifier and filters such as low- and high-pass filters with

proper bandwidth and gain selections. Hardware signal processing also includes time-varying gain control to reduce direct waves and to enhance reflected waves.

For post-processing, many methods used in seismic signal processing and general signal processing can be adopted, such as background removal, software gain adjustment, software filter, peak tracking, and common middle point.

15.2.2.7 Post-Processing Software Development

When a GPR signal is sent to the data-processing unit, usually, a computer, the signal is further processed. In modern GPR systems, a software interface is developed to simplify usage. The interface and post-processing software is usually developed using a higher level language like Visual C++, Visual Basic, MATLAB®, or C#. These development environments are increasingly user-friendly to developers.

15.2.3 Examples of GPR Applications

GPR has found many applications, including void detection, pavement thickness calculation, utility pipe leakage detection, buried pipe and cable locating, peat profiling, coal mining safety inspection, hazardous-waste mapping, oil under ice detection, through-wall imaging, life detection after natural disasters, and archeological imaging. The following sections elaborate.

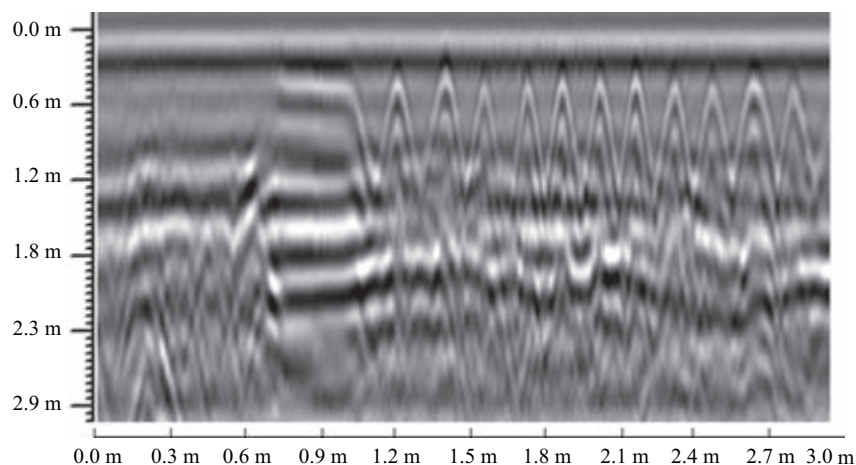
15.2.3.1 Rebar Imaging

In a construction area, reinforced concrete is widely used. When the concrete is mature, it must be inspected to see whether the rebar was placed correctly as part of quality control. In this case, GPR can be used for rebar imaging to display rebar spacing, depth, and even diameter. A color plot of such a measurement on a state highway is shown in Figure 15-8.

15.2.3.2 Pipe Detection

Figure 15-9 is the field-test result in detecting pipe in an urban area using a 400-MHz GPR. The display is in full-color mode, and the sampling mode is DMI (distance measurement instrument) trigger, and therefore the horizontal axis is the distance instead of time. The area marked with a circle is the location of a pipe.

FIGURE 15-8 ■ GPR Image of Highway Rebars. Vertical Axis is the Depth and Horizontal Axis is the Distance in Meters. Each Parabola is a GPR Image of a Rebar reflection. There are Multiple Reflections and Layer Reflections in the Image.



15.2.3.3 Through-Wall Imaging and Life Detection

GPR can also be used to detect moving or static images through walls. By processing the measured data, images of the objects on the other side of the wall can be reconstructed. Figure 15-10 shows a typical application of the application of a through wall imaging system.

The front-end hardware of the through-wall imager and the life-detection system are very similar to a GPR system. The difference between the two is the signal processing and information display. The life-detection system uses GPR data and conducts timed Fourier transform to detect heartbeat and breath information while the GPR is immobile. The through-wall imaging system, on the other hand, looks for images of the objects on the other side of the wall. Figure 15-11 shows a life-detection GPR system that was used in real rescue operation after the disastrous Wenchuan earthquake on May 12, 2008, in

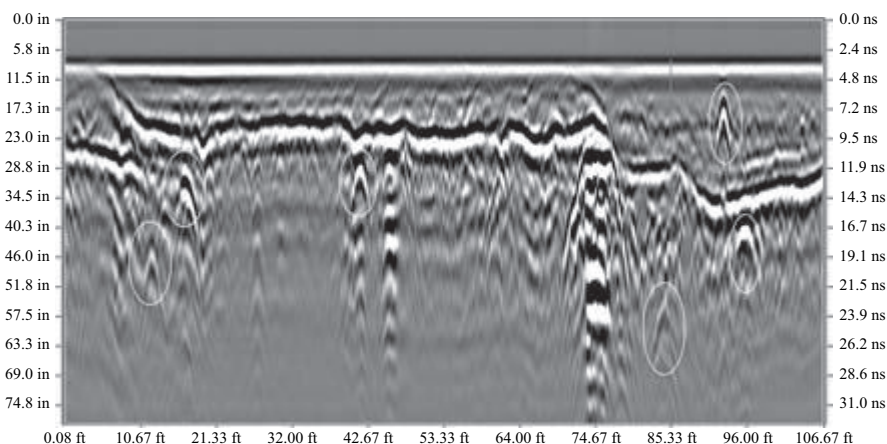


FIGURE 15-9 ■ GPR Image of Pipe Detection. The Horizontal Axis shows the Distance in Inches. Gray Scale represents Signal Amplitudes According to the Range of the Data-Acquisition System. In this Example, the Maximums are 10 V.

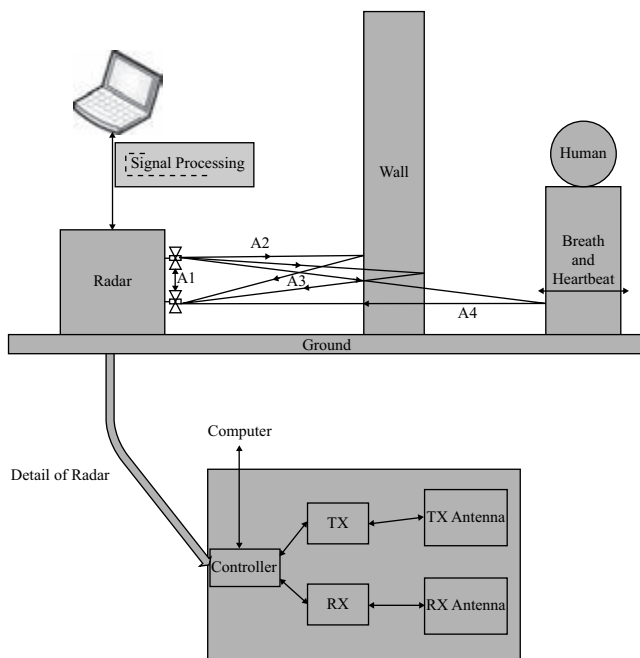


FIGURE 15-10 ■ A Simplified Life-Detection and Through-Wall Imaging System.

Sichuan Province, China. Figures 15-12 and 15-13 are the processed data from a life-detection GPR system.

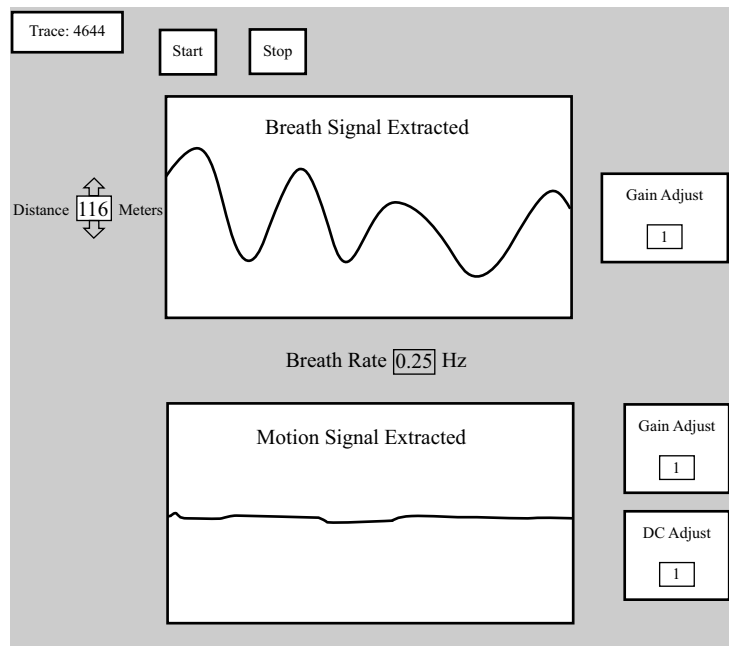
15.2.4 GPR Antennas

In most GPR systems, the bandwidth bottleneck is the antennas. In antenna theory, the gain and bandwidth product is a constant for a given antenna. Increasing bandwidth also means sacrificing antenna gain. However, due to high instant power, a pulse-GPR

FIGURE 15-11 ■ A 400-MHz Life-Detection GPR Was Used in Rescue Efforts After the Disastrous May 12, 2008, Earthquake in Wenchuan, Sichuan Province, China. Life Signatures under Earthquake Rubble Can Be Obtained by GPR Data Processing [Courtesy of Biken Co.].



FIGURE 15-12 ■ Processed Life-Detection Radar Signals [Courtesy of Biken Co.].



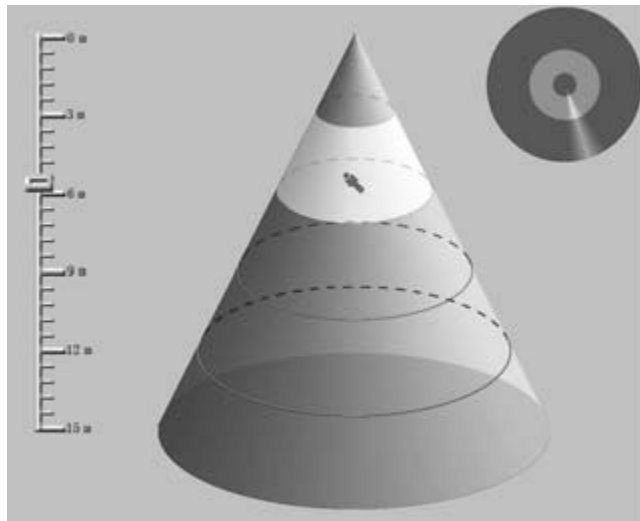


FIGURE 15-13 ■ Location of the Person in the Radar-Detection Range [Courtesy of Biken Co.].

system usually has enough system gain to cover the loss of antennas. The pulses generated in the GPR transmitter will be sent to the antenna for transmission. As discussed in the previous sections, ideally the pulse radiated from the antennas should be as narrow as possible to obtain a higher spatial resolution. In the meantime, the energy of the pulse must be large enough to penetrate through lossy materials. Therefore, the antenna used in the GPR system should have enough bandwidth to allow fast pulses to be radiated and received. For this reason, a proper compromise must be made in antenna selection. In most cases, it is much easier and more economical to generate high-amplitude pulses than to make a high-gain antenna. In the GPR antenna design, wideband becomes the design objective, and gain is somewhat compromised.

GPR antennas are ultrawideband (UWB). For an ultrawideband impulse antenna, the desire is to effectively radiate the pulse signal without distortion. Therefore, the antennas should have a wide working frequency band and a fixed phase center. Since the signal transmitted and received by the antenna usually has a bandwidth that is more than 20 percent of its center frequency, the GPR is defined as an ultrawideband system. The pulse shape carries information of the materials that the waves go through. The transmitted time-domain signal contains abundant frequency components. Thus, the radiation of a GPR antenna depends on how the characteristics change with the frequency in the required frequency band. When an antenna transmits a single frequency signal, the excitation signal changes continuously and periodically in the time domain. In the pulsed system, we need to consider the relationship between amplitude and phase at the same time in order to minimize the distortion of the pulse due to the antenna characteristics. Consider the Gaussian impulse excitation signal as an example. If the excitation of the antenna is a Gaussian pulse, due to the bandpass nature of the antennas, the radiation field from the antenna is in the differential form of its excitation signal. When the receiver antenna receives this field, if the load is matched with the impedance of the antenna, the received voltage will be completely applied to the load without reflection in the entire band. The current on the load will be proportional to the incoming field. Thus, the received waveform will keep the shape of the differential Gaussian pulse, which means the signal waveform of the receiving antenna

at the maximum receiving direction is similar to the incident signal waveform. However, the characteristics of the GPR antenna are not ideal in practice. We need to consider signal amplitude and phase when designing a GPR antenna according to the frequency response of the antennas. The other issue is that the frequency characteristics of the materials cannot be assumed to be dispersionless. Frequency dispersion will introduce distortions, so distortions may occur during transmission in a wide band in lossy media.

15.2.4.1 GPR Transmitting Pulse

The Gaussian pulse signal is a common model in time-domain analysis, which can be expressed by [22]:

$$g_n(t) = \frac{\tau^n \left(\frac{n}{2}\right)!}{n!} \frac{d^n}{dt^n} e^{-(t/\tau)^2} \quad (15.6)$$

where

$n = 0, 1, 2, \dots$ is the degree of Gaussian signal and
 $\tau =$ time constant of pulse width.

Figure 15-14(a) shows the waveform in different order when τ is equal to 1 ns. By Fourier transformation, the spectral function of the Gauss signal $g_n(t)$ is

$$G_n(\omega) = \frac{\tau^n \left(\frac{n}{2}\right)!}{n!} (j\omega)^n \sqrt{\pi\tau^2} e^{-(\tau\omega/2)^2} \quad (15.7)$$

We can obtain the maximum frequency of spectral density of the Gaussian pulse in (15.7):

$$\omega_c = \frac{\sqrt{2n}}{\tau} \quad \text{or} \quad f_c = \frac{\sqrt{2n}}{2\pi\tau} \quad (15.8)$$

If we know the bandwidth and f_c , then we can find the degree of the Gaussian pulse by (15.8).

By normalizing the spectral density of the signal in (15.7), we can obtain the power spectral density:

$$U(\omega) = \begin{cases} e^{-(\tau\omega/2)^2/2} & n = 0 \\ \left(\frac{e}{4\pi^2 f_c^2}\right)^n \omega^{2n} e^{-(\tau\omega/2)^2/2} & n > 0 \end{cases} \quad (15.9)$$

Figure 15-14(b) shows the power spectral density when $\tau = 1$ ns, which shows that when $n = 0$, the pulse has a large DC component, and when $n = 1$, the pulse becomes a bandpass signal. In practice, we usually use $n = 0$ and $n = 1$ cases to represent pulse generated from a GPR transmitter electronics and the pulse signal received from a GPR receiver, respectively. We notice that when $n = 0$, the pulse is a unipolar signal in which the DC component is dominant. If the antenna size is too small to

radiate low-frequency signal, then the low-frequency characteristic of the radiation field will be compromised. When $n = 1$, the signal is a differential Gaussian pulse that is bipolar and becomes a bandpass signal, which describes an output when a signal of $n = 0$ passes through a band-limited system such as an antenna. The Gaussian pulse is a better description of GPR transmitter signal. However, for mathematical simplicity, we can approximate the Gaussian pulse by a triangular signal without losing generality.

Figure 15-14(c) shows a triangular approximation of the Gaussian pulse when $n = 0$, which is a linear approximation of the Gaussian pulse when $n = 0$.

15.2.4.2 Bow-Tie Antennas

Bow-tie antennas [23] are widely used in GPR systems as transmitting and receiving antennas. A bow-tie antenna is a simplification of a biconical antenna. The wide-band characteristic and time-domain characteristic of a biconical antenna is ideal (Figure 15-15) because of its characteristics of frequency independency – it is impractical to use, however, due to its size and cost.

The space between the two triangle pieces forms a transmission line. If the ratio between the equivalent inductance L and equivalent capacitance C remains constant from the center to the edge, then the characteristic impedance will not change along the transmission line and wideband antenna characteristics will be present. This is similar to the biconical antenna.

Although the UWB characteristic of the bow-tie antenna (Figure 15-16) is not as good as that of the biconical antenna, it has a simple mechanical structure, is easy to manufacture, and is easy to integrate into a system. Due to these reasons, the bow-tie antenna is widely used in ground-penetrating radar systems. Note that the bow-tie antenna is a balanced antenna. If we use a parallel line feed, then balanced matching

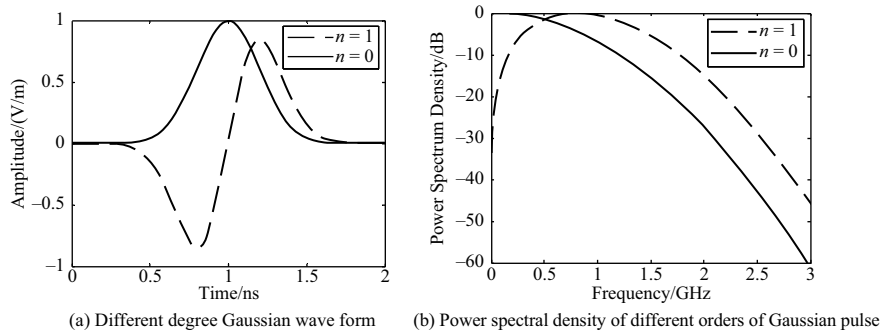
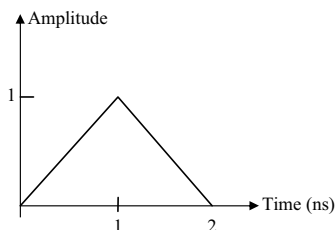


FIGURE 15-14 ■ Waveform of a Gaussian Pulse and Linearized Triangular Pulse.



(c) Linear approximation of the Gaussian pulse when $n = 0$ in Figure (a)

FIGURE 15-15 ■
Biconical Antenna.

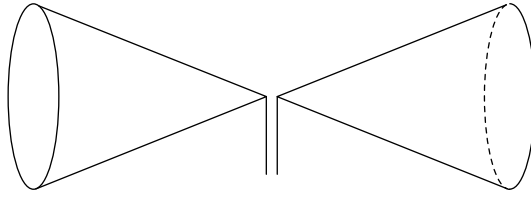
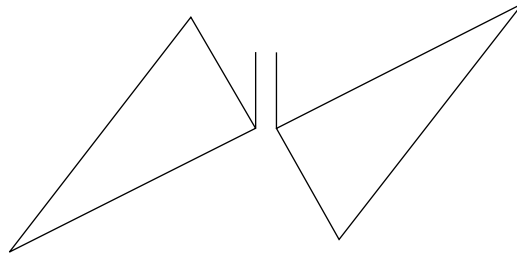


FIGURE 15-16 ■
Bow-Tie Antenna.



circuits will be needed. If we use a coaxial line to feed the antenna, then we need to add a balun to keep a balanced input.

For GPR applications, the bow-tie antenna can be categorized into three different types: unloaded, end-loaded, and distributed resistive load.

15.2.4.3 Unloaded Bow-Tie Antenna

The bow-tie antenna is shown in Figure 15-16. Due to the limited size of the antenna, there is a discontinuity at the end of the antenna, which will generate a reflection (antenna ringing). The reflected signal from the target will mix with the end reflection of the antenna and make the data interpretation difficult. Also note that the unloaded bow-tie antenna can be considered a transformed version of a dipole. In most GPR applications, bow-tie antennas are not used without adding resistive loads to reduce the end reflection and increase bandwidth.

15.2.4.4 End-Loaded Bow-Tie Antenna [24]

To make the antenna short and minimize the reflections at the end of the antenna, we can add resistive load at the end of the antenna to absorb energy reaching the ends. When the EM energy reaches the resistive load, instead of radiating the energy or reflecting it back, it is absorbed by the resistive load as if the antenna is infinitely long. To minimize the reflection, the value of the resistive load must match the impedance of the antenna ends in the entire frequency band. Therefore, the load impedance must be equal to the characteristic impedance of the antenna. We should notice that the impedance of the antenna is not a constant throughout the frequency band. On the other hand, the end resistor is a constant. The end loading method thus is of limited use when increasing bandwidth. In most cases, the end loading can improve low-frequency performance significantly if proper matching is achieved. To ensure the load current return loop, we can add metal shielding to form a shielded bow-tie antenna. The end-loaded bow-tie antenna can effectively reduce wave reflection. To reduce reflection from the back of the metal shielding, absorbing foam is usually inserted between the back of the antenna and the metal shield.

The load resistor can also cause energy loss and reduce the radiation efficiency. This method actually is a way to trade gain for bandwidth.

15.2.4.5 Definition of Ultrawideband

In a communication system, the bandwidth of a signal is defined as the ratio between 3-dB bandwidth and the center frequency, or the ratio between absolute bandwidth and center frequency:

$$B = \frac{f_h - f_l}{(f_h + f_l)/2} = \frac{\Delta f}{f_0} \quad (15.10)$$

where

f_h = upper 3-dB frequency,

f_l = lower 3-dB frequency,

$\Delta f = f_h - f_l$, absolute 3-dB bandwidth, and

$f_0 = \frac{f_h + f_l}{2}$ center frequency.

In (15.10), we see that $0 \leq B \leq 2$. When $f_h = f_l$, the signal is a single frequency signal and B is 0. When the signal high-frequency bandwidth f_h is much greater than the low-frequency limit f_l , $f_h \gg f_l$, the signal bandwidth approaches the upper limit of 2. When $B < 1\%$, the signal is a narrowband signal. When $1\% \leq B < 25\%$, the signal is generally considered to be a wideband signal. When $B \geq 25\%$, the signal is defined as ultrawideband. Most GPR systems have a bandwidth of more than 30 percent, and therefore the GPR system is an ultrawideband system.

The spatial resolution is determined by the characteristics of the antenna and signal processing employed. In general, to achieve an acceptable spatial resolution, we need a high-gain antenna. This necessitates the antenna dimensions to be able to accommodate the wavelength of the lowest frequency transmitted. To achieve small antenna dimensions and high gain, it is required to use a high carrier frequency, which generally does not penetrate the ground material with sufficient depth. An important consideration when choosing equipment for any particular application is to determine the exact trade-off between spatial resolution, antenna size, method of signal processing, and ability to penetrate the material. Figure 15-17 is a typical GPR antenna with shielding. The resistivity loading is used for increasing bandwidth trading with reduced antenna gain.

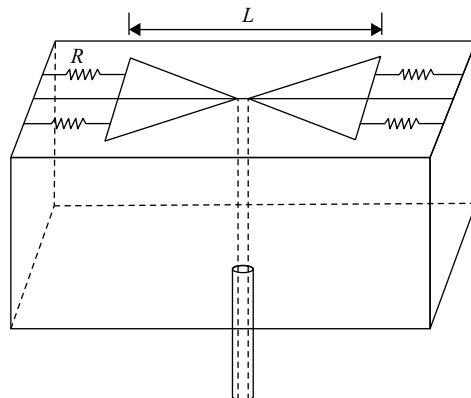


FIGURE 15-17 ■ End-Loaded Bow-Tie Antenna with Metal Shield [25].

15.2.5 Design of a GPR Transmitter

15.2.5.1 Discussions of Transmitter Pulse Width

Pulsed-GPR transmitter is a high-speed, high-voltage pulse generator. The objective of a pulsed-GPR transmitter design is to obtain a pulse that suits the GPR system antenna. The Gaussian pulse shown in Figure 15-14 is generally assumed in a GPR system. To simplify the analysis, the transmitter pulse is approximated by a triangular wave as shown in Figure 15-18. The triangular wave of the transmitter is shown in Figure 15-18(a); Figures 15-18(b) and (c) are the first- and second-order derivatives of the transmitted wave, respectively. The Fourier transform of the second-order derivative of the transmitted signal can be easily obtained from Figure 15-18(c):

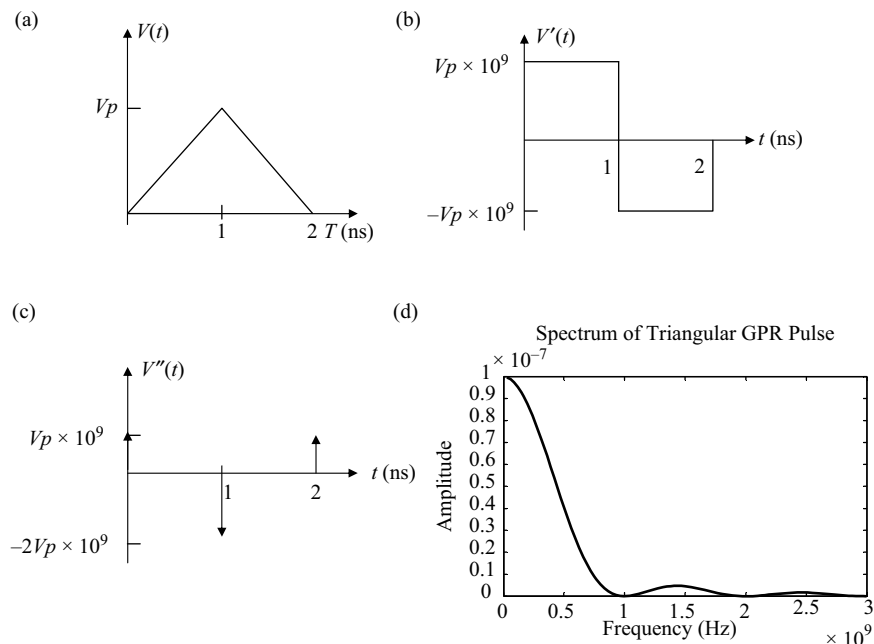
$$F(V'') = -\tau V_p \omega^2 e^{-j\omega\tau} \sin^2\left(\frac{\omega\tau}{2}\right) \quad (15.11)$$

Therefore, the spectrum of the transmitter signal can be obtained:

$$F(V) = \frac{F(V'')}{-\omega^2} = \tau V_p e^{-j\omega\tau} \sin^2\left(\frac{\omega\tau}{2}\right) \quad (15.12)$$

Figure 15-18(d) is the plot of the amplitude spectrum of the transmitter triangular signal. Note that the spectrum peak is at DC with the amplitude of $V_p\tau$. The spectrum magnitude is proportional to the area of the pulse. When pulse width is narrow, the amplitude of the spectrum will be small. We also notice that when the pulse is narrow – for example, τ is small – the spectrum tends to be flat. The amplitude decays in a squared sinc function with respect to the frequency. In the meantime, we can see that the first zero crossing of the spectrum is $f_0 = 1/\tau$, which is inversely proportional to half of the pulse duration τ , which is the rising edge of the transmitter pulse. If we define the

FIGURE 15-18 ■
GPR Transmitter
Pulse and Its
Spectrum.



maximum GPR system bandwidth as equal to the first zero crossing of the transmitted pulse spectrum, then the maximum GPR bandwidth can be written as

$$B_{max} = \frac{1}{\tau} \quad (15.13)$$

We must note that the spectrum of an impulse generated by a GPR transmitter has its major energy at DC. As previously discussed, the pulsed GPR directly transmits the impulse from the transmitter antenna without modulation. The portion of the radiated signal is only a part of the entire transmitted spectrum. When the pulse width is narrow, the spectrum tends to be flat, which means that the spectrum includes more high-frequency components. The antenna bandwidth is usually much narrower than that of the transmitted pulse. However, when the pulse rise time is very slow, the high-frequency components will have small amplitude. Due to hardware limitations, it is difficult to create narrow pulses with high amplitude. In designing a GPR transmitter, we must optimize the output energy at the specified frequency band by correctly compromising between the amplitude of the pulse and the pulse width of the transmitter pulse, which are determined by transmitter hardware. The 3-dB bandwidth of the pulse shown in Figure 15-18 can be calculated by solving

$$\sin c^2\left(\frac{\omega\tau}{2}\right) = \frac{1}{\sqrt{2}} \quad (15.14)$$

The solution can be easily found to be

$$B_{pulse} = \frac{1.8955}{\pi\tau} \quad (15.15)$$

When the pulse amplitude reduces to half its maximum, then we define the frequency as half the amplitude frequency, $f_{1/2}$:

$$f_{\frac{1}{2}} = \frac{1.392}{\pi\tau} \quad (15.16)$$

where B_{pulse} is the 3-dB bandwidth of the pulse shown in Figure 15-18. If we define the GPR center frequency equal to B_{pulse} , then we can calculate the required pulse rise time of the GPR transmitter. This definition will result in a very fast transmitter pulse, which will reduce the pulse amplitude significantly. In practice, a reasonable compromise is to select a GPR frequency equal to the frequency point that the pulse amplitude reduces to half its maximum. Based on this definition, Table 15-5 lists the pulse rise time required for typical GPR center frequencies.

From Table 15-5, we can see that in transmitter circuit design, the rise time of the transmitted pulse determines the frequency band of a GPR system. Something else to note is that as long as the first zero-crossing frequency is within the GPR antenna band, the GPR can still radiate energy to the media with compromised radiation energy.

The steeper the slope and the shorter the pulse duration, the more high-frequency components the system will have. These high-frequency components determine the system's spatial resolution. The amplitude of the transmitted pulse, on the other hand, affects the signal-to-noise ratio (SNR) of the received signal: The higher the amplitude, the greater the SNR of the receiver. However, increased transmitter amplitude will

introduce more noise into the system through the trigger paths and will raise the cost of the transmitter circuit and reduce the maximum pulse-repetition frequency (PRF). Sampling circuits in most pulse-GPR systems are based on a sequential-sampling technique. The duration of the sampling pulse applied to the sampling circuit holds the key to the time resolution of the received signal.

In receiver circuit design, the systems with shorter aperture time will have a higher time resolution, which also implies the better spatial resolution. The amplitude of the sampling pulse defines the dynamic input range of the sampling circuit. Subsequently, it affects the SNR of the GPR system. Sampling systems with higher control pulse amplitudes will provide a wider dynamic input range.

Unfortunately, shorter pulse duration and higher pulse amplitude are contradictory parameters in circuit design. PRF is another concern. Trade-offs among all these parameters have to be made in the system design.

15.2.5.2 Methods of Generating Nanosecond Pulse

The amplitude of the variable nanosecond pulse mainly affects the system in two ways. In a GPR transmitter, the amplitude of the transmitted pulse affects the SNR of the received signal. The higher the amplitude, the better the SNR of the receiver will reach. The PRF is another concern. It affects the resolution of the receiving signals. Trade-offs among all of these parameters are another necessity.

Three different methods are used to generate nanosecond pulses: (1) avalanche transistor pulse generator, (2) emitter-coupled logic pulse generator, and (3) pulse generator using high-speed gates [26, 27]. A brief comparison of these three methods is shown in Table 15-5. In the next section, we will discuss the method of using an avalanche transistor to implement the differential pulse generator as the transmitter due to its simplicity and effectiveness.

15.2.5.3 Avalanche Transistor Pulse Generator

Transistors biased in the “avalanche region” may show a negative differential resistance between the collector and the emitter. This part of a bipolar transistor is used for nanosecond pulse generation. The avalanche transistor circuit is a traditional method used to generate a nanosecond pulse. As shown in Figure 15-19, the normal range of transistor

TABLE 15-5 ■ The Comparison of the Three Nanosecond Pulse-Generating Methods

	Avalanche Transistor Pulse Generator	Emitter Coupled Logic Pulse Generator	High-Speed Logic Pulse Generator
Amplitude of the pulse	High	≤ 0.7 V	≤ 4.5 V
Rising time of the pulse	< 1 ns	≤ 160 ps	≤ 500 ps
Pulse repetition rate	Low	High	High
Jitter	Medium	Low	Low
Output format	Differential/unipolar	Differential/ Unipolar	Unipolar
Complexity of the power supply	Need high-voltage power supply	Need several voltage power supplies	Simple
Noise introduced into the whole system	High	Low	Low

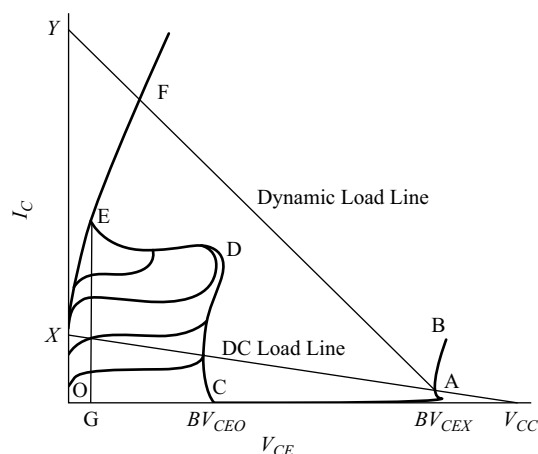


FIGURE 15-19 ■ Common Emitter Output Characteristics of a Typical Transistor.

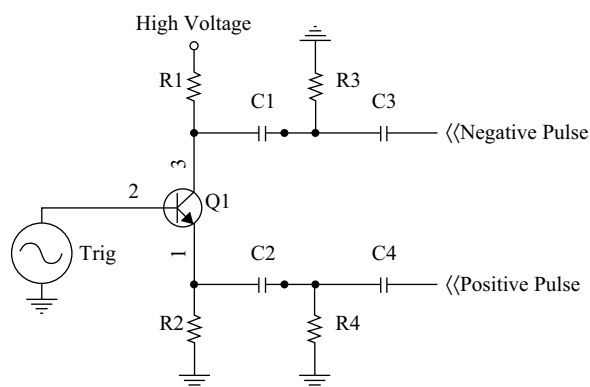


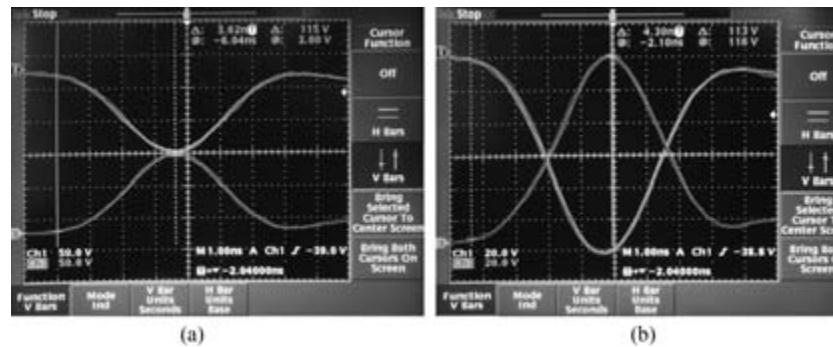
FIGURE 15-20 ■ Schematic of an Avalanche Pulse Generator with Differential Output.

operation is within the area enclosed by OCDEO, which is the safe operating active region. The avalanche of the transistor operates outside this area in the region ABFE [28].

Figure 15-20 shows the improved schematic of an avalanche circuit, which has two output ports from a single transistor: a negative pulse port and a positive pulse port. These two differential pulses are temporarily synchronized and oppositely polarized. They can be used as a differential transmitter of a GPR system and also as a differential strobe generator to drive a sampling bridge circuit without using any wideband balun, which may generate undesired ringing.

Upon application of supply voltages, capacitor C1 will charge through R1 and R3 until the voltages at the collector reaches BV_{CEX} . The transistor will reach the stable state at point A. The circuit will remain in this condition until a trigger is supplied. Application of a positive trigger pulse to the base will cause the transistor to conduct. Owing to the dynamic load C1, C2, R1, and R3, the operating point for rapid changes lies along the line AY (dynamic load line). Since this line lies completely outside the stable region, the collector voltage will collapse very rapidly along AY until the stable point F is reached. Capacitor C1 will then discharge through R3, C2, and R4, and the operating point will follow the line FE until a level is reached below which there is insufficient current to maintain the avalanche condition. The transistor will subsequently cut off and the operating point will fall to point G. Capacitor C1 will begin recharging and the operating point will move out on the BV_{CEX} curve until point A is again reached, completing a cycle.

FIGURE 15-21 ■
Output Waveform
from a GPR
Transmitter Shown
in Figure 15-20.



$C1$, $R3$, $C2$, and $R4$ determine the time constant of the differential pulses. By changing their values, different pulse widths and amplitudes can be achieved. Figure 15-21 shows the differential pulses with different pulse widths and amplitude. The pulses in Figure 15-21(a) have a 1.1-ns bottom pulse width and $\pm 6.3\text{-V}$ amplitudes generated by the circuit, while the pulses in Figure 15-21(b) have a 2.3-ns bottom pulse width and $\pm 14\text{-V}$ amplitudes. The waveform is measured by a digital sampling oscilloscope, Tek-11801B, with 22-dB attenuator.

Figure 15-21 shows the experimental result of the differential output voltages of the circuit in Figure 15-20. The signals have been attenuated by 22 dB before they are sent to the oscilloscope for display. The amplitude of each differential signal is 14 volts. The 10 percent to 90 percent rise time is about 500 ps. The pulse width, which is the time interval between the time that the pulse amplitude reaches 20 percent of the peak amplitude at the rising edge and the time that the pulse amplitude drops to 20 percent of the peak amplitude at the falling edge, is 2.3 ns.

The drawbacks of the circuit are its relatively low pulse-repetition frequency and the need of a high-voltage power supply. The PRF is controlled by the recharging time, defined as the time between the cessation of the avalanche current and the moment when the collector voltage reaches BV_{CEX} . It can be estimated as the time constant of $R1$ and the total capacitance from collector to ground. Large values of time constant of $R1C1$ circuit and BV_{CEX} will result in a low PRF. However, to obtain high output amplitude and low static current, the values of $R1$, $C1$ and BV_{CEX} must be high. Thus, a compromise must be made in the circuit design among the PRF, the cost of the high-voltage power supply, and the system SNR.

15.2.6 Design of a GPR Sampling Head

The sampling head as shown in Figure 15-7 receives signals collected by the receiving antenna and samples the signals by using a sequential-sampling method. This can benefit the system in two principal ways. First, it is easy and cost-effective to implement compared with real-time sampling for the ultrawideband input signals. Second, the ultrawideband RF signals can be down converted to the low-frequency band (normally less than 1 MHz), which is easy for the subsequent circuit for signal conditioning and processing.

The bandwidth of the sampling circuit will affect the bandwidth of the entire GPR system, so it defines the maximum resolution the system can achieve.

The sampling head, which is green in Figure 15-7, consists of a strobe generator and a sampling bridge. The strobe generator generates the strobe pulse train for the sampling bridge. The sampling bridge samples the received signal controlled by the strobe pulse train, which determines the sampling position on the received signal.

The sampling bridge includes two stages: the sampling bridge circuit and the preamplifier circuit. The sampling bridge circuit takes the samples from the ultrawideband signal under the control of the strobe trains and feeds the sampled pulses to the preamplifier circuit for amplification. Note that the sampling bridge only samples very small portions of the received signal and the preamplifier only amplifies the low-frequency components of the sampled pulses. As a result, the output of the preamplifier is a low-frequency replica of the ultrawideband signal. The strobe generator generates one pulse per transmitter pulse. In other words, the sampling bridge only samples one point each transmit cycle, which will be discussed in the next section. The simplified schematic of the sampling bridge is shown in Figure 15-22, which is a two-diode sampling circuit. The bias network places the diodes in a high-impedance reverse-biased state until the strobe fires. Each time the strobes fires, the strobe pulses forward-bias the two diodes, turning them on and lowering their impedances for a short time, which is determined by the pulse width of the strobes, the amplitude of the strobes, and the DC bias voltage. Since the large-signal strobe currents are in the same direction (shown by solid arrows in Figure 15-22) and the circuit is balanced, the effects of the strobe currents cancel at the input of the sampling circuit. While the sampling diodes are in their low-impedance state, a nonzero voltage at the input port of the sampling circuit causes a net charge to flow from the input port through the diodes to the hold capacitors. These small-signal currents, which are shown by dashed arrows in Figure 15-22, go in opposite directions in the two diodes and add a net charge on the hold capacitors, C_h . The balanced strobe configuration of the sampling circuit ensures that only the net charges from the input transferred to the hold capacitors

While the sampling diodes are in their low-impedance state, a nonzero voltage at the input port of the sampling circuit causes a net charge to flow from the input port through the diodes to the hold capacitors. These small-signal currents, which are shown by dashed arrows in Figure 15-22, go in opposite directions in the two diodes and add a net charge on the hold capacitors, C_h . The balanced strobe configuration of the sampling circuit ensures that only the net charges from the input transferred to the hold capacitors

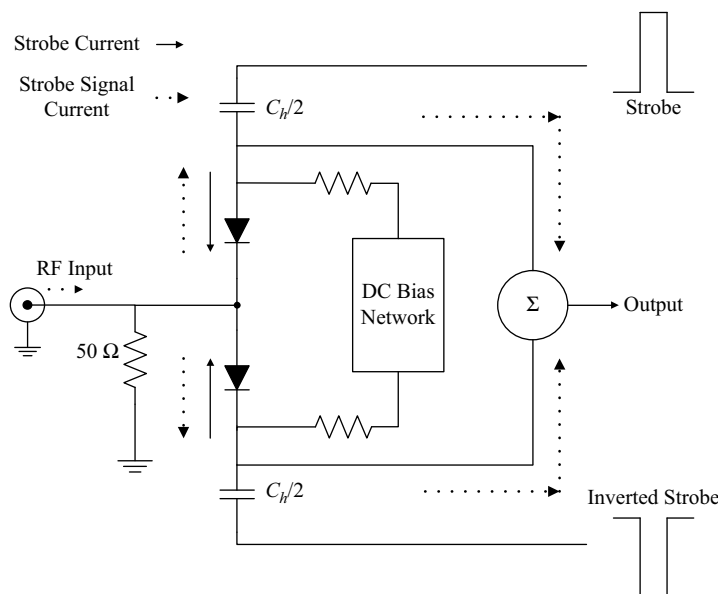


FIGURE 15-22 ■ Simplified Schematic of the Sampling Circuit Used in a GPR Receiver Front End.

produces a signal at the output. The differential charges transferred by the strobe pulses are canceled at the output.

During operation, a repetitive signal train is applied to the input port. The sampling circuit is used to reconstruct the shape of an individual pulse from the pulse train. This is accomplished by firing the strobe at a time Δt later than it fires in the previous cycle of the input signal train. In this way the strobe's firing time slowly "scans" across the input pulse being sampled. Since each successive digitized voltage sample corresponds to the input voltage at a time Δt later than the previous voltage sample, the shape of the signal in the input signal train can be reconstructed and the time stretched, which means the frequency of the signal is down-converted to the low-frequency range.

15.2.7 Design of a GPR Receiver

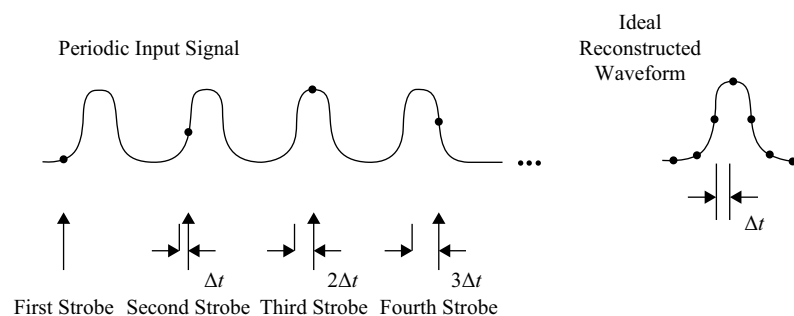
A GPR receiver must recover the pulse shape of the received signal with minimal distortion. Consider a typical GPR system with 400-MHz center frequency; if the sampling window is 33 nS (the equivalent maximum investigation distance is about 5 m in air), when the sampling point is 1,000, the equivalent-sampling interval is 33 pS. If a real-time sampling method is used, the equivalent-sampling frequency will be 30 GHz. This sampling rate is too expensive electrically and monetarily. To avoid real-time sampling, a sequential-sampling or equivalent-sampling method is generally used in a GPR system.

Equivalent time sampling is a traditional method used to sample the high-frequency signal with a relatively low sampling rate. It is based on the assumption that the received signal is repetitive during the period of a full cycle of sampling.

Sequential equivalent time sampling acquires one sample per trigger [29, 30]. Figure 15-23 shows the sampling procedure of the sequential equivalent time sampling. When a trigger comes, a sample is taken after a very short delay. When the next trigger occurs, a small time increment Δt is added to this delay and another sample is taken. The process is repeated many times, with Δt adding to each previous acquisition until all of the waveform has been scanned. The original signal can be reconstructed by putting all the samples taken in the scan together. The drawback of time-equivalent sampling is that hundreds of transmitter cycles are required to form a complete scan, which slows down the capturing process. If the waveform changes in one scan period, the sampled signal will be distorted.

If the pulse-repetition frequency of the GPR system is 200 kHz and the vehicle on which the GPR system is mounted moves at a speed of 40 miles per hour, the antenna

FIGURE 15-23 ■
The Principle of
Sequential
Sampling.



will move 0.0915 m between each scan and 1,024 sample points will be taken. In this 0.0915-m range, the waveform is assumed to have no change. This fact makes this sampling technique suitable for GPR inspection even for highway structures. With a 200-kHz PRF, the scan rate of 400 kHz is needed, but the equivalent-sampling rate can be several GHz.

From Figure 15-22 and 15-23, we can see that two factors have an impact on the time resolution of the sampling system: Δt and the width of the sampling control pulse. The Δt factor determines where to sample and how close two adjacent sampling points are. The width of the sampling control pulse or the tracking window determines the integration time on the sampling capacitor. To obtain an accurate sample at a position on the input signal, we hope that the voltage of the received signal will not change much in the tracking window. Therefore, the tracking window for the signal shown previously must be less than 500 ps in most GPR systems.

A GPR receiver will need to generate the sampling command, shifting a Δt each trigger and construct the low-frequency signal from a sampling head into a replica of the high-frequency GPR pulse. As discussed in previous sections, the receiver is one of the key components in a GPR system. The system block diagram of the receiver is shown in Figure 15-24.

As shown in Figure 15-24, the functions of receiver subsystem include:

- generating the system clock for fast ramp and slow ramp signal generators to control the sequential-sampling points and window size;
- generating the trigger signal for transmitter, which has a fixed delay with respect to the system clock;
- generating the control pulse series for sampling head, which have a small time-increment delay added to each precious pulse;

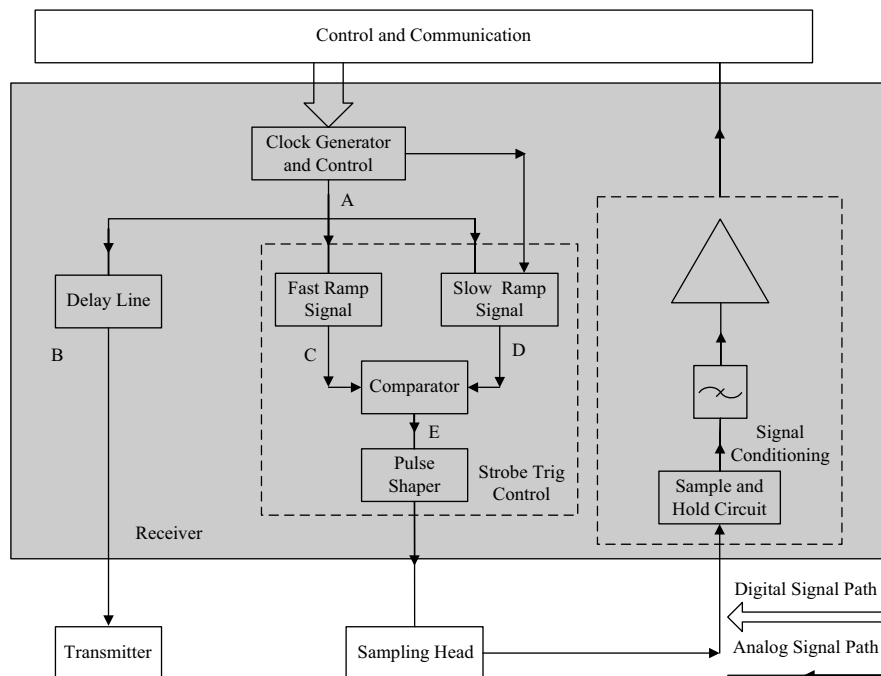


FIGURE 15-24 ■ System Block Diagram of the Pulsed-GPR Receiver.

- generating the sample-and-hold (S/H) control pulses, which have a fixed delay time with the control pulse train; and
- sampling and holding the sampled voltages from the sample circuit for signal conditioning and amplification.

15.2.7.1 Design of Fast Ramp Generator

To implement sequential sampling, two ramp signals are compared and time-stepping pulses are generated. The first ramp signal has a duration equal to the GPR time window, which is called *fast ramp*; the second ramp signal has a duration equal to the number of sampling points that the GPR receiver will sample the high-frequency signal. The linearity of the ramp generators determines the time-domain distortion of the sampled replica of the received RF signal. Due to the relative short duration of the fast ramp generator, the design of the fast ramp circuits is critical to the performance of the GPR system. The fast ramp signal must have very high linearity and relatively high amplitude. The method to generate a ramp voltage is to charge a capacitor by a constant current. The resulting voltage across the capacitor is a ramp voltage is directly proportional to time, which can be calculated by

$$V_{out}(t) = \int_0^t \frac{I_C}{C} \cdot dt = \frac{I_C}{C} \cdot t + V_{out}(0) \quad (15.17)$$

where

I_C = constant current source,

C = charging capacitor,

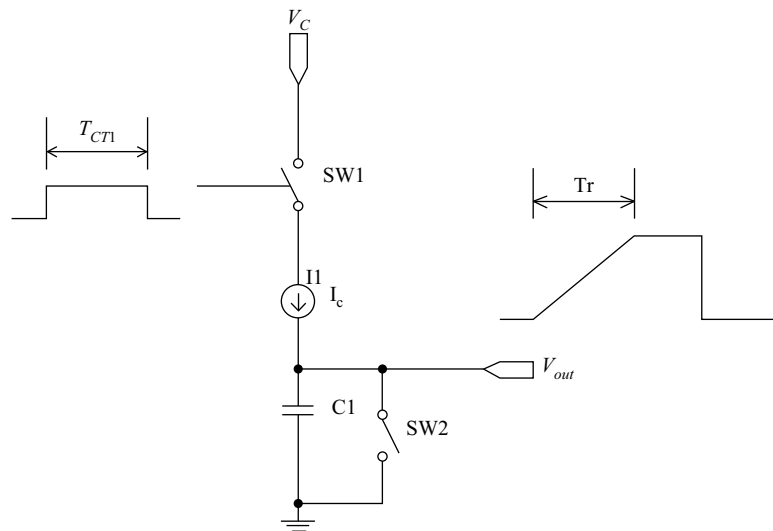
$V_{out}(0)$ = residual voltage across the charging capacitor from previous cycle, and

V_{out} = voltage across the capacitor, since

$$I_C = C \frac{dV_{out}}{dt} \quad (15.18)$$

The simplified schematic of such a ramp generator is given in Figure 15-25. It consists of a constant current source; a charging capacitor; a switch, S1, that controls the

FIGURE 15-25 ■
The Simplified
Schematic of the
Fast Ramp Signal
Generator.



duration of the ramp; and a switch, S2, that initializes the process. The S1 and S2 can also be called *control switches*. The simulation model of the fast ramp signal generator is shown in Figure 15-26. The operational amplifier, U1, and transistor, M1, form a constant current source as long as the transistor M1 operates in its forward operating region. The reference voltage comes from a +8V DC source. The simulation result is shown in Figure 15-27.

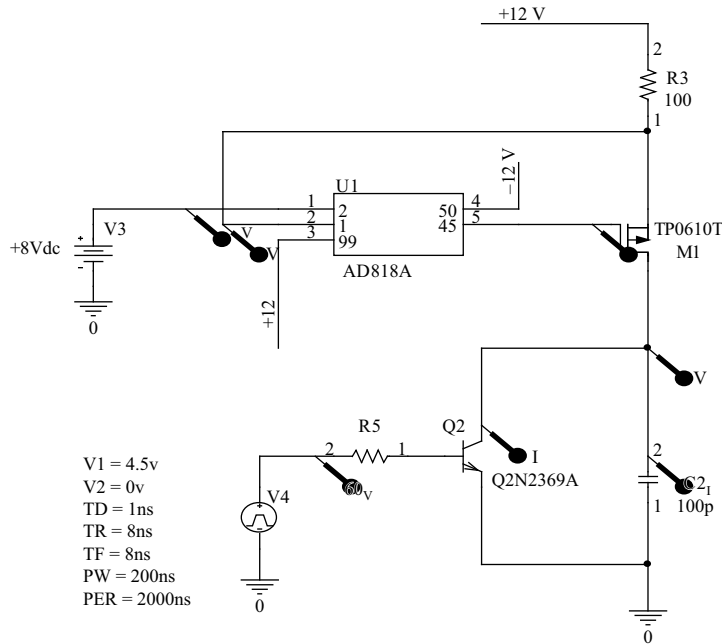


FIGURE 15-26 ■ The Simulation Model of the Fast Ramp Signal Generator.

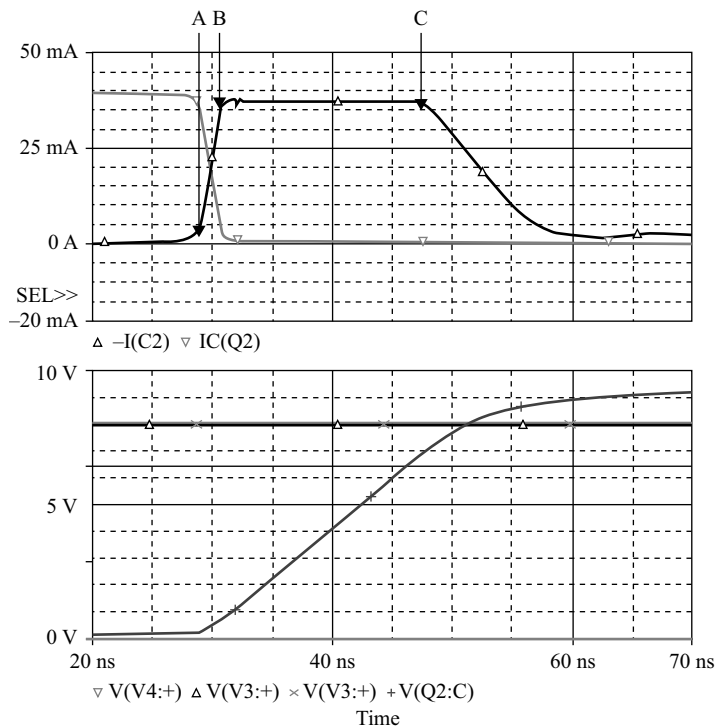


FIGURE 15-27 ■ The Time-Domain Waveform of the Simulation Results of the Ramp Generator in a GPR Receiver.

In Figure 15-26, Q2 is a high-speed bipolar transistor with a short turn-off time and small output capacitance. The operational amplifier (op amp) AD818 can provide enough linear working range. From Figure 15-27, we can see that the shutdown transition time of the transistor is only about 2 ns from point A to point B. In the transition period, nonlinearity will be introduced only in a very short time range at the beginning. After point B, the current goes to the switch, which is represented by the grey curve in the upper plot in Figure 15-27, is almost zero, and all current goes to the charging capacitor, which is represented by the black curve in the upper plot. Together, these improve the linearity from point B to point C.

15.2.7.2 Design of Slow Ramp Signal Generator

The slow ramp signal is a stair-type signal that is used to control the value of increment delay between every two pulses in the sample pulse train. A digital-to-analog converter (DAC) can be used for this task. For example, an AD7533 can serve to generate the slow ramp signal because it is easy to control the increment. The schematic of the slow ramp generator is shown in Figure 15-28.

The reference voltage is sent to AD7533 from port E and op amp U33A is used as an inverting amplifier to turn the positive reference voltage to a negative one. The output voltage of the inverting amplifier is calculated by

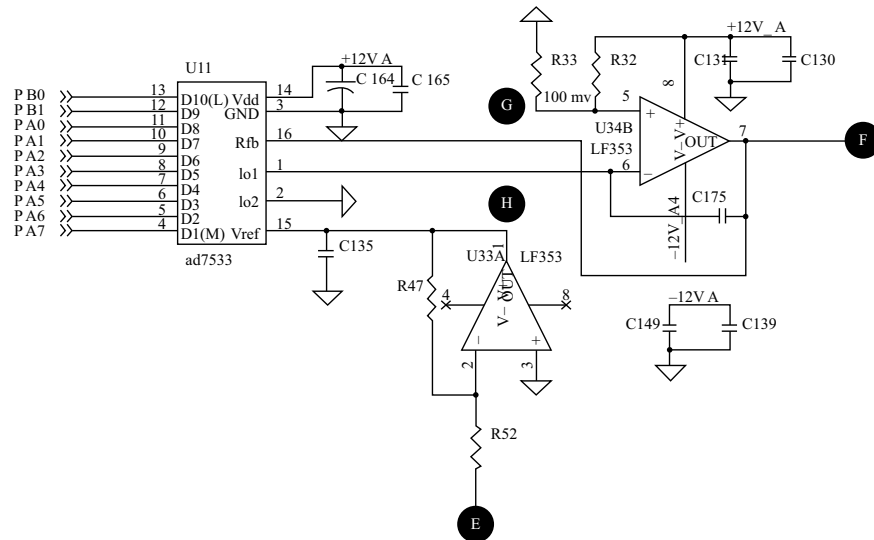
$$V_H = -\frac{R_{47}}{R_{52}} \times V_E \quad (15.19)$$

The equivalent circuit of the DAC, AD7533, is shown in Figure 15-29. The output voltage can be calculated by

$$V_{in} = V_H \times \frac{N}{1024} \quad (15.20)$$

Then the circuit can be simplified and analyzed by using the schematic shown in Figure 15-30.

FIGURE 15-28 ■
Schematic of the
Slow Ramp
Generator.



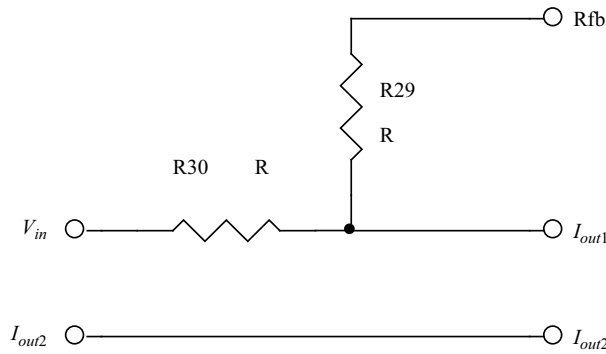


FIGURE 15-29 ■ The Equivalent Circuit of AD7533.

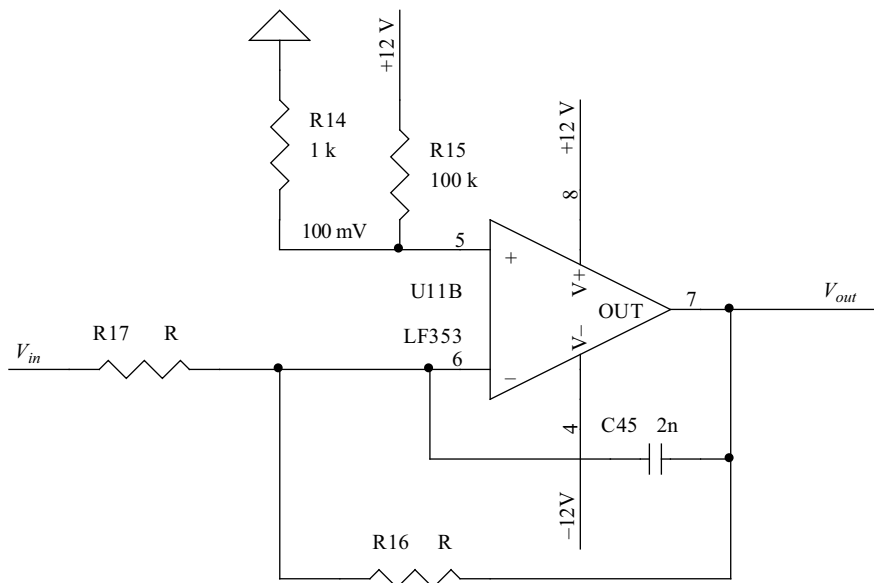


FIGURE 15-30 ■ The Equivalent Circuit of the Slow Ramp Signal Generator.

From the equivalent circuit, the voltage at point F in Figure 15-28 can be calculated by

$$\frac{V_F - V_G}{R_{29}} = \frac{V_G - V_{IN}}{R_{30}} \quad (15.21)$$

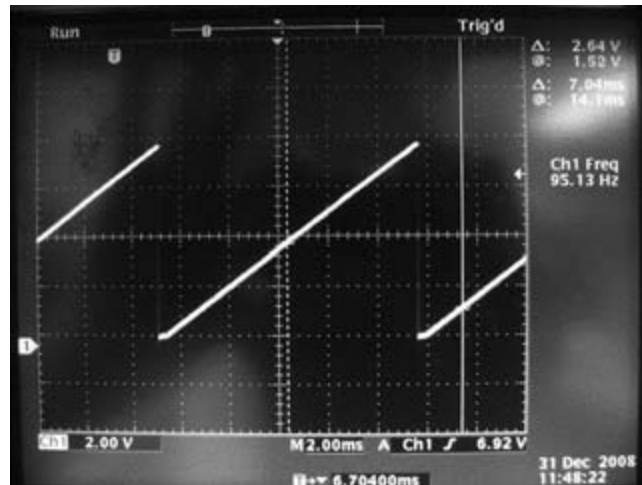
Since $R_{29} = R_{30} = 10 \text{ k}\Omega$, we have

$$V_F = 2 \times V_G - V_{IN} = 2 \times V_G - V_H \times \frac{N}{1,024} = 2 \times V_G + \frac{R_{47}}{R_{52}} \times \frac{N}{1,024} \times V_E \quad (15.22)$$

From (15.22) we can see that V_G sets up the offset voltage of the slow ramp signal. The feedback capacitor C45 in Figure 15-30 forms a low-pass filter (LPF) along with the op amp, which greatly reduces the power-supply noise coupled from E in Figure 15-28. The measured waveform of the slow ramp signal is shown in Figure 15-31.

When feeding the fast ramp signal and the slow ramp signal input into the comparator, a pulse train with a controllable increment between each two adjacent pulses is generated. This pulse train will be used for the sampling head as the sequential-sampling trigger command.

FIGURE 15-31 ■
The Measured
Waveform of the
Slow Ramp Signal.



15.2.7.3 Design of Delay Line

As shown in Figure 15-24, the transmitter pulse and receiver sampling command must be synchronized so that the sampling bridge is triggered at the time when the received signal arrives at the receiver front end. Note that the received signal exists only for several tens of nanoseconds, determined by the window size, and the transmitter and receiver delays are quite different. The receiver circuits have longer delay time than the transmitter circuits due to the complexity of the receiver system. To balance the delay difference between transmitter system and receiver circuits, an additional delay circuit is inserted into the transmitter path. The main purpose of the delay line circuit in Figure 15-24 is to adjust the sampled waveform in the sampling window. From Figure 15-24 we can see that the sampling pulse train to the sampling head will have a certain time delay as compared with the trigger at point B. This time delay is controlled by the R, C, and chips in this signal path and is a fixed value for each system, which is around 50 ns to several 100 ns. If no delay line is used, then the reflecting waveform may be out of the sampling window. As such, the delay line is needed to make sure the whole reflecting waveform can be sampled at the sampling head.

Figure 15-32 shows the simulation model of the delay line circuit, and the simulation result is shown in Figure 15-33. If the C1 and C3 are fixed, then the output delay is only controlled by the resistors R1 and R3. The simulation model has two delay channels to compare the delay differences of different circuit parameters.

15.2.7.4 Design of Sample and Hold Circuit

As previously discussed, the output waveform of the sampling head is a series of spikes, of which the envelope is the “down-converted” high-frequency waveform. In this case, a sample-and-hold circuit is needed to hold the maximum value of each spike.

The sample-and-hold circuit is the basis of the data-acquisition process. Basically, an S/H amplifier circuit has two basic and distinct operational states: *sample* and *hold*. In the sample state, an input signal is sampled and simultaneously transmitted to the output. While in the hold state, the last value of the input signal is held until the sample command is reissued. The purpose of the S/H is to maintain the analog input voltage at a constant level for the period of time required to perform an A/D conversion. In the GPR system, the S/H “freezes” the peak voltage of the sampled pulses at the time of the hold

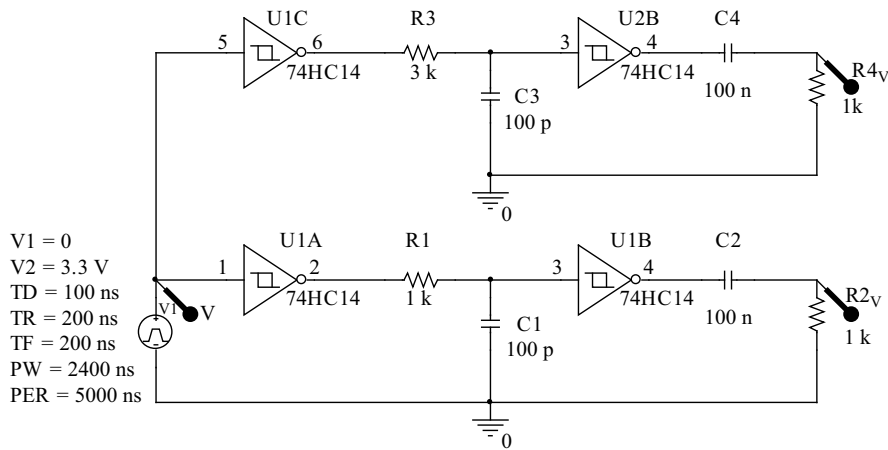


FIGURE 15-32 ■ Simulation Model of the Transmitter Delay Line Circuit in a GPR Receiver.

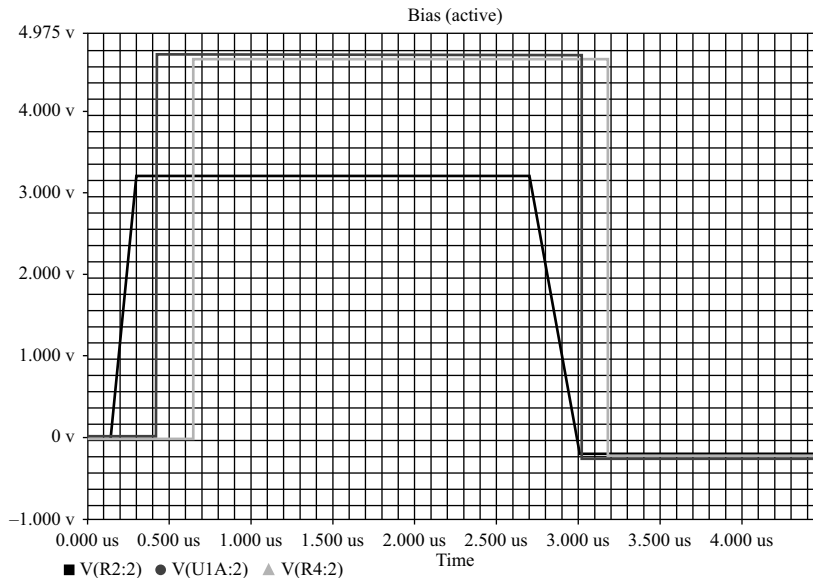


FIGURE 15-33 ■ Simulation Results of the Delay Line Circuit.

command and keeps this voltage unaltered until the next sampled command comes. By doing this, a time-stretched GPR waveform is generated. Figure 15-34 shows the input and output waveforms of the sample-and-hold circuit. The input signal is in blue and the output in yellow. There are many noise sources in this circuit. The main noise source is the sampling pulses. Acquisition time is the time required for the S/H to acquire and then track the input signal after the sample command. Acquisition should end when the signal has settled and remain within the rated error band. This is critical in the system adjustment. By adjusting the time constant of the RC circuit, the delay between sampled signal pulses and the S/H trigger can be adjusted and optimized.

15.2.7.5 Design of the Low-Pass Filter and Amplifier

The output waveform of the sample-and-hold circuit is noisy due to high-frequency sampling. A low-pass filter is needed to eliminate the high-frequency noises. Subsequently, an amplifier is needed to adjust the amplitude to increase the dynamic range.

FIGURE 15-34 ■
The Input and Output Waveforms of an S/H Circuit in a GPR Receiver.

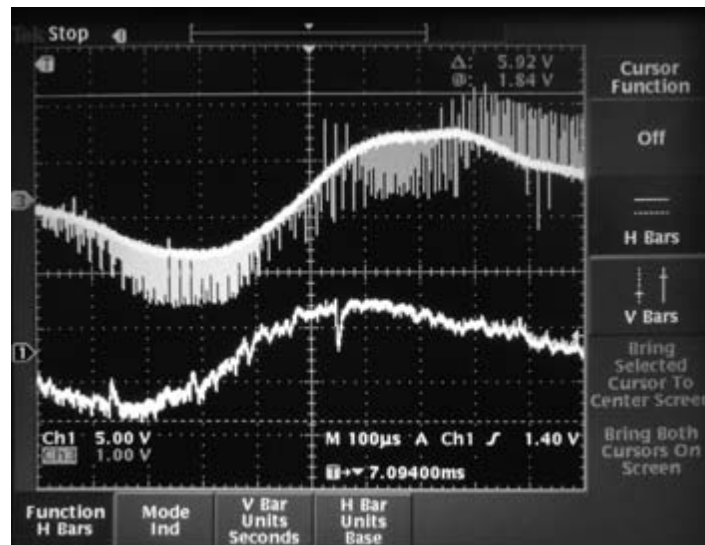
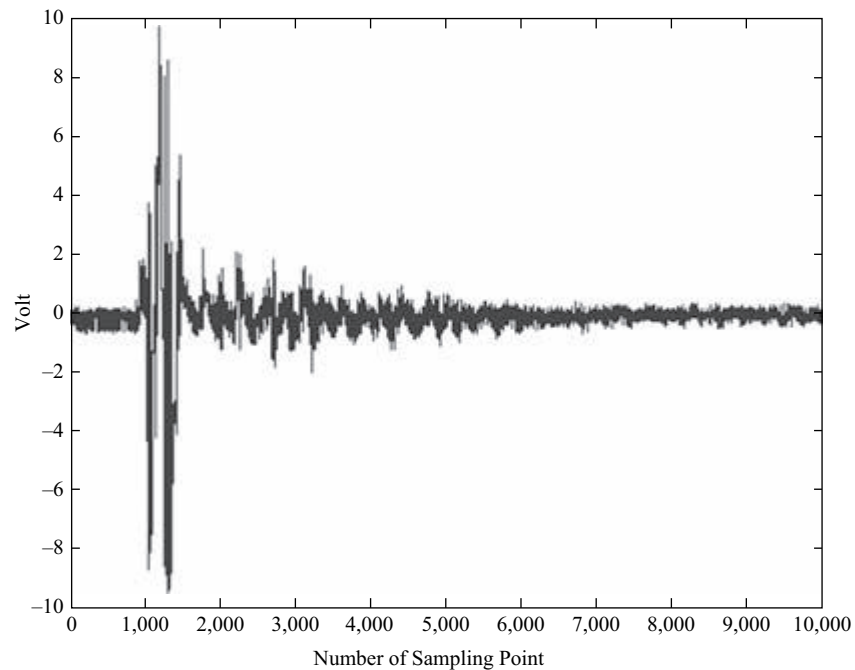


FIGURE 15-35 ■
Input Waveform of LPF.



There are several types of LPFs, including the Butterworth filter, the Chebyshev filter, the Bessel filter, and the Gaussian filter; each has a different performance and application. In terms of GPRs, we do not want the LPF to introduce distortion into the waveforms, so a safe choice is the Butterworth filter, of which the magnitude of the in-band gain is maximally flat. The input waveform is shown in Figure 15-35. MATLAB[®] is used to optimize the bandwidth of the LPF, which is shown in Figures 15-36–15-38.

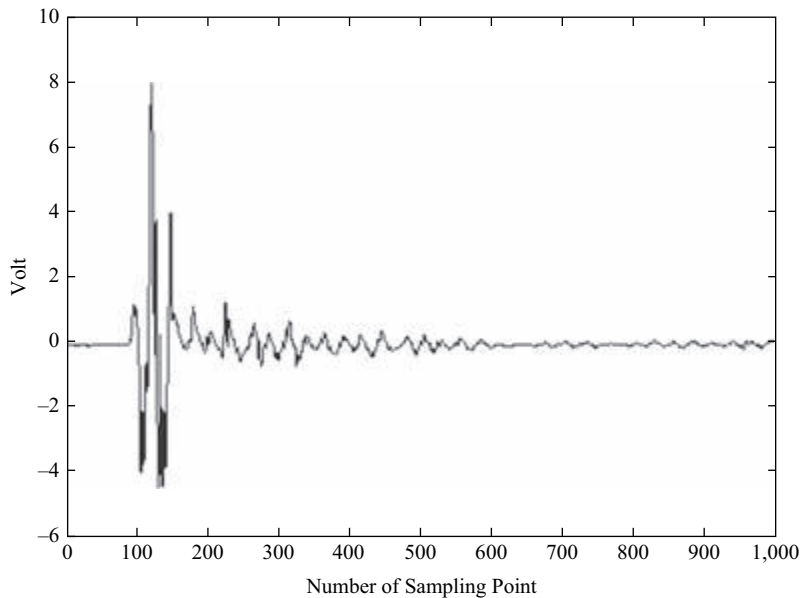


FIGURE 15-36 ■
MATLAB[®]
Simulation Results
with Second-Order
LPF; the Bandwidth
Is 20 kHz.

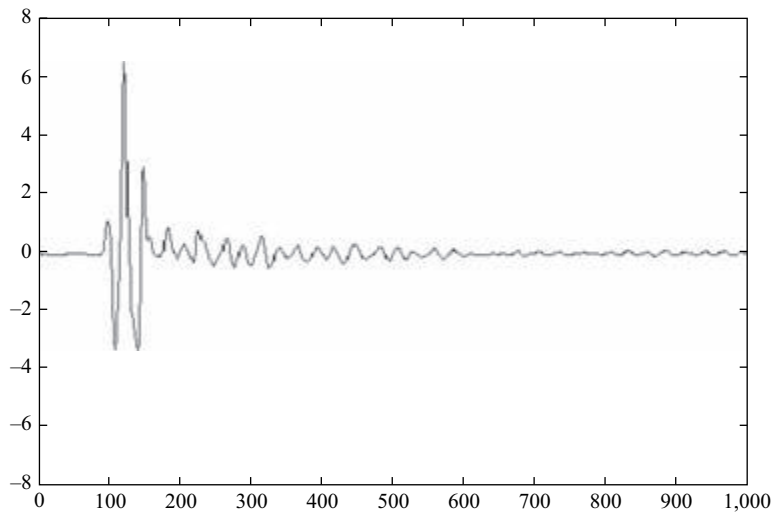


FIGURE 15-37 ■
MATLAB[®]
Simulation Results
with Second-Order
LPF; the Bandwidth
Is 10 kHz.

After comparing the simulation results with LPF with different bandwidths, the 10-kHz bandwidth is selected because it gives a smooth waveform without losing many details on each waveform signature. A more systematic way to design the filter bandwidth is to Fourier transform the GPR waveform in Figure 15-38 and design the filter based on the spectrum distribution of noises.

Figure 15-39 shows the modified Sallen–Key LPF circuit. The circuit is named after the authors of a 1950s paper describing the technique. Compared with the passive filter with the same order, it provides a higher Q (Quality Factor) by using a positive feedback amplifier with a simple structure. If the positive feedback is properly designed, almost

FIGURE 15-38 ■
MATLAB®
Simulation Results
with Second-Order
LPF; the Bandwidth
Is 5 kHz.

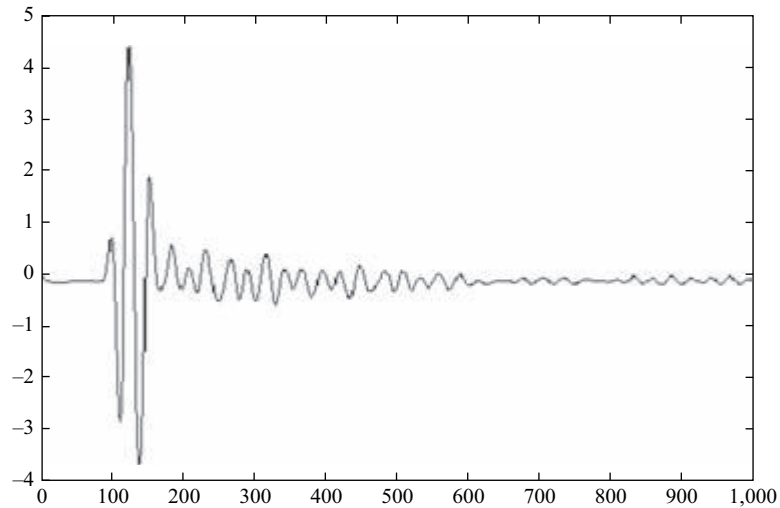
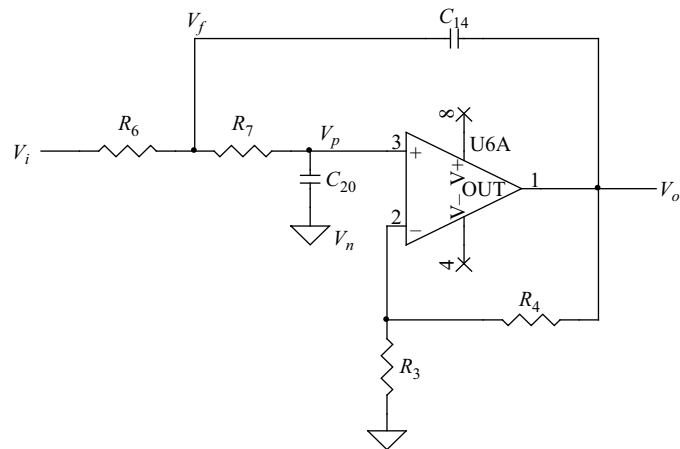


FIGURE 15-39 ■
Modified Sallen-Key
Circuit.



any Q can be realized, limited mainly by the physical constraints of the power supply and the component tolerance. The circuit shown is a two-pole low-pass filter that can be configured as any of the three basic types: Chebyshev, Butterworth, or Bessel. The mathematical equation can be driven as follows. As shown in Figure 15-39, by using Kirchoff's current law at V_f , V_p , and V_n , we get the following three equations:

$$V_f \left(\frac{1}{R_6} + \frac{1}{R_7} + sC_{14} \right) = V_i \left(\frac{1}{R_6} \right) + V_p \left(\frac{1}{R_7} \right) + V_o (sC_{14}) \quad (15.23)$$

$$V_p \left(\frac{1}{R_7} + sC_{20} \right) = V_f \left(\frac{1}{R_7} \right) \Rightarrow V_f = V_p (1 + sR_7 C_{20}) \quad (15.24)$$

$$V_n \left(\frac{1}{R_3} + \frac{1}{R_4} \right) = V_o \left(\frac{1}{R_4} \right) \Rightarrow V_n = V_o \left(\frac{R_3}{R_3 + R_4} \right) \quad (15.25)$$

Then V_p can be solved by using (15.23) and (15.24) together:

$$V_p = V_i \left(\frac{\frac{R_7}{s^2 C_{14} C_{20}}}{\frac{R_7}{s^2 C_{14} C_{20}} + \frac{R_6 R_7}{s C_{14}} + \frac{R_6 R_7}{s C_{20}} + \frac{R_7^2}{s C_{14}} + R_6 R_7^2} \right) + V_o \left(\frac{\frac{R_6 R_7}{s C_{20}}}{\frac{R_7}{s^2 C_{14} C_{20}} + \frac{R_6 R_7}{s C_{14}} + \frac{R_6 R_7}{s C_{20}} + \frac{R_7^2}{s C_{14}} + R_6 R_7^2} \right) \quad (15.26)$$

Then the ideal transfer function can be driven by setting $V_p = V_n$. By doing this, we get $H(s)$:

$$H(s) = \frac{V_o}{V_i} = \frac{K}{1 + s(C_{20}R_6 + C_{20}R_7 + C_{14}R_6(1 - K) + s^2 C_{14}C_{20}R_6R_7)} \quad (15.27)$$

The standard frequency-domain equation for a second-order LPF is

$$H(s) = \frac{K}{1 + \frac{jf}{Qf_c} - \left(\frac{f}{f_c}\right)^2} \quad (15.28)$$

where

f_c = corner frequency and
 Q = quality factor.

Following (15.28), we can set

$$f_c = \frac{1}{2\pi\sqrt{R_6R_7C_{14}C_{20}}} \quad (15.29)$$

$$Q = \frac{\sqrt{R_6R_7C_{14}C_{20}}}{C_{20}(R_6 + R_7) + R_6C_{14}(1 - K)} \quad (15.30)$$

By setting $R_6 = R_7 = R$, $C_{20} = C_{14} = C$, the f_c and Q can be written as follows:

$$f_c = \frac{1}{2\pi RC} \quad (15.31)$$

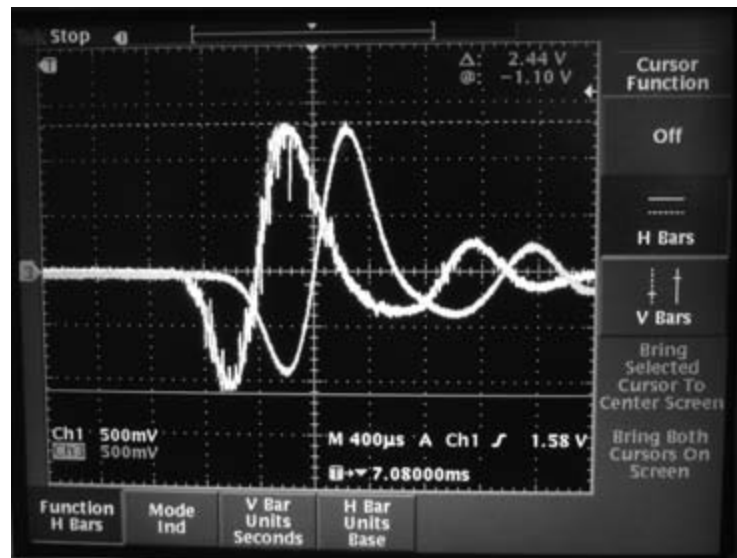
$$Q = \frac{1}{3 - K} \quad (15.31)$$

There is another way to calculate the parameters. We still set $R_6 = R_7 = R$, $C_{20} = C_{14} = C$. Then $R = k_1/C * F_{cutoff}$, and $R_4 = R_3k_2$. Table 15-6 provides the necessary information to select the appropriate resistors and capacitors.

Figure 15-40 shows the input and output waveforms of the second-order Sallen–Key low-pass filter with 10-kHz bandwidth. We can see that the LPF not only removes the

TABLE 15-6 ■ Parameters for designing Bessel, Butterworth, and Chebychev filters

# Poles	Bessel		Butterworth		Chebychev	
	k_1	k_2	k_1	k_2	k_1	k_2
2 stage 1	0.1251	0.268	0.1592	0.586	0.1293	0.842
4 stage 1	0.1111	0.084	0.1592	0.152	0.2666	0.582
stage 2	0.0991	0.759	0.1592	1.235	0.1544	1.660
6 stage 1	0.0990	0.040	0.1592	0.068	0.4019	0.537
stage 2	0.0941	0.364	0.1592	0.586	0.2072	1.448
stage 3	0.0834	1.023	0.1592	1.483	0.1574	1.846
8 stage 1	0.0894	0.024	0.1592	0.038	0.5359	0.522
stage 2	0.0867	0.213	0.1592	0.337	0.2657	1.379
stage 3	0.0814	0.593	0.1592	0.889	0.1848	1.711
stage 4	0.0726	1.184	0.1592	1.610	0.1582	1.913

FIGURE 15-40 ■ The Input and Output Waveforms of the Second-Order Sallen-Key Butterworth LPF with Bandwidth = 10 kHz.

high-frequency component generated in the S/H procedure but also removes part of the noise from the previous circuit.

15.2.7.6 Design of Time-Varying Gain Amplifier

As shown in Figure 15-5, the waveform of the received signal of the GPR system can be divided into three parts according to the sources of the signal. The first part in the signal waveform, which comes from the direct coupling between the transmitting and receiving antennas at a time range from 0 to 5 ns, carries no information from the subsurface structure but has a very large magnitude. The second part of the waveform, which is reflected by the ground surface, indicates the position of the ground surface and has a relatively large magnitude. The third part in the waveform, which comes from reflections on the boundaries of the underground structures, carries the useful information about the subsurface structure but has a low amplitude.

From Figure 15-5 we can see the amplitude of each waveform. These waveforms represent the reflections from subsurface features, and they are separated in time. The closer target has greater amplitude, and the reflection waveform comes near the direct wave. For the amplifier circuit, if a higher gain is applied to the part of the received signal that carries useful information of the underground structure, such as the third part in the received signal, then a larger dynamic range, deeper detection range, and higher SNR can be obtained, which means that the detecting range can be increased when we keep the same spatial resolution. A time-varying gain amplifier is an effective way to implement this idea. As an example, the GPR system can use LMH6503 as the variable gain-control amplifier, and an Microprocessor Unit (MCU) is used to generate the gain-control signal.

15.3 | GPR SYSTEM IMPLEMENTATION AND TEST RESULTS

15.3.1 GPR System Implementation

GPR hardware can be implemented with different center frequencies. Typical commercial GPR systems have center frequencies of 50 MHz, 100 MHz, 200 MHz, 400 MHz, and 1 GHz. As discussed in previous sections, higher GPR center frequencies result in better spatial resolutions with compromises in penetration depth. Figure 15-41 to Figure 15-43 show the measured results at the same site using 200-MHz, 400-MHz,



FIGURE 15-41 ■ Measured GPR Data over a Section of Driveway Using a 200-MHz GPR System.

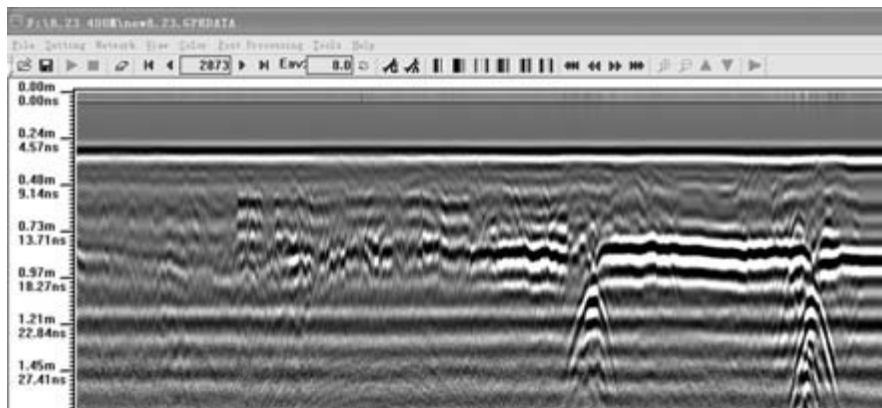


FIGURE 15-42 ■ Measured GPR Data over a Section of Driveway Using a 400-MHz GPR System.

FIGURE 15-43 ■ Measured GPR Data over a Section of Driveway Using a 1-GHz GPR System.

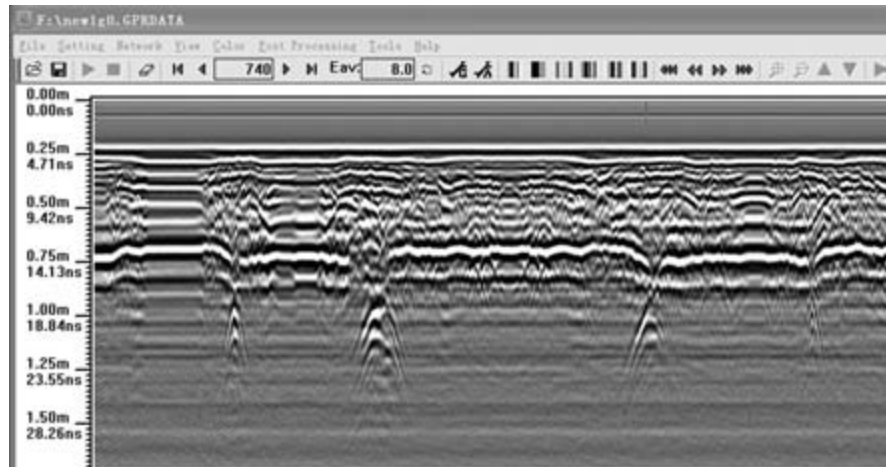
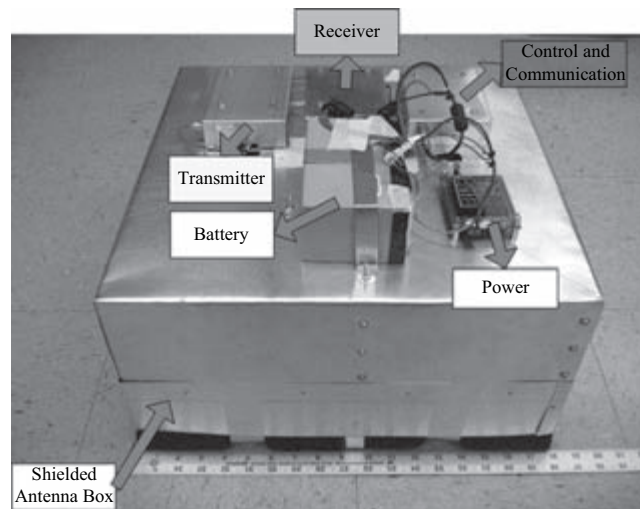


FIGURE 15-44 ■ The Internal Structure of a 200-MHz Ground-Coupled GPR System with Shielded Bow-Tie Antennas.



and 1-GHz GPR systems. Clearly, the 1-GHz GPR system has the highest spatial resolution while the 200-MHz GPR has the deepest penetration.

A ground-coupled 200-MHz GPR hardware internal structure with shielded bow-tie antennas is shown in Figures 15-44. Note that all the circuits are shielded to avoid interference from high-frequency signals. Figure 15-45 and Figure 15-46 show the structure and assembled 400 MHz GPR and 1 GHz GPR units, respectively.

The air-coupled GPR is used for top-surface thickness detection, and the required depth resolution is less than half an inch. Figure 15-47 shows an example of an air-coupled GPR unit mounted on a vehicle for road survey.

The specifications for the 200-MHz, 400-MHz, and 1-GHz GPR systems are listed in Table 15-7. The transmitter pulse waveforms of different transmitters are shown in Figures 15-48, 15-49, and 15-50, respectively. The waveform of differential strobe pulses for sequential-sampling heads is shown in Figure 15-51.

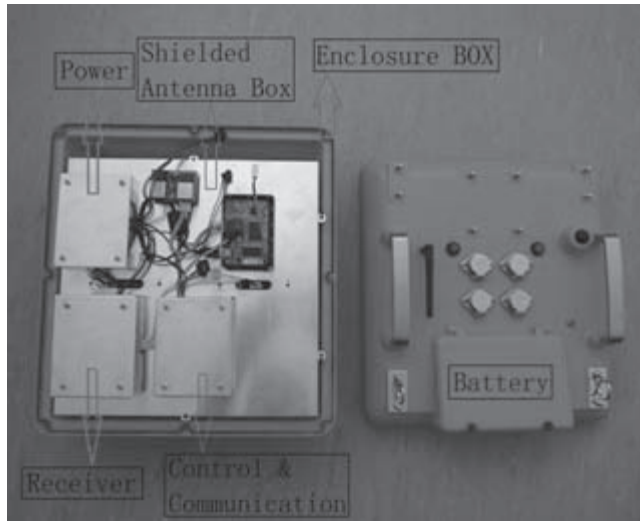


FIGURE 15-45 ■ The Internal Structure of a 400-MHz Ground-Coupled GPR System with Shielded Bow-Tie Antennas.

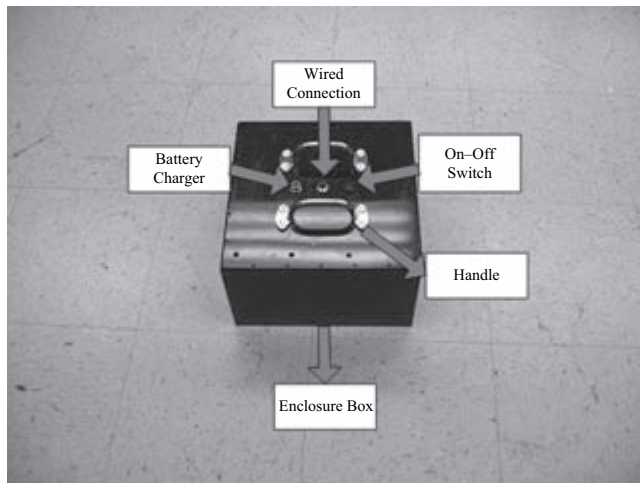


FIGURE 15-46 ■ The External Connections of a 1-GHz Ground-Coupled GPR System with Shielded Bow-Tie Antennas.

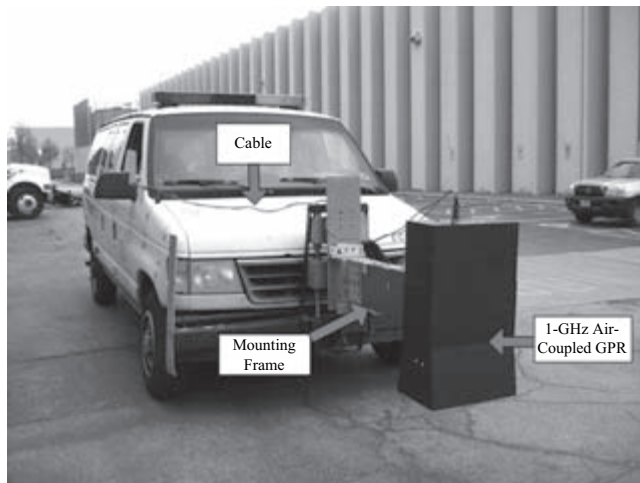


FIGURE 15-47 ■ The 1-GHz Air-Coupled GPR System Mounted on a Vehicle.

TABLE 15-7 ■ The Specifications of the Different Sub-Nanosecond Differential Pulse Generators for Sampling Head and Different Transmitters

Sampling head	PRF	200 kHz
	Sample points per cycle	1,024
	Strobe pulse rising time	371 ps
	Strobe pulse rising time	334 ps
	Strobe pulse amplitude	± 7 V
200-MHz transmitter	Pulse rising time	2.3 ns
	Pulse falling time	3 ns
	Pulse width	5.3 ns
400-MHz transmitter	Pulse amplitude	± 150 V
	Pulse rising time	860 ps
	Pulse falling time	960 ps
	Pulse width	2 ns
1-GHz transmitter	Pulse amplitude	± 58 V
	Pulse rising time	430 ps
	Pulse falling time	514 ps
	Pulse width	1 ns
	Pulse amplitude	± 30 V

FIGURE 15-48 ■ The Output Waveforms of the Differential 1-ns Transmitter Used in the 1-GHz GPR Transmitter Measured by a Tektronix 11801B Sampling Oscilloscope with Attenuator.

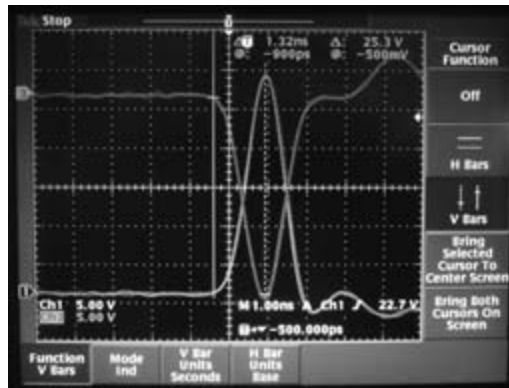
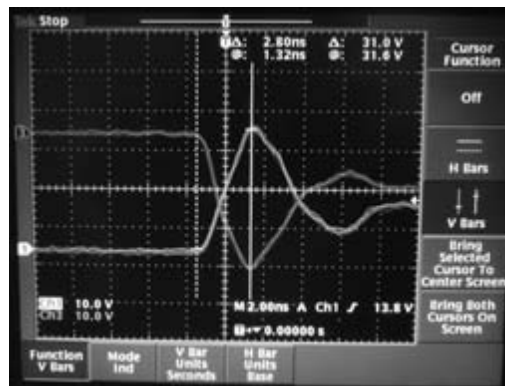


FIGURE 15-49 ■ The Output Waveforms of the Differential 1-ns Transmitter Used in the 400-MHz GPR Transmitter Measured by a Tektronix 11801B Sampling Oscilloscope with Attenuator.



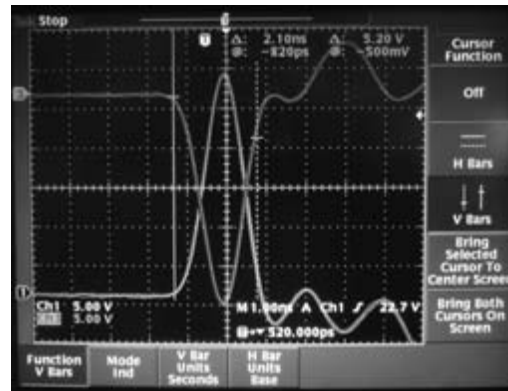


FIGURE 15-50 ■ The Output Waveforms of the Differential 1-ns Transmitter Used in the 1-GHz GPR Transmitter Measured by a Tektronix 11801B Sampling Oscilloscope Attenuator.

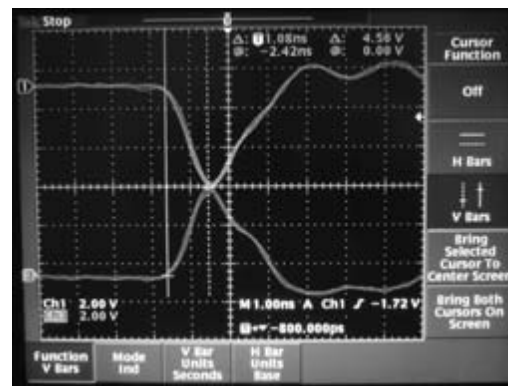


FIGURE 15-51 ■ The Waveforms of the Differential Strobe Pulses for Triggering the Sequential-Sampling Gates in a 400-MHz GPR Receiver.

The waveforms recovered by the sampling head of these 400-MHz and 1-GHz pulsed radar systems are shown in Figures 15-52 and 15-53. For each of these figures, both waveforms recovered by the sequential-sampling head we designed and by the oscilloscope TDS3052B are shown. Those figures prove that the variable nanosecond differential pulses generator works well for the pulsed-GPR system up to 1 GHz. They also prove that these GPR systems work well and that the matching for the transmitter to the transmitting antenna and for the receiving antenna to the sampling head is relatively accurate for the ultra wideband. There are however, some differences between the two recovered waveforms.

15.3.2 GPR System Tests

After system implementation, tuning, and optimization, lab tests should be done to test the performance of the GPR systems.

15.3.2.1 Air Tests

The air tests are designed to test the GPR's maximum detection range and linearity. A metal plate can be set in front of the GPR being tested and then moved away from the GPR in an open area. One test site in a crowded urban area is the roof of a building. This will allow the detecting ranges in the air for different GPR systems to be measured. Figures 15-54 to 15-56 show the test results. The reflection lines have wiggles, indicating that the metal plate stopped or moved more slowly.

FIGURE 15-52 ■
Recovered
Waveforms of the
400-MHz Pulsed-
GPR System.

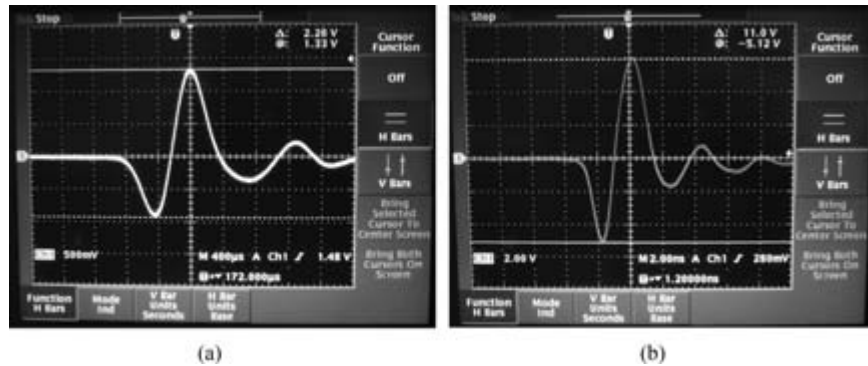
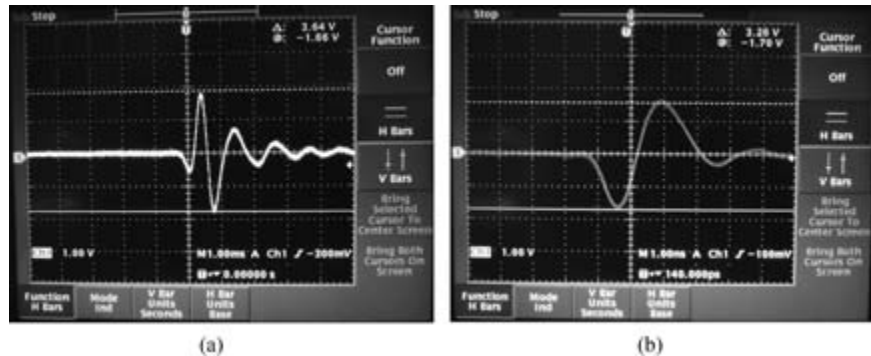


FIGURE 15-53 ■
Recovered
Waveforms of the
1-GHz Pulsed-GPR
System.



15.3.2.2 Field-Test Comparison of GPR System with Different Frequencies

GPR systems with different center frequencies show the capability of different detecting depths and spatial resolutions. In this section, we compare the differences by using the GPR systems of different center frequencies at the same test conditions. Two locations are used for the comparisons of GPR systems with three different working frequencies: 400 MHz, 600 MHz, and 1 GHz. Figures 15-57 through 15-59 show the measured raw data in location 1. Figures 15-60 through 15-62 show the measured raw data in location 2.

From the six raw data measurements taken in the two locations, we can see that the 1-GHz GPR provides the best resolution while the 400-MHz GPR has the deepest detection. Table 15-8 lists the measured depths and resolutions for the different GPR systems.

TABLE 15-8 ■ Measured Depth Detecting and Spatial Resolution for Different GPR Systems

GPR System	Depth Detecting	Spatial Resolution
200-MHz GPR	<10 m in soil	0.2 m
400-MHz GPR	<4 m in soil	0.1 m
600-MHz GPR	<2.5 m in soil	0.05 m
1-GHz GPR	<1 m in soil	0.02 m

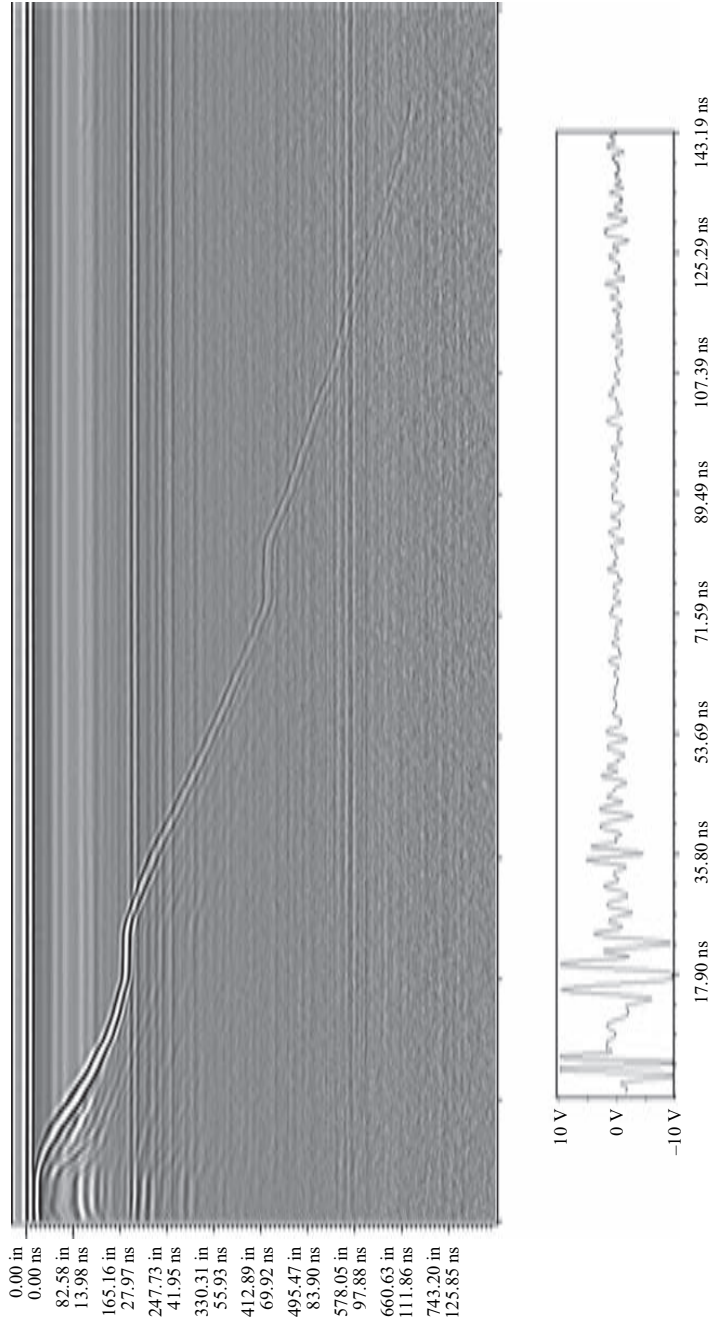


FIGURE 15-54 ■ 200-MHz GPR Detecting Range in Air.

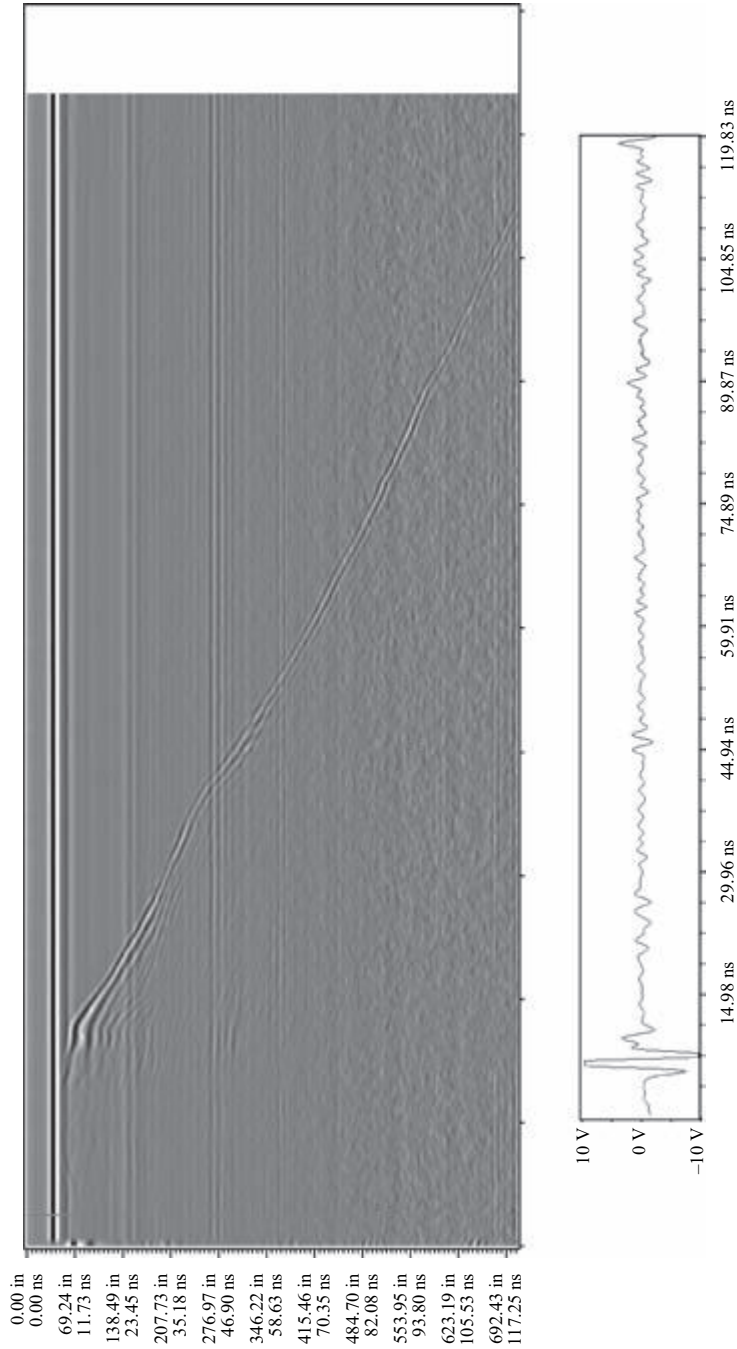


FIGURE 15-55 ■ 400-MHz GPR Detecting Range in Air.

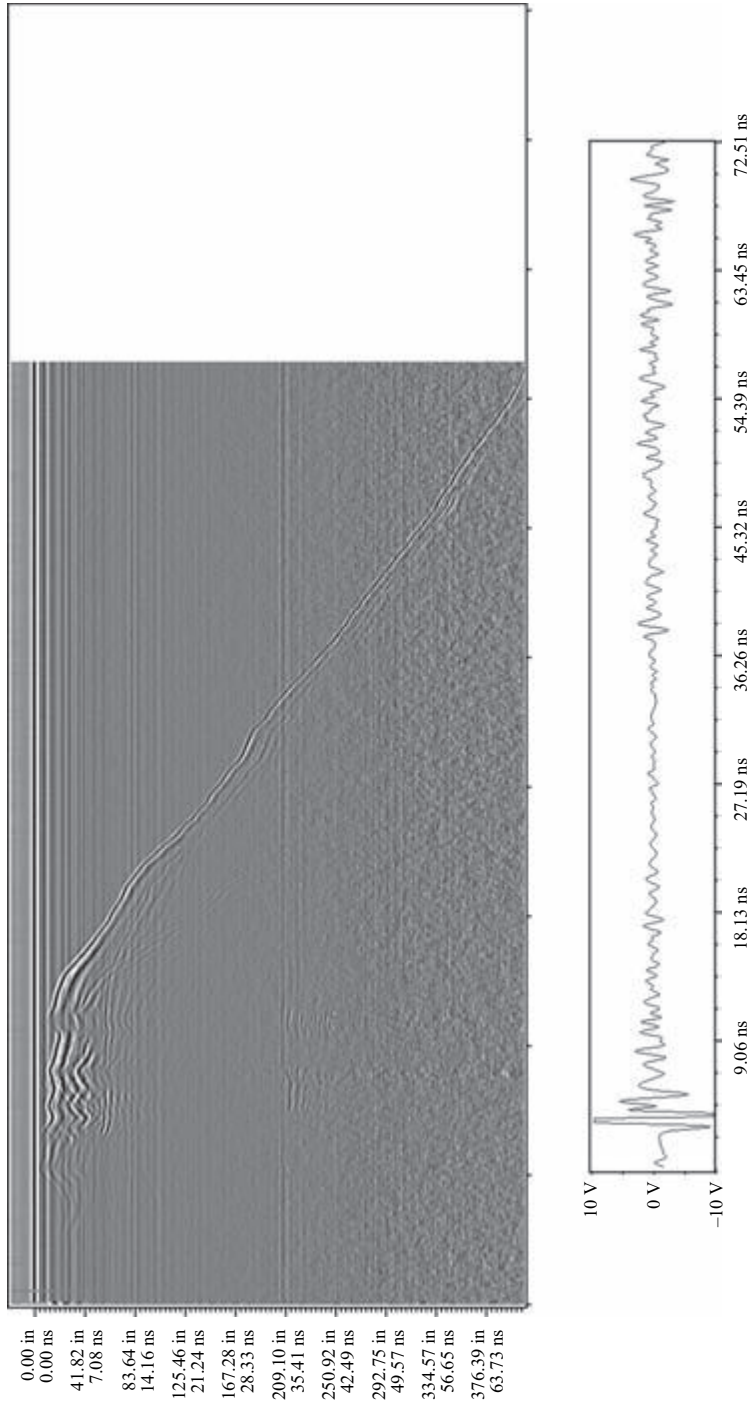


FIGURE 15-56 ■ 1-GHz GPR Detecting Range in Air.

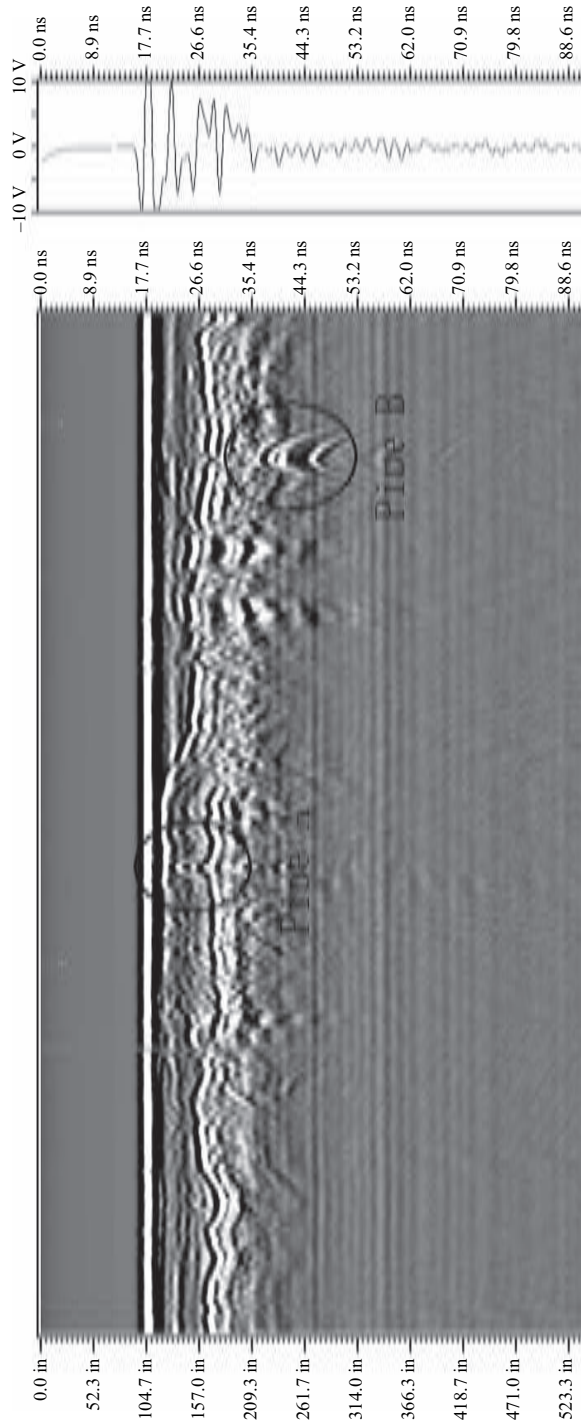


FIGURE 15-57 ■ 400-MHz Ground-Coupled GPR Measured Result, Location 1.

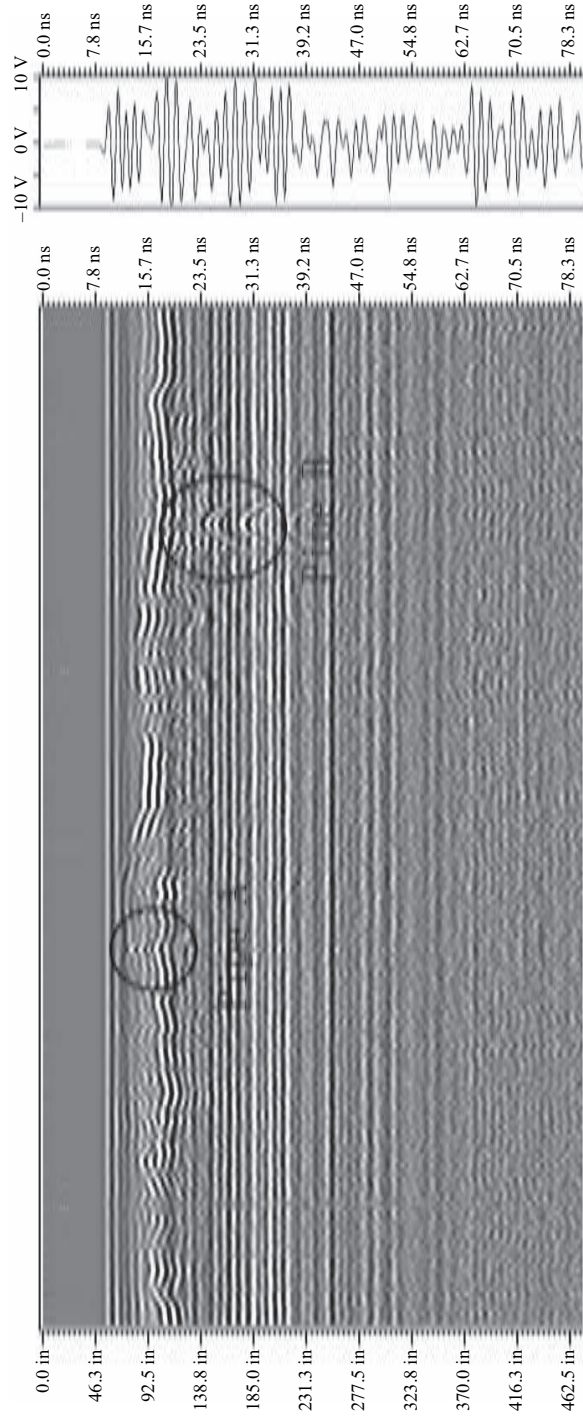


FIGURE 15-58 ■ 600-MHz Ground-Coupled GPR Measured Result, Location 1.

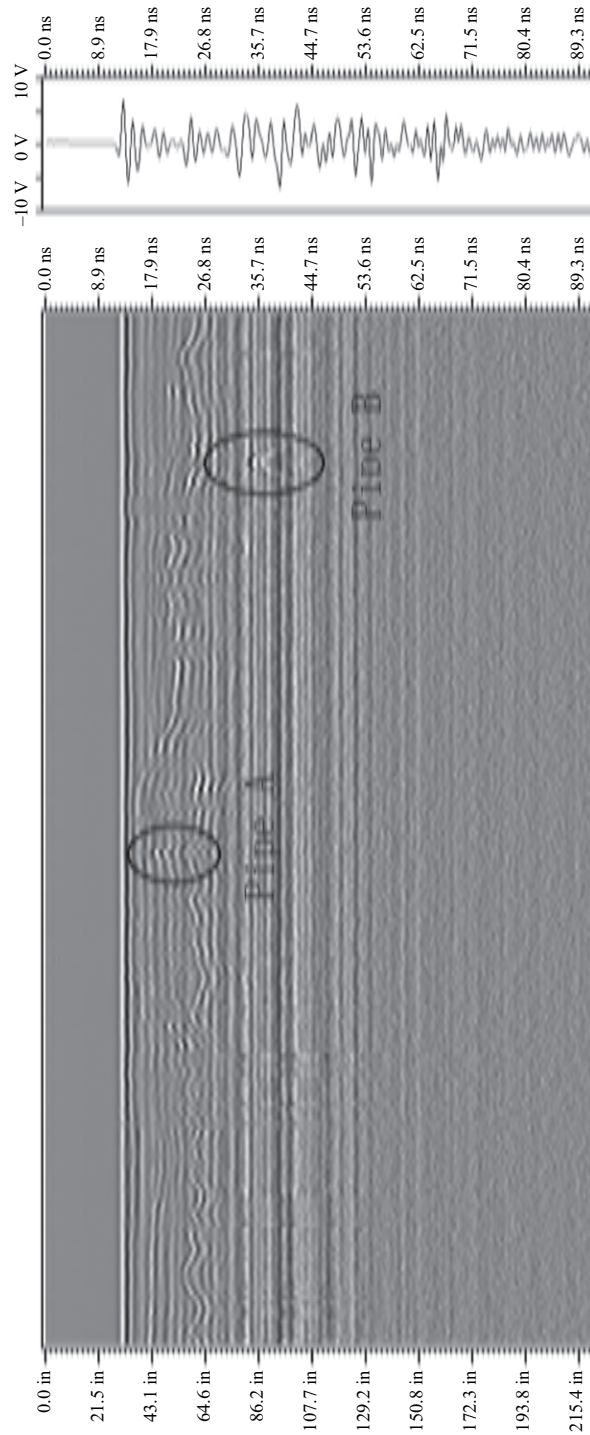


FIGURE 15-59 ■ 1-GHz Ground-Coupled GPR Measured Result, Location 1.

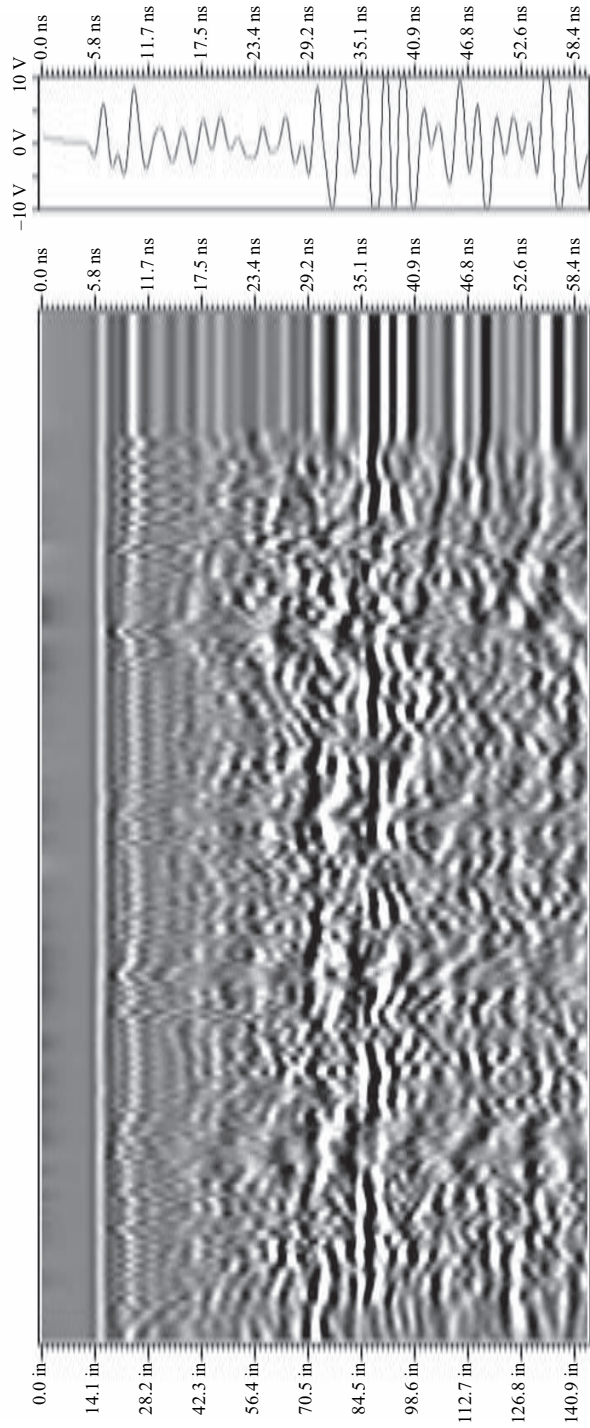


FIGURE 15-60 ■ 400-MHz Ground-Coupled GPR Measured Result, Location 2.



FIGURE 15-61 ■ 600-MHz Ground-Coupled GPR Measured Result, Location 2.



FIGURE 15-62 ■ 1-GHz Ground-Coupled GPR Measured Result, Location 2.

15.4 | CONCLUSIONS

In this chapter, a pulsed-GPR system is used as an example and GPR development efforts and methods are described. A GPR hardware system can be very complicated and changed according to different system requirements. However, basic development steps and structures will remain the same. We use the pulsed-GPR system example to show the hardware structure, typical circuit used, and typical signal waveforms such as system should have. The examples used in the chapter can be used as a reference when a GPR system is to be designed and implemented. The examples used in this chapter are intended to show the basic operating principles but by no means provide a standard. Various circuits and implementation methods can be applied as new electronics devices evolve. In the past, GPR system development was difficult and challenging. However, as new electronics components become more powerful, system development becomes much easier, which drives down system costs. As more UWB devices emerge, the portable GPR system will find its applications in everyday life for imaging, detection, and location. A new cusp of GPR is imminent.

15.5 | REFERENCES

- [1] Olhoeft, G.R., "Selected bibliography on ground penetrating radar," *Proceedings of the Symposium on the Applications of Geophysics to Engineering and Environmental Problems*, March 28–31, Golden, CO, pp. 462–520, 1988.
- [2] Davis, J.L., and Annan, A.P., "Ground penetrating radar for high-resolution mapping of soil and rock stratigraphy," *Geophysical Prospecting*, 37, pp. 531–551, 1988.
- [3] Li, J., Xing, H., Chen, X., and Liu, R., "Extracting rebar's reflection from measured GPR data," *Tenth International Conference on Ground Penetrating Radar*, June 21–24, Delft, The Netherlands, 2004.
- [4] Liu, R., Li, J., Gan, X., Xing, H., and Chen, X., "A new model for estimating the thickness and permittivity of subsurface layers from GPR data," *IEE Proceedings on Radar Sonar and Navigation*, Vol. 149, No. 6, pp. 315–319, December 2002.
- [5] Xing, H., Li, J., Chen, X., and Liu, R., "GPR reflection position identification by STFT," *Tenth International Conference on Ground Penetrating Radar*, June 21–24, Delft, The Netherlands, 2004.
- [6] Maser, K.R., "Condition assessment of transportation infrastructure using ground penetrating radar," *Journal of Infrastructure Systems*, Vol. 2, pp. 94–101, 1996.
- [7] Al-Qadi, I.L., "The penetration of electromagnetic waves into hot-mix asphalt," presented at Proceedings of the Nondestructive Evaluation of Civil Structures and Materials, Boulder, Colorado, pp. 195–209, 1992.
- [8] Davidson, N.C., Hardy, M.S.A., Broughton, J.K., Forde, M.C., and Das, P.C., "Investigation of bridge scour using digital impulse radar," presented at Proceedings of 3rd Conference on Nondestructive Evaluation of Civil Structures and Materials, pp. 69–79, 1996.
- [9] Davis, B.R., Lundien, J.R., and Williamson, A.N., "Feasibility study of the use of radar to detect surface and ground water," U.S. Army Engineer Waterways Exp.Sta.Tech.Rep. 3–727, pp. 50, 1966.
- [10] Bauman, P.D., Heitzmann, R.J., Porter, J.E., Sallomy, J.T., Brewster, M.L., and Thompson, C.J., "The integration of radar, magnetic, and terrain conductivity data in an

- archaeogeophysical investigation of a Hudson's Bay Company fur trade post," GPR '94, Kitchener, Canada, Vol. 2, pp. 531–537, 1994.
- [11] Papamarinopoulos, S.P., and Papaioannou, M.G., "Geophysical investigations with the georadar in the middle of Athens at Syntagma Square and the discovery of the subterranean river Eridanos." GPR '94, Kitchener, Canada, Vol. 2, pp. 569–576, 1994.
- [12] Barone, P.M., Bellomo, T., Pettinelli, E., and Scarpati, C., "Applications of GPR to archaeology and geology: the example of the Region III in Pompeii (Naples, Italy), *4th International Workshop on Advanced Ground Penetrating Radar*, 2007, pp. 64–68, 2007.
- [13] Montoya, T.P., and Smith, G.S., "Land mine detection using a ground-penetrating radar based on resistively loaded Vee dipoles," *IEEE Transactions on Antennas and Propagation*, Vol. 47, No. 12, pp. 1795–1806, 1999.
- [14] Tanaka, R., and Sato, M., "A GPR system using a broadband passive optical sensor for land mine detection," *Proceedings of the Tenth International Conference on Ground Penetrating Radar, 2004. GPR 2004*, Vol. 1, pp. 171–174, 2004.
- [15] Bourgeois, J.R., and Smith, G.S., "A complete electromagnetic simulation of the separated-aperture sensor for detecting buried land mines," *IEEE Transactions on Antennas and Propagation*, Vol. 46, No. 10, pp. 1419–1426, 1998.
- [16] Lubecke, V.M., Boric-Lubecke, O., Host-Madsen, A., and Fathy, A.E., "Through-the-wall radar life detection and monitoring," *IEEE/MTT-S International Microwave Symposium*, 2007, pp. 769–772, July 2007.
- [17] Chen, K.-M., Huang, Y., Zhang, J., and Norman, A., "Microwave life-detection system for searching human subjects under earthquake rubble or behind barrier," *IEEE Transactions on Biomedical Engineering*, pp. 105–114, January 2000.
- [18] Website: <http://www.wikipedia.org>
- [19] Website: http://www.taugiken.jp/tau/life_detector.pdf
- [20] D'Urso, M., Leone, G., and Soldovieri, F., "A simple strategy for life signs detection via an X-band experimental set-up," *Progress In Electromagnetics Research C*, Vol. 9, pp. 119–129, 2009.
- [21] Ralston, J.C., and Hainsworth, D.W., "Application of ground penetrating radar for coal depth measurement," *Proceedings of the 1999 IEEE International Conference on Acoustics, Speech, and Signal Processing, 1999 (ICASSP '99)*, Vol. 4, pp. 2275–2278, 1999.
- [22] Schantz, H.G. *The art and science of UWB design*, Boston: Artech House, 2005.
- [23] Leat, C.J., Shuley, N.V., and Stickley, G.F., "Triangular-patch model of bow-tie antennas: Validation against Brown and Woodward," *IEE Proceedings Microwaves, Antennas, and Propagation*, Vol. 145, No. 6, pp. 465–470, December 1998.
- [24] Lestari, A.A., Yarovoy, A.G., and Ligthart, L.P., "Numerical and experimental analysis of circular-end wire bow-tie antennas over a lossy ground," *IEEE Transactions on Antennas and Propagation*, Vol. 52, No. 1, pp. 26–35, 2004.
- [25] Nishioka, Y., and Uno, T. "Effective radiation efficiency of resistor-loaded bow-tie antenna covered with ferrite-coated conducting cavity located above ground surface." *IEICE Transactions on Communications*, E83-B, pp. 419–421, 2000.
- [26] Wang, Y., "Comparison of three nanosecond pulse generating methods in pulse GPR applications," *11th International Conference on Ground Penetrating Radar*, Columbus Ohio, USA, 2006.
- [27] Ren, W., Wang, H., Guo, C., and Liu, R., "Differential sub-nanosecond pulses generator for pulsed GPR system," *IWAGPR* 2009.

- [28] W. B. Mitchell, "Avalanche Transistors Give Fast Pulses," *Electronic Design*, Vol.6, pp. 202–209, March 14, 1968.
- [29] Technique Primer, "Sampling Oscilloscope Techniques," 47W-7209, Tektronix, 1989
- [30] Wang, Y., "Comparison of Three Nanosecond Pulse Generating Methods in Pulse GPR Applications," *11th International Conference on Ground Penetrating Radar*, Columbus Ohio, USA, 2006.

Police Radar

Gene F. Greneker, RAD, Seal, Gtri, GA Institute of Technology, Atlanta, GA

Chapter Outline

16.1	Introduction	749
16.2	The History of Technologies that Enabled Police Radar	750
16.3	Review of Homodyne Radar Principles	751
16.4	The First Police Radar	753
16.5	The Cosine Error Caused by Improper Operation	754
16.6	The Next-Generation S-band Radar	755
16.7	The Move to X-band – 10 GHz	758
16.8	A Second Method Used to Achieve the Ferro-magnetic Circulator Function	763
16.9	Moving Radar with Improved Detection Range Capability	764
16.10	Moving-Mode Police Radar Operation	766
16.11	Alternative Phase-Locked Loop Signal-Processing Approach	770
16.12	The Move to K-band Frequencies	771
16.13	Police Radar Moves to the Ka-band and Utilizes Digital Signal Processing	772
16.14	Other Police Operating Modes made Possible by DSP	774
16.15	Summary	777
16.16	References	777
16.17	Further Reading	778

16.1 | INTRODUCTION

Police radar is one of many radar systems that every reader may have had or may have an up-close and personal experience with. Police radar, when used by a properly trained operator, can be very accurate in determining a motorist's speed. When used by a poorly trained operator or within a political jurisdiction using radar as a means to raise revenue, however, an innocent motorist can be fined, get points on their driving record, and possibly lose both their driver's license and their automobile insurance. For this reason, it is important to understand not only the technology, but also the operational challenges. This chapter will *not* provide guidance related to defeating the purpose of police speed-timing radars – sorry.

The police speed-timing radar is designed to measure the Doppler frequency shift induced by a moving vehicle and display the corresponding velocity to the operator. It is also important that the system be able to isolate the vehicle whose speed is being

measured. To do this effectively, the systems usually transmit a CW (continuous wave) waveform and have a sample rate sufficient to record the Doppler frequency unambiguously. Narrow antenna beamwidths are also an important part of the isolation function. There are six basic characteristics that police radar must have to ensure proper operation:

1. Very stable transmitter with low phase noise close to the carrier.
2. Narrow antenna azimuthal and elevation beamwidth (16 degrees or less).
3. Signal processor that can accurately determine target Doppler shifts over a large range of target radar cross sections.
4. Compact package with a small footprint on the dashboard, if used in a patrol car.
5. Intuitive target speed display system for easy interpretation by the human operator.
6. Built-in error detection circuits that will determine when target data are faulty.

These required technical characteristics have not always been included in police radar designs. Also, training was not always a requirement for operators using the earlier police radars. The sections that follow present an evolutionary historical perspective of how police radar has developed from the early rudimentary systems to the sophisticated digital signal processing (DSP) police radars in use today.

16.2 | THE HISTORY OF TECHNOLOGIES THAT ENABLED POLICE RADAR

The first police radar design utilized technical advancements made during WWII, specifically those advancements relating to devices capable of generating radio frequency energy at centimetric wavelengths. When the war ended, there were millions of electronic components stockpiled in military warehouses, and these components were sold on the surplus market, providing manufacturers with an immediate and inexpensive supply of previously unavailable components. Military radar designs were being declassified, and those once-classified radar system concepts could be applied to civilian applications. These circumstances and new technology in the late 1940 time period led to the development of police radar.

16.2.1 Early Police Radar Transmitter Components

A police homodyne radar system requires a stable oscillator at the desired radio frequency (RF) operating frequency. The 846B vacuum tube was developed as a cavity oscillator for use in identification friend or foe (IFF) sets carried by all Allied aircraft to avoid being shot down by friendly fire. The 846B planer triode was known as a “lighthouse tube” because of its shape. These tubes were also used in Allied airborne active radar jamming equipment. In 1945, the Radio Corporation of America (RCA) introduced the 2C40 lighthouse tube that replaced the 846 series. The 2C40 planar triode was capable of producing 500 milliwatts of CW power at 1,000 MHz (L-band) and 60 milliwatts at 3,000 MHz (S-band). The 2C40 planar triode was designed to be mounted in a resonant cavity, and it was the design of that cavity that determined the oscillation frequency and the stability of the signal.

The reflex klystron was another technical advancement that was moved out of the laboratory and into production airborne radar systems developed in the early 1940 time period. The first reflex klystrons were used as the local oscillator (LO) in X-band radar. A later klystron, the VA-203B, produced milliwatts of power at frequencies in excess of 10 GHz (X-band). The device with a frequency-determining cavity was mounted to a waveguide flange.

16.2.2 Early Police Radar Receiver (Detector/Mixer)

The radar system also requires a means to receive and detect the signal that reflects from a vehicle. The detector used in several generations of military radars, and two generations of police radars, was the 1N23 crystal detector/mixer diode. The 1N23 diode element was mounted inside a ceramic housing that was transparent to RF. The diode was designed to be mounted inside of a waveguide or a tuned cavity. It served as both the detector and mixer.

16.2.3 The Three Devices That Served as Enabling Technology

Figure 16-1 shows the 2C40 planar triode (left), the 1N23 diode (center) with the associated waveguide mounting flange, and the VA-203B reflex klystron (right). All three of these components were used in the early homodyne police radars. The planar triode was used in the first police radar, and later the reflex klystron was used when police radars migrated to higher frequencies.



FIGURE 16-1 ■ The 2C40 Planar Triode (L), 1N23 Crystal Detector (C), and Reflex Klystron (R) [Greneker Police Radar Collection (GPRC)].

16.3 | REVIEW OF HOMODYNE RADAR PRINCIPLES

Police radars are required to measure only the speed of an approaching or receding target vehicle. The police radar must only measure the difference between the transmitted frequency and the received frequency. This difference is the Doppler frequency

shift, which is proportional to the radial component of the velocity of the “target” vehicle. Equation (16.1) describes this relationship:

$$F_d = \frac{2v_r \cdot F_t}{C} \quad (16.1)$$

where

F_d = Doppler shift (Hz),

v_r = target radial velocity (m/s),

F_t = transmitter operational frequency (Hz), and

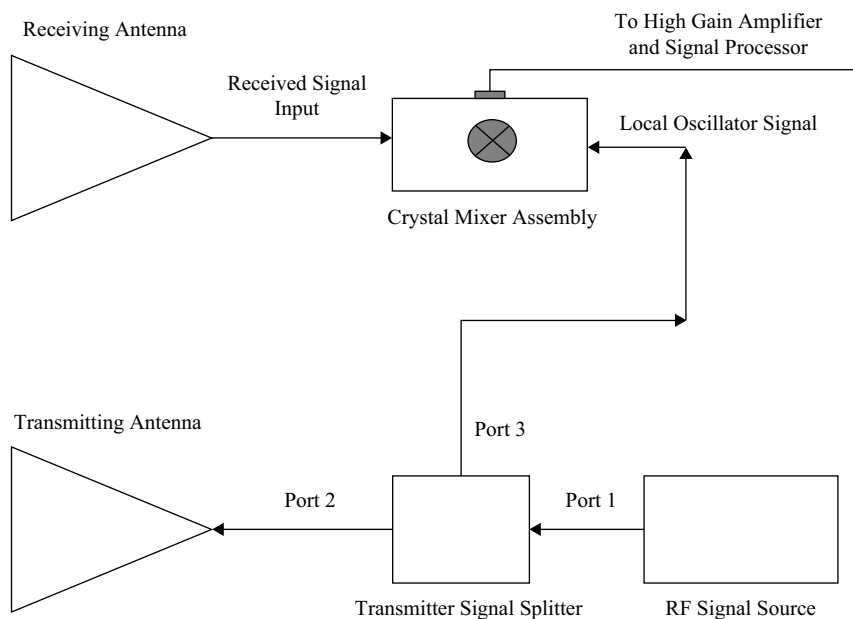
C = speed of light (m/s).

Once measured, the Doppler shift is scaled to speed in units of miles per hour (MPH). To meet this requirement, one of the simplest designs, called the homodyne radar, has been used for all police radar designs since the late 1940 time period. Figure 16-2 is a block diagram showing the homodyne concept.

The transmitter signal is developed by a device capable of generating RF power at the desired frequency of radar operation. The planar triode and the klystron are both examples of a candidate device. The signal generated by the RF power source is split into two paths. One path goes to the transmitter antenna, and that signal is radiated toward the target. The second path is sent to the detector mixer assembly, such as the 1N23 diode. The signal that goes to the mixer assembly from port 3 serves as the local oscillator (LO) and mixes with the signal that is backscattered from the target. The sum and the difference frequency are produced by the mixing process. The sum frequency is eliminated by filtering, and the difference frequency is processed as the desired Doppler signal.

When there is no target motion, the difference frequency (received frequency minus transmit frequency) is 0 Hz. If the received signal has been reflected from a moving target, the signal is Doppler-shifted. After detection and mixing, the difference between

FIGURE 16-2 ■
Block Diagram
Showing the Simple
Homodyne Radar
Concept Using Two
Antennas [GPRC].



the received frequency and the transmitted frequency is output to the signal processor where it is scaled and displayed to the police radar operator in MPH.

This simple homodyne radar system approach has been implemented in various ways, and almost all police radars still use the homodyne approach 60 years after the first police radar was designed. The advantages of homodyne radar are: (1) The transmitter serves as both the transmitter and the LO, removing the requirement that two locked RF signal sources be used to measure small Doppler shifts; and (2) the Doppler-shifted signal is always in the audio range and can be processed with inexpensive amplifiers and components. Currently, continuous wave frequency modulation (CWFM) is being used by one police radar manufacturer to provide target range information to assist the radar operator in identifying target vehicles.

16.4 | THE FIRST POLICE RADAR

In 1946, Eastern Industries, Inc., Signal Division, located in Norwalk, Connecticut, designed and manufactured the first police radar. It was called the Electro-matic, model S1. The model S1 enabling technology was the planar triode. Eastern Industries chose the RCA 2C40 planar triode as the transmitter RF source for the model S1 police radar.

The Electro-matic model S1 radar is shown in operation in Figure 16-3. The radar operator set up the S1 near the highway surface on a tripod. The fixed approach to radar operation was called the “stationary mode of operation.” The stationary mode of operation is still used by police today, and the term stationary mode is part of the police radar training lexicon.

The signal transmitted by the S1 was generated by the 2C40 planar triode tube housed in a cavity resonant at the frequency of 2.455 GHz (S-band). The short-term frequency tolerance of the transmitter was ± 1 MHz. The 2.455-GHz CW signal was transmitted toward the approaching target vehicle. When the approaching vehicle reached an approximate range of 150 to 200 feet from the radar, the speed of the approaching vehicle was displayed on the large analog meter that can be seen on the



FIGURE 16-3 ■ Operation of Stationary Radar Using the Electro-matic Model S1 Radar [Popular Mechanics].

fender of the police car. A strip chart recorder was offered as an option to record the speed of all targets.

When the police radar operator observed a passing motorist exceeding the speed limit, a description of the vehicle and the vehicle's speed was written down in a log kept by the radar operator. The officer would then radio the information to another patrol car, known as the pursuit car, farther down the road. The pursuit car would stop the speeding car and issue the driver a ticket for a court appearance.

The radar target detection and tracking range of 150 to 200 feet achieved by the S1 was poor compared to the 0.5 to 1 mile detection and tracking range achieved by modern police radar. The poor performance of the model S1 was a result of low radar transmitter power, high noise figure components, and low receiver and transmitter antenna gain. The model S1 had only four dipole antennas. Two were phased together for receiving, and the other pair was phased for transmitting. The physical spacing between the antenna pairs provided enough signal isolation to keep the transmit signal from saturating the crystal detector/mixer.

A police car using the S1 radar could be visually observed by a motorist at twice the vehicle's detection range. The frustration of watching speeding cars slow down before reaching the detection envelope led police to experiment with methods of concealing radar operation. The highway patrol in one state used unmarked cars sitting on the side of the road as the radar vehicle. The S1 was mounted in the trunk or in a cutout hole in the trunk lid. The analog meter was hung from the rearview mirror of the unmarked police car so that an approaching car could be observed in the rearview mirror while the radar operator also observed the speed meter. While successful, this method was expensive, and very few departments had the resources to operate dedicated unmarked cars for traffic enforcement.

16.5 | THE COSINE ERROR CAUSED BY IMPROPER OPERATION

The ambush mode was a more popular method used by police to avoid visual detection when using the S1. The police would park their patrol cars behind signs, trees, and other visually obscuring objects near the side of the highway. The radar would be set up on the tripod a short distance away from the patrol car, given the short length of the power and display cables. Police using the concealed method of operation noticed that almost overnight, the average speeds of approaching motorists seemed to decrease. Police radar technology was so new that none of the operators, who had only on-the-job training, were aware that the principle of physics known as the cosine error was giving the approaching driver a break.

The correct speed (Doppler shift) of a target vehicle can only be determined when the radar is located at some point along a line of radial approach. Figure 16-4 shows the radar being operated in the ambush mode, an alignment that causes the cosine error. The figure shows the example case of a 40-degree angle formed between the line of true radial approach and the modified radial approach line formed by the ambush operating geometry. The measured speed decreases as a function of the magnitude of the cosine of the angle formed between these two lines, in the example case, 40 degrees.

The cosine error can be demonstrated using the geometry shown in Figure 16-4. The Doppler shift (F_d) of an automobile approaching the radar radially and traveling at

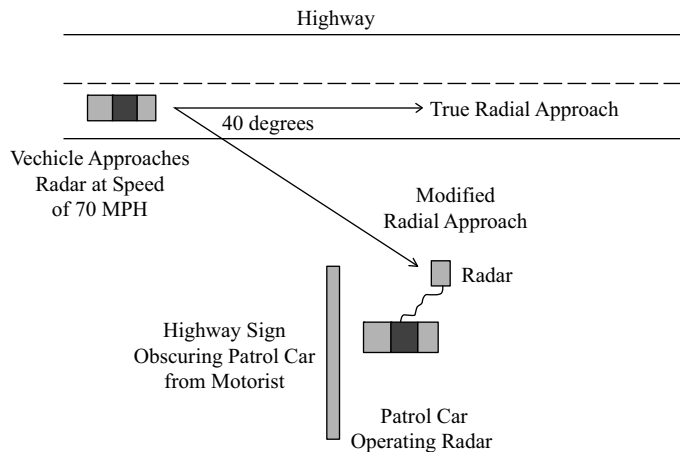


FIGURE 16-4 ■ The Cosine Error Caused by Radar Operated Away from the Roadway [GPRC].

70 MPH (31 meters/second), when measured by a radar operating at 2.455 GHz ($\lambda = .122$ M), is 507 Hz, as determined by Equation (16.1).

When the radar is offset from the line of radial approach by, say, 40 degrees, as in the example case, the Doppler shift of the 70-MPH target is reduced to 389 Hz instead of the true 507 Hz. This can be demonstrated by incorporating the cosine term in Equation (16.1), which results in

$$F_{d(meas)} = \frac{2v_r \cos(\theta) \cdot F_t}{C} \quad (16.2)$$

where

$F_{d(meas)}$ = measured Doppler shift (Hz) and

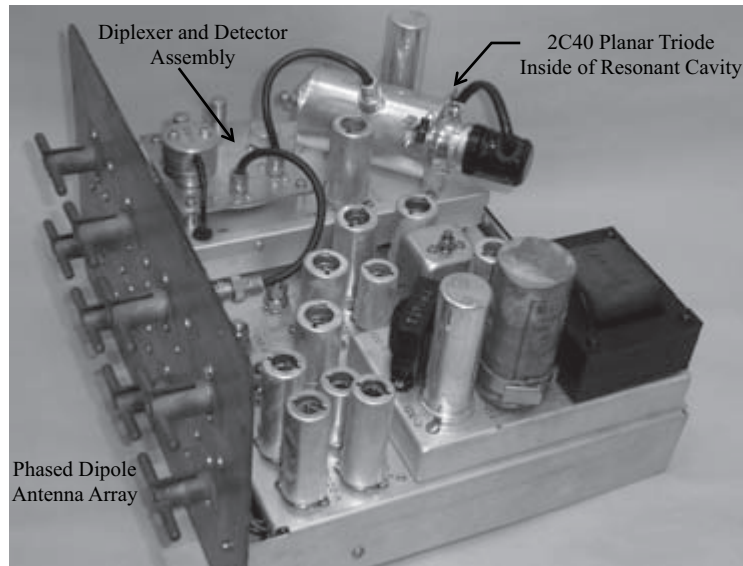
θ = angle between true radial approach and the modified angle of radial approach.

When the true target Doppler ($F_d = 507$ Hz) is multiplied by the cosine of the angle 40 degrees, the Doppler shift measured by the radar is only 389 Hz, and this to the driver's advantage. Converting Doppler shift to MPH demonstrates the magnitude of the error observed by the police radar operator. Recall that the speed of 70 MPH produced a Doppler shift of 507 Hz when a vehicle was moving radially toward the radar. When the Doppler shift was reduced to 389 Hz because of a cosine error of 40 degrees, the radar operator would read a speed of only 53 MPH on his meter. As a result, a driver driving at a speed of 70 MPH on a highway with a speed limit of 55 MPH would display only 53 MPH on the S1 radar. As radars became more sophisticated, other errors were identified.

16.6 | THE NEXT-GENERATION S-BAND RADAR

The frustrations involved with the S1's short detection range, coupled with advances in microwave engineering, led to the development of the Electro-matic model S2 police radar. Figure 16-5 shows the model S2 police radar with the protective cover and RF transparent antenna radome removed to reveal the improved eight-dipole phased array antenna.

FIGURE 16-5 ■
The Electro-matic
Model S2 with
Cover and Antenna
Radome Removed
[GPRC].



The gain of the S2 antenna was improved by abandoning the S1 design that used only two dipoles to transmit and two separate dipoles for receiving. The S2's eight-dipole design served as both the transmit and receive antenna. The eight dipoles were phased to generate a single antenna beam with additional two-way gain over the S1's two-antenna design. The combined power radiated by the eight phased dipoles formed a beam of energy that is directed toward an approaching vehicle. Power reflected off of the vehicle and back to the radar is collected by the eight dipoles and phased to sum as long as the target is inside of the geometric space defined by the eight-dipole main antenna beam.

The resonant cavity shown in Figure 16-5 contains the 2C40 planar triode. The cavity is tuned to be resonant at a frequency of 2.455 GHz. The frequency stability tolerance was certified to be ± 1 MHz. The output power of the S2 transmitter was certified to be less than 200 mw.

The assembly with the transformer mounted on it is the vibrator power supply that steps the 6 volts DC from the car battery to various higher voltages that are used for plate, grid bias, and the screen voltages required by the vacuum tubes. The other tubes shown in Figure 16-5 amplify the small signal produced by the crystal detector/mixer, level the gain of the amplified signal, and convert (scale) Doppler frequency to a speed reading.

Figure 16-6 is a block diagram of the model S2 radar that shows the signal flow. The 2C40 planar triode generates a CW signal on the frequency of 2.455 GHz. The power output is sent from the resonant cavity to a duplexer assembly via short coaxial cable. The duplexer was a new development that allowed the single eight-dipole antenna to serve as both the transmitting and receiving antenna while the CW transmitter was transmitting. A homodyne radar is very sensitive, provided the transmitter and receiver signal paths are well isolated from each other. Isolation between the transmitter and receiver signal paths is a function performed by the duplexer. Power flows from the transmitter port to the antenna port, and the signal is radiated by the antenna. Power reflected from the target is received by the antenna and flows back through the antenna

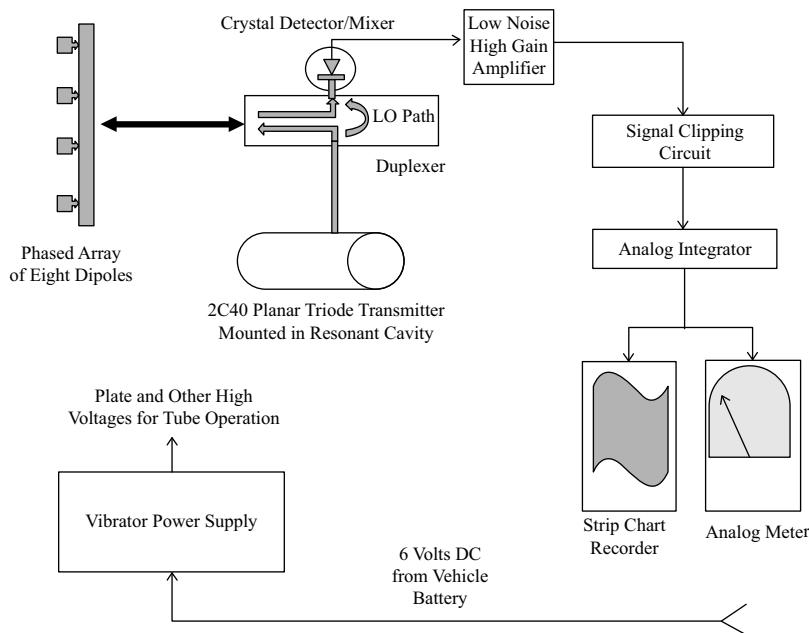


FIGURE 16-6 ■ Block Diagram of the S2 Police Radar Showing the Primary Functions [GPRC].

port to the duplexer's crystal detector/mixer diode assembly. The duplexer provides isolation between the transmitted and received signal so that the CW transmitted signal does not saturate the crystal detector/mixer diode.

There is an intentional leakage path between the transmitter output port and the crystal diode detector/mixer. This leaked signal serves as the local oscillator (LO) that mixes with the received signal. The transmitter signal serves as the LO. The LO signal that is mixed with the received signal is, by definition, extremely stable because it is a sample of the exact signal that is being transmitted at the time of transmission, minus propagation delay times.

The LO signal is mixed with the Doppler-shifted received signal in the crystal detector/mixer diode. The sum of the two frequencies and the difference between the two frequencies are produced at the output of the crystal detector/mixer. If the target vehicle is traveling at 70 MPH and the transmitted frequency is 2,455,000,000 Hz (2.455 GHz), the frequency of the received signal would be 2,455,000,507 Hz, given the 507 Hz of target-induced Doppler shift, as derived when solving Equation (16.1). The Doppler-shifted received signal plus the LO signal, after mixing, would produce a sum signal of 4,910,000,507 Hz (4.91 GHz). The Doppler-shifted receive signal of 2,455,000,507 Hz minus the transmitted signal of 2,455,000,000 Hz produced a difference frequency of 507 Hz. A 4.9-GHz signal could not be processed given the technology of the 1950 time period, but the difference frequency of 507 Hz was an audio frequency signal that could be amplified by even the most fundamental tube type amplifier.

The difference frequency waveform produced by a moving vehicle is a sine wave. After amplification, the signal was sent to a clipping circuit that turned the sine wave into a hard-clipped square wave. The square wave is integrated and converted to a voltage that is linearly proportional to the Doppler frequency of the target. The clipper and integrator form a frequency-to-voltage converter. The voltage is amplified and fed

to a strip chart recorder and an analog meter, both calibrated in MPH. The strip chart recording was saved to show the motorist their vehicle's speed and to present in court as evidence, if needed.

It was estimated that by 1962 there were 1,350 police agencies operating police radar in the United States. Signal Division of Eastern Industries, Inc., had demonstrated that there was a market for police radar with both the model S1 and S2, despite their less-than-optimum detection range, their large physical footprint, and a requirement that two patrol cars were required to conduct radar enforcement operations. Police radar designers recognized that improvements in the antenna design were the most cost-effective way to achieve long detection ranges without raising transmitter power to unacceptable levels.

16.7 | THE MOVE TO X-BAND – 10 GHZ

To a first order, the estimated beamwidth (BW) of an antenna of dimension D for a system using a wavelength λ is

$$BW = \frac{1.2\lambda}{D} \quad (16.3)$$

For a given antenna size, the shorter the wavelength, the narrower the beamwidth. Also, the wavelength λ and the RF frequency F are related by

$$\lambda = \frac{c}{F} \quad (16.4)$$

where c is the speed of propagation of an electromagnetic signal, 3×10^8 meters per second. Several manufacturers recognized that if police radar operation were moved from 2.455 GHz to 10 GHz, more compact, higher gain, tighter beamwidth antennas could be developed for a given size antenna aperture, all desirable features.

16.7.1 Vehicle Radar Cross Section at 10 GHZ

The range at which a radar target can be reliably detected depends on several radar parameters and the radar cross section (RCS) of the vehicle. It was also recognized that the RCS of a vehicular target would increase if the radar operating frequency were increased from 2.4 GHz to 10 GHz, extending the range at which a vehicle could be monitored. A vehicle's RCS is a function of both the azimuthal and the elevation angle that the vehicle presents to the radar. The 10-GHz next-generation police radar was designed to be attached to the left back window of the patrol car, and as a result, the elevation angle is fixed between 0 and 10 degrees. If the radar is operated close to the radial line of target approach, the vehicle will always present a front aspect to the radar. Figure 16-7 shows the radar cross section of a vehicle as a function of azimuthal aspect angle. Only one side of the polar plot is shown because the data from 180 through 360 degrees is identical and, therefore, redundant.

The model used to plot the radar cross section as a function of azimuthal angle was developed by Buddendick and Eibert [1] to verify the results of a cross-section

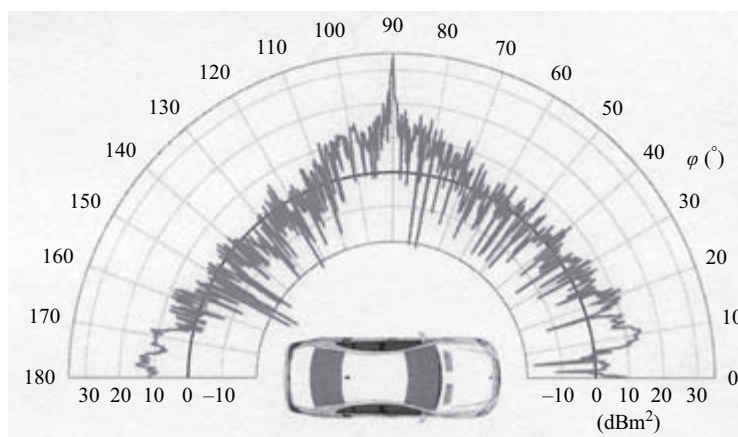


FIGURE 16-7 ■ Radar Cross Section Plotted as Function of Azimuthal Aspect Angle [IEEE].

computation that used a modern passenger car as the modeled vehicle. The radar cross section for a modern vehicle is less than vehicles manufactured in the 1950 through 1990 time period, due to the difference between the construction and size of vehicles during this time period.

The vehicle's front aspect (0 degree) radar cross section shown in Figure 16-7 is approximately 10 dB above a square meter (10 m^2). Vehicles manufactured between 1950 and 1990 had a front-aspect radar cross section as high as 20 dB above a square meter (100 m^2), and even higher over small angles. The highest radar cross section occurs at the 90-degree aspect, which is logical. The side of the vehicle forms a flat surface reflector when illuminated over a very small angle around 90 degrees. Of course, this is of little significance, since there is no Doppler frequency shift at this aspect angle, so the police speed-timing radar is not used in this geometry.

The early vehicles were designed with large chrome metal grills and fenders that extended across the entire front of the vehicle. Large flat-face radiators were behind the decorative chrome grill, making the earlier vehicles a highly reflective target when the front aspect was illuminated. In addition, the cavities where the headlights were installed formed dihedral reflectors, which added to the cross section. In summary, the cross-section plot shown in Figure 16-7 provides a very realistic pattern regarding the change in cross-section to viewing angle, but underestimates the cross-section of automobiles in the 1950 through 1990 time period.

16.7.2 X-band Microwave Technology in the 1960 Time Period

The Federal Communications Commission made a frequency assignment for police radar within the X-band during the late 1950 time period. X-band police radars were assigned to operate within the frequency range of 10.5 GHz to 10.55 GHz, a band 50 MHz wide.

Microwave hardware technology advanced by 1960 to the point where commercial off-the-shelf (COTS) components were available to design the entire RF section of a homodyne radar for operation at X-band frequencies. If cost was not a required consideration, the RF section of the radar could be designed using only four components. As an example, a four-device COTS homodyne radar is shown in Figure 16-8.

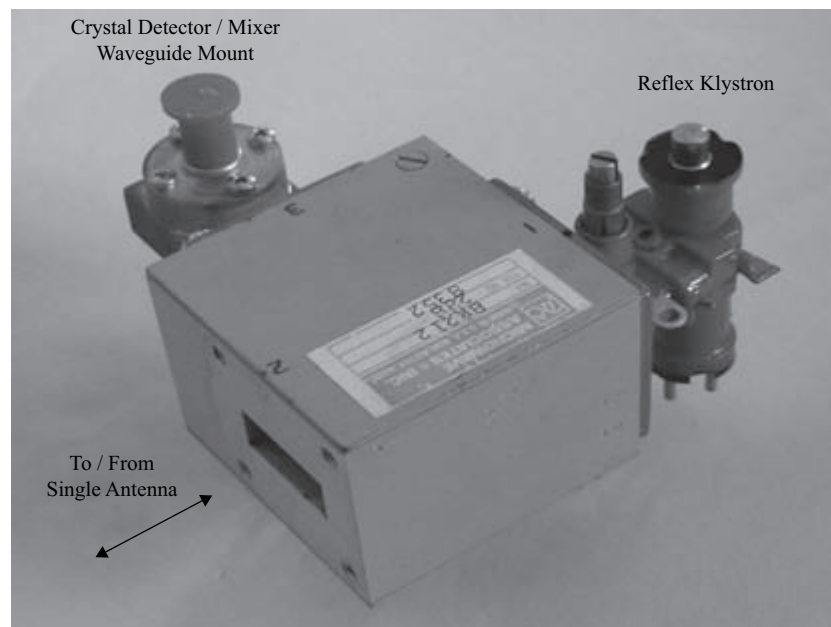
The fourth component, the single antenna used for both transmitting and receiving, is not shown.

The ferrite circulator served as the duplexer in the four-device design. It is the three-port device shown as the rectangular component in Figure 16-8. In 1960, a reflex klystron served as the CW power source. The transmitter power is applied to port 1 of the circulator. The transmitter power is circulated clockwise to port 2 under the influence of a magnetic field. A single antenna (not shown) used for both transmitting and receiving is attached to port 2. The transmitter power is radiated toward the target by the single antenna. The power reflected from the target is received by the same antenna used for transmitting. The power from the antenna enters port 2 of the ferrite circulator and is circulated clockwise to port 3. A receiver, as simple as a 1N23 crystal detector/mixer, is mounted in a waveguide on port 3. Vertical or horizontal polarization was transmitted, depending on how the radar unit was aligned.

The required LO signal is leaked between port 1 and port 3 of the circulator. The isolation between port 1 (transmit) and port 3 (receive) of a broadband circulator is approximately 20–25 dB. The leakage power level is sufficient to serve as the LO signal that mixes with the received signal in the 1N23 detector/mixer diode mounted on port 3.

The COTS ferro-magnetic circulator was the perfect component for the development of the next-generation homodyne police radar. However, in the 1960 time period, the ferro-magnetic circulator proved prohibitively expensive. Several attempts were made to produce the device at lower costs, but because the tuning of the device required human labor and laboratory equipment, a price breakthrough could not be achieved. As a result, the manufacturers of police radar were forced to look for a more inexpensive way to perform the signal duplexer function to provide isolation between transmitter and receiver for X-band police radars. Several clever police radar designs that did not use a ferro-magnetic circulator were developed and marketed in the early 1960 time period.

FIGURE 16-8 ■
Example of a
Ferro-magnetic
Circulator, Four-
device Homodyne
Radar [GPRC].



16.7.3 Electro-matic's Shift to X-band Police Radar Operation

The Automatic Signal Division, Laboratory for Electronics, Norwalk, Connecticut, developed the model S-5 X-band radar in 1961 to utilize the new frequency assignment. Table 16-1 shows the characteristics of the S-5. The model S-5 X-band radar was fully transistorized, except for the reflex klystron transmitter tube. A transistor multivibrator circuit was used to step the 12 VDC from the patrol car electrical system up to the higher voltages required for klystron operation.

TABLE 16-1 ■ Operating Characteristics of S-5 X-band Radar

Frequency of operation	Nominal 10.515 GHz plus or minus 5 MHz
Transmitter stage	Varian type VA204 klystron megahertz
Type of emission	Continuous wave
Power requirements	11 to 15 volts DC at 2 amperes
Minimum and maximum speed and accuracy of measurement	0 to 100 miles per hour plus or minus 2 miles per hour
Target detection range (controlled by a three-position switch)	150, 300, and 500 feet from radar

Figure 16-9 shows a photo of the model S-5 X-band radar. The analog meter, calibrated in units of MPH, is on the left of the figure, the control/processor unit is in the middle, and the radar transceiver assembly that contains the antenna and RF components is on the right side, mounted on a window clip.

The S-5 signal processor functional design was very similar to the design approach used for the S-2 model, shown in Figure 16-6, except for the RF assembly and the fact that all vacuum tubes were replaced with transistors. The S-5 was designed to be operated as a stationary radar only. The RF assembly (antenna unit) was designed to mount on a tripod or to clip on the outside of the left back side window of the police vehicle, radiating the transmitted signal rearward toward approaching traffic.

The S-5 allowed the target detection range to be set at 150, 300, or 500 feet by setting a three-position selector switch. Range was determined by average signal



FIGURE 16-9 ■ The Electro-matic Model S-5 X-band Police Radar System [GPRC].

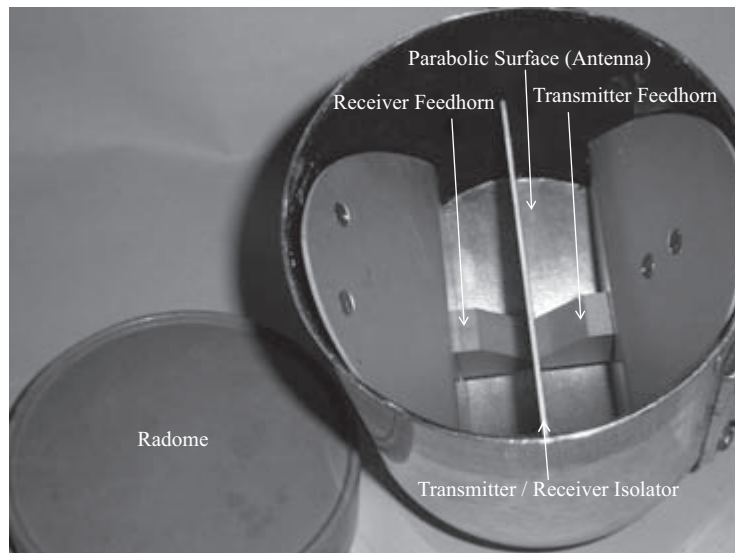
amplitude, and not by any method to extract the target range from the return signal. When operated at the specified frequency of 10.515 GHz, the Doppler shift produced by a 70-MPH target is 2,194 Hz. As discussed earlier, this frequency is in the audio range. To convert from Doppler frequency to vehicle speed in MPH at X-band requires the Doppler frequency be divided by the scaling factor of 31.4.

The S-5 design team introduced their own concept of how to achieve the ferromagnetic circulator function without using the expensive device to serve as the duplexer. Figure 16-10 shows a magnified view of the inside of the S-5 antenna unit with the radome removed. There is a parabolic reflector located in the bottom of the antenna unit. The reflector surface is divided into two sections by an aluminum plate that splits the parabolic surface in the middle. There is a waveguide feedhorn entering from the left of the assembly. The left feedhorn captures the received energy reflected from the parabolic section on the left of the assembly, and that power is transferred via short waveguide section to the crystal detector/mixer that serves as the receiver. The feedhorn on the right illuminates the parabolic surface with the power generated by the VA204 klystron (not visible).

The antenna is horizontally polarized when mounted on the rear left window using the window clip, as shown in Figure 16-9. The antenna beamwidth (half power point) is 16 degrees in the horizontal plane and 20 degrees in the vertical plane. The small antenna surface and the split reflector arrangement affect the antenna sidelobes in a negative way. The manufacturer estimated that the sidelobes are only 12 dB below the mainbeam. If the feed was illuminating a full parabolic surface and there was little blockage posed by the feed, the sidelobe suppression could be as high as between 20 and 24 dB below the mainbeam. As a result of using the split reflector, a moving target outside of the mainbeam could be detected when there was no primary target in the mainbeam.

The S-5 is a homodyne radar system and requires a sample of the transmitted signal to serve as the LO. The radome is not totally transparent to the transmitted energy by design. Some of the transmitted energy is reflected back to the receiver side of the reflector. This transmitted energy serves as the LO that mixes with the returned Doppler-shifted signal.

FIGURE 16-10 ■ Antenna Unit That Utilizes a Split Parabolic Reflector with Two Individual Feeds [GPRC].



16.8 | A SECOND METHOD USED TO ACHIEVE THE FERRO-MAGNETIC CIRCULATOR FUNCTION

A police radar developed to compete with the Electro-matic model S-5 was developed by Muni-Quip Industries, located in Deer Run, Illinois. The system was designed to operate within 10.5 to 10.55 GHz, the 50-MHz-wide X-band segment allocated to police radars.

The Muni-Quip transmitter/receiver unit is shown, with protective cover removed, in Figure 16-11. This transmitter/receiver assembly was also designed to be hung on the outside left back window of the police car and pointed back toward traffic approaching from the rear. The designers used two polyrod antennas to allow transmit while receive capability. A polyrod antenna is an end-fire directional dielectric antenna consisting of a polystyrene rod that mates to a section of waveguide. Most polyrod antennas are round; however, the design used in the Muni-Quip system was rectangular. The dielectric of the plastic material that the antenna is constructed of determines design parameters.

The transmitter polyrod antenna telescopes into a piece of rectangular waveguide that has a flange on one end. The reflex klystron transmitter is mounted to the flange hosting the transmitting polyrod. The body of the klystron has a high voltage potential applied to it, and a nylon spacer electrically isolates the klystron from the waveguide section. Nonconducting nylon screws are used to secure the klystron to the flange. An identical polyrod antenna runs parallel to the transmit antenna, and it is used for receiving. A 1N23 crystal detector/mixer assembly mounts on the waveguide flange of the receiving polyrod.

Without a coupling device, the leakage between the two polyrod antennas is low, provided the spacing of the two antennas is greater than one wavelength. In order to couple enough signal to serve as the LO, the signal leakage from the transmit antenna must be increased using the large screw that is located halfway between the transmitter

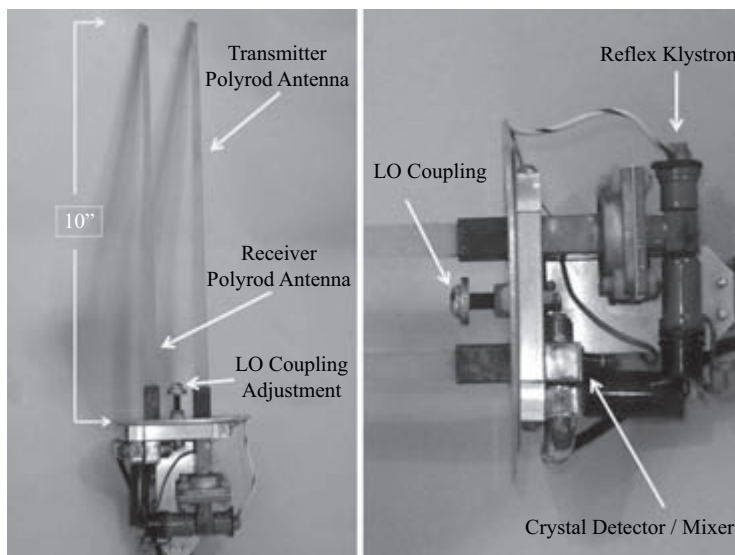


FIGURE 16-11 ■ Muni-Quip Transmitter/Receiver Unit with Protective Cover Removed [GPRC].

and receiver antennas. The amount of transmitter signal coupled to the receiver crystal diode detector/mixer is determined by the position of the screw. When the screw is close to the mounting plate, the coupling is minimized. When the screw is in the position that is shown in Figure 16-11, the coupling is maximized.

In summary, the split reflector and the polyrod antennas represents two primary approaches taken by the manufacturers of the 1960s X-band radars to achieve isolation between the transmitter and receiver paths. System sensitivity achieved through these design approaches, and the increase in target radar cross section by moving to 10 GHz, did improve the range at which a target could be detected. Police operators, while appreciative of the improvements, wanted moving radar. A company that was new to the police radar manufacturing industry provided the first moving radar design and implementation.

16.9 | MOVING RADAR WITH IMPROVED DETECTION RANGE CAPABILITY

All of the police radar systems developed from the late 1940 time period through the early 1960 period were operated in the stationary mode, requiring the radar to be mounted in one police car operating at a stationary location. A second police pursuit car had to be stationed farther down the road to pursue speed limit violators determined by radar, unless the police car with the radar served as both the radar car and the arrest car. Target detection range was limited to approximately 500 feet.

In 1970, Kustom Electronics, Inc., located in Olathe, Kansas, introduced their Model TR-6 X-band homodyne police radar that operated on a frequency of 10.525 GHz. While the TR-6 operated only in the stationary mode, it incorporated several technological breakthroughs. Kustom developed a simple, inexpensive, but very effective, duplexer that provided high signal isolation between the transmitter and receiver, and very good detection range performance. The TR-6 duplexer was a turnstile junction that allowed simultaneous transmit while receiving. A single large circularly polarized horn served as both the transmitting and receiving antenna. A 1970-model vehicle could be detected on a straight and level highway at a range of a mile or more by police using the TR-6 radar. Kustom followed the TR-6 development with the model MR-7/MR-9.

Figure 16-12 is a photograph of the MR-7/ MR-9, showing the remotely mounted antenna unit and the control/display unit that sat on the police car's dashboard. The antenna unit was designed to be mounted on the outside of the left rear window.

16.9.1 Turnstile Junction Duplexer

The turnstile junction duplexer is a device with four coplanar, rectangular ports and one circular port that is orthogonal to the rectangular ports, as shown in Figure 16-13. Not shown in the figure is a tuning element that takes the form of a pin, cut for the operating wavelength in both diameter and length, that excites the circular waveguide.

In the case of the turnstile junction used in the MR-7/MR-9, transmit power is applied to port 1. One half of the transmitted power goes into the circular waveguide port and is transmitted as a circularly polarized wave toward the target vehicle. Half of



FIGURE 16-12 ■ Kustom Electronics, Inc., Model MR-7 Stationary/Moving Police Radar [Kustom Signal, Inc.].

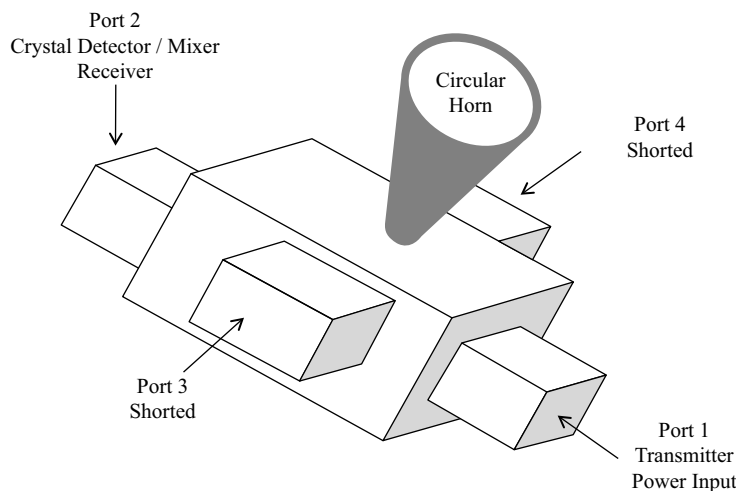


FIGURE 16-13 ■ Turnstile Junction Used as a Duplexer for Simultaneous Transmit and Receive [GPRC].

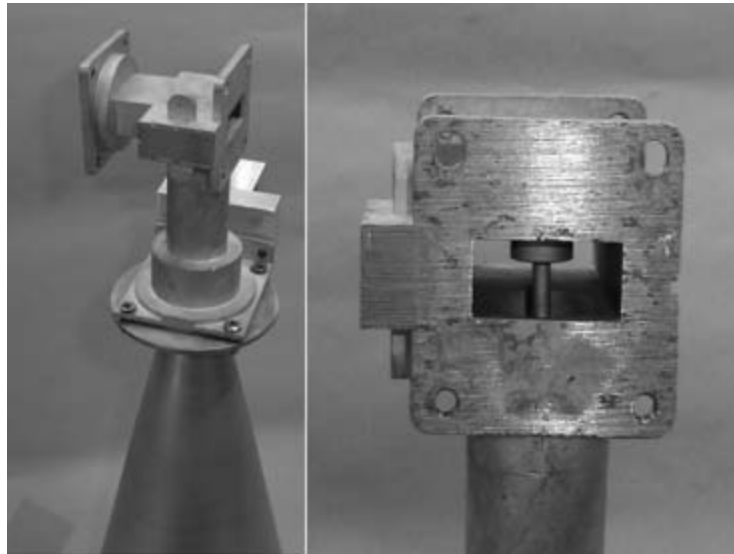
the remaining power divides equally between ports 3 and 4, with no power going to the receiver diode detector/mixer on port 2. The 90-degree time phase difference required for circular polarization is achieved by making arm 4 longer or shorter than arm 3. The exact change in length is frequency-dependent.

When the circularly polarized wave rotating clockwise (viewed from behind the antenna) strikes a flat-plate target, the wave comes back with the polarization vector rotating counterclockwise (viewed behind the antenna). The circularly polarized horn antenna receives the return signal. The received signal appears at port 2 of the turnstile junction. A 1N23 crystal detector/mixer assembly is mounted on port 2 and serves as the system receiver. The signal isolation between ports 1 and 2 can be as high as 50 dB if the turnstile junction is well designed for the exact frequency of operation. As a result, the LO signal required for homodyne operation is almost nonexistent, given the very

low-level direct leakage from port 1 to port 2. Kustom developed a plastic radome that fit over the end of the horn to purposely reflect a small amount of RF power back into port 2 and create an LO reference signal at the required mixing level.

Figure 16-14 is a composite of two photographs. The photograph on the left is the turnstile junction and the circular horn. The photograph on the right is an extreme close-up of the turnstile junction viewed through port 1. The round stepped rod element that excites the circular polarization can be seen inside of the turnstile junction assembly.

FIGURE 16-14 ■
Turnstile Junction
and Circular Horn (L)
and Turnstile
Junction Close-up (R)
[GPRC].



16.9.2 Gunn Device Solid-State Transmitter

Kustom elected to use a solid-state Gunn device rather than a reflex klystron as the transmitter. Gunn devices are diodes, but they have no rectifying characteristics. They consist of a micrometer layer of gallium arsenide mounted inside a resonant cavity. A DC voltage between 5 and 10 volts (the exact voltage is specified for every device) at a current of 100 to 300 milliamps is required to start and sustain oscillation. The output power of the Gunn device is usually less than 100 mw (20 dBm). The advantage of using the Gunn device rather than a reflex klystron as the transmitter is that only a single low-voltage power regulator is required to drop and regulate the vehicle's 12-volt supply. The lifetime of the Gunn device is much longer than that of a Klystron, and the device is physically smaller than the Klystron. In recent years, the cost of the Gunn device has been lower than the klystron's, price.

16.10 | MOVING-MODE POLICE RADAR OPERATION

The MR-7/MR-9 was a breakthrough because it could be operated in the stationary mode or in the moving mode (from a moving vehicle). A swivel allowed the antenna to be aimed forward or to the rear of the police car, depending on mode of operation. When the MR-7/MR-9 was used in the fixed mode, the antenna would be aimed rearward

toward traffic approaching from behind the police car. When the radar was used in the moving mode, the police would drive normally at highway speeds with the antenna pointed forward toward approaching traffic.

Figure 16-15 demonstrates the concept of moving-mode radar operation made possible by the MR-7/MR-9 design. The police patrol car drives from right to left in the figure, and the targets to be evaluated approach the patrol car in the opposite lane. The moving principle is applied for both two-lane and interstate highways where a median may divide the multiple-lane road surfaces. The 16-degree wide antenna beam is pointed straight ahead of the patrol car.

The forward-pointing antenna allows both the patrol car speed and the closing speed (patrol car speed plus motorist speed) to be determined. A clutter-referenced signal processing technique is used to determine the patrol car speed.

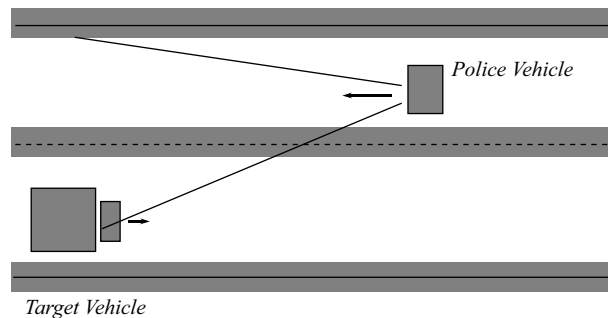


FIGURE 16-15 ■ Diagram Showing the Moving Mode of Police Radar Operation [GPRC].

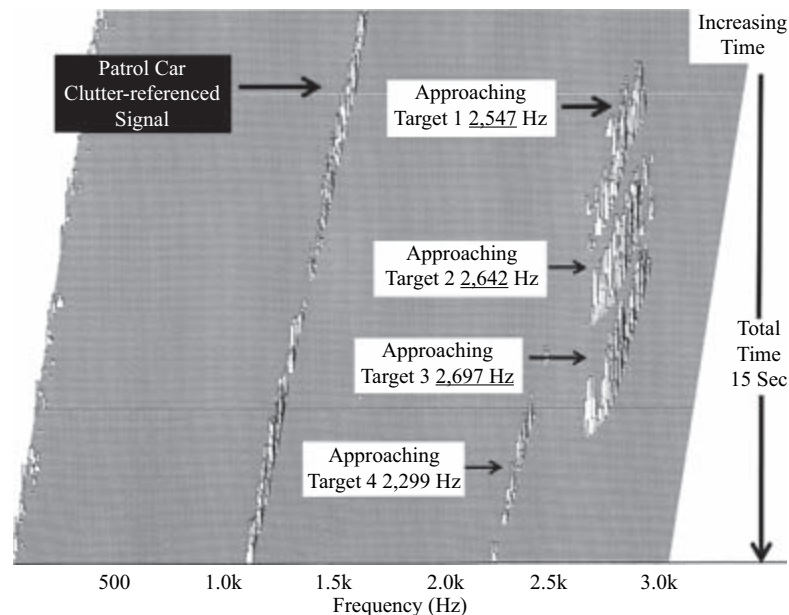
16.10.1 Clutter-Referenced Patrol Car Speed Determination

Figure 16-16 shows a waterfall spectral display of the signals produced by the homodyne police radar when it is operating in the moving mode. The display consists of approximately 300, 1,024-point Hamming windowed, fast Fourier transforms (FFTs). The frequency bin resolution is 10.7 Hz. The 300 successive spectrums are stacked from top to bottom to form the waterfall display. The waterfall display is composed of approximately 15 seconds of data. The spectral frequency scale is shown along the abscissa and ranges from 20 Hz to 3 kHz.

The patrol car clutter-referenced signal is generated as the patrol car drives at a relatively constant speed along the highway with the radar antenna directed forward. The amplitude of the patrol car clutter-referenced speed at any time is indicated by the height of the trail of spikes on the plot. Road signs, traffic signals, other fixed objects along the roadway, and the pavement backscatter the forward-directed radar signal. Due to patrol car motion, the Doppler-shifted frequency from the nonmoving clutter sources is used by the radar to compute the patrol car speed.

Figure 16-16 shows that a total of four vehicles approached and passed the police patrol car during the 15 seconds when data was taken while the radar was operated in the moving mode. The target identification number and the Doppler shift value generated by the closing velocity between the patrol car and the target vehicle are also shown in Figure 16-16. The drop in Doppler frequency just before each approaching target is lost is caused by the cosine effect, discussed in Section 16.4. When the target vehicle gets very close to the police car, the angle between the radial approach line and the actual angle

FIGURE 16-16 ■ Waterfall Display of Patrol Car Clutter-referenced and Target Doppler Frequencies [GPRC].



to the target increases at a high rate. This causes the closing Doppler frequency to drop rapidly just as the target passes the police car and moves out of the radar's antenna beam.

The speed limit where the moving-mode data were taken was 45 MPH. Analyzing the data presented in Figure 16-16, the Doppler shift generated by the moving patrol car averages approximately 1,134 Hz, which corresponds to an average patrol car speed of 36 MPH. Table 16-2 shows the target identification number in the left column. The detected Doppler shift for each target corresponding to the closing speed between the police car and the target vehicle is shown in the second column. Doppler is converted to closing speed in MPH in the third column. The true target speed is calculated by subtracting the patrol car speed from the target speed in the fourth column from the left.

TABLE 16-2 ■ Doppler Shift, Closing Speed, and Actual Speed of Target Vehicles 1 Through 4

Vehicle ID Number	Doppler Shift (Hz)	Closing Speed (MPH)	True Speed (MPH)
1	2,547	81	45
2	2,642	84	48
3	2,697	86	50
4	2,299	73	29

Figure 16-17 shows a simplified block diagram of the Kustom MR-7/MR-9 moving radar. The RF transceiver is composed of the circular horn, the solid-state Gunn device transmitter, a crystal detector/mixer assembly, and the turnstile junction duplexer. Also housed in the antenna unit is a high-gain amplifier and an automatic gain control (AGC) circuit that keeps the amplitude of the output signal relatively constant, regardless of input signal amplitude. The AGC decreases signal amplitude by electronically reducing the amplifier gain when large radar cross section targets are present in the antenna beam. This AGC action increases the dynamic range of the amplifier and keeps the output

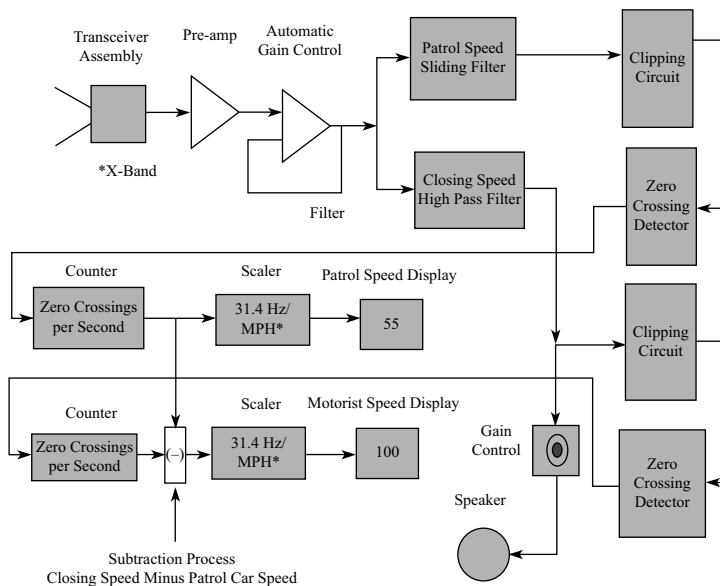


FIGURE 16-17 ■ Block Diagram of the Kustom Model MR-7/9 Moving Police Radar System [GPRC].

signal level within the narrow amplitude range required for accurate signal processing. Achieving high dynamic range is important, given that a tractor trailer truck head-on aspect can have an X-band radar cross section of over 10,000 square meters and a motorcycle and rider may have a cross section of less than 1 square meter.

The relatively constant amplitude output signal from the AGC is split. One side goes to the *patrol-speed sliding filter*. This filter is approximately 300 Hz wide. When the patrol car starts moving, the filter is electronically stepped in 10-MPH increments until the return from roadside clutter is centered in the filter. Once the sliding filter locks on to the clutter signal, the filter tracks the signal as the patrol car slows down and speeds up. To convert Doppler shift to MPH, the output of the filter is hard clipped, and the resulting signal becomes a square wave. The number of zero crossings per unit time is converted to a count corresponding to the Doppler shift generated by patrol car motion.

The other side of the split signal is applied to the *closing-speed high-pass filter*. The high-pass filter low end cutoff frequency is always offset above the frequency of the patrol-speed sliding filter upper frequency. When the patrol car increases or decreases speed, the sliding filter low end cutoff frequency increases or decreases proportionally. A simple math circuit subtracts the patrol car speed from the target closing speed. The resulting target Doppler shift is then scaled to units of MPH by dividing the target speed by 31.4, the scaling factor for X-band radar. The actual target speed is displayed to the police radar operator in MPH on a digital display.

The MR-7/9 signal processor included a logic circuit requiring the observed target Doppler frequency to remain the same over multiple successive samples within a short window of time. If all samples in the time window were not the same value, the speed display would be blanked. This circuit performed a signal quality evaluation. It was included to eliminate false alarms from interference or signals from a target environment that changed very rapidly. To further assist the operator in making decisions about the quality of the signal, the Doppler audio was sent to a small speaker mounted in the radar. The operator was instructed to listen to the target Doppler and only write tickets when the tone from the target was relatively constant in amplitude and frequency.

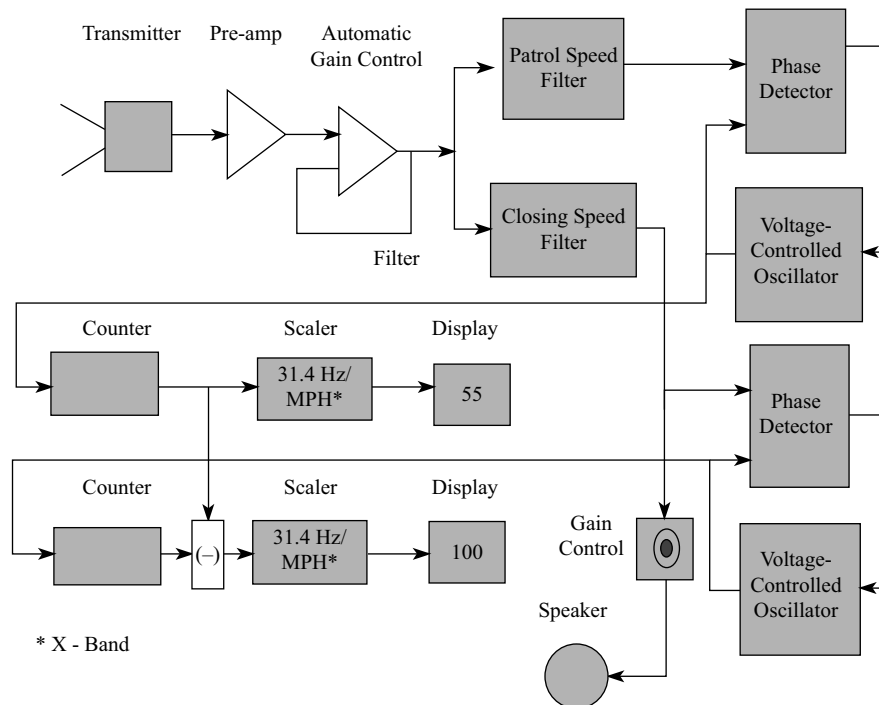
The MR-7/9 also could be operated in the stationary mode. The operating mode was selected by a front panel push-button switch. When the radar was operated in stationary mode, the patrol-speed sliding filter was reconfigured to have a broad pass band. The output signal from the zero crossing detector was fed to the target counter and after scaling to the target speed display.

16.11 | ALTERNATIVE PHASE-LOCKED LOOP SIGNAL-PROCESSING APPROACH

Several other police radar manufacturers developed an approach different from the one used by the MR-7/MR-9 to process the signal for both the stationary and moving modes of police radar operation. Figure 16-18 is a block diagram that shows the alternative approach using a phase-locked loop to regenerate the incoming Doppler frequency. The radar front-end RF hardware and signal flow are almost identical to the approach shown for the MR-7/MR-9 in Figure 16-17. However, rather than clip the signal and count zero crossings to derive Doppler frequency, the signal processor used a phase-locked loop (PLL) and a counter-circuit. The PLL consists of two primary circuits: (1) a phase detector (PD), and (2) a voltage-controlled oscillator (VCO).

The phase detector is a device with two inputs. When a first frequency is fed into one input of the phase detector and a second frequency is fed into the second input, the output of the PD is an error voltage. The greater the difference between the two input frequencies, the greater the error voltage that appears at the PD output. When the two input frequencies to the PD are the same, there is no error voltage output.

FIGURE 16-18 ■ The Use of a Phased-locked Loop to Determine Doppler Frequency [GPRC].



The second component of the PLL is the voltage-controlled oscillator. The output frequency of the VCO is voltage tuned. The output of the VCO is fed back to the phase detector input and is one of the two frequencies input to the phase detector. The error voltage output of the PD is connected to the tuning element of the VCO so that the error voltage will tune the frequency of the VCO to the frequency of the Doppler-shifted signal in a feedback loop.

In the police radar application, the Doppler signal from the patrol-speed filter is fed to one input of the phase detector. In the first few milliseconds, the Doppler signal applied to the phase detector generates an error voltage because the target Doppler and the VCO frequencies are different. In a matter of milliseconds, the error voltage feedback process drives the VCO frequency output to be the same as the Doppler input frequency. When there is no difference between the two frequencies, the VCO is effectively locked to the output of the patrol-speed filter. When a phase-locked condition is achieved, the radar is enabled to display the target speed to the operator.

The primary advantage of using a PLL is the fact that the counter circuits that follow the PLL are designed to sample and count a logic-level square wave, not a filtered analog Doppler sine wave signal. The output of the VCO is a logic-level square wave that is optimum for the input to a counter circuit.

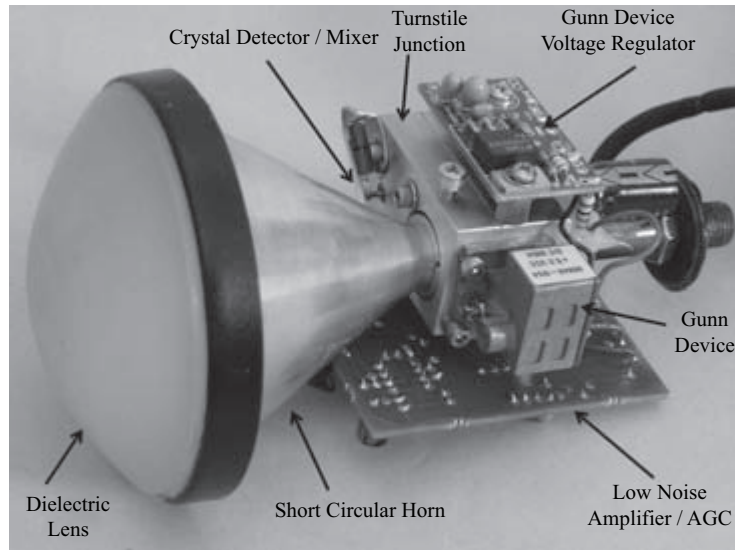
16.12 | THE MOVE TO K-BAND FREQUENCIES

When changing from S-band to X-band, the beamwidth for a given antenna size reduces and the RCS of a typical vehicle increases; so, too, will these characteristics improve when moving from X-band to the higher frequencies. The FCC made an allocation for police radar operations in the K-band from 24.05 to 24.25 GHz in 1978. By the mid-1980s, police radar manufacturers were all using the solid-state Gunn device as a transmitter, an improved Schottky crystal detector/mixer diode, and a short conical horn/turnstile junction duplexer. The first generation of the K-band radars were scaled versions of each manufacturer's existing X-band design. The X-band turnstile junction and the short conical horn design was scaled to K-band dimensions and incorporated in most manufacturers' designs. A dielectric lens was added to the short conical horn to correct associated phase distortions. The Gunn device transmitter had lower power output than the previous X-band Gunn devices (20 mW versus 100 mW). The K-band Gunn device was also smaller, given the smaller cavity size of the cavity resonator at K-band. A Schottky detector/mixer diode was developed for use at K-band.

The signal-processing circuits already used in a manufacturer's existing X-band product were modified to provide new scaling of the K-band Doppler signal. Using Equation (16.1), a 100-MPH target observed by a radar operating at 10.5 GHz will produce a Doppler shift of 3,136 Hz. The Doppler frequency was divided by a scaling factor of 31.4, and the speed was displayed in MPH. The same 100-MPH target produced a Doppler shift of 7,252 Hz at 24.2 GHz. The existing X-Band processor that used PLL technology was modified to operate at K-Band by shifting the PLL operating range to 7,252 Hz and adjusting the scaling factor to 72.5 Hz.

In 1991, Decatur Electronics, located in Decatur, Illinois, had developed their next generation of K-Band radar that was typical of the radars designed by other police radar manufacturers during the period. The Genesis I radar was small, yet sensitive. The Genesis I RF assembly, shown in Figure 16-19, utilized the same basic design of

FIGURE 16-19 ■
Decatur Electronics
Genesis I K-band
Radar Typical of the
Designs Sold in
1991 [GPRC].



their first-generation K-Band system. However, the design was implemented in a much smaller package. The conical horn with the dielectric lens mated with the turnstile junction. The Gunn Device transmitter was mounted to port 1 of the turnstile junction, and the Schottky detector/mixer was installed inside of a cavity in the turnstile junction assembly. The turnstile junction was cast or milled aluminum. The aluminum turnstile junction duplexer was very inexpensive to make. Variants of this design of the RF homodyne assembly are used in almost all police radar designs on the market today.

The voltage supply for the Gunn device was 5.5 volts DC. The Gunn device generated approximately 20 mW of transmit power. The voltage regulator board shown on top of the turnstile junction regulated the 12-volt vehicle battery voltage down to the required 5.5 volts DC. The circuit board hosting the high-gain amplifier/AGC circuit is mounted on the bottom of the turnstile junction. A connecting cable supplies voltage to the regulator and amplifier boards. The amplified and leveled Doppler signal is transmitted to the operator control/display unit via the connecting cable.

The Decatur Genesis I radar could be used as a stationary radar or a moving radar. The small size of the antenna unit allowed it to be mounted behind the rear window of the patrol car for stationary operation, or behind the windshield for moving operation. The footprint of the operator control/display unit was small. This allowed it to sit on the dashboard out of harm's way if the passenger airbag was deployed. The Genesis I control/display unit had three display windows. When operated in the moving mode one display showed the patrol car speed. A second allowed the radar operator to lock the target vehicle speed into the display to be shown to the speeding motorist, and the third window displayed the speed of the target vehicle the entire time it was being tracked, allowing changes in target speed to be noted.

16.13 | POLICE RADAR MOVES TO THE KA-BAND AND UTILIZES DIGITAL SIGNAL PROCESSING

The FCC made a Ka-band allocation of 34.2 to 35.2 GHz for police radar use in 1983. However, the price of 35-GHz microwave components prohibited their use in police

radar when the Ka-band was first allocated. The spectrum approved for police radar use was later expanded to 33.4–36 GHz in 1992, and by 1992, the price of 35-GHz RF components had dropped to the point that they could be used in cost-sensitive police radar applications. In 1992, Applied Concepts Incorporated (ACI) in Plano, Texas, developed one of the first Ka-band radars to use DSP technology. Figure 16-20 shows the Stalker Ka-band police radar system developed by ACI.

The radar RF assembly utilizes a conical horn with dielectric lens. A turnstile junction serves as the duplexer. A Gunn device is used as the transmitter, and a Schottky diode mounted in the turnstile junction serves as the detector/mixer. The Stalker control unit/digital signal processor has three display windows to provide additional display capability for several modes of operation made possible by DSP techniques. All of the functions of the unit are controlled by the radar operator using the hand-operated remote control shown on the right in Figure 16-20.

Figure 16-21 shows a generic block diagram of a police radar that uses DSP to determine both patrol and target vehicle speed. This diagram is not specific to police radar models, but rather incorporates the high-level design features of several of the



FIGURE 16-20 ■ The Stalker Ka-band Police Radar with DSP Capability [GPRC].

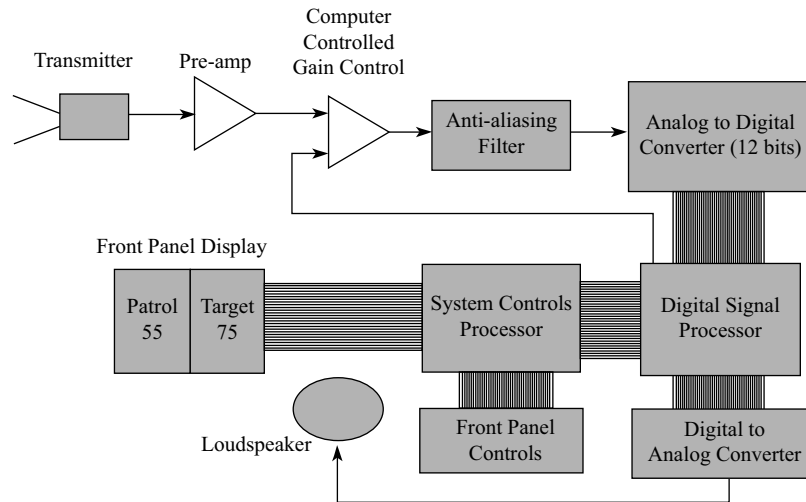
leading police radar that utilize DSP to provide speed information. The transmitter receiver section shown in Figure 16-21 is the conical horn; the turnstile junction design was already discussed. It operates at Ka-band frequencies.

The amplified signal from the radar transmitter receiver assembly is sent to a processor-controlled electronic attenuator. A low-pass filter follows the attenuator to ensure that the spectral data are not aliased. After filtering, the signal is digitized by a 12-bit analog-to-digital converter (ADC). The digital value representing signal amplitude is monitored by a signal-leveling algorithm in the DSP. Before the maximum value (4,096) is reached and saturates the ADC, the DSP algorithm commands the attenuator to reduce the gain of the input radar signal. This feedback action ensures that the ADC is not saturated by a close target. The processor-controlled attenuator is similar to the AGC circuit used in the analog radars to keep the amplitude of the signal to the processor relatively constant.

The digitized representation of the signal is processed by the DSP. The signal is windowed, and a real FFT is computed. The Doppler from each vehicle in the antenna beam

is assigned to a corresponding FFT frequency bin. The system control processor (SCP) is programmed to analyze the contents of the FFT bins, based on the radar mode of operation.

FIGURE 16-21 ■ Simplified Block Diagram of a Generic Police Radar That Utilizes DSP [GPRC].



When the radar is being operated in the moving mode, the SCP will identify the FFT bin where the referenced patrol car signal is centered. The bin index number is converted to a corresponding Doppler frequency, a scaling factor is applied, and the resulting speed value in MPH is displayed as patrol speed on the front panel. The SCP next determines the bin index number containing the energy from an approaching target and converts the bin index number to the closing Doppler frequency. A scaling factor would be applied to convert from Doppler closing speed to MPH. The SCP subtracts the patrol speed from the closing speed and displays the target speed display window.

The Doppler tone produced by the moving target is converted to an audio signal using a digital-to-analog converter (DAC). It is amplified and presented to the radar operator via a small loudspeaker. The radar operator monitors the amplitude and stability of the tone to judge target quality. The actual tone presented to the operator of a Ka-band radar may be divided down in frequency from the actual Doppler frequency generated by the target. Applying Equation (16.1), we can see that a 100-MPH target generates a Doppler frequency of 10,343 Hz by a police radar operating at approximately 36 GHz. Many veteran police officers' hearing range cuts off below this frequency. Thus, the Doppler frequency presented to the radar operator may be divided (translated down) by a factor of three or four to allow it to be heard. The same approach to lower the true Doppler frequency is used in some K-band radars.

16.14 | OTHER POLICE OPERATING MODES MADE POSSIBLE BY DSP

The early police radars measured Doppler frequency using a frequency counter, which typically “locked onto” the highest signal level, even if there were more than one frequency in the signal. Modern high-speed DSP engines make it possible to simultaneously compute the Doppler of all target vehicles in the antenna beam in milliseconds.

The processing algorithm uses the fast Fourier transform (FFT), a common radar digital signal-processing technique used to measure all Doppler frequencies in the signal. The FFT output is a complete spectrum containing the Doppler shift of all moving targets in the antenna beam. Given that the velocity of all targets in the antenna beam is available for processing by the radar SCP, new operational modes have been developed for the latest-generation DSP police radars. The author demonstrated this capability through research in 1981. A paper [2] was published in 1981 on how to resolve the speed of multiple simultaneous targets in the antenna beam using digital signal processing. Today several police radar manufacturers hold patent claims on the technique even though the concept has been in the open literature since 1981.

16.14.1 Largest Radar Cross Section or Fastest Target Mode of Operation

The ACI Stalker radar was one of the first to allow the radar operator to select for display the speed of either the target with the largest radar cross section or the fastest target. For example, if a motorcycle rider was passing a tractor trailer truck and if the fastest target mode was selected for display, the motorcycle speed would be displayed in the target window. The speed of the 10,000-square meter tractor trailer would not be displayed even though the amplitude of the tractor trailer truck is several orders of magnitude larger. The fastest/largest target mode was not possible in the previous generation of analog radars that used zero crossing and PLL methods to extract target Doppler speeds. In most cases, the analog radars always displayed the speed of the target with the largest radar cross section.

16.14.2 Same-Direction Moving Mode

The moving mode had been introduced in an earlier generation of police radar. Figure 16-15 shows the patrol car being driven in one lane, while the radar provides the speed of approaching vehicles in the opposite lane. The DSP radar made not only moving radar possible, but also made it possible to track targets moving in the same direction. Figure 16-22 shows a diagram demonstrating the tracking of targets moving in the same direction of travel for the overtaking target and for the target in front of and moving away from the police car.

When a vehicle is behind a police car and overtaking the police car (the radar antenna is pointed rearward), the speed of the overtaking vehicle can be determined. If a

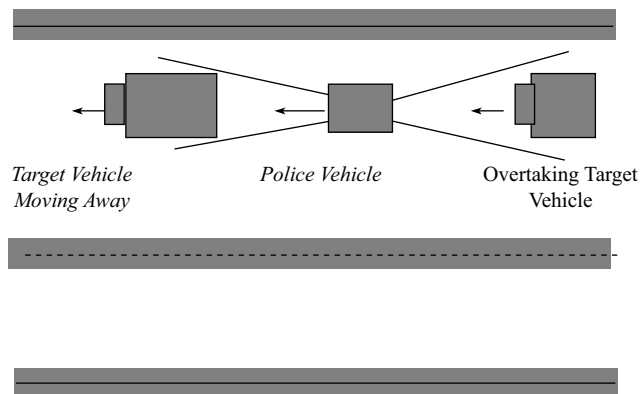


FIGURE 16-22 ■ Diagram Showing the Principle of Same-lane Police Radar Operation [GPRC].

vehicle is in front of the police car and moving away from the police car (the radar antenna is pointed forward), the lead vehicle's speed can be determined.

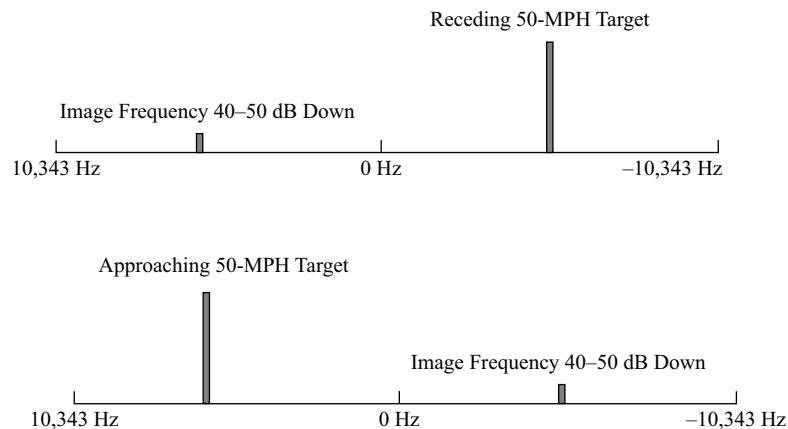
16.14.3 Target Direction Discrimination Mode

A police radar with target direction discrimination allows the radar's operator to select tracking of either an approaching or a receding target for processing and speed display. Why select target direction? Recall that when a radar is being operated in stationary mode, the radar normally detects and tracks target vehicles approaching the stationary police car from the rear. However, as vehicles in the opposite lane pass the police car and move rearward and away from the police car, they are illuminated by the police radar's rear-pointing antenna beam for a short time. These opposite-lane targets can be false targets if they have a large radar cross section. An RF system modification was necessary to implement target direction selection.

The DSP radar with target direction selection utilizes a detector/mixer that has both an in-phase (I) and quadrature (Q) output. The I and Q signal components are processed using a complex FFT, and a two-sided spectrum is produced. Each of the two spectrums shown in Figure 16-23 is presented as examples only, because no spectrum is ever presented to the operator.

The example case of a double-sided spectrum at the top of Figure 16-23 is centered at 0 Hz. A receding target has a Doppler shift lower than the transmitter frequency. As a result, the receding target line appears within the right side of the zero-centered spectrum (negative frequency Doppler shift).

FIGURE 16-23 ■
Two Zero-centered Spectrums Showing How Receding Targets Are Rejected [GPRC].



The Doppler shift of an approaching target is above the transmitter frequency. The spectrum at the bottom of Figure 16-23 allows the visualization of how the approaching target would appear within the positive side of the hypothetical zero-centered spectrum.

If the radar operator selects approaching targets to be displayed, the SPC would analyze only the FFT bins in the positive side of the zero-based spectrum to determine which bin contained maximum power. The FFT bin containing the greatest power corresponds to the Doppler frequency of the approaching target. The frequency is scaled to units of MPH for display.

Figure 16-23 also shows that a small amount of power from the receding target appears in the left side of the spectrum. The energy from the receding target that appears in the positive side of the spectrum is called the image frequency. In order to keep the image frequency to a minimum, each manufacturer of a DSP radar has to ensure that the fixed phase difference between the I and Q mixers is exactly 90 electrical degrees and that the signals from both mixers are balanced in amplitude. If this design goal is achieved, the image amplitude may be suppressed 30 to 40 dB, which would ensure the image would not be mistaken for an approaching target. If the design goal is not achieved, a high-amplitude image will be present, and the SCP may not be capable of discriminating the image of a receding target from the signature of an approaching target when the receding target has a large radar cross section.

16.15 | SUMMARY

The Electro-matic model S1 was the first commercially successful police radar. It was designed after WWII using transmitter technology developed for use by the military. The next generation was the Electro-matic model S2 police radar. Both systems were homodyne CW radars, and the S2 utilized a single antenna to transmit while receiving. This was made possible by a duplexer that isolated the receiver from the transmitter. As both civilian and military radar technology advanced, police radar took advantage of higher-frequency allocations while utilizing inexpensive design approaches to maintain low selling prices. Since the development of the model S1, the basic homodyne design approach has not changed. Antenna designs have been improved and the less-than-optimum methods to allow simultaneous receive while transmitting have been improved upon. The turnstile junction duplexer and conical horn have become standard aspects of RF section design. This duplexer design is currently used by all police radar manufacturers as an inexpensive substitute for the much more expensive ferro-magnetic circulator.

The introduction of the DSP engine has made high-speed processing of the Doppler signal possible. The speed of multiple targets can be resolved by the complex FFT. The radar's ability to resolve the speed of multiple targets and to resolve the targets' direction of travel makes different radar operational modes possible. The next revolutionary advancement in police radar will be methods that make identification of individual targets possible in a multiple-target environment. However, even with better technology, the reliability of police radar operations is totally dependent on the radar operator interpreting the data properly. Operator training and experience are key to proper data interpretation.

16.16 | REFERENCES

- [1] H. Buddendick and T. F. Eibert, "Acceleration of Ray-Based Radar Cross Section Predictions Using Monostatic-Bistatic Equivalence," in *IEEE Transactions on Antennas and Propagation*, Vol. 58, No. 2, February 2010.
- [2] E. F. Grenaker and M. A. Corbin, "Speed Timing Radar – New Methods to Quantify Accuracies Achievable Under Various Target Conditions," in Carnahan Conference on Security Technology, Lexington, Kentucky, 12–14 May 1982.

16.17 | FURTHER READING

- E. F. Greneker, “The Source of Errors Most Frequently Encountered in Speed Timing Law Enforcement Radar,” presented in the *Proceedings of the Third International Conference Security through Science and Engineering*, Berlin, 1980.
- E. F. Greneker, J. L. Geisheimer, and D. Asbell, “Extraction of Micro-Doppler Data from Vehicles at X-Band Frequencies,” in *Proceedings of SPIE Aerosense*, Vol. 4374, pp. 1–9.
- E. F. Greneker, J. Geisheimer, and E. O. Rausch, “Farm Equipment Collision Avoidance Using Only Homodyne Radar,” in *SPIE Proceedings of the Aerosense 2000 Conference, Sensor Technology V, Session 1, Radar Systems and Phenomenology Orlando, FL, April 2000*, pp. 22–32.
- W. E. Mueller and W. A. Tyrrell, “Polyrod Antennas,” in *Bell System Technical Journal*, Vol. 26, 1947, pp. 837–857.
- M. A. Meyer and H. B. Goldberg, “Applications of the Turnstile Junction,” in *IRE Transactions, Theory and Techniques*, December 1955, pp. 40–45.
- L. Sun, E. L. Hines, and C. Mias, “Quarter-Wave Phase Compensating Multidielectric Lens Design Using Genetic Algorithms”, *Microwave and Optical Technology Letters / Vol. 44, No. 2, January 20, 2005*, pp. 165–169.
- W. G. Lotz, R. A. Rinsky, and R. D. Edwards, “Occupational Exposure of Police Radar Operators to Microwave Radiation from Traffic Radar Devices,” *National Technical Information Service (NTIS) Publication Number PB95-261350*, June 1995.
- R. C. Baird, R. L. Lewis, D. P. Kremer, S. B. Kilgore, “Field Strength Measurements of Speed Measuring Police Radar Units”, *Technical Report DOT HS-805 928*, June, 1981. pp 1–59.

Index

1-dB compression point (1 dBcp) 344, 348, 368
1N23 diode 751
2C40 planar triode 751
3-D beam-scanning techniques 336–40
3-D radar 335
743D radar 336

A

A-35 305
acquisition and air-combat mode 130–1
across-track interferometric SAR (InSAR) 478
active electronically scanned arrays (AESAs) 121, 147–9, 151, 156, 163, 253, 276–9, 285, 299, 308, 311, 487
active homing missiles 164, 168
active layered theater ballistic missile defense (ALTBMD) 329
active protection system (APS) 10, 76, 111
AD9858 62
AD9912 63
adaptive beam forming (ABF) for multiple jammers 122, 156, 171
adaptive constant false-alarm rate 566–7
adaptive cruise control (ACC) 76–7, 110
adaptive digital beamforming (ADBF) 279
adaptive displaced phase-center antenna 413–15
adaptive Doppler processing 410–13
adaptive matched filter (AMF) 420
adaptive resource management 273
adaptive RFI removal process 674–6
adaptive SINR loss 403, 417
advanced audio coding (AAC) 516
advanced land observing satellite (ALOS) 446–7
Advanced Research Projects Agency (ARPA)
Lincoln C-Band Observables Radar (ALCOR) 288

Long-Range Tracking and Instrumentation Radar (ALTAIR) 288
advanced synthetic aperture radar (ASAR) 444–6, 449
Aegis ballistic missile defense (ABMD) 287
Aegis BMD SPY-1 286
against antiship cruise missiles (ASCM) 162
Agilent E5500 phase noise measurement system 572
AGM-154 joint standoff weapon (JSOW) 137
aim point+seeker area 144
air and missile defense (AMD) engagements 255
Airborne Cloud Radar 111
airborne early warning (AEW) radar scanning 8
airborne fire-control radar 123
E-SCAN FCR 147–9
E-SCAN-only functionalities 151–4
modern functionalities not directly related with 154–6
new modes enabled by 151
technological aspects 149–50
future of 156–60, 161
heads-up displays 142
M-SCAN FCR 123–5
air-to-air modes 125–31
air-to-ground modes 131–40
air-to-sea modes 140–1
multifunction displays 141–2
weapon modes 142
air-to-air missile mode 142–5
air-to-ground missile mode 146
air-to-sea missile mode 146–7
cannon mode 146
airborne IFMCW imaging radar 43
airborne moving target indication (AMTI) radar 350–1, 392
airborne pulse-Doppler radar 3, 175, 203, 555

blind zones 223
range 223–4
velocity 224–6
clutter-fill pulses 221–3
conceptual approach 203
coherent integration of digital samples 210–12
Doppler filter response 212–14
Doppler frequency, extracting 208–9
overview of operation 206–7
pulse-Doppler waveform 204–6
pulsed versus CW operation 203–4
range-Doppler map 215–16
reduction of Doppler sidelobes 214–15
sampled waveform 209–10
synchronous detection 207–8
contours of constant Doppler and range 196
iso-Doppler contours 196–8
iso-range contours 198–9
co-range mainlobe clutter conditions of 183
signal-to-clutter ratio for 184–5
Doppler shift 181–2
example scenario 199–203
folded clutter 220–1
geometry 177
angle relative to radar velocity vector 179
coordinate system 177–8
range and elevation angle to a point on earth surface 179–81
high pulse repetition frequency (HPRF) mode 228–35
medium pulse repetition frequency (MPRF) mode 235–48
PRF regimes 226–8
range ambiguity 217–18
range and Doppler distribution of clutter 185, 195–6
altitude return Doppler extent 194–5
altitude return range 193–4
clutter spectrum 185–6

- airborne pulse-Doppler radar (*cont.*)
 - mainlobe clutter range and Doppler extent 190–3
 - sidelobe clutter range and Doppler extent 186–90
 - range-Doppler spectrum, folding of 220
 - unambiguous range and velocity, interdependence of 219–20
 - velocity ambiguity 218–19
- Air Command and Control System (ACCS) 329
- aircraft landing and obstacle avoidance 74–6
- air defense radars 323
- Air Force Cambridge Research Laboratory 592
- Air Force Space Surveillance System (AFSSS) 81, 288
- air-interception missiles (AIM) 143, 145
- air interceptor (AI) radar scanning 8
- airport surveillance radar (ASR) 544–8, 553, 555, 556, 558–9, 561–2
 - performance characteristics of 554
- air route surveillance radar (ARSR) 545–7, 553, 555, 556, 558, 559, 561–2, 564–5
 - performance characteristics of 554
- air route traffic control center (ARTCC) 545
- air superiority 125
- air tests, GPR 735, 737–9
- air-to-air missile modes 142–5
- air-to-air mission 125
- air-to-air modes, of M-SCAN FCR 125–31
- air-to-ground missile mode 146
- air-to-ground modes, FCR in 131–40, 246, 249, 257
- air-to-ground ranging (AGR) 132, 136
- air-to-sea missile mode 146–7
- air-to-sea modes 140–1
- air traffic control (ATC) radars 323, 543
 - design issues 581–2
 - future of 582
 - organization 547–8
 - primary surveillance radar (PSR): *see* primary surveillance radar (PSR)
 - radar advancements for 583–4
 - reliability, maintainability, and availability (RMA) 581
 - secondary surveillance radar (SSR): *see* secondary surveillance radar (SSR)
 - surveillance systems for 584–5
- air traffic control beacon interrogator (ATCBI) system 546, 577–8
- air traffic control radar beacon system (ATCRBS) 545, 557, 577
- air traffic control radar systems 13
- air traffic management (ATM) 582, 584
- Air Weather Service (AWS) 591
- Alliant Techsystems FMCW radar 56
- Allied Command Europe (ACE) 329
- Almaz-1 438
- along-track interferometry (ATI) 386, 449, 478–81, 493, 494
- ALOS PALSAR 446–7
- alpha-beta filtering 128, 273, 355
- altitude return (ALT) 185
 - Doppler extent 194–5
 - range extent 193–4
- ambiguities 217
 - for bistatic radar 507–9
 - function 507
 - range 217–18
 - range/velocity extent 219–20
 - resolving 242–5
 - velocity 218–19
- amplifier and low-pass filter design 725–30
- amplitude modulated (AM) noise levels 35–43
- AMTI (adaptive moving target indicator) filters 350–1
- Analog Devices AD9858 62
- Analog Devices AD9912 63
- analog-to-digital converter (ADC) 30, 50, 343, 346, 394, 407, 446, 568, 574–5, 773, 774
- analog TV 510–12
 - examples of systems 527–9
- AN/APG-63 10, 229
- AN/APN-232 Combined Altitude Radar Altimeter (CARA) 73, 74
- AN/APQ-13 radar 591
- AN/APY-1 radar 10
- AN/APY-2 radar 10
- AN/FPS-85 286, 289
- angle deception 172
- angle-of-arrival (AOA) 262
- AN/SPY-1 10
- AN/SPY-3 ship self-defense radar 253, 256
- Antei-2500 306
- antenna 101–4, 405
 - along-track antenna length 405–6
 - antenna height 406–7
 - of ASR-9 545, 546
 - auxiliary 124
 - beamwidth 93–4
 - bow-tie 709–10
 - GPR 706–11
 - guard 245
 - high-gain, flat-slotted 123
 - and MMW sensing 101
 - on MPARS performance 265–8
 - phased array: *see* phased array antenna
- RADARSAT-2 SAR 449
 - selection 701–2
 - subarray design considerations 407–9
 - TerraSAR-X 484–6
 - ultra-low sidelobe 372
 - waveforms 409–10
- antenna coordinate system (ACS) 422–3
- antenna scanning modulation 563
- antenna subsystem 11
- anti-aircraft (AA) guns 71
- antiaircraft artillery (AAA) 160, 162
- antiballistic missile 359
 - anti-radar missile (ARM) detection and alert 372–3
 - BM kinematic model 361–3
 - BM tracking 363–8
 - prediction of BM RCS 360–1
 - Simulated Scenarios and Results 368–71
- Anti-Ballistic Missile (ABM) Treaty 299
- anti-radar missile detection and alert 372–3
- antiradiation missiles 502
- AN/TPQ-53 10
- AN/TPY-2 11, 253, 286, 295
- AN/TPY-2/THAAD radar 303
- “AN” equipment-designation system 172–3
- apoapsis 451
- apogee 451
- applications of radar 1
 - ISR radar 12–13
 - specialized applications 13–14
 - tactical radar 10–12
 - see also* continuous wave (CW) radar, applications
- Applied Concepts Incorporated (ACI) 773
- APS-15 radar 592
- AR327 336
- area clutter RCS 43–4
- area coverage rate (ACR) 386, 392, 404, 494, 642, 644
- argument of latitude 451
- argument of the perigee/periapsis 451
- ascending node 451
- ascension radar 288
- atmospheric sensing 111
- attenuation of weather-radar signals 613
- auto-acquisition (AACQ) 130, 131
- autodyne CW radar configuration 23–4
- automated landing guidance (ALG) 110–11
- automatic dependent surveillance (ADS) 546
- automatic dependent surveillance-broadcast (ADS-B) 524, 557, 582
- automatic gain control (AGC) 29, 768
- automotive CW radars 76–7

- automotive MMW radar 110
- auxiliary antenna 124, 171, 245
- avalanche transistor pulse generator 714–16
- aviation radars 597
- AWS-9 336
- azimuth beam steering 474
- azimuth estimation, moving window technique for 352
- azimuth scan range 474, 486
- B**
- back projection algorithm (BPA) 659–60, 663, 664
- BAE SYSTEMS AR327
 - COMMANDER 332
- BAE SYSTEMS COMMANDER SL 331
- BAE SYSTEMS S743D
 - MARTELLO 331
- ballistic missile defense (BMD) radar 11
 - ballistic missile threat, overview of 292–4
 - cross-range resolution of 312–13
 - design 307–12
 - engagement implementation 294–8
 - frequency considerations 307–8
 - implementation
 - search and acquisition 308–9
 - tracking and discrimination 309–10
 - international BMD radar
 - deployment 306
 - missile warning (MW) fidelity 287
 - performance estimation 312–20
 - BMD CSO performance 316–20
 - track prediction performance 313–16
 - radar development for 298–306
 - Russian BMD radar deployment 304–6
 - system requirements 292–8
 - technologies
 - RF aperture 310–11
 - signal and data processing 311–12
 - U.S. BMD radar deployment 301–4
 - U.S. detection fence and mechanically scanned radars currently supporting SSA 288
 - view of threat complex 313
- ballistic missile defense system (BMDS) 287, 297, 299, 301
- ballistic missile early warning system (BMEWS) 286, 302, 308, 328
- ballistic missiles (BMs)
 - detection 363
 - kinematic model 361–3
 - RCS, prediction of 360–1
 - tracking 363–8
- ballistic targets (BTs) 324
- barrage noise 170
- Barratt, Peter 592
- battlefield combat identification system (BCIS) 112
- battlefield surveillance radar, history of 637–41
- battlefield target identification device (BTID) 112
- beam-limited altimeters 433
- beam-scanning technique (BST) 324, 330, 332, 336
- beam-steering computer 263
- beamwidth
 - azimuth 405, 449, 468, 473, 485
 - Doppler beamwidth 411
 - elevation 464–5
- beat frequency 26, 30, 38, 45, 47, 49, 57
 - bandwidth 47
 - spectrum 61
- Bessel filter 726, 730
- biconical antenna 709–10
- binary hypothesis test 564
- bistatic equivalence theorem 507
- bistatic hosting, denial of 375–6
- bistatic radar
 - ambiguity function for 507–9
 - and multistatic radar geometry 505–6
 - radar equation 506
 - target signatures 506–7
- Blake charts 258
- Blighter radar 71, 72
- blind speeds 560
- blind-zone charts 237–8
- blind zones 223
 - range 223–4
 - velocity 224–6
- block adaptive quantization (BAQ) 471–2
- block floating point quantization (BFPQ) 471
- bombing using ground mapping 137–8
- boresight acquisition (BACQ) 131
- bounded weak echo region (BWER) 617
- bow echoes 621, 622
- bow-tie antennas 709–10
 - end-loaded 710
 - unloaded 710
- bright band 615–16
- Brimstone anti-armor missile 76
- British Chain Home radar system 3, 12, 327
- Browne, Ian 592
- Butterworth filter 726, 730
- C**
- Camp Sentinel II service test system 639
- Canadian Spaceborne SARs 447–9
- cancellation filter and insertion map 350–1
- cancellation phase 40
- cannon mode 146
- Cat House 304
- C-band 8, 461
- CELLDAR 531
- cell phone 513–14
 - examples of systems 530–1
- Center for Severe Weather Research (CSWR) 624
- Chain Home Low 327
- Chebyshev filter 726, 730
- China 439
- chip length 64–5
- chips 678
- circular error probable (CEP) 293, 405
- circular orbits 452–4
- civilian radars 323
- clairvoyant SINR loss 402
- classification 9
- CLOCK 344
- closely spaced objects (CSOs)
 - performance, BMD 289–90, 316–20
- closing-speed high-pass filter 769
- cloud-profiling radar (CPR) 111
- clouds 460
- CloudSAT 111
- clutter 552
 - attenuation ratio 560
 - and clutter processing 566–7
 - mapping 561
- clutter Doppler spectrum 185–6
 - altitude return Doppler extent 194–5
 - altitude return range 193–4
 - mainlobe clutter range and Doppler extent 190–3
 - sidelobe clutter range and Doppler extent 186–90
- clutter-fill pulses 221–3
- clutter improvement factor (CIF) 317
- clutter map constant false-alarm rate 567
- clutter-mitigation approaches 410
 - nonadaptive and adaptive Doppler processing 410–13
 - nonadaptive and adaptive DPCA 413–15
 - STAP and STAP Variants 415–18
- clutter-referenced patrol car speed determination 767–70
- clutter-referenced signal processing technique 767
- clutter-reflectivity values 93
- clutter spreading due to LFM ranging 233–4
- CNAPS 110
- coambiguous range 243–5
- “coarse weather information” 547
- Coastal Border Surveillance System (CBSS) 70, 71

- COBRA DANE radar 286, 299, 303
 coded orthogonal frequency-division multiplex (COFDM) modulation 512
 coherent all radio band system (CARABAS I) 645, 652
 coherent change detection (CCD) 6
 coherent continuous wave radars 3
 coherent oscillator (COHO) 206, 207, 571
 coherent-processing interval (CPI) 204, 208, 222, 223, 242, 248, 390
 coherent radar 3
 COHO (coherent oscillator) 206, 207, 344, 571
 Collaborative Adaptive Sensing of the Atmosphere (CASA) 632
 combat identification systems 88, 112
 Combined Altitude Radar Altimeter (CARA) 73
 Command Guidance 167
 commercial off-the-shelf (COTS) components 759
 communication and synchronization, in radar system 703
 cone angles 407
 cone of silence 562, 598, 632
 constant false-alarm rate (CFAR) 216, 351–2, 387
 detection 566
 constantly computed release point (CCRP) 136–7
 continental United States (CONUS) 546
 continuous wave (CW) Doppler 175, 186
 continuous wave (CW) radar 10, 17, 21
 applications 67
 aircraft landing and obstacle avoidance 74–6
 automotive CW radars 76–7
 CW radar altimeters 73–4
 level-measurement FMCW radars 78
 over-the-horizon radar (OTHR) 80–1
 seekers and active protection system sensors 76
 space 81
 surveillance 68–73
 weather sensing 78–80
 configuration types 23–6
 disadvantage of 22
 frequency modulated (FMCW) 26
 amplitude and phase noise 35–43
 applications 67
 area clutter RCS 43–4
 direct digital chirp synthesizers 62–3
 frequency sweep nonlinearity 52–62
 linear waveform 26–9
 linear waveform trades 29–31
 range resolution 44–52
 signal-to-noise ratio (SNR) estimation 31–5
 waveform designs 63–7
 continuous wave frequency modulation (CWFM) 753
 controlled airspace 544, 557
 cooperative bistatic radar 5, 6
 cooperative sensor 122, 159
 cooperative systems 5, 121, 160
 coordinate system 177–8
 co-range mainlobe clutter 183
 conditions of 183
 signal-to-clutter ratio for 184–5
 correlation 129
 correlation coefficient 626–7
 correlation logics 356–7
 cosecant 163
 cosecant-squared coverage pattern 562
 cosine error caused by improper operation 754–5
 Cosmos 1870 438
 COSMO/Skymed 438, 450
 CRM-100 72–3
 cross-eye 172
 crossing tracks 129
 cross-polarization 172
 Crotale NG system 165
 cumulative probability 152
 of detection and false alarm 239–42
- D**
 DBS TV 518
 debris balls 608, 620–1
 Decatur Electronics 771–2
 decision-level fusion 107
 Defense Advanced Research Projects Agency (DARPA) 385, 638
 defense radars 323
 see also ballistic missile defense (BMD) radar
 degree of freedom (DoF) 387
 delay line cancellers: *see* moving target indication (MTI), pulse cancellation filters
 delay line design 724
 deployable GBWR 332
 deramp RFI removal algorithm 671–4
 derechos 621
 descending node 451
 dielectric resonant oscillators (DROs) 42
 differential phase 629–31
 differential reflectivity 627–9
 digital beamforming (DBF) 4, 279, 412
 digital elevation model (DEM) 644, 661
 Digital Radio Mondiale (DRM) format 516
 digital radio/TV 512–13
 examples of systems 529–30
 digital signal processing (DSP) 13, 50, 207, 556, 772–4
 radar cross section or fastest target mode of operation 775
 same-direction moving mode 775
 target direction discrimination mode 776–7
 digital-to-analog converter (DAC) 346, 574–5, 774
 digital up-conversion (DUC) 346
 direct digital chirp synthesizers 62–3
 direct digital synthesizer (DDS) technology 62
 direct sequence spread spectrum (DSSS) 514
 direct wave 694
 Discrete Address Beacon System (DABS) 557
 discrete Fourier transform (DFT) 555
 discrimination 9, 296, 309–10
 displaced phase-center antenna (DPCA) 135, 387, 480
 distance measuring equipment (DME) 577
 Distant Early Warning Line (DEW Line) 328
 Distributed Collaborative Adaptive Sensing (DCAS) 632
 distrometers 610–11
 Dog House 304
 Don-2N radar system 305, 306
 Doppler ambiguity/aliasing 213, 218, 220, 225, 226, 664
 Doppler analysis 141
 Doppler beam sharpening (DBS) 132, 246
 Doppler beamwidth 411
 Doppler contours 196
 iso-Doppler contours 196–8
 iso-range contours 198–9
 Doppler dilemma 595, 605
 Doppler effect 17, 18, 28, 141, 569, 592
 Doppler filtering resolution 253
 Doppler frequency 17–18, 209, 218–19, 226, 228, 230, 247, 395, 406, 604, 608, 767, 769, 770, 771, 774
 equation development 603–4
 extracting 208–9
 Doppler-frequency-shift resolution 66
 Doppler navigation 140
 Doppler processing 603
 Doppler dilemma 605
 Doppler-frequency equation development 603–4
 Doppler spectrum 606–8

- maximum unambiguous range and velocity 604
 - range folding and velocity aliasing 609
 - spectrum width 608
 - Doppler processing, motivation for 182
 - co-range mainlobe clutter conditions of 183
 - signal-to-clutter ratio for 184–5
 - Doppler radar 13, 604, 609, 621
 - see also* airborne pulse-Doppler radar
 - Doppler resolution 30, 130, 214, 253, 275, 318, 404, 411, 507–8, 515
 - Doppler sensitivity 64, 68
 - Doppler shift 3, 176, 181–2, 186, 191–3, 196–8, 200, 203, 207, 208, 210, 230, 233, 432, 457, 754–5, 757, 762, 768–9, 771
 - Doppler spectrum 186, 210, 224, 246, 606–8
 - double sideband (DSB) 573
 - downsweep beat frequency 28
 - drop size distributions 606, 610–11, 614
 - dual-beam configuration 562
 - dual Doppler 570, 594, 624–5
 - dual polarization 5, 625
 - correlation coefficient 626–7
 - differential reflectivity 627–9
 - specific differential phase 629–31
 - dual-sensor systems 122
 - Dunay-class battle-management radars 304
 - dwelt time 153, 404, 409, 461
 - dynamic range 35, 348, 520, 555, 567–9, 580
- E**
- E-8C Joint STARS aircraft 154
 - early police radar receiver (detector/mixer) 751
 - early police radar transmitter
 - components 750
 - early warning radars (EWRs) 12, 285, 304–5, 323, 328
 - earth-orbiting satellites, deploying radar on 12
 - effective isotropic radiated power (EIRP) 510, 518, 531, 557, 666, 668
 - effective noise power in post-processing noise bandwidth 488–9
 - electromagnetic compatibility (EMC) 6, 576
 - electromagnetic interference (EMI) 6, 576, 582
 - electromagnetic pulse (EMP)
 - effects 311
 - electro-matic model
 - S1 radar 753
 - S2 police radar 755, 756
 - S-5 X-band police radar system 761–2
 - electronically scanned array 101, 254, 262, 264, 277
 - antenna impacts on MPARS performance 265–8
 - array principles 262–4
 - multiple target tracking considerations in radar control 275–6
 - radar resources and constraints 269–71
 - resource management implementation 271–5
 - electronic attack (EA) 125, 281, 298
 - electronic counter countermeasures (ECCM) 121, 126, 170, 330, 332
 - angle deception 172
 - capabilities 357–9
 - noise jamming 170
 - ECCM against 170–1
 - gated 171–2
 - range and velocity deception 172
 - electronic protection techniques 126, 312
 - electro-optical (EO) system 70, 88, 97, 141
 - electro-optical targeting system (EOTS) 120
 - elevation error 460
 - elevation scan range 485
 - elliptical error probable (EEP) 405
 - elliptical orbits 455–6
 - ELVA-1 millimeter wave (MMW) FMCW radar 38, 55
 - ELVA FMCW radar system 38
 - EM equivalent principle 361
 - emitter-coupled logic pulse generator 714
 - energy-on-target 548, 563–4
 - en route phase of flight 544–5
 - en route radar 553
 - Enterprise Electronics Corporation (EEC) 592
 - Environmental Research Institute of Michigan (ERIM) 474, 644
 - ENVISAT 438
 - ASAR 444, 445, 518
 - equivalent radiated power (ERP) 81, 144, 528
 - ERS-1 438, 443, 445, 446, 518
 - ERS-2 438, 443, 445, 446, 518
 - E-SCAN fire-control radar 132, 147–9
 - AESA radars 147–8
 - E-SCAN-only functionalities 151–4 and M-scan 149
 - modern functionalities not directly related with 154–6
 - new modes enabled by 151
 - PESA radars 147
 - technological aspects 149–50
 - escort jamming 170
 - European Galileo systems 517
 - European Space Agency (ESA)
 - spaceborne SARs 286, 438, 443–6, 518
 - excess range delay 459–60
 - exoatmospheric BMD 292–3, 311–12
 - extended factored algorithm (EFA) 417
 - extended Kalman filter (EKF) 360, 363, 365, 368, 369, 372, 526
 - extratropical storms and stratiform precipitation 615–16
- F**
- false alarm density (FAD) 319, 392, 401, 402, 648
 - false-alarm suppression 272
 - false replies uncorrelated in time (FRUIT) 557
 - fan beam 302, 337, 339, 562, 580
 - Faraday rotation 458, 460
 - far-field sidelobes 263
 - fast Fourier transform (FFT) 30, 210, 213, 608, 662, 673, 775
 - FFT-generated Doppler filter 214
 - fast ramp generator design 720–2
 - FCR tracking and seeker 144
 - feature-level fusion 107
 - Federal Aviation Administration (FAA) 14, 543, 544, 547, 557, 581, 583, 584, 595, 631
 - Federal Communications Commission (FCC) 665, 759
 - ferrite circulator 760
 - ferro-magnetic circulator function 760, 763–4
 - field programmable gate arrays (FPGAs) 342, 556
 - filtering logics 355–6
 - fire-and-forget missile 105, 109, 144
 - fire-control assembly 162
 - fire-control computer (FCC) 136, 137, 166
 - fire-control-quality tracks 282
 - fire-control radar (FCR) 11, 109, 117, 255, 304
 - airborne 123
 - E-SCAN FCR 147–56
 - future of 156–60, 161
 - heads-up displays 142
 - M-SCAN FCR 123–41
 - multifunction displays 141–2
 - weapon modes 142–7
 - “AN” equipment-designation system 172–3
 - electronic counter
 - countermeasures 170
 - against noise jamming 170–1
 - angle deception 172

- fire-control radar (FCR) (*cont.*)
 - gated noise jamming 171–2
 - noise jamming 170
 - range and velocity deception 172
 - functionality 121–2
 - kill chain and 121–2
 - surface-based 160
 - antiaircraft artillery (AAA) 160, 162
 - principles of missile guidance 166–70
 - surface-to-air missile systems 163–5
 - surface-to-surface fire-control radar 165
 - systems 11
 - and weapon systems 117–21
 - fire-finder radar 166
 - first police radar 750, 751, 753–4
 - fixed-parameter filters 355–6
 - flat-earth approximation 179–80, 233, 466–7
 - flexible block adaptive quantizer (FBAQ) 446
 - flight information service-broadcast (FIS-B) 584
 - fluctuation loss 400
 - folded range-Doppler spectrum 220–1, 222, 237
 - foliage-penetrating (FOPEN) radar 6, 14, 635
 - battlefield surveillance radar, history of 637–41
 - clutter characteristics 645–54
 - foliage attenuation 651–4
 - FOLPEN II 644, 645, 647
 - image formation 654–64
 - SAR phase history 658–9
 - M-FOPEN 640–1
 - polarization whitening 678–80
 - radio frequency interference (RFI) 665
 - cancellation of 670–6
 - notched linear FM waveform 668–70
 - transmit waveform design for RFI environment 666–8
 - synthetic aperture radar (SAR) systems 635, 642–5
 - target characterization 680–1
 - target detection processing 677–8
 - target features, four types of 681–4
 - forward edge of battle area (FEBA) 637
 - forward-firing rocket (FFR) 136
 - forward-looking infrared (FLIR) 120
 - forward scatter 502, 507
 - Fourier transform relationship 263
 - free-running dielectric resonant oscillator (FRDRO) 42, 43
 - French AASM 137
 - frequencies, radar 6–8
 - frequency bands 7, 462
 - frequency-division duplex (FDD) 513
 - frequency modulated continuous wave (FMCW) radar 18, 26, 77, 694–5
 - amplitude and phase noise 35–43
 - applications 67
 - area clutter RCS 43–4
 - direct digital chirp synthesizers 62–3
 - equation 27
 - frequency sweep nonlinearity 52–62
 - linear waveform 26–9
 - linear waveform trades 29–31
 - range resolution 44–52
 - signal-to-noise ratio (SNR) estimation 31–5
 - frequency-shift keying (FSK) CW modulation 65, 67
 - frequency sweep nonlinearity 52–62
 - frequency tuning word (FTW) 63
 - full-body imaging systems 109–10
 - full field of view (FFOV) 264, 285, 304
 - functions of radar 8–9
- G**
- GaAs technology 150
 - gain 485
 - gallium nitride (GaN) technology 278
 - gated noise jamming 171–2
 - Gaussian filter 726
 - Gaussian minimum-shift keying (GMSK) modulation 513
 - GBU-31 137
 - geographic synthetic aperture radar system (GeoSAR) 644, 674, 676
 - geoid 432–3
 - German FREYA 327, 328
 - German SAR Programs 450–1, 461, 474
 - German TerraSAR-X 482–4
 - noise 488
 - return power and noise summary 491
 - target, terrain, and noise power 487
 - target return signal power 487
 - terrain return power 487–8
 - TerraSAR-X antenna 484–6
 - TerraSAR-X orbit 483–4
 - ghosting 242, 243
 - global navigation satellite systems 534–6
 - global optimum approach 356
 - global positioning system (GPS) 405, 582
 - Globus II 288
 - GLONASS (GLObalnaya NAvigatsionnaya Sputnikovaya Sistema) 517–18, 534
 - GMTI modes 133, 246, 386
 - GNSS 517–18, 534
 - Goalkeeper System 163
 - Goodyear Aircraft Company 4
 - GPS-guided weapons 137
 - ground-based early warning radar (GBEWR) 323
 - antiballistic missile 359–73
 - azimuth estimation, moving window technique for 352
 - cancellation filter and insertion map 350–1
 - CFAR techniques 351–2
 - commercial systems 330–1
 - denial of bistatic hosting by waveform design 375–6
 - deployable 332
 - distinctive characteristics of 334–5
 - electronic counter-countermeasures (ECCM) capabilities 357–9
 - historical perspective 327–8
 - low probability of intercept (LPI) 373–5
 - mobile 331–2
 - NATO Air Defense Ground Environment (NADGE) 328–9
 - operative frequency 335
 - phased array antenna 335–42
 - platform 330–2
 - requirements for 332–4
 - sidelobes reduction, pulse compression filters for 349–50
 - tracking 352–5
 - correlation logics 356–7
 - filtering logics 355–6
 - scan to scan correlation (SSC) 357
 - transceiver 342–3
 - classic architecture of 344–6
 - modern architecture 346–8
 - parameters 348
 - typical characteristics 329–30
 - waveforms 348–9
 - ground-based midcourse defense (GMD) 297
 - Ground-Based Radar–Prototype (GBR-P) 303
 - ground-based radars 287, 330
 - ground clutter 387, 395, 413, 552
 - ground-moving target indication (GMTI) 12, 133, 227, 383, 481, 637
 - ground-penetrating radar (GPR) 14
 - antennas 706
 - bow-tie antennas 709–11
 - GPR transmitting pulse 708–9
 - applications
 - pipe detection 704
 - rebar imaging 704
 - through-wall imaging and life detection 705–6

- design consideration 697–8
 - center frequency 698
 - sampling interval 700
 - window size 698–700
 - hardware architectures of
 - frequency-modulated CW (FMCW) radar 694–5
 - impulse radar 694
 - stepped frequency CW (SFCW) radar 695–6
 - hardware block diagram
 - antenna selection 701–2
 - communication and synchronization 703
 - digital circuit and analog circuit 703
 - high sampling rates data acquisition 702–3
 - microcontroller 703
 - microprocessor 703
 - post-processing software development 704
 - signal processing 703–4
 - operating principle 692
 - pulsed-GPR system design 696–731
 - receiver design 718
 - delay line 724
 - fast ramp generator 720–2
 - low-pass filter and amplifier 725–30
 - sample and hold circuit 724–5
 - slow ramp signal generator 722–4
 - time-varying gain amplifier 730–1
 - sampling head design 716–18
 - system implementation 731–5, 736
 - system tests
 - air tests 735, 737–9
 - field-test comparison, with different frequencies 736, 740–5
 - transmitter design
 - generating nanosecond pulse, methods of 714–16
 - transmitter pulse width, discussions of 712–14
 - GSM system, for cell phone 513
 - guard antenna 245, 359
 - Gunn device solid-state transmitter 766
 - Gunn diode oscillator 53
 - gust fronts and outflow regions 617
- H**
- hail measurements 612–13
 - HAWK System 164
 - Haystack auxiliary radar 288
 - heads-up display acquisition (HACQ) 131
 - heads-up displays (HUDs) 110, 131, 142
 - air-to-air cannon symbology 146
 - Hellfire missile 109
 - helmet-mounted display (HMD) 155
 - HEN HOUSE BM EWRs 328
 - Hen House frequency-scanned radar system 304–5
 - heterodyne CW radar configuration 25
 - HF (short-wave) broadcasting 516–17
 - HG-9550 radar altimeter 73
 - high mobility multipurpose wheeled vehicle (HMMWV) 70, 168
 - high-power amplifier (HPAs) 206, 225, 271, 572
 - High Power Illuminator Doppler Radar (HIPIR) 164, 165
 - high pulse repetition frequency (HPRF) 121, 124, 127, 176, 227, 228, 348
 - linear frequency modulation ranging 231–4
 - range eclipsing 234–5
 - range-gated 234
 - representative characteristics of 229
 - velocity search 229–31
 - high-range resolution (HRR) 97, 121, 391
 - high-range resolution profiles (HRRP) 44, 141, 409
 - high-speed logic pulse generator 714
 - historical perspective of radar 2–5
 - hitchhiker 499, 500
 - HMMWV AMRAAM Launcher 169
 - homodyne CW radar configuration 24, 25
 - homodyne radar principles 751–3
 - advantages of 753
 - Honeywell 64, 73, 76
 - hook echoes 592, 618
 - horizontal polarization (HH) 439, 485, 628, 646, 650, 651, 760
 - HPRF (high-pulse repetition frequency) waveforms 121, 176, 225, 226, 231, 234, 348–9
 - human machine interface (HMI) 155, 340
 - hurricanes 621–2
 - hydrological measurements 609
 - attenuation from precipitation 613–15
 - hail measurements 612–13
 - rain measurements 610–12
 - snow measurements 613
- I**
- identification of friend or foe (IFF) info 129
 - IF receiving board 346
 - IMM (interactive multiple model) filter 129, 310, 355, 356, 357
 - improved HAWK (I-HAWK) system 164
 - improved pulse acquisition radar (I-PAR) 164
 - impulse radar 694
 - impulse response (IPR) 472
 - inclination 439, 451
 - incremental-length diffraction coefficients (ILDC) 361
 - independent and identically distributed (iid) 403, 424
 - India 306, 439, 461, 591
 - INDRA 3D LANZA 331
 - inertial navigation system (INS) 112, 132–3, 140
 - guided weapons 137
 - inertial navigation unit (INU) data 405
 - infrared search-and-track (IRST) system 120
 - Inmarsat service 518
 - instantaneous band 7, 348, 418
 - instrument flight rules (IFR) 544
 - instrument meteorological conditions (IMC) 544
 - integrated collision warning 110
 - integrated phase noise power 575, 576
 - integrated sidelobe ratio (ISLR) 472, 473
 - Integrated Tactical Warning and Attack Assessment (ITWAA) 285
 - intelligence, surveillance, and reconnaissance 2, 10
 - interacting multiple model (IMM) 129, 310, 360
 - intercontinental ballistic missile (ICBM) 295, 297, 300, 305, 306, 328
 - interference sidelobe suppression (ISLS) 577
 - interferometric synthetic aperture radar - elevation (IFSARE) system 644, 645
 - intermediate frequency (IF) 25, 206
 - international BMD radar deployment 291, 306
 - international frequency allocations for active earth exploration satellites below 100 GHz 462
 - International Telecommunication Union (ITU) 461
 - interrupted FMCW (IFMCW) 42
 - intruder detection and tracking 109
 - inverse fast Fourier transform (IFFT) 662, 673
 - inverse synthetic aperture radar (ISAR) 141
 - iso-Doppler contours 176, 196–8, 221
 - iso-range contours 198–9, 221
 - Israel 306, 439, 474, 477
 - ISR radar systems 12–13
 - Italian COSMO/SkyMed System 450, 461
- J**
- Japanese Earth Resources Satellite (JERS) 446
 - Japanese Spaceborne SARs 446–7

- Japan Resources Observation System Organization (JAROS) 446–7
- JERS-1 438, 446
- jet-engine modulation (JEM) 130
- joint direct attack munition (JDAM) 137
- joint domain optimal (JDO) 417
- Joint Doppler Operational Project (JDOP) 592
- Joint Electronics Type Designation System (JETDS) 9, 172
- Joint Surveillance Targeting Attack Radar System (Joint STARS) 154, 384, 638
- JPDA (joint probabilistic data association) 356
- K**
- Ka-band and utilizes digital signal processing 772–4
- Ka-band radar 88, 104, 773, 774
- Kalman filter (KF) 129, 273, 309, 355, 356, 360, 368, 526
- K-band 7, 88
- frequencies 771–2
- kill chain 121–2, 162, 281, 295, 297
- kill vehicle (KV) 296, 297, 299, 314
- Klein Heidelberg 500
- Ku-band 7, 518
- Kustom Electronics, Inc. 764, 765
- L**
- Lake Kickapoo 81
- Land Warfare Laboratory (LWL) 638, 640
- latitude–longitude–altitude (LLA) 405
- launch-detection satellite (LDS) 295
- L-band 7, 9, 517, 518
- L-band Green Pine multiple-function AESA 306
- “leakage” in signal processing 473
- Lear Astronics and Technology Service Corporation 75, 110
- least common multiple 245
- “leaves” 484
- Lemon technique 617
- level gauge measurement 10
- level-measurement FMCW radars 78, 80
- lighthouse tube 750
- limited field-of-view (LFOV) AESA 303
- linear FMCW waveform 26–9, 55, 81
- trades 29–31
- linear frequency modulation (LFM) 303, 311–12, 390
- modulator 449
- ranging HPRF 231–4
- LNA (low-noise amplifier) 340, 344, 703
- local optimum approach 356
- local oscillator (LO) 23, 344, 751, 752, 757
- LOCKHEED MARTIN AN/TPS-77 332
- LOCKHEED MARTIN FPS-117 331
- longbow MMW radar 109
- long-term duty cycle 270
- low earth orbit (LEO) 432, 517
- regime 287
- synthetic aperture radar 518
- lower probability of intercept (LPI) 23
- low level windshear alert system (LLWAS) 547
- low noise amplifier (LNA) 26, 150
- low-pass filter (LPF) 207, 208, 773
- and amplifier design 725–30
- low-pressure compressor blade 130
- low probability of intercept (LPI) 373–5
- low pulse repetition frequency (LPRF) 176, 227, 246–8
- representative characteristics of 229
- waveforms 349
- M**
- mainbeam 545
- mainlobe clutter (MLC) 185, 224
- co-range 183–4
- signal-to-clutter ratio for 184–5
- Doppler extent 191–3
- Doppler return 186
- range extent 190–1
- Maisel sidelobe blanking 359
- maritime communications 518
- maritime surface-to-surface fire-control systems 165
- Marshall–Palmer distribution 611
- masking signal radiation 376
- master oscillator power amplifier implementation 206
- material-penetrating radar (MPR) 692
- maximum unambiguous range and velocity 604
- mean sea level (MSL) 544
- mean time between critical failures (MTBCF) 581
- mean time to repair (MTTR) 581
- measurements, radar 5–6
- mechanically scanned radars 288–9
- medium pulse repetition frequency (MPRF) 124, 127, 176, 235
- blind-zone charts 237–8
- detection and false alarm 239–42
- examples 236–7
- representative characteristics of 229
- resolving ambiguities 242–5
- sidelobe blanking 245–6
- metal semiconductor field effect transistor (MESFET) 341
- metrics 400
- area coverage rate 404
- false alarm density 401–2
- minimum detectable velocity 403–4
- parameter estimation accuracy 405
- probability of detection 400–1
- signal-to-interference-plus-noise ratio loss 402–3
- M-FOPEN man-transportable radar 640
- microburst phenomena 547
- microcontroller 703
- micro-Doppler information 515
- microprocessor 703
- microwave hardware technology 759
- midrange munition (MRM) 109
- millimeter wave (MMW) radar 10–11, 87, 288
- for advanced imaging technology 97–8
- advantage of 87
- antenna beamwidth considerations 93–4
- applications for 88, 108
- active protection system (APS) 111
- atmospheric sensing 111
- automated landing guidance (ALG) 110–11
- automotive MMW radar 110
- combat identification systems 112
- full-body imaging systems 109–10
- intruder detection and tracking 109
- obstacle avoidance (OA) system 111–12
- terrain following (TF) system 111–12
- weapons 108–9
- wireless communications systems 112
- comparison with other systems 97
- disadvantage of 88
- FMCW radar 55
- future trends 112
- performance limitations 94–8
- propagation at higher frequency 89
- atmosphere 90–1
- target RCS characteristics 91–2
- terrain patches 93
- smart weapon configurations 98
- components 101–4
- multispectral implementations 106–7
- seeker spectra and modes 105–6
- typical waveforms 107–8
- spectrum 88–9
- millimeter wave integrated circuit (MMIC) 104, 112–13
- Millstone Hill radar 288
- minimum detectable velocity (MDV) 392, 637
- minimum discernable signal (MDS) level 568
- minimum received signal power 203

- minimum variance distortionless response (MVDR) 397
 - missile defense agency (MDA) 299
 - missile guidance
 - modes 167–70
 - principles of 166
 - surface-to-air missile (SAM) 166–7
 - missiles
 - with electromagnetic seekers 143
 - with passive infrared seeker 143
 - missile-seeker design 76
 - missile warning (MW) sensors 288
 - MISTRAL 71
 - mobile GBEWR 331–2, 334
 - mobile ground surveillance radar system (MGSRS) 70
 - mobile radar systems 624
 - modern multifunction phased array radar systems (MPARS) 257
 - mode-S/automatic dependent surveillance broadcast (ADS-B) receiver 524
 - modulation bandwidth 26
 - decreasing 29
 - modulation period, decreasing 29
 - monopulse difference channels 264
 - monostatic radar 5, 90, 499
 - moving-mode police radar operation 766–7
 - clutter-referenced patrol car speed determination 767–70
 - moving object detection experiment (MODEX) 386
 - moving radar with improved detection range capability 764
 - Gunn device solid-state transmitter 766
 - turnstile junction duplexer 764–6
 - moving target detection (MTD) 449, 555
 - filter 330
 - moving target indication (MTI) 8, 175, 555, 651
 - filter 330, 350
 - gain 560
 - pulse cancellation filters 560
 - moving window technique, for azimuth estimation 352
 - MRCS403 336
 - M-SCAN fire-control radar 123–5
 - air-to-air modes 125–31
 - air-to-ground modes 131–40
 - air-to-sea modes 140–1
 - MSSC 68, 70
 - Multi-Channel Airborne Radar
 - Measurements (MCARM) 397
 - multifunction displays (MFDs) 141–2, 155, 159
 - multifunction phased array radar systems (MPARS) 11, 14, 251, 583, 631–2
 - electronically scanned array (ESA) 262
 - antenna impacts 265–8
 - array principles 262–4
 - multiple target tracking considerations 275–6
 - radar resources and constraints 269–71
 - resource management implementation 271–5
 - modern MPARSs 257
 - netcentric applications 281–2
 - operational concepts and military utilities 254–7
 - organization 253–4
 - sizing and performance evaluation 257
 - search sizing 259–61
 - track sizing 261–2
 - technologies 276–80
 - testing and evaluation 280–1
 - multifunction sensor 159
 - multifunction systems 121
 - Multi-Platform Radar Technology Insertion Program (MP-RTIP) 384–5
 - multiple false-target generation 172
 - multiple frequency (MF) technique 65, 580
 - multiple hypothesis tracking (MHT) 356, 357
 - multiple independent scanning (MIS)
 - beam technique 337, 339–40
 - multiple launch rocket system (MLRS) 109
 - multiple model (MM) approaches 368
 - multiple radar modes 105
 - multiplicative noise ratio (MNR) 472, 473
 - multiscan correlation 356
 - Multi Spectral Response Simulation (MRSIM) 92
 - multispectral seeker 105, 107
 - multistatic radar 6, 499
 - multitarget tracking issues 129
 - multitrip echoes 609
 - Muni-Quip Industries 763
- N**
- nanosecond pulse, generating 714–16
 - narrowband passive bistatic radar 500
 - National Airspace System (NAS) 544
 - National Space Development Agency of Japan (NASDA) project 446
 - National Telecommunications and Information Administration (NTIA) 665, 666
 - National Weather Radar Testbed (NWRT) 632
 - National Weather Service (NWS) 579, 592
 - NATO Airborne Early Warning (NAEW) aircrafts 329
 - NATO Air Defense Ground Environment (NADGE) 328–9
 - Naval Space Surveillance (NAVSPASUR) 287
 - NavCom Defense Electronics, Inc. 73
 - nearest neighbor (NN) 356
 - Next-Generation Air Transportation System (NextGen) 582
 - next generation radar (NEXRAD) 547, 593, 594, 595–6
 - next-generation S-band radar 755–8
 - Neyman-Pearson criterion 565, 566
 - NLFM (nonlinear frequency modulation) code 349, 565, 566
 - node 452
 - node line 452, 454
 - noise 31, 488
 - noise-equivalent sigma zero (NESZ) 489, 490
 - noise figure (NF) 78, 94, 113, 348, 527
 - noise jamming 170
 - ECCM against 170–1
 - gated 171–2
 - nonadaptive displaced phase-center antenna 413–15
 - nonadaptive Doppler processing 410–13
 - noncoherent pulsed radar systems 3, 185
 - noncooperative bistatic radar 5
 - noncooperative target recognition (NCTR) 125, 130
 - nonlinearities in frequency sweep 44, 47, 52, 54, 57, 61, 108
 - nonrecursive cancellers: *see* moving target indication (MTI), pulse cancellation filters
 - normalized time 362, 365, 366
 - North Atlantic Treaty Organization (NATO) 386
 - north-east-down (NED) 405
 - North Warning System 328
 - notched linear FM waveform 668–70
 - notch filtering 225, 393, 560
 - N-pulse MTI cancellers 560
 - nuclear blackout 308
 - Nyquist frequency 604
- O**
- observable phase change 480
 - observation geometry nomenclature 463, 464
 - obstacle avoidance (OA) system 111–12
 - and aircraft landing 74–6
 - offset aim-point bombing 137–8
 - operational loss factor 258
 - operative band 348

- orbits 451
 - circular orbits 452–4
 - elliptical orbits 455–6
 - target Doppler shift 457
- orthogonal frequency division
 - multiple access (OFDMA) modulation 516
- orthogonal frequency division multiplexing (OFDM) 514, 516
- over-the-horizon (OTH) radar system 23, 328
- over-the-horizon backscatter (OTHB) radar 328
- over-the-horizon radar (OTHR) systems 80–1, 301
- P**
- P-3 UWB SAR system 644, 649, 668, 671, 674, 678
- PAGE 71, 72
 - Air Surveillance FMCW 72
- PALSAR (phased array type L-band SAR) 446, 447, 449
- passive beam 545
- passive bistatic radar (PBR) 13, 499, 521
 - applications 502
 - examples of systems 529–36
 - historical perspective 500–1
 - performance prediction 527
 - signal environment 519
 - direct signal interference 519–20
 - direct signal suppression 520–1
 - processing 521–2
 - range-Doppler plots 522–4
 - tracking 525–6
 - triangulation 524–5
 - waveforms 509
 - analog TV 510–12
 - cell phone 513–14
 - digital radio/TV 512–13
 - HF broadcasting 516–17
 - spaceborne illuminators 517–18
 - VHF FM 510
 - WiFi and WiMAX 514–16
- passive electronically scanned antenna (PESA) radar 147–8, 149
- Patriot Track-via-Missile TVM Tracking 169
- patrol-speed sliding filter 769
- PAVE Phased Array Warning System (PAVE PAWS) 286, 302, 304, 308, 328
- PDA (probabilistic data association) 356
- peak sidelobe ratio (PSLR) 472, 473
- Pechora-class Large Phased Array Radars 304
- pencil beam 337, 338
- penetrator munition 99
- periapsis 452
- perigee 452
- Perimeter Acquisition Radar (PAR) 300
- Perimeter Acquisition Radar Characterization System (PARCS) 286, 302
- Phalanx 162
- phase alternating line (PAL) modulation format 511
- phase and amplitude adjustment modules (PAAMs) 340, 341, 342
- phased array antenna 264, 335
 - 3-D beam-scanning techniques 336–40
 - architecture 340–1
 - radiating network technology 342
 - transmit-receive module 341–2
- phased array radar 4, 11, 12, 304
 - multifunction: *see* multifunction phased array radar systems (MPARS)
- phased array radar systems (PARSs) 275
- Phased Array Type L-band Synthetic Aperture Radar (PALSAR) 446–7
- phase-locked dielectric resonant oscillator (PLDRO) 43
- phase-locked loop signal-processing approach 770–1
- phase-modulated CW radar 64
- phase modulated noise levels 35–43
- phase modulation 63
- phase noise 570
- phase noise correlation factor 37, 38
- phase-only modulation 63
- phase stability affecting cancellation 348
- physical theory of diffraction (PTD) 361
- PILOT radar system 31, 32, 38–9, 41, 43, 45, 68, 69, 70
- plan position indicator (PPI) 615
- pixel-level fusion 107
- Plextek 70
- pointing error versus frequency 486
- point spread function (PSF) 472
- polarization 485, 663
 - dual 625–31
 - whitening 678–80
- polar orbit 452
- police radar 749
 - alternative phase-locked loop signal-processing approach 770
 - characteristics of 750
 - cosine error caused by improper operation 754–5
 - DSP 774–5
 - ferro-magnetic circulator function 763–4
 - first police radar 753–4
 - homodyne radar principles 751–3
 - Ka-band and utilizes digital signal processing 772–4
- K-band frequencies 771–2
- moving-mode police radar operation 766–7
- moving radar with improved detection range capability 764
- next-generation S-band radar 755–8
- technologies, history of 750
- X-band 758
- postdetection integration (PDI) 391, 401
- power density 510
- preamplifier circuit 717
- precision guided munition (PGM) 98
- precision standoff weapons 137
- precision track 296
- precision velocity update 140
- primary surveillance radar (PSR) 545, 552–6
 - design issues for 558
 - clutter and clutter processing 566–7
 - dynamic range 567–9
 - energy-on-target 563–4
 - radar antenna aperture 562–3
 - radar system stability 569–77
 - radar transmitter
 - considerations 561–2
 - waveform design 565–6
 - for weather radar detection 579–81
- printed circuit board (PCB) 575
- probability density function (PDF) 564
- probability of detection 239, 241, 392, 400–1
- prograde orbit 452
- ProSensing Inc. 78
- pulsed ground-penetrating radar (GPR) system design 696–731
- pulse-Doppler radar: *see* airborne pulse-Doppler radar
- pulse-Doppler waveform 11, 175
- pulse generator using high-speed gates 714
- pulse-limited altimeters 433
- pulse-pair processing 607
- pulse repetition frequency (PRF) 124, 175, 218, 260, 432
- pulse repetition interval (PRI) 242, 244, 245, 390
- purple haze 609
- Q**
- quadrature amplitude modulation (QAM) mapping 517
- R**
- radar absorbing material (RAM) 520
- radar altimeters 432–3
- radar antenna aperture 562–3
- radar control program 269, 272
- radar cross section (RCS) 307, 324, 360–1, 386, 647, 677

- radar forward air controller beacon (RABFAC) 138, 139
 - radar imaging 8
 - radar line of sight (RLOS) 295
 - radar-offset aim point 137
 - “radar-on-a-chip” technologies 279
 - radar-range equation, for weather radar
 - characteristics of precipitation 598
 - final form 602–3
 - nature of weather-radar measurements 598
 - raindrop-scattering cross sections 601–2
 - reflectivity factor 602
 - volume scattering 599–600
 - RADARSAT-1 386, 438, 447–8
 - RADARSAT-2 386, 438, 449
 - radar signal processing (RSP) 555
 - radar stability 560
 - radar system stability 569–77
 - radar target detection 564, 754
 - radar-to-scatterer range 182, 208
 - radar transmitter considerations 561–2
 - radial velocity 182
 - radiated power 73, 486
 - radiating network technology 342, 343
 - radio frequency (RF) aperture 310–11
 - radio frequency interference (RFI) 386, 665
 - cancellation of 670
 - adaptive RFI removal 674–6
 - deramp RFI removal 671–4
 - notched linear FM waveform 668–70
 - transmit waveform design for the RFI environment 666–8
 - radiometric calibration 461
 - radome material 101, 102
 - raid assessment 130
 - rain attenuation 460
 - rain measurements 610
 - drop size distributions 610–11
 - radar reflectivity and rainfall rate 611–12
 - ram air turbine (RAT) 130
 - RAN 40 L 336
 - range ambiguity 217–18
 - range and azimuth gates (RAGs) 562
 - range and velocity deception 172
 - range blind zones 223
 - range-Doppler coupling 48
 - range-Doppler map (RDM) 215–16, 391
 - range-Doppler plots 522–4
 - range-Doppler spectrum, folding of 220, 221
 - “range-Doppler” coupling 28
 - range folding and velocity aliasing 609
 - range gate pull-off (RGPO) 172
 - range height indicator (RHI) plot 615
 - range instrumentation radar (RIR) 545
 - range migration algorithm (RMA) 659–60, 677
 - range only radar (ROR) 164
 - range resolution 44–52, 253
 - range while search (RWS) mode 126, 128, 231
 - RAT31DL 336
 - RAT31SL 336
 - Rayleigh approximation 601
 - Rayleigh scattering 89–90
 - RBS70 71
 - Reagan, Ronald 301
 - real-beam ground mapping (RBGM) 132
 - receiver operating characteristic (ROC) curve 400, 565
 - recognition, defined 9
 - reduced-dimension STAP (RD-STAP) 416
 - Reed-Mallett-Brennan rule 403
 - reentry vehicles (RVs) 285, 292
 - reflected-power canceller (RPC) 38–9
 - reflectivity factor 602
 - reflex klystron 751, 763
 - refraction 460
 - remotely piloted vehicle (RPV) 635
 - remote maintenance monitoring subsystem (RMMS) 581
 - remote monitoring subsystem (RMS) 576, 581
 - resident space objects (RSOs) 287
 - resonant scatter 507
 - retransmission homing guidance 169–70
 - retrograde orbit 452
 - return power and noise summary 491
 - RISAT-1 439
 - RISAT-2 439, 461
 - Rockwell Collins weather radar 597
 - roost rings 623
 - root mean square (RMS) error 392, 572
 - round-trip propagation time 27
 - Russian BMD radar deployment 304–6
- S**
- Saab Bofors Dynamics RBS-15 76
 - Saab TankRadar 78
 - Sallen–Key LPF circuit 727
 - sample-and-hold circuit design 724–5
 - sample matrix inversion (SMI) 412, 416
 - sampling bridge circuit 717
 - SAR ambiguities and associated trade-offs 464
 - aperture height 464–8
 - block adaptive quantization (BAQ) 471–2
 - Doppler (azimuth) ambiguities and PRF selection 468–70
 - minimum aperture area requirement for SAR 470–1
 - PRF selection 464–8
 - range ambiguities 464–8
 - SAR image quality metrics 472–3
 - SAR/GMTI 133, 134, 135
 - SAR-Lupe 450–1
 - satellite television (DBS TV) transmissions 518
 - S-band Missile Site Radar (MSR) 300
 - scanSAR 476–7
 - scan to scan correlation (SSC) 357
 - scattered radiation 519
 - scatterometers 432, 433–4
 - SCOUT radar 68–70
 - Sea-Based X-Band (SBX) radar system 286, 303
 - search radar 162, 559
 - search while track (SWT) 151–3, 257
 - Seasat mission 438, 439
 - Sea Sparrow semi-active guidance 168
 - secondary surveillance radar (SSR) 545, 556–8
 - design issues 577
 - link calculation 578–9
 - seeker-only area 144
 - seekers and active protection system sensors 76
 - Selex ES RAT 31DL/M 331–2
 - Selex EX RAT 31 DL 330–1
 - SELEX Sistemi Integrati sensors 336
 - self-ambiguity function 508
 - self-protection jamming 170
 - semi-active homing guidance 167
 - sense and destroy armor (SADARM) 109
 - sensitivity time control (STC) 35, 330, 553, 569
 - sensor fusion, levels of 106
 - Service Life Extension Program (SLEP) 546
 - Sherwood Forest 644
 - short-wave infrared (SWIR) 285
 - shuttle imaging radar (SIR) missions 438
 - SIR-A 439
 - SIR-B 439
 - Shuttle Radar Topography Mission (SRTM) 438, 478
 - sidelobe blanking (SLB) 245–6, 358–9
 - side lobe canceller 170
 - sidelobe clutter 562
 - Doppler extent 187–90
 - Doppler spectrum 185
 - range extent 186–97
 - sidelobes reduction, pulse compression filters for 349–50
 - sidelobe suppression 124
 - side-looking array radar (SLAR) 637, 638
 - SiGe technology 150

- signal models 393–5
 interference 399
 space–time snapshot 399–400
 surface clutter 395–8
 targets 398–9
 signal-to-clutter ratio (SCR) 185, 317
 signal-to-distortion noise ratio (SDNR) 472
 signal-to-interference-plus-noise ratio (SINR) 384
 Signal to Jamming Ratio 171
 signal-to-noise ratio (SNR) 31–5, 94, 409, 432, 666
 “Singer” target model 128–9
 single-antenna CW radar configuration 24
 single integrated air picture (SIAP) 282
 single sensor but dual-function system 121–2
 single sideband (SSB) 573
 power density 570
 single spectral seeker 105
 single-target tracking (STT) radars 130, 143, 276
 SIR-C/X-SAR (1994) 443, 444
 slow-moving targets, detection of 134–5
 slow ramp signal generator design 722–4
 small area ground (SAG) 383, 391
 smart weapon configurations 98
 components 101–4
 multispectral implementations 106–7
 seeker spectra and modes 105–6
 typical waveforms 107–8
 snow measurements 613
 solid-state high-power amplifier (HPAs) 271
 space-based SAR for remote sensing 431
 German TerraSAR-X 482–4
 historical perspective 438–9
 orbits 451
 radar altimeters 432–3
 SAR waveform 491–3
 scatterometers 433–4
 spaceborne SARs 431–2
 special modes and capabilities 473
 spaceborne illuminators 517
 DBS TV 518
 global navigation satellite systems (GNSS) 517–18
 low-earth orbit synthetic aperture radar 518
 maritime communications 518
 spaceborne SAR 12, 431–2, 439, 457
 Canadian 447–9
 European Space Agency 443–6
 Japanese 446–7
 observable characteristics 461–3
 observation geometry nomenclature 463
 propagation phenomena 458–60
 radar frequency selection 460–1
 SAR ambiguities and associated trade-offs 464
 U.S. 439, 443
 Space Fence radar systems 81
 Space Shuttle Challenger 439
 Space Shuttle Endeavour 443
 space situational awareness (SSA) 287, 288, 289
 space-surface bistatic synthetic aperture radar (SS-BSAR) 534
 Space Surveillance Network (SSN) 287
 space–time adaptive processing (STAP) 4, 122, 135, 156–8, 383, 415–18, 481
 specialized applications 2, 13
 spectral band replication (SBR) 516
 spectrum width 608
 specular scattering 507
 spherical earth 464–5
 approximation 180–1
 spongy hail 612
 spurious free dynamic range (SFDR) 348
 SPY-1 10
 squall lines 621
 squawk codes 545
 SQUIRE radar 69, 70, 71
 SSR link calculation 578–9
 in MATLAB® 578
 stable local oscillator (STALO) 206, 207, 344, 571
 Stalker Ka-band police radar 773
 Standard NATO Agreement (STANAG) 386
 stand-off target acquisition system (SOTAS) 637, 638
 STARSTREAK 71
 stationary mode of operation 753
 stepped frequency continuous wave (SFCW) radar 695–6
 STINGER 71
 strip map mode 469
 subclutter visibility (SCV) 552, 560, 565
 Sugar Tree 501
 sun echoes and roost rings 623
 sun-synchronous orbit 443, 454
 dawn–dusk orbit 454
 dawn-to-dusk 454
 supercells 617
 thunderstorms and 617
 surface-based fire-control radar 160
 antiaircraft artillery (AAA) 160, 162
 missile guidance modes 167–70
 surface-to-air missile (SAM) 166–7
 surface-to-air missile systems 163–5
 surface-to-surface fire-control radar 165–6
 surface-based radar system 3, 275
 surface moving target indication (SMTI) 12, 383
 angle and Doppler estimation 421–3
 antenna and waveform considerations 405
 bistatic and multistatic configurations 425
 clutter-mitigation approaches 410–15
 detection processing 418–21
 dismount detection 425–6
 heterogeneous clutter 424
 key points 387–8
 metrics 400
 area coverage rate 404
 false alarm density 401–2
 minimum detectable velocity 403–4
 parameter estimation accuracy 405
 probability of detection 400–1
 signal-to-interference-plus-noise ratio loss 402–3
 radar operation 390–3
 SAR-GMTI 424–5
 signal models 393–5
 interference 399
 space–time snapshot 399–400
 surface clutter 395–8
 targets 398–9
 surface reflection wave 694
 surface-to-air missile (SAM) 166–7
 surveillance radar 8
 surveillance systems 68–73
 synchronous detection 207–8
 synthetic aperture radar (SAR) 3–4, 92, 132, 227, 385, 431
 FOPEN 635, 642–5
 satellite and radar characteristics 441–2
 timeline of 440
 synthetic array time and post-processing noise bandwidth 488
 synthetic pulse radar: *see* Stepped frequency continuous wave (SFCW) radar
 system automation 155
 system control processor (SCP) 774
 system loss factor 258
 system phase error 570, 571
- T**
 tactical radar systems 2, 10–12
 TanDEM-X 438, 451, 461
 tank extended range munition (TERM) 109
 target, terrain, and noise power 487
 target Doppler shift 457

- target fading 390, 398
 - target object map (TOM) 296
 - Target Resolution and Discrimination Experiment (TRADEX) 288
 - target return signal power 487
 - targets directions of arrival (TDoA) 375
 - target tracking 127, 128, 153
 - TecSAR 439, 461
 - terminal Doppler weather radar (TDWR) 547, 596–7
 - Terminal High Altitude Area Defense (THAAD) radar 11, 253, 287, 297, 304
 - terminal phase, of flight 544
 - terminal radar 545, 546, 553
 - terminal radar approach control (TRACON) 545
 - terrain avoidance (TA) 138–9
 - terrain following (TF) system 111–12, 139–40
 - terrain observation by progressive scan (TOPS) 477
 - terrain patches 93
 - terrain return power 487–8
 - TerraSAR-X 438, 451, 461, 482–3, 485
 - antenna 484–6
 - orbit 483–4
 - Thales Naval Nederland 71, 73
 - AHV-2100 73, 74
 - AHV-2500 74, 75
 - AHV-2900 74, 75
 - THALES RAYTHEON SYSTEM MASTER-M 332
 - THALES RAYTHEON SYSTEMS GROUND MASTER 400 331
 - theater ballistic missile defense (TBMD) 295, 299, 301, 329
 - theater ballistic missiles (TBMs) 301, 306
 - threat complex 292, 313
 - thunderstorms, detection and tracking of 617
 - time-division duplex (TDD) 513
 - time-division multiple access (TDMA) 513, 514
 - timeline occupancy 269–70
 - time-varying gain amplifier design 730–1
 - tornadoes 618
 - debris balls 620–1
 - hook echoes 618
 - velocity couplets 618–20
 - tornado vortex signature (TVS) 620, 621
 - total electron content (TEC) 458, 459
 - TPQ-53 10
 - track designation 129–30
 - track during scan (TDS) 255, 256, 273
 - track files 129–30
 - tracking 8, 352–5
 - correlation logics 356–7
 - and discrimination processes 309–10
 - filtering logics 355–6
 - scan to scan correlation (SSC) 357
 - tracking gate 127–8
 - track prediction performance, for BMD sensors 313–16
 - track via missile (TVM) 169, 170
 - track while scan (TWS) 9, 127–8, 255, 276, 561
 - Traffic Alert and Collision Avoidance System (TCAS) 557
 - traffic information service-broadcast (TIS-B) 584
 - transceiver 104, 342–3
 - classic 344–6
 - modern 346–8
 - parameters 348
 - transmit-and-receive module (TRM) 149, 150
 - transmit-receive module (TRM) 341–2
 - transmitter pulse width, GPR 712–14
 - transmit waveform design, for RFI environment 666–8
 - traveling wave tube (TWT) 124
 - Tropical Rainfall Measuring Mission (TRMM) 461
 - true anomaly 452
 - tube-based transmitters 94
 - turnstile junction duplexer 764–6
 - two-dimensional (2-D) bistatic radar 522–3
- U**
- ultrahigh frequency (UHF) 638, 642, 643, 655, 668
 - ultrawideband (UWB) 707, 711
 - uncontrolled airspace 544
 - Universal Mobile Telecommunication System (UMTS) 513–14
 - unmanned aerial system (UAS) 383
 - unmanned aerial vehicle (UAV) 11
 - unmodulated CW radar system 18, 26
 - upsweep beat frequency 28
 - U.S. AN/CPS-6 327, 328
 - U.S. BMD radar deployment 301–4
 - U.S. CXAM 327, 328
 - U.S. military radar nomenclature 9–10
 - U.S. SCR-270 327, 328
 - U.S. spaceborne SARs 439, 443
- V**
- VA-203B reflex klystron 751
 - Vaisala WRK-200 system 596
 - variable-weights filter 355
 - Vega Controls Ltd. 78
 - Vehicle and Dismount Exploitation Radar (VADER) 385
 - vehicle radar cross section at 10 GHz 758–9
 - velocity aliasing 609
 - velocity ambiguity 218–19
 - velocity blind zones 224–6
 - velocity couplets 618–20
 - velocity gate pull-off (VGPO) 172
 - velocity search (VS) 126
 - HPRF mode 229–31
 - vernal equinox direction 452
 - vertical acquisition (VACQ) 131
 - vertical polarization (VV) 485, 646
 - very high frequency (VHF) 638, 640, 642, 643, 652, 655, 668
 - VHF FM 510, 527–9
 - visual flight rules (VFR) 544
 - voltage-controlled oscillators (VCOs) 19, 53, 770
 - volume coverage pattern (VCP) 598
 - volumetric clutter 43, 292, 313, 317, 318
 - Voronezh radars 305
- W**
- Walsh–Hadamard coding 513
 - Warsaw-based Prezemyslowy Instytut Telekomunikacji 72
 - waveforms 107–108
 - antenna and 409–10
 - design 565–6
 - for GBEWs 348–9
 - passive bistatic radar (PBR) 509
 - analog TV 510–12
 - cell phone 513–14
 - digital radio/TV 512–13
 - HF broadcasting 516–17
 - spaceborne illuminators 517–18
 - pulse Doppler 11, 176, 204–5
 - W-band sawtooth FMCW prototype radar 75
 - weapon modes 142
 - air-to-air missile modes 142–5
 - air-to-ground missile mode 146
 - air-to-sea missile mode 146–7
 - cannon mode 146
 - weapon-quality track (WQT) 152, 153
 - weapons system 117
 - weather radar
 - advanced processing and systems 623–32
 - applications of 593–4
 - aviation radars 597
 - bow echoes, squall lines, and derechos 621
 - CASA and DCAS concepts 632
 - commercial concerns 596
 - current innovations 594
 - Doppler processing 603–9
 - dual Doppler 624–5

- weather radar (*cont.*)
 - dual polarization 625–31
 - extratropical storms and stratiform precipitation 615–16
 - hardware 595–7
 - history of 591–3
 - hurricanes 621–2
 - hydrological measurements 609
 - attenuation from precipitation 613–15
 - hail measurements 612–13
 - rain measurements 610–12
 - snow measurements 613
 - mobile radar systems 624
 - Multifunction Phased Array Radar (MPAR) 631–2
 - NEXRAD 595–6
 - radar-range equation for
 - characteristics of precipitation 598
 - final form 602–3
 - nature of weather-radar measurements 598
 - raindrop-scattering cross sections 601–2
 - reflectivity factor 602
 - volume scattering 599–600
 - sun echoes and roost rings 623
 - terminal Doppler weather radar (TDWR) 596–7
 - thunderstorms and supercells
 - bounded weak echo region (BWER) 617
 - gust fronts and outflow regions 617
 - tornadoes
 - debris balls 620–1
 - hook echoes 618
 - velocity couplets 618–20
 - weather sensing 78–80
 - weather systems processor (WSP) 547
 - W-FMCW 111
 - wide acquisition (WACQ) 130
 - wide area search (WAS) 133, 134, 135, 383, 391
 - wideband CDMA (WCDMA) 513
 - wideband PBR 500
 - WiFi 514–16, 531–4
 - Wiley, Carl 4
 - WiMAX 514–16, 531–4
 - wireless communications
 - systems 112
 - World Geodetic System (WGS)
 - standards 405
 - World War II, radar development during 2–3
 - WSR-57 radars 592, 593
 - WSR-88Ds 547, 584, 595
- X**
- X-band 7, 8, 9, 253, 461, 758
 - electro-matic's shift to 761–2
 - fire-control radars 14
 - microwave technology 759–60
 - vehicle radar cross section at 10 GHz 758–9
- Z**
- zero-centered spectrums 776
 - zero Doppler 22, 224–5
 - zero-Doppler direction 470, 493
 - zero-padding technique 50

Fundamental Relations and Terminology

Major Forms of the Radar Range Equation

Peak power form, single pulse	$SNR = \frac{P_t G_t G_r \lambda^2 \sigma}{(4\pi)^3 k T_0 B F L_s R^4}$		
Search form:	$\frac{P_{avg} A_e}{L_s T_0 F} \geq SNR_{min} 4\pi k \left(\frac{R^4}{\sigma}\right) \left(\frac{\Omega}{T_{fs}}\right)$		
Track form:	$\frac{P_{avg} A_e^3 k_m^2}{\lambda^4 L_s T_0 F} = \left(\frac{\pi^2}{2}\right) \left(\frac{k r N_t R^4}{\sigma \cdot \sigma_\theta^2}\right) \left(\frac{1}{\cos^5(\theta_{scan})}\right)$		
Definition of Terms:			
SNR	Signal-to-noise ratio	B	Receiver bandwidth
SNR_{min}	Minimum detectable SNR	L_s	System losses
P_t	Peak transmitted power	F	Noise figure
P_{avg}	Average transmitted power	k	Boltzmann's constant
G_t	Transmit antenna gain	Ω	Search area solid angle
G_r	Receive antenna gain	T_{fs}	Frame search time
A_e	Effective aperture	k_m	Track measurement error slope
λ	Wavelength	r	Track measurement rate
σ	Target radar cross section	N_t	Number of targets
R	Range to target	σ_θ	Track angle estimate precision (std. dev.)
T_0	Standard temperature (270 K)	θ_{scan}	Scan angle, electronically-scanned array

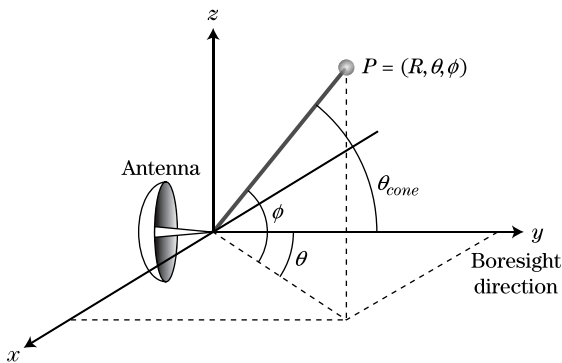
Radar Bands

Band	Frequency Range	ITU Radar Frequency
High frequency (HF)	3–30 MHz	
Very high frequency (VHF)	30–300 MHz	138–144 MHz 216–225 MHz
Ultra high frequency (UHF)	300 MHz–1 GHz	420–450 MHz 890–942 MHz
L	1–2 GHz	1.215–1.400 GHz
S	2–4 GHz	2.3–2.5 GHz 2.7–3.7 GHz
C	4–8 GHz	5.250–5.925 GHz
X	8–12 GHz	8.500–10.680 GHz
Ku (“under” K-band)	12–18 GHz	13.4–14.0 GHz 15.7–17.7 GHz
K	18–27 GHz	24.05–24.25 GHz 24.65–24.75 GHz
Ka (“above” K-band)	27–40 GHz	33.4–36.0 GHz
V	40–75 GHz	59.0–64.0 GHz
W	75–110 GHz	76.0–81.0 GHz 92.0–100.0 GHz
mm	100–300 GHz	126.0–142.0 GHz 144.0–149.0 GHz 231.0–235.0 GHz 238.0–248.0 GHz

Time Delay

A time delay of is approximately equivalent to a range of ...
1 nanosecond (ns)	0.15 meters (m)
	15 centimeters (cm)
	0.5 feet (ft)
	6 inches (in)
1 microsecond (μs)	0.15 km
	150 meters (m)
	0.1 (0.093) miles
	500 (492) feet (ft)

Definition of Azimuth, Elevation, and Cone Angles



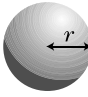
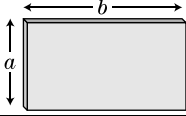
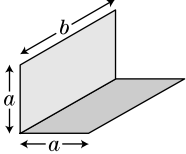
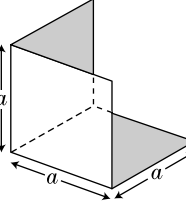
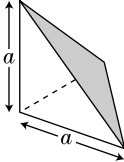
Antenna Directivity, Gain, and Beamwidth

Maximum Directivity D_{max} and Gain G
$D_{max} \approx \begin{cases} \frac{4\pi}{\theta_3 \phi_3} \alpha^2, & \theta_3, \phi_3 \text{ in radians} \\ \frac{129,600}{\pi^2 \theta_3 \phi_3} \alpha^2, & \theta_3, \phi_3 \text{ in degrees} \end{cases}$
Gain G (dB) = D_{max} (dB) – antenna losses (dB)
3 dB Beamwidth θ_3
$\theta_3 \approx \begin{cases} \frac{\alpha \lambda}{D} \text{ radians} \\ \frac{180 \alpha \lambda}{\pi D} \text{ degrees} \end{cases}$
D = aperture size
α = aperture factor
θ_3, ϕ_3 = azimuth and elevation 3 dB beamwidths

Peak Sidelobe Level, dB	Aperture Factor α
–13	0.88
–12	0.98
–25	1.05
–30	1.12
–35	1.18
–40	1.25
–45	1.30

Radar Phenomenology

Maximum RCS of Simple Shapes, $\lambda \ll \text{Object Size}$

Shape		RCS
Sphere, radius r		πr^2
Flat plate, edge lengths a and b		$4\pi(ab)^2/\lambda^2$
Dihedral, edge lengths a and b		$8\pi(ab)^2/\lambda^2$
Trihedral, square sides, edge length a		$12\pi a^4/\lambda^2$
Trihedral, triangular sides, edge length a		$4\pi a^4/3\lambda^2$

Swerling Models

Probability Density Function of RCS σ	Decorrelation	
	Scan-to-Scan	Pulse-to-Pulse
Exponential, $p_\sigma(\sigma) = \frac{1}{\bar{\sigma}} \exp\left[-\frac{\sigma}{\bar{\sigma}}\right]$	Case 1	Case 2
Chi-square, degree 4, $p(\sigma) = \frac{4\sigma}{\bar{\sigma}^2} \exp\left[-\frac{2\sigma}{\bar{\sigma}}\right]$	Case 3	Case 4

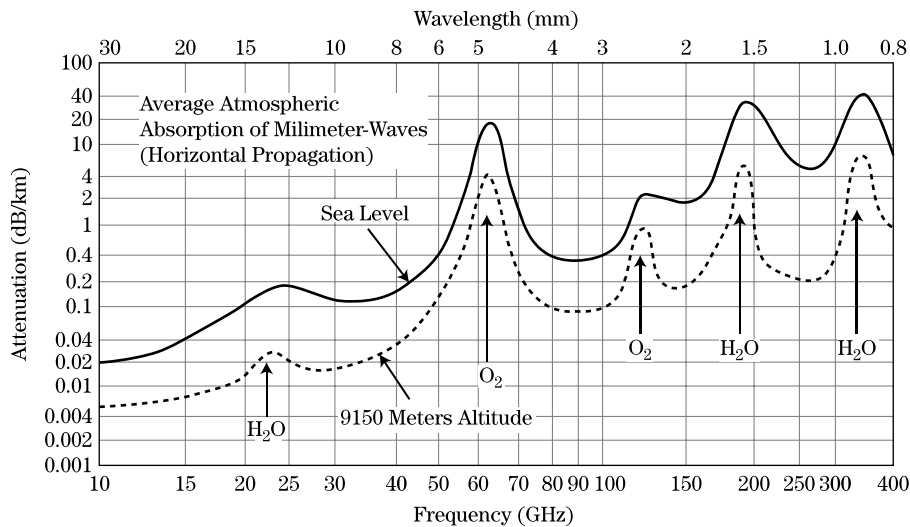
RCS Decorrelation

Variable	Required Change	Comment
Aspect angle (rad)	$\frac{c}{2Lf} = \frac{\lambda}{2L}$	L = width as viewed along radar line of sight
Frequency (Hz)	$\frac{c}{2L}$	L = depth as viewed along radar line of sight

Values of Doppler Shift

Radio frequency f		Doppler Shift f_d (Hz)		
Band	Frequency (GHz)	1 m/s	1 knot	1 mph
L	1	6.67	3.43	2.98
S	3	20.0	10.3	8.94
C	6	40.0	20.5	17.9
X	10	66.7	34.3	29.8
K _u	16	107	54.9	47.7
K _a	35	233	120	104
W	95	633	326	283

Atmospheric Attenuation



Signal Analysis and Processing

Select Fourier Transforms and Properties

Continuous Time	
$x(t)$	$X(f)$
$\begin{cases} A, & -\frac{\tau}{2} \leq t \leq \frac{\tau}{2} \\ 0, & \text{otherwise} \end{cases}$	$A\tau \frac{\sin(\pi f \tau)}{\pi f \tau} \equiv A\tau \text{sinc}(\pi f \tau)$
$\begin{cases} A \cos(2\pi f_0 t), & -\frac{\tau}{2} \leq t \leq \frac{\tau}{2} \\ 0, & \text{otherwise} \end{cases}$	$\frac{A\tau}{2} \text{sinc}[\pi(f - f_0)\tau] + \frac{A\tau}{2} \text{sinc}[\pi(f + f_0)\tau]$
$\sum_{n=-\infty}^{\infty} \delta_D(t - nT)$	$\sum_{k=-\infty}^{\infty} \delta_D(f - k \cdot PRF)$
$AB \frac{\sin(\pi Bt)}{\pi Bt} \equiv AB \text{sinc}(\pi Bt)$	$\begin{cases} A, & -\frac{B}{2} \leq t \leq \frac{B}{2} \\ 0, & \text{otherwise} \end{cases}$
$x(t - t_0)$	$e^{-j2\pi f t_0} X(f)$
$e^{+j2\pi f_0 t} x(t)$	$X(f - f_0)$
Discrete Time	
$x[n]$	$X(\hat{f})$
$Ae^{j2\pi \hat{f}_0 n}, \quad n = 0, \dots, N - 1$	$A \frac{1 - e^{-j2\pi(\hat{f} - \hat{f}_0)N}}{1 - e^{-j2\pi(\hat{f} - \hat{f}_0)}} \equiv NAe^{-j\pi(\hat{f} - \hat{f}_0)(N-1)} \text{asinc}(\hat{f} - \hat{f}_0, N)$
$A\delta[n - n_0]$	$e^{-j2\pi \hat{f} n_0}$
$\sum_{n=-\infty}^{\infty} \delta_D(t - nT)$	$\sum_{k=-\infty}^{\infty} \delta_D(f - k \cdot PRF)$
$A\hat{B} \frac{\sin[\pi \hat{B}n]}{\pi \hat{B}n} \equiv A\hat{B} \text{sinc}[\pi \hat{B}n]$	$\begin{cases} A, & \hat{f} < \hat{B} \\ \hat{B} < \hat{f} < \pi, & \text{otherwise} \end{cases}$
$x[n - n_0]$	$e^{-j2\pi \hat{f} n_0} X(\hat{f})$
$e^{+j2\pi \hat{f}_0 n} x[n]$	$X(\hat{f} - \hat{f}_0)$

Window Properties

Window	3 dB Mainlobe Width, relative to rectangular	Peak Sidelobe (dB)	Sidelobe Rolloff (dB per octave)	SNR Loss (dB)	Maximum Straddle Loss (dB)
Rectangular	1.0	-13.2	6	0	3.92
Hann	1.68	-31.5	18	-1.90	1.33
Hamming	1.50	-41.7	6	-1.44	1.68
Taylor, 35 dB, $\bar{n} = 5$	1.34	-35.2	0/6	-0.93	2.11
Taylor, 50 dB, $\bar{n} = 5$	1.52	-46.9	0/6	-1.49	1.64
Dolph-Chebyshev (50 dB equiripple)	1.54	-50.0	0	-1.54	1.61
Dolph-Chebyshev (70 dB equiripple)	1.78	-70.0	0	-2.21	1.19

Resolution

Dimension	Resolution with Matched Filter	Comments
Range (ΔR)	$\frac{c\tau}{2}$	simple pulse, length τ
	$\frac{c}{2B}$	arbitrary waveform, bandwidth B Hz
Cross-range (ΔCR)	$R\theta_3$	real beam imaging
	$\frac{\lambda R}{2vT_a} = \frac{\lambda R}{2D_{SAR}}$	synthetic aperture imaging v = platform velocity T_a = aperture time D_{SAR} = synthetic aperture size
	$\frac{\lambda}{2\gamma}$	synthetic aperture imaging γ = integration angle

Simplified Probability of Detection Estimates

Nonfluctuating target, Noncoherent integration of N samples (Albersheim's equation)	$P_D = \frac{1}{1 + e^{-B}}, \quad A = \ln\left(\frac{0.62}{P_{FA}}\right),$ $Z = \frac{SNR_{1dB} + 5 \log_{10} N}{6.2 + \sqrt{N + 0.44}}, \quad B = \frac{10^Z - A}{1.7 + 0.12A}$
Swerling 1 Fluctuating Target, No Noncoherent Integration	$P_D = (P_{FA})^{\frac{1}{1+SNR}}$

Miscellaneous Relations

Linear \leftrightarrow dB Scale

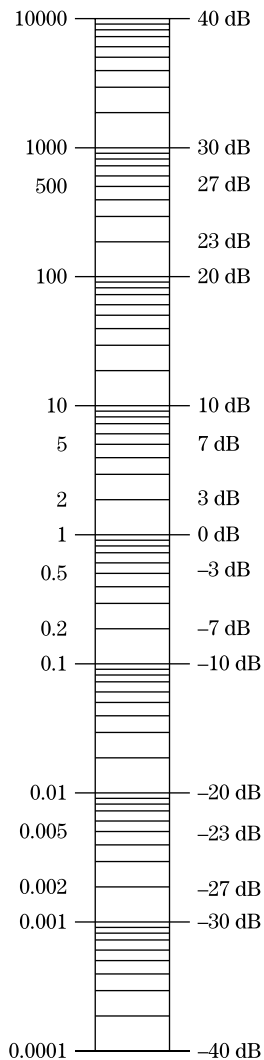


Table of Constants

Constant	Symbol	Value
Speed of light	c	2.99792458×10^8 m/s $\approx 3 \times 10^8$ m/s
Permittivity of free space	ϵ_0	8.85×10^{-12} F/m
Permeability of free space	μ_0	$4\pi \times 10^{-7}$ H/m
Impedance of free space	η	377Ω
Boltzmann's constant	k	1.38×10^{-23} J/K

Subset of AN Nomenclature Applicable to US Radar Systems

First Letter (Type of Installation)		Second Letter (Type of Equipment)		Third Letter (Purpose)	
A	Piloted aircraft	L	Countermeasures	D	Direction finder, reconnaissance, or surveillance
F	Fixed Ground	P	Radar	G	Fire control or searchlight directing
M	Ground, mobile (installed as operating unit in a vehicle which has no function other than transporting the equipment)	Y	Signal/data processing	K	Computing
P	Pack or portable (animal or man)			N	Navigational aids (including altimeter, beacons, compasses, racons, depth sounding, approach, and landing)
S	Water surface craft			Q	Special, or combination of purposes
T	Ground, transportable			R	Receiving, passive detecting
U	Ground utility			S	Detecting or range and bearing, search
V	Ground, vehicular (installed in vehicle designed for functions other than carrying electronic equipment, etc., such as tanks)			Y	Surveillance (search, detect, and multiple target tracking) and control (both fire control and air control)

Supplements and errata available at
www.scitechpub.com/pomr3